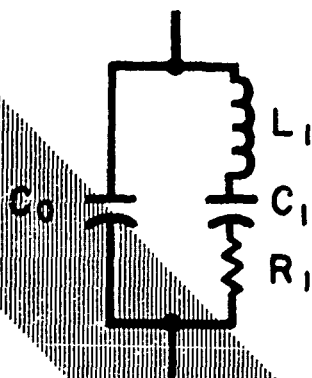
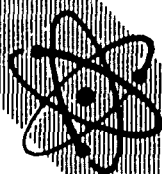
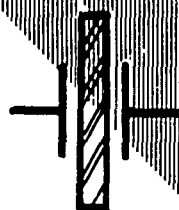


RTM FILE COPY

C

**AD-A213 670 PROCEEDINGS
OF THE
34th ANNUAL SYMPOSIUM ON FREQUENCY CONTROL
1980**



DTIC
ELECTE
S **D**
OCT 20 1989

DISTRIBUTION STATEMENT A

Approved for public release
Distribution Unlimited

28-30 May 1980

**U.S. Army Electronics Research And
Development Command**

89 10 20 247

PROCEEDINGS
of the
THIRTY FOURTH ANNUAL FREQUENCY CONTROL SYMPOSIUM
1980
Sponsored by



U.S. ARMY ELECTRONICS RESEARCH AND DEVELOPMENT COMMAND
Major General Albert N. Stubblebine III
Commanding

ELECTRONICS TECHNOLOGY AND DEVICES LABORATORY
Dr. C. G. Thornton
Director

© Electronic Industries Association 1980
All rights reserved
Printed in U.S.A.

Copies of the Proceedings are available from:

Electronic Industries Association
2001 Eye Street, N.W.
Washington, D.C. 20006

~~PRICE PER COPY \$16.00~~

Accession For	
NTIS CRA&I	<input checked="" type="checkbox"/>
DTIC TAB	<input type="checkbox"/>
Unannounced	<input type="checkbox"/>
Justification	
By <i>ph form 50</i>	
Distribution <i>out of stock</i>	
Availability Codes	
Dist	Avail and/or Special
<i>A-1</i>	

None of the papers contained in the Proceedings may be reproduced in whole or in part, except for the customary brief abstract, without permission of the author, and without due credit to the Symposium.

28-30, MAY 1980

Marriott Hotel
Philadelphia, Pennsylvania

THIRTY-FOURTH ANNUAL FREQUENCY CONTROL SYMPOSIUM

Sponsored By

**U.S. ARMY ELECTRONICS RESEARCH AND DEVELOPMENT COMMAND
ELECTRONICS TECHNOLOGY AND DEVICES LABORATORY**

Fort Monmouth, New Jersey

28-30, MAY 1980
Marriott Hotel
Philadelphia, Pennsylvania

SYMPOSIUM EXECUTIVE COMMITTEE

Chairman
Executive Secretary

Dr. Erich Hafner
Mrs. Lee Hildebrandt

TECHNICAL PROGRAM COMMITTEE

Dr. Erich Hafner — Chairman
U.S. Army Electronics Technology and Devices Laboratory

Mr. E. J. Alexander
Bell Laboratories

Dr. R. Kagiwada
TRW-DSSG

Dr. A. Ballato
U.S. Army, ERADCOM

Mr. A. Kahan
U.S. Air Force, RADC

Dr. J. A. Barnes
National Bureau of Standards

Mr. D. Kemper
Tyco Crystal Products

Mr. M. Bloch
Frequency Electronics, Inc.

Mr. E. Kentley
Roditi, Inc.

Dr. R. Chafin
Sandia Laboratories

Mr. J. A. Kusters
Hewlett-Packard

Mr. A. R. Chi
NASA — Goddard Space Flight Center

Mr. T. Lukaszek
U.S. Army, ERADCOM

Dr. L. T. Claiborne
Texas Instruments

Mr. G. Lussler
Savoy Electronics

Dr. L. S. Cutler
Hewlett-Packard

Dr. T. Meeker
Bell Laboratories

Mr. V. L. Friedrich
Ofc. Asst. Sec'y of the Army (R&D)

Mr. D. Relfel
Motorola, Inc.

Dr. H. Hellwig
Frequency & Time Systems

Mr. S. Schodowski
U.S. Army, ERADCOM

Mr. J. D. Holmbeck
Northern Engineering Laboratories

Dr. E. Staples
Rockwell Science Center

Dr. W. H. Horton
Piezo Technology, Inc.

Dr. J. R. Vig
U.S. Army, ERADCOM

Dr. G. M. R. Winkler
U.S. Naval Observatory

CONTENTS!

CHAIRMEN FOR TECHNICAL SESSIONS

FUNDAMENTAL PROPERTIES OF PIEZOELECTRIC MATERIALS

Dr. J. C. King, Sandia Laboratories

RESONATOR PROCESSING

Mr. D. Reifel, Motorola

CRYSTAL SYNTHESIS AND RADIATION EFFECTS

Mr. J. H. Sherman, Jr., General Electric Company

NOVEL RESONATORS

Dr. E. P. EerNisse, Quartex, Inc.

UHF AND MICROWAVE FREQUENCY GENERATION

Dr. S. Stein, National Bureau of Standards

SURFACE ACOUSTIC WAVE DEVICES

Dr. L. T. Claiborne, Texas Instruments

PRECISION TIMEKEEPING, GENERATION, DISTRIBUTION AND APPLICATION

Dr. L. S. Cutler, Hewlett-Packard

RESONATOR THEORY AND DESIGN

Dr. T. R. Meeker, Bell Telephone Laboratories

QUARTZ CRYSTAL OSCILLATORS

Mr. M. Bloch, Frequency Electronics, Inc.

QUARTZ CRYSTAL SEMINAR

Dr. A. Ballato, USAERADCOM

Fundamental Properties of Piezoelectric Materials

Point Defects in Synthetic Quartz: A Survey of Spectroscopic Results with Application to Quality Assurance

- L. E. Halliburton, M. E. Markes, and J. J. Martin, Oklahoma State University 1

Electrical Conductivity and Dielectric Loss of Quartz Crystals Before and After Irradiation

- A. S. Nowick and H. Jain, Columbia University..... 9

Studies of Micron Order Defects in Quartz by a High Angular Resolved X-Ray Small Angle Scattering Technique

- C. K. Suzuki, University of Tokyo, F. Iwasaki, Kinsekisha Laboratory Ltd., and K. Kohra, National Laboratory for High Energy Physics..... 14

A New Method for Predicting the Temperature Dependence of Elastic Compliance in Simple Proper Ferroelectrics

- L. E. Cross, R. Betsch, H. McKinstry, T. Shrout, The Pennsylvania State University and R. Neurgaonkar, Rockwell International Science Center 25

Resonator Processing

An On-Wafer Detection Method of the Imbalance of Quartz Tuning Fork Resonators

- P.E. Debely and R. J. Dinger, ASULAB..... 34

A Micro-Processor Assisted Baseplating Apparatus with Improved Plateback Distribution

- D. Ang, Tyco Crystal Products 41

Analysis of Quartz Resonator Electrodes Using the Rutherford Backscattering Technique

- G. L. Dybwad, Bell Telephone Laboratories 46

Digital Temperature Control for Ultrastable Quartz Oscillators

- G. Marianneau, J. J. Gagnepain, CNRS..... 52

A New Equivalent Circuit for Piezoelectric Ceramic Disc Resonators

- M. Toki, Y. Tsuzuki and O. Kawano, Yokohama National University 58

Crystal Synthesis and Radiation Effects

Factors Affecting the Quality and Perfection of Hydrothermally Grown Quartz

- J. F. Balascio and N. C. Lias, Motorola, Inc..... 65

Radiation Effects in Quartz Oscillators, Resonators and Materials

- F. Euler, H. G. Lipson and P. A. Ligor, RADC..... 72

The Acoustic Loss Spectrum of 5 MHz 5th Overtone AT-CUT Deuterated Quartz Resonators

- J. J. Martin and S. P. Doherty, Oklahoma State University..... 81

The Temperature Coefficient of Frequency of AT-CUT Resonators Made from Cultured r-Face Quartz

- T. R. Meeker and A. J. Miller, Bell Telephone Laboratories, Inc. 85

Experimental Thermal Behavior of Berlinite Resonators

- J. Detaint, H. Poignant, Y. Toudic, CNET..... 93

Netplane Data for Quartz, Berlinite, LiTaO₃ and LiNbO₃

- E. Knolmayer, Quarzkeramik GmbH..... 102

New Method to Saw Quartz Slides	
- H. Merigoux, J. F. Darces and J. Lamboley, Besancon.....	112
Highly Precise Measurement of Orientation Angle for Crystal Blanks	
- N. Asanuma and J. Asahara, Toyo Communication Equipment Co., Ltd.....	120
<u>Novel Resonators</u>	
New Frequency Temperature Characteristics of Miniaturized GT-CUT Quartz Resonators	
- H. Kawashima, H. Sato and O. Ochiai, Daini Seikosha Co., Ltd.....	131
Frequency Temperature Behavior of Miniaturized Circular Disk-AT-CUT Crystal Resonator	
- Y. Oomura, Tokyo Metropolitan University.....	140
Improving Frequency-Temperature Characteristics of Grooved AT-CUT Plates	
- M. Nakazawa, Shinshu University.....	152
New Type Twin Mode Resonator	
- S. Kogure, E. Momosaki and T. Sonoda, Suwa Seikosha Co., Ltd.....	160
Production Statistics of SC (or TTC) Crystals	
- J. A. Kusters and C. A. Adams, Hewlett Packard Co.....	167
Further Advances on B.V.A. Quartz Resonators	
- R. J. Besson, ENSMM, and U. R. Peier, Oscilloquartz S.A.....	175
Further Developments on 'SC' Cut Crystals	
- B. Goldfrank and A. Warner, Frequency Electronics, Inc.....	183
Fundamental Mode SC-Cut Resonators	
- R. L. Filler and J. R. Vig, USAERADCOM	187
Internal Heating and Thermal Regulation of Bulk Quartz Resonators	
- J. P. Valentin, ENSMM	194
<u>UHF AND MICROWAVE FREQUENCY GENERATION</u>	
An L- and S-Band Radar Exciter Using Agile Low Noise Phase Locked Loop Synthesizers	
- C. Andricos, ITT Gilfillan.....	202
High Speed, Broadband Tuneable Microwave Synthesizer	
- E. M. Perdue, Raytheon Company.....	213
Digital Generation of Wideband Linear FM Waveforms	
- F. W. Hopwood, R. A. Tracy, Westinghouse Electric Corporation.....	217
SAW Stabilized 1680 MHz Microwave Oscillator	
- D. J. Dodson, K. F. Lau, M. Y. Huang, TRW DSSG, and T. J. Lukaszek, USAERADCOM.....	221
Application of Modern Time Series Analysis to High Stability Oscillators	
- B. F. Farrell, E. M. Mattison, and R. F. C. Vessot, Smithsonian Astrophysical Observatory.....	228
UHF Oscillator Using SC Cut Quartz Crystal, with Low Noise Performances and High Long Term Stability	
- C. Pegéot, Quartz et Electronique and G. Sauvage, Adret Electronique.....	233
A Temperature Stable 2 GHz SBAW Delay Line Oscillator	
- K. F. Lau, K. H. Yen, R. S. Kagiwada and A. M. Kong, TRW DSSG.....	237
High Q Bulk Acoustic Resonators for Direct Microwave Oscillator Stabilization	
- R. A. Moore, J. Goodell, A. Zahorchak, R. A. Sundelin, W. Hopwood and T. Haynes, Westinghouse D&E Systems Center, and B.R. McAvoy, J. Murphy, Westinghouse R&D Center.....	243

	<u>Page</u>
Frequency Stable Sources Using Superconducting Microstrip Resonators	
- R. Davidheiser, TRW DSSG	252
<u>Surface Acoustic Wave Devices</u>	
Non-Linear Propagation of Surface Acoustic Waves on Quartz	
- M. Planat, D. Hauden, J. Gros Lambert and J.J. Gagnepain, CNRS.....	255
Theoretical Analysis of Second-Order Effects in Surface-Wave Gratings	
- P. V. Wright and H. A. Haus, Massachusetts Institute of Technology.....	262
Surface Acoustic Wave Resonators with Hermite-Gaussian Transverse Modes	
- F. Pirio and P. Desrousseaux, CNET.....	269
SAW Resonator 2-Pole Filters	
- E. J. Staples, J. Wise, J. S. Schoenwald, and T.C. Lim, Rockwell International Corporation	273
UHF SAW Resonators and Applications	
- W. J. Tanski, Sperry Research Center.....	278
SH-Type Surface Acoustic Waves on Rotated Y-Cut Quartz	
- T. Nishikawa, A. Tani, K. Shirai and C. Takeuchi, Fujitsu Limited.....	286
Analysis of Aging Data on SAW Oscillators	
- T. E. Parker, Raytheon Research Division.....	292
Numerical Analysis of Doubly Rotated Cut SAW Devices	
- D. F. Williams and F. Y. Cho, Motorola Government Electronics Division.....	302
Observations of Effects Induced by Dielectric Coatings on SSBW and SAW Devices	
- C. N. Helmick, Jr. and D. J. White, Naval Weapons Center.....	307
Sensitivities of SAW Oscillators to Temperature, Forces and Pressure: Application to Sensors	
- D. Hauden, S. Rousseau and J. J. Gagnepain, CNRS.....	312
<u>Precision Timekeeping, Generation, Distribution and Application</u>	
Longevity Performance of Cesium Beam Frequency Standards	
- A. C. Johnson, US Naval Observatory, M. M. Force and T. N. Osterdock, Hewlett-Packard Company.....	320
Initial Test Results of USNO GPS Time Transfer Unit	
- K. Putkovich, US Naval Observatory.....	326
Accurate Time and Frequency Transfer During Common-View of a GPS Satellite	
- D. W. Allan and M. A. Weiss, NBS.....	334
Time Related Aspects of the Position Location Reporting System	
- J. E. Lloy, FLRS/TIDS.....	347
Mercury Ion Frequency Standard: Preliminary Results	
- M. Jardino, M. Desaintfuscien, R. Barillet, J. Viennet, P. Petit and C. Audoin, CNRS	353
New Hydrogen Maser Designs	
- H. E. Peters, Sigma Tau Standards Corporation.....	360
An Oscillating Compact Hydrogen	
- H. T. M. Wang, Hughes Research Laboratories.....	364
Results of the Development of the Light Weight Cesium Standard	
- M. Meirs, I. Pascaru and Martin Bloch, Frequency Electronics, Inc.....	370

Possible Avenues of Improvement of the Short and Long Term Stability of Optically Pumped Passive Rubidium Frequency Standards	
- L. G. Bernier, A. Brisson, M. Têtu, J. Y. Savard and J. Vanier, Laval University.....	376
<u>Resonator Theory and Design</u>	
Temperature Induced Frequency Changes in Electroded AT-Cut Quartz Trapped Energy Resonators	
- D. S. Stevens and H. F. Tiersten, Rensselaer Polytechnic Institute.....	384
Transient Thermally Induced Frequency Excursions in Doubly-Rotated Quartz Thickness-Mode Resonators	
- B. K. Sinha, Schlumberger-Doll Research and H. F. Tiersten, Rensselaer Polytechnic Institute.....	393
Nonlinear Effect of Initial Stresses in Doubly-Rotated Crystal Resonator Plates	
- P. C. Y. Lee and K-M Wu, Princeton University.....	403
The Frequency and Motional Capacitance of Partial Contoured Crystal Resonators	
- D. C. L. Vangheluwe, N. V. Phillips' Gloeilampenfabrieken.....	412
Decoupled Families of Contour Modes of Planar Thin Plates	
- C. Bourgeois, Centre Electronique Horloger S.A.....	419
Temperature Dependence of the Force Frequency Effect for the AT-, FC-, SC-, and Rotated X-Cuts	
- E. P. EerNisse, Quartex, Inc.....	426
Subtle Effects in High Stability Vibrators	
- A. Ballato, T. J. Lukaszek and G. J. Iafrate, USAERADCOM.....	431
The Overlapping Ground - A New Monolithic Crystal Filter Configuration	
- J. L. Dailing, Motorola, Inc.....	445
<u>Quartz Crystal Oscillators</u>	
Tactical Miniature Crystal Oscillator	
- H. W. Jackson, Bendix Corporation.....	449
Performance of New Oscillators Designed for "Electrodeless" Crystals	
- R. J. Besson, ENSMM, D. A. Emmons, Frequency and Time Systems, Inc., P. G. Girardet and E. P. Graf, Oscilloquartz S.A.....	457
A Fast Warmup, SC Cut Crystal Oscillator	
- M. Meirs, P. Sheiman, M. Bloch and J. Ho, Frequency Electronics, Inc.....	463
Requirements and Evaluation of the Circuitry, Excluding the Crystal, in Crystal Oscillators	
- B. Parzen, Frequency Electronics, Inc.....	471
Miniature Packaged Crystal Oscillators	
- D. M. Embree, R. E. Paradysz, V. R. Saari, Bell Telephone Laboratories, Inc., R. J. McClure, Western Electric Company.....	475
Direct-Temperature Compensated Crystal Oscillator for Advanced VHF/UHF Radio Communication Systems	
- S. Okano, T. Mitsuoka and T. Ohshima, Toyo Communication Equipment Co., Ltd.....	488
Integrated Circuit Compensation of A.T. Cut Crystal Oscillators	
- T. Keller, D. Marvin, and R. Steele, Motorola Communications Group.....	498
TCXO Error Due to Aging Adjustment	
- W. D. Galla, Isotemp Research, Inc., and E. S. McVey, University of Virginia.....	504
<u>Precision Frequency Control and Selection - A Bibliography, continued</u>	
- E. A. Gerber.....	510

POINT DEFECTS IN SYNTHETIC QUARTZ: A SURVEY OF SPECTROSCOPIC RESULTS

WITH APPLICATION TO QUALITY ASSURANCE

L. E. Halliburton, M. E. Markes, and J. J. Martin
Physics Department, Oklahoma State University
Stillwater, Oklahoma 74078

Summary

The behavior of point defects in commercially available high-quality synthetic quartz is reviewed with special emphasis being put on precision applications where radiation effects are important. Models are presented for the major defects and the modification of quartz as a result of electrodiffusion (sweeping) is described. The present understanding of the fundamental mechanisms leading to the radiation-induced steady state and transient response of quartz-stabilized oscillators is outlined. Finally, a reliable procedure to evaluate the quality of quartz material prior to fabrication of devices is described.

Introduction

Stringent sensitivity and stability requirements for many applications of quartz serve to emphasize the need for systematic, and thus reliable, procedures to evaluate the quality of quartz material prior to fabrication of devices. Accurate screening tests for use in material selection would greatly increase the uniformity and reliability of quartz-containing devices, as well as save time and reduce costs associated with the fabrication processes.

The quality of quartz is, of course, directly related to both the number and type of defects present in the material. In general, defects can be divided into two classes; point defects such as isolated impurities and vacancies and extended defects such as dislocations and inclusions. The point defects in quartz have been studied for over twenty-five years with considerable progress being made. A number of reviews have summarized much of this work.¹⁻⁵ Recently, attention has also been given to investigating the extended defects.⁶⁻¹⁰

In the present paper, we provide detailed spectroscopic data (primarily infrared and electron spin resonance) describing the nature and behavior of specific point defects in quartz and suggest ways in which such techniques can be used as reasonable screening tests for material selection. Our discussion is restricted to high-quality

quartz designed for use in precision applications where radiation effects are important. First, we introduce the models for the various point defects. Then, the electrodiffusion (sweeping) process is described and the radiation damage mechanisms are detailed. Finally, these results are used to discuss the present quartz evaluation procedure and to introduce new, more informative evaluation procedures.

Point Defect Models

Aluminum, lithium, sodium, hydrogen, and iron are among the impurities normally found in quartz. The aluminum substitutes for silicon while the protons and monovalent alkalis enter the quartz lattice as interstitials where they charge compensate the aluminum and other electron-excess defects. All chemical analyses of commercial synthetic quartz have indicated the presence of iron, but electron spin resonance has failed to find evidence either before or after irradiation of isolated Fe^{3+} ions in undoped samples. It is now generally believed that the iron is located in particulate inclusions within the quartz, possibly as particles of acmite ($\text{Na}_2\text{O} \cdot \text{Fe}_2\text{O}_3 \cdot 4\text{SiO}_2$) which have broken loose from the autoclave wall, been transported to the crystal surface, and been enclosed by the growing crystals.¹¹ The acmite is initially formed on the autoclave walls when the mineralizer solution reacts with the steel.¹² Recent results have suggested the particulate inclusions in the quartz are tuhualite, a more complex sodium iron silicate than acmite.⁹

In this section we describe some of the various point defects which have been observed in synthetic quartz.

Compensated Aluminum Centers

Aluminum is found in all synthetic quartz grown using natural quartz as nutrient. The trivalent aluminum ions easily substitute for silicon and thus, require charge compensation (i.e., an aluminum ion needs an additional positive-charged entity in the lattice to compensate for the charge of the replaced silicon). Examples of such charge compensators in quartz are H^+ , Li^+ , or Na^+ ions at interstitial sites or holes trapped at oxygen ions. Because of the strong Coulombic attraction force of the interstitial ions and the holes with the aluminum and because of the high mobility of both the interstitial ions and the holes, these charge compensators are usually lo-

cated adjacent to the substitutional aluminum ions and this gives rise to either Al-OH^- , Al-Li^+ , Al-Na^+ , or $[\text{Al}_{\text{e}+}]^0$ centers. Schematic representations of the compensated aluminum centers are given in Fig. 1. These defect centers can be observed by widely varying experimental techniques; infrared absorption in the case of Al-OH^- centers, acoustic loss in the case of Al-Na^+ centers, and electron spin resonance in the case of $[\text{Al}_{\text{e}+}]^0$ centers.

The Al-OH^- center, shown in Fig. 1a, is formed when an interstitial proton bonds to an oxygen ion, thus forming an OH^- molecule adjacent to a substitutional aluminum. Stretching vibrations of the OH^- molecule lead to infrared absorption and two bands, at 3367 and 3306 cm^{-1} , have been attributed to the Al-OH^- center. The initial observation of these two infrared bands was made by Kats¹³ and additional studies were made by Dodd and Fraser,¹⁴ Brown and Kahan,¹⁵ and Lipson et al.^{16,17} Recently, Sibley et al.¹⁸ found that the relative intensity of the two bands changes with sample treatment; an intense 77 K irradiation destroys the two bands but upon subsequent annealing, they recover with nearly equal intensities up to approximately 200 K while in the $200\text{--}270\text{ K}$ anneal region the 3367 cm^{-1} band continues to grow and the 3306 cm^{-1} band decreases in intensity. This suggests the two bands arise from OH^- molecules in two different but closely related orientations and that a transfer from one orientation to the other occurs in the $200\text{--}270\text{ K}$ region.

Figure 1b shows the Al-M^+ center, where M^+ represents either Li^+ or Na^+ . This type of center consists of an interstitial alkali ion located adjacent to a substitutional aluminum and can give rise to one or more characteristic acoustic loss peaks because of the stress-induced motion of the alkali ion from one equilibrium position to another about the aluminum ion. An acoustic loss peak near 50 K in 5 MHz 5th overtone AT-cut quartz resonators was initially observed by Bümmel et al.^{19,20} and later work by King²¹ and Fraser^{2,22} led to the assignment of this peak to the Al-Na^+ center. Doherty et al.²³ have further characterized the effects of irradiation and electrodiffusion on this 50 K Al-Na^+ acoustic loss peak. The dielectric loss of the Al-Na^+ center has been studied by Stevels and Volger²⁴ and Nowick and co-workers.^{25,26} Much less is known about the Al-Li^+ center; Fraser^{2,22} has suggested a small acoustic loss peak near 105 K is due to the Al-Li^+ center but this must be verified by further experiments.

The much discussed aluminum-hole center (usually written as the $[\text{Al}_{\text{e}+}]^0$ center) consists of a hole trapped in a nonbonding p orbital of an oxygen ion located adjacent to a substitutional aluminum, as shown in Fig. 1c. Formation of the hole (i.e., removal of the electron) leaves an unpaired electron in the oxygen nonbonding p orbital, thus making the $[\text{Al}_{\text{e}+}]^0$ center paramagnetic and easily detectable by electron spin resonance (ESR). The ESR spectrum of the $[\text{Al}_{\text{e}+}]^0$ center, shown in Fig. 2 for the case when the magnetic field is parallel to the crystal c axis, consists of a

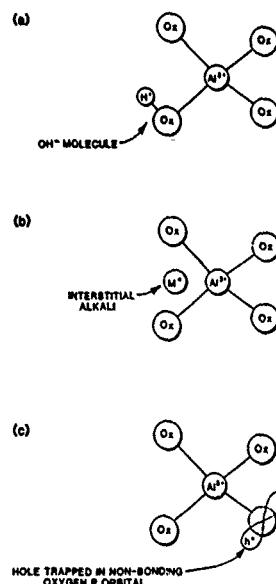


Fig. 1 Schematic representation of (a) the Al-OH^- center, (b) the Al-M^+ center where M^+ is either Li^+ or Na^+ , and (c) the $[\text{Al}_{\text{e}+}]^0$ center.

number of overlapping lines covering a 30 gauss region and centered at $g_c = 2.0183$. This complex ESR spectrum was first observed by Griffiths et al.²⁷ and then immediately explained by O'Brien.²⁸ The four oxygens surrounding a silicon (or aluminum) are only pairwise equivalent, short- and long-bond oxygens, and the ground state of the $[\text{Al}_{\text{e}+}]^0$ center corresponds to localization of the

hole on a short-bond oxygen neighbor. However, Schnadt and Schneider²⁹ have shown that only 0.03 eV of energy is required to transfer the hole from a short-bond to a long-bond oxygen neighboring the aluminum. This means that at room temperature the hole is rapidly jumping among the four oxygens surrounding the aluminum ion. Recently, Markes and Halliburton³⁰ have investigated the production and stabilization conditions for $[\text{Al}_{\text{e}+}]^0$ centers,

Koumvakalis³¹ has correlated the $[\text{Al}_{\text{e}+}]^0$ center ESR spectrum with a visible optical absorption, and Martin and Doherty³² have suggested that acoustic loss peaks at 25 K and 100 K and a broad loss over the $125\text{--}160\text{ K}$ range in 5 MHz 5th overtone AT-cut resonators is due to the $[\text{Al}_{\text{e}+}]^0$ center. King³³

had earlier attributed the 100 K loss peak and the broad loss from $125\text{--}160\text{ K}$ to the $[\text{Al}_{\text{e}+}]^0$ center.

The comprehensive review by Weil³ summarizes much additional work on the aluminum-associated hole centers in quartz.

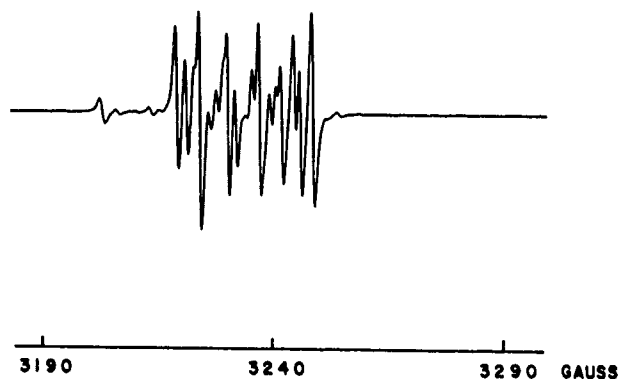


Fig. 2 ESR spectrum of the $[Al_e^+]^0$ center taken at 77 K and 9.13 GHz with the magnetic field parallel to the crystal's c axis

Hydrogen Atoms

When quartz is irradiated near 77 K, hydrogen atoms are formed. These centers were initially reported by Weeks and Abraham³⁴ and a later, more detailed, investigation was made by Perlson and Weil.³⁵ Presumably the radiation leads to dissociation of OH^- molecules followed by displacement of the hydrogen to an isolated interstitial site where it becomes stably trapped. Because of its single unpaired electron, the hydrogen atom is paramagnetic and its c-axis ESR spectrum consists of a doublet exhibiting a characteristic hyperfine splitting of 520 gauss. The ESR linewidths are extremely narrow, approximately 0.05 gauss, and the spectrum is easily saturated with microwave power because of a very long spin-lattice relaxation time. The hydrogen atoms thermally decay near 125 K.

Oxygen Vacancy Centers

Another class of point defects which has been extensively investigated in quartz is the oxygen vacancy centers, better known as the E^- -type centers. The simplest of these defects, the E_1 center, consists of an oxygen vacancy and a single unpaired electron. This electron is localized on only one of the neighboring silicons in an sp^3 hybrid orbital extending into the vacancy. Weeks³⁶ first observed the ESR spectrum of the E_1 center. This work was later extended by Silsbee.³⁷ Nelson and Weeks³⁸ and Arnold³⁹ examined the ultraviolet optical absorption of samples containing E_1 centers. The excellent theoretical work of Feigl, Fowler, and Yip^{40,41} has provided insight to the electronic and ionic structure of the E_1 center. They explain the localization of the unpaired electron on only one silicon in terms of an asymmetrical lattice relaxation of the two silicons adjoining the vacancy. Two additional

E^- -type centers, the E_2 and E_4 centers, have been investigated. The E_2 center, first discovered by Weeks,⁴² and the E_4 center, reported by Weeks and Nelson,⁴³ both exhibit a proton hyperfine splitting. In the case of the E_4 center, four hyperfine lines are observed in the ESR spectra but data taken at 9 and 20 GHz by Halliburton et al.⁴⁴ clearly show that two of the four lines are "forbidden" transitions and that the hyperfine interaction actually is with an $I = 1/2$ nucleus. Isoya et al.⁴⁵ using the GAUSSIAN 70 quantum chemistry computer program, have shown that the model for the E_4 center consists basically of an H^- ion trapped in the oxygen vacancy with an unpaired electron in the sp^3 hybrid orbital on one of the adjoining silicons. A definitive model for the E_2 center has not yet been presented.

Thermal Annealing Behavior

Figure 3 shows ESR data taken during a pulsed thermal anneal experiment on an as-received Premium Q sample which had first been irradiated (1.5 MeV electrons, 3×10^6 rads) at 300 K and then at 77 K. Data points were taken approximately 25 degrees apart and were obtained by holding the sample at the given temperature for five minutes then cooling to 90 K where the ESR spectrum of each center was monitored.

The $[Al_e^+]^0$ (aluminum-hole) center has three thermal decay stages, at 125-130 K, 430-440 K, and 540-550 K. The first $[Al_e^+]^0$ center decay step, at 125-130 K, correlates directly with the decay of the hydrogen atom. The second $[Al_e^+]^0$ center decay step, at 430-440 K, correlates with the decay of the E_2 and E_4 centers. However, absolute concentration measurements indicate there are too few E_2 and E_4 centers to account for the observed decrease in $[Al_e^+]^0$ centers at this temperature and thus, there must be one or more additional defects which are active in this 430-440 K region. Also, the formation of the E_2 and E_4 centers is not clear and is not shown in Fig. 3. Because of strongly overlapping ESR lines from other unidentified defects, it could not be determined if the E_2 and E_4 centers were produced by the 77 K irradiation or whether they appeared as a result of the hydrogen atom anneal. The third $[Al_e^+]^0$ center decay step, at 540-550 K, correlates with a growth of the E_1 center. Again, the increase in concentration of the E_1 centers is not sufficient to account for the decrease in the $[Al_e^+]^0$ centers. Finally, the E_1 centers thermally decay over the 600-675 K range.

Electrodiffusion (Sweeping)

Quartz has large c-axis channels along which interstitial ions can migrate. King,²¹ making use of this characteristic of quartz, developed the electrodiffusion (sweeping) process as a method for changing the concentration of specific interstitial cations (i.e., H^+ , Li^+ , Na^+ , etc.) within a given quartz crystal.

This sweeping technique consists of applying

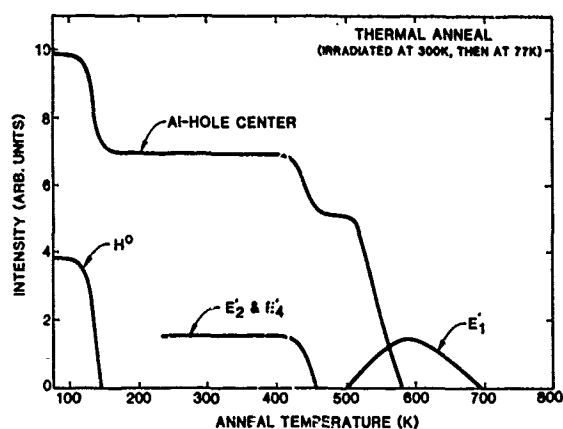


Fig. 3 Pulsed thermal anneal of as-received Premium Q sample after irradiation at 300 K and then 77 K.

an electric field parallel to the c-axis of the crystal while maintaining the sample temperature in the 400-550°C range. Either a vacuum or an inert gas, air, or hydrogen atmosphere surrounds the crystal. As positive-charged species are pulled along the large c-axis channels and out of the crystal by the electric field, additional positive-charged species of a similar or different nature are taken into the crystal at the opposite electrode in order to maintain charge neutrality for the sample as a whole. For example, if either air or a hydrogen atmosphere surrounds the crystal, the sweeping process will remove interstitial alkali ions from the crystal and replace them with H^+ ions. The removal of interstitial Na^+ ions by sweeping in a hydrogen atmosphere is illustrated in Fig. 4. In this case, the resonator itself was swept after obtaining the as-received data. The 50 K acoustic loss peak due to the $Al-Na^+$ center, initially present, is effectively eliminated by the sweeping. Figure 5 shows that as the interstitial alkali ions are removed by sweeping in a hydrogen atmosphere, protons are entering the crystal. After sweeping, the initial infrared absorption peaks are unchanged but the two bands at 3367 and 3306 cm^{-1} , due to the $Al-OH^-$ centers, have increased significantly.

Numerous cases exist in the literature where the sweeping process has greatly helped in clarifying the behavior of point defects in quartz. 13,22,23,20,46,47

Radiation Response Mechanisms

Ionizing radiations (i.e., x-rays and gamma rays as well as high energy electrons and protons) create large numbers of uncorrelated electron-hole pairs in quartz. Such behavior is important in all

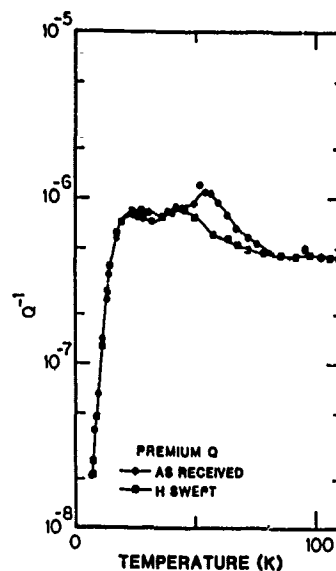


Fig. 4 Acoustic loss (Q^{-1}) versus temperature for a 5 MHz 5th overtone AT-cut resonator before and after sweeping in a hydrogen atmosphere.

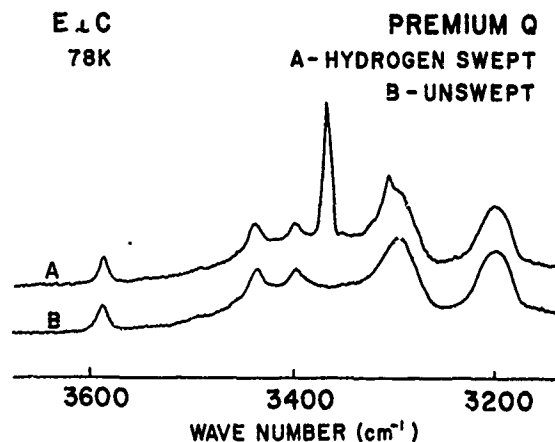


Fig. 5 Infrared absorption spectra taken at 78 K of a Premium Q sample before (B) and after (A) sweeping in a hydrogen atmosphere.

insulator materials, but it is especially crucial in quartz because it leads to clearly observable effects in the behavior of interstitial cations and has major ramifications with regard to quartz device operation. If the recombination of a radiation-induced electron and hole occurs at or very near an interstitial monovalent cation, the energy given up by the recombining electron and hole may be used to free the interstitial from its trapping site. Thus, energy that was initially carried by the irradiating photon or particle is at least partially transferred, via the intermediate formation of the electron-hole pairs, to kinetic energy of the interstitial cations. Questions concerning the valence state of the interstitial during the induced motion are unanswered at this time and details of the dissociation mechanisms of the interstitial and its trapping entity are still not clear. As a result, considerable study of the fundamental radiolysis (photochemical) processes in quartz must be done in the years to come.

As an example of radiation-induced mobility of interstitials, Fig. 6 shows the infrared absorption of an Electronic Grade sample in the as-received state and after an electron irradiation at 300 K. The infrared peaks initially present have decreased as a result of the irradiation while two bands have increased. This shows that protons trapped at sites giving rise to the infrared bands at 3585, 3440, and 3400 cm^{-1} have moved over to aluminum sites where they give rise to bands at 3367 and 3306 cm^{-1} . Additional experiments by Sibley et al.¹⁸ and Markes and Halliburton³⁰ have shown that movement of the protons can be induced by radiation at temperatures as low as 10 K.

In contrast to the behavior of hydrogen under

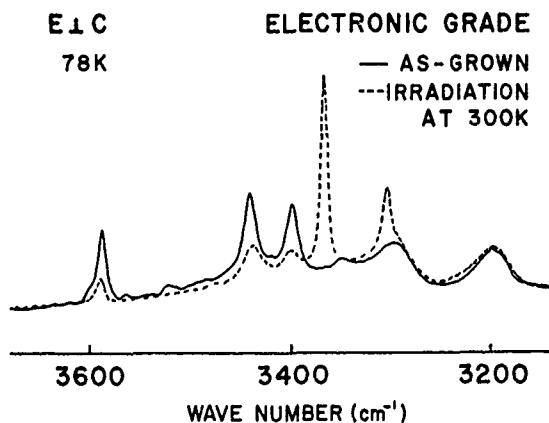


Fig. 6 Infrared absorption of an Electronic Grade sample before and after electron irradiation.

irradiation, the interstitial alkalis can not be induced to move at all temperatures. Markes and Halliburton³⁰ have shown that the onset of radiation-induced mobility of the alkali interstitials occurs at approximately 200 K. Below this temperature, the interstitial is in the form of Al-M^+ centers and is unaffected by radiation while above this temperature, the radiation dissociates the Al-M^+ center and allows Al-OH^- and $[\text{Al}_{\text{e}}^+]^0$

centers to be formed. After removal from the aluminum ion, the interstitial alkali ion becomes trapped at an unknown site in the crystal. Heating the crystal to the 400-500°C region causes the interstitial alkali ions to return to the aluminum ions and, thus, restores the crystal to its pre-irradiated state. Of course, in hydrogen-swept crystals, the interstitial alkali ions have already been removed and no effects due to alkali mobility are observed.

Quartz-stabilized oscillators exposed to ionizing radiation may exhibit transient and steady-state changes in frequency and Q. Figure 7

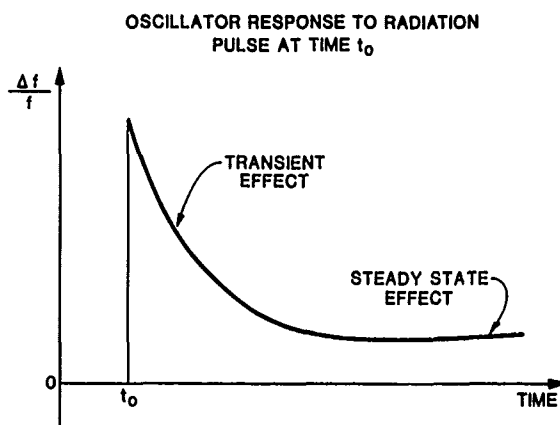


Fig. 7 Simplified representation of the response of a quartz-stabilized oscillator to a short pulse of radiation at time t_0 .

shows, in a greatly simplified fashion, the response of a quartz oscillator to a short pulse of radiation at time t_0 . The oscillator will experience a transient offset which usually decays within seconds to a smaller steady-state offset (usually negative). In severe cases, the oscillator will stop until the transient decreases sufficiently to allow oscillation to resume.

If precautions have been taken in oscillator design, then interstitial ions become the major cause of radiation effects. For irradiations at or above room temperature, both hydrogen and alkali

interstitials will be displaced. The hydrogen, initially in the form of Al-OH^- centers, is moved out into the lattice during irradiation, but because there are no other stable trapping sites it quickly returns to the aluminum. While the hydrogen is gone from the aluminum site, a hole will become trapped as an $[\text{Al}_e^+]^0$ center and the

acoustic loss of the sample will change. King and Sander³³ have proposed that the radiation-induced transient oscillator frequency changes result from this transient motion of the hydrogen away from and then back to the aluminum site. Interstitial alkali ions, initially in the form of Al-M^+ centers, are also displaced from the aluminum during irradiation at or above room temperature. However, the interstitial alkali ions become trapped at sites not yet identified and there are no transient effects. Aluminum-hole centers are stably formed as the alkalis are removed from the aluminum ion and this will change the acoustic loss of the sample in a steady-state manner. Thus, we believe the hydrogen plays a crucial role in the transient response of oscillators while the alkalis are important in the steady-state response to radiation.

Quality Assurance Procedures

As can be seen from the previous section, impurities in quartz have a direct effect on device performance in a radiation environment. Aluminum is the key impurity since its need for charge compensation leads to the introduction of the positive interstitial cations. Efforts to reduce the aluminum content and related interstitial content should lead to more radiation-hardened devices.

Commercial quartz growers have responded to the various needs of the industry by offering several grades of material. For example, Sawyer produces Electronic Grade, Premium Q, and Optical Grade. Infrared absorption spectra taken at 78 K from an Electronic Grade sample and a Premium Q sample are shown in Fig. 8. The two bands at 3300 and 3200 cm^{-1} are intrinsic and must be the same intensity in both samples. The remaining bands at 3585, 3440, and 3400 cm^{-1} are much smaller in the Premium Q than in the Electronic Grade material.

At the present time, the commercial growers use a room temperature infrared test to determine in which category a quartz bar should be placed. This test compares the infrared absorption at 3500 cm^{-1} with that at 3900 cm^{-1} and the difference is used to predict the Q of the material.⁴⁸ Essentially, this infrared test provides a rough measure of the OH^- content of the crystal and, since the concentration of other impurities appears to scale with the OH^- , the test provides a good initial screen of quartz quality. However, for precision applications, additional information can be obtained from the infrared absorption if the data are obtained at liquid nitrogen temperature and a scan from 3700 to 3200 cm^{-1} is made. Figure 9 compares the infrared absorption from an Electronic Grade sample at 78 K and 300 K. Two of the bands, at 3440 and 3400 cm^{-1} , are extremely sensitive to the observation temperature.

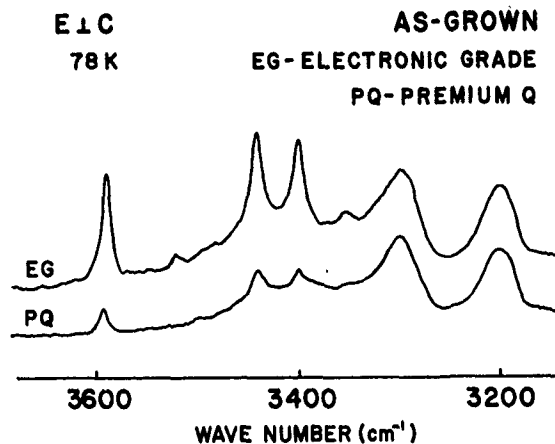


Fig. 8 Comparison of the infrared absorption of an Electronic Grade and Premium Q sample.

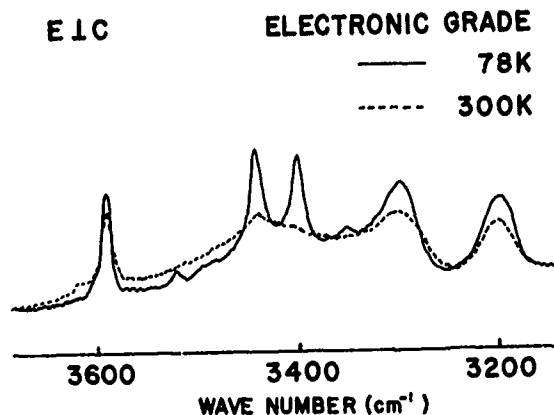


Fig. 9 Infrared absorption of an Electronic Grade sample taken at 78 K and 300 K.

In the course of our investigations, we have surveyed a number of samples for aluminum content using the electron spin resonance technique. The results for ten Premium Q samples are given in Fig. 10. Each vertical bar represents a different sample and the aluminum content varies from less than 1 ppm (Si) to near 15 ppm. From this, it is easy to understand the large variations that have been found in the radiation response of quartz

oscillators.

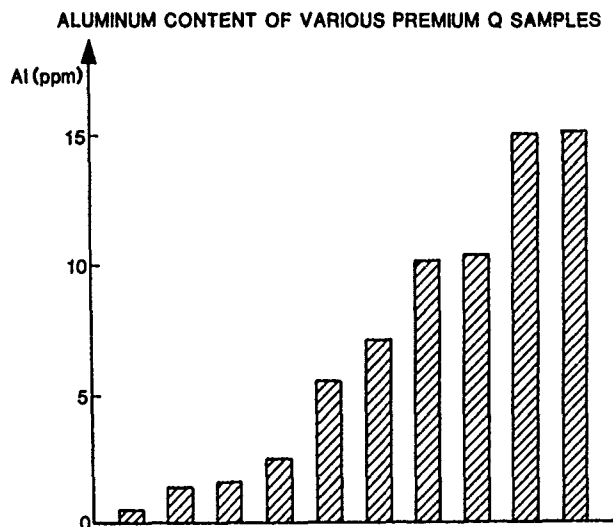


Fig. 10 Aluminum content of ten randomly selected Premium Q samples as determined by electron spin resonance.

We propose that quartz which is to be used in precision oscillators for radiation environments be evaluated by electron spin resonance to determine the aluminum content. An ESR test developed by Markes and Halliburton³⁰ not only gives the aluminum content but also determines the effectiveness of any sweeping previously performed on the bar. This ESR test consists of subjecting a sample to three irradiations; the first at 77 K, the second at room temperature, and the third at 77 K. After each of the 77 K irradiations, the $[Al_{e+}]^0$ center ESR spectrum is taken. The intensity of the $[Al_{e+}]^0$ center spectrum after the third irradiation is a direct measure of the aluminum content and the ratio of the intensities of the $[Al_{e+}]^0$ center spectra after the first and third irradiations is a measure of the effectiveness of any previous sweeping. This ratio indicates the percentage of alkalis that were removed from the crystal by the sweeping. Figure 11 shows the application of this ESR test to an unswept and a swept sample, both cut from the same initial bar. The unswept sample, shown on the left of Fig. 11, shows a dramatic increase in the $[Al_{e+}]^0$ center spectrum from the first to the second 77 K irradiation. The two irradiations give nearly identical spectra for the swept sample, shown on the right side of Fig. 11, indicating that it is 100% swept.

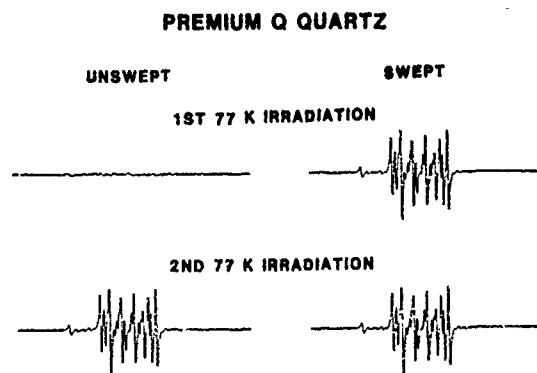


Fig. 11 Example of the ESR evaluation test applied to an unswept and a swept quartz sample.

References

1. E. Iell, N.J. Kreidl, and J.R. Hensler, *Progress in Ceramic Science*, Vol. 4, edited by J.E. Burke (Pergamon Press, Oxford, 1966) pp. 1-93.
2. D.B. Fraser, *Physical Acoustics*, Vol. 5, edited by W.P. Mason (Academic Press, New York, 1968) pp. 59-110.
3. J.A. Weil, *Radiation Effects* **26**, 261 (1975).
4. A. Kahan, presentation at NBS Seminar on Time and Frequency: Standards, Measurements, Usage, Boulder, Colorado, August 25, 1977.
5. D.L. Griscom, *Proceedings of the 33rd Annual Symposium on Frequency Control*, June 1979, pp. 98-109.
6. J. Yoshimura and K. Kohra, *J. Cryst. Growth* **33**, 311 (1976).
7. F. Iwasaki, *J. Cryst. Growth* **39**, 291 (1977).
8. K. Moriya and T. Ogawa, *J. Cryst. Growth* **44**, 53 (1978).
9. R.L. Barns, P.E. Freeland, E.D. Kolb, R.A. Laudise, and J.R. Patel, *J. Cryst. Growth* **43**, 676 (1978).
10. K. Moriya and T. Ogawa, *Philos. Mag. A* **41**, 191 (1980).

11. Technical Brief No. 3, Sawyer Research Products, 35400 Lakeland Blvd., Eastlake, OH 44094
12. R.A. Laudise, The Growth of Single Crystals (Prentice-Hall, Inc., New Jersey, 1970).
13. A. Kats, Phillips Res. Rep. 17, 133 (1962).
14. D.M. Dodd and D.B. Fraser, J. Phys. Chem. Solids 26, 673 (1965).
15. R.N. Brown and A. Kahan, J. Phys. Chem. Solids 36, 467 (1975).
16. H.G. Lipson, F. Euler, and A.F. Armington, Proceedings of the 32nd Annual Symposium on Frequency Control, 11 (1978). Copies available from the Electronic Industries Association, 2001 Eye Street, N.W., Washington, D.C. 20006.
17. H.G. Lipson, F. Euler, and P.A. Ligor, Proceedings of the 33rd Annual Symposium on Frequency Control, 122 (1979). Copies available from the Electronic Industries Association, 2001 Eye Street, N.W., Washington, D.C. 20006.
18. W.A. Sibley, J.J. Martin, M.C. Wintersgill, and J.D. Brown, J. Appl. Phys. 50, 5449 (1979).
19. H.E. Bommel, W.P. Mason, and A.W. Warner, Phys. Rev. 99, 1894 (1955).
20. H.E. Bommel, W.P. Mason, and A. W. Warner, Phys. Rev. 102, 64 (1956).
21. J.C. King, Bell System Technical Journal 38, 573 (1959).
22. D.B. Fraser, J. Appl. Phys. 35, 3913 (1964).
23. S.P. Doherty, J.J. Martin, A.F. Armington, and R.N. Brown, J. Appl. Phys. (in press).
24. J.M. Stevels and J. Volger, Phillips Res. Repts. 17, 283 (1962).
25. A.S. Nowick and M.W. Stanley, J. Appl. Phys. 40, 4995 (1969).
26. D.S. Park and A.S. Nowick, Phys. Stat. Sol.(a) 26, 617 (1974).
27. J.H.E. Griffiths, J. Owen, and I.M. Ward, Report of the Bristol Conference - Defects in Crystalline Solids (The Physical Society, London, 1955) p. 81.
28. M.C.M. O'Brien, Proc. Roy. Soc. (London) A231, 404 (1955).
29. R. Schnadt and J. Schneider, Phys. kondens. Materie 11, 19 (1970).
30. M.E. Markes and L.E. Halliburton, J. Appl. Phys. 50, 8172 (1979).
31. N. Koumvakalis (unpublished).
32. J.J. Martin and S.P. Doherty, Proceedings of the 34th Annual Symposium on Frequency Control, Philadelphia, May, 1980.
33. J.C. King and H.H. Sander, IEEE Trans. Nucl. Sci. NS-19, 23 (1972).
34. R.A. Weeks and M. Abraham, J. Chem. Phys. 42, 68 (1965).
35. B.D. Perlson and J.A. Weil, J. Magn. Res. 15, 594 (1974).
36. R.A. Weeks, J. Appl. Phys. 27, 1376 (1956).
37. R.H. Silsbee, J. Appl. Phys. 32, 1459 (1961).
38. C.M. Nelson and R.A. Weeks, J. Am. Ceram. Soc. 43, 396 (1960).
39. G.W. Arnold, Phys. Rev. 139, A1234 (1965).
40. F.J. Feigl, W.B. Fowler, and K.L. Yip, Solid State Commun. 14, 225 (1974).
41. K.L. Yip and W.B. Fowler, Phys. Rev. B 11, 2327 (1975).
42. R.A. Weeks, Phys. Rev. 130, 570 (1963).
43. R.A. Weeks and C.M. Nelson, J. Am. Ceram. Soc. 43, 399 (1960).
44. L.E. Halliburton, B.D. Perlson, R.A. Weeks, J.A. Weil, and M.C. Wintersgill, Solid State Commun. 30, 575 (1979).
45. J. Isoya, J.A. Weil, L.E. Halliburton (unpublished).
46. J.H. Mackey, Jr., J. Chem. Phys. 39, 74 (1963).
47. J.H. Mackey, J.W. Boss, and D.E. Wood, J. Magn. Res. 3, 44 (1970).
48. B. Sawyer, IEEE Trans. Sonics and Ultrasonics SU-19, 41 (1972).

Acknowledgements

This work supported by the U. S. Air Force and monitored by Dr. Alton F. Armington, Hanscom AFB, Boston, Mass.

ELECTRICAL CONDUCTIVITY AND DIELECTRIC LOSS OF QUARTZ CRYSTALS BEFORE AND AFTER IRRADIATION

A. S. Nowick and H. Jain*

Henry Krumb School of Mines
Columbia University
New York, New York 10027

Summary

Dielectric relaxation and electrical conductivity measurements have been used to study defects of the type which may be responsible for frequency changes in quartz crystals, viz., Al-M pairs, where M denotes an interstitial alkali ion. For the Al-Na defect two dielectric and two corresponding anelastic peaks have been well established. The existence of analogous peaks for Al-Li is not as clear.

Electrical conductivity is believed to be due to the migration of dissociated M^+ ions down c-axis channels of the crystal. The conductivity of natural and several synthetic crystals is studied, both in the unirradiated state and following exposure to X-rays or γ -rays. Room-temperature irradiation is shown to produce a greatly enhanced conductivity attributed to the freeing of alkali ions from bound pairs. Appropriate activation energies and pre-exponential quantities for both irradiated and unirradiated samples are analyzed. There are striking differences between the natural and synthetic crystals. The results for the synthetic crystals are interpreted in terms of the Al-M pair and its dissociation. In the case of the natural crystals, however, the quantitative aspects of the interpretation remain unresolved.

Introduction

The defect in α -quartz consisting of an Al^{3+} ion substituting for Si^{4+} together with a nearby charge-compensating monovalent ion, M^+ , has been widely recognized as an important contributor to resonator frequency instability, especially under irradiation.¹ One of the most direct ways to study this defect is through electrical measurements. In particular, the associated Al-M pair can give rise to dielectric relaxation phenomena, while the dissociation of the pair leads to the presence of interstitial M^+ ions which constitute, perhaps, the principal source of electrical conductivity in such crystals. The present paper is concerned with the use of these two types of electrical measurements to attempt to learn more about these basic defects, and as a tool to better characterize quartz crystals.

*Now at Argonne National Laboratory.

Dielectric Relaxation

If a defect pair in a crystal possesses more than one equivalent orientation, the application of an electric field can split the energy levels of these orientations so that certain orientations will be preferred over others. If sufficient time is allowed, reorientation will then occur so as to increase the relative occupancy of the preferred orientations. For an alternating electric field, this gives rise to an electric displacement that lags behind the field by an angle δ given by the well-known Debye equation

$$\tan \delta = (\Delta\epsilon/\epsilon)\omega\tau/(1 + \omega^2\tau^2) \quad (1)$$

where ω is the circular frequency, ϵ the dielectric constant, $\Delta\epsilon$ the "relaxation of ϵ " which measures the magnitude of the effect, and τ is the "relaxation time".² Eq. (1) takes the form of a symmetric peak ("Debye peak") in a plot of $\tan \delta$ versus $\log \omega\tau$. Since the relaxation time, τ , often results from an activated atomic process it may be expected to take the form

$$\tau = \tau_0 \exp(E_p/kT) \quad (2)$$

where E_p is the activation energy for relaxation and kT has its usual meaning. Accordingly, the relaxation phenomenon can be observed as a symmetric peak of $\tan \delta$ versus $1/T$ at a fixed frequency (i.e., varying τ instead of ω , by varying the temperature).

In an analogous way, the same defect can give rise to anelastic relaxation peaks of the Debye form under an alternating applied stress.³ Further, a change in the magnitude of such a peak will produce a corresponding resonant frequency shift at all temperatures above that of the peak.^{1,3}

In a classic study of dielectric relaxation in quartz, Stevels and Volger⁴ observed a number of such loss peaks, (in the direction parallel to the crystalline c-axis) over a wide range of temperatures and conditions. Most importantly, they established that a particular pair of low-temperature peaks, whose heights always occurred in a fixed ratio, were due to the presence of both Al and Na. These peaks, which were observed at 38 and 95°K at a frequency of 32 kHz, were attributed by these authors to the Al-Na pair. Figure 1 shows an illustration of these peaks.⁵ They occur at slightly lower temperatures since the frequency,

in this case, is 2 kHz. (There are also two additional peaks at higher temperatures whose origin is not yet established). The height of either of the Al-Na peaks is directly proportional to the concentration of these defects and, therefore, can be used as an analytical technique.

It is appropriate to ask why a particular defect pair should produce two peaks instead of just one. The answer is that two peaks result when the pair can exist in two non-equivalent states, say a nearest and next-nearest neighbor (nn and nnn) configuration.²⁻⁴ Nowick and Stanley⁶ and Park and Nowick⁵ have developed a rather explicit model to explain the details of the two Al-Na peaks. In this model, the lower peak is due to a flip-flop motion between the two equivalent nn Na sites on a given AlO₄ distorted tetrahedron, while the upper peak involves relaxation of the nnn defect. Locations of the Na in relation to the four O²⁻ ions of the distorted tetrahedron are proposed, both for the nn and nnn configurations.

An analogous pair of peaks has also been found in anelastic relaxation,^{7,8} as summarized in Table I. Because of the higher frequency employed (5 MHz) these peaks occur at a higher temperature than the dielectric peaks; however, when the corresponding activation energies (E_r) are calculated excellent agreement is found, thus supporting the claim that the two types of peaks have the same origin.

For other alkalis (Li⁺ and K⁺, in particular), Stevels and Volger⁴ report dielectric loss peaks, but only a single one for each alkali. These, and possible corresponding anelastic peaks^{7,8} are also listed in Table I. For the Li Peak, the E_r values do not agree well; in addition, the anelastic peak is rather broad. We conclude that there is a need for further study before these dielectric and anelastic peaks can be used to identify the Al-Li defect with the same confidence with which we now can identify the Al-Na pair.

TABLE I. SUMMARY OF DATA ON ANELASTIC AND DIELECTRIC LOSS PEAKS, GIVING FREQUENCY, PEAK TEMPERATURE (T_p), ACTIVATION ENERGY AND PROPOSED ALKALI ION.

Type	Freq. (MHz)	T_p (°K)	E_r (eV)	M ⁺ ion
Die1.	.03	38	.062	Na
	.03	95	.154	Na
Anel.	5	50	.059	Na
	5	135	.160	Na
Die1.	.03	60	.097	Li
Anel.	5	105	.125	Li
Die1.	.03	140	.227	K
Anel.	5	208	.246	K

Electrical Conductivity

Background

Because of the very large band gap (~ 9 eV) of crystalline quartz,⁹ the electrical conductivity of

an unirradiated crystal may be expected to be totally ionic. In terms of the Al-M defect model, conductivity is most reasonably attributed to M⁺ interstitials that have dissociated and are migrating freely down the open c-axis (i.e., Z-axis) channels of the crystal. Because of the structure of quartz, one would then expect a high degree of anisotropy, with the conductivity measured perpendicular to the c-axis being much lower than that parallel to this axis. Such anisotropy has indeed been observed.¹⁰ In the present paper, we will concern ourselves primarily with the conductivity along the c-axis.

The expression for the conductivity, σ , is

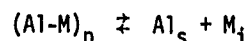
$$\sigma = n_i e \mu_i = c_i N_0 e \mu_i \quad (3)$$

where n_i and c_i denote the concentration of free interstitial ions (in number/vol. and mole fraction, respectively), μ_i is the mobility of these ions, e the electronic charge and N_0 the concentration of Si atoms in the crystal. The mobility μ_i is given by¹¹

$$\mu_i = (ed^2/kT)\Gamma_i = (ed^2/kT)v_0' \exp(-E_m/kT) \quad (4)$$

where d is the jump distance, Γ_i the jump frequency, v_0' the oscillation frequency (including the activation entropy term) and E_m the activation energy for the elementary interstitial migration step.

The quantity c_i is controlled by the dissociation equilibrium of the pair:



where Al_s refers to the isolated substitutional Al³⁺ ion. Since Al_s and M_i are formed together, their concentrations may be taken as equal. Thus, the corresponding mass-action equation for the above equilibrium is

$$c_i^2/c_p = \frac{1}{2} \exp(-E_A/kT) \quad (5)$$

c_p being the concentrations of pairs and E_A the association energy of the pair, and the factor $\frac{1}{2}$ occurs because the pair has two equivalent orientations. Anticipating almost complete association in the range of the experiments, we set $c_p \approx c_t$, the total mole fraction of Al in the crystal. Thus,

$$c_i = (c_t/2)^{1/2} \exp(-E_A/2kT) \quad (6)$$

Inserting Eqs. (6) and (4) into (3) gives the standard form for the dependence of σ on T :

$$\sigma T = A \exp(-E_\sigma/kT) \quad (7)$$

in which the activation energy, E_σ , is given by

$$E_\sigma = E_m + \frac{1}{2}E_A \quad (8)$$

and the pre-exponential factor by

$$A = (c_t/2)^{1/2} N_0 e^2 v_0' d^2 / k \quad (9)$$

Eq. (7) suggests that, one should plot $\log \sigma T$ versus $1/T$, and obtain E_σ from the slope and A from

the intercept. It is important to note that once c_t is known, all quantities in the expression for A are known. (There is some uncertainty in the term v_0^1 , which is expected to be $\sim 3 \times 10^{13} \text{sec}^{-1}$ to within a factor ~ 3 .)

The above theory must be applied with caution, since it is based on only one type of defect pair and its dissociation equilibrium. It is well recognized that quartz crystals often contain other defects, particularly hydrogen at various types of sites.^{12,13}

In the literature there is much electrical data for quartz based on d.c. measurements or a.c. measurements at a fixed frequency.¹⁰ Such results can be complicated by secondary processes such as space charge formation, electrode processes, etc. In the present work, we have used a.c. bridge measurements over a wide range of frequencies with complex-impedance analysis.¹⁴ In this way, it is possible to separate out extraneous effects from the true lattice conductivity process. Details will be presented elsewhere.¹⁵

Results on Unirradiated Crystals

A high quality natural crystal from Arkansas and three synthetic crystals were studied. The latter include one Electronic Grade and one Premium Q Grade from Sawyer Research Products, as well as a small crystal (denoted S4) grown several years earlier by Sawyer at a moderately rapid rate. The results, in Fig. 2, show a striking difference between the natural crystal and the three synthetics, in that the natural one has a much higher conductivity and a lower E_σ . (Such a difference between natural and synthetic crystals has already been reported.¹⁶) On the other hand, differences among the three synthetics are surprisingly small. For comparison, we present below the activation energies and pre-exponentials for the Premium Q synthetic and the natural crystal:

TABLE II. SOME RESULTS OF CONDUCTIVITY EXPERIMENTS.

	$E_\sigma(\text{eV})$	$A(^{\circ}\text{K}/\Omega\text{-cm})$
Prem. Q	1.33	1.1×10^6
Natural	0.82	2.2×10^4

In addition, hydrogen sweeping (under a high d.c. field and high temperature) was carried out for several of the samples; the effect was always to reduce σ by about a factor of 10, but leaving the slope almost unchanged. This suggests that H^+ is more tightly bound than alkali ions and does not contribute appreciably to the conductivity so long as some alkali remains.

It is important to examine the pre-exponential factor closely. Eq. (9) gives a complete expression for A in which all quantities are known except for c_t . For the Premium Q crystal, ESR studies following irradiation (in which Al-hole centers are generated)¹⁷ show that, for this material,

$c_t \approx 6 \text{ ppm}$. Substituting into Eq. (9) gives $A \approx 1.5 \times 10^3 ^{\circ}\text{K}/\Omega\text{-cm}$. On the other hand, the experimental value of A (Table II) is about 10^3 times larger than this calculated value. There is no way to reconcile this discrepancy without a significant change in the assumptions on which Eq. (9) is based. The most reasonable such change is to regard that the jump distance d must be replaced by a larger value ℓ . This could come about if there exist secondary barriers to the migration, with activation energy $E_m^1 (> E_m)$, spaced at intervals ℓ along the c-axis. In this case, E must be interpreted as

$$E_\sigma = E_m^1 + \frac{1}{2}E_A \quad (10)$$

rather than by Eq. (8), while Eq. (9) for A would have ℓ in place of d . In the present case $\ell/d \sim 30$, i.e. the secondary barriers are spaced at intervals ~ 30 interatomic distances, in order to account for the factor of 10^3 .

These remarks relate primarily to the synthetic crystals. The question of interpretation of the data on natural crystals will be discussed in the closing section.

Results on Irradiated Crystals

While electronic defects are not involved in unirradiated quartz crystals because of the large band gap, irradiation does generate electrons and holes, thus making possible the liberation of alkalis from Al-M pairs. It has been shown repeatedly (through infrared and ESR studies) that alkalis become mobile during irradiation only at temperatures above $200\text{-}250^{\circ}\text{K}$, but certainly at room temperature.^{17,18} This result can be very significant to conductivity studies, since the observed activation energy for unirradiated crystals involves the sum of motion and association energies [Eq. (8) or (10)] which cannot be obtained separately. On the other hand, the same theory shows that if the value of c_i were fixed (e.g., as a concentration generated in an irradiation experiment), σ will vary with temperature only through a motion energy. In fact, combining Eqs. (3) and (4) for a fixed c_i gives: $E_\sigma = E_m$ and

$$A = c_i N_0 e^2 v_0^1 d^2 / k \quad (11)$$

We have carried out long time (1-4 hr) X-ray and γ -ray irradiations of quartz crystals and studied the conductivity at room temperature over periods from minutes to hours after cessation of the irradiation. A considerably enhanced conductivity is observed at room temperature, with σ values $\sim 10^5$ larger than the values obtained by extrapolation of the curves in Fig. 2. This radiation-induced conductivity decays with time, however, showing that the enhanced carriers are being continuously trapped or immobilized (see Fig. 3). It is, therefore, difficult to obtain σ as a function of T for constant c_i . If, however, the specimen is cooled to temperatures below $\sim 0^{\circ}\text{C}$, the decay process slows down so considerably that measurements as a function of temperature can be made reversibly in this range. Figure 4 provides an example of such data for a synthetic crystal,

both swept and unswept. A relatively low activation energy $E_G = 0.14$ eV is consistently observed for synthetic crystals in this way. This radiation induced conductivity is highly anisotropic; values for σ perpendicular to the c-axis are generally too small to measure.

Similar experiments were carried out for natural crystals. In this case a higher activation energy ~ 0.45 - 0.50 eV was obtained. (Note that this is the reverse of the situation for unirradiated crystals where E_G was smaller for the natural crystals. See Table II.)

It is interesting to compare these results with the work of Hughes,¹⁹ who irradiated crystals with very short X-ray pulses and made observations of subsequent conduction over short time periods. He found an initial very rapid decay process (times $\lesssim 30$ nsec) during which there was no strong anisotropy in the conductivity, followed by a long tail in times \sim msec to seconds, which effect showed high anisotropy. He suggested that the short time effect relates to electronic carriers while the longer time effect could be attributed to ionic carriers, viz., released alkali ions. The present results support this notion. The small activation energy of 0.14 eV that we measure for synthetic crystals can reasonably be attributed to E_m , the jump activation energy of free alkali ions along the c-axis channels. Further, taking the value of the pre-exponential factor from the upper curve of Fig. 3 and substituting it in Eq. (11), we obtain $c_i \sim 10^{-5}$ ppm. This is an extremely small value, only $\sim 10^{-6}$ - 10^{-7} of the total Al content, but it is consistent with the expectation that irradiation and subsequent decay can only leave a small fraction of the total available alkali ions as free carriers. The reason that such a small c_i can still produce an appreciable conductivity is, of course, the low value of E_m .

If, in Eq. (11), ℓ^2 were substituted in place of d^2 (where ℓ is the spacing of the larger secondary barriers), the value of c_i would come out $\sim 10^3$ smaller, which would be unreasonable. It is appropriate to ask, then, why E_m appears in the unirradiated case [Eq. (10)] while E_m appears after irradiation. The answer is¹⁵ that in the higher temperature range of measurements on unirradiated crystals, the mean migration distance of a free carrier during one-quarter cycle of the applied field is $\gg \ell$, while for the low temperatures used after irradiation this distance is $< \ell$.

Concluding Remarks

We have shown that dielectric relaxation provides an excellent tool for monitoring of Al-Na pairs in α -quartz. In the case of Li, it would be very desirable to have this same capability (especially because Li is so difficult to determine chemically); it appears, however, that further work will be required before this goal is achieved.

In the study of conductivity, the results on synthetic crystals have been interpreted quite reasonably. Results on radiation-induced conductivity give a value E_m for alkali migration down a

a c-axis channel of 0.14 eV. This is quite a low value, but remembering that the hopping of Na between two nn sites of the bound Al-Na pair is only 0.06 eV (see Table I), it seems quite reasonable. The behavior of the unirradiated synthetic material, however, is dominated by secondary barriers giving rise to an increase in E_G and an anomalously high pre-exponential factor A .

The very different behavior of the natural crystals is puzzling. In the past, the lower E_G of the unirradiated natural crystals had often been interpreted as due to migration of Li^+ in these crystals, while it is Na^+ that dominates in the synthetics.^{16,20-22} This interpretation cannot be correct, however; the difference in activation energy is so large that even if the faster migrating species (e.g., Li) were present only as a very small fraction of the total alkali, it would still dominate the behavior. In fact, chemical analysis consistently shows that both Li and Na are present to some extent in natural as well as synthetic crystals.

An intriguing interpretation is that the value $E_G = 0.82$ eV of the unirradiated natural crystals represents simply $E_m + \frac{1}{2}E_A$ [Eq. (8)], i.e., without the intervention of secondary barriers. Since $E_m = 0.14$ eV, this means that $E_A = 1.36$ eV. There then remains, however, the problem of interpreting why post-irradiated natural crystals do not give the correct value for E_m . This may be related to a more rapid decay of liberated alkali ions in the natural crystals than in the synthetics. Much of the difficulty centers on the lack of detailed knowledge about defects in natural crystals. To obtain such information requires careful chemical analysis, dielectric relaxation measurements, and the types of ESR and infrared experiments recently used so successfully in the study of synthetic crystals.^{17,18} It is hoped that such information will be forthcoming.

This work was supported by the National Science Foundation under grant DMR 77-07141.

References

1. I.C. King and H.H. Sander, IEEE Trans. on Nuc. Sci., **NS-19**, 23 (1972), Rad. Effects **26**, 203 (1975).
2. A.S. Nowick, in Point Defects in Solids, J.H. Crawford, Jr., and L.M. Slifkin, eds., Volume 1, Plenum Press, New York, 1972, Chapter 3.
3. A.S. Nowick and B.S. Berry, Anelastic Relaxation in Crystalline Solids, Academic Press, New York, 1972, Chapters 8-11.
4. J.M. Stevels and J. Volger, Philips Res. Rep. **17**, 283 (1962).
5. D.S. Park and A.S. Nowick, Phys. Stat. Sol. (a) **26** 617 (1974).
6. A.S. Nowick and M.W. Stanley, in Physics of the Solid State, S. Balakrishna, Editor, Academic Press, New York, 1969, p. 183.
7. D.B. Fraser, J. Appl. Phys. **35**, 2913 (1964).
8. D.B. Fraser, in Physical Acoustics, Volume V, W.P. Mason, editor, Academic Press, New York, 1968, Chapter 2.
9. H.R. Philipp, Sol. St. Comm. **4**, 73 (1966).

10. S.V. Koloieva and M.M. Firsova, Sov. Phys.-Cryst. 13, 540 (1969), and references therein.
11. A.B. Lidiard, Handbuch der Physik 20, 246 (1957).
12. A. Kats, Philips Res. Rept. 17, 133 (1962).
13. R.N. Brown and A. Kahan, J. Phys. Chem. Solids 36, 467 (1975).
14. I.M. Hodge, M.D. Ingram and A.R. West, J. Electroanal. Chem. 74, 125 (1976).
15. H. Jain and A.S. Nowick, to be published.
16. T.M. Glushkova and M.M. Firsova, Sov. Phys.-Cryst. 12, 871 (1968).
17. M.E. Markes and L.E. Halliburton, J. Appl. Phys. 50, 8172 (1979).
18. L.E. Halliburton, M. Markes, J.J. Martin, A.F. Armington and R.N. Brown, IEEE Trans. on Nuc. Sci. NS-26, 4851 (1979).
19. R.C. Hughes, Rad. Effects 26, 225 (1975).
20. J. Verhoogen, Am. Mineralogist 37, 637 (1952).
21. M.R. Stuart, J. Appl. Phys. 26, 1399 (1955).
22. R.C. Vogel and G. Gibson, J. Chem. Phys. 18, 490, 1094 (1950).

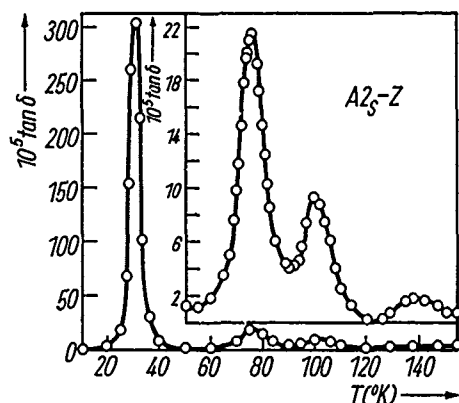


Fig. 1 : Plot of $\tan \delta$ (at 2 kHz) versus temperature for a synthetic quartz crystal. (the inset shows the higher temperature region on an enlarged scale.) The peaks at 32 and 76°K are the Al-Na peaks, while the smaller peaks above 90°K are unidentified.

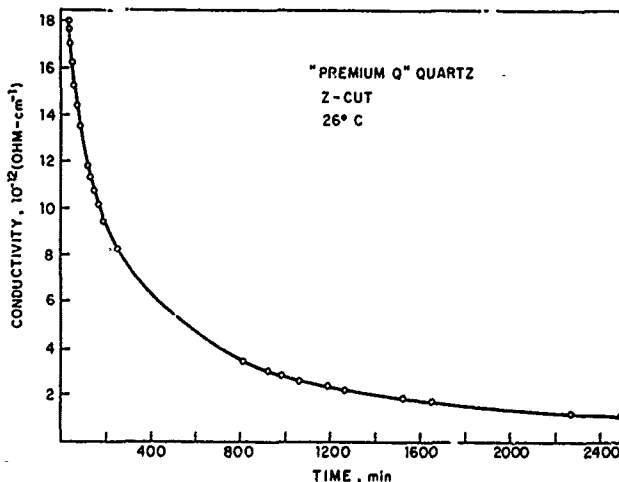


Fig. 3 : Variation of conductivity at room temperature with time, for a Premium Q crystal, following a 4 hr X-ray irradiation (total dose $\sim 3 \times 10^6$ R).

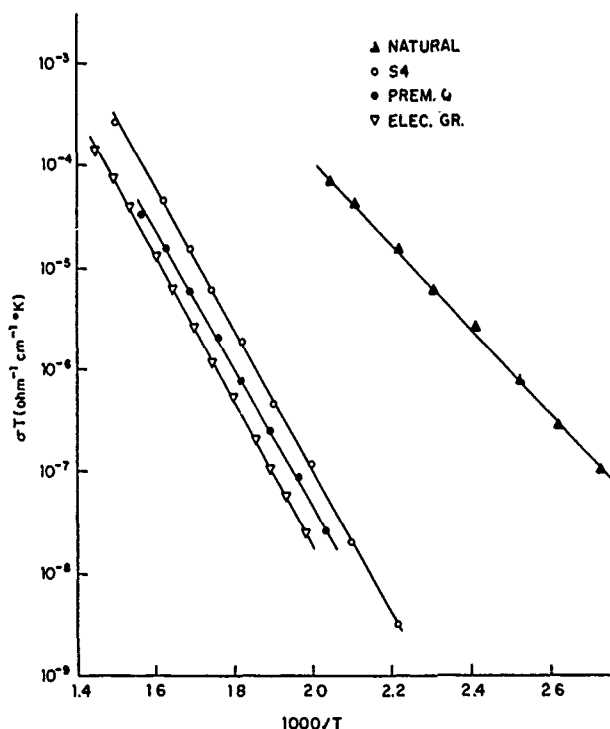


Fig. 2 : Conductivity plots ($\log \sigma T$ vs. $1/T$) for a natural crystal and three synthetic crystals.

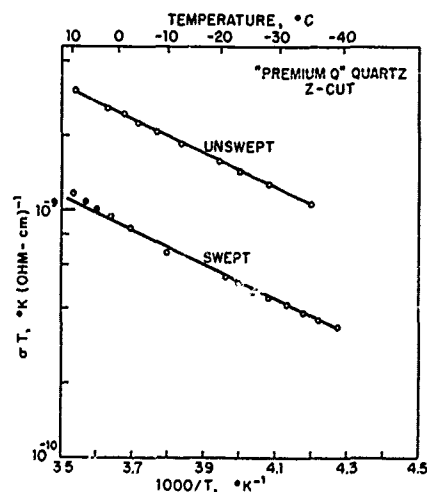


Fig. 4 : Variation of conductivity with $1/T$ following X-irradiation for Premium Q quartz (both unswept and swept) in the range where the decay process is very slow.

STUDIES OF MICRON ORDER DEFECTS IN QUARTZ
BY A HIGH ANGULAR RESOLVED X-RAY SMALL ANGLE SCATTERING TECHNIQUE

Carlos K. Suzuki*
University of Tokyo, Faculty of Engineering
Dept. of Applied Physics, Bunkyo-ku, Tokyo

Fumiko Iwasaki
Kinsekisha Laboratory Ltd., Komae-shi, Tokyo

and

Kazutake Kohra
National Laboratory for High Energy Physics
Tsukuba-gun, Japan

Summary

A very-small angle X-ray scattering technique with capability to explore an angular range down to 0.1 sec. of arc, consequently extending the measurement limit of radius of gyration up to several tens microns is briefly described.

Using this technique we studied the growth process of milky precipitates in a Y-bar synthetic quartz crystal annealing at a temperature range 520°C-800°C for 20 hours, and annealing at 660°C at various times between 2 and 26 hours. X-ray topographic studies were also performed for comparison. Annealing performed below and above the alpha-beta phase transition revealed a remarkable discontinuity in precipitates size. Activation energy for growth process of milky precipitates was estimated at $Q \approx 0.73 \text{ eV}$.

Key words: Very-Small Angle X-Ray Scattering VSAXS, Radius of Gyration R_g , X-Ray Topography, Annealing, Milky Quartz, Precipitates.

Introduction

In the usual small angle X-ray scattering SAXS studies, scattered intensities are measured in an angular range from a few degrees down to several minutes of arc separation from the incident direction, and consequently the measurable size of lattice defects is less than a few hundred angstroms. The use of the Bonse-Hart diffractometer¹ has enabled SAXS measurements at much lower angles. Renninger and Uhlmann² thus measured X-ray scattering of amorphous SiO_2 in an angular range as low as 20 sec. of arc.

Recently, interest in very small angle X-ray scattering VSAXS has been increasing because of usefulness in the understanding of micron order defects in materials, such as electronic density fluctuations and precipitates, which are usually related to very important physical properties.

Using the principle of a channel-cut monochromator system (Bonse-Hart diffractometer), we

have developed a technique to observe extremely small angle scattering down to 0.1 sec. of arc^{3,4} which means that the detection limit of defect size, or more precisely the radius of gyration R_g is extended up to few tens microns.

Applying this technique to study amorphous SiO_2 ⁵, we have observed that before irradiation the material is very homogeneous with no scattering in VSAXS; neutron irradiation gives rise to electronic inhomogeneities of 5 microns (radius of gyration). On the other hand, as-grown amorphous $\text{Pd}_{80}\text{Si}_{20}$ ribbons have presented electronic inhomogeneities of few microns (radius of gyration), but by mechanical treatment (rolling) they become very homogeneous with no central scattering peak⁶. We have also observed VSAXS in $(\text{BaPb}_{1-x}\text{Bi}_x\text{O}_3)$ superconductors⁷, with structure inhomogeneities changes in the interval of 3.0-5.4 microns (radius of gyration) with varying compositions ($0.05 < x < 0.30$).

In this paper we report the results of application of VSAXS on milky precipitates in Y-bar synthetic quartz. It is well known^{8,9,10,11} that when quartz crystals with a high concentration of hydrogen bonded OH are annealed at $T \geq 500^\circ\text{C}$, milky precipitates are produced. Infra-red absorption data and X-ray topography of milky precipitates have been previously reported¹. We have observed that both the effects of annealing temperature and time for the growth process of precipitates, as well as their average size are distinct for different growth regions (e.g. Z-sector and -X-sector). An abrupt change in size of precipitates was observed below and above the alpha-beta phase transition temperature.

This technique can be extended to study effects of irradiation in amorphous and crystalline quartz.

Experimental Procedure

The multiple crystal arrangement of the monochromator system is presented in figure 1, in which Mo K α Si (111) diffractions are used with the three crystals arranged in parallel setting^{13,14}. In order to diminish or to enlarge the spatial cross-section of the exploring beam band, an asymmetric-cut crystal is used (fore crystal); so

that depending on the size of the specimen or of the region inside the specimen to be examined, a convenient choice of the beam band can be made. The beam successively diffracted in the groove undergoes a sharp cut in its diffraction tails. Three-fold reflections were used in the present experiment. The first grooved crystal is used as a collimator and the second crystal as an analyser, thus, with the specimen between them, if scattering takes place, this intensity can be measured and its angular distribution determined by rotating the analyser crystal (2nd grooved). The curve of X-ray intensity versus scattered angle obtained without the specimen is the instrumental curve or parasitic scattering. In figure 1.b, the calculated instrumental curve⁵ for this arrangement is shown (the experimentally measured instrumental curve agrees quite well with the calculated curve) by the solid line; an experimentally measured curve with the specimen present, is schematically represented by broken lines.

In previous experiments^{1,2} Ge grooved crystals and CuK α radiation were used, but presently, with MoK α and Si(111) reflections the instrumental curve is much sharper, with half-maximum width of 3.3 sec. of arc.

Details of Experimental Apparatus

To take measurements of VSAXS, a very precise goniometer with microcomputer control was used for the analyser crystal. The experiment was carried out in two different settings:

- (A) Conventional X-ray tube with apparent focus $1.0 \times 1.0 \text{ mm}^2$, operated at 40kV, 26mA. In this case the peak intensity of the instrumental curve is 8.000 counts per sec., detected by a scintillation counter with pulse height analyser. The peak to back-ground ratio in this case is 10^{-5} for ϵ (scattering angle) at 11.5 sec. of arc. The minimum angular step of the goniometer used in this setting was $\Delta\epsilon = 0.1$ sec. of arc. So, VSAXS curves were measured point by point with angular step 0.1 sec of arc in the range $-6 \leq \epsilon \leq +6$ sec. of arc; and with angular step 0.6 for $6 \leq \epsilon \leq 50$ sec. of arc. In order to improve the statistics, the counting time was 10^3 seconds for each point in the interval $6 \leq \epsilon \leq 50$; so about 24 hours were required to measure one curve.
- (B) Super rotating-anode generator with apparent focus $0.1 \times 0.1 \text{ mm}^2$ operated at 50kV, 40mA and with a spatial cross-section of the exploring beam band of 0.1 mm. In this case the X-ray intensity was about 10 times more intense as compared with (A), so in order to take measurement over the same interval $-6 \leq \epsilon \leq 50$ sec. of arc, about 3 hours were enough to complete one curve. The goniometer used in this setting was developed by Takahashi et al.¹⁶; its precision is exceptionally

high, and the minimum angular step can be 0.005 sec. of arc. If normal focus ($1.0 \times 1.0 \text{ mm}^2$ apparent) with full power (60kV, 1A) and larger spatial cross-section of the beam band are used, the peak intensity of such arrangement can be improved by a factor of two orders of magnitude.

Accurate temperature control of the multiple crystal arrangement is very important to get good reproducibility of data. In the present experiment, temperature was carefully controlled with a precision of $\pm 0.1^\circ\text{C}$ for both settings (A) and (B).

The silicon crystal used to construct the monochro-analyser system were dislocation free F.Z. crystals from Komatsu Electronic Metals Co.

Method of Analysis

The observed or measured profile of scattered intensity with the specimen present $I'(\epsilon)$, is the result of the convolution of the true distribution of intensity $i(\epsilon)$ with the instrumental profile (obtained without the specimen) $I(\epsilon)$:

$$I'(\epsilon) = i(\epsilon) * I(\epsilon), \quad (1)$$

where ϵ is the scattered angle.

If both, $i(\epsilon)$ and $I(\epsilon)$ are Gaussian distributions in the range of very-small angle X-ray scattering, their convolution will also be Gaussian. In all our measurements in the VSAXS region we have verified that the instrumental profile $I(\epsilon)$ as well as the observed profile $I'(\epsilon)$, are Gaussians in the angular range ± 3 sec. of arc, which is the same as to say that the logarithmic plots of X-ray intensities against squares of the scattering angles (Guinier's plot) are rectilinear in an angular range up to 3 sec. of arc.

As an illustration of the above statements, figure 2 shows the Guinier's plot for:

- (a) no specimen present (instrumental or parasitic scattering),
- (b) unirradiated amorphous SiO_2 ,
- (c) neutron irradiated amorphous SiO_2

which are strictly rectilinear in the range considered. So, the half-maximum width of the curves (b) and (c) can readily be deconvoluted from the instrumental distribution (a).⁵

Therefore in the exponential or Guinier's approximation¹⁷:

$$i(\epsilon) = i_0 \exp[-4\pi^2 R_g^2 \epsilon^2 / 3\lambda^2], \quad (2)$$

where ϵ is the scattering angle, R_g the radius of gyration, and λ the wavelength of the radiation employed, the substitution of the deconvoluted half-maximum width $\epsilon_{1/2}$ in equation (2) gives an expression for the radius of gyration:

$$R_g = \frac{\lambda\sqrt{3} \cdot 0.8325}{2\pi\epsilon_{1/2}} \quad (3)$$

Specimen Preparation and Infra-red Absorption in the As-grown State

Y-bar synthetic quartz was grown at a fast rate, 1.0 mm/day in the Z-direction (sodium carbonate solution) by conventional hydrothermal method. Y-cut specimens were isochronally annealed in the temperature range 520°C-800°C for 20 hours, except for the specimen annealed at 520°C, for which about 60 hours was necessary to produce some traces of precipitates. Annealing times in the interval 2-26 hours at 660°C were also carried out on another set of Y-cut specimens.

In order to estimate the concentration of hydrogen bonded OH, infra-red absorption measurements¹² were performed on samples in the as-grown state. The dotted lines 1-6 and 7-12 in figure 3.a show the lines along which the concentrations in the Z-sector and ±X-sectors were measured. The corresponding positional change of the extinction coefficient are shown in figures 3.b and 3.c respectively. As sketched in figure 3.a, the growth rate was intentionally increased half-way through the growing process from 0.8 mm/day to 1.0 mm/day in Z-direction. Accordingly cross-hatched areas A or A' (Z-sector) and B (-X-sector) in figure 3.a were selected for the VSAXS measurements. Direct observations of defects in the A region by X-ray topography were carried out, but in the B region (-X-sector), due to the high concentration of precipitates, topographic images could not be resolved.

Results and Discussions

VSAXS and X-ray Topography of Milky Precipitates

Figure 4 shows typical plots of the logarithms of measured intensities versus scattering angles for Z-sector specimens annealed at 660°C for 2 and 8 hours. In the angular interval considered, the sample annealed for 8 hours presents a sharp increase in scattered intensity, indicating the nucleation of precipitates, most of which are in the submicron range. X-ray scattered intensities at much lower angles are represented by Guinier's plot (inserted in the same figure, but with the logarithmic scale changed): Plots (1), (2) and (3) correspond to samples 8h, 2h, and as-grown, respectively; as plots (1) and (2) have the same slope as that of plot (3), we can immediately conclude that there is no detectable amount of micron order precipitates. Examination of Z-sector samples annealed at the same temperature (660°C) for 15, 20, and 26 hours reveals an interesting feature: there is no appreciable changes in the size submicron order precipitates, as shown in figure 5, but in the extremely small angle X-ray scattering region represented by Guinier's plot in this same figure there is a considerable change in their slopes, which means an increase in average size of precipitates of micron order. With the same annealing condition

-X-sector presents a quite different nucleation process in the submicron range with a gradual increase in concentration for 15, 20 and 26 hour heat-treatments. Curves are shown in figure 6. The radii of gyration R_g of Z- and -X-sectors are estimated using the method of analysis described above. The values of R_g of samples annealed in beta-phase (660°C) as a function of annealing temperature are presented in figure 7. From this figure we can directly deduce that the growth rate of precipitates is distinct for -X- and Z-sectors. Their R_g values are approximately comparable at 30 hours of annealing.

X-ray topographs of the same specimens are shown in figure 8 in the sequence: as-grown state 2, 8, 15, 20 and 26 hour 660°C annealing. Molybdenum radiation, (00.3) diffracting planes, and the condition $\mu t = 1.0$, where μ is the linear absorption coefficient for the radiation employed and t the thickness of the sample, were used. In the as-grown state the presence of Pendellösung fringes¹⁸ indicates that the crystal is perfect. For 2 hours annealing the Pendellösung fringes persist, which means that the milky precipitates even though not detectable in this topograph, are very small in this stage (the existence of very small precipitates is known from previous X-ray small angle scattering measurements) and homogeneously distributed; most of the black contrast belongs to the dynamical image of dislocations. As each heat-treatment was performed on a different sample cut adjacent to each other, the image of each topograph belongs to a different region of the crystal. After annealing for 8 hours, the concentration of precipitates is high enough to extinguish the Pendellösung fringes, although these precipitates are still not well resolved by X-ray topography; the black contrast is due to other defects instead of milky precipitates. Treatment at 15 hours gives rise to bigger precipitates and their progression can be followed in the topographs of 20 and 26 hour annealed samples. The X-ray topographic image is caused by the strain field around the defects, and so, their real size can not be obtained, but this technique can provide a useful qualitative view of the process.

X-ray topography with (22.0) diffraction shows a much sharper image: figures 9.a and 9.b are for 520°C, 60 hour and 660°C, 20 hour annealings respectively. From these images we can construct a tridimensional model for the growth process in the Z-sector, which develops with precipitates contained in layers perpendicular to the direction of crystal growth (approximately the Z-direction). Figures 9.a' and 9.b' are spatial representations of the topographs 9.a and 9.b respectively. The average distance between layers of precipitates are $\sim 26\mu\text{m}$ and $\sim 110\mu\text{m}$ for 520°C and 660°C respectively.

For 20 hour annealing at temperatures in the interval 550°C-800°C, the calculated radius of gyration of precipitates in the -X- and Z-sectors as a function of temperature are shown in figure 10. The corresponding diameter D assuming spherical precipitates [from X-ray topography of

figure 9 such a hypothesis is reasonable] are presented on the right vertical axis. Observe the remarkable discontinuity that takes place in the size of precipitates just on the neighborhood of the alpha-beta phase transition temperature (573°C).

Alpha-Beta Phase Transition

The size of precipitates for 20 hour heat-treatment just below and above the alpha-beta phase transition shows an abrupt change, being about 35 times greater on the beta-phase side. Annealings of samples performed in the alpha-phase reveal a very low concentration of much smaller precipitates. This is better seen in the picture of figure 9.a, where only thin layers of precipitates are visible, the particles being unresolved. By VSAXS measurement their size are estimated to be on the order of 0.1 micron.

Little is known about the mechanism by which the rate of nucleation and growth of precipitates differs on the alpha-phase and beta-phase sides.

Direct observation by X-ray topography¹⁹ in the neighborhood of the alpha-beta phase transition temperature in synthetic quartz shows that in most cases the alpha-phase is transformed to a Dauphiné twinned region [from the crystallographic point of view the crystal is rotated 180° in relation to the matrix or alpha-phase; as the structure factor for the Dauphiné twinned region is different, the X-ray diffracted intensity reveals a clear contrast in the topographic image] prior to the appearance of beta-phase. Then the beta-phase transition proceeds preferentially over the twinned region. The temperature range of the transformation process is variable from sample to sample, but we can roughly estimate from the work of reference¹⁹ that $\Delta T \approx 10^\circ\text{C}$. The rapid diffusion of small precipitates through a pressure difference during the crystallographic symmetry and structure transformation process is apparently the main mechanism to explain the observed discontinuity in size.

Activation Energy of the Precipitates Growth Process

The activation energy of the growth process of milky precipitates annealed in beta-phase is estimated by assuming a simple model for spherical grain-growth²⁰. If D represents the mean diameter of precipitates, and supposing that the size of precipitates D_0 at the beginning is very small, the growth law can be expressed as a function of both annealing time t , and annealing temperature T by the following expression:

$$D^2 = K t \exp[-Q/k T], \quad (4)$$

where K is a constant of proportionality, Q the activation energy, k Boltzmann's constant and T the temperature in degrees Kelvin. For isochronal annealings, expression (4) can be simplified to:

$$D^2 = C \exp[-Q/k T], \quad (5)$$

where C is a constant. Therefore, from the plot of $\log D$ versus $1/T$ (figure 11), the value of activation energy is estimated to be:

$$A \approx 0.73 \text{ eV.}$$

This value of Q is valid for the Z-sector, in which growth of the nucleus progresses in the form of "layers of precipitates". For the -X-sector, due to the very high concentration of nuclei, and consequently because of the excessive strain, the layers of precipitates could not be verified by X-ray topography. Nevertheless the data on the -X-sector for $\log D$ versus $1/T$ plot as presented in figure 11 can roughly be taken to present the same value of activation energy as above calculated.

Conclusion

Accurate measurements of very-small angle X-ray scattering of milky quartz have provided new information concerning the nucleation and growth of precipitates. Further studies of milky precipitates in the neighborhood of the alpha-beta phase transition temperature using a high temperature camera and very intense X-ray source, can provide an "almost live" measurement of nucleation and growth processes of the precipitates.

Acknowledgements

The authors would like to acknowledge Prof. S. Kikuta, Dr. T. Takahashi and Mr. T. Ishikawa for helpful discussions on experimental details and assistance in the experiment. We also wish to acknowledge Dr. K. Doi for advice and helpful discussions. One of us (C.K.S) acknowledges the support of Capes (Coordenação do Aperfeiçoamento de Pessoal de Nível Superior), and Profs. C.A. Argüello, J.E. Ripper Filho, and S. Caticha-Ellis.

References

1. U. Bonse and M. Hart, Z. Physik **189**, 151 (1966).
2. A.L. Renninger and D.R. Uhlmann, J. Non-Cryst. Sol. **16**, 325 (1974).
3. C.K. Suzuki and K. Kohra, Proc. of First Japan-Brazil Symposium on Science & Technology, Tokyo (1979).
4. C.K. Suzuki and K. Kohra, To be published.
5. C.K. Suzuki, K. Doi and K. Kohra, Japan. J. Appl. Phys.-Lett **19**, 205 (1980).
6. K. Doi and C.K. Suzuki, Private Communication.
7. C.K. Suzuki, T.D. Thanh, and S. Kikuta, To be published.
8. D.M. Dodd and D.B. Fraser, J. Phys. Chem. Solids **26**, 673 (1965).

9. D.M. Dodd and D.B. Fraser, Amer. Mineral. 52, 149 (1967).
 10. K. Moriya and T. Ogawa, J. Crystal Growth 44 (1978) 53.
 11. F. Iwasaki and M. Kurashige, Japan. J. Appl. Phys. 17, 817 (1978).
 12. F. Iwasaki, Japan. J. Appl. Phys. To be published in Vol. 19 (1980).
 13. S. Kikuta and K. Kohra, J. Phys. Soc. Japan, 29, 1322 (1970).
 14. K. Kohra, International Summer School on X-ray Dynamical Theory and Topography, Limoges, France (1975).
 15. M. Ando. Private Communication.
 16. T. Takahashi, T. Ishikawa, T. Matsushita, S. Kikuta and K. Kohra, Read at the Annual Meeting of the Crystallographic Society of Japan, Nagoya (1979).
 17. A. Guinier, La Théorie et Technique de la Radio-cristallographie, 2nd. ed., (Dunod. Paris, 1964) Chap. XIV.
 18. N. Kato, X-Ray Diffraction, edited by L.V. Azaroff, (MacGraw-Hill, 1974) Chap. IV.
 19. N. Inoue, A. Iida and K. Kohra, J. Phys. Soc. Japan 37, 742 (1974).
 20. R.E. Reed-Hill, Physical Metallurgy Principles, 2nd. ed., (D. Van Nostrand Co., 1973) Chap. VII.
-

* On leave from the University of Campinas, Brazil

Work in part supported by the Ministry of Education of Japan.

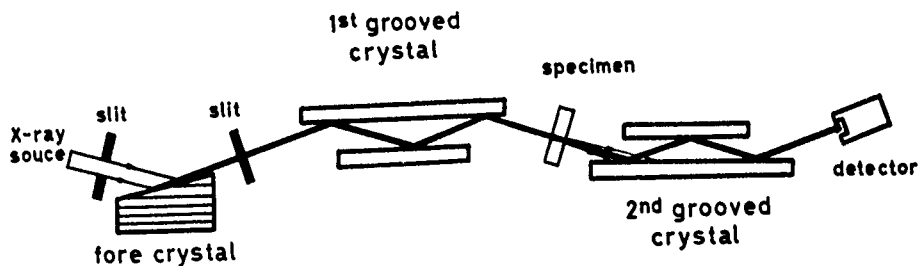


Fig. 1a

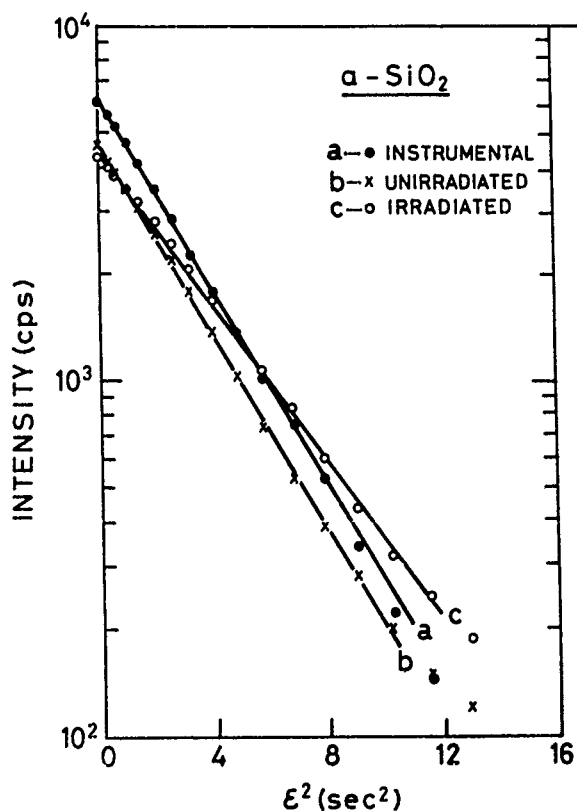


Fig. 2 Guinier's plot of amorphous SiO_2 with: (a) instrumental curve, (b) before irradiation, (c) neutron irradiated. The change in the slope of plot (c) is to be observed. From Ref. [5].

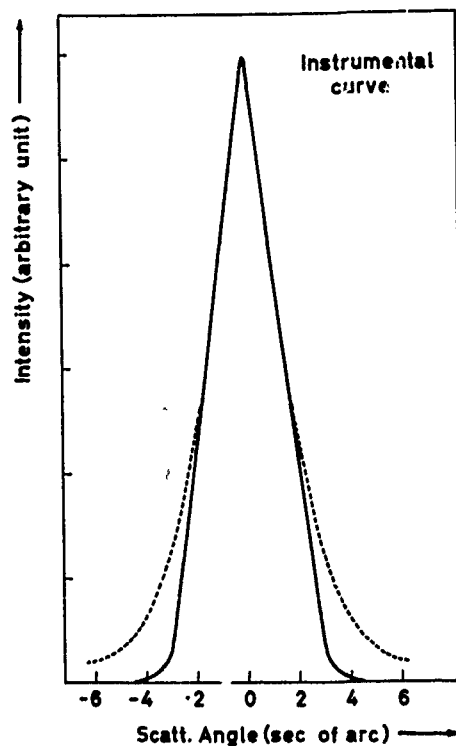


Fig. 1 (a) Schematic drawing of multiple crystal arrangement of very-small angle X-ray scattering. MoK α and Silicon (111) diffracting planes are used. (b) Calculated instrumental curve (solid line), the broken line represents the curve measured with specimen.

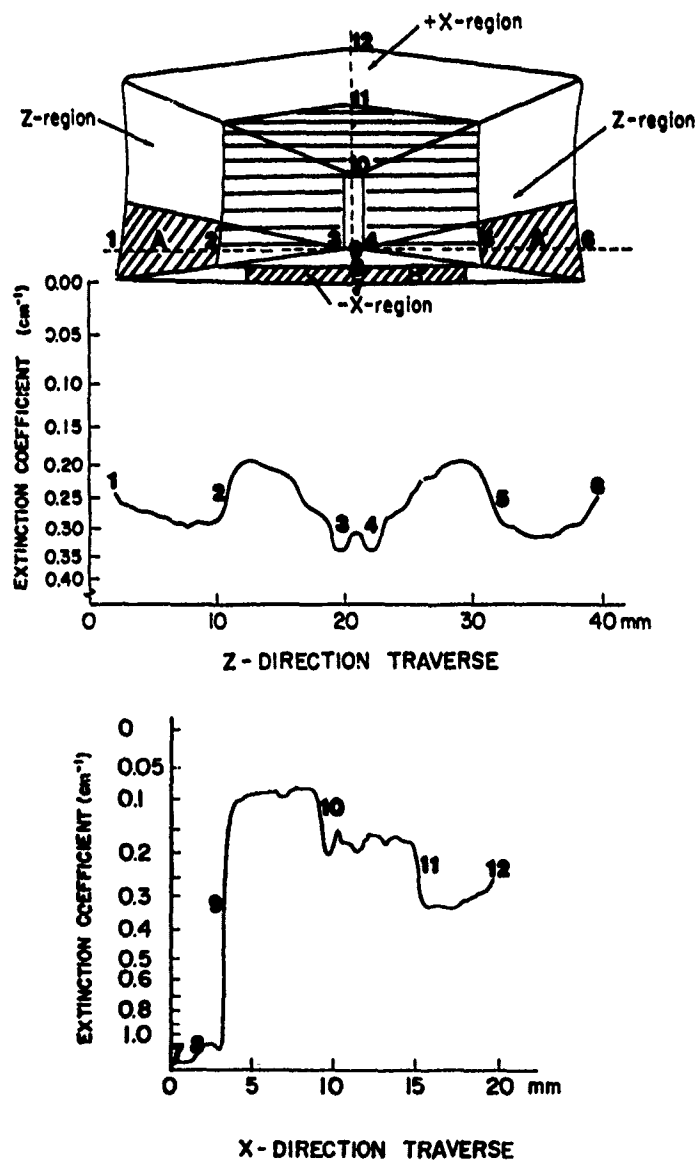


Fig. 3 (a) Y-cut specimen of fast-growth synthetic quartz. In the ribboned region the growth rate was 0.8 mm/day (in Z-direction); outside the ribboned region, 1.0 mm/day. Cross-hatched area A or A' and B were selected for VSAXS measurement. (b) Positional change of infra-red absorption coefficient along line 1-6. (c) Positional change of infra-red absorption coefficient along line 7-12. Ref. [12].

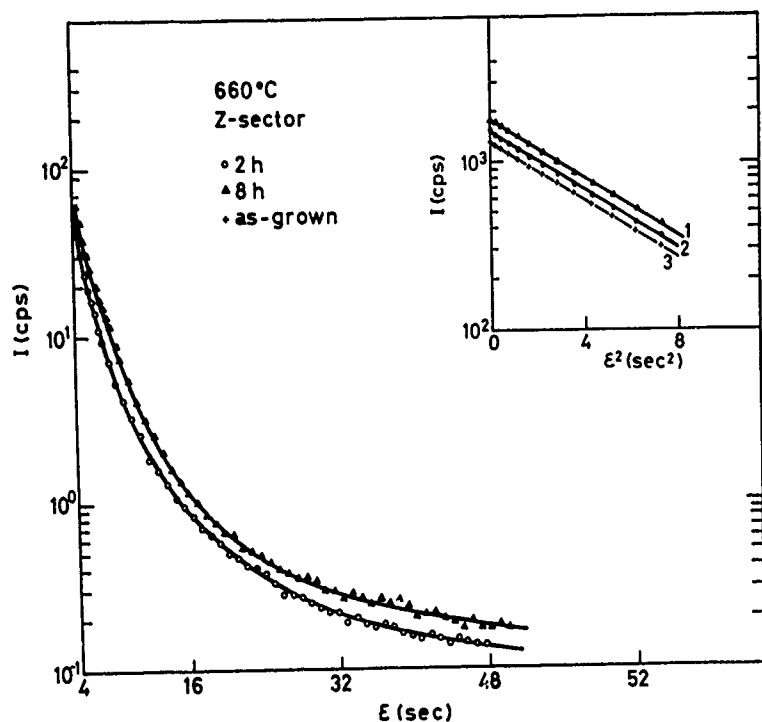


Fig. 4

Very-small angle X-ray scattering for Z-sector, 660°C annealed sample. The sample annealed at 8h denotes a considerable increase of scattered intensity. The region of extremely small angle X-ray scattering is represented by Guinier's plots, which were translated on the vertical axis to facilitate comparison. There is no change in the slope of the three plots, which means there is no detectable amount of precipitates of micron order.

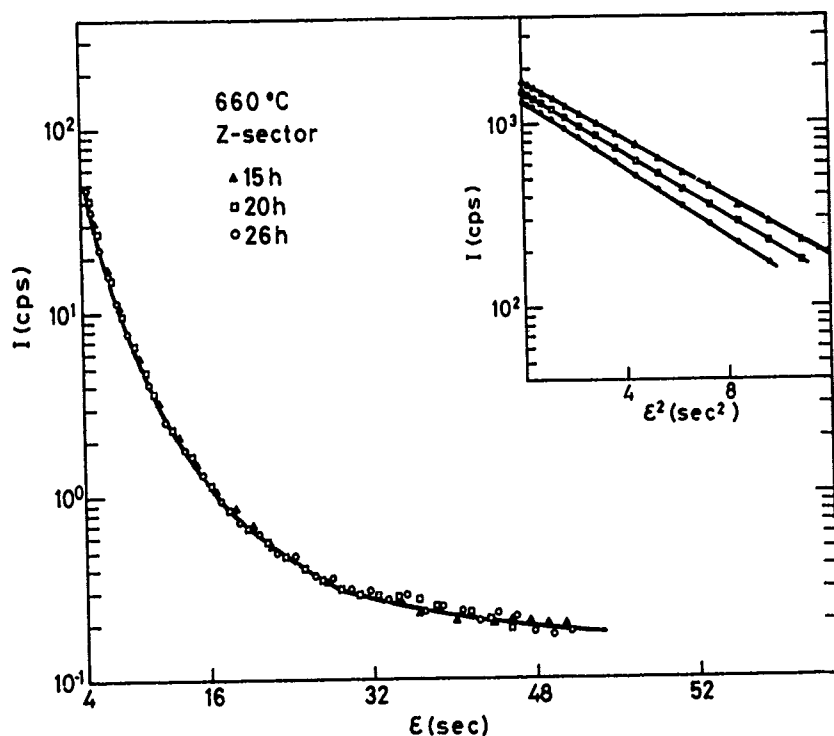


Fig. 5 The change in the slopes of Guinier's plot indicates the growth of big Precipitates of the order of several microns. Scattering due to precipitates of sub-micron order presents no appreciable change.

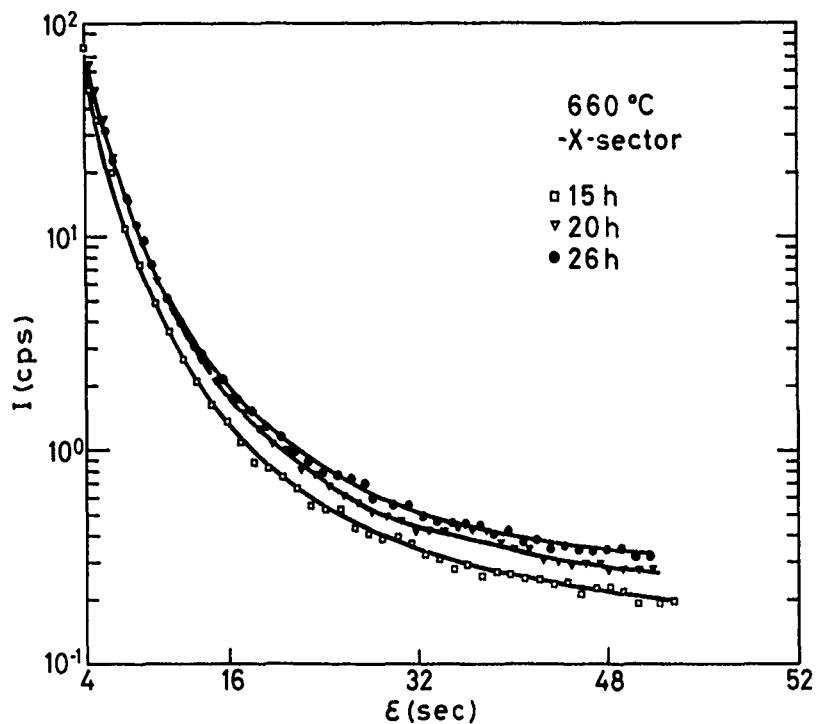


Fig. 6 -X-sector samples annealed at the same conditions of Z-sector sampler (fig. 5) show a quite different behavior.

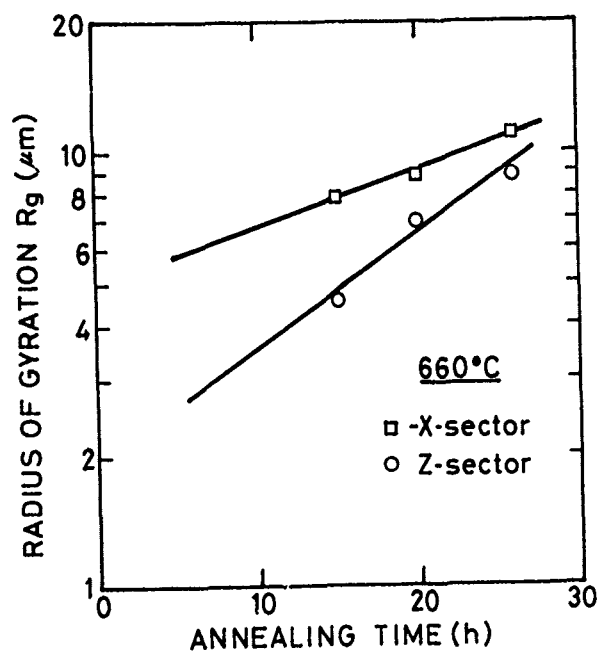


Fig. 7 Radius of gyration R_g as function of annealing temperature.

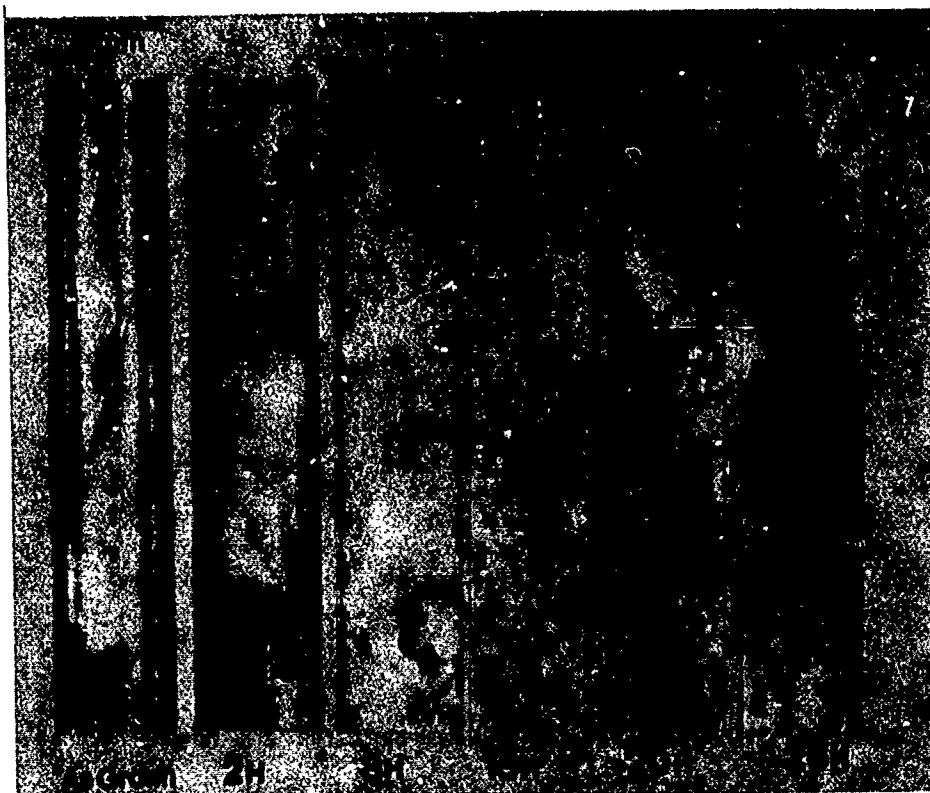


Fig. 8 X-ray section topography of Z-sector synthetic quartz. $\text{Mo K}\alpha$, (00.3) reflection. The sequence of pictures show that in as-grown state the crystal is nearly

perfect due to the presence of Pendellösung fringes; and gradual change is observed with increasing time. The topographs for 15, 20 and 26 hours annealings show big milky precipitates.



Fig.9a



Fig.9b

Fig. 9 X-ray section topography with $\text{Mo K}\alpha$, (22.0) diffraction planes for: (a) 520°C, 60 hour and (b) 660°C, 20

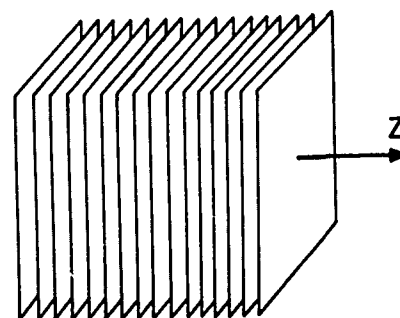


Fig.9a'

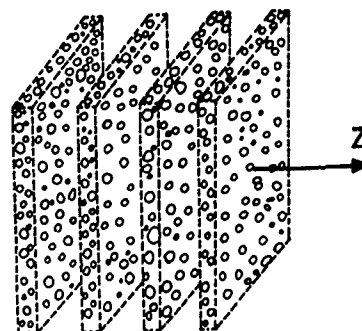


Fig.9b'

hour annealing. From these topographs we can observe that the precipitates are distributed inside ordered layers. The spatial representation of picture (a) and (b) are shown in (a') and (b') respectively.

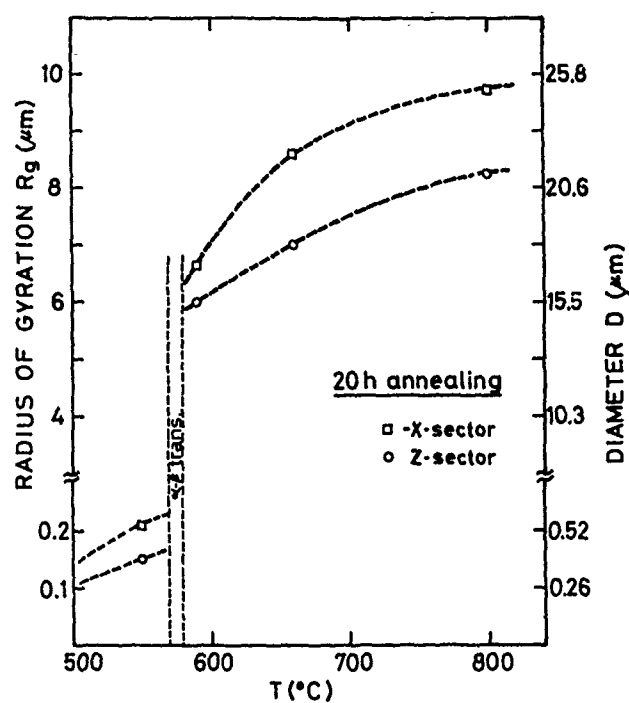


Fig. 10 Radius of gyration R_g of precipitates as function of temperature.

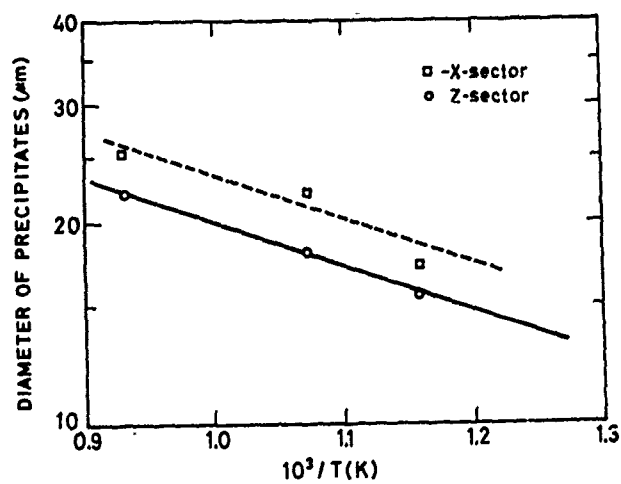


Fig. 11 Diameter of precipitates of samples annealed for 20 hours as function of the inverse of annealing temperature.

A NEW METHOD FOR PREDICTING THE TEMPERATURE DEPENDENCE OF ELASTIC COMPLIANCE IN SIMPLE PROPER FERROELECTRICS

L.E. Cross, R. Betsch, H. McKinstry, T. Shrout
Materials Research Laboratory, The Pennsylvania State University
R. Neurgaonkar
Rockwell International Science Center

Summary

The Landau-Ginsburg-Devonshire phenomenological theory for simple proper ferroelectrics has been extended to include all elasto:electric coupling terms up to sixth order. For the elastic behavior in the single domain ferroelectric phase it appears that the sixth order electrostriction constants ϕ_{ijklmn} play a most important role. This analysis has been applied to study the elastic behavior of ferroelectric crystals in the tungsten bronze structure family.

A feature that makes the phenomenology potentially valuable is that the higher order dielectric stiffnesses and coupling terms do not change markedly with temperature or with cationic makeup. Thus in principle it is possible to predict semiquantitatively the trends for the dielectric, thermal, piezoelectric, and elastic constants for a wide compositional range of ferroelectric bronze compounds, from a limited set of prototypic constants.

Introduction

For many acoustic wave devices it is desirable that the propagation time τ for the elastic wave be independent of ambient temperature change. The temperature coefficient of delay for a bulk wave may be simply written¹

$$1/\tau \left(\frac{\partial \tau}{\partial T} \right)_X = \alpha_L - \frac{1}{2} \alpha_V - \frac{1}{2} \frac{1}{c} \left(\frac{\partial \bar{c}}{\partial T} \right)_X \quad (1)$$

where τ is the propagation (or delay) time measured at constant stress X , α_L the coefficient of linear thermal expansion in the direction of propagation, α_V the volume coefficient of expansion, and \bar{c} a combination of elastic constant depending on the type, polarization, and propagation direction of the elastic wave.

In many "normal" crystals this expression is dominated by the temperature coefficient of \bar{c} which is usually negative (crystals soften on heating) and of order 10^{-3} to 10^{-4} K^{-1} . For many device structures it is desirable that the crystal itself be piezoelectric, and for several classes of broadband devices high piezoelectric coupling (k_{ij}) and low impedance (high permittivity ϵ_{ij}) are desirable, so that it is natural to explore simple proper ferroelectric crystals which often combine suitable magnitudes in these parameters. The proper as distinct from improper or extrinsic ferroelectrics are characterized by the fact that the electric spontaneous

polarization P_s is an effective order parameter describing the phase change from paraelectric to ferroelectric form. Changes of properties in the ferroelectric phase can be traced to essential consequences of the onset of polarization in the paraelectric phase, and their temperature dependence can be described by a simpler family of temperature independent coupling parameters in the paraelectric prototype.

In the thermodynamic phenomenological modeling the non-zero stiffnesses and coupling parameters are determined by the prototypic symmetry, and it does appear that the higher order stiffnesses which control the magnitude of P_s mutate only slowly with cationic composition in a given symmetry group, while the coupling parameters change hardly at all with composition or temperature.

It is the purpose of this paper to demonstrate (i) that if higher order electrostriction is considered, the onset of polarization P_s has a direct effect upon the stiffened ferroelectric compliances s_{ij}^P ; (ii) that for the tungsten bronze simple proper ferroelectric ($Sr_{0.61}Ba_{0.39}Nb_2O_6$) the elastic compliances in the paraelectric phase have the predicted behavior under induced polarization $P_I(3)$; (iii) the compliances in the ferroelectric single domain and their temperature dependence can be predicted from the measured paraelectric constants; (iv) provided the diffuse nature of the phase transition in this SBN bronze is taken into account by a suitable distribution of Curie points, the phenomenology is able to derive a rather complete family of low temperature dielectric, elastic, piezoelectric, and thermal expansion parameters from a limited family of high temperature prototypic constants.

Thermodynamic Phenomenology

In general, the thermodynamic function of interest to describe the isothermal, isobaric properties of a polarizable deformable insulator is the elastic Gibbs function G_1 defined by

$$G_1 = U - TS - Xx \quad (2)$$

where U is the internal energy, S the entropy, T the temperature, X the elastic stress, and x the strain.

T and S are scalar, but X and small x will be second rank tensors.

The increment of G_1 dG_1 will be made up from

$$dG_1 = -SdT - x dX + E dP \quad (3)$$

where E is the electric field, P the electric polarization, and E and P are polar vectors. Thus from the partial derivatives of G_1 we may derive the strain x as

$$\left(\frac{\partial G_1}{\partial X}\right)_{TP} = -x \quad (4)$$

the electric compliance at constant P (stiffened)

$$\left(\frac{\partial^2 G_1}{\partial X^2}\right)_{TP} = s^P \quad (5)$$

electric field E

$$\left(\frac{\partial G_1}{\partial P}\right)_{TX} = E \quad (6)$$

dielectric stiffness χ

$$\left(\frac{\partial^2 G_1}{\partial P^2}\right)_{TX} = \chi^X \quad (7)$$

and the piezoelectric polarization constant b

$$\left(\frac{\partial^2 G_1}{\partial P \partial X}\right)_T = \left(\frac{\partial E}{\partial X}\right)_T = b^T \quad (8)$$

which is related to the more frequently used d constant by

$$d^T = \left(\frac{\partial P}{\partial X}\right)_T = \left(\frac{\partial E}{\partial X}\right) \left(\frac{\partial P}{\partial E}\right) = b/\chi^X \quad (9)$$

It is conventional in Landau-Ginsburg-Devonshire phenomenological theory to take out the elastic Gibbs energy of the unpolarized undeformed crystal and write

$$\Delta G_1 = G_1(\text{polarized}) - G_1(\text{unpolarized}) = f(P, X, T) \quad (10)$$

and to separate the function f into three components

$$\Delta G_1 = f(P, T) + f(X, T) + f(X, P) \quad (11)$$

Inserting now the vector nature of P and E , and the tensor form of X , $f(P, T)$ is expressed as a power series expansion

$$f(P, T) = \alpha_{ij} P_i P_j + \alpha_{ijk} P_i P_j P_k + \dots \quad (12)$$

where the α_{ijk} are limited by the prototype symmetry and only the α_{ij} are temperature dependent. If the ferroelectric transition is first order, it is necessary to include at least the first 6th power terms in P .

Usually only "Hookian" elastic behavior is considered and $f(X, T)$ takes the simple form

$$f(X, T) = -\frac{1}{2} s_{ijkl} X_{ij} X_{kl} \quad (13)$$

It has been considered necessary only to include the lowest power symmetry allowed coupling terms

between P and X , so that $f(X, P)$ is given by either

$$f(X, P) = -b_{ijk} P_i X_{jk} \quad (14)$$

or

$$f(X, P) = -Q_{ijkl} P_i P_j X_{kl} \quad (15)$$

where Q_{ijkl} are the symmetry permitted electrostriction constants.

For centric prototype structures of the type to be considered all $b_{ijk} \equiv 0$, and the phase change at T_c is first order. Since 6th power terms in P are absolutely necessary it seems illogical to consider only the 4th rank coupling terms, and we propose to add terms of the form

$$-[\phi_{ijklmn} P_i P_j X_{kl} X_{mn}] - [W_{ijklmn} P_i P_j P_k P_l X_{mn}] \quad (16)$$

For the elastic behavior clearly the ϕ terms are most important. In the unmodified LGD theory in the spontaneously polarized phase taking second partial derivatives with respect to the X_{ij} obviously all Q terms drop out so that

$$s_{klmn}^P(\text{polarized}) = s_{klmn}^P(\text{unpolarized})$$

whereas if the ϕ constants have significant magnitude

$$s_{klmn}^P(\text{polarized}) = s_{klmn}^P(\text{unpolarized}) + \phi_{ijklmn} P_i P_j$$

since the polarization components $P_i P_j$ in the simple ferroelectric have strong temperature dependence, the electrostrictive term may be most important in dictating the elastic compliances in the ferroelectric phase.

Application of the Phenomenology to Tungsten Bronze Structure Ferroelectrics

Introduction

The tetragonal bronze structure ferroelectrics form a very large family with over 100 known individual ferroelectric compounds and innumerable² possible solid solutions between these end members. Paraelectric prototypic point symmetry is $4/mmm$ and though seven ferroelectric species are theoretically possible, only two different ferroelectric forms are known: an orthorhombic form in which the spontaneous polarization is along 110 , $\bar{1}\bar{1}0$, $1\bar{1}0$, or $\bar{1}10$, which is in polar $mm2$ symmetry, and a tetragonal form in which P_s lies along 001 or $00\bar{1}$ and which has polar tetragonal $4mm$ symmetry.

To characterize the elastic wave behavior completely in the orthorhombic case it is necessary to know 9 elastic constants, 5 piezoelectric constants, 3 dielectric constants and their temperature derivatives, and 3 thermal expansions. For the tetragonal form there are 8 elastic constants, 3 piezoelectric and 2 dielectric parameters and their temperature derivatives and 2 thermal expansions. Clearly, if this measurement burden were to be repeated for each end member compound of interest and iterated across

each solid solution the task of choosing an optimum bronze for elastic wave applications is horrendous. The objective of the present study is to attempt to provide more rational guidelines for this choice by making use of a limited family of paraelectric parameters which hopefully will not change rapidly with composition.

Symmetry Constraints

For the prototypic 4/ $\overline{3}2$ centric group the permitted dielectric stiffnesses α_{ij} , fourth order stiffnesses α_{ijkl} , electrostrictive Q_{ijkl} and elastic compliance constants s_{ijkl} are listed in Table I. The sixth order stiffnesses α_{ijklmn} are listed in Table II, and the sixth order electrostriction constants ϕ_{ijklmn} in Table III.

The LGD phenomenological elastic Gibbs function³ has the form

$$\begin{aligned} \Delta G = & \alpha_1 (P_1^2 + P_2^2) + \alpha_3 P_3^2 + \alpha_{11} (P_1^4 + P_2^4) + \alpha_{33} P_3^4 \\ & + \alpha_{13} (P_1^2 P_3^2 + P_2^2 P_3^2) + \alpha_{12} P_1^2 P_2^2 + \alpha_{333} P_3^6 \\ & + \alpha_{111} (P_1^6 + P_2^6) - \frac{1}{2} s_{11} (X_1^2 + X_2^2) - s_{12} X_1 X_2 \\ & - s_{13} (X_1 + X_2) X_3 - \frac{1}{2} s_{33} X_3^2 - \frac{1}{2} s_{44} (X_4^2 + X_5^2) \\ & - \frac{1}{2} s_{66} X_6^2 - Q_{11} (P_1^2 X_1 + P_2^2 X_2) - Q_{12} (P_1^2 X_2 + P_2^2 X_1) \\ & - Q_{13} (P_1^2 X_3 + P_2^2 X_3) - Q_{31} (P_3^2 X_1 + P_3^2 X_2) \\ & - Q_{33} P_3^2 X_3 - Q_{44} (P_2 P_3 X_4 + P_1 P_3 X_5) \\ & - Q_{66} P_1 P_2 X_6 \end{aligned} \quad (17)$$

The first partial derivatives with respect to the polarization give the field components

$$\begin{aligned} \frac{\partial \Delta G}{\partial P_1} = E_1 = & 2\alpha_1 P_1 + 4\alpha_{11} P_1^3 + 2\alpha_{13} P_1 P_3^2 \\ & + 2\alpha_{12} P_1 P_2^2 + 6\alpha_{111} P_1^5 - 2Q_{11} P_1 X_1 \\ & - 2Q_{12} P_1 X_2 - Q_{13} P_1 X_3 - Q_{44} P_3 X_5 - Q_{66} P_2 X_6 \\ \frac{\partial \Delta G}{\partial P_2} = E_2 = & 2\alpha_1 P_2 + 4\alpha_{11} P_2^3 + 2\alpha_{13} P_2 P_3^2 \\ & + 2\alpha_{12} P_2 P_1^2 + 6\alpha_{111} P_2^5 - 2Q_{11} P_2 X_2 \\ & - 2Q_{12} P_2 X_1 - 2Q_{13} P_2 X_3 - Q_{44} P_3 X_4 - Q_{66} P_1 X_6 \\ \frac{\partial \Delta G}{\partial P_3} = E_3 = & 2\alpha_3 P_3 + 4\alpha_{33} P_3^3 + 2\alpha_{13} (P_1^2 + P_2^2) P_3 \\ & + 6\alpha_{333} P_3^5 - 2Q_{31} P_3 (X_1 + X_2) \\ & - 2Q_{33} P_3 X_3 - Q_{44} (P_2 X_4 + P_1 X_5) \end{aligned} \quad (18)$$

It is the solutions of these equations with $E_i = 0$ which determine the ferroelectric states. For the tetragonal case, the dielectric data in the paraelectric phase indicate that α_3 is a linearly decreasing function of T passing through zero near T_c , that is

$$\alpha_3 = \alpha_{30} (T - \theta_3) \quad (19)$$

where θ_3 is close to T_c whereas α_1 also has the same form

$$\alpha_1 = \alpha_{10} (T - \theta_3) \quad (20)$$

but θ_1 is very much below T_c .

For temperatures less than the ferroelectric Curie point T_c in this case, the spontaneous polarization along the tetrad axis is given by the solution of

$$0 = 2\alpha_{30} (T - \theta_3) + 4\alpha_{33} P_3^2 + 6\alpha_{333} P_3^4 \quad (21)$$

and

$$P_1 = P_2 = 0 \quad (22)$$

The isothermal dielectric stiffnesses are

$$\begin{aligned} \chi_{11}^T &= 2\alpha_1 + 2\alpha_{13} P_3^2 \\ \chi_{22}^T &= 2\alpha_1 + 2\alpha_{13} P_3^2 \\ \chi_{33}^T &= 2\alpha_3 + 12\alpha_{33} P_3^2 + 30\alpha_{333} P_3^4 \\ \chi_{12}^T = \chi_{13}^T = \chi_{23}^T &= 0 \end{aligned} \quad (23)$$

The tetragonal spontaneous strains are given by

$$\begin{aligned} x_1 &= Q_{31} P_3^2 & x_4 = x_5 = x_6 &= 0 \\ x_2 &= Q_{31} P_3^2 \\ x_3 &= Q_{33} P_3^2 \end{aligned} \quad (24)$$

and the piezoelectric b coefficients by

$$\begin{aligned} b_{11} &= 0 & b_{21} &= 0 & b_{31} &= 2Q_{31} P_3 \\ b_{12} &= 0 & b_{22} &= 0 & b_{32} &= 2Q_{31} P_3 \\ b_{13} &= 0 & b_{23} &= 0 & b_{33} &= 2Q_{33} P_3 \\ b_{14} &= 0 & b_{24} &= Q_{44} P_3 & b_{34} &= 0 \\ b_{15} &= Q_{44} P_3 & b_{25} &= 0 & b_{35} &= 0 \\ b_{16} &= 0 & b_{26} &= 0 & b_{36} &= 0 \end{aligned}$$

If the sixth order ϕ terms are added to equation (17), then the second derivatives with respect to the stress give the stiffened elastic compli-

ances s_{ij}^P which take the form

$$\begin{aligned} S_{11}^P(P) &= S_{22}^P(P) = S_{11}^P(0) + \phi_{311} P_3^2 \\ S_{12}^P(P) &= S_{12}^P(0) + \phi_{312} P_3^2 \\ S_{13}^P(P) &= S_{23}^P(P) = S_{13}^P(0) + \phi_{313} P_3^2 \\ S_{33}^P(P) &= S_{33}^P(0) + \phi_{333} P_3^2 \\ S_{44}^P(P) &= S_{55}^P(P) = S_{44}^P(0) + \phi_{344} P_3^2 \\ S_{66}^P(P) &= S_{66}^P(0) + \phi_{366} P_3^2 \end{aligned} \quad (26)$$

where the suffix (P) indicates the S value at polarization level P and the suffix (0) the prototypic value when $P=0$.

Derivation of the Thermodynamic Constants for Ba_{0.39}Sr_{0.61}Nb₂O₆ Bronze

The most important initial consideration was to determine whether the ϕ constants that are symmetry permitted have magnitudes which make a significant contribution to the s_{ijkl}^P and thus are of importance in determining the elastic response and its temperature behavior in the polarized ferroelectric phase.

Fortunately because of the very high polarizability along the 4-fold axis for temperatures above T_c where $P_3=0$ it is possible to determine the ϕ_{3ij} constants by a very simple direct experimental test. If a suitable bar-shaped sample of SBN is subjected to a DC field E_3 at a temperature above T_c , a high non-zero P_3 may be induced in the bar, which induces through equations (2) non-zero values of the piezoelectric constants. If the electrical impedance of the bar is now explored with a low level probing field, the resonance and antiresonance frequencies corresponding to the different modes of elastic vibration of the bar may be excited (Figure 1), and the elastic parameters s_{ij}^P , s_{ij}^P deduced from the resonance frequencies and the dimensions and density of the bar.

By repeating the measurement at a sequence of different E field levels, different values of P may be induced and the relationships expected in equations (26) explored. It may be noted that in these extremely polarizable crystals the dielectric properties exhibit significant nonlinearity at quite low E_3 levels so that it is necessary to measure the P_3 value for each field level using a slow sweep Sawyer and Tower method³.

Typical measurements of S_{11}^P and S_{33}^P as a function of induced P_3 taken from resonance data on an x-cut bar at 141°C are shown in Figure 2, and of S_{33}^P and S_{44}^P taken from the resonance of a z-cut bar at 131°C are shown in Figure 3. Clearly, both S_{11}^P and S_{33}^P are linear functions of P_3^2 and the magnitudes of ϕ_{311} and ϕ_{333} can be deduced at the two temperatures from measurement of the slopes of the S_{ij}^P lines. It may be noted that from the separation of S_{11}^P and S_{33}^P the coupling coefficient can

be calculated, and since the permittivity at each P level is known from the P vs E Sawyer and Tower loops, the Q constant may be derived.

By repeating measurements of the field (polarization) dependence of the resonances at a sequence of temperatures above T_c it has been shown that ϕ_{333} and ϕ_{311} (Figure 4) are of opposite sign and change little with temperature. Thus the importance of the sixth order electrostriction coupling upon the elastic constant in the bronze ferroelectrics is clearly established.

The next question that must be addressed is whether the values of the ϕ_{ijklmn} constants measured under induced polarization in the paraelectric phase can be used as would be suggested by equations (26) to describe the changes in elastic behavior associated with the onset of spontaneous polarization in the ferroelectric phase. To make this next step, however, a special feature of ferroelectricity in the bronze structure materials must first be recognized. For many of these materials including the SBN bronze, it has been determined^{4,5,6} that the phase change at T_c is not abrupt, but is diffuse. Thus over a limited range of temperatures close to T_c paraelectric and ferroelectric phases coexist. The thermodynamic description which has been given above is appropriate for a completely homogeneous crystal which has an abrupt phase change at T_c . It may be used, however, also in good approximation to describe a crystal with diffuse transition if the transition temperature T_c is presumed to be distributed.

The choice of the distribution function and the stiffness parameters is rigorously limited by the need to fit the observed dielectric permittivity and spontaneous electric polarization data. For the 65:35 SBN the chosen parameters are

$$\begin{aligned} \alpha_3(0) &= 2.52 \cdot 10^{-6} / \text{o} \\ T_c - \theta &= 1 \text{ K} \\ P_0 &= 1.7 \text{ } \mu\text{C}/\text{cm}^2 \\ \bar{T}_c &= 350 \text{ K} \end{aligned}$$

The distribution of Curie points is gaussian with a halfwidth $\Delta T = 8 \text{ K}$.

For these parameters, measured and calculated polarization P_3 is shown in Figure 5, and the measured and calculated dielectric permittivity ϵ_3 in Figure 6.

Using precise x-ray diffraction measurements, the spontaneous elastic strain can be determined, and for a Q_{33} value of $0.40 \text{ m}^4/\text{C}^2$ the calculated strain is shown in Figure 7, and thus the ferroelectric contribution to α_c the linear thermal expansion along "c" in Figure 8.

A more detailed description of the simple LGD thermodynamic phenomenology for these diffuse transition crystals is being prepared for publication elsewhere. To accommodate the objectives of the present study the essential requirement was merely

to derive phenomenological values for $P_s(T)$, $x_1(T)$ and $x_3(T)$ over the ferroelectric temperature range. Taken together with the ϕ_{ijklmn} values derived from the higher temperature paraelectric measurements these could then be used to develop phenomenological s^P values which may be compared with the measured values obtained by extending the simple resonance studies down into the ferroelectric temperature region.

Comparison between the predicted and measured values for s_{11}^P , s_{12}^P and for a rotated cut (s_{11}^P) are shown in Figures 9, 10, and 11.

Discussion and Conclusions

The direct measurements by induced piezoelectric resonance in the paraelectric phase of SBN do show that in this crystal there is a clear coupling between the stiffened elastic compliance and the electric polarization level in the crystal. That the coupling is of the form which can be described by the sixth order electrostriction constants ϕ_{ijklmn} and that these constants derived from direct measurement over a range of temperatures above T_c do not change significantly with temperature.

Application of the full phenomenological theory in the bronze structure ferroelectrics is complicated by the fact that the phase change into the ferroelectric form in SBN and in many other members in this family of ferroelectrics is diffuse not sharp, a facet of behavior which has been postulated to occur due to local fluctuations in the cation site populations in the complex bronze structure leading to local fluctuations in the ordering temperature.

To first approximation, the equilibrium properties may be derived by applying a suitable distribution function to describe the Curie temperature distribution and then summing the contributions from ferroelectric and paraelectric volume fractions. The P_s data derived in this manner agrees well with measured data. Clearly, however, for dynamical properties such as the permittivity under AC field and the elastic compliance to alternating stress there may be time dependent rearrangement in the distribution of microvolumes and heterophase fluctuations which cannot be accounted for. This is manifest in the dielectric permittivity by a strong dispersion in the Curie range of temperatures, and only the very high frequency permittivity agrees with that derived from the distribution function which fits the polarization data.

In the elastic compliance measurements, which are taken from dimensional resonances at low radio frequencies, we believe that the compliance maxima at the Curie maximum are probably associated with an additional "softness" due to the mixed phase character near T_c . Outside the Curie range, the phenomenology does predict the trends of the observed elastic behavior and again it is clear that the sixth order constants play a very important role. If we assume that the compliance maximum at T_c is extrinsic and symmetric in temperature, and that we may subtract the additional extrinsic compliance the agreement near T_c is considerably improved.

A facet of the behavior of the SBN bronze which is particularly interesting is the observation that ϕ_{333} in this crystal is positive, so that the compliance s_{33}^P increases as the crystal polarizes. In the ferroelectric phase then, it is to be expected that as the P_s value is reduced on heating, the large positive ϕ_{333} will lead to an anomalous elastic stiffening.

Unfortunately, present attempts to verify directly the s_{33}^P values in the ferroelectric phase have been frustrated by the very large softening contribution from the diffuse broadening of the Curie point. We need to increase the measuring frequency to suppress the dispersive component and work is progressing in this direction.

Taken together with the strong dimensional coupling through Q_{33} which leads to the "anomalous" negative thermal expansion $\alpha(3)$ (Figure 8), the positive ϕ_{333} value does suggest that the bronze structure family will be of considerable interest as temperature compensated acoustic wave materials. Measurements which tend to confirm these characteristics for the SBN will be reported elsewhere.

There is as yet too little experimental information from other bronze family crystals to confirm the general utility of the phenomenological approach. The fact that seven ferroelectric species are theoretically possible while only two are actually observed in the hundreds of bronze ferroelectrics so far studied suggests that the higher order dielectric stiffnesses (α_{ijkl} , α_{ijklmn}) have a very limited range of values. That the Q constants change little with cationic makeup is confirmed by available data on Q_{11} from spontaneous polarization and spontaneous strain measurements in the orthorhombic bronzes.

If the Q constants do not change significantly, it is then logical to expect that the higher order ϕ constants will also be insensitive to cationic makeup but there is urgent need for more experimental data to confirm this hypothesis.

In conclusion

(i) The LGD phenomenology for simple proper ferroelectrics has been extended to include sixth order coupling parameters.

(ii) For the SBN ferroelectric bronze, the electric polarization does have a strong influence upon the elastic compliances s_{11}^P , s_{12}^P in a manner consistent with that predicted from the sixth order electrostriction.

(iii) Sixth order ϕ_{ijklmn} constants can be used to predict the elastic behavior for temperatures outside the Curie range in these diffuse phase transition crystals, but additional "anomalous" softening occurs in the mixed phase Curie region.

(iv) The observed behavior is consistent with higher order constants being only weakly composition and temperature dependent, but additional measurements of the ϕ constants in other ferroelectric bronzes are urgently needed.

(v) The phenomenological method does permit the correlation of low temperature data in the ferroelectric phase with a limited family of temperature independent higher order constants of the simpler

paraelectric symmetry and with accumulating experience, the possibility of predicting dielectric, thermal, piezoelectric and elastic response and its temperature dependence for all simple proper bronze ferroelectrics.

Acknowledgment

This work was supported by the Air Force Office of Scientific Research through Contract No. F49620-78-C-0093.

References

- 1) Barsch, G.R. and Newnham, R.E. (1975) Piezoelectric Materials with Positive Elastic Constant Temperature Coefficients. AFRL-TR-75-0163 Final Report No. 19628-73-C-0108.
- 2) Landolt Börnstein (1969 and 1973) Ferro and Antiferroelectric Crystals, New Series, Vol. 3 and Vol. 9.
- 3) Jana, F. and Shirane, G. (1962) Ferroelectric Crystals, p. 15-23.
- 4) Glass, A.M. (1969) J. Appl. Phys. 40, 4699.
- 5) Goodman, G. (1953) J. Amer. Ceram. Soc. 36, 368.
- 6) Baxter, P.A. and Hellicer, N.J. (1960) J. Amer. Ceram. Soc. 43, 578.

Figure Captions

1. Typical resonance spectrum for an SBN bar under DC bias above the Curie temperature \bar{T}_c .
2. Elastic compliances s_{11}^E, s_{11}^P as a function of induced electrical polarization in SBN at a temperature of 141°C.
3. Elastic compliances s_{33}^E, s_{33}^P as a function of induced electrical polarization in SBN measured at 131°C.
4. Measured values of ϕ_{333}, ϕ_{311} , and ϕ for a rotated cut taken from the slopes of s_{11}^P vs P^2 curves taken over a range of temperatures above \bar{T}_c .
5. Comparison of the measured P_s in SBN and the derived phenomenological P_s values using the distributed LGD model.
Experimental points derived from pyroelectric discharge and slow speed Sawyer and Tower measurements.
Dotted curve is distributed LGD using distribution parameters listed in the text.
6. Measured high frequency (1 MHz) weak field permittivity ϵ_3 for SBN compared to the calculated ϵ_3 (dotted line) using the distributed LGD model.
7. Comparison of measured and calculated spontaneous strain x_3 experimental data from x-ray lattice parameter measurement. Phenomenological fitting ($Q_{33} = 0.04 \text{ m}^4/\text{C}^2$) dotted curve.
8. Measured and derived thermal expansion α_3 .

9. s_{12}^P measured from piezoelectric resonance data, compared to s_{12}^P derived using ϕ value determined in the paraelectric phase.
— Experimental data
↔ Corrected for compliance maximum at \bar{T}_c
*** Phenomenological derivation
10. s_{11}^P measured from resonance data compared to s_{11}^P calculated using paraelectric ϕ values.
— Experimental data
↔ Corrected for compliance maximum at \bar{T}_c
**** Phenomenological values
11. $s_{11}^{P'}$ measured on a rotated cut, compared to $s_{11}^{P'}$ values calculated from high temperature ϕ values.
— Experimental data
↔ Corrected values
***** Phenomenological theory

Table I

Symmetry permitted second and fourth rank polar tensor for point symmetry 4/mmm

α_{ij} dielectric stiffnesses at constant stress
 α_{ijkl} fourth order stiffnesses at constant stress
 Q_{ijkl} quadratic electrostriction in polarization notation
 s_{ijkl} elastic compliances at constant P

WYE'S MATRIX NOTATION		FULL TENSOR NOTATION		No. of Equiv. Terms
Term	Symmetry Equivalent Terms	Term	Symmetry Equivalent Terms	
α_1	α_2	α_{11}	α_{22}	2
α_3		α_{33}		1
α_{11}	α_{22}	α_{1111}	α_{2222}	2
α_{12}	α_{21}, α_{66}	α_{1122}	$\alpha_{1212}, \alpha_{2211}, \alpha_{2112}, \alpha_{2121}, \alpha_{2211}$	
α_{13}	$\alpha_{31}, \alpha_{23}, \alpha_{32}, \alpha_{44}, \alpha_{55}$ ($\alpha_{44} = 4\alpha_{55}$)	α_{1133}	$\alpha_{3311}, \alpha_{2233}, \alpha_{3322}, \alpha_{1313}, \alpha_{1331}, \alpha_{3131}, \alpha_{2323}, \alpha_{2332}, \alpha_{3223}, \alpha_{3232}$	12
α_{33}		α_{3333}		1
Q_{11}	Q_{22}	Q_{1111}	Q_{2222}	2
Q_{12}	Q_{21}	Q_{1122}	Q_{2211}	2
Q_{13}	Q_{23}	Q_{1133}	Q_{2233}	2
Q_{31}	Q_{32}	Q_{3311}	Q_{3322}	2
Q_{33}		Q_{3333}		1
Q_{44}	Q_{55}	Q_{2323}	$Q_{2332}, Q_{3223}, Q_{3232}, Q_{1313}, Q_{1331}, Q_{3113}, Q_{3131}$	8
Q_{66}		Q_{1212}	$Q_{1221}, Q_{2112}, Q_{2121}$	4
S_{11}	S_{22}	S_{1111}	S_{2222}	2
S_{12}	S_{21}	S_{1122}	S_{2211}	2
S_{13}	S_{31}, S_{23}, S_{32}	S_{1133}	S_{2233}, S_{3322}	4
S_{33}		S_{3333}		1
S_{44}	S_{55}	S_{2323}	$S_{2332}, S_{3223}, S_{3232}, S_{1313}, S_{1331}, S_{3113}, S_{3131}$	8
S_{66}		S_{1212}	$S_{1221}, S_{2112}, S_{2121}$	4

Table II

Symmetry permitted sixth rank dielectric stiffness components α_{ijklmn} for point symmetry 4/mmm

TERM	SYMMETRY RELATED TERMS	NUMBER OF EQUIVALENT TERMS
1. α_{111}	222	2
2. α_{112}	166, 121, 616, 661, 211, 221, 266, 212, 626, 662, 122	30
3. α_{113}	155, 131, 515, 551, 331, 223, 244, 232, 424, 442, 322	30
4. α_{123}	144, 132, 525, 645, 546, 636, 663, 564, 654, 552, 321, 441, 231, 455, 366, 235, 456, 213, 414, 312	90
5. α_{133}	535, 553, 331, 355, 313, 233, 434, 443, 332, 344, 323	30
6. α_{333}		1

Table III

Sixth order electrostriction constants ϕ_{ijklmn} for point symmetry 4/mmm

TERM	SYMMETRY RELATED TERMS	NUMBER OF EQUIVALENT TERMS
1. ϕ_{111}	222	2
2. ϕ_{112}	121, 221, 212	4
3. ϕ_{113}	131, 223, 232	4
4. ϕ_{166}	266	8
5. ϕ_{244}	166	8
6. ϕ_{122}	211	2
7. ϕ_{123}	132, 213, 231	4
8. ϕ_{144}	255	8
9. ϕ_{133}	233	2
10. ϕ_{616}	661, 626, 662	16
11. ϕ_{636}	663	8
12. ϕ_{645}	664	16
13. ϕ_{424}	442, 515, 551	16
14. ϕ_{456}	445, 546, 564	32
15. ϕ_{414}	441, 525, 552	16
16. ϕ_{434}	443, 535, 553	16
17. ϕ_{311}	322	2
18. ϕ_{312}	321	2
19. ϕ_{313}	331, 323, 332	4
20. ϕ_{366}		4
21. ϕ_{344}	355	8
22. ϕ_{333}		1

Table IV

Values of the electrostriction constant Q_{11} for several ferroelectric bronze crystals calculated from spontaneous polarization and spontaneous strain values in the orthorhombic ferroelectric species

Compound	Electrostriction Constant	Reference
$0.25 \times \text{PbTa}_2\text{O}_6$	$Q_{11} \sim 5.3 \times 10^{-2} \text{ m}^4/\text{C}^2$	Subbarao, <i>et al.</i> , 1960
$0.75 \times \text{PbNb}_2\text{O}_6$		Francombe, <i>et al.</i> , 1958
$0.95 \times \text{PbNb}_2\text{O}_6$	$Q_{11} \sim 5.4 \times 10^{-2} \text{ m}^4/\text{C}^2$	Subbarao, <i>et al.</i> , 1960
$0.05 (2\text{PbTiO}_3)$		
$\text{Na}_2\text{Nb}_2\text{O}_{15} (\text{NN})$	$Q_{11} \sim 1 \times 10^{-2} \text{ m}^4/\text{C}^2$	Gautier, <i>et al.</i> , 1967
$(\text{Pb}_{0.8}\text{Ba}_{0.4/3})\text{Nb}_2\text{O}_6$	$Q_{11} \sim 5.7 \times 10^{-2} \text{ m}^4/\text{C}^2$	Subbarao, <i>et al.</i> , 1962
$\text{K}_2\text{BiNb}_2\text{O}_{15}$	$Q_{11} \sim 4 \times 10^{-2} \text{ m}^4/\text{C}^2$	Isaevskaya, <i>et al.</i> , 1963
		Krainik, <i>et al.</i> , 1964
$(\text{Ba}_{0.75}\text{Ca}_{0.25})\text{Nb}_2\text{O}_6$	$Q_{11} \sim 4.9 \times 10^{-2} \text{ m}^4/\text{C}^2$	Isaevskaya, 1960
$0.95 \times \text{PbNb}_2\text{O}_6$	$Q_{11} \sim 6.8 \times 10^{-2} \text{ m}^4/\text{C}^2$	Subbarao, 1960
$0.05 (2\text{PbZrO}_3)$		
$\text{Pb}_{1.05}(\text{Nb}_{0.95}\text{Sb}_{0.05})_2\text{O}_6$	$Q_{11} \sim 5.6 \times 10^{-2} \text{ m}^4/\text{C}^2$	Subbarao, <i>et al.</i> , 1960

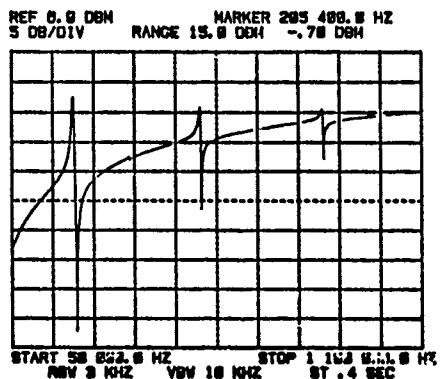


Figure 1

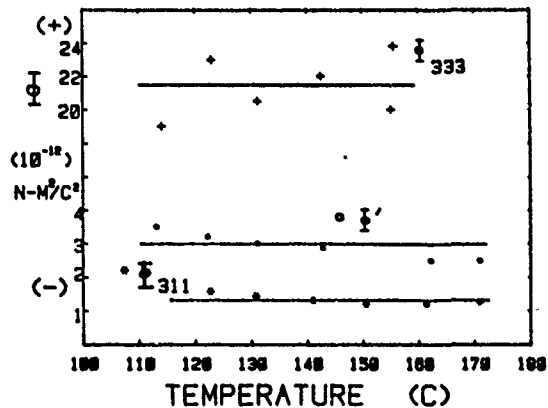


Figure 4

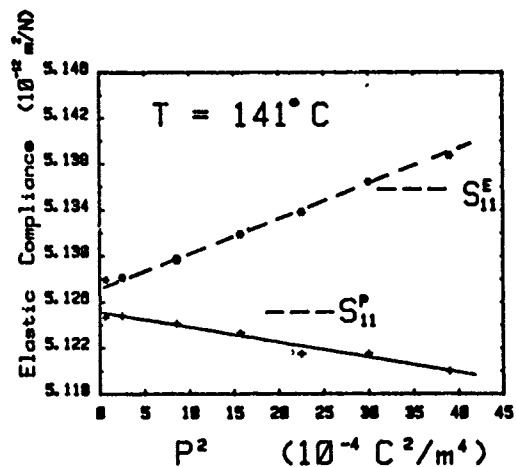


Figure 2

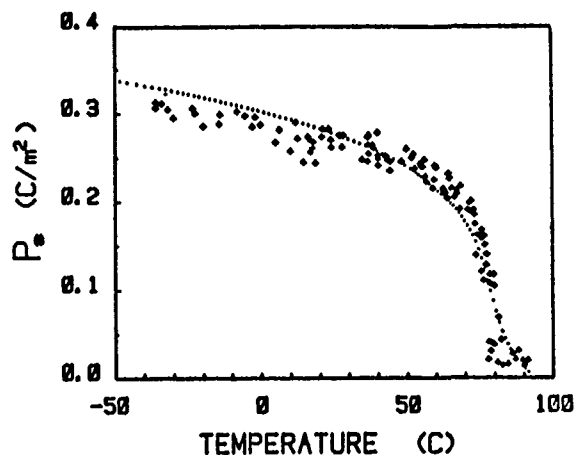


Figure 5

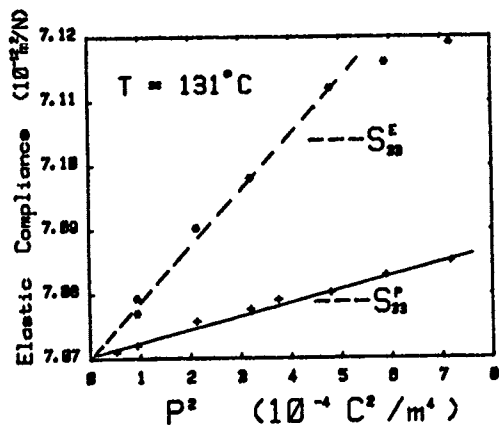


Figure 3

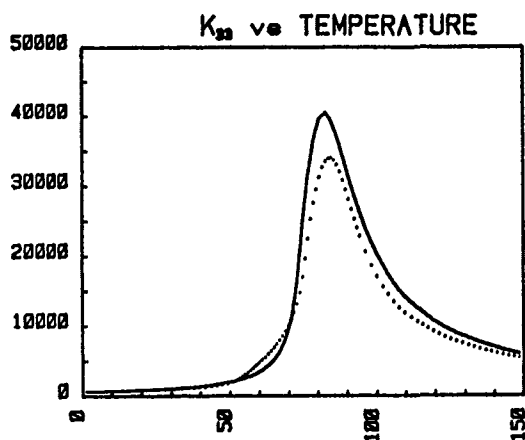


Figure 6

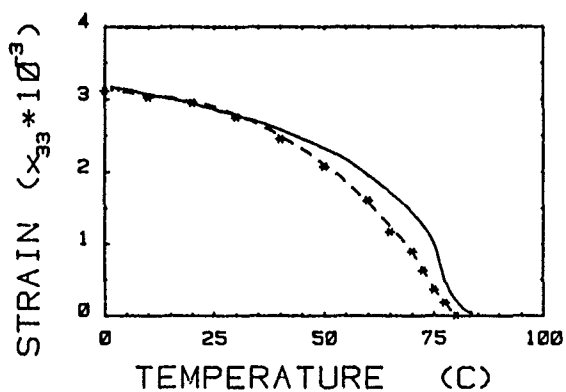


Figure 7

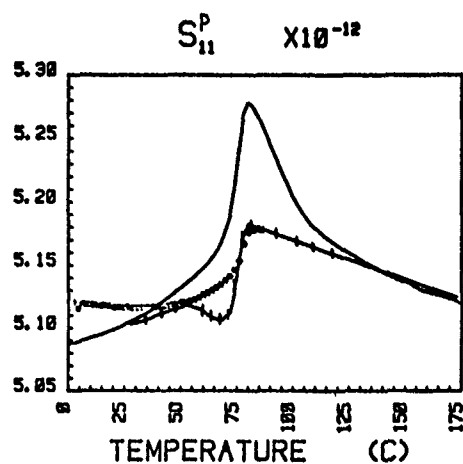


Figure 10

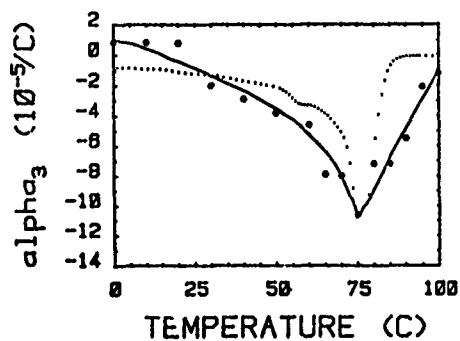


Figure 8

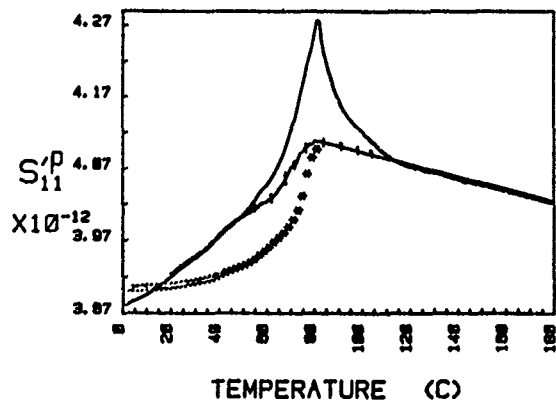


Figure 11

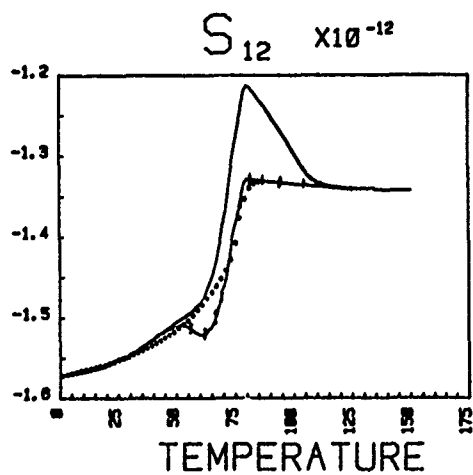


Figure 9

AN ON-WAFER DETECTION METHOD OF THE IMBALANCE OF QUARTZ TUNING FORK RESONATORS

P.E. Debély and R.J. Dinger

ASULAB SA - Neuchâtel - Switzerland

Abstract

A measurement technique for the asymmetry of tuning fork quartz resonators is presented. The method is capable of quantitatively measuring the imbalance of tuning forks made by photolithographic methods while the resonators are on the wafer. For watch size tuning forks vibrating at 32768 Hz a sensitivity of 10 μ V per Hz of imbalance may be achieved and the detection limit is approximately 1 Hz.

1. Introduction

The tuning fork has in recent years become the dominant design for low frequency quartz resonators. Especially for wrist watch applications, tuning fork resonators vibrating at 32768 Hz have almost completely eliminated previous designs (such as the flexure bar type resonators). This is mainly due to the easier mounting of the tuning fork which results in improved shock and aging characteristics and lower manufacturing costs.

Many of the mechanical and electrical parameters of a quartz tuning fork, however, depend to some extent on the imbalance or asymmetry of the resonator. This phenomena is well known from tuning forks manufactured by mechanical techniques (1-3). The improved accuracy of the photolithographic manufacturing technique (4,5) rendered the problem less important. To take full advantage of its potential for miniaturisation and to obtain the best possible parameters with a given resonator size, balance becomes more important as the devices decrease in size.

As an illustration, Table 1 shows the mechanical parameters of a tuning fork of watch size dimensions (total length 3.6mm, tine length 2.4mm, tine width 0.22mm, thickness 0.125mm) as a function of the imbalance. The latter was varied by adding a small droplet of epoxy to the top of the tine.

Test condition	Frequency Hz	Imbalance Hz	Q (1000)	T ₀ (°C)
Initial condition	33'000	-17	50	+7.5
Added drop to tine A	32'955	+28	33	+25.5
Added 2nd drop to tine A	32'905	+78	7	-18.5
Added drop to tine B	32'875	+48	14	+15.9
Added 2nd drop to tine B	32'799	-28	34	+25.6

Table 1: Quality factor Q and inversion temperature T₀ as a function of the imbalance.

The table shows that the quality factor Q as well as the temperature behavior of the tuning fork (shown is the inversion temperature T₀ of the f(T) parabola) are strongly influenced by the imbalance of the tuning fork. The imbalance is expressed in Hz, the frequency shift caused at the tuning fork by the added mass of the epoxy drop.

The degradation of the quality factor and the frequency temperature behavior depends on the imbalance, the tuning fork design and to a large extent on the mounting conditions. Figure 1 shows

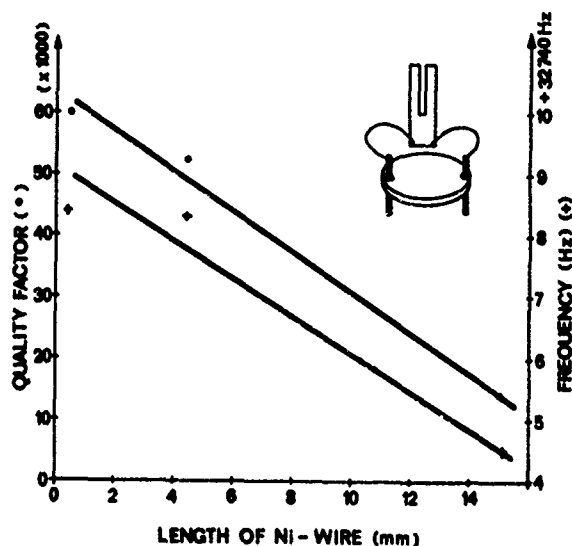
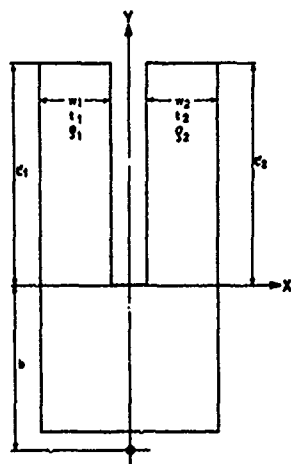


Fig. 1 - Quality factor (•) and frequency (+) of a tuning fork mounted with 2 Ni-alloy wires as a function of the wire length.

the frequency and quality factor of a tuning fork (5mm long, tine length 3mm, tine width 0.4mm, thickness 0.1mm) mounted with two low-loss nickel alloy wires as shown in the insert. The length of the wires was shortened successively without modifying the bond of the wire at the tuning fork. It may be seen that the quality factor as well as the frequency strongly depend on the length of the wires.

2. Symmetry Condition for a Tuning Fork

We consider a tuning fork with small symmetry defects and ask for the minimum requirement for zero energy loss (due to the imbalance). Using the nomenclature shown in figure 2 for the



homogeneous tines and neglecting all movements except the displacement parallel to the x-axis we may assume the displacement $X(y, t)$ of the tines to be

$$X(y, t) = A \cdot X\left(\frac{y}{L}\right) \cdot \cos \omega t$$

$$= A X(\xi) \cdot \cos \omega t$$

where ω is the frequency, A the amplitude of vibration and ξ the dimensionless coordinate which takes the values

$$0 \leq \xi \leq 1.$$

Fig. 2 - Tuning fork with small symmetry derivations. L' length, w width, t thickness and ρ density of the homogeneous tines.

$X(\xi)$ shall be a function which is the same for both arms of the tuning fork (as long as the asymmetry is small). In general the tuning fork will move around a pivot which shall have the y-coordinate of $-b$.

Neglecting the x-dimension of the tuning fork (but taking into account the arm width w) we now ask for conservation of momentum and angular momentum with respect to the pivot. Assuming the base portion of the tuning fork does not contribute we obtain

$$0 = A_1 w_1 t_1 \rho_1 L'_1 + A_2 w_2 t_2 \rho_2 L'_2 \quad \text{and} \quad (2)$$

$$0 = A_1 w_1 t_1 \rho_1 L'_1 [L'_1 c_1 + b c_2] + A_2 w_2 t_2 \rho_2 L'_2 [L'_2 c_1 + b c_2] \quad (3)$$

$$\text{where } c_1 = \int_0^1 \xi \cdot X(\xi) d\xi \text{ and}$$

$$c_2 = \int_0^1 X(\xi) d\xi.$$

Combination of eq. 2 and 3 yields

$$L'_1 = L'_2 \quad \text{and} \quad (4)$$

$$\frac{A_1}{A_2} = - \frac{w_1 t_1 \rho_1}{w_2 t_2 \rho_2} = - \frac{m_1}{m_2} \quad (5)$$

where m_1 and m_2 stand for the mass of the two tines.

Eq. 4 shows that conservation of momentum and angular momentum requires the tine lengths to be equal. This means that uneven tine length inevitably leads to momentum (and energy) transfer to the mount. In eq. 2 and 3 there is no contribution from the base part of the tuning fork, which was assumed not to move. This means that the torque acting on the base must also vanish. Using eq. 1, 4 and the fact that the torque is proportional to the second derivative of the displacement and to the moment of inertia of the section of the tine, one obtains

$$A_1 w_1^3 t_1 = A_2 w_2^3 t_2 = 0 \quad (6)$$

Combination of eq. 5 and 6 leads to

$$\frac{w_1^2}{\rho_1} = \frac{w_2^2}{\rho_2} \quad (7)$$

If the proper frequency of the tuning fork's tines are calculated using the model of the clamped cantilever (6) one finds

$$\omega \approx \sqrt{\frac{E}{\rho}} \cdot \frac{w}{L'^2} \quad (8)$$

E being the elastic modulus. Since L' must be equal, eq. 7 obviously means that the proper frequencies of the tuning fork's tines must also be equal. (The tuning fork always vibrates at the mean frequency of its tines). In conclusion one

may say that in order not to transmit imbalance energy to the mount a tuning fork must satisfy the following conditions:

1. Equal tine length
2. Equal proper frequency of its tines.

3. Measurement of the Asymmetry

The measurement technique for the asymmetry has been developed for quartz tuning fork resonators made by the photolithographic process. In this process, which has been introduced by STATEK Corp. (4) and has been adopted by SEIKO (5) and ASUAG, the resonators are manufactured by batch processing from a polished and metallized wafer by photolithographic techniques and chemical milling. During the manufacturing process the individual resonators remain attached to a frame-work consisting of unetched parts of the quartz wafer as shown in fig. 3. The connection between

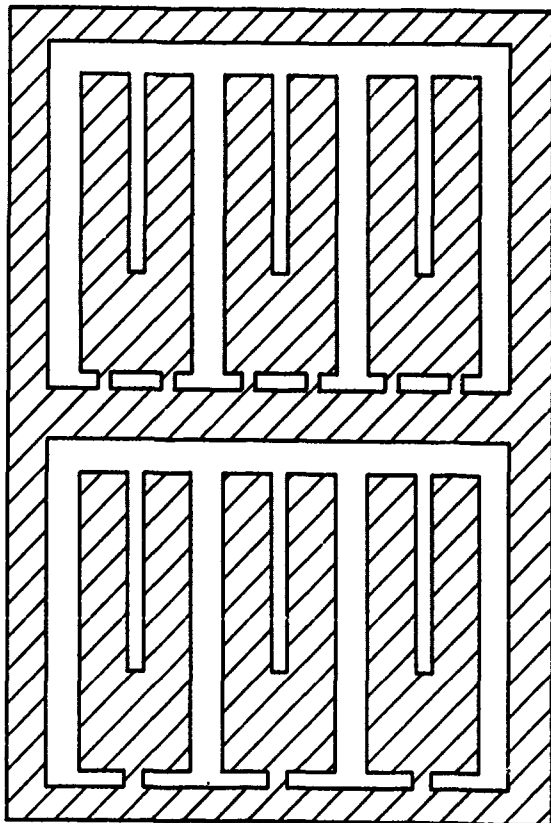


Fig. 3 - Quartz wafer with tuning forks. Upper half: two-stem arrangement, lower half: one-stem arrangement.

the tuning forks and the frame of the wafer is realized by one or two little stems which are broken once all the on-wafer operations are finished and the parts are ready for assembly. Since the base region of an unsymmetrical tuning

fork moves with respect to the symmetry plane of the tuning fork the little stems can be used to measure the asymmetry by covering them with the appropriate electrodes to capture the piezoelectric signal due to deformation of the stems. For the arrangement using one stem per tuning fork a flexure signal must be detected. For the arrangement using two stems per tuning fork the stems are alternatively compressed and expanded. The electrode system used to capture these stresses is shown in fig. 4. The resonator is driven through

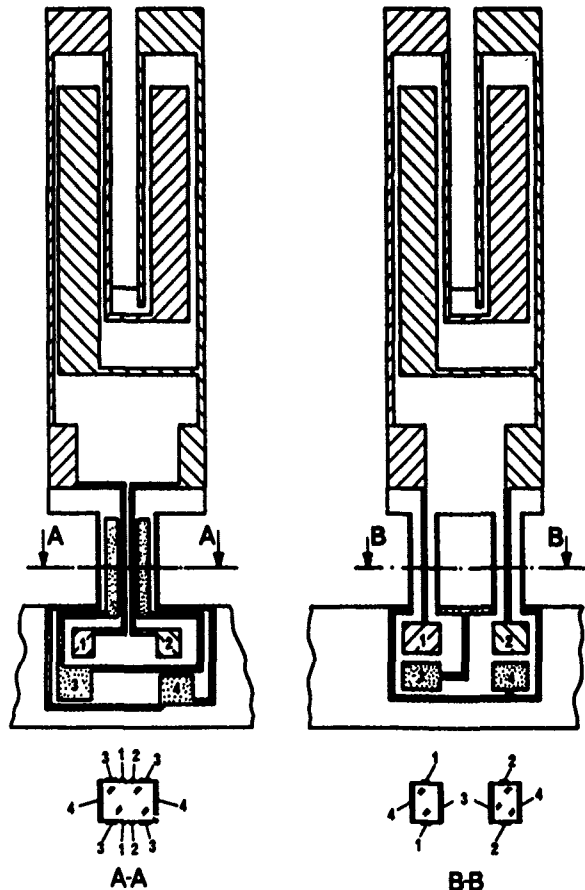


Fig. 4 - Electrode design and tuning fork geometry. Tuning fork length=5.3mm, tine length=3.1mm, tine width=0.4mm, thickness=0.1mm, stem width=0.15mm, stem length=0.4mm, stem separation=0.27mm.

contacts 1 and 2 and the signal due to the asymmetry is picked up at contacts 3 and 4. For one-stem resonators the electrode arrangement is similar and acts in the same manner as the main electrodes on the tuning forks tines. The stems of the two-stem arrangement are covered with the electrode system of a x-cut length extension resonator connected antiparallel.

The sensitivity of the two stem arrangement may be calculated if we assume that the clamping effect due to the stems is negligible which means that we may consider the resonator as moving freely.

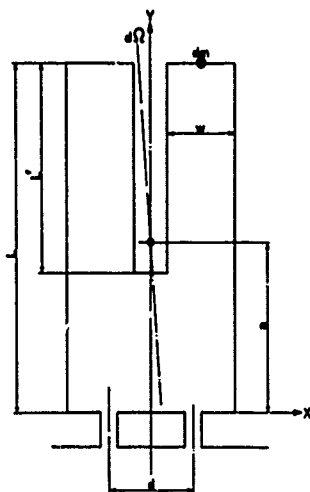


Fig. 5

Explanation see text

We start with a perfectly symmetrical tuning fork and add a small additional mass dm to one of its tines. Conservation of angular momentum requires that the entire tuning fork moves around its center of gravity to compensate the angular momentum of dm . This is equivalent to stating that the heavier tine of the tuning fork moves with a smaller amplitude. If A is the amplitude of the symmetric tuning fork and Θ its moment of inertia with respect to the center of gravity, the tuning fork moves with an angular amplitude $d\Omega$ given by

$$d\Omega = A \frac{L-a}{\Theta} \cdot dm \quad (9)$$

where a is the distance of the center of gravity from the base and L the length of the tuning fork. This movement causes a length extension at the stems of amplitude $d\xi$ where

$$d\xi = \frac{1}{2} d \cdot d\Omega \quad (10)$$

d being the distance between the two stems. This will cause a piezoelectric charge dQ at the transducers electrodes

$$dQ = 2 d_{11} E \cdot t \cdot d\xi \quad (11)$$

where d_{11} is the piezoelectric constant, E the elastic modulus and t the thickness of the resonator. Combining eq. 9 to 11 one obtains

$$dQ = E \cdot d_{11} \cdot t \cdot d \cdot \frac{L-a}{\Theta} \cdot A \cdot dm. \quad (12)$$

For practical purposes the driving current I is substituted into the equation in place of the amplitude A of the resonator. To do so, we

consider the energy of the vibrating tuning fork which in terms of the equivalent circuit is

$$E_{el} = \frac{1}{2} L_1 I^2 = \frac{1}{2} \frac{I^2}{\omega^2 C_1} \quad (13)$$

where L_1 and C_1 are the motional inductance and capacitance of the resonator and ω its resonant frequency. The elastic energy of the tuning fork may be calculated assuming the tuning fork as composed of two cantilevers clamped at one end. The elastic energy is given by

$$E_{mech} = \frac{1}{2} E \int_0^L I_x \left(\frac{\partial x}{\partial y} \right)^2 dy \quad (14)$$

where $x(y)$ is the displacement of the tine, the y -coordinate is parallel to the length of the tine and I_x is the moment of inertia of the cross section of the tine. The integral may be solved and the mechanical energy of both tines is

$$E_{mech} = \frac{1}{2} E A^2 t \frac{w^3}{L^3} \times 20.98 \quad (15)$$

where w , is the width and L' the length of the tines. Combination eq. 12, 13 and 14 we obtain

$$dQ = 0.22 \frac{d_{11} L' d \cdot (L-a)}{\omega \cdot w \cdot \Theta} \sqrt{\frac{E t L'}{w C_1}} \cdot I \cdot dm \quad (16)$$

Finally, replacing dm by the induced frequency shift according to

$$\frac{df}{f} = \frac{dm}{m} \quad (17)$$

where m is the mass of one tine and df the frequency shift of the tuning fork due to dm , we obtain

$$dQ = 0.44 \pi \frac{d_{11} d (L-a) L'^{5/2} t^{3/2} E^{1/2} \rho}{\omega^2 \Theta w^{1/2} C_1^{1/2}} \cdot I \cdot df \quad (18)$$

where ρ is the density of the tuning fork. Some comment is necessary to avoid misinterpretation of the above formula. Although it appears that the charge dQ is proportional to the separation of the two stems d , it should be noted that we derived this equation under the assumption of a free moving resonator. The larger the separation d the more closely the system approaches a clamped tuning fork's behavior.

With the dimensions shown in fig. 4 one obtains a numerical value of

$$dQ = 8.45 \times 10^{-12} \frac{C}{V} \cdot I \cdot df.$$

If the charge is measured with charge sensitive preamplifiers of a differential input capacity of 5 pF one obtains a sensitivity of

$$\frac{dV}{I df} = 2.02 \frac{\mu V}{\mu A \cdot Hz}.$$

4. Experimental Arrangement

To measure the small voltages generated by the stems phase-lock measurement techniques must be used. The block diagram of the setup is shown in fig. 6. The resonator is driven by the synthe-

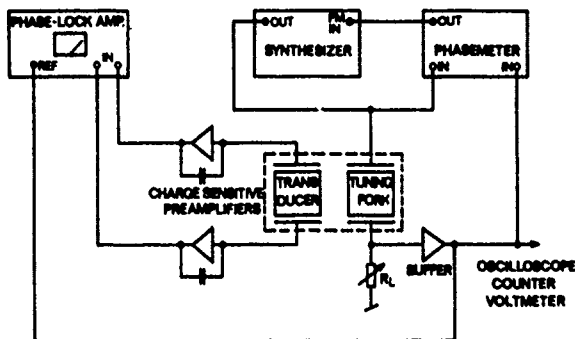


Fig. 6 - Block diagram of the experimental arrangement.

sizer - phasemeter loop. The current signal of the tuning fork serves as a reference for the phase-lock amplifier which measures the imbalance voltage. The charge generated by the transducer is measured with charge sensitive preamplifiers. Due to the capacitive input impedance of these amplifiers there is a 90° phase-shift between the reference signal and the transducer signal which suppresses the capacitive pick-up signal due to the driving voltage of the resonator. (With a capacitive input impedance at the charge sensitive preamps the latter is in phase with the driving current). Even with the suppression due to the phase-lock technique it is important to control the geometry of the leads connecting the tuning fork and the transducer stems for compensation of the capacitive pick-up. An alternative technique has also been used to suppress the influence of the stray-capacitance for laboratory type measurements: variation of the quality factor of the tuning fork by variation of the pressure in the measuring chamber allows one to maintain the driving voltage and the voltage across the load resistor R_L at a constant level, as well as to vary the resonator current. Since the asymmetry signal is proportional to the resonator current it may be found even on a strong background of capacitive signal.

5. Experimental Results

Watch size tuning forks have been made using both arrangements discussed in part 3. The geometry used is shown in fig. 4. The imbalance signal observed with a resonator of the two-stem configuration is shown in fig. 7 and 8 as a function of

the resonator current. These results were obtained using the technique of varying the quality factor to demonstrate and suppress the influence of the stray capacitors discussed in part 4. Figure 7 shows the tuning fork in its initial condition.

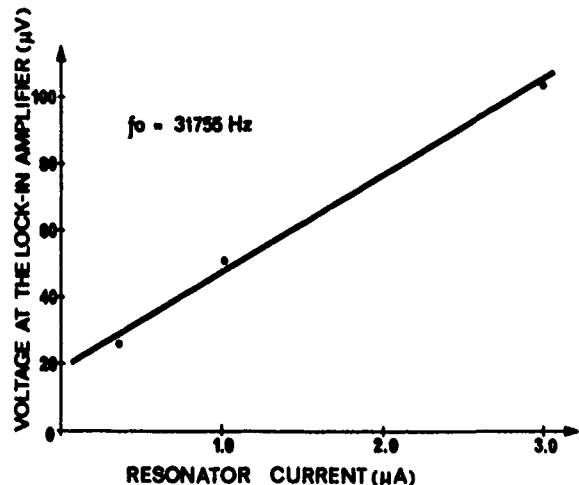


Fig. 7 - Imbalance voltage vs. resonator current of an unmodified tuning fork with the two-stem transducer.

It can be seen that the experimental points are on a straight line as predicted by eq. 18. The slope of the straight line gives the asymmetry and the zero intercept the influence of the capacitive pick-up. The imbalance of this tuning fork was then increased by adding a small drop of epoxy to the right tine. This caused the resonant frequency to decrease by 308 Hz and increase the imbalance signal as shown in fig. 8.

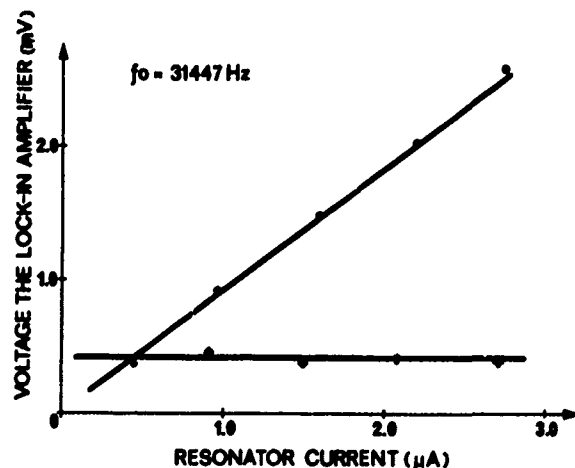


Fig. 8 - Imbalance voltage vs. resonator current of the tuning fork of fig. 7 after adding a drop of epoxy to the right tine. (•) signal at 90° , (+) signal at 0° .

From this measurement one obtains a sensitivity of

$$\frac{dV}{I df} = 3.24 \frac{\mu V}{\mu A \cdot Hz}$$

Considering the numerous approximations used in part 3 (especially the use of the clamped cantilever model to calculate the relationship between the amplitude and the current), the agreement between the above result and the theoretical result is satisfactory.

As indicated in part 4, the signal due to the imbalance shows a 90° phase shift with respect to the current signal of the tuning fork. In fig. 8 both components of the signal are plotted and it may be seen that the in phase component remains constant, which clearly demonstrates that it is due to capacitive pick-up only. This pick-up voltage is in the order of $400 \mu V$. The detection limit of the present imbalance measuring system may be given by the imbalance voltage causing a signal that is equal to the pick-up signal in the 90° component. If we assume a phase adjustment error of 2° we obtain an error voltage due to pick-up of about $15 \mu V$ (which corresponds to the zero intercept in fig. 7) giving a detection limit (at a tuning fork driving current of $5 \mu A$) of about 1 Hz.

The electrical parameters of the tuning fork have been measured before and after the addition of the imbalance mass. Of special interest is the quality factor which was in both cases about 130'000. This justifies the assumption made in part 3 of a free moving tuning fork because a clamped fork shows a strong degradation of the quality factor if it is as asymmetric as the one shown in fig. 8.

The same measurements have been performed with tuning forks of the one stem transducer configuration. The results are shown in the figures 9-11. Figure 9 shows the resonator in its initial

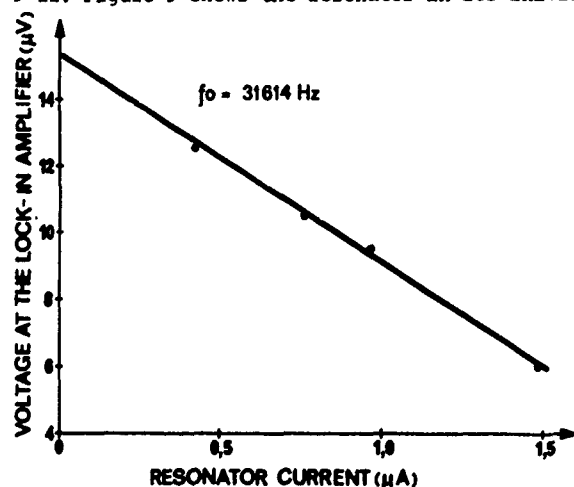


Fig. 9 - Imbalance voltage vs. resonator current of an unmodified tuning fork with the one-stem transducer.

condition. It may be seen (from the negative slope of the straight line) that this fork has a negative imbalance voltage (with respect to the one discussed in fig. 7 and 8) which means that the heavier tine is now on the left. Fig. 10 shows

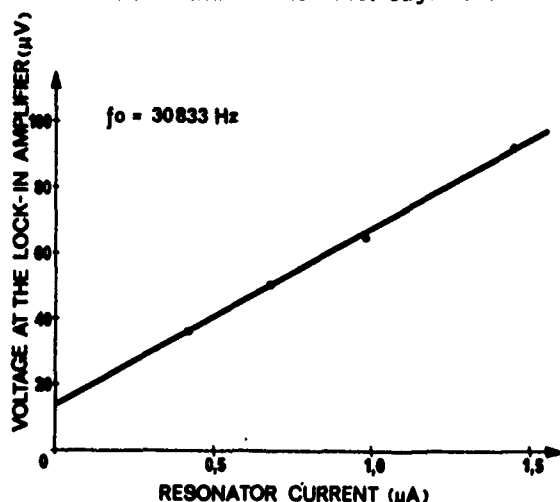


Fig.10 - Imbalance voltage vs. resonator current of the tuning fork of fig. 9 after adding a drop of epoxy to the right tine.

the same resonator after a drop of epoxy has been added to the right tine. The imbalance has changed sign and increased greatly, as may be seen from the transducer response. The asymmetry was then reduced by adding a drop of epoxy to the left tine and the result is shown in fig. 11. The sensitivity of this arrangement is considerably lower

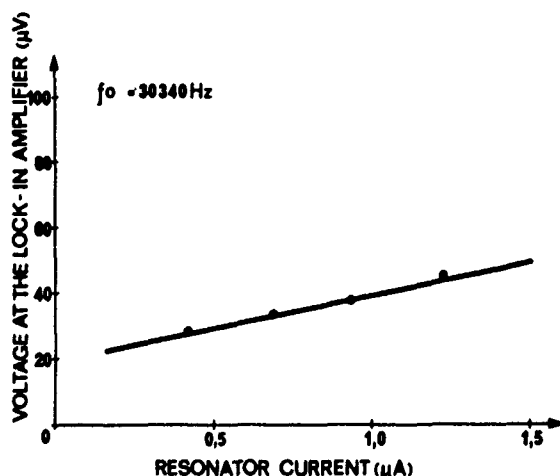


Fig.11 - Imbalance voltage vs. resonator current of the tuning fork of fig. 10 after adding a drop of epoxy to the left tine.

than the one of the two stem arrangement. From these measurements

$$\frac{dV}{I df} = 0.07 \frac{\mu V}{\mu A Hz}.$$

It should be mentioned, however that the measurements with the one stem tuning forks were done using two bonded gold wires instead of the metalization strips 1 and 2 (cf. fig. 4) to contact the tuning fork. These gold bonds clamp the tuning fork considerably which reduces the sensitivity of the arrangement. The clamping effect of the bonds may be seen also in the quality factor, which was 81000 for the tuning fork in its initial condition, decreased to 59000 after the drop to the right tine (fig. 10) and increased to 71000 after the "compensation" drop to the left tine.

6. Conclusion

This paper presents a method for measuring the imbalance of quartz tuning fork resonators manufactured by the photolithographic process. The measurement may be performed while the resonators are still on the wafer and the information obtained may be used to correct the imbalance in this stage of the manufacturing process. Using the cantilever model for the tuning fork, it is shown that the conditions for a "symmetric" tuning fork (a tuning fork that does not transmit energy to the mount due to imbalance) are:

1. The length of the two tines must be equal.
2. The proper frequency of the two tines must be equal.

This means that symmetry defects (except for differences in the tine length) can be corrected using the known means of frequency adjustment of a tuning fork (laser or evaporator) if these equipments are modified to act on one tine only. The measurement system for the imbalance presented in this paper is capable of determining without trial and error which of the two tines of the tuning fork must be treated to correct for the imbalance. This is particularly advantageous for control of the correction tool.

The method is capable of measuring the imbalance quantitatively. Depending on the geometry, a sensitivity in the order of 10 μV per Hz of imbalance may be achieved for watch size tuning forks vibrating at 32768 Hz. The imbalance detection limit is about 1Hz.

Acknowledgements

The authors would like to thank Jean Beiner and Hubert Portmann for stimulating discussions and Jean-Baptiste Vienot for technical assistance.

References

- (1) T. Koyama, Jap. Pat. Appl. No.52-126 950
- (2) F. Katon, Jap. Pat. Appl. No.52-38083
- (3) Y. Kato, Jap. Pat. Appl. No.50-71495
- (4) J.H. Staudte, Proceedings of the 27th Symp. on Frequency Control (1974) p. 50
- (5) K. Oguchi et al., Proceedings of the 32nd Symp. on Frequency Control (1978) p. 277
- (6) L.D. Landau und E.M. Lifshitz: Elastizitätstheorie, Akademie-Verlag, Berlin 1966 p. 129
- (7) same as (6) p. 88.

A MICRO-PROCESSOR ASSISTED BASEPLATING APPARATUS
WITH IMPROVED PLATEBACK DISTRIBUTION

Dick Ang

Tyco Crystal Products
Phoenix, Arizona

Summary

Baseplating is a first metalization procedure for the electrodes of quartz resonators which are processed in large quantities. Ideally we would like the thickness as uniform as possible and of the desired thickness such that subsequent processing to adjust each resonator to its target frequency can be performed as efficiently as possible. This paper attempts to describe a simple method of supporting baseplating masks in a vacuum system to achieve good uniformity and the associated electronics which is utilized to manage the deposition process.

Introduction

Although many deposition fixtures have been devised and manufactured for the semiconductor industry, few if any are available for the quartz industry. With the exception of uniform thickness distribution of evaporant on all the blanks, the requirements of thin film deposition on semiconductor blanks differ from quartz crystals. For example both surfaces on the quartz blank (in bulk resonators) have to be metallized, only one surface is metallized on semiconductor device fabrication. In general semiconductor blanks are metallized without a pattern on it, the pattern is generated subsequently using photolithography or other suitable methods. Quartz blanks for bulk resonators are generally metallized via a shadow mask; excessive vibrations during deposition can result in electrode misalignment. Therefore complex motion fixtures which are utilized in semiconductor applications designed to achieve film uniformity generally are not readily applicable to quartz crystal industry. As a result most crystal manufacturers improvise their own methods to achieve good thickness uniformity in their deposition procedures. A paper by Dybwad¹ describing a deposition fixture for monolithic crystal filters

is perhaps some supporting evidence on this conjecture.

In this paper I will try to explain what has been done at TYCO to improve the thin film thickness distribution over our previous system.

Optimization Procedure

As is well known the amount of evaporant incident upon a surface is dependent on the source distribution, i.e. the type of source; the distance from the source to the target (blanks or wafers) and the angle of incidence of the evaporant flux onto the target. The source distribution at some fixed distance from the source can be described in terms of θ , ϕ , and R_o . If the source is isotropic, then the distribution is only a function of R_o . By defining the distance from the source to the substrate as R_i , and the angle of incidence of the flux as ψ_i ($\psi = 0$ is normal incidence), the amount of mass at any position R_i can be expressed as:

$$M_i \propto F(\theta, \phi, R_o) \frac{R_o^2}{R_i^2} \cos \psi_i$$

Our previous fixturing for baseplating consists of a flat holder which holds four 5" x 5" baseplating masks in a horizontal plane at about 16" from the evaporant source, see figure 1. The typical electrode distribution is shown in figure 2. Several factors result in the large non uniform distribution of the film thickness. The blanks furthest from the source receives much less evaporant than those which are centrally located and closest to the source. Those which are centrally located receive the evaporant flux at about normal incidence while those at the outer parts receives the evaporant flux at more oblique angles. The effects of the inverse square law on the distance between the target and the source reduce the flux still further and finally the decrease of the flux from the source due to the non-isotropic behaviour results in a plate-back which is not uniform. In fact the data for a flat mask configuration shown in figure 1 results in a standard deviation of about $0.12 F^2$ for

a 1.00 F^2 mean plateback.

Our present fixturing for baseplating is shown schematically in figure 3. To compensate for the decrease in the evaporant incident on the outer areas of the masks it is necessary to decrease the distance of the outer areas to the source by drooping the masks. By supporting the masks at a dihedral angle instead of in a flat plane, we are also improving the angle of incidence of the evaporant flux (Ψ) closer to normal incidence such that $\cos \Psi$ approaches 1. In contrast the evaporant arriving at the central areas of the fixture will now have to travel a further distance and arrive at angles of incidence which are more oblique. By computing the value for each M_i equation 1 for a specific source distribution (i.e. type of boat) and optimizing the distribution of M_i ; an angle can be found which will yield the minimum non-uniformity in the evaporant thickness over the whole mask.

For a dimple type of source we found that the "droop angle" or dihedral angle which gives us the best distribution is about 30° from the horizontal. The results of the "drooping mask support" can be contrasted to that of the flat mask fixture of figure 2. The standard deviation of the compensated fixture is about $0.03 F^2$ while that of the non compensated fixture is $0.12 F^2$; both are for a $1.00 F^2$ mean plate back.

Instrument Description

The actual system is shown in figure 6. It consists of a hub with four dihedral shafts at an angle of 30° and one vertical shaft. The mask holders are attached at the end of the four dihedral shafts. Each of the four $5" \times 5"$ baseplating masks can be slipped in and out of the mask holders. They are held in place during the baseplating cycle by a "spring loaded ball detent retainer".

The vertical shaft drives the four dihedral shafts via 5 identical bevel shaped gears. The vertical shaft is in turn driven by a reversible ferrofluidic sealed motor. With the exception of the gears, all the parts are manufactured from stainless steel and is therefore bakeable at moderate temperatures. No attempt was made to seal the hub which encloses the gear and shaft mechanisms. In fact large holes are drilled on the top surface of the hub to facilitate vacuum pump out. The hub assembly including the mask holders, ferrofluidic motor, are supported by two vertical stainless steel posts from the baseplate. The entire assembly is designed such that it can be disassembled and re-assembled easily. Acid cleaning can be

performed on the system because most of the parts are made of stainless steel.

In this configuration the masks are rotated about the dihedral shafts for deposition on the second surface. Although a further improvement could have been obtained by rotating the masks about an axis in the plane of the baseplate; i.e. an axis which is orthogonal to the present axis; the additional improvement would have been obtained by an imbalance of plating between the quartz surfaces. A substantial amount of imbalance of plating between the quartz resonator surfaces can result in the excitation of even ordered overtone modes of the crystal and on occasions may result in "activity dips" over temperature. Therefore we decided to maintain our present axis of rotation. As mentioned earlier, a ferrofluidic motor drives the shaft over an angular rotation of 180° . This angle is ascertained by mechanical stops which prevents the shaft from turning beyond 180° . The ferrofluidic motor is de-energized at the end of its travel by a current overload sensor.

In view of the fact that we have had problems with training baseplating operators, we incorporated a micro-processor to aid the operation of the baseplating system. The micro-processor used in this system utilizes high level language (basic), because we intend to retain a large portion of flexibility for future modifications. All the pertinent deposition parameters and tasks are controlled by the micro-processor. Parameters such as pressure, pump down performance, plate back on the blanks are measured directly via A to D convertors or entered as data on the CRT monitor. All other parameters which have to be transmitted to the baseplating system is done via D to A convertors through appropriate interface. All that is required from the operator, after the masks are inserted and the source replenished with new evaporant material, is to enter the average frequency of the blanks and the target frequency. The required plateback on the blanks and on the deposition monitor crystal is automatically computed from these data. The micro-processor is programmed to sense the vacuum system performance and performing the deposition tasks; i.e. preheating the filaments, outgassing the evaporant, opening the shutter for evaporation and terminating the evaporation process; then rotating the masks after the first half of the deposition cycle and completing the second half of the cycle. The deposition pressure is sampled periodically and compared to the limit programmed into the system. Deposition failures are analyzed in terms of pressure failure, evaporation exhaustion, broked filament, transformer failure or monitor failure, and are displayed as a specific abort message.

Conclusion

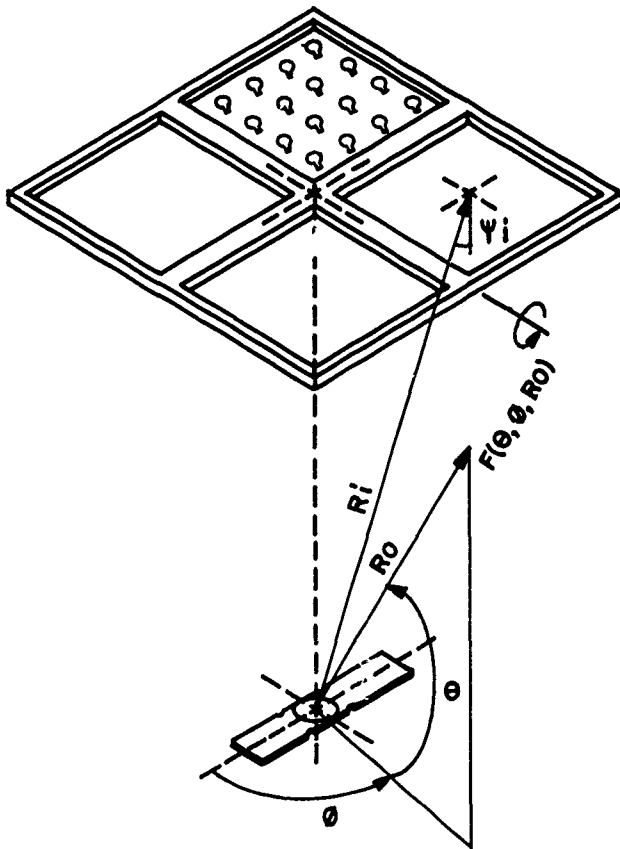
A simple compensated fixturing for baseplating has been described. The compensation is obtained by "drooping" the mask at a dihedral angle. For a "dimple" type source the dihedral angle is about 30° . The plateback uniformity is improved by about a factor of four over a flat fixture. The entire baseplating procedure associated with the actual deposition is simplified considerably to entering the average blank frequency and target frequency and replenishing the evaporant.

Aknowledgements

I would like to thank Mr. E. Kimberly for his technical support in this project. I would like to acknowledge the support of the Electronics and Machine shop of TYCO for their excellent work.

References

1. G. L. Dybwad, "Simplified Fixtures With Improved Thin Film Deposition Uniformity On Quartz Crystals", Proceedings of the 32nd Annual Symposium on Freq. Control, pp. 286-289, 1978.



$$M_i \propto F(\theta, \theta, R_0) \frac{R_0^2}{R_i^2} \cos \psi_i$$

Fig. 1 FLAT FIXTURE

PLATE BACK UNIFORMITY FOR
 $\frac{1}{S} F^2$ PLATE BACK
 $\frac{1}{S} \approx 0.12 F^2$

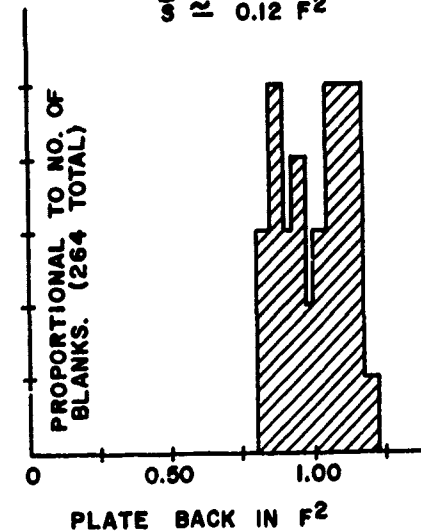


Fig. 2 FLAT FIXTURE DATA

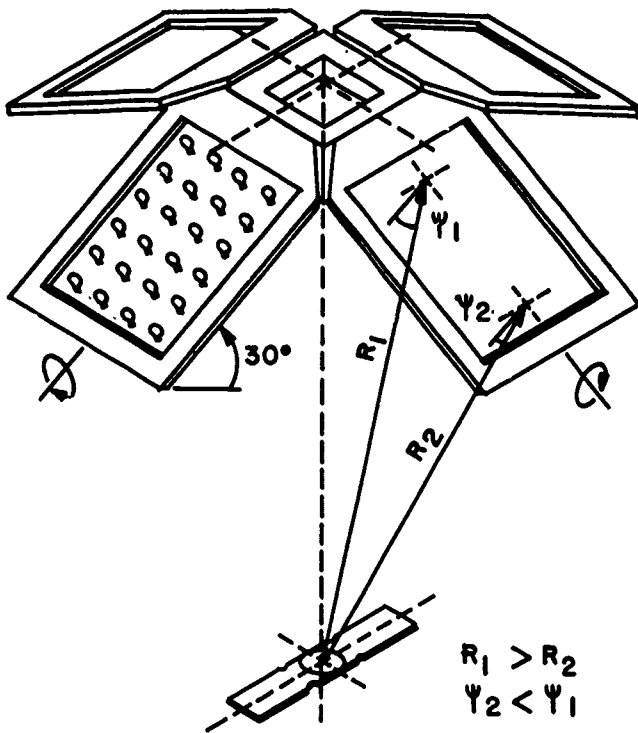


Fig. 3 COMPENSATED FIXTURE

PLATE BACK UNIFORMITY FOR
1 F² PLATE BACK
 $S \approx 0.03 F^2$

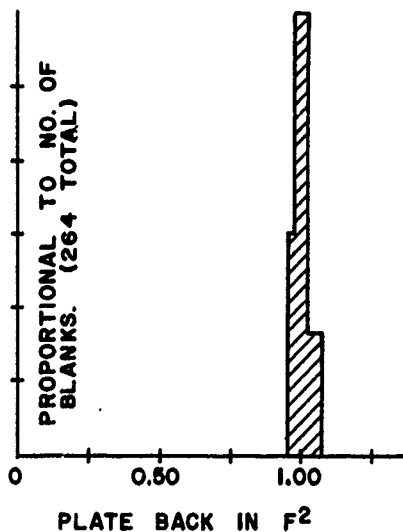


Fig. 4 COMPENSATED FIXTURE DATA

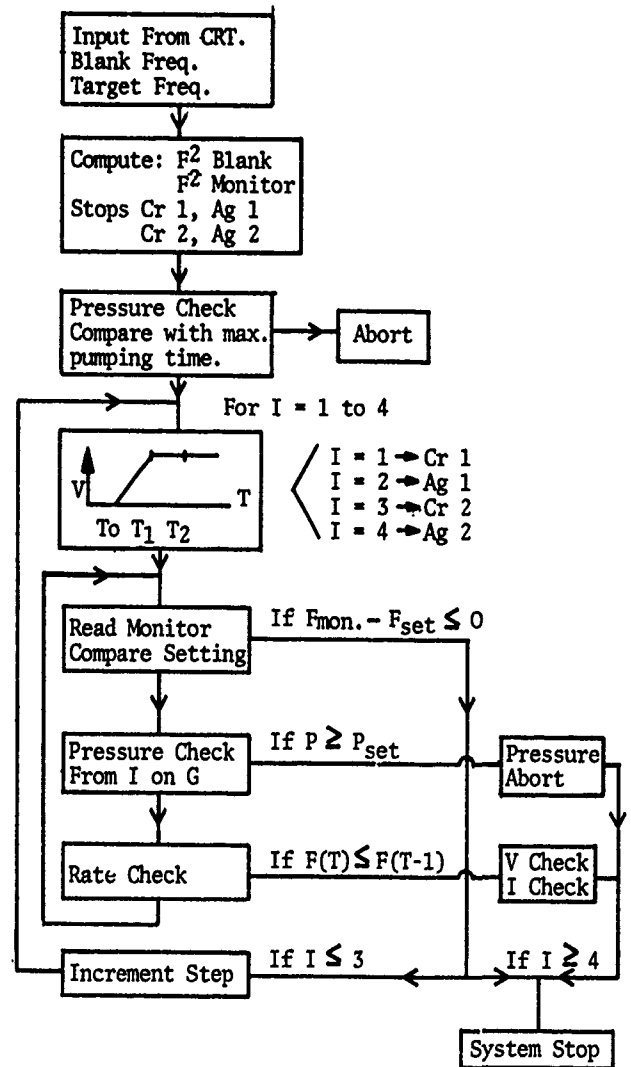


Fig. 5 SOFTWARE OUTLINE

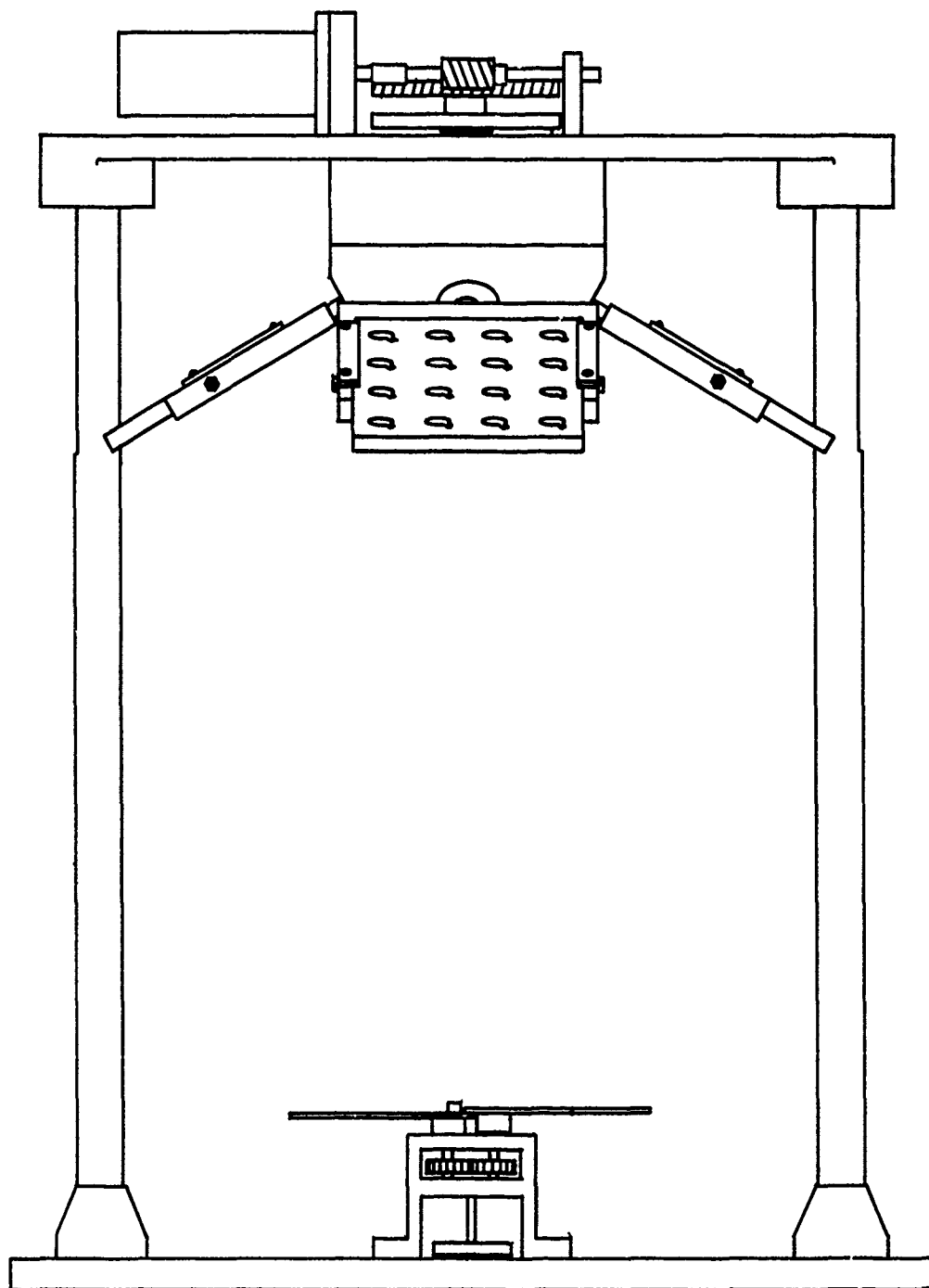


Fig. 6 COMPENSATED FIXTURE ASSEMBLY

ANALYSIS OF QUARTZ RESONATOR ELECTRODES USING THE
RUTHERFORD BACKSCATTERING TECHNIQUE

by

G. L. Dybwad

Bell Telephone Laboratories, Incorporated
Allentown Pennsylvania, 18103**Abstract**

Most quartz resonators have metal electrodes on two or more faces of the crystal. The electrodes may be deposited in an appropriate design pattern by any of several techniques. The electrodes must exhibit several properties: they must adhere well to the quartz, provide reliable electrical connection to the header contact pins, be easy to clean, and be stable with time. Various quality tests and analysis techniques have been devised over the years to ensure design performance of production electrodes.

In this paper we review the analysis principals of Rutherford backscattering as it applies to thin film electrodes on quartz. In this method, monoenergetic helium nuclei are accelerated in a Van de Graff generator toward the sample electrode. The nuclei, (AMU 4), with positive charge, pass through the film or are absorbed in the film if nuclear collisions occur. A small fraction of the incident particles are in fact reflected 180° back out of the film, i.e. backscattered. The energy of the reflected helium nuclei depends on the mass of the atoms constituting the substrate and the thickness of the substrate. This nondestructive analysis technique is called Rutherford backscattering in honor of the man who first described the physical principles of nuclear collisions.

We also describe here the application of Rutherford backscattering to analysis of films on AT-cut shear mode resonators and X-cut extensional resonators. In both cases, film interfaces were found to be partially oxidized. In the AT-case this has been related to the aging stability, i.e. mass stability of the electrodes (TiPdAu). For the X-cut resonators, the degree of oxidation of the NiCr-Au interface was related to the pull test performance of solder bond leads. The less oxidation the higher is the average pull value. The Rutherford backscattering analysis thus implied that for both devices the vapor deposition process should take place under relatively good vacuum conditions ($< 5 \times 10^{-6}$ Torr) in order to prevent interface oxidation and thus the generation of defects. Improved deposition vacuum is being employed for both types of devices as a result of the Rutherford film analysis.

Introduction

Processing of piezoelectric quartz devices usually includes some method of depositing electrode patterns on one or more faces of the single crystal blank. The electrodes cover considerable surface area and represent the interface between the electrical driving circuits and the desired mechanical vibrations of the crystal. Hence, the mechanical and electrical quality of the deposits are expected to influence the performance of the finished devices. Many methods have been devised to qualify electrode deposits; we review here one of the more recent analysis techniques which is not widely known but is very powerful in its application - namely Rutherford Backscattering. The method gives non-destructive depth profiles of the electrodes, chemical composition of the electrodes, and information on stability of interfaces the electrodes may have.

Rutherford Backscattering

The basis for this nuclear method of film analysis begins with the analysis of the momentum and energy of colliding nuclei. Figure 1 shows such a collision between an incoming particle, m_1 , and a target atom m_2 . If we restrict ourselves to low projectile energies, the process will be elastic in nature, and we can then write classical conservation equations immediately.

$$\begin{array}{ccc} \rightarrow & \rightarrow & \rightarrow \\ P_{1I} + P_{2I} = P_{1F} + P_{2F} & \text{Momentum} & (1) \end{array}$$

$$T_{1I} + T_{2I} = T_{1F} + T_{2F} \quad \text{Kinetic Energy} \quad (2)$$

Because of the idealized geometry we have chosen, where the process takes place in the plane of the paper, with m_2 being at rest initially, we can simplify 1 and 2:

$$P_{1I} = P_{1F} \cos \theta_1 + P_{2F} \cos \theta_2 \quad (\text{Horizontal Component}) \quad (3)$$

$$P_{2I} = 0 \quad (m_2 \text{ at rest}) \quad (4)$$

$$P_{1F} \sin \theta_1 - P_{2F} \sin \theta_2 = 0 \quad (\text{Vertical Component}) \quad (5)$$

$$T_{2I} = 0 = \frac{P_{2I}^2}{2m_2} \quad (m_2 \text{ at rest}) \quad (6)$$

$$\frac{P_{1I}^2}{2m_1} + \frac{P_{2I}^2}{2m_2} = \frac{P_{1F}^2}{2m_1} + \frac{P_{2F}^2}{2m_2} \quad (7)$$

where the kinetic energy is $T = P^2/2m$. This simpli-

ties to:

$$P_{1I} = P_{1F} \cos\theta_1 + P_{2F} \cos\theta_2 \quad (8)$$

$$0 = P_{1F} \sin\theta_1 - P_{2F} \sin\theta_2 \quad (9)$$

$$\frac{P_{1I}^2 - P_{1F}^2}{2m_1} = \frac{P_{2F}^2}{m_2} \quad (10)$$

The Rutherford backscattering case allows further simplification, i.e., we consider only head on direct collisions, with $m_1 < m_2$.

$$P_{1I} + P_{1F} = P_{2F} \quad (11)$$

$$\frac{P_{1I}^2 - P_{1F}^2}{2m_1} = \frac{P_{2F}^2}{2m_2} \quad (12)$$

That is, θ_1 , is 180° for this case. Combining terms leaves

$$m_2 (P_{1I} - P_{1F}) = m_1 (P_{1I} + P_{1F}) \quad (13)$$

Or, in a more useful form

$$\frac{T_{1F}}{T_{1I}} = \left| \frac{m_2 - m_1}{m_2 + m_1} \right|^2 \quad (14)$$

Equation 14 relates then the incident energy to the backscattered energy solely as a function of the masses of the two particles involved. Hence, if we let a monoenergetic beam of accelerated particles of known mass, m_1 , strike a target and then analyze the energies of the recoiling particles, m_2 , we can determine the chemical composition of the unknown target m_2 , the only unknown in (14).

Figure 2 shows the expected spectrum from a one component, infinite target. Notice that the detected energies start at T_{OUT} , which determines m_2 by (14), and continue down to lower energies. This occurs since the collision process is not truly energy conservative. Some projectile energy is lost by coulomb interactions with the electrons surrounding the target nuclei. The spectrum intensity should have a nearly flat top except at low energies, the height of which is governed by the differential scattering cross section³

$$\frac{d\sigma}{d\Omega} = 1.296 \left| \frac{Z_1 Z_2}{T_{1N}} \right|^2 \left| 1 - \frac{m_1}{2m_2} \right|^2 \times 10^{-27} \text{ cm}^2/\text{str} \quad (15)$$

That is, the probability of collision is large for heavy targets with high atomic number, Z_2 . This is ideal then for analysis of metal electrodes. For these thin electrodes, the spectrum would appear as shown in Figure 3. The width of the spectrum in energy space then gives information on target thickness, t , if the value of dT/dt_{m_2} is known.

For targets with several components on a substrate, we would have a spectrum like that of Figure 4. The different components are resolved in energy space by the backscattering; this tends to aid identification. However, the heavier components effectively push the lighter components to lower energies because of dT/dt , the rate of energy loss, which

must be applied as a correction to the mass equation 14. Mass identification can be aided by taking long counts and comparing peak heights on a relative basis. The statistical nature of the backscattering process and channeling processes in single crystal materials will limit this resolution. The properties of the detector will also limit the resolution in energy, which is related to mass or thickness resolution. The detector used in these experiments can discriminate ΔT in increments of 4keV which corresponds to a gold film thickness of 32A. Experimental conditions reduce this resolution further to about 120A.

Apparatus

The incident particles used in these experiments were singly ionized helium nuclei with atomic mass number 4. This probe atom is easy to accelerate, will not react chemically with the target, and is light enough to prevent significant transfer of energy to the target which could cause damage. The accelerator used here was a 2 MEV Van de Graff machine; the incident energy was 1.8 MEV.³ This energy prevents target damage (i.e., elastic collisions) and gives good energy resolution. Also, extensive data exists in this energy range on dT/dt , the stopping power of metal targets.

Figure 5 shows the details of accelerating the monoenergetic beam towards the target.³ Electrostatic deflectors are used to align the beam correctly vertically and horizontally. A series of collimating apertures control the beam diameter (0.060 degrees). Small beam diameters aid in detection of lateral variations on the target surface, but require correspondingly longer accumulation times at the detector. The detector is an annular ring with 50 mm² area. The target is rigidly mounted on a copper block attached to a goniometer head. The block is equipped with heater elements so that diffusion experiments can be carried out on the sample without breaking vacuum. Liquid nitrogen cold traps maintained a vacuum level of about 10^{-8} torr for these experiments.

A 2048 bin multichannel analyzer is used to display the backscatter information from the detector (Figure 6). The total energy range which can be detected is thus approximately 1 MEV, sufficient for most analyses. A computer and keyboard are used to control the helium beam by means of shutters, accumulate and analyze the data, and print or plot the results if a permanent record is desired. Figure 7 is an example of a typical analysis spectrum.

QUARTZ RESONATOR APPLICATIONS

Thin film analyses using Rutherford backscattering have been completed on two resonator codes in our laboratory. A brief description of each will serve to illustrate the method.

A. The Monolithic Crystal Filter (MCF)

The MCF (Figure 8) is an 8-pole Chebyshev

filter with a 4 kHz bandwidth and used for voice channel communications.⁶ Titanium-palladium-gold films are e-beam evaporated onto the AT-cut substrate. Short and long term aging studies on these devices typically displayed frequency shifts as shown in Figure 9. The negative frequency shifts at long times were attributed to accumulation of mass on the electrodes. Since the top gold layer was intended to protect the active metal layers below (Ti-Pd), it was suspected that the mass was passing through pinholes in the top film. Rutherford backscattering analysis was used to confirm this model. Figure 10 shows the spectra after a long annealing time. The three metals forming the electrode are still well defined implying that little diffusion took place during the in situ annealing process. Other experiments with Ti-Pd-Au thin films deposited under carefully controlled conditions gave the reference spectra shown in Figure 10. The interdiffusion of the interfaces is well developed. We conclude that ambient mass, most likely oxygen or water vapor, has indeed diffused through the MCF gold electrode and oxidized the interfaces of the titanium and palladium layers. Oxides of metals generally exhibit lower diffusion rates than the pure metal. Aging performance was improved on this device by reducing the ambient contamination levels, and depositing films with fewer pinhole defects. It was noted that the improved devices exhibited increased electrode interface diffusion. Hence, the backscatter diffusion results could be correlated with filter frequency stability.

B. Extensional Resonators (E-elements)

Figure 11 shows an extensional mode resonator which is part of a larger band pass filter assembly. The 5° x-cut blank has a pair of split electrodes; the electrodes are filament evaporated nichrome and gold. Four, headed, wire leads are soldered to the electrodes to provide electrical connections. The detailed characteristics of these bonds were expected to influence device performance. Based on the MCF results discussed above, a backscatter study was undertaken to determine if film quality could be correlated with lead pull strength.

Two groups of test resonators were fabricated: one group received normal electrode processing, and the other group had electrodes deposited under improved vacuum conditions (6×10^{-6} torr). Samples from the two groups were analyzed by Rutherford backscattering. Figure 12 summarizes the results. Initially, both groups gave identical spectra. After a high temperature anneal period (500°C for 30 minutes) only a small amount of interface diffusion was observed for the improved vacuum deposition group. The group processed normally did not show any additional diffusion on annealing. We conclude that the film interfaces were oxidized in both sets of samples. On a relative basis, the improved vacuum group showed the least oxidation.

Wire leads were then attached to all the test crystals by standard solder bonding techniques (60/40 lead tin). The leads were pull tested to destruction, and the pull values in kilograms noted.

The average values and standard deviations for the two groups are listed below.

	Test Pull Values (K gm)
(N=20)	
Improved Vacuum Group:	$\bar{P} = 1.16 \pm 0.127$
Normal Product:	$\bar{P} = 0.98 \pm 0.158$

The samples made under controlled deposition conditions exhibited improved lead adherence. We conclude that less oxidation of metal film interfaces as determined by backscattering and other experiments improves the solderability of nichrome-gold electrodes.

Summary

I have reviewed here the principles governing Rutherford Backscattering analysis. This nuclear technique involves the acceleration of monoenergetic He towards the sample. Nuclei are detected which have suffered an elastic collision with the target nuclei and been reflected 180°. The energy spectrum of the detected particles contains chemical and thickness information about the target. Diffusion of interfaces can be monitored in situ by annealing.

The method lends itself to non-destructive testing of thin metal films. I have described here the application of this important analysis technique to two types of quartz resonators with metal electrodes. In the one case, interface oxidation observed in the backscatter data was related to device aging stability. In the other case, interface oxidation has been correlated with pull strengths of wire leads solder bonded to the nichrome-gold electrodes on extensional resonators.

Acknowledgements

I would like to especially thank J. M. Poate for acquainting me with the backscatter methods. He also performed the experiments on the quartz samples using the accelerator and Rutherford facility at Bell Laboratories, Murray Hill, New Jersey. I also thank W. C. Morse and W. G. Harmon for depositing the electrodes on the extensional resonators.

REFERENCES

- [1] J. M. Poate, K. N. Tu, and J. W. Mayer, "Thin Films-Interdiffusion and Reactions," Wiley and Sons, New York, 1978.
- [2] K. R. Symon, "Mechanics," Addison-Wesley, Reading, Mass., 1961.
- [3] T. M. Buck, J. M. Poate, K. A. Pickar, and C. M. Hsieh, *Surface Science*, **35**, 362 (1973).
- [4] J. M. Poate, P. A. Turner, and W. J. DeBonte, *JAP*, **46**, 10, 4275 (1975).

- [5] J. M. Poate, P. A. Turner, and W. J. DeBonte, *JAP*, **46**, 10, 4284 (1975).
- [6] S. H. Ooster, et. al., *29th Annual Symp. on Freq. Control*, 1975, p. 105.
- [7] G. L. Dybwad, *31st Annual Symp. on Freq. Control*, 1977, p. 144.
- [8] L. I. Maissel and R. Glang, "Handbook of Thin Film Technology," McGraw-Hill Co., New York, 1970, p. 23-15.
- [9] T. H. Simmonds, *Proceedings of the IEEE*, **67**, No. 1, 109 (1979).

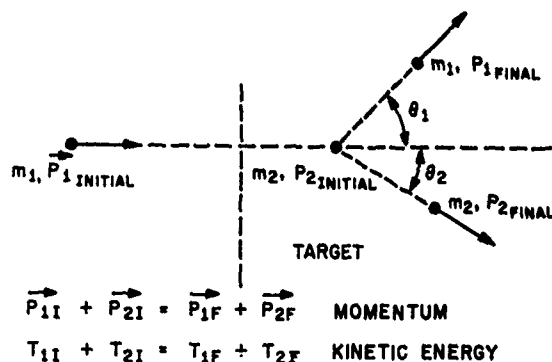


FIGURE 1 ELASTIC RUTHERFORD COLLISIONS
 $\theta_1 = 180^\circ$

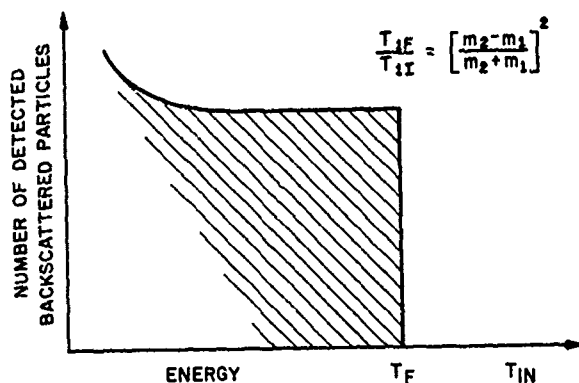


FIGURE 2 IDEAL RUTHERFORD SPECTRUM
 $\theta_1 = 180^\circ$

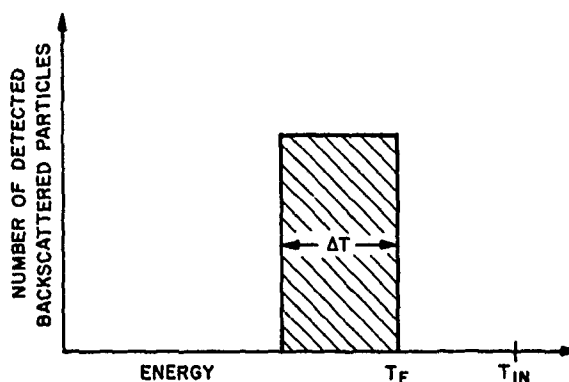


FIGURE 3 RUTHERFORD SPECTRUM OF A THIN TARGET

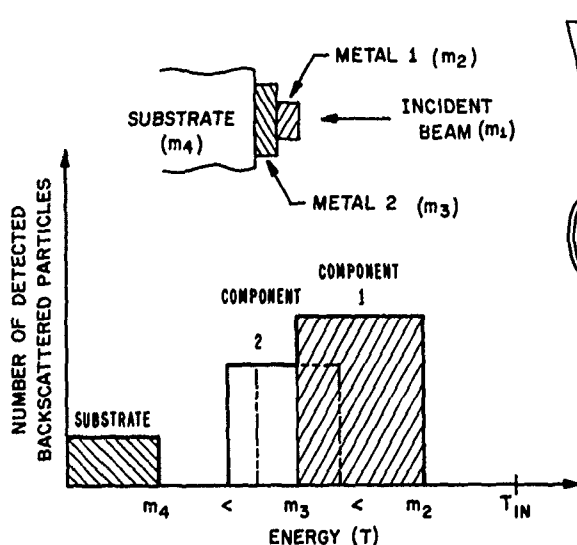


FIGURE 4 IDEAL TWO COMPONENT ELECTRODE
ON AN INFINITE SUBSTRATE

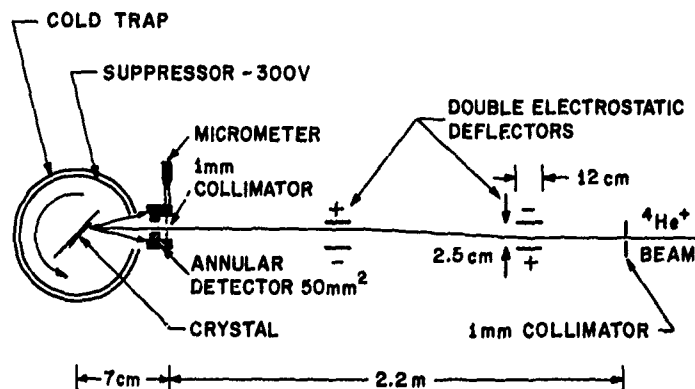


FIGURE 5. DIAGRAM OF THE SAMPLE HOLDER AND DETECTOR

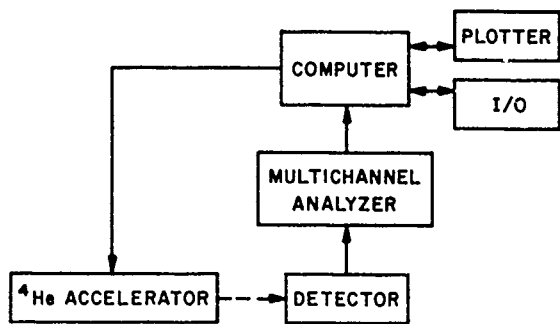


FIGURE 6 SCHEMATIC OF THE RUTHERFORD BACKSCATTERING FACILITY

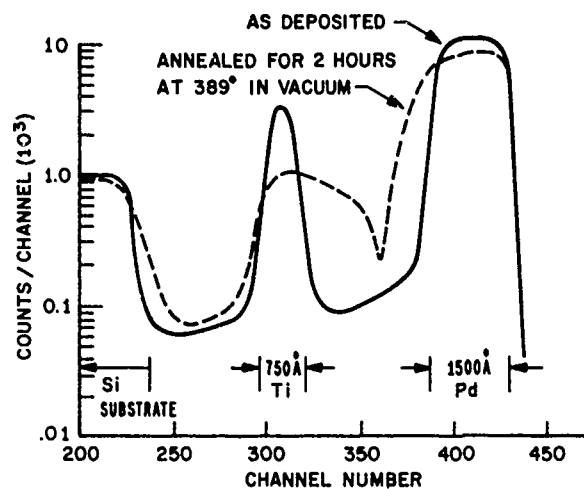


FIGURE 7 TYPICAL RUTHERFORD SPECTRUM

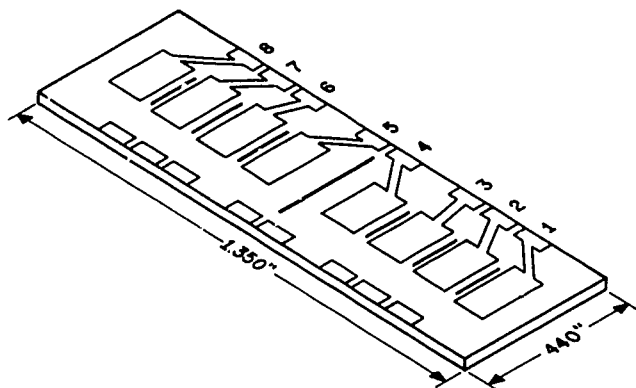


FIGURE 8 THE MONOLITHIC CRYSTAL FILTER

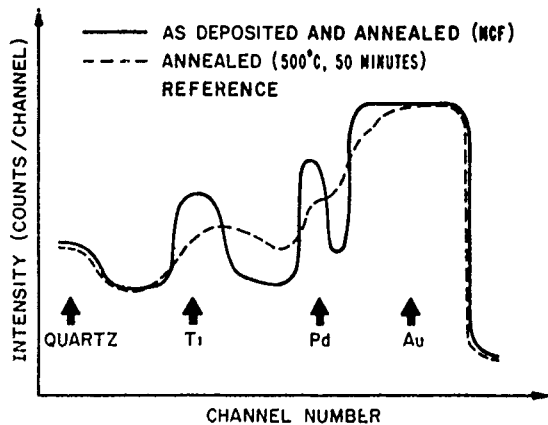


FIGURE 10 RUTHERFORD BACKSCATTERING OF AN ANNEALED MONOLITHIC CRYSTAL FILTER ELECTRODE

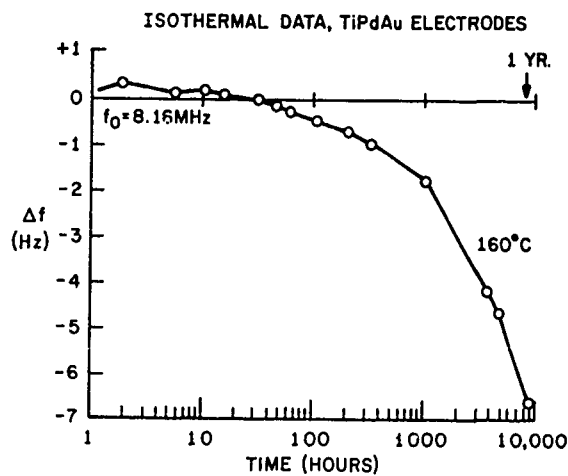


FIGURE 9 MCF AGING BEHAVIOR

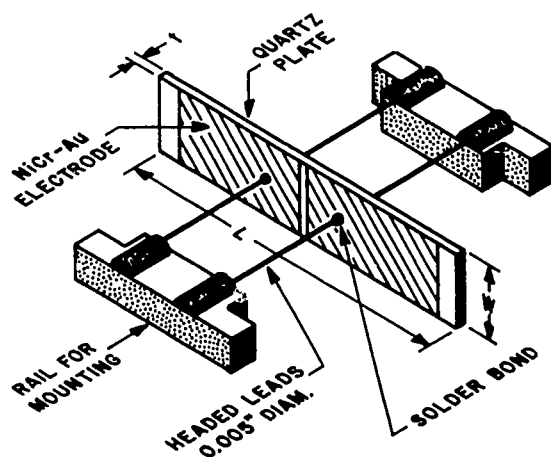


FIGURE 11 5° X-CUT EXTENSIONAL QUARTZ RESONATOR

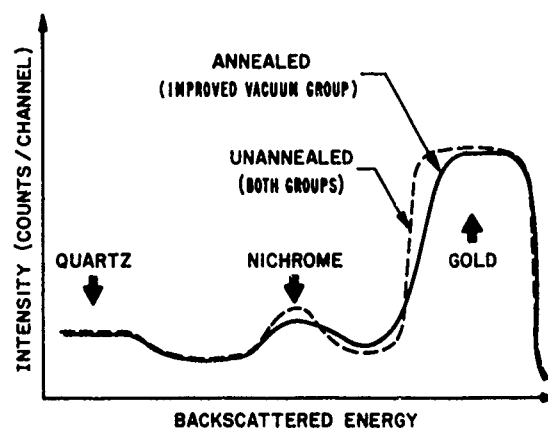


FIGURE 12 RUTHERFORD BACKSCATTERING SPECTRA FROM EXTENSIONAL RESONATORS AFTER ANNEALING AT 500°C FOR 30 MINUTES

DIGITAL TEMPERATURE CONTROL FOR ULTRASTABLE QUARTZ OSCILLATORS

G. Marianneau, J.J. Gagnepain

Laboratoire de Physique et Métrologie des Oscillateurs du C.N.R.S.
associé à l'Université de Franche-Comté-Besançon
32, av. de l'Observatoire - 25000 Besançon - France

Abstract

The sensitivity of quartz resonators to temperature gradients, known as the dynamic thermal behavior, is one of the main causes of instability in oscillators. When using AT cut resonators it is necessary to control short term temperature fluctuations at a level below $1 \mu^\circ\text{C}$ and to maintain a drift lower than 0.001°C/day . Such specifications are not easy to achieve with regular analog temperature controlled ovens, the resolution of which is limited by temperature probes such as thermistors, platinum resistors, etc, by the signal over noise ratio and by the difficulty of introducing appropriate correcting networks in the servo loop for lower frequencies. The principle of the device which is presented consists in using a quartz resonator, with a large temperature coefficient, as temperature to frequency transducer, and after frequency multiplication and mixing a digital electronics for driving the oven heater. The oven itself is to be designed with thermal shunts and discontinuities so that it filters the residual fluctuations at higher frequencies. Accurate digital control and thermal filtering enable to reach temperature stabilities better than $.1 \mu^\circ\text{C}$ over a few seconds and $.001^\circ\text{C}$ per day.

Introduction

Previous studies, on the dynamic thermal behavior of quartz resonators^{1,2} showed the large influence of temperature gradients on the frequency of quartz oscillators and led to a simple model consisting in an additional term proportional to the time derivative of temperature. The complete frequency-temperature characteristic, including both static and dynamic effects then is

$$\begin{aligned} (f-f_0)/f_0 = & \tilde{\alpha} dT/dt + a_0(T-T_0) \\ & + b_0(T-T_0)^2 + c_0(T-T_0)^3 \end{aligned} \quad (1)$$

where $\tilde{\alpha}$ is called dynamic temperature coefficient and a_0 , b_0 and c_0 are the 1st, 2nd and 3rd order static temperature coefficients.

If considering only the static behavior of an AT cut quartz resonator operated at its turn-over temperature point, the F-T characteristic is

parabolic with an equivalent coefficient of $10^{-5}/^\circ\text{C}^2$. Therefore the achievement of a 10^{-13} frequency stability would need only an accuracy in temperature of $.01^\circ\text{C}$ which can be easily obtained. But for the same AT cut resonator the $\tilde{\alpha}$ coefficient is $10^{-5} \text{ s}/^\circ\text{C}$. This roughly means that the same frequency variation (frequency step for instance) can be obtained with linear-in-time temperature changes as low as $0.01 \mu^\circ\text{C/s}$ at short term and $0.001^\circ\text{C/per day}$ at long term.

The exact transformation from temperature to frequency fluctuations can be made if the former ones are defined with the same mathematical tools as for the last ones, i.e., mean value and variance. Let $\Delta T(t)$ be the absolute temperature variations and $y(t)$ the fractional frequency variations.

Both are related following the equation

$$\sigma_y(\tau) = (\tilde{\alpha}/\tau) \sigma_{\Delta T}(\tau) \quad (2)$$

as illustrated on figure 1.

For SC cut resonators, the $\tilde{\alpha}$ coefficient is lower by a factor hundred. Therefore the accuracy in temperature can be advantageously reduced by the same factor. Such thermal specifications are not easy to achieve in regular analog temperature controlled oven. Effectively thermistors, platinum resistors or thermocouple, do not offer a sufficient signal over noise ratio and are not stable enough at long term. In analog servo loop the correcting networks practically are not usable for the lowest frequencies and therefore unwanted oscillations are difficult to avoid.

The device which has been studied is based on the principle of digital temperature control. The key element is the quartz resonator used as temperature sensor, which drives an oscillator and is chosen with a large first order static temperature coefficient. The information is almost digitally available as a frequency. After multiplication and mixing, if necessary for increasing the resolution, and comparison with respect to a stable frequency reference, this information equivalent to temperature is taken into account by a μ processor which drives the oven heater. The oven design is not so different of the previous ones, but is to be adapted to the

quartz probe shape and characteristics, and a maximum of care is taken to minimize thermal coupling along the connecting cables. The oven is as low as possible, thermal low-pass filter.

Temperature sensors

Bulk waves resonators and SAW delay lines or resonators can be used as temperature sensors. Several crystallographic cuts are available, as shown in table I, where are presented their sensitivities and linearities.

cut	sensitivity absolute (Hz/°C)	relative ppm/°C	2nd order T.C. (10 ⁻³ /°C)	frequency MHz
LC	1000	36	0	28
Y+4°	460	92	60	5
SC B Mode	125	25	-35	5
LST (SAW)	3100	31	-2	100

Table I : Comparison between different resonators used as temperature sensors

These different cuts have their own advantages and inconvenients :

a) LC cut is sensitive and linear. The resonators which were used have a small size (mounted in a TO39 enclosure) and time constants of a few seconds. Their peculiar frequency noise was measured and is presented on fig. 2. Two different noise sources are observed : 1/F noise and frequency random walk (1/F²). This last one is directly related to temperature fluctuations (the dynamic thermal behavior is involved in this frequency range) of the oven which was used during the measure. The 1/F spectrum is not correlated to temperature fluctuations, at least at room temperature, and will constitute the limit of resolution of the probe. At 1 Hz this resolution is of the order of 6 μ C (independantly of other additive noise sources in the electronic associated to the sensor).

b) The rotated Y+4° cut presents the largest first order T.C. (92 ppm/°C) but also a large second order T.C. Therefore the resolution will depend on the operating temperature.

c) The B mode of SC cut offers a good sensitivity but also a linearity which is not sufficient if the temperature range is wide. The main advantage of this cut is to have an intrinsic stability, which is expected to be same one for the B mode as for the C mode (at constant temperature). The stability of this last one being in the range of 10⁻¹³, and exceptionally of 10⁻¹⁴ for EVA resona-

tors³, the resolution in temperature measurement will be the best one, but with much larger time constants related to the crystal size and to its mounting.

d) The LST cut SAW sensor leads to comparable relative sensitivities, but to higher absolute sensitivities (this aspect is not negligible because larger the frequency shift/°C simpler the electronics), and also has a good linearity⁴. It can be used over a large temperature range. Its main advantage certainly is the small time constant (below 1 s) due to the structure of the SAW oscillator itself. But, the intrinsic stability is between 10⁻⁹ and 10⁻¹⁰ typically and lower by several order of magnitude when compared to SC cut.

Description of the thermostat

The schematic diagram of the temperature control presented on fig. 3 is adapted to a 28 MHz LC cut sensor which has a sensitivity of 1000 Hz/°C. The frequency is compared to a 25 MHz reference obtained from a multiplied 5 MHz stable oscillator. The beat frequency after multiplication by 10 will give a resolution of 10⁻⁴°C/Hz. If necessary this resolution can be increased to 10⁻⁵°C/Hz with a second step of mixing and multiplication.

A counter measures the final beat frequency over a time interval $\tau = 1$ s. The data of the counter then are introduced in a μ processor and compared to the operation temperature T displayed by means of a thumbwheel. The signal error delivered by the μ p in the form of incremental current steps of .1 mA drives after amplification the oven heater.

The versatility of such a system is attributable to the μ p. The parameters of the servo loop can be modified just by changing instructions in the program and all corrections necessary to avoid spurious oscillations can be also introduced directly in the program. However the linearity of the temperature sensor is not so important because after calibration it can be corrected also by programing adequately the μ p. A second temperature probe enables to measure the residual temperature fluctuations by means of a similar system used as a thermometer, but independently of the first one.

The oven itself is to be carefully designed in order to avoid thermal coupling between its inner part and the surrounding medium. Direct heat exchange along the cables are minimized by means of thermal discontinuities and shunts made with thin wires of stainless steel or argentan. Several types of ovens were built as shown on fig. 4 :

a) a single oven made with a block of brass which contains the probe ; a resistive coil in contact is used as heater. The oven is thermally protected with fiberglass.

b) a double oven made with a copper block similar to the previous one is placed in a stainless steel box.

c) a threefold oven constituted with a copper block, which contains the probes and the heater, placed in two boxes of copper and stainless steel. Thermally insulated connectors were used with this more sophisticated oven.

The volume and weight and therefore time constants of the ovens increase with the number of layers, but the thermal filtering becomes more efficient.

At this filtering effect of the oven is to be added the effect of the resonator enclosure with its own thermal time constant, which still minimizes the residual fluctuations.

Short and long term temperature stabilities

As indicated above, the temperature in the oven was measured independantly of the controlling system itself by using also a quartz resonator as temperature sensor. It is important to note that the temperature is locally measured and the obtained value does not reflect the temperature of the all oven but only of an average over a small volume : the volume of the measurement probe indeed. The thermostats which were studied being to be used for controlling the temperature of quartz crystal, it is mostly interesting to measure this temperature by means of a quartz probe in order to be in the same conditions as during operation. Two types of sensors were used for these measures, LC cut and SC cut. The first one gives informations on the thermal fluctuations as they are seen by the temperature control system and will show its operating range and its limitations. With the second one, the B mode will give the temperature of the resonator which will be operated effectively in a frequency standard, and therefore its true temperature can be determined.

If the same oven is utilized for both measurements the differences which appear in the results are to be attributed to the different thermal constants of the resonators.

On fig. 5 are presented the temperature stabilities obtained when measuring the thermal fluctuations in the threefold oven with an LC cut probe, with a regular commercially available SC cut resonator and with a BVA SC cut high performance resonator.

It can be seen that as predicted the measured temperature stability depends on the type of probe and more precisely on their thermal time constant. The LC resonator has the faster response. The time constants introduce a cut-off in the stability curves. These curves increase as τ and go to a same floor, which will correspond to the resolution of the servo loop, but which could be observed only over very large time intervals in

account of the several hour time constant of the oven. At short term the three stabilities merge in one single curve and the fluctuations seem to follow a $1/\tau$ law. In fact this corresponds to the electronic noise of the measurement system itself and is not to be attributed to temperature.

The best short term stability was obtained for $\tau = 10$ s with the BVA resonator and is equal to $.04 \mu^\circ\text{C}$. For shorter times the curves can be extrapolated, in this case the measurement system noise is not to be taken into account.

The influence of the oven design was also studied. On fig. 6 are presented the temperature stabilities measured in the three different ovens with the same LC cut probe.

The long term temperature stability was measured in the threefold oven when controlled with a 10^{-4}°C resolution. Temperature was recorded every 1000 s during several days and the results are presented on fig. 7. A mean drift of the order of 3.10^{-5}°C per day was observed and is attributed to the resonator frequency aging ; this resonator was operated only for two days before the beginning of the measurements. The random variations, which are superposed on the mean drift, is due to the influence of the room temperature changes on the probe oscillator which was outside the oven.

Conclusion

This study shows that the accuracy in temperature control can be improved by using a digital control. The stabilities which were obtained at short term are closed to the specifications necessary to achieve frequency stabilities of 10^{-13} with AT cut resonators and sufficient with SC cut resonators. At long term the observed temperature drift is lower than $0.0001^\circ\text{C}/\text{day}$ and the peak to peak variations remain within 0.001°C . These results are still perfectible and improvements are expected by using miniaturized probe oscillators located inside the oven, and not outside as presently. In this first work the maximum of care was taken in the design of the oven, without considerations of size. The second step will consist in cancelling all that what is not necessary in order to decrease the size, weight and cost of such thermostats.

Acknowledgements

The authors wish to thank C. Ferrandez and R. Grand who achieved the μ electronics and the frequency multiplication. They are also grateful to R. Pr  tot and J. Gros Lambert for their advices. The LC probes were provided by C. Peugeot of Quartz et Electronique (France) and by Mrs Gniewinska of the Institute of Teleradiotechnic (Poland) and the BVA resonators by Professor R. Besson.

References

1. A. Ballato and J.R. Vig, "Static and dynamic frequency-temperature behavior of singly and doubly rotated oven-controlled quartz resonators", Proc. 32nd An. Freq. Cont. Symp., 1978.
2. G. Théobald, G. Marianneau, R. Prétot, J.J. Gagnepain, "Dynamic thermal behavior of quartz resonators, Proc. 33rd An. Freq. Cont. Symp., 1979.
3. S. Stein, C. Manney, F. Walls, J. Gray, R. Besson, "A systems approach to high performance oscillators", Proc. 32nd An. Freq. Cont. Symp., 1978.
4. D. Hauden, S. Rousseau, J.J. Gagnepain, "Sensitivities of SAW oscillators to temperature, forces and pressure : application to sensors", This meeting.

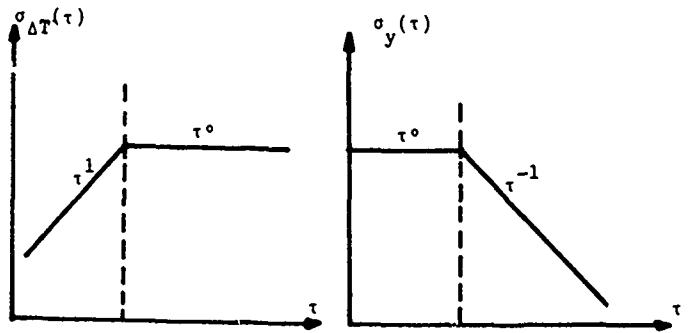


Fig. 1

Absolute temperature stability and frequency stability.

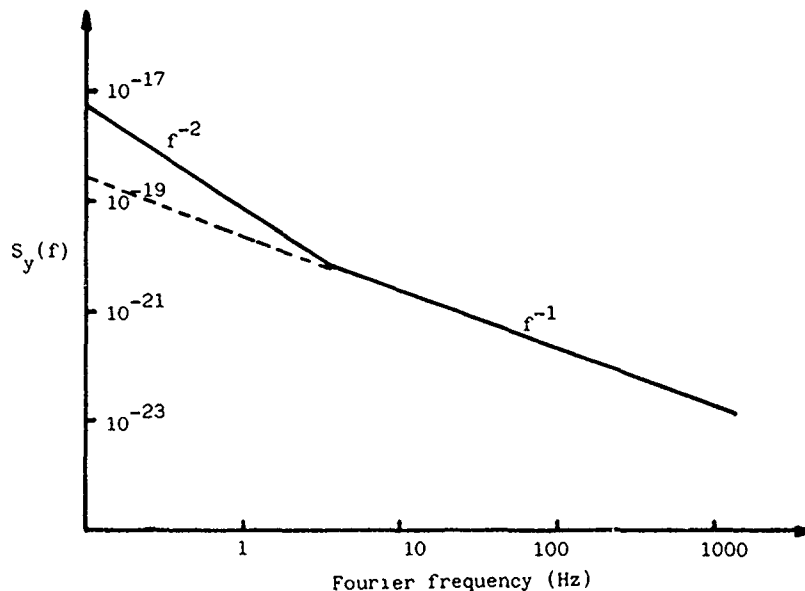


Fig. 2 : Fractional frequency fluctuation's density power spectrum of the LC cut temperature sensor.

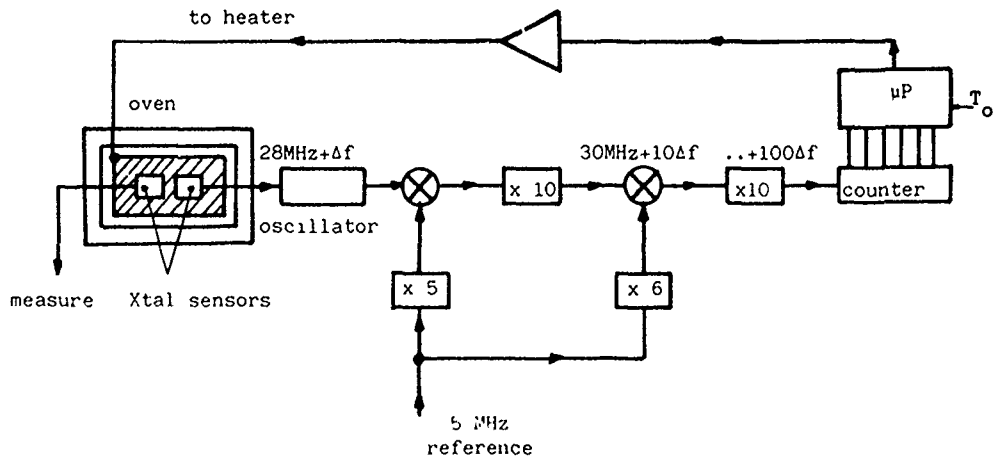


Fig. 3 : Schematic diagram of the electronic system used for controlling the temperature

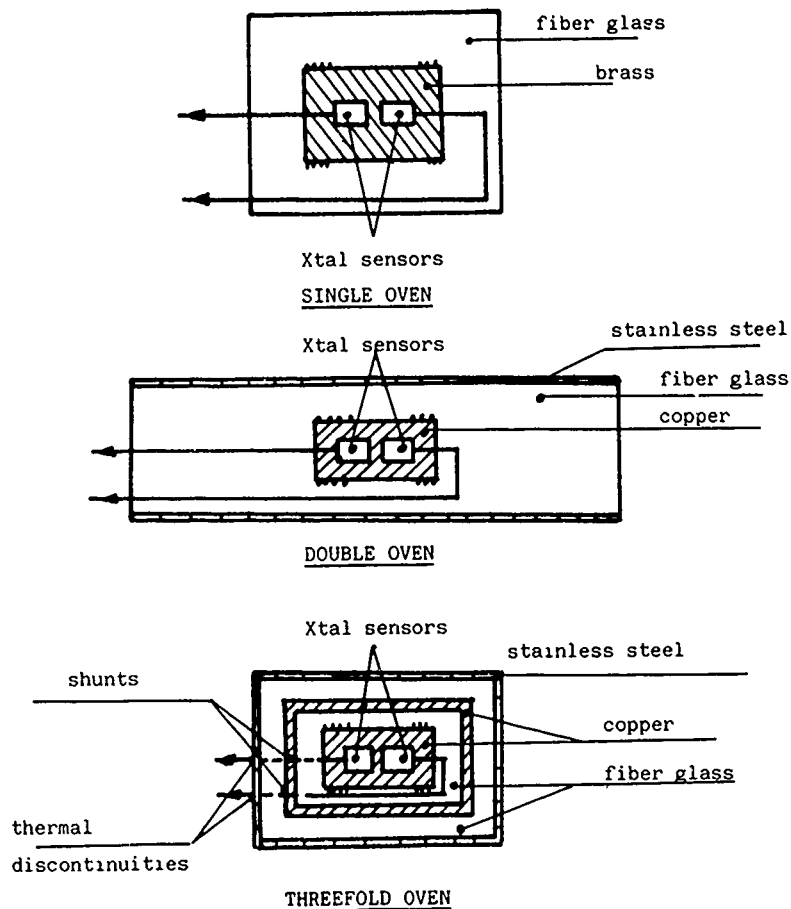


Fig. 4 : Different types of ovens

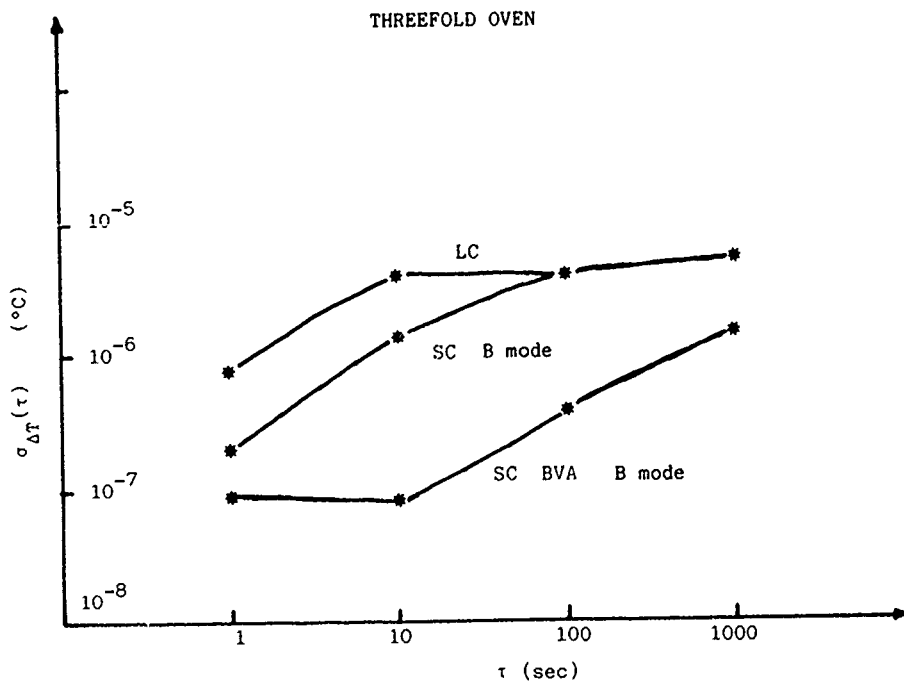


Fig. 5 : Temperature fluctuations in the threefold oven measured with LC cut, regular SC cut and BVA SC cut resonators.

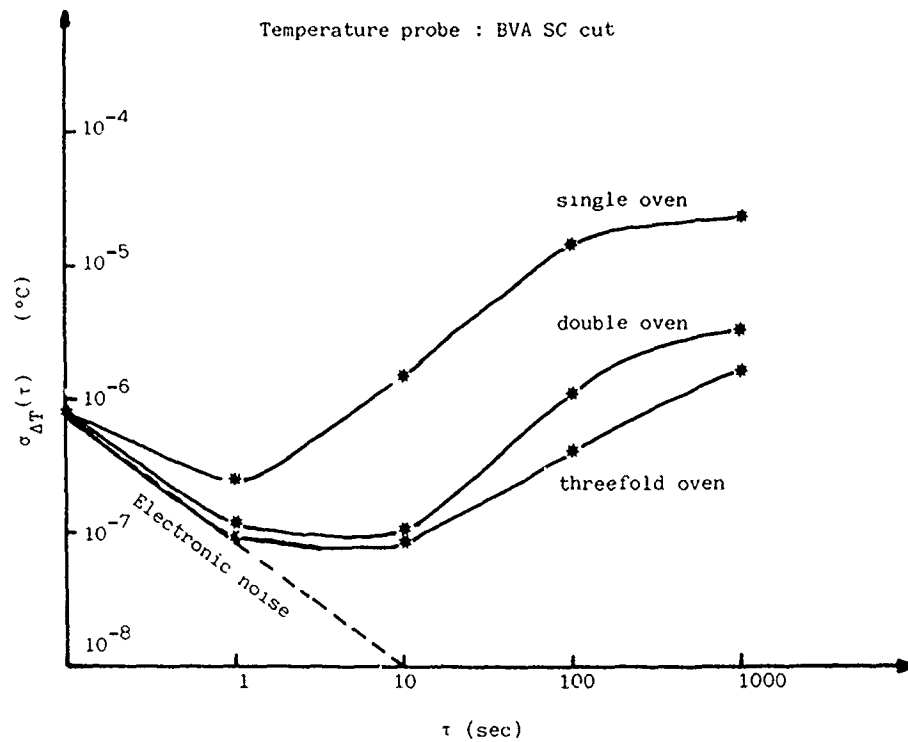


Fig. 6 : Influence of the oven design on the temperature stability (measured with the same SC cut probe for the three ovens).

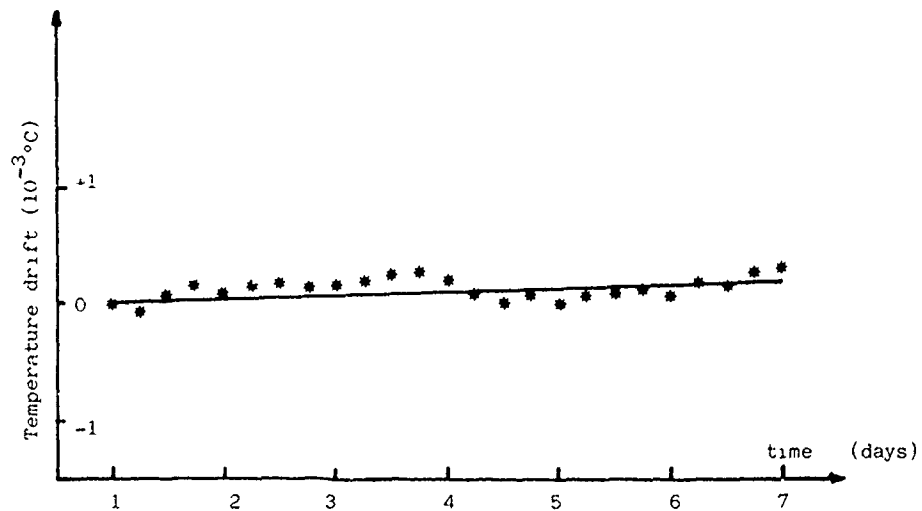


Fig. 7 : Long term temperature drift.

A NEW EQUIVALENT CIRCUIT FOR PIEZOELECTRIC CERAMIC DISC RESONATORS

Masahiro Toki, Yasuo Tsuzuki and Osamu kawano

Yokohama National University
Hodogaya-ku, Yokohama 240
Japan

Summary

A new equivalent circuit has been considered, so that it can be usable for a better simulation of the impedance characteristics of ceramic resonators.

Characteristics of the resonator impedance have been investigated on radial mode ceramic disc resonators, and it has been indicated that the frequency characteristics of the test resonator impedance over a wide frequency range including the series and parallel resonance frequencies can not be simulated, if all the parameters of a commonly used equivalent circuit are made constant.

A new equivalent circuit, then, has been considered. The configuration of the new circuit consists of a commonly used equivalent circuit and a resistance element connected in series. It has been verified that the new equivalent circuit represents well the resonator impedance characteristics over the wide frequency range. The new circuit configuration is applicable to all the resonator samples which have an arbitrary thickness and diameter, and the ones which have different values of piezoelectric coupling factor and quality factor.

Introduction

Piezoelectric ceramic disc resonators have been in wide use in filters and transducers. In order to represent the characteristics of the ceramic resonators, an equivalent circuit, consisting of $R_1 L_1 C_1$ series resonance circuit with equivalent parallel capacitance C_0 as shown in Fig. 1(a), is commonly used in the vicinity of the resonance frequency. In recent investigation, however, it has been found that the characteristics of the resonator impedance in the vicinity of the series and parallel resonance frequencies can not be simulated simultaneously, if all the elements of the commonly used equivalent circuit are made constant.

In this paper a precise measuring method of equivalent circuit parameters, recently developed by the authors[1][2], is used in order to investigate the impedance characteristics of the radial mode ceramic disc resonators. Both the series and parallel resonance characteristics of the resonator are investigated, and frequency characteristics of the equivalent circuit parameters are obtained.

Then a new equivalent circuit, consisting of parameters of constant values, is considered so that it is usable for a better simulation of the resonator impedance over a wide frequency range including the series and parallel resonance frequencies. Applicability of the new circuit configuration is shown by measuring the circuit parameters on various resonators having different values of piezoelectric coupling factor k_p and quality factor Q .

Precise measuring method of equivalent circuit parameters

An automatic precise measuring system[2] is shown in Fig. 2(a). The RF output signal of the Frequency Synthesizer is led to the Measuring Circuit[3] in which a resonator sample is inserted, and the values of the voltage transfer ratio $A = |V_2/V_1| = R_L / |R_L + Z|$ in the vicinity of the series and parallel resonance frequencies, as shown in Fig. 2(b), are automatically measured at a number of frequencies of equal frequency separation. Then the values of equivalent circuit parameters, series resonance frequency $f_s = 1/2\pi\sqrt{L_1 C_1}$, parallel resonance frequency $f_p = f_s \sqrt{1 + C_1/C_0}$, equivalent series resistance R_1 and motional inductance L_1 , are determined by a computer data processing so that the frequency characteristics calculated from these values give the best agreement with the measured data. Other parameters C_1 , Q , k_p and C_0 are determined from these four parameters by using the relations: $C_1 = 1/[(2\pi f_s)^2 L_1]$, $C_0 = C_1/[(f_p/f_s)^2 - 1]$, $Q = 2\pi f_s L_1/R_1$ and $1/k_p^2 = 0.395 f_s / (f_p - f_s) + 0.574$ (formula for k_p [3] for Poisson's ratio of 0.30).

In the data processing the series and parallel resonance frequencies f_s and f_p are determined by using the measured data in the vicinity of the respective resonance frequencies. While the equivalent series resistance R_1 and the motional inductance L_1 are determined by using the measured data in the vicinity of either the series or the parallel resonance frequencies, and the best simulations of corresponding either the series or parallel resonance characteristics of the resonator are obtained.

In the data measurement the initial calibration of the measuring system is made by using precision attenuator so that the systematic errors produced by the system become as small as possible.

Using this measuring method, then, the equivalent circuit parameters can be obtained precisely without personal errors. The simulating accuracy of the measured data by the equivalent circuit parameters can be estimated in terms of the root mean square deviation of the residual differences between the calculated and measured values of the voltage transfer ratio $\Delta A/A$.

Frequency characteristics of the equivalent circuit parameters between the series and parallel resonance frequencies can be obtained, if we shift the resonance frequencies f_s or f_p to new resonance frequencies f'_s or f'_p by connecting a capacitance C of a known value in series or in parallel with the resonator, and measure the voltage transfer ratio data in the vicinity of either one of the new resonance frequencies.

Frequency characteristics of ceramic resonator

Measurements have been made on a radial mode ceramic disc resonator which has a high k_p of 60 % and low Q of 100. The resonator has a diameter $d = 18\text{mm}$ and a thickness $t = 3.15\text{mm}$. The series resonance frequency f_s is about 110KHz. It has been confirmed, prior to the data measurements, that the value of the voltage transfer ratio does not change practically over the Synthesizer output level from -20dBm to 0dBm, then the output level has been set at -15dBm for every measurements of the voltage transfer ratio data. The values of the voltage transfer ratio over a frequency range about five times as wide as the respective 3dB widths. The load resistances of 5.10 ohms and 574 ohms have been used for the measurements in the vicinity of the series and parallel resonance frequencies, respectively.

Fig. 3 shows the measured data together with the simulated curve by using the commonly used equivalent circuit. Parallel resonance data have been shown in the form of $1/A = |R_L + Z|/R_L$ in the figure. When the equivalent circuit parameters were determined so as to simulate the series resonance characteristics the best, it was found that the parallel resonance characteristics calculated from these parameters considerably differ from the measured data as shown in Fig. 3(a). In the parallel resonance the Q of the measured data is much higher than that of the calculated one. While when the parameters were determined so as to simulate the parallel resonance characteristics the best, a considerable discrepancy in the vicinity of the series resonance was found such that the measured Q is much lower than that of the calculated one. Comparing the each parameters which have been obtained in the above described two ways, it has been shown that the value of R_1 which is obtained so as to simulate the series resonance characteristics the best is much larger than the one obtained in the other way. While all the reactance parameters L_1, C_1 and C_0 are practically the same, respectively.

Frequency characteristics of the equivalent circuit parameters

In the previous section it has been shown that the equivalent resistance in the series resonance is much larger than the one in the parallel resonance. In this section, then, the frequency characteristics of the equivalent resistance and of all the reactance parameters over the frequency range between the series and parallel resonance frequencies have been investigated.

Measurements have been made on the same resonator, and the frequency characteristics of the equivalent circuit parameters have been obtained as shown by small circles in Fig. 4. It has been shown that the value of the equivalent resistance parameter decreases as the frequency increases, while the values of all the reactance parameters are practically unchanged by the frequency. In the measurement it has been checked that the measured values of the parameters at a couple of frequencies in both methods of connecting the capacitance C in either series or parallel with the resonator give a good agreement each other.

A new equivalent circuit

In this section a new equivalent circuit has been considered on the basis of the fact that only the equivalent resistance has such frequency characteristics as investigated in the previous section.

The configuration of the new circuit consists of the commonly used equivalent circuit and another resistance element R_s connected in series, as shown in Fig. 1(b). The sum of the values of the resistance elements R_1 and R_s gives the resonator resistance at the series resonance frequency, $R_1(f_s)$, and the value of R_1 gives the resonator resistance at the parallel resonance frequency, $R_1(f_p)$. Conversely, the parameters R_1 and R_s of the new equivalent circuit can be determined as $R_1 = R_1(f_p)$ and $R_s = R_1(f_s) - R_1(f_p)$.

The characteristics of the resonator resistance calculated by using the new equivalent circuit parameters have been shown by a solid curve in Fig. 4(a). The difference between the calculated and the measured values of the equivalent resistance is less than some five percent, and the new equivalent circuit gives a good agreement with the measured resistance characteristics of the resonator.

Both the series and parallel resonance characteristics of the resonator are simultaneously simulated well, as shown in Fig. 3(c), by using the new equivalent circuit.

Applicability of the new equivalent circuit

In order to consider the applicability of the new equivalent circuit, the relation between the configuration of the new circuit and the dimensions of the resonator has been investigated. Relations

between the resistance ratio $(R_1+R_s)/R_1$ and the parameters which represent the material properties of the resonator have been investigated also.

Measurements have been made on resonators having different diameters and thicknesses. Fig. 5 shows the measured values of the circuit parameters. It has been shown that the parameter L_1 is not changed by the diameter d of the resonator but is proportional to the thickness t , while both the parameters R_1 and R_s are inversely proportional to d (hence proportional to the resonance frequencies f_s ~~or f_p~~) and proportional to t . Then it has been confirmed that the resistance ratio $(R_1+R_s)/R_1$ [$= R_1(f_s)/R_1(f_p)$] is the same for all the resonators of different d and t , and it has been verified that the configuration of the new equivalent circuit is applicable to the sample resonators which have an arbitrary diameter and thickness.

Measurements have been also made on various resonators having different k_p in the range from 15 to 60 percent and different Q from 98 to 1030, and it has been shown that for all the resonators the resistance ratio $R_1(f_s)/R_1(f_p)$ is larger than the unity, being in the range from 1.05 to 1.42. TABLE I shows the measured values of the resistance ratio of a few typical resonators made in the United States. The resistance ratio varies with the material property of the resonator, and it is especially large for high k_p and low Q . These measured values of the resistance ratio of all the resonators used for the measurement have been rearranged in terms of k_p as shown in Fig. 6. An obvious relationship has been found between the resistance ratio and k_p , such that the resistance ratio is especially large for k_p higher than some 50 percent.

Conclusions

A new equivalent circuit has been considered so that it is usable for a better simulation of the impedance characteristics of the radial mode ceramic disc resonators.

It has been shown that the new circuit is applicable to all the resonator samples of arbitrary diameter and thickness. The resistance ratio $(R_1+R_s)/R_1$ is larger for higher piezoelectric coupling factor k_p , and is especially large for k_p higher than some 50 percent for various resonator samples. No obvious relationships have been found between the resistance ratio and the measured values of $\tan\delta$ of the resonators.

From the physical point of view the new circuit has such a configuration as the one taking the dielectric loss into account, however, it is not obvious whether the new equivalent circuit can immediately give quantitative informations concerning the dielectric loss of ceramic material.

Acknowledgement

The authors wish to thank Mr S. Fujishima of Murata Mfg. Co., Ltd. for providing the resonator samples.

References

- [1] Y. Tsuzuki and M. Toki, "Precise Determination of Equivalent Circuit Parameters of Quartz Crystal Resonators," Proc. IEEE, vol. 64, pp 1249-1250 (Proc. Letters), August 1976.
- [2] M. Toki, Y. Tsuzuki and O. Kawano, "Precise Measurements of Equivalent Circuit Parameters of Ceramic Resonators," Trans. IECE of Japan, vol. 62-A, No. 8, pp493-498, August 1979. (in Japanese)
- [3] H. Jaffe, et. al, "IRE Standards on Piezoelectric Ceramics, 1961," Proc. IRE, vol. 49, p 1165, July 1961.

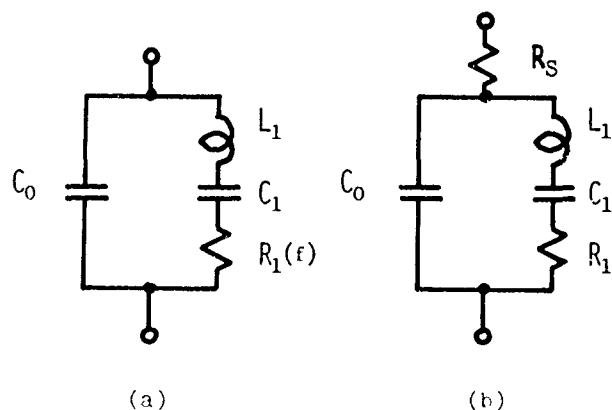


Fig. 1. Equivalent circuits for ceramic resonators: (a) Commonly used circuit
(b) New circuit considered in this paper where $R_1 = R_1(f_p)$ and $R_S = R_1(f_S) - R_1(f_p)$.

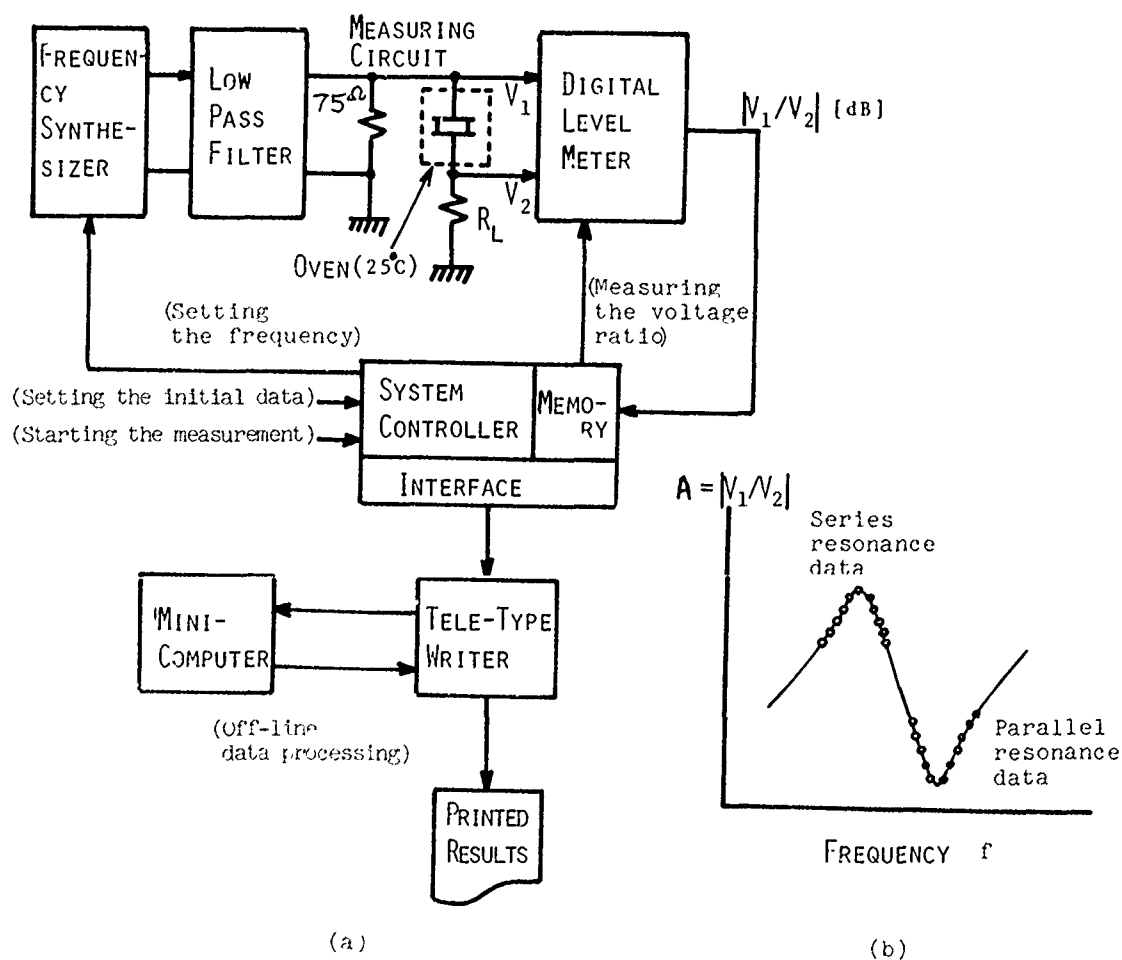
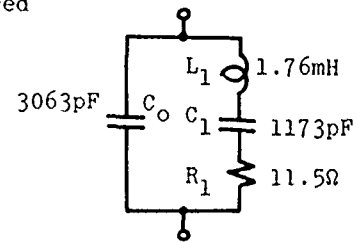
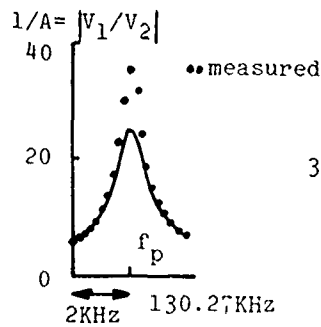
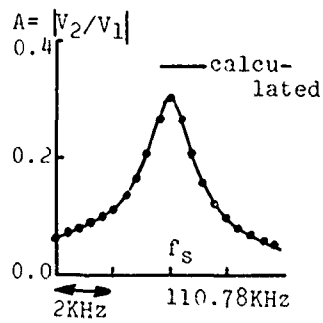


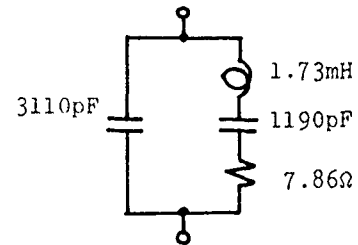
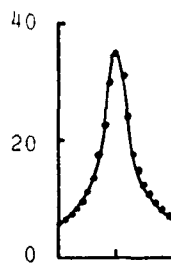
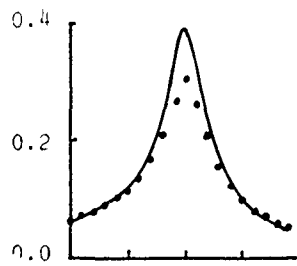
Fig. 2. Automatic measuring system of equivalent circuit parameters of ceramic resonators (a) and characteristics of the voltage transfer ratio (b).

SERIES RESONANCE

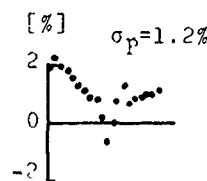
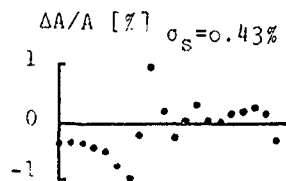
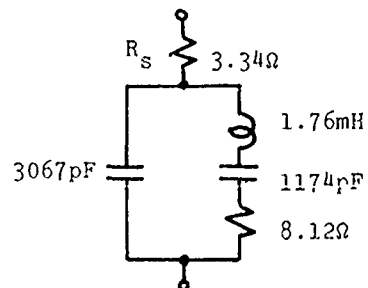
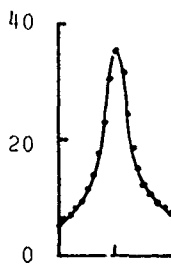
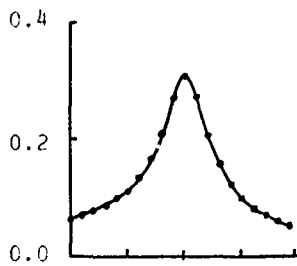
PARALLEL RESONANCE



(a)



(b)



(c)

Fig. 3. Simulation of (a) the series or (b) the parallel resonance characteristics by using the commonly used equivalent circuit and (c) of both the series and parallel resonance characteristics by using the new equivalent circuit.

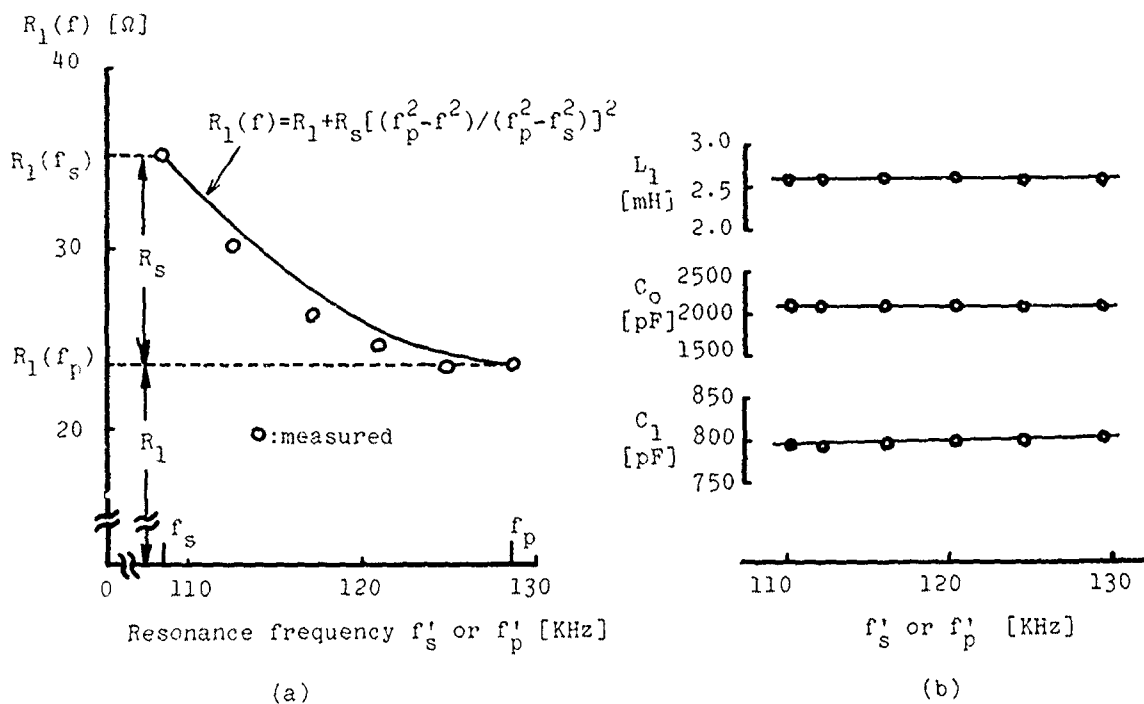


Fig. 4. Frequency characteristics of (a) the equivalent series resistance, and of (b) the reactance parameters.

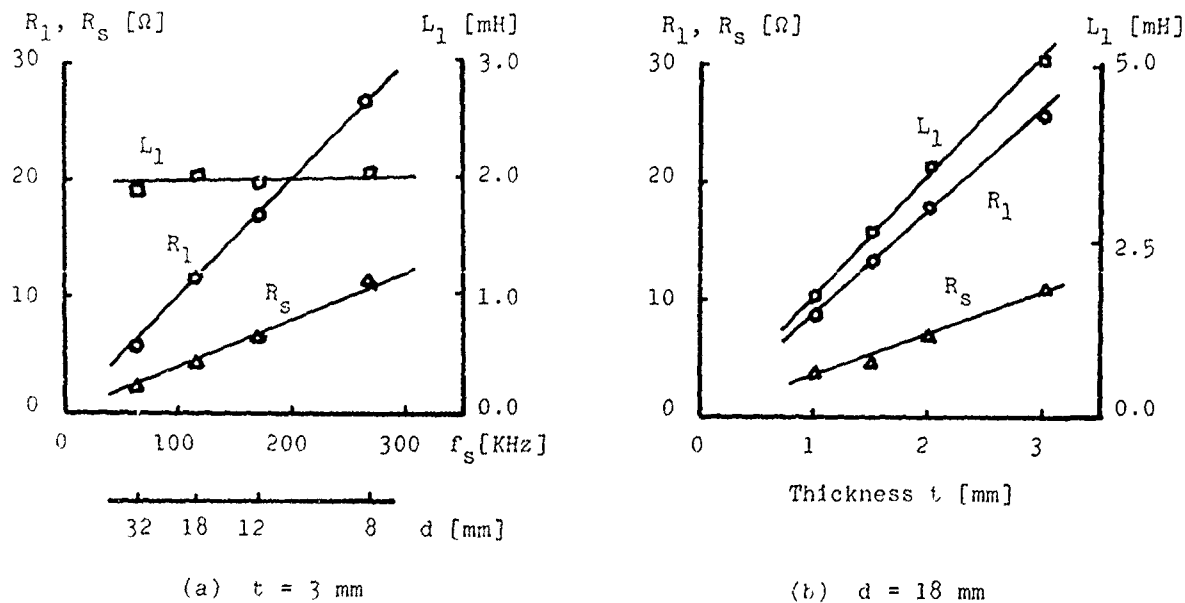


Fig. 5. Parameters of the new equivalent circuit (a) versus the diameter (or versus the resonance frequency) and (b) versus the thickness of a set of radial mode ceramic disc resonators. The resistance ratio $(R_1 + R_s)/R_1$ has been found to be 1.42.

TABLE I Values of $R_1(f_s)$ and the resistance ratio $R_1(f_s)/R_1(f_p)$ of a few typical radial mode ceramic disc resonators.

Resonators	f_s [KHz]	k_p [%]	Q	$R_1(f_s)$ [Ω]	$R_1(f_s)/R_1(f_p)$
No. 1	104.68	58.7	98.4	15.1	1.37
No. 2	118.30	53.2	978	2.6 ₁	1.16
No. 3	116.11	16.4	894	44.1	1.05

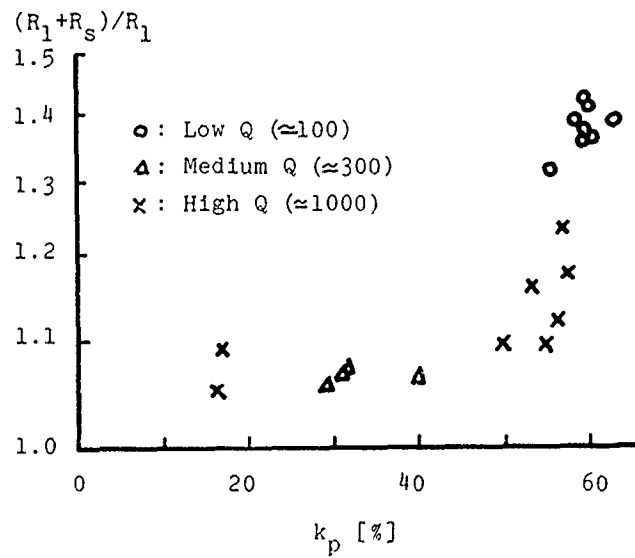


Fig. 6. Relationships between $(R_1+R_s)/R_1$ and k_p .

FACTORS AFFECTING THE QUALITY AND PERFECTION OF HYDROTHERMALLY GROWN QUARTZ

Joseph F. Balascio and Nicholas C. Lias

Motorola, Inc.
Carlisle, Pennsylvania

Summary

The two factors that greatly influenced the degree of etch channel formation in cultured quartz were the control of the initial seed-crystal interface and the maintenance of a uniform growth rate throughout the course of a run. The relative change in both of these factors can be obtained from the analysis of data obtained by the infrared scanning technique.¹⁻³ By controlling both of these factors an eight to tenfold reduction in etch channel density was achieved in production vessels. Average etch channel densities were found to be 118cm^{-2} when grown from sodium hydroxide and 169cm^{-2} from the sodium carbonate mineralizer. The use of electrically swept quartz as seed material further reduced the etch channel density by seventeen percent in the as-grown bar.

Introduction

Alpha quartz has been employed for many years as crystal oscillators and filters. More recent applications for α -quartz include employment as high Q resonators in SAW devices and as narrow bandpass optical filters in the near ultraviolet region of the spectrum. As technologies improve, two natural developments occur. One is the better utilization of component materials and the other is the discovery of new potential uses for component parts. Both of these developments require a high degree of reliability in the component materials employed. The component's reliability, in this case, α -quartz, is important especially with respect to the reproducibility of its desired physical properties.

A present and continuing application for α -quartz is as high precision and high frequency resonators possessing good mechanical strength. It is important to be able to confidently process α -quartz into resonators that will withstand a high shock.⁴ A relative measure of the anticipated mechanical strength of quartz is its etch channel density. Some factors affecting etch channel formation in hydrothermally grown quartz, on a laboratory scale, was presented by Barns et al.⁵ This paper contains a substantial list of references of vari-

ous contributors to this subject. Hydrothermal growth and characterization data on α -quartz have recently been published by a number of investigators⁶⁻⁹ utilizing sodium hydroxide as the mineralizer and by Chakraborty and Saha^{10,11} in the sodium carbonate system.

The objective of this investigation was the correlation of etch channel density to process variables and their control on a production basis. The variables studied during this investigation were the nature of the mineralizer, the thermal gradient, nutrient source and seed preparation techniques.

Experimental

Growth runs were conducted in regular steel autoclaves with inside diameters equal to or greater than ten inches in the production vessels and four inches in the experimental vessels. All vessels were instrumented in similar fashion and were monitored and controlled by an on-line process control computer.

The typical mineralizer concentrations employed during this study were between 0.5 to 1.0 molal. Thermal gradients between the crystallization and nutrient zones were varied from 2° to 50°C . Two types of α -quartz nutrient were employed: natural and cultured. The cultured α -quartz nutrient used was natural quartz recrystallized hydrothermally. Only 0°X seeds were employed and all seeds were inspected between crossed polarizers to be certain they were of uniform quality.⁸ In addition to the regularly processed 0°X seeds used during this investigation, other seed material was electrically swept¹²⁻¹⁷ and these swept 0°X seeds were then placed in selected growth runs for direct comparison with regular 0°X seeds. The sweeping arrangement employed was modeled after that described by Lipson et al.¹⁷ The electric field was varied between 2-5 KV/cm and was applied in the Z direction. Gold plated electrodes were used and the furnace temperature was maintained at $500^\circ\text{C} \pm 0.5^\circ\text{C}$.

Q values were determined by the infrared absorption technique utilizing the 3800 and

3500cm⁻¹ wavenumbers.² Two spectrophotometers were employed for these measurements, a Perkin-Elmer 457 and a Beckman ACTA MIV. Typically, a 2mm round aperture was used when scanning various sections of a quartz Y-cut slice. Each slice was mechanically polished to at least a 3µm finish on a P.R. Hoffman planetary lapping machine before infrared measurements were made.

Etch channel densities were determined on slices cut approximately parallel to the AT plane. These slices were adjacent cuts from the same bars utilized for their respective Q determinations. All samples were etched for two hours at 75°C in a saturated ammonium bifluoride solution. Each etched sample was then viewed under 30X magnification and etch channel counts were made. At least eight different cm x cm areas were counted per sample. The etching arrangement was similar to that described by Vig et al.⁴

Results and Discussion

Growth data were collected from a series of consecutive hydrothermal runs utilizing NaOH as the mineralizer. All these runs were conducted in the same production vessel operated under identical conditions with only the thermal gradient and nutrient source being varied. These data are shown in Figure 1. The bars sectioned and analyzed for these data were located in identical positions in all the runs listed here. The second column lists the average Q values determined from the infrared absorption data obtained on polished Y-cut samples. All slices were scanned along the Z axis. The third column lists the average thermal gradient recorded and controlled during each run. An average value is listed here because it was necessary to program the temperature in order to maintain a uniform growth rate throughout the run. The thermal gradient during growth was not varied more than 15% from the value listed for that run. The last column lists the nutrient source used in each run. To the right of each set of data are portions of the 3500cm⁻¹ infrared scan recorded on identical samples from these runs. These infrared scan portions show the central area of each Y-cut slice containing the original 00X seed employed for growth. These scan portions are to scale and reflect the actual differences between and among them. As the average thermal gradient was lowered, an improvement in the seed-crystal interface occurred. This improvement can be followed, at least qualitatively, by observing the decrease in disruption when scanning the Y-cut slice through the original seed. The areas under the curves for runs 563 and 594 were approximately three times the area shown for 622 and seven times that shown for X95. It should also be noted that the Q value listed does not reflect this change in the seed-crystal interface. The data do show an improvement in Q occurs when cultured nutrient is employed.

The second factor that influenced the etch

channel density in α-quartz was the maintenance of a uniform growth rate throughout the run. The uniformity of growth can also be followed by further analysis of infrared scan data. Figure 2 compares 3500cm⁻¹ scan data on three different polished Y-cut slices. These slices were cut from large pure Z bars grown from the sodium hydroxide mineralizer. The run number and Z dimension of the Y-cuts are shown with each scan segment. The large, almost parabolic, disruption near the center of each scan segment is the seed. In run 577 three thermal setpoint changes were made. Two of these step changes are designated by the letters A and B. With these thermal event markers in the grown bar it is possible to check the calculated growth rate with the actual growth rate during this segment of the growth cycle. The calculated growth rate is obtained by measuring the external Z dimension, subtracting the original seed thickness and then dividing by the length of the run in days.¹⁸ In run 577, the calculated growth rate was measured to be 39 mils/day. Utilizing this growth rate value one would have anticipated 156 mils or approximately 4mm between thermal setpoint changes A and B. The actual value measured was 110 mils and is shown in Figure 2. This value indicates that the actual growth rate in this portion of the run would be 0.70 times that of the calculated growth rate. Another feature that should be noted is the time required for the thermal setpoint changes to abate. The fact that one thermal setpoint change has interfered with another is an indication of sluggishness in the reaction kinetics in this particular system at this point in time. The final point to be made is that better scanning symmetry is evident when better thermal programming is employed. In 577, the asymmetry between the two Z regions separated by the seed is quite noticeable. This asymmetry is an indication of a non-uniformity, radially, in the thermal environment. The thermal gradient in run 577 was 50°C whereas, for both 599 and 675 the average gradient was 40°C. In the latter two scan segments shown in Figure 2, the thermal setpoint changes were programmed and resulted in calculated growth rates of 37.3 and 36.3 mils/day.

Another measure of growth uniformity is the size distribution of grown bars in a vessel. The size distribution reflects the degree of thermal uniformity in the crystallization zone. Table 1 shows the size variations of as-grown bars within and between the top and bottom tiers in run X95. Standard deviations were calculated for each dimension. The average Q value was determined from infrared absorption measurements. A ΔZ of 78 mils (1.98mm) was found between the top and bottom tiers with an average deviation of 33 mils (0.84mm) within a tier.

For comparison with these growth rate data, runs were also conducted employing static thermal setpoints throughout the length of the run. These data were gathered from our experimental vessel program and some of these data are shown in Table 2. In this run natural α-quartz nutri-

ent was employed, as well as, regularly processed 00X seeds. In this table, T_c is the crystallization temperature and T_n the nutrient temperature. The \bar{X} and \bar{Z} growth rates were calculated from end-run measurements of the dimensions of all the as-grown bars. Q values were calculated from the infrared absorption measurements made at 3800cm^{-1} and 3500cm^{-1} on the polished Y-cut slices. Since no thermal event marker is present in this run, the only indication of a change in growth rate is the change in Q during the course of the run. In the series of runs performed with fixed thermal setpoints, the minimum Q invariably occurred early in the run.

Figure 3 is a photomicrograph of a mechanically polished and etched Y-cut slice grown in the sodium carbonate mineralizer utilizing fixed thermal setpoints. This figure illustrates that etch channels can originate at the seed-crystal interface, as well as, further out in the grown material. The two parallel lines in the center of the photomicrograph are the outer boundaries of the original seed used in this run. The etch channels are seen as white lines, some of which are so close together that they appear to be a larger white area.

The reduction in etch channel densities by controlling the seed-crystal interface and maintaining a uniform growth rate are shown in Tables 3 and 4. These tables compare the average etch channel densities and their standard deviations on sample bars grown in both mineralizers. The run numbers listed for the hydroxide mineralizer data coincide with those employed for demonstrating the relationship between the seed-crystal interface and the thermal gradient in Figure 1. One additional run was added to these namely, 533. The growth rate data listed in these two tables are average calculated rates determined from end-run dimensions. The Q values listed in both tables are average values calculated from their respective infrared absorption measurements. Etch channel densities were determined on slices cut approximately parallel to the AT plane. In Table 3, a relative reduction in etch channel density of 8.5X occurred while in Table 4 a reduction of 10X was observed. The sodium hydroxide mineralizer data show no correlation between either the calculated growth rate and etch channel density or between the average Q and the etch channel density.

A series of samples with relatively low etch channel densities were analyzed for their respective iron and aluminum levels (Table 5). These samples were randomly selected from recent production runs without regard to a particular set of PT conditions or mineralizer. The etch channel densities were determined by the procedure listed in the experimental section. Impurity levels were determined by ion microprobe and are in weight percent. These impurity analyses were performed on sample sections prior to any etching of these sec-

tions. The first column lists the mineralizer employed during growth and the state of the sample used for the data determined in the following columns. The letter (A) denotes that the electrically swept hydroxide sample was a section from the same as-grown hydroxide bar marked with that letter. Minimum Q values were determined as previously described. These values were the lowest ones determined when scanning completely across the Z region of the Y-cut slice. In all samples ± 0.060 inches from the seed center was eliminated for this minimum Q determination. Inspection of these data show that the impurity uptake of iron and aluminum in the as-grown bars was essentially equivalent regardless of the mineralizer. Also, no change in either the impurity levels or Q_{\min} was found between the as-grown and electrically swept (A) samples. All bars analyzed in this table were grown utilizing natural quartz nutrient and regularly processed 00X seeds. No correlation is readily discernible between these substitutional impurities, at these levels, and their respective etch channel densities. However, a significant reduction in etch channel density does occur upon electrically sweeping without apparently affecting the iron or aluminum level in the bar.¹⁹ Most of the as-grown bar data in this table are included in Table 6 which compares a wider distribution of randomly selected bars grown in both mineralizers utilizing natural quartz as the nutrient. Regularly processed 00X cultured α -quartz seeds and electrically swept 00X seeds were employed. This table compares the etch channel density with minimum Q for various α -quartz samples. The top section of this table lists data gathered on various samples examined from bars grown in NaOH; the middle section lists data gathered from bars grown in Na_2CO_3 and the bottom section compares etch channel densities among bars grown in the same hydrothermal run utilizing different seed preparation techniques.

The average etch channel density for all hydroxide grown bars listed in the top third of this table is $118 \pm 69\text{cm}^{-2}$. This average excludes the swept seed result. In the carbonate mineralizer group, also excluding the swept seed result, the average etch channel density was found to be $169 \pm 158\text{cm}^{-2}$. In both of these cases it would appear that the etch channel density of swept seeds was greater than that of regularly processed 00X seeds. However, when a direct comparison is made between swept and unswept seeds in the same hydrothermal run, the etch channel density was found to be approximately seventeen percent lower in the swept seeds. These data are shown in the bottom third of Table 6. The letters T and B denote that those bars examined were taken from the top and bottom tiers in that growth run. These two bars were in identical positions within their respective tiers. The swept seeds were interspersed in the top four tiers of that run.

Conclusions

The results of this investigation have demonstrated that the quality and perfection of hydrothermally produced α -quartz are considerably affected by both the initial seed-crystal interface and the maintenance of a uniform growth rate. The relative change or the degree of improvement, with respect to etch channel formation, can be followed, at least qualitatively, through the analyses of infrared scan data. The data gathered during this study showed that the nature of the mineralizer and the nutrient source had little effect upon the etch channel density compared to the thermal gradient. The change in etch channel density between swept and unswept quartz did not correlate to either a change in the substitutional cation level or the minimum Q of the material. However, electrically swept seeds did further lower this density by approximately 17%.

Acknowledgements

The authors would like to acknowledge the contributions of the following individuals to this investigation: Dennis Reifel and Len Tyler of Motorola's Franklin Park, Ill. facility for initial discussions on this subject; Gary Hunt and Thomas Walker of Motorola's Carlisle, Pa. facility for contributions in all aspects of sample preparations and measurements and finally to Dr. John Vig of ECOM for many discussions concerning various aspects of etch channel formation.

References

1. Rudd, D.W.; Houghton, E.E. and Carroll, W.J., *The Engineer*, Western Electric, 22 (1966).
2. Sawyer, B., *IEEE Trans. Sonics and Ultrasonics*, SU-19, 41 (1972).
3. Brice, J.C. and Cole, A.M., *Proc. 32nd Annual Freq. Control Symposium*, 1 (1978).
4. Vig, J.R.; LeBus, J.W. and Filler, R.L., *Proc. 31st Annual Freq. Control Symposium*, 131 (1977).
5. Barns, R.L.; Freeland, P.E.; Kolb, E.D.; Laudise, R.A. and Patel, J.R., *J. Crystal Growth* 43 676 (1978).
6. Kolb, E.D.; Pinnow, D.A.; Rich, T.C.; Laudise, R.A.; Tynes, A.R.; Lias, N.C. and Grudenski, E.E., *Mat. Res. Bull.* 7 397 (1972).
7. Lias, N.C.; Grudenski, E.E.; Kolb, E.D. and Laudise, R.A., *J. Crystal Growth* 18 1 (1973).
8. Barns, R.L.; Kolb, E.D.; Laudise, R.A.; Simpson, E.E. and Kroupa, K.M., *J. Crystal Growth* 34 189 (1976).
9. Asahara, J. and Taki S., *Proc. 26th Annual Freq. Control Symposium*, 117 (1972).
10. Chakraborty, D. and Saha, P., *Indian J. Phys.* 48 439 (1974).
11. Chakraborty, D. and Saha, P., *Indian J. of Technology*, 11 No. 3 127 (1973).
12. King, J.C., *Proc. 13th Annual Freq. Control Symposium*, 1 (1959).
13. Dodd, D.M. and Fraser, D.B., *J. Chem. Phys. Solids*, 26, 673 (1965).
14. Brown, R.N. and Kanan, A., *J. Phys. Chem. Solids*, 36, 467 (1975).
15. Koehler, D.R., *Proc. 33rd Annual Freq. Control Symposium*, 118 (1979).
16. Brown, R.N.; O'Connor, J.J. and Armington, A.F., *Rome Air Development Command*, TR-79-175 (1979).
17. Lipson, H.G.; Euler, F. and Armington, A.F., *Proc. 32nd Annual Freq. Control Symposium*, 11 (1978).
18. Conlee, L. and Reifel, D., *Proc. 28th Annual Frequency Control Symposium*, 1 (1974).
19. Martin, J.J.; Doherty, S.P.; Halliburton, L.E.; Markes, M.; Koumvakalis, N.; Sibley, W.A.; Brown, R.N. and Armington, A.F., *Proc. 33rd Annual Freq. Control Symposium*, 134 (1979).

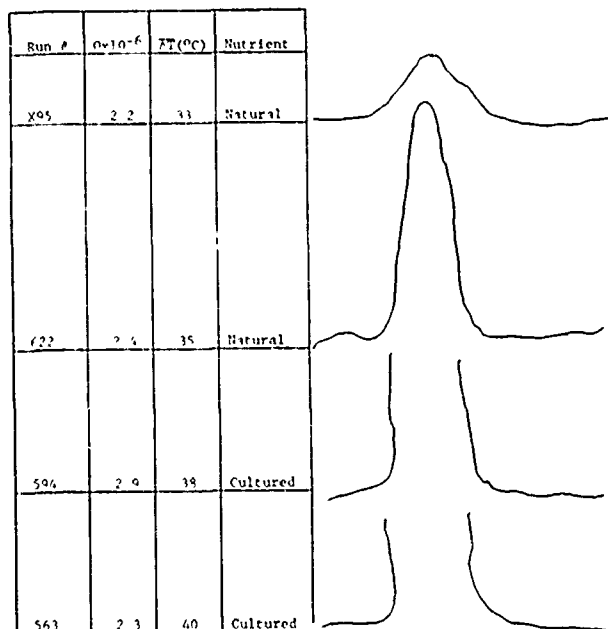


FIGURE 1 - COMPARISON OF SEED-CRYSTAL INTERFACE WITH THERMAL GRADIENT

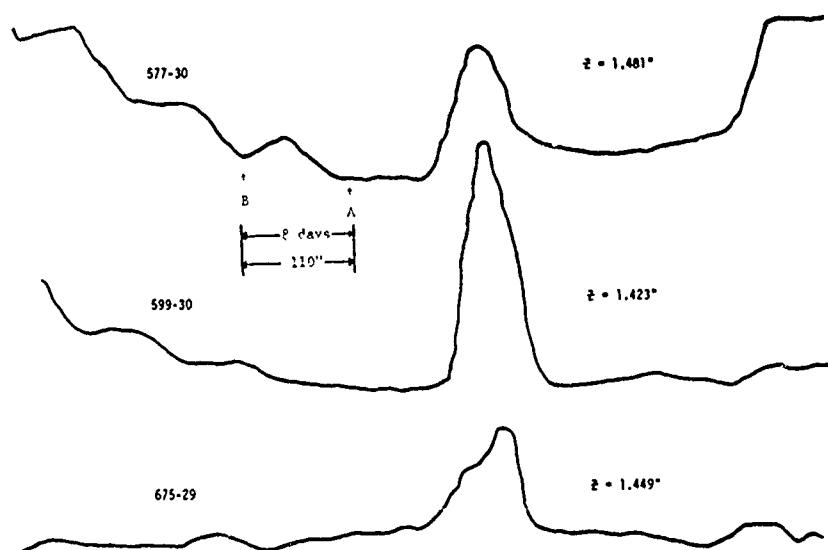


FIGURE 2 - COMPARISONS OF IR SCANNING PROFILES OF LARGE PURE Z SLICES

	TOP TIER	BOTTOM TIER
\bar{Z} (IN.)	0.944 \pm .031	1.022 \pm .036
\bar{X} (IN.)	1.858 \pm .025	1.877 \pm .025
\bar{X}/\bar{Z}	.603	.574
$\bar{\alpha} \times 10^{-6}$	2.302	2.227

TABLE 1 - COMPARISON OF AVERAGE GROWTH DIMENSIONS AND $\bar{\alpha}$ IN RUN X95

Run #	RD-17	G.R. \bar{X} (mil/day)	18.1
Mineral.	Na ₂ CO ₃	G.R. \bar{Z} (mil/day)	29.0
% Fill	75	\bar{X}/\bar{Z}	.624
T _c (°C)	333	$\bar{Q}_{min}(\times 10^{-6})$	1.804
T _n (°C)	335	$Q_{max}(\times 10^{-6})$	2.567
KPSI	8.5	$\Delta \bar{Q}(\times 10^{-6})$.763

TABLE 2 - TYPICAL Q VARIATION UNDER STATIC THERMAL SETPOINT CONDITIONS



FIGURE 3 - PHOTOMICROGRAPH OF ETCHED Y-CUT α -QUARTZ (6X)

Run No.	Growth Rate (mils/day)	$\bar{Q} \times 10^{-6}$	Channel Density (cm ⁻²)
533-16	19.4	2.7	848 \pm 339
563-16	22.1	2.3	893 \pm 360
594-16	24.5	2.9	903 \pm 372
622-16	22.6	2.4	543 \pm 175
X95-16	22.8	2.2	107 \pm 26

TABLE 3 - COMPARISON OF ETCH CHANNEL DENSITIES WITH SELECTED FACTORS IN HYDROXIDE MINERALIZER

Run No.	Growth Rate (mils/day)	$\bar{Q} \times 10^{-6}$	Channel Density (cm^{-2})
549-2	13.2	1.6	561+165
833-2	13.7	1.9	54+ 16

TABLE 4 - COMPARISON OF ETCH CHANNEL DENSITIES WITH SELECTED FACTORS IN CARBONATE MINERALIZER

Sample Description	Etch Channel ρ (cm^{-2})	Fe(ppm)	Al(ppm)	$Q_{\min} \times 10^6$
Hydroxide - as grown	33	6	10	1.441
Hydroxide - as grown	175	6	8	1.672
Hydroxide - as grown (A)	95	6	10	2.100
Carbonate - as grown	140	5	10	1.884
Carbonate - swept	5	5	3	2.300
Hydroxide - swept (A)	5	6	10	2.100

TABLE 5 - COMPARISON AMONG ETCH CHANNEL DENSITIES, Q AND SUBSTITUTIONAL IMPURITY LEVELS IN α -QUARTZ

Description	Minimum Q ($\times 10^6$)	Channels(cm^{-2})
Hydroxide - regular seed	1.441	33
Hydroxide - regular seed	1.672	175
Hydroxide - regular seed	2.000	95
Hydroxide - regular seed	2.500	85
Hydroxide - regular seed	1.410	202
Hydroxide - swept seed	1.441	175
Carbonate - regular seed	1.940	474
Carbonate - regular seed	1.884	140
Carbonate - regular seed	2.720	42
Carbonate - regular seed	1.315	135
Carbonate - regular seed	1.613	54
Carbonate - swept seed	1.633	300
Hydroxide - swept seed	1.441	175
Hydroxide - regular seed T	1.410	202
Hydroxide - regular seed B	1.410	220

TABLE 6 - COMPARISON OF ETCH CHANNEL DENSITIES WITH MINIMUM Q FOR VARIOUS α -QUARTZ SAMPLES

RADIATION EFFECTS IN QUARTZ OSCILLATORS, RESONATORS AND MATERIALS

Ferdinand Euler, Herbert G. Lipson and Paul A. Ligor

Rome Air Development Center
Deputy for Electronic Technology
Hanscom AFB, MA 01731

Summary

A number of different quartz growing and sweeping processes have been evaluated for radiation sensitivity, utilizing measurements of oscillator frequency, resonator transient resistance, acoustic loss and infrared impurity spectra. Considering all aspects of expected ionizing radiation effects, swept Premium-Q or equivalent is the recommended commercially available quartz with the lowest sensitivity to radiation. Any quartz containing even traces of sodium impurity should be rejected. Sweeping quartz will effectively eliminate alkali impurity, and reduce short-term transients and permanent frequency offset. Slow growth with lithium salt added to the mineralizer reduces radiation-induced drift rate changes. Even with high quality swept quartz, there is at least an order of magnitude variation in the radiation-induced steady-state frequency offset. Our results are consistent with the radiation response of the three principal aluminum related defect centers, $Al-M^+$, $Al-OH^-$ and $Al-e^+$, but these do not account for all of the observed effects.

Key words: Quartz Oscillators, Resonators, Radiation Effects, Acoustic Losses, Premium-Q, Infrared Spectra, Impurity Bands, Defect Centers.

Introduction

In this paper we present additional results on the effects of ionizing radiation on crystal oscillators, resonators, and quartz. As reported in previous publications,¹⁻⁴ it is our objective to characterize the radiation response of high-grade quartz, and to determine material processing procedures necessary to satisfy stringent military requirements for high stability frequency standards. At the same time it is our desire to elucidate the mechanisms responsible for observed radiation effects.

The phenomenological model utilized in interpreting data on electrodiffused (swept) or irradiated quartz involves an aluminum impurity substitutional for silicon in the SiO_2 lattice. A recent extensive review of this model has been given by L. Halliburton at this Symposium⁵, and we will outline only the highlights.

Trivalent aluminum (Al^{3+}), and possibly iron (Fe^{3+}), is incorporated substitutionally in silicon (Si^{4+}) sites. Monovalent ions, H^+ , Li^+ , Na^+ , and

K^+ tend to be interstitial near the trivalent ion to maintain charge neutrality. Charge compensation can also be provided by a hole trapped at an oxygen site. The impurity and its compensator gives rise to aluminum-hydroxide ($Al-OH^-$), aluminum-metal ($Al-M^+$), and aluminum-hole ($Al-e^+$) defect centers.

As grown, synthetic quartz contains $Al-M^+$, with $Al-Na^+$ as the dominant defect center. Lithium salt added to the mineralizer during crystal growth inhibits the formation of $Al-Na^+$, and presumably forms $Al-Li^+$. Sweeping quartz in air dissociates $Al-M^+$ and forms $Al-OH^-$. Irradiating unswept quartz at room temperature or above also converts $Al-M^+$ into $Al-OH^-$ and $Al-e^+$ centers. The factors controlling the concentration ratio of these new centers are unclear. Irradiating swept samples at room temperature and above may create additional defect species or change the ratio of $Al-OH^-$ and $Al-e^+$ concentration.

The $Al-OH^-$ center can be experimentally observed in the infrared at 3306 and 3366 cm^{-1} . The $Al-e^+$ center is EPR active, whereas some $Al-M^+$ centers show anelastic loss peaks in the Q^{-1} spectrum of resonators as a function of temperature. Specifically, the loss peak near 50 K is attributed to $Al-Na^+$. The identification of Q^{-1} peaks with $Al-Li^+$ and $Al-K^+$ is not as clearcut. There is also indication that a broad maximum observed at approximately 100 K may be attributed to $Al-e^+$.

Our measurement techniques include: (1) low temperature infrared spectroscopy before and after sweeping and irradiating quartz, (2) Q^{-1} of resonators as a function of temperature before and after ionizing irradiation, and (3) transient and permanent oscillator frequency offsets as a function of irradiation. During the last year we have expanded our data base to include almost all commercially available high quality quartz, sweeping techniques, and precision resonator fabrication procedures.

The main difficulties in identifying the mechanisms responsible for observed radiation effects in oscillators are that: (1) the specific radiation responses of $Al-OH^-$ and $Al-e^+$ have not been separated, (2) there is no direct, sufficiently sensitive measurement technique to monitor $Al-Li^+$, and (3) there are indications of additional unidentified sweeping-and radiation-induced defect centers.

Experimental Procedures

We report results on Premium-Q, High-Q, and Electronic Grade synthetic commercial quartz. Electronic Grade material was obtained from Bliley, Motorola, and Western Electric. Premium-Q and High-Q quartz was grown at Sawyer Research Products (SARP) by the same process, except that for Premium-Q lithium salt was added to the mineralizer. We evaluated six different sweeping processes: SARP I, SARP II, Bliley, and sweeping in air, vacuum, or dried nitrogen ambient. In addition, Li^+ , Na^+ , and K^+ ions were introduced by electrodiffusion into swept Premium-Q quartz.⁶ Precision 5 MHz, 5th overtone, AT cut quartz resonators were fabricated from these materials by Bliley Electric Co. and Frequency Electronics, Inc. (FEI). Table I presents an updated^{1,4} pedigree of these resonators.

The measurement and irradiation procedures involved in our investigations have been described before^{2,4} and are briefly summarized here. The resonator region of the oscillator test bed was irradiated with 10 MeV electrons to a total dose of 1 Mrad. After each exposure the oscillator frequency was measured together with the oven control

Table I. Resonator identification and pedigree.

resonator series	growth	bar	refs
Bliley	FEI		
BE	B	SARP	A 6-24 A4I 2-4
24334		SARP	A14-23 C7C 2-4
BA	E,F	SARP	A14-27 2-4
BB,BC,BI		SARP	A14-27 4
	I	SARP	A14-27 β 1 2,3
	K	SARP	A14-27 θ 2
BF,BH	R	SARP	D14-45 4
BD	G	SARP	D14-45 39a 2,4
BG	N	SARP	D14-45 10b 4
	L,M	SARP	D14-45 Ea,b
	EA,EB,EC	SARP	D14-45 2a,b
	T	SARP	E42-21 19a
	U	SARP	E42-21 18b
BNN,BNns	P,Q	Bliley	A12-35 QNU1 1,2
BNc,BNcs,BJ		Bliley	A 1-35 QCU1
BLn,BLns,BK		Bliley	A 4-42 QNL1
BLc,BLcs,BL		Bliley	A 2-33 QCL1 1,2
	C,H,J	Motorola	176-16 MH1 1,2
	ED,EE	W.E.	R-face 20 1

Table II. Steady-state fractional frequency offset $\Delta f/f$ after 1 Mrad irradiation.

quartz growth and sweeping G M A N S	resonator series and offset Bliley $\Delta f/f$ pp 10 ⁹	FEI $\Delta f/f$ pp 10 ⁹	Legend
E OH Li n -		ED +1370	G quartz grade
E C - n -	BNN +7330		E Electronic Grade
E C - c -	BNc +1560		HQ High-Q
E C Li n -	BLn +26		PQ Premium-Q
E C Li c -	BLc +280		M mineralizer
HQ C - c -		T +1650,+1400*	OH NaOH
PQ C Li c -		I +26*, +23*	C Na ₂ CO ₃
PQ C Li c -	BD -31	G -5* a	A additive to mineralizer
E OH Li n R		EE -24	- none
E OH Li c R		H;J -78; -70	Li lithium salt
E C - n B	BNns -200*	Q -66 a	N nutrient
E C - n R	(300 krad)	P -29	n natural (lascas)
E C - c B	BNcs -80		c cultured (synthetic)
E C - c R	BJ +30		S sweeping process
E C Li n B	BLns -58		B Bliley
E C Li n R	BK -54		R RADC/ES (dried N ₂ ambient)
E C Li c B	BLcs -20*(300 krad)		I SARP I
E C Li c R	BL -38		II SARP II
HQ C - c II		U -10	Sa Sandia Labs., air ambient
PQ C Li c I	BE -440	B -270 to -420* a	Sv Sandia Labs., in vacuum
PQ C Li c I	BB -34	R -6, -20	
PQ C Li c II	BF;BC -20; -84*	K -21	
PQ C Li c II	BG +7	N -12 a	
PQ C Li c R	BH;BI +12; +8		
PQ C Li c Sa		E -30*, -40*	
PQ C Li c Sa		L -11	
PQ C Li c Sv	BA -250, -325	F -8*, -20* b	
PQ C Li c Sv		M -40	
PQ C Li c R	doped with Li	EA -35, -41	
PQ C Li c R	doped with Na	EB +760, +400*	
PQ C Li c R	doped with K	EC +4, -515 c	

and AGC voltages. Resonator resistance changes were calculated from the AGC voltage. Post irradiation frequency drift was measured for periods ranging from 4 days to several weeks. Quartz samples and resonators were also irradiated with ^{60}Co gamma rays. Resonator Q was obtained as a function of temperature, between 4.5 and 420 K. For infrared spectroscopy, quartz samples were prepared with polished faces normal to the crystallographic X-, Y-, and Z-directions. Transmission was measured at 35 K between 3100 and 3700 cm^{-1} with 1 cm^{-1} resolution, using unpolarized or polarized radiation.^{4,15}

Results and Discussion

Radiation Effects on Oscillators and Resonators

Figure 1 depicts the terminology used in this paper for the short-intermediate-, and long-term radiation response of the oscillator frequency. Single pulse exposures are essential to measure short-term transients. The steady-state offset was defined as the value after the decay of the short- and intermediate-term transients.

Steady-State (Permanent) Frequency Offset. Figure 2 shows the dose dependence of the steady-state fractional frequency offset of four selected resonators. The positive offset for the unswept High-Q quartz resonator is attributed to the conversion of Al-Na^+ into Al-OH^- or Al-e^+ centers. The offset for unswept Premium-Q is smaller by 1 to 2 orders of magnitude, showing the effectiveness of lithium salt addition in reducing the radiation sensitivity of quartz. Swept Premium-Q samples demonstrate a wide variation in frequency offset.

Table II lists all steady-state offset values measured after 1 Mrad irradiation. The unswept Electronic Grade data included in this Table are shown for comparison only. We do not expect any application of these materials in situations where radiation hardness is required. Sweeping any of these Electronic Grade or High-Q materials leads to a drastic reduction in radiation sensitivity. The listed offset values for all swept quartz resonators lie between +30 and -420 pp 10^{-9} and the differences over this wide range cannot clearly be attributed to any growth, sweeping, or resonator fabrication process.

Sweeping in air forms Al-OH^- , whereas sweeping in vacuum should result in Al-e^+ . In fabricating resonators from vacuum swept material one has to be careful not to change Al-e^+ into Al-OH^- , for example, by exposing the material to a high temperature hydrogen atmosphere heat treatment, as practiced by some manufacturers. This difference in fabrication process is a possible explanation for the drastic differences in frequency offset for series BA and F.

Among the three series of alkali-ion-doped quartz resonators, sodium doping shows the expected

positive offset and lithium-doping shows characteristics of both unswept and swept Premium-Q quartz. At the present time we cannot explain the differences for the two potassium-doped resonators, series EC. Additional acoustic loss and frequency offset measurements are in progress to determine the characteristics of potassium-doping.

We consistently find the steady-state frequency offset for unswept Premium-Q comparable to or smaller than for swept Premium-Q. At the time when King introduced the sweeping process in the late 1950s,⁷ synthetic quartz had low Q-values, $1-5 \times 10^6$. Sweeping increased the Q-value to over 2×10^6 . At the same time, the removal of sodium ions during the sweeping process has also decreased the radiation sensitivity. Consequently, radiation insensitive quartz has become associated with swept quartz. It was also shown² that the addition of lithium salt to the mineralizer during growth inhibits the incorporation of sodium ions and increases the as-grown Q-value to $2-3 \times 10^6$. Therefore, sweeping high quality quartz is not absolutely essential for radiation hardness. One is then bound to ask: why should one sweep Premium-Q? It is true that sweeping does not necessarily decrease the steady-state offset of Premium-Q quartz, but we have shown^{2,4} that other oscillator performance characteristics are dramatically affected by the use of unswept material.

Short-Term Transients. Figure 3 shows that the short-term frequency and resistance transients of Premium-Q crystal resonators have similar time dependencies.⁴ The changes for unswept quartz are about 20 times larger than for swept material and their maxima occur later. The resistance changes increase with dose and may exceed the oscillator AGC control range. This will cause the oscillation to stop. Oscillator stoppage may be prevented either by modifying the oscillator and AGC circuitry or by using swept quartz.⁹ Resistance transients for selected resonators are shown in Figure 4 and additional data is listed in Table III.

Two types of short-term transient characteristics, slow and fast, can be discriminated by whether the time t_m at which maximum resistance change ΔR_m occurs is longer or shorter than approximately 30 msec. Slow type transients are found with unswept High-Q, Premium-Q, and Na-doped quartz and have been attributed⁷ to mobility of alkali ions freed from Al^{3+} and other trapping sites. Fast type transients were found with swept quartz. A comparison between unswept (resonator G-1) and swept Premium-Q quartz (resonator BC-81), evaluated in the same oscillator test bed shows $t_m = 150$ msec and $t_m = 17$ msec, respectively.

In addition to material effects, t_m is also influenced by individual oscillator test beds. The ones used here are of identical design, yet we find that, in spite of precautions not to irradiate any electronic components, for swept resonators

$t_m \leq 3$ msec in test bed 7211, and $t_m = 17$ msec in test bed 7214. For swept quartz, ΔR_m varies from 5 to 40 ohms/krad. We are not able to attribute differences within this range to any particular sweeping process or quartz grade. It is therefore difficult to correlate the fast type transients with specific atomic defects.

The curve shown for the lithium-doped swept Premium-Q resonator exhibits a fast type maximum superimposed on a slow type transient. From infrared measurements we know that the sweeping-in of Li^+ ions was not complete and $Al-OH^-$ centers are still present in the material. Therefore, it is not surprising that the transient response of this resonator exhibits both the characteristics of unswept and swept Premium-Q quartz.

From the standpoint of minimizing radiation-induced short-term transients, well-swept quartz of Premium-Q, High-Q, and possibly even of Electronic Grade appears to be equally useful.

Intermediate-term Transients. The time range between 1 and 1000 seconds shows effects of energy deposition by irradiation particles with subsequent heating of the resonator components.^{10,11} At turn-over temperature, the inner oven of our oscillator test beds is sensitive to minute temperature changes, and we find that it shuts off for a number of seconds, or minutes, after exposures exceeding several kilorads. Table IV shows the shut-off time per unit dose for various unswept and swept resonators. We find that, as a class, swept quartz resonators cause the oven to shut off for a substantially shorter time than some unswept quartz resonators. This difference between unswept and swept material, and the large shut-off time variations between unswept resonators indicate that the temperature rise in the material is influenced by crystal impurities.

Radiation-Modified Drift. We reported²⁻⁴ previously a number of different frequency drift patterns for irradiated resonators. We observed increases and decreases of the drift rate as well as spontaneous and stimulated frequency changes. The pattern we find most frequently is shown in Figure 5. It is characterized by a frequency minimum, occurring shortly after irradiation, and a subsequent increase which levels off after several days. Table V lists calculated drift rates (in $pp\ 10^9/day$) for 1, 2, and 4 days after irradiation for selected resonators.

Pre-irradiation drift rates for all listed samples were in the $pp\ 10^{-9}/day$ range, and irradiation has increased these values by an order of magnitude. The high drift rates persist for several days. Swept Electronic Grade resonators show consistently higher post-irradiation drift rates than swept Premium-Q. We find that the radiation-induced drift change is not correlated with the steady-state frequency offset. For example, a comparison of unswept and swept Electronic Grade and High-Q resonators show offset values differing by two orders of magnitude (Table II), whereas their drift rates are

Table III. Transient resistance change after single 10 MeV electron pulse.

quartz	reso-nator	osc.	dose rad	ΔR_m ohm	t_m msec	Δt_h msec
High-Q (unswept)	T-99	7212	820*	1270	50	150
			2400	1850	50	140
Premium-Q (unswept)	I-15	7212	700*	317	60	450
	G-1	7214	600	220	150	
			1100	285	150	
Na-doped	EB-27	7212	200	76	120	
Li-doped	EA-53	7212	1550*	f 46	8	20
				s 34	100	
K-doped	EC-36	7214	600	10	20	60
			850	17		
High-Q (swept)	U-72	7211	1550	15	<2	23
			3300	18		
Premium-Q (swept)	B-4	7211	270	5		
			320	13		
			450	13		
			840*	25	3	23
	BH-68	7211	250	10	3	60
			860	34	3	60
	F-2	7211	960	33	3	25
			1650	48		
	BC-81	7214	200	4		
			840*	12	17	30
	BI-76	7214	200	6		
			560	17	17	94
			2100	18		
	BA-72	7214	330	5		
			700	13	17	70
			1030	15		
	M-1	7214	700	12	17	30
			1200	12		
SC-cut	D-14	7212	550*	29	2	4

ΔR_m - maximum resistance change
 t_m - time of resistance maximum
 Δt_h - time interval between $\Delta R = \Delta R_m/2$
 f - fast component
 s - slow component
 * - time dependence shown in Figure 4

Table IV. Inner oven shut-off time after 10 MeV electron irradiation.

quartz	reso-nator	time off sec/krad
High-Q (unswept)	T-99	10 - 30
Premium-Q (unswept)	I-15	10 - 14
	G-1	2 - 2.5
Na-doped	EB-27	1 - 3
Li-doped	EA-53	11
Electronic (swept)	BNns-65	0.7 - 1.0
High-Q (swept)	U-72	1.5
Premium-Q (swept)	BA-72	1.5
	BC-81	0.8 - 1.5
	24334	0.7 - 1.1
	F-6	0.7
	F-2	0.2 - 0.4
	B-5	0.4 - 0.5
	E-3	0.2 - 0.4

comparable. Similarly, the lowest drift rate change was observed with a vacuum swept Premium-Q resonator, in spite of its relatively high steady-state offset.

Acoustic Losses as Function of Temperature

A representative selection of acoustic loss curves is shown in Fig. 6. A strong Al-Na⁺ peak near 50 K is present for the unswept High-Q resonator. The peak value of Q^{-1} decreases after 1 Mrad irradiation by 1.6×10^{-5} . The corresponding fractional frequency increase at 60 K is 1.35×10^{-5} , in good agreement with the model relating frequency and Q^{-1} changes.^{7,12} With increasing temperature, $\Delta f/f$ decreases monotonically to 2×10^{-6} at room temperature and to 1.4×10^{-6} at 75°C. In unswept Premium-Q, there is a small trace of the 50 K peak and in swept quartz, including swept Electronic Grade, it is absent. Doping swept Premium-Q with Na⁺ produced a 50 K peak with $Q^{-1} = 1.2 \times 10^{-5}$ for resonator EB-27.

In some Electronic Grade material there is a series of sweeping-induced peaks. The data in Fig. 6 for swept Electronic Grade resonator J-1 shows peaks at 40, 110 and 170 K. The nature of these has not been identified. It has been suggested¹³ that some of these loss peaks are related to Al-e⁺. In our experiments, the peak indicative for the Al-Li⁺ center¹⁴ at 105 K is not found with certainty, neither with unswept Premium-Q (grown with lithium salt added to the mineralizer) nor with swept Premium-Q doped with Li⁺ by electrodiffusion. With respect to swept Premium-Q resonators, the acoustic losses show no systematic radiation effects. Similarly, we find substantial variations⁴ in the acoustic losses of vacuum swept resonators, even when fabricated from the same bar. Peaks near 40 K and in the range between 120 and 140 K appear with some samples but not with others. Thus, except for the 50 K Na⁺ peak, it is difficult to relate radiation-induced acoustic loss changes with frequency offset.

Radiation Effects on Infrared Impurity Spectra

We have shown¹ that high grade synthetic quartz can be characterized by its low temperature impurity spectrum, consisting of four bands occurring in all synthetic quartz, designated as s-bands, and two others produced by electrodiffusion or radiation, designated as e-bands. All these bands are generated by O-H vibrations, with the e-bands being associated with Al-OH⁻. The strongest of these bands, s_4 at 3581 cm^{-1} and e_2 at 3366 cm^{-1} , are of interest here. Polarization studies indicate that the vibrations responsible for s_3 , s_4 , e_1 and e_2 take place in the basal plane, and $E \perp c$ measures the full band strength.

Figure 7 shows $E \perp c$ spectra for swept High-Q and swept Premium-Q material. The Al-OH⁻ band strength for this particular swept High-Q sample is about 4 times stronger than for the swept Premium-Q. Resonators fabricated from quartz of these two species, however, do not show marked dif-

Table V. Drift rate after 1 Mrad ⁶⁰Co irradiation.

quartz	reso-nator	drift rate (pp 10 ⁹ /day) after		
		1	2	4 days
Electronic				
Grade	BNC-69	4.4	4.8	2.2
Swept	Q-41	13.5	7.2	3.8
Electronic	BLns-70	11	3.8	2.3
	BNCs-59	6.2	4.4	2.8
	H-2	6	3	1.6
	BK-9	5.5	2.5	
	P-86	4.2	3.3	1.7
	BJ-21	3	1.9	0.7
High-Q	T-102	11	8	4.5
Swept High-Q	U-72	3.5	1.5	0.5
Swept	L-5	3.3	1.2	0.9
Premium-Q	BB-80	3	1.3	
	N-169	3	1	
	BF-97	3	0.5	
	BI-76	2.3	1.1	0.7
	M-5	2	1.5	0.8
	BG-5	1.2	0.3	
	BA-72	0.5	0.3	0.15

ferences in radiation-induced steady-state frequency offset, short-term transients, long-term post-irradiation drift or acoustic losses. The s-band strength is similar in both materials, indicating that it is independent of Al³⁺ concentration.

In Fig. 8 we show radiation effects on the e_2 and s_4 band strengths of unswept, swept and doped Premium-Q quartz. For unswept material e_2 is produced at the expense of the s-bands. The s-band centers release H⁺ ions which take part in the formation of Al-OH⁻, replacing some of the dissociating Al-M⁺ centers. In addition, radiation also produces Al-e⁺ centers.

Irradiating swept quartz decreases both the e_2 and s_4 band strengths. The amount of this decrease varies widely among different swept samples. We do not observe formation of new bands or an increase in existing band strengths, and we can conclude that the hydrogen released from the dissociation of these centers is infrared-inactive.⁵ The compensation mechanism for the affected Al³⁺ has not been elucidated.

Figure 8 also shows the effect of sweeping and subsequent doping on e_2 and s_4 . The strength of the sweeping-induced e_2 band is reduced by doping as the Al-OH⁻ is replaced by Al-M⁺. However, as the data indicates, this replacement is incomplete in both the Li⁺ and the Na⁺ doped sample. The radiation effects on these bands are commensurate with those expected for unswept quartz.

Acknowledgments

The authors wish to thank their colleagues and associates at RADC: C. P. Werner for his acoustic loss measurements, L. F. Lowe, D. C. LaPierre and J. Capelli for the irradiations, A. F. Arrington and R. N. Brown for providing samples of swept and doped quartz. They also wish

to show their appreciation to L. E. Halliburton and J.J. Martin of Oklahoma State University for helpful discussions and for sharing their results with us prior to publication.

References

- 1 H. G. Lipson, F. Euler and A. F. Armington, "Low Temperature Infrared Absorption of Impurities in High Grade Quartz", Proc. 32nd Annual Symposium on Frequency Control, 11 (1978).
- 2 F. Euler, P. Ligor, A. Kahan, P. Pellegrini, T. M. Flanagan, and T. F. Wrobel, "Steady-State Radiation Effects in Precision Quartz Resonators", Proc. 32nd Annual Symposium on Frequency Control, 24 (1978).
- 3 P. Pellegrini, F. Euler, A. Kahan, T. M. Flanagan and T. F. Wrobel, IEEE Trans. Nuclear Science, NS25, 1267 (1978).
- 4 H. G. Lipson, F. Euler and P. A. Ligor, "Radiation Effects in Swept Premium-Q Quartz Material, Resonators and Oscillators", Proc. 33rd Annual Symposium on Frequency Control, 122 (1979).
- 5 L. E. Halliburton, "Point Defects in Synthetic Quartz: Survey of Spectroscopic Results", Proc. 34th Annual Symposium on Frequency Control, (1980).
- 6 Sweeping in air and vacuum was performed at Sandia Laboratories under the direction of T. J. Young; sweeping and doping in dried nitrogen ambient was performed by A. F. Armington and R. N. Brown, Rome Air Development Center (RADC/ES).
- 7 J. C. King, Bell System Tech. J., 38, 573 (1959).
- 8 J. C. King, A. A. Ballman and R. A. Laudise, J. Phys. Chem. Solids, 23, 1019 (1962).
- 9 J. C. King and H. H. Sander, Radiation Effects, 26, 203 (1975).
- 10 T. J. Young, D. R. Koehler and R. A. Adams, "Radiation-Induced Frequency Changes in Electrolyzed High Purity Quartz Resonators", Proc. 32nd Annual Symposium on Frequency Control, 34 (1978).
- 11 D. R. Koehler, "Radiation-Induced Frequency Transients in AT, BT and SC Cut Quartz Resonators", Proc. 33rd Annual Symposium on Frequency Control, 118 (1979).
- 12 J. C. King and H. H. Sander, IEEE Trans. Nucl. Science, NS19, 23 (Dec. 1972).
- 13 J. J. Martin and S. P. Doherty, "Acoustic Loss Spectrum of 5 MHz, 5th Overtone AT-Cut Deuterated Quartz Resonators", Proc. 34th Annual Symposium on Frequency Control, (1980).
- 14 D. B. Fraser, "Impurities and Anelasticity in Crystalline Quartz", in Physical Acoustics, W. P. Mason, editor, Volume V, Academic Press, New York 1968, pp. 59 - 110.
- 15 H. G. Lipson, "Infrared Impurity Absorption Spectra of Premium-Q Quartz", in Basic Optical Properties of Materials, A. Feldman, editor, NBS Special Publication No. 574, 36 (1980).

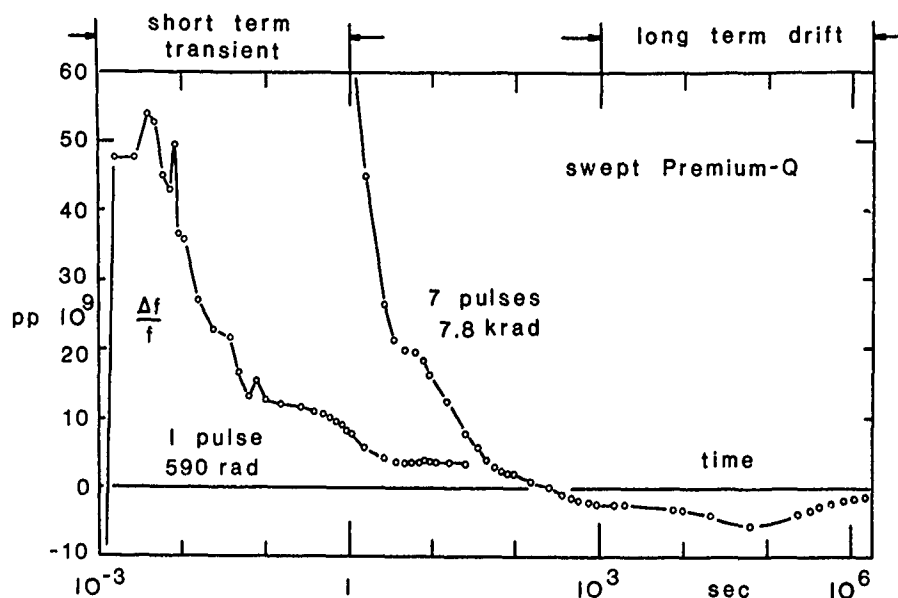


Fig. 1. Time dependence of 10 MeV electron irradiation-induced fractional frequency change $\Delta f/f$, for swept Premium-Q resonator E-3.

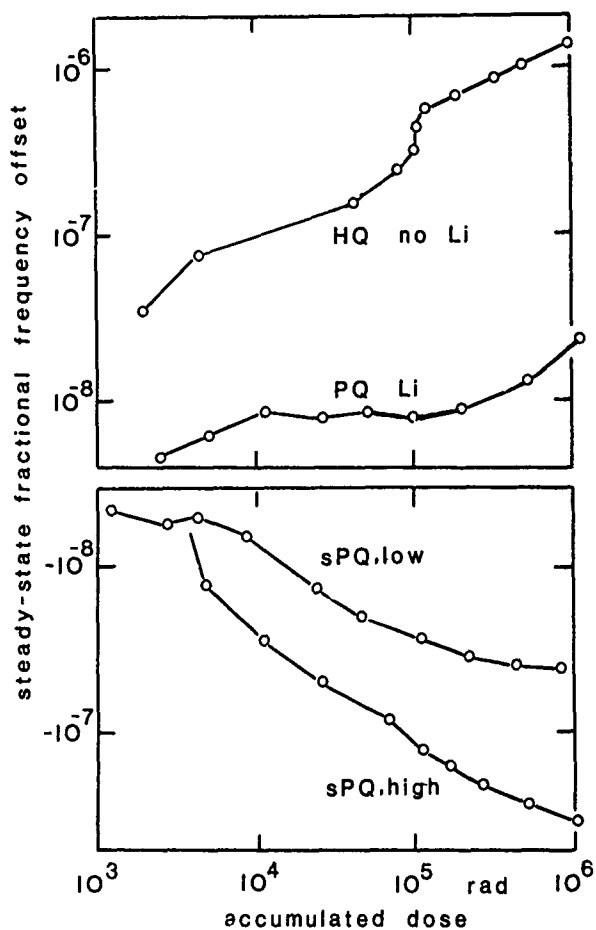
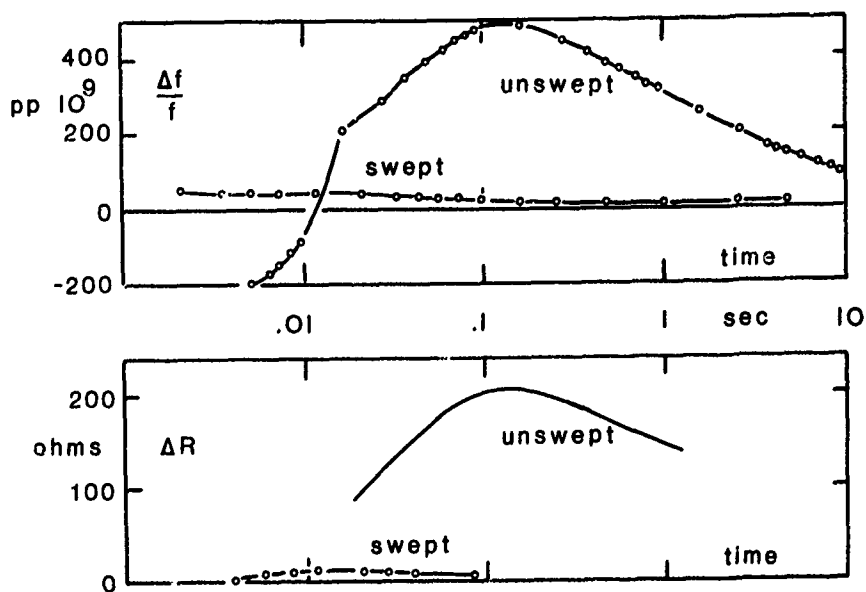


Fig. 2. Steady-state fractional frequency offset as function of accumulated 10 MeV electron dose.

	quartz	resonator
HQ	unswept High-Q	T-99
PQ	unswept Premium-Q	I-5
SPQ	swept Premium-Q, low:	E-1
	high:	B-4

Fig. 3. Short-term transient fractional frequency change $\Delta f/f$ (top), and resonator series resistance change ΔR (bottom), for Premium-Q resonators. Unswept: G-1 after 580 rad; swept: BC-81 after 840 rad single pulse 10 MeV electron dose.



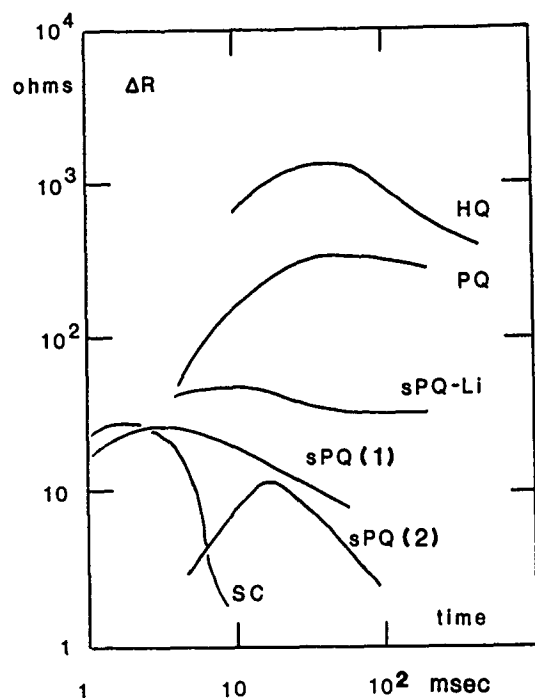


Fig. 4. Short-term transient series resistance change ΔR for selected resonators

	quartz	resonator	test bed
HQ	unswept High-Q	T-99	7212
PQ	unswept Premium-Q	I-15	7212
sPQ	swept Premium-Q, (1)	B-4	7211
		BC-81	7214
sPQ-Li	swept Premium-Q, Li-doped	EA-53	7212
SC	SC cut	D-14	7212

See Table III for 10 MeV electron pulse doses.

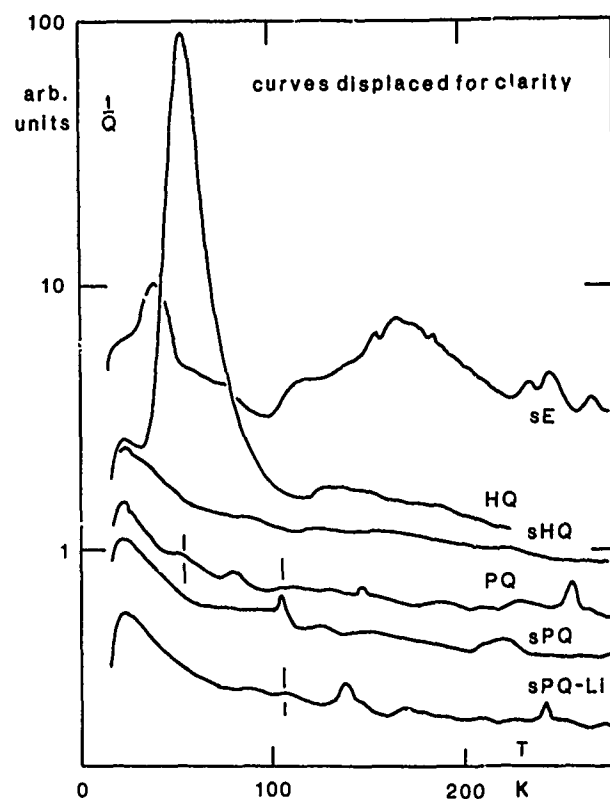
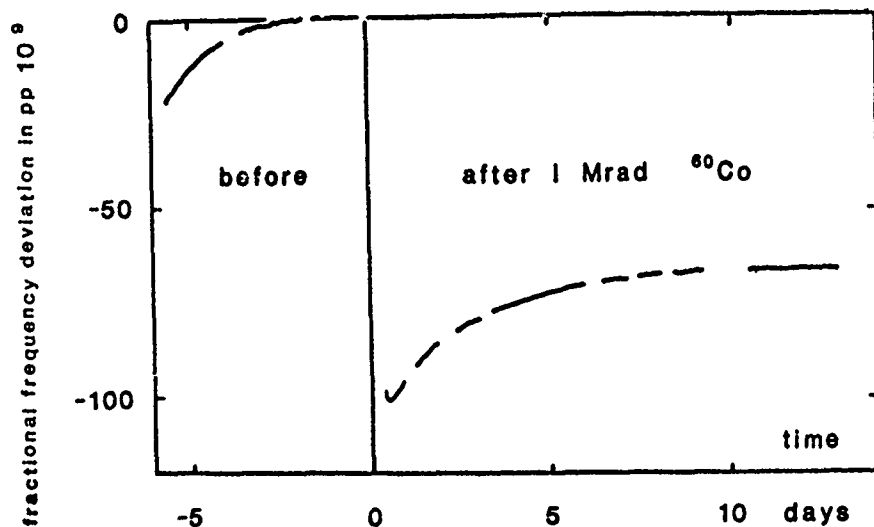


Fig. 6. Acoustic losses Q^{-1} as function of temperature T , before irradiation.

	quartz	resonator
sE	swept Electronic Grade	J-1
HQ	unswept High-Q	T-99
sHQ	swept High-Q	U-76
PQ	unswept Premium-Q	G-4
sPQ	swept Premium-Q	N-170
sPQ-Li	swept Premium-Q, Li-doped	EA-51

Fig. 5. Pre- and post-irradiation frequency drift for swept Electronic Grade quartz resonator Q-41.



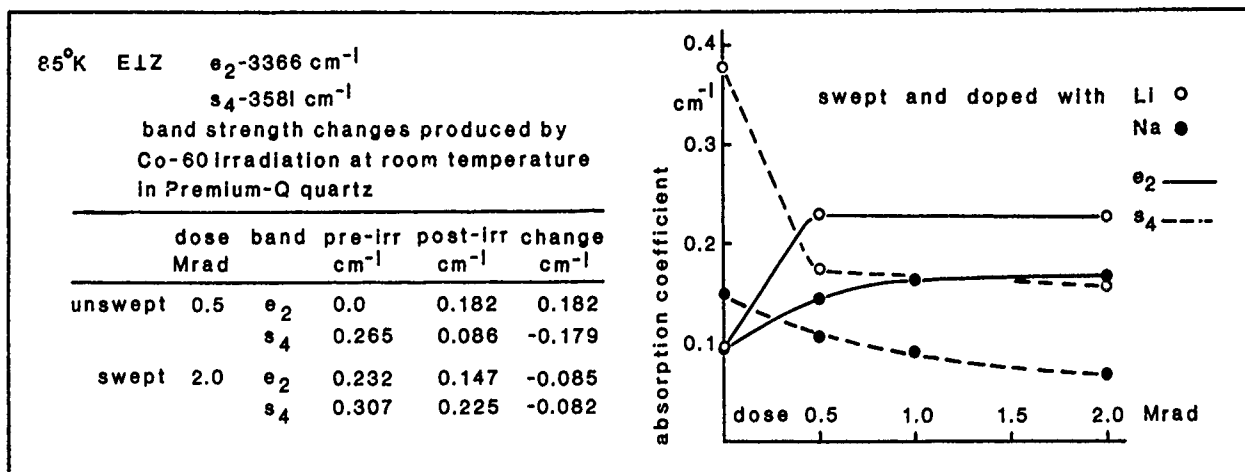
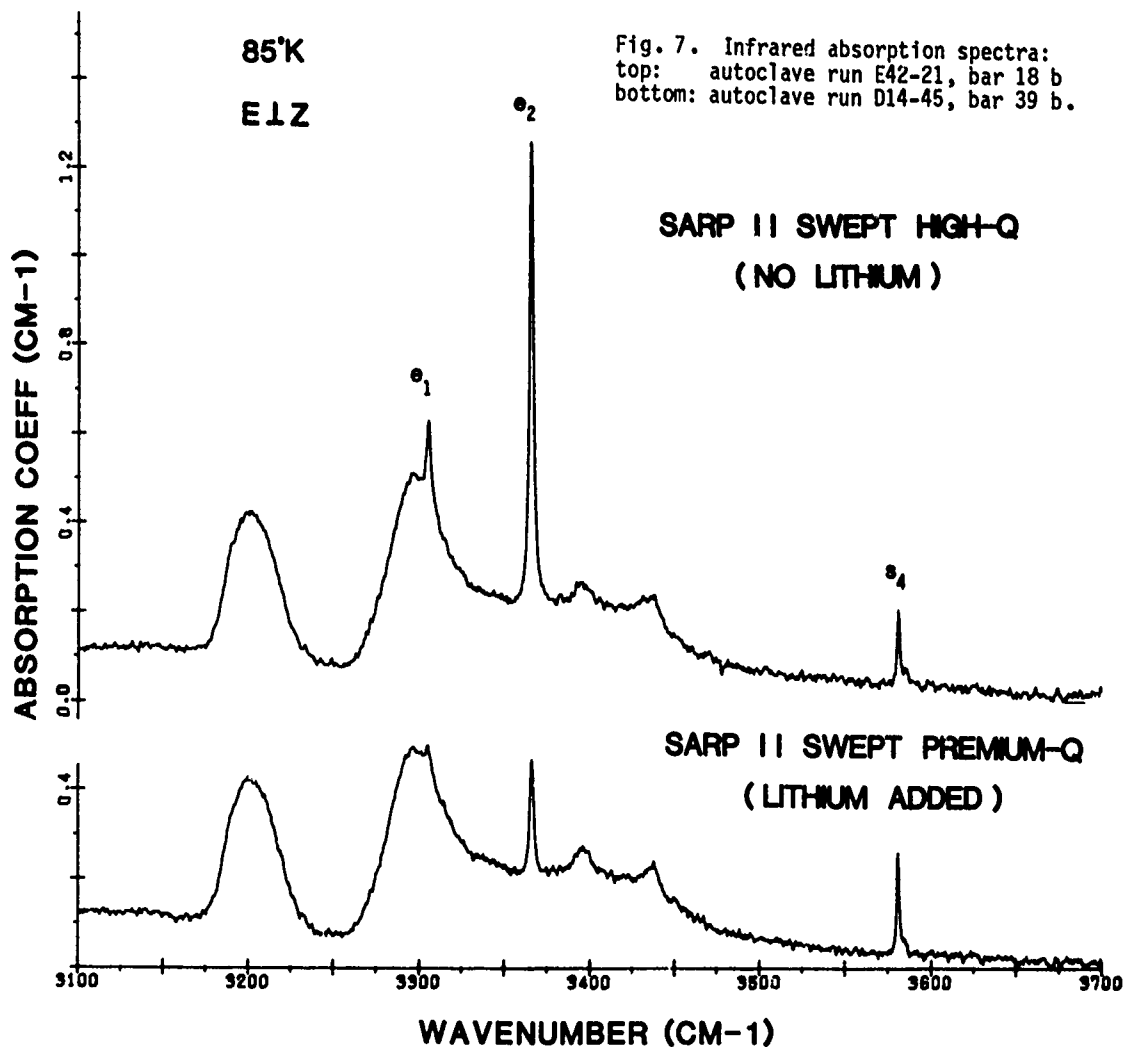


Fig. 8. Radiation effects on impurity bands.

	autoclave run	bar
unswept	D14-45	43 a sec.4
swept	A14-27	2
Li-doped	D14-45	D a
Na-doped	D14-45	2 b sec.i

THE ACOUSTIC LOSS SPECTRUM OF 5 MHz 5th OVERTONE AT-CUT DEUTERATED QUARTZ RESONATORS

J. J. Martin and S. P. Doherty

Department of Physics
Oklahoma State University
Stillwater, Oklahoma 74078

Summary

The acoustic loss spectra in 5 MHz 5th overtone AT-cut resonator blanks fabricated from well characterized Sawyer Premium Q quartz have been measured as a function of hydrogen, deuterium sweeping and of irradiation. No loss peaks that can be associated with the Al-OH center were found. Irradiation at room temperature introduced loss peaks at 25 K, 100 K and a broad shoulder on the side of the 100 K peak extending to 160 K. These loss peaks are probably caused by the $[Al_e]^0$ center.

Introduction

Acoustic loss peaks in the 250 K to 500 K temperature range are thought to be due to OH related defects.^{1,2} Irradiation at room temperature does not cause a steady state alteration of the OH defects as monitored by infrared, IR, measurements on high quality electrolyzed synthetic quartz. However, transient effects are possible since hydrogen is mobile at all temperatures in a radiation field.^{3,4} By measuring the acoustic loss spectrum of deuterated 5 MHz 5th overtone AT-cut resonator blanks we hope to pin down the effects of OH on resonator performance. The principal defect in high quality synthetic quartz is an aluminum atom substituting for a silicon atom. This substitutional Al is charge compensated by either an interstitial alkali or by a hydrogen on a non-bonding p orbital of an adjacent oxygen atom. Quartz which has not been electrolyzed always contains interstitial alkalis. Irradiation at room temperature of such material replaces the alkali at the Al site with a hydrogen. This modification of the Al site causes most of the steady state frequency offset observed in unswept quartz. Electrolysis (sweeping) developed initially by King⁵ which in the conventional process completely removes the alkalis from the quartz and substitutes hydrogen greatly reduces the steady state radiation induced offset.⁶ Recently, Koumvakalis and Markes have demonstrated an electrolytic process which produces a nearly complete replacement of the H⁺ ions with D⁺ ions.⁷ We present here the results of an ongoing study of the acoustic loss in 5 MHz 5th overtone AT-cut

blanks fabricated from well characterized Sawyer Premium Q material as a function of sweeping hydrogen and deuterium into the blank. Radiation effects on these samples will also be discussed.

Experimental Procedure

5 MHz 5th overtone plano convex AT-cut resonator blanks were fabricated for this study by K&W Mfg., Prague, Ok. from a Sawyer pure Z growth Premium Q bar of synthetic quartz. Samples from this bar have been extensively studied at Oklahoma State University by ESR, IR and thermal conductivity techniques. This bar has been given an in-house label PQ-E and resonator blanks are then coded by the letter R with a serial number; thus, PQ-ER5 is the fifth resonator blank fabricated from bar PQ-E. A chemical analysis of this bar reported by Markes and Halliburton⁴ shows that it contains 16 molar ppm Al, 9 molar ppm Na, and less than 9 molar ppm Li. This value for the Al content is in excellent agreement with the value determined by ESR reported earlier at this meeting. While the Al content of this bar is somewhat high for Premium Q quartz, the high Al content aids this type of study since we can then have a high concentration of the desired defects. An infrared absorption scan taken at liquid nitrogen temperature on resonator blank PQ-ER3 in the as-received condition with $\vec{E}||x$ is shown as curve A in Fig. 1. The scan is fairly typical of unswept Premium Q material.

The Al-OH and Al-OD centers were produced in resonator blanks PQ-ER2 and PQ-ER5 respectively by direct electrolysis of the blank in either a H₂ or D₂ atmosphere. Curve B in Fig. 1 shows the IR scan for the H₂ swept blank PQ-ER2; the strong 3367 cm⁻¹ and 3306 cm⁻¹ absorption peaks are characteristic of the Al-OH center. Curve C in Fig. 1 shows the corresponding scan for the D₂ swept blank PQ-ER5; the absorption peak at 2492 cm⁻¹ is the Al-OD analog of the 3367 cm⁻¹ peak, the analog of the 3306 cm⁻¹ peak is obscured by the strong intrinsic absorption. The Al-OH content in PQ-ER2 is estimated from the IR came to be about 15 ppm. The Al-OD content in PQ-ER5 is estimated to be about 9 ppm. The Al-OH center is not present in the unswept sample PQ-ER3.

The internal friction, Q⁻¹, of the resonator blanks was measured as a function of temperature by the log decrement method. The measurements were

made in a variable temperature helium Dewar with the blanks mounted in a gap holder similar to the one described by Fraser.² The resonator blank was driven for 10 ms at its series resonant frequency and then allowed to freely decay. The decaying rf signal was detected with a superheterodyne detector and displayed on a variable persistence storage oscilloscope. The exponential decay times were measured using a window detector to gate a digital timer.

Irradiations were carried out at room temperature using 1.7 MeV electrons from a Van de Graaff acceleration with the resonators mounted in the optical Dewar. Typical doses were approximately 2000 J/cm³ ($\sim 10^8$ rads). This dose is not expected to produce significant amounts of knock-on damage, but it has been shown to saturate the impurity related defects. The production of Al-OH centers by the irradiation was measured by an infrared scan at liquid nitrogen temperatures on the resonator blank.

Results and Discussion

Fig. 2 shows the acoustic loss, Q^{-1} , versus temperature spectrum for resonator blank PQ-ER5 in the as-received unswept condition and after electrolysis in a D₂ atmosphere. Before the D₂ electrolysis the Al-Na center loss peak at 54 K is clearly shown. A broad loss peak near 240 K is also present in the sample. When the blank was electrolyzed in a D₂ atmosphere both the Na loss peak and the broad peak near 240 K disappeared. The phonon-phonon loss near 25 K increased slightly, no other significant change in the Q^{-1} spectrum was observed. Blanks PQ-ER3 and PQ-ER1 were also measured in the as-received condition. The results for both were identical to the results of PQ-ER5 in the as-received unswept condition except that the broad 240 K peak was missing. Consequently, we believe that the 240 K loss peak is a spurious response and cannot be attributed to an impurity related defect. The 54 K Na loss peak was the same height in all three blanks.

Fig. 3 shows the acoustic loss spectrum for blank PQ-ER2 which had been electrolyzed in H₂. It contains approximately 15 ppm Al-OH centers. As expected the 54 K Na loss peak is absent. The large broad loss peak near 200 K is probably a mode crossing. This mode crossing which has been previously observed⁶ is present in our other blanks from this series. Usually, the resulting loss covers a narrower temperature range. Thus, at this stage of the investigation it appears that there is no significant loss mechanism related to the Al-OH (or Al-OD) center in the 5 K to 350 K temperature range for samples with an Al-OH content of 15 ppm or less. As shown by Fig. 1 the Premium Q quartz samples, from bar PQ-E, do not have significant amounts of the other OH related defects which cause IR absorptions at, for example, 3437 cm⁻¹ and 3400 cm⁻¹ in synthetic quartz.^{1,3} These defects may give rise to the OH related loss peaks reported by Dodd and Fraser.¹

Resonator blanks PQ-ER3 (unswept) and PQ-ER5

(D₂ swept) were irradiated at room temperature with 1.75 MeV electrons to a dose of approximately 10⁸ rads. The IR spectrum was measured at 77 K for both resonator blanks after the irradiation. No significant change was observed in the spectrum for the swept blank, PQ-ER5. In the unswept blank approximately 8 ppm Al-OH centers were produced (as shown by the 3367 cm⁻¹ and 3306 cm⁻¹ bands) by the irradiation. A room temperature irradiation moves alkali ions away from the Al site and either a proton or a hole is subsequently trapped on an adjacent oxygen. The proton then forms the Al-OH center which is IR active. The hole center, $[Al_{e+}]^0$, can be observed with ESR techniques. ESR studies on samples from the original bar, PQ-E, suggest that this irradiation also produced an equal number of $[Al_{e+}]^0$ centers in the unswept blank.⁴ The swept blank is expected to contain fewer hole centers following the room temperature irradiation. The acoustic loss spectrum for the unswept blank is shown in Fig. 4. Large loss peaks near 25 K, 100 K and a broad loss over the 125 K to 160 K range were produced by the room temperature irradiation. Fig. 5 shows that these same peaks are also present in the swept sample although they are greatly reduced in strength. Fig. 6 shows a difference curve for the irradiation induced loss in the two resonator blanks. The loss peak at 100 K with the broad shoulder extending to near 160 K shown in Fig. 6 is in excellent agreement with the much earlier results of King^{8,9} for his low temperature irradiation and subsequent anneal. He attributed the loss to the $[Al_{e+}]^0$ center. The large loss peak near 25 K is tentatively also caused by the hole center. Taylor and Farnell¹⁰ and Schnadt and Schneider¹¹ have extensively studied the electronic structure of the $[Al_{e+}]^0$ center with magnetic resonance and dielectric loss techniques. The dielectric loss results of Taylor and Farnell suggest that at liquid helium temperatures the hole is trapped on one of the two "short bond" oxygens adjacent to the aluminum and that slightly above 4 K the hole starts to jump between these two oxygens. Perhaps the onset of this motion is responsible for the 25 K anelastic loss peak. The 100 K loss peak can possibly be attributed to the onset of the hole jumping to the "long bond" oxygens. This jumping has been observed in the ESR results of Schnadt and Schneider. The broad higher temperature loss may correspond to the rapid motion of the hole between oxygens. This motion causes the ESR spectrum to broaden beyond recognition.

This work was supported in part by the U. S. Air Force, monitored by A. F. Armington, RADC, Hanscom AFB, MA 01731.

References

1. D. M. Dodd and D. B. Fraser, *J. Phys. Chem. Solids* **26**, 673 (1965).
2. D. B. Fraser, *Physical Acoustics*, (W. P. Mason, ed.) Vol. III-Part A, pp. 1-42, Academic Press, New York (1966).
3. W. A. Sibley, J. J. Martin, M. C. Wintersgill and J. D. Brown, *J. Appl. Phys.* **50**,

5449 (1979).

4. M. E. Markes and L. E. Halliburton, J. Appl. Phys. **50**, 8172 (1979).

5. J. C. King, Bell System Technical Journal **38**, 573 (1959).

6. B. R. Capone, A. Kahan, R. N. Brown and J. R. Buckmelter, IEEE Trans. on Nuc. Sci. **NS-17**, 217 (1970).

7. Nicholas Koumvakalis and Mark Markes, J. Appl. Phys. (in press).

8. J. C. King. Fundamental Studies of Natural and Synthetic Quartz, 15th Int. Rpt. Contract DA36-039 sc 64586 (January, 1960).

9. Cited in J. C. King and H. H. Sander, IEEE Trans. on Nuc. Sci. **NS-19**, 23 (1972).

10. A. L. Taylor and G. W. Farnell, Canad. J. Phys. **42**, 598 (1964).

11. R. Schnadt and J. Schneider, Phys. Kondens Materie **11**, 19 (1970).

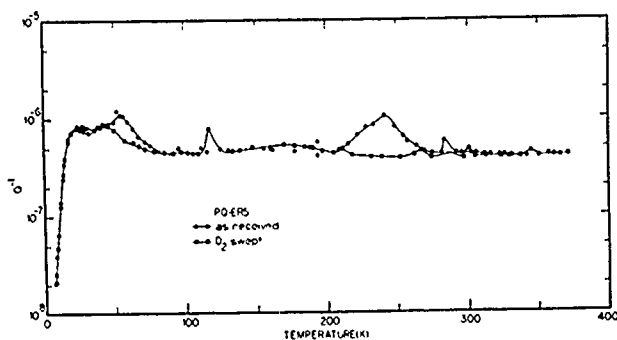
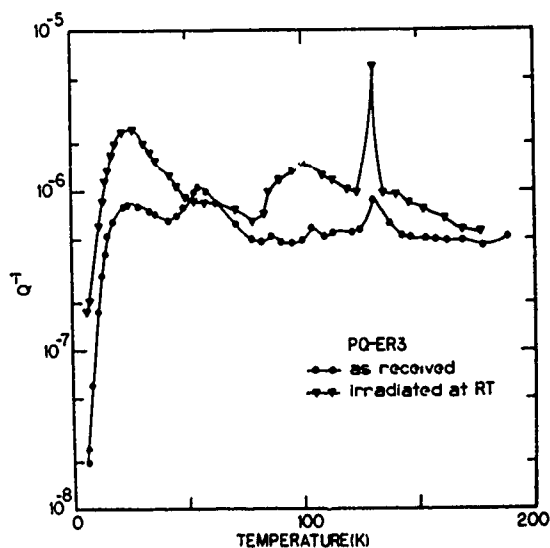


Fig. 2 shows the acoustic loss, Q^{-1} , versus temperature spectrum for resonator blank PQ-ER5 in the as-received unswept condition and after electrolysis in a D_2 atmosphere. Before the D_2 elec-



The acoustic loss spectrum for the unswept blank is shown in Fig. 4. Large loss peaks near 25 K, 100 K and a broad loss over the 125 K to 160 K range were produced by the room temperature irradiation.

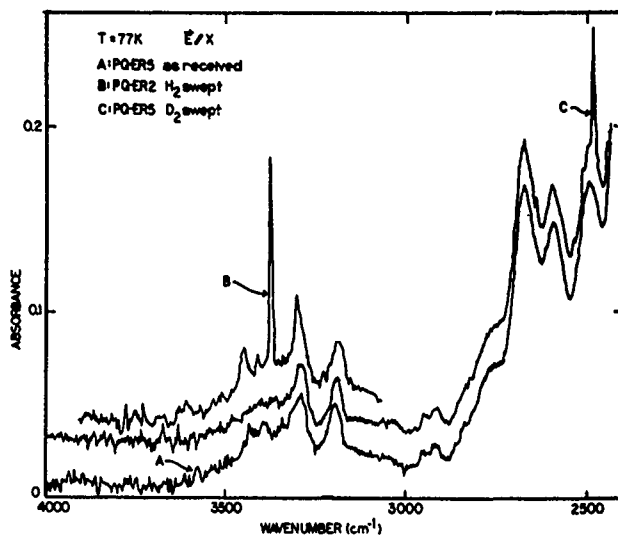


Fig. 1 shows the IR scan for the H_2 swept blank PQ-ER2; the strong 3367 cm^{-1} and 3306 cm^{-1} absorption peaks are characteristic of the Al-OH center.

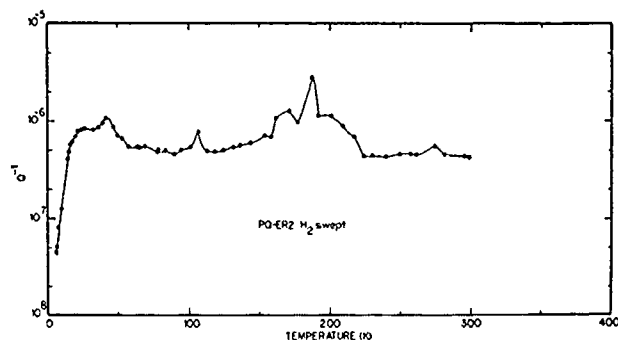


Fig. 3 shows the acoustic loss spectrum for blank PQ-ER2 which had been electrolyzed in H_2 .

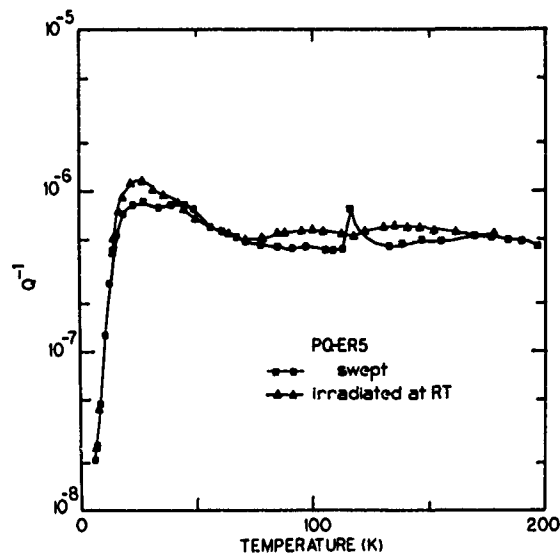


Fig. 5 shows that these same peaks are also present in the swept sample although they are greatly reduced in strength.

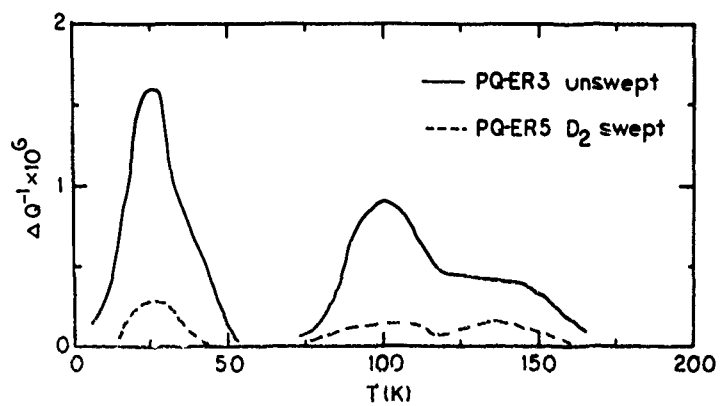


Fig 6 shows a difference curve for the irradiation induced loss in the two resonator blanks. The loss peak at

THE TEMPERATURE COEFFICIENT OF FREQUENCY OF AT-CUT RESONATORS MADE FROM CULTURED r-FACE QUARTZ

T. R. Meeker and A. J. Miller
Bell Laboratories, Incorporated
555 Union Boulevard
Allentown, Pennsylvania 18103

Abstract

Good correlation between the quartz crystal orientation angle and the dependence of resonator frequency on temperature is important when it is necessary to use the lower cost crystal orientation angle control rather than the higher cost actual frequency measurement over the temperature range of interest. Adequate correlation also allows the use of low cost orientation angle sorting and correction techniques in the development of high yield manufacturing processes.

The dependence of the frequency of a large number of AT-quartz filters on temperature is discussed. These results show what has been achieved in production under conditions of careful process control. For a smaller number of discrete AT-quartz resonators the crystal orientation angles for each resonator plate were also measured. The dependence of the frequency on temperature depends mostly on the orientation angle of the resonator plate.

A significant fraction of the resonators and filters showed an abnormal dependence of frequency on temperature. A careful examination of the crystal plates for these resonators showed that crystal defects (grown-in strain associated with dislocations) are largely responsible for the unusual temperature coefficient. The results of this examination are discussed. Also discussed are observations related to the initiation and propagation of grown-in strain and how strain in thick r-face bars and thin plates was inspected.

Introduction

During 1970 and 1975, several reports were given on design^(1,2), development^(3,4) and manufacturing aspects^(5,6) of 8-resonator Monolithic Crystal Filters (MCFs) intended for A6 Channel Banks at about 8.140 MHz. This report will describe a quartz material problem that affected the frequency-temperature (f-T) behavior of these filters. We will first introduce the problem by (A) showing its effects on the f-T behavior of MCFs made from non-selected cultured r-face bars, (B) describe grown-in strain - the actual problem - based on observations we made during the critical period, and (C) discuss the results of an evaluation of the effects of grown-in strain on the f-T behavior and Q of a group of 8 MHz fundamental mode discrete resonators.

We hope that our results may contribute to a better understanding of structural defects in r-face quartz in particular, and to the practical aspects of cultured quartz with respect to crystal design in general.

A. f-T Behavior of A6 MCFs Made From Non-Selected r-face Quartz Materials

The principle part of the MCF is a rectangular AT-cut quartz crystal plate which provides space for eight pairs of evaporated electrodes with coupling stripes, and sixteen pads for mechanical and electrical interconnections. A sample of this filter is shown in Figure 1.

Figure 2 shows graphically the orientation of the AT plate relative to the coordinate axial system of quartz. This figure gives an idea of how these plates are cut and machined from hydrothermally grown r-face bars. (The number of plates obtained from one r-face bar is much larger than shown.) The principle orientation angle required by the MCFs is $35^{\circ}12'30''$ relative to the Z axis. At this angle the frequency change as a function of temperature is minimum from 0 to 50°C. This is also the orientation angle of seed plates from which r-face bars are grown. (The seed plate in the figure is indicated by a dotted section.) Since minimum frequency change is one of the most important objectives the A6 MCFs have to meet, tight angle control is an important factor in the preparation of these plates. We measure the angle (using X-ray double diffraction techniques) after wafering and angle correction where plates are still relatively thick. By controlling all subsequent plate machining processes, we are then able to meet the final objective of $\pm 45''$ at the end of the overall plate process at about 8.140 MHz without the need for additional X-ray testing. Also indicated in Figure 2 is the point of observation for strain inspection. This point will become important in the following description of strain.

In spite of tight angle control and control of other variables which also influence the f-T behavior of MCFs (e.g. mass loading), we have experienced poor correlation between AT-orientation angles and f-T drifts. What we mean by poor correlation is shown in Figure 3 where f-T drifts of a large number of experimental and production MCFs are plotted against the AT-orientation angles of

the plates used for these filters. Each data point represents the 50°C frequency of one MCF minus the 25°C frequency as measured at the -3db point. (This approach of comparing angles and drifts has been chosen because of its simplicity. The insert in Figure 3 shows that the f-T curves of AT plates over this relatively narrow temperature range are sufficiently consistent with respect to angular intervals to allow this way of displaying variations without much loss of accuracy). Some scattering of data points is expected because many process and design related variables (in addition to orientation angle) have some influence on the f-T characteristic. However, the scatter shown in this figure seemed excessive. We have found that this poor correlation was related to quartz material defects, particularly grown-in strain closely associated with dislocations, rather than to process or design related variables.

B. Description of Grown-In Strain in r-face Quartz

Model on How Strain Originates

Because strain modifies the birefringence of quartz, strain areas can be made visible with the aid of polarized, monochromatic light. Figure 4 shows the typical appearance of strain in an approximately 1.5cm thick r-face bar. Strain is represented by several starlike clusters. The point of observation was at about 25° relative to the optic axis as indicated in Figure 2. This angle has been found optimum for this method of inspection. A polariscope was used which basically consisted of a sodium light source, a light diffuser and a polarizer and analyzer in crossed position. For this test the major faces of a quartz sample must be fairly transparent and parallel. Transparency was obtained by using polished cover glasses and a fluid of matching index of refraction which fills the gaps between the cover-glasses and the otherwise non-transparent (ground) major faces of the quartz. The sequence of the uniformly spaced, straight and horizontal light bands result from the interactions between the fast and slow optical wavefronts in quartz. No attempt was made to eliminate these bands (as is in other strain-inspection methods). In the present method these bands are needed as background reference in the qualification of strain. Material completely free of structural defects, such as grown-in strain or optical twins, will display uniformly spaced, straight and continuous bands. Large sections of the r-face bar in Figure 4 indicate this ideal condition. Any anomalous deviation from straightness, or discontinuities (e.g., the starlike clusters) may then be interpreted as structural defects. In a later section of the paper we will show that resonators cut from such strain sections may have undesired f-T characteristics.

The method may be equally used to observe structural differences within seed or bulk related to, for instance, the different growth regions in cultured quartz.

In Figure 5 we observe the interaction of polarized, monochromatic light along the X-axis of quartz which is along the width dimension of an r-face bar. In the top picture, two quartz sections are shown within the outline of natural quartz and the important pyramidal faces. It is apparent that along X there is less contrast, and there are no straight interference bands available for reference. However, this view along X is of interest because it reveals the following characteristics:

- a. Strain appears in the shape of cones (several strain cones appear in the top picture of Figure 5).
- b. Strain initially originates near the seed.
- c. Strain apparently propagates during growing toward the pyramidal faces of quartz.

Two of the cones labeled A and B can be seen magnified in the lower two microphotographs where strain is represented by light-toned, comet-like tails which originate near the seed plate. (A closer look reveals that cone A consists of two cones nearly parallel to each other.) A section of the seedplate is shown on the bottom part of these two pictures. The seed section is represented by dark pipes, or etch channels, related to hydrothermal etching which takes place during the warm-up period of a growing run. Next to the seed section is the seed-bulk interface, here only revealed by a layer-like accumulation of small particles. These particles range from several microns down to submicron dimensions. Generally referred to as sodium-iron-silicates, and quite common in cultured quartz, these particles prefer sites at or near the seed, especially in r-face quartz bars. (A washboard-like pattern covering the entire pictures should be ignored. These unwanted interferences are related to a wedged filter in the light path of the microscope.)

It is now important to note that within the immediate areas from which strain cones originate, there is usually also an accumulation of apparently similar particles. (In the figure, these particles appear about the center of the lower two pictures). Although most particles were found to be also of the usual sodium-iron-silicate flakes, not all have been identified. From our limited observations it appears that only some of these particles are capable of initiating harmful dislocation growth and the associated strain. We have also observed that these certain particles are mostly small, may sometimes have faces in crystallographic terms, and are often attached to other larger particles. Other apparently important factors in the initiation of strain are the seed orientation and the orientation of these certain particles relative to the seed orientation. It should be noted that Barns et al. (1) have related similar particles within strain areas in r-face quartz to crystallites of the rare mineral Tuhualite (which is structurally similar to lithium sodium iron silicate). Further, no initial strain cones have been detected in r-face bars grown in (laboratory) silver- or platinum-lined vessels under similar growing conditions.

It has been considered possible that micro-quartz crystallites known to spontaneously nucleate within the vessel in every growing run may become embedded in the bulk during growing and cause growth defects.⁽⁸⁾ Although we have seen such micro-quartz crystallites on the surface of the X-growth regions of r-face quartz bars, we have not found any evidence of them on the surfaces or within the bulk of the all-important Z-growth regions using optical inspection techniques. For instance, none of the particles at the origin of the strain cones A and B in Figure 5 appears in the classical shape of crystal quartz.

Strain Intensity and Distribution

Grown-in strain in the form of well defined cones as shown in Figure 5 exists only in the initial state, that is when strain is generated within the bulk. This state, to which we may now refer as first order strain, is graphically shown in a cross section in Figure 6a. First order strain may convert into second or higher order strain as follows. First, the strain, once generated, will "grow" from its point of origin usually near the seed, through the remaining half sections of the r-face bar. When a seed plate obtained from an r-face bar containing first order strain is used to grow another (next generation) bar, the strain will propagate from within the seed into the bulk (both half sections now) of the new bar. This new strain we may call second order strain. When the cycle is repeated with a seed containing second order strain, we will get a bar with third order strain, and so on. An example of this is graphically shown in Figure 6b. Because of the coned shape with which strain propagates within the bulk, each new (higher order) strain section will cover a large area. When uncontrolled, strain would eventually cover the entire stone. Such extreme conditions are prevented by rejuvenation of seed inventories through proper seed selection.

Grown-in strain is generally most intense in the initial state and proportionally less in states of higher order. Moreover, the intensity within a strain area is highest near the seed and proportionally less away from the seed. (Fractures usually originate near the seed).

There are situations, as shown in Figure 6c, where first order strain originates within another high-order strain section. These situations have usually resulted in very intense strains and often led to cracking, or in extreme cases even to the formation of electrical twinning. This process is complex and not well understood.

Grown-in strain has been the subject of other investigations in connection with cracking of r-face bars^(9,10).

Although strain appears in r-face bars in the basic shape of cones, it also prefers to spread out in branchlike formations. This may have already become evident from Figure 4, where the view is along the center of first order strain cones. In

the direction of this view, the branchlike formation can easily be observed. These formations become even more evident from Figure 7 where two photographs show first order strain (reflected light) contained in two thin 8.1 MHz AT-cut plates cut from the same straincone. The one on the left is a section from near the origin close to the seed, and the other from a location far away from the origin. The branchlike formations are particularly noticeable in the latter plate. These plates have been extensively etched in a saturated solution of ammonium bifluoride to reveal the structural defects (dislocations) in form of etch pits and etch channels. The etch time was approximately 30 minutes. Chemical etching is a good method of evaluating the size, shape, location and intensity of grown-in strain in thin quartz plates. Low levels of strain are difficult to observe in thin plates by optical methods. These etch patterns correlate with strain patterns revealed by X-ray topology, but etching is quicker and simpler.

Figure 7, especially the picture on the left, also gives an indication of the two principle appearances of dislocations in r-face quartz represented by etch pits and etch channels: Type (1) dislocations are (more or less) uniformly distributed throughout the z-growth region, propagate from the seed into the bulk apparently without making contact or being attracted to each other, and are not associated with any optically detectable strain. Type (2) dislocations are condensed to cone-shaped, branch-like formations initiated near the seed or propagating from strain areas within the seed, and are associated with optically measurable strain as demonstrated.

Type (1) dislocations are of no concern because after etching, they apparently have no effect on Q, f-T behavior, inductance and aging of resonators and filters below about 10 MHz. (The frequency range above 10 MHz has not yet been sufficiently explored for r-face quartz.) During etching, type (1) dislocations convert first into etch pits and then into etch channels at a relatively slow etch rate with the occasional exceptions of some isolated, rapidly etching dislocations of unknown origin.

Type (2) dislocations are of much concern because they may considerably affect the f-T behavior of resonators and filters as demonstrated in the next paragraph. This type converts into etch channels at a much faster rate than type (1). (Note that the terms type (1) and (2) have been arbitrarily chosen for this simplified description. These terms have no relation to the general terminology of dislocation.)

The highest dislocation activity in r-face quartz occurs in the slow X-growth region - the region not used in production. Under the present growing conditions, type (1) dislocations seem to be more represented in r-face quartz than in Y-bar quartz.

C. Effects of Grown-in Strain on Resonator Characteristics

Resonators Preparation and Test Procedure

Crystal plates from two different r-face production bars grown in steel vessels during 1975 were selected to include a wide range of relative intensities, shapes and sizes of strain. The intrinsic Q of all of these bars was about 1.5 million as determined by the infrared method. To reduce the number of variables which could have influenced the outcome of the evaluation, we decided on round 15mm diameter crystal plates (instead of the rectangular type for MCFs) and on only one pair of round 4mm diameter electrodes per plate (instead of the eight pairs per MCF plate). The area of the round electrodes approximated that of the square or rectangular electrodes of MCFs. Other design and processing parameters such as finish, amount of etching, plate back and the frequency adjustment method were the same as those for the MCF. After plate preparation (which included X-ray testing of the AT-orientation angle to within ± 10 seconds of arc), base plating and assembly, the units were evacuated and sealed. This was followed by testing the frequency, resistance and inductance of each unit over a temperature range.

Effect of Grown-In Strain on f-T Behavior

Figure 8 shows the f-T drifts of the fifteen resonators of the evaluation plotted against the AT-orientation angles. Individual resonators are identified by numbers. Scales and units of the coordinates agree with those of Figure 3. Circles versus double circles differentiate between plates from the two r-face bars (identified as r-face stones A and B in the figure).

Two best-fit reference lines appear in Figure 8: one applies to the present single resonators, and the other (a dashed line) to the MCFs of Figure 3. Why these two lines do not coincide is probably related to differences in plate shape, effective plate aspect ratio and ratio of total electrode area versus plate area. Some of this offset may also be related to differences in electrode composition. Although the plate back (2%) was kept identical, the single resonators had one pair of Au electrodes while the MCFs had eight pairs of TiPdAu electrodes.

The difference between these two reference lines becomes insignificant when we now look at the overall distribution of data points. The relatively large scatter of data points is apparently related to grown-in strain. We observe that four of the fifteen data points indicate poor correlation between f-T drifts and measured AT-orientation angles. With the aid of the etch patterns displayed in Figure 9 we can compare given strain conditions with the quality of correlation. These etch patterns, when properly illuminated as here with transmitted light, will provide sufficient contrast for observation of the position, size, shape and relative intensity of a strain area. To

obtain these etch patterns, the 4mm diameter electrodes had to be removed for subsequent etching where approximately 5 μ m of material was etched away from each side of a plate. This amounted to a total frequency change of 325 KHz at 8 MHz, which is equivalent to $\Delta f/f = 5$. All fifteen plates are shown arranged with respect to their correlation errors (frequency offset from reference line in ppm). For a more detailed view, plate #8 is also shown magnified in the upper part of the figure. (Two broken plates, #1 and 2, were rejoined with the aid of a tape indicated by dark bands). Periodically appearing white spots on the periphery of plates were caused by the holding arrangement used in the photographing process.

That grown-in strain affects the f-T behavior of resonators becomes especially evident from the plates of four resonators (#1, 3, 4 and 8) all of which contain strain at or near the acoustically most active center portion of the plates normally covered by the electrodes. Worst of all is #1 with a correlation error of 14 ppm equivalent to an angular error of about 4.5 minutes of arc. Next is #8 with an error of 9.2 ppm, equivalent to 2.5 minutes of arc. In contrast, the f-T behavior of other resonators apparently free of grown-in strain (#10, 11, 12, 13, 14 and 15), or resonators with strain safely away from the active plate-center (#2 and 9) correlates well with the measured AT-orientation angles.

When we compare the data points of Figure 8 and Figure 3, it can be seen that the scatter of data points of single resonators is much larger. Although we have not individually tested these MCFs for grown-in strain, we know that many of them contained strain regions (though probably not of the intensity of resonator #1 of the experiment). We know, for instance, that they were processed from the same sort of r-face material at about the same time as the single resonators. The smaller distribution related to MCFs is not surprising considering that intense strain incidences are usually limited to small lateral dimensions. A strain section will therefore occupy only a limited portion of an MCF; for instance, only an area of one or two of the eight resonators. Since the measured f-T drift of the MCF is then represented by the average f-T drift of all eight resonators on one plate, the effects of the strain are reduced.

Figure 8 shows also that resonators made from r-face bar A (represented by single circles) occupy more the upper section of the distribution while those from bar B (represented by double circles) the lower section. The reason for this duality is not known nor does the limited number of samples allow serious speculations. More experimental work on a larger scale would be needed for a meaningful assessment.

Effect of Grown-In Strain on Resonator Q

The strain intensity, size and location of the strained area and the correlation errors are tabulated in Table 1. In the last two columns the individual Q and resistance values are listed. No apparent differences in Q, effective resistance and

inductance between resonators processed from strained or unstrained sections could be detected. The Q and inductance values also compared well with those of individual resonators of A6 MCFs.

The resistances of all fifteen plates are also shown in Figure 10 in form of cumulative percent. Plates with strain within the electrode area can be found near the upper end of this 4.8 Q to 6Q range as well as near the lower end. The difference between 5.44Q and 5.24Q, the two average values of strained and unstrained plates, is less than the overall standard deviation. Even the worst resonator of the experiment which contained very intense strain that grossly affected the f-T behavior did not indicate any unreasonable resistance increase.

Summary

Grown-in strain, closely associated with dislocations, is one of the basic structural defects in cultured quartz. In a large-scale growing process it can be controlled but not totally eliminated. When cultured quartz, such as the relatively fast-grown r-face type originally designed for one specific application, is considered for high frequency resonators or filters with tight requirements on the f-T characteristic, careful process controls (e.g. seed selection) are required. When the growing process is insufficiently controlled, grown-in strain may reach very high intensity levels or cover large areas. Although grown-in strain does not affect the Q and inductance of fundamental mode 8 MHz resonators, it does have a large effect on the f-T characteristic. Errors in the correlation between f-T drifts and AT-orientation angles equivalent to angular errors of up to several minutes of arc have been found in single resonators. Correlation errors are apparently smaller in multi-resonators (MCFs) than in single resonators because of an "averaging" of the individual f-T drifts of all resonators on one plate. The correlation error is obviously also a function of position, size and intensity of a strained area relative to the acoustically most active plate center.

Grown-in strain can be observed and qualified in cultured r-face bars, regardless of thickness, by optical methods. On the basis of observations made several years ago when strain was insufficiently under control, a model on how strain originates and spreads from one to another growing generation has been proposed.

The density of etch pits and etch channels at and about strained areas was found to be a sufficient and quick indicator for grown-in strain in thin crystal plates.

It is not known what caused an apparent duality in the distribution of data points of resonators made from two r-face bars each from a different autoclave load. A full assessment of effects on f-T behavior should include not only material defects, but also other material, growing and process related variables. More work on the effects of these variables needs to be done to fully evaluate all parameters.

Acknowledgments

The authors gratefully acknowledge the contributions of the following members of Western Electric and Bell Labs: S. H. Olster, K. M. Kroupa, D. G. Mattis, G. T. Pearman, E. E. Simpson, K. K. Simpson, and E. C. Thompson.

References

- [1] T. R. Meeker, "Plate Constants and Dispersion Relations for Width-Length Effects in Rotated Y-cut Quartz Plates", (Proceedings of the Twenty-Ninth Annual Symposium on Frequency Control, May 1975, pp.s 54-64).
- [2] An Equivalent Circuit Approach to the Design and Analysis of Monolithic Crystal Filters, R. C. Rennick (IEEE Transactions on Sonics and Ultrasonics, October 1973).
- [3] G. T. Pearman, R. C. Rennick, Monolithic Crystal Filters, IEEE Transactions on Sonics and Ultrasonics, Vol. SU-21, October 1974).
- [4] A6 Monolithic Crystal Filter Design for Manufacture and Device Quality, S. H. Olster, I. R. Oak, G. T. Pearman, Rennick, and T. R. Meeker (Proceedings of the Twenty-Ninth Annual Symposium on Frequency Control, May 1975).
- [5] Manufacture of Monolithic Crystal Filters for A-6 Channel Bank, H. F. Cawley, J. D. Jennings, J. I. Pelo, P. R. Perri, F. E. Snell, and A. J. Miller (Proceedings of the Twenty-Ninth Annual Symposium on Frequency Control, May 1975).
- [6] Preparation of Quartz Crystal Plates for Monolithic Crystal Filters, A. J. Miller (Proceedings of the Twenty-Fourth Annual Symposium on Frequency Control, April 1970).
- [7] R. L. Barns, P. E. Freeland, E. D. Kolb, R. A. Laudise and J. R. Patel, Dislocation - Free and Low - Dislocation Quartz Prepared by Hydrothermal Crystallization, Journal of Crystal Growth 48 (1978), 676-686.
- [8] P. N. Kotru, Microcrystals as Nucleus Centres on Rhombohedral Surfaces of Cultured Quartz, Japanese Journal of Applied Physics. Vol. 12, No. 6, June, 1973.
- [9] R. L. Barns, E. D. Kolb, P. L. Key, R. A. Laudise, E. E. Simpson, K. M. Kroupa, Production and Perfection of r-Face quartz, (Proceedings of the Twenty-Ninth Annual Symposium on Frequency Control, 1975).
- [10] D. L. Brownlow, Fracture Resistance of Synthetic Alpha-Quartz Seed Plates, (Proceedings of the Thirtieth Annual Symposium on Frequency Control, 1976).

TABLE 1

	STRAIN INTENSITY	STRAINED AREA	COVERED BY ELECTRODE	CORRELATION ERROR $\frac{\Delta f}{f}$	EFFECTIVE RESISTANCE Q	DYNAMIC Q
Plate 1	Very High	Very Large.	Fully	114.1 ppm	5.9	240000
2	Medium	Small	Not	0.2	5.3	269000
3	Medium	Large	Fully	5.7	5.9	240000
4	High	Large	Partially	4.0	5.2	263000
5	Very Low	Large	Not	2.2	4.9	231000
6	High	Small	Not	2.3	5.0	275000
8	High	Large	Fully	9.1	4.9	231000
9	High	Small	Not	0.8	6.0	233000
16	Very Low	Very Large	Partially	2.4	5.3	261000
10	No Strain Detectable			0.12	4.9	233000
11	No Strain Detectable			0.36	5.2	266000
12	No Strain Detectable			0.0	5.0	275000
13	No Strain Detectable			0.24	5.4	262000
14	No Strain Detectable			0.24	4.8	295000
15	No Strain Detectable			0.61	5.9	240000

Table I Relative intensity of strain, size of strain, correlation error, effective resistance and Q of experimental 8.1 MHz single resonators made from strained and unstrained r-face quartz.

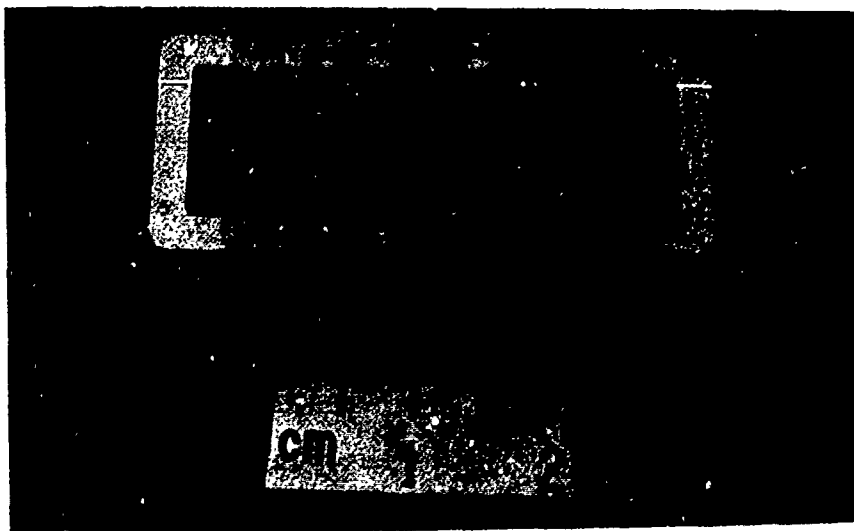


Figure 1 8-resonator Monolithic Crystal Filter (A6 MCF)

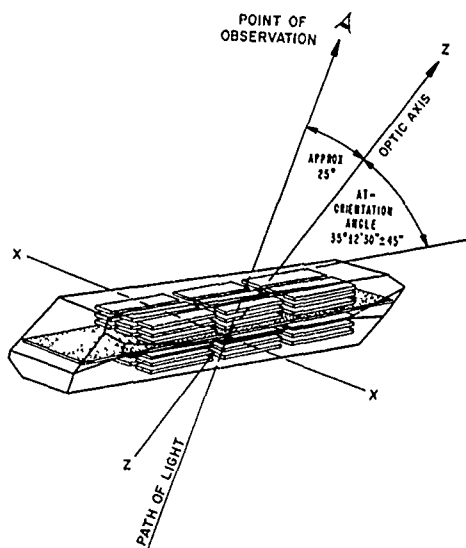


Figure 2 Schematic of cultured r-face bar showing AT-orientation and preferred point of observation for strain inspection.

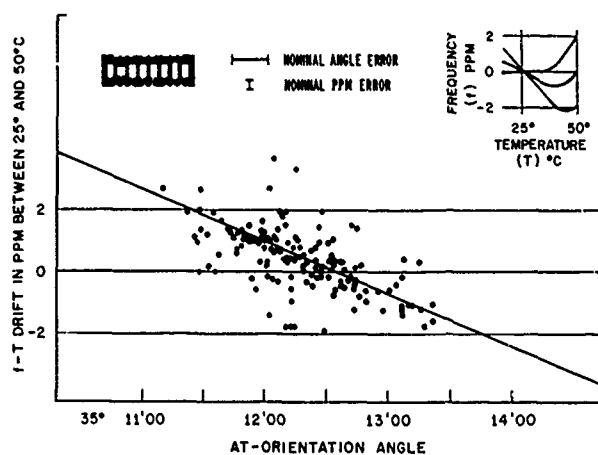


Figure 3 Correlation of AT-orientation angle and frequency-temperature drift of 8-resonator MCFs made from (non-selected) r-face quartz.

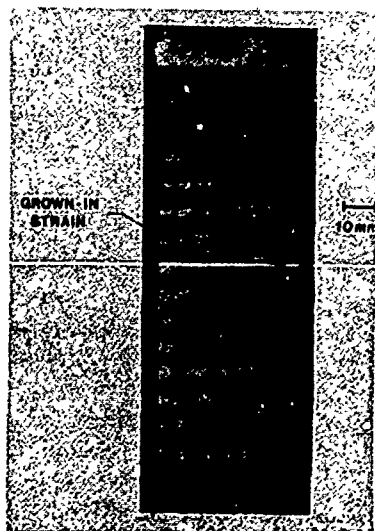


Figure 4 Typical appearance of grown-in strain in a thick r-face quartz section observed 25° off Z axis.

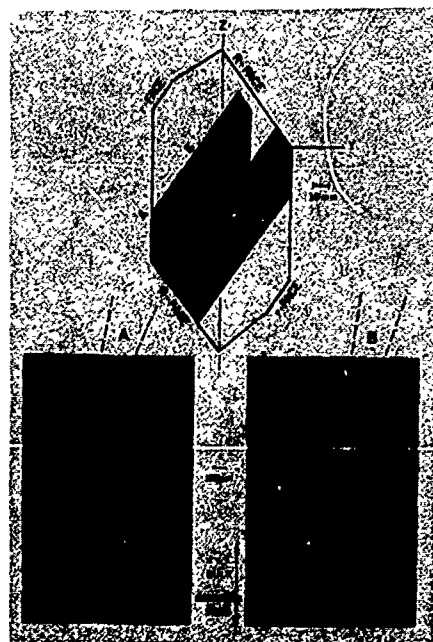


Figure 5 Typical cone-shaped appearance of initial (first order) grown-in strain in thick r-face quartz sections as seen along X axis.

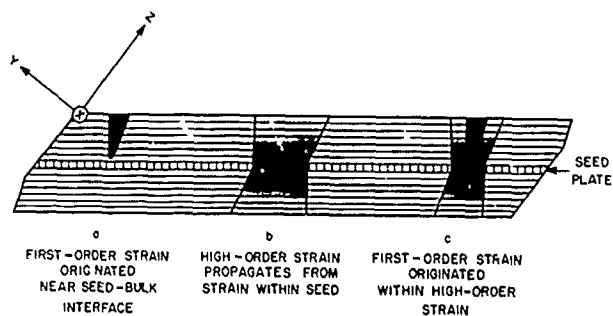


Figure 6 Schematic of cross section of r-face quartz bar with first-order and higher-order strain.

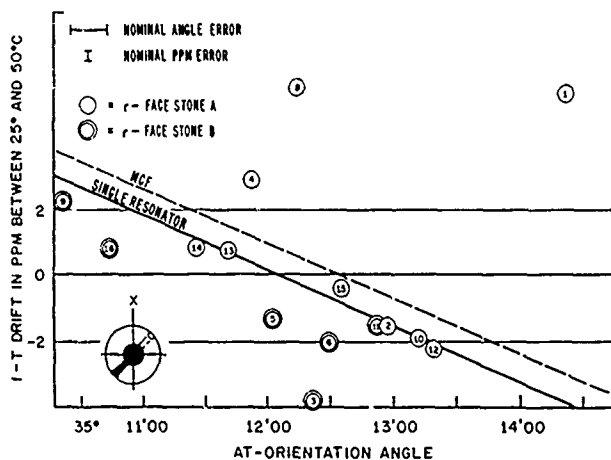


Figure 8 Correlation of AT-orientation angles and frequency-temperature drifts of 8.1 MHz single resonators made from strained and unstrained r-face quartz.

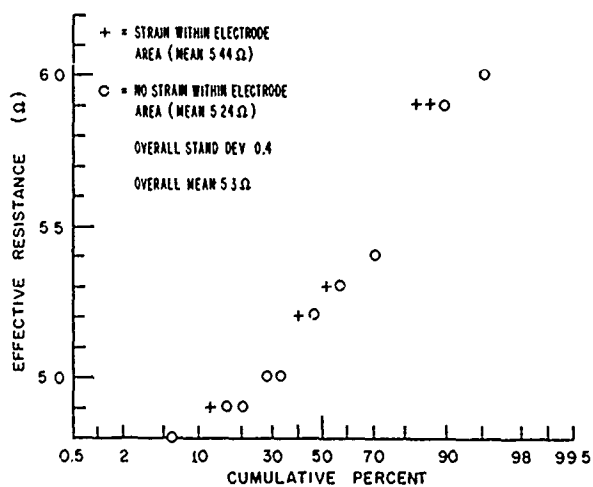


Figure 10 Effective-resistance values of 8.1 MHz single resonators made from strained and unstrained r-face quartz.

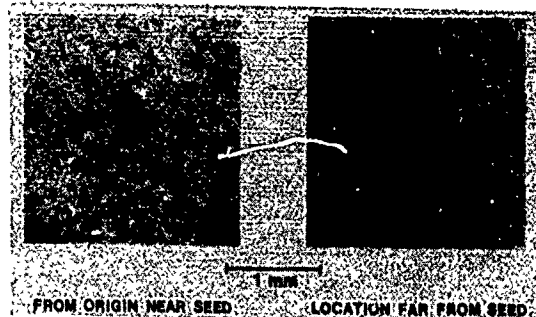


Figure 7 Etch patterns show branch-like formations representing dislocations and associated grown-in strain in thin r-face (AT-cut) crystal plates cut from areas near seed (left) and far from seed (right).

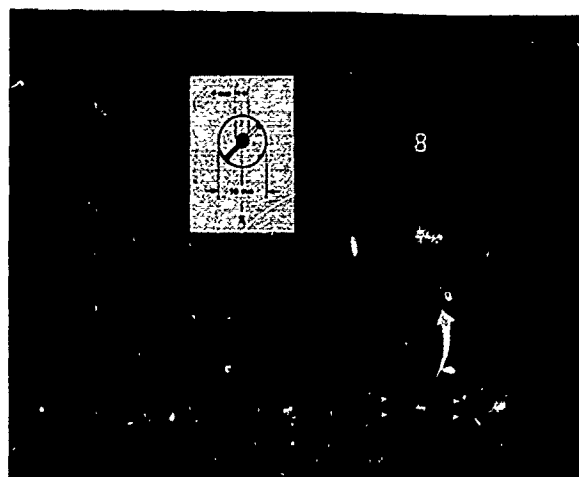


Figure 9 Comparison of etch patterns and correlation errors of crystal plates made from strained and unstrained r-face quartz.

EXPERIMENTAL THERMAL BEHAVIOUR OF BERLINITE RESONATORS

J. DETAINT, H. POIGNANT, Y. TOUDIC

CENTRE NATIONAL D'ETUDES DES TELECOMMUNICATIONS
92131 ISSY-LES-MOULINEAUX, 23301 LANNION (FRANCE)

ABSTRACT

In order to improve the crystal quality of hydrothermally grown Berlinite a study of the evolution of impurities concentration during growth was made as a function of experimental conditions (Temperature) and methods (Slow heating or reverse temperature gradient).

Crystals with different seeds orientations were grown (0001 = z plate ; 1010 = m face ; 1011 = r face 0111 = z face).

From these crystals, Y rotated resonators with six orientations ranging from $\theta = -38^\circ$ to $\theta = +30^\circ$ were cut. Extensive use of acid etching figures inspection was done to ensure that the plates used were as free as possible from macroscopic twinning and other major defects. An experimental study of the thermal behaviour of the resonant frequencies F_r has indicated like cubical variations for all the Y rotated cuts we have made.

On the whole the results indicate the important potentialities of this material (coupling coefficient and thermal behaviour) together with the need of a further advance towards the crystal perfection and in direction of a refinement of the knowledge of the thermal derivatives of the material constants.

Introduction

After the pioneer work of Stanley (1), the decisive contribution of Chang and Barsch (2) has shown that berlinite is, as quartz, a thermally compensated material but with a much higher coupling coefficient. Since, interest for this material was renewed and the published results of many research groups in USA, Great Britain, Germany and France have extend the knowledge of Berlinite by their contribution to :

- Experimental assesment of piezoelectric devices made with Berlinite^{5,9,11,12}.
- Crystal growth and fundamental studies of the material^{6,7,8,9,10}.
- Theoretical Evaluation of the properties of devices^{3,4}.

These works have confirmed the high coupling of the material and the good thermal properties of devices.

At the Centre National d'Etudes des Télécommunications all the aspects of berlinite development were considered. First, at the Lannion Research Center a study of solubility of $AlPO_4$ in H_3PO_4 was done¹⁰, then two crystal growth methods were set up while the physico-chemical characterization of the crystals took place. At the Paris research center computation of expected properties of bulk and surface wave devices were done while first devices experiments took place.

Recently, refinements of the crystal growth methods were studied in order to produce the more perfect and larger crystal that are needed in devices applications and for a better fundamental knowledge of the material. Among them it was recognised that advances in starting material purification and enhancements of seed selection and preparation was necessary. In this contribution we give results concerning advances in crystal growth, together with new results concerning the thermal behaviour of resonators of several cuts. A discussion is then made of the influence of still existing defects on devices.

1. Influence of crystallization conditions on the impurity content-Purification

The impurities were analysed by atomic absorption spectrometry on crystals grown by both methods used for berlinite growth: The slow increase of temperature method (Method I) and the reverse temperature gradient method (Method II)¹⁴.

Method I :

The starting material used is $AlPO_4$ "Selectipur" quality powder (Merck). The experiments were made in a sealed glass container inside the autoclave. Two solvents were used : orthophosphoric Acid (H_3PO_4) and hydrochloric Acid (HCl). The Table I give the impurity concentration in the starting powder and in the crystal obtained respectively in HCl and H_3PO_4 as solvent. Experimental conditions are given in table 2.

As expected, a purification of $AlPO_4$ was observed by crystallization.

Higher impurity concentration remains in the case of H_3PO_4 solvent particularly for Na and Si. This is probably due to the higher glass attack during the experiment.

TABLE 1

ELEMENTS	STARTING POWDER SELECTIVUM ALPO ₄	CRYSTALS A HCL SOLVENT	CRYSTALS B H ₃ PO ₄ SOLVENT
Al	105.	16.	18.
Zn	15.	5.	5.
Na	6500.	.5	14.
Ca	127.	110.	170.
Si	257.	30.	210.

Table 1 : Impurity content of starting material and crystal grown in HCL or H_3PO_4 (In $\mu g/g$).

TABLE 2.

HCL SOLVENT	H ₃ PO ₄ SOLVENT
HCL = 3.2 M ALPO ₄ = 1.7 MOLE/L HCL HEATING RATE 4°C/DAY T INITIAL = 190°C T FINAL = 200°C	H ₃ PO ₄ = 9.5 M ALPO ₄ 28 MOLE/L H ₃ PO ₄ HEATING RATE 4°C/DAY T INITIAL = 190°C T FINAL = 200°C

Table 2 : Experimental conditions of crystallisation experiments.

Figure I represents the impurity concentration as a function of the heating rate. The high impurity content of crystals grown with 10°C/day heating rate results probably from the crystal inclusions.

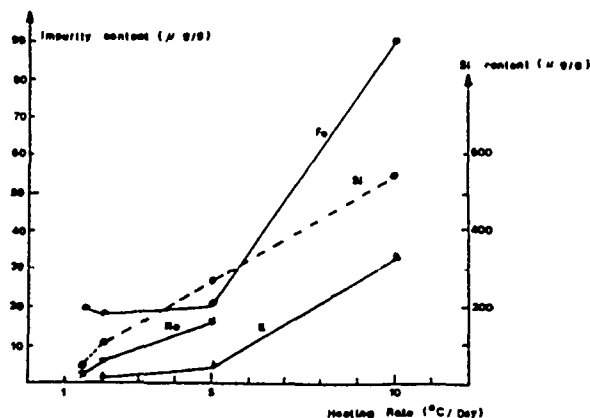


Figure 1 : Impurity content as a function of heating rate.

Method II

The starting product (nutrient) was crystals obtained by the first method (B crystals in Table 1) we used $H_3PO_4/AlPO_4$ solutions presaturated at the crystallization temperature to prevent unwanted dissolving of the seeds during the initial heating of the autoclave. Impurity content as a function of crystallization temperature (Between 190° and 280°C) is shown in figure 2.

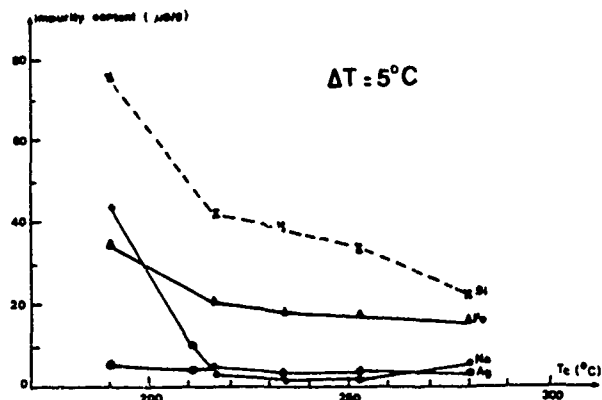


Figure 2 : Impurity content as a function of crystallization temperature.

II. Crystal growth

In an initial paper we have reported berlinite crystal growth by the slow heating method and the reverse gradient method.

In the slow heating method, the growth rate (0001) versus ΔT is about 0.5-0.8 mm by day with a heating rate of 1.5-2°C by day. In the crystals obtained in those conditions inclusions are initiated near the seed and consequently other defects as cracks and twins appear. Those inclusions are particularly increased by the inhomogeneous attack of the seed during the initial heating of the autoclave, the high growth rate at the beginning of the growth cycle due to the profile of the solubility curve ($\Delta S/\Delta T$ is higher in this temperature region). In order to diminish the crystal inclusion content, we have tried to lower the initial seed attack and the growth rate. So we have studied berlinite crystal growth of m (1010), r (1011) and z (0111) cuts corresponding to natural faces. In those cases we have noted an improvement of the optical crystal quality (Figures 3 and 4). Inclusions are not formed at the beginning of the growth process. The growth rate (1010) versus ΔT is given on Figure 5. On the other hand, in the reverse gradient method, we obtain good quality crystals because the growth rate is constant during all the experiment and is lower than in the slow heating method at the beginning of the growth process.



Figure 3 : Crystals grown from a m (1010) seed.

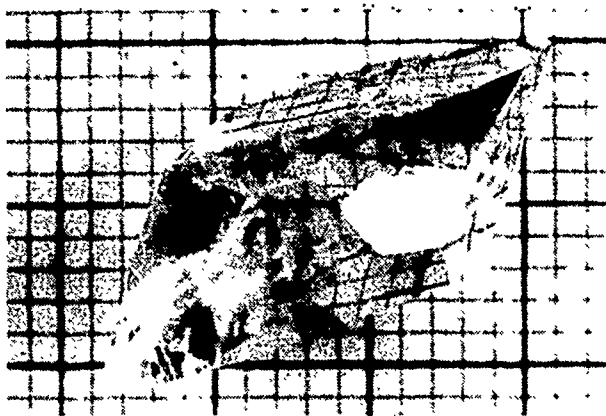


Figure 4 : Crystal grown from a r ($10\bar{1}1$) seed.

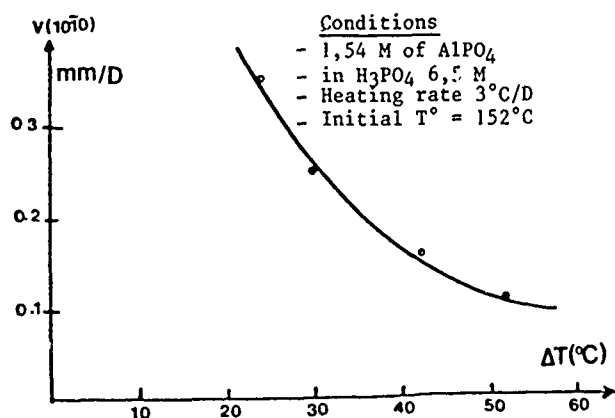


Figure 5 : Growth rate: from m ($10\bar{1}0$) seed as a function of ΔT

During the autoclave cooling, there is crystal etching, and it appears on crystal faces etch figures which allow us to determine the crystal orientation as shown on Figure 6; twins may be observed on R faces as well by looking at growth figures. Figure 7 shows a twin boundary as observed in quartz crystals.

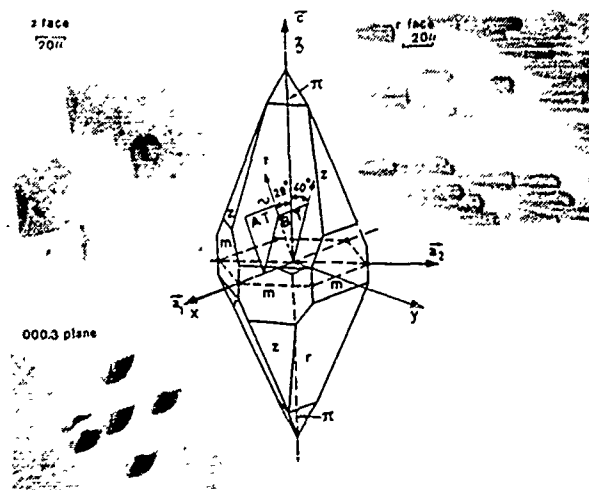


Figure 6 : Cooling etch figure on natural faces and orientation of important cuts of berlinite.

tals in the case of Dauphiné twins (R figures on the top and z figures on the bottom). Figures 8a and 8b show Brazil twins respectively on R faces and m faces.

(The presence of twins are now the main problem in the crystal growth of berlinite).



Figure 7 : Dauphiné (Electrical) twinning as observed in a r face.

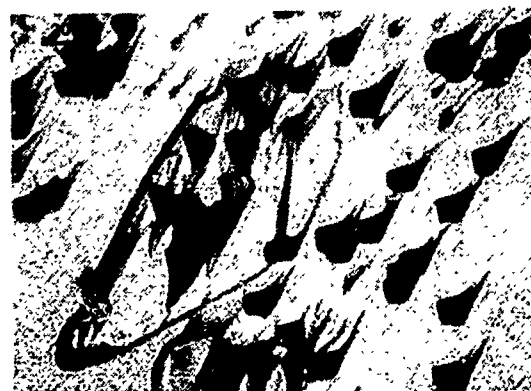


Figure 8 : Brazil (optical) twinning in a z face (8a) and in a m face (8b).

III Preparation of resonators

Resonators are made using a modified natural quartz processing technique. First, by examination of natural faces of the crystals, x direction is found and a precise X section is made for further orientation purpose. For $Y + \theta$ resonators, a face $Y + \theta$ is made from a natural z face (Positive angles) or from a r face (Negative angles) Figure 6. These faces are always existing in crystals grown from any kind of seed used (§II) they can be easily distinguished by etch figures (Figure 6). Plates parallel to this $Y + \theta$ face are then sawn with a very thin (0,1 mm) annular diamond saw ; the plates are reoriented and lapped to final thickness with 305 Al_2O_3 . They are left with natural contours except for those which are polished (with cerium oxyde or alumina) that are squared. Four to six plates are generally obtained general from a 2-2.5 cm crystal. The precision on θ is usually in the range of several minutes and the thickness variations across the plates less than 1 μm . As a whole, in terms of workability, berlinite is a good material, and appears to be berlinite similar to a borosilicate glass.

Polished plates are generally examined by conventional microscopy to search for liquid inclusions, then all plates are slightly etched in a 3 % HF 15 % H_3PO_4 solution for five to ten minutes. This etchant give well defined etch figures sufficiently small for a proper work of resonators. A stronger etchant is used for X plates. In most cases X ray-topography examination is also made on etched plates.

Electrodes deposition 1000 Å gold, or, more recently 2000 Å Aluminium is made on zones of the plates that are free of imperfections observed by acid etching. Electrode diameter is chosen to occupy only a small fraction of this zone.

Observation of defects in plates.

The principal defects observed were Dauphiné and Brasil twins, Cracks and liquid inclusions. Their number and size were observed to decrease strongly as progress occured in the crystal growth studies, however some may still be present on a more or less important fraction of the plates.

Twinning according to the Brasil Law is now the more common defect. The presence of such twins can be assessed on as grown crystal by careful examination of r,z,m faces ; the most revealing sign of their presence are V shaped figures on the z faces).

Two principal morphologies of Brasil twins can be observed in plates :

- The first is characterised by acicular prismatic or pyramidal twins with generally a V shaped base section that are generally very small and hard to detect. . They seem to appear in last stage of growth originating from a point often close to the final surface of the crystal. They are evidently related to the V shapes observed on natural faces.

Some examples of such twins in X plates are given on Figure 9. The traces of the same twins in a Y rotated plate are displayed in Figure 10 where, also, etch figures, typical of near AT cuts of berlinite can be seen. This type of optical twinning appears to be much less common in reverse gradient crystals and in small slow heating crystals ; it seems to be related to impurity content of the nutrient solution and with solid inclusions in the crystal.

- The second type, which was common on earlier crystals, consists in bulky twins with regular limiting surfaces that were seen inside the crystals generally nearby the seed or its attaching wire. This kind of twins is now almost eliminated by progress in seed selection and preparation^{7,12}.

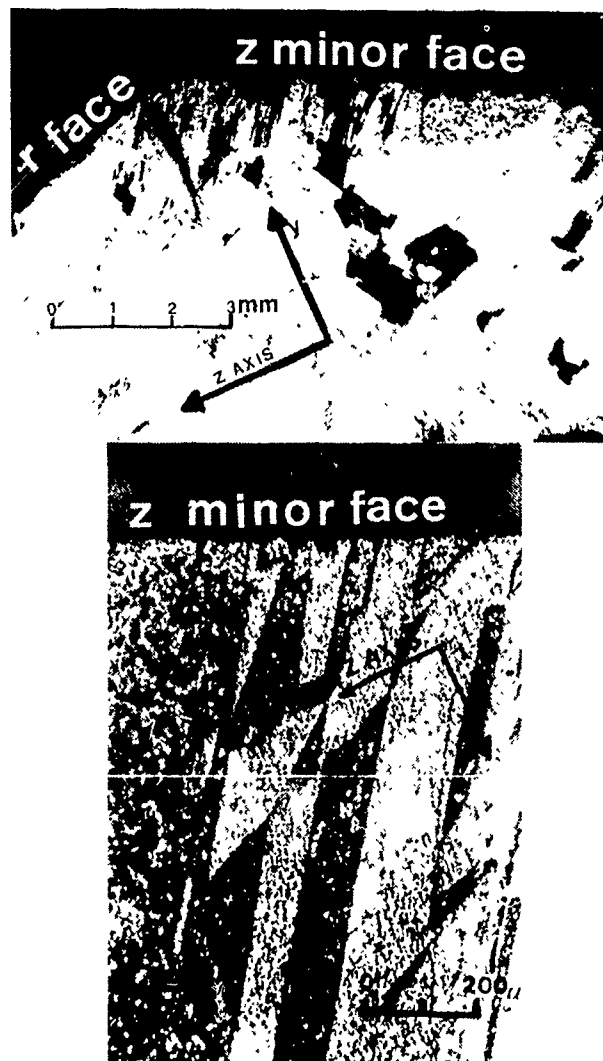


Figure 9 : Optical twinning in an X cut.

Twinning according to the Dauphiné law was also found in plates. It has a compact shape with irregular limiting surfaces. The twins sections in plates are scarcely of very small dimensions so that they can easily be avoided in resonators.



Figure 10 : Optical twinning in a Y+29° cut.

Electrical twinning can often be detected on as grown crystals since when it occurred near a rhomboedral face it was revealed by a step in this face (Figure 7) that results from the difference of growth rate between r and z faces. Etch figures on as grown crystals or on Y rotated plates allowed to identify readily this kind of twinning. In Figure 11 a typical example of Dauphiné twinning in a Y rotated plate is given.



Figure 11 : Electrical twinning in a Y rotated cut.

Electrical twinning which, as noted in reference is much less common than Brasil twinning, was observed in some case in the vicinity of the supporting wire or near cracks.

Liquid Inclusions were reported by Kolb and Laudise. CHAI et al¹¹ have measured a high water content of berlinite crystals that is probably in relation with inclusions. In our polished plates, they are easily revealed by conventional microscopy; their shapes are round to oblate and at room temperature, the liquid fills most of their volumes.

Important concentration of such inclusions may, sometimes, be assembled in surfaces near twins boundaries (veiling). A such zone of high concentration of liquid inclusions in a Y rotated plate is shown on Figure 12.

In good quality regions of present ^{crystals} can often be observed. They are less common in gradient crystals.

Cracks were common in earlier crystals. Now they have been eliminated from the reserve gradient crystals.



Figure 12 : Liquid inclusions in a Y rotated cut.

IV Experimental results with Y rotated resonators

Plates with orientations Y-38°05', Y, Y + 21°22', Y + 25°15', Y + 27°30', Y + 29°00' were cut as described in § III from crystals grown in second half of 1979 by methods described in reference¹⁴. Most of these cuts are in a lattice plane direction. Two to four resonators with no major defects under or nearly the electrodes were obtained from one crystal in each case. A polished resonator is displayed in Figure 13. Plates were measured in a network comprising two 10 dB attenuators on each side of the resonator with a Hewlett Packard 8045A Vector voltmeter in a set up which was otherwise the one described in the IEC 444 recommendation. Maximum and minimum amplitude frequencies and zero phase frequencies, when permitted by the Q factor, were measured together with attenuation at resonance. Estimated precision on remarkable frequencies is + 10⁻⁵. Temperature measurements were made with a platinum resistance thermometer which has a resolution of 10⁻²°C.

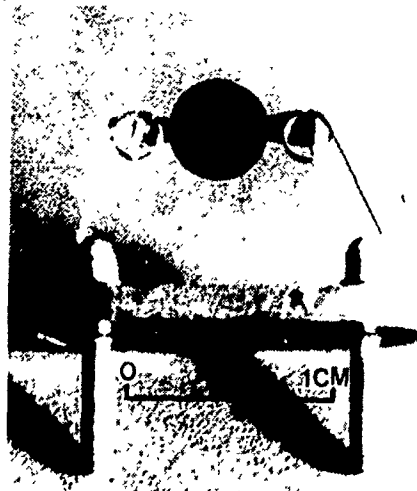


Figure 13 : Polished Y + 29° resonator.

At room temperature, Q_3 factors of the resonators are in the range of 10^3 to $5 \cdot 10^3$.

The frequency constants at room temperature, reproducible from sample to sample of same orientation, are in good agreement with the computed values obtained as described earlier⁵. They are given in table 3 where the precision of experimental values is assumed to be better than a few percent (Mass loading effect + thickness measurement errors).

In these experiments, the coupling coefficients were generally lower than the theoretical values, this may be due, in part, to an energy trapping effect related to the fact that we use electrodes much smaller to what may be permitted by spectral purity criterium. This effect was already encountered with another high coupling material¹³. An other explanation will be given in the discussion.

Table 3

	$\gamma=38^\circ 05'$	γ	$\gamma=21^\circ 22'$	$\gamma=23^\circ 15'$	$\gamma=27^\circ 30'$	$\gamma=29^\circ 00'$
MEAN THICKNESS(MM)	.1725	.191	.194	.180	.185	.243
NFR MEASURED	2099.	1662.	1452.	1455.	1474.	1443.
NF _A MEASURED	2107.	1668.	1460.	1458.	1468.	1455.
NF _R COMPUTED	2100.	1665.	1453.	1444.	1434.	1432.
NF _a COMPUTED	2122.	1695.	1477.	1466.	1450.	1448.

Table 3 : Frequency constants at 20°C for six γ rotated cuts (kHz.MM).

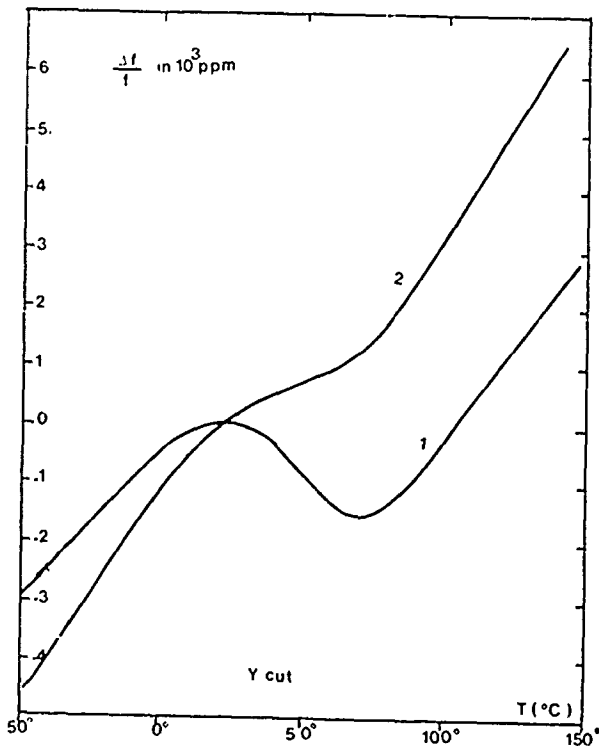


Figure 14 : Experimental thermal behaviour of a γ resonator.

Thermal variations of the remarkable frequencies were measured from -50° to $+150^\circ$. The results are displayed in Figure 14 to 17. (Other results are in Figure 19). Generally, only slight differences are observed between samples of same orientation, a typical case being those of Figure 17. However for γ plates, a large difference was recently observed (Figure 14).

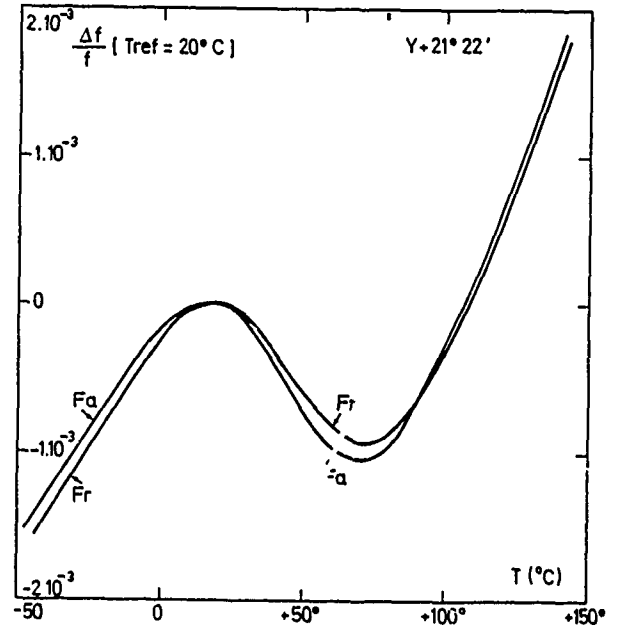


Figure 15 Thermal Behaviour of a $\gamma+21^\circ$ Berlinite Resonator

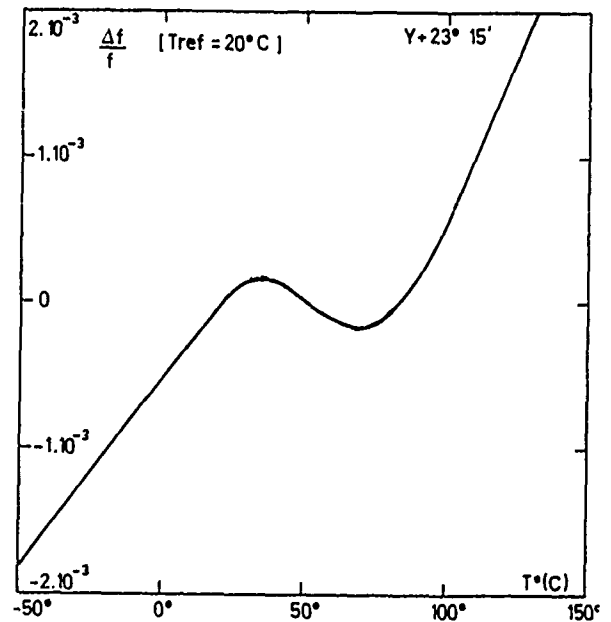


Figure 16 Thermal behaviour of a $\gamma+23^\circ$ Berlinite resonator

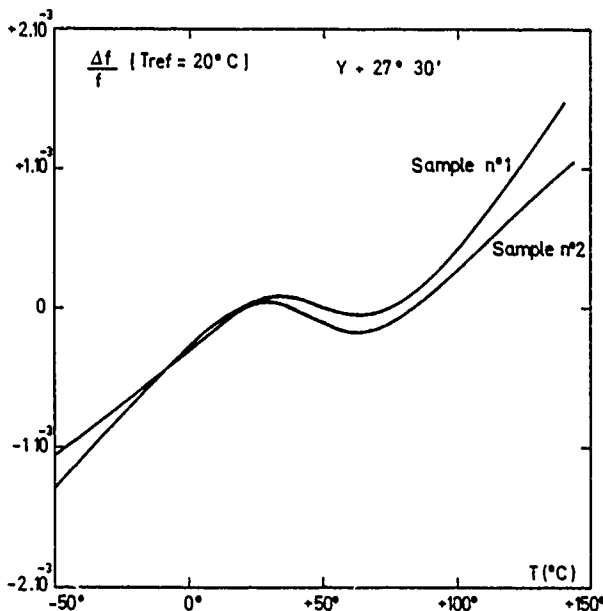


Figure 17 Experimental Frequency - Temperature Behaviour of a Y+27° 30' Cut

An "apparent" third order behaviour was observed for all Y rotated cuts already experimented with inflexion temperatures in the range 45°-50°C.

In several cases the variations of the resistance versus temperature was observed to have a maximum near the inflexion temperature. Such a behaviour is shown in Figure 18 for a Y + 21° 22' resonator.

The coupling coefficients of the resonators as computed by the relation $k^2 = \frac{\pi f_r}{2 f_a} \cotg \frac{\pi f_r}{2 f_a}$ have small temperature variations in the range -50° to + 150°C.

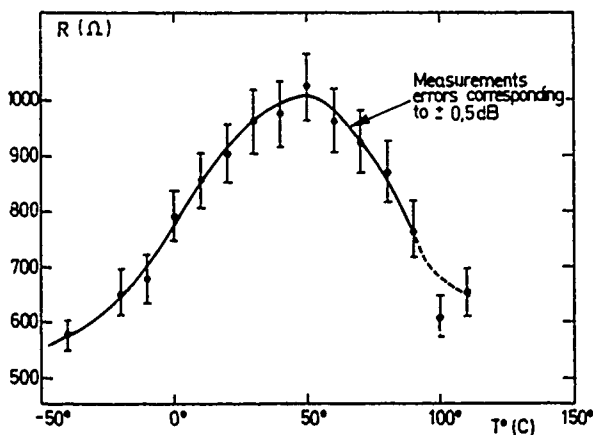


Figure 18 Thermal behaviour of the resistance of a Y+21° 22' Berlinité resonator

The experimental difference between thermal behaviour of f_a and f_r is much smaller to what can be expected from our previous theoretical calculation⁵. On Figure 15 we can see a typical example of this fact.

Comparison of thermal behaviour with Quartz

On Figure 19 we have put together our results now referred to the temperature of the inflexion point in each case. Computed results for corresponding cuts of quartz are displayed on Figure 20. From the comparison we can infer that except near the AT and BT cut that are not, now determined with a sufficient precision for Berlinité (The AT cut is expected to lie between $\theta = 28^\circ$ and $\theta = 30^\circ$), Temperature behaviour of this material seems to be more favourable, so is the angular sensitivity of the temperature coefficient. The results of figure 19 seem to be in good agreement with those already published in reference¹. On Figure 21 a comparison is made of the electrical response of resonators made of quartz and of berlinité.

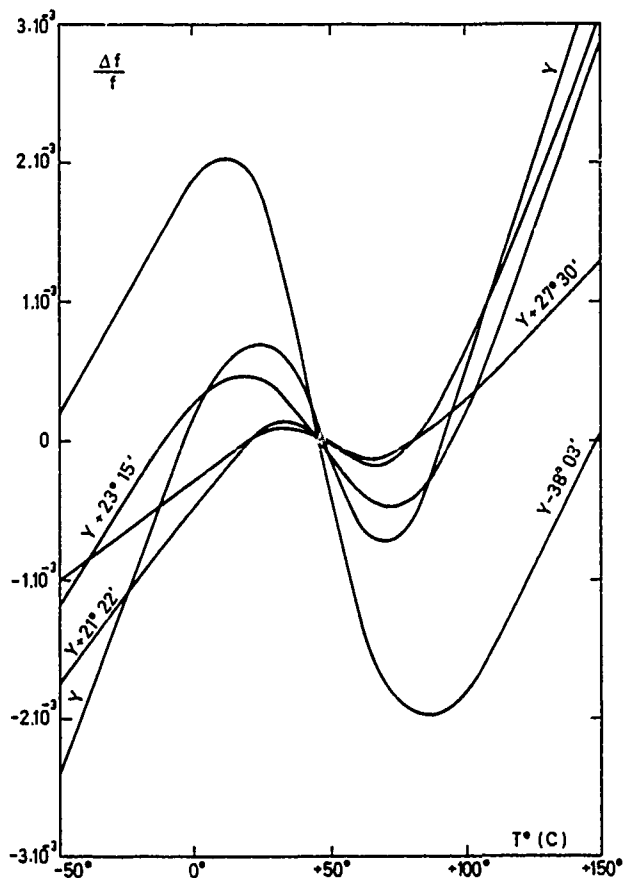


Figure 19 Summary of principal results now referred to the inflexion temperature of each case

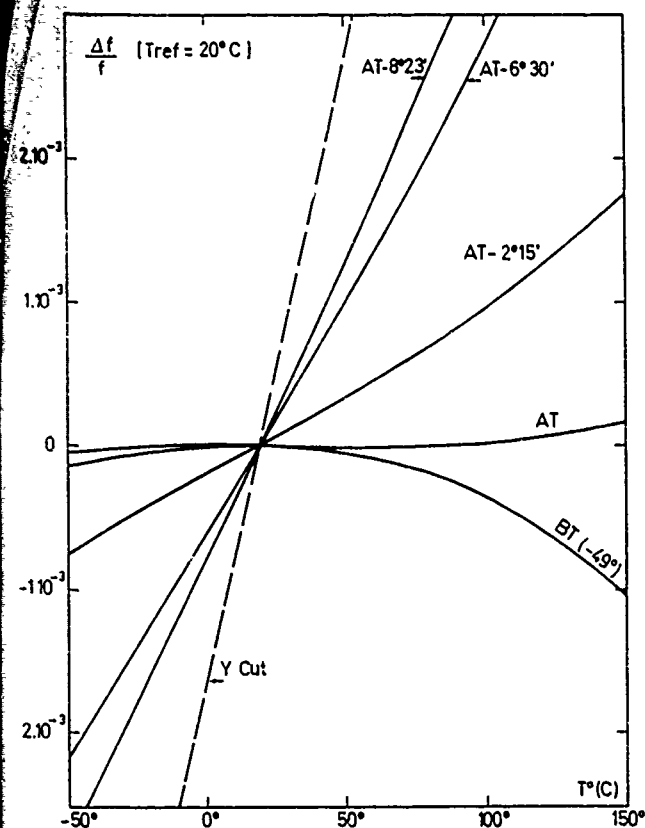


Figure 20 Computed results for similar cuts of quartz
(Same scale as figure 19)

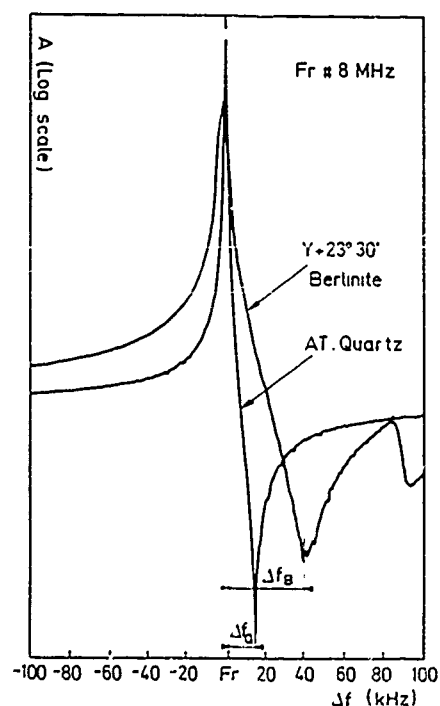


Figure 21 Compared amplitude versus frequency
response of quartz and Berlinite resonators

V Discussion of the results

Several facts indicate that parts of the obtained results may not be intrinsic features of perfect berlinite material :

1) The differences observed, for the thermal variations of the frequencies and for the coupling coefficients, of samples with identical orientation are larger than can be explained by orientation or measurement errors (Figure 17).

2°) A careful examination of present $\Delta f/f(T^\circ)$ results by polynomial least squares analysis indicate that they cannot be fitted exactly by polynomials of third or even fourth degree so that temperature coefficients with orders greater to 3 have with present samples a much larger value than for usual piezoelectric material.

3°) New experiments with Y plates indicate a different thermal behaviour as can be see in Figure 14.

4°) In this discussion we must indicate, that one of us, in collaboration with C. Ecolivet of the Rennes University¹⁵ has made Brillouin scattering measurements of the thermal variations of some berlinite elastic constants from room temperature to the transition temperature. The obtained results indicate, at all temperature a thermal behaviour of the elastic constants quite similar to those of the corresponding constant of quartz.

The higher order temperature coefficient of material constant that can be obtained from these measurements are much lower than values derived from CHANG and BARSCH experiments² or that computed from results of Figure 19.

Effect of impurities on Q, k, N_{fr} .

In our plates may exist very small Brasil twins that can not be seen by etch figures examination and liquid inclusions together with impurities, point defects, dislocations etc...

Liquid inclusions must introduce a strong dissipation in the plates especially in our case of a shear wave propagation. This attenuation can be temperature dependant since the filling of inclusions is varying with temperature.

The liquid inclusions may also, by a short circuiting effect lower the coupling coefficient but, in this matter, the major influence seems to be assigned to Brasil twinning : In Y rotated plate electrically excited, with twins, the shear motion take place in a direction ($\pm x$) which is given by the majority twin while the minority twin destroys the charge build up on electrodes and adds inertia, hence reduces the coupling coefficient (All this is due to the reverse direction of its x axis). This leads also to electrical dissipation which lowers the Q factor.

Since the phase velocities in the two parts of a Brasil twinning are the same, this defect can be assumed to introduce in first approximations no important effect on frequency constants. The other defects may also be supposed to give no major change on that properties.

All the previously considered defects may have 2nd order influences on frequency through :

- 1°) The composite nature of the resonators when twins or inclusions are present.
- 2°) The eventual modification of material constants they involve (Impurities...).
- 3°) Their influence on energy trapping (Dau-phiné Twins).

In some case these influences may be temperature dependant so that differences between $\Delta f/f(T)$ results, which are small and sensitive quantities may be explained.

Recently, experiments made with deeply twinned plates have confirmed that twins (or the associated defects) have negligible influences on frequency constants but that they modify the $\Delta f/f(T)$ results in increasing the value of the two extrema while slightly shifting the temperature of these extrema (the shape of $\Delta f/f(T)$ remains apparently cubical). Twinning appears thus to increase greatly the higher order temperature coefficients of frequency.

Conclusion

An efficient method was presented to reduce the impurity content of the crystals together with new advances in crystal growth methods. Experimental results with Y rotated resonators have given further evidences of the interest of berlinite for frequency control devices.

This material seems to have the following advantages over quartz :

- A much higher coupling coefficient
- A lower angular sensitivity of the temperature coefficients of frequency.

Further evidences of the possibility of an intrinsic excellent (similar to those of AT Quartz) thermal behaviour of devices were obtained and it appears that, as crystal quality increases the higher order temperature coefficients of the material constants seem to decrease.

On the whole, this material already surpasses quartz for several properties that are of major importance in frequency control devices. This fact is a full justification to the new researches toward further advances in crystal perfection and size that are planned in many country and that are needed before an industrial development can take place.

Acknowledgment

The authors would like to thank :

MM. Le Marechal, Gaillard, Servajean for their skillful contributions ; Mme Guenais and her staff of Physicochemical analysis laboratory for impurity analysis, MM. Ecolivet and Sanquer of the Rennes University for helpful discussions about their Brillouin scattering measurements. M. Lefèvre for his cooperation and M. Feldmann, Mme Henaff, M. Bon for kind encouragement and interest in Berlinite development.

References

- (1) J.M. STANLEY
Indust. Eng. Chem. 46 n°8 pp. 1684-1689 (1954).
- (2) Z.P. CHANG ; G.R. GARSCH
IEEE Trans. Sonics. Ultrason.
SU 23 p. 127 (1976).
- (3) A.D. BALLATO ; G.z. LAFRATE
Proc. 30th Symposium Frequency Control pp.141 156 (1976).
- (4) P.H. CARR, R.M. O'CONNELL
Proc. 30 Symposium Frequency Control
pp. 129 (1976).
- (5) J.DETAINT, M.FELDMANN, J.HENAFF, H.POIGNANT, Y.TOUDIC
Proc. 33rd Symposium Frequency Control
pp. 7079 (1979).
- (6) E.D. KOLB ; R.A. LAUDISE
J. Crystal growth 43 pp. 313-319 (1978).
- (7) E.D.KOLB, R.A. LAUDISE
Proc. 33rd Symposium Frequency Control
pp.88-98 (1979).
- (8) E.J. OZIMEK ; B.H.T. CHAI
Proc. 33rd Symposium Frequency Control
pp.80-87 (1979).
- (9) D.F. CROXALL ; L.R. A CHRISTIE ;
B.J. ISHERWOOD ; A.G. TODD ; J. BIRSH
2nd European Conference on Crysta Growth
Lancaster UK (1979).
- (10) H.POIGNANT, L. LE MARECHAL, Y. TOUDIC
Mat. Res. Bull. 14 pp. 603-612 (1979).
- (11) B.H.T. CHAI ; M.L. SHAND ; E. BUEHLER ;
M.A. GILLES
Proc. IEEE Ultrasonics Symposium.
Sept. 1979 New-Orleans (1979).
- (12) H.POIGNANT "Synthèse hydrothermale de la
Berlinite- AlPO 4)
Thesis University of Rennes (France)
25 oct. 1979.
- (13) J. DETAINT, R.LANCON
Proc. 30th Symposium Frequency Control
p. 132 (1976).
- (14) H.POIGNANT, L.LE MARECHAL, Y. TOUDIC
Proc. 7eme Conf. Int. Hte Pessions AIRAPT Le
CREUSOT-France Juillet 1979.
- (15) C. ECOLIVET, H. POIGNANT
to be published.

Netplane Data for Quartz, Berlinite, LiTaO_3 and LiNbO_3

Ernst Knolmayer

Quarzkeramik GmbH D-8035 Stockdorf (West Germany)

Summary

For Quartz and berlinite the data are computed for the same small positive indices because these crystals belong to the same space group. For LiTaO_3 and LiNbO_3 the data are computed for the following range of indices $h = -5$ to 5 , $k = -5$ to 5 , $l = 0$ to 9 . These two crystals belong to the same space group. For these two crystals the data are computed only for those indices which satisfy the conditions for possible reflections and for which the sum of the absolute values of the indices is smaller than 13 and for which the Bragg angles are smaller than 70° . The data are computed for 20°C and 25°C . Half circle diagrams were made for the netplanes and cuts parallel to the X-axis. The data are computed for the $\text{CuK } \alpha_1$ line. The data for quartz are more accurate than the data for the other three crystals.

Introduction

For the X-ray orientation of a crystal plate there are three important angles. Two of these determine the position of the netplane. Fig. 1. The third angle is the Bragg angle

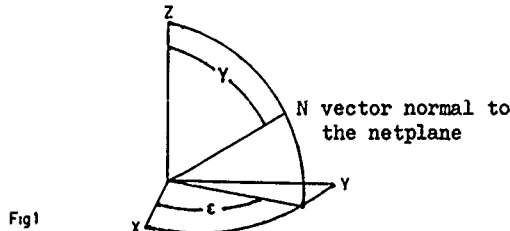


Fig 1

These angles depend on the Miller indices of the netplanes and on the lattice parameters. Because the lattice parameters are temperature dependent these angles are also temperature dependent. The three angles may be computed by the following equations (1)

$$\gamma = \cos^{-1} \left(\frac{1}{(c/a) \sqrt{S}} \right) \quad \text{where } S = h^2 + (h+2k)^2/3 + \frac{l^2}{(c/a)^2}$$

$$\epsilon = \tan^{-1} \left(\frac{h+2k}{hy/3} \right)$$

$$\Theta = \sin^{-1} \left(\frac{\lambda}{2d} \right) \quad \text{where } d = \frac{a}{\sqrt{\frac{4}{3}(h^2 + hk + k^2) + \frac{l^2}{(c/a)^2}}}$$

h, k, l indices
 c, a lattice parameters
 Θ Bragg angle
 λ X-ray wavelength

Because equation for ξ do not contain the lattice parameters this angle is temperature independent.

The lattice parameters

The data are computed from the following values of the lattice parameters

Lattice parameters in nm ($10\text{\AA} = 1 \text{ nm}$)

Crystal	a		c	
	20°C	25°C	20°C	25°C
Quartz	0.491291 ± 2	0.491323 ± 2	0.540461 ± 1	0.540485 ± 1
Berlinite	0.494276	0.494316	1.09737	1.09741
LiTaO_3	0.515383	0.515426	1.376276	1.376351
LiNbO_3	0.514806	0.514844	1.386291	1.386323

$\text{CuK } \alpha_1 = 0.1540562 \text{ nm}$

For Berlinite, LiTaO_3 and LiNbO_3 these values are calculated by means of the thermal expansion coefficients from values measured at other temperatures. If only one reflection is measured the change of Θ by temperature causes an error of the measured cut angle. The data are applicable to evaluate this error even if the seconds of the angles themselves are not accurate.

The Conditions for Possible Reflections

At LiTaO_3 and LiNbO_3 (space group $R3C$) only those netplanes are reflecting which satisfy the following conditions

$$-h+k+l = 3n, \quad l = 2n \text{ if } h = -k, \quad n \text{ integer}$$

Therefore it is not reasonable to compute the data only for positive indices.

References: 1. Heising; 2. International Tables for x-ray Crystallography; 3. Landolt-Börnstein

Berlinite

	20°C	25°C	30°C	35°C	40°C	45°C	50°C	55°C	60°C	65°C	70°C	75°C	80°C	85°C	90°C	95°C	100°C	105°C	110°C	115°C	120°C	125°C	130°C	135°C	140°C	145°C	150°C	155°C	160°C	165°C	170°C	175°C	180°C	185°C	190°C	195°C	200°C	205°C	210°C	215°C	220°C	225°C	230°C	235°C	240°C	245°C	250°C	255°C	260°C	265°C	270°C	275°C	280°C	285°C	290°C	295°C	300°C	305°C	310°C	315°C	320°C	325°C	330°C	335°C	340°C	345°C	350°C	355°C	360°C	365°C	370°C	375°C	380°C	385°C	390°C	395°C	400°C	405°C	410°C	415°C	420°C	425°C	430°C	435°C	440°C	445°C	450°C	455°C	460°C	465°C	470°C	475°C	480°C	485°C	490°C	495°C	500°C	505°C	510°C	515°C	520°C	525°C	530°C	535°C	540°C	545°C	550°C	555°C	560°C	565°C	570°C	575°C	580°C	585°C	590°C	595°C	600°C	605°C	610°C	615°C	620°C	625°C	630°C	635°C	640°C	645°C	650°C	655°C	660°C	665°C	670°C	675°C	680°C	685°C	690°C	695°C	700°C	705°C	710°C	715°C	720°C	725°C	730°C	735°C	740°C	745°C	750°C	755°C	760°C	765°C	770°C	775°C	780°C	785°C	790°C	795°C	800°C	805°C	810°C	815°C	820°C	825°C	830°C	835°C	840°C	845°C	850°C	855°C	860°C	865°C	870°C	875°C	880°C	885°C	890°C	895°C	900°C	905°C	910°C	915°C	920°C	925°C	930°C	935°C	940°C	945°C	950°C	955°C	960°C	965°C	970°C	975°C	980°C	985°C	990°C	995°C	1000°C	1005°C	1010°C	1015°C	1020°C	1025°C	1030°C	1035°C	1040°C	1045°C	1050°C	1055°C	1060°C	1065°C	1070°C	1075°C	1080°C	1085°C	1090°C	1095°C	1100°C	1105°C	1110°C	1115°C	1120°C	1125°C	1130°C	1135°C	1140°C	1145°C	1150°C	1155°C	1160°C	1165°C	1170°C	1175°C	1180°C	1185°C	1190°C	1195°C	1200°C	1205°C	1210°C	1215°C	1220°C	1225°C	1230°C	1235°C	1240°C	1245°C	1250°C	1255°C	1260°C	1265°C	1270°C	1275°C	1280°C	1285°C	1290°C	1295°C	1300°C	1305°C	1310°C	1315°C	1320°C	1325°C	1330°C	1335°C	1340°C	1345°C	1350°C	1355°C	1360°C	1365°C	1370°C	1375°C	1380°C	1385°C	1390°C	1395°C	1400°C	1405°C	1410°C	1415°C	1420°C	1425°C	1430°C	1435°C	1440°C	1445°C	1450°C	1455°C	1460°C	1465°C	1470°C	1475°C	1480°C	1485°C	1490°C	1495°C	1500°C	1505°C	1510°C	1515°C	1520°C	1525°C	1530°C	1535°C	1540°C	1545°C	1550°C	1555°C	1560°C	1565°C	1570°C	1575°C	1580°C	1585°C	1590°C	1595°C	1600°C	1605°C	1610°C	1615°C	1620°C	1625°C	1630°C	1635°C	1640°C	1645°C	1650°C	1655°C	1660°C	1665°C	1670°C	1675°C	1680°C	1685°C	1690°C	1695°C	1700°C	1705°C	1710°C	1715°C	1720°C	1725°C	1730°C	1735°C	1740°C	1745°C	1750°C	1755°C	1760°C	1765°C	1770°C	1775°C	1780°C	1785°C	1790°C	1795°C	1800°C	1805°C	1810°C	1815°C	1820°C	1825°C	1830°C	1835°C	1840°C	1845°C	1850°C	1855°C	1860°C	1865°C	1870°C	1875°C	1880°C	1885°C	1890°C	1895°C	1900°C	1905°C	1910°C	1915°C	1920°C	1925°C	1930°C	1935°C	1940°C	1945°C	1950°C	1955°C	1960°C	1965°C	1970°C	1975°C	1980°C	1985°C	1990°C	1995°C	2000°C	2005°C	2010°C	2015°C	2020°C	2025°C	2030°C	2035°C	2040°C	2045°C	2050°C	2055°C	2060°C	2065°C	2070°C	2075°C	2080°C	2085°C	2090°C	2095°C	2100°C	2105°C	2110°C	2115°C	2120°C	2125°C	2130°C	2135°C	2140°C	2145°C	2150°C	2155°C	2160°C	2165°C	2170°C	2175°C	2180°C	2185°C	2190°C	2195°C	2200°C	2205°C	2210°C	2215°C	2220°C	2225°C	2230°C	2235°C	2240°C	2245°C	2250°C	2255°C	2260°C	2265°C	2270°C	2275°C	2280°C	2285°C	2290°C	2295°C	2300°C	2305°C	2310°C	2315°C	2320°C	2325°C	2330°C	2335°C	2340°C	2345°C	2350°C	2355°C	2360°C	2365°C	2370°C	2375°C	2380°C	2385°C	2390°C	2395°C	2400°C	2405°C	2410°C	2415°C	2420°C	2425°C	2430°C	2435°C	2440°C	2445°C	2450°C	2455°C	2460°C	2465°C	2470°C	2475°C	2480°C	2485°C	2490°C	2495°C	2500°C	2505°C	2510°C	2515°C	2520°C	2525°C	2530°C	2535°C	2540°C	2545°C	2550°C	2555°C	2560°C	2565°C	2570°C	2575°C	2580°C	2585°C	2590°C	2595°C	2600°C	2605°C	2610°C	2615°C	2620°C	2625°C	2630°C	2635°C	2640°C	2645°C	2650°C	2655°C	2660°C	2665°C	2670°C	2675°C	2680°C	2685°C	2690°C	2695°C	2700°C	2705°C	2710°C	2715°C	2720°C	2725°C	2730°C	2735°C	2740°C	2745°C	2750°C	2755°C	2760°C	2765°C	2770°C	2775°C	2780°C	2785°C	2790°C	2795°C	2800°C	2805°C	2810°C	2815°C	2820°C	2825°C	2830°C	2835°C	2840°C	2845°C	2850°C	2855°C	2860°C	2865°C	2870°C	2875°C	2880°C	2885°C	2890°C	2895°C	2900°C	2905°C	2910°C	2915°C	2920°C	2925°C	2930°C	2935°C	2940°C	2945°C	2950°C	2955°C	2960°C	2965°C	2970°C	2975°C	2980°C	2985°C	2990°C	2995°C	3000°C	3005°C	3010°C	3015°C	3020°C	3025°C	3030°C	3035°C	3040°C	3045°C	3050°C	3055°C	3060°C	3065°C	3070°C	3075°C	3080°C	3085°C	3090°C	3095°C	3100°C	3105°C	3110°C	3115°C	3120°C	3125°C	3130°C	3135°C	3140°C	3145°C	3150°C	3155°C	3160°C	3165°C	3170°C	3175°C	3180°C	3185°C	3190°C	3195°C	3200°C	3205°C	3210°C	3215°C	3220°C	3225°C	3230°C	3235°C	3240°C	3245°C	3250°C	3255°C	3260°C	3265°C	3270°C	3275°C	3280°C	3285°C	3290°C	3295°C	3300°C	3305°C	3310°C	3315°C	3320°C	3325°C	3330°C	3335°C	3340°C	3345°C	3350°C	3355°C	3360°C	3365°C	3370°C	3375°C	3380°C	3385°C	3390°C	3395°C	3400°C	3405°C	3410°C	3415°C	3420°C	3425°C	3430°C	3435°C	3440°C	3445°C	3450°C	3455°C	3460°C	3465°C	3470°C	3475°C	3480°C	3485°C	3490°C	3495°C	3500°C	3505°C	3510°C	3515°C	3520°C	3525°C	3530°C	3535°C	3540°C	3545°C	3550°C	3555°C	3560°C	3565°C	3570°C	3575°C	3580°C	3585°C	3590°C	3595°C	3600°C	3605°C	3610°C	3615°C	3620°C	3625°C	3630°C	3635°C	3640°C	3645°C	3650°C	3655°C	3660°C	3665°C	3670°C	3675°C	3680°C	3685°C	3690°C	3695°C	3700°C	3705°C	3710°C	3715°C	3720°C	3725°C	3730°C	3735°C	3740°C	3745°C	3750°C	3755°C	3760°C	3765°C	3770°C	3775°C	3780°C	3785°C	3790°C	3795°C	3800°C	3805°C	3810°C	3815°C	3820°C	3825°C	3830°C	3835°C	3840°C	3845°C	3850°C	3855°C	3860°C	3865°C	3870°C	3875°C	3880°C	3885°C	3890°C	3895°C	3900°C	3905°C	3910°C	3915°C	3920°C	3925°C	3930°C	3935°C	3940°C	3945°C	3950°C	3955°C	3960°C	3965°C	3970°C	3975°C	3980°C	3985°C	3990°C	3995°C	4000°C	4005°C	4010°C	4015°C	4020°C	4025°C	4030°C	4035°C	4040°C	4045°C	4050°C	4055°C	4060°C	4065°C	4070°C	4075°C	4080°C	4085°C	4090°C	4095°C	4100°C	4105°C	4110°C	4115°C	4120°C	4125°C	4130°C	4135°C	4140°C	4145°C	4150°C	4155°C	4160°C	4165°C	4170°C	4175°C	4180°C	4185°C	4190°C	4195°C	4200°C	4205°C	4210°C	4215°C	4220°C	4225°C	4230°C	4235°C	4240°C	4245°C	4250°C	4255°C	4260°C	4265°C	4270°C	4275°C	4280°C	4285°C	4290°C	4295°C	4300°C	4305°C	4310°C	4315°C	4320°C	4325°C	4330°C	4335°C	4340°C	4345°C	4350°C	4355°C	4360°C	4365°C	4370°C	4375°C	4380°C	4385°C	4390°C	4395°C	4400°C	4405°C	4410°C	4415°C	4420°C	4425°C	4430°C	4435°C	4440°C	4445°C	4450°C	4455°C	4460°C	4465°C	4470°C	4475°C	4480°C	4485°C	4490°C	4495°C	4500°C	4505°C	4510°C	4515°C	4520°C	4525°C	4530°C	4535°C	4540°C	4545°C	4550°C	4555°C	4560°C	4565°C	4570°C	4575°C	4580°C	4585°C	4590°C	4595°C	4600°C	4605°C	4610°C	4615°C	4620°C	4625°C	4630°C	4635°C	4640°C	4645°C	4650°C	4655°C	4660°C	4665°C	4670°C	4675°C	4680°C	4685°C	4690°C	4695°C	4700°C	4705°C	4710°C	4715°C	4720°C	4725°C	4730°C	4735°C	4740°C	4745°C	4750°C	4755°C	4760°C	4765°C	4770°C	4775°C	4780°C	4785°C	4790°C	4795°C	4800°C	4805°C	4810°C	4815°C	4820°C	4825°C	4830°C	4835°C	4840°C	4845°C	4850°C	4855°C	4860°C	4865°C	4870°C	4875°C	4880°C	4885°C	4890°C	4895°C	4900°C	4905°C	4910°C	4915°C	4920°C	4925°C	4930°C	4935°C	4940°C	4945°C	4950°C	4955°C	4960°C	4965°C	4970°C	4975°C	4980°C	4985°C	4990°C	4995°C	5000°C	5005°C	5010°C	5015°C	5020°C	5025°C	5030°C	5035°C	5040°C	5045°C	5050°C	5055°C	5060°C	5065°C	5070°C	5075°C	5080°C	5085°C	5090°C	5095°C	5100°C	5105°C	5110°C	5115°C	5120°C	5125°C	5130°C	5135°C	5140°C	5145°C	5150°C	5155°C	5160°C	5165°C	5170°C	5175°C	5180°C	5185°C	5190°C	5195°C	5200°C	5205°C	5210°C	5215°C	5220°C	5225°C	5230°C	5235°C	5240°C	5245°C	5250°C	5255°C	5260°C	5265°C	5270°C	5275°C	5280°C	5285°C	5290°C	5295°C	5300°C	5305°C	5310°C	5315°C	5320°C	5325°C	5330°C	5335°C	5340°C	5345°C	5350°C	5355°C	5360°C	5365°C	5370°C	5375°C	5380°C	5385°C	5390°C	5395°C	5400°C	5405°C	5410°C	5415°C	5420°C	5425°C	5430°C	5435°C	5440°C	5445°C	5450°C	5455°C	5460°C	5465°C	5470°C	5475°C	5480°C	5485°C	5490°C	5495°C	5500°C	5505°C	5510°C	5515°C	5520°C	5525°C	5530°C	5535°C	5540°C	5545°C	5550°C	5555°C	5560°C	5565°C	5570°C	5575°C	5580°C	5585°C	5590°C	5595°C	5600°C	5605°C	5610°C	5615°C	5620°C	5625°C	5630°C	5635°C	5640°C	5645°C	5650°C	5655°C	5660°C	5665°C	5670°C	5675°C	5680°C	5685°C	5690°C	5695°C	5700°C	5705°C	5710°C	5715°C	5720°C	5725°C	5730°C	5735°C	5740°C	5745°C	5750°C	5755°C	5760°C	5765°C	5770°C	5775°C	5780°C	5785°C	5790°C	5795°C	5800°C	5805°C	5810°C	5815°C	5820°C	5825°C	5830°C	5835°C	5840°C	5845°C	5850°C	5855°C	5860°C	5865°C	5870°C	5875°C	5880°C	5885°C	5890°C	5895°C	5900°C	5905°C	5910°C	5915°C	5920°C	5925°C	5930°C	5935°C	5940°C	5945°C	5950°C	5955°C	5960°C	5965°C	5970°C	5975°C	5980°C	5985°C	5990°C	5995°C	6000°C	6005°C	6010°C	6015°C	6020°C	6025°C	6030°C	6035°C	6040°C	6045°C	6050°C	6055°C	6060°C	6065°C	6070°C	6075°C	6080°C	6085°C	6090°C	6095°C	6100°C	6105°C	6110°C	6115°C	6120°C	6125°C	6130°C	6135°C	6140°C	6145°C	6150°C	6155°C	6160°C	6165°C	6170°C	6175°C	6180°C	6185°C	6190°C	6195°C	6200°C	6205°C	6210°C	6215°C	6220°C	6225°C	6230°C	6235°C	6240°C	6245°C	6250°C	6255°C	6260°C	6265°C	6270°C	6275°C	6280°C	6285°C	6290°C	6295°C	6300°C	6305°C	6310°C</
--	------	------	------	------	------	------	------	------	------	------	------	------	------	------	------	------	-------	-------	-------	-------	-------	-------	-------	-------	-------	-------	-------	-------	-------	-------	-------	-------	-------	-------	-------	-------	-------	-------	-------	-------	-------	-------	-------	-------	-------	-------	-------	-------	-------	-------	-------	-------	-------	-------	-------	-------	-------	-------	-------	-------	-------	-------	-------	-------	-------	-------	-------	-------	-------	-------	-------	-------	-------	-------	-------	-------	-------	-------	-------	-------	-------	-------	-------	-------	-------	-------	-------	-------	-------	-------	-------	-------	-------	-------	-------	-------	-------	-------	-------	-------	-------	-------	-------	-------	-------	-------	-------	-------	-------	-------	-------	-------	-------	-------	-------	-------	-------	-------	-------	-------	-------	-------	-------	-------	-------	-------	-------	-------	-------	-------	-------	-------	-------	-------	-------	-------	-------	-------	-------	-------	-------	-------	-------	-------	-------	-------	-------	-------	-------	-------	-------	-------	-------	-------	-------	-------	-------	-------	-------	-------	-------	-------	-------	-------	-------	-------	-------	-------	-------	-------	-------	-------	-------	-------	-------	-------	-------	-------	-------	-------	-------	-------	-------	-------	-------	-------	-------	-------	-------	-------	-------	-------	-------	-------	-------	-------	--------	--------	--------	--------	--------	--------	--------	--------	--------	--------	--------	--------	--------	--------	--------	--------	--------	--------	--------	--------	--------	--------	--------	--------	--------	--------	--------	--------	--------	--------	--------	--------	--------	--------	--------	--------	--------	--------	--------	--------	--------	--------	--------	--------	--------	--------	--------	--------	--------	--------	--------	--------	--------	--------	--------	--------	--------	--------	--------	--------	--------	--------	--------	--------	--------	--------	--------	--------	--------	--------	--------	--------	--------	--------	--------	--------	--------	--------	--------	--------	--------	--------	--------	--------	--------	--------	--------	--------	--------	--------	--------	--------	--------	--------	--------	--------	--------	--------	--------	--------	--------	--------	--------	--------	--------	--------	--------	--------	--------	--------	--------	--------	--------	--------	--------	--------	--------	--------	--------	--------	--------	--------	--------	--------	--------	--------	--------	--------	--------	--------	--------	--------	--------	--------	--------	--------	--------	--------	--------	--------	--------	--------	--------	--------	--------	--------	--------	--------	--------	--------	--------	--------	--------	--------	--------	--------	--------	--------	--------	--------	--------	--------	--------	--------	--------	--------	--------	--------	--------	--------	--------	--------	--------	--------	--------	--------	--------	--------	--------	--------	--------	--------	--------	--------	--------	--------	--------	--------	--------	--------	--------	--------	--------	--------	--------	--------	--------	--------	--------	--------	--------	--------	--------	--------	--------	--------	--------	--------	--------	--------	--------	--------	--------	--------	--------	--------	--------	--------	--------	--------	--------	--------	--------	--------	--------	--------	--------	--------	--------	--------	--------	--------	--------	--------	--------	--------	--------	--------	--------	--------	--------	--------	--------	--------	--------	--------	--------	--------	--------	--------	--------	--------	--------	--------	--------	--------	--------	--------	--------	--------	--------	--------	--------	--------	--------	--------	--------	--------	--------	--------	--------	--------	--------	--------	--------	--------	--------	--------	--------	--------	--------	--------	--------	--------	--------	--------	--------	--------	--------	--------	--------	--------	--------	--------	--------	--------	--------	--------	--------	--------	--------	--------	--------	--------	--------	--------	--------	--------	--------	--------	--------	--------	--------	--------	--------	--------	--------	--------	--------	--------	--------	--------	--------	--------	--------	--------	--------	--------	--------	--------	--------	--------	--------	--------	--------	--------	--------	--------	--------	--------	--------	--------	--------	--------	--------	--------	--------	--------	--------	--------	--------	--------	--------	--------	--------	--------	--------	--------	--------	--------	--------	--------	--------	--------	--------	--------	--------	--------	--------	--------	--------	--------	--------	--------	--------	--------	--------	--------	--------	--------	--------	--------	--------	--------	--------	--------	--------	--------	--------	--------	--------	--------	--------	--------	--------	--------	--------	--------	--------	--------	--------	--------	--------	--------	--------	--------	--------	--------	--------	--------	--------	--------	--------	--------	--------	--------	--------	--------	--------	--------	--------	--------	--------	--------	--------	--------	--------	--------	--------	--------	--------	--------	--------	--------	--------	--------	--------	--------	--------	--------	--------	--------	--------	--------	--------	--------	--------	--------	--------	--------	--------	--------	--------	--------	--------	--------	--------	--------	--------	--------	--------	--------	--------	--------	--------	--------	--------	--------	--------	--------	--------	--------	--------	--------	--------	--------	--------	--------	--------	--------	--------	--------	--------	--------	--------	--------	--------	--------	--------	--------	--------	--------	--------	--------	--------	--------	--------	--------	--------	--------	--------	--------	--------	--------	--------	--------	--------	--------	--------	--------	--------	--------	--------	--------	--------	--------	--------	--------	--------	--------	--------	--------	--------	--------	--------	--------	--------	--------	--------	--------	--------	--------	--------	--------	--------	--------	--------	--------	--------	--------	--------	--------	--------	--------	--------	--------	--------	--------	--------	--------	--------	--------	--------	--------	--------	--------	--------	--------	--------	--------	--------	--------	--------	--------	--------	--------	--------	--------	--------	--------	--------	--------	--------	--------	--------	--------	--------	--------	--------	--------	--------	--------	--------	--------	--------	--------	--------	--------	--------	--------	--------	--------	--------	--------	--------	--------	--------	--------	--------	--------	--------	--------	--------	--------	--------	--------	--------	--------	--------	--------	--------	--------	--------	--------	--------	--------	--------	--------	--------	--------	--------	--------	--------	--------	--------	--------	--------	--------	--------	--------	--------	--------	--------	--------	--------	--------	--------	--------	--------	--------	--------	--------	--------	--------	--------	--------	--------	--------	--------	--------	--------	--------	--------	--------	--------	--------	--------	--------	--------	--------	--------	--------	--------	--------	--------	--------	--------	--------	--------	--------	--------	--------	--------	--------	--------	--------	--------	--------	--------	--------	--------	--------	--------	--------	--------	--------	--------	--------	--------	--------	--------	--------	--------	--------	--------	--------	--------	--------	--------	--------	--------	--------	--------	--------	--------	--------	--------	--------	--------	--------	--------	--------	--------	--------	--------	--------	--------	--------	--------	--------	--------	--------	--------	--------	--------	--------	--------	--------	--------	--------	--------	--------	--------	--------	--------	--------	--------	--------	--------	--------	--------	--------	--------	--------	--------	--------	--------	--------	--------	--------	--------	--------	--------	--------	--------	--------	--------	--------	--------	--------	--------	--------	--------	--------	--------	--------	--------	--------	--------	--------	--------	--------	--------	--------	--------	--------	--------	--------	--------	--------	--------	--------	--------	--------	--------	--------	--------	--------	--------	--------	--------	--------	--------	--------	--------	--------	--------	--------	--------	--------	--------	--------	--------	--------	--------	--------	--------	--------	--------	--------	--------	--------	--------	--------	--------	--------	--------	--------	--------	--------	--------	--------	--------	--------	--------	--------	--------	--------	--------	--------	--------	--------	--------	--------	--------	--------	--------	--------	--------	--------	--------	--------	--------	--------	--------	--------	--------	--------	--------	--------	--------	--------	--------	--------	--------	--------	--------	--------	--------	--------	--------	--------	--------	--------	--------	--------	--------	--------	--------	--------	--------	--------	--------	--------	--------	--------	--------	--------	--------	--------	--------	--------	--------	--------	--------	--------	--------	--------	--------	--------	--------	--------	--------	--------	--------	--------	--------	--------	--------	--------	--------	--------	--------	--------	--------	--------	--------	--------	--------	--------	--------	--------	--------	--------	--------	--------	--------	--------	--------	--------	--------	--------	--------	--------	--------	--------	--------	--------	--------	--------	--------	--------	--------	--------	--------	--------	--------	--------	--------	--------	--------	--------	--------	--------	--------	--------	--------	--------	--------	--------	--------	--------	--------	--------	--------	--------	--------	--------	--------	--------	--------	--------	--------	--------	--------	--------	--------	--------	--------	--------	--------	--------	--------	--------	--------	--------	--------	--------	--------	--------	--------	--------	--------	--------	--------	--------	--------	--------	--------	--------	--------	--------	--------	--------	--------	--------	--------	--------	--------	--------	--------	--------	--------	--------	--------	--------	--------	--------	--------	--------	--------	--------	--------	--------	--------	--------	--------	--------	--------	--------	--------	--------	--------	--------	--------	--------	--------	--------	--------	--------	--------	--------	--------	--------	--------	--------	--------	--------	--------	--------	--------	--------	--------	--------	--------	--------	--------	--------	--------	--------	--------	--------	--------	--------	--------	--------	--------	--------	--------	--------	--------	--------	----------

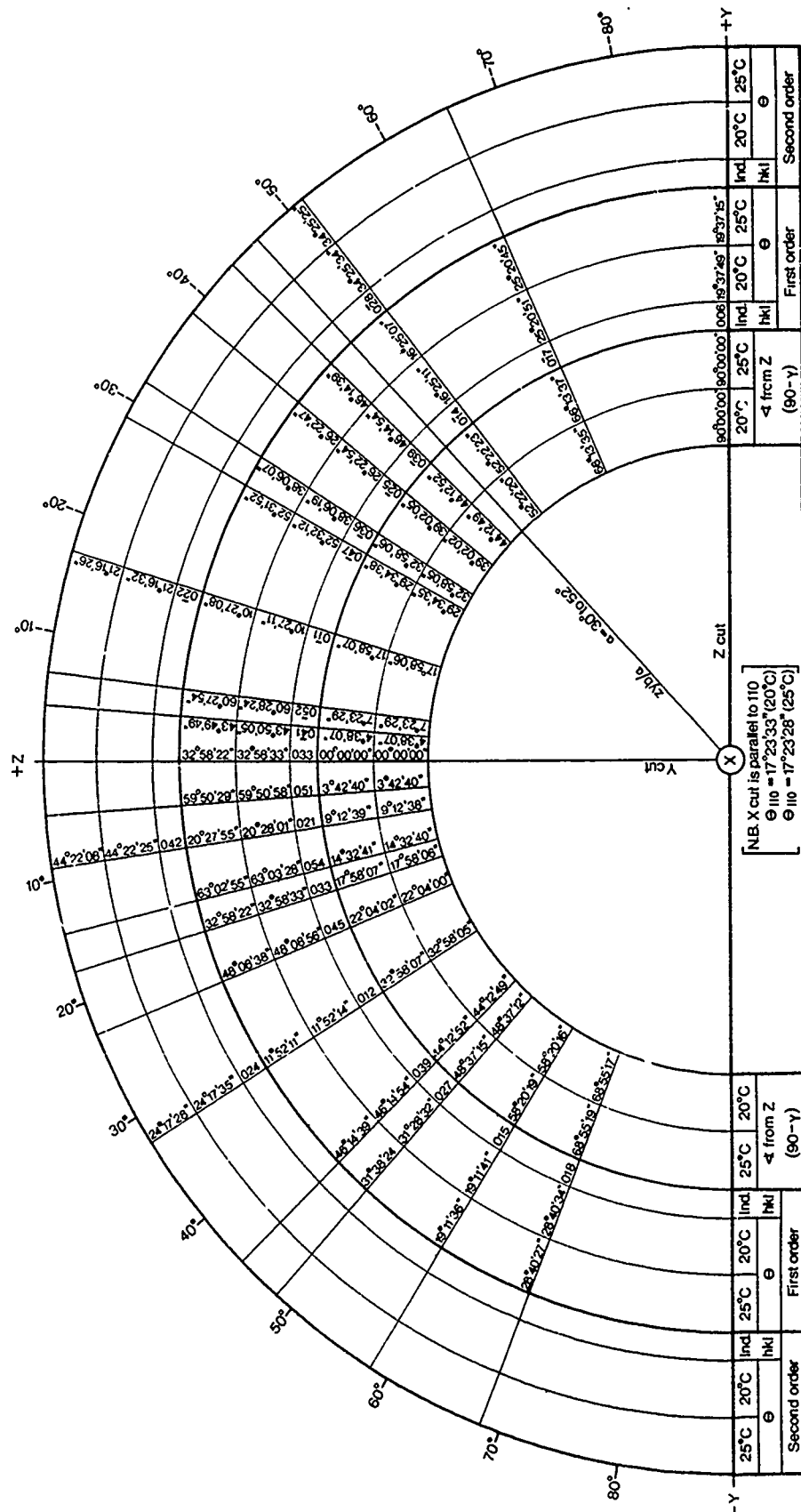
Quartz

[illegible]

[illegible]

	20°C	25°C	Θ	20°C	25°C	Y	20°C	25°C	ε
l	1	4	0	0	0	0	1	4	0
k	0	0	0	0	0	0	0	0	0
h	1	5	0	0	0	0	1	5	0
g	1	5	0	0	0	0	1	5	0
f	1	5	0	0	0	0	1	5	0
e	1	5	0	0	0	0	1	5	0
d	1	5	0	0	0	0	1	5	0
c	1	5	0	0	0	0	1	5	0
b	1	5	0	0	0	0	1	5	0
a	1	5	0	0	0	0	1	5	0
z	1	5	0	0	0	0	1	5	0
y	1	5	0	0	0	0	1	5	0
x	1	5	0	0	0	0	1	5	0
w	1	5	0	0	0	0	1	5	0
v	1	5	0	0	0	0	1	5	0
u	1	5	0	0	0	0	1	5	0
t	1	5	0	0	0	0	1	5	0
s	1	5	0	0	0	0	1	5	0
r	1	5	0	0	0	0	1	5	0
q	1	5	0	0	0	0	1	5	0
p	1	5	0	0	0	0	1	5	0
o	1	5	0	0	0	0	1	5	0
n	1	5	0	0	0	0	1	5	0
m	1	5	0	0	0	0	1	5	0
l	1	5	0	0	0	0	1	5	0
k	1	5	0	0	0	0	1	5	0
j	1	5	0	0	0	0	1	5	0
i	1	5	0	0	0	0	1	5	0
h	1	5	0	0	0	0	1	5	0
g	1	5	0	0	0	0	1	5	0
f	1	5	0	0	0	0	1	5	0
e	1	5	0	0	0	0	1	5	0
d	1	5	0	0	0	0	1	5	0
c	1	5	0	0	0	0	1	5	0
b	1	5	0	0	0	0	1	5	0
a	1	5	0	0	0	0	1	5	0
z	1	5	0	0	0	0	1	5	0
y	1	5	0	0	0	0	1	5	0
x	1	5	0	0	0	0	1	5	0
w	1	5	0	0	0	0	1	5	0
v	1	5	0	0	0	0	1	5	0
u	1	5	0	0	0	0	1	5	0
t	1	5	0	0	0	0	1	5	0
s	1	5	0	0	0	0	1	5	0
r	1	5	0	0	0	0	1	5	0
q	1	5	0	0	0	0	1	5	0
p	1	5	0	0	0	0	1	5	0
o	1	5	0	0	0	0	1	5	0
n	1	5	0	0	0	0	1	5	0
m	1	5	0	0	0	0	1	5	0
l	1	5	0	0	0	0	1	5	0
k	1	5	0	0	0	0	1	5	0
j	1	5	0	0	0	0	1	5	0
i	1	5	0	0	0	0	1	5	0
h	1	5	0	0	0	0	1	5	0
g	1	5	0	0	0	0	1	5	0
f	1	5	0	0	0	0	1	5	0
e	1	5	0	0	0	0	1	5	0
d	1	5	0	0	0	0	1	5	0
c	1	5	0	0	0	0	1	5	0
b	1	5	0	0	0	0	1	5	0
a	1	5	0	0	0	0	1	5	0
z	1	5							

LiTaO_3



LiNbO₃

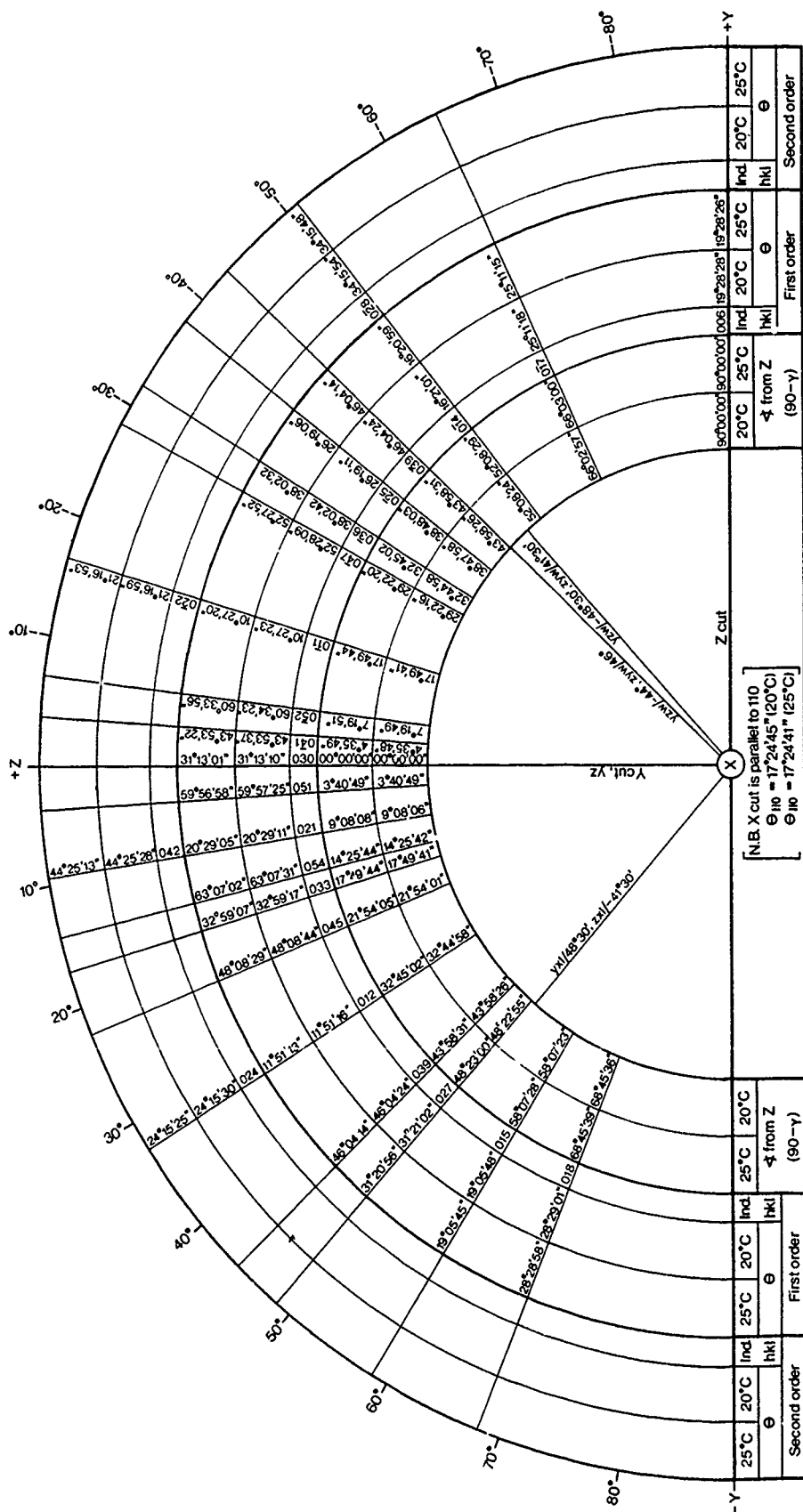
	20°C	25°C	Y	20°C	25°C	ε
h	1	1	1	1	1	1
k	1	1	1	1	1	1
l	1	1	1	1	1	1
ε	20 52 51 50 49 48 47 46 45 44 43 42 41 40 39 38 37 36 35 34 33 32 31 30 29 28 27 26 25 24 23 22 21 20 19 18 17 16 15 14 13 12 11 10 9 8 7 6 5 4 3 2 1 0	20 52 51 50 49 48 47 46 45 44 43 42 41 40 39 38 37 36 35 34 33 32 31 30 29 28 27 26 25 24 23 22 21 20 19 18 17 16 15 14 13 12 11 10 9 8 7 6 5 4 3 2 1 0	20 52 51 50 49 48 47 46 45 44 43 42 41 40 39 38 37 36 35 34 33 32 31 30 29 28 27 26 25 24 23 22 21 20 19 18 17 16 15 14 13 12 11 10 9 8 7 6 5 4 3 2 1 0	20 52 51 50 49 48 47 46 45 44 43 42 41 40 39 38 37 36 35 34 33 32 31 30 29 28 27 26 25 24 23 22 21 20 19 18 17 16 15 14 13 12 11 10 9 8 7 6 5 4 3 2 1 0	20 52 51 50 49 48 47 46 45 44 43 42 41 40 39 38 37 36 35 34 33 32 31 30 29 28 27 26 25 24 23 22 21 20 19 18 17 16 15 14 13 12 11 10 9 8 7 6 5 4 3 2 1 0	20 52 51 50 49 48 47 46 45 44 43 42 41 40 39 38 37 36 35 34 33 32 31 30 29 28 27 26 25 24 23 22 21 20 19 18 17 16 15 14 13 12 11 10 9 8 7 6 5 4 3 2 1 0

LiNbO₃

	20°C	25°C	Y	20°C	25°C	ε
h	1	1	1	1	1	1
k	1	1	1	1	1	1
l	1	1	1	1	1	1
ε	20 52 51 50 49 48 47 46 45 44 43 42 41 40 39 38 37 36 35 34 33 32 31 30 29 28 27 26 25 24 23 22 21 20 19 18 17 16 15 14 13 12 11 10 9 8 7 6 5 4 3 2 1 0	20 52 51 50 49 48 47 46 45 44 43 42 41 40 39 38 37 36 35 34 33 32 31 30 29 28 27 26 25 24 23 22 21 20 19 18 17 16 15 14 13 12 11 10 9 8 7 6 5 4 3 2 1 0	20 52 51 50 49 48 47 46 45 44 43 42 41 40 39 38 37 36 35 34 33 32 31 30 29 28 27 26 25 24 23 22 21 20 19 18 17 16 15 14 13 12 11 10 9 8 7 6 5 4 3 2 1 0	20 52 51 50 49 48 47 46 45 44 43 42 41 40 39 38 37 36 35 34 33 32 31 30 29 28 27 26 25 24 23 22 21 20 19 18 17 16 15 14 13 12 11 10 9 8 7 6 5 4 3 2 1 0	20 52 51 50 49 48 47 46 45 44 43 42 41 40 39 38 37 36 35 34 33 32 31 30 29 28 27 26 25 24 23 22 21 20 19 18 17 16 15 14 13 12 11 10 9 8 7 6 5 4 3 2 1 0	20 52 51 50 49 48 47 46 45 44 43 42 41 40 39 38 37 36 35 34 33 32 31 30 29 28 27 26 25 24 23 22 21 20 19 18 17 16 15 14 13 12 11 10 9 8 7 6 5 4 3 2 1 0

LiNbO_3 [illegible] LiNbO_3

	20°C	25°C	30°C	35°C	40°C	45°C	50°C	55°C	60°C	65°C	70°C	75°C	80°C	85°C	90°C	95°C	100°C	105°C	110°C	115°C	120°C	125°C	130°C	135°C	140°C	145°C	150°C	155°C	160°C	165°C	170°C	175°C	180°C	185°C	190°C	195°C	200°C	205°C	210°C	215°C	220°C	225°C	230°C	235°C	240°C	245°C	250°C	255°C	260°C	265°C	270°C	275°C	280°C	285°C	290°C	295°C	300°C	305°C	310°C	315°C	320°C	325°C	330°C	335°C	340°C	345°C	350°C	355°C	360°C	365°C	370°C	375°C	380°C	385°C	390°C	395°C	400°C	405°C	410°C	415°C	420°C	425°C	430°C	435°C	440°C	445°C	450°C	455°C	460°C	465°C	470°C	475°C	480°C	485°C	490°C	495°C	500°C	505°C	510°C	515°C	520°C	525°C	530°C	535°C	540°C	545°C	550°C	555°C	560°C	565°C	570°C	575°C	580°C	585°C	590°C	595°C	600°C	605°C	610°C	615°C	620°C	625°C	630°C	635°C	640°C	645°C	650°C	655°C	660°C	665°C	670°C	675°C	680°C	685°C	690°C	695°C	700°C	705°C	710°C	715°C	720°C	725°C	730°C	735°C	740°C	745°C	750°C	755°C	760°C	765°C	770°C	775°C	780°C	785°C	790°C	795°C	800°C	805°C	810°C	815°C	820°C	825°C	830°C	835°C	840°C	845°C	850°C	855°C	860°C	865°C	870°C	875°C	880°C	885°C	890°C	895°C	900°C	905°C	910°C	915°C	920°C	925°C	930°C	935°C	940°C	945°C	950°C	955°C	960°C	965°C	970°C	975°C	980°C	985°C	990°C	995°C	1000°C	1005°C	1010°C	1015°C	1020°C	1025°C	1030°C	1035°C	1040°C	1045°C	1050°C	1055°C	1060°C	1065°C	1070°C	1075°C	1080°C	1085°C	1090°C	1095°C	1100°C	1105°C	1110°C	1115°C	1120°C	1125°C	1130°C	1135°C	1140°C	1145°C	1150°C	1155°C	1160°C	1165°C	1170°C	1175°C	1180°C	1185°C	1190°C	1195°C	1200°C	1205°C	1210°C	1215°C	1220°C	1225°C	1230°C	1235°C	1240°C	1245°C	1250°C	1255°C	1260°C	1265°C	1270°C	1275°C	1280°C	1285°C	1290°C	1295°C	1300°C	1305°C	1310°C	1315°C	1320°C	1325°C	1330°C	1335°C	1340°C	1345°C	1350°C	1355°C	1360°C	1365°C	1370°C	1375°C	1380°C	1385°C	1390°C	1395°C	1400°C	1405°C	1410°C	1415°C	1420°C	1425°C	1430°C	1435°C	1440°C	1445°C	1450°C	1455°C	1460°C	1465°C	1470°C	1475°C	1480°C	1485°C	1490°C	1495°C	1500°C	1505°C	1510°C	1515°C	1520°C	1525°C	1530°C	1535°C	1540°C	1545°C	1550°C	1555°C	1560°C	1565°C	1570°C	1575°C	1580°C	1585°C	1590°C	1595°C	1600°C	1605°C	1610°C	1615°C	1620°C	1625°C	1630°C	1635°C	1640°C	1645°C	1650°C	1655°C	1660°C	1665°C	1670°C	1675°C	1680°C	1685°C	1690°C	1695°C	1700°C	1705°C	1710°C	1715°C	1720°C	1725°C	1730°C	1735°C	1740°C	1745°C	1750°C	1755°C	1760°C	1765°C	1770°C	1775°C	1780°C	1785°C	1790°C	1795°C	1800°C	1805°C	1810°C	1815°C	1820°C	1825°C	1830°C	1835°C	1840°C	1845°C	1850°C	1855°C	1860°C	1865°C	1870°C	1875°C	1880°C	1885°C	1890°C	1895°C	1900°C	1905°C	1910°C	1915°C	1920°C	1925°C	1930°C	1935°C	1940°C	1945°C	1950°C	1955°C	1960°C	1965°C	1970°C	1975°C	1980°C	1985°C	1990°C	1995°C	2000°C	2005°C	2010°C	2015°C	2020°C	2025°C	2030°C	2035°C	2040°C	2045°C	2050°C	2055°C	2060°C	2065°C	2070°C	2075°C	2080°C	2085°C	2090°C	2095°C	2100°C	2105°C	2110°C	2115°C	2120°C	2125°C	2130°C	2135°C	2140°C	2145°C	2150°C	2155°C	2160°C	2165°C	2170°C	2175°C	2180°C	2185°C	2190°C	2195°C	2200°C	2205°C	2210°C	2215°C	2220°C	2225°C	2230°C	2235°C	2240°C	2245°C	2250°C	2255°C	2260°C	2265°C	2270°C	2275°C	2280°C	2285°C	2290°C	2295°C	2300°C	2305°C	2310°C	2315°C	2320°C	2325°C	2330°C	2335°C	2340°C	2345°C	2350°C	2355°C	2360°C	2365°C	2370°C	2375°C	2380°C	2385°C	2390°C	2395°C	2400°C	2405°C	2410°C	2415°C	2420°C	2425°C	2430°C	2435°C	2440°C	2445°C	2450°C	2455°C	2460°C	2465°C	2470°C	2475°C	2480°C	2485°C	2490°C	2495°C	2500°C	2505°C	2510°C	2515°C	2520°C	2525°C	2530°C	2535°C	2540°C	2545°C	2550°C	2555°C	2560°C	2565°C	2570°C	2575°C	2580°C	2585°C	2590°C	2595°C	2600°C	2605°C	2610°C	2615°C	2620°C	2625°C	2630°C	2635°C	2640°C	2645°C	2650°C	2655°C	2660°C	2665°C	2670°C	2675°C	2680°C	2685°C	2690°C	2695°C	2700°C	2705°C	2710°C	2715°C	2720°C	2725°C	2730°C	2735°C	2740°C	2745°C	2750°C	2755°C	2760°C	2765°C	2770°C	2775°C	2780°C	2785°C	2790°C	2795°C	2800°C	2805°C	2810°C	2815°C	2820°C	2825°C	2830°C	2835°C	2840°C	2845°C	2850°C	2855°C	2860°C	2865°C	2870°C	2875°C	2880°C	2885°C	2890°C	2895°C	2900°C	2905°C	2910°C	2915°C	2920°C	2925°C	2930°C	2935°C	2940°C	2945°C	2950°C	2955°C	2960°C	2965°C	2970°C	2975°C	2980°C	2985°C	2990°C	2995°C	3000°C	3005°C	3010°C	3015°C	3020°C	3025°C	3030°C	3035°C	3040°C	3045°C	3050°C	3055°C	3060°C	3065°C	3070°C	3075°C	3080°C	3085°C	3090°C	3095°C	3100°C	3105°C	3110°C	3115°C	3120°C	3125°C	3130°C	3135°C	3140°C	3145°C	3150°C	3155°C	3160°C	3165°C	3170°C	3175°C	3180°C	3185°C	3190°C	3195°C	3200°C	3205°C	3210°C	3215°C	3220°C	3225°C	3230°C	3235°C	3240°C	3245°C	3250°C	3255°C	3260°C	3265°C	3270°C	3275°C	3280°C	3285°C	3290°C	3295°C	3300°C	3305°C	3310°C	3315°C	3320°C	3325°C	3330°C	3335°C	3340°C	3345°C	3350°C	3355°C	3360°C	3365°C	3370°C	3375°C	3380°C	3385°C	3390°C	3395°C	3400°C	3405°C	3410°C	3415°C	3420°C	3425°C	3430°C	3435°C	3440°C	3445°C	3450°C	3455°C	3460°C	3465°C	3470°C	3475°C	3480°C	3485°C	3490°C	3495°C	3500°C	3505°C	3510°C	3515°C	3520°C	3525°C	3530°C	3535°C	3540°C	3545°C	3550°C	3555°C	3560°C	3565°C	3570°C	3575°C	3580°C	3585°C	3590°C	3595°C	3600°C	3605°C	3610°C	3615°C	3620°C	3625°C	3630°C	3635°C	3640°C	3645°C	3650°C	3655°C	3660°C	3665°C	3670°C	3675°C	3680°C	3685°C	3690°C	3695°C	3700°C	3705°C	3710°C	3715°C	3720°C	3725°C	3730°C	3735°C	3740°C	3745°C	3750°C	3755°C	3760°C	3765°C	3770°C	3775°C	3780°C	3785°C	3790°C	3795°C	3800°C	3805°C	3810°C	3815°C	3820°C	3825°C	3830°C	3835°C	3840°C	3845°C	3850°C	3855°C	3860°C	3865°C	3870°C	3875°C	3880°C	3885°C	3890°C	3895°C	3900°C	3905°C	3910°C	3915°C	3920°C	3925°C	3930°C	3935°C	3940°C	3945°C	3950°C	3955°C	3960°C	3965°C	3970°C	3975°C	3980°C	3985°C	3990°C	3995°C	4000°C	4005°C	4010°C	4015°C	4020°C	4025°C	4030°C	4035°C	4040°C	4045°C	4050°C	4055°C	4060°C	4065°C	4070°C	4075°C	4080°C	4085°C	4090°C	4095°C	4100°C	4105°C	4110°C	4115°C	4120°C	4125°C	4130°C	4135°C	4140°C	4145°C	4150°C	4155°C	4160°C	4165°C	4170°C	4175°C	4180°C	4185°C	4190°C	4195°C	4200°C	4205°C	4210°C	4215°C	4220°C	4225°C	4230°C	4235°C	4240°C	4245°C	4250°C	4255°C	4260°C	4265°C	4270°C	4275°C	4280°C	4285°C	4290°C	4295°C	4300°C	4305°C	4310°C	4315°C	4320°C	4325°C	4330°C	4335°C	4340°C	4345°C	4350°C	4355°C	4360°C	4365°C	4370°C	4375°C	4380°C	4385°C	4390°C	4395°C	4400°C	4405°C	4410°C	4415°C	4420°C	4425°C	4430°C	4435°C	4440°C	4445°C	4450°C	4455°C	4460°C	4465°C	4470°C	4475°C	4480°C	4485°C	4490°C	4495°C	4500°C	4505°C	4510°C	4515°C	4520°C	4525°C	4530°C	4535°C	4540°C	4545°C	4550°C	4555°C	4560°C	4565°C	4570°C	4575°C	4580°C	4585°C	4590°C	4595°C	4600°C	4605°C	4610°C	4615°C	4620°C	4625°C	4630°C	4635°C	4640°C	4645°C	4650°C	4655°C	4660°C	4665°C	4670°C	4675°C	4680°C	4685°C	4690°C	4695°C	4700°C	4705°C	4710°C	4715°C	4720°C	4725°C	4730°C	4735°C	4740°C	4745°C	4750°C	4755°C	4760°C	4765°C	4770°C	4775°C	4780°C	4785°C	4790°C	4795°C	4800°C	4805°C	4810°C	4815°C	4820°C	4825°C	4830°C	4835°C	4840°C	4845°C	4850°C	4855°C	4860°C	4865°C	4870°C	4875°C	4880°C	4885°C	4890°C	4895°C	4900°C	4905°C	4910°C	4915°C	4920°C	4925°C	4930°C	4935°C	4940°C	4945°C	4950°C	4955°C	4960°C	4965°C	4970°C	4975°C	4980°C	4985°C	4990°C	4995°C	5000°C	5005°C	5010°C	5015°C	5020°C	5025°C	5030°C	5035°C	5040°C	5045°C	5050°C	5055°C	5060°C	5065°C	5070°C	5075°C	5080°C	5085°C	5090°C	5095°C	5100°C	5105°C	5110°C	5115°C	5120°C	5125°C	5130°C	5135°C	5140°C	5145°C	5150°C	5155°C	5160°C	5165°C	5170°C	5175°C	5180°C	5185°C	5190°C	5195°C	5200°C	5205°C	5210°C	5215°C	5220°C	5225°C	5230°C	5235°C	5240°C	5245°C	5250°C	5255°C	5260°C	5265°C	5270°C	5275°C	5280°C	5285°C	5290°C	5295°C	5300°C	5305°C	5310°C	5315°C	5320°C	5325°C	5330°C	5335°C	5340°C	5345°C	5350°C	5355°C	5360°C	5365°C	5370°C	5375°C	5380°C	5385°C	5390°C	5395°C	5400°C	5405°C	5410°C	5415°C	5420°C	5425°C	5430°C	5435°C	5440°C	5445°C	5450°C	5455°C	5460°C	5465°C	5470°C	5475°C	5480°C	5485°C	5490°C	5495°C	5500°C	5505°C	5510°C	5515°C	5520°C	5525°C	5530°C	5535°C	5540°C	5545°C	5550°C	5555°C	5560°C	5565°C	5570°C	5575°C	5580°C	5585°C	5590°C	5595°C	5600°C	5605°C	5610°C	5615°C	5620°C	5625°C	5630°C	5635°C	5640°C	5645°C	5650°C	5655°C	5660°C	5665°C	5670°C	5675°C	5680°C	5685°C	5690°C	5695°C	5700°C	5705°C	5710°C	5715°C	5720°C	5725°C	5730°C	5735°C	5740°C	5745°C	5750°C	5755°C	5760°C	5765°C	5770°C	5775°C	5780°C	5785°C	5790°C	5795°C	5800°C	5805°C	5810°C	5815°C	5820°C	5825°C	5830°C	5835°C	5840°C	5845°C	5850°C	5855°C	5860°C	5865°C	5870°C	5875°C	5880°C	5885°C	5890°C	5895°C	5900°C	5905°C	5910°C	5915°C	5920°C	5925°C	5930°C	5935°C	5940°C	5945°C	5950°C	5955°C	5960°C	5965°C	5970°C	5975°C	5980°C	5985°C	5990°C	5995°C	6000°C	6005°C	6010°C	6015°C	6020°C	6025°C	6030°C	6035°C	6040°C	6045°C	6050°C	6055°C	6060°C	6065°C	6070°C	6075°C	6080°C	6085°C	6090°C	6095°C	6100°C	6105°C	6110°C	6115°C	6120°C	6125°C	6130°C	6135°C	6140°C	6145°C	6150°C	6155°C	6160°C	6165°C	6170°C	6175°C	6180°C	6185°C	6190°C	6195°C	6200°C	6205°C	6210°C	6215°C	6220°C	6225°C	6230°C	6235°C	6240°C	6245°C	6250°C	6255°C	6260°C	6265°C	6270°C	6275°C	6280°C	6285°C	6290°C	6295°C	6300°C	6305°C	6310°C</
--	------	------	------	------	------	------	------	------	------	------	------	------	------	------	------	------	-------	-------	-------	-------	-------	-------	-------	-------	-------	-------	-------	-------	-------	-------	-------	-------	-------	-------	-------	-------	-------	-------	-------	-------	-------	-------	-------	-------	-------	-------	-------	-------	-------	-------	-------	-------	-------	-------	-------	-------	-------	-------	-------	-------	-------	-------	-------	-------	-------	-------	-------	-------	-------	-------	-------	-------	-------	-------	-------	-------	-------	-------	-------	-------	-------	-------	-------	-------	-------	-------	-------	-------	-------	-------	-------	-------	-------	-------	-------	-------	-------	-------	-------	-------	-------	-------	-------	-------	-------	-------	-------	-------	-------	-------	-------	-------	-------	-------	-------	-------	-------	-------	-------	-------	-------	-------	-------	-------	-------	-------	-------	-------	-------	-------	-------	-------	-------	-------	-------	-------	-------	-------	-------	-------	-------	-------	-------	-------	-------	-------	-------	-------	-------	-------	-------	-------	-------	-------	-------	-------	-------	-------	-------	-------	-------	-------	-------	-------	-------	-------	-------	-------	-------	-------	-------	-------	-------	-------	-------	-------	-------	-------	-------	-------	-------	-------	-------	-------	-------	-------	-------	-------	-------	-------	-------	-------	-------	-------	-------	-------	--------	--------	--------	--------	--------	--------	--------	--------	--------	--------	--------	--------	--------	--------	--------	--------	--------	--------	--------	--------	--------	--------	--------	--------	--------	--------	--------	--------	--------	--------	--------	--------	--------	--------	--------	--------	--------	--------	--------	--------	--------	--------	--------	--------	--------	--------	--------	--------	--------	--------	--------	--------	--------	--------	--------	--------	--------	--------	--------	--------	--------	--------	--------	--------	--------	--------	--------	--------	--------	--------	--------	--------	--------	--------	--------	--------	--------	--------	--------	--------	--------	--------	--------	--------	--------	--------	--------	--------	--------	--------	--------	--------	--------	--------	--------	--------	--------	--------	--------	--------	--------	--------	--------	--------	--------	--------	--------	--------	--------	--------	--------	--------	--------	--------	--------	--------	--------	--------	--------	--------	--------	--------	--------	--------	--------	--------	--------	--------	--------	--------	--------	--------	--------	--------	--------	--------	--------	--------	--------	--------	--------	--------	--------	--------	--------	--------	--------	--------	--------	--------	--------	--------	--------	--------	--------	--------	--------	--------	--------	--------	--------	--------	--------	--------	--------	--------	--------	--------	--------	--------	--------	--------	--------	--------	--------	--------	--------	--------	--------	--------	--------	--------	--------	--------	--------	--------	--------	--------	--------	--------	--------	--------	--------	--------	--------	--------	--------	--------	--------	--------	--------	--------	--------	--------	--------	--------	--------	--------	--------	--------	--------	--------	--------	--------	--------	--------	--------	--------	--------	--------	--------	--------	--------	--------	--------	--------	--------	--------	--------	--------	--------	--------	--------	--------	--------	--------	--------	--------	--------	--------	--------	--------	--------	--------	--------	--------	--------	--------	--------	--------	--------	--------	--------	--------	--------	--------	--------	--------	--------	--------	--------	--------	--------	--------	--------	--------	--------	--------	--------	--------	--------	--------	--------	--------	--------	--------	--------	--------	--------	--------	--------	--------	--------	--------	--------	--------	--------	--------	--------	--------	--------	--------	--------	--------	--------	--------	--------	--------	--------	--------	--------	--------	--------	--------	--------	--------	--------	--------	--------	--------	--------	--------	--------	--------	--------	--------	--------	--------	--------	--------	--------	--------	--------	--------	--------	--------	--------	--------	--------	--------	--------	--------	--------	--------	--------	--------	--------	--------	--------	--------	--------	--------	--------	--------	--------	--------	--------	--------	--------	--------	--------	--------	--------	--------	--------	--------	--------	--------	--------	--------	--------	--------	--------	--------	--------	--------	--------	--------	--------	--------	--------	--------	--------	--------	--------	--------	--------	--------	--------	--------	--------	--------	--------	--------	--------	--------	--------	--------	--------	--------	--------	--------	--------	--------	--------	--------	--------	--------	--------	--------	--------	--------	--------	--------	--------	--------	--------	--------	--------	--------	--------	--------	--------	--------	--------	--------	--------	--------	--------	--------	--------	--------	--------	--------	--------	--------	--------	--------	--------	--------	--------	--------	--------	--------	--------	--------	--------	--------	--------	--------	--------	--------	--------	--------	--------	--------	--------	--------	--------	--------	--------	--------	--------	--------	--------	--------	--------	--------	--------	--------	--------	--------	--------	--------	--------	--------	--------	--------	--------	--------	--------	--------	--------	--------	--------	--------	--------	--------	--------	--------	--------	--------	--------	--------	--------	--------	--------	--------	--------	--------	--------	--------	--------	--------	--------	--------	--------	--------	--------	--------	--------	--------	--------	--------	--------	--------	--------	--------	--------	--------	--------	--------	--------	--------	--------	--------	--------	--------	--------	--------	--------	--------	--------	--------	--------	--------	--------	--------	--------	--------	--------	--------	--------	--------	--------	--------	--------	--------	--------	--------	--------	--------	--------	--------	--------	--------	--------	--------	--------	--------	--------	--------	--------	--------	--------	--------	--------	--------	--------	--------	--------	--------	--------	--------	--------	--------	--------	--------	--------	--------	--------	--------	--------	--------	--------	--------	--------	--------	--------	--------	--------	--------	--------	--------	--------	--------	--------	--------	--------	--------	--------	--------	--------	--------	--------	--------	--------	--------	--------	--------	--------	--------	--------	--------	--------	--------	--------	--------	--------	--------	--------	--------	--------	--------	--------	--------	--------	--------	--------	--------	--------	--------	--------	--------	--------	--------	--------	--------	--------	--------	--------	--------	--------	--------	--------	--------	--------	--------	--------	--------	--------	--------	--------	--------	--------	--------	--------	--------	--------	--------	--------	--------	--------	--------	--------	--------	--------	--------	--------	--------	--------	--------	--------	--------	--------	--------	--------	--------	--------	--------	--------	--------	--------	--------	--------	--------	--------	--------	--------	--------	--------	--------	--------	--------	--------	--------	--------	--------	--------	--------	--------	--------	--------	--------	--------	--------	--------	--------	--------	--------	--------	--------	--------	--------	--------	--------	--------	--------	--------	--------	--------	--------	--------	--------	--------	--------	--------	--------	--------	--------	--------	--------	--------	--------	--------	--------	--------	--------	--------	--------	--------	--------	--------	--------	--------	--------	--------	--------	--------	--------	--------	--------	--------	--------	--------	--------	--------	--------	--------	--------	--------	--------	--------	--------	--------	--------	--------	--------	--------	--------	--------	--------	--------	--------	--------	--------	--------	--------	--------	--------	--------	--------	--------	--------	--------	--------	--------	--------	--------	--------	--------	--------	--------	--------	--------	--------	--------	--------	--------	--------	--------	--------	--------	--------	--------	--------	--------	--------	--------	--------	--------	--------	--------	--------	--------	--------	--------	--------	--------	--------	--------	--------	--------	--------	--------	--------	--------	--------	--------	--------	--------	--------	--------	--------	--------	--------	--------	--------	--------	--------	--------	--------	--------	--------	--------	--------	--------	--------	--------	--------	--------	--------	--------	--------	--------	--------	--------	--------	--------	--------	--------	--------	--------	--------	--------	--------	--------	--------	--------	--------	--------	--------	--------	--------	--------	--------	--------	--------	--------	--------	--------	--------	--------	--------	--------	--------	--------	--------	--------	--------	--------	--------	--------	--------	--------	--------	--------	--------	--------	--------	--------	--------	--------	--------	--------	--------	--------	--------	--------	--------	--------	--------	--------	--------	--------	--------	--------	--------	--------	--------	--------	--------	--------	--------	--------	--------	--------	--------	--------	--------	--------	--------	--------	--------	--------	--------	--------	--------	--------	--------	--------	--------	--------	--------	--------	--------	--------	--------	--------	--------	--------	--------	--------	--------	--------	--------	--------	--------	--------	--------	--------	--------	--------	--------	--------	--------	--------	--------	--------	--------	--------	--------	--------	--------	--------	--------	--------	--------	--------	--------	--------	--------	--------	--------	--------	--------	--------	--------	--------	--------	--------	--------	--------	--------	--------	--------	--------	--------	--------	--------	--------	--------	--------	--------	--------	--------	--------	--------	--------	--------	--------	--------	--------	--------	--------	--------	--------	--------	--------	--------	--------	--------	--------	--------	--------	--------	--------	--------	--------	--------	--------	--------	--------	--------	--------	--------	--------	--------	--------	--------	--------	--------	--------	--------	--------	--------	--------	--------	--------	--------	--------	--------	--------	--------	--------	--------	--------	--------	--------	--------	--------	--------	--------	--------	--------	--------	--------	--------	--------	--------	--------	--------	----------



Netplanes and cuts parallel to the X axis

LiNbO_3

$\text{CuK}\alpha_1$ radiation

NEW METHOD TO SAW QUARTZ SLIDES

H. MERIGOUX, J.F. DARCES, J. LAMBOLEY

Laboratoire de Cristallographie - Université de Franche-Comté
Route de Gray, 25030 BESANCON CEDEX - FRANCE

SUMMARY

To cut a slide in a quartz block, whether synthetic or natural, the block's orientation at the moment it is attached to the sawing table must first be known.

With the presently proposed method, the quartz block is placed directly on the saw. A particular reference surface is not delimited, but the slide's angular position with respect to both the saw and the crystal lattice is determined.

This method is applicable if orientation of the two preliminary slides can be determined. The orientation measurement is made by X ray diffraction. From the values obtained this way, the angular positions which will give the expected slide orientation are calculated. Rotation calculation principles needed for sawing are based on the possibility of positioning, in the crystal system, the goniometric device axis which remains fixed with respect to the block.

Results are given for several doubly rotated cuts.

Key-words

Crystal sawing methods, quartz slides, orientation measurements, X-ray goniometry, doubly rotated cuts.

INTRODUCTION

When cutting a quartz slide with a specific orientation the spatial geometry of the quartz must be taken into consideration. To overcome this spatial geometry problem when cutting a quartz slide with a predetermined orientation a series of operations must be done to position the quartz in front of the saw. GORDON and al. (1943)(1) have suggested rather complex solutions.

Once a block without any optical twinning has been selected the reference surfaces are defined: the X and Z cuts are checked by X-ray diffraction. The + and - direction of the electrical axis of the observed block is determined. These preliminary operations are facilitated if a cultured instead of a natural quartz is used. However, the highly accurate checking of the X and Z faces is not eliminated. Then, once the position of the quartz axis system is known, the block is set on the saw table so that the crystal axis system coincides with that of the goniometric device axis. Now, the angular positions to be displayed on the saw

graduations for the required cut can be calculated. W.L. BOND and al. (1977) (2). If an X-ray goniometer is available to measure the blank of any orientation, J.F. DARCES and al. (1978) (3), a more direct method can be used. Instead of having to prepare the reference faces before setting the block on the goniometric saw device the block that is free of optical twinning is put directly onto the saw table.

The block can be of almost any shape and is glued onto a glass plate which is firmly attached to the goniometric device. Two slides are then cut and the angular position of the saw is read off for each cut. These two slides are then used as reference surfaces. Their orientations are measured and then the two angular positions to be displayed on the saw graduations to obtain the required cut are calculated.

Basically the principles of these two methods are the same, but instead of using common reference planes two general ones were chosen. The advantage of this will be shown later.

DESCRIPTION OF APPARATUS

To follow the calculations required for cutting we will begin by defining the three axis systems and the effect of the two rotation movements that have to be used.

1 - AXIS SYSTEMS

- OXYZ saw axis system
- O_{xyz} goniometric device axis system
- a,b,c crystal axis system

To illustrate this presentation we have shown photos of the laboratory saw that was used to develop this method.

- OXYZ axis system (saw coordinates)

This is attached to the saw frame. The OZ axis is vertical and corresponds to the rotation axis on the goniometric device on which the crystal is fixed. The OY axis coincides with the saw cutting disk rotation axis. This OX axis is perpendicular to the OZ and OY axes.

Whatever the crystal position on the saw table may be later, the sawing plane is always XOZ. This means that when an (yxw) ϕ/θ cut is made the geometric perpendicular to the slide N_g is the OY direction. (Figure 1).



Figure 1

OXYZ axis system (saw coordinates).

- Oxyz axis system

This is attached to the goniometric device. The crystal is fixed to this axis system. The Ox direction is parallel to the goniometric device horizontal rotation axis. Then using this Oy and Oz are defined as the directions which are parallel to the OY and OZ directions when all the goniometric device graduations are on zero. (Figure 2).

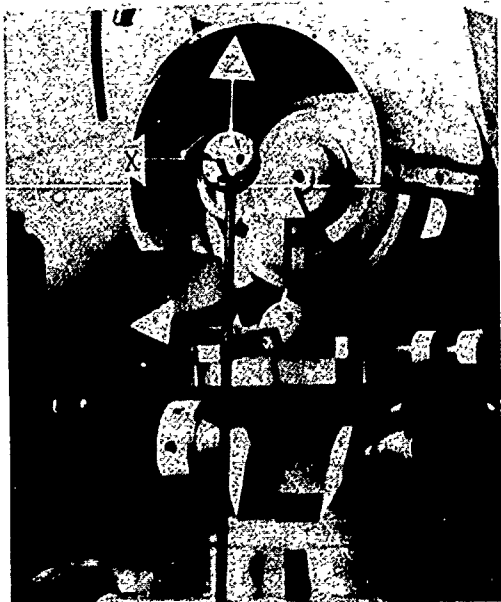


Figure 2

Oxyz and OXYZ axis systems.

- $\vec{a}, \vec{b}, \vec{c}$ axis system (crystal coordinates)

This is a crystal axis system that is fixed in the former axis system. This can be in any position in relation to this Oxyz axis system. This method is very different from the classical methods where the crystal axis system is the axis system defined by the IRE convention i.e. the electrical, mechanical and optical axes. Before sawing, these three orthogonal axis systems are superimposed. With the present method there is no need to use the IRE convention axis system and the $\vec{a}, \vec{b}, \vec{c}$ cell axis system, which is closer to the diffraction phenomenon, is easier to handle.

2. THE EFFECTS OF THE ROTATION MOVEMENT OF THE GONIOMETRIC HEAD

The origins on the saw graduations are defined when the Oxyz axes are parallel to OXYZ. Sawing, we can obtain any N_{g_i} direction after two rotations:

one round the vertical OZ axis, the other round the horizontal Ox axis.

After the first rotation round the OZ axis, the Ox direction is on the Ox_i direction, and after the second rotation round the Ox_i axis, the Oz direction is on the Oz_i direction. The displayed angles on the goniometric device are r_{x_i} and r_{z_i} .

N_{g_i} is given by r_{x_i}, r_{z_i} .

With this geometrical situation, the rotation order is of no importance because the Ox axis is carried by the rotation round the other, i.e. OZ axis. If we measure this slide orientation of an X-ray goniometer, the same N_{g_i} cut is defined by

the goniometer graduations, r_{x_i} and r_{z_i} , and by its crystal axis system coordinates: y_{i1}, y_{i2}, y_{i3} .

- Going from one slide to another which is differently orientated.

Let N_{g_i} and N_{g_j} be two different orientated cuts. If N_{g_i} is obtained with r_{x_i} and r_{z_i} and N_{g_j} with r_{x_j} and r_{z_j} we go from one to the other by the angular variation:

$$r_x = r_{x_j} - r_{x_i}$$

$$r_z = r_{z_j} - r_{z_i}$$

r_x and r_z mean only a position variation on the saw graduations, i.e. we go from N_{g_i} to N_{g_j} with rotations round the Ox and OZ axes of r_x and r_z amplitudes.

- Particular function of the Ox axis

Between the quartz crystal and the saw, the goniometric device acts as Hooke's coupling. A part of the goniometric device is part of the saw and the other part is attached to the crystal. The horizontal Ox axis is a direction bound to the saw but motionless in the crystal. It is used to define the required cuts in the crystal space.

Remark : According to the saw type, this axis may be in a vertical position. This is not of importance for the principle calculations.

CALCULATIONS REQUIRED FOR SAWING

N_{g_i} and N_{g_j} : two slides which are obtained without rotation round the horizontal Ox axis and which only rotate round the vertical OZ axis. Consequently $r_{x_1} = r_{x_2}$ and the slides are situated in the plane which is perpendicular to OZ. We can express \vec{Ox} in terms of \vec{N}_{g_1} and \vec{N}_{g_2} by the following relation :

$$\vec{Ox} = p \vec{N}_{g_1} + q \vec{N}_{g_2}$$

p and q are such that $|\vec{Ox}| = 1$.

To know the Ox orientation in the crystal space, p and q are calculated. The $(\vec{Ox}, \vec{N}_{g_1})$ and $(\vec{Ox}, \vec{N}_{g_2})$ angles can be defined either from reading on the saw graduations, or from scalar products.

- By reading

The $(\vec{Ox}, \vec{N}_{g_1})$ angle is equal to the (\vec{Ox}, \vec{OY}) angle when the N_{g_1} blank is cut. (Figure 3)

We have :

$$(\vec{Ox}, \vec{N}_{g_1}) = \frac{\pi}{2} - r_{Z_1}$$

and

$$(\vec{Ox}, \vec{N}_{g_2}) = \frac{\pi}{2} - r_{Z_2}$$

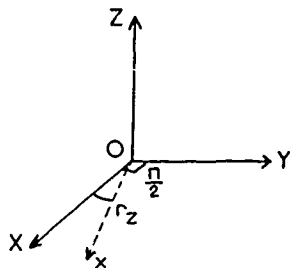


Figure 3

- From scalar products

$$\vec{Ox} \cdot \vec{N}_{g_1} = |\vec{N}_{g_1}| |1| \cos(\vec{Ox}, \vec{N}_{g_1}) = N_{g_1} \sin r_{Z_1}$$

$$\vec{Ox} \cdot \vec{N}_{g_2} = |\vec{N}_{g_2}| |1| \cos(\vec{Ox}, \vec{N}_{g_2}) = N_{g_2} \sin r_{Z_2}$$

$$\begin{aligned} \text{but } \vec{Ox} \cdot \vec{N}_{g_1} &= (p \vec{N}_{g_1} + q \vec{N}_{g_2}) \cdot \vec{N}_{g_1} \\ &= p \vec{N}_{g_1}^2 + q \vec{N}_{g_1} \cdot \vec{N}_{g_2} \end{aligned}$$

$$\text{and } \vec{Ox} \cdot \vec{N}_{g_2} = p \vec{N}_{g_1} \cdot \vec{N}_{g_2} + q \vec{N}_{g_2}^2$$

$$\text{Let } |\vec{N}_{g_1}| = M_1$$

$$|\vec{N}_{g_2}| = M_2$$

$$\vec{N}_{g_1} \cdot \vec{N}_{g_2} = M$$

There are two unknowns p and q in two equation system which must be solved.

$$pM_1^2 + qM = M_1 \sin r_{Z_1}$$

$$pM + qM_2^2 = M_2 \sin r_{Z_2}$$

Once p and q are known, the Ox direction is defined in the crystal space by the following numbers :

$$h_x = py_{11} + qy_{21}$$

$$k_x = py_{12} + qy_{22}$$

$$l_x = py_{13} + qy_{23}$$

Remark I : It is possible that, because of the crystal symmetry, we do not use the same axis system for the two N_{g_1} and

N_{g_2} slides when calculating their

orientation. The previous condition have to be checked to see that the calculated angle for these two directions is really equal to the r_z angle which is the rotation angle round the vertical axis. If this is not so, we have to change the axis sign for one of the measures.

Remark II : To calculate the Ox position in the crystal, it is possible to define the two cuts N_{g_1} and N_{g_2} differently,

particularly with a rotation round the Ox axis. The solution which is suggested here corresponds to the simplest calculations.

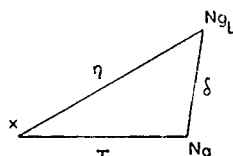
ROTATIONS TO BE DISPLAYED

We want to obtain a N_g blank that will be defined $(\gamma\omega\lambda)\phi/\theta$ using the IRE conventions. In the $\vec{a}, \vec{b}, \vec{c}$ crystal axis system, this direction corresponds to the y_1, y_2, y_3 numbers. Let the last measured slide N_{g_L} be one of the slides which are used to define the Ox direction. We must find the r_x and r_z rotation values which will change N_{g_L} to N_g .

In the crystal space, three directions are known.

- The \vec{N}_g direction is the expected direction
- The \vec{N}_{g_L} direction, the last measured direction
- The \vec{Ox} direction, defined from calculations.

These three directions define a spherical triangle. From the scalar products, we calculate the three following angles :

$$\begin{aligned}\tau &= (\vec{Ox}, \vec{N}_g) \\ \delta &= (\vec{N}_g, \vec{N}_{g_L}) \\ \eta &= (\vec{Ox}, \vec{N}_{g_L})\end{aligned}$$


When turning round the Ox and Oz axes, this triangle turns without distorting. Taking into consideration how the apexes shift, we can see that the r_x and r_z angle calculations are very simple. When the goniometric device moves, the OY axis does not move, defining the cutting plane, and the Ox axis stays in an horizontal plane which is perpendicular to OZ . When cutting from N_{g_L} to N_g , the spherical triangles moves in space. (Fig. 4.)

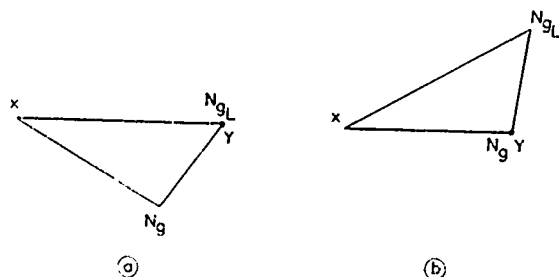


Figure 4.

For the first blank, N_{g_L} coincides with Y

(Figure 4a) for the second blank, N_g coincides again with Y (Figure 4b). Ox remains in the horizontal plane. The N_g cut is deduced from the N_{g_L} cut by the r_x and r_z angles. By developing the two possible cases, we can see that the rotation order is of no importance.

- First rotation round Ox (Figure 5)

When the N_{g_L} slide is cut, the xY arc is equal to η (figure 5a). We turn round the Ox axis to keep N_{g_L} in the horizontal plane (figure 5b). The r_x angle around which we turned is the $(N_g \times N_{g_L})$ angle of the spherical triangle. From this position, we turn the goniometric head around the OZ axis of an angle $r_z = \eta - \tau$ to bring N_g on Y (figure 5c). Then, the saw is in right position to cut the expected blank.

All these movements are summarized (figure 5d) by the spherical triangle $x N_g S$.

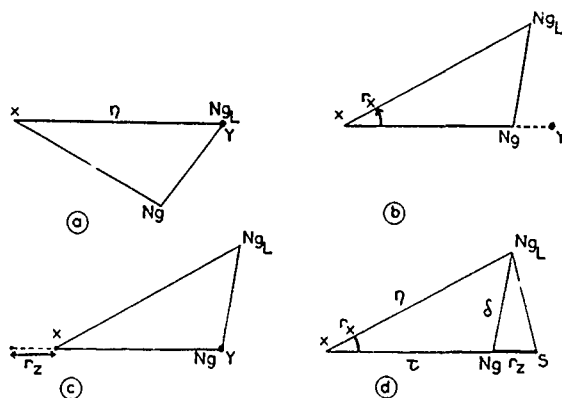


Figure 5.

- First rotation round OZ (figure 6)

The same starting position is described in figure 6a. The rotation around the OZ axis maintains x and N_{g_L} in the horizontal plane, N_{g_L} goes to S (figure 6b). The second rotation round Ox sets N_g on Y (figure 6c). The movements are summarized in figure 6d. We can see there the same spherical triangle as in figure 5d. Both ways are equivalent.

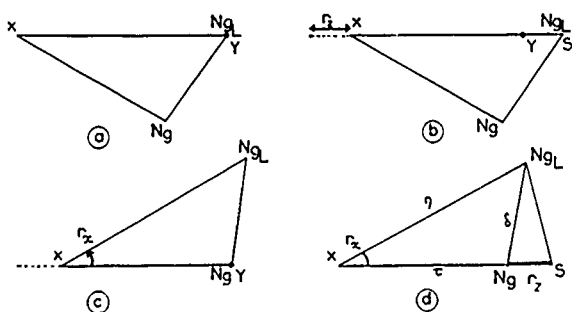


Figure 6

The angle of the x apex is the required r_x angle. When solving the T spherical triangle the r_x angle is given by :

$$\cos r_x = \frac{\cos \delta - \cos \tau \cos \eta}{\sin \tau \sin \eta}$$

the r_x sign is the same as that of the Ox , N_g , N_{g_L} axis system.

The arc $N_g S$ equal to the expected r_z angle is

$$r_z = \eta - \tau$$

Results are given for doubly rotated cuts in table I, II, III. These cuts are arbitrary cuts without applications.

The r_x and r_z angular positions displayed are in fact the sum of the displayed angles with the N_{g_L} cut and the calculated values by spherical trigonometry.

SAWING ACCURACY

- First the effects of errors during the orientation measurements giving r_x and r_z are calculated.

- Then an ϵ angle divergence between the expected slide and the obtained one is determined when all the possible errors have been taken into account.

Finally by finding the right position of the crystal on the table the divergence ϵ can be reduced.

- Calculation of Δr_x and Δr_z

Mismeasurements of the orientation of the two preliminary slides N_{g_1} and N_{g_2} modify the position of Ox in space. An analytical determination of these effects is difficult. The result are obtained by spherical trigonometry. But a computerized method taking into account all the possible errors provides the numerical value of the dr_x and dr_z errors on r_x and r_z . If the misread errors are added we obtain Δr_x and Δr_z which represent the total error on r_x and r_z .

- Calculation of the ϵ divergence

From Δr_x and Δr_z we now obtain the ϵ divergence between the expected orientation and the obtained one.

Suppose that E is a spherical triangle (figure 7) with the apexes x, $N_{g \text{ exp}}$, $N_{g \text{ obt}}$.

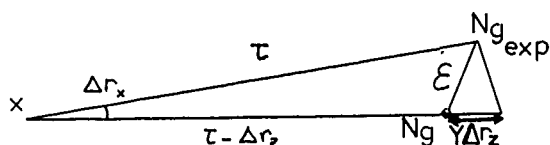


Figure 7

The obtained quartz slide N_g is on the Y axis. ϵ is the arc ($N_{g \text{ exp}}$, $N_{g \text{ obt}}$). As the T triangle has just been solved and then using E, ϵ can be calculated from Δr_x and Δr_z .

The E and T spherical triangles are almost similar, but now the unknown value is ϵ instead of r_x and r_z .

- Best crystal position

When the spherical triangle T is solved the choice of the last preliminary slide N_g may have an influence on the magnitude of the orientation accuracy.

Effect on dr_x :

When the differential is written as

$$dr_x = \frac{\partial r_x}{\partial \delta} d\delta + \frac{\partial r_x}{\partial \tau} d\tau + \frac{\partial r_x}{\partial \eta} d\eta$$

then if δ is small we only have :

$$dr_x = \frac{d\delta}{\sin \tau}$$

where dr_x is a minimum value if τ equals $\pi/2$.

and δ the (N_{g_i} , N_g) arc.

N_g is the expected orientation without errors, the uncertainty of δ is only linked to the mis-orientation Δm of the last slide N_{g_L} .

Thus if δ is small and τ near $\pi/2$, dr_x is close to Δm in the upper values.

Effect on dr_z :

r_z is equal to $\eta - \tau$ and under the former condition the spherical triangle T is quite flat and the position of Ox does not change the difference between η and τ . The errors can only come from the position of N_g and N_{g_L} . In the same way,

dr_z is equal to Δm .

The highest accuracy is obtained if the quartz block is placed on the table in such a position that the expected slide is almost parallel to the Ox direction, which is the direction of the goniometric table axis attached to the crystal (condition $\tau = \pi/2$).

As well it is useful to select one of the two preliminary slides close to the expected cut (δ small condition).

Naturally, after checking the expected cut, the δ small condition is convenient. If the first cut is not the correct one, we may use the values of this slide in the Ox calculation, instead of N_{g_L} . The accuracy is improved as shown in table III.

The differences between this method and a classical one is in the quartz block preparation, and in the saw correction when the cut is not the expected one.

When a classical method is used, great attention must be paid to all details before sawing. Two very simple planes in relation to the crystal space, are prepared by successive mechanical adjustments and X ray controls, then the block is fixed and glued. On the saw table, if the first blank is not exactly the expected one by trial and errors we correct the readings on the two rotation axis using our method. The quartz block is placed on the saw table so as to put the expected cut nearly parallel to the horizontal axis of the goniometric device. After the quartz is attached, two preliminary slides are sawn and their orientation measured. The angular positions to be displayed are calculated.

If the first slide is not exactly the expected one, the angular positions are recalculated, using now, instead of the preliminary slide, the first cut. This method directly gives the corrections in sized and signs.

CONCLUSION

This method provides considerable economy, greatly reduces waste when cutting and eliminates unnecessary tooling. It is most suitable when a set of different θ, ϕ slides is needed for research purposes. At the present time a model is being developed for industrial use.

ACKNOWLEDGEMENTS

We would like to express our thanks to the D.R.E.T. (Direction des Recherches, Etudes et Techniques) of the Ministry of Defense who sponsored this research.

REFERENCES

- 1 - W. PARRISH and S.G. GORDON - Precise angular control of quartz cutting by X-rays. Am. Miner. 30, 326, 1945.
- 2 - W.L. BOND and J.A. KUSTERS - Making doubly rotated quartz plates. Proc. of the 31st Annual Symposium on Frequency Control, 153, 1977.
- 3 - J.F. DARCES and H. MERIGOUX - Final X-ray control of the orientation of round or rectangular quartz slides for industrial purposes. Proc. of the 32nd Annual Symposium on Frequency Control, 304, 1978.

REQUIRED CUT $\phi = 9.50$ $\theta = -30.00$

		ANGULAR POSITIONS DISPLAYED		MEASURED ORIENTATION		
		N°	r_x	r_z	ϕ	θ
PRELIMINARY CUTS		1	28.50	-7.50	9.42	-31.29
		2	28,50	26.00	-29,57	-28.54
OBTAINED CUTS	Computed from N° 1	3	27,21	-7.69	9,49	-30,02
	Divergence		$(\vec{N}_{g_{obt}}, \vec{N}_{g_{req}}) = 0,02$		$\Delta \phi = 0.01$	$\Delta \theta = 0,02$

TABLE N° I

REQUIRED CUT $\phi = 0.00$ $\theta = 78.05$

		ANGULAR POSITIONS DISPLAYED		MEASURED ORIENTATION		
		N°	r_x	r_z	ϕ	θ
PRELIMINARY CUTS		1	0.00	-26,00	7.64	- 64.95
		2	0.00	26.00	7,07	62.61
OBTAINED CUTS	Computed from N° 2	3	-3.55	10,78	0.17	78.00
	Divergence		$(\vec{N}_{g_{obt}}, \vec{N}_{g_{req}}) = 0,06$		$\Delta \phi = 0.17$	$\Delta \theta = 0.05$

TABLE N° II

REQUIRED CUT $\phi = 9,92$ $\theta = 72,35$

			ANGULAR POSITIONS DISPLAYED		MEASURED ORIENTATION	
		N°	r_x °	r_z °	ϕ °	θ °
PRELIMINARY CUTS		1	0,00	-26,00	7.64	- 64.95
		2	0,00	26.00	7.07	62.61
OBTAINED CUTS	Computed from N° 2	3	-6,70	16.19	10.17	72.21
	Divergence		$(\vec{R}_{g_{obt}}, \vec{R}_{g_{req}}) = 0.16$		$\Delta \phi = 0.25$	$\Delta \theta = 0.14$
	Computed from N° 3	4	-6.59	16,20	9.74	72,32
	Divergence		$(\vec{R}_{g_{obt}}, \vec{R}_{g_{req}}) = 0.06$		$\Delta \phi = 0.17$	$\Delta \theta = 0.03$

TABLE N° III

HIGHLY PRECISE MEASUREMENT OF ORIENTATION ANGLE FOR CRYSTAL BLANKS

N.Asanuma and J.Asahara

Toyo Communication Equipment Co., Ltd.

SUMMARY

The relationship between the measurement error produced when measuring the orientation angle of a crystal blank and the various factors affecting this measurement error have been systematically clarified. For example, the main factors in the measurement error of an AT-cut crystal, which has the tightest angle tolerance of any crystal unit, today, has been found by analyzing the "reference surface angle of lumbered quartz", "XX' angle of the crystal blank", "plate rotation angle", and "reproducibility of angle reading of the micrometer". Reliable, stable manufacture of crystal blanks that require tight angle of cut tolerance is first made possible by incorporating the results of these analyses into the quality control standards of crystal blank manufacturing process.

The reference angle, which is the angle formed by the optical axis and atomic plane (01.1) of synthetic quartz, has been measured as $38^{\circ} 12' 39'' \pm 0.5''$. This value is extremely stable without regard to the Q of the synthetic quartz itself, and shows that use as a standard reference angle is possible.

Key words

Angular Deviation, Equivalent Angle Factor, Geometry, Lumbered Reference Surface, Optical Alignment, Reference Surface Angle, Crystal Blank.

INTRODUCTION

Of all the factors affecting the quality of a crystal unit, the angle of cut of the crystal blank with respect to the crystallographic axes is the most important in deciding the frequency-temperature characteristic (F/t characteristic) and frequency warm-up characteristic specifications of the crystal unit. Increased demand for communications in recent years has been accompanied by a narrowing of the frequency bandwidth of each communication system, resulting in tighter crystal unit F/t characteristic specifications. The frequency change ($\Delta f/f$) of a crystal unit at a given temperature range is mainly determined by the

angle of cut of the crystal blank. Therefore, the use of a crystal blank having a reliable, guaranteed angle of cut is a prerequisite for stable manufacture of crystal units having a tight F/t characteristic. The angle of cut of the crystal blank is found by measuring the angular deviation, i.e., the angle formed by the angle of cut and atomic plane of the crystal blank, with an X-ray goniometer.

For example, for reliable, stable manufacture of a crystal blank having a tight angle tolerance of ± 15 seconds, the various factors affecting the angular deviation measurement error must be correctly grasped and quality control standards for each manufacturing process must be established to reflect the interrelationship between these factors in the crystal blank manufacturing process. However, until now few of the factors affecting the measurement error have been systematically analyzed, and the results of such analysis have only been introduced into the crystal blank manufacturing process under special limited conditions.⁽¹⁾

Therefore, the factors affecting the measurement error of crystal blanks is systematically analyzed to permit application of not only singly rotated crystal blanks, but also of doubly rotated crystal blanks. An example of a crystal blank having the tightest angle of cut angle tolerance, today, is the AT-cut crystal. Therefore, we experimented and analyzed the relationship with the various factors affecting the measurement error of an AT-cut crystal to allow reliable, stable manufacture of AT-cut having a tight angle tolerance of ± 15 seconds. The following three factors affecting the measurement error are described.

(I) Angular deviation measurement error due to geometrical factors:

Measurement error caused by the angle of cut and atomic plane of the crystal blank mounted to the goniometer and the goniometer geometrical factors.

(II) Angular deviation measurement error due to angle reading accuracy:

Measurement error caused by micrometer dial angle reading accuracy on the X-ray rocking curve peak position measurement accuracy.

(III) Angular deviation measurement error due to reference surface angle accuracy:

Measurement error caused by the precision of

the reference surface angle, i.e., the angle formed by the optical axis and atomic plane (01.1) of the crystal.

I ANGULAR DEVIATION MEASUREMENT ERROR DUE TO GEOMETRICAL FACTORS

The angle of cut of a crystal blank is the angle at which the blank is cut with respect to the crystallographic axes of the crystal. Fig. 1 shows the orientation angle of AT-cut and SC-cut crystal blanks. An x-ray goniometer is used to measure the orientation angle of crystal blanks. The atomic plane of a crystal blank parallel to, or nearly parallel to, the plate face of the crystal blank. In this case, the angular deviation of the crystal blank is measured. The orientation angle of the crystal blank is then easily found from the measured angular deviation.

"Angular deviation measurement error due to geometrical factors" is the measurement error caused by the plate face and atomic plane of the crystal blank mounted on the goniometer and the goniometer geometrical factor when the angular deviation of the crystal blank is measured.

IDEAL GEOMETRY

Fig. 2 shows the ideal geometry. Under the ideal geometry state, the normal direction of the plate face and atomic plane of the crystal blank is parallel to the plane of instrument, i.e., the plane of the goniometer. "Plane of instrument" and "axis of instrument" are terms taken from Heising's book⁽¹⁾. The plane of the instrument is a plane normal to the axis of rotation of the instrument and containing the incident beam. Further, under the ideal geometry state, the diffracted plane which contains the incident beam, atomic plane normal, and diffracted beam is parallel to the plane of the instrument. In Fig. 2, the diffracted plane is the same as the plane of the instrument.

The x-ray goniometer actually measures the angle projected on the plane of the instrument instead of the diffraction angle in the x-ray diffracted plane. Since the x-ray diffracted plane and the plane of the instrument are mutually parallel under ideal geometry conditions, if the angular deviation of the crystal blank is made μ , the x-ray incident angle is made g_0 , and the diffraction angle is made θ , the following equation is established:

$$\theta = \mu + g_0. \quad (1)$$

In other words, diffraction angle θ is equal to the angle $\mu + g_0$ actually measured, and "angular deviation measurement error due to geometrical factors" is not produced.

GENERAL GEOMETRY

As shown in Fig. 3, the normal direction of plate face and atomic plane of the crystal blank mounted on the goniometer are generally not perpendicular to the plane of the instrument. That is, the x-ray diffracted plane and the plane of the

instrument are not parallel. Under these conditions, the geometrical relationship of the plate face and atomic plane of the crystal blank and the goniometer is called the "general geometry".

The general geometry can be described by introducing the three rotating operation parameters δ , φ , and ε as shown in Fig. 2 and Fig. 3. That is,

a) the atomic plane is δ rotated around the intersection formed by the atomic plane and reference edge of the crystal blank.

b) the crystal blank is φ rotated around the plate face normal.

c) the crystal blank is ε rotated around the intersection formed by the plate face and the plane of the instrument.

The sign of the rotating angle at these rotating angle at these rotating operations is plus when rotation is in the counterclockwise direction. The rotating angles will be designated "equivalent angle factor" " δ ", " φ ", and " ε " hereafter. Under the general geometry state, angle $\mu' + g$ projected on the plane of instrument is actually measured instead of the diffraction angle θ (in the case of ideal geometry, $\theta = \mu + g_0$) in the diffracted plane. From Fig. 3, the relationship of this angle is expressed by the equation:

$$\sin(\mu' + g) = \sin(\mu + g_0) / \cos \delta' \quad (2)$$

Where, $g = g_0$ when $\delta' = 0$. (For ideal geometry) In addition, the "angular deviation measurement error due to geometrical factors" Δg is given by the following equation.

$$\Delta g \equiv g_0 - g = \mu' - \mu - \frac{\theta}{2} \delta'^2 \quad (3)$$

EQUIVALENT ANGLE FACTOR AND ANGULAR MEASUREMENT ERROR

The general relations of expression of equivalent angle factors δ , φ , ε and angular deviation measurement error Δg caused by δ , φ , ε are introduced.

The fundamental equations needed by each equivalent angle factor and the expressions of measurement error introduced from these equations are given in Table 1. (Refer to the appendix for a description of introduction of the fundamental equations and the expressions of measurement error.)

Today, AT-cut crystal blanks are the most mass produced and have the tightest angle tolerance. The expressions of relation converted to practical angle units to simplify use of the equivalent angle factors and the expression of relation with the measurement error are also given in Table 1. Only the equivalent angle factors and expressions of relation with the measurement error for an AT-cut crystal blank will be described below. Here diffraction angle θ is assumed to be 13.3° and angular deviation (ZZ' angle) μ is assumed to be 3° .

Moreover, Δg [SECONDS], δ [MINUTES], φ [MINUTES], and ε [MINUTES] are expressed in the units. In this case, equivalent angle factors δ , φ , ε , and the measurement error Δg are expressed by the following equations

$$\delta: \Delta g \approx -\frac{\theta}{2} \delta^2 = -2 \times 10^{-3} \times \delta^2 \quad (4)$$

δ is the angular deviation corresponding to the XX' angle of the crystal blank. Its angle tolerance is generally specified to be less than ± 30 minutes. If δ is assumed to be 30 minutes, Δg is -1.8 seconds and can be disregarded.

$$\begin{aligned} \varepsilon: \Delta g' &\approx \mu \varepsilon \left(\delta + \frac{\varepsilon}{2} \right) - \frac{\theta}{2} (\delta + \varepsilon)^2 \\ &= 9.21 \times 10^{-4} \times \varepsilon \left(\delta + \frac{\varepsilon}{2} \right) - 2.04 \times 10^{-3} (\delta + \varepsilon)^2 \end{aligned} \quad (5)$$

ε is the equivalent angle factor produced when the crystal blank is mounted on the goniometer. If its angle is assumed to be 30 minutes, Δg is 1.1 seconds and can also be disregarded. However, since this equivalent angle factor ε directly affects on the half-width of the x-ray rocking curve, care must be exercised. (This will be described later in "angular deviation measurement error due to angle reading accuracy".)

$$\begin{aligned} \varphi: \Delta g' &\approx \delta \varphi - \frac{\mu}{2} \varphi^2 \\ &= 1.75 \times 10^{-2} \times \delta \varphi - 4.6 \times 10^{-4} \times \varphi^2 \end{aligned} \quad (6)$$

The angle of φ at the crystal blank manufacturing process is generally considered to be less than about 60 minutes. If φ is assumed to be 30 minutes, since δ is 30 minutes, $\Delta g'$ is 15.4 seconds. The measurement error of this angular deviation shows that manufacture of a crystal blank demanding a tight ± 15 seconds angle tolerance is impossible if the equivalent angle factors δ and φ are also ± 30 minutes. For reliable, stable manufacture of crystal blanks requiring a tight angle tolerance, the relationship between equivalent angle factors δ and φ and the measurement error $\Delta g'$, must be grasped and its cause and effect relationship must be introduced in each manufacturing process. The calculated measurement error $\Delta g'$ versus φ as a function of δ is shown in Fig. 4. Fig. 5 is the magnified scale when the angles of δ and φ in Fig. 4 are both less than 60 minutes. If the angles of δ and φ are both less than 60 minutes, $\Delta g'$ is nearly proportional to the product of δ and φ and is expressed by $\Delta g' \approx 1.75 \times 10^{-2} \times \delta \varphi$.

One of the plate faces of the crystal blank mounted on the goniometer, is designated the "head" and the other is designated the "tail". The sign (plus or minus) of δ depends on whether the "head" or "tail" of the plate face is measured. However, the sign of φ does not change without regard to the "head" and "tail" when the crystal is mounted on the same goniometer. If the measurement error is made $\Delta g'$ (H) when the angular deviation of the "head" of the crystal blank is measured, and the measurement error is made $\Delta g'$ (T) when the angular deviation of the "tail" of the crystal blank is measured, the sign of δ is different at

the "head" and "tail," but the sign of φ remains unchanged. Therefore, the value of $\Delta g'$ (H) or $\Delta g'$ (T) takes the plus sign and the other takes the minus sign. Fig. 6 shows the typical measurement error signed in this way. $\Delta g'$ (T) is plus in Fig. 6. Referring to Table 1, since $\Delta g' = \mu' - \mu$, the apparent angular deviation μ' of the crystal blank at measurement is always larger than the true angular deviation μ of the crystal blank. On the other, $\Delta g'$ (H) is the opposite, as shown in Fig. 6. The absolute value of the difference in measurement error between of the "head" and "tail" of the crystal blank is expressed by the following equation.

$$\Delta G \approx |\Delta g'(\text{H}) - \Delta g'(\text{T})| = 2 |\delta \varphi| \quad (7)$$

Fig. 7 shows the relationship between ΔG and δ calculated with φ as the variable. Examples of the measured results are shown in Fig. 8. The crystal blank used in this measurement was cut from the lumbered quartz with its reference surface angle tolerance θY , θZ of $\pm 3'$ or less. Fig. 8 shows that the calculated measurement error and measured error are in good agreement. From Fig. 4 and Fig. 5, the following main problem factors depend on equivalent angle factors δ and φ .

1. The difference in the angles of cut measured values between "head" and "tail" in the crystal blank is mainly caused by the parallelity of the crystal blank produced at the lapping process.

2. The orientation angle of a circular crystal blank is measured by several methods. However, the following method cannot be used to measure the orientation angle of circular blanks requiring tight angle tolerance. A circular crystal blank does not have a reference edge. Therefore, the orientation angle is found to measure the maximum angular deviation while rotating the circular crystal blank mounted on the holder of the goniometer. This measurement method is only applicable when $\delta = 0$; otherwise, it cannot be used.

3. Generally, when measuring and classifying the orientation angle of crystal blanks, only the "head" or "tail" is measured and selected within the specified angle range. When the sorted crystal blanks is remeasured, the distribution of the remeasured angles is wider than the distribution of the angles before remeasurement.

CRYSTAL BLANK MANUFACTURING PROCESS AND EQUIVALENT ANGLE FACTOR

The following two factors produce angular deviation measurement error at the crystal blank manufacturing process:

- i) Errors in fabricating the crystal blank,
- ii) Errors in mounting the crystal blank on the holder of the goniometer.

These factors are given in Table 2 by process from lumbering to X-raying. Equivalent angle factors δ , φ , and ε are represented by the some of the angle factors produced at each process. Therefore, from this table, to hold the measurement error to within a certain limit, the previously described equivalent angle factors and the

measurement error expressions of relation must be used to establish the quality control standards for each crystal blank manufacturing process. Table 3 shows the calculated relationship between the angle factors δL and φL produced by lumbered reference surface angle tolerance ΘY , ΘZ and the measurement error $\Delta g'_L$ of an AT-cut crystal produced by only the angle factors δL and φL . According to IEC/49 (Secretariat) 129, the angle tolerance of the lumbered reference surface must be within ± 15 minutes for both ΘY and ΘZ . From Table 3, when φL is ± 21 minutes, δL is ± 3.6 minutes and the measurement error $\Delta g'_L$ caused by only the angle tolerance of lumbered reference surface is -1.3 seconds and can be ignored. However, the specified XX' angle of an AT-cut crystal, that corresponds to the equivalent angle factor δ is generally less than ± 30 minutes. Therefore, from Fig. 5, the measurement error $\Delta g'$ of an AT-cut crystal is approximately 12 seconds. This measurement error is too large in the manufacture of an AT-cut crystal requiring a tight angle tolerance of ± 15 seconds. For stable, reliable manufacture of a crystal blank requiring such a tight angle tolerance, the measurement error $\Delta g'$ must be at least ± 5 seconds. If the angle tolerances ΘY and ΘZ are both made less than ± 15 minutes, from Table 3, φL is ± 21 seconds. If dicing and mounting are assumed to be ideally done (i.e., $\varphi D = \varphi M = 0$), the value of φ will be the angle of φL only. That is, it will be ± 21 minutes. From Fig. 5, $\delta = \pm 14$ minutes. Therefore, the XX' angle of the crystal blank must be at least ± 14 minutes or less.

II ANGULAR DEVIATION MEASUREMENT ERROR DUE TO ANGLE READING ACCURACY

The rocking curve is defined by plotting the relationship between the diffraction intensity and the diffraction angle of goniometer according to Bragg's law. As shown in Fig. 9, the x-ray diffraction intensity is found by a ratemeter reading the magnitude of the diffraction beam, and the diffraction angle is found by a micrometer reading angle when the diffraction intensity is maximum. In other words, the orientation angle of the crystal blank is found by reading the diffraction angle corresponding to the peak position of the rocking curve obtained in this manner. This diffraction angle is called the Bragg angle. When the backlash of the micrometer is removed, the angle reading accuracy is primarily determined by sharpness that determines the peak position accuracy of the rocking curve. This is an extremely important item when an especially tight angle tolerance are required. When measuring the orientation angle of such a crystal blank, the following conditions must also be satisfied by the rocking curve profile:

- (i) The rocking curve half-width must be as narrow as possible.
That is, the curve must be as sharp as possible.
- (ii) The x-ray diffraction intensity must be sufficiently high in order to overcome background noise, and this can not be controlled by increasing the ratemeter sensitivity.

Currently, a double crystal goniometer are used to meet these conditions instead of a single crystal goniometer and the crystal blanks are etched to remove its surface damage⁽²⁾. As a result, the angle reading accuracy of a common x-ray goniometer can be raised to about ± 10 seconds. However, for reliable measurement of crystal blanks requiring a tight angle tolerance of ± 15 seconds, the angle reading accuracy must be held to at least ± 5 seconds. To satisfy this condition, the optical alignment of the double crystal goniometer must be adjusted to near the ideal state.

OPTICAL ALIGNMENT ADJUSTMENT AND HALF-WIDTH

The optical alignment at a double crystal goniometer is ideal when the atomic planes of the reference crystal and crystal blank are perpendicular to the plane of the instrument as shown in Fig. 10. However, when measuring the orientation angle of a crystal blank with a double crystal goniometer, the atomic planes are generally not perpendicular to the plane of the instrument. If the angle formed by the atomic plane normal direction of reference crystal and crystal blank and the plane of the instrument (called the tilt angle hereafter) are made ϵ_1 and ϵ_2 , the half-width W of the rocking curve of a double crystal goniometer in such an optical alignment stable is given by the following equation⁽³⁾.

$$W = W_0 + \Phi_m \cdot |\epsilon| \cdot \tan \Theta$$

Where, Φ_m : Vertical angle of incident beam maximum

ϵ : Absolute value of the angular error of ϵ_1 and ϵ_2 , i.e., $\epsilon = \epsilon_1 - \epsilon_2$

For an AT-cut crystal,

Θ : Bragg angle, 13.3 degrees

W_0 : Rocking curve ideal half-width

$$W_0 = w_0 \times \sqrt{1 + \frac{1}{b}} \approx 6.65 \text{ secs}$$

w_0 : Intrinsic diffraction profile, 4.45 arc of seconds (01.1)

b : Asymmetric factor

$$b = \sqrt{\sin(\Theta - \mu) / \sin(\Theta + \mu)}$$

μ : Angular deviation, $2^\circ 50'$

Typical results obtained by plotting the relationship between the half-width W and diffraction intensity I when the crystal blank tilt angle ϵ_2 was fixed and the reference crystal tilt angle ϵ_1 was changed, using the double crystal goniometer shown in Fig. 9, are shown in Fig. 11. These measured results show good agreement with the theoretic expression described above. That is,

a) Half-width W is proportional to the relative tilt angle ϵ . Therefore, if the optical alignment is ideally adjusted and controlled ($\epsilon = 0$), the half-width W will be equal to the ideal half-width W_0 (6.65 seconds) regardless of the aperture of the goniometer slit.

b) When the relative tilt angle ϵ is $\epsilon \neq 0$, the half-width W is proportional to the product of Φ_m and ϵ determined by the aperture of the goniometer slit.

c) The diffraction intensity I is strongest in the ideal optical state ($\varepsilon=0$) and suddenly weakens further away from the ideal state. As the slit aperture increases, the diffraction intensity also increases. Therefore, if the optical alignment of a double crystal goniometer is maintained in the ideal state, the half-width of the rocking curve will be minimum, i.e., about equal to the theoretical value, and the diffraction intensity will be maximum. As a result, a high angle reading accuracy can be controlled.

d) Because of the S/N, when $\varepsilon \neq 0$, even if the diffraction intensity I is increased by making the slit aperture larger, the half-width W will also widen, resulting in no increase in angle reading accuracy.

HALF-WIDTH AND ANGLE READING ACCURACY

We experimented with the relationship between the rocking curve half-width and angle reading accuracy when the double crystal goniometer optical alignment is slightly distorted from the ideal state. The orientation angle of the same face of the same crystal blank was measured 100 times and the blank was mounted to a goniometer three-point vacuum chuck. The half-width of the double crystal goniometer was changed by rotating (ε_1) the reference crystal. The measured crystal blank was etched to eliminate the affects of spreading width of the rocking curve due to the surface damage of the crystal. As a result, the half-width of the rocking curve of crystal blanks other than #800 lapped blanks was 7 seconds, or about the same as the theoretical value. The affect of the surface damage is considered to be removed. Typical standard deviation of repeatability of micrometer reading angle examples are given in Table 4.

From this table, the following can be stated:

1. As the half-width W of the rocking curve is widened by optical alignment, the standard deviation of the angle reading accuracy increases.
2. Since the crystal blank is mounted on a three-point chuck for measurement, the roughness of the crystal blank finish also affects the standard deviation of the angle reading accuracy.

For reliable, stable measurement of crystal blanks requiring a tight angle tolerance of ± 15 seconds, for example, the angle reading accuracy must be maintained at ± 5 seconds or less. Therefore, the following are necessary:

1. The optical alignment of the double crystal goniometer must be adjusted and managed so that the half-width W of the rocking curve is always less than 10 seconds.
2. The crystal blank to be measured must be lapped with #3000 or finer abrasive, then etched.

III ANGULAR DEVIATION MEASUREMENT ERROR DUE TO REFERENCE SURFACE ANGLE ACCURACY

An AT-cut crystal is generally cut near $35^\circ 15'$ with respect to the optical axis around its x axis. In this case, the orientation angle of crystal

blank is represented by the angle Θ formed by the optical axis and the angle of cut. If the angular deviation is made μ and the reference surface angle (angle formed by the optical axis and atomic plane (01.1) of the crystal blank) is made α , the orientation angle Θ is represented by the sum of the angular deviation μ and reference surface angle α as shown in Fig. 12. The orientation angle Θ is found by measuring the angular deviation μ with an x-ray goniometer. Therefore, in order to accurately determine the orientation angle Θ with respect to the optical axis, it is necessary to know the exact value of reference surface angle α .

However, reference surface angle α is not uniform at each manufacturing process and may extend from $38^\circ 12'$ to $38^\circ 14'$. Of these values, the most widely used is near $38^\circ 13'$. And also these reference surface angles are the measured values in natural quartz. Today, high measurement accuracy has been obtained through advanced in measurement technology and synthetic quartz are today replacing natural quartz. Considering these points, to measure the reference surface angle of synthetic quartz, and to use this measured values as "standard reference surface angle" are significant. As a result,

1. The orientation angle of a crystal blank is the more absolute angle with respect to the optical axis.
2. The orientation angle of AT-cut crystal blanks can be commonly used at each manufacturing process.

Therefore, we measured the reference surface angle with careful attention, and also studied the inter-relationship between the "Q value" of synthetic quartz⁽⁴⁾⁽⁵⁾ and reference surface angle in order to make this value into general use. Fig. 13 shows the equipment used to measure the reference surface angle. The reference surface angle α formed by the optical axis and atomic plane (01.1) is found by measuring the inter planar angle 2α with the atomic plane (01.1) and (01.1) forming the equal angle with respect to the optical axis. Since the affect of the x-ray dispersion $\Delta\lambda/\lambda$ can be disregarded,⁽⁶⁾ this method provides an extremely high measurement accuracy. The measurement accuracy of the experimental equipment is guaranteed within ± 0.5 second. Measurement values obtained with this method are shown in Table 5. This table shows that the reference surface angle α measured values have no affect on the "Q value" of synthetic quartz within a measurement accuracy and show an extremely stable angle. Therefore, this predicts that the $38^\circ 12' 39''$ measured reference surface angle can be used as the "standard reference surface angle" of synthetic quartz.

CONCLUSION

1. The angular deviation measurement error $\Delta\theta$ produced by the geometrical relationship between the orientation angle and atomic plane of the crystal blank mounted to the goniometer and the goniometer is caused by equivalent angle factors ε and φ . The expression of relation is expressed

by,

$$\Delta g = \delta \varphi - \frac{\mu}{2} \varphi^2 - \frac{\theta}{2} (\delta - \mu \varphi)^2$$

This expression of relation can be used to analyse all crystal blank angular deviation measurement errors. For example, in order to make the angular deviation measurement error of an AT-cut crystal ± 5 seconds or less, each crystal blank must be quality controlled in manufacturing process so that δ (corresponds to the XX' angle) is held to ± 14 minutes and φ (corresponds to the surface rotating angle) is held to less than ± 21 minutes, if the crystal is assumed to be cut from lumbered quartz with its reference surface angle tolerance θY and θZ of ± 15 minutes.

2. The angle reading error produced when reading the scale of a micrometer is caused by the half-width of the rocking curve. The half-width of the rocking curve can be held to less than 10 seconds, or almost the theoretical value, by adjusting the tilt angle of the double crystal goniometer reference crystal. As a result, high angle reading accuracy reproducibility was obtained. For example, an angle reading reproducibility standard deviation of 1.73 seconds was obtained as an experimental value for a #3000 lapped and etched AT-cut crystal at an 8 seconds rocking curve half-width.

3. A reference surface angle (angle formed by the optical axis and atomic plane (01.1) of the crystal) measured value of $38^\circ 12' 39'' \pm 0.5''$ was obtained without regard to the "Q value" of the synthetic quartz itself. Obtaining such an extremely stable measured value without regard to the "Q value" of the synthetic quartz itself predicts that this measured value of $38^\circ 12' 39''$ can be used as the "standard reference surface angle".

ACKNOWLEDGEMENTS

The authors are grateful to Dr. J. Yoshimura, Institute of Inorganic Synthesis, Faculty of Engineering, Yamanashi University, for his helpful discussions and to Dr. T. Matsushita, Department of Applied Physics, Faculty of Engineering, University of Tokyo, for measuring the interplanar angle of material crystals.

REFERENCES

1. R.A. Heising, "Quartz Crystal for Electrical Circuits," Chapter III, D. Van Norstrand Co., Inc., New York 1946
2. W.L. Bond, "A Double-Crystal X-Ray Goniometer for Accurate Orientation Determination," Proceedings of The I.R.E., PP.886-889 (1950)
3. R. Bubakova, "Exact Adjustment of Monocrystals on Many-Crystal X-Ray Equipment," Czech. J. Phys. vol.12, PP.695-702 (1962)
4. IEC49 (Central Office) 127, "Specification for Synthetic Quartz Crystal," clause 4.6.1, "Evaluation of Q by infrared absorption"
5. J. Asahara and S. Taki, "Physical Property of Synthetic Quartz and Its Electrical Characteristics," Proc. 26th Annual Frequency Control Symposium, PP.93-103 (1972)

6. A.H. Compton and S.K. Allison, "X-Rays in Theory and Experiment," D.Van Norstrand Co., Inc., New York 1949

APPENDIX

The unit vector of the normal direction of the atomic plane (hk.l) is made \vec{n} . If the vector components of $\vec{n}(n_1)$ in the crystal axes X, Y, and Z and direction are made n_1 , n_2 , and n_3 respectively, \vec{n} is expressed by the following equation at the O-XYZ coordinates system.

$$\vec{n} = \begin{pmatrix} n_1 \\ n_2 \\ n_3 \end{pmatrix} = \frac{1}{S} \cdot \begin{pmatrix} h \\ \frac{h+2k}{\sqrt{3}} \\ l/a \end{pmatrix} \quad (A-1)$$

Where, S is the normalized factor $[h^2 + (h + 2K)^2/3 + 12/(c/a)^2]^{1/2}$. h, k, and l are the Miller-Bravais indices, and a and c are the lattice constants of quartz crystal. The unit vector of normal direction of the crystal blank atomic planes (hk.l) is made \vec{N} . The vector components (N_1) of \vec{N} with respect to the blank which have the length L, thickness T, and width W are made N_1 , N_2 , N_3 . In general for a doubly rotating crystal blank (YXW) \oplus / \ominus , O-X, Y, Z coordinates system and the vector components (N_1) at the O-L, T, W coordinates system is expressed by the following equation.

$$\vec{N} = \begin{pmatrix} N_1 \\ N_2 \\ N_3 \end{pmatrix} = \begin{pmatrix} 1 & 0 & 0 \\ 0 & \cos\theta & \sin\theta \\ 0 & -\sin\theta & \cos\theta \end{pmatrix} \begin{pmatrix} \cos\phi & \sin\phi & 0 \\ -\sin\phi & \cos\phi & 0 \\ 0 & 0 & 1 \end{pmatrix} \begin{pmatrix} n_1 \\ n_2 \\ n_3 \end{pmatrix} \quad (A-2)$$

In the case of a singly rotating crystal blank, for example AT-cut crystal blank, which is very commonly used in actual production line. (A-2) is simplified and expressed by the following equation.

$$\vec{N} = \begin{pmatrix} N_1 \\ N_2 \\ N_3 \end{pmatrix} = \begin{pmatrix} 1 & 0 & 0 \\ 0 & \cos\theta & \sin\theta \\ 0 & -\sin\theta & \cos\theta \end{pmatrix} \begin{pmatrix} n_1 \\ n_2 \\ n_3 \end{pmatrix} \quad (A-3)$$

The atomic plane of an ideally cut crystal blank is perpendicular to the reference edge of the crystal blank. However, the atomic plane of an actual cut crystal blank is not generally perpendicular to this reference edge. (Fig. 14) In this case, the angular deviation, μ and δ are expressed by the following equation.

$$\tan \mu = \frac{N_3}{N_2}, \quad \tan \delta = \frac{N_1}{N_2} \quad (A-4)$$

The atomic plane of a doubly rotating crystal blank is not perpendicular to the reference edge of the blank. In addition, Eq. (A-4) is a general

equation that is also applicable to doubly rotating crystal blanks.

Equivalent angle factor δ and angular deviation μ measurement error Δg

If the x-ray incident angle on the plate face of the crystal blank is made g , the conditions that diffract the x-rays are given by the following equation.

$$\sin(\mu + g) = \sin \theta / \cos \delta \quad (A-5)$$

Where, θ is the Bragg angle. g of Eq. (A-5) is approximated by the following equation.

$$g = \theta - \mu + \frac{\theta}{2} \delta^2 \quad (A-5)'$$

If the x-ray incident angle on the plate face of an ideally cut crystal blank ideally mounted on the goniometer (Fig. 2, $\delta = \varphi = \varepsilon = 0$) is made g_0 , from Eq. (A-5), g_0 is given by the following equation.

$$g_0 = \theta - \mu \quad (A-5)''$$

The crystal blank angular deviation μ measurement error Δg caused by only the equivalent angle factor δ is given by the following equation.

$$\Delta g \equiv g_0 - g = -\frac{\theta}{2} \delta^2 \quad (A-6)$$

Equivalent angle factor φ and angular deviation μ measurement error $\Delta g'$

If a crystal blank is φ rotated in the counterclockwise direction around T axis of crystal blank, unit vector \bar{N} is converted to unit vector \bar{N}' . The relationship between vector components (N_i) and (N_i') at the O-L', T', W' coordinates system after rotation is given by the following equation.

$$\begin{pmatrix} N_1' \\ N_2' \\ N_3' \end{pmatrix} = \begin{pmatrix} \cos \varphi & 0 & -\sin \varphi \\ 0 & 1 & 0 \\ \sin \varphi & 0 & \cos \varphi \end{pmatrix} \begin{pmatrix} N_1 \\ N_2 \\ N_3 \end{pmatrix} = \begin{pmatrix} N_1 \cos \varphi - N_3 \sin \varphi \\ N_2 \\ N_1 \sin \varphi + N_3 \cos \varphi \end{pmatrix} \quad (A-7)$$

If the angle projected on the plane of the instrument from angular deviation μ and δ are made μ' and δ' , the same as at (A-4), the relationship between μ' , δ' , and the vector component (N_i') is given by the following equations:

$$\tan \mu' = \frac{N_3'}{N_2'} = \tan \delta \sin \varphi + \tan \mu \cos \varphi \quad (A-8)$$

$$\tan \delta' = \frac{N_1'}{N_2'} = \tan \delta \cos \varphi - \tan \mu \sin \varphi \quad (A-8)'$$

The diffraction condition of the x-rays are given by the following equation, the same as at Eq. (A-5).

$$\sin(\mu' + g) = \sin \theta / \cos \delta' \quad (A-9)$$

g is approximated by the following equation by substituting μ' and δ' of Eqs. (A-8) and (A-8)' into Eq. (A-9).

$$g = \theta - \mu - \delta \varphi + \frac{\mu}{2} \varphi^2 + \frac{\theta}{2} (\delta - \mu \varphi)^2 \quad (A-10)$$

The angular deviation measurement error $\Delta g'$ is given by the following equation including the equivalent angle factor φ .

$$\Delta g' \equiv g_0 - g = \delta \varphi - \frac{\mu}{2} \varphi^2 - \frac{\theta}{2} (\delta - \mu \varphi)^2 \quad (A-11)$$

Angular deviation μ measurement error $\Delta g''$ due to equivalent angle factor

If a crystal plate is ε rotated in the counterclockwise direction around the width axis W, the unit vector \bar{N} is converted to unit vector \bar{N}'' after rotation. The relationship between the vector components (N_i) and (N_i'') at the O-L'', T'', W'' coordinates system after rotation is given by the following equation.

$$\begin{pmatrix} N_1'' \\ N_2'' \\ N_3'' \end{pmatrix} = \begin{pmatrix} \cos \varepsilon & \sin \varepsilon & 0 \\ -\sin \varepsilon & \cos \varepsilon & 0 \\ 0 & 0 & 1 \end{pmatrix} \begin{pmatrix} N_1 \\ N_2 \\ N_3 \end{pmatrix} = \begin{pmatrix} N_1 \cos \varepsilon + N_2 \sin \varepsilon \\ -N_1 \sin \varepsilon + N_2 \cos \varepsilon \\ N_3 \end{pmatrix} \quad (A-12)$$

If the angles projected on the plane of the instrument from angular deviation μ and δ are made μ'' and δ'' , the same as at Eq. (A-4), the expression of relationship between μ'' , δ'' , and vector component (N_i'') is given by the following equations.

$$\tan \mu'' = \frac{N_3''}{N_2''} = \frac{\tan \mu}{\cos \varepsilon - \tan \delta \sin \varepsilon} \quad (A-13)$$

$$\tan \delta'' = \frac{N_1''}{N_2''} = \frac{\tan \delta + \tan \varepsilon}{1 - \tan \delta \tan \varepsilon} \quad (A-13)'$$

The diffraction conditions of the x-rays are given by the following equation, the same as at Eq. (A-5).

$$\sin(\mu'' + g) = \sin \theta / \cos \delta'' \quad (A-14)$$

g is approximated by the following equation by substituting μ'' and δ'' of Eqs. (A-13) and (A-13)'

into Eq. (A-14).

$$g = \theta - \mu - \mu \delta \varepsilon - \frac{1}{2} \{ \mu \varepsilon^2 - \theta (1 + \delta \varepsilon)^2 (\delta + \varepsilon)^2 \} \quad (\text{A-15})$$

The angular deviation measurement error $\Delta g''$ is given by the following equation including the equivalent angle factor ε .

$$\Delta g' \equiv g_0 - g = \mu \delta \varepsilon + \frac{1}{2} \{ \mu \varepsilon^2 - \theta (1 + \delta \varepsilon)^2 (\delta + \varepsilon)^2 \} \quad (\text{A-16})$$

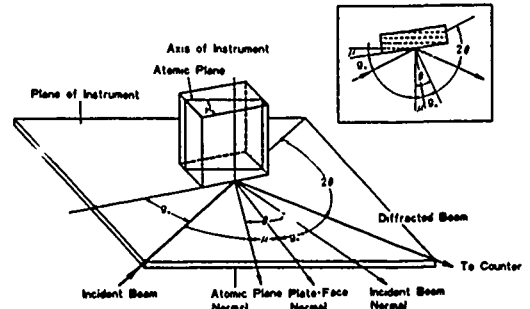


Fig.2 Ideal geometry.

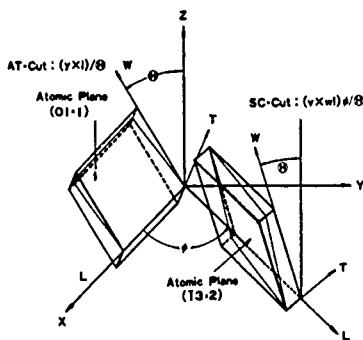


Fig.1 Orientation angle of AT-Cut and SC-Cut crystal blank.

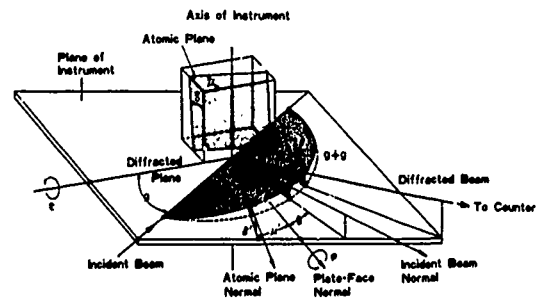


Fig.3 General geometry.

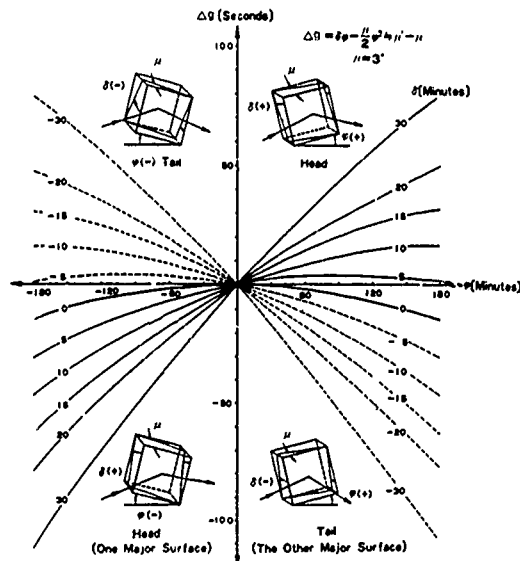


Fig.4 Calculated measurement error $\Delta g'$ vs ϕ , as a function of δ .

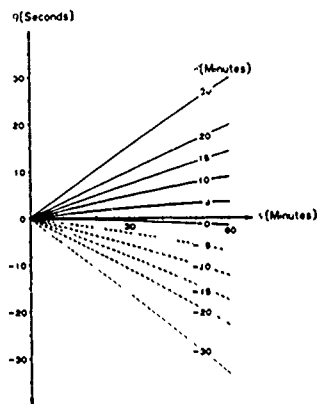


Fig. 5 Magnified scale in Fig. 4

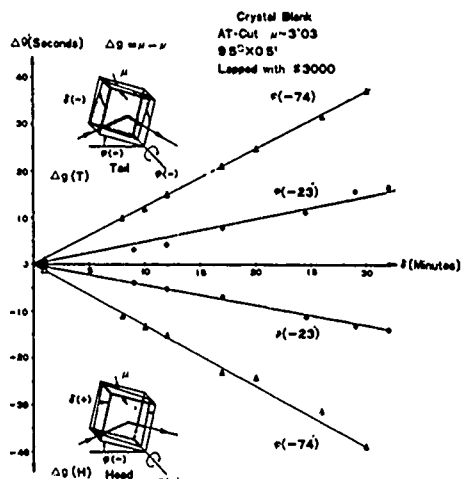


Fig. 6 Typical measurement error $\Delta g'$ due to sign of δ .

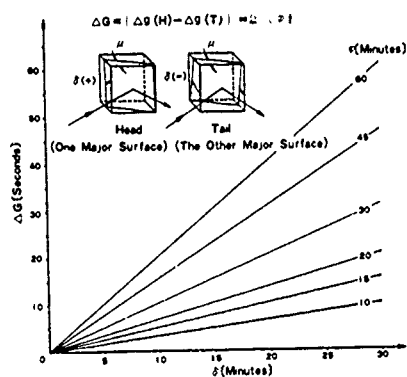


Fig. 7 Calculated difference in the measurement error between "Head" and "Tail".

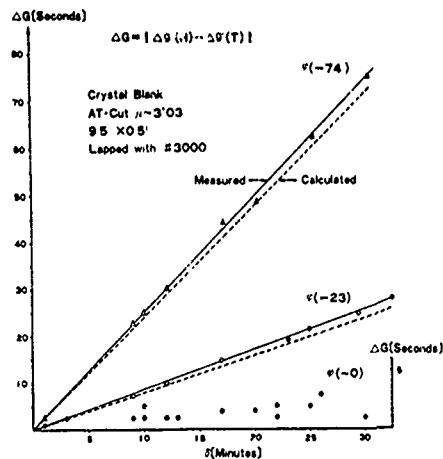


Fig. 8 Measured Difference in measurement error between "Head" and "Tail"

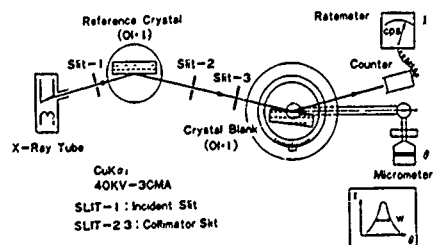


Fig. 9 Diagram of double crystal goniometer.

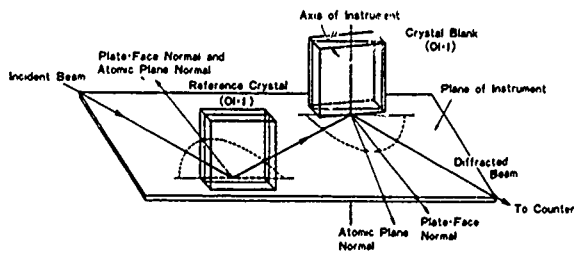


Fig. 10 Ideal geometry of double crystal arrangement.

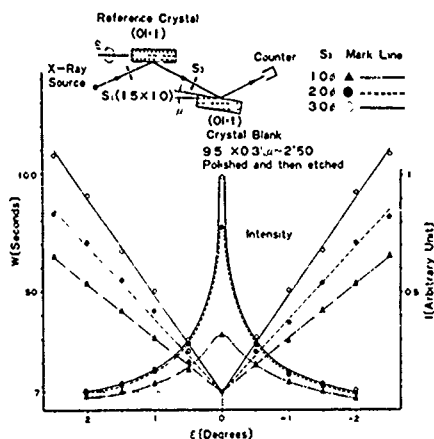


Fig.11 Measured rocking curve and its intensity, as a function of slit's size.

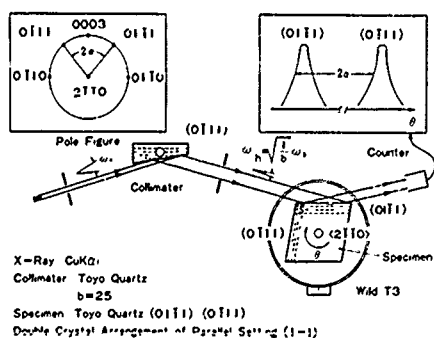


Fig.13 Double crystal arrangement of parallel setting (1.-1).

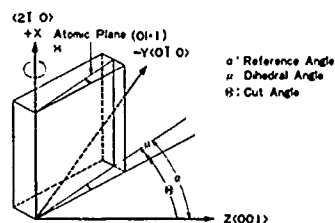


Fig.12 Orientation angle of AT-Cut crystal blank and coordinate system.

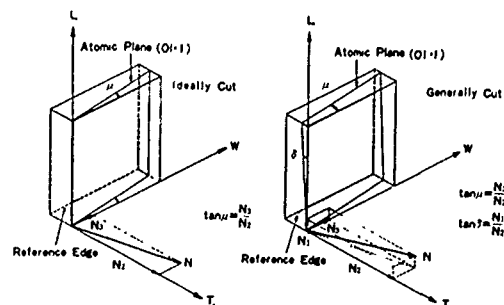


Fig.14 Orientation of the (01-1) atomic plane in AT-Cut crystal blank.

Table1. Fundamental equations and measurement error by equivalent angle factor.

Factors	Fundamental Equations	Errors in μ Measurement	
δ	$g_1 = \delta - \mu \dots \dots \dots (1)$ $\tan \mu = N_2/N_1, \tan \delta = N_2/N_1 \dots \dots (2)$ $\sin(\mu + g) = \sin \delta / \cos \delta \dots \dots \dots (3)$	$\Delta g = g_1 - g$ $\mu = \frac{\delta}{2}$ $\mu = \mu_0$ $(\mu = \mu_0 \text{ at } \delta = 0)$	$\Delta g \approx -\frac{\delta}{2} \delta^2$ $= -1.5 \times 10^{-4} \times \delta \delta^2$ $= -2 \times 10^{-4} \times \delta^3$
φ	$\tan \mu' = \tan \delta \sin \varphi + \tan \mu \cos \varphi \dots (2-1)$ $\tan \delta' = \tan \delta \cos \varphi - \tan \mu \sin \varphi \dots (2-2)$ $\sin(\mu' + g) = \sin \delta / \cos \delta' \dots \dots \dots (3)$	$\Delta g' = g_1 - g$ $= \delta \varphi - \frac{\mu}{2} \varphi^2 - \frac{\delta}{2} (\delta - \mu \varphi)^2$ $\approx \delta \varphi - \frac{\mu}{2} \varphi^2$ $\approx \mu' - \mu$	$\Delta g \approx \delta \varphi - \frac{\mu}{2} \varphi^2$ $= 1.75 \times 10^{-4} \times \delta \varphi - 1.53 \times 10^{-4} \times \mu \varphi^2$ $= 1.75 \times 10^{-4} \times \delta \varphi - 4.6 \times 10^{-4} \times \varphi^2$
ϵ	$\tan \mu' = \tan \mu / (\cos \epsilon - \tan \delta \sin \epsilon) \dots (2-1')$ $\tan \delta' = (\tan \delta + \tan \epsilon) / (1 - \tan \delta \tan \epsilon) \dots (2-2')$ $\sin(\mu' + g) = \sin \delta / \cos \delta' \dots \dots \dots (3)$	$\Delta g' = g_1 - g$ $= \mu \delta \epsilon + \frac{1}{2} [\mu \epsilon^2 - \delta (1 + \delta \epsilon)^2 (\delta + \epsilon)^2]$ $\approx \mu \epsilon (\delta + \frac{\epsilon}{2}) - \frac{\delta}{2} (\delta + \epsilon)^2$	$\Delta g' \approx \mu \epsilon (\delta + \frac{\epsilon}{2}) - \frac{\delta}{2} (\delta + \epsilon)^2$ $= 3.07 \times 10^{-4} \times \mu \epsilon (\delta + \frac{\epsilon}{2})$ $- \frac{\delta}{2} (\delta + \epsilon)^2$ $= 9.21 \times 10^{-4} \times \epsilon (\delta + \frac{\epsilon}{2}) - 2.04 \times 10^{-4} (\delta + \epsilon)^2$
Note	1 For AT-Cut Crystal Blank, μ : xx' Angle, δ : xx Angle Bragg Angle, δ : 13.3' μ : -3' 2 Units: Δg (Second) $\delta, \varphi, \epsilon$ (Minute) δ, μ (Degree) 3 Sign: For counterclockwise rotation, δ, ϵ and φ are plus, while δ and μ are only plus		

Table2. Angle factor and equivalent angle factor by process.

Process	$\delta = \delta_1 + \delta_2$	$\varphi = \varphi_1 + \varphi_2 + \varphi_3$	$\epsilon = \epsilon_1$
Lumbering	○	○	
Cutting	○		
Dicing		○	
Mounting		○	○

Lumbering and Cutting

Dicing

Mounting

■ In AT-Cut $\varphi_1 \approx 0.82 \times \delta_1 + 0.58 \times \delta_2$; $\delta_1 \approx \pm 0.58 \times \delta_2 \mp 0.82 \times \delta_2$

Table3. Reference surface angle of lumbered quartz and measurement error.

Accuracy of Orientation Angle: θ_1 and θ_2	Maximum rotation Angle: α	Maximum Measurement Error: α_{gl}
$\pm 30'$	42'	5.3'
$\pm 20'$	28'	2.4'
$\pm 15'$	21'	1.3'
$\pm 10'$	14'	0.6'
$\pm 5'$	7'	0.1'

For AT-Cut $\mu \approx 0.82 \times \delta_1 + 0.58 \times \delta_2$
 $\delta_1 \approx \pm 0.58 \times \delta_2 \mp 0.82 \times \delta_2$
 For counterclockwise rotation, θ_1 and θ_2 are plus.

Table4. The standard deviation of repeatability of micrometer reading angle.

Crystal Blank Surface Finish	W on Optical Alignment itself		
	W=8'	W=15'	W=30'
Polished with CeO_2	0.89'	0.94'	1.00'
Lapped with #3000	1.73'	2.02'	2.81'
Lapped with #2000	2.09'	2.48'	3.29'
Lapped with #800	7.50'	—	—

Table5. Measured reference surface angle in synthetic quartz, as a function of its Q-value.

Lot Number	Estimated "Q" of Quartz ($\times 10^4$)	Reference Surface Angle
A	148	38° 12' 38.9" $\pm 0.5'$
B	174	38° 12' 36.8" $\pm 0.5'$
C	220	38° 12' 39.0" $\pm 0.5'$
D	237	38° 12' 39.4" $\pm 0.5'$

NEW FREQUENCY TEMPERATURE CHARACTERISTICS OF MINIATURIZED GT-CUT QUARTZ RESONATORS

Hirofumi Kawashima, Hirochika Sato and Osamu Ochiai

Daini Seikosha Co., Ltd.
6-31-1, Kameido, Koto-ku, Tokyo 136, Japan

Summary

This paper describes the shape, size and frequency-temperature characteristics of a miniaturized GT cut quartz resonator. We have developed a new GT cut quartz resonator, which is greatly miniaturized, highly shock resistant and has excellent frequency-temperature characteristics over a wide temperature range. In order to obtain sufficient processing accuracy, this quartz resonator is manufactured by a lithographic process, and, by means of a one-body formation of a vibrational portion and supporting portions of the quartz resonator, it can be made small. To describe it in still more detail, in order to minimize the energy losses caused by vibrations of the supporting portions, the quartz resonator has been designed such that the amplitude of vibrations, derived from the vibrational portion and transmitted to the supporting portions, which have the function of changing the length-extensioral vibration derived from the vibrational portion into a flexural mode vibration, is minimized at the end of the supporting portions and thus there is hardly any distortion.

The optimum shape and size for this quartz resonator have been analyzed by the finite element method. The calculated results show that the analysis of displacement of the vibrational portion and the supporting ones can be made as a one-body problem. The quartz resonator, therefore, has excellent electrical characteristics, even if it is mounted on the pedestal without great care.

It has been found that this miniaturized GT cut quartz resonator not only has excellent frequency-temperature characteristics but also extremely good electrical characteristics, and in particular, that its frequency-temperature characteristics are more excellent than that of an AT cut resonator within a wide temperature range, such as -30°C to $+70^{\circ}\text{C}$.

Introduction

Since CT and DT cut resonators were introduced by Hight and Willard, there have been numerous studies of contour mode resonators. In particular, in 1940 the GT cut quartz resonator, introduced by

W.P. Mason¹, showed excellent frequency-temperature behavior over a wide temperature range. This quartz resonator does not change in accuracy by more than one part in a million over a 100-degree centigrade range of temperature. Therefore, it was applied to many standard quartz crystal oscillators and crystal filters used under severe temperature conditions. However, notwithstanding that its frequency-temperature behavior is the best of all known crystal resonators, as things are, it is not used much today except in some specialized fields, because its supporting method and miniaturization are difficult, and also its sensitivity of frequency to the width to length ratio is high. Furthermore, there are few theoretical studies concerning the GT cut quartz resonator except those of Bechmann and Nakazawa.

Now it has been about ten years since quartz wrist watches were realized. They have been remarkably improved in terms of time accuracy and now have a monthly error of only 5 to 20 seconds. Recently, however, a wrist watch of even higher accuracy is being sought in the watch industry. In order to achieve this goal, it is necessary to obtain a quartz resonator having excellent frequency-temperature characteristics. At the same time, other severe conditions must be met, such as that it must be easy to support, highly shock resistant, easy to process and not difficult to miniaturize. At present, as a resonator for high accuracy wrist watch use, AT and M cut quartz resonators are being proposed. However, in mass production, the former has some problems particularly concerning supporting method, processing accuracy and miniaturization; and the latter also has some problems particularly concerning processing accuracy and the supporting method.

We took notice of two significant features of GT cut quartz resonators: excellent frequency-temperature characteristics and their ability to make use of a thin quartz plate. Furthermore, by adopting a photolithographic process, which makes it possible to form any shape of quartz resonator, we have developed a new type GT cut quartz resonator for high accuracy wrist watch use, which satisfies the required electrical characteristics.

Design Procedure

The main characteristics of a quartz

resonator required for electronic instruments, and in particular, for high accuracy wrist watches, for example, yearly accuracy within ± 5 seconds, are as follows:

- (a) excellent frequency-temperature characteristics.
- (b) small in size to allow freedom in watch design.
- (c) highly shock resistant.
- (d) easy to process and assemble.
- (e) small frequency aging.
- (f) of adequate frequency to prolong battery life.

Rectangular AT cut quartz resonators and M cut quartz resonators now meet these requirements. Their development has made progress. However, they are not used much in wrist watches. When utilizing a GT cut quartz resonator for wrist watches, the most well-known type being mounted with two supporting lead wires at the center of a quartz plate, it cannot be expected to satisfy requirements (b) - (d) at all. Therefore, a novel supporting method for quartz resonators has been developed and these problems have been worked out.

Processing Method

Fig. 1 shows cut angle (ϕ, θ) and a quartz plate of a GT cut quartz resonator. The cut angle (ϕ, θ) is expressed by an IRE standard $yxwt(\phi/\theta)$. After a quartz plate cut like this is polished to the desired constant thickness, a photolithographic process, as well as that of the tuning fork type quartz resonator of $+5^\circ X$ -cut, is employed to form the shape and electrode patterns of a GT cut quartz resonator. With this process there are two remarkable benefits:

- (1) It is possible to process the intricate shape of a quartz resonator with high accuracy.
- (2) It is possible to reduce costs in mass production.

Supporting Method

Recently, a few attempts¹¹ to reduce the influence of the supporting portions of a quartz resonator by means of a one-body formation of the vibrational portion and supporting portions of the quartz resonator and by mounting it at the supporting ones, have been made. The way of thinking behind this is that as long as a quartz resonator is mounted at its nodal points, the vibration energy of the quartz resonator can be trapped inside its vibrational portion. However, a trapped energy condition is not satisfactory, if the shape of the supporting portions and the pedestal are not specifically devised for this purpose. Therefore, a quartz resonator must be dealt as a resonance system including its supporting portions and pedestal. Great care is not only needed in the pedestal design, but also the size of the supporting system

per se becomes a problem.

We have constructed a resonance system including supporting portions such that resonance frequency of this whole resonance system becomes approximately equal to that of the vibrational portion alone, a vibration derived from the vibrational portion is not transmitted to the ends of the supporting portions. First of all, the resonance system has been determined by taking the ease of analysis and mode of a vibrational portion into account. Hence, it consists of a beam vibrating in a flexural mode. Fig. 2 shows the concrete shape of a GT cut quartz resonator comprising a vibrational portion and supporting portions. Fig. 3 shows the supporting portion of the quartz resonator described in Fig. 2 in enlarged detail. To describe the principle briefly, a vibration in the directions of the arrows in Fig. 3 of the vibrational portion is restricted, because of the elastic portion connected through the bridge portion. In other words, its vibration is transmitted to the elastic portion through the bridge portion. By this method, the elastic portion which works as a both end supported beam, vibrates in a flexural mode. When the resonant frequency of the elastic portion is approximately equal to that of the vibrational portion, a vibration derived from the vibrational portion is hardly transmitted to attenuate portion and mounting ones. Since the energy loss caused by vibrations at the end of the supporting portion hardly takes place, the quartz resonator has excellent electrical characteristics, even if it is mounted on the pedestal without great care.

The optimum shape, size and vibrational mode for this quartz resonator have been analyzed by the finite element method wherein anisotropic isoparametric planar quadrilateral elements stored in the NASA structural analysis program are used so as to improve the analysis accuracy of the flexural mode. An example of the shape and size of a quartz resonator having good electrical characteristics with a resonant frequency about 2.3MHz is shown in Fig. 4. Furthermore, its distribution of displacement is shown in Fig. 5. It is understood from Figs. 4 and 5 that the effect of the supporting portions appears sufficient. For the quartz resonator shown in Fig. 4, the relationship between its resonant frequency when its mounting portions are free (f_{Free}) and when they are fixed (f_{Fixed}) is as follows:

$$(f_{\text{Fixed}} - f_{\text{Free}}) / f_{\text{Free}} < 1.0 \times 10^{-6} \dots (1)$$

On the basis of this result it is possible to ignore the influence of the supporting portions. Accordingly, the vibrational portion and supporting portions of a quartz resonator can be dealt with as a one-body problem. Consequently, since the quartz resonator is not only easy to assemble but also is firmly mounted on the pedestal, it is highly shock resistant and furthermore, it is possible to miniaturize.

Fig. 6 shows a mode chart for the quartz resonator in Fig. 4 and Fig. 7 shows its three

modes (A), (B) and (C) respectively. A GT cut quartz resonator's electrical characteristics are influenced by the intensity of the coupling between the width-extensional vibration (A) of the fundamental vibration and the length-extensional vibration (C) of the sub-vibration. The (B) mode is called the edge mode, however its intensity is so weak as to enable us to ignore its influence on the fundamental vibration. In order to maintain a constant frequency difference between the fundamental vibration and the sub-one as well as that of the conventional GT cut quartz resonator itself, that is to say, to obtain a constant intensity of coupling between the fundamental vibration and the sub-one, from which excellent frequency-temperature characteristics are to be obtained, it is found from Fig. 6 that the width to length ratio, also called the dimensional ratio, becomes larger than the conventional one, because mode (C) is suppressed by the addition of the supporting portions.

The conventional rectangular GT cut quartz resonator has its best frequency-temperature characteristics with a width to length ratio of approximately 0.86, but the new type GT cut quartz resonator proposed by us, as predicted in Fig. 6, has its best frequency-temperature characteristics with a width to length ratio of approximately 0.96.

Now, there are many possible shapes for the supporting portions of a quartz resonator using the principle described in this study. In this paper, however, only the shape shown in Fig. 2 is described as an example.

Size

For a quartz resonator for wrist watches a small size is desirable. More precisely, it is to be desired that the dimension of the short side of the vibrational portion is smaller than 2.0^{mm} so as to allow freedom in watch design. Since a GT cut quartz resonator's frequency-temperature characteristics are directly dependent upon the width to length ratio of its vibrational portion, its optimum ratio must be chosen with this in mind. First of all, we analyzed the frequency-temperature characteristics, using a frequency equation (2), of the rectangular GT cut quartz resonator, and, in particular, carefully examined the relationship between the width to length ratio and frequency-temperature characteristics. Taking these results into account, an analysis was made by the finite element method concerning the shape proposed by us.

$$f = \frac{1}{2W} \sqrt{\frac{P_{11}}{\rho}} \sqrt{\frac{1}{2} [1 + k_1 R^2 + \sqrt{(1 - k_1 R^2) + 4k_2 R^2}]} \quad \dots\dots\dots (2)$$

where, w: a dimension of width
 R: the width to length ratio
 ρ : density
 $k_1 = P_{33}/P_{11}$, $k_2 = P_{13}/P_{11}$

$$\begin{pmatrix} P_{11} & P_{13} & P_{15} \\ P_{13} & P_{33} & P_{35} \\ P_{15} & P_{35} & P_{55} \end{pmatrix} = \begin{pmatrix} s_{11} & s_{13} & s_{15} \\ s_{13} & s_{33} & s_{35} \\ s_{15} & s_{35} & s_{55} \end{pmatrix}^{-1}$$

s_{ij} : elastic compliance

Figs. 8 and 9 show temperature coefficients of the first order and the second order versus cut angle, when the width to length ratio of the rectangular quartz plate is changed.

Experimental Results

According to the results of the above mentioned analysis, we have actually manufactured resonators and have experimentally examined their various electrical characteristics.

Investigation of a Dimensional Ratio

Fig. 10 illustrates the relationship between the dimensional ratio (R) and the temperature coefficients (α , β) of the first order and the second order at 20°C of a GT cut quartz resonator having supporting portions as shown in Fig. 4 and a cut angle of $\gamma_{\text{cut}}(55.5/45^\circ)$. As shown in Fig. 10, when the dimensional ratio is about 0.96, α and β approach zero. The dimensional ratio becomes larger than the conventional one. This is why, by arranging the supporting portions connected at the ends of the vibrational portion, the length-extensional vibration of the sub-vibration is suppressed a little as compared with that of the conventional rectangular resonators. In other words, the sub-vibration becomes lower than the conventional one. Therefore, in order for temperature coefficients α , β to approach to zero, the resonant frequency between the fundamental vibration and the sub-vibration must approach each other. This experimental result is in firm agreement with theoretical prediction.

Fig. 11 shows the temperature coefficient α versus the dimensional ratio (R) when the dimensions of the supporting portions are changed. The sign E in Fig. 11 is the curve for a quartz resonator having the dimension of the supporting portions shown in Fig. 4, and the sign F is the curve for a quartz resonator in which the dimensions of the bridge portions and the attenuate ones are larger than those of the one in Fig. 4. Since the length-extensional vibration of the quartz resonator F is suppressed more than that of the quartz resonator E, in order to make the first order temperature coefficient α of the quartz resonator F approach zero, its dimensional ratio R must be larger than that of the quartz resonator E. And furthermore, as shown in Fig. 11 the change of α versus R at the dimensional ratio $w/L=0.96$ is expressed by the following equation (3):

$$\frac{\partial \alpha}{\partial R} = 1.7 \text{ ppm}/^\circ\text{C}/\% \dots\dots\dots (3)$$

This value is small in comparison with that of the conventional rectangular GT cut quartz resonator, which has a value of 2.4 to 2.5 ppm/°C/%, and so the dependence of the first order temperature coefficient versus the dimensional ratio is eased up. The dimensional ratio R is one factor in representing intensity of the coupling between a width-extensional vibration and a length-extensional vibration. However, taking into consideration that the quartz resonator is to be formed by a photolithographic process, as a still more practical way of showing the intensity of the coupling between them we have adopted δ together with the dimensional ratio R, and it is defined as follows:

$$\delta = (f_H - f_L) \times 100 / f_H \dots\dots\dots (4)$$

where, f_H : high resonant frequency for (A) mode in Fig. 6.

f_L : low resonant frequency for (C) mode in Fig. 6.

Fig. 12 illustrates the change of δ versus R, in which the dots are experimentally measured values and the solid line is a calculated value determined by the finite element method. The experimental result is in good agreement with the theoretical prediction. Fig. 13 shows the experimental results of temperature coefficients of the first order and the second order (α, β) versus the factor δ . The change of α versus δ at $\delta = 10\%$ is approximately expressed by the following equation (5):

$$\frac{\partial \alpha}{\partial \delta} = -2.19 \text{ ppm}/^\circ\text{C}/\% \dots\dots\dots (5)$$

Investigation of Cut Angle

Fig. 14 illustrates the experimental results of three temperature coefficients (α, β, γ) for a GT cut quartz resonator having a dimensional ratio $w/L=0.96$ and thickness $t=50 \mu\text{m}$. There are two cut angles ϕ , 52.5° and 55.5° , for which the first order temperature coefficient is almost zero. The temperature coefficients of the second order and the third order (β, γ) are as follows when the cut angle ϕ is about 52.5° :

$$\begin{aligned} |\beta| &< 2 \times 10^{-9} / ^\circ\text{C}^2 \dots\dots\dots (6) \\ |\gamma| &< 5 \times 10^{-12} / ^\circ\text{C}^3 \end{aligned}$$

Then, the sensitivity of the first order temperature coefficient (α) versus cut angle ϕ at $\phi=52.5^\circ$ is as follows:

$$\frac{\partial \alpha}{\partial \phi} = 0.9 \times 10^{-6} / ^\circ\text{C}/\text{deg} \dots\dots\dots (7)$$

Investigation of Thickness

Figs. 15 and 16 show the relationship between the temperature coefficients (α, β) and thickness respectively. Both the temperature coefficients have nothing to do with the thickness, when the thickness is less than $70 \mu\text{m}$. Namely:

$$\frac{\partial \alpha}{\partial t} = \frac{\partial \beta}{\partial t} = 0 \dots\dots\dots (8)$$

Therefore, the thickness of a quartz resonator is determined so as to avoid unwanted spurious vibrations which are dependent upon the thickness, and, moreover, so as to take the processing accuracy of the photolithographic process into account.

Characteristics

We have manufactured resonators, for example, the width, length (not including supporting portions), thickness and cut angle of which have values of 1.41mm, 1.47mm, 0.07mm (a dimensional ratio 0.96) and 53° respectively, and have experimentally examined their various electrical characteristics. The quartz resonator is firmly mounted on the pedestal by adhesive and is enclosed in a vacuum. The main characteristics of this design are summarized as follows:

- (1) frequency: 2.3MHz
- (2) motional capacitance: 2.5fF
- (3) quality factor: 200 to 300 $\times 10^3$
- (4) series resistance: 110 Ω
- (5) frequency temperature coefficients: $\alpha : 1 \times 10^{-8} / ^\circ\text{C}$
 $\beta : 4.5 \times 10^{-12} / ^\circ\text{C}^2$

Furthermore, the experimental results show three noteworthy features:

- (1) The relationship between the width to length ratio and cut angle remarkably differs from that of the well-known GT cut quartz resonator. For a dimensional ratio of about 0.93 to 0.98 and a cut angle of about 52° to 60° all three temperature coefficients are almost zero, yielding excellent frequency-temperature characteristics.
- (1i) The temperature coefficients differ markedly from those of the well-known GT cut quartz resonators; namely, the temperature of the inflection point is lowered and the frequency shift is less than four parts per million within the temperature range of -30°C to $+70^\circ\text{C}$.
- (1ii) The temperature coefficients in relation to the width to length ratio is decreased. It is therefore easy to process the quartz resonator.

Fig. 17 shows an experimental example of the frequency-temperature characteristics of a new GT cut quartz resonator together with that of an AT

cut quartz resonator and a +5°X-cut quartz resonator of the tuning fork type. It has experimentally been confirmed that frequency-temperature characteristics are changed remarkably by changes in the shape, size and cut angle of a quartz resonator.

Crystal Unit

Photo 1 shows an oscillator, which has a length of 6.0mm, a width of 3.2mm, and a thickness of 0.8mm, developed by us, in which a resonator having the above-mentioned electrical characteristics is housed.

Conclusion

In this paper, the GT cut quartz resonator described has been analyzed by the finite element method. The vibrational portion and supporting portions of the quartz resonator are one-body-formed by a photolithographic process, and the shape of the supporting portions is greatly improved. As a result, the energy losses caused by vibrations at the supporting portions are extremely reduced and so it is possible to miniaturize this quartz resonator easily. It has been found that it is possible to obtain excellent frequency-temperature characteristics with the conventional GT cut quartz resonator, even if the supporting portions are connected and added to the vibration portion of the quartz resonator, by properly combining the dimensional ratio and cut angle of the quartz resonator. By adding the supporting portions, the dependence of the frequency-temperature characteristics to the dimensional ratio is eased up. Therefore, it becomes easy to manufacture this quartz resonator. This quartz resonator not only receives great attention as a resonator for wrist watches, but also is applicable to other electronic instruments.

The shape for the quartz resonator in this study is applicable to other contour vibration modes, such as a pure width-extensional resonator, and will also be applicable to still other types of quartz resonators.

Acknowledgements

The authors would like to thank Messrs. Kubota, Watanabe, Ebiyara, and Kai for their help and encouragement, and in particular, to thank Mr. Osawa and other many people for their help in the experimental work leading to the realization of the GT cut quartz resonator.

References

- 1) W.P.Mason; "A New Quartz-Crystal Plate, Designated the GT", Proc. I.R.E., PP220-223, 1940
- 2) R.Bechmann; "Contour Mode of Square Plate

excited piezoelectrically and Determination of Elastic and Piezoelectric Coefficients", Proc. Soc (London), B, PP323-337, 1951

3) M. Nakazawa, "Analysis on the GT Quartz crystal Vibrator", IEE. Japan, US76-6 PP7-12, 1976

4) A.E.Zumsteg and P.Suda; "PROPERTIES OF 4MHZ MINIATURE FLAT RECTANGULAR QUARTZ RESONATOR VIBRATING IN A COUPLED MODE" Proc. 30th AFCS, pp196-201 1976

5) S. Yamashita, et al.; New Frequency-Temperature Characteristics of 4.19MHz Beveled Rectangular AT-cut Quartz, Proc. 33rd AFCS, pp277-285, 1979

6) E.Momomaki et al.; New Quartz Tuning Fork with Low Temperature Coefficient, Proc. 33rd AFCS, pp247-254, 1979

7) K.Oguchi et al.; Proc. 32nd AFCS, pp277, 1978

8) NASTRAN LEVEL 15.6, Theoretical Manual Additions NASA

9) H.Sato and O.Ochiai; Technical Report of Daini Seikosha Co., Ltd. (unpublished)

10) R.Bechmann, A.D.Ballato, and T.J.Lukaszek: High-Order Temperature Coefficients of the Elastic Stiffness and Compliances of Alpha-Quartz proc. IRE. 1962

11) For example, U.S.Patent 4139793

12) M.Ariger,Bull. Tokyo Inst. Tech.A-No.2, 1956 Piezoelectric Coefficients. Proc.phys.Soc.(London), B, pp323-, 1951

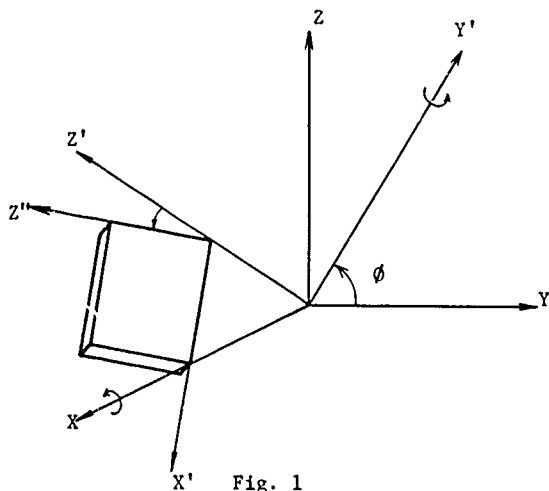


Fig. 1 shows a coordinate system, in which cut angle $yxwt(\phi/\theta)$ and a quartz plate of a GT cut quartz resonator are illustrated.

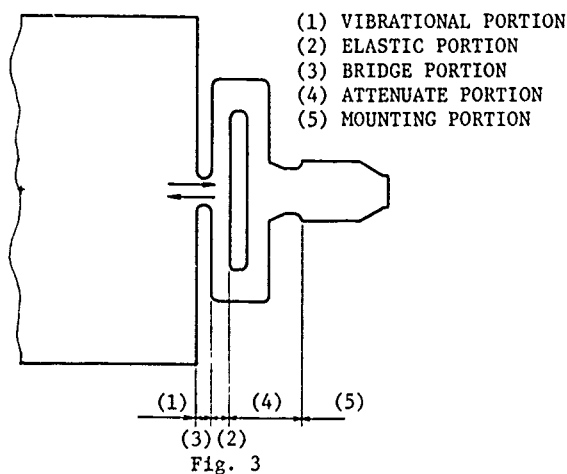


Fig. 3 shows enlarged detail of the supporting portion of the quartz resonator described in Fig. 2.

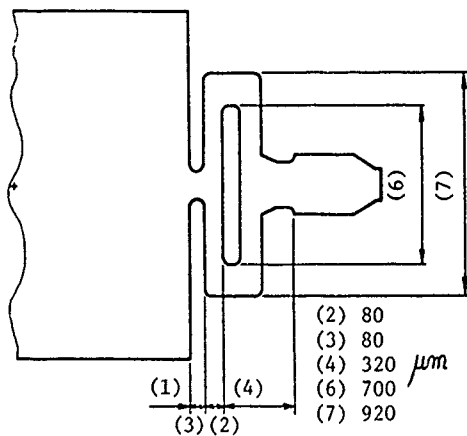


Fig. 4 shows an example of the shape and size obtained by an analysis of the finite element method.

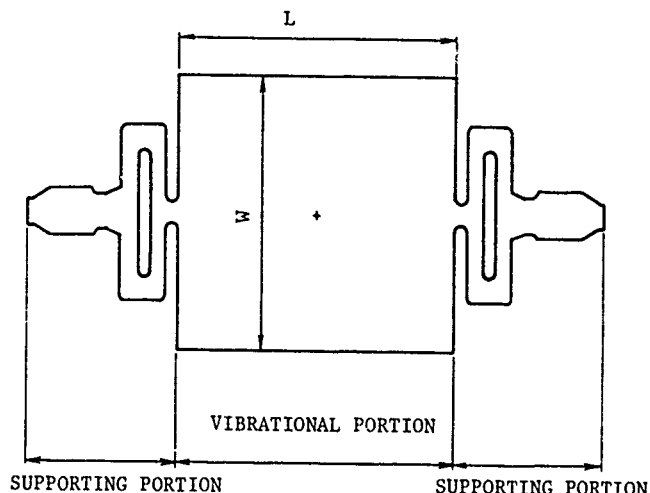
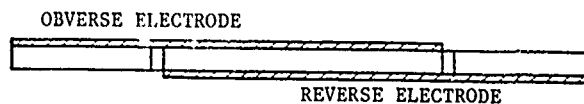


Fig. 2

Fig. 2 shows a concrete shape and electrode disposition of a GT cut quartz resonator consisting of a vibrational portion and supporting portions.

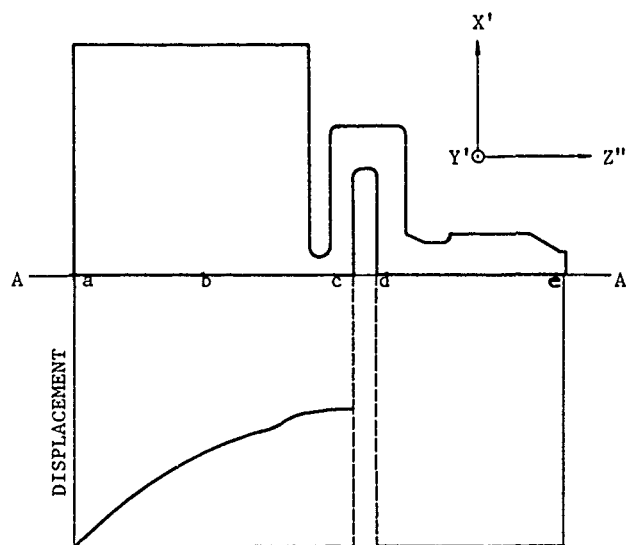


Fig. 5

Fig. 5 shows distribution of displacement on A-A line of a GT cut quartz resonator analyzed by the finite element method.

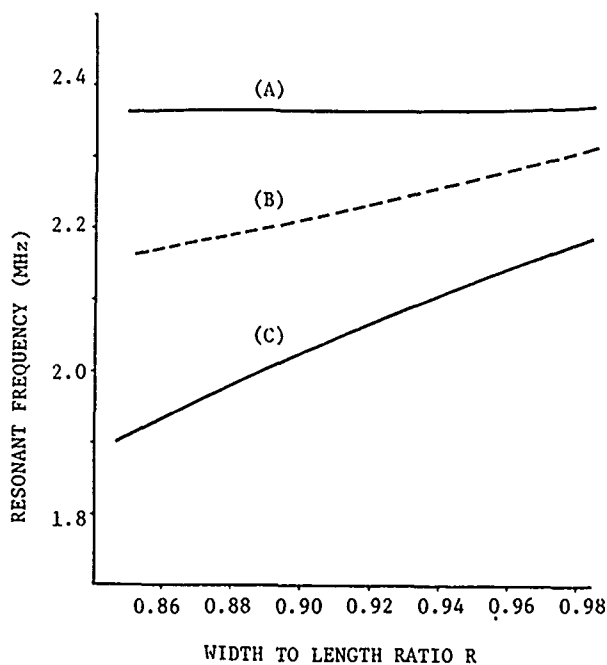


Fig. 6

Fig. 6 shows a mode chart for the quartz resonator illustrated in Fig. 4.

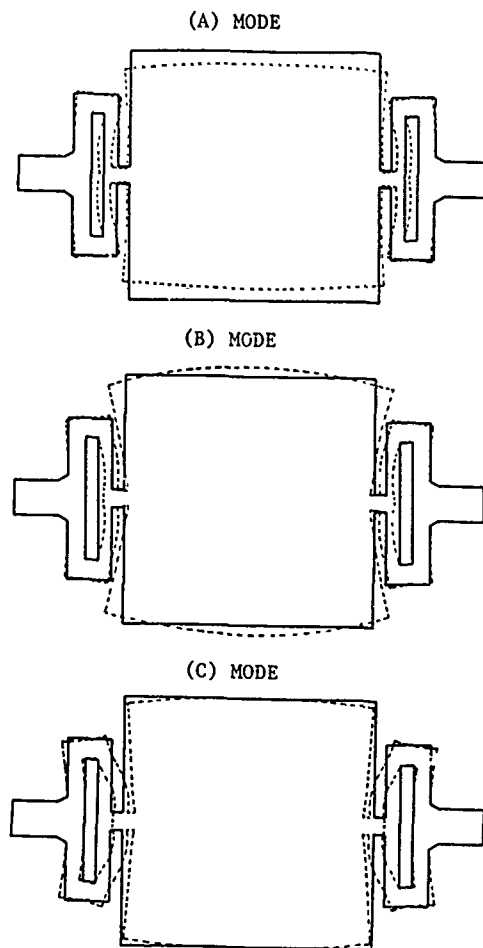


Fig. 7

Fig. 7 shows vibrational distortion for three modes (A), (B), (C) of the GT cut quartz resonator in Fig. 4.

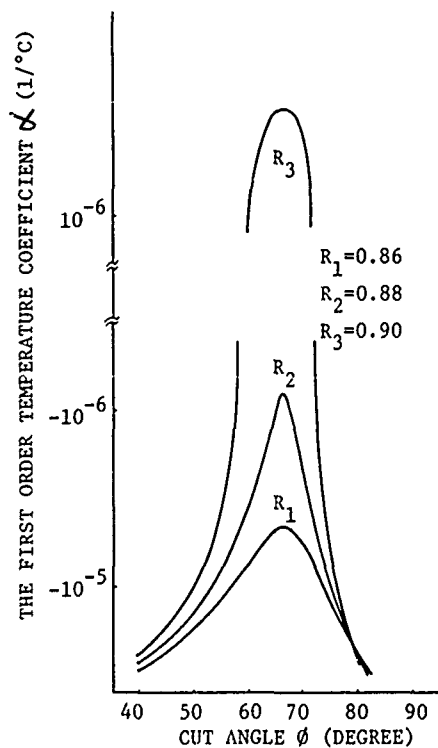


Fig. 8

Fig. 8 shows the relationship between the first order temperature coefficient and cut angle versus the width to length ratio R_1 of the rectangular GT cut quartz resonator.

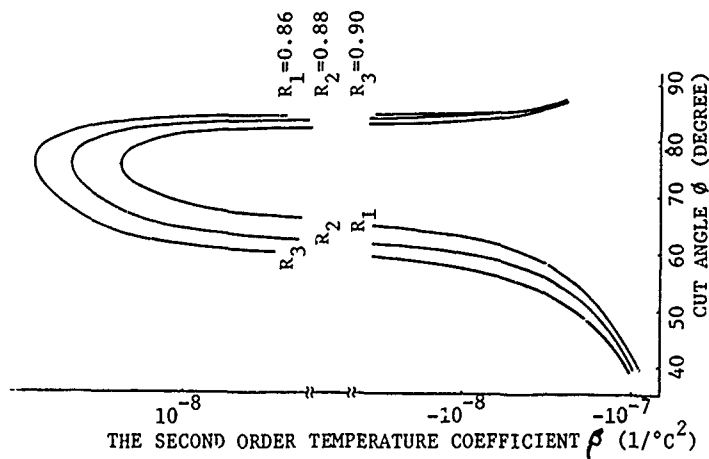


Fig. 9

Fig. 9 shows the relationship between the second order temperature coefficient and cut angle versus the width to length ratio R_1 of the rectangular GT cut quartz resonator.

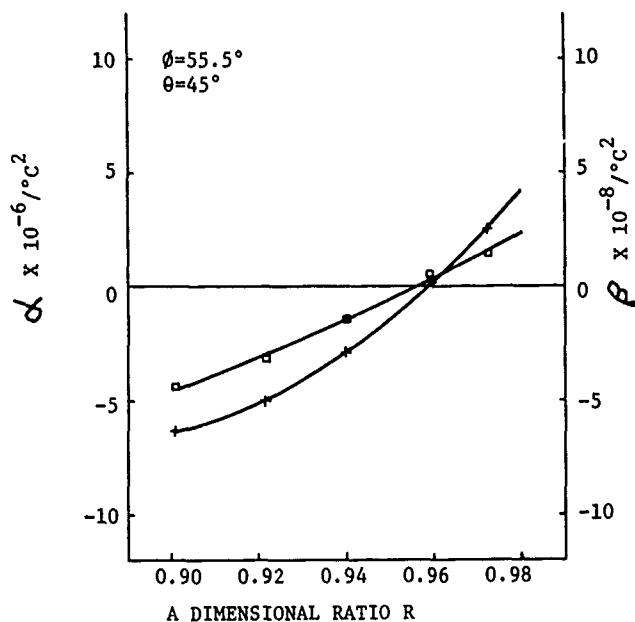


Fig. 10

Fig.10 illustrates the relationship between a dimensional ratio R and temperature coefficients (α, β) at 20°C.

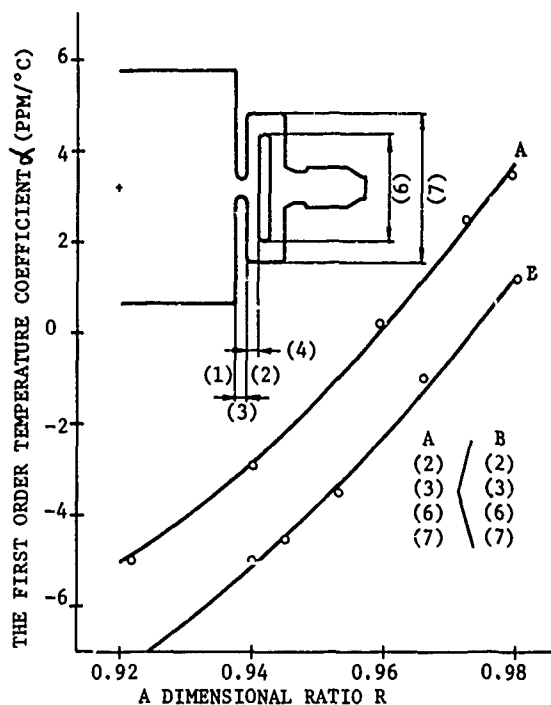


Fig. 11

Fig. 11 shows the relationship between temperature coefficient and dimensional ratio R versus the change of supporting portions

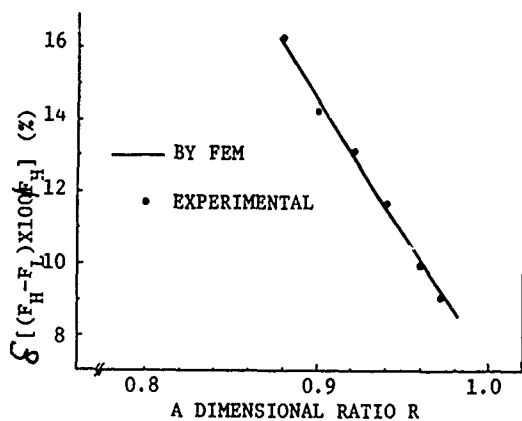


Fig. 12

Fig. 12 illustrates the relationship between δ and R of a quartz resonator calculated by FEM, and obtained by the experiment.

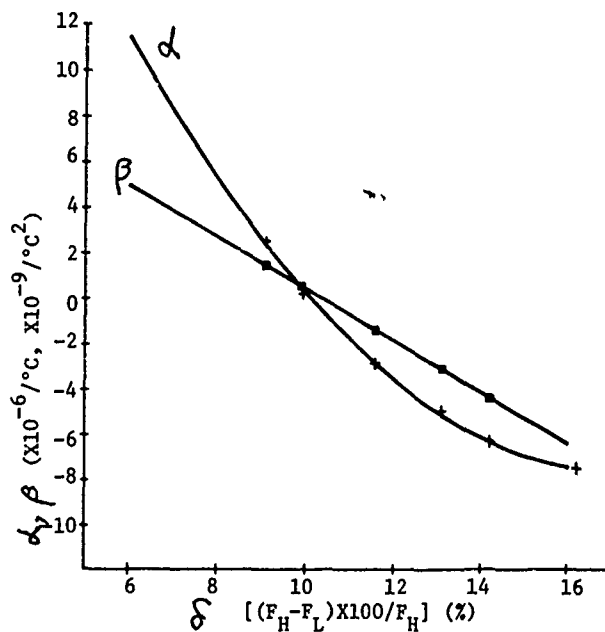


Fig. 13

Fig. 13 shows the experimental results of temperature coefficients of the first order and second order ($d_y \beta$) versus the factor

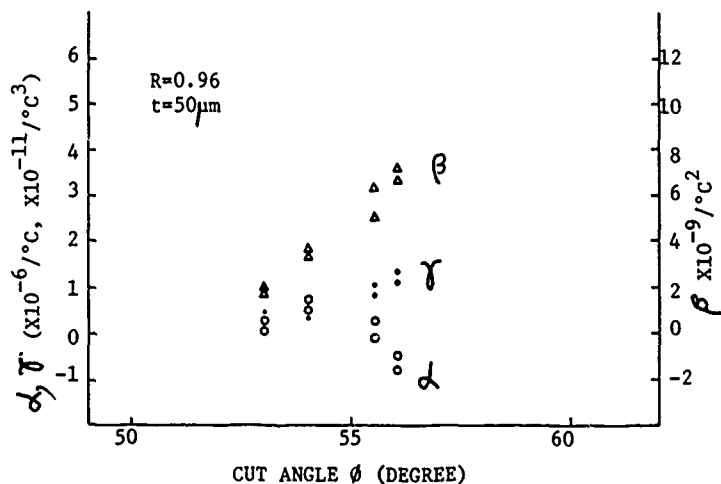


Fig. 14

Fig. 14 illustrates the experimental results of three temperature coefficients (α, β, γ) versus cut angle.

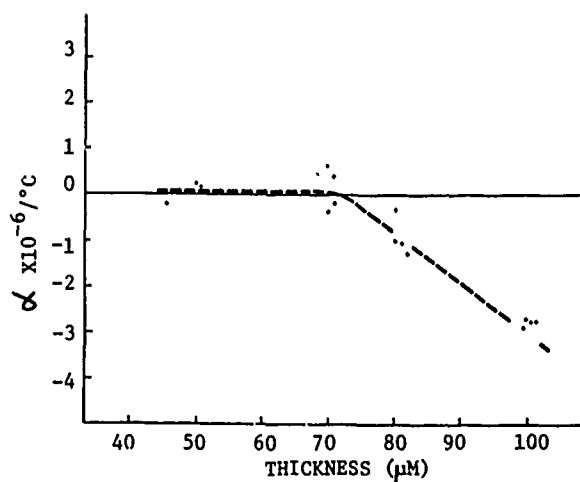


Fig. 15

Fig. 15 shows the first order temperature coefficient versus thickness

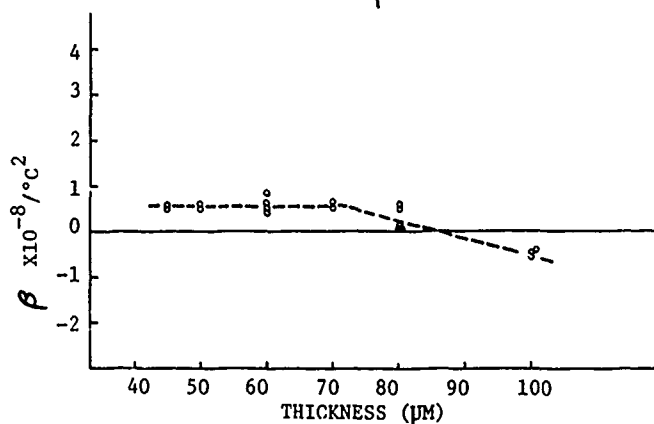


Fig. 16

Fig. 16 shows the second order temperature coefficient versus thickness.



Photo 1 shows an oscillator developed by us.

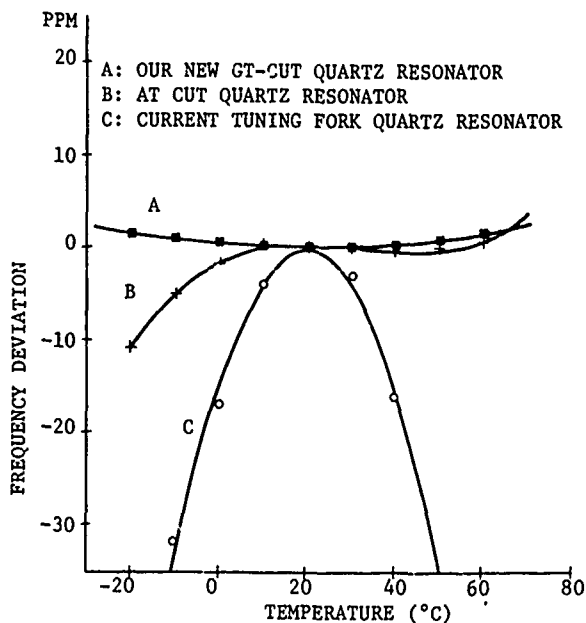


Fig. 17

Fig. 17 shows an experimental example of frequency-temperature characteristics of a new GT cut quartz resonator together with that of an AT cut quartz resonator and a +5°X-cut quartz tuning fork resonator.

FREQUENCY TEMPERATURE BEHAVIOR OF MINIATURIZED
CIRCULAR DISK AT-CUT CRYSTAL RESONATOR

Yoshimasa Oomura

Faculty of Technology
Tokyo Metropolitan University
Setagaya, Tokyo, JAPAN

Summary

The requirement for the practical application of miniaturized AT-cut crystal resonator, of which frequency temperature behavior is cubic curve, has increased in accordance with the development of miniaturization of electronic components. The ratio of diameter to thickness of the conventional circular disk AT-cut plate is usually more than 15, but the ratio of miniaturized one described in this paper is ranged from 4.338 to 4.683; (diameter: from 6.329 mm to 6.832 mm, thickness: 1.457 or 1.459 mm, resonance frequency: about 1.2 MHz).

The cut angle of specimen is decided by the coupling modulus g , which is the ratio of the thickness shear modulus to the plate flexure modulus. The frequency temperature behavior of different cut angle was measured. With changing the diameter of specimen, the same measurement was also carried on.

The inflection temperature and a very little change in resonance frequency within wide temperature range are discussed by the experimental results.

Introduction

The miniaturized crystal resonator, of which shape is almost the tuning fork type, has been put into practice in the industry of wrist watch in compliance with the development of miniature electronic components.

Owing to the electrical behaviors of the tuning fork crystal resonator, the temperature compensating circuit and the combination of twin quartz crystals are necessary for keeping accuracy.

The miniaturized crystal resonator, which shows the frequency temperature behavior of cubic curve, has been urged by recent development of application of IC and LSI. Recently the tuning fork type crystal resonator with cubic frequency temperature behavior has been produced, and its resonance frequency is approximately 100KHz.

The miniaturization of AT-cut crystal plate, on the other hand, has been studied, and a bar type resonator and a biconvex bar type resonator have been put into practical use at resonance frequency of about 4.19MHz. The small size circular disk AT-cut crystal resonator had been already reported at the 30th Annual Symposium on Frequency Control.

Present paper is concerned with its frequency temperature behavior. The following subjects are described in this paper.

1) Although the ratio of diameter to thickness is small, the cubic characteristics in frequency temperature behaviors have been obtained by the proper combination of cut angle and ratio.

2) A very little change in the resonance frequency is found within wide temperature range (e.g. about from -10°C to 40°C).

3) The second order temperature coefficient of frequency shows negative value in case of cut angle $4^{\circ}15' \sim 5^{\circ}10'$, positive value in case of $6^{\circ}55' \sim 7^{\circ}30'$ and almost zero at $6^{\circ}50'$.

4) The inflection temperature is changed between 50°C and -10°C by the adequate selection of both cut angle and ratio of diameter to thickness.

Decision of the ratio of diameter to thickness

The chart, which shows the relation between the resonance frequency and the ratio of diameter to thickness of the disk, is basically necessary for the design of the circular disk crystal resonator. A part of the chart obtained from the experiment is shown in Fig.1. It is understood from Fig.1 that only dominant frequency response is appeared within the ratio of 4.300 \sim 4.800.

The designed ratio in this paper is decided to be 4.338 \sim 4.683 by the chart.

The specimen is obtained by polishing its diameter by a few micron meter without decreasing its thickness, that is to say, the thickness is 1.459 or 1.457 mm.

Specimen for measurement

When the circular disk AT-cut crystal resonator is miniaturized by polishing its diameter, the fundamental resonance frequency response contains the coupling between thickness shear mode and flexural mode.

The coupling modulus between thickness shear mode and flexural one is explained in Ref. (2) and it is expressed by formula (1),

$$g = \frac{\pi^2 C_{66}}{12 (C_{11} - C_{12}^2 / C_{22})} \quad (1)$$

where $\pi^2 C_{66} / 12$ is the thickness shear modulus, $(C_{11} - C_{12}^2 / C_{22})$ is the flexural modulus, and g is the coupling modulus.

The value of g varies in accordance with the variation of elastic constants depending on cut angle. Fig.2 shows the variations of thickness shear modulus, the flexural modulus and the coupling modulus g normalized at the value of cut angle $2^\circ 58'$ from Z-minor face. The minimum value of g corresponds to approximately $6^\circ 50' \sim 6^\circ 55'$, and in this part the thickness shear modulus also is almost minimum value, on the other hand, the value of flexural modulus (denoted by S in Fig.2) increases with cut angle. The value of g between $4^\circ 15'$ and $5^\circ 10'$ is declining, but the minimum value of g appears in the range of $6^\circ 50' \sim 7^\circ 30'$. Two groups of cut angle, i.e. $4^\circ 15' \sim 5^\circ 10'$ and $6^\circ 50' \sim 7^\circ 30'$, are chosen for the specimen.

The each specimen was gradually polished its diameter, and its frequency temperature behavior was measured by the π network system as shown in Fig.3. Fig.4 shows the construction of air gap type holder used in measurement. The picture of air gap type holder is shown in Fig.5. The crystal current was held to be 0.2mA during measurement.

Experimental results

The frequency temperature behaviors for crystals of various cut angles from Z-minor face were measured at constant ratio 4.677. Fig.6 shows the experimental results. It is shown in Fig.6 that the resonance frequency scarcely changes in the range of $45^\circ \text{C} \sim 55^\circ \text{C}$ at cut angle $4^\circ 15'$. Although the ratio of diameter to thickness is 4.677, the frequency temperature behavior is shown by cubic curve.

Fig.7 (a) \sim (n) show the experimental results of the frequency and the crystal impedance (CI) - temperature behaviors. The frequency temperature behaviors were measured, when the specimen's diameter was changed by polishing.

It is shown in Fig.7 (c) and (1) that a little change in the resonance frequency is found within wide temperature range, e.g. $20^\circ \text{C} \sim 70^\circ \text{C}$ at the ratio 4.635 and $-10^\circ \text{C} \sim 40^\circ \text{C}$ at the ratio 4.362 respectively.

If a proper selection between cut angle and ratio of diameter to thickness is made in case of another cut angle, it is expected by Fig.7 that same characteristics as mentioned above in the wide temperature range will be obtained.

Discussion

The frequency temperature behavior of piezoelectric resonator depends on cut angles, ratio of dimension, order of overtone, shape of plate, and type of mounting.³ The dependence of both cut angle and ratio of dimension on the frequency temperature

behavior has been mainly studied by experimental results in this paper. The measured frequency, f , of a miniaturized circular disk crystal resonator as a function of the temperature, T , can be developed in power series in the vicinity of the frequency, f_0 , at the arbitrary temperature, T_0 , shown as formula (2),

$$\frac{f - f_0}{f_0} = \frac{\Delta f}{f_0} = A(T - T_0) + B(T - T_0)^2 + C(T - T_0)^3 + \dots \quad (2)$$

where A , B , and C are the first, second, and third-order temperature coefficients of frequency.

The temperature coefficient of the frequency, Tf , is given by formula (3),

$$Tf = \frac{1}{f_0} \cdot \frac{\partial f}{\partial T} = A + 2B(T - T_0) + 3C(T - T_0)^2 \quad (3)$$

Temperature coefficients of the frequency Tf

Fig.8 (a) \sim (f) show the relations between Tf and temperature with changing the ratio of diameter to thickness at the cut angle from $4^\circ 15'$ to $5^\circ 10'$. Fig.9 (a) \sim (f) show same relations ranging from $6^\circ 50'$ to $7^\circ 30'$ in order to compare with Fig.8.

The inflection temperature corresponding to the minimum value of Tf increases gradually with decreasing the ratio of diameter to thickness as shown in Fig.8. But, the inflection temperature in Fig.9 decreases except for $6^\circ 50'$. Tf value at small frequency change within wide temperature range is nearly equal to zero.

The reproducibility of the experimental result was taken into consideration by another polished specimen. Fig.10 shows the reproducibility of frequency temperature behavior. The reliability of experimental results is considered to be good by comparing Fig.7 (c) with Fig.10.

The first, second, and third order temperature coefficients

Fig.11 (a) \sim (f) are the relations between the first, second, and third order temperature coefficients of frequency and the ratio at each cut angle ranging from $4^\circ 15'$ to $5^\circ 10'$, and Fig.12 (a) \sim (f) are the same relations ranging from $6^\circ 50'$ to $7^\circ 30'$.

The second order temperature coefficient B in Fig.11 has negative values; increasing the ratio of diameter to thickness the values of B decrease at $4^\circ 15'$ and $4^\circ 20'$; keep approximately constant at $4^\circ 30'$ and $4^\circ 40'$; increase at $5^\circ 00'$ and $5^\circ 10'$.

On the other hand, the B values in Fig.12 are positive, and decrease with increasing the ratio.

The inclinations of the first, second, and third order temperature coefficients with the ratio in Fig.12 are larger than those in Fig.11.

Inflection temperature

The inflection temperature T_p is obtained by the next formula (4),

$$T_p = -\frac{B}{3C} + T_0 \quad (^\circ\text{C}) \quad (4)$$

where B, C are same as formula (2), T_0 is 25°C .

It is obvious from Fig.7 (a) ~ (h) and Fig.8 (a) ~ (f) that the small size disk crystals of cut angle ranging from $4^\circ15'$ to $5^\circ10'$ show increasing inflection temperature from 40°C to 60°C with the descent of the ratio. These crystal resonators are, therefore, not suitable for watches.

The discussion on inflection temperature is restricted within cut angle from $6^\circ50'$ to $7^\circ30'$.

Fig.13 shows the relations of inflection temperature versus the ratio of diameter to thickness. The inflection temperature of the miniaturized circular disk declines with the decrease of the ratio.

If the cut angle as $7^\circ10'$ and the ratio as 4.3 62 are decided, the miniaturized circular disk crystal, of which inflection temperature is about 15°C and the change of resonance frequency is almost negligible in the wide temperature range (-10°C ~ 40°C), will be obtained.

The relation between g and manufacturing accuracy

The frequency temperature behavior is influenced by the ratio as mentioned above. The relation between the ratio and the coupling modulus g is expressed by formula (5),

$$g = \frac{A^4 - 3A^2}{3A^2 - 9(1 - (\bar{\omega}/\omega)^2)} \quad (5)$$

where $\omega > \bar{\omega}$, $A = \gamma / (d/h)(\omega/\bar{\omega})$, d : diameter, h : thickness, ω : resonance angular frequency at the arbitrary ratio of dimension, $\bar{\omega} = (C_{66}/\rho)^{1/2}\pi/h$, ρ : density of quartz crystal, γ : solution of secular equation explained in Ref. (2).

The normalized frequency varies with the ratio of diameter to thickness, and its experimental results are shown in Fig.14. Fig.15 shows the linear relation between normalized coupling modulus and ratio of diameter to thickness calculated by formula (5). Fig.16 shows the normalized coupling modulus variation with cut angle at the ratio in case of a very little change in resonance frequency. In Fig.16 point A is a calculated value at $2^\circ58'$ by formula (1), but group of points, marked B, are calculated by experimental values at 25°C .

Comparing Fig.2 with Fig.16, Fig.2 seems to be corresponded to the relation between normalized

coupling modulus and cut angle at the constant ratio, but Fig.16 is the same relation accompanied with variation of ratio.

It is obvious that the changing rate of the coupling modulus in Fig.16 is greater than that in Fig.2 by approximately 80 times for having an effect of the ratio in addition to the cut angle.

It is, therefore, desired that an accuracy less than 2 micron meter is required for polishing the diameter of miniaturizing circular disk crystal.

For example, the diameter at the ratio 4.630 as shown in Fig.7 (d) differs from that at 4.629 by approximately 1.5 micron meter, and the difference of the frequency temperature behavior between them is less than 2 ppm.

Conclusion

Generally speaking, the inflection temperature is seemed to increase with the miniaturization of the crystal resonator. But it was explained in this paper that the inflection temperature decreases in case of miniaturized circular disk crystal resonator by the adequate selection between the cut angle and the ratio of dimension to thickness, and also a very little change of resonance frequency within wide temperature range is obtained by above mentioned selection.

References

1. Y. Oomura, "Miniaturized Circular Disk AT-Cut Crystal Vibrator," Proc. 30th Annual Symposium on Frequency Control, pp. 202 - 208, 1976.
2. R. D. Mindlin and H. Deresiewicz, "Thickness-Shear and Flexural Vibrations of Circular Disk," J. Appl. Phys., Vol.25, No. 10, pp.1320 -1337, (Oct. 1954)
3. R. Bechmann, "Frequency-Temperature-Angle Characteristics of AT-Type Resonators Made of Natural and Synthetic Quartz," Proc. of the I. R. E. pp. 1600-1607, (Nov. 1956).

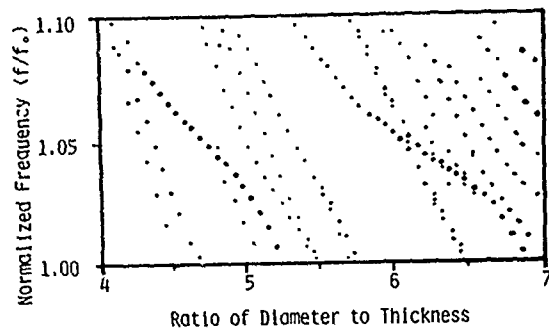


Fig. 1 - Chart of Resonance Frequency versus Ratio of Diameter to Thickness.

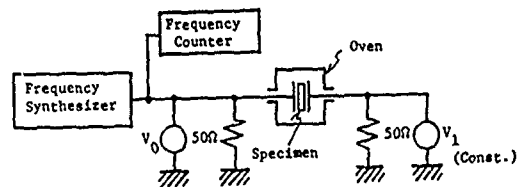


Fig. 3 - Measuring Circuit for Temperature Behavior of Resonance Frequency and Crystal Impedance (CI).

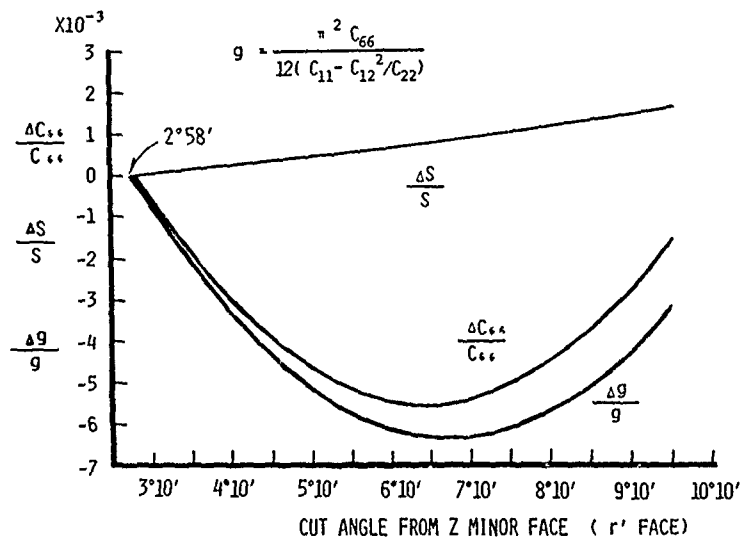


Fig. 2 - Variations of the thickness shear modulus, the plate flexure modulus and g (the ratio of the thickness shear modulus to the plate flexure modulus) with the cut angle of quartz crystal.

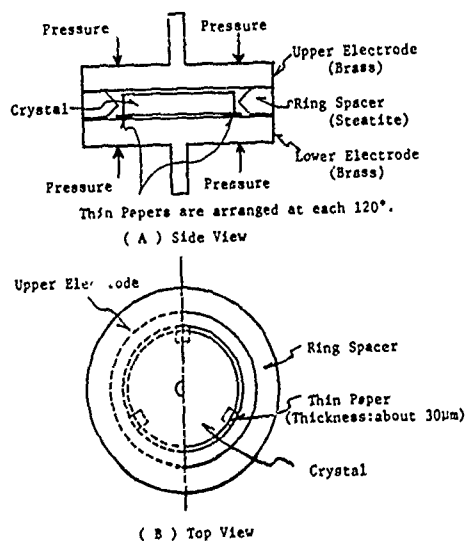


Fig. 4 - Air Gap Type Holder.

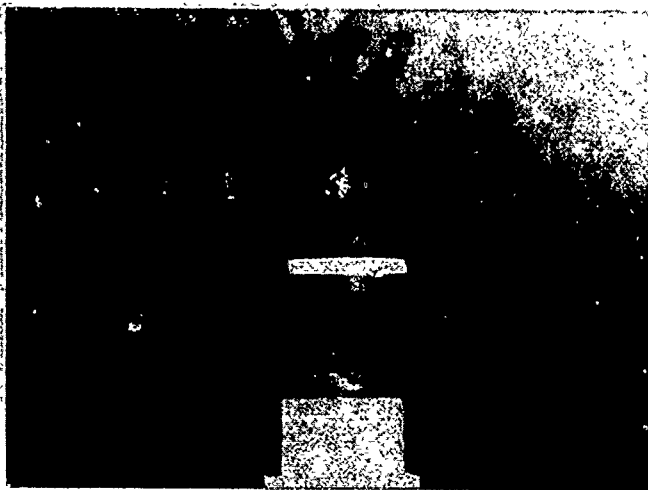


Fig. 5- Picture of Air Gap Type Holder.

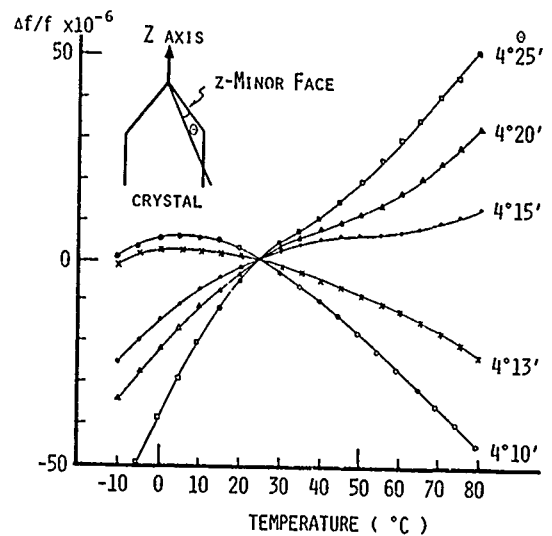


Fig. 6 - Frequency Temperature Behaviors for various Cut Angles from Z-Minor Face (Diameter:6.824mm, Thickness:1.459mm, Crystal Current:0.2mA).

Fig. 7 - (a), (b), (c), (d), (e), (f), (g), (h), (i), (j), (k), (l), (m), (n) - Frequency and Crystal Impedance-Temperature Behaviors.
 (a); Cut Angle 4°15', (b); Cut Angle 4°18', (c); Cut Angle 4°20',
 (d); Cut Angle 4°23', (e); Cut Angle 4°30', (f); Cut Angle 4°40',
 (g); Cut Angle 5°00', (h); Cut Angle 5°10', (i); Cut Angle 6°50',
 (j); Cut Angle 6°55', (k); Cut Angle 7°00', (l); Cut Angle 7°10',
 (m); Cut Angle 7°20', (n); Cut Angle 7°30'.

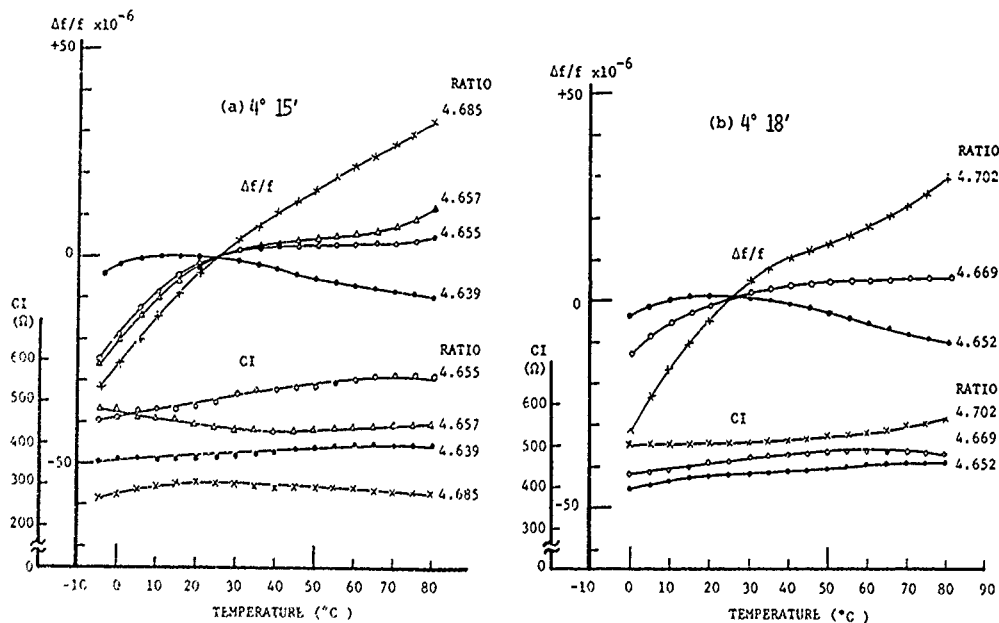


Fig. 7- (a), (b): Frequency and Crystal Impedance -Temperature Behaviors
 (a); Cut Angle 4°15', (b), Cut Angle 4°18'.

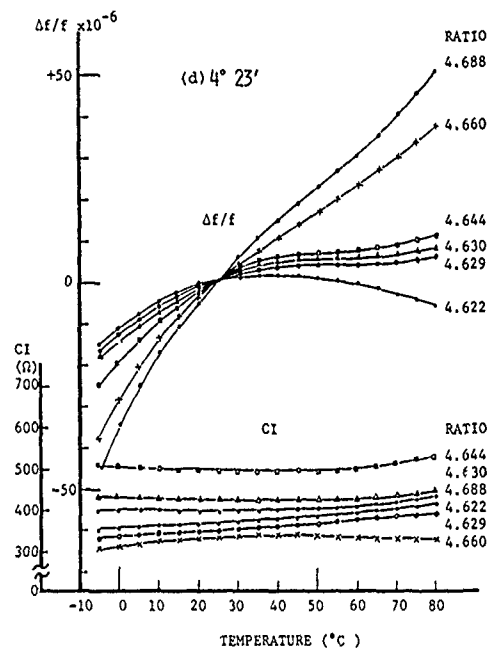
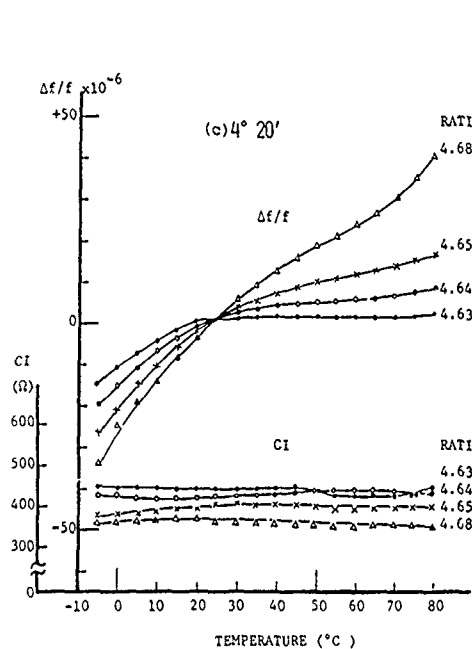


Fig. 7 - (c), (d): Frequency and Crystal Impedance - Temperature Behaviors
(c); Cut Angle $4^{\circ}20'$, (d); Cut Angle $4^{\circ}23'$.

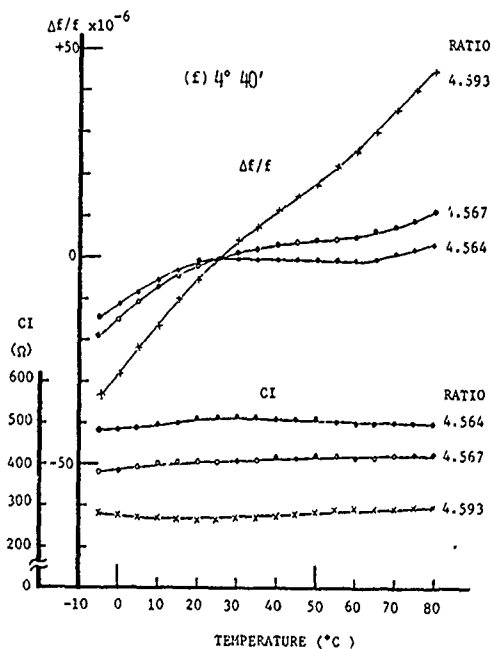
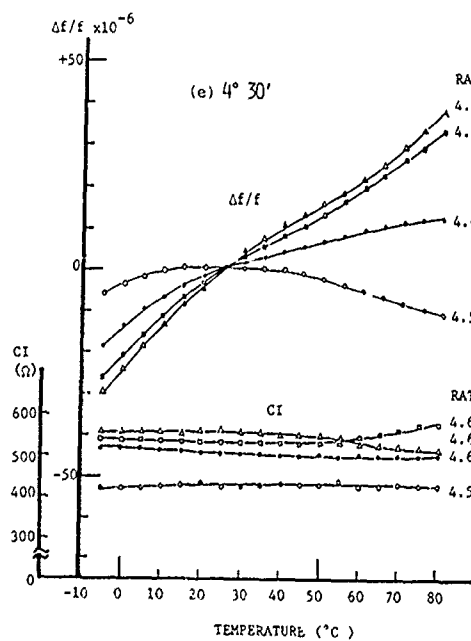


Fig. 7 - (e), (f): Frequency and Crystal Impedance - Temperature Behaviors
(e); Cut angle $4^{\circ}30'$, (f); Cut angle $4^{\circ}40'$.

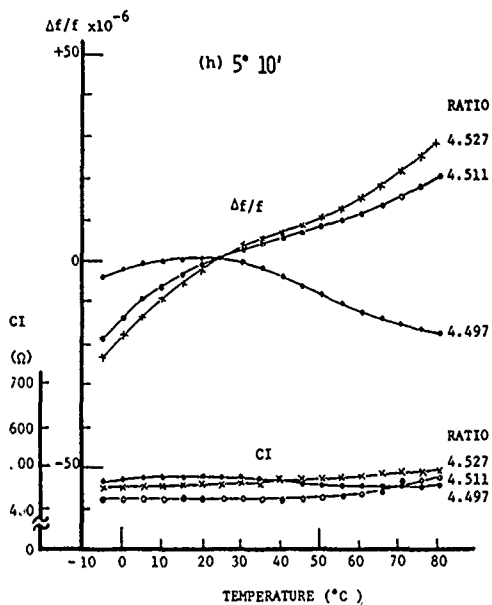
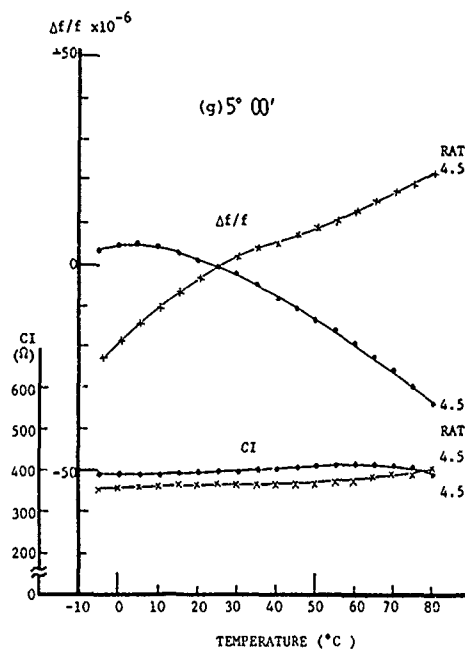


Fig. 7 - (g), (h): Frequency and Crystal Impedance - Temperature Behaviors
(g); Cut Angle $5^{\circ}00'$, (h); Cut Angle $5^{\circ}10'$.

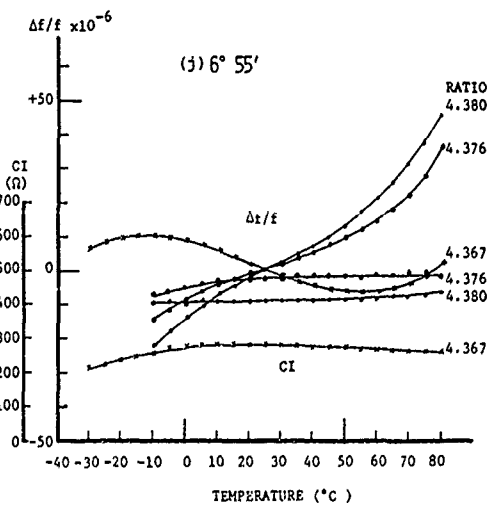
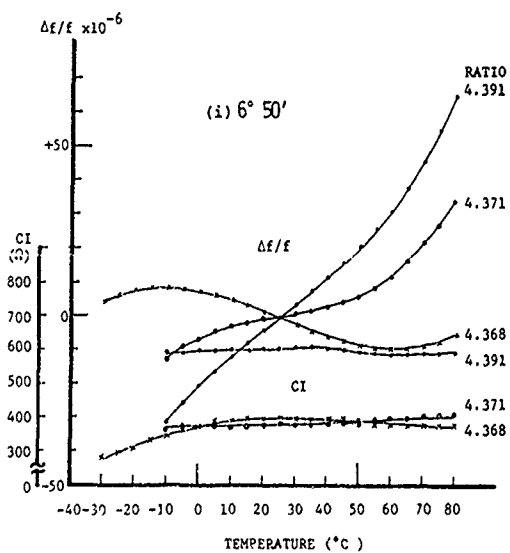


Fig. 7 - (i), (j): Frequency and Crystal Impedance - Temperature Behaviors
(i); Cut Angle $6^{\circ}50'$, (j); Cut Angle $6^{\circ}55'$.

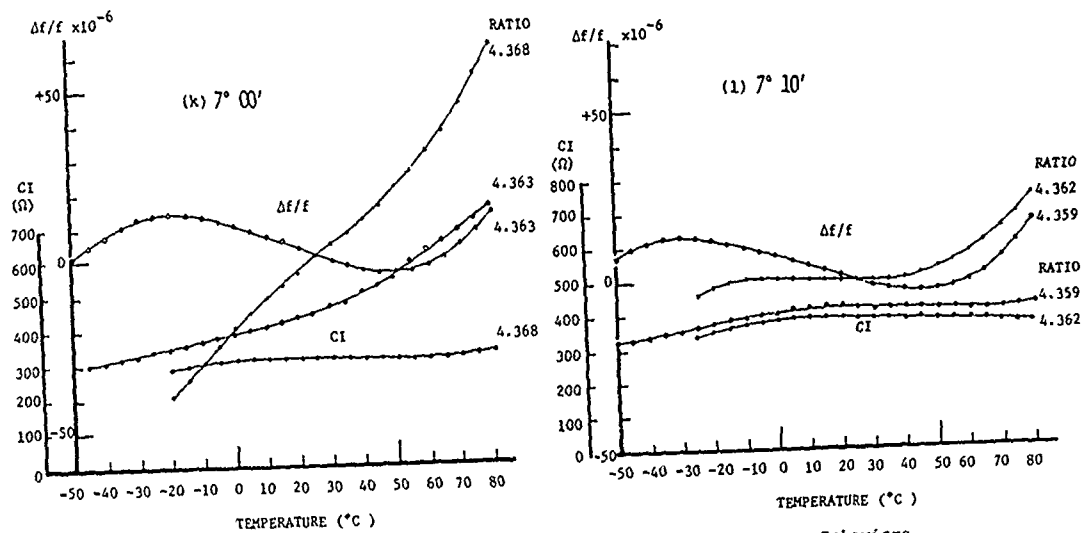


Fig. 7 - (k), (l): Frequency and Crystal Impedance -Temperature Behaviors
(k); Cut Angle $7^\circ 00'$, (l); Cut Angle $7^\circ 10'$.

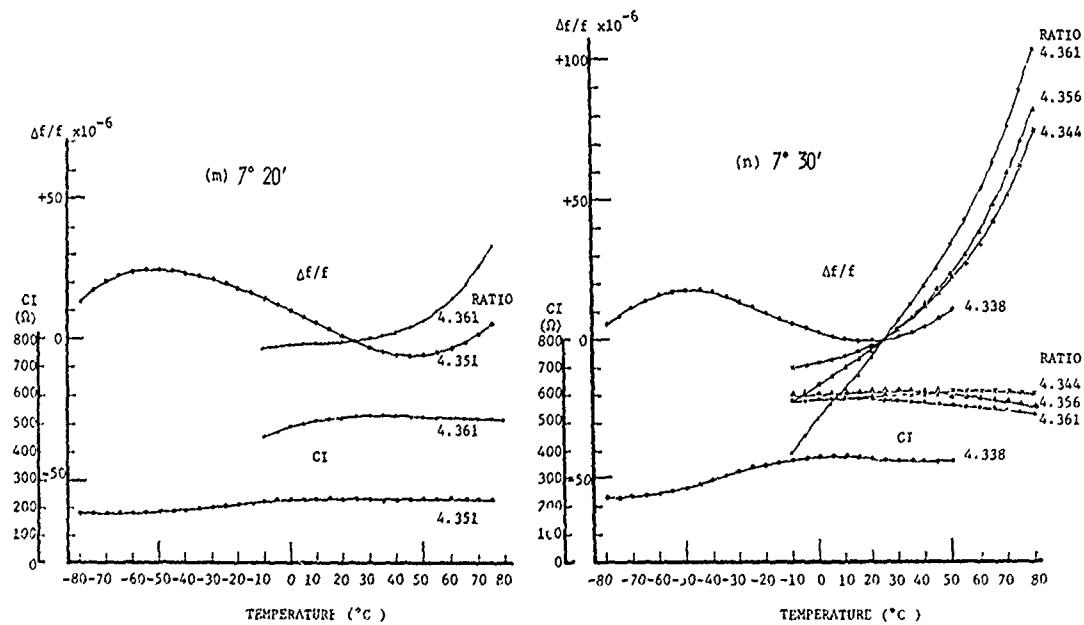


Fig. 7 - (m), (n): Frequency and Crystal Impedance -Temperature Behaviors
(m); Cut Angle $7^\circ 20'$, (n); Cut Angle $7^\circ 30'$.

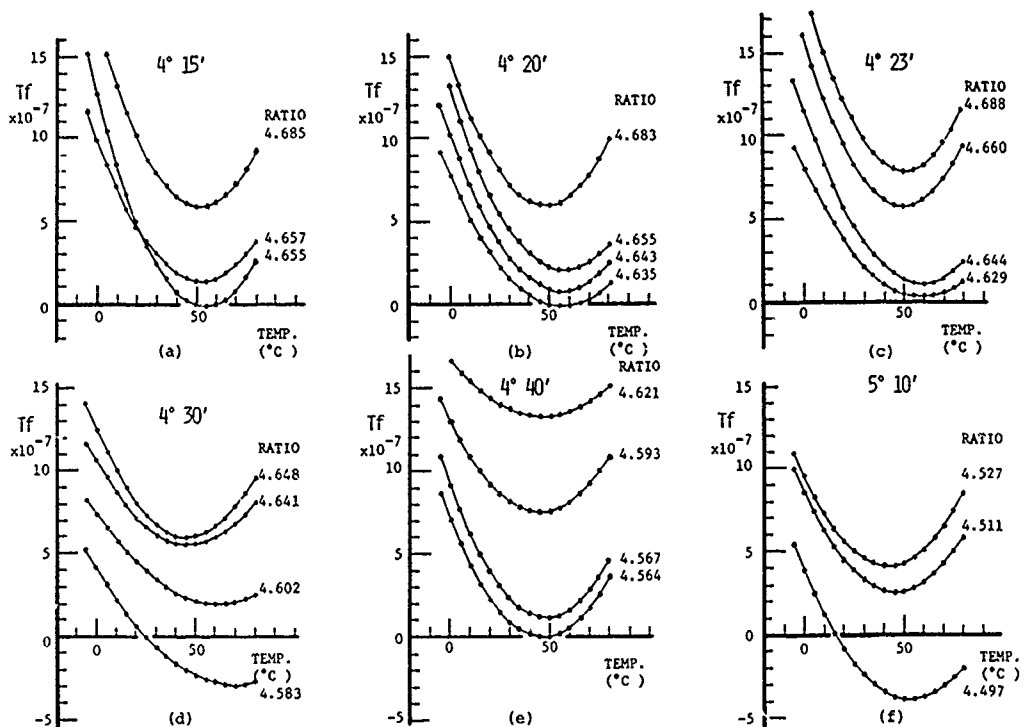


Fig. 8 - T_f versus Temperature Behavior by means of Ratio of Diameter to Thickness at each Angles.

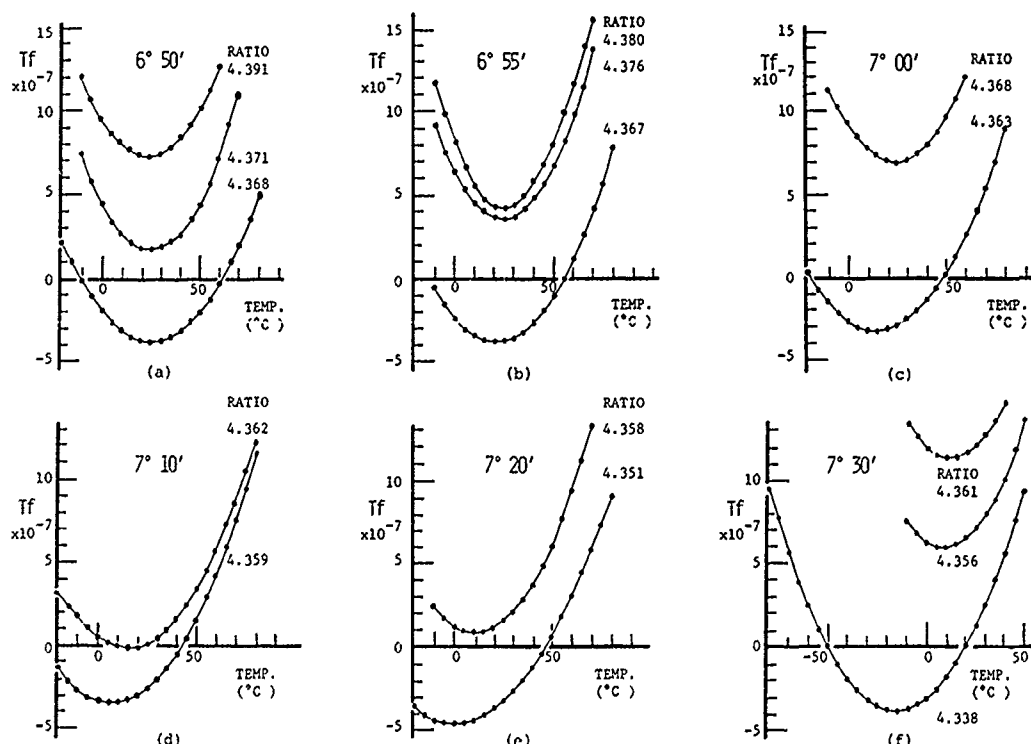


Fig. 9 - T_f versus Temperature Behavior by means of Ratio of Diameter to Thickness at each Angles

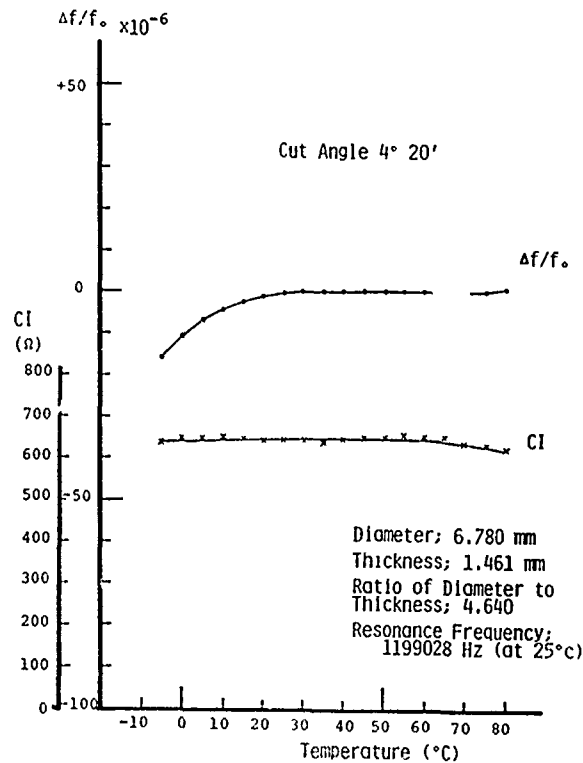
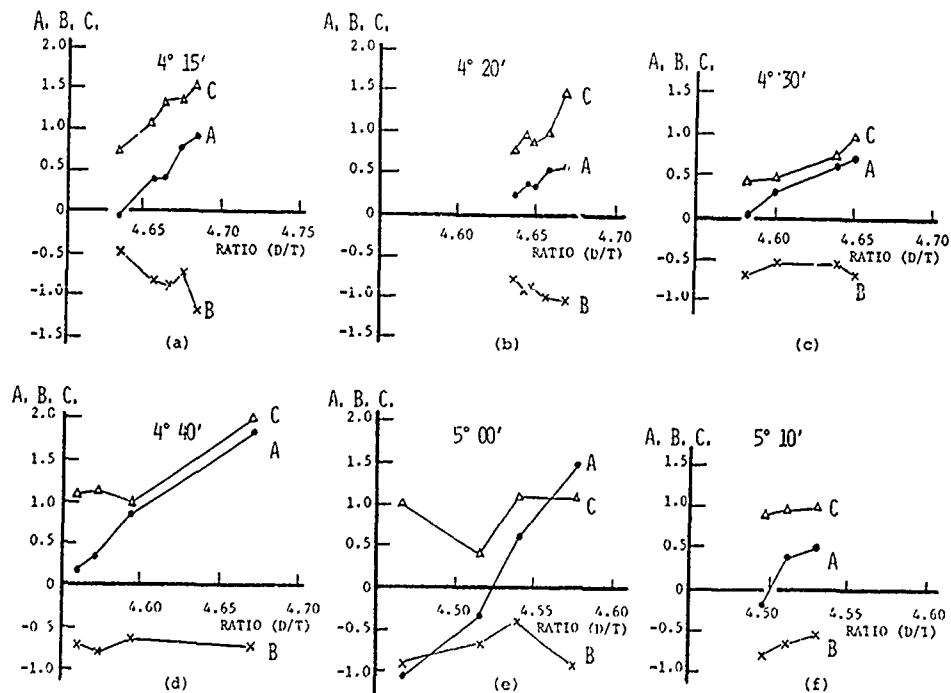


Fig. 10 - Reproducibility of Frequency Temperature Behavior at $T_f=0$ in case of Cut Angle 4°20'. Specimen's plane surface is polished by # 2000 emery, and also side surface by # 500 diamond hand stone.



A : $\times 10^{-6}$, B : $\times 10^{-8}$, C : $\times 10^{-10}$

Fig. 11 - (a)~(f): The first, second, and third order Temperature Coefficients versus Ratio of Diameter to Thickness, calculated by Experimental Result (Cut Angles are from 4°15' to 5°10').

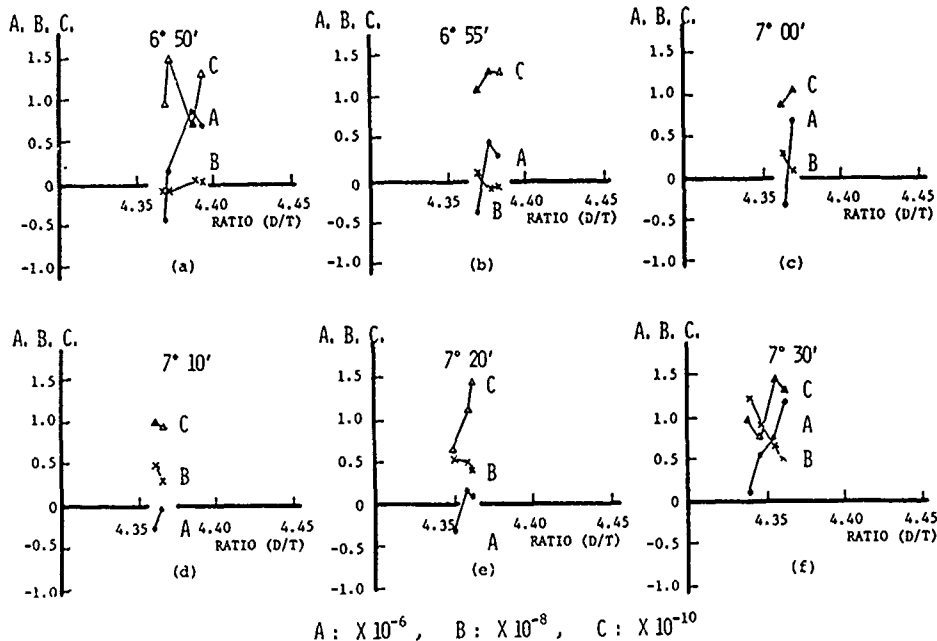


Fig. 12 - (a)~(f): The first, second, and third order Temperature Coefficients versus Ratio of Diameter to Thickness, calculated by Experimental result (Cut Angles are from 6°50' to 7°30').

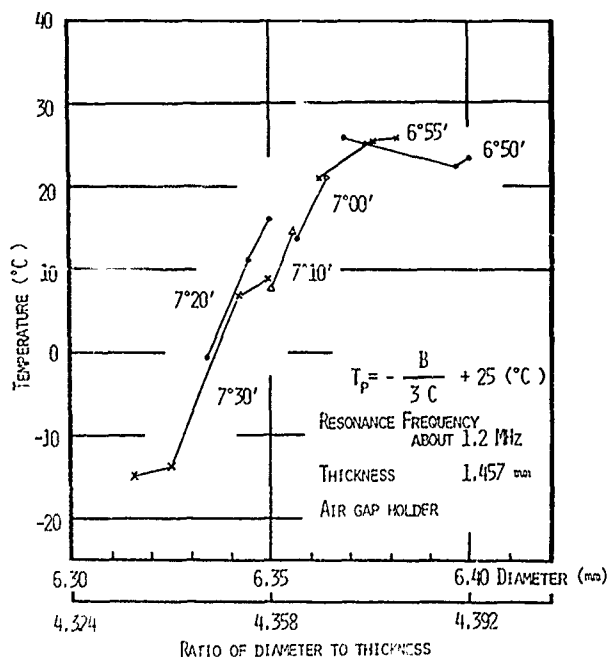


Fig. 13 - Variations of Inflection Temperature at each Cut Angles and Ratios.

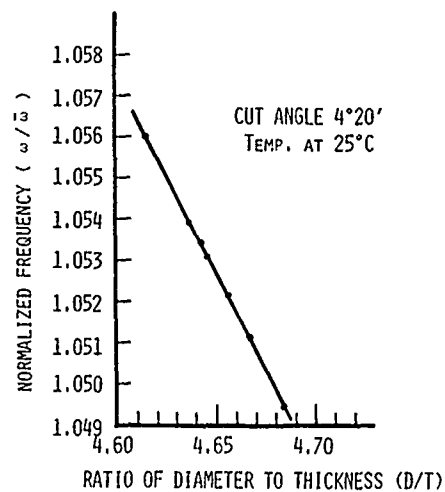


Fig. 14 - Normalized Frequency Variation with Ratio of Diameter to Thickness.

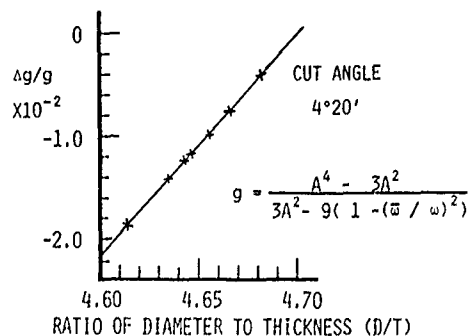


Fig. 15- Normalized g Variation with Ratio of Diameter to Thickness.

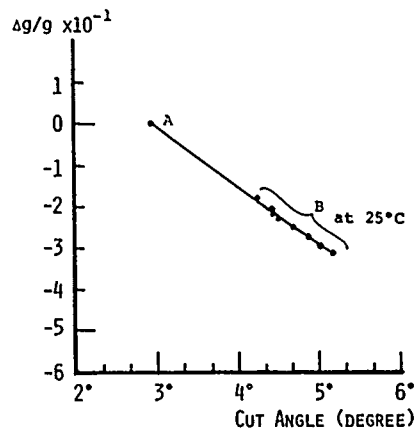


Fig. 16 - Normalized Coupling Modulus Variation with Cut Angle for Ratio in case of a very little change in Resonance Frequency; Point A is a calculated value by formula (1), Group B points are calculated by measuring results.

IMPROVING FREQUENCY-TEMPERATURE CHARACTERISTICS OF GROOVED AT-CUT PLATES

Mitsuo Nakazawa
Shinshu University
Nagano, Japan

Summary

The aim of this study has been to further improve the frequency-temperature characteristics of grooved AT-cut plates.

Carefully applying the similitude principle, we cut a rectangular or a circular groove in the middle of standard AT-cut plates and finished the floor of the groove to resemble the surface of a plano-convex lens. The basic characteristics of grooved AT-cut plates were clarified by experiments, and the frequency equation of these plates is developed. Through experiments to find the most suitable relationship between the ratio of the thickness of the grooved area to that of the surrounding material and the outside dimensions, and through a theoretical analysis, we have been able to produce grooved AT-cut plates which show the best frequency-temperature characteristics.

Introduction

Accompanying progress in IC technology over the past few years, quartz crystal resonators have come to play a central part in the clock and watch making, communications and measuring instrument industries as functional components in which it is possible to rather easily achieve high performance and high stability and the part thus played will probably become even more important from now on and no doubt there will be a need to develop quartz crystal resonators offering even higher performance and ultra high stability. At the present time it is essential in practical resonators that

- (1) they are small,
- (2) unwanted responses are reduced to zero,
- (3) crystal impedances are minimal,
- (4) they are easy to support,
- (5) frequency-temperature characteristics are good,
- (6) stability is high, and so on.

In particular, as far as support structures are concerned, there are such as the tuning fork type quartz crystal resonators for watches which are superior to older ones in the low frequency range. However, when it comes to supports for the quartz crystal resonators used in the high frequency range, a pair of wire clips or metal ribbons are used to connect directly to the conventional vibration nodal point. With these structures, the nonlinear effects on crystal resonators due to support power slightly affect the main vibration

and, in addition to this, further improvement in vibration and shock resistance is necessary. Recently, as the thickness of quartz crystal plates has continued to be reduced to meet high frequency requirements in particular, this problem has been magnified.

Over the past few years the new resonators have been studied intensively to try to find a way to simply and effectively solve problems (1) and (4), referred to above [1-4]. This is done by grooving or reducing the thickness of the central area of quartz plates used in thickness vibration. To fulfil requirements (1) to (5) the resonators have been improved by cutting a rectangular groove or a circular groove in the central area and finishing the floor of the cut-out portion in the shape of a plano-convex lens to be the main vibrator (Fig.1) a so called "quartz crystal plate with a distorted convex lens shaped groove". This present study deals with grooved AT-cut plates of this type and sets out to show their various basic characteristics experimentally and, in particular, to improve their frequency-temperature characteristics (5).

Basic Characteristics

What are the basic and ordinary characteristics of so-called grooved quartz crystal plates?

This chapter endeavours to clarify the basic characteristics of grooved quartz crystal plates and experiments are carried out to determine the following:

- (1) What laws do the frequency mode charts for thickness obey?
- (2) What are the vibration modes?

The experimental quartz crystal plates used in these tests are the rectangular and circular grooved AT-cut types.

Frequency Mode Chart and Frequency Constants

Fig.2 shows samples No.1, No.2 and No.3, three identically shaped rectangular quartz crystal AT plates having the same dimensions and samples No.1 and No.2 are cut, according to the same procedure, on an ultrasonic wave processing machine. In the middle of sample No.1 a groove or cutaway section, similar in shape to the surrounding plate, is cut. The outside dimensions

of this grooved area in sample No.2 are exactly the same as those in No.1 but the floor of the groove in No.2 is finished in the shape of a plano-convex lens whose radius of curvature R is 100mm. Sample No.3 is a standard quartz crystal. The external shape and dimensions of No.3 are exactly the same as those of Nos.1 and 2.

First of all we prepare a frequency mode chart for the thickness of sample No.1. As indicated in Fig.1, the thickness of the surrounding material and that of the grooved portion have been referred to as y_0 and y_0' , respectively, where R is infinite. Now, keeping thickness ($y_0 - y_0'$) constant, we continually observe resonant frequency as affected by minute changes in y_0 or y_0' .

Fig.3 is a measured frequency mode chart for sample No.1 when readings are taken in the manner described above. The large and small black circles seen in Fig.3 are in direct proportion in size to the strength of vibration produced in the quartz crystal plates. Again when the y_0'/y_0 ratio exceeds 0.7893, the amount by which y_0 is reduced by grinding each time is approximately 350 μ m, but when the ratio is less than the above figure, y_0 is reduced by about 100 μ m each time. From Fig.3 then we learn the following:

As y_0 is reduced in size, the frequencies of groups (a) and (b) change as shown in the hyperbola curves. Group (c) is not greatly dependent on a reduction in y_0 , and group (d) which is scarcely related to the reduction in y_0 at all, and so on. Group (a) is produced in the high frequency range and its vibration strength also is great. Group (b) is produced in a lower frequency area than (a) and, when the y_0'/y_0 ratio is great, vibration is great but as this ratio becomes smaller, vibration strength decreases. In the case of group (c), frequency gradually increases as y_0 is reduced but vibration strength is still small. However, as far as y_0 is concerned, it is periodically bound to group (a) or (b).

From what has been seen so far, it can be said that in the periphery of group (a), which are the main vibration of sample No.1, there exist a lot of unwanted modes which have an undesirable effect on group (a). In order to eliminate these unwanted modes and to increase the Q value of the main vibrations, sample No.2 is designed and made. On the basis of the principle of analogy, it is possible to get a general idea of the frequency mode chart for sample No.2 from Fig.3.

However, since the floor of the grooved or cutaway portion of sample No.2 is in the form of a plano-convex lens, as far as the frequency mode chart related to y_0' is concerned, few unwanted modes are produced on the periphery of the main vibration belonging to group (a). In this way frequency mode charts are prepared for the y_0' of the main vibrations. For purpose of comparison, both the experimental and theoretical values for the main vibration frequency constants for the standard AT-cut plate (sample No.3) are obtained.

The frequency constants for samples No.1 to No.3, are obtained by the least square method from a large volume of data. Strictly speaking, these constants $f_1'y_0'$ and $f_2'y_0$ are seen to become slightly smaller each time that y_0' or y_0 is reduced. From these data, we can learn the following:

Accompanying the change from sample No.3 type flat AT-cut plates to grooved AT-cut plates such as samples Nos.1 and 2, the frequency constant $f_1'y_0'$ for the main vibration, as taken from the experimental result, increases from 1.675MHz-mm to 1.777MHz-mm and 1.789MHz-mm, an increase of about 1.1% and 1.3%.

Next, concerning the effect on the frequency constant due to the difference between the shape of the grooves in samples Nos.1 and 2, we obtain

$$\text{and } [f_1'y_0']_{\text{No.2}}/[f_1'y_0']_{\text{No.1}} \approx 1.007$$

$$[f_2'y_0]_{\text{No.2}}/[f_2'y_0]_{\text{No.1}} \approx 1.002$$

In other words, because the floor of the groove or cutaway in No.2 sample is in the form of a plano-convex lens, when compared with No.1, it is seen that there is an increase in the frequency constants of the groove area itself and of the quartz material surrounding the groove of 0.7% and 0.2%, respectively.

It is well known that as y_0 decreases, the value for sample No.3 gradually approaches the calculated value of 1.664MHz-mm and we observed one example of this in these experiments.

Frequency Constants of Practical Grooved AT-cut Plates

We built an experimental precision grinding machine to use in making practical grooved AT-cut plates.

The sample of crystal is fixed in the frame in the middle of the fixed plate of the grinder and directly above the center of it a cylindrical hard metal cutting tool is placed.

The grinding liquid used is a solution of green carbon in water and this is poured on the quartz while gradually rotating the grinding tool.

Fig.4 sets out the $f_1'y_0'$ frequency constants found in relation to y_0' for practical square AT-cut plates (length \times width \times thickness: $x_0 \times z_0 \times y_0$) with a circular groove (diameter \times thickness \times radius of curvature: $d' \times y_0' \times R$) in the middle and circular disk AT-cut plates (diameter \times thickness: $d \times y_0$) with a circular groove (diameter \times thickness \times radius of curvature: $d' \times y_0' \times R$) in the middle, the readings for the former being indicated by mark O and for the latter by mark \bullet . $f_1'y_0' \sim y_0'$ characteristics fluctuated a little and any such fluctuation is regarded as probably due to coarsenesses of the surface of the crystal plates. The radii of curvature of the floor of the groove in both

plates are approximately 36mm.

In Fig.4 if the method of least squares is used to find $f_1'y_0'$ of the square plates, the value obtained is 1.757MHz-mm and the result in the case of the circular plates is 1.770MHz-mm making the average for these two 1.764MHz-mm or a little smaller than the $f_1'y_0'$ for Nos.1 and 2 samples referred to above. From these results we see that when using the kind of grooved crystal plate with the dimensions shown in Fig.4, if it is so designed that the thickness of the middle of the grooved area is around $y_0' = 0.418 \sim 0.422$ mm, it will be possible to obtain the 2^{22} Hz frequency required for watch resonators.

Fig.5 shows the $f_1'y_0'$ characteristics for R in circular grooved AT-cut plates. It can be seen that the smaller R becomes, the greater $f_1'y_0'$ becomes.

Vibration Modes

In order to understand the main vibration mode for the grooved AT-cut resonators, electric probe experiments are carried out.

As shown in the left side in Fig.6, sample No.2 is placed in an electric probing device and the main vibration belonging to group (a) is excited. Again together with the upper electrode, sample No.2 is moved horizontally from A to B by means of a motor. At the same time, the induction current based on the piezoelectric effect passing through the probe is amplified and the output is pictured on a recorder. Then we learn the relationship between the position on the crystal and the intensity of the induction current to the probe, as shown in the right side in Fig.6. The four areas of distribution show the readings obtained. When the y_0'/y_0 ratio is close to unity, the electrical polarization distribution for sample No.2 is very close to that for No.3 and in this case the ratio $y_0'/y_0 = 0.949$ corresponds to this and along the AB line the main vibrations are distributed in almost a sine wave form. However, there is higher order vibration in combination with higher contour modes and it is seen that peaks are superposed on the sine waves referred to above. As the y_0'/y_0 ratio decreases, electrical polarization distribution gradually comes to be concentrated in the ab area of the grooved part of sample No.2.

From what has been set out in this section and above, it is concluded that the main vibration belonging to group (a) of grooved AT-cut plates samples Nos.1 and 2 is the thickness-shear mode.

We shall now discuss another example. Fig.7 shows the three-dimensional distribution of electrical polarization in a small grooved AT-cut plate. The diameter (d') of the circular groove of this rectangular plate is 4.5 mm and the radius of curvature of the groove is 100mm. When the thickness at the middle is $y_0' \approx 99\mu\text{m}$, the main resonant frequency is 17.72525MHz at 25°C.

It follows, in view of the distribution pattern shown in Fig.7, that any distortion in the grooved crystal plate will reach its maximum at the middle of the groove and that at its immediate circumference distortion will be down almost to zero.

We may conclude from this that most of the main vibration energy of the grooved plate will be concentrated inside the groove area, as mentioned above. From these facts and taking into account the distribution of electrical polarization shown in Figs.6 and 7, it may be said that it is best to try to support these grooved AT-cut plates at the most suitable sides.

Frequency Equation

It is possible to think of the central grooved domain (I) of a rectangular grooved AT-cut plate and the surrounding material (II) separately and also to think of the main vibrations belonging to group (a) produced in the domain (I) and vibrations belonging to group (b) produced in the domain (II) as mechanically linked. Fig.8 shows this relationship in equivalent circuits. M is mutual inductance governing electromagnetic coupling. C_0 is the electrical capacitance of the quartz crystal plate. If ω is the angular frequency of circuits for exciting voltage E, then

$$Z_1 = R_1 + j \omega L_1 + \frac{1}{j \omega C_1}$$

shows the motional impedance for the main vibrations of region (I), in which j is an imaginary unit. Further, the motional impedance for region (II) becomes

$$Z_2 = R_2 + j \omega L_2 + \frac{1}{j \omega C_2}$$

Now if in Fig.8 we call the current passing through regions (I) and (II), I_1 and I_2 , respectively, then according to Kirchhoff's laws,

$$\begin{aligned} Z_1 I_1 + j \omega M I_2 &= E, \\ j \omega M I_1 + Z_2 I_2 &= 0, \\ \omega &= 2 \pi f, \quad M = k \sqrt{L_1 L_2}, \quad (1) \end{aligned}$$

in which f and k are frequency and coupling coefficient, respectively.

Generally, since R_1 and R_2 are quite small, if we disregard them, we obtain the following formula for resonant frequency f :

$$f = f_1 \sqrt{1+r_0} \sqrt{\frac{1+\sqrt{1-\frac{4r_0(1-k)^2}{(1+r_0)^2}}}{2(1-k^2)}}, \quad (2)$$

Where

$$f_1 = \frac{1}{2\pi \sqrt{L_1 C_1}},$$

$$f_2 = \frac{1}{2\pi \sqrt{L_2 C_2}},$$

$$r_0 = (f_2/f_1)^2 \quad (3)$$

If, taking report [5] into account, f_1 and f_2 are the resonant frequencies showing the thickness-shear modes of regions (I) and (II) of sample No.1, respectively, then we obtain the following equations without the effect of electrode:

$$f_1 = \frac{q}{2y_0'} \sqrt{\frac{C_{66}}{\rho}} \left\{ 1 + \frac{C_{11}}{C_{66}} \left(\frac{py_0'}{qx_0z_i'} \right)^2 \Delta_i' + \frac{C_{55}}{C_{66}} \left(\frac{ry_0'}{qz_0z_i'} \right)^2 \Delta_{ii}' \right\}^{1/2},$$

$$f_2 = \frac{q}{2y_0'} \sqrt{\frac{C_{66}}{\rho}} \left\{ 1 + \frac{C_{11}}{C_{66}} \left(\frac{py_0'}{qx_0z_i'} \right)^2 \Delta_i' + \frac{C_{55}}{C_{66}} \left(\frac{ry_0'}{qz_0z_i'} \right)^2 \Delta_{ii}' \right\}^{1/2},$$

(p, q, r = integer, $i = 1, 2$), (4)

in which ρ is the density of the quartz crystal and C_{11} , C_{55} and C_{66} are the elastic stiffness constants converted to a coordinate system for AT-cut quartz crystal plates. Δ_i' , Δ_{ii}' and so on show the correction coefficients. These show the values for rectangular AT-cuts at $i = 1$, and also show those for circular disk AT-cuts at $i = 2$.

Hence we obtain, from equation (2) ~ (4), the resonant frequency f showing the mode (p=1, q=1, and r=0) of rectangular grooved AT-cuts as

$$f = \frac{1}{2y_0'} \sqrt{\frac{C_{66}}{\rho}} \sqrt{1 + \left(\frac{y_0'}{x_0} \right)^2 \frac{a_2}{a_1}} \sqrt{1 + \frac{1 - \frac{4 \left(\frac{y_0'}{x_0} \right)^2 (1-k^2) \frac{a_2}{a_1}}{\left\{ 1 + \left(\frac{y_0'}{x_0} \right)^2 \frac{a_2}{a_1} \right\}^2}}{2(1-k^2)}},$$

(5)

where

$$a_1 = 1 + \frac{C_{11}}{C_{66}} \left(\frac{y_0'}{x_0z_i'} \right)^2 \Delta_i',$$

$$a_2 = 1 + \frac{C_{11}}{C_{66}} \left(\frac{y_0'}{x_0z_i'} \right)^2 \Delta_{ii}',$$

($i = 1, 2$).

(6)

The plus and minus signs in equations (5) correspond to the main frequency groups (a) and (b), respectively. In order to apply the similitude principle we shall make the y_0'/x_0z_i' ratio of sample No.1 equal to the y_0/x_0z_i' ratio of it. Then we obtain the relation $a_1 = a_2$ in equations (4) ~ (5).

By using those results and the measured values for $[f_1' y_0']$ of Nos. 1, 2 and 5, we find the curves k vs y_0'/y_0 , as shown in Fig.9. The curves also show the k characteristics for the different shapes of these resonators. From Fig.9 it is found that the great part of k exists between zero and 0.3.

Frequency-Temperature Characteristics

Frequency f obtained by equation (5) is well known as a function of temperature T and it is approximately expanded by Taylor series as

$$f(T) = f(T_0) \{ 1 + \alpha(T - T_0) + \frac{\beta}{2}(T - T_0)^2 + \frac{\gamma}{6}(T - T_0)^3 + \dots \},$$

(7)

where T_0 is reference temperature and α , β and γ are the first, second and third order frequency-temperature coefficients, respectively. For instance, α is defined as

$$\alpha = \left(\frac{1}{f} \frac{\partial f}{\partial T} \right)_{T_0}.$$

(8)

We assume here that coupling coefficient k is independent of temperature. Hence, we obtain

$$\alpha = \alpha_1 + A_0(\alpha_2 - \alpha_1),$$

(9)

where A_0 is a constant which includes k and r_0 , and α_1 and α_2 is defined as

$$\alpha_1 = \left(\frac{1}{f_1} \frac{\partial f_1}{\partial T} \right)_{T_0},$$

$$\alpha_2 = \left(\frac{1}{f_2} \frac{\partial f_2}{\partial T} \right)_{T_0}.$$

(10)

From equation (9), to obtain the best frequency-temperature characteristics of the grooved AT-cut plates, we can choose as

$$\alpha_1 = \alpha_2,$$

$$|\alpha_1| = \text{minimum}$$

(11)

by making use of the similitude principle. Hence, the following relationship is required for mode (110):

$$\left(\frac{y_0' x_0 z_i'}{y_0 x_0 z_i'} \right)^2 \cdot \frac{\Delta_i'}{\Delta_{ii}'} = 1,$$

(12)

and simultaneously, the grooved AT plates have to be selected according to equation (11), in which it is necessary that the values for k are not too small.

Fig.10 shows the measured values for resonant frequency-temperature characteristics for sample No.2 when y_0'/y_0 is taken as the parameter. The reference temperature T_0 is 25°C. From Fig.10 the smaller the y_0'/y_0 ratio becomes, the smaller the frequency fluctuation in relation to temperature also becomes.

Similarly, Figs.11 and 12 show the measured values for resonant frequency-temperature for samples 4 and 5. The external shape of No.4 is a rectangular and it has a circular groove at the middle, as shown in Fig.11. The floor of the groove is then finished to resemble the surface of a plano-convex lens having a radius of curvature of 21 mm. On the other hand the external shape of No.5 is a circular disk and it has a circular groove at the middle, as shown in Fig.12. The floor of groove is formed to the plano-convex with radius $R=68.5\text{mm}$.

For sample No.2 it is theoretically seen that

when y_0'/y_0 ratio is about 0.4, the best frequency-temperature characteristics will be obtained, and the frequency accuracy will be a few ppm over the temperature range $-10^\circ\text{C} \sim 60^\circ\text{C}$. Fig.10 shows the experiment proof.

Similarly, for sample No.4 it is theoretically seen that the best frequency-temperature characteristics will be obtained at $y_0'/y_0=0.5$, and the frequency accuracy will be within a few ppm over temperature range $-10^\circ\text{C} \sim 60^\circ\text{C}$. Fig.11 data confirms this.

For sample No.5 it is also found that the best frequency-temperature characteristics will be obtained at $y_0'/y_0 = 0.66$. Fig.12 makes this clear.

Conclusion

In this study, the following conclusions are drawn:

(1) To improve supportability, and to reduce the unwanted responses and the crystal impedances, special grooved AT-cut plates are proposed [6-8].

(2) It is possible to improve the frequency-temperature characteristics by finding the most suitable relationship between the ratio of the thickness of the grooved area to that of the surrounding material and outside dimensions. Through these optimum designs of grooved AT-cut plates, we can also make small resonators.

Acknowledgements

The author wishes to thank Drs. E. Hafner and A. Ballato, USAERADCOM, Ft. Monmouth, NJ and Messrs. K. Ichikawa and T. Sumita of Fujikoshi Machinery Co., Ltd. and Mr. S. Wakui of Daini Seikosha and Mr. H. Matsuzaka of Yamada Seisakusho Co., Ltd. for their help in making the grooved AT-cut plates and for discussing the project. This research was supported in part by the Saneyoshi Fund.

References

- [1] G. K. Guttwein, A. D. Ballato and T. J. Lukaszek, "VHF-UHF Piezoelectric Resonators", US Patent, 3694677, Sept. 26, 1972.
- [2] M. Berte, "Acoustic Bulk Wave Resonators and Filters Operating in the Fundamental Mode at Frequencies Greater than 100MHz", Proc. 31st AFCS, 122-125, June 1977.
- [3] M. Nakazawa and M. Miyazawa, "Trial Production of High Frequency AT-cut Quartz Crystal Vibrators", Paper of T.G. on US, E.C.I. of Japan, US NO.76, 7-11, June 1976.
- [4] M. Nakazawa and S. Wakui, "Frequency-Temperature Characteristics of Grooved Quartz Crystal", Paper of T.G. on US, E.C.I. of Japan, US 79, 29-31, Oct. 1979.

- [5] H. Fukuyo, "Researches in Modes of Vibrations of Quartz Crystal Resonators by Means of the Probe Method", Bulletin of Tokyo Institute of Technology, A-1, 28-67, Mar. 1955.
- [6] H. Fukuyo, H. Yoshie and M. Nakazawa, "The Unwanted Responses of the Crystal Oscillator controlled by AT-cut Plate", Proc. 21st AFCS, 402-419, June 1967.
- [7] P. C. Y. Lee and K. M. Wu, "Coupled Resonances in Doubly Rotated Crystal Plates", Proc. 33rd AFCS, May 1979.
- [8] A. Ballato, "Force-Frequency Compensation Applied to Four-Point Mounting of AT-cut Resonators", IEEE Trans. Sonics and Ultrason., Vol. SU-25, 223-226, 1978.

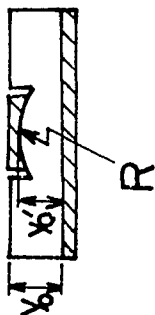
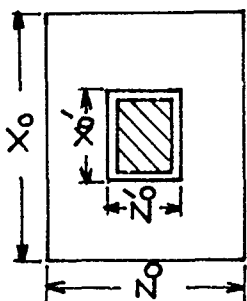


Fig.1. Rectangular grooved AT-cut plate (R: Radius of curvature).

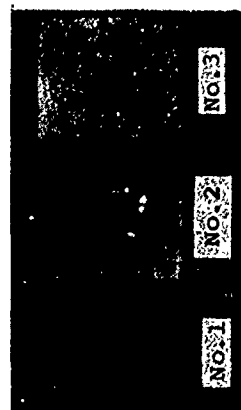


Fig.2. Rectangular grooved AT-cut plates and standard AT-cut plate (No.1: $R=\infty$, No.2: $R=100\text{mm}$, No.3: Flat).

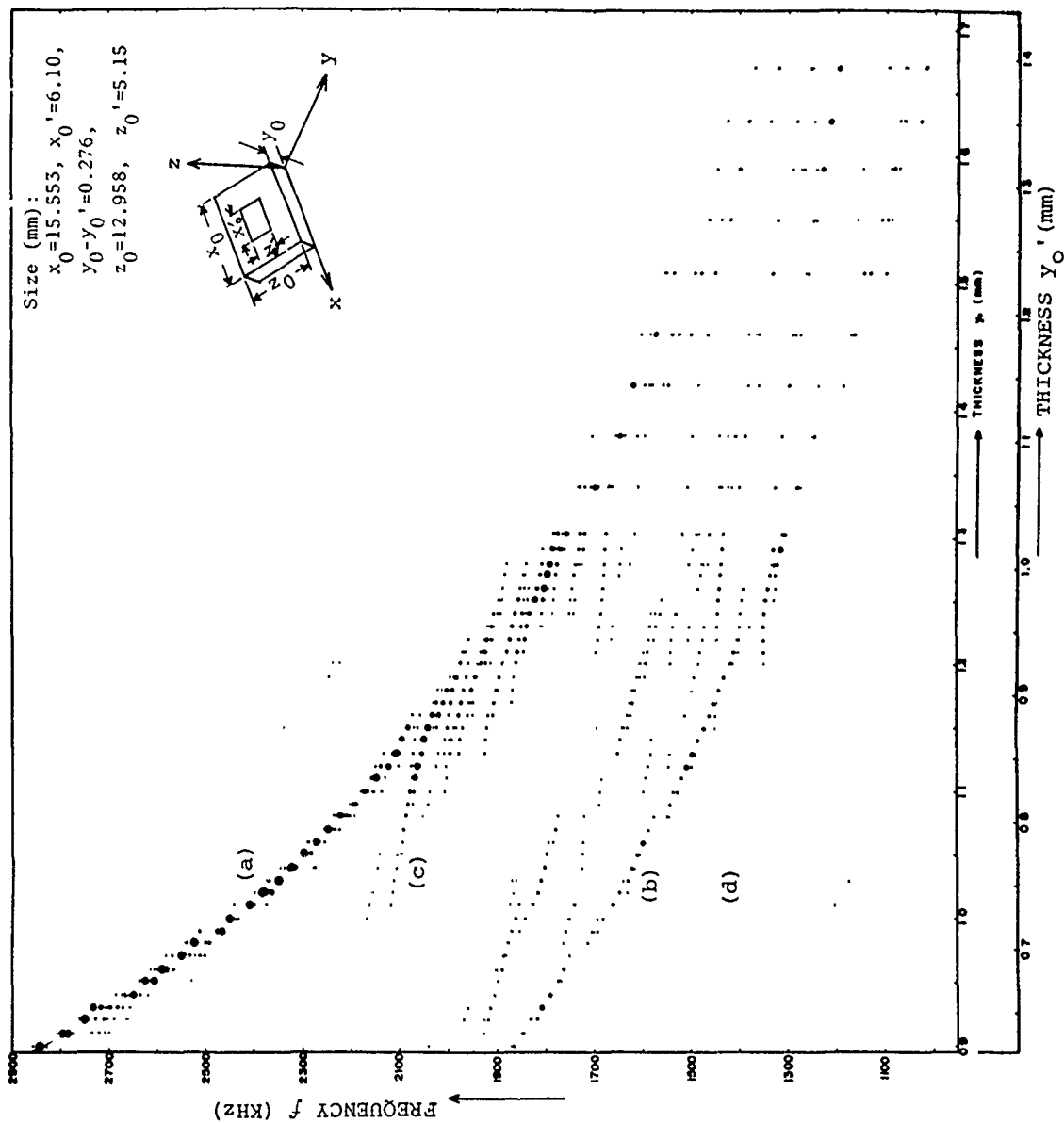


Fig.3. Frequency mode chart of rectangular grooved AT-cut plates (Sample No.1).

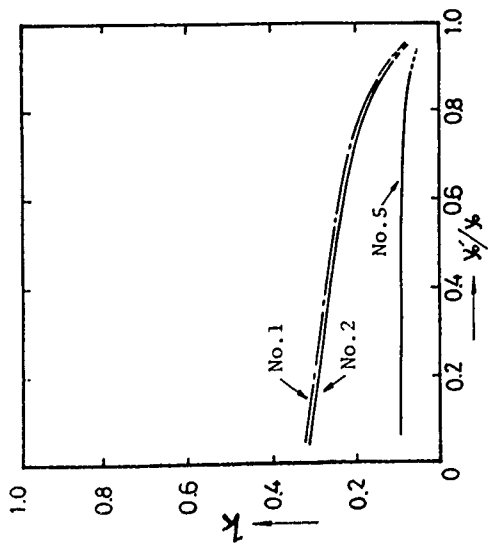


Fig. 9. k - y_0'/y_0 characteristics curves of grooved AT-cut plates.

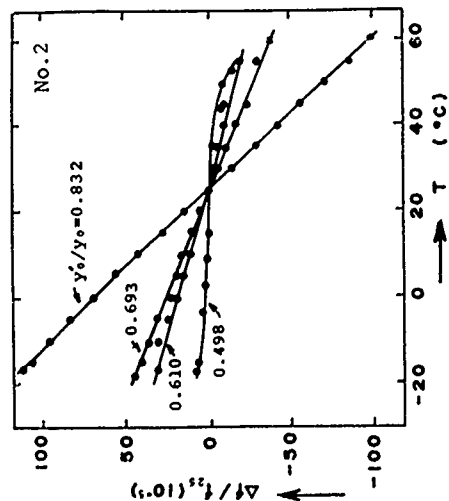


Fig. 10. Frequency-temperature characteristics of sample No. 2 (Size (mm): $x_0 \times z_0 = 15.553 \times 12.958$, $x_0' \times z_0' = 6.10 \times 5.15$, $y_0 - y_0' = 0.276$).

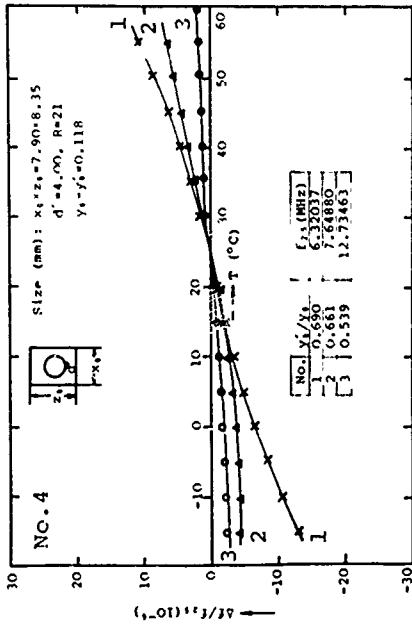


Fig. 11. Frequency-temperature characteristics of circular grooved AT-cut plates (No. 4), taking the y_0'/y_0 ratio as the parameter.

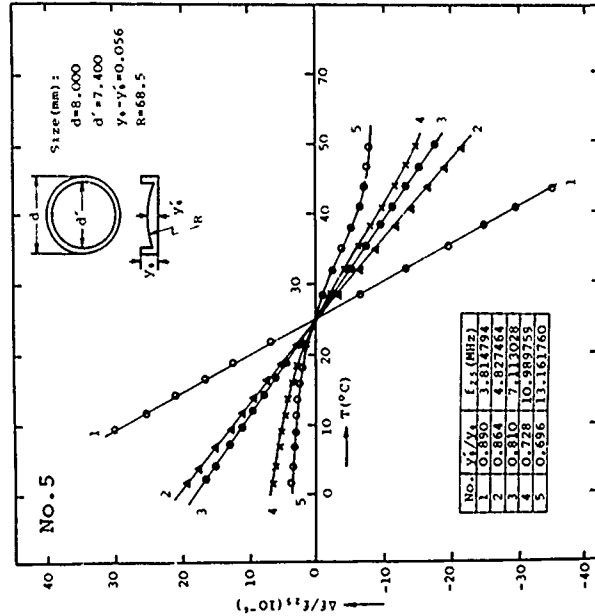


Fig. 12. Frequency-temperature characteristics of circular grooved AT-cut plates (No. 5), taking the y_0'/y_0 ratio as the parameter.

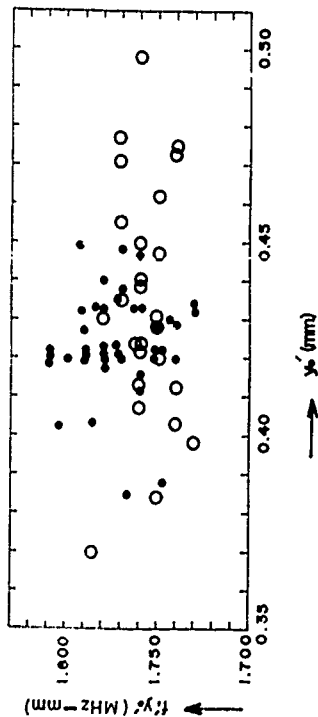


Fig. 4. Frequency-constant characteristics for y' in grooved AT-cuts:
 O..... Square plates (Size (mm): $x_0 \times z_0 \times y_0 = 8 \times 8 \times 0.528$, $d \times R = 4 \times 36$),
 ●..... Circular disks (Size (mm): $d \times y_0 = 8 \times 0.528$, $d \times R = 4 \times 36$).

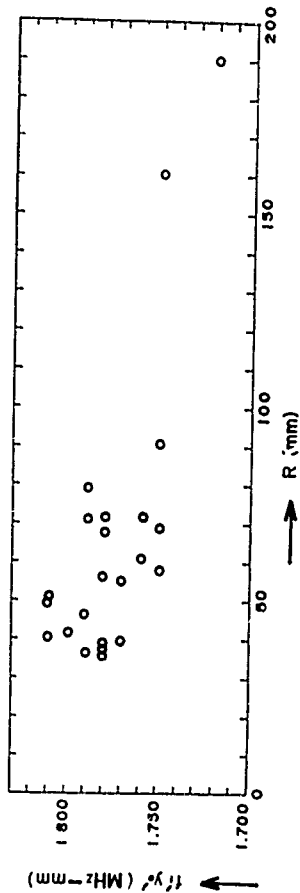


Fig. 5. Frequency-constant characteristics for R in circular grooved AT-cuts (Size (mm): $d \times d' \times y_0 = 8 \times 4 \times 0.528$).

Size (mm):

$x_0 = 15.553$
 $z_0 = 12.958$
 $x'_0 = 6.100$
 $z'_0 = 5.150$

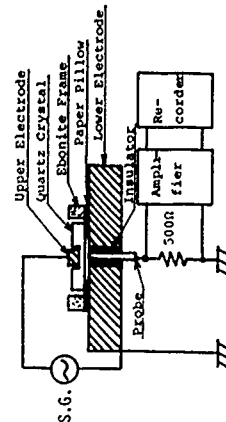
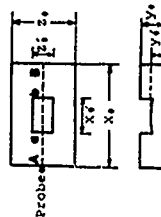


Fig. 6. Electric polarization pattern of sample No. 2 measured by probe method.

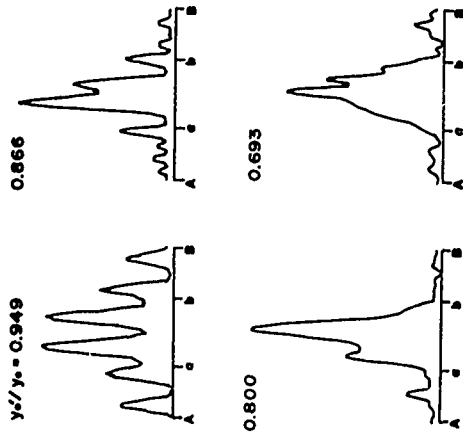


Fig. 7. Solid distribution of electric polarization of a grooved AT-plate.

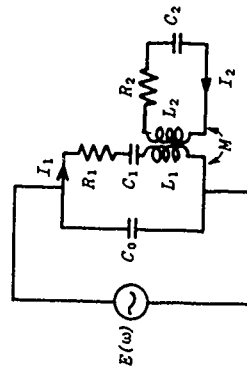


Fig. 8. Equivalent electric circuits of a grooved AT-cut plate.

NEW TYPE TWIN MODE RESONATOR

Shigeru Kogure, Eishi Momosaki and Tetsumi Sonoda

Suwa Seikosha Co., Ltd.

Suwa Japan

Summary

In the quartz crystal tuning fork at the angle of cut near the M_1 cut, we coupled the first overtone of the flexural mode (F_1 mode) with the fundamental vibration of the torsional mode (To mode) and could make both the 1st- and 2nd-order-frequency-temperature coefficients zero.

The frequency-temperature characteristics (f-T characteristics) of this resonator disperse due to the dispersion of the coupling resulting from the dimensional dispersion in the manufacturing processes. We established the adjustment method of the f-T characteristics by adding or reducing the mass at the vibrational node of the F_1 mode.

This resonator is designated new type Twin Mode (TM) Resonator.

Introduction

In recent years, 32 kHz quartz crystal tuning fork with $+5^\circ X$ cut is mainly used in the electronic wristwatches. It is because this resonator features the parabolic f-T characteristics in the room temperature and low power consumption due to a low frequency. But, even if this resonator is used, time error of about 20 seconds per month may occur. Therefore, in order to realize the electronic wristwatches with high accuracy and long life, we developed a new quartz crystal tuning fork with a low frequency and the excellent f-T characteristics by using the coupling between two modes, and reported about it at the last symposium.¹ This resonator is designated TM Resonator.

Because the coupling is used in the TM Resonator, the dispersion of the coupling results in the dispersion of the f-T characteristics. In order to manufacture TM Resonator in high productivity, the coupling must be adjusted. We used the F_1 mode in order to adjust the coupling easily.

Hereinafter, we describe the calculated results and the experimental results as to the

matters of the f-T characteristics and the adjustment of the f-T characteristics.

Analysis

Model of calculations

We theoretically analysed the matters of the coupling, f-T characteristics and the adjustment of the f-T characteristics with the computer program of the finite element method called NASTRAN. The tuning fork is divided into the finite hexahedron elements as shown in Fig. 1. Fig. 2 represents the coordinate system. Detailed calculation method is referred to the appendix in the literature.¹

f-T characteristics

For a long time, the f-T characteristics have been recognized to be affected by the coupling between the main mode and the spurious mode. TM Resonator uses this coupling for improving f-T characteristics. Let's consider f-T characteristics in terms of the frequency-temperature coefficients. The resonant frequency $f(T)$ of the F_1 mode at a given temperature can be expressed as

$$f(T) \approx f(20) \{ 1 + \alpha(T-20) + \beta(T-20)^2 + \gamma(T-20)^3 \} \quad (1)$$

, where α : 1st-order temperature coefficient
 β : 2nd-order temperature coefficient
 γ : 3rd-order temperature coefficient
 T : Temperature

As our aim is to obtain the cubic f-T characteristics in the room temperature, both α and β must be made zero.

We noticed that in the quartz crystal tuning fork, whose arms are directed along the Y axis, cut from the Z plate rotated clockwise around the X axis by several degrees, the 1st-order temperature coefficient of the flexural mode was negative and the 1st-order temperature coefficient of the torsional mode positive. Then, we think it possible to change the 1st-order temperature coefficient of the flexural mode from negative to zero by coupling the flexural mode with the torsional mode, and confirmed it actually.¹ In order to make the 1st- and 2nd-order temperature coefficients zero simultaneously, the cutting angle must be

adjusted. That is, in order to make both the 1st- and 2nd-order temperature coefficients zero, two parameters of coupling and the angle of cut must be adjusted.

Fig. 3 represents the frequency spectrum. The pictures in the parentheses represent the typical chart for the vibrational modes of the two arms. The F_1 mode is coupled with the T_0 mode in the vicinity of $160\mu\text{m}$ in thickness. Fig. 4 represents α , β and γ derived by means of the least square method from the calculated resonant frequencies of the coupled F_1 mode for eight temperatures with the thickness in the vicinity of $160\mu\text{m}$. Fig. 4 represents the calculated results α , β and γ for two thicknesses with \circ , \times and Δ . By obtaining α , β and γ for the thickness between the above two thicknesses by means of the linear approximation and substituting these α , β and γ into the equation (1), the maximum variation from 0°C to 40°C of $\{f(T) - f(20)\}/f(20)$ of the coupled F_1 mode is obtained. Similar calculation is performed for ϕ other than -12.5° , and the result is shown in Fig. 5. From Fig. 5, Δ of the coupled F_1 mode is predicted to be minimum at -12.5° in ϕ near the M_1 cut, that is 0.2ppm . Fig. 6 represents the theoretically predicted f-T characteristics for the different thicknesses. As shown in this figure, the Δ is 0.2ppm for $158.02\mu\text{m}$ in thickness. And for the variation of only $0.01\mu\text{m}$, the f-T characteristics so much change. Similarly, the f-T characteristics so much change for the dimensional dispersion other than thickness. Therefore, in the mass-production it is necessary to exactly control the dimensions and adjust the f-T characteristics finally. And it is theoretically predicted that the dispersion of ϕ must be restricted within $\pm 2.5'$ ($5'$ range) in order to make Δ to be less than 1ppm .

Adjustment of f-T characteristics

When the resonator are produced with the aim to obtain the theoretically predicted f-T characteristics, the angle of cut and the dimensions inevitably disperse.

As mentioned above, if the dimensions do not disperse and are equal to the optimal values, Δ can be made to be less than 1ppm by restricting the dispersion of the angle of cut to be within $\pm 2.5'$, and it is possible with today's manufacturing techniques. The factors that may affect the coupling so much are l , w and t . The dispersions of l , w and t are written as Δl , Δw and Δt , and these dispersions are several microns. As l is large in comparison with w and t , the effect of Δl on the coupling is regarded small and can be neglected. Therefore, the dispersions which affects the coupling so much are considered to be Δw and Δt . When $b=0$, the optimal values are as follows :

$$\phi_{\text{opt}} = -12.5^\circ, t_{\text{opt}} = 158.02\mu\text{m}, w_{\text{opt}} = 370\mu\text{m}, \\ l_{\text{opt}} = 2890\mu\text{m} \text{ and } d_{\text{opt}} = 900\mu\text{m}.$$

The f-T characteristics can be adjusted by compensating the Δw and the Δt occurred in

manufacturing processes. Hereafter we mention the basic concepts for this compensation. The resonant frequencies of the F_1 mode and the T_0 mode at 20°C are written as f_F and f_T , and the ratio of f_T to f_F is written as $R (=f_T/f_F)$. We considered that the dispersion of the f-T characteristics was caused by the dispersion of the R mainly derived from the dimensional dispersion from the fact that one of the f-T characteristics corresponds one R for the individual resonator experimentally. That is, we considered the cause to consist in the fact that R dispersed from the optimal R for the individual resonator.

Fig. 7 shows the displacements of the F_1 mode and the T_0 mode. The displacements in this figure represent those on the line AB on the mid-plane. U_x is the displacement in the X direction and U_T the torsional angle about the Y'-axis (the line AB). For the F_1 mode, there is a vibrational node at the position 0.22 from the top of the arm when the length of the arm is regarded as l . For the T_0 mode, there is not a vibrational node on the arm. The equivalent mass of the F_1 mode at the node is very large and that of the T_0 mode at the same position is small. Therefore, if the mass is reduced or added at this position, it is possible to change f_T so much without changing f_F so much. That is, it is possible to change R . It is necessary to use the node of the flexural vibration for the adjustment of the f-T characteristics, and for this reason 1st overtone is used instead of the fundamental mode. By using 1st overtone, some favorable effects are also expected, that is the high Q, the small frequency deviation due to gravity and the improvement of the aging rate of the frequency.

So as to ascertain whether it is possible to adjust the f-T characteristics by reducing or adding the mass at the node, in other words, whether it is possible to compensate Δw and Δt with the mass at the node, we performed the vibrational analysis with NASTRAN.

At first, we consider whether it is possible to compensate Δt with the mass at the node when w does not disperse and only t disperses. Fig. 8 represents the relationship between R and the frequency variation $\Delta' (= \{f(40) - f(20)\}/f(20))$ of the coupled F_1 mode. The solid line represents the relationship between R and Δ' for the different thicknesses without evaporating the metal films. Points 1 and 3 show the calculated results when the metal films are evaporated over $900\mu\text{m}$ in width on the both sides of the arms at the nodes. Points 2 and 4 show the calculated results when the metal films are reduced over $150\mu\text{m}$ in width on the both sides of the arms at the nodes. Point 5 is the calculated result when the metal films are reduced over $450\mu\text{m}$ in width on the both sides of the arms at the nodes. Arrows represent the behavior of the adjustment. The points 1, 2, 3, 4 and 5 are on the solid line and this shows that the dispersion of the thickness Δt can be compensated by reducing the metal films on the both sides of the arms at the nodes. This

shows that Δt is equivalent to the mass at the nodes, too.

Fig. 9 represents α and β on the α - β plane which are obtained from the f-T characteristics in Fig. 8. Points 1', 2', 3', 4' and 5' correspond to the points 1, 2, 3, 4 and 5 in Fig. 8, respectively. It is known that points (α, β) get toward the the origin by reducing the metal films on the both sides of the arms at the nodes. This corresponds to the compensation of Δt .

Fig. 10 represents the relationship between R and Δ' similarly. The solid line represents the relationship between R and Δ' for the different thicknesses without evaporating the metal films. Point 6 shows the calculated result when the metal films are not evaporated. Point 7 shows the calculated result when the metal films are evaporated over 350 μm on the both sides of the arms at the nodes. Points 6 and 7 are on the solid line and this shows that Δt can be compensated by evaporating the metal films on the both sides of the arms at the nodes. This shows that Δt is equivalent to the mass at the nodes, too.

As mentioned above, it becomes clear when only thickness disperses, Δt can be compensated and consequently the f-T characteristics can be also adjusted by evaporating the metal films on the both sides at the nodes or reducing the evaporant at the same position. Calculations are performed for the model which has the concentrated mass at the grid points as the effect of the metal films. In all the calculations, the masses on the both sides at the nodes are equal.

Next, we considered whether it is possible to compensate Δt and Δw with the mass at the nodes when w disperses in addition to Δt . The solid line in Fig. 11, which is equal to the solid line in Fig. 10, represents the relationship between R and Δ' for the different thicknesses with $w = w_{\text{opt}}$. The broken lines in Fig. 11 represent the relationships between R and Δ' for the different thicknesses with $\Delta w = \pm 2 \mu\text{m}$. The broken lines are adjacent to the solid line, but the R's for $\Delta' = 0$ with $\Delta w = \pm 2 \mu\text{m}$ are slight different from the R for $\Delta' = 0$ with $w = w_{\text{opt}}$. Therefore, the f-T characteristics must be adjusted twice actually, that is, the coarse adjustment and the fine adjustment. From the relationship between R and Δ' after the coarse adjustment, the R for $\Delta' = 0$ can be predicted. And then the fine adjustment is performed for the desired R. The Δw can be restricted within about $\pm 2 \mu\text{m}$ with today's manufacturing techniques.

Fig. 12 represents the relationship between t and Δ when w is larger than w_{opt} by 20 μm . This figure represents that the thickness must be 176.6 μm in order to obtain the best f-T characteristics. That is, if the thickness is increased by 18.6 μm , the f-T characteristics is equal to that of the resonator with the optimal dimensions. Therefore, the dispersion of w is equivalent to the dispersion of $t \pm 0.9 \mu\text{m}$. From this result it is known that Δw and Δt must be restricted to the same extent.

With today's manufacturing techniques, $|\Delta w| \leq 2 \mu\text{m}$ and $|\Delta t| \leq 1 \mu\text{m}$ are possible. As the f-T characteristics smoothly change by the mass at the nodes, it is possible to adjust the f-T characteristics by adjusting the mass with today's manufacturing techniques. As mentioned above, it is theoretically predicted that even if both w and t disperse, these dispersions can be compensated and the f-T characteristics can be adjusted by evaporating the metal films on the both sides at the nodes or reducing the evaporant at the same positions.

Experiments

f-T characteristics

We actually produced the resonator by the lithographic technique² and confirmed that the theoretically predicted f-T characteristics could be obtained. Figs. 13 and 14 show the experimental results of the frequency spectrum and the f-T characteristics at the angle of cut near the M_1 cut respectively, and these results correspond to the calculated results as shown in Figs. 3 and 6. Especially, the resonant frequency of the coupled F_1 mode does not change by more than 1 ppm over the temperature range from 0°C to 40°C. However, sign of γ is negative in the calculation and positive in the experiment. Probably, this is a matter of the precision in the calculations.

Adjustment of f-T characteristics

Fig. 15 represents α and β of the f-T characteristics which are obtained by reducing with the laser beam the evaporant on the both sides of the arms at the nodes at the angle of cut near the M_1 cut. Closed and open circles are the points before and after the adjustment, respectively. Closed and open circles are on a straight line, and this corresponds to the calculated result as shown in Fig. 9. Open circles concentrate near the origin, and this shows that the adjustment of f-T characteristics was achieved.

The adjustment is also possible by evaporating the metal films on the both sides of the arms at the nodes.

Electric characteristics

In order to excite the F_1 mode in high efficiency, we use the special electrode in which the direction of the exciting electric field changes at the position where the sign of the strain of the F_1 mode changes. By using this electrode, the resonant resistance decreased so much and the series capacitance increased. Electric characteristics are as follows:

Oscillation frequency	~ 200 kHz
Quality factor	30×10^4
Resonant resistance	3 k Ω
Series capacitance	1.0×10^{-3} pF
Parallel capacitance	1.0 pF

Conclusions

In the new type Twin Mode Resonator, whose F_1 mode is coupled with T_0 mode at the angle of cut near the M_1 cut, we established the adjustment methods of f-T characteristics and could have the prospect of producing this resonator in high productivity. When this resonator is used in the electronic wristwatches, oscillation frequency is adjusted to 196.608 kHz with the digital trimming owing to the dispersion of oscillation frequency. However, we are also investigating the adjustment method of the oscillation frequency now, and the digital trimming will be unnecessary in the future. Furthermore, we must investigate the aging rate of the frequency which is one of the important terms as the frequency stability.

New type Twin Mode Resonator, which features miniature size, low frequency and excellent frequency-temperature characteristics, is expected to find an extensive range of application in many industrial fields.

Acknowledgements

The authors are indebted to Mr. H. Yasukawa, Mr. K. Fujita and Mr. T. Abe for their encouragement throughout the course of this work.

The authors would like to thank Mr. M. Inoue for valuable advices throughout this research.

The authors would like to thank the co-workers of Suwa Seikosha Co., Ltd. and those of Matsushima Kogyo Co., Ltd. for their direct cooperation in this work, too. Particular thanks are due to Mr. M. Imai, Mr. K. Miyasaka and other members of the Data Processing Department for their valuable advices and cooperation in our use of computer.

References

1. Momosaki, E., Kogure, S., Inoue, M. and Sonoda, T., "New Quartz Tuning Fork with Very Low Temperature Coefficient", Proceedings of the 33rd Annual Symposium on Frequency Control, pp247-254, 1979.
2. Oguchi, K. and Momosaki, E., "+5°X Micro Quartz Resonator by Lithographic Process", Proceedings of the 32nd Annual Symposium Frequency Control, pp277-281, 1978.

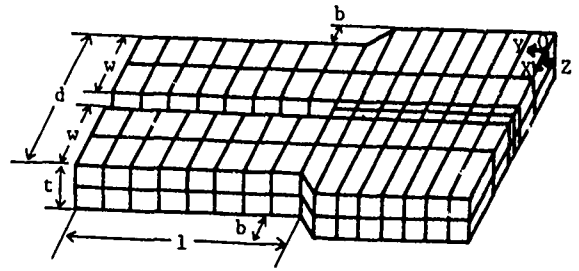


Fig. 1 Model of a tuning fork

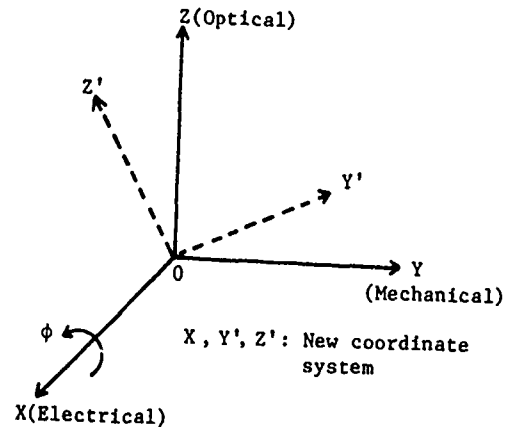


Fig. 2 Coordinate system

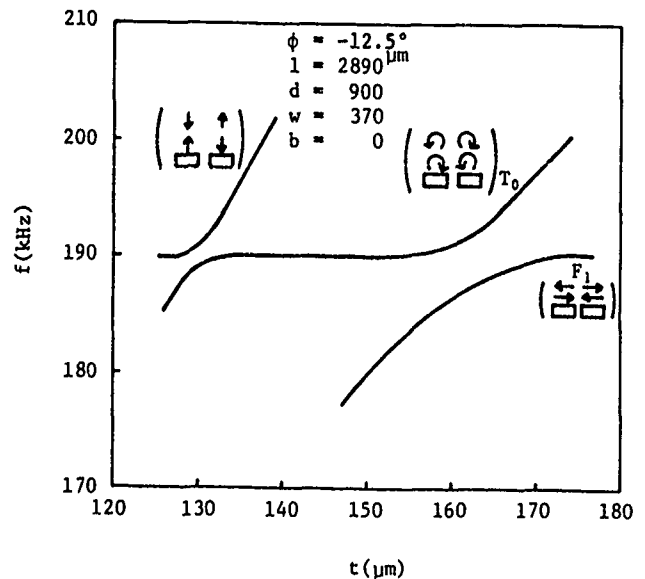


Fig. 3 Frequency spectrum

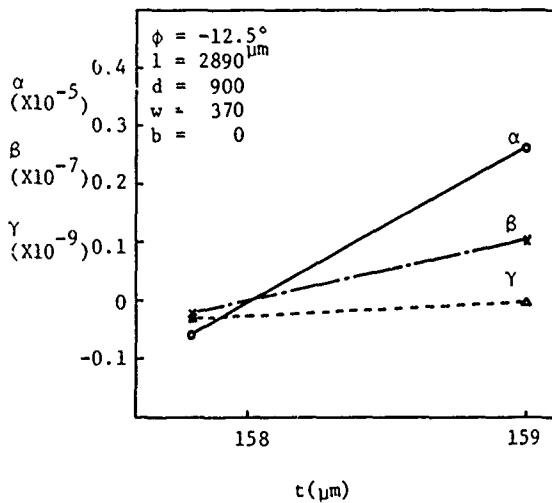


Fig. 4 α , β and γ by means of linear approximation

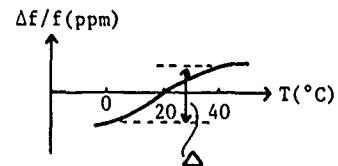
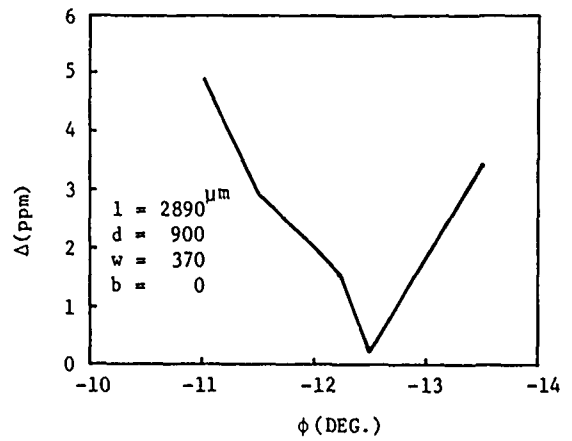
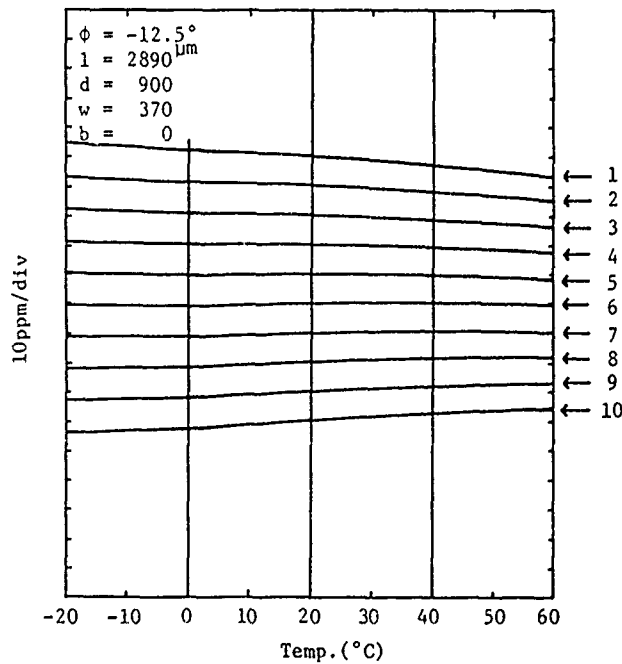


Fig. 5 Δ vs. angle of cut



	1	2	3	4	5
$t(\mu\text{m})$	157.98	.99	158.00	.01	.02
$\Delta(\text{ppm})$	4.4	2.8	2.8	0.8	0.2

	6	7	8	9	10
$t(\mu\text{m})$.03	.04	.05	.06	.07
$\Delta(\text{ppm})$	1.2	2.0	3.2	4.0	5.2

Fig. 6 Variations of f - T characteristics for the different thicknesses

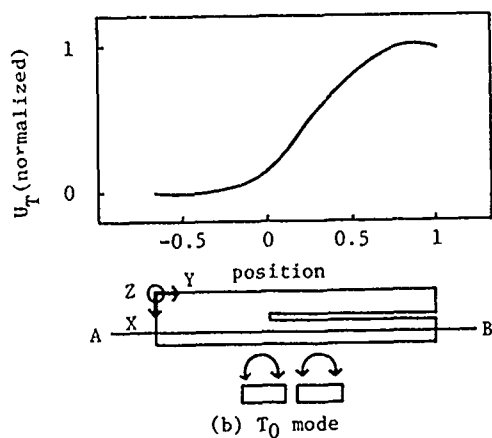
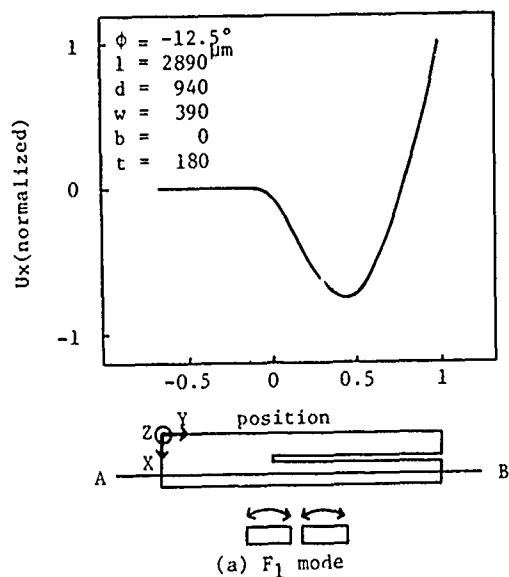


Fig. 7 Displacements of F_1 mode and T_0 mode

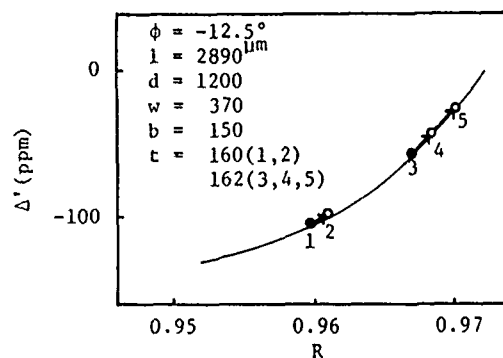


Fig. 8 Relationship between Δ' and R where the metal films are reduced on the both sides of the arms at the nodes

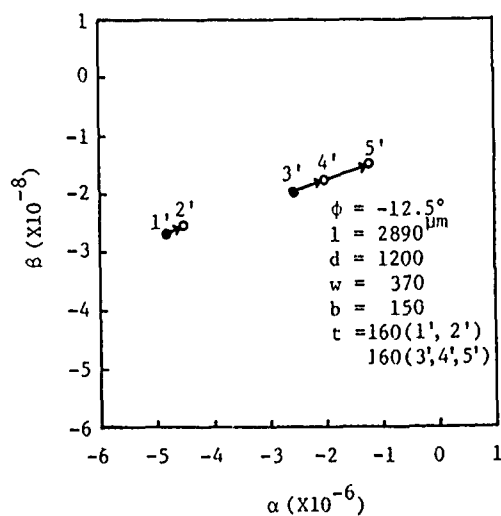


Fig. 9 Behavior of α and β before and after the adjustment

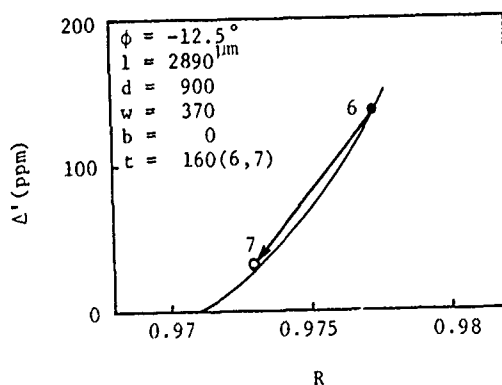


Fig. 10 Relationship between Δ' and R where the metal films are evaporated on the both sides of the arms at the nodes

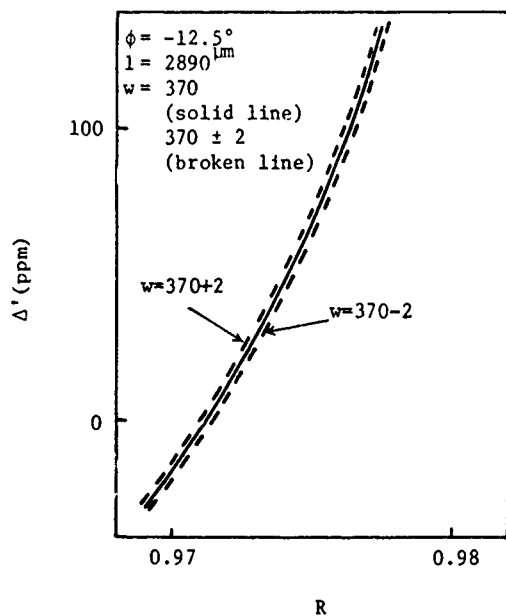


Fig. 11 Relationship between Δ' and R when w disperses in addition to Δt

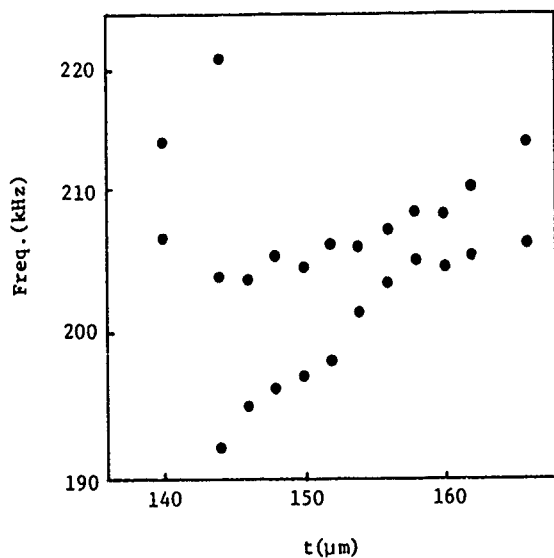


Fig. 13 Frequency spectrum

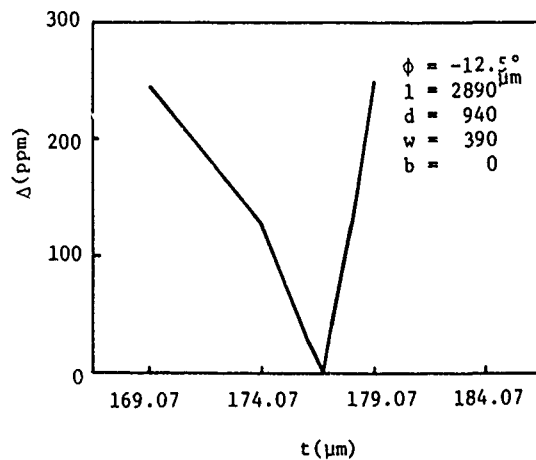


Fig. 12 Δ vs. thickness t

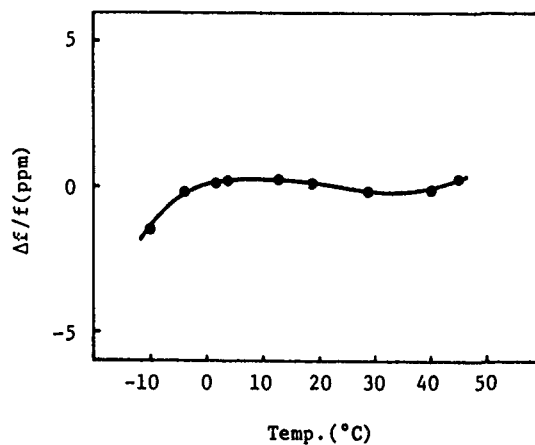


Fig. 14 f - T characteristics

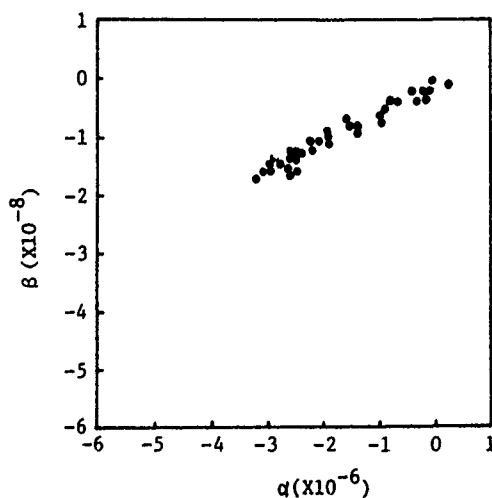


Fig. 15 α and β before and after the adjustment of f - T characteristics

PRODUCTION STATISTICS OF SC (or TTC) CRYSTALS

John A. Kusters and Charles A. Adams

Hewlett Packard Co.
Santa Clara, California

Continued volume production of the SC type crystal has given a more complete picture of the ability of any manufacturing process to produce these doubly-rotated cuts reliably.

We have produced in excess of 1000 of the 10 MHz, 3rd overtone, 15 mm. diameter units to date. Each crystal produced is measured in an automatic test system which records crystal Q, resistance, and frequency at multiple temperatures. As all test data is stored on magnetic disk, a relatively simple data retrieval program allows us to track small changes in the manufacturing process. In addition, the system allows easy determination of the equivalent circuit parameters and their expected range of value.

The data also allows a backward look at the precision obtained in X-ray orientation of the crystal blanks. This is done by comparing temperature coefficient data against a model developed using a variety of precisely known orientations in the vicinity of the SC-cut.

In addition, limited data is given on the B-mode of this cut which indicates the repeatability of the temperature characteristics which have a direct relationship on the suitability of these doubly-rotated dual mode cuts for digitally compensated TCXO operation.

Finally, data on 317 BT-cut units with heavy etch channels indicate that, under the right conditions, a significant improvement in aging rate can be obtained.

Introduction

Since its introduction in November 1974,¹ the SC-cut,² or as it is also known, the TS-cut¹ or the TTC-cut³ has been the subject of a number of papers detailing its virtues and faults.¹⁻⁸ In particular, several papers have commented on the relative difficulty of producing these units reliably in a manufacturing environment due to orientational requirements for this doubly-rotated cut. Hewlett Packard has been producing doubly-rotated cuts, the LC-cut, for use in thermometry for many years.⁹ As a result, our process is uniquely set up to produce SC-cut crystals reliably and efficiently.

An automatic test system was set up to test these crystals in large quantities.¹⁰ This is a synthesizer-vector voltmeter based system tied to a calculator and magnetic disks, printers, plotters, etc. All units are checked for Q, frequency, resistance, temperature coefficients, frequency-temperature slope in the operating range, and equivalent circuit parameters. All of the data is stored for future retrieval. This forms our production data base.

Normally, crystals are measured only in the C, or slow-shear, acoustic mode. However, the data base does include limited data on the B, or fast-shear, acoustic mode also.

Crystal Parameters

A brief list of our current crystal parameters is shown in Table I.

The crystal is specifically designed for operation in a new oscillator, the Hewlett Packard 10811A and 10811B. This crystal is a 10 MHz, 3rd overtone, 15 mm. diameter plano-convex blank, with a 0.5 diopter curvature, and 6.4 mm. diameter electrodes.

An important point to note is that the crystal is not necessarily operated at a turnover temperature.¹¹ The oscillator is designed to operate continuously between 80 and 84°C. At the operating temperature, the frequency-temperature slope can be no larger than 1.5 parts in 10⁶/°C. This slope, coupled with the very high thermal gain made possible by a unique oven design, permits satisfactory operation from -55°C. to 71°C.

C Mode Data

This section covers experimental data taken on over 1000 production quality units. Figs. 1 through 7 presents histogram data as a percent measured of the total number tested. Each horizontal axis is divided up into 100 measurement slots on these graphs. Each curve is roughly Gaussian as might be expected. Of primary interest on each curve are the values plotted on the horizontal axis, the mean value for the measurement, and its standard deviation. The data presented, in order, are the resistance, Q, motional capacitance, motional inductance, and the first, second, and third-order temperature coefficients.

One parameter of interest in SC units is the performance under acceleration. We have no automatic way to test this, so Fig. 8 shows data taken manually on the last 68 production 10811A and 10811B oscillators. This data is for an acceleration change of 2g. The crystals used are mounted in a two-point mount, oriented optically using crossed polarizers, and fixed to the mount using a metallic brazing technique.

Of interest is that the worst case in the 68 oscillators is 4.7 parts in 10^{10} /g with a specification limit of 2 parts in 10^9 /g.

Fig. 9 shows the expected turnover temperature for a change in θ based on previously published data. Because of the method of operating with a frequency-temperature slope specification instead of turnover temperature, we can actually use units with total effective angle changes from about 25" to about 90" of arc. If all of the temperature data spread is due entirely to orientational errors in the blank, the temperature coefficient data and this data indicate that we are holding a standard deviation, due to all causes, of roughly 20" of arc.

Fig. 10 shows essentially the same data as a function of ϕ . The horizontal axis has been contracted 20-fold to present essentially the same form of the curve. This again points out that temperature performance is about 20 times more dependent on θ than on ϕ .

B Mode Data

Two years ago, we presented a paper on a novel dual mode concept which permitted digital compensation of an oscillator for temperature effects.¹² One question unanswered at that time was whether or not the results presented could be obtained without individually calibrating each crystal. Ideally, one would measure a representative sample of units, then simply burn or mask a generalized ROM suitable for all units.

To test this, limited 10.96 MHz B-mode data was taken on 37 production units. Fig. 11 shows the measured resistance data for the 37 units. Mean value is about 38.5 ohms in comparison with the 51 ohm mean seen for the C-mode. Figs. 12 through 14 present the measured first, second, and third-order temperature coefficients for this mode. In general, the first-order coefficient is -25ppm/°C, or about 280 Hz/°C. This again points out the high temperature sensitivity which makes this mode useful for digital temperature compensation.

The problem shows up in Fig. 15. This is the spread in measured frequency at 65°C. A standard deviation of almost 520 Hz with extremes differing by 2,000 Hz from the mean. At the C-mode, the same crystals show a standard deviation of frequency of less than 1 Hz. Taking into account all of the above B-mode data, a generalized masked ROM will yield digital compensation to no better than 10 parts per million.

A possible explanation is shown in Table II. Whereas, for proper C-mode temperature performance, θ must be held as tight as possible, letting ϕ more or less wander, a simple calculation of sensitivity of the frequency-thickness constant to either ϕ or θ indicates that proper tracking of the B and C-mode frequencies can be achieved only with a much tighter control on ϕ than on θ . The first-order derivative of the frequency-thickness constant is 15 times more sensitive to ϕ than to θ for the C-mode, and two times more sensitive to ϕ than to θ for the B-mode.

Elimination of individual calibration can apparently be achieved only by a rather significant leap forward in orientational control. The B-mode data presented here indicates that if the trouble really lies with the sensitivity of the frequency-thickness constant with ϕ , then ϕ must be held to about 3" of arc to be able to achieve one part in 10^7 over the temperature range from -20° C. to 80°C.

ANHARMONIC MODE DATA

Fig. 16 shows the anharmonic frequency spectrum for the C-mode as a function of contour. In each case, only the two main modes of each group is shown. The general anharmonic mode spectrum is very similar to an AT-cut. Moving from the main response, the groups represent a doublet, a triplet, then a quadruplet. From this plot, a rough idea of the frequency mode spacing as a function of contour can be determined.

An equally important question is the one of anharmonic mode response amplitude. Fig. 17 shows this data. Only the mode closest to the main 10 MHz response is shown. The numbers on the left represent the attenuation from the main response seen for an electrode diameter of 11.4 mm. Those on the right represent similar data for a 6.4 mm. diameter electrode. The data is for a 15 mm. diameter crystal blank.

Identical data is shown in Figs. 18 and 19 for the B-mode.

Etch Channels

This section departs from the topic represented by the title of this paper. It is not concerned with SC-cuts, but with similar 10 MHz, 3rd overtone, BT-cuts. Because of a manufacturing process problem, several thousand blanks received a heavy etching before final finishing which resulted in a rather heavy etch channel density, about 200 per cm^2 . As part of a controlled experiment, these were systematically fed into the normal manufacturing system.

The crystals were 15 mm. diameter blanks, plano-convex with .33 diopter contour, and mechanically polished with cerium oxide after the heavy etching. Side lighting the blanks indicate that the vast majority of the pits were essentially normal to the blank surface and extending completely through the crystal. Normal cleaning, including UV-ozone, was used prior to vacuum processing.

The finished crystals were tested on the automatic system and had Q's, resistance, and temperature characteristics, that were statistically identical to units without etch channels. All units had resistances in the range of 14 to 30 ohms, with a measured Q in excess of 2,500,000 for all units. This is almost at the material limit for a 10 MHz BT-cut which indicates that etch channels do not increase apparent acoustic loss.

The major difference observed - in an oscillator, they age better!

Table III shows the oscillator yield as a percent of all units tested. Each period represents 26 days of testing. Each oscillator must be within specifications continuously for 5 days before shipping. No oscillator is tested for more than 15 days. During the last 12 periods before May 1980, 63.3% of all units tested shipped. This represents data on at least 1000 oscillators. During the last 4 periods, not including data on oscillators containing crystals with known etch channels, a minor increase to 64.5% was seen. These crystals were manufactured at the same time, with the same equipment, as those with etch channels. Runs were interleaved to obtain a more valid data base. This group also represents data on at least 1000 oscillators.

During the same period of time, oscillators containing crystals with heavy etch channels were also tested with a rather significant shipment increase to 73.4%. This group numbered 317, so the data is statistically significant. All crystals were identified only by normal production code numbers. Only the crystal production supervisor knew which were which until the data were analyzed.

More interesting is when the units with etch channels shipped. Figs. 20 through 22 indicate that the significant difference is that far more etch channel units are within specifications at an earlier time in the test sequence than units without etch channels.

This data does not imply that heavy etch channels are desirable in all crystals. For the thickness-mode units described here, made with our processes, no reasons seem evident to avoid etch channels. Future development in cultured quartz crystal growth may indeed result in units without etch channels with as good or better aging performance.

Several explanations have been postulated for the better performance of units with etch channels. Our data does not support the competing contamination hypothesis since the aging rate slope follows our normal pattern of aging performance, but starting at a significantly lower aging level.

We also see no reason for concern about the long term effect of etch channels on operating oscillators. Several of the original units, after three months of continuous operation, are aging within several parts in 10^{12} per day. These units also show none of the frequency micro-jumps usually

evident in "young" crystals. It is extremely difficult to believe that, with performance like this, it will suddenly degrade by several orders of magnitude after a year or so.

A possible explanation lies in the known mechanisms for aging in quartz crystals. One of the causes of long-term aging in resonators is the relaxation of internal lattice stresses, induced during either growth or manufacturing of the resonator blank. Etch channels occur because of a high preferential etch rate along regions of stress and seem to be related to the growing process, at least for cultured quartz. Allowing the channels to etch completely through the blank must accomplish at least some internal stress relief which would help to reduce the aging rate. Further investigations are under way.

Acknowledgements

The authors would like to acknowledge that most of the data relating to anharmonic modes were measured several years ago by Jerry Leach, now with Hewlett Packard, Andover, Mass. We would also like to thank Rob Burgoon for sharing his '2-g' data with us for this paper.

References

1. R. Holland, "Nonuniformly Heated Anisotropic Plates: II, Frequency Transients in AT and BT Quartz Plates," 1974 Ultrasonics Symposium Proceedings, pp. 593-598.
2. E. EerNisse, "Quartz Resonator Frequency Shifts Arising from Electrode Stress," Proc. 29th Annual Symposium on Frequency Control, pp. 1-4, 1975.
3. J. Kusters, "Transient Thermal Compensation for Quartz Resonators," IEEE Trans. Sonics and Ultrasonics, SU-23, pp. 273-276, July 1976.
4. J. Kusters and J. Leach, "Further Experimental Data on Stress and Thermal Gradient Compensated Crystals," Proc. IEEE, Vol. 65, pp. 282-284, Feb. 1977.
5. J. Kusters, C. Adams, H. Yoshida, and J. Leach, "TTC's - Further Developmental Results," Proc. 31st Annual Symposium on Frequency Control, pp. 3-7, 1977.
6. A. Ballato, E. EerNisse, and T. Lukaszek, "The Force-Frequency Behavior of Doubly Rotated Quartz Resonators," Proc. 31st Annual Symposium on Frequency Control, pp. 8-16, 1977.
7. J. Gagnepain, J. Poncot, and C. Pequeot, "Amplitude-Frequency Behavior of Doubly Rotated Quartz Resonators," Proc. 31st Annual Symposium on Frequency Control, pp. 17-22, 1977.

SPECIFICATIONS

8. A. Warner, B. Goldfrank, M. Meirs, and M. Rosenfeld, "Low 'g' Sensitivity Crystal Units and Their Testing," Proc. 33rd Annual Symposium on Frequency Control, pp. 306-310, 1979.
9. D. Hammond, C. Adams, P. Schmidt, "A Linear, Quartz-Crystal, Temperature-Sensing, Element," ISA-Trans., Vol. 4, pp. 349-354, Oct. 1965.
10. The system is an automated version of that discussed in: C. Adams, J. Kusters, and A. Benjaminson, "Measurement Techniques for Quarta Crystals," Proc. 22nd Annual Symposium on Frequency Control, pp. 248-258, 1968.
11. R. Burgoon and R. Wilson, "Design Aspects of an Oscillator using the SC Cut Crystal," Proc. 33rd Annual Symposium on Frequency Control, pp. 411-416, 1979.
12. J. Kusters, M. Fischer, and J. Leach, "Dual Mode Operation of Temperature and stress Compensated Crystals," Proc. 32nd Annual Symposium on Frequency Control, pp. 389-397, 1978.

MODE	C mode - 3rd overtone
FREQUENCY (16 pF)	10 MHz
SERIES RESISTANCE	36 - 60 Ohms
EQUIVALENT Q	0.8M minimum
OPERATING TEMPERATURE	80 - 84 °C
SLOPE AT TEMPERATURE	$< 1.5 \times 10^{-8}/^{\circ}\text{C}$
MOTIONAL CAPACITANCE	0.26 - 0.40 fF

WHEN USED IN 10811A/B OSCILLATORS:

DRIVE LEVEL	1 mA typical
ACCELERATION SENSITIVITY	$< 2 \times 10^{-9}/\text{g}$
AGING RATE	$< 5 \times 10^{-10}/\text{day}$

Table I - SC-Cut Crystal Specifications

MODE	PHI	THETA
B	7.1	3.6
C	11.9	0.8

OSCILLATOR YIELD

Last 12 periods - all crystals	63.3%
Last 4 periods - no etch channels	64.5%
Last 4 periods - etch channels	73.4%

DERIVATIVE OF f_t CONSTANT

WITH RESPECT TO ANGLE (KHz-mm/Deg)

Table II - Orientation Sensitivity of Frequency-Thickness Constant

Table III - Oscillator Yields vs. Time

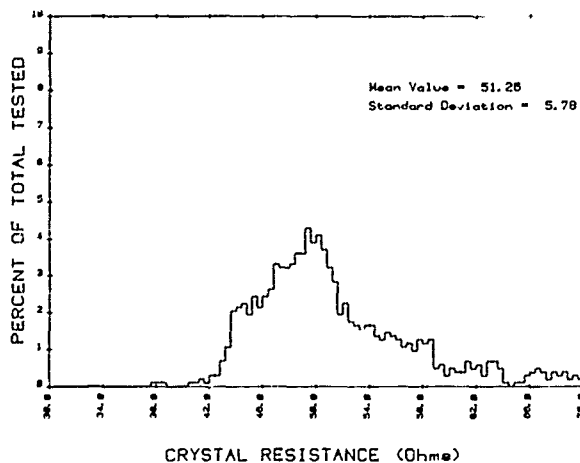


Fig. 1 - C Mode Resistance

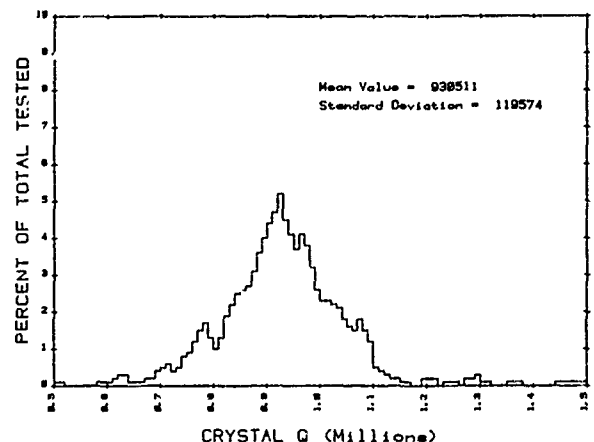


Fig. 2 - C Mode Q

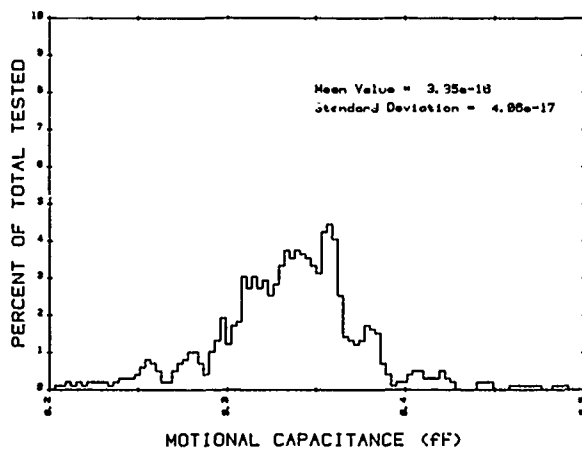


Fig. 3 - C Mode Motional Capacitance

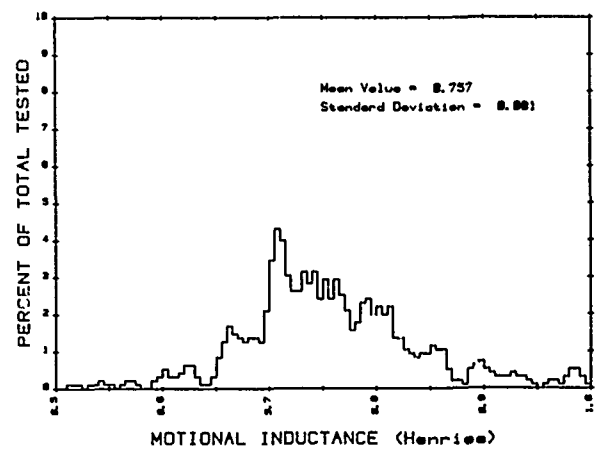


Fig. 4 - C Mode Motional Inductance

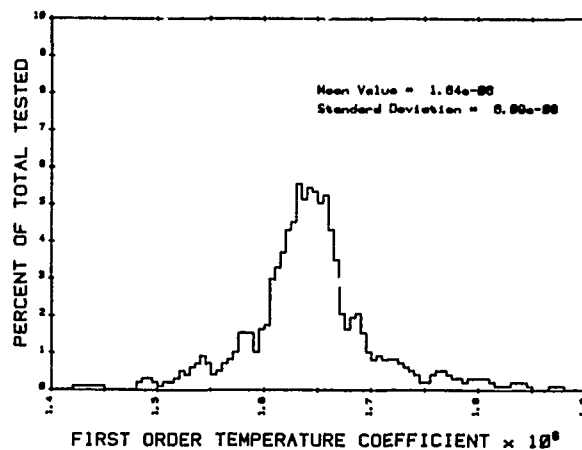


Fig. 5 - C Mode First Order Temperature Coefficient

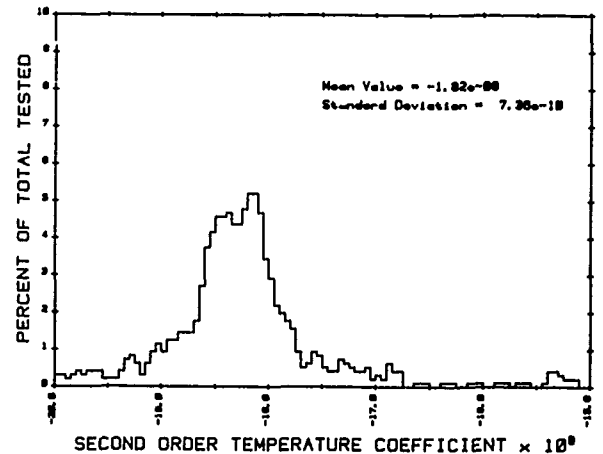


Fig. 6 - C Mode Second Order Temperature Coefficient

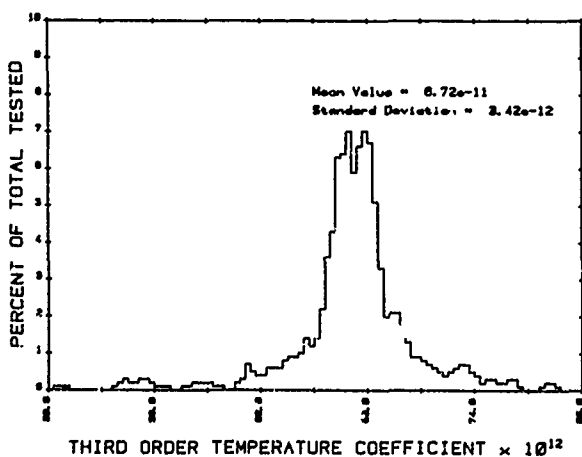


Fig. 7 - C Mode Third Order Temperature Coefficient

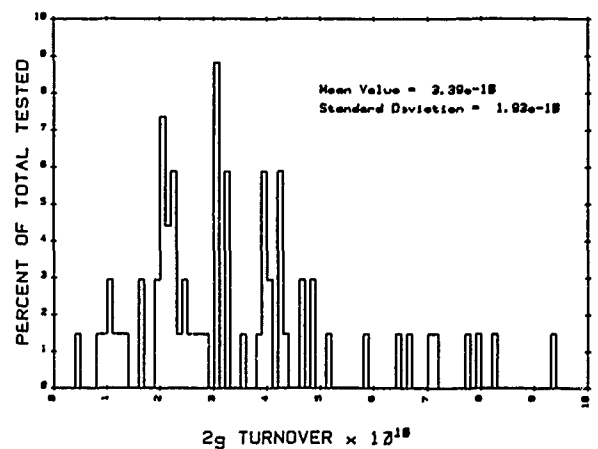


Fig. 8 - C Mode - 68 Oscillators - 2g Turnover

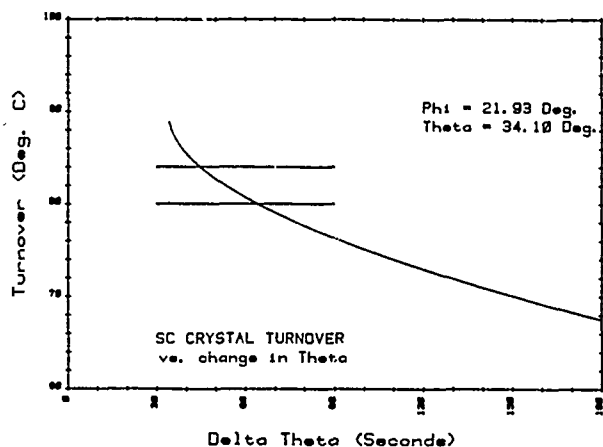


Fig. 9 - C Mode - Turnover Sensitivity to Theta

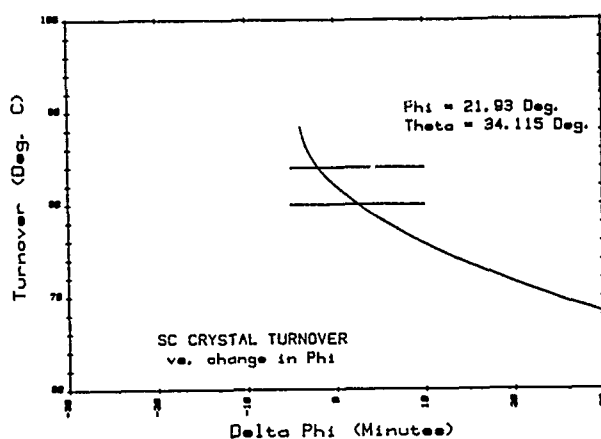


Fig. 10 - C Mode - Turnover Sensitivity to Phi

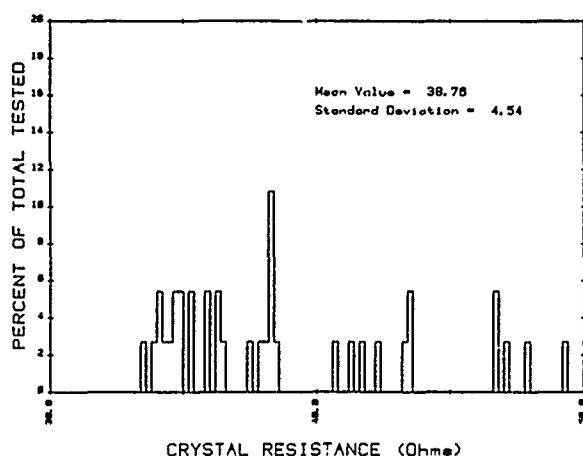


Fig. 11 - B Mode Resistance

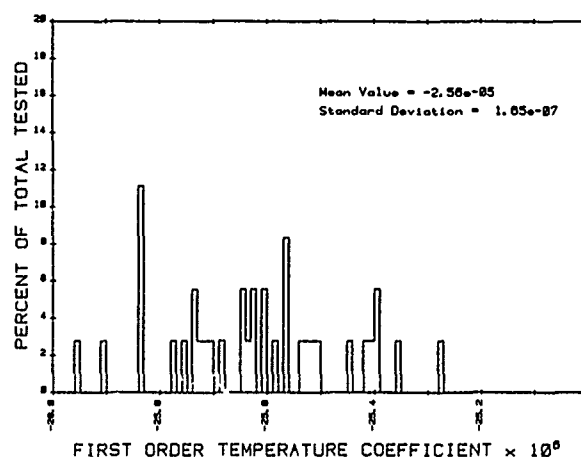


Fig. 12 - B Mode First Order Temperature Coefficient

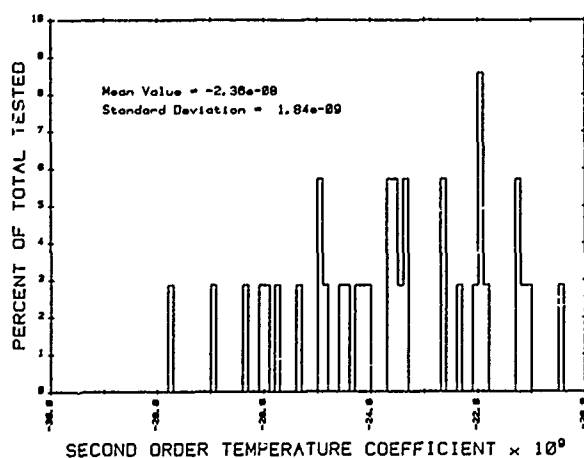


Fig. 13 - B Mode Second Order Temperature Coefficient

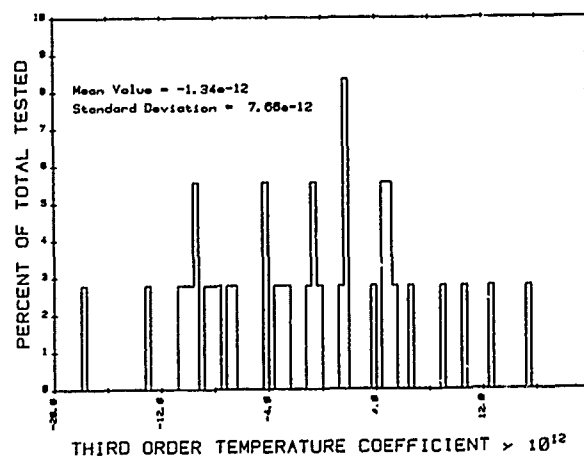


Fig. 14 - B Mode Third Order Temperature Coefficient

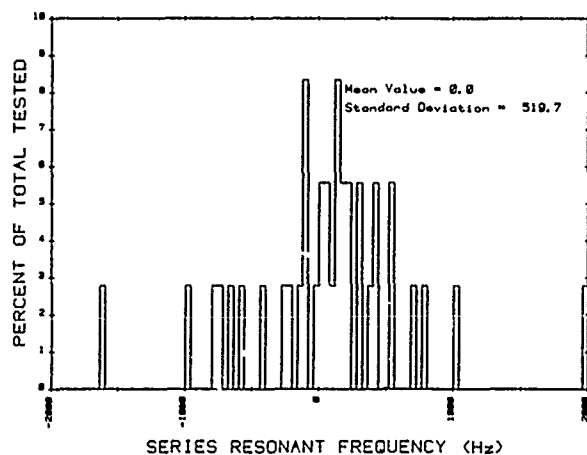


Fig. 15 - B Mode Frequency Deviation from Mean Mode Frequency

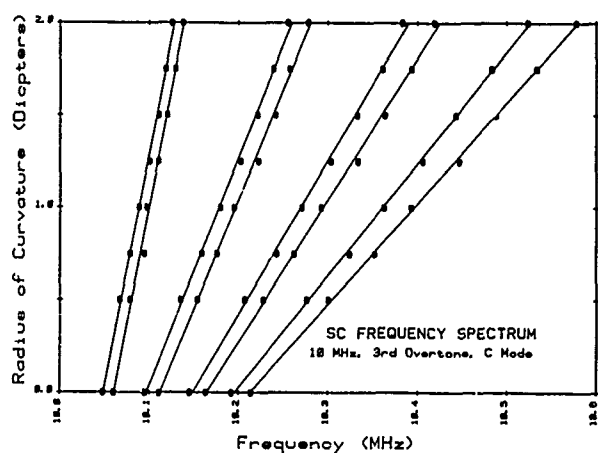


Fig. 16 - C Mode Anharmonic Mode Frequency Spectrum

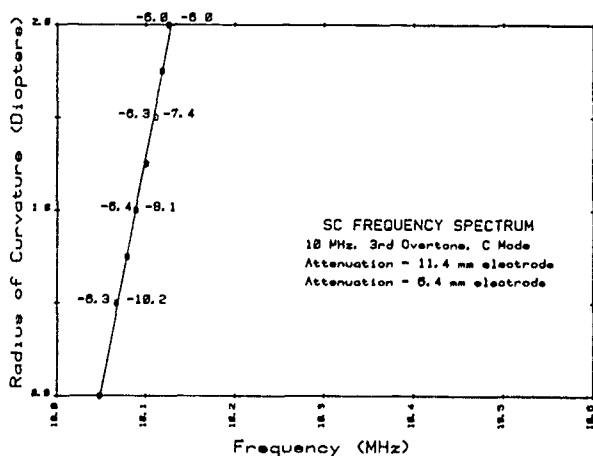


Fig. 17 - C Mode Anharmonic mode attenuation

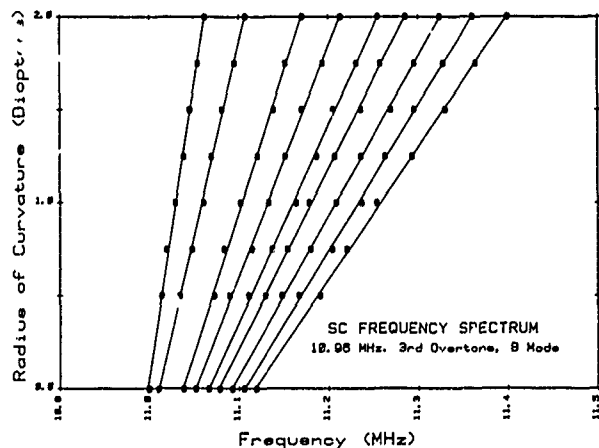


Fig. 18 - B Mode Anharmonic Mode Frequency Spectrum

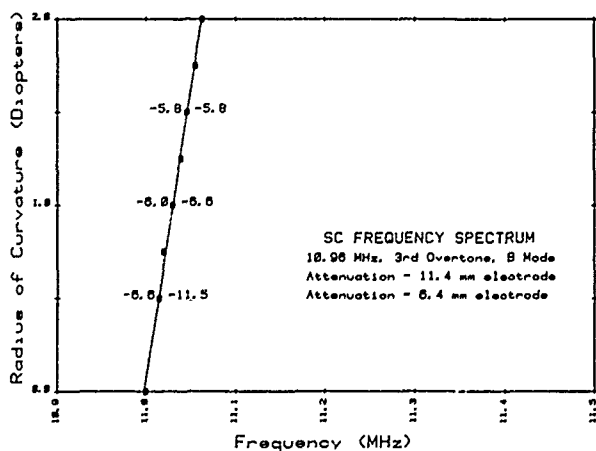


Fig. 19 - B Mode Anharmonic mode attenuation

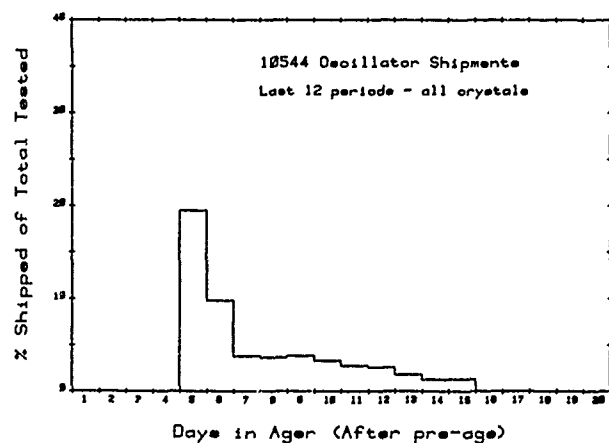


Fig. 20 - BT Cut Oscillator Shipments - Last 12 periods

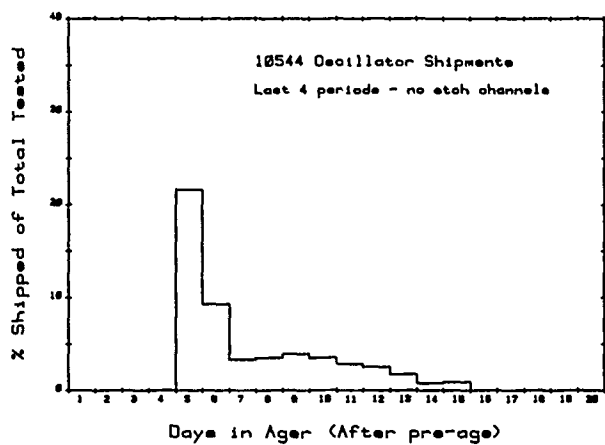


Fig. 21 - BT Cut Shipments - Last 4 periods without Etch Channels

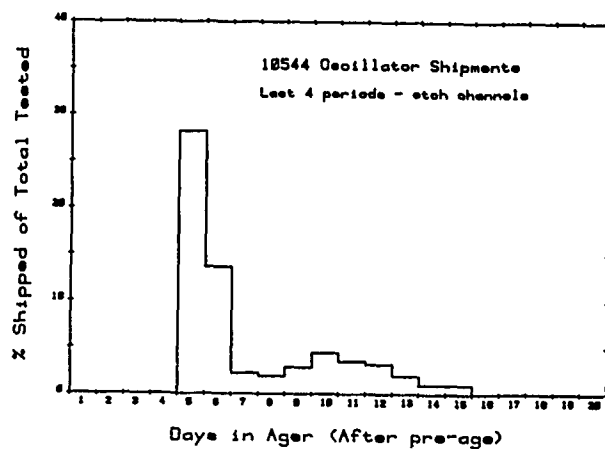


Fig. 22 - BT Cut Shipments - Last 4 periods, etch channel units only

FURTHER ADVANCES ON B.V.A. QUARTZ RESONATORS

R.J. Bessor * and U.R. Peier**

*Ecole Nationale Supérieure de Mécanique
et des Microtechniques - Besançon - France

**Oscilloquartz S.A. - CH-2002 - Switzerland

ABSTRACT

In the 1976 and 1977 Annual Symposia on Frequency Control a new piezo-electric resonator design was introduced.

The recent results on 5 MHz resonators concerning amplitude frequency effect, aging (versus drive level and quartz material) will be given. Especially it will be shown that extremely high drive levels can be used (up to 30 mW) and that the increase in drive level does not destroy aging performances. In addition, a "zero aging rate" is possible at a given drive level. By "zero aging drive level" we mean that the aging rate crosses zero for this given power dissipation.

Finally, the industrial aspects of the production of B.V.A. units will be discussed.

INTRODUCTION

Piezoelectric resonator has a long story since it began in 1918. Most important improvements were performed by R.A. Sykes who introduced the universal use of coated units in 1948 and A.W. Warner who achieved in 1952 the design which is still used without any major change. Then for a time, improvements appeared as asymptotical and interest decreased. Quartz crystal oscillators already provide us with small, rugged, low consumption, low cost units of excellent short term stability. The main effort has gone toward decreased aging, lower amplitude-frequency effect (then as a consequence better short term stability), low thermal transient sensitivity, and low environmental dependance (acceleration, vibration, ...).

A very promising development has been the introduction of doubly rotated crystals (1), (2), interesting for their low sensitivities to stresses in the plane of the cut (2) their excellent thermal behavior including thermal transients (3) and their low amplitude frequency effect.

It is also possible to make drastic changes in the conventional design which obviously exhibits badly or incompletely solved boundary problems, at least to the high degree of perfection we need.

The main problems of the conventional design come through plating (surface perturbation, ion migration, and as consequences Q reduction, noise, aging...), frequency adjustment and mounting structure (stress relaxation and contamination) see ref. (4) (5).

Research type BVA₂ resonators have been evaluated covering approximately 10 different types of versions according to various goals of frequency range, type of mounting, size, environment, etc. At this point, some types are close to the industrial preproduction stage (6).

Results have been obtained at various frequencies including 100 MHz and ultrahigh (7). The BVA₂ 5 MHz type resonator has been the most extensively studied.

In this paper, the most interesting results previously obtained are reviewed and some new results are given. Particular attention is given to drive level capabilities and aging versus drive level questions. Frequency and phase stability performance and frequency retrace following power interruption are discussed.

BVA₂ RESONATOR

This paper only deals with resonators of the BVA₂ design. Basically, BVA₂ resonator construction includes :

1. An "electrodeless" design. All problems of damping, stresses, contamination, ion migration, etc., which relate to electrode deposition are removed. (see fig. 1).

2. A crystal mounting made of quartz. Small "bridges" connect the vibrating part of the crystal to the dormant part. (see fig. 2). Key advantages are :

- no discontinuities nor stresses in mounting points
- very high precision in shape and location of "bridges"
- symmetry and reproducibility when needed

3. Additional parameters. (compared to classical designs). The design exhibits additional construction parameters :

- the electrode (and thus the electric fields) can have a radius of curvature different from the radius of curvature given to the vibrating crystal.
- heaters and sensors can be placed in vacuum close to the crystal without contacting the vibrating crystal.
- connecting "bridges" can have a great various other features.

4. Provision for any material, crystal cut or frequency (including very high frequencies.).

5. Use of technological means (i.e. ultrasonic machining) which allow reproducibility or versatility (for example the external shape of crystal does not need to be circular or rectangular).

BRIEF REVIEW OF PREVIOUS RESULTS

In this section, only results dealing the 5 MHz AT or SC cut units will be discussed. The easiest is to list the results pointing out interesting figures already available. Very roughly speaking, the BVA design is capable of an order of magnitude improvement in short term stability (8), long term drift and acceleration sensitivity (9). More precisely, the following features can be listed from previous results .

1. Higher Q factor : 5 MHz fifth overtone AT (Oscilloquartz, Switzerland)

yielded $Q = 3.5 \cdot 10^6$ together with

$$\begin{aligned}R_1 &= 80.7 \Omega \\C_1 &= 1.02 \cdot 10^{-4} \text{ pF} \\C_0 &= 4.1 \text{ pF}\end{aligned}$$

2. Better frequency adjustment (by a factor of 2 to 5 depending of technology). Adjustment within ± 1 Hz for 5 MHz unit is possible.

3. Better short term stability. 5.9×10^{-14} for 128 s has been achieved (8) and 10^{-13} (for integration time in the order of 100 s) has been reproduced since. More recent results see paper of E. Graf elsewhere in this proceedings.

4. Lower drift rate. 5×10^{-12} /day drift has been measured at NBS Boulder and at ENSCM Besançon as well. Also important is the fact that final aging is established within hours or days and remains constant (10) (11). Results recently obtained will be discussed in the next section.

5. Lower g sensitivity (9). A maximum sensitivity of the order of $10^{-10}/g$ can be achieved in the case of AT cut units. A sensitivity lower than $5 \times 10^{-11}/g$ can be achieved in the case of SC cut single crystals.

6. Reduced amplitude frequency effect : Reduction by a factor of 2 to 15 (11). A factor of 2 is obtained with a concave electrode and a convex resonator, a factor of 10 with a plano and 15 with a concave electrode.

RECENT ADVANCES

1. Extremely high drive level

The usual drive level for conventional units ranges from 0.1 μW to some 20 or 30 μW , at least in ultrastable 5 MHz oscillators. Precision oscillators with an aging rate lower than $10^{-10}/\text{day}$ usually operate at less than a few μW . In the case of high spectral purity oscillators, the crystal can be driven slightly harder but this causes the aging rate to increase by an order magnitude or two. If the crystal is driven harder, non-linear effects (12) interfere and with still higher levels the crystal can even fracture.

Aging measurements as a function of drive level started 18 months ago. Indeed, the B.V.A. resonators (they do have reduced frequency - power effect that is 3 to 15 times smaller than for plated crystals) not only survived very high drive levels, they show also a modest aging rate. Some 20 resonators have been used at high drive levels and several of them have been measured for more than one year. BVA₂ resonators withstand drive levels in the mW or even 10 mW range.

For instance, the BVA₂ 2-77, 5 MHz, natural quartz, AT cut, fifth overtone unit has now been running for 16 months at a 1600 μW drive level. The oscillator and the single oven are of very simple design. Nevertheless the drift has remained very constant at $3.3 \pm 0.2 \times 10^{-10}/\text{day}$ after 72 hours. After power interruption the oscillator retraces to within 2 or 3 $\times 10^{-10}$ and the aging comes back to the previous value.

Another similar resonator of synthetic unswept material (BVA₂ 2-119) has been driven at 2.8 mW and exhibits an aging of approximately 10⁻⁹/day. Some 5 MHz resonators have been driven up to 30 mW but aging experiments have not been carried out for these drive levels (Influence Temperature on aging, see Ref. (15)).

2. Aging versus drive level.

The aging rate for BVA₂ resonators is a non monotonic function of drive level. Preliminary data (aging experiments unfortunately require long time periods !) on 7 resonators, and theoretical considerations show that the resulting aging a_r may be modeled by the following formula :

$$a_r = a_i + kP \{1 + a \exp(-\sqrt{\frac{P}{P_0}} \frac{t}{\tau}) + \dots\} \quad (1)$$

where : a_i is an intrinsic aging highly depending on material and cut
 k is a constant depending on material and cut
 P is the power dissipated in motional resistance R
 P_0 is a reference power level
 τ is a time constant
 t is time

This formulation is valid for a first operation; there is some evidence that the exponential part decreases for further operations. At this point, it is premature to quote precise figures for each parameter. However, orders of magnitude can be given for SC cut Natural quartz third overtone crystals :

$a_i \rightarrow \text{some } 10^{-10} \text{ /day}$
 $k \rightarrow \text{some } 10^{-12} \text{ /d/}\mu\text{W}$
 $a \rightarrow \text{order of } 10 \text{ to } 100$
 $\tau \rightarrow \text{several days}$

The number obtained with various units of the same material are consistent.

For these units the aging is predictable and also settable. Moreover it is possible to change the aging rate by changing the drive level. In particular it is possible to obtain, by slight changes of drive level, slightly positive or slightly negative aging. There is a drive level \bar{P}_1 , called "zero aging drive level", since it yields an aging rate crossing zero.

Three oscillators operating at this "zero aging drive level" remained to within 3×10^{-10} over 5 months. For AT cut, natural quartz, 5 MHz, fifth overtone, four bridge units a drive level of 70 to 90 μW appears to be optimum. For SC cut, natural quartz, 5 MHz, third overtone four bridge units a level of $\sim 160 \mu\text{W}$ is suitable for the so called "zero aging".

3. Internally heated crystals (13) :

Using very high drive levels, it is possible to directly heat the crystal by energy dissipation in the motional resistance R_1 . Units specially devoted to internal heating have been designed (12). These special units are described elsewhere in the proceedings (15).

4. Frequency retrace following power interruption:

Extensive retrace experiments have been conducted with resonator BVA₂ 2-77 already mentioned. This resonator retraced to within 2 or 3×10^{-10} following power interruption ranging between 12 and 48 hours. An example is given in fig. 3 for an interruption of 2 hours. Another crystal retraced after a power interruption of 24 hours as follow :

time elapsed	offset
1 h	$6 \cdot 10^{-9}$
2.5 h	$1.4 \cdot 10^{-9}$
5 h	$5 \cdot 10^{-10}$
7 h	$3 \cdot 10^{-10}$

The crystal was driven at its "zero aging power level" in a 200 W sec/^oC oven. Some other experiments with similar resonators but different drive levels have been conducted yielding similar results. Nevertheless, some particular resonators has shown a frequency versus temperature hysteresis effect which at this point seems to be related to the old mounting structure and packaging of prototype BVA₂ units.

The frequency retrace problem depends largely on the BVA mounting structures. These new structures based on principles already discussed (9) have been designed (one structure is already in the industrial stage). The structure must allow a large degree of symmetry and also mounting stresses must be avoided; especially the crystal must be frequency independent from the enclosure. Also the time constant of heat transfer is to be considered.

At this time preliminary results show that there are preferred ways to design a crystal which could retrace to within 2 or 3×10^{-10} almost in any conditions. More precisely, measurements have been performed on resonators during the fabrication process with greatly improved retrace (factor larger than 10) with respect to retrace obtained with the previous mounting structures. However, the encapsulated crystals have not been extensively tested yet.

DESIGN

The first few BVA-Resonators we made at Oscilloquartz had exactly the same design as the BVA₂ resonators that had been made in the laboratories of the ENSMB. During industrialisation we replaced the brass pieces by stainless steel. The feedthrus, that had been accorced glass, are replaced by compressed glass. Details are in Fig. 4.

The resonator itself is shown in Fig. 2. It's a planoconvex design. The vibrating part is separated by bridges from the corona that is intended for suspension purposes. The whole "sandwich" is held together with a sort of clips and suspended with springs to the rigid cage consisting of the lower and the upper plate that are connected by bolts.

PRODUCTION

Sawing is done on an ordinary diamond saw. First lapping is made on a planetary lapping machine. After X-Ray check the blanks are angle-corrected manually. It appears that this operation is somewhat easier to do because the blanks are very large. The large size helps especially in correction SC-Cut blanks : a correction to tolerance of $\pm 15''$ for both angles ϕ and θ is very easily achieved. We even use BVA SC blanks for operator training. The blanks for the capacitor are cut out of the same way but corrected in angle to only $\pm 1'$. Next lapping operations are made on pin lap machines that have been built in house. They are on conventional design, only a little bit larger in size. Here also we can profit of the larger size: uniformity becomes excellent.

The slots that separate the vibrating part from the corona are made by ultrasonic machine. Ultrasonic machining is a fast and problemless method, if one knows how to use the equipment. For this application it is the ideal method, it gives very high precision in locating the bridges, much more precise than any cementing or thermocompression bonding. The resonator diameter can be guaranteed to $\pm 50 \mu$ with a run out of the cylindric part of less than 5μ . US Machining gives also the possibility to a further reduction of mounting influences by making a double decoupling of the vibrating zone as in Fig. 5.

A form like this is absolutely possible. The bridges are 300μ .

The bridges are further machined by grinding from both sides, of course giving attention to the fact that one side will be of convex shape. These bridges are somewhat difficult to grind : they have a thickness of only 220μ m and have to be placed exactly into π -plane of the resonator.

Contouring is made on an optical polishing machine. We are using a method which uses both a mechanical polish and an etching process to get both a very smooth surface and a good approach to the spheric form.

The capacitors are produced in a similar manner. The ultrasonic machining is the same only that the dimensions are much less critical, the slots are intended only to improve pumping in the gaps. The gaps are made by lapping and have a dimension of 6μ for the plano gap and 10μ for the convex one.

The final assembly and testing is entirely made in a glove box filled with dry nitrogen. This working condition is not very comfortable but it makes sure that we do not have problems with dust, humidity or oxydation. Fig. 6 shows the glovebox with solid state heat test chamber where we measure the parameters at the turnoverpoint. This is necessary because we have a tolerance in final frequency adjustment of $\pm .2$ ppm. In the moment the gaps are individually manufactured to match these specifications, later we plan to have a stack of prepared capacitors with different gap sizes so that we can choose the right one.

Determination of the turnoverpoint is made in a temperature test chambre under vacuum. Temperature change is less than 10^0 C/hour.

Next operation is cold welding the can. During this operation the pinch of cheminee is still open so that we can mount the resonator on the bakeout equipment (fig. 8). The system is pumped by a sorption pump for rough pumping, then a turbomolecular pump connected in parallel with an ion pump. This is an ideal combination : the turbomolecular pump prefers the heavier molecules while the ion pump pumps best small molecules.

Bakeout temperature is 250^0 C.

In a next step we plan to replace the glass parts by stainless steel equipment and to use a cryopumping system to speed up the bakeout operation, and to have the possibility to pump 12 crystals at the time.

The can is finally closed by pinch-off.

The method for measuring the parameters follows IEC 444. We made our equipment ourselves (fig. 7). It's a vector voltmeter that locks automatically a synthesizer at the series resonance frequency. Actually the resolution is 1. Hz but it will be increased to 0.001 Hz in near future. Optionally the equipment can also be used to trace f-T and R-T curves or to detect spurious responses.

This slow temperature change has necessitated the set up an automatic measuring system containing a desk top calculator with tape cartridge to record the data. The system is operated over night and is protected against power failure. 6 crystals are measured at a time. Each crystal is operated in a small ECL-Gate type oscillator with it's appropriate load capacitor.

CONCLUSIONS

1. At the time an excellent aging and a very good spectral density can be achieved with the same resonator.
2. It's the first time that aging is modella-ble and settable (by means of the drive level).
3. Because of the high degree of symetrie in the mounting structure the BVA has a lower 2 g semitivity. The location of the bridges is much easier to control than with any other method.
4. The final frequency adjustment can be done within ± 1 Hz what allows to maintain a high loaded Quality factors in the oscillators circuit.
5. The BVA design larger variety of design parameters when other crystal designs, so that it is possible to adapt it for almost any special application but a high degree of precision work is required.

REFERENCES

- (1) A. Ballato, "Doubly Rotated thickness mode Plate vibrators, "Physical Acoustics, vol XIII, pp 115-181, Ac. Press NY (1978)
- (2) E.P. Eer Nisse, "Quartz Resonator Frequency Shifts Arising from Electrode Stress Compensated (S.C.-Cut) Quartz Resonator, Proc. 30th AFCS, pp 8-11 (1976)
- (3) J.Kusters, "Transient Thermal Compensation for Quartz Resonators", IEEE Trans. Sonics and Ultrasonics, SU-23, pp 276 (1976)
- (4) R.J. Besson, "A New Piezoelectric Resonator Design", Proc. 30th AFCS, pp 78-83 (1976)
- (5) R.J. Besson, "A New Electrodeless Resonator Design", Proc. 31st AFCS, pp 147-152 (1977)
- (6) R.J. Besson, U. Peier Conf. A 1.8 Proceedings Congres International de Chronometrie pp 57-61 Sept. 1979
- (7) J.P. Valentin, J.P. Michel and R.J. Besson, CR Acad Sc Paris 15. Oct. 1979
- (8) S.R. Stein, C.M. Manney Jr. F.L. Walls, J.E. Grey, NBS and R.J. Besson, ENSCMMB Proc. 32nd AFCS pp 527-530 (1978)
- (9) R.J. Besson, J.J. Gagnepain, D. Janiaud and M. Valdois, Proc. 33 th AFCS (1979)
- (10) R.J. Besson, C.R. Acad Sc Paris t 288 (2 mai 1979) serie B 245-248
- (11) A. Berthaut and R.J. Besson, CR Acad Sc Paris, Nov. 1979
- (12) J.J. Gagnepain, R.J. Besson, Physical Acoustics Volume XI Acad Press pp 245-288
- (13) J.P. Valentin and R.J. Acad. SC. Paris B138 24 Sept. 1979
- (14) R.J. Besson, J.P. Valentin, French patent application Nr. 7918553.
- (15) J.P. Valentin, 34th AFCS, Philadelphia, 1980

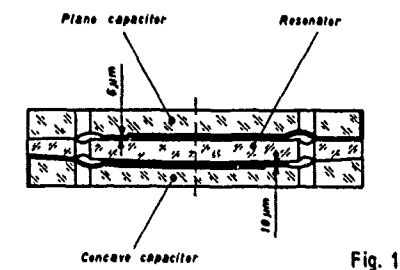


Fig. 1

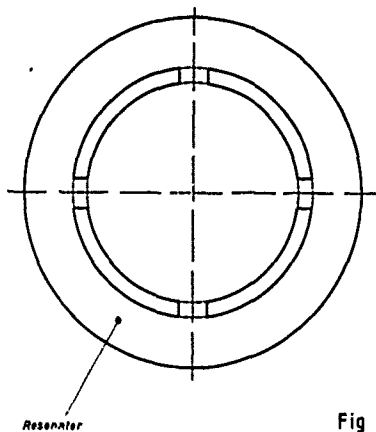


Fig 2

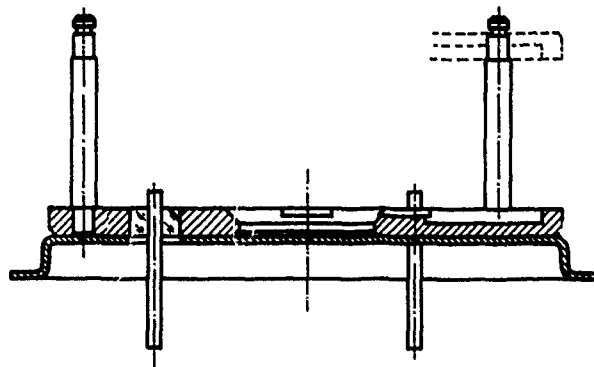


Fig.4 Baseplate of BVA enclosure with compressed glass feedthrus

Fig. 1/2 BVA₂ design consisting of Top capacitor (plano), Resonator and Bottom Capacitor (concave).

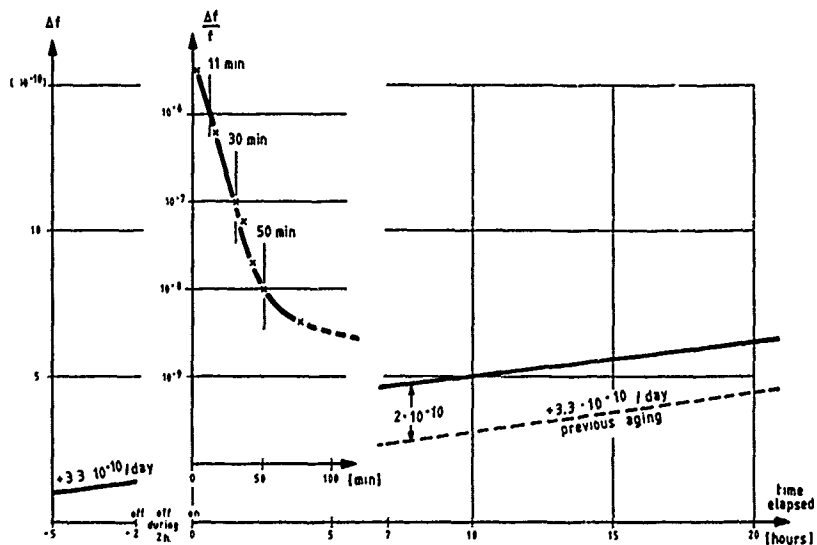


Fig. 3 Retrace characteristic of BVA₂ resonator after power interruption of 2 hours.



Fig. 5 Resonator with double bridge system, machined by ultra sonic means, width of the bridges : 0.3 mm.

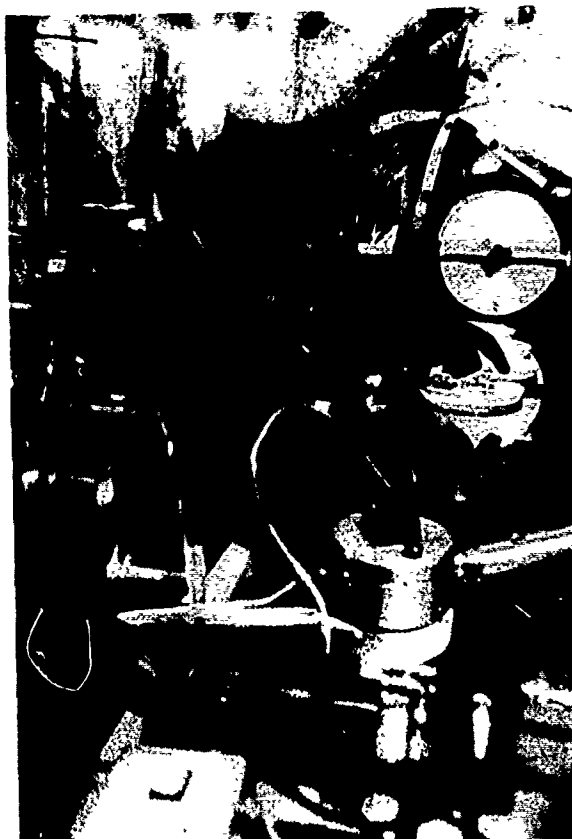


Fig. 6 Glovebox for assembly and measurement, filled with dry nitrogen.

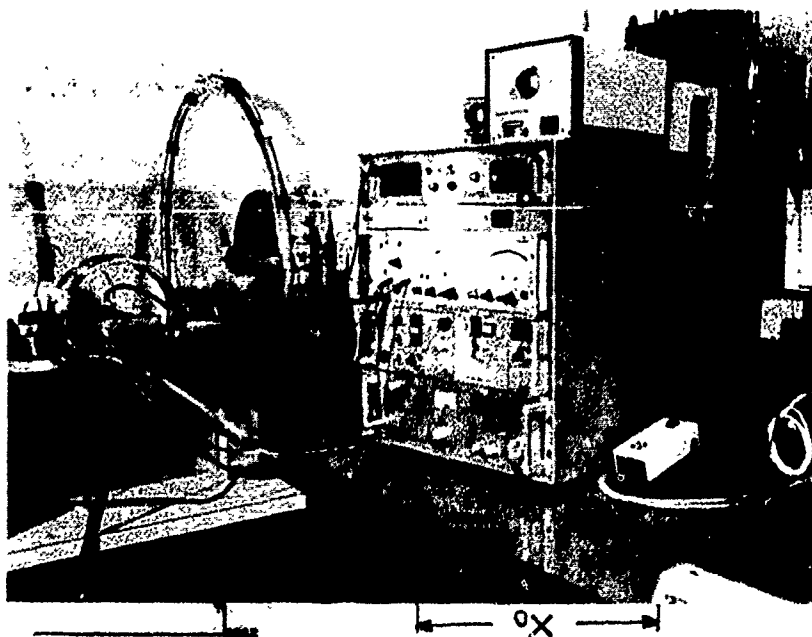


Fig. 7 Zero phase measuring equipment.



Fig. 8 BVA resonators mounted on
the bakeout system.

FURTHER DEVELOPMENTS ON 'SC' CUT CRYSTALS

Bruce Goldfrank and Art Warner

Frequency Electronics, Inc.
New Hyde Park, New York 11040

Introduction

'SC' cut crystals have found their way into many new designs. The applications, though many and varied, center around the requirements of good 'g' sensitivity, resistance to radiation, fast warmup and good temperature characteristics. The temperature and strain effects on the 'SC' cut crystal are such that a large improvement over AT cut crystals is possible. In particular, data will be given on the improvement in radiation resistance of the 'SC' over the 'AT'.

In order to produce a successful SC crystal unit, i.e., one that exploits this design to the fullest, significant changes in design philosophy, design parameters, measuring techniques, testing methods, and production tools must be made. Three of the more important changes involve angle control prior to final lapping, angle measurements, and frequency adjustment. Where low 'g' sensitivity is important, the crystal plates must be thermo-compression bonded using small, uniform, very precisely located mounting spots.

Orientation

That the orientation of the plate must be closely controlled can be understood when we consider the typical AT frequency versus temperature curve. The center of the curve which is the inflection point, is at room temperature, and as the specified operating temperature goes higher, angle control becomes easier. For the SC, the inflection point is near 100°C and as the operating temperature approaches that point the angle control becomes difficult. 70°C to 80°C zero temperature coefficient (ZTC) for the SC cut is like 40°C to 50°C for the AT cut. At 80°C, one minute of arc error can shift the ZTC by 20°C. The benefit is, of course, that once angle control is achieved the temperature curve is much flatter.

Figure 1 shows a quartz bar and the stages of orientation, following the IEEE standard nomenclature, $YX\omega\theta\psi$. Visualize a starting plate which is a Y cut, rotate it about the Z axis by the angle ϕ and then rotate it about its new length, X' , by the angle θ . The usual illustrations show the plate rectangular in shape. The final doubly oriented plate is usually shown the same size and shape as the starting plate. However, one can see that if we arrange to saw the

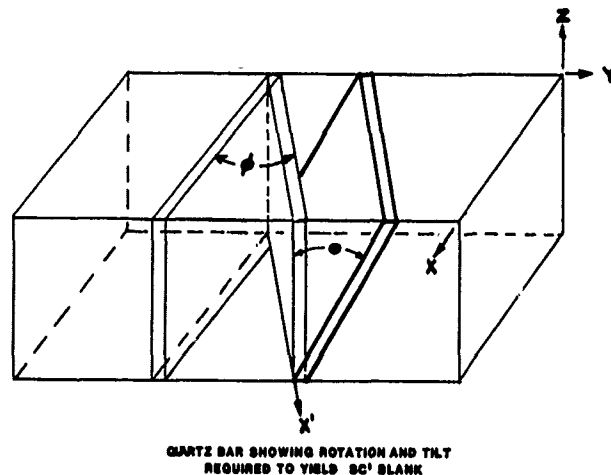
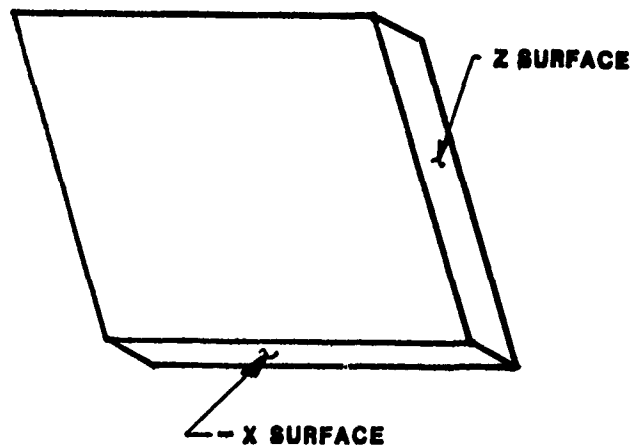


Figure 1. Stages of Orientation for a $YX\omega\theta\psi$ Blank



'SC' CUT CRYSTAL BLANK AS CUT FROM BAR

Figure 2. Quartz Blank As Cut From a Y Bar

doubly oriented plate from the bar, the shape will not be rectangular but will be as shown in Figure 2. If this were an AT, usual practice would be to simply mount it in the X-ray with the X axis vertical and compare the crystal face with the nearby 01.1 crystal plane at $38^\circ 12.7'$. However, with the SC we must first "undo" the ϕ angle, that is tilt the plate until the 01.1 plane is in a vertical position. The tilt itself is not particularly critical, but now the mounting flat, or if you will, the rotation of the plate about its thickness, becomes extremely critical, since this rotation will now tilt the reference plane.

Our answer to this problem is to highly correct the -X and one Z surface of the quartz bar itself before cutting. This is straight forward since, of course, there are X-ray planes parallel to these surfaces. These highly corrected surfaces are then used not only to orient the bar in the saw, but also to orient the blank in the X-ray goniometer.

Now, which edge surface should we use for the X-ray reference flat? The X' axis lies in the Z surface, some 14° away from using the -X surface as a reference flat and the X' would be the normal choice.

In either case, the equation to convert from the angle measured by the X-ray, to the specified θ angle is fairly simple, but it turns out there is an advantage to using the -X surface 14° away from the X' to locate the axis about which the X-ray angle is to be measured.

Figure 3 shows the relationship between the specified θ angle for various ϕ angles. The outer curve shows the equation developed by Ballato and Iafrate, and the other two curves show the corresponding angles θ' and θ'' measured by the tilt-back method for both X' axis and the -X surface. We can see that the angle measured using the -X surface, the upper curve, is much closer to the $38^\circ 13'$ reference plane, even closer than that of the AT. Also we can see the slope is about 1 in 6 or 6' error in measuring ϕ results in 1' error in measuring θ . You may also have noticed that for the SC cut at $\phi = 23^\circ$, that the 14° shift in reference flat location corresponds to a 5 or 6 degree shift in indicated angle, or almost 2 to 1. Two minutes error in reference flat equals one minute error in angle measurement. To keep this error to an absolute minimum, we use, as indicated earlier, the actual corrected surface generated on the quartz bar before it is cut. In addition we use a special jig that avoids any error due to chipping at the edges. Figure 4 shows the tilt back vacuum jig used with the X-ray. The reference surface makes contact along a line away from the crystal edge. Figure 5 shows this reference contact a little more clearly. Repeatability using this method is about 10 seconds of arc. The ϕ angle is measured by a 90° turn of the quartz blank. No tilt is needed in this case, because the X-ray plane in this position is within $1\frac{1}{2}$ degrees of vertical, again closer than the AT for this measurement.

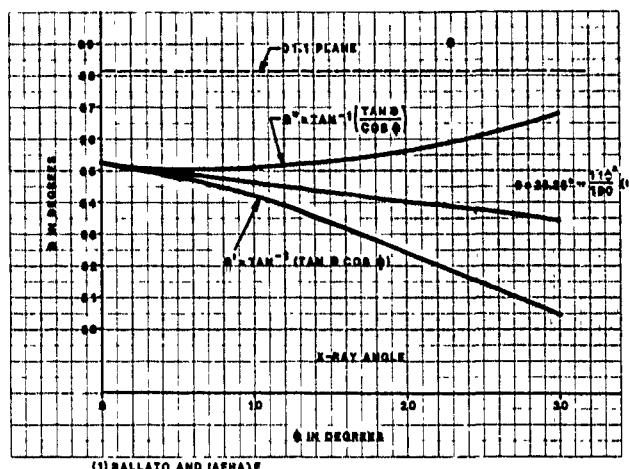


Figure 3. Relationship Between Specified ϕ and θ Angles and Those Measured By The Tilt-Back X-ray Method

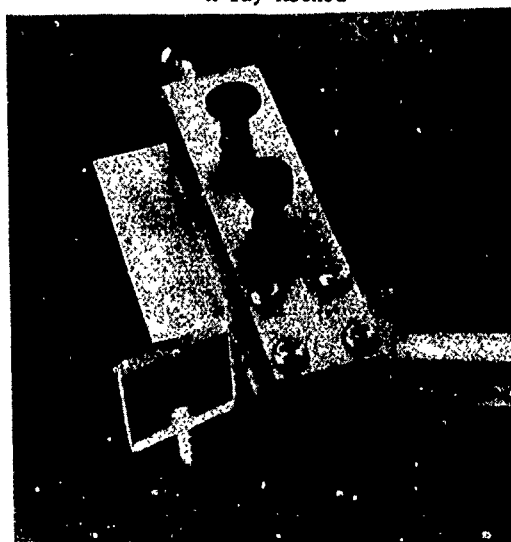


Figure 4. Tilt-Back Vacuum Jig Used With The Double-Crystal X-ray Goniometer

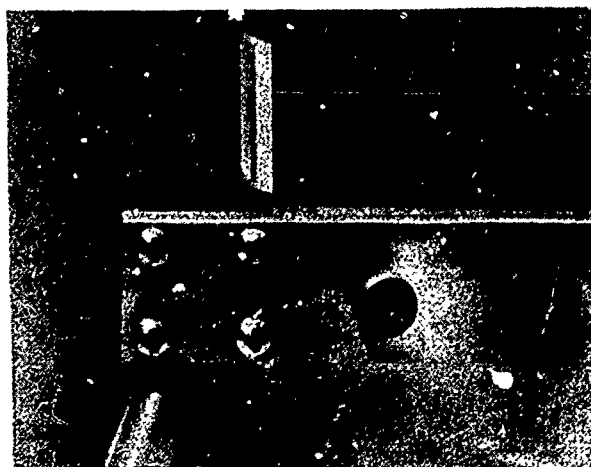


Figure 5. Tilt-Back Jig Showing -X Surface Contact

Figure 6 shows the precision saw. The setting is accomplished by a tilt and a rotation. Figure 7 is another view. One advantage of the tilt and rotation, rather than a double tilt is that the tilt and the rotation angles are exactly those measured by the X-ray. So necessary corrections to the saw table are directly applied from the X-ray reading. To obtain actual specified θ and ϕ angles, in practice, it is only necessary for the operator to enter the X-ray dial reading into a pre-programmed calculator and push the button.

Advantages of -X Surface Reference and Tilt Method of Orientation

1. An existing double crystal X-ray goniometer set for AT cut can be used with no change other than the tilt jig.
2. The angle is close enough to 01.1 plane for calibrating of standards by a turnover method.
3. Orientation of the sensitive reference flat is generated right on the quartz bar before cutting.
4. The ϕ angle is determined without a tilt jig and is simply measured by the X-ray.
5. By using a standard reference crystal, accuracies of a few seconds of arc are possible.
6. There is a direct correspondence between saw table angles and the angles measured by the X-ray.
7. Specified angles are obtained easily by using a simple programmed calculator.
8. The 14° psi angle generated automatically turns out to be the correct mounting point for the crystal plate.

Frequency Adjustment

The fact that the inflection point of the SC temperature frequency curve is above the operating temperature makes room temperature frequency adjustment a disaster. The slope is about 10 Hz per degree at 5 MHz. In addition frequency adjustment by circuit means is limited to about 1/4 of that of the AT. Therefore frequency adjustment at or near the temperature at which the crystal is to be operated is imperative. Figure 8 shows a small heater used in the vacuum deposition chamber. Temperature sensing control is by a thermistor bridge, the lead wires from the crystal are of special material and pass thru the temperature controlled block on their way to a network which sets the operating phase conditions. Deposition is by evaporation from a small tungsten filament.

Crystal Mounting

Figure 9 shows an experimental approach to thermo-compression (TC) ribbon mounting of the crystal plate. The ribbon is nickel, and it has a gold triangular strip bonded thereon. The TC bond will be gold to gold, and in the shape of a long thin rectangle, about 5 x 50 mils. This method permits a better location of the mounting points with respect to the center of the plate, and also permits TC bonding to very thin plates.

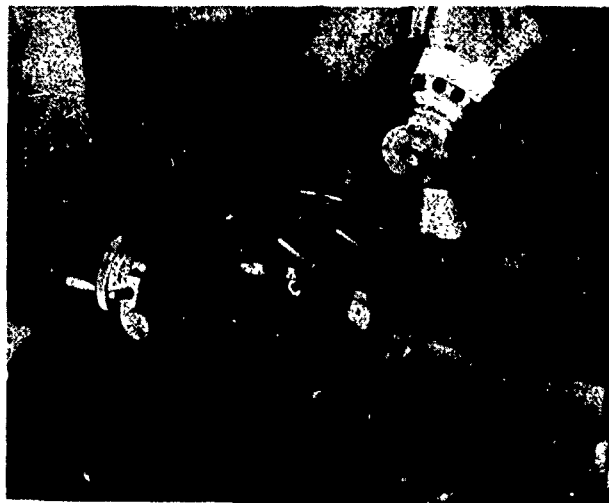


Figure 6. One View of the Precision Saw

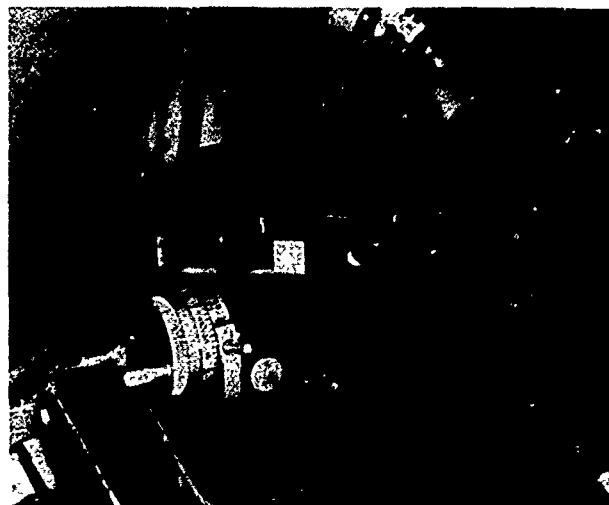


Figure 7. One View of the Precision Saw

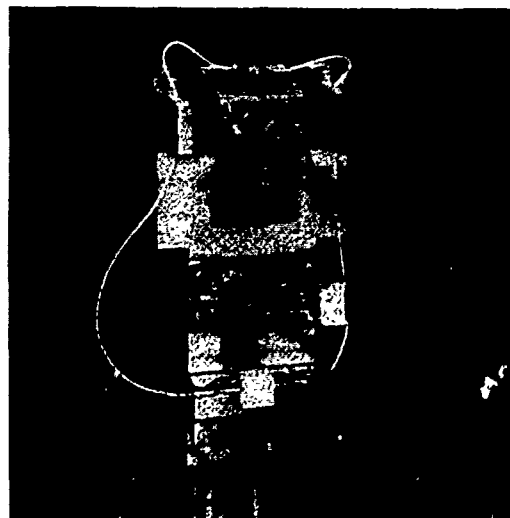


Figure 8. Crystal Unit Heater For Gold Evaporation in Vacuum

Figure 10 is a photo of one such bond on a 5 MHz 5th overtone plate. Figure 11 is a drawing of a typical thermocompression bond. Recent discussions with and calculations by Prof. Peter Lee, of Princeton University, have indicated the extreme importance of the mounting points in obtaining a low 'g' sensitivity crystal unit. He indicates a ψ angle near -15° as optimum for a 3 point 90° mount. It is interesting to note that the natural angle generated in cutting the blank, (-14.8°) which Frequency Electronics uses, the experimental angle reported by Kusters, Adams, and others of Hewlett Packard in 1977, and Peter Lee's calculated angle are all essentially the same. I believe the naturally generated angle is the correct one, but further experimentation will be necessary with precisely mounted units, to verify this.

Radiation Effects

An unexpected bonus came to light when some 24 MHz SC units in oscillators intended for use in the Galileo Probe of Jupiter were subjected to radiation of 1.0 megarads. The SC units changed 1 part in 10^{14} /rad versus 2 parts in 10^{12} per rad for AT units. This is about 2 orders of magnitude improvement in radiation susceptibility. This again needs further study.

Conclusion

Figure 12 shows a graph of one 5 MHz doubly contoured SC unit made at Frequency Electronics, Inc. subjected to a 2G acceleration by a simple turn-over test. Plate up to plate down was $1\text{PP}10^{11}$. Rotation in the vertical plane shows less than $1\text{PP}10^{10}$ per G. Future studies will be aimed at increasing the yield of such units.

Acknowledgment

This work was supported in part by a grant from USAERDCOM, #DAAK20-79-C-0272.

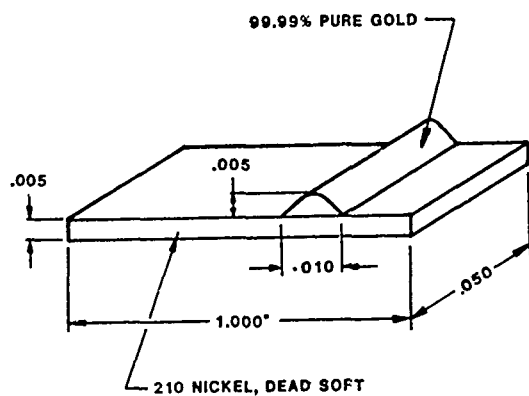


Figure 9. Experimental Gold Bonded Nickel Mounting Ribbon

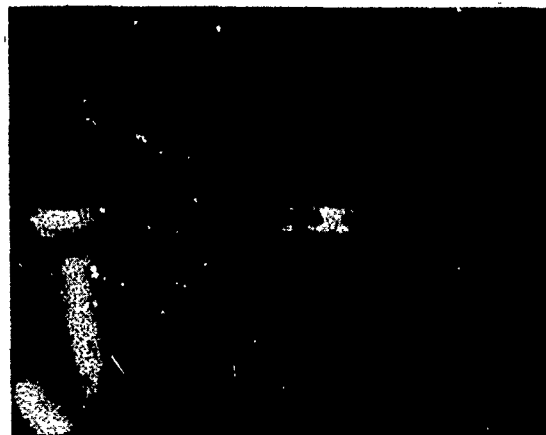


Figure 10. Experimental Thermo-Compression Bond To A 5 MHz SC Plate

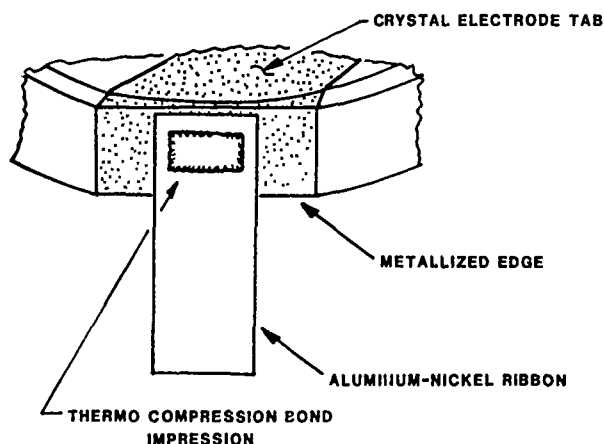


Figure 11. Typical Thermo-Compression Bond

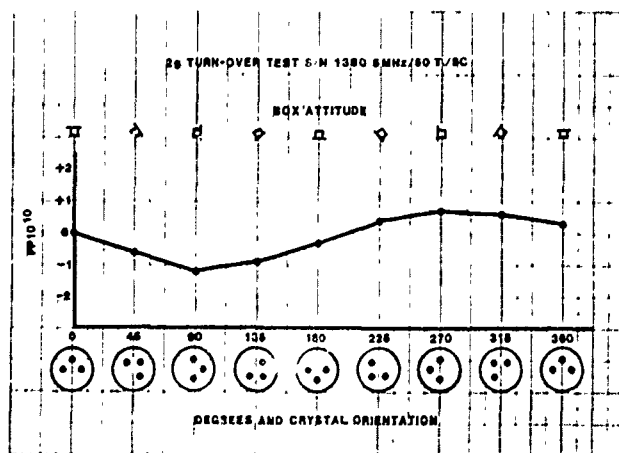


Figure 12. Turn-Over Test of One 5 MHz, 5th Overtone SC Unit Showing a 'g' Sensitivity of Less Than $1\text{PP}10^{10}$

FUNDAMENTAL MODE SC-CUT RESONATORS

RAYMOND L. FILLER and JOHN R. VIG

US ARMY ELECTRONICS TECHNOLOGY AND DEVICES LABORATORY
USAERADCOM, Fort Monmouth, NJ 07703

SUMMARY

The properties of fundamental mode SC-cut quartz crystal resonators have been studied, primarily as a function of blank contour and mounting orientation. When the crystal is mounted along the ZZ' axis, the resistance of the b-mode is consistently higher than the resistance of the c-mode. Q's above 1×10^6 have been observed for a contour of 1.37 diopter. The capacitance ratios ranged from 1000 at 0.37 diopter to 1700 at 2.5 diopter. For a 5.115 MHz fundamental mode resonator, the frequency sensitivity to d.c. voltage is 7×10^{-9} /volt. The implications of this voltage sensitivity are discussed. The sensitivity of apparent angle of cut to mass loading is shown to be substantially less for the SC-cut than for similarly fabricated A'-cuts. On the other hand, the equivalent series resistance of SC-cut resonators is more sensitive to ambient pressure variations than similarly fabricated AT-cuts'. The vibration sensitivities and the dependence of the mode spectrum on blank contour are also discussed.

KEY WORDS

Quartz, quartz resonators, resonators, SC-cut, frequency control, voltage sensitivity, Q, vibration resistance, mode spectrum.

INTRODUCTION

Overtone crystals are generally used in quartz crystal oscillators designed to attain the highest possible stability. Properly designed and fabricated fundamental mode resonators can, however, provide stabilities that are adequate for many "high stability" applications. It has now been confirmed¹, for example, that 5 MHz fundamental mode, AT-cut, ceramic flatpack enclosed resonators²⁻⁴ can exhibit short term stabilities of parts in 10^{17} per one second, aging of 2×10^{-10} per day after one week at 90°C, retrace of 5×10^{-10}

at the upper turnover temperature, and warmup to 1×10^{-8} (from -40°C to +90°C) in less than three minutes. If such respectable results can be achieved with fundamental mode AT-cut resonators, then, due to the now well known advantages of the SC-cut,⁵⁻⁷ it was felt that with properly designed and fabricated fundamental mode SC-cut resonators, even better performance could be achieved.

This paper is a progress report on investigations aimed at developing designs suitable for high stability, fundamental mode SC-cut resonators. Unfortunately, SC-cut resonators have a known disadvantage in that an undesirable mode of vibration, the b-mode, is always excited together with the (desired) c-mode. The b-mode, which is about 10% above the c-mode frequency, has had to be suppressed in the past by means of oscillator circuitry^{8,9}. Since simpler oscillator circuitry would result if the resonator could be designed to consistently have a higher b-mode resistance, a secondary goal of these investigations was to develop SC-cut resonator designs which assure the suppression of the b-mode.

RESONATOR FABRICATION PARAMETERS

The particle displacement for the c-mode is substantially along the XX' axis. The particle displacement for the b-mode, being substantially along the ZZ'-axis, is nearly perpendicular to that of the c-mode⁶. In an attempt to take advantage of these different particle displacements, initially two variables were investigated: 1) the orientation of the mounting points with respect to the crystallographic axes of the blank and 2) the blank contour.

The other resonator fabrication parameters were held constant, as follows: the frequency was 5.115 MHz on the fundamental mode, the blanks were natural quartz, 14 mm diameter, plano-convex, chemically polished¹⁰ and bonded at two diametrically opposite points with silver filled polyimide adhesive¹¹ to stainless steel mounting clips. The electrodes were 7 mm diameter, gold; the plateback was 1f². The resonators were packaged in HC-36 enclosures which were cold-weld sealed at 10^{-7} torr (fig 1).

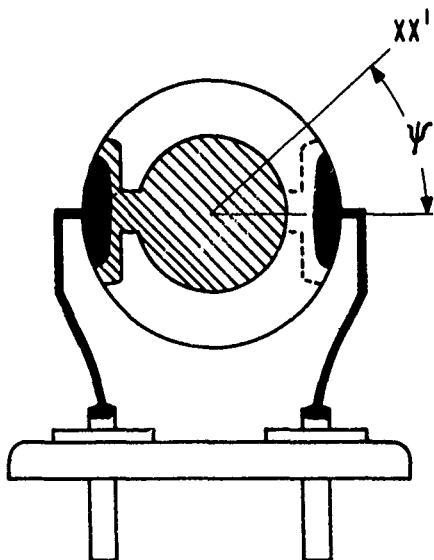


FIGURE 1: RESONATOR CONFIGURATION

The resonator parameters were measured with a microcircuit bridge¹². The frequency vs. temperature characteristics were measured with a crystal impedance meter.

Q VS. CONTOUR

The initial experiment was aimed at determining the dependence of Q on blank contour. The blanks were mounted on ZZ' in an attempt to suppress the b-mode. Figure 2 shows the Q of the c-mode vs. blank contour. The range of contours was from 0.37 diopter to 3.0 diopter. The initial groups of resonators indicated that 1.37 diopter provided the highest average Q , although no large variations in average Q were observable at diopter values from 1.0 to 3.0. The 1.37 diopter design was selected for further study. The additional units fabricated with this diopter are included in Figure 2. The maximum Q observed, 1.8×10^6 , occurred at the 1.37 diopter contour. The average Q at 1.37 diopter was about 1.0×10^6 , which corresponded to an equivalent series resistance of 7 ohms. As one would expect, the Q falls off rapidly at low diopter values, probably because the edges become more active.

The typical Q of these SC-cut resonators was about 30% higher than the Q of similarly fabricated AT-cut resonators.

R_b/R_c VS. CONTOUR

The second part of the experiment was to determine the ratio of the resistance of the b-mode, R_b , to the resistance of the c-mode, R_c . A ratio of R_b to R_c which is greater than one is desirable, because a wide-band oscillator circuit will tend to oscillate at the frequency of the mode with the lowest resistance.

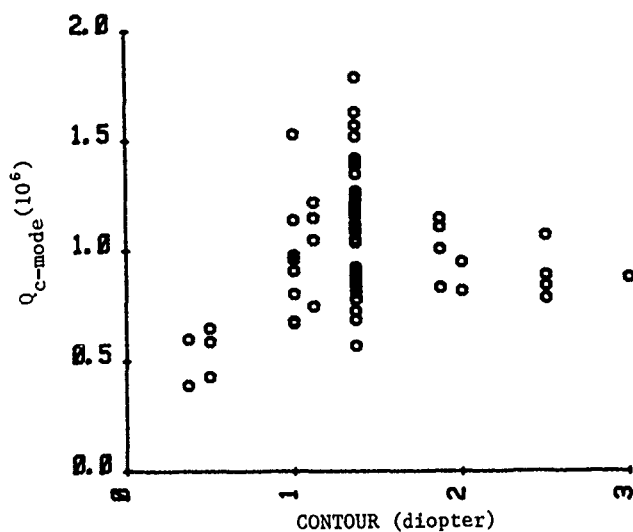


FIGURE 2: $Q_{c\text{-mode}}$ VS. CONTOUR

Figure 3 shows R_b/R_c vs. contour for all units of figure 2. Nearly all units (49 out of 50) had a b-mode resistance greater than the c-mode resistance. The ratios range from around 1 to over 100. The peak, or maximum b-mode suppression, occurs around 1.0 diopter. This appears to be a slightly lower contour than that at which the Q is a maximum.

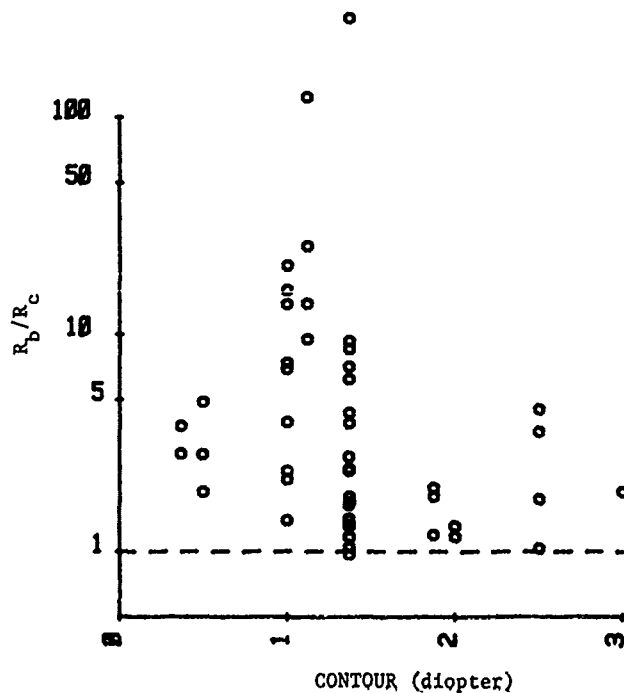


FIGURE 3: R_b/R_c VS. CONTOUR

The data points depicted in figures 2 and 3 represent all resonators that had a c-mode resistance less than 15 ohms. A 15 ohm cut-off value was chosen because the resistances fell mainly into two groups, those below 15 ohms and those above 40 ohms. Anomalously high c-mode resistances were observed for approximately 30% of all units fabricated. It should be noted that in the group with the anomalously high R_c , nearly 50% had a R_b/R_c ratio less than one. Reprocessing the blanks from these units usually resulted in a ratio greater than one. The fabrication parameter that degraded the c-mode resistances is yet to be identified.

The suppression of the b-mode has also been observed in plano-plano, 6.4 mm diameter, 20 MHz resonators. Of 45 resonators fabricated, 42 had an R_b greater than R_c , regardless of the resistance of the c-mode.

The suppression of the b-mode can, therefore, be achieved in fundamental mode SC-cut resonators.

R_b/R_c VS. MOUNTING ORIENTATION

In order to test the assumption that the mounting orientation has a significant effect on b-mode suppression, a group of nine blanks with the 1.37 diopter contour was reprocessed so as to change the mounting orientation from ZZ' to XX'.

Figure 4 depicts the ratio of R_b to R_c for the two different mounting orientations. It can be seen that most of the units had significantly higher b-mode suppression when mounted on ZZ'. One odd unit had a very high ratio on ZZ' and an even higher one on XX'. The other anomaly was the one unit in figure 3 which had a ratio less than 1.

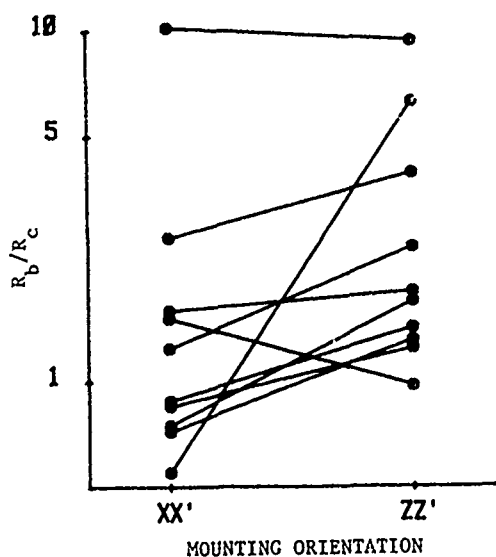


FIGURE 4: R_b/R_c VS. MOUNTING ORIENTATION

These results seem to confirm the original assumption that the different particle motions of the two modes may be of some aid in suppressing the unwanted b-mode. The probability of success in suppressing the b-mode is much higher when the resonator is mounted on ZZ' instead of XX'.

C_0/C_1 VS. CONTOUR

As is true for the AT-cut¹³, the capacitance ratio, C_0/C_1 , increases with increasing contour. Figure 5 depicts the C_0 to C_1 ratio vs. contour. The capacitance ratio ranges from approximately 1000 for a contour of 0.37 diopter to 1700 for 2.5 diopter. The capacitance ratio was measured to be 500 for an identically fabricated AT-cut resonator with a contour of 2.5 diopter. This data point is included in Figure 4 for comparison. The C_1 of SC-cut resonators is thus slightly less than one-third of the C_1 for identically fabricated AT-cut resonators. The SC-cut is, therefore, more difficult to "pull" than the AT-cut. For a given overtone, the SC-cut is more suitable for high precision applications, because the effects of circuit induced instabilities will be less.

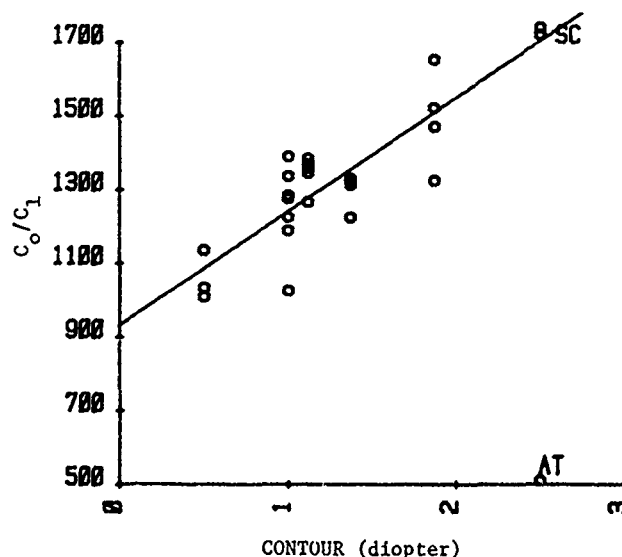


FIGURE 5: C_0/C_1 VS. CONTOUR

FREQUENCY VS. VOLTAGE

It has been reported^{14,15} that doubly rotated resonators are sensitive to d.c. voltages. The frequency of a fundamental mode 5.115 MHz SC-cut resonator, with a 1.37 diopter blank, was measured as a function of d.c. voltage applied to the electrodes. At each point, the frequency was measured 20-30 seconds after application of the voltage, after equilibrium had been reached¹⁴.

Figure 6 shows the fractional frequency change versus applied voltage. The frequency

change is linear, with a slope of about 7×10^{-9} /volt (or 2.53×10^{-12} meters/volt). Kusters¹⁶ measured 2.3×10^{-12} meters/volt while Hruska¹⁵ reported 1.33×10^{-12} meters/volt. The value for AT-cut resonators is theoretically zero⁸, but actually measures about 0.04×10^{-12} meters/volt¹⁶.

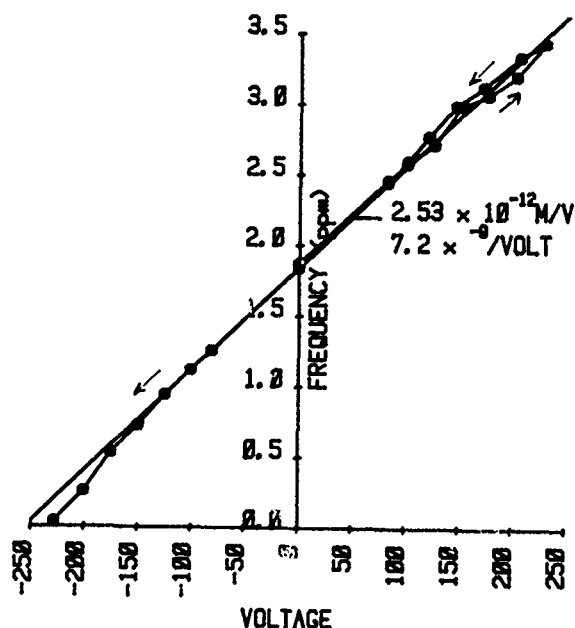


FIGURE 6: FREQUENCY VS. D.C. VOLTAGE - open circles are increasing voltage, closed circles are decreasing voltage, straight line is best fit.

This phenomenon is of interest because it has an effect on the proper choice of fabrication techniques and circuit configurations to be employed. It is well known that, especially under low humidity conditions, large electrostatic potentials can be developed in the course of normal, routine activities. For example, a person walking on a carpet can develop an electrostatic potential as high as 30,000 volts, and a clean room smock can become charged to over 20,000 volts if not treated with static retarding chemicals. When a person who is charged to such a high potential touches a good insulator, such as clean quartz, static charges are transferred which can remain on the surfaces for long times, at localized areas and at high potential.

If in the course of cleaning and handling a 5 MHz fundamental mode SC-cut resonator, an electrostatic potential of only 150 volts remains on the resonator when it is sealed hermetically, the contribution of this electrostatic charge to the initial aging of the

resonator will be about 1 ppm. It is therefore important that during the fabrication of SC-cut resonators static charges be eliminated from the surfaces before the resonators are sealed. The UV/ozone cleaning technique¹⁷ is a simple method of eliminating static charges (while also maintaining surface cleanliness). More elaborate techniques are used in the semiconductor industry where static charges can permanently damage many types of devices.

APPARENT ANGLE SHIFT VS. PLATEBACK*

It has been reported^{18,19} that mass loading shifts the apparent angle of cut of AT-cut resonators. This effect was of interest as a possible method of "angle correcting", i.e., fine-tuning the frequency vs. temperature characteristics of SC-cut resonators.

A convenient method of monitoring changes in the frequency vs. temperature characteristic of a resonator is to monitor the variation in the frequency difference between turning points, TP_1 - TP_2 . Figure 7 shows the variation of (TP_1 - TP_2), for identically fabricated AT and SC-cut resonators, as the thicknesses of the gold electrodes are increased. It can be seen that SC-cut resonators are less sensitive to plateback. It is likely that the effect we were measuring for the AT-cuts, was a combination of mass loading and electrode stress. Because it is known that the SC-cut is compensated for electrode stresses²⁰, and, it is now also known that the SC-cut is also relatively insensitive to plateback, one may expect less fabrication induced miscorrelation between the frequency vs. temperature characteristic and the x-ray angles for SC-cut resonators than for AT-cut resonators.

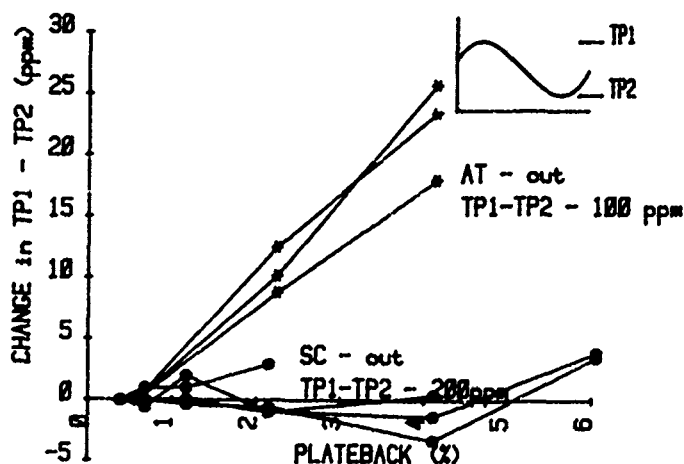


FIGURE 7: APPARENT ANGLE SHIFT ($TP_1 - TP_2$) VS. PLATEBACK

* The resonators used in this experiment were backfilled with 1 atmosphere of nitrogen and solder sealed (HC-6) to facilitate reprocessing.

PRESSURE DEPENDENCE

The particle displacements for both the b and the c modes of SC-cut resonators are slightly out of the plane of the blank⁶. It may therefore be expected that an SC-cut resonator's properties would be more sensitive to variations in the ambient gas pressure than an AT-cut's¹.

As the ambient pressure surrounding an SC-cut resonator was increased, a large increase in equivalent series resistance was observed. Figure 8 shows the change in equivalent series resistance for 5.115 MHz SC and AT-cut resonators. The pressure was varied from 2×10^{-2} torr to 1 atmosphere (of air). The resistance change for the SC-cut was nearly a factor of six. The AT-cut changed by a factor of 3. At low pressure, the slope of the resistance vs. pressure curve of the SC-cut resonator is about 3 times larger than that of the AT.

The frequency change between 2×10^{-2} torr and 1 atmosphere was measured (in a non-temperature controlled environment) to be less than 1 ppm, the estimated resolution of the measurement.

VIBRATION RESISTANCE

The effect of vibration²¹ was measured along the three major axes of the HC-36 enclosure. For SC-cut resonators mounted on ZZ' or XX', the lowest vibration sensitivity was along the direction parallel to the pins. The highest sensitivity was along the direction perpendicular to both the pins and the normal to the face of the quartz blank.. For SC-cut resonators mounted on ZZ', the sensitivities ranged from $2.5 \times 10^{-10}/g$ to $8.5 \times 10^{-10}/g$ for the best direction and from $2.0 \times 10^{-9}/g$ to $6.0 \times 10^{-9}/g$ for the worst direction. For an SC-cut resonator mounted on XX', the values were $3.0 \times 10^{-10}/g$ for the best direction and 2.0×10^{-9} for the worst direction. The worst direction for an identically fabricated AT-cut resonator was normal to the blank, where it has a vibration sensitivity of $7.4 \times 10^{-9}/g$. The best direction for this AT-cut was, as for the SC-cut, parallel to the pins, where the value was $7.6 \times 10^{-10}/g$. The scatter in the data did not allow for a determination of whether or not there is a relationship between the vibration sensitivity and the suppression of the b-mode.

MODE SPECTRUM

The mode spectrum for an SC-cut resonator with a 1.37 diopter contour is shown in figure 9. The resistances, in ohms, of all modes are also shown. The lowest frequency mode, at 5.115 MHz and 3.97 ohms, is the c-mode. The mode near 5.6 MHz, 9.59 ohms, is the b-mode.

The frequency difference to the first anharmonic mode is shown in figure 10 as a function of contour. It can be seen that the frequency difference increases for increasing

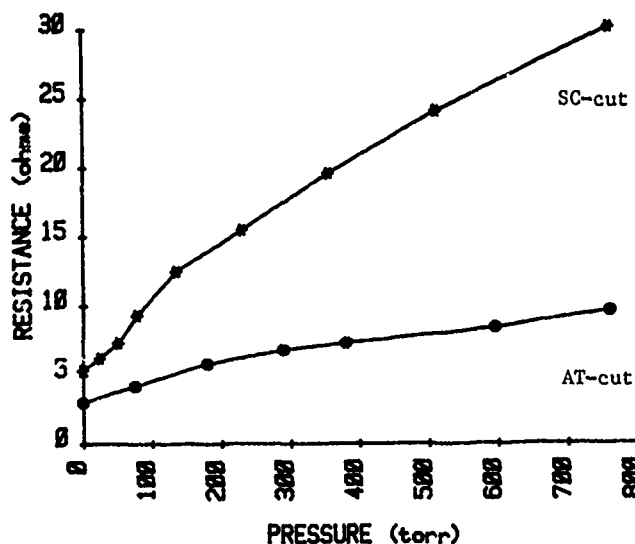


FIGURE 8: RESISTANCE VS. AMBIENT GAS PRESSURE

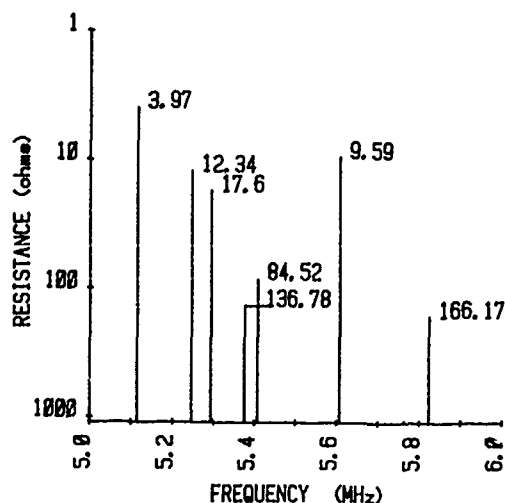


FIGURE 9: MODE SPECTRUM

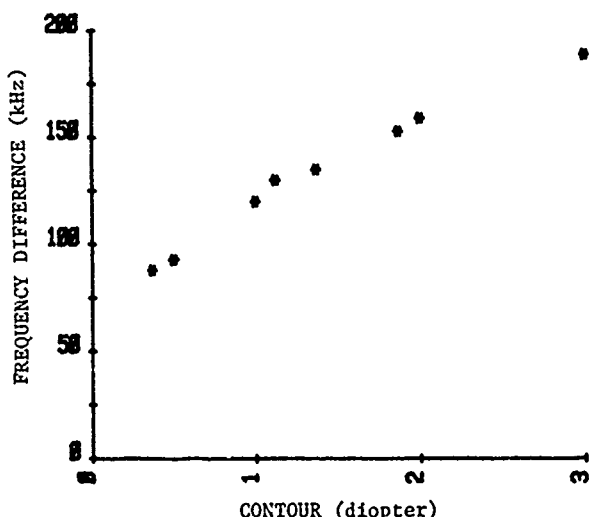


FIGURE 10: MODE SPACING VS. CONTOUR - frequency difference between first anharmonic mode and c-mode, in kHz.

contour. This behavior is similar for all of the anharmonic modes. The spacings between the b and the c modes, however, are much less sensitive to contour. The spacing for the first anharmonic mode increases from 1.72% of the c-mode frequency at 0.37 diopter to 3.6% at 3.0 diopter. The b-mode to c-mode spacing, for one particular angle of cut, increases from 10.23% to only 10.33% over the same range of contours.

CONCLUSION

Suppression of the b-mode with crystal design is possible for fundamental mode SC-cut resonators. The Q's of these units are acceptable for many high precision applications. The question of whether or not the b-mode suppression can be achieved while optimizing other parameters, such as vibration sensitivity, has yet to be determined.

ACKNOWLEDGEMENTS

The authors wish to thank R. Brandmayr, H. Spaghts and W. Washington for their skillful contributions in preparing the quartz plates used in these experiments, and D. Boyce and E. Simon for their assistance with resonator evaluation.

REFERENCES

1. H. W. Jackson, "Tactical Miniature Crystal Oscillator", these proceedings.
2. J. R. Vig and E. Hafner, "Packaging Precision Quartz Crystal Resonators", Technical Report ECOM-4134, US Army Electronics Command, Ft. Monmouth, NJ,

July 1973. Copies available from NTIS, accession no. AD 763215.

3. P. D. Wilcox, G. S. Snow, E. Hafner and J. R. Vig, "A New Ceramic Flatpack for Quartz Resonators", Proc. 29th ASFC*, 1975, pp. 202-210.
4. R. D. Peters, "Ceramic Flatpack Enclosures for Precision Quartz Crystal Units", Proc. 30th ASFC*, 1976, pp. 224-231.
5. J. A. Kusters, et. al., "TTC's - Further Developmental Results", Proc. 31st ASFC*, 1977, pp. 3-7.
6. A. Ballato, "Doubly Rotated Thickness Mode Plate Vibrators", in Physical Acoustics: Principles and Methods, Vol. 13, W. P. Mason and R. N. Thurston, Eds., New York: Academic Press, 1977, Chapter 5, pp. 115-181.
7. A. Ballato and J. R. Vig, "Advances in the Stability of High Precision Crystal Resonators", Proc. of the Eleventh Annual Precise Time and Time Interval (PTTI) Applications and Planning Meeting, NASA Conference Publication 2129, 1979, pp. 403-440.
8. R. Burgoon and R. L. Wilson, "Design Aspects of an Oscillator Using the SC-cut Crystal", Proc. 33rd ASFC*, 1979, pp. 411-416.
9. M. Bloch, et. al., "Galileo Quartz Clock", Proc. of the Eleventh Annual Precise Time and Time Interval (PTTI) Applications and Planning Meeting, NASA Conference Publication 2129, 1979, pp. 441-455.
10. J. R. Vig, R. J. Brandmayr and R. L. Filler, "Etching Studies on Singly and Doubly Rotated Quartz Plates", Proc. 33rd ASFC*, 1979, pp. 351-358.
11. R. L. Filler, et. al., "Polyimide Bonded Resonators", Proc. 32nd ASFC*, 1978, pp. 290-298.
12. G. Malinowski and E. Hafner, "Automatic Microcircuit Bridge for Measurements on Quartz Crystal Units", Proc. 32nd ASFC*, 1978, pp. 354-364.
13. A. W. Warner, "High-Frequency Crystal Units for Primary Frequency Standards", Proc. IRE, Vol. 40, Sep 1952, pp. 1030-1033.
14. J. A. Kusters, "The Effect of Static Electric Fields on the Elastic Constants of α Quartz", Proc. 24th ASFC*, 1970, pp. 46-54.

15. C. K. Hruska, "Zero Polarizing Effect with Doubly Rotated α Quartz Plates Vibrating in Thickness", IEEE Trans. Sonics and Ultrasonics, Vol. SU-27, March 1980, pp. 87-89.
16. J. A. Kusters, private communication, 1977.
17. J. R. Vig, "UV/Ozone Cleaning of Surfaces: A Review", in Surface Contamination: Genesis, Detection and Control, Vol. 1, K. L. Mittal, Ed., New York: Plenum Press, 1979, pp. 235-254.
18. A. Ballato and T. Lukaszek, "Higher Order Temperature Coefficients of Frequency of Mass Loaded Piezoelectric Crystal Plates", Proc. 29th ASFC*, 1975, pp. 10-25.
19. A. Ballato, T. J. Lukaszek and G. J. Iafrate, "Subtle Effects in High Stability Vibrators", these proceedings.
20. E. P. EerNisse, "Calculations on the Stress Compensated (SC-cut) Quartz Resonator", Proc. 30th ASFC*, 1976, pp. 8-22.
21. R. L. Filler, "The Effect of Vibration on Quartz Crystal Resonators", Technical Report DELET-TR-80-10, ERADCOM, Ft. Monmouth, NJ, 1980, Available from NTIS, AD A085642.

* ASFC: Annual Symposium on Frequency Control,
 US Army Electronics R&D Command, Ft.
 Monmouth, NJ, 07703. Copies available from
 Electronics Industries Association, 2001
 Eye Street, NW, Washington, DC 20006

INTERNAL HEATING AND THERMAL REGULATION OF BULK QUARTZ RESONATORS

Jean - Pascal Valentin

Ecole Nationale Supérieure de Mécanique et des Microtechniques
La Bouloie - Route de Gray - 25030 Besançon Cedex - FRANCE

SUMMARY

In this paper, the possibility to keep a quartz resonator at its turning point temperature, only by means of the drive power, is studied.

Coated units first, then "electrodeless" resonators are considered. The latter, which stands high power levels and nevertheless maintains low aging rates, can be, after various modifications of its thermal insulation, maintained at its turn-over temperature with approximately 20mW.

Various applications are proposed. In particular it is possible to design an accurate portable unit using a very rough oven and a laboratory oscillator in a liquid helium environment.

INTRODUCTION

In a classical resonator thermal transfers occur through the crystal surface which plays a fundamental part. Thermal exchanges, by conduction and radiation, depend on the crystal surface and involve a temperature gradient in the crystal. Energy dissipation inside the crystal is very small and actually does not contribute to the thermal balance of the "resonator/oven" system. The internal temperature of the crystal is regulated by the crystal surface temperature and the average thermal energy through the resonator surface is null.

EXTERNAL AND INTERNAL FLUX

Basically, two thermal flux control the thermal balance of a bulk quartz resonator :

1) The external flux which corresponds to the resonator exchanges with its oven. At equilibrium its average is null. The exchanges correspond to the oven fluctuations and occur through the resonator surface. Accordingly, the crystal internal temperature is regulated by the resonator surface temperature. As a consequence a temperature gradient inside the crystal (entirely depending on the oven fluctuations) is involved.

2) The internal flux due to vibrational energy dissipation. Vibrational energy is dissipated in the whole bulk crystal, essentially in the nodal planes of vibration. Thus, the whole bulk crystal plays an important part in a self

thermal regulation process. Then a more homogeneous inner crystal temperature is obtained.

Of course, thermal conduction effects inside the crystal tend to make the internal and the surface temperatures uniform, since quartz material is a fairly good thermal conductor.

Note that, for a classical coated resonator, drive levels usually range from 0.1 microwatt to several tens microwatts (low aging rate units commonly correspond to some microwatts drive levels). Under those conditions the internal thermal flux is very small and cannot be used for thermal regulation.

However, recent works have shown that the new "electrodeless B.V.A." resonators can stand extremely high drive levels (up to 60 mW for a 5 MHz unit). Nevertheless good aging rates (for instance $3.3 \cdot 10^{-10}$ /day for sixteen months and for 1.6 mW, in a 5 MHz fifth overtone AT cut resonator) are obtained^{1,2}.

In this particular case the internal thermal flux is no more negligible. So we recently proposed the internal flux utilization to keep constant and adequate the crystal temperature³.

Of course, for an accurate device, it is not possible to modulate the drive level, because of "amplitude to frequency effect". Then, for the thermal regulation, it is necessary to use an other mode (overtone, anharmonic, B or C mode, ...) with a low coupling factor. On the other hand the A.F. effect is considerably reduced for an "electrodeless" resonator. Nevertheless, for warm up applications the metrologic mode may be used : the greater the power on the crystal is, faster the warm up.

Note that a high drive level is very suitable for spectral purity improvement. Other interesting technics contribute to this improvement, but at the price of more sophisticated electronics^{4,5}.

INTERNAL HEAT SOURCE

The inner flux comes from the electrical energy dissipated into heat. It is useful to analyse the transformation mechanism in order to calculate its efficiency. It can be shown that the efficiency is greater than 99%³. Then, the internal heat source produces a thermal power equal to the drive power.

Then, what should be the drive level in order to keep the resonator temperature at the turning point, only with the internal heat source? The answer needs an analysis of the resonator specific thermal losses.

Let us consider first coated resonators.

COATED RESONATORS

(For this section, all numerical values are calculated deal with a very general case : AT cut, 5 MHz, 5ft overtone Xtal, gold coating, glass enclosure, turning point = 350°K).

Conduction thermal losses :

They include :

1/ Losses by wires

2/ Losses by residual gas.

Losses P_w by wires are ruled by the FOURIER's law :

$$dP_w = - \lambda \frac{\partial T}{\partial n} dS$$

The thermal conductance C_w is calculated from :

$$P_w = C_w \Delta T$$

In the case of wires, obviously :

$$C_w = AS/\ell \text{ where } S \text{ is the surface, } \ell \text{ the length}$$

with ⁶ :

$$\lambda_{\text{nichrome}} = 13W/m^{\circ}K, \lambda_{\text{nickel}} = 59W/m^{\circ}K$$

For both wires, the average value of C_w is :

$$C_w \approx 2 \cdot 10^{-4} W/^{\circ}K$$

Losses P_g due to residual gas are ruled by KNUDSEN'S law ⁷ :

$$dP_g = - \lambda p \frac{\partial T}{\partial n} dS$$

where :

$$\Lambda = \frac{1}{2} \frac{\gamma + 1}{\gamma - 1} \left(\frac{R}{2\pi M T_e} \right)^{1/2}$$

with p : residual pressure in the enclosure

S : enclosure surface

γ : specific heats ratio

R : perfect gas constant

M : molar mass

T_e : enclosure temperature (°K)

For air $\Lambda \approx 1,6 W/m^2 \times P_a \times ^{\circ}K$ at $T_e = 350^{\circ}K$

Obviously, the thermal power dissipated by gaseous conduction is :

$$P_g = C_g \Delta T \text{ with } C_g = \Lambda p S$$

For $p \approx 10^{-3}$ mbar, we obtain :

$$C_g \approx 0.7 \cdot 10^{-4} W/^{\circ}K$$

This conductance is not negligible compared to C_w .

Nevertheless, for precision resonators the residual pressure is $\ll 10^{-3}$ mbar and C_g is negligible.

Radiation thermal losses :

Thermal exchanges by radiation obey the PLANCK's law. In this case ($T \approx 350^{\circ}K$) the energy spectral density is maximum for wavelengths of approximately 8 μm . Then, the quartz crystal is not transparent and we shall consider its transmission factor as null. It is also the case for the enclosure (glass, metal or ceramic).

On the other hand the crystal and the enclosure will be considered as grey bodies obeying the LAMBERT's law.

The net flux exchanged from the crystal to its enclosure will be calculated when the system is at the steady state characterized by constant temperatures (T_q for the quartz crystal surface and T_e for the enclosure). Two difficulties appear :

1/ the enclosure is a hollow body : the radiation emitted by its inner surface is partly absorbed by itself.

2/ It is not possible to neglect the multiple reflections between the quartz crystal and its enclosure.

Then, the following assumption is made : the quartz emission and the enclosure emission are independent. The effects of both emissions calculated independently may be added up.

Thus, the whole energy flux ϕ_q gathered by the quartz from the enclosure (multiple reflections included) is considered. In addition the quartz thermal emission is assumed null.

Likewise, the whole energy flux ϕ_e gathered by the enclosure from the quartz (multiple reflections included) is considered. Then, the enclosure thermal emission is assumed null.

The net thermal power P_r radiated from the quartz to its enclosure is written :

$$P_r = \alpha_e \phi_e - \alpha_q \phi_q$$

with :

α_e = energetical absorption factor of the enclosure inner surface.

α_q = energetical absorption factor of the quartz crystal.

Determining the various terms in this relation needs knowledge of :

ϵ_e = energetical emission factor of the enclosure inner surface.

ϵ_q = energetical emission factor of the quartz crystal.

ρ_e = energetical reflection factor of the enclosure inner surface.

ρ_q = energetical reflection factor of the quartz crystal.

ϕ_{te} = total flux emitted from the enclosure inner surface, multiple reflections included (the quartz thermal emission being assumed null).

ϕ_{tq} = total flux emitted from the quartz crystal, multiple reflections included (the enclosure thermal emission being assumed null).

-sure thermal emission being assured null).

It can be easily seen that :

$$\phi_e = \phi_{tq}$$

$$\phi_q = f \phi_{te}$$

Here f is a coefficient < 1 , which only depends on the "quartz-enclosure" system geometry. On the other hand :

$$\phi_{te} = \epsilon_e \sigma T_e^4 S_e + \rho_e \rho_q \phi_q$$

$$\phi_{tq} = \epsilon_q \sigma T_q^4 S_q + f \rho_e \rho_q \phi_e$$

In these equations, the first terms correspond to the thermal emissions, σ being the STEFAN's constant, the second terms correspond to the multiple reflections on the enclosure inner surface S_e and the quartz crystal surface S_q . Taking the radiation KIRCHHOFF's law and the energy conservation law into consideration, we obtain :

$$\tau_r = \frac{\epsilon_e \epsilon_q \sigma (S_q T_e^4 - f S_e T_q^4)}{1 - f (1 - \epsilon_e) (1 - \epsilon_q)}$$

The f coefficient calculation can be done using the following remark : f being only depending on the system geometry, we can consider the quartz and its enclosure as black bodies exchanging exclusively together. Then, at the thermal balance, P_r is null and :

$$f = \frac{S_q}{S_e}$$

Similarly to the case of conduction losses, a radiation conductance C_r can be defined from :

$$P_r = C_r \Delta T \quad \text{with } \Delta T = T_q - T_e$$

Obviously :

$$C_r = \frac{\epsilon_e \epsilon_q \sigma S_q (T_e + T_q) (T_e^2 + T_q^2)}{1 - (1 - \epsilon_e) (1 - \epsilon_q) \frac{S_q}{S_e}}$$

In the classical case of a resonator in an oven ($T_e = T_q$), this relation is simplified. For an AT cut, 5 MHz, 5th overtone, in cylindrical glass enclosure ($h \approx 2\text{cm}$, $\phi \approx 2\text{cm}$), turning point $\approx 350^\circ\text{K}$, the computed value of C_r is :

$$C_r \approx 23 \cdot 10^{-4} \text{ W/}^\circ\text{K}$$

To summarize, radiation losses are, by far, the most important. For a precision resonator they represent 92% of the thermal losses. and the losses by wires conduction only 8%. Experimental data can be obtained from transient measurements (the time constant which depends on the total conductance is obtained).

Transient process :

A variation ΔT_e of the enclosure temperature T_e induces a transient response ruled by :

$$P_e dt = k c_p dT_i + \frac{C_q}{1-k} (T_i - T_q) dt$$

and

$$\frac{C_q}{1-k} (T_i - T_q) dt = C_t (T_q - T_e) dt$$

with :

P_e = electrical power

c_p = crystal thermal capacity

C_t = total conductance ($C_w + C_g + C_r$)

C_q = crystal conductance

T_i = inner heat source temperature

T_q = crystal surface temperature.

The whole crystal material cannot be considered as a heat source but only a part of it, let us say k , corresponding to regions close to the nodal planes. By X-rays topography⁸ the coefficient k can be estimated to 0.5.

The solution of the previous equations-system is an exponential variation with a given time constant τ :

$$\tau = \frac{k c_p (1-k)}{C_q C_t} (C_t + \frac{C_q}{1-k})$$

Here, C_t is approximately $25 \cdot 10^{-4} \text{ W/}^\circ\text{K}$, and c_p is easily calculated : $c_p \approx 0,55 \text{ J/}^\circ\text{K}$. The thermal conductivity λ in a direction perpendicular to the AT plan is given by :

$$\lambda^2 \left(\frac{\cos^2 \phi}{a^2} + \frac{\sin^2 \phi}{b^2} \right) = 1$$

with $\phi = 35^\circ$, $a = 5,9 \text{ W/m}^\circ\text{K}$, $b = 11 \text{ W/m}^\circ\text{K}$

This relation give : $\lambda = 6,7 \text{ W/m}^\circ\text{K}$

Then, in this case : $C_q \approx 7900 \cdot 10^{-4} \text{ W/}^\circ\text{K}$

and $\tau \approx 110\text{s}$

This numerical value is in very good agreement with the experimental results⁹. It should be observed that the glass enclosure conductance is around $3 \text{ W/}^\circ\text{K}$ for a typical enclosure. Compared with C_t this conductance is very large and does not interfere in the time constant measurement.

Steady State :

At the thermal balance, P_e is given by :

$$P_e = \frac{C_q}{1-k} (T_i - T_q) = C_t (T_q - T_e)$$

With the above numerical values, we calculate the differences $T_i - T_q$ and $T_q - T_e$:

1/ At low drive level (1μW)

$$T_i - T_q \approx 6 \cdot 10^{-7} \text{°K} \text{ and } T_q - T_e \approx 4 \cdot 10^{-4} \text{°K}$$

2/ At high drive level (50μW)

$$T_i - T_q \approx 3 \cdot 10^{-5} \text{°K} \text{ and } T_q - T_e \approx 2 \cdot 10^{-2} \text{°K}$$

In both cases the inner temperature inhomogeneity ($T_i - T_q$) is considerably smaller than the surface temperature variations induced by the oven fluctuations. Thus, the resonators' inner thermal gradients depend always only on oven fluctuations.

But it is different for the quantity ($T_q - T_e$). For a low oscillating level this quantity is completely instable because its average value is comparable to the fluctuations of the best ovens. The thermal flux exchanged between the crystal and its enclosure can be directed either way, and its variation can be very large (even 100%). It must be pointed out that the surface stress is connected to these flux variations, and may involve oscillator frequency variations.

For high drive levels, the crystal being in an oven at $\pm 10^{-3} \text{°K}$, the difference $T_i - T_e$ is twenty times larger than oven fluctuation. The thermal flux flows out permanently from crystal to enclosure and carries variations of about 5% only. The frequency variations connected to thermal flux variations are then smaller than previously. However, non linear effects have to be considered and probably ruin part of the improvement.

Fast variations of drive level :

Let us impose a 10% relative variation on the drive level, the oven temperature T_e being assumed constant. The ($T_i - T_q$) and ($T_q - T_e$) variations subsequent to this jump are:

1/ At low drive level (1μW)

$$d(T_i - T_q) \approx 6 \cdot 10^{-8} \text{°K} \text{ and }$$

$$d(T_q - T_e) \approx 4 \cdot 10^{-5} \text{°K}$$

2/ At high drive level (50μW)

$$d(T_i - T_q) \approx 3 \cdot 10^{-6} \text{°K} \text{ and }$$

$$d(T_q - T_e) \approx 2 \cdot 10^{-3} \text{°K}$$

In the first case the thermal variations subsequent to a 10% power jump may always be ignored by respect to variations involved by the oven fluctuations. For a high drive level ($T_i - T_e$) variations subsequent to a 10% power jump are in the order of magnitude of oven fluctuations. The surface temperature changes of $2 \cdot 10^{-3} \text{°K}$, involving a similar evolution of the inner temperature. Then, the resonator frequency changes in agreement with the usual frequency-temperature curve. For high drive levels the effect on frequency of an inner temperature gradient variation has been very carefully studied¹⁰. It has been shown that

this variation induces an elastic strain related to the vibration by non linear elastic effects. This causes variation of the resonator frequency.

"ELECTRODELESS" RESONATORS

These resonators have already been presented². Basically it includes :

1/ a vibrating quartz crystal. The active part of the crystal is connected to the dormant part by little quartz bridges.

2/ a quartz condenser made of two disks of the same cut and orientation on which the electrodes are deposited.

3/ means to maintain the condenser and crystal tightened together.

4/ a metallic enclosure.

Those resonators exhibit thermal properties completely different from the properties of other units. This is connected, on the one hand, to the thermal inertia of the device, on the other, to the high conductance between the condenser and the enclosure

Thermal conductances :

C_w and C_g do not differ from the same quantities in coated resonators. However, the radiation conductance C_r , turns out to be (all numerical applications are made for an AT cut, 5 MHz, 5th overtone, turning point 350°K, nickeled enclosure):

$$C_r \approx 13.7 \cdot 10^{-4} \text{ W/°K}$$

Taking into account various data on the mechanical fixation structure, the total conductance C_t between condenser surface and enclosure (wires, residual gas, radiation and suspension) is found to be :

$$C_t \approx 1500 \cdot 10^{-4} \text{ W/°K}$$

On the other hand, the internal conductance C_i between the inner heat sources (in the crystal) and the condenser surface must be taken into account. This last conductance interferes through the bridges' conduction and the radiation process between the crystal surface and the condenser inner surface. For an ordinary construction, the bridges' conductance is approximately $\approx 50 \cdot 10^{-4} \text{ W/°K}$.

The radiation inner conductance is easily computed and found to be $\approx 24 \cdot 10^{-4} \text{ W/°K}$. Note that the quartz crystal and the two disks of the condenser are actual thermal "short - circuits". Thus, the internal conductance C_i is simply the sum of both previous conductances, and :

$$C_i \approx 74 \cdot 10^{-4} \text{ W/°K}$$

Transient Process :

A variation ΔT_e of T_e induces a transient response ruled by :

$$P_e dt = k c_p dT_i + C_i (T_i - T_q) dt$$

and

$$C_i(T_i - T_q)dt = C_p dT_q + C_t(T_q - T_e)dt$$

C_p being the condenser thermal capacity. This system is equivalent to :

$$\frac{k_c C_p}{C_i} \ddot{T}_i + (k_c C_p + C_p + k_c \frac{C_t}{C_i}) \dot{T}_i + C_t T_i = C_t T_e + (1 + \frac{C_t}{C_i}) P_e \quad (1)$$

Equation whose the solution is always aperiodic :

$$\Delta T_i = \Delta T_e \{1 - e^{-t/\tau} (A \sinh \omega t + ch \omega t)\}$$

Here $C_t/C_i \gg 1$. This condition give :

$$\begin{aligned} \tau &\approx 2k_c C_p C_i / (k_c \frac{C_t}{C_i} + C_p) \\ \omega &\approx C_i (k_c \frac{C_t}{C_i} - C_p) / 2k_c C_p \\ A &\approx (k_c \frac{C_t}{C_i} + C_p) / (k_c \frac{C_t}{C_i} - C_p) \end{aligned}$$

The response-time t_r cannot be defined simply and differs from the time-constant τ . Nevertheless, it is possible to give an approximation for t_r :

$$t_r \approx \frac{k_c C_p + C_p}{C_i C_t / (C_i + C_t)} \quad \text{which correspond to} \quad t_r \approx 650 \text{ s.}$$

The response-time depends only on C_i when $C_t/C_i \gg 1$. It should be pointed out that C_i depends on the bridges number, on their location and on the reflection factor of the electrodes. Usually for "electrodeless" resonators, the experimental measurement yield : $500_s < t_r < 850_s$.

Here, the response-time is several times that of a coated resonator. This situation explains the "electrodeless" resonator thermal hysteresis is larger compared to the case of a coated resonator. Indeed, for a given temperature slope the thermal lag is proportional to the response-time. On fig. 1, are represented a temperature slope imposed to the enclosure and the corresponding crystal temperature. If the "frequency-temperature" curve is known for increasing temperatures, then, the "frequency-temperature" curve for decreasing temperatures can be inferred. For instance at the time t_1 , the enclosure temperature is T_A and the crystal temperature T_B . To the temperature T_B corresponds the point C on the first part of the curve (frequency f_1). The point D of the second part of the curve is located at the intersection between the axis T_A and the axis f_1 . The point D' is obtained for the time t_2 in a similar way. This explanation of the observed "frequency-temperature" curve is reinforced by both following experiments :

1/ for a given device, the thermal hysteresis is always larger for the crystal under vacuum

than for the crystal under atmospheric pressure, the thermal conductance being larger in the second case.

2/ for a given device, the thermal hysteresis is always larger for a fast temperature slope than for a slow one, the thermal lag being proportional to the speed.

Internal Gradient :

At the thermal balance :

$$P_e = C_i (T_i - T_q) = C_t (T_q - T_e)$$

The numerical application give :

1/ At low drive level (1μw) :

$$T_i - T_q \approx 1.5 \cdot 10^{-4} \text{°K}$$

2/ At high drive level (50μw) :

$$T_i - T_q \approx 7 \cdot 10^{-3} \text{°K}$$

In the latter case, the internal difference $T_i - T_q$ is larger than the variations of the surface temperature T_q , induced by the oven fluctuations. Thus, the internal gradient of temperature is more permanent with the time.

Internal Heating :

Usual "electrodeless" resonators must be modified for internal heating applications. Indeed, to maintain the crystal temperature at 350°K with an external temperature of 293°K, it would be necessary to drive the crystal with a power :

$$\begin{aligned} P_e &= (T_i - T_e) C_i C_t / (C_i - C_t) \\ &\approx 400 \text{ mW} \quad \text{which is not adequate.} \end{aligned}$$

ISOLATED "ELECTRODELESS" RESONATOR

For an internal heating device, the last calculation shows it is necessary to decrease :

- 1/ the radiation losses between the condenser and the enclosure.
- 2/ the conduction losses of the wires.
- 3/ the conduction losses of the whole fixation structure.
- 4/ the internal losses by radiation and conduction between the crystal and the condenser.

Decreasing of radiation losses :

The thermal conductance by radiation between the condenser and the enclosure is given by :

$$C_r = \frac{\epsilon_q \epsilon_e \sigma S_q (T_q + T_e) (T_q^2 + T_e^2)}{1 - (1 - \epsilon_e)(1 - \epsilon_q) \frac{S_q}{S_e}}$$

For practical reasons the ratio S_q/S_e is about 0.5. It is difficult to decrease this ratio. Likewise the surface S_q is imposed by the frequency and by the need of good quality coefficients.

Then, it is possible to change ϵ_q and ϵ_e by use of coated condensers and coated enclosures. A gold coating is recommended. Indeed, for a wavelength of 10 μm :

$$C_r \approx 0.35 \cdot 10^{-4} \text{ W/}^\circ\text{K} \quad \text{at } T_q = T_e = 350^\circ\text{K}$$

Thus, C_r is divided by forty by respect of its value in the case of a normal electrodeless resonator.

Decreasing of conduction losses of wires :

Some alloys as Nichrome, Hastelloy C or even stainless steel can be used. For Nichrome, a diameter of 100 μm is correct. Then, for both wires :

$$C_w \approx 0.2 \cdot 10^{-4} \text{ W/}^\circ\text{K} \\ \rho \approx 1.4\Omega$$

Decreasing of conduction losses of fixation structure :

It is necessary to be very careful because these losses are, by far, the most important. Indeed, for a normal "electrodeless" resonator the conductance of the fixation is :

$$\approx 1500 \cdot 10^{-4} \text{ W/}^\circ\text{K}$$

A novel fixation structure has been designed in this case and allows in principle :

$$C_t \approx 5 \cdot 10^{-4} \text{ W/}^\circ\text{K}$$

Some more effort is needed on that point.

Decreasing of internal losses :

Two points can be studied :

1/ The bridges can be reduced and manufactured following the X-axis of the AT cut. Then, bridges conductance can become :

$$\approx 20 \cdot 10^{-4} \text{ W/}^\circ\text{K}$$

2/ In order to decrease the radiation losses between the crystal and the condenser, the inner surface of this can be gilded, except a fine line round the electrodes. Thus, the energetic emission factor of the condenser inner surface is reduced to the minimum, and the thermal conductance by radiation between the crystal and the condenser is calculated :

$$\approx 1.7 \cdot 10^{-4} \text{ W/}^\circ\text{K}$$

Taking those two conductances into consideration, the internal conductance C_i is :

$$C_i \approx 22 \cdot 10^{-4} \text{ W/}^\circ\text{K}$$

Response-Time :

With the new values for C_t and C_i , t_r becomes :

$$t_r \approx 3 \text{ hours}$$

This response-time corresponds to an excellent thermal insulation ; it has advantage to make the inner crystal practically insensitive to the periodic temperature variations when the variations period is not too slow.

In order to calculate this insensitivity, let us impose to the enclosure by the intermediary of the oven, the following temperature variation :

$$T_e = T_o + \Delta T_e \sin \Omega t$$

Then, the second part of the equation (1) includes a variable term and, in the steady state, the internal temperature T_i of the resonator becomes :

$$T_i = T_o + \frac{C_t + C_i}{C_i C_t} P_e + \Delta T_i \sin (\Omega t + \phi)$$

with

$$\Delta T_i = \frac{C_t \Delta T_e}{C_t \cos \phi - \{C_p + k C_p (1 + \frac{C_t}{C_i} + \frac{C_p}{C_i} \Omega)\} \Omega \sin \phi}$$

and

$$\text{tg } \phi = \frac{\{C_p + k C_p (1 + \frac{C_t}{C_i})\} \Omega}{\frac{k C_p C_p}{C_i} \Omega^2 - C_t}$$

For periodic variations of period ≈ 1 hour, ΔT_i is computed :

$$|\Delta T_i| \approx 5 \cdot 10^{-2} |\Delta T_e|$$

And for periodic variations of period ≈ 1 minute :

$$|\Delta T_i| \approx 10^{-3} |\Delta T_e|$$

Of course, this last result is much interesting for the medium term frequency stability.

Drive levels needed for internal heating :

At the thermal balance the electrical power is connected to the conductances and the temperatures by the relation :

$$P_e = \frac{C_i C_t}{(C_i + C_t)} (T_i - T_e)$$

In order to keep, only with the electrical power, at its turning point (350°K) the isolated "electrodeless" resonator described previously, which sits in an environment at 293°K, it is necessary to rise the drive level to :

$$P_e \approx 23 \text{ mW}$$

Those drive levels have proved to be possible for B.V.A. resonators. Under, these conditions the temperature difference between the crystal and the condenser is :

$$T_i - T_q \approx 10^\circ\text{K}$$

and the difference between the condenser and the enclosure is :

$$T_q - T_e \approx 46^\circ\text{K}$$

VARIOUS APPLICATIONS ¹¹

Oscillator of medium accuracy :

Such an oscillator have the following characteristics :

1/ an internal heating, the traditional oven being suppressed (in general, this oven requires several watts).

2/ an aging rate which is basically constant.

3/ a resonator temperature regulation by the intermediary of the drive level. In order to avoid the frequency variations related to the A.F. effect, it is proposed to apply a constant power on the metrologic mode and to heat the crystal with another vibration mode ¹². Of course, this latter mode must be uncoupled with the metrologic mode, at least to a large extent.

The temperature sensor can use a third mode, for instance the mode B in a SC cut, like that has already been proposed ^{13,14}.

4/ a very fast warm up : the warm up time can be approximated very simply, since the condenser temperature is supposed constant and equal to T_e . Then :

$$T_i = T_e + \frac{P}{C_i} (1 - e^{-t/\tau})$$

with

$$\tau = k_c P / C_i$$

The superior limit of the warm up time can be computed using this relation.

Thus, using an isolated "electrodeless" resonator and with an electrical power of only 60 mW applied directly on the crystal, the warm up time is :

$$t \approx 10\text{s}$$

This time is the necessary time to obtain the turning point at 350°K , with an environment temperature at 293°K .

Accurate oscillator with rough oven :

If the necessary power in order to supply an oven is available, it is interesting to take advantage of the excellent insulation of the isolated "electrodeless" resonator. This can be set in a rough oven producing an temperature oscillation of $\pm 1^\circ\text{K}$, for instance. The various advantages are :

1/ a simple oven, little cumbersome and little breakable. With this, for oven thermal variation periods next to one minute, the crystal temperature fluctuations are 0.001°K .

2/ a little aging rate, in so far as the resonator is driven at $90 \mu\text{W}$ for an AT cut and at $160 \mu\text{W}$ for a SC cut ¹ (natural crystals).

3/ an internal gradient of temperature which is constant/time. Indeed, with a drive level of $90 \mu\text{W}$, the temperature difference $T_i - T_e$ is 0.2°K , i.e. two hundred times the crystal temperature fluctuation induced by the oven temperature oscillation. Thus, the thermal flux is constant and the resonator internal gradient variations are completely negligible.

4/ under these conditions, a frequency stability which would otherwise be obtained with a sophisticated oven, is obtained with a poor oven.

5/ a very fast warm up, because, like previously, the warm up time for the crystal is about 10 secondes (with a power of 60 mW applied directly on the crystal).

Hyper regulated oscillator :

In laboratory conditions, the fixation of the isolated "electrodeless" resonator can be modified and replaced by fine wires. At the same time radiation losses can be enlarged. These, with frosted surfaces, can give a thermal conductance, by radiation, of approximately :

$$C_r \approx 33 \cdot 10^{-4} \text{ W/}^\circ\text{K}$$

while the fixation thermal conductance can be decreased to :

$$C_{\text{fix}} \approx 0,5 \cdot 10^{-4} \text{ W/}^\circ\text{K}$$

Under these conditions the thermal losses are only radiative and at the thermal balance :

$$\frac{dT_i}{T_i} = \left(\frac{C}{C_i}\right)^4 \frac{dT_e}{T_e} + \frac{1}{4} \left(1 - \frac{T_e}{T_i}\right)^4 \frac{dP}{P_e}$$

Such a resonator is placed in a bath of liquid helium. Its internal temperature is kept at the turning point. Then, the ratio $(T_e/T_i)^4$ is :

$$\approx 4 \cdot 10^{-8}$$

Under those conditions using an usual helium bath, the crystal temperature T_i can be maintained very accurately :

$$T_i = 350^\circ\text{K} \pm 10^{-5}^\circ\text{K}$$

It is possible, with a helium bath whose the pressure would be controlled, to obtain $\pm 10^{-6}^\circ\text{K}$. But this is probably very difficult because of the electrical power control requirement. Under these conditions, in order to keep the crystal at the

turning point, the needed drive level is :

$$P_e \approx 1 \text{ watt}$$

This heating power can be directly applied on the condenser, by means of a resistor bonded on its external surfaces.

ACKNOWLEDGMENTS

The autor would like to thank especially Professor R. BESSON for work participation and many helpful discussions. He also would like to thank various coworkers in the laboratory, especially MM. BERTHAUT, GUERIN and MOUREY.

REFERENCES -

- 1 - A. Berthaut et R. Besson
Comptes-rendus 289 - Série B - 1979 - p.223.
- 2 - R. Besson
"A new electrodeless resonator design"
Proc. 31st - Annual Symposium Frequency Control
p.147 - 1977.
- 3 - J.P. Valentin et R. Besson
Comptes-rendus - 289 - Série B - 1979 - p.119.
- 4 - F.L. Walls et S.R. Stein
"A frequency - Lock system for improved quartz crystal oscillator performance"
I.E.E.E. Transactions - Vol. IM - 27 - N°3 - September 1978.
- 5 - R. Besson et M. Decailiot
Comptes-rendus - 288 - Série B - 1979 - p.57.
- 6 - Handbook of Chemistry and Physics - 57th Edition 1976 - 1977.
- 7 - R.P. Henry
Science et Technique du Vide - Tome 1 -
- 8 - G. Genestier
Doctoral thesis - July 1980 - Besançon University.
- 9 - J. Chauvin
Doctoral thesis - "Régimes transitoires dans les résonateurs à quartz soumis à des variations rapides de température"
1975 - Besançon University.
- 10 - G. Theobald - J.J. Gagnepain
"Frequency variations in quartz crystal resonators due to internal dissipation"
J. Appl. Phys. 50 (10) - 1979 - p. 6309.
- 11 - R. Besson et J.P. Valentin
Brevet d'Invention Etat Français - FR 79 18 553.
- 12 - C. Guerin
Work currently done in the laboratory.
- 13 - J.A. Musters - M.C. Fischer et J.G. Leach
"Dual mode operation of temperature and stress compensated crystals"
Proc. 32nd Annual Symposium Frequency Control
p. 389 - 1978.
- 14 - J. Kusters
"Transient thermal compensation for quartz resonators"
I.E.E.E. Trans. Sonics and Ultrasonics SU-23
p.273 - 276 - 1976.

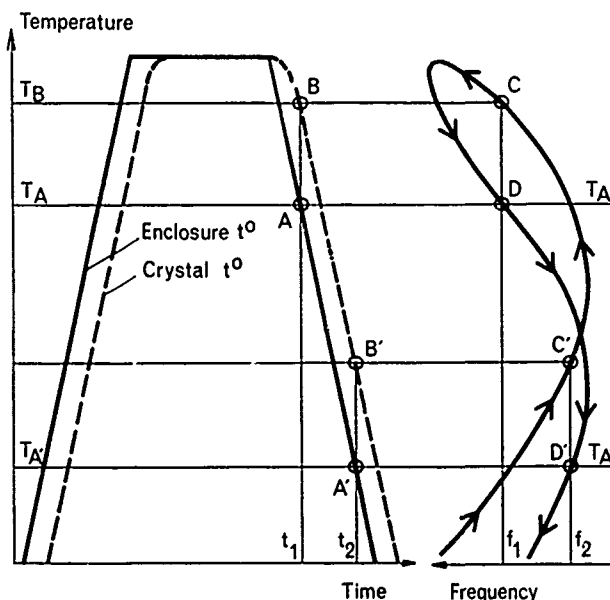


(fig. 1)

"Frequency - temperature" curve and thermal lag.

AN L- AND S-BAND RADAR EXCITER USING AGILE LOW NOISE PHASE LOCKED LOOP SYNTHESIZERS

Constantine Andricos
ITT GILFILLAN
Van Nuys, California 91406

SUMMARY

An exciter using phase locked loops (PLL) to generate radar frequencies was built and tested at ITT Gilfillan. Its performance was superior in many respects to standard direct synthesizer configurations. In addition to being less complex, the phase locked loop approach proved more versatile for changing frequency bands for different systems and augments a modular approach for frequency generation in radar systems.

The basic exciter was built at L-band covering 1.2 to 1.4 GHz, and extended to 3.1 to 3.6 GHz by the addition of an S-band synthesizer and upconverter.

The measured short term stability at L- and S-band was $\leq 3 \times 10^{-10}$ for a 1 msec sample time. A 250 kHz step size over a 500 MHz bandwidth was achieved with a total settling time of $< 60 \mu\text{sec}$ to within 0.1 degree phase for any frequency change.

The exciter was constructed entirely using thick and thin film hybrid and microwave integrated circuit technology. The result was improved performance, increased MTBF and reduced size, weight, and power.

Key Words (for information retrieval). Synthesizer, Phase Locked Loop, Radar Exciter, Thick Film Substrates, Radar Improvement Factor.

INTRODUCTION

The main driving functions for new applications of search radars are improved clutter performance, antijamming capability and higher reliability and reduced LCC. The resulting requirements for high MTI performance and frequency agility place stringent demands upon the frequency synthesizers of radar systems.

PERFORMANCE REQUIREMENTS

Frequency agile radars require programming of local oscillator frequencies over wide bandwidths typically, 200 to 500 MHz. In addition, the radar hopping scheme is such that comparatively fast settling times at each frequency are required, typically to within 0.1 degrees in $< 60 \mu\text{sec}$. The conflicting additional requirement of very low phase noise

and spurious outputs makes the synthesizer design an exacting task.

Typical synthesizer performance requirements include:

- L- and S-band transmit frequency
- 200 MHz to 500 MHz band coverage
- 250 kHz minimum step; full band maximum step
- $< 60 \mu\text{sec}$ switching to 0.1 degree phase
- Short term stability 3×10^{-10} at 1 msec
- Phase noise floors - 115 dBc
- Improvement factors $> 55 \text{ dB}$
- Spurious signals 80 dB down.

SYNTHESIZER TRADEOFFS

The performance requirements are achieved in standard configurations using direct synthesizers which select frequencies from a bank of crystal oscillators, mixing to obtain the sum or difference frequency and then multiplying to produce the desired output frequency.

Since the crystal oscillators are always in the on position, frequency switching speed can be quite rapid (approximately $10 \mu\text{sec}$). The existence of many simultaneous frequencies, however, presents a problem in maintaining a spurious-free output. The spectral purity of the output depends to a large degree not only on the selected oscillator, but also on the selector switch isolation, the mixer's inter-modulation, and the filter's rejection characteristics. As the radar bandwidth requirements increase, the direct synthesizer becomes less able to maintain an acceptable spurious-free output.

The direct synthesizer is also relatively bulky and expensive due to the large number of mixers, amplifiers, switches, oscillators and filters required. This imposes a restriction on reliability and maintainability. Additionally, periodic alignment of the multiple RF circuits is a necessity and adaptability to different systems is difficult.

Microwave synthesis is usually accomplished by multiplying or upconverting the low frequency output of a direct synthesizer. The crystal oscillator frequencies are selected by a switch matrix at a relatively low frequency to achieve high isolation. The multiplication effect imposes tight specifications on the low frequency synthesizer. For

example, the requirement for switching times of $<60 \mu\text{sec}$ for 0.1 degree phase at X-band (100 times multiplication) necessitates a specification of 0.001 degree phase settling or run out at the low frequency synthesizer.

Buffering at each oscillator output required to achieve the very high isolation and low phase disturbance with switching can lead to excessive signal attenuation which can increase the phase noise at the final output.

Because of these inherent limitations of direct synthesizers, other configurations were studied. The primary areas of interest in the analysis were phase noise, settling time, maximum bandwidth, minimum step size and simplicity.

The phase locked loop approach was selected because of its simplicity, and frequency agility, and because it offered superior noise and spurious signal performance. Several types of loops were studied including those using analog direct feedback with microwave phase detection and programmable divider feedback.

IMPROVEMENT FACTOR

In search radars, the unwanted clutter and background returns are removed by moving target indicator (MTI) operation which relies on the Doppler frequency shifts produced by the movement of the target for discrimination.

The phase reference is generated by the local oscillators producing the radar signals. Good clutter cancellation requires high phase stability on the synthesizers. A measure of the effectiveness of the MTI is the clutter attenuation CA.² CA is defined as the ratio of input clutter power C_i to output clutter power C_o . The improvement factor, I, is defined as the average improvement in the signal-to-clutter ratio introduced by the canceller, including the canceller average gain G .²

$$I = \frac{\bar{S}_o/C_o}{S_i/C_i} \quad (1)$$

\bar{S}_o = Average output signal power

S_i = Input signal power

In terms of the clutter attenuation ratio²

$$I = G \times CA \quad (2)$$

where G = the signal power gain when averaged over all possible target-Doppler frequencies.

The clutter attenuation is given to be²

$$CA = \frac{1}{\Delta\phi^2} \quad (3)$$

where $\Delta\phi$ is the interpulse period phase change. The improvement ratio for a double canceller is²

$$I = \frac{3}{\Delta\phi^2} \quad (4)$$

or

$$I_{dB} = 10 \log \frac{3}{\Delta\phi^2} \quad (5)$$

The cancellation occurs on a pulse-to-pulse basis with phase comparison times related to the interpulse period T , and τ , the round trip time to target. Typically τ is of interest from $25 \mu\text{sec}$ (2 miles) to $1236 \mu\text{sec}$ (100 miles) and $T = 2 \text{ msec}$ so that synthesizer noise sidebands above 10 Hz are the ones limiting the cancellation that can be obtained.

Because of the difficulty of measuring the single sideband noise of microwave oscillators close in to the carrier, it is convenient to specify short term stability in the time domain.

For this, a computing counter is used and a plot of fractional frequency deviation $\Delta F/F_0$ versus sampling time is obtained. The improvement factor I in terms of $\langle \sigma_y^2(2,T,\tau) \rangle$ the averaged value of the standard deviation of $\Delta F/F_0$ is given by Equation (6).

$$I = \frac{3}{\omega_0^2 2\tau^2 \langle \sigma_y^2(2,T,\tau) \rangle} \quad (6)$$

$$\psi_x^2(T,\tau) = 2\tau^2 \langle \sigma_y^2(2,T,\tau) \rangle^s \quad (7)$$

$\psi_x^2(T,\tau)$ = mean square time for Doppler radar

τ = sampling time

$\omega_0 = 2\pi F_0$

I = improvement factor for a double canceller

Although the time domain measurement is convenient and relatively simple, the numbers offer no insight directly on the synthesizer design requirements.

A phase noise versus frequency offset from the carrier plot is preferable for the design and specification of the local oscillators. The relation of the improvement factor to the phase spectral density is given by

$$I = \frac{3}{16 \int_0^F S_\phi(f) \sin^2(\pi \tau f) \sin^2(\pi T f) df} \quad (8)$$

- I = the improvement factor for a double canceller
 $S_{\phi}(f)$ = the power spectral density of the oscillator phase noise.
 τ = roundtrip time to target, equivalent to the sampling time above.
 F = $\frac{1}{2}$ the bandwidth of radar IF
 T = $1/\text{PRF}$ of radar

The $\sin^2(\pi fT)$ terms are weighting functions applied to the phase spectral density $S_{\phi}(f)$ peaking at $f = 1/2T$ and dropping rapidly for $F < 1/2T$ as shown in Figure 1.

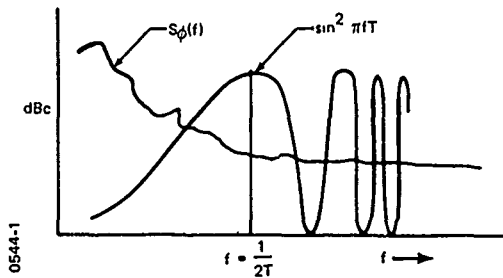


Figure 1. Weighting function of phase noise spectral components

The dominant weighting function is the time-to-target τ term since $\tau < T$.

When the main contribution to the MTI improvement factor is the noise floor, the T term has only a small contribution to the overall integration. This is so because for the higher frequency components of $S_{\phi}(f)$ there is little correlation between pulse transmission intervals.

As the time to target τ is increased, the weighting function is heavier on the lower frequency components of the synthesizer phase noise spectral density. The contributions of the various parts of the noise curve to the MTI stability factor can be estimated for different τ 's. Thus, for $\tau = 1$ msec (81 miles) the weighting function peaks at 500 Hz (0 dB) and is -30 dB at 10 Hz offset. For the synthesizer noise floor extending out to F_2 when $F \gg 1/\tau$, a weight of $\frac{1}{2}$ is applied to $S_{\phi}(f)$.

IMPROVEMENT FACTOR CALCULATIONS

Calculations using Equation (8) showing the contributions of various parts of the noise spectrum for different τ (round-trip times to target) appear below. The spectrum $S_{\phi}(f)$ is for the L-band synthesizer at 1.03 GHz shown in Figure 2. The PRF is 2 msec and the system video bandwidth = 500 kHz.

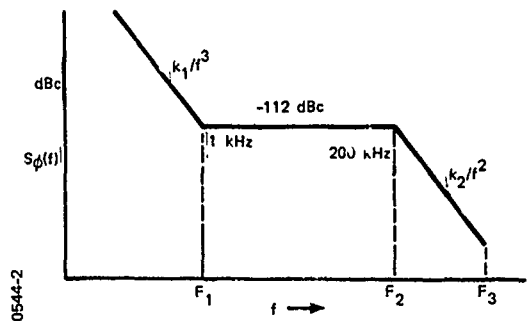


Figure 2. L-Band synthesizer phase noise spectral density

Improvement Factor dB	Integrating Interval kHz	τ μsec
64.5	0.1	1000
56.9	0.200	1000
55.2	0.500	1000
69.4	0.1	500
57.5	0.200	500
55.5	0.500	500
82.9	0.1	100
57.7	0.200	100
55.6	0.500	100

The individual segments are summed as

$$\frac{1}{I_T} = \frac{1}{I_1} + \frac{1}{I_2} + \frac{1}{I_3} \quad (9)$$

where I_T = the synthesizer improvement factor

and, I_1, I_2, I_3 are the improvement factors for the individual frequency segment, $0-F_1, F_1-F_2, F_2-F_3$.

From the table, it can be seen that the main contribution to the improvement factor is the synthesizer noise floor. The low frequency noise becomes more important as the radar range increases. The frequency span above 200 kHz contributes about -2 dB to the improvement factor.

The slope of the noise beyond the second breakpoint F_2 is $1/f^2$ and corresponds to the slope of the VCO alone.

As F_1 moves higher in frequency, the effect of the $1/f^3$ noise increases and the improvement factor decreases rapidly.

This effect of the low frequency breakpoint F_1 , in the noise spectrum on the MTI improvement factor appears below for the $T = 2$ msec.

Improvement Factor dB	Integrating Interval kHz	τ μsec	F_1 kHz
55.2	0.500	1000	1
51.7	0.500	1000	3
34.9	0.500	1000	10

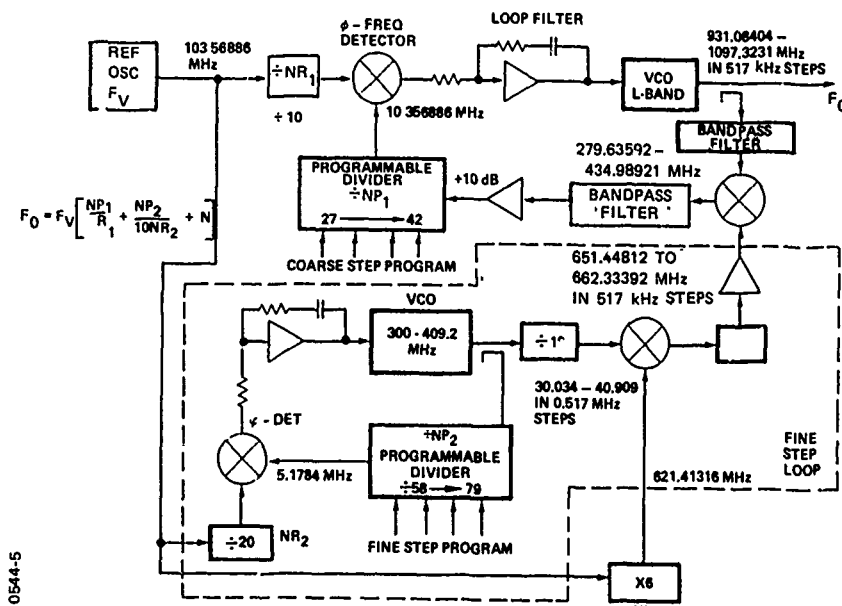


Figure 5. L-Band fmc frequency step PLL synthesizer

Noise Performance of the Digital PLL

The curves in Figure 6 show the measured single sideband phase noise and the estimated noise as contributed from the elements in the loop. All the active components in the loop contribute to the overall output phase noise.

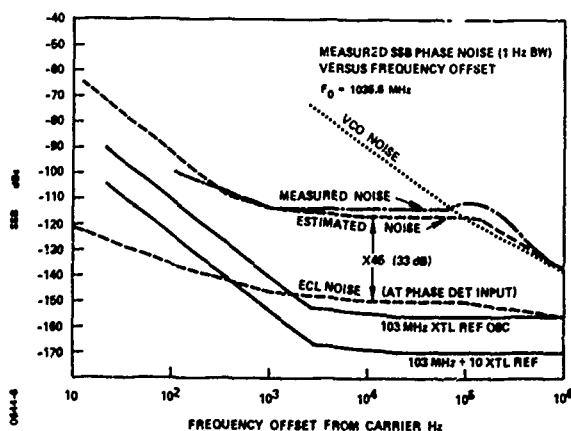


Figure 6. L-Band synthesizer noise

The phase locked loop acts as a low pass filter for the reference and multiplied reference noise and acts as a high pass filter for the VCO noise. The filters cutoff at approximately the loop bandwidth.

The long term stability and the noise close in to the carrier is attributable directly to the reference oscillator. This is the $1/f^3$ term in the previous discussion. The noise from this source is multiplied at the output by the N_p (feedback division ratio).

The phase detector and programmable counters establish the noise floor in the intermediate frequency range of 1 kHz to 200 kHz. Above the loop bandwidth, the noise is established by the VCO.

For optimum noise performance, the loop bandwidth is set at the intersection of the VCO noise and the divider noise floor.

The output phase noise was minimized by observing the following points:

- The division ratio was set as low as possible.
- Specification for good short term stability of the reference oscillators since the close-in noise is not filtered by the loop.
- Use of hybrid low noise operational amplifiers for the loop filter. (1 nV/√Hz input noise level).
- Use of logic circuits with low jitter for the reference and programmable dividers. ECL logic/-150 dBc noise floor.
- Selection of low noise components, resistors, amplifiers, etc.
- Design of VCO with low noise for frequencies outside the loop bandwidth. Selected varactors, high Q, low leakage.
- Optimization of loop parameters, gain, damping factor, use of shaping network to maintain constant loop bandwidth.
- Proper shielding and grounding techniques. This was especially important to reduce power line pickup very close in to the carrier.

Spurious Outputs

The spurious components at the output of the loop were maintained below 80 dB.

The spurious outputs were attributed to the following:

- Phase detector reference leakage.
- Down converter intermodulation products and leakage.
- VCO spurious generation.
- Power supply pickup.
- Fine step loop products.

The first item was minimized by using a three-state digital phase detector and a high reference frequency with subsequent low pass filters.

The down converter spurs are maintained at a low level by proper selection of the frequencies and suitable bandpass filters and isolators at the mixer terminals.

The contribution from the VCO is minimal since a wideband tunable oscillator was designed with a relatively high Q which has a spur free output in the operating band.

Adequate shielding, grounding, and power supply ripple filtering prevented power supply coupling and degradation of the output spectrum.

When the auxiliary loop was used for the fine step size and the down conversion frequency was not an integral multiple of the PLL reference, spurious products resulted but were removed by sharply filtering the fine tune loop output

Switching Speed

The PLL must settle to within 0.1 degree of final phase in less than 60 μ sec for any frequency change. This imposes a minimum value for the bandwidth.

The total switching time T_T of the loop is the sum of the frequency slew time T_F and the phase lock in time T_ϕ

$$T_T = T_F + T_\phi \quad (10)$$

The frequency discriminator initially slews the loop to within the capture range where the loop phase lock-in transient occurs. The rate at which the frequency slew occurs depends on the average pump voltage available (taken to be $V_p/2$). For the active loop filter shown in Figure 7, (second order loop)

$$\Delta E_0 = \frac{1}{C} \int \frac{V_p}{2R_1} dt \quad (11)$$

or

$$T_F = \frac{2\Delta E_0}{V_p} \frac{K_V K_\phi}{N\omega_n^2} \quad (12)$$

where

ΔE_0 is the maximum slew voltage

V_p is the pump voltage

$$T_1 = R_1 C \quad T_2 = R_2 C$$

ω_n = loop natural frequency³

$$= \left[\frac{K_V K_\phi}{N T_1} \right]^{1/2} \quad (13)$$

ξ = loop damping factor³

$$= \frac{\omega_n T_2}{2} \quad (14)$$

N = divide ratio

K_ϕ = phase detector constant

K_V = VCO gain constant

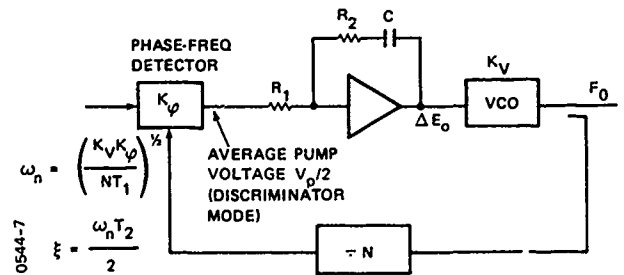


Figure 7. Second order PLL

The time to acquire phase lock when the PLL output frequency is within the capture range is given by⁴

$$T_\phi = \frac{2}{\frac{K_\phi K_V}{N} \cos \epsilon_{ss}} \ln \frac{2}{\gamma_{lock}} \quad (15)$$

where

γ_{lock} = phase error at time T_ϕ in radians

$$\epsilon_{ss} = \sin^{-1} \frac{\Delta\omega}{\Delta\omega_{capture}} \quad (16)$$

$\Delta\omega$ = initial frequency offset

for $\Delta\omega = 1/2 \Delta\omega_{capture}$

$$\cos \epsilon_{ss} = 0.86$$

With the loop constants set by the noise considerations to give a loop bandwidth of 200 kHz

$$\omega_n = 1.25 \times 10^5 \text{ rads/sec}$$

$$K_\phi = 0.4 \text{ volts/rad}$$

$$K_V = 8.3 \times 10^7 \text{ rad per second/volt}$$

$$T_1 = 4.23 \times 10^{-7} \text{ and } T_2 = 1.1 \times 10^{-6}$$

$$\xi = 0.7 \text{ and } V_p = 2.5V \text{ For } \gamma_{\text{lock}} = \frac{0.1^0}{57.3}$$

From Equation (12) $T_F \approx 5 \mu\text{sec}$

$$(15) T_\phi \approx 24.5 \mu\text{sec}$$

$$(10) T_T \approx 29.5 \mu\text{sec.}$$

The 200 kHz bandwidth is sufficient to satisfy the phase settling requirement.

Test Results

Test results for the first LO appearing in Figure 8 indicate a settling time to within 0.1 degree of final phase in $<50 \mu\text{sec}$ for any step frequency up to a maximum of 200 MHz was achieved. Short term stability $\Delta F/F$ was measured at 3×10^{-10} for a 1 msec sample time and 300 kHz bandwidth. The improvement factor calculated from the single sideband noise plot is 55 dB at 1 msec.

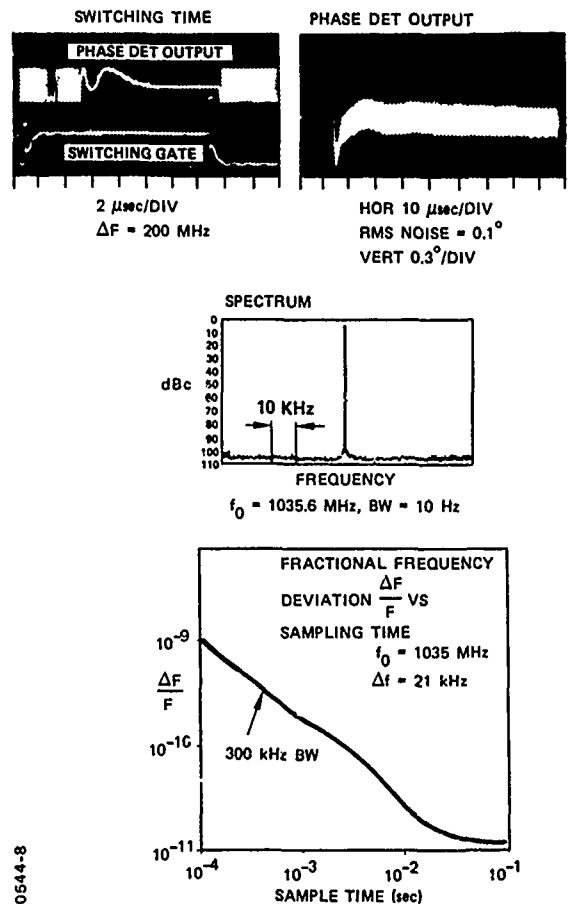


Figure 8. First LO test results

S-BAND EXCITER

2nd LO and COHO Synthesizers

The second LO and COHO synthesizer configurations are similar to the first LO phase locked loop except for the down converter. The noise floors for both are below -120 dBc. The COHOs operate at a fixed frequency so that the loop bandwidth is reduced to about 10 kHz for improvement factors of >65 dB.

S-BAND EXCITER

The table summarizes the measured performance of the S-Band Exciter. Full frequency coverage of 3.1 to 3.59 GHz was obtained with a maximum frequency step of 494 MHz and a minimum step of 517.8 kHz. Parameters of settling time and FM noise were within the goals necessary to establish an MTI improvement factor of 55 dB. The S-Band Exciter block diagram appears in Figure 9.

Parameters	Measured Performance
Frequency Coverage	3102 to 3596 MHz
Step Size	
Minimum	517.8 kHz
Maximum	494 MHz
Switching Time	$<60 \mu\text{sec}$ to within 0.1 degree for a maximum step of 500 MHz
Short Term Stability $\Delta F/F$ for 1 msec Sampling Time	1.5×10^{-10}
Power Output	+10 dBm
Flatness Over Band	± 1 dB
Output VSWR	1.5:1
Pulsed On-Off Ratio	100 dB
Pulsewidth	0.1 μsec to 100 μsec
Phase Code	180 ± 3 degrees
Spurious Output	60 dB down from carrier
MTI Improvement Factor	55 dB

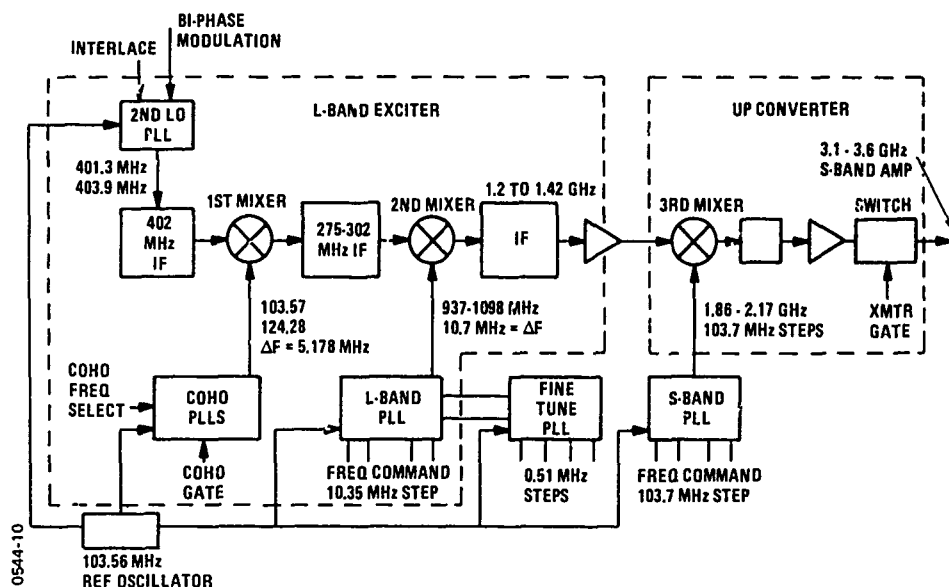


Figure 9. S-Band exciter block diagram

A modular approach was adapted to extend the frequency range of the synthesizers using the existing L-Band Exciter in conjunction with an S-Band Synthesizer and upconverter to implement the S-band unit. This modular technique minimized the number of new designs required and allowed a frequency extension by the addition of add-on modules to the basic L-band frequency generator and modulator.

All synthesizers are composed of phase locked loops coherently tied to a master reference. The use of common programmable dividers, reference dividers, and phase detector on thick film substrates greatly reduced the number of different substrates used throughout the exciter.

The L-Band Exciter provides a phase coded pulse modulated signal at 1215-1410 MHz to the up-converter where it is mixed with an S-band local oscillator to generate the 3.1 to 3.6 GHz output.

The up-converter combines the L-band phase and pulse coded signal with the S-band LO to produce the 3.1 to 3.6 GHz output.

To minimize spurious inband signals, the 500 MHz frequency excursion is achieved by stepping the L-band and S-band synthesizer over the bands shown in Figure 9.

S-BAND SYNTHESIZER

The S-Band Synthesizer generates the wide step fast hopping 1.8 to 2.17 GHz signal to up-convert the L-band output to the 3.1 to 3.6 GHz range.

To achieve low noise performance and wide bandwidth, a circuit using a sampling phase detector was employed as shown in the block diagram of Figure 10.

The 103.5 MHz reference generates a narrow pulse to sample the RF output directly at 2 GHz in the phase detector. This comparison technique without the intervention of digital programmable dividers allows for a wider bandwidth loop and lower noise performance than is possible with the standard divider feedback configuration. The fast switching time and low noise performance is gained, however, at the expense of a relatively broad frequency step size, 103.5 MHz.

Since the sampling phase detector has no frequency discrimination, it will lock up at harmonics of the reference. A D/A converter is used to set the VCO to within the desired frequency beat. For the extreme conditions where the frequency offset is outside the loop bandwidth, a fast sweep is initiated to bring the VCO into the reference frequency multiple to achieve a lock.

The total time to acquire lock for this loop T_T is

$$T_T = T_d + T_s + T_\phi \quad (17)$$

where

$$\begin{aligned} T_d &= \text{slew time with the D/A preset voltage} \\ T_s &= \text{slew time with the sweep search} \\ T_\phi &= \text{phase lock-in time of the loop within the capture range} \\ T_d &= 5 \mu\text{sec} \quad T_s = 15 \mu\text{sec.} \end{aligned}$$

For the loop constants

$$\begin{aligned} K_V &= 2.8 \times 10^8 & \omega_n &= 18.8 \times 10^6 \\ K_\phi &= 1.27 & N &= 1 \\ \cos \epsilon_{ss} &= 0.86 & \gamma &= 0.1/57.3 \end{aligned}$$

from Equation (15)

$$T_\phi = 0.045 \mu\text{sec}$$

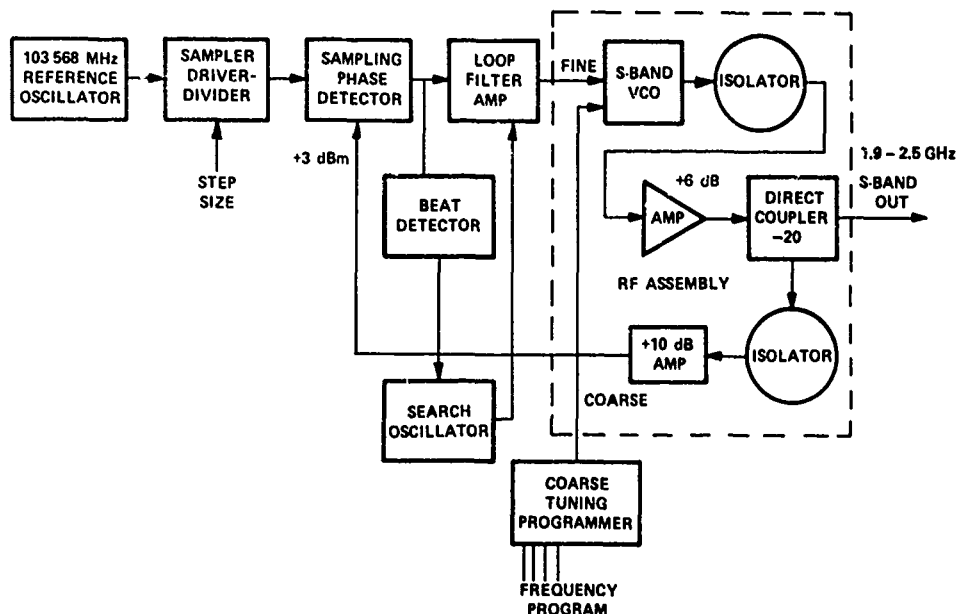


Figure 10. S-Band PLL synthesizer

therefore

$$T_T = 20 \mu\text{sec.}$$

S-Band Synthesizer Performance

The phase noise output of the S-Band Synthesizer was evaluated by measuring the fractional frequency deviation, $\Delta F/F$, and by performing single sideband noise measurements

The measured $\Delta F/F$ versus sampling time of the synthesizer appears in Figure 11 for 300 kHz and 3 MHz measurement bandwidths. Figure 11 shows that the short term stability of the S-band unit is superior to that of the L-band PLL. This lower noise level is confirmed by the

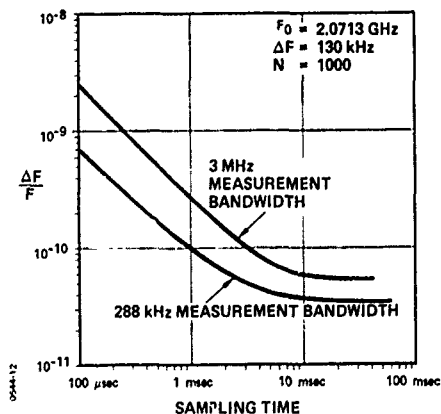


Figure 11 S-Band synthesizer (fractional frequency deviation vs sampling time)

plot of the measured single sideband noise versus carrier offset frequency appearing in Figure 12. This noise floor level is about 8 dB lower than for the L-band synthesizer output. This curve also shows the relative contribution of the measured S-band VCO and the estimated multiplied reference noise.

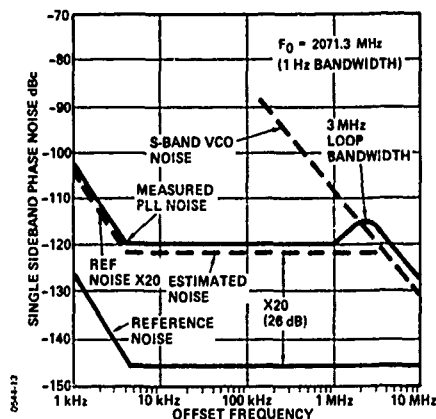


Figure 12. S-Band synthesizer (single sideband noise vs offset frequency)

The improvement factor calculated from the single sideband noise for the S-Band Synthesizer was 56 dB.

The switching total time to less than 0.1 degree phase was measured at 30 μsec . This is the worst case when the offsets are such that fast sweep is initiated to bring the VCO to within the loop capture range.

THICK FILM HYBRIDS

The exciter was constructed entirely using thick and thin film hybrids and microwave integrated circuit technology. The result was improved performance, improved MTBF, and reduced size, weight and power.

A photograph of the complete L-Band Exciter showing the 1st LO, 2nd LO and COHO, and the up-converter appears in Figure 13.

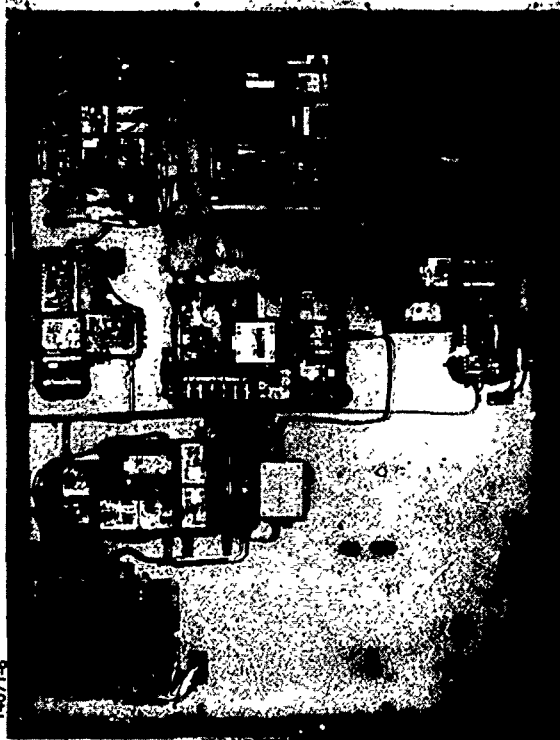


Figure 13. The complete L-Band Exciter

The phase locked loops use common thick film programmable dividers operating up to 600 MHz; common phase detectors, loop filters and reference dividers.

An example of a thick film substrate utilizing chip carrier integrated circuits appears in the photo of the reference divider (Figure 14).

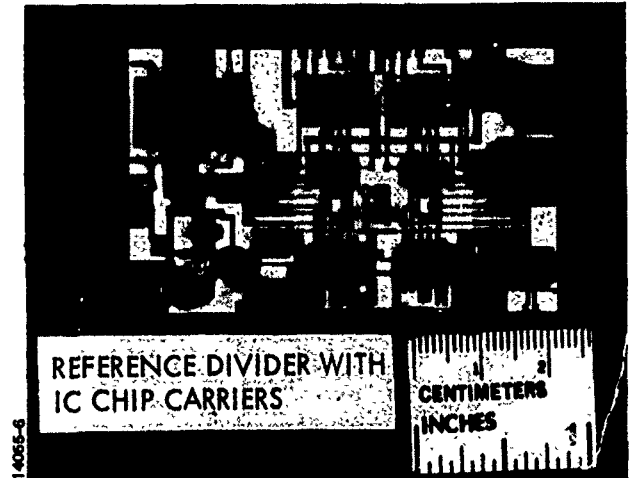


Figure 14. Reference divider with IC chip carriers

The integrated circuits are packaged and pretested as leadless chip carriers and are then assembled on the substrates and reflow soldered.

These substrates are interconnected with other modules such as isolators, filter, mixers to form a complete assembly using SMA connectors for signal leads and feedthrough filters for power and programming leads.

A typical assembly is the fine tune loop synthesizer appearing in Figure 15. This module contains the VCO, programmable and reference dividers, phase detector loop filter substrates, as well as built-in power regulators and self-test circuits.

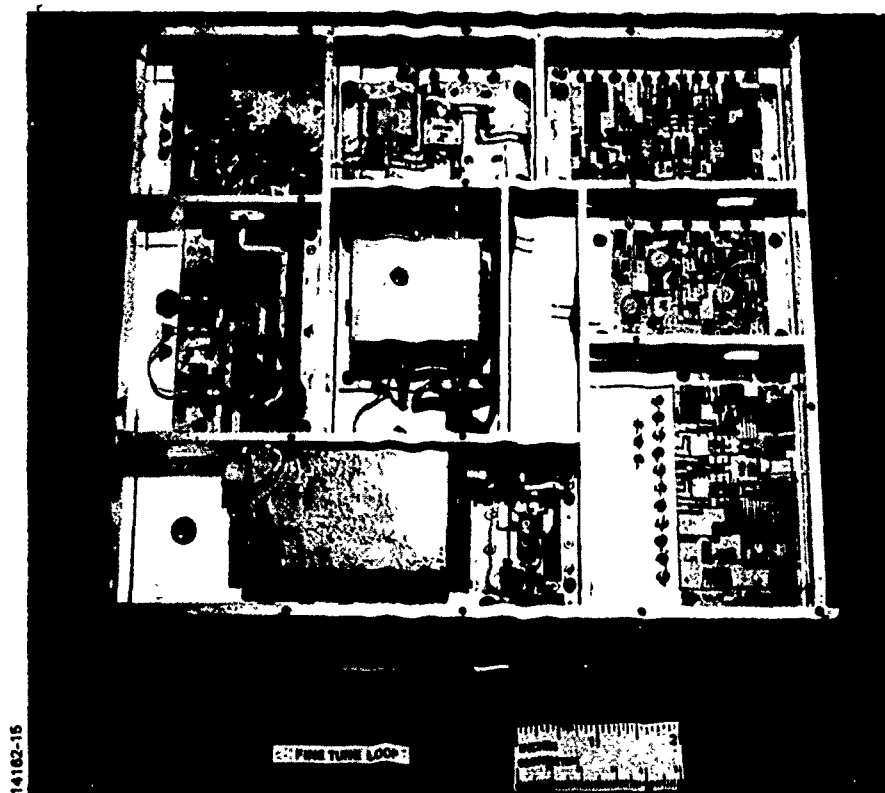


Figure 15. Fine tune loop

CONCLUSIONS

The overall measured performance of the exciters indicate successful achievement of the following key goals for radars.

1. Fully coherent, fast switching frequency generation, $<60 \mu\text{sec}$ settling to 0.1 degree phase.
2. High MTI improvement factor $>55 \text{ dB}$ (low phase noise).
3. High degree of electrical and mechanical design commonality (phase locked loops, microwave integrated circuits (MIC)).
4. High reliability (thick/thin hybrid film technology).

REFERENCES

1. Skolnik, Merrill I., Radar Handbook, McGraw-Hill Book Co., 1970, Chapter 17.
2. Nathanson, Fred E., Radar Design Principles, McGraw-Hill Book Co., 1969, Chapter 8.
3. Gardner, Floyd M., Phase Lock Techniques, John Wiley & Sons, Inc., 1966, Chapter 2.
4. Manassewitsch, Vadim, Frequency Synthesizers Theory and Design, John Wiley & Sons, Inc., 1976, Chapter 5.
5. Characterization of Frequency Stability, J.A. Barnes, et al, IEEE Transactions on Instrumentation and Measurement, Vol. IM-20, No. 2, May 1971.

HIGH SPEED, BROADBAND TUNEABLE MICROWAVE SYNTHESIZER*

Edward M. Perdue

Raytheon Company
Equipment Division
Communication Systems Laboratory
Sudbury, Massachusetts 01776

ABSTRACT

Microwave synthesizers are being developed to meet specific requirements. In this paper it is shown that a microwave synthesizer can be built embodying rapid, broadband tuning, accuracy and resolution to institute doppler correction, spectral purity for low data rate transmission, remote control, and be small in size for airborne operation. The work discussed here is directly adaptable to any band of communication, radar, etc. Various disciplines in the field of frequency generation are brought together in the design of the microwave synthesizer.

The paper is composed of two parts; the first part details the system approach and the second presents the results obtained and a review of the hardware.

INTRODUCTION

Microwave synthesizers have been developed to meet the diverse requirements of various radio communication systems. The development of the local oscillator chains has progressed from fixed frequency generators to agile frequency generators capable of rapid tuning pseudo-randomly to meet the present day jamming scenarios. This technology applies not only to communication links, but is expandable to radars, etc. This paper will discuss the ongoing work in this area. The synthesizer itself has many features:

- carrier frequency
- tuning bandwidth
- accuracy and resolution
- remote control
- spectral purity
- size

The work has been adapted to several programs having such a large set of requirements:

- Ka/Q-band airborne-satellite link
- 15 GHz line-of-sight radio
- SHF/EHF Airborne-satellite system

*The work reported here was sponsored in part by Raytheon Company and in part by AFAL under contract F33615-73-C-4036.

SYSTEM CONFIGURATION FOR USAGE OF SYNTHESIZER

Figure 1 illustrates the utilization of the synthesizer in the terminal. All frequencies required for the operation of the terminal are derived from a Rubidium standard. All channel frequency selections are entered at the Remote Control Unit, processed by the Frequency/Terminal Control Unit, and routed to the Exciter/Receivers where the microwave synthesizers reside. The frequency generation subsystem (see Figure 2 for the microwave synthesizer) maintains the channel frequency with exceptionally high spectral purity and accuracy. These two requirements are necessitated by injection of doppler in the system, low data rates used for transmission of information, and by the high carrier frequency of transmission/reception.

Thus, in a system such as this, the microwave synthesizer must accept commands that include channel selection, doppler information, and/or fast updates. It must be capable of coherency over a limited range for doppler updates in a fixed channel airborne operation. It must be capable of switching and settling at high speeds with the application of pseudo-random frequency selection (plus doppler).

FREQUENCY SYNTHESIZER

The frequency generation subsystem is illustrated in the block diagram in Figure 2. All of the basic ingredients of a tuneable microwave synthesizer are included:

- a Rubidium standard and fixed frequency synthesizer to form the high spectral purity of the reference signal
- a frequency control unit to accept serial frequency control words and convert to parallel
- two digitally programmable tuned synthesizers
 - coarse synthesizer, step size of 4 MHz
 - fine synthesizer, 2-6 MHz tuning range with minimum step size of 0.09 Hz
- microwave phase lock loop including necessary high speed acquisition circuitry.

The desired output frequency and tuning bandwidth to meet a specific requirement is determined by:

$$F_o = F_r + F_f + M \cdot F_c \quad (1)$$

where

F_r is the reference frequency of 100 MHz,

F_f is the fine frequency,

F_c is the coarse frequency,

and

M is the microwave PLL multiplicative factor.

Note the tuning bandwidth is set by:

$$BW = F_f + M \cdot F_c \quad (2)$$

This approach has been directed at minimization of the hardware but still perform the desired function. Such things as using the available 100 MHz reference, 5 MHz, and the tunability of the two synthesizers is an example.

Reference Generator

For this type of synthesizer, the reference generator provides the high spectral purity required of the local oscillator. The Rubidium standard, the 100 MHz VCXO, and the multiplier make up the reference generator. As noted by equation (1), any output frequency can be selected by selecting N appropriately during the initial design.

Figure 3 illustrates the phase noise as predicted and measured for the reference. The low noise quartz oscillators used in the Rubidium standard have been measured at the National Bureau of Standards at Boulder, Colorado, and is displayed on Figure 3. The prediction for the VCXO and xM multiplier is included since they enhance the phase noise by $20 \log N$. To ensure the VCXO locking and tracking over a -55°C to $+75^\circ\text{C}$ temperature range, the loop bandwidth is set at 1 kHz. For low data rate transmission of PSK data, the phase noise close to the generated carrier is of great concern. Improving the phase noise is approaching the limit. Work by Efratom and Austron shows that some difficulty still exists in obtaining low noise crystals for the oscillators. The yield of good, low noise crystals is very low. With the requirement of 0.05 radians (3 degrees) of integrated phase noise from 1 Hz to 150 Hz from the carrier, measurements indicate a value of approximately 0.02 - 0.03 radians.

Fine Synthesizer

Different configurations of digital synthesizers have been reported in the literature (1) designed around TTL (0-2 MHz) and lightly mentioning possibilities of higher frequency operation (upper limit of 12 MHz). There are two commercially available TTL digital frequency synthesizers; one by Rockland (0-3 MHz) and another by

Proton (0-2 MHz). The microwave synthesizer reported here contains a digital frequency synthesizer constructed entirely of emitter coupled logic (ECL) for their speed.

In the overall system design of the microwave synthesizer, one must look at the total requirements; i.e., spurious requirements, size, etc. The use of the image reject mixer to inject the fine synthesizer frequency into the feedback path of the PLL does not enhance the spurious level of the fine digital synthesizer through the PLL. The loop rejection characteristics will reduce any sidebands as a result of the mixing in the image reject mixer. Thus injection of the fine synthesizer at this point creates spurious at the output related only by:

- (1) the spurious level on the fine frequency, and
- (2) the rejection of the loop of the signal out of the image reject mixer.

One would like to use a digital synthesizer capable of operating over a 5-15 MHz range; while keeping the coarse synthesizer simple (minimum number of tones, large separation). Detailed analysis, coupled with experience gained in another division of Raytheon showed that a practical digital synthesizer could be built to operate from 2 to 6 MHz using available ECL components and limited mainly by aliasing or foldback frequency from the clock. The final fine frequency synthesizer has the following operating characteristics:

- frequency range 2-6 MHz
- resolution 0.09 Hz
- spurious better than -60 dBc
- power requirement 50 watts

In actuality, the synthesizer will operate down to 0 MHz, but due to a 100-200 kHz microwave PLL bandwidth and spurious requirements, the lower operating frequency is chosen at 2 MHz. It should be noted that the low spurious obtained is a result of the design in using separate analog and digital grounds, use of multilayered printed wiring boards and attention to placement of layers and the use of microstrip for RF signals.

In addition, the fine frequency synthesizer has sufficient tuning range outside the 2-6 MHz range to allow for overlap.

Coarse Synthesizer

Having selected an operating range for the fine synthesizer ($\Delta F = 2-6$ MHz) also determines the separation of tones required of a coarse synthesizer. Depending on the division factor in the microwave synthesizer feedback loop, the tone separation will be:

$$X = \frac{4}{M} \text{ MHz} \quad (3)$$

The number of selectable tones will be set by the desired output tuning bandwidth divided by the fine frequency tuning range:

$$Q = \frac{BW}{4} \text{ tones} \quad (4)$$

Having determined the number of tones, an optimum circuit design is chosen to minimize the hardware. The coarse synthesizer consists of generating a comb (using the 100 MHz reference appropriately), using a bank of monolithic crystal filters, and ECL devices to select frequencies. Broadband image reject mixers combine the selected frequencies to produce an output. Separation of spurious components are such that the PLL reduces them to an acceptable level at the microwave PLL output. The critical elements in the coarse synthesizer are monolithic crystal filters and the image reject mixers. Improper filter layout will degrade comb rejection.

Microwave Synthesizer - PLL

The basic microwave synthesizer PLL as shown in Figure 2 is the second order loop with special coarse acquisition circuitry. The VCO is capable of tuning over a board band having a fine loop bandwidth of 100-200 kHz under lock conditions.

To meet the fast acquisition requirements of the project, special consideration was given to the design of the microwave PLL, and the acquisition circuitry and to their interaction. Timing circuits make decisions in times less than a microsecond. The VCO is capable of large steps (full bandwidth) in less than 0.5 microseconds. No linearization circuitry is used (eliminating 20-30 dB from VCO free running noise). Temperature has no effect on the ability of the loop to tune the VCO near enough for acquisition. The successive approximation approach is used for the fastest means to coarsely tuning the VCO to within locking range of the fine loop. During the acquisition process, time to determine the appropriate timing process is gated by the beat note between where the VCO has been set and the desired frequency. Thus coarse and fine acquisition time is a summation of the preset time, the successive approximation, and final fine loop locking time:

$$T_{acq} = T_{preset} + \sum_{i=1}^n \left(\frac{1}{f_{a_i} - f_{b_i}} \right) + T_{fine} \quad (5)$$

The total time to acquire is variable; depending on how close the coarse tuning voltage places the VCO such that $F_a - F_b$ is small or large. Thus acquisition time can be as little as 20 microseconds up to tens of microseconds.

Due to tuning sensitivity of the VCO, special attention is given to power supply ripple, ground loops, etc. Post tuning drift (PTD) of the VCO effects the acquisition process and must be minimized; acceptable PTD of 1 MHz after 1000 microseconds have been obtained.

SYNTHESIZER PERFORMANCE

A synthesizer of this type has to rank its performance against the requirements. Bandwidth, center frequency, and output power are easily obtainable. This leaves two very important specifications; phase-noise and speed of acquisition. Figure 3 illustrates data taken with the synthesizer. Data taken close to the carrier, 0.2 to 10 Hz, is measured via the HP-5390 Frequency Analysis System. From 10 Hz to 10 kHz, a Modified HP-302 with 1 Hz bandwidth is used. From 10 kHz to 1 MHz, the spectrum analyzer is used. The integrated phase noise from 1 Hz to 150 Hz is that of the reference; approximately 0.03 radian. All spurious levels are below -60 dBc at any point in the band. As far as switching speed, an operator may take one-half a minute (less than one microsecond for per-programmed pseudo-random frequency selection) to load in a request for a new frequency. It will take one microsecond to relay this information to the microwave synthesizer which in turn will take tens of microseconds to lock to a new frequency.

ACKNOWLEDGEMENT

The author would like to acknowledge the contributions of V. Norden for his expert technical assistance in solving problems associated with the phase lock loop and the improvement of the high speed acquisition. In addition, V. Norden with the assistance of Carlos Caicedo developed the high speed digital synthesizer surpassing our expectations in the area of spurious content. Finally, I want to thank Joe Havel for the frequency control circuitry necessary for remote control.

REFERENCES

1. J. Tierney, "Digital Frequency Synthesizers" Frequency Synthesis: Techniques and Applications, edited by Jerzy Gorski-Popiel (IEEE Press, New York, 1975).
2. A. Blanchard, Phase-Locked Loops - Application to Coherent Receiver Design, A Wiley Intersciences Publication, New York, 1976.
3. V. Manassewitsch, Frequency Synthesizers, Theory, and Design, A Wiley Interscience Publication, New York, 1976.
4. F.M. Gardner, Phase Lock Techniques, Second Edition, A Wiley Interscience Publication, 1979.

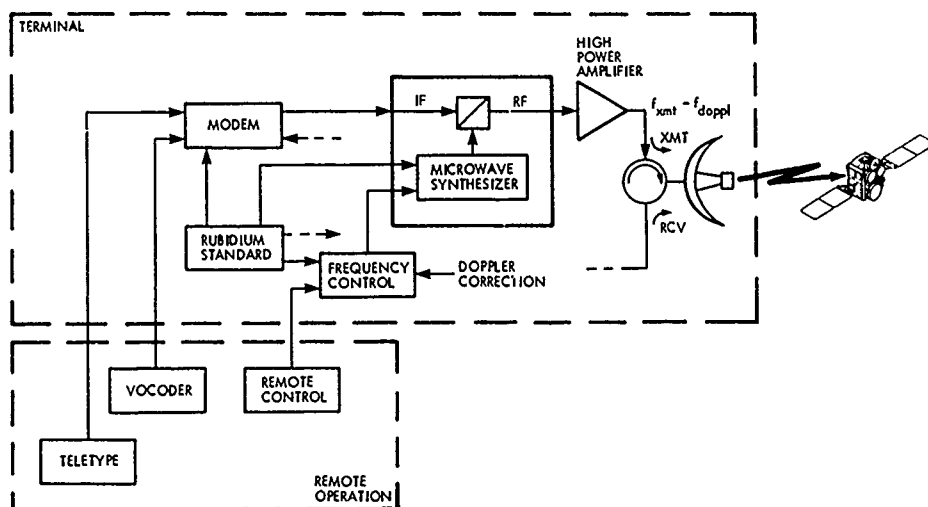


Figure 1. System Configuration

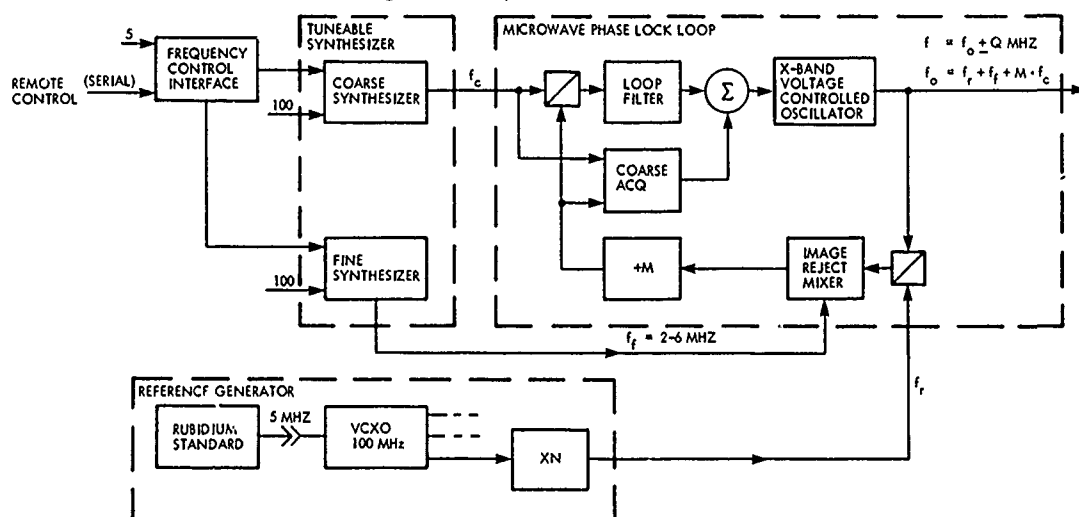


Figure 2. Frequency Generator Subsystem

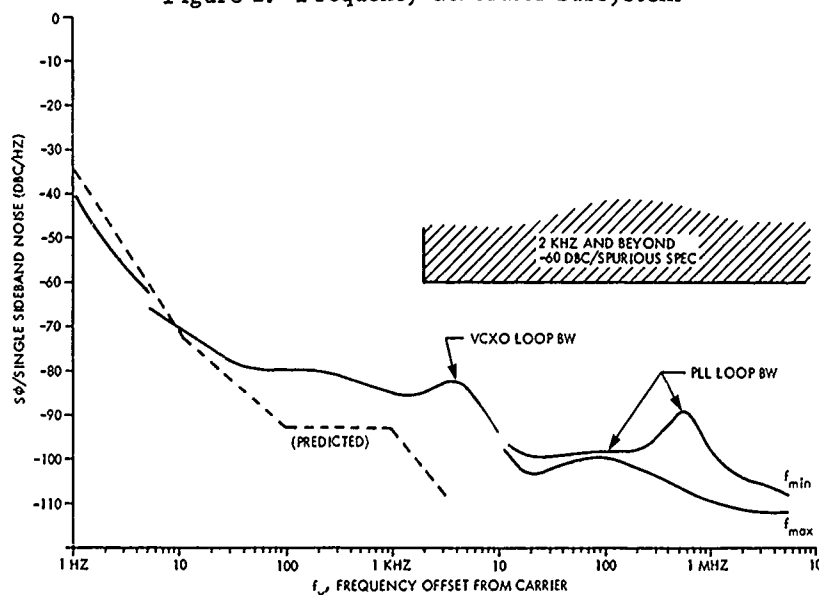


Figure 3. Microwave Synthesizer Phase Noise

DIGITAL GENERATION OF WIDEBAND LINEAR FM WAVEFORMS

F. W. Hopwood
R. A. Tracy

WESTINGHOUSE ELECTRIC CORPORATION
Mail Stop 378, Box 746
Baltimore, Maryland 21203

ABSTRACT

A technique for the direct digital generation of linear FM waveforms with up to 900 MHz bandwidth and T-B products to 450,000 is presented. The technique is applicable to high resolution Synthetic Aperture Radars, and to target identification and target count modes in multimode airborne radars. Origins of representative system requirements are outlined, mechanization details are described, and testing methods and results showing waveforms of excellent coherence and fidelity are presented.

I. INTRODUCTION

The Synthetic Aperture Radar (SAR) mode in modern, multimode airborne radars requires broadband microwave signals to measure range profiles of targets of interest and opportunity. Regardless of waveform format, range resolution R_R requires transmitted bandwidth B of at least $B = ac/2R_R$, where C is the propagation velocity of light and a is a constant (usually 1 to 1.2) related to signal processing weighting.

Systems utilizing large signal bandwidths may utilize "stretch" waveforms as described by Caputi¹ to reduce IF and signal processing bandwidths by transmitting waveforms of duration longer than the range swath collection time. Stretch systems can require waveforms of 900 MHz bandwidth and 500 μ sec duration.

The system time-bandwidth product TB is thus 450,000 and the waveform slope k is 1.8×10^{12} Hz/second.

Linear FM waveforms of very large time-bandwidth product (greater than 10,000) are difficult to generate using passive techniques. The survey by Godfrey, et al,² shows that surface wave devices are not now practical for such applications, although tremendous advances are being made in that area. In addition, passive techniques generally provide one waveform slope per device, requiring a line or line pair for each slope in a multi-slope system. These considerations, plus the fact that modern radars already use frequency synthesizers to generate a large number of microwave channels, make it practical to consider the use of active techniques to generate linear FM waveforms of very large time-bandwidth product selected from a large number of available slopes. We present here a tech-

nique wherein an ordinary phase-locked synthesizer can be adapted to the generation of such waveforms with exceptionally good fidelity and coherence. The methodology is particularly well suited to the introduction of high resolution capability into multi-mode airborne radars since it requires only moderate changes to hardware which often already exists in such systems.

II. WAVEFORM REQUIREMENTS

The "stretch" radar is a convenient means of realizing range resolution without carrying commensurately wideband signals through the receiver, A/D converters, and signal processor. Such signals are difficult to handle, at best. Stretch systems, however, utilize RF bandwidth commensurate with the required range resolution, but require signal processing bandwidths of perhaps a few tens of MHz. A linear FM waveform of bandwidth B and duration T is transmitted and a similar waveform delayed by nominal round trip time T_{RT} is used as a correlation waveform at the receiver first LO. We assume that $T_{RT} > T$, although this need not be true for certain classes of systems. Received signals from many ranges are down-converted by the swept LO to form an intermediate frequency which is proportional to range. Returns from the "nominal" range of interest fall at the center of the IF. The IF bandwidth is B_I , thus passing only signals from a limited range swath T_s . These quantities are related as:

$$B/T = B_I/T_s$$

Waveform Linearity Considerations

Low order (quadratic) frequency errors degrade range resolution by smearing the return over a number of range cells. The low order waveform nonlinearity can be expressed as:

$$F(t) = Bt/T + B_E t^2/T^2$$

The waveform from some point in the range swath is delayed from this by T_D . Its frequency is:

$$F(t - T_D) = B(t - T_D)/T + B_E(t - T_D)^2/T^2$$

Their difference is time dependent and can move across a number of range filters of width $1/T$. To restrict this to 1/2 range cell requires that:

$$B_E < 1/4 T_D$$

High order non-linearities in the FM waveform result in undesirable range sidelobes on strong radar returns. These appear on the imagery as faint reproductions of the strong returns at other ranges. The effect is quantized as follows:

The correlation (LO) waveform can be represented by:

$$F(t) = Bt/T + \sum_n F_E(n) \cos(2\pi nt/T + \phi_n)$$

where $F_E(n)$ is the n th Fourier coefficient of frequency nonlinearity, and t is time from the initiation of the correlation waveform. If an exact replica of this waveform has been transmitted and is being received at time T_D relative to nominal round trip time, the IF signal is composed of a carrier offset from the nominal IF frequency by $(B \times T_D/T \text{ Hz})$, with phase sideband pairs each of which is below the carrier by $10 \log D_R(n)$.

$$D_R(n) = \left[\frac{F_E(n) T}{n} \sin \left[\pi n T_D/T \right] \right]^2$$

$D_R(n)$ is the n 'th order range sidelobe, and:

$$-T_S/2 \leq T_D \leq T_S/2$$

For low order ($n < T/\pi T_D$) nonlinearities and returns from the edge of the range swath, the waveform linearity requirement is found to be:

$$F_E = 2 D_R^{1/2} / \pi T_{SW}$$

Phase Noise Considerations

Discrete range sidelobes can be caused by waveform phase noise as observed in matched filter bandwidth $1/T$. The spectral density requirement is then:

$$L(f) = DT, f > 1/2T$$

The integrated noise requirement arises from the fact that in the ground mapping application, the contrast between contiguous regions of strong and weak radar backscatter is degraded by the total (integrated) phase noise. This requires that the two-sided noise power be less than some value I_R , which can be expressed as:

$$I_R = 2 \int L(f) df$$

If the phase noise consists of a white floor L_F observed through servo bandwidth f_L , the integrated noise requirement is satisfied when:

$$L(f) = I_R / \pi f_L$$

In this case, the integrated noise consideration imposes a less severe phase noise floor requirement than does the discrete noise. It is not unusual, however, for the opposite to be true.

These considerations impose phase noise floor requirements on any stable source used as the waveform reference. In addition, if the waveform is generated by a tuned oscillator controlled by servo bandwidth f_L , these considerations determine the VCO phase noise at modulation rate f_L .

Range information is determined by observing a single pulse of width T . Azimuth information is determined by observing many pulses over integration period T_i , ranging from a few milliseconds to many seconds depending on aircraft velocity, range, geometry, and resolution. Low frequency stability required for discrete and integrated azimuth sidelobes is computed using the same considerations as for range, except that round trip time is used instead of range swath, and integration time is used instead of pulse width.

III. WAVEFORM SYNTHESIS

The literature^{3,4,5,6} describes various means of generating wideband linear FM waveforms of large T-B product. These generally involve either sampling linearizers or delay line linearizers. Both are capable of good performance under certain conditions but neither, due to servo bandwidth and microwave component limitations, provides adequate waveform linearity for good range sidelobe performance in systems with large range swath. In addition, neither method easily provides the large number of waveform slopes which are desirable for certain multi-mode systems.

Westinghouse has expended considerable effort toward the development of direct digital generation of wideband linear FM waveforms, resulting in the simple but exceptionally versatile methodology shown in Figure 1. Described in U.S. Patent 4,160,958, the approach consists of a stable source whose phase is set by

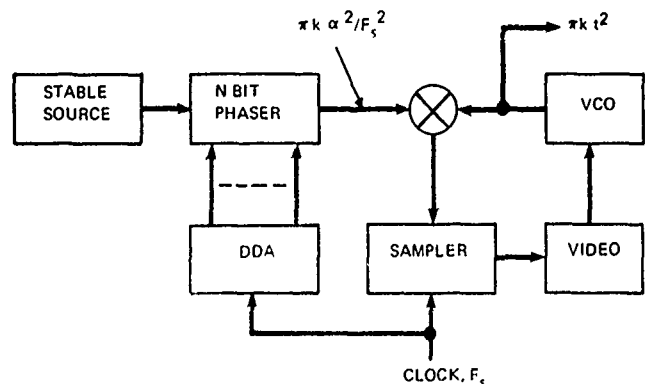


Figure 1
DIGITAL WAVEFORM GENERATOR

80 0107-V-3

a binary phaser, and a tuned oscillator (VCO) which is locked to the phased source via a sampled phase-lock loop. The instantaneous phase of the desired linear FM waveform is computed by a Differential Data Analyzer (DDA), a common digital computer element, which drives the phaser through the desired progression. A balanced mixer compares the phase of the VCO to that digitally generated. The difference is sampled, forming the error signal for the wideband phase-lock loop. The VCO acts as a smoothing filter and reproduces the desired waveform. The computation is performed and the phaser updated at rate F_s , typically 30 MHz. Since we wish to generate waveforms of 900 MHz bandwidth, the sample aperture must be less than 200 picoseconds. The phaser spectrum of bandwidth F_s is impulse sampled at rate F_s , causing the phaser spectrum to be reproduced continuously over the large bandwidth determined by the narrow sample pulse. The 30 MHz phaser update rate serves the entire 900 MHz desired waveform bandwidth.

As described in Figure 2, the phase computa-

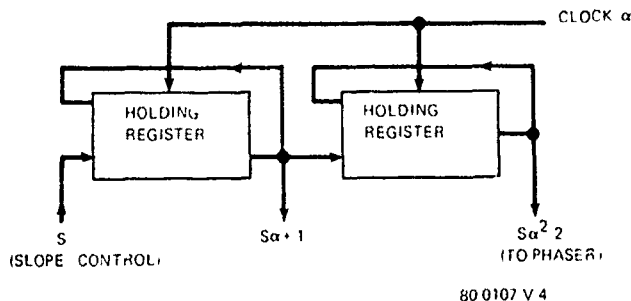


Figure 2

DDA PHASE COMPUTATION ALGORITHM

tion is performed by a cascade of DDA stages whose function is described by:

$$W_u(i+1) = W_u(i) + W_{u-1}(i)$$

where $W_u(i)$ is the output of the u 'th stage after the i 'th pulse of clock rate F_s . We use two stages of N parallel bits for linear FM of slope k , whose phase progression is:

$$\phi(i) = 2\pi s i^2 / 2^N$$

The DDA output to the phaser is $W_2(i)$, where

$$W_2(i) = si^2$$

Then: $W_1(i) = W_2(i+1) - W_2(i) = 2Si + S$

and: $W_0(i) = W_1(i+1) - W_1(i) = 2S$

S is the slope designator. The resultant phase progression is $2\pi W_2(i)/2^N$ or:

$$\phi(i) = 2\pi k i^2 / F_s^2$$

Then: $k = SF_s^2 / 2^{N-1}$

The desired slopes k may be realized by the appropriate choice of F_s and N which can be fixed within a system, and by the selection of slope number S which can be under system software control and selectable from a large number of values. For example, with 16 bits, 30 MHz sampling rate and 1024 selections, one can choose any slope up to 28 MHz/μsec in 0.027 MHz/μsec steps. This should be an adequate selection for most radar system designers. The 16 bit DDA in this example represents a moderate amount of digital hardware. The accompanying 16 bit phaser is, however, more difficult. In practice, the 16 digital bits are truncated to seven phaser bits, which is consistent with -40 dB range sidelobes. The 16 digital bits are necessary to achieve the slope resolution. Only seven of these are actually connected to a phaser. The remaining nine are considered "fractional" bits and are necessary for computational purposes.

The seven bit phaser (Figure 3) is an array of quadrature hybrids with individual PIN diode reflection elements. Bit size is determined by coupled line

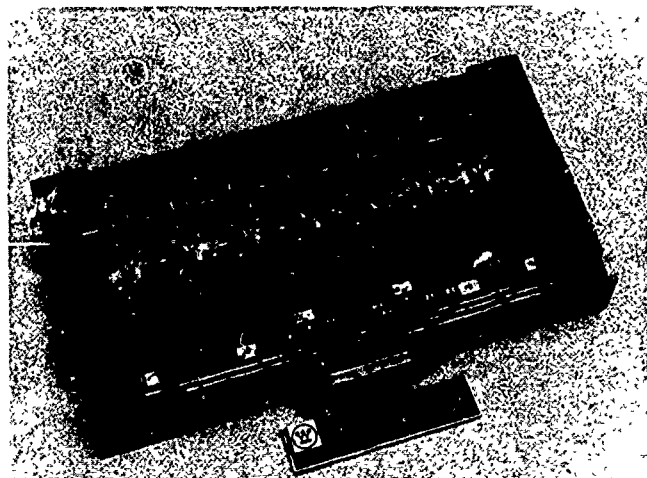


Figure 3

SEVEN BIT BINARY PHASER

transformers which also serve as DC blocks. Isolators between bits and on input and output reduce cross-talk to levels necessary for seven bit accuracy. RMS phase error is about 0.47 degrees and switching speed is about 1.8 nanoseconds. The diode drivers, Optimax DS07, were found to exhibit excellent switching speed when used in combination with high speed PIN diodes.

The VCO⁷ (Figure 4) consists of a silicon bipolar transistor oscillator with GaAs hyperabrupt tuning diode, followed by a FET power amplifier. Including the power amplifier within the linearizing servo loop eliminates the need for low order amplifier phase linearity, although amplitude flatness remains important.

Typical low order VCO nonlinearity is about 5 MHz, while the system requirement is about 500 Hz. The gain required is then simply 5 MHz/500 Hz or 80 dB at video frequency $1/T$. This calls for a Type III servo with several MHz bandwidth, which is the reason for choosing such a high (30 MHz) sampling rate.



Waveform linearity and coherence is measured by cross-correlating two similar units, with selectable time delay to detect any correlated nonlinearity. The resulting amplitude and phase error data is analyzed using a Discrete Fourier Transform. If $A(J)$ and $\phi(J)$ are the amplitude and phase error functions, the impulse response is calculated from:

$$F(k) = \sum A(J) W(J) e^{i(\phi(J) - 2\pi JK/N)}$$

$W(J)$ is the Hamming weighting function. Figures 5 and 6 are representative phase errors and their resultant impulse response, which is adequate for most mapping systems.

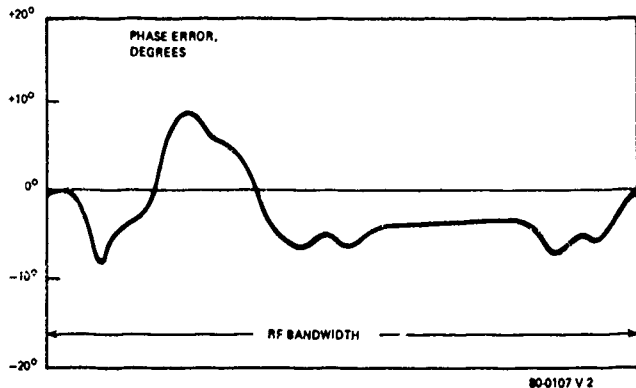


Figure 5
MEASURED PHASE NONLINEARITY

CONCLUSIONS

Digital generation of linear FM waveforms of large bandwidth and T-B product has been successfully demonstrated, with performance and versatility for high resolution mapping radars and other applications. The

technique uses readily reproduced microwave hardware whose requirements are not difficult to achieve.

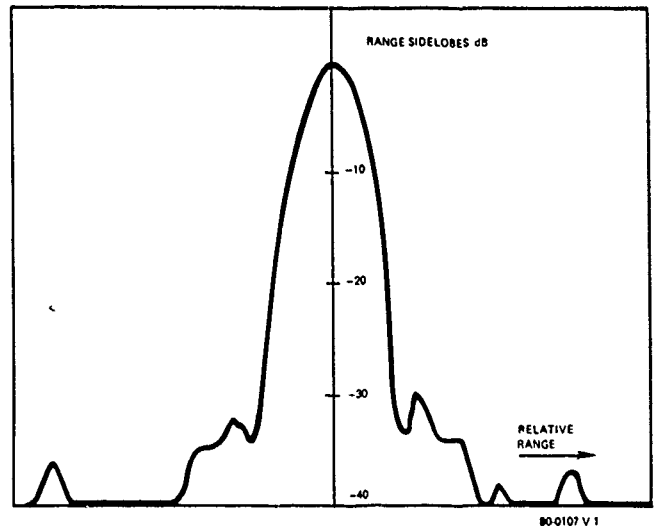


Figure 6
WEIGHTED IMPULSE RESPONSE

ACKNOWLEDGEMENT

The authors wish to acknowledge the advice of Jim Mims and Jerry Kane, and the efforts of the various microwave and digital engineers who participated in this effort.

REFERENCES

- ¹W. Caputi, "Stretch: A Time Transformation Technique," IEEE Trans. Aerospace and Electronic Systems, Vol. AES-7, March 1971.
- ²J. T. Godfrey, C. H. Grauling, C. E. Nothnick, "Pulse Compression Results using Metallic Reflective Array Lines," Trans. Aerospace and Electronic Systems, Vol. AES15-5, pp. 673-682, September, 1979.
- ³W. J. Caputi, "Stabilized Linear FM Generator," IEEE Trans. Aerospace and Electronic Systems, Vol. AES-9, pp. 670-678, 1973.
- ⁴C. H. Gager and R. B. Van Densen, "Generation of Flexible Pulse-Compression Waveforms with Computer Control," In-Proc. IEEE 1977 International Conf. Radar, pp. 488-492.
- ⁵B. D. Campbell, "High Resolution Radar, Coherent Linear FM Microwave Source," IEEE Trans. Aerospace and Electronic Systems, Vol. AES-6, pp. 62-72, January, 1970.
- ⁶"High Accuracy Control of Linearity for MM-Wave BWO," Summaries of Papers of International Conf. on Microwaves, Circuit Theory and Information Theory, pt. 1, pp. 54-62, September, 1964.
- ⁷E. C. Niehenke, R. D. Hess, "A Microstrip Low Noise X-Band Voltage Controlled Oscillator," Trans. on Microwave Theory and Techniques, Vol. MTT-27-7, December, 1979.

SAW STABILIZED 1680 MHz MICROWAVE OSCILLATOR*

D.J. Dodson, K.F. Lau, M.Y. Huang
TRW Defense and Space Systems Group
Redondo Beach, CA

T.J. Lukaszek
U.S. Army ET&D Lab., ERADCOM
Ft. Monmouth, NJ

Abstract

A SAW stabilized oscillator circuit has recently been designed and breadboarded to provide 300 ppm frequency stability over a -70°C to +70°C environment in the frequency band from 1660 to 1700 MHz. The circuit transmits 0.5 watt output power, provides both AM and FM capability, and is frequency selectable to ± 50 kHz. The circuit consists of two functional modules; a SAW oscillator module consisting of a loop amplifier, a tuned phase shifter and a four-channel SAW delay line which operates at 1/3 the output frequency, and a frequency multiplier/power amplifier module. The prototype development was implemented using low-cost circuit board techniques conducive to future large volume production. Design and performance details are provided.

Summary

To meet the requirements of meteorological radiosondes used by the US Army in the near future, a SAW stabilized, microwave oscillator providing .5W RF power from 1660 to 1700 MHz has been developed. The circuit was designed to provide a significant improvement in frequency stability so that more sondes can be used in a given area without interference. The high Q of the surface acoustic wave device and the relative temperature stability of ST-cut quartz have yielded a design with better than 300 ppm stability over the -70°C to +70°C temperature range.

The circuit consists of two modules; a four-channel SAW delay line oscillator operating in a 13.33 MHz band at 560 MHz, and an output module consisting of a tripler and power amplifier. Frequency modulation is accomplished by varying the transmission phase in the oscillator feedback path. Pulse amplitude modulation is accomplished through bias switching in the output module. The circuit was designed for eventual large volume production.

Two prototype circuits have been fabricated and tested. Test results demonstrate that temperature stability of approximately 260 ppm has been achieved. Output power in excess of .5W was typical.

*Supported by the US Army under Contract No. DAAB07-78-C-2992.

Introduction

By the late 1980s the design of radiosondes used by the US Army must be significantly improved both to increase frequency stability and to incorporate frequency modulation. The current design uses a free-running, amplitude-modulated, transistor oscillator. The instability of the oscillator limits the number of sondes which can be used in a given area without interference. It is expected that future applications will require 300 ppm frequency stability over a -70°C to +70°C environment. In addition, the circuits will be required to transmit .5W over the 1660-1700 MHz band, and be capable of both pulse amplitude modulation and frequency modulation. The required performance is summarized in Table 1.

Table 1

OSCILLATOR REQUIREMENTS

FREQUENCY	1660-1700 MHz
SETTABILITY	200 ppm (± 168 KHz)
STABILITY	< 300 ppm
OUTPUT POWER	500 mW
MODULATION	PAM (DC TO 2000 pps) FM (100 KHz, > 300 KHz/V)
FREQUENCY PULLING	$\leq \pm 1$ MHz
TEMPERATURE	-70°C TO +70°C

Since the circuits will be used in an expendable radiosonde, cost, size, weight, and power are important design considerations.

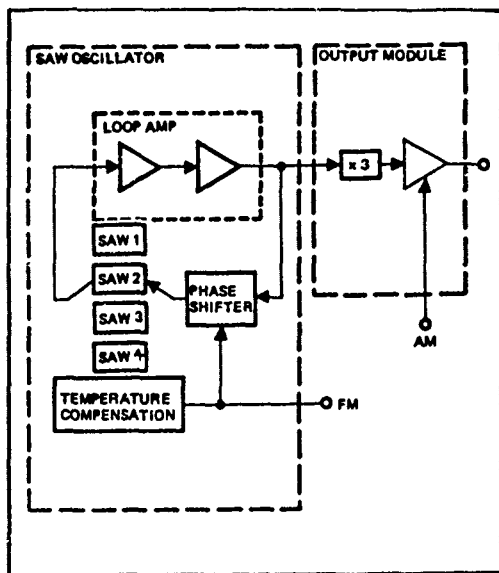
An attractive approach to these circuit requirements is a SAW stabilized oscillator. Surface acoustic wave delay lines can provide excellent uncompensated temperature stability, excellent phase noise, and their use greatly reduces circuit complexity (as compared to a crystal oscillator-multiplier chain). Whereas unstabilized microwave oscillators can be expected to have temperature stabilities between 100 ppm/°C and 1000 ppm/°C, SAW stabilized oscillators can achieve stabilities 2 to 3 orders of magnitude better than this unstabilized performance. SAWs yield this improved performance due to their high Q, Q here referring specifically to their large phase slope.

The requirements for stability, moderate tuning bandwidth, and FM complicate the oscillator design. Stability is enhanced by increased phase slope - with the resulting narrow bandwidth delay lines. Tuning and frequency modulation are enhanced by reducing phase slope. A compromise between these requirements has been made through the use of multiple SAW delay lines and temperature compensation.

System Considerations

A block diagram of the oscillator design is shown in Figure 1.

Figure 1. OSCILLATOR BLOCK DIAGRAM



The circuit consists of two functionally separate modules. One module is a SAW oscillator with output frequency at one-third the desired radiosonde transmission frequency. The second module, or output module, consists of circuitry which both frequency multiplies (X3) and amplifies the SAW oscillator output. The SAW oscillator consists of four selectable delay lines, each covering a quarter of the 553.3-566.7 MHz band, a quadrature hybrid phase shifter, and loop amplifier. The loop oscillates over the 553.3 to 566.7 MHz band, providing approximately +12 dBm output power. The oscillator frequency is adjustable through a potentiometer and can be modulated electronically. The output module consists of a $\lambda/3$ transistor multiplier and power amplifier. The output of this module can be amplitude modulated.

For loops of this type the conditions for oscillation are 1) gain around the loop must exceed all losses and (2) phase around the loop must equal a multiple of 2π radians. These conditions can be expressed as

$$L_S(f) + L_I(f) \leq G(f,A) \quad (1)$$

and

$$\frac{2\pi f_N \ell}{V} + \phi = 2N\pi \quad (2)$$

where

- f_N = oscillation frequencies
- ℓ = center-to-center transducer separation
- V = surface wave velocity
- ϕ = phase shift through all elements except SAW delay line
- N = an integer
- $L_S(f)$ = insertion loss of SAW delay line
- $L_I(f)$ = insertion loss of feedback loop components
- $G(f,A)$ = amplifier gain as a function of f and output level, A
- A = output power level

The frequency of oscillation can be determined from Equation (2), where

$$f_N = \frac{V}{\ell} \left(N - \frac{\phi}{2\pi} \right). \quad (3)$$

For single-mode operation, the SAW delay line is designed such that there is only one solution for Equation (3) that is in the passband of the delay line. As a general rule, the loss associated with the feedback loop components, $L_I(f)$, and the amplifier gain, $G(f,A)$, are slowly varying functions of frequency over a broad range around the frequency for which the oscillator is being designed, and the SAW response, $L_S(f)$, is a very strong function of frequency. The SAW oscillator is designed so that the combination of SAW delay line loss plus amplifier gain exceeds unity over a desired frequency band around the desired operating frequency. As long as only one solution to (3) falls within the passband response of the SAW delay line, single-mode operation of the SAW oscillator is guaranteed.

The loop amplifier provides gain to overcome losses around the loop - thereby meeting the first condition for oscillation. The amplifier is designed to have linear gain well in excess of the loop losses. The required gain margin is a function of the saturation characteristics of the amplifier chain, but typically must be greater than 4 dB. Measurements made at TRW have shown that a minimum of 4 dB gain margin will provide maximum output power and minimum phase noise. For a circuit with adequate gain margin, the oscillator output power will equal the saturated output power of the amplifier minus the power coupled back into the loop.

The second condition for oscillation is met through use of the phase shifter. The frequency of oscillation is set by varying ϕ in (3). It is necessary for the phase shifter to provide adequate phase variation to tune across the required frequency band. This phase variation will be defined by the phase slope of the delay line. It is generally necessary to provide tuning phase in excess of that required for any given SAW to accommodate the variation in absolute transmission phase from SAW to SAW. It is reasonable to expect variations in absolute delay for SAWs to be as large as $\pm 0.1\%$.

For typical delay lines of 100λ electrical length, this equates to $\pm 36^\circ$ variation in transmission phase. The data from measurements of 16 delay lines, shown in Table 2, demonstrates typical variation in absolute phase.

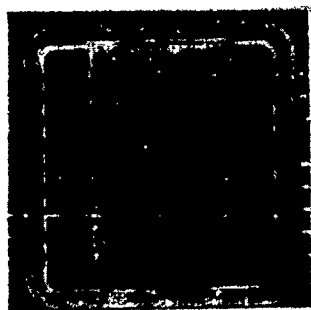
Table 2. MEASURED VARIATIONS IN ABSOLUTE PHASE

SAW DESIGNATION	DESIGN FREQUENCY	TRANSMISSION PHASE	MAXIMUM PHASE DIFFERENCE
B1-1 B2-1 B3-1 B4-1	555.0 MHz	76.5 112.5 110.0 80.0	36°
B1-2 B2-2 B3-2 B4-2	558.3	-128.0 -102.6 -145.0 -162.0	59.4°
B1-3 B2-3 B3-3 B4-3	561.7	108.0 +85.5 +95.0 +68.0	40°
B1-4 B2-4 B3-4 B4-4	565.0	-157.5 -144.0 -98.0 +165.0	107°

Saw Delay Line Design

As mentioned above, four SAW delay lines are used to cover the frequency bands from 553.3 to 566.7, 556.7 to 560, 560 to 563.3, and 563.3 to 566.7 MHz. The SAWs are shown in Figure 2.

Figure 2. FOUR CHANNEL SAW DELAY LINE



The SAW delay lines have been designed to achieve the required passband frequencies and delay times while maintaining a minimum insertion loss and good temperature stability. The delay time is important since it directly determines the mode spacing and thus the tuning range of the SAW oscillator.

The rationale for segmenting the passband into four sub-bands is as follows: The delay line bandwidth or tunability range of a SAW delay line is inversely proportional to its time delay and oscillator Q. In order to achieve a single mode frequency selectability from 1660 to 1700 MHz, a ± 12000 ppm frequency band, the center separation between the input and output transducers must be less than $33\lambda_0$. This separation creates two

problems. First, the direct feedthrough can enhance the sidelobe levels and if sufficient excess gain exists in the loop, more than one mode of oscillation can exist. Secondly, the delay line insertion loss becomes excessive due to the limited number of finger pairs in the transducer.

A delay line on ST-cut quartz with $30\lambda_0$ transducer separation was projected to have insertion loss in excess of 40 dB. To reduce this large loss it was decided to divide the 1660 to 1700 MHz frequency band into several channels. By a trade-off analysis considering insertion loss, sidelobe rejection, circuit complexity, and yield, four channels were used as a baseline design.

With the number of channels optimized, the choice of the SAW delay line frequency was considered. Frequencies to be considered include the fundamental oscillator frequency and the various subharmonics. With the present state-of-the-art, it is extremely difficult, if not impossible, to mass produce SAW delay lines operating at the fundamental. Either an embedded transducer finger configuration or an extremely thin interdigital finger metallization layer (200Å) would have to be employed if mode conversion at the surface discontinuities were to be minimized and if insertion losses were to be less than 30 dB. Even using these techniques, the typical variation of delay line frequency due to fabrication tolerance is estimated to be ± 10 MHz, too large to be of practical use.

Design of the delay line at a subharmonic of 1680 MHz is a more practical approach for a circuit requiring mass production. Both one-half and one-third output frequencies were considered. Delay lines operating at the one-half frequency can be produced using photolithographic techniques, however, center frequency reproducibility and insertion loss are not easily controlled. Again, this is mainly due to fabrication tolerances and mode conversion which could be improved by using embedded transducers or very thin electrode metallization, but both of these approaches would lead to increased SAW production costs.

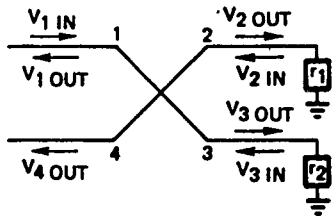
These production problems can be alleviated by lowering the delay line frequency to the third subharmonic. The device design would be similar to a one-half frequency design, but with increased line widths. Hence, for this application, four delay lines with center frequencies at 555 MHz, 558-1/3 MHz, and 565 MHz were designed on a single substrate. Each of the delay lines consists of two identical interdigital transducers with split electrode configuration. The choice of identical transducer design minimizes or eliminates fabrication errors that can cause the passbands of input and output transducers to differ, resulting in an increase in insertion loss. The split electrode configuration allows the delay line to operate at the third harmonic so that linewidth resolution for the fingers stays above $2.2\mu\text{m}$. This linewidth can easily be fabricated using conventional photolithographic techniques.

The center-to-center separation between the input and output transducers determines the time delay for the SAW delay line. The time delay then limits the length of the transducer, which in turn gives a lower bound for the delay line bandwidth. The mode spacing and the tuning range are inversely proportional to the time delay. To ensure wide tuning range and single mode operation, the transducers have to be placed very close to one another and contain the maximum allowable finger pairs. For the present design, this center-to-center separation was set at $98 \lambda_0$, where λ_0 is the acoustic wavelength at the center frequency of each delay line. The transducers each consist of 29 finger pairs, and the edge-to-edge separation between transducers is only $10 \mu\text{m}$. Fortunately, it was found that with proper packaging, the direct electromagnetic feedthrough at this separation can still be suppressed to below 20 dB of the passband peak. The acoustic aperture for these delay lines was designed to be $200 \lambda_0$.

Phase Shifter Design

The phase shifter forms a key part of the microwave oscillator since by varying phase around the loop the desired frequency of oscillation can be selected and the oscillator frequency can be modulated. The circuit selected for the phase shifter is a reactively loaded hybrid coupler design. The circuit is shown in Figure 3.

Figure 3. HYBRID PHASE SHIFTER



To operate as a phase shifter, a quadrature hybrid is connected to two reflective networks, one on port 2 and one on port 3. Ports 1 and 4 form the input and output ports, respectively. Let

$V_{1in} = Ae^{j\omega t}$ be the signal input to port 1. The hybrid coupler splits the input signal such that $V_{2out} = \frac{A}{\sqrt{2}} e^{j\omega t}$ and $V_{3out} = \frac{A}{\sqrt{2}} e^{j(\omega t + \pi/2)}$; i.e., half of the power input to port 1 goes to each of ports 2 and 3, with a 90° phase shift between them. If the networks connected to ports 2 and 3 have reflection coefficients of r_1 and r_2 respectively, then the signals input to ports 2 and 3 are given as

$$V_{2in} = \frac{A}{\sqrt{2}} e^{j\omega t} r_1 \quad (4)$$

$$V_{3in} = \frac{A}{\sqrt{2}} e^{j(\omega t + \pi/2)} r_2 \quad (5)$$

The power out of ports 1 and 4 is given by

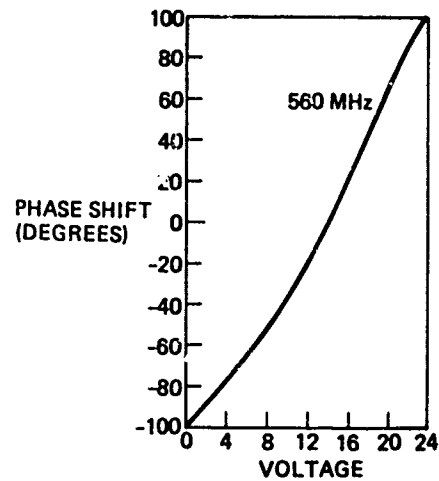
$$V_{1out} = \frac{A}{2} [e^{j\omega t} r_1 + e^{j(\omega t + \pi)} r_2] \quad (6)$$

$$V_{4out} = \frac{A}{2} [e^{j(\omega t + \pi/2)} r_1 + e^{j(\omega t + \pi/2)} r_2] \quad (7)$$

It is apparent that if $r_1 = r_2$, no power is reflected to port 1 and all power incident on port 1 is delivered to port 4.

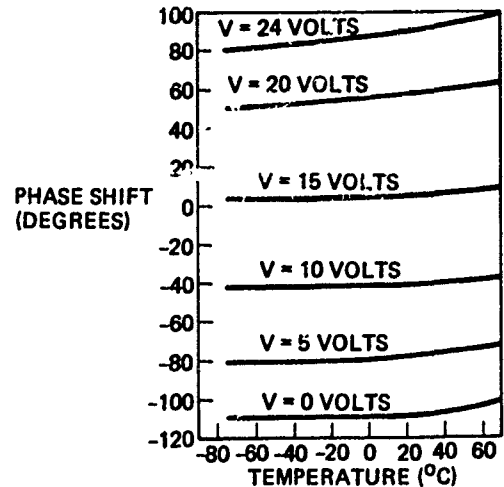
Networks of a shorted stub in parallel with a varactor diode were chosen for the load circuits in this application. This design produced the performance shown in Figure 4. Amplitude variation was less than 2 dB for nearly 200° of phase shift. Tuning voltage was 0 to 24V. Figure 4 shows the measured plot of phase shift versus voltage taken at $+70^\circ\text{C}$. Note the almost linear tuning characteristics obtained by a compensation of the phase shifter design and the capacitance change characteristic of the varactor diode.

Figure 4. PHASE SHIFT vs VOLTAGE AT $+70^\circ\text{C}$



Unfortunately, a major problem with the varactor diode is its sensitivity to temperature. Figure 5 is a measured plot of the phase shift versus temperature at 560 MHz. Note that at 20V one

Figure 5. PHASE SHIFT vs TEMPERATURE AT 560 MHz



obtains over 10° of phase variation with temperature. A sensistor-resistor network was used to temperature compensate the varactors.

Loop Amplifier

The loop amplifier is a three-stage, common emitter, bipolar transistor design providing approximately 40 dB gain. The circuit is more broadband than required, and special precautions were taken to assure out-of-band stability. The large mismatch presented by SAW devices far from center band has a tendency to cause spurious modes of oscillations. For this application a lossy tank was used to assure unconditional stability.

Output Module

The Output Module consists of a transistor tripler and power amplifier. The tripler and amplifier are each common base, bipolar transistor designs using distributed matching networks. Output power for this module was typically in excess of +28 dBm.

Microwave Oscillator Hardware and Performance

Figure 6 is a photograph of the prototype oscillator. Figure 7 shows details of the SAW oscillator module. The tripler and power amplifier are mounted beneath this board. Output power vs frequency is plotted in Figure 8. Note that a minimum of +26.8 dBm (480 mW) was achieved.

Figure 9 shows the frequency settability and turn-on drift characteristics of the oscillator in the various channels. When the oscillator had stabilized (at f_0), the power was turned off, and after cooling, turned on again. Note that the worse case drift was about ± 50 kHz. After warm-up, (T_{∞}), the oscillator returned to the initial frequency setting.

Figure 10 shows plots of the frequency stability vs temperature for each channel. This stability is the combined effects of the SAW parabolic characteristic, phase shifter drift, and sensistor compensation. Table 3 summarizes performance of the circuit. Finally, Table 4 shows a comparison of the performance of the existing oscillator and the circuits discussed here.

Conclusion

This work has demonstrated an ideal application for surface acoustic wave devices. Stable microwave frequencies were obtained which far exceeded the stability of currently available radiosondes. Improved stability and settability can also be expected with more advanced electronic compensation methods and SAW fabrication, mounting, and sealing techniques.

Acknowledgements

The authors wish to express their appreciation to M. D. Brunsman and L. Z. Marosi for their contribution to the development of this circuitry.

Figure 6. PROTOTYPE OSCILLATOR



Figure 7. SAW OSCILLATOR MODULE



Figure 8. OUTPUT POWER vs FREQUENCY

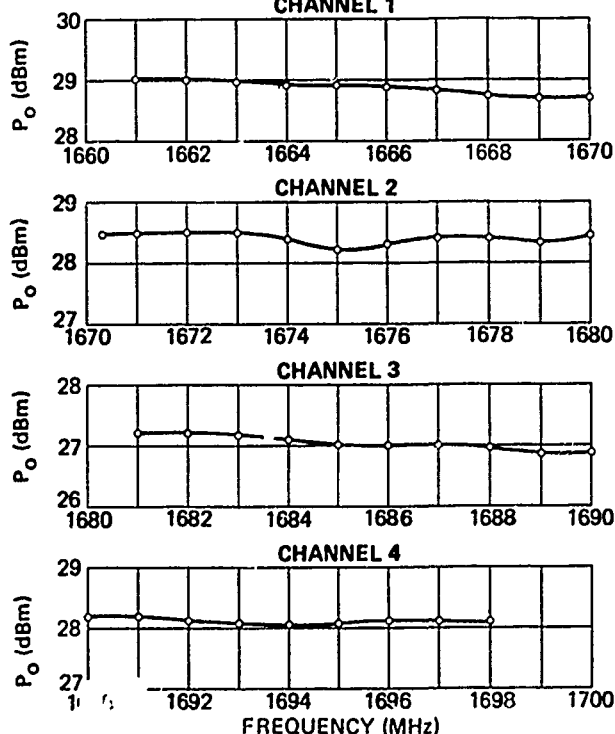


Figure 9. FREQUENCY SETTABILITY AND TURN-ON DRIFT CHARACTERISTICS

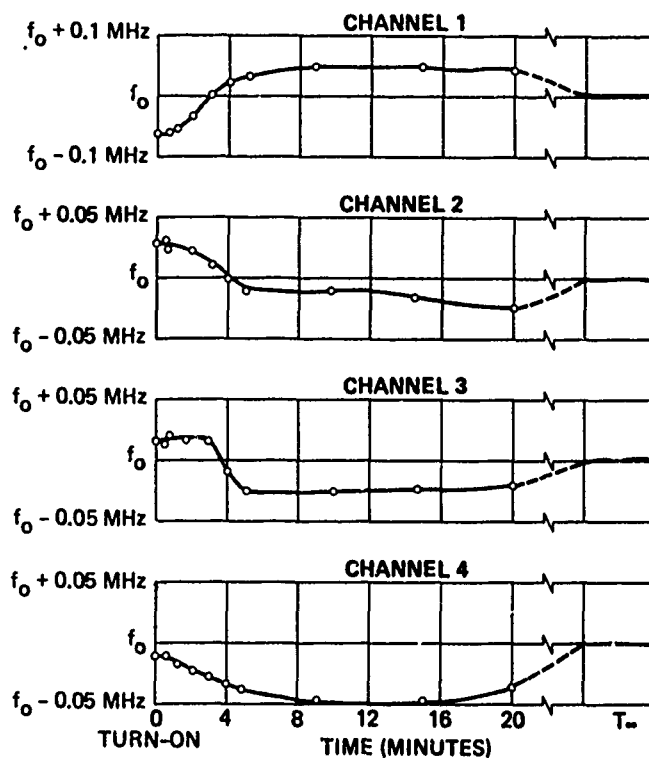


Figure 10. FREQUENCY STABILITY vs TEMPERATURE

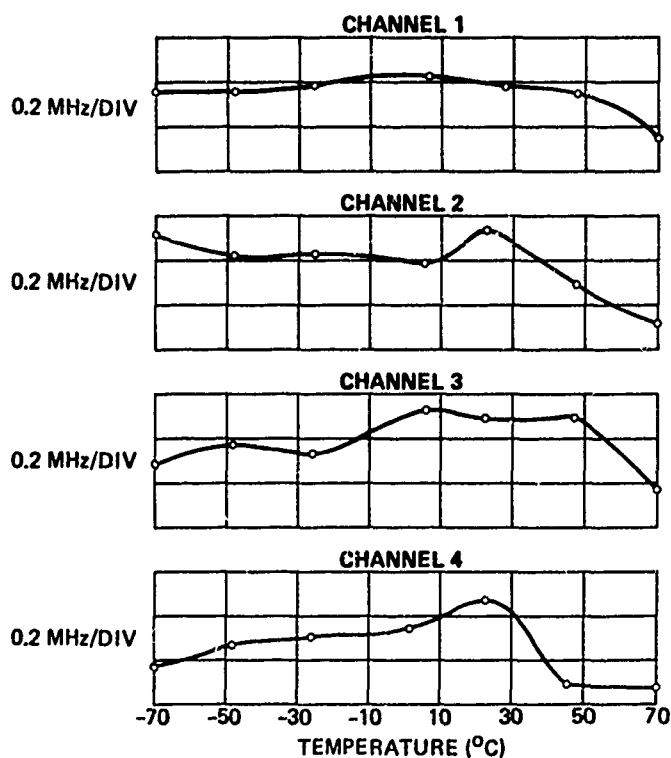


Table 3. PERFORMANCE SUMMARY

TEMPERATURE STABILITY/P _{OUT}			
CHANNEL	CENTER FREQUENCY (MHz)	P _{OUT} (dBm) MIN.	Δf (ppm)
1	1665.0	+28.10	242
2	1675.0	+28.40	257
3	1685.0	+28.00	214
4	1695.0	+27.80	222
SPURIOUS LEVEL			
FREQUENCY (MHz)	ORIGIN	(dBm)	P _{OUT} (dBm)
555.0	SAW FREQUENCY	-25.5	54.5
1110.0	2X SAW FREQUENCY	-25.5	54.5
3330.0	2X F _{OUT}	+ 9.5	19.5
5071.0	3X F _{OUT}	-28.0	57.0
FREQUENCY PULLING			
ΔF = 286 KHz (± 143 MHz)			
AM (V _{IN} = 1.414V)			
P _{ON} = +28.9 dBm			
P _{OFF} = -10.0 dBm			

Table 4. PERFORMANCE COMPARISON

OSCILLATOR	FREQUENCY STABILITY		FREQUENCY SETTABILITY	TOTAL BANDWIDTH
	TEMPERATURE -70 °C TO +70 °C	OTHER (ELECTRONICS, ETC.)		
PRESENT L.C. OSCILLATOR	1500 ppm		100 ppm	1600 ppm
	2.52 MHz		168 KHz (±84 KHz)	2.69 MHz
PROJECTED CAPABILITIES (CONTRACT REQUIREMENTS)	300 ppm		200 ppm	500 ppm
	160 ppm	140 ppm	336 KHz	840 KHz
	269 KHz	235 KHz	(±168 KHz)	
ACHIEVED PERFORMANCE	260 ppm		40 ppm	300 ppm
	160 ppm	100 ppm	67 KHz (±33.5 KHz)	504 KHz
	269 KHz	168 KHz		

APPLICATION OF MODERN TIME SERIES ANALYSIS TO HIGH STABILITY OSCILLATORS

Brian F. Farrell, Edward M. Mattison, and Robert F.C. Vessot

Smithsonian Astrophysical Observatory, Cambridge, Mass.

Summary

Modern techniques of time series analysis provide sensitive means of characterizing the frequency behavior of oscillators and are particularly useful for identifying the presence and sources of systematic frequency perturbations. We illustrate these techniques by describing the analysis of an experiment in which the frequencies of superconducting cavity-stabilized oscillators and hydrogen masers were compared.

The techniques we used to identify the presence of spurious variations in the frequency difference between two oscillators are autocorrelation of the time series of the frequency data, and cross-correlation of the frequency series with the candidate perturbation. To achieve high sensitivity in the correlation results, it was important to induce stationarity in the frequency data series by differentiating the data. Autocorrelations of the transformed series revealed the presence of perturbing signals. To identify the period of these perturbations we applied superresolution techniques; the period was found to correspond to that of the semi-diurnal lunar tide.

Cross-correlation of the differentiated frequency data with candidate perturbations then confirmed the identity of the source of the perturbations: barometric pressure fluctuations caused largely by atmospheric tides. The perturbation was removed from the frequency data by a least squares regression and also by a more sensitive calculation involving the maximum likelihood estimation of a second order linear transfer function; this technique allowed us to characterize the transfer functions of systematic perturbations affecting the oscillators.

Introduction

The quantity of ultimate importance to those working with high stability oscillators is the frequency of the oscillator, and, in particular, the behavior of the frequency as a function of time. Analysis of the frequency is necessary for characterizing the noise processes affecting the oscillator's performance and for identifying systematic perturbations of the

frequency. Traditional methods of treating oscillator frequency include Fourier analysis and measurement of the Allan variance. We shall discuss some recently applied techniques of time series analysis that provide sensitive means for characterizing the frequency behavior of oscillators, and are particularly useful for identifying the presence and sources of systematic perturbations of the frequency. These techniques include transformation of the frequency (expresses as a function of time) to a stationary process, autocorrelation and cross-correlation, superresolution and determination of transfer function between a perturbing influence and the frequency. We will illustrate these methods by describing the analysis of an experiment investigating theories of gravitation.

Description of Experiment

According to a conjecture proposed by Clifford Will, ¹ non-metric theories of gravitation predict that clocks based upon different physical principles will undergo different frequency shifts when the local gravitational potential changes, while metric gravitational theories (including Einstein's General Relativity) predict identical "gravitational redshifts" for all types of clocks.

In the experiment that provided the data to be discussed, the frequencies of superconducting-cavity stabilized oscillators (SCSO's) and the hydrogen masers were compared, with the aim of determining whether the frequency difference between the two types of oscillators is affected by changes in the local gravitational potential. The frequencies of three SCSO's in a common dewar were compared with the frequencies of two hydrogen masers in the same laboratory. The ten frequency difference combinations possible among the five oscillators were measured over a period of eleven days. The local gravitational potential due to the sun varied sinusoidally with a period of one solar day due to the rotation of the earth. Furthermore, the experiment was carried out during March and April of 1978, when the earth's motion in its eccentric orbit was carrying it away from the sun at its fastest rate of the year, thus adding a nearly linear time variation of the gravitational potential to the diurnal variation. From these two causes, the time-varying component

of the gravitational potential, normalized to the square of the speed of light, was approximately

$$\frac{\Delta\phi}{c^2} = 3 \times 10^{-12}t + 3 \times 10^{-13} \cos(2\pi t) \quad (1)$$

where t is measured in solar days, and $t=0$ corresponds to noon on April 4, 1978. The aim of the data analysis was to determine whether the difference frequencies between oscillators whose frequencies are governed by different physical principles varied in time according to eq. 1, and to set limits on the extent to which the gravitational potential can affect these frequency differences.

A typical maser SCSO fractional frequency difference signal as a function of time over the experiment is shown in Fig. 1. It can be seen that, although the signal is homogenous (any short section resembles any other short section), it is not stationary, in that it does not possess a fixed mean. (In general, a signal is stationary if and only if all of its moments--mean, variance, etc.--are independent of time.) Inspection of Fig. 1 suggests that the spectrum of the time series is "red", that is, the series is dominated by low-frequency fluctuations. This is confirmed by the Fourier transform, shown in Fig. 2; most of the spectral power is at low frequencies, and no spectral component extends more than roughly one standard deviation above the trend of the spectrum.

Homogeneous, non-stationary time series similar to that of Fig. 1 are observed in a wide variety of disciplines, from industrial process control to stock market price analysis. The significance of stationarity lies in the fact that for a stationary process probability structure of data depends only upon time differences, and not upon the absolute time. This assumption is at the foundation of most commonly used calculations such as Fourier transforms and correlation functions. Traditional methods of transforming a function with a non-fixed mean to approximate stationarity include trend removal (least square fitting of a polynomial to the function) and functional transformations (taking the logarithm, square root, etc. of the function). Another highly useful technique is to characterize the non-stationary stochastic signal as being produced by a linear system acting upon white noise. A transformation that has gained wide acceptance is the autoregressive moving-average model.⁽³⁾

$$(1 - \phi_1 B - \phi_2 B^2 - \dots) X_t = (1 - \theta_1 B - \theta_2 B^2 - \dots) A_t \quad (3)$$

where X_t = non-stationary signal at time t .

A_t = stationary white noise signal at time t

B = backshift operator defined by

$$BX_t = X_{t-1}$$

The versatility of this approach is apparent when it is viewed as the finite difference analog of the arbitrary differential operator connecting a system input and output. Usually the infinite series operating on X_t and A_t can be truncated, and in many cases X_t can be rendered stationary simply by the first difference operator:

$$(1-B) X_t \equiv X_t - X_{t-1} = A_t \quad (3)$$

This was approximately true in the experiment described here and since the first difference is the analog of the first derivative, we examined the time derivative of the relative frequency difference. The derivative of the frequency data of Fig. 1 is shown in Fig. 3.

It is apparent from Fig. 3 that the data have components fluctuating at roughly half-day and one-day periods. This can be seen more clearly in the autocorrelation function, Fig. 4, which displays a distinct period of approximately one-half day. In order to determine the source of this semi-diurnal fluctuation, we needed to know its period more exactly. The frequency resolution of Fourier analysis is limited to the reciprocal of the length of the data sample. We adopted a more powerful technique, which does not have this limitation, for determining a signal's period. This method, known as superresolution, in a trigonometric function

$$A \cos\left(\frac{2\pi t}{T} + \phi\right)$$

is fitted to the data by non-linear least squares regression. The amplitude (A), period (T), and phase (ϕ) of the function are adjusted for the best fit. The period resolution of this technique is limited only by noise, not by data length.

The period of the semi-diurnal perturbation was determined to be 0.507 ± 0.002 solar days. This is significantly longer than half a solar day, and suggests the effect of the lunar tide. Possible mechanisms of lunar perturbation are changes in the local gravitational acceleration g (the effect that causes ocean tides), and variations in the barometric pressure, which is affected by changes in g that result in the so-called "atmospheric tides". To determine the source of the perturbation, we cross-correlated the time derivatives of the candidate functions with the derivatives of the frequency differences. Fig. 5 shows the local barometric pressure during the experiment; we see that this function has a very distinct signature. Between days 3 and 5 a weather front passed through the area, and after day 6 the weather was quite stable, revealing the semi-diurnal variations of the atmospheric tides. Fig. 6 compares the time derivative of the barometric pressure, dp/dt , with the derivative of the frequency; the resemblance is striking. This is verified by the cross-correlation of dp/dt with f (Fig. 7), which has a strong peak at zero time lag.

When a systematic perturbation is identified, it is often desirable to remove its effect from the data. In the experiment, we accounted for

the influence of barometric pressure on oscillator frequencies by two methods. A traditional method is to perform a least squares regression of p on f , thereby obtaining a single value for the pressure sensitivity. p can then be multiplied by the sensitivity and subtracted from f . A more informative method of investigating the influence of the pressure is to calculate the transfer function between pressure and frequency:

$$\dot{f}_t = \frac{(1 - \phi_1 B - \phi_2 B^2)}{(1 - \theta_1 B - \theta_2 B^2)} \dot{p}_t + \eta_t \quad (4)$$

where B is the backshift operator and η is a white noise process. We determined the values of the ϕ_i and θ_i using a maximum likelihood method.⁽³⁾ The transfer function of eq. 3 gives not only the magnitude of the response of frequency to barometric pressure, but also its time evolution, and permits calculation of the impulse response,⁽³⁾ which is shown in Fig. 8 for the frequency differences between three pairs of oscillators. (Masers are labeled M5 and M6; SCSO's are labelled S1, S2, and S3.) It is apparent that the impulse response of the pair S2-M6 has a high initial amplitude and that a larger fraction of the area under curve is near $t=0$ than is the case for the other pairs. Furthermore, pair S2-M5 has a smaller amplitude and a slower response, suggesting that maser M6 had the highest barometric sensitivity. This was subsequently found to be caused by a mechanical interference within the maser, which was corrected. The barometric response of the frequency difference between SCSO's arises from flexure of the plate from which they are suspended in their dewar.⁽⁵⁾ The derivatives of the frequency differences for the three pairs of oscillators are shown in Fig. 9, along with dp/dt . The consequences of their different impulse responses are readily apparent in the data.

Conclusion

We have explored the application of several techniques of modern time series analysis that are useful for analyzing the characteristics of high-stability oscillators and for identifying systematic perturbations to the frequency. The techniques discussed here are:

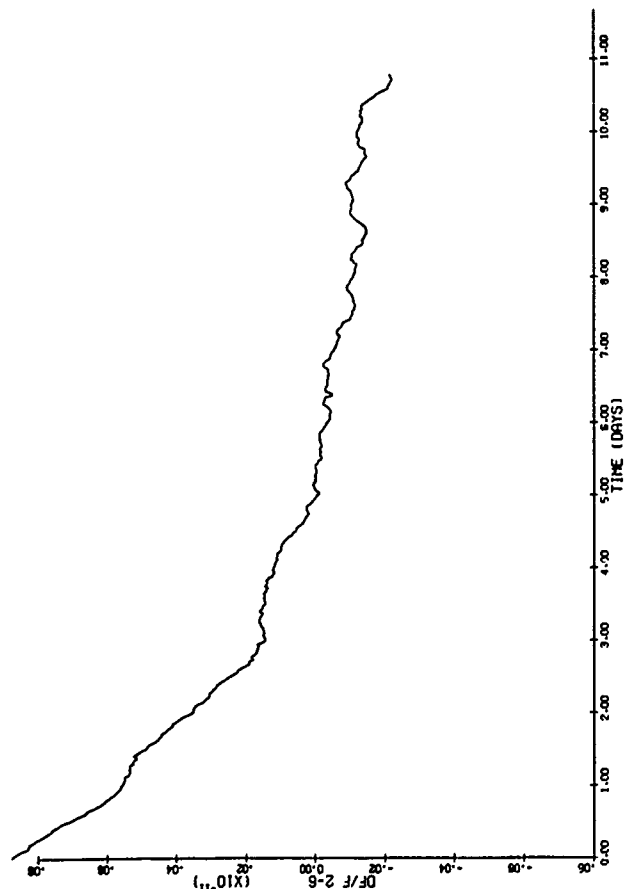
- transformation to stationarity
- autocorrelation and cross-correlation
- superresolution
- transfer function determination

Acknowledgement

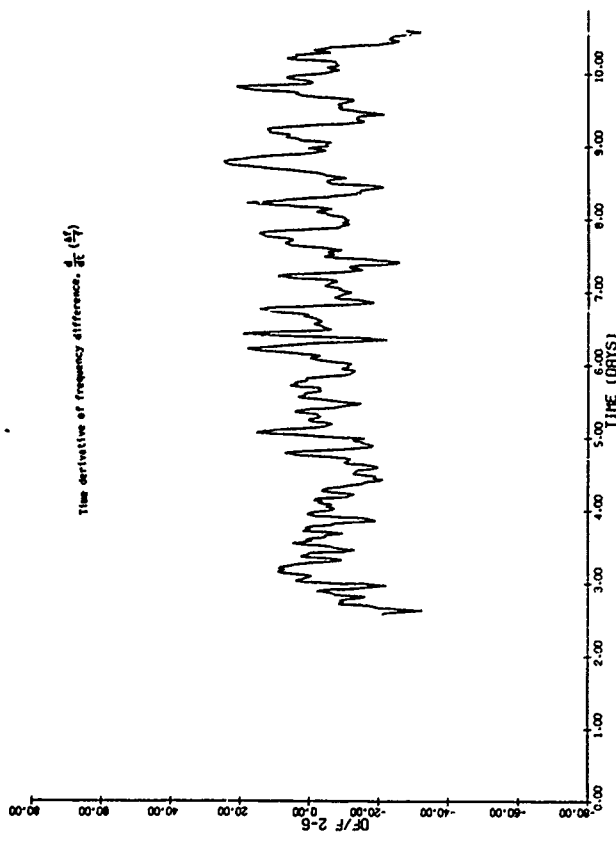
This work was supported by the Marshall Space Flight Center of the National Aeronautics and Space Administration.

References

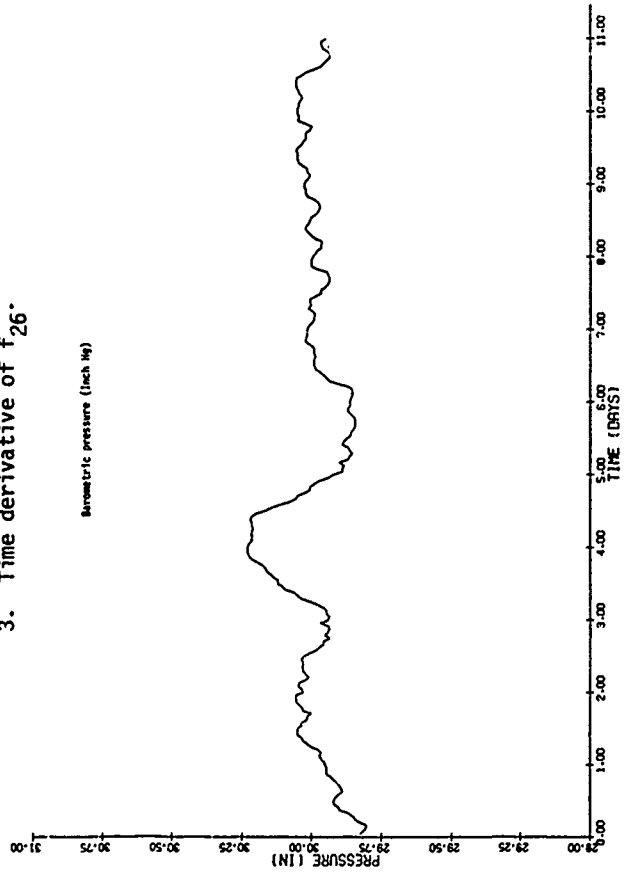
1. Will, Clifford M., *Metrologia* **13**, 95 (1977)
2. Farrell, B., E. Mattison, J. Turneaure, R. Vessot, C. Will, to be published.
3. Box, G.E.P. and G.M. Jenkins, *Time Series Analysis: Forecasting and Control*. Holden-Day (San Francisco), 1976.
4. Bloomfield, P., *Fourier Analysis of Time Series: an Introduction*. Wiley, 1976
5. Turneaure, J., Stanford University. Private communication.



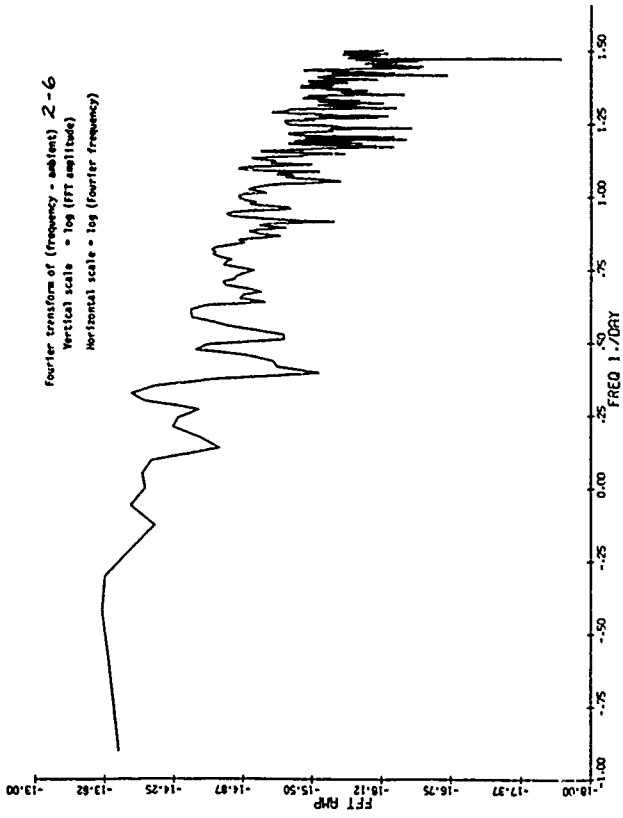
1. Fractional frequency differences, f_{26} , between SCSO S2 and maser M6.



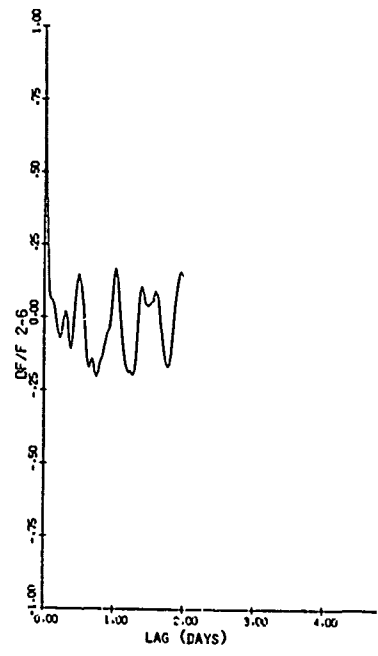
3. Time derivative of f_{26} .



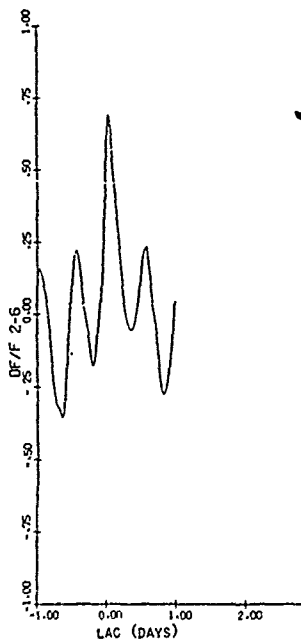
5. Local barometric pressure p , during experiment.



2. Fourier spectrum of f_{26} .



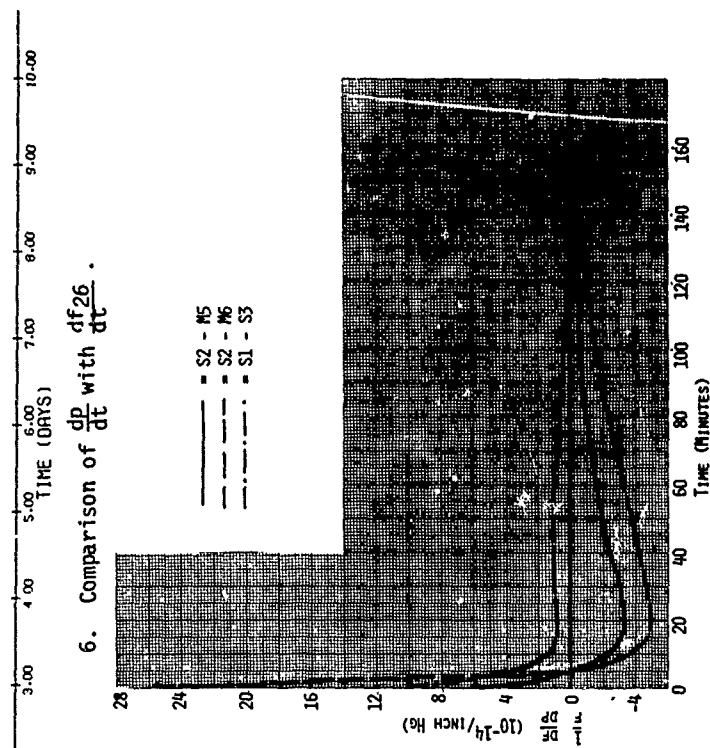
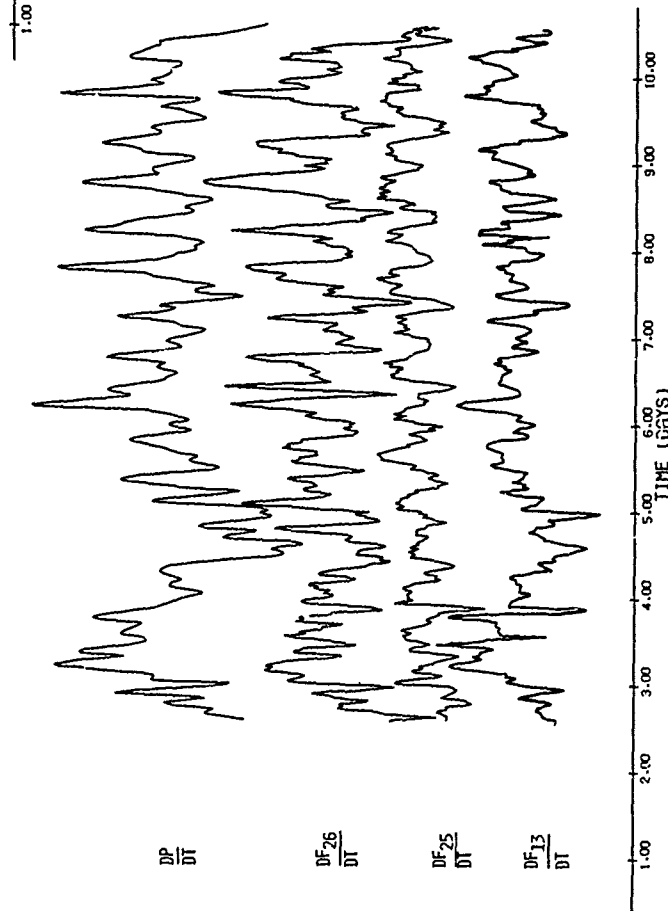
4. Autocorrelation function of $\frac{df}{dt}$.



7. Cross-correlation of $\frac{dp}{dt}$ with $\frac{df_{26}}{dt}$



8. Fractional frequency response to impulse change in barometric pressure for three pairs of oscillators. 9. Comparison of $\frac{dp}{dt}$ with $\frac{df}{dt}$ for three pairs of oscillators.



6. Comparison of $\frac{dp}{dt}$ with $\frac{df_{26}}{dt}$.

UHF OSCILLATOR USING SC CUT QUARTZ CRYSTAL,
WITH LOWNOISE PERFORMANCES AND HIGH LONG TERM STABILITY.

C. Pegeot
Quartz et Electronique - 92602 Asnières France

G. Sauvage
Adret Electronique - 78190 Trappes France

SUMMARY

Crystal oscillators are well known for short and medium term stability. Optimum performances are obtained at 5 and 10 MHz with a AT cut crystal. They are closely associated with the notion of stability in time. Another notion, spectral purity, will result in searching for a frequency generator. Let us consider the conventional AT cut crystal oscillator at 10 MHz. Low performances of such an oscillator are due, firstly to a too low frequency and secondly to an drive level wich must be low. To achieve -140 dB/Hz signal/noise ratio at 10 kHz of the 500 MHz carrier, -174 dB/Hz must be reached at 10 MHz. At this 10 MHz frequency the long term stability (aging) must be better than $5 \cdot 10^{-7}$ per year.

The oscillator presented provides directly, without multiplication to 80 MHz, the following performances :

- Spectral purity of -162 dB/Hz at 80 MHz.
- Long-term stability (aging) $< 5 \cdot 10^{-7}$ per year.

Such performances are obtained in using an SC cut crystal at 80 MHz.

Key words : Crystal oscillators- doubly rotated cuts - resonateurs - stability - spectral purity - noise - aging.

Introduction

The best performances of crystal oscillators take place at 5 MHz and 10 MHz with an AT cut crystal. They are closely associated with the notion of stability in time. Another notion, spectral purity, will result in searching for a frequency generator, performances such as -120 dB/Hz signal/noise ratio at 1 kHz and -140 dB/Hz at 10 kHz for a 500 MHz carrier frequency are necessary for a lot of applications in telecommunications. This notion of spectral purity requires the development of the design of generators, frequency synthesizers, spectrum analyzers and results in expanding prospects.¹

Let us consider the conventional AT cut crystal oscillator at 10 MHz. Low performances of such an oscillator are due firstly to a too low frequency and secondly to a drive level wich must be low (a few tens of microwatt), so that non-linearities in the operation of the resonator do not result in hardly controllable frequency variations and in addition, do not lower the long-term stability of the oscillator. To achieve a -140 dB/Hz signal/noise ratio at 10 kHz of the 500 MHz carrier, -174 dB/Hz must be reached at 10 MHz. Futher-more, to get to UHF, insolved studies on frequency multipliers are required.

The long term stability of this 500 MHz frequency must be better than $5 \cdot 10^{-7}$ per year. This long term stability may be obtained with a 10 MHz oscillator. That is the reason why the 10 MHz oscillator was choosen.

In this paper we present a 80 MHz oscillator using SC cut quartz crystal.

This 80 MHz oscillator paccent, without multiplication, the two performances : noise and long term stability.

Description and results

The choice of this 80 MHz frequency has been made according to the characteristics of crystal. It's difficult to get an industrial crystal at a frequency higher than 100 MHz, with an easy technology for getting a low aging rate and a low noise. This limit of 80 MHz is mainly determined by the thickness of the blank. The thickness of the 10 MHz blank (AT cut, overtone 3) is 500 μm . The thickness of the 80 MHz blank (SC cut, overtone 3) is 68 μm .

We will classify the following oscillators in 2 types :

- the first one : oscillators for satellite Communications applications (SATCOM)
- the second one : generators used for VHF and UHF receiver (telecommunications applications).

All the following values, will be given at 100 MHz frequency.

On figure 1, for these two applications, we can see the necessary specifications at 100 MHz.

The main difficulty for the spectral density of phase fluctuations in the case shown by the curve called SATCOM, is situated between a few Hz and 100 Hz.

For example the European Spatial Agency needs -120 dB/Hz at 160 Hz from the carrier frequency and -85 dB/Hz at 10 Hz from the carrier frequency.

In the case shown, by the curve called TELECOM, the noise specified is at more than 5 kHz.

-144 dB/Hz at 500 MHz, that is 160 dB/Hz at 100 MHz are needs.

For the aging rate, we must get several 10^{-7} per year.

On figure 2, we can see the standard oscillator performances.

The lower curve shows the values of an AT cut 10 MHz oscillator transposed at 100 MHz.

The noise is too high over 100 Hz from the carrier. That is due to the low oscillating power (a few 10 μ W). This low power is necessary to meet aging rate.

To used this kind of oscillator it is necessary to add a 100 MHz crystal filter. This is an expensive solution.

The second curve shows the values of a 100 MHz oscillator using an AT cut crystal.

The noise value agree with the specifications, but the aging rate is more than several ppm per year. For using this second kind of oscillator it's necessary to lock it on a 10 MHz oscillator, to get a good aging rate. This is also an expensive solution.

The figure 3 shows the values of a 80 MHz oscillator translated to 100 MHz, using a SC cut crystal.

On this SC cut oscillator, the noise value is -162 dB per Hz at 10 kHz from the carrier frequency, wich corresponds to -146 dB/Hz at 500 MHz and -180 dB/Hz at 10 MHz.

The aging rate is less than 5.10^{-7} per year.

These characteristics of the 80 MHz crystal resonator are the following :

- For the AT cut crystal : $R_1 = 15\Omega$
 $L_1 = 2,3 \text{ mH}$, $Q = 75 \text{ OOO}$.

- For the SC cut crystal : $R_1 = 65\Omega$
 $L_1 = 11 \text{ mH}$, $Q = 86 \text{ OOO}$.

The relative frequency deviation due to non-linear effects of these two kinds of crystal are the following :

- For the AT cut crystal : $\frac{\Delta F}{F} = 20.10^{-7}$
between two power levels of 45 and 400 μ W

- For the SC cut crystal : $\frac{\Delta F}{F} = 4.10^{-7}$
between two power levels of 45 and 400 μ W.

The SC crystal is 5 times better than the AT crystal.³

This good performance is interesting for the frequency adjustment at room temperature because the power level in the crystal is not crucial, and we imagine also, that the aging is better when the non linear effects are few.

The diagram of this 80 MHz oscillator is given on figure 4. The crystal works on its serial mode. The power level in the crystal is around 300 μ W.²

On figure 5 we can see the frequency temperature deviation for an AT and SC cut crystal about 70° celcius. The accuracy of the inversion point of the frequency-temperature curve for the SC cut, is $\pm 2^\circ\text{C}$.⁴

Figure 6 shows SC cut crystal aging curves.⁵

These results were made on 10 oscillators. The top curve shows the minimum aging rate in one year.

The inferior curve shows the maximum aging rate in one year. The middle curve shows the average value of the aging of the 10 oscillators (1.10^{-7} per year.)

Figure 7 compares the average value of the aging of AT and SC cuts. The average aging of the AT cut crystal is $10 \cdot 10^{-6}$ per year and the average aging of the SC cut crystal is $1 \cdot 10^{-7}$ per year. The ratio is 100.

Conclusion

The noise values are a few better for the SC cut crystal oscillators (about 3 dB), but the aging rate is 100 times better.

Without a filter or another lock oscillator a SC cut crystal oscillator solves the two problems, noise and aging, (only with one crystal).

It's also a less expensive and easier solution.

We think that this new 80 MHz oscillator could be applied in many ways in the telecommunications field.

References

1. G. Sauvage, "Short term instability of oscillators : Study of new measurements in frequency domain and Time domain". Thesis Univ. Paris VI. Nov. 1974. Paris.
2. G. Sauvage, "Phase noise in oscillators : A mathematical Analysis of Leeson's model" IEEE Transactions on Instrumentation and Measurement. Vol. I.M.-26, N°4 December 1977.
3. J.J. Gagnepain, J.C. Ponçot, C. Pegeot. "Amplitude Frequency Behavior of Doubly Rotated Quartz Resonators". Proceedings of the 31th Annual Symposium on Frequency Control, U.S. Army Electronics Command, Fort Monmouth, N.J. (1977).
4. J. Clastre, C. Pegeot, P.Y. Leroy. "Goniometric Measurements of the Angles of Cut of Doubly Rotated Quartz Plates". Proceedings of the 32th Annual Symposium on Frequency Control, U.S. Army Electronics Command, Fort Monmouth, N.J. (1978).

5. C. Pegeot. "Etude comparative entre des oscillateurs à quartz en coupe AT et en coupe SC". Revue l'Onde Electrique, novembre 1979. Vol. 59. N° 11.

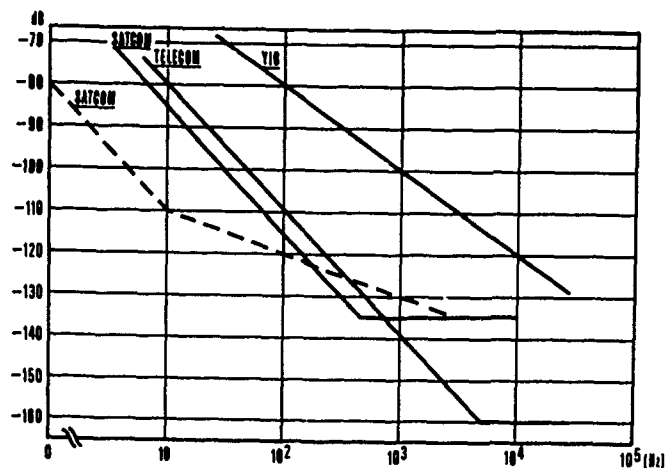


Figure 1
 $\mathcal{L}(f)$ specifications at 100 MHz

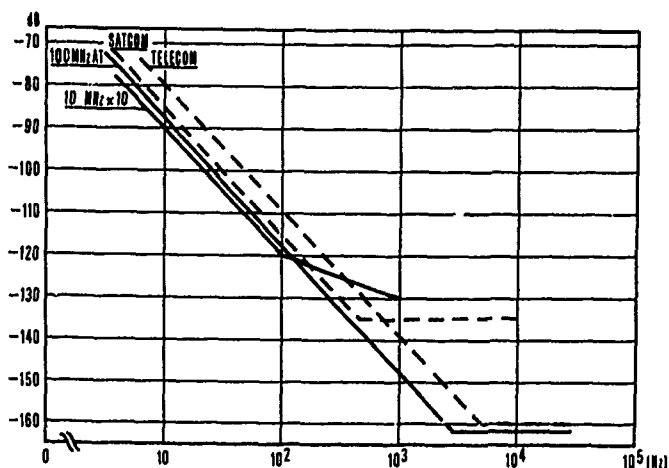


Figure 2
 $\mathcal{L}(f)$ of the standard oscillators

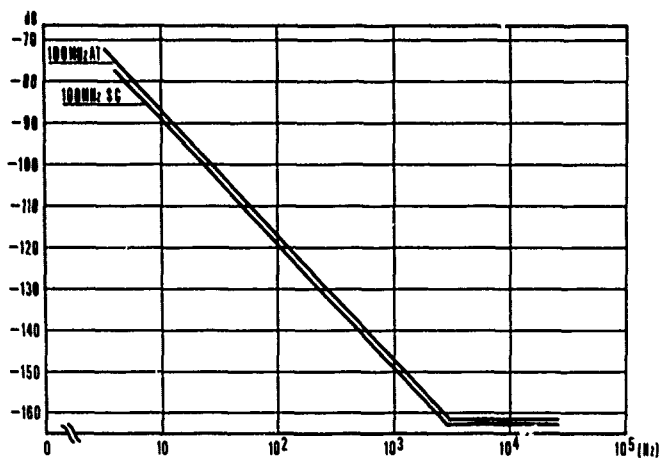


Figure 3
SC cut crystal oscillator performances

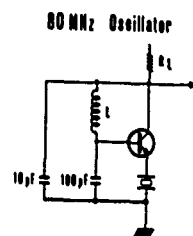


Figure 4
Diagram of the 80 MHz oscillator

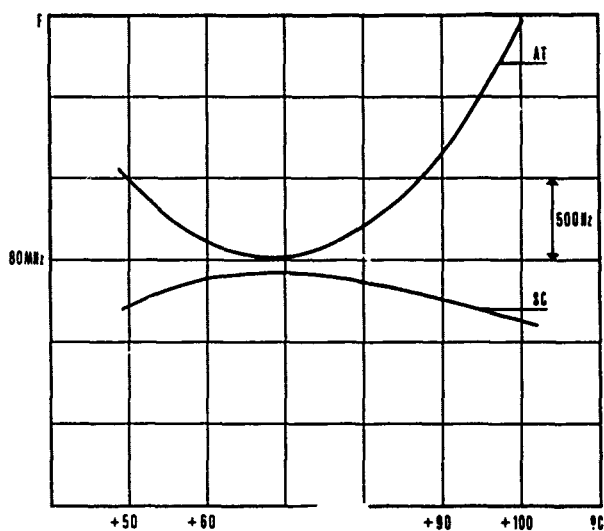


Figure 5
Frequency-Temperature deviation

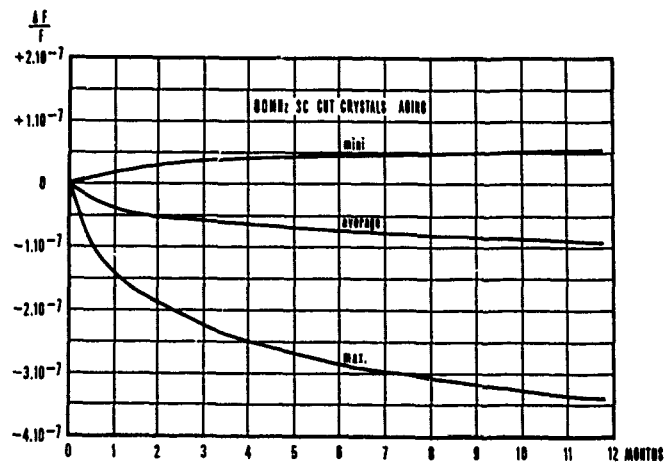


Figure 6
80 MHz SC cut crystal oscillators aging

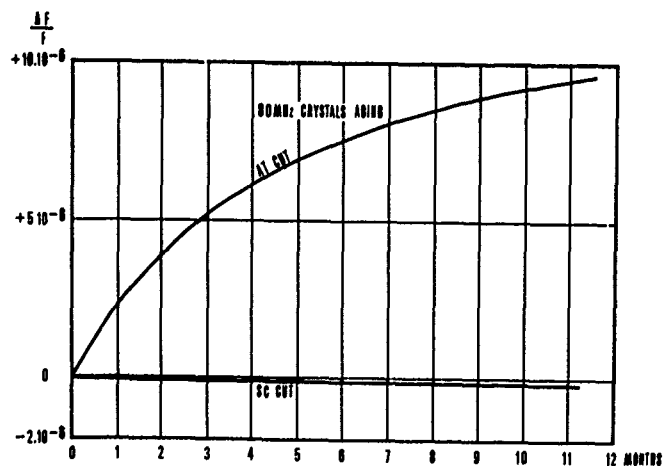


Figure 7
80 MHz AT and SC cut crystal oscillators aging

A TEMPERATURE STABLE 2 GHz SBAW DELAY LINE OSCILLATOR*

K. F. Lau, K. H. Yen, R. S. Kagiwada and A. M. Kong

TRW Defense and Space Systems Group
Redondo Beach, California

Summary

With wave velocities 1.1 to 1.7 times that of the Surface Acoustic Waves (SAW), the Shallow Bulk Acoustic Waves (SBAW) are particularly attractive for high frequency applications. In this paper an experimental 2 GHz SBAW delay line oscillator is described and its performance analyzed. The SBAW delay lines are fabricated on rotated Y-cut quartz substrates with angle θ near the AT-cut angle of 35.25° . For these substrates the SBAW has high velocity and a zero first order temperature coefficient of delay near room temperature. Each delay line consists of two identical transducers with split finger configuration and operates at the third harmonic. Very thin aluminum metallization is used for the transducers. In addition, the fingers are embedded into the substrate surface in order to minimize diffraction loss at finger edges. The untuned insertion losses of these SBAW delay lines are consistently less than 25 dB.

The 2 GHz SBAW delay line oscillator is constructed with discrete components which include the SBAW delay line, amplifier, external delay, and output coupler. Its short-term stability or phase noise is measured in the frequency domain and the result compared with theory. The medium stability of temperature effect is measured as a function of the metallization thickness and the crystal cut angle θ . Data on initial device burn-in drift are also presented as an indication of the long-term aging characteristic of the SBAW oscillator.

This work demonstrates the applicability of SBAW devices for frequency control above 2 GHz using conventional photolithographic techniques. By using transducers operating at the fifth harmonic, the practical frequency range of SBAW devices is expected to extend above 3 GHz.

Introduction

The shallow bulk acoustic wave (SBAW) propagating at 90° off the X-axis of the rotated Y-cut quartz has been studied extensively over the past few years.¹⁻⁶ It is well known from these

studies that temperature compensated cuts exist in two ranges of the rotated Y-cut angle θ . For substrates with angle θ near -50.5° , the shallow bulk acoustic wave is a slow shear wave with temperature characteristics similar to that of an AT bulk crystal. For substrates with θ near 35.5° , on the other hand, the shallow bulk acoustic wave is a fast shear wave with temperature characteristics similar to those of the BT bulk crystal. In high frequency applications, the fast shear wave is desirable not only because its wave velocity is 1.6 times that of the surface acoustic wave (SAW), but also because the attenuation due to material viscosity is much lower.^{2,7} It is for these reasons that the $+35.5^\circ$ rotated Y-cut quartz was chosen for the construction of the 2 GHz SBAW oscillator.

The purpose of this paper is to demonstrate the applicability of SBAW device for direct frequency control above 2.0 GHz by describing in detail the construction and performance of an experimental 2.0 GHz SBAW oscillator. The areas of investigation include delay line design and fabrication, metallization effects on frequency and temperature characteristics, short-term phase noise spectrum, and temperature stability. Data on initial burn-in drift are also presented as an indication of the long-term aging characteristic of the oscillator.

Construction of the SBAW Oscillator

The SBAW oscillator is very similar to the surface acoustic wave (SAW) delay line oscillator, as shown schematically in Figure 1. A SBAW oscillator consists basically of a SBAW delay line and an amplifier in a feedback loop circuit. The conditions for oscillation are (1) gain around the loop must exceed all losses, and (2) phase around the loop must be equal to a multiple of 2π radians. For single mode operation, the SBAW delay line must have a sufficiently narrow passband so that it covers only one oscillation mode in its passband. All other modes satisfying condition (2) will lie in the rejection band of the delay line and will not oscillate due to lack of gain.

The photograph of the SBAW oscillator is shown in Figure 2. Discrete components are used in the construction of the oscillator. These include the SBAW delay line, amplifier, attenuator, some external delay and an output coupler. The

* This work was partially supported by the Army Office of Research Contract No. DAAG26-78-C-0043.

amplifier has a maximum gain of 29 dB and can be reduced by adding attenuators in the loop if required. The use of discrete components allows maximum flexibility in interchanging individual components. Many different SBAW delay lines can be incorporated into the oscillator circuit and their performances analyzed.

Delay Line Design and Fabrication

The SBAW delay line was designed to satisfy the single mode requirement. It consists of two identical transducers with split finger design as shown schematically in Figure 3. This configuration allows the transducer to operate at the third space harmonics. The number of finger pairs in each transducer is 75, and the center-to-center separation between transducers is 286λ , where λ is the acoustic wavelength at the operating frequency. The linewidth of the transducer is $0.95 \mu\text{m}$, and the transducer aperture is 90λ .

The SBAW delay lines were fabricated using basically the lift-off technique. However, in the case of 2 GHz delay lines, it was necessary to embed the metallization fingers into the quartz substrate in order to minimize scattering loss at the finger edges.

The fabrication process for the embedded transducer is shown schematically in Figure 4. After the photoresist pattern was developed, the substrate was ion-milled to create the desired groove depth. Aluminum metallization was then evaporated to fill up the grooves. The metal thickness was usually within 100 \AA that of the groove depth. This was verified by surface profile measurement using a Dektak machine. In some devices a titanium layer of $30\text{--}40 \text{ \AA}$ were placed between the substrate and the aluminum to improve film adhesion. No significant difference in device characteristics were observed for these two types of metallization schemes.

Frequency Characteristics

A typical frequency response of one SBAW delay line is shown in Figure 5. The device shown in this figure was fabricated on 35.5° rotated Y-cut quartz with wave propagation at 90° off the X-axis. The metallization used was 40 \AA Ti/ 420 \AA Al, and the groove depth was 400 \AA . The device has an untuned insertion loss of 22.5 dB and a 3 dB bandwidth of 5.4 MHz. Its phase slope was equal to 360° per 7 MHz and the single mode requirement is easily met. The only other "spurious" response of the delay line is the fundamental frequency response at 671 MHz. The insertion loss of the fundamental response is 32 dB and is 10 dB down from the third harmonic passband. By matching the delay line at the third harmonic, the fundamental frequency response can be further suppressed by at least another 10 dB.

Similar to high frequency SAW devices, the electrode width (or finger width) and the metal film thickness of the SBAW transducers have a significant effect upon the center frequency and the temperature characteristics of the SBAW delay line. To

investigate this effect, up to 30 delay lines with eight different metallization thicknesses were fabricated on 35.5° rotated Y-cut quartz. The finger-to-gap ratios for these delay lines are generally of the order of 5 to 1 due to overdevelopment of photoresist pattern during fabrication. Figure 6 shows the measured center frequency of these delay lines as a function of normalized metal thickness t/λ where t is the metal thickness and λ is the wavelength at the center frequency. The dependence on metal thickness is less critical for thin metallizations. At 400 \AA metallization, for example, a variation of 25 Å in metallization thickness causes a 1 MHz change in center frequency.

No special effort was made during the present investigation to control the finger/gap ratio. As a result, the effect of finger width on center frequency has not been thoroughly investigated. Table 1 lists the response of five delay lines fabricated simultaneously on a single substrate of 35.5° rotated Y-cut quartz. The photoresist pattern was developed by dipping the substrate into a bath of resist developers. Different finger/gap ratios were found in each of the five delay lines. The center frequency was found to be lower for wider fingers. A total of 7 MHz variation was found for a variation of metal coverage δ from 0.66 to 0.89, where δ is the ratio of metallized area/total area in the transducer region. For a more typical fabrication run, a control of center frequency to within 2 MHz can usually be achieved.

The center frequency of the SBAW delay line can also be adjusted by fabricating the delay line on substrate with different rotation angle θ . Figure 7 shows the dependence of SBAW velocity as a function of θ near the 35.5° region. The theoretical solid line has been calculated using a method reported previously.⁹ The experimental points were obtained by dividing the center frequency of the delay line with the acoustic wavelength λ of $2.533 \mu\text{m}$. The data for the 38° rotated Y-cut quartz were collected by measuring four separate delay lines.

Phase Noise - Short Term Stability

For a feedback oscillator such as the SBAW delay line oscillator, the amplifier is operating in a saturated condition suppressing the AM noise. The dominant noise is thus FM.¹⁰ The equation for the single-sideband noise spectrum of such an oscillator has been worked out by Parker for the case of SAW delay line oscillator.¹¹ It is expression gives the FM single-sideband noise power relative to the carrier in a 1 Hz bandwidth as a function of the Fourier or modulation frequency ω .

$$\left[\frac{P_{sb}}{P_c} \right]_{\text{dB}_c} = 10 \log \left[\frac{\alpha}{\omega^3 \tau^2} + \left(\frac{GFkT}{P_c} \right) \left(\frac{1}{\omega^2 \tau^2} + 1 \right) \right], \quad (1)$$

where

- α = flicker noise parameter (sec^{-1})
- τ = group delay
- G = amplifier gain
- F = noise figure
- P_c = loop power
- kT = thermal energy

Application of this noise theory to the 2 GHz SBAW delay line oscillator yields a theoretical noise floor of -153 dBc/Hz and a noise floor intercept point at 1.12 MHz. The parameters used in this calculation are summarized in Table 2. Figure 8 shows the theoretical and experimental single-sideband noise spectrum of the 2 GHz SBAW delay line. The experimental data was obtained by using the SBAW delay line on 35.5° rotated Y-cut quartz whose frequency response was shown in Figure 5. The amplifier gain was set so that it is 3 dB more than the delay line insertion loss. The measurement was done at TRW Metrology using the single oscillator technique.¹² The phase noise spectrum shows a 20 dB/decade decrease in noise for Fourier frequency (modulation frequency) between 2 kHz and 1.12 MHz. Below 2 kHz the $1/f$ noise results in a 30 dB/decade slope. For this result, the flicker noise parameter α is estimated to be $6 \times 10^{-12} \text{ sec}^{-1}$. This value is comparable to values between $2 \times 10^{-10} \text{ sec}^{-1}$ and $6 \times 10^{-13} \text{ sec}^{-1}$ measured for SAW delay line oscillators.¹¹

Temperature Coefficient of Delay - Medium Term Stability

The temperature stability of the SBAW delay line oscillator is controlled by the temperature behavior of the SBAW delay line. For SBAW in rotated Y-cut quartz with θ near 35 degrees, the temperature behavior is parabolic with zero first order coefficient of delay occurring at some turn-over temperature T_0 and a second order temperature coefficient of delay of approximately $52 \times 10^{-9}/^\circ\text{C}^2$. The dependence of the turn-around temperature T_0 on the rotation angle θ of the substrate is shown in Figure 9. This theoretical curve is obtained by methods described in Reference 9. By choosing the proper θ , one selects the temperature characteristics of the SBAW oscillator.

The temperature behavior of two specific substrates is shown in Figure 10. Experimentally, however, the curves are all shifted toward lower temperatures. The reason for this is because the substrate surface is covered by metal. Similar to the center frequency, the temperature characteristic of the SBAW delay line is affected by both the metal thickness and the percent of metal coverage. Figure 11 is an attempt to indicate the magnitude of such an effect due to metal thickness. The data were collected on both 35.5° and 38° rotated Y-cut substrates. The dotted line is just an eyeball fit to the experimental points. This investigation of the temperature effect is only preliminary since no special effort was made to control the finger/gap ratio to high accuracy. Scattering of T_0 at the order of 30°C can sometimes be observed for similar metallization thicknesses.

Initial Aging Data

To get an estimate of the aging characteristics of the SBAW oscillator, a delay line using 38° rotated Y-cut quartz was hermetically sealed in a nitrogen environment and tested for initial burn-in drift. In this experiment the substrate was mounted on a flatpack using RTV. The device is then cleaned and vacuum baked before sealing. A leak test was performed to insure the hermeticity

of the package. The oscillator is then placed in an oven at 50.5°C . For this test, the short-term oscillator stability as indicated from the frequency counter is better than $10^{-8}/\text{sec}$. The initial aging data over a period of 48 hours is shown in Figure 12.

Conclusion

In conclusion, we have demonstrated the applicability of SBAW for direct frequency control at frequencies above 2 GHz using only conventional photolithographic techniques. Oscillators with characteristics similar to this experimental 2 GHz delay line oscillator, as summarized in Table 3, can be produced in large quantity and at a low cost. Previous oscillators using SAW delay lines at comparable frequencies required either electron beam lithographic technique¹³ for device fabrication or $\text{AlN}/\text{Al}_2\text{O}_3$ as SAW substrates.¹⁴ This $\text{AlN}/\text{Al}_2\text{O}_3$ substrate has so far been found to be very difficult to prepare. Using a linewidth of $0.6 \mu\text{m}$, the present design can be extended to above 3 GHz. Higher harmonic SBAW transducers have also been demonstrated at TRW. Preliminary data shows that using fifth harmonic transducers a 3.5 GHz SBAW delay line can be fabricated with an insertion loss of less than 35 dB.

Acknowledgement

The help by J. C. Thorpe, F. Miller, and N. Hudson in the phase noise measurement is gratefully acknowledged.

References

1. Yen, K. H., K. L. Wang and R. S. Kagiwada, "Efficient bulk wave excitation on ST-quartz," Electronics Letters, Vol. 13, 1977, pp. 37-38.
2. Lewis, M., "Surface skimming bulk waves, SSBW," Proc. IEEE Ultrasonics Symposium, October 1977, pp. 744-752.
3. Yen, K. H., K. F. Lau, and R. S. Kagiwada, "Recent advances in shallow bulk acoustic wave devices," Proc. IEEE Ultrasonics Symposium, September, 1979, pp. 776-785.
4. Lee, D. L., "Excitation and detection of surface skimming bulk waves on rotated Y-cut quartz," IEEE Transactions on Sonics and Ultrasonics, Vol. SU-27, No. 1, January 1980, pp. 22-30.
5. Jhunjunwala, A. J., J. F. Vetelino, Harman and N. Soluck, "Theoretical examination of surface skimming bulk waves," Proc. IEEE Ultrasonics Symposium, September, 1978, pp. 670-674.
6. Ballato, A., and T. Lukaszek, "Shallow bulk acoustic wave devices," 1979 MTT Symposium Digest, pp. 162-164.
7. Slobodnik, A. J., and J. U. O'Brien, "Complete theory of acoustic bulk wave propagation in

anisotropic piezoelectric media," AFCRL-71-0601, November 1971, pp. 86.

8. Weglein, R. D., "1.2 GHz temperature stable SAW oscillator," Proc. 31st Annual Symposium on Frequency Control, 1977, pp. 225-230.
9. Lau, K. F., K. H. Yen, J. Wilcox and R. S. Kagiwada, "Analysis of shallow bulk acoustic wave excitation by interdigital transducers," Proc. 33rd Annual Frequency Control Symposium, May, 1979, pp. 388-395.
10. Parker, T. E., "Current developments in SAW oscillator stability," Proc. of the 31st Annual Symposium on Frequency Control, 1977, pp. 359-364.
11. Parker, T. E., "1/f phase noise in quartz SAW devices," Proc. IEEE Ultrasonics Symposium, 1979, pp. 878-881.
12. Lance, A. L., W. D. Seal, F. G. Mendoza and N. W. Hudson, "Automatic phase noise measurements in the frequency domain," Proc. of the 31st Annual Frequency Control Symposium, June, 1977, pp. 347-358.
13. Weglein, R. D., and O. W. Otto, "Microwave SAW Oscillators," Proc. IEEE Ultrasonics Symposium, October 1977, pp. 913-921.
14. Thorpe, J. C. and K. H. Yen, "2.148 GHz Surface Acoustic Wave Oscillator," Proc. IEEE Ultrasonics Symposium, 1979, pp. 882-885.

Table 1. Reproducibility Data of 2 GHz SBAW Delay Line on 35.5° Rotated Y-Cut Quartz.

GROOVE DEPTH/ METAL THICKNESS (Å)	CENTER FREQUENCY (MHz)	INSERTION LOSS (dB)	3 dB BANDWIDTH (MHz)	% META ¹ COVERAGE (6 x 100%)
400/460	2014.3	22.5	5.40	0.66
400/460	2010.78	22.5	3.60	0.92
400/460	2010.04	24.0	4.06	0.85
400/460	2009.15	25.0	5.42	0.87
400/460	2007.46	24.0	3.64	0.89

Table 2. Oscillator Parameters.

AMPLIFIER GAIN	G	25 dB
NOISE FIGURE	F	6 dB
LOOP POWER	P _c	10 dBm
GROUP DELAY	τ	0.142 μSEC

Table 3. Characteristics of the 2 GHz SBAW Oscillator.

FREQUENCY	2014.5 MHz
LOOP POWER	10 dBm
POWER OUTPUT	~ 0.5 dBm
DELAY LINE INSERTION LOSS	22 dB
FREQUENCY STABILITY (PHASE NOISE)	- 55 dBc/Hz AT 100 Hz - 84 dBc/Hz AT 1 kHz NOISE FLOOR AT 1 MHz - 144 dBc/Hz
TEMPERATURE STABILITY	ZERO 1st ORDER COEFF. AT - 15°C 2nd ORDER COEFF. ≈ 52 × 10 ⁻⁹ /°C ²

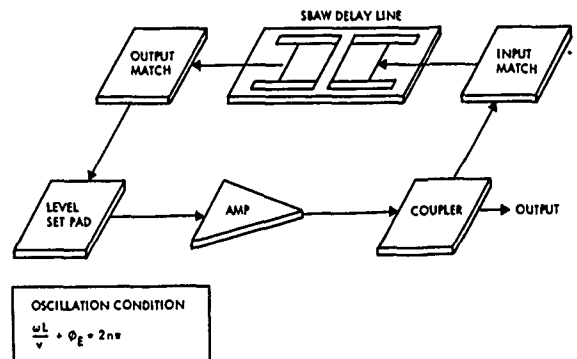


Figure 1. SBAW Oscillator Schematic.

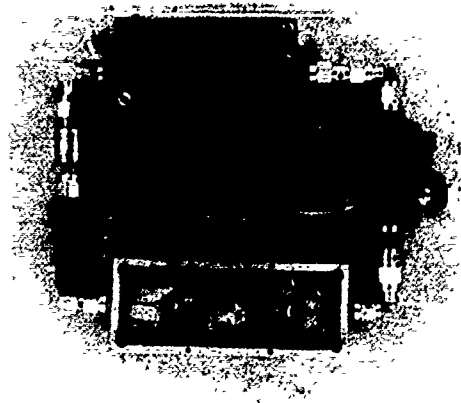


Figure 2. 2 GHz SBAW Delay Line Oscillator.

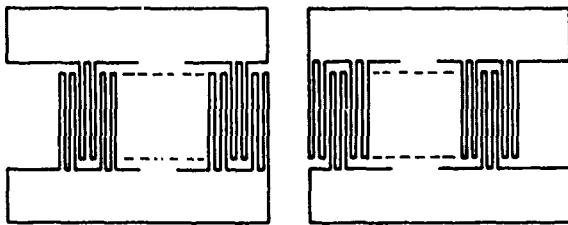


Figure 3. SBAW Delay Line Design.

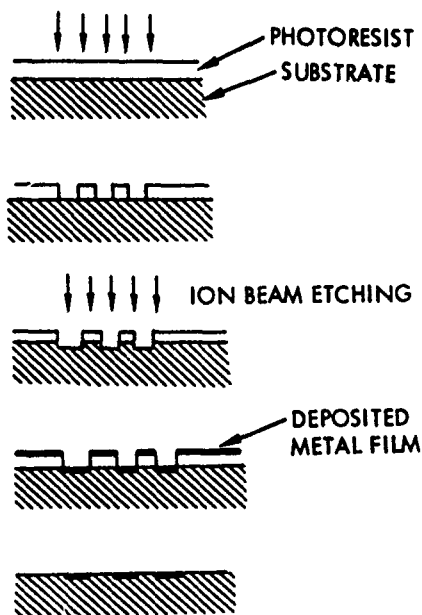


Figure 4. SBAW Delay Line Fabrication.

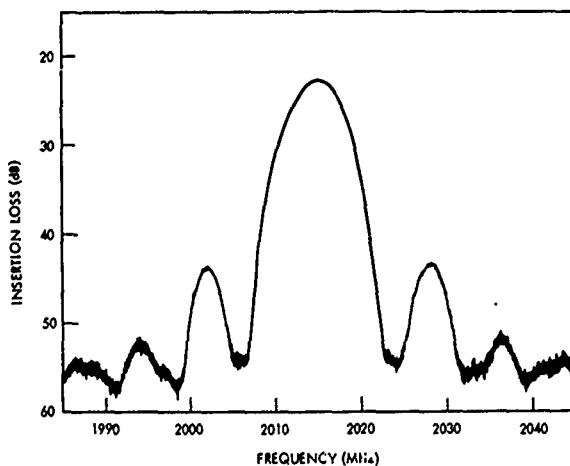


Figure 5. 2 GHz SBAW Delay Line on 35.5° Rotated Y-Cut Quartz.

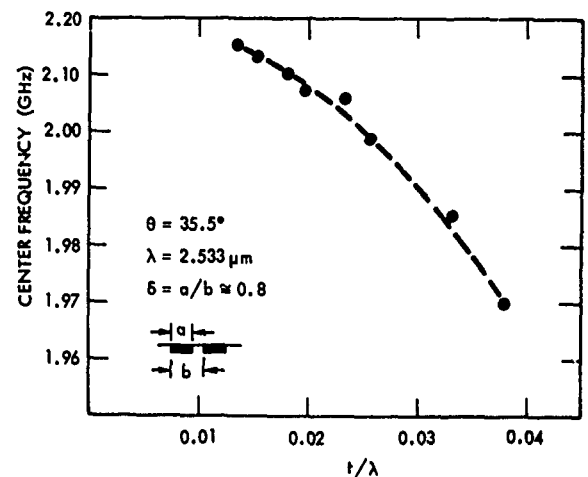


Figure 6. Dependence of Center Frequency as a Function of Normalized Metal Thickness.

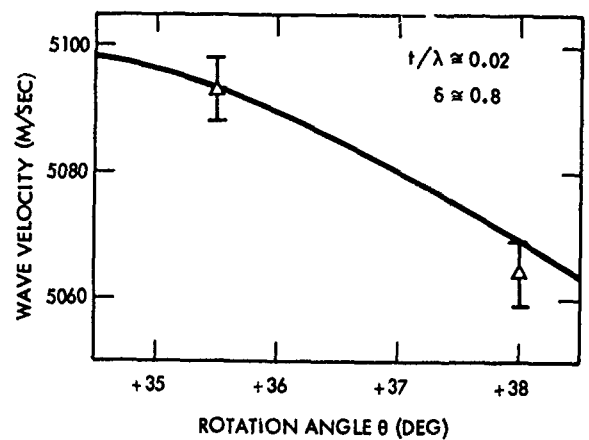


Figure 7. Dependence of SBAW Velocity as a Function of θ in Rotated Y-Cut Quartz.

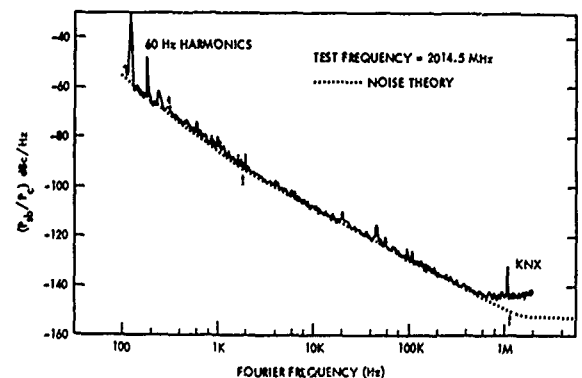


Figure 8. Single Sideband Phase Noise of the 2 GHz SBAW Oscillator.

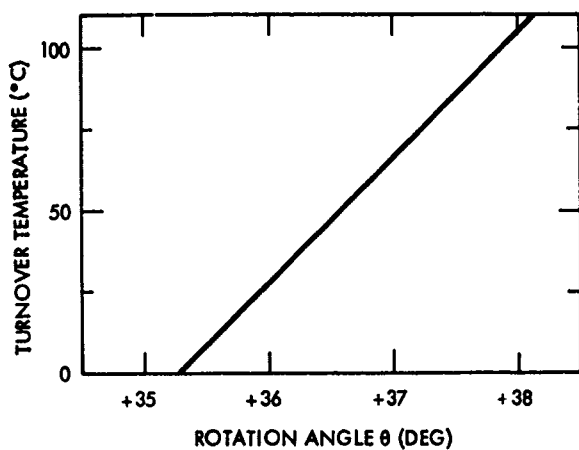


Figure 9. Dependence of Turnover Temperature on θ for SBAW in Rotated Y-Cut Quartz

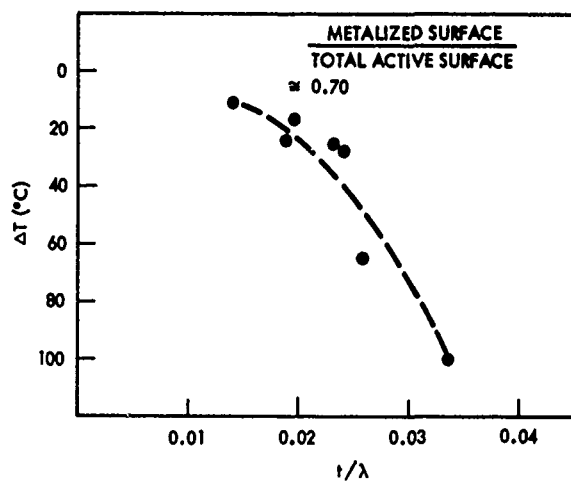


Figure 11. Turnover Temperature vs. Normalized Thickness of Aluminum Film on Rotated Y-Cut Quartz Near AT-Cut.

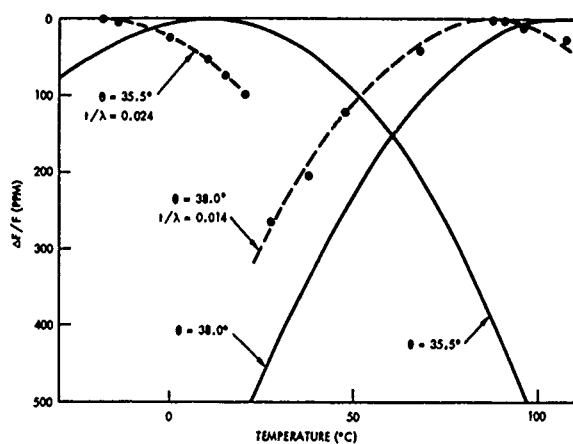


Figure 10. Theoretical and Experimental Temperature Behavior of SBAW Delay Line on Rotated Y-Cut Quartz.

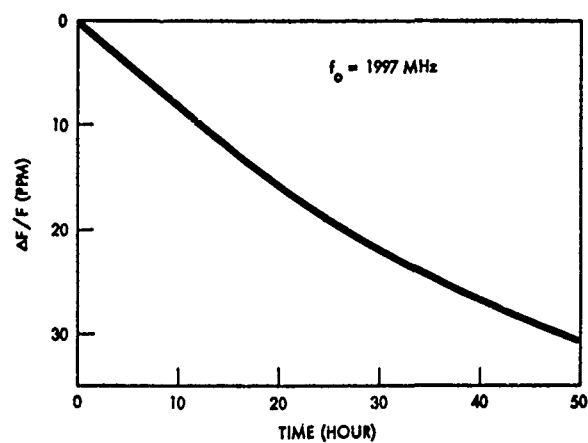


Figure 12. Initial Aging Data of the 2 GHz SBAW Oscillator.

HIGH Q BULK ACOUSTIC RESONATORS FOR DIRECT *
MICROWAVE OSCILLATOR STABILIZATION

R.A. Moore, J. Goodell, A. Zahorchak
R.A. Sundelin, W. Hopwood, T. Haynes
Westinghouse Defense & Electronic Systems
Center
Baltimore, MD 21203

B.R. McAvoy, J. Murphy
Westinghouse R&D Center
Pittsburgh, PA 15235

Abstract

Direct Microwave Bulk Acoustic Resonator Oscillator Stabilization has previously been identified as a possible low cost alternative to the quartz crystal multiplier chain. The bulk acoustic resonator additionally has the potential for frequency agility. Previously the resonator based on several high Q media has been described, though none with zero temperature coefficient. The resonator geometry and oscillator noise performance have been given only limited characterization.

In this paper zero temperature coefficient cuts of lithium tantalate will be mapped. Though previously identified to exist in shear mode, extensive mapping of these zero temperature cuts has not been carried out. Mapping will be presented for a one dimensional one-half wavelength resonator geometry for both resonance and anti-resonance. Complete families of orientations will be provided. It should be noted that orientations for each order of resonator overtone must be individually computed. Only the first order are presented. Results are compared with computed and measured results from the literature.

The effect of anisotropy on Q of trapped modes will also be presented. For this purpose anisotropy has been expressed in a circularly symmetric manner. For orientations close to the propagation direction this leads to a good approximation of actual performance. Anisotropy has been found to be very critical to high Q. Curves of Q value vs. wave propagation anisotropy, based on crystallographic data show expected Q values for resonator mode from spinel, sapphire, and diamond.

Noise measurements are provided for a microwave bulk acoustic resonator stabilized oscillator operating at x-band.

Introduction

The thrust for a technically and economically well-balanced hardware realization of low noise microwave stable local oscillators has led to the examination of alternatives to the quartz crystal-multiplier chain. One such alternative is the high overtone acoustic bulk mode resonator. Our examination of the properties of this type of resonator has initially centered on the longitudinal mode over a frequency range of 300 MHz to 12 GHz.

Operation of the high overtone resonator, previously described by Moore, et al., is somewhat

analogous to an optical Fabray-Perot Resonator.^{1,2} A transducer as suggested in Figure 1 launches an acoustical wave toward the opposite face. For frequencies for which the round trip distance is a multiple of an acoustic wavelength, phase support and a resonant build up of energy occurs. For most cases for which resonators have been fabricated two transducers were used on the opposite crystal-faces for operation as a transmission resonator.

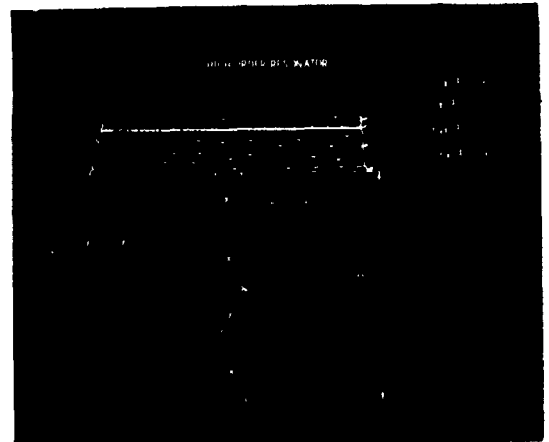


Figure 1. Geometry of high overtone Microwave Acoustic Resonator showing substrate and transducer detail.

The use of a separate resonant body and electro-acoustical coupling mechanism has two key advantages:

- (a) A much higher overtone resonance becomes practical
- (b) The resonator itself is not restricted to being piezoelectric.

By using a separate transducer, coupling is not limited by high overtone levels of operation. Operation at these frequencies is allowed even with

* The work reported in this paper has been supported in part by Contract F19628-78-C-0108, Hanscom Air Force Base, Massachusetts 01731

resonator thickness up to a large fraction of a millimeter. Figure 2 shows the periodic response of a high overtone resonator. Because the substrate need not be piezoelectric for coupling, a large variety of media with Q's an order of magnitude greater than quartz are available. Curves of crystalline Q vs. frequency previously have been provided for sapphire, YAG, spinel and lithium niobate in comparison to that of quartz.^{1,2}

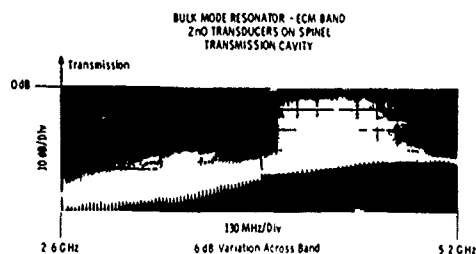


Figure 2. Frequency response of high overtone bulk acoustic microwave resonator.

Resonators have been fabricated for a variety of substrate media and overtone levels. Table 1 provides an example of typical parameters achieved for a variety of materials. Though these measurements do not represent a sufficiently large scope to completely parameterize the resonator, certain trends can be identified. At least three of the materials, sapphire, YAG, spinel have reasonably high Q's. Diamond by contrast shows a lower Q. Also, higher overtone (same wavelength) resonators typically display higher Q's. The reason for this would appear to be transducer loading, degrading reflecting surface effects, diffraction and lack of parallelism. Even so a Q of 20,000 is identified and Q's of 5,000 to 10,000 appear to be typical. For all but the diamond, frequency - Q (FQ) products are greater than 10^{13} from L through X bands.

Further, previous reports have provided an initial description of the resonator geometry, example responses at microwave frequencies and example velocities, two dimensional power flow angle and temperature coefficients for circular cuts, in lithium niobate, sapphire, diamond and spinel.^{1,2,3} In this paper, besides intrinsic Q, effects of key crystalline and geometric parameters critical to achieving high Q, crystalline anisotropy and reflecting surface parallelism are reported. Temperature characteristics of a zero temperature cut of lithium tantalate, not previously provided are given. Further, the use of the resonator for direct microwave oscillator stabilization is described and an example phase noise profile provided.

Crystalline Anisotropy

As Fabry-Perot optical resonators, losses which detract from Q include coupling or external Q, lack of parallelism and diffraction. One crystalline mechanism which can be used to minimize diffraction losses in beam mode acoustic resonators is crystalline anisotropy. Positive (converging) anisotropy has the effect of tending to collimate the acoustic energy leaving transducers or reflected from either surface. Spread of the energy beyond the areas covered by the transducers is reduced, reducing diffraction losses and increasing Q.

It might be suggested that an increase in the transducer aperture dimensions would have an equivalent effect. Though this is true in principle, to minimize diffraction losses by transducer aperture alone would have serious disadvantages: (1) the size of the transducer required to achieve Q's equivalent to those achieved could be excessive, (2) losses due to other mechanisms beyond the transducer aperture would be more difficult to control, (3) transducer loading of a transducer sufficiently large to control diffraction losses would itself incur excessive transducer loading.

Computation of the effect of anisotropy on Q has been carried out by an approach analogous to that used by Goodell to evaluate acoustic energy distribution in high overtone beam mode acoustic resonators.⁴ Goodell computed the acoustic energy distribution by iterating a reverberating wave between two reflecting surfaces, one containing a transducer, until the wave substantially repeated itself on successive reverberations. The energy distribution of the reverberating wave was assumed to be an approximation of the energy distribution in the resonator. Resonance was identified by the frequency for which a maximum energy build up occurs. Q was measured by varying the frequency through resonance in sufficiently small steps that a resonance curve could be drawn and bandwidth determined.

Functions expressing a circularly symmetric anisotropy were introduced into the integral equation for the reverberating wave to provide an approximate evaluation of the effect of anisotropy. In the analysis assuming isotropic media the phase functions were expressed as

$$e^{i \vec{k} \cdot \vec{R}} \quad (1)$$

where \vec{k} is the vector number $2\pi (\vec{i} \frac{1}{\lambda_x} + \vec{j} \frac{1}{\lambda_y} + \vec{k} \frac{1}{\lambda_z})$

and \vec{R} is the position vector $i(x-x_0) + j(y-y_0) + k(z-z_0)$

For anisotropic media, Eq. (1) is replaced by

$$e^{i k R F(\theta)} \quad (2)$$

where $k = 2\pi/\lambda$, $R = \sqrt{(x-x_0)^2 + (y-y_0)^2 + (z-z_0)^2}$. Two forms of $F(\theta)$ were explored, a first order and a second order, respectively.

$$F_1(\theta) = 1 - K|\theta|$$

$$F_2(\theta) = 1 - K'\theta^2 \quad (3)$$

TABLE I

Example Resonators Tested From L to X Band Frequencies

Material	Q	Frequency GHz	$\frac{FQ}{10^{13}}$	Loss dB	Overtone Number	Temp. Co-ef. of Delay PPM/ $^{\circ}$ C	
						Measured	Calculated
Diamond (111)	1567	2.7117	.42	22	33.3	8.14	8
Diamond (111)	2697	2.5885	.70	23	33.4	7.4	8
Diamond (111)	1385	2.5244	.35	31	38.8	6.5	8
Sapphire	8532	2.7155	2.32	10	30.0	31.92	34
Sapphire	8521	2.1179	1.80	22	4.3	31.45	34
Sapphire	8938	3.7086	3.31	19	5.0	28.84	34
Sapphire (X-Band)	6454	7.6623	4.94	39	60.0	33.19	34
YAG (100)	4508	3.4147	1.54	31	5.0	37.86	41
YAG (100)	7659	3.3887	2.60	22	5.0	37.60	41
YAG (100)	7899	3.4439	2.72	32	5.0	37.78	41
Spinel (111)	4763	3.3460	1.59	10	12.8	32.84	28
Spinel (111)	5329	3.3415	1.78	22	12.5	32.78	28
Spinel (111)	14926	2.1311	3.18	35	15.7	32.07	28
Spinel (111)	20000	1.2168	2.43	22	16.0	Not Measured	28

In both cases θ is the angular deviation from the axis of the resonator. Values of K and K' were determined empirically to provide a best fit to computed velocity curves.

After the process of iteratively determining the steady state acoustic energy distribution, at successive frequencies, a resonance curve and the value of Q were computed. This process was repeated for a sequence of values of anisotropy. An example curve for which a first order anisotropy approximation was used is shown in Figure 3. Also indicated in Figure 3 are the anisotropies of crystalline types used for experimentation. The range of experimental Q's obtained for each material are indicated. It should be noted that the curves denote the diffraction limited Q's for the indicated anisotropy. Less Q may be experienced due to other sources of loss. Figure 3 it appears that sapphire and from

diamond display Q's which reasonably approximate that obtained experimentally. However, the Q's of spinel and YAG were greater than indicated by the curve. This is, at least, partly because the resonators evaluated cover a wider range of parameters than are covered in Figure 3. Further computations are being carried out to achieve an improved correlation with anisotropy and Q values over a wide range of potential resonator parameters. A family of curves is anticipated.

Parallelism of Reflecting Surfaces

Lack of complete parallelism between the resonators degrades Q values because energy fed back from the tilted face only partially interacts with the driver due to lateral beam displacement. Thus a tilted resonator face introduces an additional loss factor into the resonator which degrades Q values by amounts roughly proportional to the tilt. Figure 4 shows typical computed Q value

degradation vs. plate tilt in a single port resonator comprising Z cut Al_2O_3 (optimum anisotropy). The resonator is $0.020''^2$ thick and contains a $0.004''$ by $0.006''$ transducer.

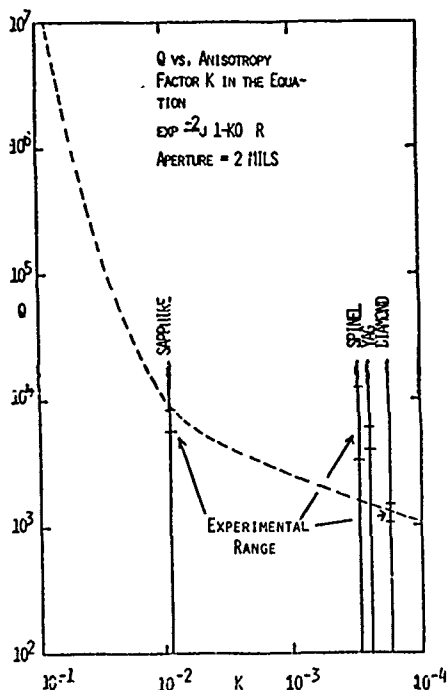


Figure 3. Curve of Q vs. anisotropy for a transducer aperture of 2 mils.

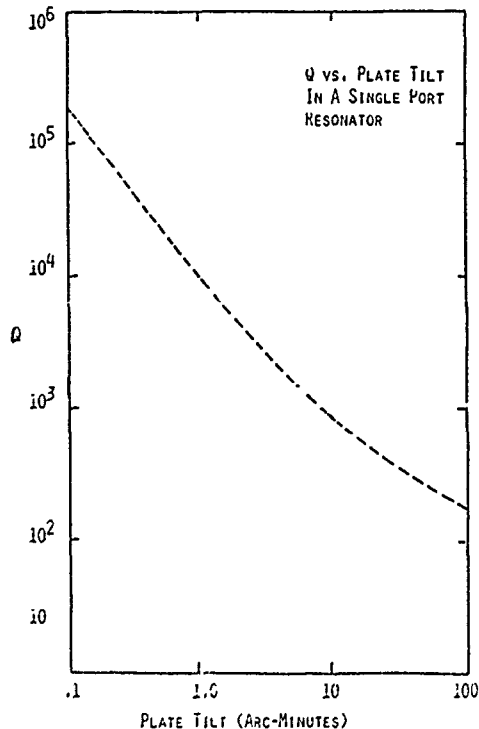


Figure 4. Q vs. deviation from parallel faces for Z cut Al_2O_3 for optimum anisotropy.

Microwave Oscillator

With the availability of high Q microwave resonators, an order of magnitude higher than could be projected for quartz even if they were available, it is natural to explore means for direct stabilization of low phase noise microwave oscillators. Further, by virtue of the high overtone nature of the resonator, the possibility of selectively stabilizing over any one of the overtones on command suggests the possibility of a direct microwave frequency stabilized low phase noise synthesizer. This suggests the possibility of a synthesizer with an immensely reduced mechanization when it is considered that all other forms of low noise rapidly switchable microwave oscillators require a low frequency reference source. Typical competing oscillators along with a summary comparison of these oscillator types to the bulk acoustic stabilized oscillators are given in Table II. Though this comparison is very brief it does suggest that the bulk acoustic oscillator can provide low phase noise multiplier selectable frequency operation with considerably less hardware than present techniques.

To achieve rapid tuning and select the resonant frequency of interest, a low noise VCO is used in a phase reference feedback loop containing the bulk acoustic resonator. An example implementation is shown in Figure 5. The useful output is generated by a voltage controlled oscillator (1). A sample of the frequency of the VCO (1) is applied to the bulk mode resonator (2) and to the digitally controlled phase shifter (3). Both signals are then applied to I-Q mixers, (4&5) as commonly practiced in radar receivers. When phase shifter (3) is correctly adjusted, the voltage out of Q mixer (4) is proportional to the error between the VCO frequency (1) and that of the desired transmission response of the bulk resonator (4), if the VCO is within the bandwidth of the desired resonator response. This error signal is amplified by the video amplifier (6), whose output is used to tune the VCO (1) to the desired frequency.

The digital controller (8) tunes the VCO (1) to the nominal desired frequency by addressing the digital-to-analog converter (7) with the appropriate control word, as determined by stored data or some means of active calibration. The digital controller (8) also adjusts phase shifter (3) to the correct setting by means of monitoring the I-Q mixers, (4) and (5), adjusting the phase shifter until the desired signals appear at these mixers. The phase shifter is assumed to be correctly set when approximately zero volts appears at Q mixer (4) and a positive voltage of some minimum amplitude appears at the I mixer.

Short term stability of the bulk acoustic resonator (BAR) synthesizer is limited to modulation rates between several Hz and several KHz by resonator Q, video amplifier noise, and VCO AM noise is detected by the mixer. Above several KHz it is limited by VCO phase noise as modified by loop gains.

The low frequency phase noise contributed by the loop video is:

TABLE II
COMPARISON OF LOW NOISE MICROWAVE
OSCILLATORS FOR FREQUENCY AGILE RADAR REQUIREMENTS

Type	Mechanization Single Freq.	Multiple dFreq.	Switching Speed	Useful Freq. Range	Size* (Cu. In.)	Weight lb.
Bulk Acoustic Wave BAR Stabilized	On Frequency OSC with phase reference to feedback loop.	Digital Controlled VCO with phase reference to feedback loop.	$\frac{3Q}{f}$ 3-10 μ s	200 MHz to 10 GHz. (multiplication to higher frequency).	72 5 μ	1.2
VHF Crystal Controlled Oscillator Multiplier	Direct output.	Multiple crystals.	$\frac{3Q}{f}$ (f VHF) lms	100MHz to 100 GHz.	480	8
Overtone Oscillator with phase locked Microwave oscillator	Single conversion phase lock loop.	Variable IF phase lock loop.	Limited by VCO post tuning drift 3 - 10 μ s.	100 MHz to 20 GHz (multiplication to higher frequencies).	360	66
Count down Microwave oscillator Phase locked to VHF Crystal	VCO frequency counted down to crystal controlled phase locked loop.	Variable count ratio.	Limited by narrow loop band width lms	100 MHz to 2 GHz (extended multiplication).	240	4

*Based on 50 switchable output frequencies.

$$L_L(f) = \frac{B^2 \overline{e_o^2}}{8 E^2 f^2}$$

where:

$L_L(f)$ is the single side phase spectral density (Hz^{-1})

B is the BAR bandwidth

$\overline{e_o^2}$ is the video amplifier white noise voltage density at frequencies f_o (volts²/Hz)

E is the mixer phase sensitivity (volts/radian)

f is the modulation rate of interest

The AM noise on the VCO and its power amplifier result in FM noise since the mixer LO Port act as an (inefficient) AM detector. AM noise on the LO port produces a video noise voltage in the loop which modulates the close loop frequency. This effect is quantified as

$$L_A(f) = \frac{B^2 I^2 f_o M(f_o)}{2f^3}$$

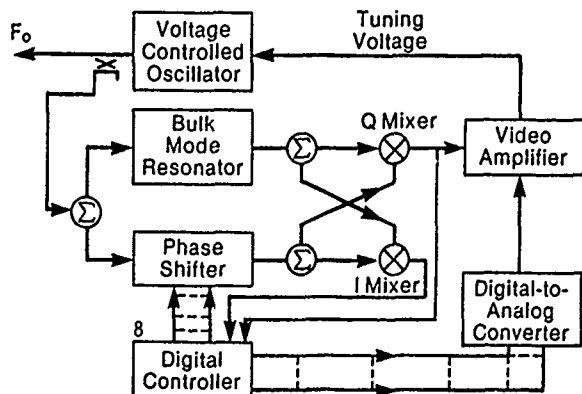


Figure 5. Implementation of BAR Synthesizer at X-Band.

where:

$L_A(f)$ is the resultant phase spectral density at frequency f

B is the BAR bandwidth

I is the fractional change in mixer video voltage per fractional change in LO power, as calculated from typical mixer data.

$M(f_o)$ is the $1/f$ AM spectral density at frequency f_o .

The f_o
The following set of values are assumed as an example

$F = 8 \text{ GHz}$, $Q = 6000$, $B = 1.3 \text{ MHz}$

$e_o^2 = 4 \times 10^{-18} \text{ volt}^2/\text{Hz}$ at $f_o = 1000$

$E = 0.1 \text{ volts/Radian}$

$f = 1000 \text{ Hz}$

$I = 0.12$, for a typical X-band mixer

$M(f_o = 1) = 10^{-11}$ for an X-band bipolar transistor

Then $L_L(f) = -100.7 \text{ dB/Hz}$, falling at 20 dB decade. These numbers relate to measured characteristics of an X-band BAR and to realistic video amplifier and mixer parameters. Currently $L_A(f=1000) = -99 \text{ dB/Hz}$. Had an FET been used with noise 30 dB greater than the bipolar transistor, the $L_A(f)$ would have been -69 dB/Hz .

The high frequency noise floor associated with the BAR stabilized source is only weakly influenced by the resonator Q . Rather, it is determined by the open loop VCO phase noise and stabilization loop servo bandwidth.

The phase noise floor in such a loop is approximately the value of the VCO phase noise at the loop bandwidth. X-Band VCOs tuning 600 MHz reach -130 dB/Hz at $f = 1 \text{ MHz}$, if mechanized with low power bipolar transistors. One MHz is reasonable loop bandwidth so a noise floor of -130 dB/Hz is reasonably achievable.

The predicted noise performance with a BAR synthesizer, based on measured data for various components, is described in Figure 6 where it is seen to compare favorably with typical airborne RADAR stability requirements at X-band.

Stabilization of an X-band source with a bulk acoustic resonator has been achieved. The resonators has a Q of approximately 3500 and the sources operated at 8 GHz.

Phase noise was investigated using a phase lock method. The experimental results shown in Figure 7 offer promise of radar application of BAR stabilized sources. The discrepancy between experimental results and theoretical predictions, approximately 7db, is the subject of on going studies.

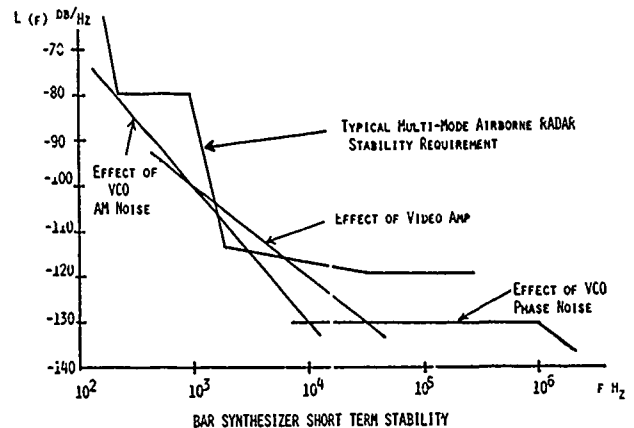


Figure 6. Predicted BAR Stabilized Microwave Oscillator Phase Noise.

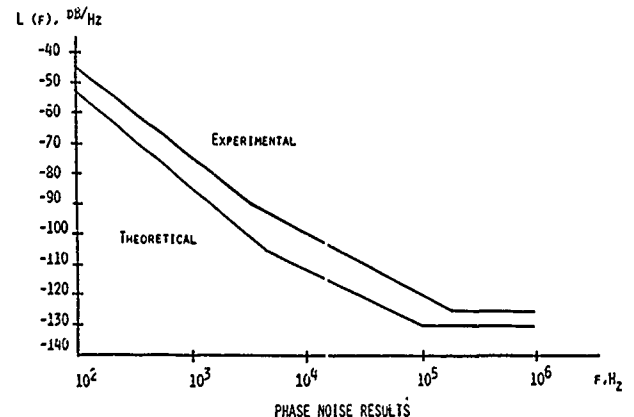


Figure 7. Measured and Computed Noise on Same Scale.

Temperature Coefficient

A high Q resonator is most attractive if it has a zero temperature coefficient for much if not all of the temperature range in which equipment must normally perform. Previously we have presented data^{1,2,3} on all the high Q media discussed in this paper. None except lithium tantalate appear to offer any possibility of a zero temperature cut. Lithium tantalate suggests the possibility of shear mode operation with zero temperature coefficient. This possibility has been presented previously by Murphy, et.al., who discussed zero temperature coefficient from the point of view of infinite medium plane

wave propagation. In this paper we discuss zero temperature cuts of lithium tantalate for which reflective surface boundaries exist.

The electrical impedance of a thickness mode resonator was calculated first by Tiersten and later in a more elegant manner by Yamada and Niizeki. The expression derived by Yamada and Niizeki for the reactance of a fully electroded infinite plate resonator is

$$Z = \frac{1}{j\omega C_0} \left[1 - \sum_{i=1}^3 k_i^2 \frac{\tan X_i}{X_i} \right] \quad (6)$$

where $X_i = \frac{\omega h}{2V_i^1}$

and ω = angular frequency

h = plate thickness

V_i^1 = phase velocity of i^{th} acoustic wave in the direction of h

k_i^2 = the bulk wave coupling factors $\frac{2\Delta V_i}{V_i}$

C_0 = free capacitance of the plate

The anti-resonance frequencies occur at the poles of Eqn (6) so that

$$\omega_{an}^i = \frac{2n+1}{2} \cdot \frac{(2V_i)}{h} \quad (7)$$

The fundamental anti-resonance frequencies are therefore

$$\omega_{a1}^i = \frac{\pi V_i^1}{h} \quad (8)$$

The fundamental resonances occur at the zeros of Eqn (6). These always occur at lower frequencies than the corresponding anti-resonances by an amount depending upon the value of the k_i^2 quantities. The coupling factors for the resonator modes, defined by

$$K^2 = \frac{(\omega_a^i)^2 - (\omega_r^i)^2}{(\omega_r^i)^2} \quad (9)$$

differ slightly from the k_i^2 calculated for the bulk waves in an infinite medium because of the admittance of modes by the resonator boundaries. Ballato⁽⁷⁾ shows the effect of the proximity of resonances on each other.

Following the work of Lancon and Detaint⁸ we have calculated the temperature dependance of the resonances and anti-resonances and the coupling factors by computing the quantities at two temperature and using the finite difference definition

$$TC = \frac{FR(T+\Delta T) - FR(T)}{\Delta T \cdot FR(T)} \quad (10)$$

when FR stands for the either resonance or anti-resonances. The anti-resonance modes are identical with the bulk waves in an infinite medium so that for these modes, the temperature coefficient of frequency is just the negative of the temperature coefficient of delay.

The resonance modes on the other hand can behave very differently because they are affected by the temperature dependance of the coupling constant k_i^2 as well as on the position of the anti-resonance mode. Figure 8 shows the definition of angles for the plate orientation and Figure 9 through 17 show the first order temperature coefficients of the resonances and the anti-resonances and the coupling factors defined by Eqn 6 all as a function of plate orientation.

We will shortly select orientations that show zero first order temperature coefficients with large coupling factors and fabricate resonators to test these results.

Conclusions

Examples of extremely high overtone microwave resonators have been presented previously. In this paper key advances in design analysis, stabilized oscillator performance and temperature coefficient computations are reported. Advances in design include effects of crystalline anisotropy and resonator surface parallelism. Crystalline anisotropy helps to account for previous transducer anomalies and provides an additional criterion for selection of the substrate crystal orientation. A method of determining optimum anisotropy for minimizing diffraction losses was identified. The test of an X-band oscillator is described which provides phase noise performance to within 7 dB theoretical. This work is on going with noise performance approaching values of interest for RADAR systems. Temperature stable cuts of lithium tantalate have been identified with an improved formulation which account for two parallel reflecting surfaces.

References

1. R.A. Moore, F.W. Hopwood, T. Haynes, B.R. McAvoy, "Bulk Acoustic Resonators for Microwave Frequencies," Proc. 33rd Annual Frequency Control Symposium, Atlantic City, NJ, 1979, pp. 444-448.
2. R.A. Moore, B.A. Newman, B.R. McAvoy, J. Murphy, "Temperature Characteristics of Microwave Acoustic Resonators." MTT Interactive Symposium, Orlando, FL, 1979.
3. J. Murphy, B.R. McAvoy, R.B. Feldman, "Three Dimensional Representation of the Bulk Acoustic Wave Properties of Anisotropic Crystals," Proc. 1979 Ultrasonics Symposium, CH 1482-9/79/000-157, pp. 157-160.
4. J. Goodell, R. Sundelin, "Frequency Characteristics of Bulk Microwave Acoustic Resonators," Proc. 1979 Ultrasonics Symposium, CH 1482-9/79-0000-0123, pp. 123-127.

5. H.F. Tiersten, J. Acoust. Sec. 35, 53 (1963).
6. T. Yamada and Niizeki, Proc. IEEE. 59, 941 (1970).
7. A. Ballatto, Physical Acoustic Vol. III, Ch. 5, p. 123, (Academic Press, Mason & Thurston - Eds.).
8. J. Detaint and R. Lancon, Proc. 30th Annu. Freq. Control Symp., pp. 132-140.

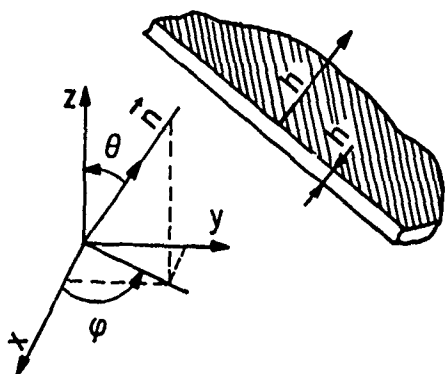


Figure 8. Plate orientation.

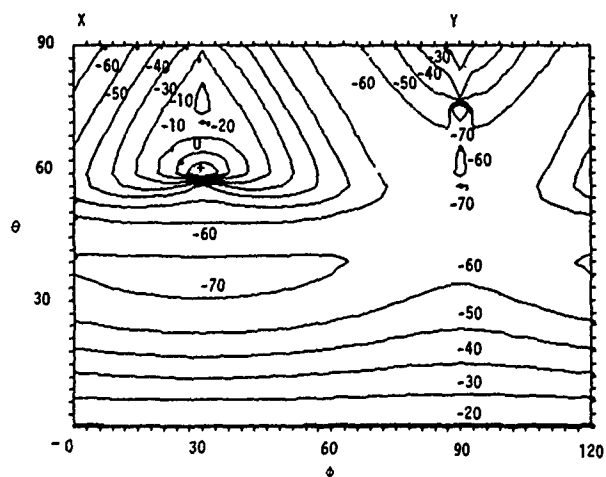


Figure 9. Temperature coefficient of frequency C mode resonance: LiTaO_3 .

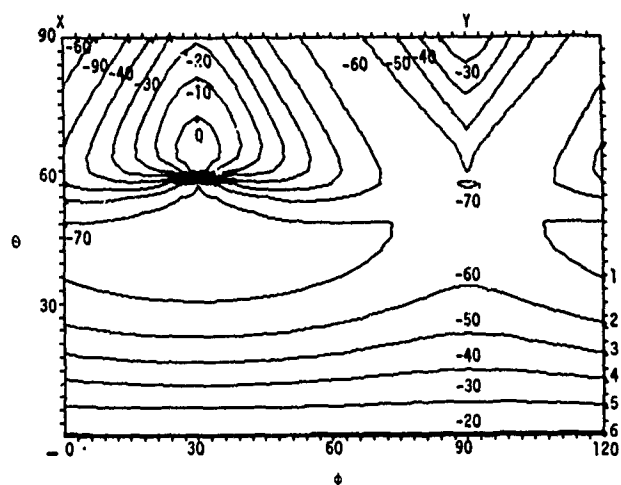


Figure 10. Temperature coefficient of frequency C mode antiresonance: LiTaO_3 .

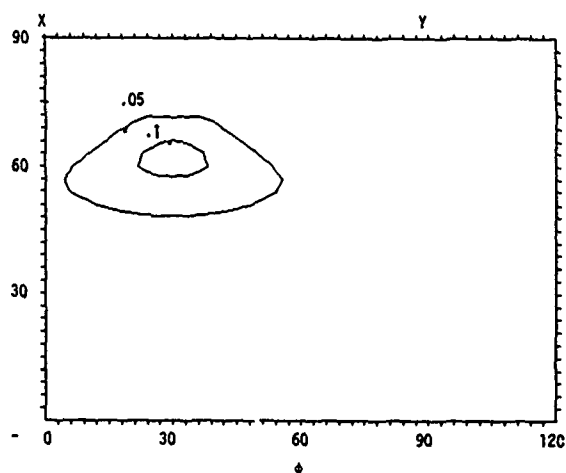


Figure 11. Coupling factor (k^2) C mode: LiTaO_3 .

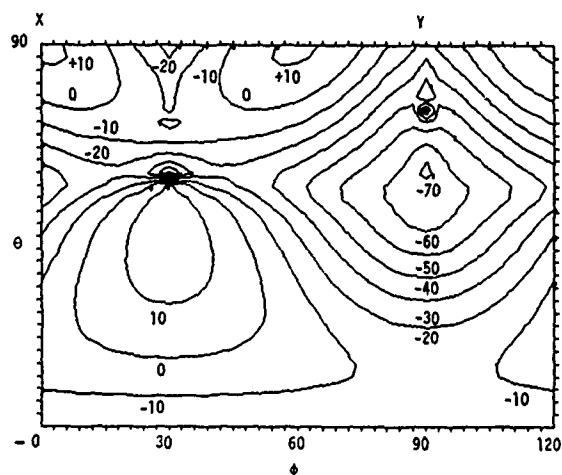


Figure 12. Temperature coefficient of frequency B mode resonance: LiTaO_3 .

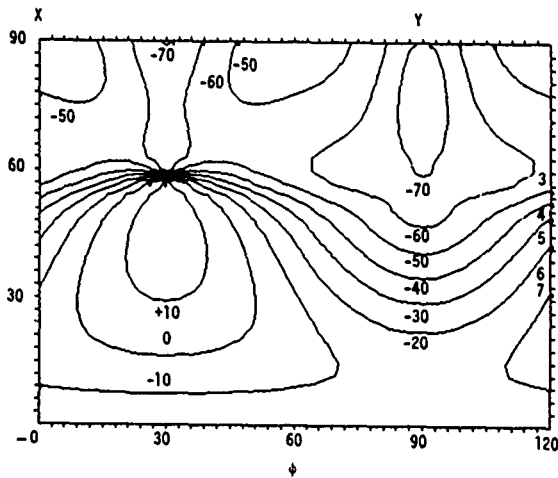


Figure 13. Temperature coefficient of frequency B mode antiresonance: LiTaO_3 .

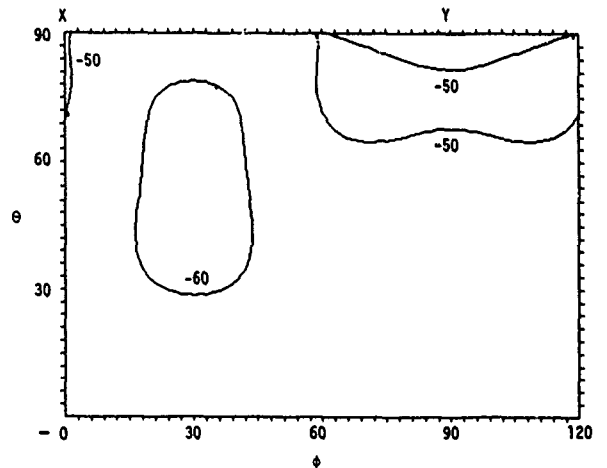


Figure 16. Temperature coefficient of frequency A mode resonance: LiTaO_3 .

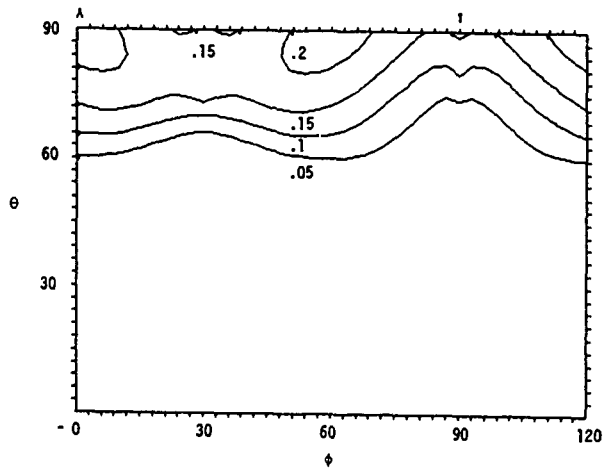


Figure 14. Coupling factor (k^2) B mode: LiTaO_3 .

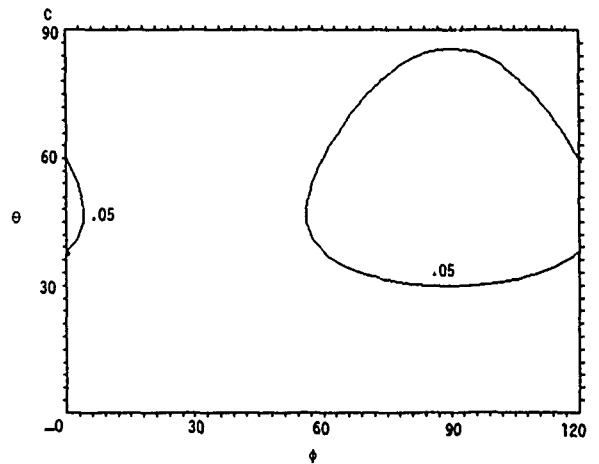


Figure 17. Coupling factor (k^2) A mode: LiTaO_3 .

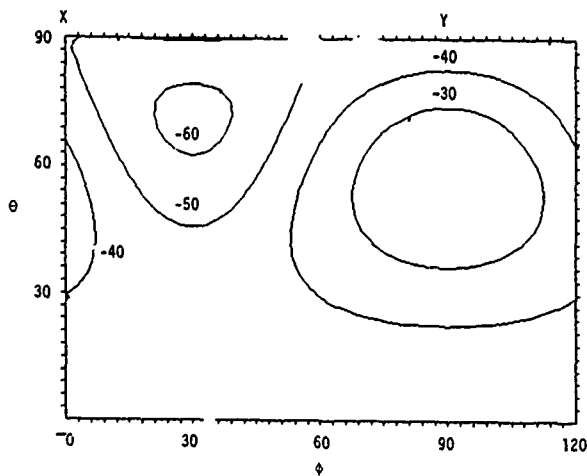


Figure 15. Temperature coefficient of frequency A mode resonance: LiTaO_3 .

FREQUENCY STABLE SOURCES USING SUPERCONDUCTING MICROSTRIP RESONATORS

Roger Davidheiser

TRW Defense and Space Systems Group

Redondo Beach, California 90278

Summary

A superconducting microstrip resonator has demonstrated its application in a stable frequency source. The resonator, constructed from thin film Pb deposited on synthetic sapphire, operates at liquid helium temperatures. The demonstration stable oscillator consists of a voltage controlled backward wave oscillator, a phase detector, and a superconducting resonator used in a negative feedback loop.

This paper presents experimental resonator results ($Q_0 = 40,000$), correlates these with previous theoretical predictions, summarizes performance of the oscillator in the time domain, and outlines methods to improve oscillator stability. The stabilized oscillator operates at 2.94 GHz, and exhibits a stability of 1.3×10^{-7} for 10 sec samples. The temperature coefficient of the resonator is cubic in absolute temperature and is $2.7 \times 10^{-8}/^\circ\text{K}$ at 2°K. Aging characteristics have not been measured, but are expected to be excellent.

The extremely low microwave surface resistances of superconducting metal films allow high Q elements to be constructed in a convenient stable form for application at microwave and millimeter wave frequencies. Thus, superconducting microstrip resonators will provide a means to produce lightweight, low cost, multiple frequency sources directly stabilized at millimeter wavelengths. Sources completely contained in liquid helium for use in multiple frequency systems are possible.

Introduction

Microstrip circuitry is a very convenient medium to transmit and manipulate microwave signals. Its properties are well understood and its low cost desirable. Microstrip has consequently earned a dominant position in microwave system hardware. The loss properties of microstrip, however, are less desirable. To control radiation from the open-walled structure, the designer must use a relatively thin substrate and keep both elements of the transmission line close together. Typically, the substrate thickness is held to less than $0.03 \lambda_0$, where λ_0 is the wavelength of the transmitted signal. The field energy stored in such a geometry, for a given current density, is exceedingly low, and a relatively large fraction

is dissipated per angular radian. Thus, resonator quality factors are low; $Q = 100$ -500 are typical values. (Equivalent values for the transmission line loss per wavelength are 0.25 dB and .05 dB.)

Superconducting digital and microwave circuitry will offer a number of impressive advances for future systems. To date the advantages of the superconducting mainframe computer or digital processor,^[1] superconducting low noise receiver,^[2] and superconducting millimeterwave detector^[3] have been largely demonstrated. Integrated superconducting signal filters would have attractive features.^[4] Superconducting cavity resonators have demonstrated unequalled performance in stabilizing oscillators for short and medium sample durations. Frequency stabilities of 6×10^{-16} ^[5] and 3×10^{-16} ^[6] for 10 to 1000 sec samples are reported for Gunn diode oscillators stabilized with the use of vacuum fired niobium, microwave cavities.

Resonator Design and Performance

This paper reports the use of a superconducting microstrip resonator to stabilize a commercial backward wave oscillator. The resonator is a two-port transmission filter whose output phase is the frequency selecting quantity. It is constructed from thin film Pb evaporated onto both sides of a crystalline sapphire substrate. The Pb is lithographically patterned into a resonator and input and output coupling lines on one side, and the Pb on the other side acts as a ground plane. A photo of the Pb structure is shown in Figure 1. The substrate's surface has a polished, scratch-free, 1 microinch finish. The substrate thickness for the 3 GHz resonator is .006 in. and the lead thickness 3000 Å. No adhesion metallization was used.

Radiation losses from the resonator were strictly controlled. The substrate housing was non-resonant and non-propagating. Losses due to finite substrate thickness were determined by the radiation resistance analysis of Denlinger.^[7] The expected Pb microwave dissipation was assumed to be that reported by Turneaure and Weissman.^[8] The sapphire dielectric loss tangent was taken to be 10^{-5} . The predicted resonator Q as a function of substrate thickness, h, is shown in Figure 2. A similar analysis for a normal Cu resonator is also shown in the figure. The superconducting

Pb resonator was designed to have an $h/\lambda_0 = 1.5 \times 10^{-3}$.

Additionally, coupling coefficients, or external quality factors, for the open ended transmission lines adjacent to the resonator had to be determined. Although this coupling technique is common for copper microstrip resonators, the exceedingly light coupling appropriate for the superconducting resonator required coupling geometries not characterized in the literature. The results of experimentation are shown in Figure 3. Q_0 and Q_{ext} versus the ratio of microstrip separation to substrate height, S/h , is plotted. As expected, the unloaded quality factors, Q_0 , of the copper resonators are not a function of separation, while the external Q , Q_{ext} , rises monotonically in separation and is a function of S/h alone.

The resonator can be characterized by an unloaded quality factor, $Q_0 = 40,000$, external quality factors, $Q_{ext} = 18,000$, a loaded quality factor, $Q_L = 7,000$, and a resultant insertion loss of 1.5 dB.

An Oscillator Stabilization

Frequency stabilization of a voltage controlled backward wave oscillator is achieved with a feedback loop employing a frequency discriminator. This configuration is shown in Figure 4. The resonator output phase variation is 2.1×10^{-4} deg/Hz, the phase comparator's output is 9×10^{-7} V/Hz, and the overall loop gain is 7200. The oscillator's open loop stability of 1×10^{-6} for a 10-second two-sample Allan variance was reduced to 1.3×10^{-9} for a 10 sec sample.

The plot of observed Allan variance versus sampling time is shown in Figure 5. Stability is superior to that of surface acoustic wave devices. However, the stability observed for sample times longer than 10 sec degrades badly. Sample points on the upper line of the shaded section represent the variance of all sequential data pairs, while the lower line represents data from which 3 σ points have been removed. The major contribution to the observed variance is thought to result from mechanical vibration of the parallel coaxial loops of the discriminator. Each loop which passes from 293°K into the liquid helium dewar at 4.2°K and back to room temperature is four feet long. No frequency compensation scheme [9] was employed, nor was any attempt made to include power splitter and phase comparator in the liquid helium. Thus, no real test of long-term stability has been made.

Temperature dependence of the stabilized oscillator was measured by variation of the helium bath temperature. As expected, data, shown in Figure 6, reveal an approximate cubic dependence in absolute temperature. Thus, at 2.0°K, the stability is a remarkably low $3 \times 10^{-8}/^\circ\text{K}$. Combined with an ability to tightly control the helium bath temperature, resonator temperature dependence makes no significant contribution to frequency drift.

Several techniques are available to trim fabricated and tested resonators to produce exact frequency performance. These techniques include laser trimming of material at very low or very high impedance points. The stability of the resonator after thermal cycling is exceedingly good.

Conclusion

This work represents a new type of resonator used for source stabilization. The microstrip resonator is the only resonator of integrated format usable directly at microwave frequencies. Direct stabilization avoids costly, performance degrading frequency multiplication or the use of frequency synthesis. Thus, systems requiring multiple, exact frequency microwave outputs in a compact format may prove important applications. The extensive use of superconductive electronics for such systems, or the development of miniature refrigerators, would remove the inconvenience of cryogenic temperatures.

References

1. Anacker, W., "Josephson Computer Technology: An IBM Research Project," IBM Journal 24, #2, pp. 107-112 (March 1980).
2. Shen, T. M., et al., "Conversion Gain in mm-Wave Quasiparticle Heterodyne Mixers," Appl. Phys. Letters 36 (9), pp. 777-779 (1 May 1980).
3. Richards, P. L., et al., "Superconductor-Insulator-Superconductor Quasiparticle Junctions as Microwave Photon Detectors," Appl. Phys. Letters 36 (6), pp. 480-482 (15 March 1980).
4. Davidheiser, R. A., "Superconducting Microstrip Filters," AIP Conf. Proc. 44, Future Trends in Superconducting Electronics, AIP, pp. 219-222 (1978).
5. Stein, S.R., and J.P. Turneaure, "Superconducting Cavity Stabilized Oscillators with Improved Frequency Stability," Proc. IEEE 63, 8, pp. 1249-1250 (1975).
6. Stein, S.R., and J.P. Turneaure, "Superconducting Resonators: High Stability Oscillators and Applications to Fundamental Physics and Metrology," AIP Conf. Proc. 44, Future Trends in Superconducting Electronics, AIP, pp. 192-213 (1978).
7. Denlinger, E. J., "Radiation from Microstrip Resonators," IEEE-MTT 17, 235 (1969).
8. Turneaure, J.P., and I. Weissman, "Microwave Surface Resistance of Superconducting Niobium," J. Appl. Phys. 39, 4417 (1958).
9. Stein, S. R., and J. P. Turneaure, "Superconducting-Cavity-Stabilized Oscillator of High Stability," Electronic Letters 8, 13, pp. 321-323 (1972).



Figure 1. The superconducting Pb microstrip resonator shown with input and output coupling lines.

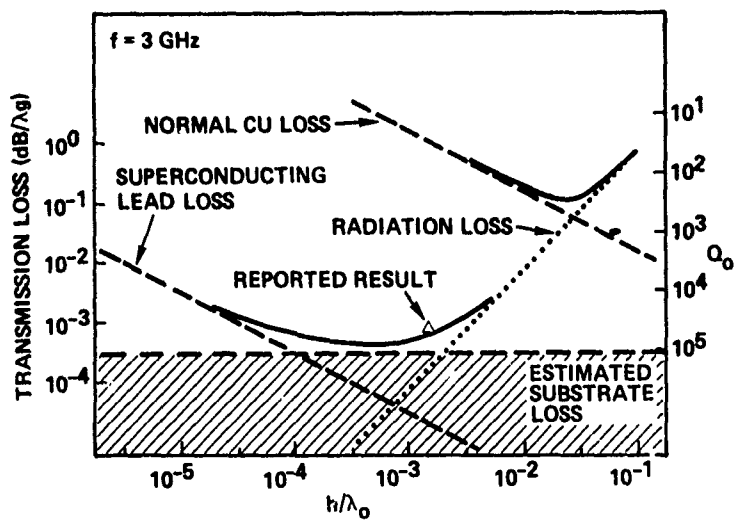


Figure 2. Comparison of copper and superconducting lead microstrip resonators.

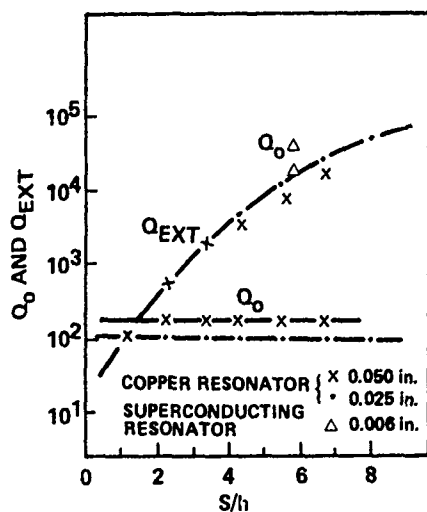


Figure 3. Resonator separation versus quality factors.

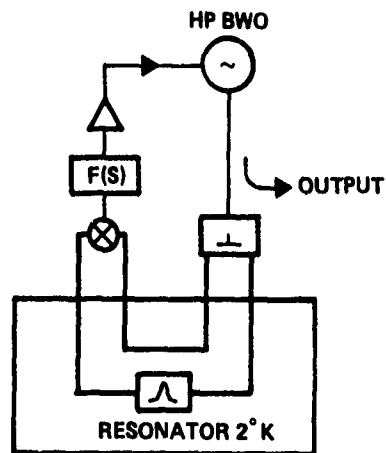


Figure 4. Discriminator stabilized oscillator.

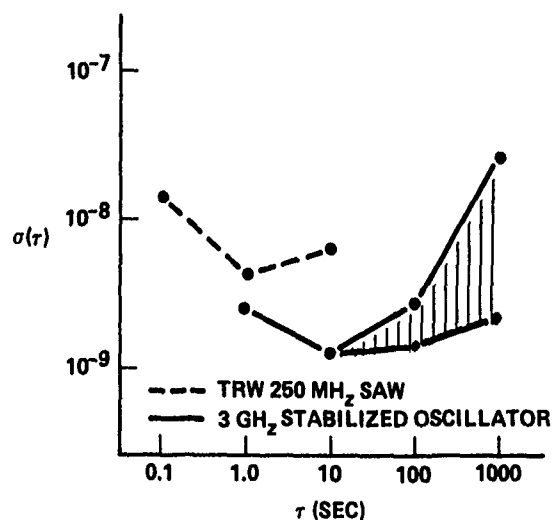


Figure 5. Closed loop stability.

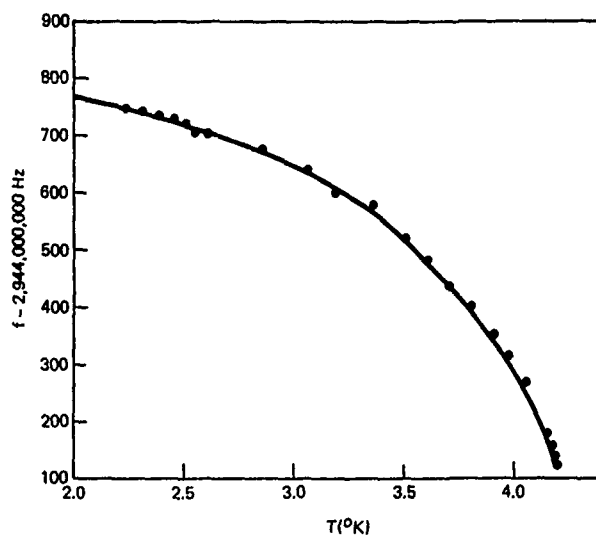


Figure 6. Temperature dependence of the stabilized oscillator.

NON-LINEAR PROPAGATION OF SURFACE ACOUSTIC WAVES ON QUARTZ

M. Planat, D. Hauden, J. Gros Lambert, J.J. Gagnepain

Laboratoire de Physique et Métrologie des Oscillateurs du C.N.R.S.
associé à l'Université de Franche-Comté-Besançon
32, av. de l'Observatoire - 25000 Besançon - France

Abstract

The non-linear elastic characteristics of quartz crystal are at the origin of harmonic generation, amplitude-frequency (A-F) effect in oscillators, intermodulation in filters. The measurement of A-F effect generally is perturbed by the spurious influence of temperature which results from the modification of the oscillation level. A new method, using amplitude modulation and phase detection, enables to separate elastic and thermal effects. This method is applied to ST cut SAW resonators, and comparisons are made with AT cut bulk wave resonators. Intermodulation measurements confirm the previous ones, and both show that SAW has lower non linearities than B.W.

By using the exact state and constitutive equations of elasticity, the general non linear wave propagation equations and boundary conditions are obtained. Solutions are calculated up to the second step of approximation. They lead to the determination of the second harmonic level and of the A-F effect.

Introduction

The propagation of elastic waves in solids can be described by the linear theory of elasticity only in the case of small amplitude waves. In fact the amplitude is finite and the propagation medium is not linear in account of its own structure and of the finite deformation induced by the wave. Intrinsic non-linearities and induced non linearities can be distinguished. They are at the origin of harmonic generation, amplitude-frequency (AF) effect in resonators and oscillators, intermodulation in filters. These phenomena generally are undesirable because they are among the main causes of instabilities and troubles. However sometimes they can be advantageously used in devices such as acoustic convolvers and correlators.

The non-linear properties of bulk waves were intensively studied during these past years, but very few studies were devoted to surface acoustic waves. The calculation of second harmonic generation was performed by Tiersten¹ in isotropic bodies and by Vella² in the anisotropic ones. In the case of quartz crystal the experiments were also limited to the measurement of the second harmonic level^{3,4,5,6}

In the present work these phenomena are studied both theoretically and experimentally. Experimental methods are defined for measuring the A-F effect and intermodulation. The theory is extended to the second step of approximation and leads to the calculation of the A-F effect.

Comparison between bulk waves and surface waves, by means of devices at the same frequencies, are performed in order to answer the question : are SAW more linear than B.W. or not ?

Amplitude Frequency Effect

The measurement of resonator A-F effect generally consists in recording the amplitude and/or phase resonance curves for different values of the oscillation level. The inconvenient of such a method is to be sensitive to temperature : when increasing the oscillation level for instance, the crystal is warmed up and therefore its frequency is modified. The phenomenon is minimized by operating at the turn-over temperature. With high Q resonators the A-F effect can be measured at low level and therefore in this case the thermal effect is not too important. But with low Q devices higher powers are necessary and the temperature influence becomes predominant.

A first improvement can be obtained by processing the measurement quickly, i.e, in a time shorter than the thermal relaxation time. To this end the resonator is excited in a π transmission network by a synthesizer, the frequency of which is locked to the resonator frequency with a phase bridge. When changing the excitation level, the corresponding frequency shift can be measured directly on the source.

The method which was effectively used consists in modulating the amplitude of the source at a frequency F (fig. 1). At the phase bridge output the error signal, used to lock the source, contains three components : a DC component, and two AC components at the frequencies F and 2F.

The total A-F effect, including both elastic and thermal effects can be represented by the relation :

$$\Delta\omega/\omega = kI^2 + \lambda\theta(I^2) \quad (1)$$

which gives the fractional frequency shift as a function of the current I and of the temperature θ .

This last one is itself dependent on the current. The modulated signal amplitude can be written:

$$I = I_0 + I_1 \cos \Omega t \quad (2)$$

When using (2) in (1) it is obvious that the frequency shift is composed of a DC part and of two components at F and $2F$. The DC part is a function of k which characterizes the elastic effect to be measured, and of λ . Therefore both phenomena cannot be distinguished in the DC component. But if the frequency modulation is much larger than the thermal relaxation frequency, related to the heat diffusion constant, the components of thermal origin at F and $2F$ will be strongly attenuated. At those frequencies only remains the purely elastic effect. Thus, the measure of the spectral lines F and $2F$ enables, with redundancy, to obtain the value of the A-F coefficient k .

This method was applied to ST cut quartz resonators. In order to check the validity, measurements were repeated at three different temperatures, one corresponding to the turn-over temperature, the two other ones being located on each side of the F-T characteristic. As shown on fig. 2 the three results are identical as expected.

Comparisons are made in table I between SAW resonators and BW resonators.

It can be observed that the ST cut SAW A-F effect is lowered in a ratio of the order of 200 in comparison with AT cut BW resonators.

Intermodulation

Two signals are simultaneously applied on the resonator or delay line (fig. 3). Their angular frequencies ω_1 and ω_2 are within the device bandwidth and symmetrically located on both sides of the central frequency. In this case, the intermodulation frequencies $\Omega = 2\omega_1 - \omega_2$ and $\Omega' = 2\omega_2 - \omega_1$ also are symmetrical and in the bandwidth. Impedances are to be carefully adapted in order to avoid spurious reflexion which would perturb the measurement.

The intermodulation ratio is characterized by P/P_0 , ratio of the test tone power P ($P = P_1 = P_2$) over the intermodulation power P_0 ($P_0 = P_1 = P_2$) measured across a 50Ω load resistor.

Intermodulation was measured on a 110 MHz SAW resonator (its motional parameters are: $R_1 = 136 \Omega$, $L_1 = 7.8 \text{ mH}$, $C_1 = 0.27 \text{ pF}$, $C_0 = 3.7 \text{ pF}$, $Q_0 = 33\,000$) placed in a 50Ω circuit, and is presented on fig. 4.

A measure on a SAW delay line was attempted. But because of the low equivalent Q factor, it was not possible to reach its intermodulation, which was below the circuit intermodulation level.

Comparison can also be made between SAW and BW resonators. The easiest way is to compare the locations of their intercept points given in table II.

These results confirm the previous ones and show also the better linearity of surface acoustic waves.

Theoretical approach

The non linear equilibrium equations and boundary conditions of a semiinfinite anisotropic solid, limited by a free surface $a_2 = 0$ may be written in a Lagrangian reference system

$$\rho_0 \ddot{u}_j = P_{ij,i} \quad (3)$$

$$n_i P_{ij} = 0 \text{ on the surface} \quad (4)$$

where ρ_0 is the specific mass, u_j the displacement field and n_i the director cosines of the unit outward normal to the free surface. P_{ij} is the Piola-Kirchhoff tensor, which corresponds to the stress field in the material coordinates system. When limited to the third and fourth order non linearities P_{ij} is given by the relation:

$$P_{ij} = c_{ijkl} u_{k,l} + \gamma_{ijklmn} u_{k,l} u_{m,n} + \delta_{ijklmnpq} u_{k,l} u_{m,n} u_{p,q} \quad (5)$$

c_{ijkl} are the second order elastic constants; γ_{ijklmn} and $\delta_{ijklmnpq}$ are related to the third and fourth order elastic constants c_{ijklmn} and $c_{ijklmnpq}$ by:

$$\gamma_{ijklmn} = c_{inkl} \delta_{jm} + \frac{1}{2} c_{ijnl} \delta_{km} + \frac{1}{2} c_{ijk lmn} \quad (6)$$

$$\begin{aligned} \delta_{ijklmnpq} = & \frac{1}{2} c_{iqnl} \delta_{km} \delta_{jp} + \frac{1}{4} c_{ijk lqn} \delta_{pm} \\ & + \frac{1}{4} c_{ijqlmn} \delta_{kp} + \frac{1}{2} c_{iqk lmn} \delta_{pj} \\ & + \frac{1}{6} c_{ijklmnpq} \end{aligned} \quad (7)$$

By using (6) and (7) into (3) and (4) the general wave propagation equations and boundary conditions are obtained.

They are solved by using a method of successive approximations. The solution is written

$$u_j = u_j^0 + u_j^1 + u_j^2 \quad (8)$$

where u_j^n are the solutions at the different steps of approximation.

u_j^0 verifies the unperturbed homogeneous system:

$$\rho_0 \ddot{u}_j - c_{ijkl} \dot{u}_{k,li} = 0 \quad (9)$$

$$c_{2jkl} \dot{u}_{k,l} = 0 \text{ at } a_2 = 0 \quad (10)$$

and has the regular form :

$$\dot{u}_j = u_0 \sum_r C_j^{(r)} e^{i(\omega t - k_0 a_1 - k_0 n_2^{(r)} a_2)} \quad (11)$$

$r = 1, 2, 3$

for a wave propagating in the a_1 direction. k_0 is the wave number and $n_2^{(r)}$ the depth penetration coefficients.

a) Second harmonic generation

At the first step of approximation the system becomes

$$\rho_0 \ddot{u}_j - c_{ijkl} \dot{u}_{k,li} = \bar{\gamma}_{ijklmn} \dot{u}_{k,li} \dot{u}_{m,n} \quad (12)$$

$$c_{2jkl} \dot{u}_{k,l} = -\gamma_{2jklmn} \dot{u}_{k,l} \dot{u}_{m,n} \text{ for } a_2 = 0 \quad (13)$$

$$\text{with } \bar{\gamma}_{ijklmn} = \delta_{ijklmn} + \gamma_{ijmnlk}$$

When \dot{u}_j is replaced by eq. (11) in the inhomogeneous parts of (12), (13) a linearized system is obtained :

$$\rho_0 \ddot{u}_j - c_{ijkl} \dot{u}_{k,li} = \frac{1}{2} k_0^3 u_0^2 \times \sum_{r,s} \left(\bar{D}_j^{(r,s)} e^{2i\psi(r,s)} + \bar{D}_j^{(r,s)} e^{i\phi(r,s)} \right) \quad (14)$$

$$c_{2jkl} \dot{u}_{k,l} = -\frac{1}{2} k_0^2 u_0^2 \times \quad (15)$$

$$\sum_{r,s} \left(H_{2j}^{(r,s)} e^{2i\psi(r,s)} + \bar{H}_{2j}^{(r,s)} e^{i\phi(r,s)} \right) \text{ at } a_2 = 0$$

$$\text{where } \psi(r,s) = \omega t - k_0 a_1 - k_0 \left(\frac{n_2^{(r)} + n_2^{(s)}}{2} \right) a_2$$

$$\text{and } \phi(r,s) = k_0 (n_2^{(r)*} - n_2^{(s)}) a_2$$

The amplitudes of the driving terms are given in annex.

The inhomogeneous part of eq. (14) is composed of a time independent term and of a term at the frequency 2ω .

The particular solution independent of time is :

$$\dot{u}_k = k_0 u_0^2 \sum_{r,s} \alpha_k^{(r,s)} e^{i\phi(r,s)} \quad (16)$$

$\alpha_k^{(r,s)}$ is completely determined and given as function of $D_j^{(r,s)}$.

The homogeneous part of the propagation equation (14) is verified by a solution at the frequency 2ω proportional to the unperturbed solution constituting the SAW

$$u_k^1 = \lambda u_0^2 k_0 \sum_r C_k^{(r)} e^{2i\phi(r,r)} \quad (17)$$

λ is a constant.

The driving terms of (14) are small perturbations. Therefore a general solution can be chosen from (17) by perturbing the wave number k_0 , the penetration coefficients $n_2^{(r)}$ and the amplitudes $C_k^{(r)}$. In the first study of the isotropic solid by Tiersten the proposed solution was equivalent to a perturbation of the wave number. A similar solution was utilized by Planat for calculating the second harmonic level in quartz. It led to values in agreement with the experimental data of Gibson and Alippi for Y-cut quartz, but for ST and X cuts the results of the calculation were too high. Vella also observed too high values with a similar method, not only for X cut but also for Y cut. He proposed a method where complementary solution colinear and orthogonal to the eigen vectors are added. This method is equivalent to perturbing at the same time wave number, penetration and amplitude.

This type of solution is used in the present study by taking for $r = s$.

$$u_k^1 = \lambda u_0^2 k_0 \sum_r \left(C_k^{(r)} + \Delta C_k^{(r)} \right) e^{2i\{\omega t - (k_0 + \Delta k_0) a_1 - (k_0 n_2^{(r)} + \Delta(k_0 n_2^{(r)})) a_2\}} \quad (18)$$

Approximated at the first terms of the development, (18) becomes

$$u_k^1 = \lambda u_0^2 k_0 \sum_r C_k^{(r)} e^{2i\psi(r,r)} \times \left\{ 1 + \frac{\Delta C_k^{(r)}}{C_k^{(r)}} - 2i \Delta k_0 a_1 - 2i \Delta(k_0 n_2^{(r)}) a_2 \right\} \quad (19)$$

This solution must verify equation (14).

For $r \neq s$ none of the driving terms of the propagation equation being synchronous with any of the homogeneous solution (17), the amplitude of the corresponding particular solution is independent of a_1 and a_2 . This suggests :

$$u_k^1 = k_0 u_0^2 \sum_{r,s} \beta_k^{(r,s)} e^{2i\psi(r,s)} \quad (20)$$

$\beta_k^{(r,s)}$ is completely determined when using (20) into (14), and given as a function of $D_j^{(r,s)}$.

Then the general solution is obtained by adding (16), (19) and (20). It must verify the boundary conditions. This determines completely the unknowns Δk_0 , $\Delta(k_0 n_2^{(r)})$ and $\Delta C_k^{(r)}$.

For a_1 larger than a few wave lengths the term proportional to a_1 in this general solution becomes predominant - this is equivalent to Tiersten's asymptotic condition - and the solution reduces to

$$u_k = -2i U_0^2 k_0 \lambda \Delta k_0 a_1 \int_r C_k^{(r)} e^{2i\psi(r,r)} \quad (21)$$

The general solution could also have, to verify an excitation condition, for instance $u_k = 0$ for $a_1 = a_2 = 0$ if no second harmonic is generated by the source. It can be seen that this condition cannot be satisfied by the present solution. Therefore this last one is to be completed, and the complementary term corresponds to a bulk wave propagating radially from the source point (this is equivalent to a S.S.B.W. at the frequency 2ω). But its calculation has not been carried out yet, because it is of no importance for the determination of the main parts of the second and third harmonics.

The second harmonic level is defined as the ratio between the amplitudes U_0 and U_1 of the solutions at the frequencies ω and 2ω . From (21) and (11) it follows

$$U_1/U_0 = 2i U_0 k_0 \lambda \Delta k_0 a_1 \quad (22)$$

It is more convenient to give this level at a distance a_1 normalized to unity, and also with respect to unitary amplitude U_0 and wave number k_0 . The results of the calculation for quartz are given in table III and compared with the theoretical values of Vella² and the experimental data of Gibson, Alippi^{5,6} and Lopen.

b) Amplitude-frequency effect

After a second iteration the equilibrium equations and boundary conditions at the second order of approximation become

$$\begin{aligned} \ddot{u}_j - c_{ijkl} u_{k,li} = & \\ \gamma_{ijklmn} (u_{k,li}^0 u_{m,n}^1 + u_{k,li}^1 u_{m,n}^0) & \quad (23) \\ + \delta_{ijklmnpq}^0 u_{k,li}^0 u_{m,n}^0 u_{p,q}^0 & \end{aligned}$$

$$\begin{aligned} c_{2jkl}^2 u_{k,l}^2 = -\gamma_{2jklmn}^0 (u_{k,l}^0 u_{m,n}^1 + u_{k,l}^1 u_{m,n}^0) & \quad (24) \\ - \delta_{2jklmnpq}^0 u_{k,l}^0 u_{m,n}^0 u_{p,q}^0 & \text{ at } a_2 = 0 \end{aligned}$$

with

$$\delta_{ijklmnpq}^0 = \delta_{ijklmnpq} + \delta_{ijmnklpq} + \delta_{ijpqmnkl}$$

By replacing u_k^0 and u_k^1 by their expressions, the driving terms at the frequencies 3ω

and ω are obtained. They lead to solutions corresponding respectively to the third harmonic generation and to amplitude and phase perturbations at the fundamental frequency, i.e., to the A-F effect. The study was limited to this last phenomenon and therefore only solutions of (23) (24) at the frequency ω were calculated.

By using the same method as previously it can be easily shown that the general solution u_k is composed of particular solutions on the one end related to γ_{ijklmn} and with amplitudes constant or proportional to a_1 or to a_2 and on the other end related to $\delta_{ijklmnpq}$ with constant amplitude.

These particular solutions are easily calculated because none of the driving terms of (23) is synchronous with any of the partial waves of the SAW. They are written :

$$u_k = U_0^3 k_0^2 \int_{r,s} e^{i\psi(r,s)} \quad (25)$$

$$\times \{k_0 \gamma_k^{(r,s)} a_1 + k_0 \delta_k^{(r,s)} a_2 + \epsilon_k^{(r,s)}\}$$

where

$$\psi(r,s) = \omega t - k_0 a_1 - k_0 (2n_2^{(s)} - n_2^{(r)*}) a_2$$

$\gamma_k^{(r,s)}$ and $\delta_k^{(r,s)}$ are function of γ_{ijklmn} and therefore only of the second and third order elastic constants. $\epsilon_k^{(r,s)}$ is related to γ_{ijklmn} and $\delta_{ijklmnpq}$ and depends also on the fourth order elastic constants.

In order to satisfy the boundary conditions a general solution of the homogeneous part of (23) is to be added. This solution is built up by perturbing the amplitude, wave number and penetration of the homogeneous solution :

$$u_k = U_0^3 k_0^2 \int_r C_k^{(r)} e^{i(\omega t - k_0 a_1 - k_0 n_2^{(r)} a_2)}$$

The perturbed solution is approximated, as in (19), but at one more step of approximation.

$$\begin{aligned} u_k = \mu k_0^2 U_0^3 \int_r C_k^{(r)} e^{i\psi(r,r)} & \\ \times \left\{ -i \frac{\Delta^2 k_0}{2} a_1^2 - i \frac{\Delta^2 (k_0 n_2^{(r)})}{2} a_2^2 - \Delta k_0 \Delta (k_0 n_2^{(r)}) a_1 a_2 \right. & \\ - i \frac{\Delta C_k^{(r)}}{C_k^{(r)}} (\Delta k_0 a_1 + \Delta (k_0 n_2^{(r)}) a_2) & \quad (26) \\ + 1 + \frac{\Delta C_k^{(r)}}{C_k^{(r)}} - i \Delta k_0 a_1 - i \Delta (k_0 n_2^{(r)}) a_2 \} & \end{aligned}$$

The complete solution is obtained by adding (25) and (26). The same remark as previously can be made : for a_1 larger than a few wave lengths

the term proportional to a_1 becomes predominant and the solution reduces to :

$$u_k = -k_0^2 u_0^3 i \frac{\Delta^2 k_0}{2} \mu a_1^2 \int_r e^{i\psi(r,r)} \quad (27)$$

The component proportional to a_1^2 is function of the second and third order elastic constants but not of the fourth ones. If for some particular crystal orientation the $\mu \Delta^2 k_0$ coefficient becomes small the component proportional to a_1 will be to be conserved, but in this case the fourth order elastic constants (which are not known for quartz) are to be introduced.

In eq. (27) the constant $\mu \Delta^2 k_0$ is a complex quantity, which induces phase velocity and amplitude perturbation given by

$$\begin{aligned} V &= V_0 (1 + k_0^3 u_0^2 f_1 a_1^2) \\ U &= U_0 (1 + k_0^4 u_0^2 e_1 a_1^2) \end{aligned} \quad (28)$$

$$\text{where } e_1 + if_1 = -(4/2) \mu \Delta^2 k_0 / k_0^2$$

The A-F effect of a resonator or delay line can be calculated from (28) by integrating with respect to a_1 over the effective wave path length. The results of this calculation are shown on table IV.

In this table the SAW A-F effect is defined as the fractional velocity or frequency change for wave number and amplitude normalized to unity and calculated for a wave path length equal to 100 wave lengths. Comparison is made with bulk waves (for these last ones a_1 is of the order of one wave length) for the same crystal cuts.

The A-F effect of SAW ST cut is found to be near zero. This is due to the fact that in the solution u_k the terms proportionnal to a_1 and constant were neglected. They are to be taken into account in the case of ST cut for a better evaluation.

Conclusion

This study shows that the intensities of the non linear elastic phenomena of SAW are lower than the corresponding ones observed in bulk waves, at least for regular ST and AT cuts. It appears from the calculation that the amplitude-frequency effect is mainly related to the third order elastic constants, the values of which all are measured for quartz. This gives the possibility of calculating the influence of cut angles and propagation direction in order to find configurations with the lowest possible non linearities.

Acknowledgements

The SAW resonators used in this work were prepared by Thomson-CSF-DASM Cagnes/s/mer, France. The authors wish to thank Drs. C. Lardat,

C. Maerfeld and P. Tournois for providing the samples and for helpfull discussions.

References

1. H.F. Tiersten and J.C. Baumhauer, "Second Harmonic Generation of surface waves in isotropic elastic solids", J. Appl. Phys., 45, 4272, 1974.
2. P.J. Vella, G.I. Stegeman and V.M. Ristic, "Analysis of parametric mixing and harmonic generation of surface acoustic waves", J. Appl. Phys., 50, 81, 1979.
3. P.O. Lopen, "Second-harmonic generation in an elastic surface wave in alpha-quartz", J. Appl. Phys., 39, 5400, 1968.
4. J.W. Gibson and P. Meijer, "Non linearly generated harmonics and attenuation of Rayleigh waves on crystalline quartz", J. Appl. Phys., 45, 3288, 1974.
5. A. Alippi, A. Palma, L. Palmieri and G. Socino, "Phase and amplitude relations between fundamental and second harmonic acoustic surface waves in SiO_2 and LiNbO_3 ", J. Appl. Phys., 48, 2182, 1977.
6. A. Alippi, A. Palma, L. Palmieri, G. Socino and E. Verona, "Experimental evidence of distorted rippling profiles of finite amplitude acoustic surface wave", J. de Physique, Colloque C8, supplément au n° 11, tome 40, novembre 1979, page C8-249.
7. J.C. Baumhauer, H.F. Tiersten, "Non linear electroelastic equations for small fields superposed on a bias", J. Acoust. Soc. Am., 54, n°4, 1017, 1973.
8. M. Planat, C.R. Acad. Sc. Paris, t. 289 (5 novembre 1979).
9. P.J. Vella, J.C. Padmore, G.I. Stegeman et V.M. Ristic, "Non linear surface wave interactions : parametric mixing and harmonic generation", J. Appl. Phys., 45, 1993, 1974.

Annex

Coefficients of the inhomogeneous parts of propagation equations and boundary conditions at the first order of approximation :

$$D_j^{(r,s)} = -i \{ 2H_{1j}^{(r,s)} + H_{2j}^{(r,s)} (n_2^{(r)} + n_2^{(s)}) \}$$

$$\bar{D}_j^{(r,s)} = i H_{2j}^{(r,s)} (n_2^{(r)*} - n_2^{(s)})$$

$$H_{ij}^{(r,s)} = \gamma_{ijk\ell mn} b_\ell^{(r)} b_n^{(s)} c_k^{(r)} c_m^{(s)}$$

$$\bar{H}_{ij}^{(r,s)} = \gamma_{ijk\ell mn} b_\ell^{(r)*} b_n^{(s)} c_k^{(r)*} c_m^{(s)}$$

$$\text{with } b_1^{(r)} = -i ; b_2^{(r)} = -in_2^{(r)} ; b_3^{(r)} = 0$$

	cut	Frequency	Q factor	A-F coef. k
SAW resonator	ST	110 MHz	26 000	$1.1 \cdot 10^{-3}/A^2$
BW resonator	AT	100 MHz	63 000	$2.5 \cdot 10^{-1}/A^2$
BW resonator	AT	5 MHz	$2 \cdot 10^6$	$2 \cdot 10^{-1}/A^2$

Table I : Amplitude-Frequency Effect

	cut	Frequency	Q factor	intercept point
SAW resonator	ST	110 MHz	33 000	45 dBm
BW resonator	AT	100 MHz	63 000	15 dBm

Table II : Intermodulation

	calculated		measured		
	present work	Vella 1978	Lopen 1968	Gibson 1974	Alippi 1977 1979
Y cut prop. X	0.04	0.07	/	0.065	0.035
X cut prop. Y	0.11	0.07	0.18	/	0.068 0.07
ST cut prop. X	0.23	/	/	/	/

Table III : Second harmonic level $U_1/U_0^2 k_0 a_1$

	$\frac{1}{k_0^2 U_0^2} \frac{\Delta V}{V_0}$ of SAW for $a_1 = 100$ wave lengths	SAW A-F effect BW A-F effect
Y cut	0.16	0.025
X cut	2.0	0.30
ST cut	0 if the next terms in the solutions are neglected.	/

Table IV : Calculated A-F effect

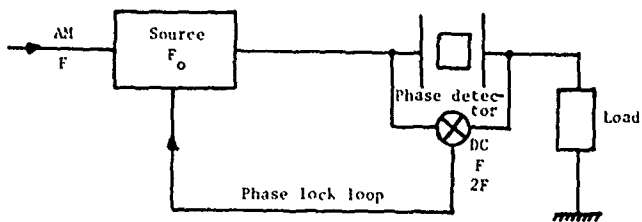


Figure 1. Schematic diagram of the amplitude-frequency effect measurement set

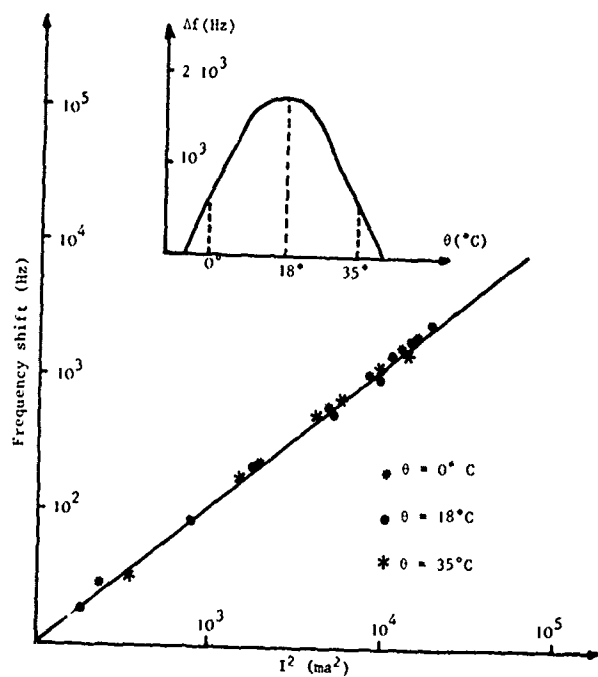


Figure 2. Amplitude-frequency effect of a SAW resonator, measured at three different temperatures.

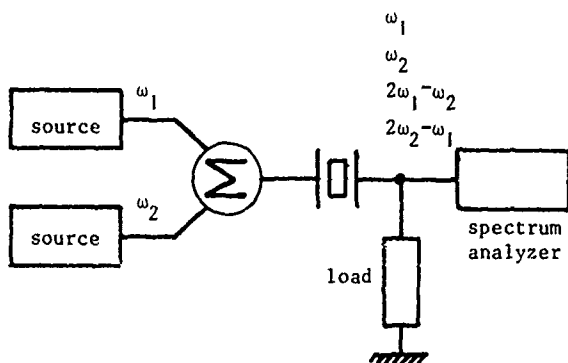


Figure 3. Schematic diagram of the intermodulation measurement set.

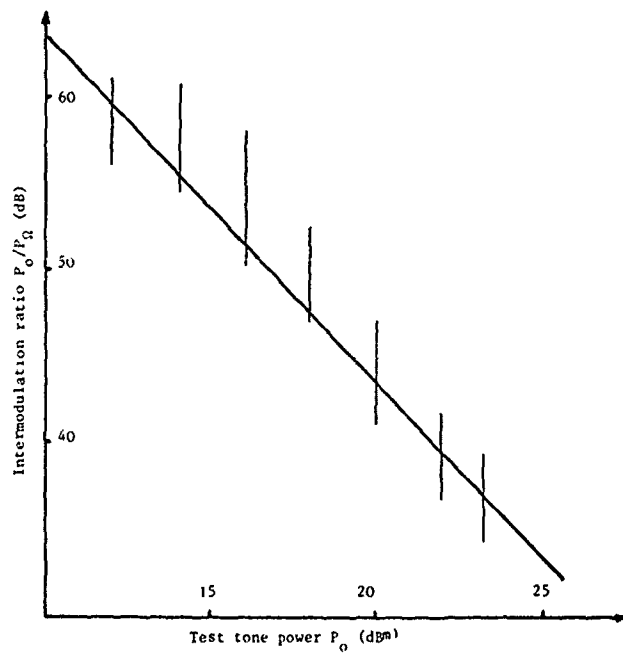


Figure 4. Intermodulation of a SAW resonator.

THEORETICAL ANALYSIS OF SECOND-ORDER EFFECTS IN SURFACE-WAVE GRATINGS

Peter V. Wright and Hermann A. Haus
Massachusetts Institute of Technology
Cambridge, Massachusetts

Abstract

This paper presents a theoretical analysis of second-order effects that have been observed with surface acoustic wave (SAW) gratings. The term "second-order" refers to effects that vary quadratically with groove depth. In the past such effects were assumed to be very small and because a theoretical analysis of the latter appeared to be too involved they were ignored by most theories.

However, in recent years several papers have been presented stressing the importance of second-order effects on SAW grating design.¹⁻⁸ In particular the second-order reduction in the free surface wave velocity within a grating has been found to be a major source of phase error often necessitating empirical adjustments in design.

We develop here a new, relatively straightforward theory for predicting second-order effects in normal incidence grooved gratings. Closed form expressions are derived for all the second-order parameters without the need for invoking perturbation theories, truncation or numerical integration in the analysis. Using the theory we examine grating responses near Bragg and second-harmonic and compare the results with experimental data. In the light of the analysis we suggest how second-order effects may be controlled or even used to advantage.

Introduction



FIG. 1. GRATING CONFIGURATION

This paper will deal specifically with normal incidence grooved gratings (Fig. 1). We shall concentrate on analysing second-order effects in such a grating near the Bragg frequency and its second-harmonic. These frequencies are defined by

$$\text{Bragg: } \Lambda = \lambda_r / 2,$$

$$\text{Second harmonic: } \Lambda = \lambda_r$$

$$\lambda_r = \text{Rayleigh wavelength.}$$

To first-order in the grating depth, near Bragg, the reflection of a wave incident on the grating is a maximum: the reflections from the front and back of each groove add in phase. At second-harmonic the latter reflections are out of phase and no reflection is expected. To second-order however we shall see that the latter is not the case. In practice strong grating reflections have been observed at the second-harmonic³ that are comparable with, or even greater than those at Bragg. In addition, the Bragg frequency itself, or frequency of maximum reflection of the grating is found experimentally to be lower than that predicted by the first-order theory. This effect can be attributed to a slowing down of the surface wave that occurs under the grating compared to the velocity on a free surface. This reduction in the wave velocity under the grating may also be observed in the grating transmission phase response. The reduction in the velocity is a second-order effect, varying quadratically with the groove depth of the grating.

The major second-order effects we thus seek to predict from our theoretical second-order analysis are:

1. Resonator frequency shift
2. Grating phase shift
3. Strong second-harmonic reflection

Objectives

The main objectives in embarking on this second-order analysis are:

1. To predict observed second-order effects entirely theoretically without the use of empirical parameters
2. To understand which grating parameters most strongly influence the second-order grating effects
3. To use second order effects for design optimization.

Theory

Assumptions

In the analysis that follows we shall make the following assumptions:

1. Isotropic substrate
2. Shallow grooves (i.e. small reflection/groove)
3. Many grooves
4. Ignore diffraction (i.e. wide grooves).

The first assumption is not as restrictive as it may first appear. To enable the results of the analysis to be applicable to common anisotropic substrate materials, such as $y-z$ LiNbO_3 and ST Quartz, we shall use an "equivalent Poisson ratio" for such materials as suggested by several authors.^{8,9} In particular, we shall use the equivalent Poisson ratios derived theoretically by Shimizu et al. of $\nu = .335$ for $y-z$ LiNbO_3 , and $\nu = .41$ for ST quartz.

The next assumption of many and shallow grooves is valid for typical SAW grating devices. Groove heights are usually less than approximately 2% of the Rayleigh wavelength ($h/\lambda_r \leq .02$) and typical gratings comprise 100 or more grooves. This assumption permits a "coupling of modes" analysis of the grating.

The last assumption that ignores diffraction is justified for most practical gratings as typical groove widths are of the order of $100 \lambda_r$.

First-Order Analysis

Before going on to a second-order analysis we briefly summarize the results of a first order grating analysis.

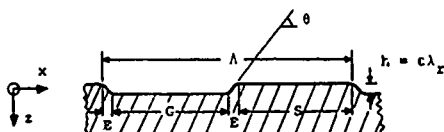


FIG. 2. GRATING PROFILE, $\Lambda = (\lambda_r/2)$,
 $c = (h/\lambda_r) \approx .02$, $\theta = 60^\circ$

Figure 2 shows in cross-section a small section of a typical SAW grating of the type we shall analyze. Note that we have assumed a finite width to the groove edge, namely E , and a slope to the groove edge of θ , ($\theta \leq 90^\circ$). For the first-order analysis the details of the groove edge are relatively unimportant. However, we shall show that in the second-order analysis the shape of the groove edge is crucial in determining the second-order effects.

Assuming the grating to comprise an infinite number of grooves we may describe the grating surface by

$$z = \epsilon \lambda_r f(x)$$

$$= \epsilon \lambda_r \sum_{m=1}^M A_m \cos\left(\frac{2m\pi}{\Lambda} x\right)$$

$$\lambda_r = \text{Rayleigh wavelength.}$$

The Fourier coefficients of the grating serve to couple energy out of an incident Rayleigh wave into a backward, or reflected wave and also into higher-order Brillouin components. Near Bragg the latter are all evanescent and result in energy storage in the region of the grating discontinuities. At the second-harmonic in addition to energy storage they are also responsible for the radiation of energy into the bulk.

Consider a normal incidence grating. If the grating were not present the free surface could support Rayleigh waves propagating in both the forward and backward directions, with propagation constants k_r and $-k_r$ respectively. The waves would be uncoupled. However, with the grating present the forward and backward Rayleigh waves in the grating are coupled by the $2k_r$ Fourier component of the grating. This is the cause of the first-order grating reflection coefficient. At Bragg the fundamental Fourier component A_1 of the grating has dependence $2k_r$, thus the first-order reflection coefficient is strong. However, at the second-harmonic a trapezoidal grating with a groove/stripe ratio of 1 has only Fourier coefficients with wavenumber $k_r, 3k_r, \dots$. Thus to first-order there is no reflection from the grating at the second-harmonic.

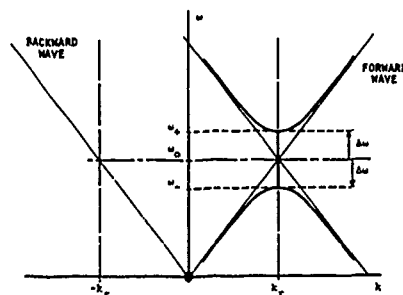


FIG. 3. FIRST-ORDER GRATING DISPERSION DIAGRAM NEAR BRAGG.

The first-order grating dispersion diagram is shown in Fig. 3. The important point to note is that the split in the dispersion diagram is entirely symmetric about the "unperturbed" center frequency ω_0 . To first-order $\Delta\omega$, or the reflection coefficient of the grating is only a function of A_1 , the $2k_r$ Fourier coefficient of the grating. There is no shift in the resonant frequency of the grating to first-order.

Second-Order Analysis

In general, the upper and lower frequencies

of the band gap of the dispersion relation, ω_+ and ω_- respectively, will also be functions of the higher powers of ϵ , i.e.

$$\left(\frac{\Delta\omega}{\omega_0}\right)_{\pm} = \pm \epsilon f_1(A_1) + \epsilon^2 f_2^{\pm}(A_1, A_2, \dots, A_M) + \dots$$

In contrast with the first-order coefficient we shall show that the second-order coefficient is

1. A function of all the Fourier coefficients of the surface
2. In general has both a symmetric and an antisymmetric component.

The antisymmetric component of the second-order split in the dispersion diagram is responsible for a resultant shift downward in the band gap.

To derive the second-order dispersion relation theoretically, we match the boundary conditions on the surface of the grating for $\Lambda = \lambda_r/2$ or $\Lambda = \lambda_r$. The stress on the perturbed boundary $\vec{\sigma} \cdot \hat{n}$ must be zero, where $\vec{\sigma}$ is the stress tensor and \hat{n} the surface normal. This determines the amplitude of all the Brillouin components to first-order. The Brillouin components having propagation constants of $\pm nk_r$ ($0 \leq n \leq (M+1)$, $n \neq 1$) are all first-order in ϵ , (M = number of Fourier coefficients of the surface).

We next match boundary conditions to second-order. The Brillouin components need only be determined to first-order, however, because the second-order dispersion relation arises from matching the stress components having the dependence $\exp(\pm jk_r)$ to second-order. Since the Brillouin components couple into these equations by the surface perturbation to order ϵ , all stress components of the Brillouin waves of order ϵ^2 couple into the equations to the order ϵ^3 . Thus to derive the second-order dispersion relation the Brillouin components need only be defined to first-order. The technique is therefore somewhat analogous to a variational principle.

The result of the analysis is that we obtain the upper and lower frequencies of the band gap, ω_+ and ω_- respectively, in closed form to second-order. The solutions contain infinite sums (for $M = \infty$), consisting of contributions from all the Brillouin components. However, it is important to note that the solutions are derived in closed form by this method, no perturbation techniques, truncation or numerical integrations are employed in the analysis after the initial coupling of modes assumptions. Defining,

k_r = Rayleigh wave propagation constant

k_1 = compressional wave number

k_2 = shear wave number

and the decay constants q and r of the shear and compressional waves respectively by:

$$q^2 = k_r^2 - k_2^2$$

$$r^2 = k_r^2 - k_1^2,$$

we obtain for the second-order frequency shifts at Bragg,

$$f_2^+ = - \frac{qr}{4(k_r^2 q - k_r^2 r - 2q^2 r)} \cdot [(q^3 - q^2 r - 3k_r^2 q - k_r^2 r) A_1^2 + (k_r^2 + q^2)(q + r) \sum_{m=1}^{M-1} A_m A_{m+1}] - q^4 \frac{A_1^2}{2} \left[\frac{(k_r^2 q^2 + k_r^2 r^2 + 2k_r^2 qr + 5q^2 r^2)}{(k_r^2 q - k_r^2 r - 2q^2 r)^2} + \frac{2k_r^2 q^2 r (q^2 + 3r^2)}{(k_r^2 q - k_r^2 r - 2q^2 r)^3} \right] - \frac{qr [2jk_r q T_1 + (k_r^2 + q^2) T_2]}{4\mu k_r^2 (q - r) (k_r^2 q - k_r^2 r - 2q^2 r)}$$

with,

$$T_1 = \frac{1}{2} \sum_{n=1}^{M+1} [A_n^- S_i^n \sigma_{ixz}^n(0) + jk_r (A_n^+ - nA_n^-)]$$

$$S_i^n \sigma_{ixx}^n(0)]$$

and

$$T_2 = \frac{1}{2} \sum_{n=1}^{M+1} [A_n^+ S_i^n \sigma_{izz}^n(0) + jk_r (A_n^- - nA_n^+)]$$

$$S_i^n \sigma_{ixz}^n(0)]$$

Also,

$$f_2^- = - \frac{qr}{4(k_r^2 q - k_r^2 r - 2q^2 r)} [(q^3 - q^2 r - 3k_r^2 q - k_r^2 r) A_1^2$$

$$\begin{aligned}
& - (k_r^2 + q^2)(q + r) \sum_{m=1}^{M-1} A_m A_{m+1} \\
& - q^4 \frac{A_1^2}{2} \left[\frac{(k_r^2 q^2 + k_r^2 r^2 + 2k_r^2 q r + 5q^2 r^2)}{(k_r^2 q - k_r^2 r - 2q^2 r)^2} \right. \\
& \quad \left. + \frac{2k_r^2 q^2 r (q^2 + 3r^2)}{(k_r^2 q - k_r^2 r - 2q^2 r)^3} \right] \\
& - \frac{q r [2j k_r q T_3 + (k_r^2 + q^2) T_4]}{4 \mu k_r^2 (q - r) (k_r^2 q - k_r^2 r - 2q^2 r)}
\end{aligned}$$

with

$$T_3 = \frac{1}{2} \sum_{m=1}^{M+1} [A_n^+ S_i^n \sigma_{ixz}^n(0) + j k_r (A_n^- - n A_n^+)]$$

$$S_i^n \sigma_{ixz}^n(0)]$$

and

$$T_4 = \frac{1}{2} \sum_{n=1}^{M+1} [A_n^- S_i^n \sigma_{ixz}^n(0) + j k_r (A_n^+ - n A_n^-)]$$

$$S_i^n \sigma_{ixz}^n(0)]$$

$$i = \begin{cases} 1, & \text{denotes compressional wave} \\ 2, & \text{denotes shear wave} \end{cases}$$

S_i^n denotes the amplitude of the Brillouin stress component σ_i^n with dependence $\exp(-j n k_r x)$.

$$A_n^+ = (A_{n-1} + A_{n+1})$$

$$A_n^- = (A_{n-1} - A_{n+1})$$

and μ is a Lamé constant. Similar relations are obtained at the second harmonic.

The width of the band gap $2\Delta\omega_g$ may be determined from

$$\Delta\omega_g = \frac{(\Delta\omega_+ - \Delta\omega_-)}{2}$$

and the new center frequency of the grating ω' may be determined from

$$(\omega' - \omega_0) = \Delta\Omega = \frac{(\Delta\omega_+ + \Delta\omega_-)}{2}$$

where $\Delta\Omega$ is the second-order shift in the resonant frequency of the grating.

The reflection coefficient of the grating may be determined to second-order from $\Delta\omega$. Using a modified form of conventional coupling of modes¹⁰ we may extend the dispersion relation away from the gap to obtain the response of the grating in the region of Bragg or second-harmonic.

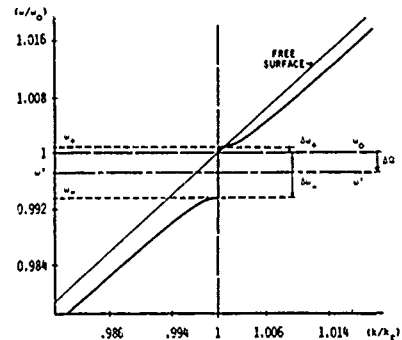


FIG. 4. THEORETICAL SECOND-ORDER DISPERSION DIAGRAM NEAR BRAGG FOR GRATING ON $y = x \sin \theta_0$. ($\nu = .335$, $(h/\lambda_0) = .016$, $\theta = 45^\circ$)

Figure 4 shows a theoretical plot of the dispersion relation to second-order for a typical grating. The downward second-order shift in the grating center frequency $\Delta\Omega$ is clearly predicted by the theory.

Defining the coefficient K_2 of the quadratic shift in the grating center frequency by

$$(\omega'/\omega_0) = 1 - K_2 (h/\lambda)^2$$

we plot K_2 in Fig. 5 as a function of Poisson ratio (ν) for a Bragg grating of height $h/\lambda_r = .01$ and for various groove slopes (θ). It can be seen that the second-order frequency shift is very sensitive to the shape of the grooves. The frequency shift is greatest for steep grooves and in fact is INFINITE for grooves with vertical sides ($\theta = 90^\circ$). This is because to second-order for grooves with 90° corners, the stresses in the region of the corners become infinite. If such corners could be made in practice of course the material would flow plastically in the region of the sharp corner to remove the singularity.

The "blow-up" of the coefficient K_2 is however very weak, in that it blows up logarithmically. For a grating with a square wave profile

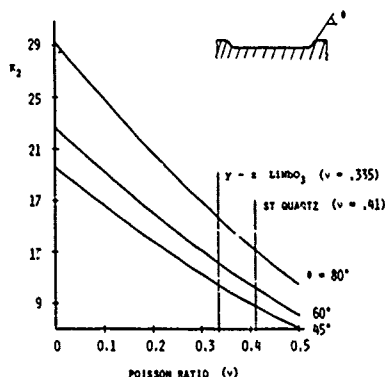


FIG. 5. THEORETICAL DEPENDENCE OF SECOND-ORDER COEFFICIENT ON POISSON RATIO FOR AN ISOTROPIC SUBSTRATE NEAR BRAGG. $(h/\lambda)^2 = 0.11$. $(\omega/\omega_0) = 1 - K_2(h/\lambda)^2$

i.e. vertical groove edges, the contributions of the Brillouin components to the frequency shift decrease inversely with the mode order. The latter can be determined from the form of our closed form solution. However, if it were not for the closed form nature of our solution such a blow-up would be extremely difficult to detect. To realise that $K_2 \rightarrow \infty$ as $\theta \rightarrow 90^\circ$ would require summing an almost infinite sum of ever decreasing terms. It is for this reason that theoretical analyses of second-order effects requiring perturbation techniques, truncation or numerical integration in their solution should be avoided. Such an attempt was made by Shimizu et al.⁸ and led them to the incorrect result that K_2 remains finite for vertical grooves.

Experimental Verification

We now seek to confirm our theoretical analysis by comparison with experimental data that has been reported in the literature.

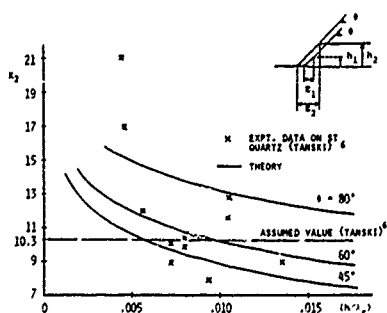


FIG. 6. THEORETICAL VARIATION OF SECOND-ORDER COEFFICIENT WITH GROOVE DEPTH NEAR BRAGG ON ST-QUARTZ ($\nu = .41$).

Figure 6 shows experimental measurements of K_2 for gratings at Bragg, on ST Quartz made by Tanski.⁶ We also show theoretical plots from the present theory of K_2 (assuming an equivalent $\nu = .41$) for various groove slopes. From the experimental data Tanski inferred an average value of K_2 of approximately 10.3. However, he noted that he found it "very disturbing indeed" that for small groove depths K_2 appeared to increase significantly. The present theory predicts that such an effect is likely to occur. There are two reasons

1. For small groove depths the groove edges are likely to be steeper because of the fabrication processes involved.
2. Even for grooves with constant edge slope θ , shallower grooves have a narrower edge width, E . It is the ratio (E/Λ) that determines the Fourier coefficients of the grating, not the groove slope. As E decreases the second order effects increase and as $E \rightarrow 0$, $K_2 \rightarrow \infty$.

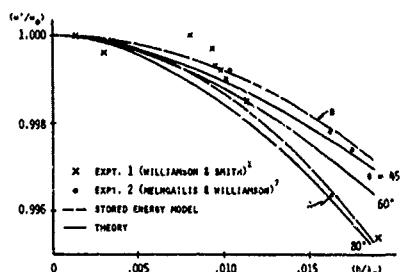


FIG. 7. THEORETICAL DEPENDENCE OF SHIFT S OF BAND WITH GROOVE DEPTH FOR GRATING ON $y-z$ LiNbO_3 ($\nu = .335$). STORED ENERGY MODEL, A: 'LI AND HELMINIAK', ASSUMED $K_2 = 13.8$, B: (HELMINIAK AND WILLIAMSON), ASSUMED $K_2 = 8.0$

In Fig. 7 we show data taken by Williamson et al.^{1,7} of the resonator frequency shift at Bragg, of gratings on $y-z$ LiNbO_3 . We also show the quadratic dependence on (h/λ) predicted by the stored energy model of Li et al.³ using two different empirically determined values for K_2 .^{3,7} For comparison we show the behavior predicted by the present theory (assuming an equivalent $\nu = .335$) for various groove slopes. Important to note is that these curves are not exactly parabolic because of the dependence of K_2 on (h/λ) discussed above. However the departure from quadratic behavior is well within the experimental uncertainty of such measurements. Finally we note from the theoretical curves that although $K_2 \rightarrow \infty$ as $(h/\lambda) \rightarrow 0$ the frequency shift $K_2(h/\lambda)^2 \rightarrow 0$ as $(h/\lambda) \rightarrow 0$ as the logarithmic blow-up of K_2 is so weak.

We now examine the theoretical behavior of a

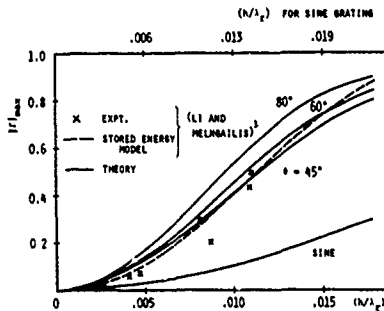


FIG. 8. THEORETICAL DEPENDENCE OF MAXIMUM REFLECTION COEFFICIENT WITH GROOVE DEPTH NEAR SECOND HARMONIC FOR 100 GROOVES ON $y-z$ LiNbO_3 , ($v = .335$), STORED ENERGY MODEL (LI AND MELNGAILIS), ASSUMED $\theta = 45^\circ$.

grating expected near second-harmonic. Figure 8 shows experimental measurements of the maximum grating reflection coefficient (Γ), as a function of groove height, near second-harmonic, made by Li et al.³ for gratings on $y-z$ LiNbO_3 . We again show the behavior predicted by their stored energy model (incorporating an empirically derived constant) and the theoretical behavior predicted by the present theory for various groove slopes. The stored energy model and the present theory both predict Γ to within the experimental uncertainty of the data. In addition, however, our theoretical analysis also predicts bulk radiation loss at this frequency.

In Fig. 8 we show also the second-order reflection coefficient predicted by the theory for a sinusoidal grating having the same Bragg reflection coefficient as a trapezoidal grating. The reflection of the sinusoidal grating at second-harmonic is very much reduced from that of a trapezoid. The message here is that second-order effects can be considerably reduced in a grating that avoids sharp corners and vertical sides. A sinusoidal grating ideally has the lowest second-order effects.

We now examine the transmission phase response through a SAW grating predicted by the present theory. As we have demonstrated the theory predicts a second-order reduction in the surface wave velocity beneath a grating, compared with that on a free surface. This reduction in the wave velocity causes a wave travelling under the grating to suffer an increased phase delay compared to a wave travelling an equal distance on the free surface. In Fig. 9 we show such a phase delay for a grating on $y-z$ LiNbO_3 as measured by T. Melngailis (Lincoln Lab., unpublished). The measured phase delay is shown as a function of frequency in the neighborhood of Bragg.

Assuming an arbitrary groove slope of 45° , and a grating depth of $(h/\lambda_c) = .015$ we used a

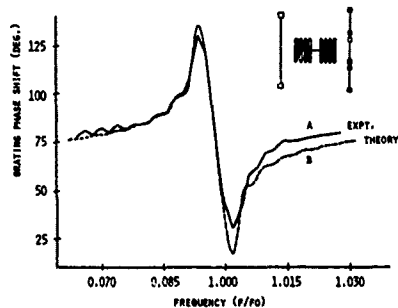


FIG. 9. GRATING PHASE SHIFT VS. FREQUENCY NEAR BRAGG (f_0). A: EXPERIMENT, 200 GROOVES $y-z$ LiNbO_3 , $(h/\lambda_c) = .015$ (T. MELNGAILIS, UNPUBLISHED). B: THEORY, 200 GROOVES $v = .335$, $(h/\lambda_c) = .015$, $\theta = 45^\circ$ (ASSUMED).

coupling of modes analysis, together with our center of the gap analysis to predict the theoretical phase response around Bragg. The result of the analysis is also shown in Fig. 9. The agreement of the theory to experiment is very good; the theory even succeeds in closely predicting the structure of the observed ripples in the response. Such good agreement may make the measurement of grating depth and groove profile possible by such electrical measurements.

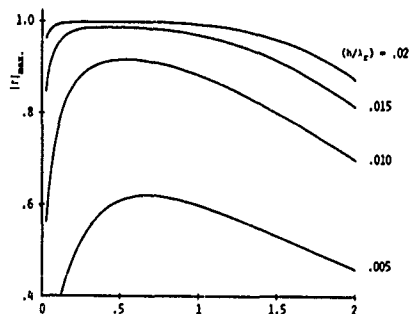


FIG. 10. THEORETICAL DEPENDENCE OF MAXIMUM REFLECTION COEFFICIENT WITH GROOVE/STRIP RATIO NEAR BRAGG FOR 200 GROOVES ON $y-z$ LiNbO_3 ($v = .335$, $\theta = 45^\circ$).

In Fig. 10 we show the dependence of the maximum grating reflection coefficient (Γ) on the groove to strip ratio (G/S) for a typical grating, taking into account second-order effects. This dependence is shown for several groove heights. The magnitude of the reflection coefficient is skewed about $G/S = 1$ by second-order effects. To first-order we would expect Γ to be a maximum for $G/S = 1$. However, as G/S is reduced (< 1) the increase in the second-order grating reflection more than compensates for the

decrease in the first-order coefficient. If the G/S ratio is increased (> 1) in addition to the reduction in the first-order reflection coefficient the second-order reflection is out of phase and thus Γ decreases rapidly. To minimize the sensitivity of Γ to fabrication tolerances for G/S, Fig. 10 suggests that a groove strip ratio of < 1 may be desirable.

In Fig. 11 we show the theoretical second-order frequency shift of a grating on $y - z$ LiNbO_3 ($v = .335$). It can be seen that the latter is not a strong function of the G/S ratio for $G/S > \sim 5$. We thus can control the second-order reflection coefficient and frequency shift relatively independently. The former is most sensitive to the groove/stripe ratio while the latter is most sensitive to the groove slope. Such control may find useful application in the trimming of gratings after fabrication.

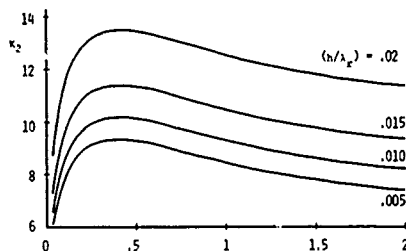


FIG. 11. THEORETICAL DEPENDENCE OF SECOND-ORDER COEFFICIENT WITH GROOVE/STRIP RATIO NEAR BRAGG FOR GRATING ON $y - z$ LiNbO_3 ($v = .335$, $\theta = 45^\circ$).

Conclusions

The second-order theory developed has:

1. Derived second-order quantities theoretically without the need for empirical constants. No perturbation techniques, truncation of numerical integration are required in the solutions.
2. Demonstrated the critical importance of groove shape in determining second-order effects. Vertical grooves have ideally infinite second-order effects.
3. Predicted the second-order resonator frequency shift observed in SAW gratings.
4. Suggested how gratings with low second-order effects may be designed. A pure sinusoidal grating profile produces the lowest second-order effects.
5. Predicted the transmission phase response through a SAW grating.
6. Predicted the strong reflection observed in gratings at the second-harmonic.

Acknowledgments

The authors would like to thank J. Melngailis (MIT) for many helpful contributions in the course of this work and also for supplying the experimental phase data. We also wish to acknowledge several very helpful discussions with W. J. Tanski (Sperry Research Center).

Finally we are grateful for the support of the National Science Foundation Grant ENG7909980.

References

1. R. C. Williamson and H. I. Smith, "The Use of Surface-Elastic-Wave Reflection Gratings in Large Time-Bandwidth Pulse-Compression Filters," *IEEE Trans. MTT-21*, pp. 195-205, April 1973.
2. R. C. M. Li and J. Melngailis, "Second-Order Effects in Surface-Wave Devices due to Stored Energy at Step Discontinuities," *IEEE Ultrasonics Symposium Proceedings*, pp. 503-505, Monterey, CA, November 1973.
3. R. C. M. Li and J. Melngailis, "The Influence of Stored Energy at Step Discontinuities on the Behavior of Surface-Wave Gratings," *IEEE Trans. on Sonics and Ultrasonics*, Vol. SU-22, No. 3, pp. 189-198, May 1975.
4. J. Melngailis, R. C. Williamson, J. H. Holtham and R. C. M. Li, "Design of Reflective-Array Surface Wave Devices," *Wave Electronics*, Vol. 2, pp. 177-198, 1976.
5. W. R. Shreve, "Surface Wave Resonators and their use in Narrowband Filters," 1976 *Ultrasonics Symposium Proceedings*, IEEE Cat. No. 76CH1120-5SU, pp. 706-713.
6. W. J. Tanski, "Developments in Resonators on Quartz," 1977 *Ultrasonics Symposium Proceedings*, IEEE Cat. No. 77CH1264-1SU, pp. 900-904.
7. J. Melngailis and R. C. Williamson, "Interaction of Surface Waves and Bulk Waves in Gratings: Phase Shifts and Sharp Surface-Wave/Reflected Bulk Wave Resonances," 1978 *Ultrasonics Symposium Proceedings*, IEEE Cat. No. 78CH1344-1SU, pp. 623-629.
8. H. Shimizu and M. Takeuchi, "Theoretical Studies of the Energy Storage and the Second Harmonic Responses of SAW Reflection Gratings," 1979 *Ultrasonics Symposium Proceedings*, IEEE Cat. No. 79CH1482-9SU, pp. 1-6.
9. R. C. M. Li, "Analysis of Surface Wave Reflection from a Periodic Array of Grooves," 1972 *Ultrasonics Symposium Proceedings*, pp. 263-266, Oct. 1972.
10. H. Kogelnik and C. V. Shank, "Coupling-Wave Theory of Distributed Feedback Lasers," *J. Appl. Phys.*, Vol. 43, pp. 2328-2335, May 1972.

SURFACE ACOUSTIC WAVE RESONATORS WITH HERMITO-GAUSSIAN TRANSVERSE MODES

by Francis PIRIO and Patrick DESROUSSEAUX
PAB - DTS

Centre National d'Etudes des Télécommunications
38-40 rue du Gal Leclerc
92131 Issy-les-Moulineaux France

Summary.

In this paper, we first briefly examine the principal characteristics of acoustic surface wave Hermito-Gaussian beams in amplitude and phase. We then describe a resonator supporting these transverse modes.

Some theoretical diffraction loss curves are given showing the new resonator geometry advantages. Measured transverse amplitude profiles in such a resonator will be presented and compared with theory. Then a resonator excited by a combination of two transverse modes will be discussed.

Introduction.

Conventional acoustic surface wave resonators are analogous to the well-known plane-parallel Fabry-Perot configuration in optics with the difference of distributed reflectors.

Haus¹ has theoretically calculated the transverse modes due to guidance at grating edges, which exist in surface acoustic wave distributed reflectors. These modes have rather complicated and variable shape when frequency varies, and do not lead to easy determination of diffraction losses caused by the non-guiding cavity between the two reflectors. Experimental verification has confirmed the presence of noticeable acoustic energy at grating edges which can lead to extra-losses due to non ideal grating edges and to diffraction in non guided modes².

Using analogy with a concave mirror laser cavity, we propose a new geometry for surface acoustic wave gratings where curved elementary reflectors follow equiphasic lines of Gaussian acoustic beams.

Hermito-Gaussian A.S.W. beams.

Background :

It has been shown³ that if A.S.W. velocity has a parabolic behaviour versus propagation angle around a central propagation direction (and in a sufficiently wide angular aperture determined by transverse source size), then a beam with transverse

Hermito-Gaussian shape can freely propagate and diffracts, without losing its shape, according to simple mathematical expressions. This parabolic velocity behaviour is found for X propagating-ST Quartz which is often used in a.s.w. resonators.

Mathematical formulation :

We write the a.s.w. field as :

$$a_n(y, z) \cdot \exp[j \Phi_n(y, z)] \quad (1)$$

z being the longitudinal coordinate, y the transverse one ; a_n denotes the amplitude, Φ_n the phase of the a.s.w. beam.

Amplitude is given by :

$$a_n(y, z) = \sqrt{W_0/W(z)} \cdot H_n\left(\frac{y}{W(z)}\right) \cdot \exp\left[-\frac{y^2}{2W^2(z)}\right] \quad (2)$$

The first term $\sqrt{W_0/W(z)}$ gives amplitude dependence with distance of propagation. The two other terms give amplitude transverse dependence and its spreading along distance according to a characteristic transverse dimension $W(z)$. One has :

$$W(z) = W_0 \sqrt{1 + (z/z_0)^2} \quad (3)$$

H_n : Hermite polynomial of order n (1 if $n=0$).

W_0 : beam spot size.

$z_0 = k_0 W_0^2 / p$: characteristic longitudinal dimension.

k_0 : wave number for central propagation direction.

p : coefficient for parabolic anisotropy (1.37 for ST-Quartz).

Phase is given by :

$$\Phi_n(y, z) = k_0 z - (n+1/2) \arctg(z/z_0) + k_0 \left[\frac{y^2}{2R(z)} \right] \quad (4)$$

$$\text{with } R(z) = pz [1 + (z/z_0)^2] \quad (5)$$

$k_0 z$ is the usual propagation term.

The second term in (4) represents a phase shift of the gaussian beam with respect to a plane wave reference.

The third term gives the shape of equiphase lines which are parabolas in the paraxial approximation used to derive gaussian beams. $R(z)$ is their radius of curvature along longitudinal axis. These equiphase lines do not depend of mode order n .

Characteristic parameters for Hermito-Gaussian a.s.w. beams are :

1. p : coefficient of parabolic anisotropy.
2. W : beam spot size (expressed in wavelength).
3. n^0 : order of the mode.

A.S.W. resonators with Hermito-Gaussian modes.

Principle :

If, in an a.s.w. distributed grating, the elementary reflectors' shape follow equiphase lines of a given Hermito-Gaussian beam, elementary reflections will give rise to a backward propagating a.s.w. beam identical in shape to the incident one.

It must be noted that with this geometry, we shall have the same simple transverse dependance of the standing wave amplitude pattern inside gratings and inside the resonant cavity. Another characteristic is that no guidance effect occurs at grating edges ; so a.s.w. energy can be theoretically as low as desired at these edges if the reflector width is large enough.

Design :

The following scheme has been used to design a.s.w. resonators supporting Hermito-Gaussian modes :

1. choose beam parameters (we took fundamental mode : $n=0$ so that amplitude has a gaussian transverse shape).
2. Draw elementary reflectors having the parabolic shape of equiphase lines. The position is slightly corrected with respect to the usual case of straight reflectors to take into account the extra phase shift of gaussian beams.
3. Use curved apodized transducers matching in phase and amplitude the gaussian beam.

Figure (1) schematizes one half of such a resonator. b is the cavity length, a its half transverse width. Since our purpose was to experimentally verify the resonant mode transverse amplitude distribution, we have designed input and output a.s.w. transducers outside cavity in order to be free from parasitic light reflections when using a laser probe.

Potential advantages :

Since no guidance occurs at grating edges, losses due to edges' imperfections are avoided.

Amplitude and phase distributions are given by simple mathematical expressions inside gratings and cavity, leading to more precise matching of input-output transducers to the chosen resonant mode.

Diffraction losses are expected to be lower

than in plane-parallel configuration for the same transverse dimensions :

In order to evaluate diffraction losses in a.s.w. resonators, we transpose theoretical and numerical results established years ago concerning diffraction losses in various laser cavities^{4,5}. Losses per half-round trip are given versus the Fresnel number N :

$$N = \frac{a^2}{b\lambda} \quad (6)$$

We recall that b is the cavity length, a its half-width. In a.s.w. resonators it is not obvious to define the cavity length since mirrors are of a distributed type. We have assumed that the effective length b is close to the geometrical value. This assumption is based on the fact that acoustic energy rapidly exponentially decreases while going inside reflectors. Another intricacy, in plane-parallel configuration, comes from the fact that mirrors are in fact resonant waveguides with their transverse modes set to which the diffracting a.s.w. field inside cavity should be matched in order to get exact diffraction losses. This may lead to slightly higher losses than the discrete plane mirrors case.

With these restrictions, figure (2) compares diffraction losses of a plane-parallel cavity (curve 2) and of a confocal cavity (curve 1). For a given Fresnel number N , a confocal configuration may have losses orders of magnitude smaller than a plane-parallel one. Another formulation is that for given losses, a confocal cavity may be transversally smaller.

From curves given in^{4,5}, diffraction losses per half-round trip are approximately :

$$\alpha_D = 9 \cdot 10^{-2} N^{-1.4} \quad (7)$$

for plane parallel configuration.

$$\alpha_D = 7.26 \cdot 10^{-5.15N} \quad (8)$$

in confocal case.

These formulas may be used to evaluate diffraction Q in a.s.w. resonators.

Experimental verification.

We have designed and fabricated a.s.w. "parabolic" resonators in order to test in a first time the transverse standing wave pattern.

Characteristics of these resonators were :

1. Substrate : X propagating ST-Quartz.
2. Wavelength : $34.14 \mu\text{m}$ (resonant frequency close to 92.4 MHz).
3. Gratings : 400 grooves for each reflector etched between 1 % and 1.3 % wavelengths.
4. Cavity length : $b = 70$ wavelengths.
5. Cavity half-width : $a = 40$ wavelengths (much larger than necessary in order to be sure to have unmodified resonant mode).
6. Mode : fundamental gaussian mode ($n=0$) with spot size $W_0 = 10$ or 5 wavelengths.

Experimental results :

With a laser probe, we made, near cavity

center, successive longitudinal scans beginning on cavity longitudinal axis and then moving towards edges with constant increment between each scan.

Figure (3) gives a pseudo perspective view of the standing wave amplitude pattern (50 μ m between successive scan lines) inside a parabolic resonator with $W_0 = 10$ wavelengths (irregularities are caused by stepping motor displacement).

Transverse amplitude profile, easily deduced from preceding results, is given in figure (4) and compared with theoretical curve. Agreement is very good ; experimentally deduced W_0 fits with theoretical value within 1 - 2 %.

Gratings edges are shown by arrows. It is clear that almost no a.s.w. energy is present near these edges as expected.

For a resonator with $W_0 = 5$ wavelengths, we still have good agreement as shown on figure (5). Standing wave amplitude is more transversely confined (by a factor 2) and grating edges are well out of scale on this figure.

Electrical transfer function of this resonator is shown on figure (6). Q value slightly higher than 30,000 is a little bit better than values obtained on plane-parallel resonators we have fabricated in the same conditions.

So, we have experimentally verified that it is possible to design a.s.w. resonators supporting gaussian modes with the aid of simple formulas and with good experimental agreement.

Transversely multimoded a.s.w. resonators.

In conventional s.a.w. resonators, transverse monomode operation is useful since it allows higher Q. This is obtained by weighting s.a.w. transducers. But one can take benefit of multimoded resonators.

For example, suppose that each a.s.w. transducer generates a combination of two adjacent Hermite-Gaussian resonator modes. The total electrical transfer function will be a combination of two partial ones, each corresponding to a specific transverse mode. These partial transfer functions mainly differ in their peak transmission frequency so that we generally obtain a double peaked electrical response. By correctly choosing the gap between the two modes resonant frequencies (this gap depends on the characteristic transverse dimension W_0 and is easily calculated), a flat top transfer function is obtained.

So, such a multimoded resonator can be used to design flat-top bandpass filters without the use of coupling mechanism between two identical a.s.w. resonators as it is usually done.

Figure (7) gives the result of a preliminary experiment illustrating this possibility. The double peaked response is clearly visible but important losses are present and the two successive transverse resonances are too much distant in frequency. We hope that these troubles will be removed by much care in transducers design and also in resonator geometry. We are working now in that way and in testing higher order Hermite-Gaussian modes resonances in "parabolic" a.s.w. resonators.

Conclusion.

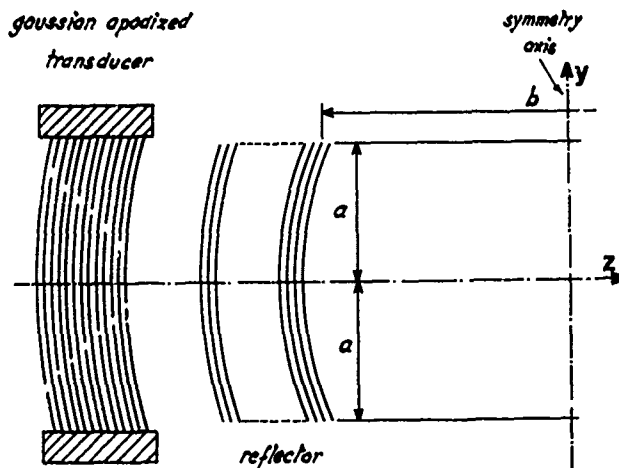
A.s.w. resonators with Hermite-Gaussian transverse modes have been described and successfully tested. They have some potential advantages compared with plane-parallel configuration. Preliminary results on transversely multimoded resonators indicate the possibility of designing flat top bandpass resonators filters without the use of coupling mechanism between two resonators.

Acknowledgements.

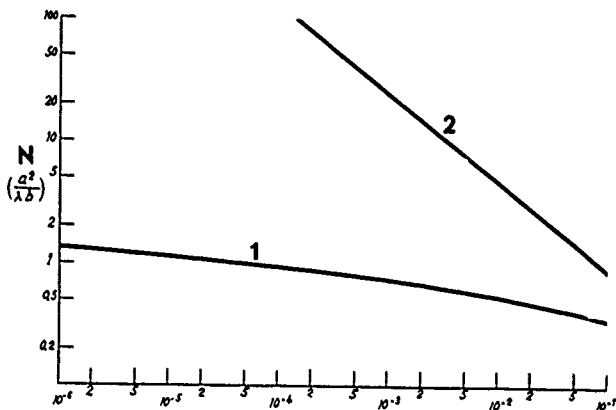
The authors would like to thank Mr Favennec for supplying etched gratings, Mme Duchenois and Mr Devinat for crystal-transducers fabrication, Mme Feuillade, Mr Sainson and Mlle Baud for paper preparation.

References

1. H.A. Haus : "Modes in S.A.W. grating resonators". J.Appl. Phys. 48 (12) December 1977.
2. L.A. Coldren, H.A. Haus and K.L. Wang : "Experimental verification of mode shape in S.A.W. grating resonators". Electronics Letters Vol.13 n°21 13th October 1977.
3. See for example : I.M. Mason and E.A. Ash : "A.S.W. beam diffraction on anisotropic substrates". J.Appl.Phys.42, 5343-5351 (1971).
4. A.G. Fox and Tingye Li : "Resonant modes in a maser interferometer". Bell Syst. Tech. Journal. March 1961.
5. G.D. Boyd and J.P. Gordon : "Confocal multimode resonator for millimeter through optical wavelength masers". Bell Syst. Techn. Journal. March 1961.



Geometry of a SAW resonator supporting transverse gaussian modes. Fig.1



Diffraction losses for confocal (1) and plane parallel (2) resonator **Fig. 2**

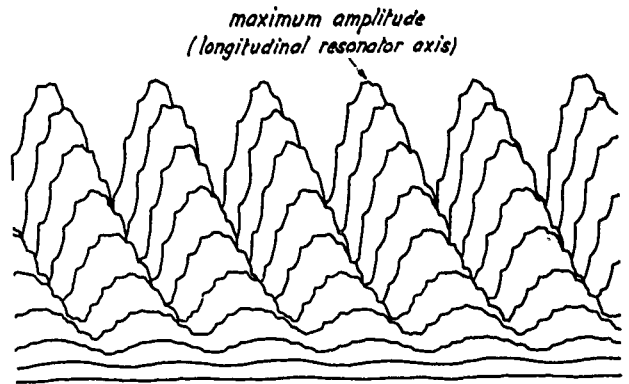
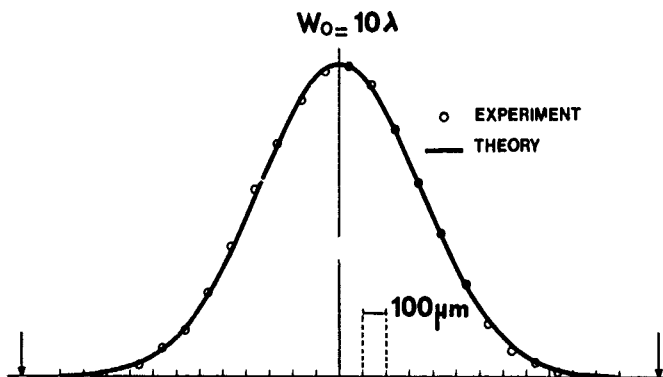
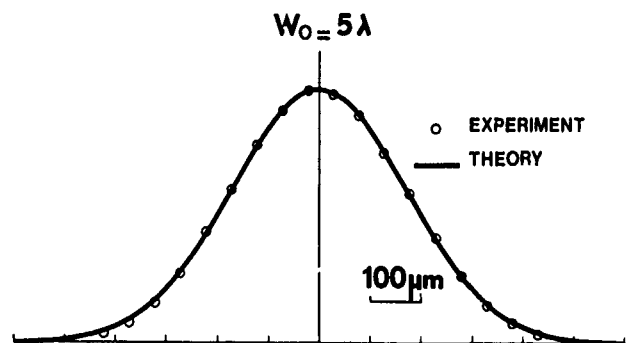


Fig 3 Experimental standing wave pattern inside a S.A.W. resonator supporting transverse gaussian mode $W_0 = 10 \lambda$. 50 μm between successive longitudinal scan lines



Transverse amplitude profile at resonator center $W_0 = 10 \lambda$ **Fig. 4**



Transverse amplitude profile at resonator center $W_0 = 5 \lambda$ **Fig. 5**

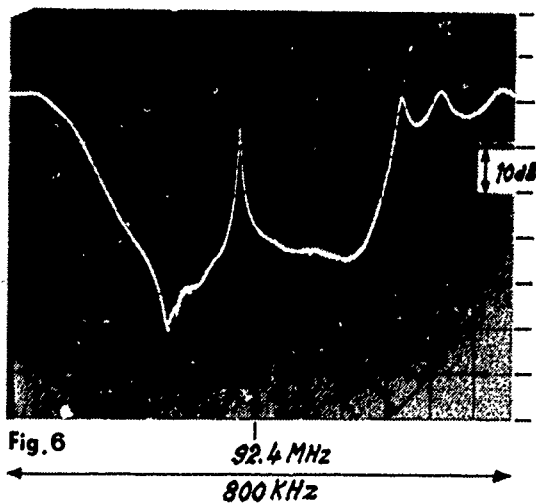


Fig. 6
TRANSFER FUNCTION OF PARABOLIC
A.S.W. RESONATOR
 $W_0 = 5 \lambda$. $Q \geq 30,000$

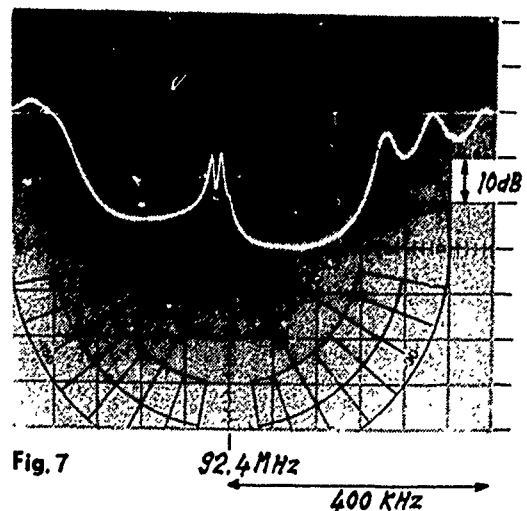


Fig. 7
TRANSFER FUNCTION OF RESONATOR
WITH TWO TRANSVERSE MODES

SAW RESONATOR 2-POLE FILTERS

E.J. Staples, J. Wise, J.S. Schoenwald, and T.C. Lim

Rockwell International Corporation
Thousand Oaks, California 91360

Summary

Multipole crystal filter technology performs a uniquely accurate filtering function in RF communications systems. Described in this paper is a type of coupled crystal resonator or monolithic crystal filter using surface acoustic wave (SAW) resonators. Design and fabrication of 2-pole filters with insertion loss less than 3 dB, pass-band ripple less than 0.2 dB, and a 0.07% bandwidth at 173.91 MHz are described.

Low loss, narrowband multipole crystal filters in the VHF-UHF range will allow signal processing normally performed at lower frequencies to be done at much higher frequencies. Because the SAW crystal is a "chip" component, these filters are well suited to hybrid microelectronics manufacturing methods.

1.0 Introduction

Associated with modern RF communications systems is the need to perform complex signal processing. Multipole crystal filter technology performs a uniquely accurate filtering function in these systems. The monolithic crystal filter building block is the 2-pole section depicted in Fig. 1. A classical "bulk" coupled resonator is achieved by coupling two thickness-mode resonances on the same quartz blank. Frequency is determined by the blank thickness and coupling is controlled

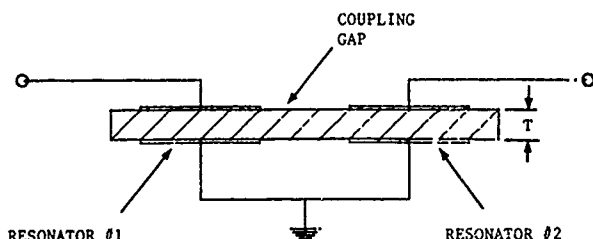


Fig. 1 Bulk wave, monolithic 2-pole crystal filter.

by the proximity of the resonators and their electrode thickness. These types of filters have become common components in intermediate (IF) signal processing at 10.7 and 22.4 MHz. As the frequency of operation goes beyond 30 MHz, the bulk wave

filters must be designed on harmonics of the crystal because the thickness of the quartz blank becomes prohibitively small for low cost and high yield fabrication methods to be used.

Described in this paper is a type of coupled crystal resonator or monolithic crystal filter using surface acoustic wave (SAW) resonators.^{1,2} The SAW crystal frequency is independent of blank frequency and SAW resonator structures, both one and two-port as shown in Fig. 2, can be fabricated at frequencies up to 1 GHz and more.³ In order to achieve a two pole filter response two crystals must be coupled together using an LC network to control the coupling. However, by placing a periodic grating between the transducers of two-port structure, as shown in Fig. 3, a two pole filter response can be achieved using only one crystal. This type of crystal uses in-line or longitudinal elastic coupling between resonant SAW cavities formed by the reflective gratings.

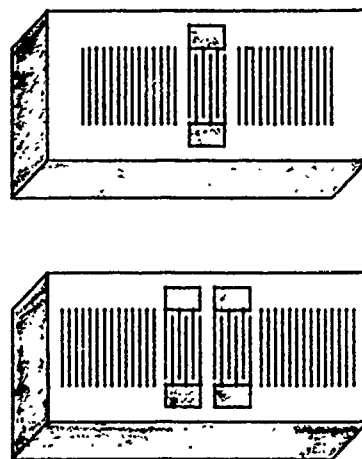


Fig. 2 One and two-port SAW resonator structures.

2.0 2-Pole Crystal Fabrication

The electrode structure of the SAW 2-pole crystal contained three periodic grating arrays with 400, 175, and 400 lines respectively. The three gratings had lines 130 wavelengths long and a line to gap ratio of 1.3. Experimentally this

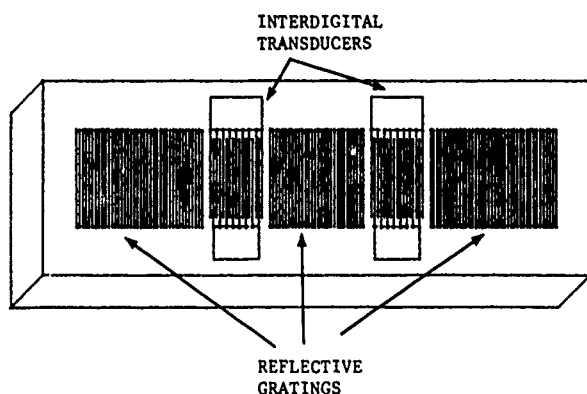


Fig. 3 In-line coupled SAW monolithic 2-pole crystal filter.

value of λ/g was found to give maximum Q. This is supportive of the theory of reflective arrays proposed by Wright and Haus.⁴

Two 40 wavelength (40 finger-pair) transducers were symmetrically placed within 42.75 wavelength gaps separating the reflective arrays. The transducers were apodized with a cosine (10% pedestal) amplitude weighting to reduce spurious mode generation. The periodicity of the gratings was slightly larger (0.5%) than the interdigital transducers, nominally 0.05 millimeters, for a final operating frequency of 173.91 MHz on ST-quartz.

The fabrication process is depicted in Fig. 4. After delineating the electrode pattern in a Cr-Al film (50Å and 1000Å), RF probing was used to measure the device unmatched bandpass filter response. RF probing provided a convenient and practical method of monitoring each process step following metalization. Shown in Fig. 5 is a typical filter response relative to the design frequency. Because of the dispersion in the electrode design, the periodic reflectors show a weak stopband 0.5% above F_0 .

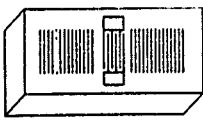
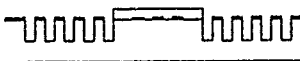

- | | |
|---|---|
| 1. METALIZATION - MASK #1 (+) | 7. SAW INTO CHIPS |
| 2. RF - PROBE - PROCESS CHARACTERIZATION |  |
| 3. TRANSDUCER PROTECT - MASK #2 (-Y+) | 8. RF-PROBE (SORT) |
| 4. PLASMA ETCH (BATCH) | 9. MOUNT AND CALIBRATE |
|  |  |
| 5a. STRIP METALIZATION | 10. SEAL |
| 5b. STRIP RESIST | 11. PRE-AGING TEST |
| 6. RF PROBE - PROCESS CHARACTERIZATION | 12. AGING |
| | 13. FINAL TEST |

Fig. 4 Fabrication process for SAW resonators.

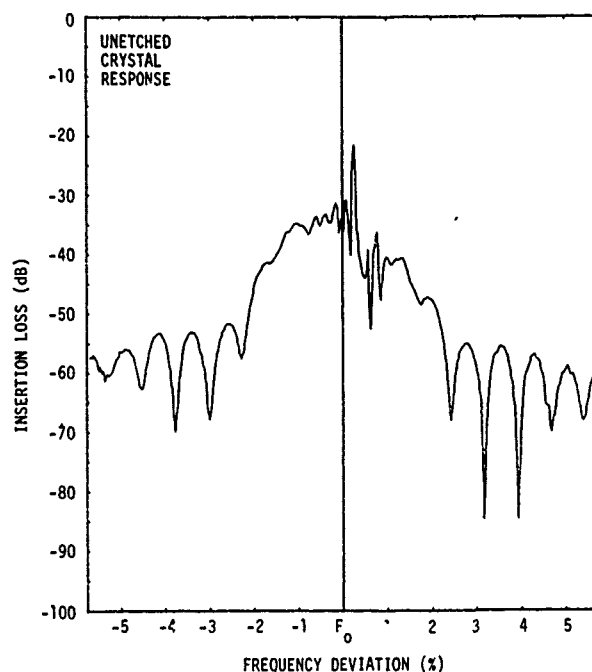


Fig. 5 Unetched and unmatched 2-pole filter response.

A second photomask is used to pattern photoresist with windows over the reflecting arrays. The resist is used to protect the transducer electrodes during the next step, a reactive parallel plate plasma etch in CF_4 and 5% O_2 . Quartz grooves are anisotropically etched between the Al lines in the reflectors. Etch selectivity between the quartz and the aluminum in this plasma is 10:1. The quartz was etched to a depth of 2500Å.

After etching the quartz, the metalization in the reflectors and photoresist was removed and the wafer again RF probed. Shown in Fig. 6 is the unmatched filter response after etching. Due to the dispersion as a result of energy storage in the reflector grooves,⁴ the reflective array stopbands are now centered about the design frequency as shown. In Fig. 7 an expanded plot of the coupled 2-pole crystal filter response is shown. The small ripples in the passband are due to spurious transverse modes not completely suppressed by the transducer apodization.

After probing, the wafers were diced into chips approximately 7.5 x 2.5 mm. The chips were mounted to a 16 pin dual in-line header as shown in Fig. 8 using polyimide epoxy⁵ and then gold leads were thermocompression bonded. The crystals were calibrated using a low power CF_4 plasma etch immediately prior to sealing under vacuum in a capacitively discharged resistance welder. Calibration was done such that the center frequency was equal to the frequency of the second transverse mode as shown in Fig. 7, and this provided a response which was optimal for a $\pm 75^\circ C$

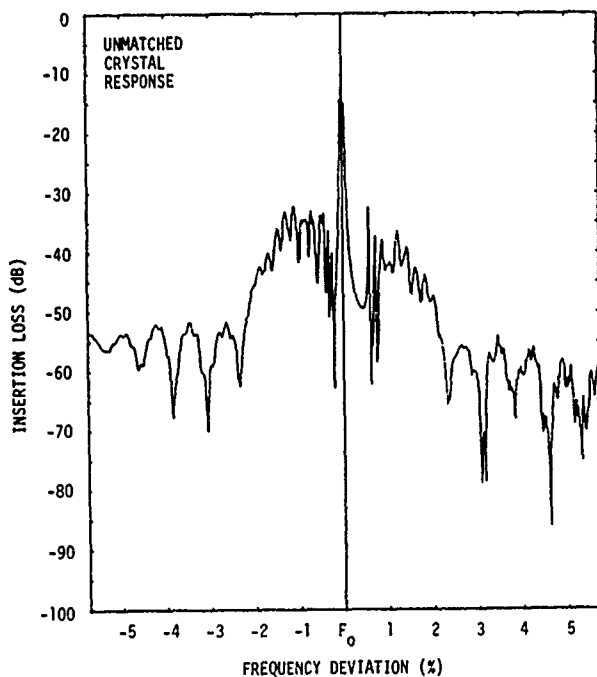


Fig. 6 Unmatched crystal filter response after plasma etching.

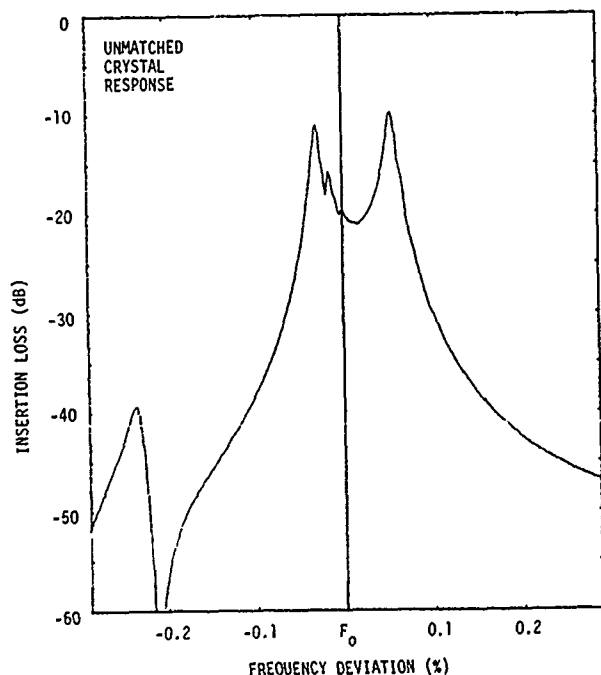


Fig. 7 Expanded filter response showing mode coupling.

temperature excursion about the crystal turning point temperature.



Fig. 8 16-pin, dual-in-line crystal package used for filters.

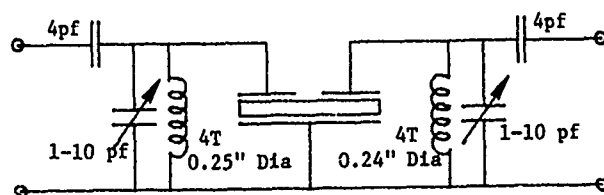


Fig. 9 Electrical matching circuit used for 2-pole filters.

3.0 Matched 2-Pole Filter

To obtain a maximally flat bandpass filter response the 2-pole crystal was matched to its characteristic impedance, typically 200 ohms, using the LC transformers shown in Fig. 9. The shunt inductors were tuned using capacitive trimmers to give zero input/output reactance at the center frequency of the filter. The series capacitor was selected to give the correct transformed impedance ratio, 4:1 for a 50 ohm output. Shown in Fig. 10 is a typical tuned filter response. The 3 dB bandwidth is approximately 0.07% or 122 kHz at 173.91 MHz, and the insertion loss was 3 dB maximum. Approximately 1 to 2 dB of loss was found to be in the matching networks, primarily in inductive losses.

Out-of-band rejection for the 2-pole filter was limited by direct electrical and elastic feedthru. For frequencies close to the passband, $\pm 1\%$, the feedthru was elastic and resulted from relatively wideband transducer to transducer delay line transmission. Beyond $\pm 2\%$ the feedthru was electrical in nature and nominally -50 dB per 2-pole section.

The phase response of two separate crystal filters is shown in Fig. 11 and was linear with a negative slope of -1.5 deg/kHz.

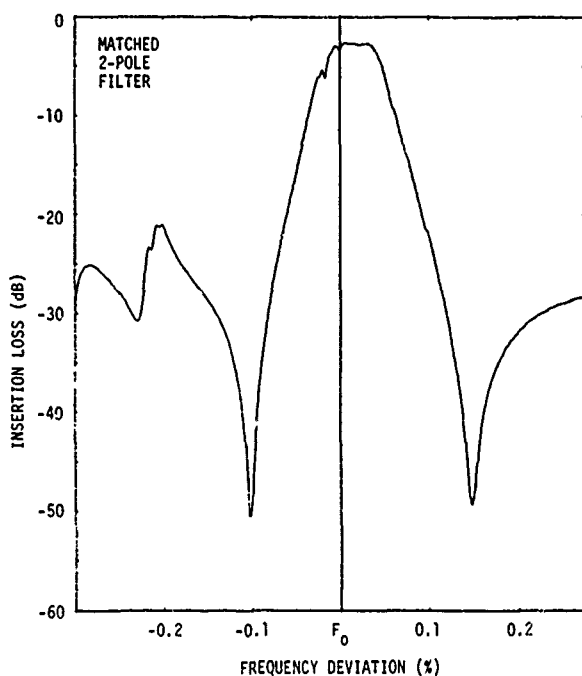


Fig. 10 Electrically tuned 2-pole filter response.

Repeatability and uniformity of batch processed and calibrated filter chips is evident in Fig. 11, and in Fig. 12 the phase difference over the passband of the two filters is shown. Phase tracking between filter pairs was typically ± 2.5 over a 50 kHz information bandwidth as shown in Fig. 12.

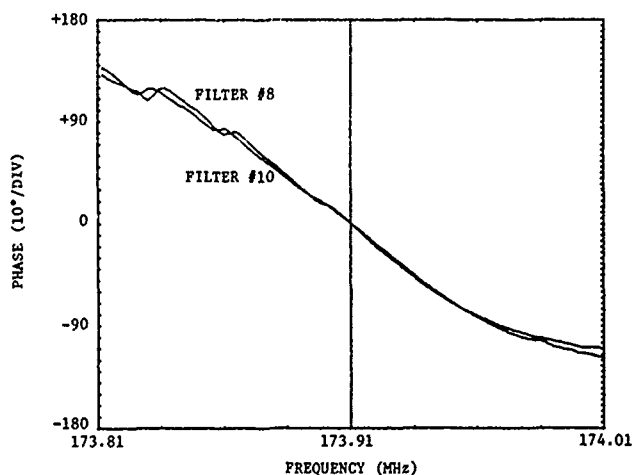


Fig. 11 Phase response for two, 2-pole, crystal filters.

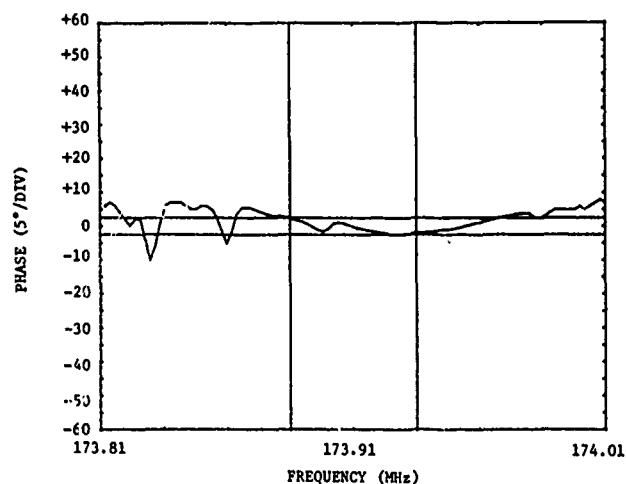


Fig. 12 Phase tracking for two, 2-pole crystal filters.

4.0 Discussion of Results

2-Pole monolithic crystal filters using surface acoustic waves have been demonstrated which had insertion losses less than 3 dB at 173.91 MHz. These crystal filters are "chip" mounted and compatible with standard RF hybrid manufacturing techniques. Bandwidths of the experimental filters were typically 0.07%.

Controlling the number of grooves and the groove depth in the center reflective array of the electrode pattern provides a convenient design method for filter bandwidths 0.01 to 0.15%.

The 2-pole crystal filter is the basic building block for filters with more than two poles of selectivity. Although involving more than just cascading 2-pole lattice sections,⁶ the design techniques are well known and are not presented here. The procedure is to adjust the coupling between lattice sections electrically. The main limitation on the number of poles of selectivity that can be achieved is the SAW resonator Q. Functional dependence is commonly described in terms of resonator Q normalized to the Q of the filter being synthesized. For example assuming an individual resonator Q of 25,000 and a filter bandwidth of 1000 ppm, the normalized resonator Q would be 25. Using multipole filter design tables⁷ with a 0.1 dB passband ripple, and information on the maximum achievable resonator Q as a function of frequency,⁸ the minimum filter bandwidth as a function of frequency with the number of poles as a parameter is shown in Fig. 13.

The absolute minimum bandwidth (dotted line) is arbitrarily selected as 100 ppm because this is the amount of temperature instability associated

with ST-cut crystals over a nominal 125°C temperature range. These design curves show that an 8-pole SAW multipole filter may be fabricated at 150 MHz with a minimum 400 ppm bandwidth or 60 kHz.

In summary, surface acoustic wave structures with responses similar to monolithic "bulk" crystal filters have been achieved which show extremely low insertion loss in the VHF-UHF range, typically 1 - 3 dB. Applications for these filters include the following: front-end filters for single channel receivers, image rejection filters for mixer outputs in frequency translators, and in oscillator or multiplier chain output sections.

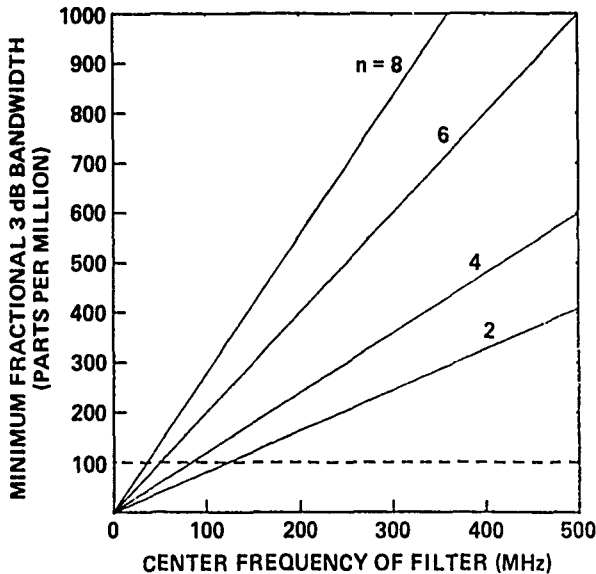


Fig. 13 Minimum achievable 3 dB bandwidth for multipole crystal filters with 0.1 dB ripple.

The availability of low loss, narrowband 8-pole crystal filters in the UHF range will enable RF signal processing normally performed at lower frequencies to be done at much higher frequencies. Because the SAW crystal is a "chip" component, these types of filters are well suited to hybrid microelectronics fabrication methods.

References

1. E.J. Staples and R.C. Smythe, "SAW Resonators and Coupled Resonator Filters," Proceedings of the 30th Annual Symposium on Frequency Control, Atlantic City, June 1976, p. 322-7.
2. J.S. Schoenwald, "Tunable Variable Bandwidth/Frequency SAW Resonators," Proceedings of the 31st Annual Frequency Control Symposium, Atlantic City, N.J., p. 240-5.
3. W.J. Tanski, "UHF SAW Resonators and Applications," Proceedings of the 34th Annual Symposium on Frequency Control, May 1980 (this issue).
4. P.V. Wright and H.A. Haus, "Theoretical Analysis of Second-Order Effects in Surface-Wave Gratings," Proceedings of the 34th Annual Symposium on Frequency Control, May 1980 (this issue).
5. J.R. Vig, J.W. LeBus, and R.I. Filler, "Further Results on UV Cleaning and Ni Electro-bonding," Proceedings of the 29th Annual Frequency Control Symposium, Atlantic City, N.J., p. 220-9.
6. E.J. Staples, J.S. Schoenwald, J. Wise, and T.C. Lim, "Low Loss Multipole SAW Resonator Filters," IEEE International Microwave Symposium Digest, May 1980, Washington, D.C., pp. 34-6, IEEE Catalog No. 80CH1545-3 MTT.
7. A.I. Zverev, Handbook of Filter Synthesis, John Wiley and Sons, New York, 1967.
8. R.C. Li, J.A. Slusow, and R.C. Williamson, "Experimental Exploration of the Limits of Achievable Q of Grooved Surface Wave Resonators," Proc. 1975 Ultrasonics Symposium, pp. 279-283, IEEE Cat No. 75CHO 994-4SU.

*Available from Electronic Industries Association, Washington, D.C.

UHF SAW RESONATORS AND APPLICATIONS

William J. Tanski

Sperry Research Center
Sudbury, MA 01776Abstract

Surface acoustic wave (SAW) resonators suitable for systems applications are being produced in our laboratory at frequencies as high as 1.43 GHz. These two-port single-pole devices, which have distortionless response characteristics and high Q values [$Q_u \geq 10,400/F(\text{GHz})$] may be used to stabilize UHF oscillators or as narrowband filters. These resonators have the advantages of small size, low matched insertion loss ($\approx 3\text{dB}$ at 1 GHz), and relatively high input power levels ($\approx 15\text{dBm}$). Design techniques used to eliminate distortions and reduce losses, and the fabrication steps used to produce devices with linewidths down to 0.55 microns, are outlined.

Resonators are currently in production, or are under development, in our laboratory for use in a radar system test set oscillator (at 840 MHz) and as a frequency source noise suppression filter (at 500 MHz). These devices and the applications are described and resonators are seen to contribute significantly to the reduction in size, complexity and power consumption of UHF sub-systems. Phase locking a UHF SAW oscillator to a low frequency bulk mode source is also discussed as a method of obtaining optimum UHF source performance.

Introduction

The single-pole SAW resonator has been developed to the extent that the systems designer now has available a class of high Q devices at frequencies far above those of bulk mode crystal resonators. Resonators have been fabricated at frequencies in excess of 1.4 GHz, with unloaded Q values approaching or exceeding the published material limits, and with distortionless response characteristics. These devices offer the advantages of small size, relatively high power handling capacity, linear phase characteristics, and the potential for a substantial reduction in sub-system complexity, weight, and power consumption.

In this report we shall discuss the characteristics of state-of-the-art two-port SAW resonators being produced in our laboratory, the design and fabrication techniques used to attain low-loss distortion-free characteristics, and two applications of these devices in UHF frequency sources. Aspects of resonator performance requiring further development are also summarized.

Two-Port Resonator Characteristics and Uses

At present we can reliably produce SAW resonators at frequencies up to 1.43 GHz on quartz. This upper limit is set by the availability of good quality photolithographic masks with linewidths down to 0.55 microns. The lower frequency limit is about 100 MHz which is due to the large device size (>2 inches in length) at or below this frequency. The maximum possible unloaded Q values are determined by the inherent material losses due to viscosity. The published¹ value (measured at 1 GHz) of surface wave attenuation for the ST-cut of quartz (42.75° rotated Y) results in an expected unloaded Q value given by: $Q_u = 10,400/F(\text{GHz})$. In Fig. 1 we show the expected Q_u and the maximum unloaded Q 's of four two-port SAW resonator designs. This data is summarized in Table 1 below.

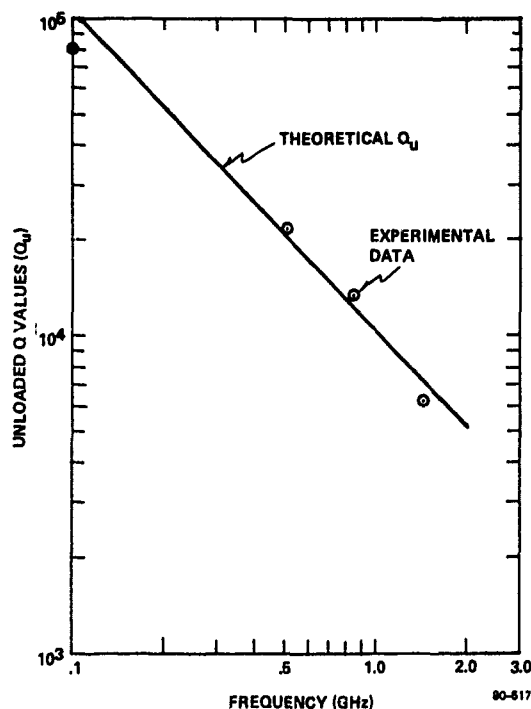


Fig. 1 Predicted and experimental values of unloaded Q for two-port SAW resonators.

Table 1

Frequency (MHz)	Expected Max: Q_{um}	Experimental: Q_{uE}	Q_{uE}/Q_{um}
98.5	105,500	80,500	.76
500	20,800	22,050	1.06
840	12,400	13,900	1.12
1430	7,370	6,080	.84

From these data one can see that improvements are necessary at the low and high end of the frequency range, but that the expected values of Q_u are lower than those actually obtained in the UHF frequency range. We conclude that the quartz we use is lower loss than that on which the published¹ attenuation data were taken.

Narrow and wideband views of the frequency response of a two-port SAW resonator filter operating at 1.43 GHz are shown in Fig. 2. The 3dB bandwidth was 280 KHz measured in a 50 Ω system, electrically unmatched, in air. The associated Q values are: Q_L = 5100 (loaded in air), Q_V = 5750 (loaded in vacuum) and Q_u = 6080 (unloaded). The unloaded Q is about 84% of the reported material limit of 7370 at this frequency. The resonance is seen to be free of distortions and unwanted resonances and the out-of-band rejection is about 28 dB. The ripple off-resonance has been suppressed to a relatively low level by withdrawal weighting the reflectors². The photograph in Fig. 3 shows a 1.43 GHz resonator mounted in a T0-5 header where a 1 cm line is given for comparison.

The response of a 500 MHz two-port resonator designed to be a frequency source noise suppression filter is shown in Fig. 4. This response is also seen to be symmetric with no unwanted resonance modes. The electrically matched response is given in section (a) with a loss level of 1.9 dB. The matched Q is 2500, and the off-resonance peak-to-peak ripple is about 1 dB. This low value of ripple has been achieved using a new type of reflector utilizing withdrawal weighting and segmented lines. The unmatched response with a loss of 12.6 dB, and a Q = 10,000 is shown in Fig. 4(b).

In actual operation, the input power level to the 500 MHz devices will be +15 dBm. SAW resonators at 840 MHz are presently being used in a radar system oscillator with an input power level of +14 dBm, and for these devices response degradation did not occur until the input power approached +30 dBm. These results demonstrate that SAW resonators can be operated at relatively high input power, a fact which will allow lowered noise levels in SAW resonator stabilized oscillators, for example.

The device size is typically 1600λ long and 50λ (plus two connecting pad widths) wide. At 800 MHz, for example where the wavelength, λ , is about 4 microns, a device substrate is about 6 mm long by 1 mm wide. This small size at UHF frequencies makes SAW resonators very attractive for applications where space and weight must be reduced. In addition, the high power handling capacity and

relatively low matched loss (<3dB) permits further reductions in component count as compared with SAW delay line filters.

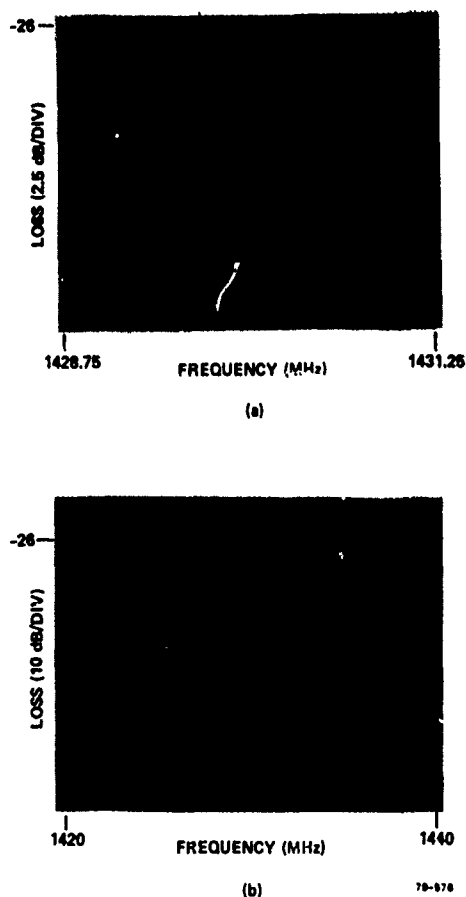


Fig. 2 Frequency response of a 1.43 GHz two-port SAW resonator. The narrow-band view covering 3.5 MHz about resonance is shown in (a) and a wideband view covering 40 MHz is in (b). The unloaded Q is about 6100 or 84% of the maximum expected value.

The temperature coefficient of frequency for the ST and related cuts of quartz is zero to first order, but they have second order frequency changes given by $\Delta F/F_0 \approx 30 \times 10^{-9} (T-T_0)^2$ where T is in $^{\circ}\text{C}$, and T_0 depends on the exact cut angle. For the ST cut, an unmetallized surface has $T_0 = 20^{\circ}\text{C}$, but this decreases by 10°C or so when interdigital electrode transducers are placed on the surface. Other cuts of quartz, some doubly rotated, have been found³ with second order coefficients as low as 17×10^{-9} but most have non-zero power flow angles, or lower electroacoustic coupling coefficients. These cuts, particularly the 23° rotated Y cut (propagation at 41° from the x axis), deserve experimental investigation, however, as a possibility for improved temperature performance. Surface waves have also been predicted⁴ to have a zero first order

temperature coefficient of frequency on the SC cut (Euler angles 22.4° , 34.3° , 0°) with propagation at -15° from the X_1 direction.

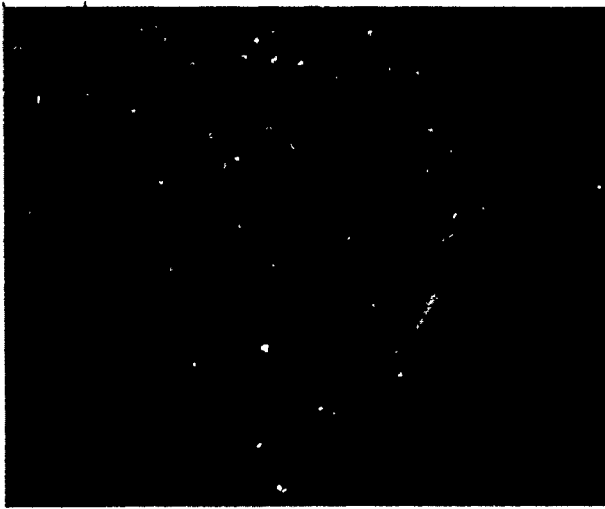


Fig. 3 Photograph of a 1.43 GHz SAW resonator in a TO-5 header.

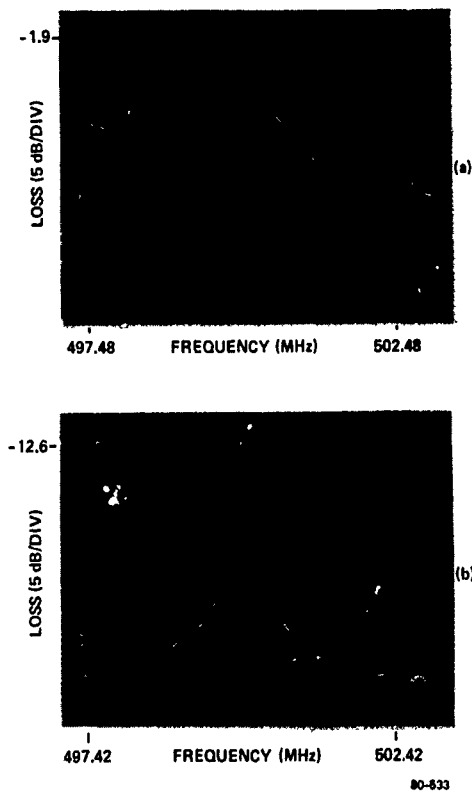


Fig. 4 Frequency response of a 500 MHz two-port SAW resonator. The electrically matched loss level, shown in (a), is 1.9 dB with a loaded Q of 2500. In section (b) the unmatched response is given where the loss is 12.6 dB and the Q is 10,600.

The aging characteristics of UHF SAW resonators have not been investigated thus far to our knowledge. Investigations⁵ at 160 MHz show that, with good packaging techniques, aging rates on the order of 0.5×10^{-9} /day can be achieved. Thus, in the UHF range, aging rates on the order of 1 to 2×10^{-9} /day should be achievable using currently available packaging methods.

Multipole filters may also be made using SAW resonators and a number of coupling schemes have been investigated⁶. We have made two-pole resonator filters, by cascading single-pole 500 MHz two-port devices, which have 5dB loss and in excess of 50 dB out-of-band rejection. We plan further work in the development of UHF multipole resonator filters.

Resonator Design

A single-pole SAW resonator utilizes two distributed-grating surface wave reflectors forming a resonant cavity. The cavity may contain either one or two interdigital transducers. These elements which are fabricated on the highly polished surface of a piezoelectric plate, are shown diagrammatically in Fig. 5 (a) for a two-port device. Distributed-grating-reflectors, consisting of long arrays of

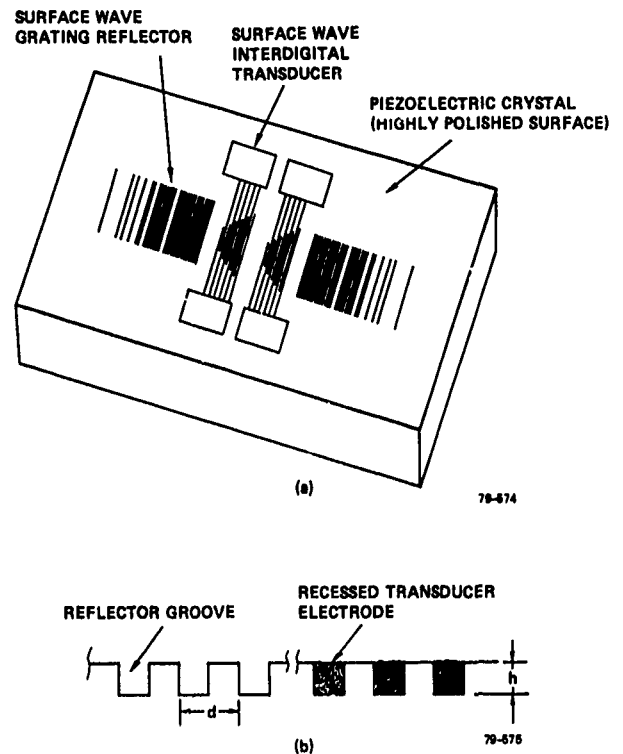


Fig. 5 (a) Diagram of a two-port SAW resonator showing overlap weighted transducers and withdrawal weighted reflectors, and (b) a section view of the recessed-aluminum-transducer/etched-groove-reflector configuration used to fabricate UHF devices.

lightly reflecting elements, are used since they are the only low loss surface wave reflectors known. Reflectors must be long enough to reflect most of the incident energy, they should be weighted to reduce reflection-side-lobes, spaced to allow only one symmetric, resonance mode (the reflector stopband width is about 0.5%) and of such a nature as to reduce scattering losses and minimize aging. In order to meet these requirements we have chosen to use reflectors consisting of grooves etched into the substrate surface which are on the order of $.01 \lambda_0$ deep, where λ_0 is twice the groove period (d) shown in Fig. 5 (b). Design data for uniform and withdrawal weighted reflectors has been presented previously^{2,7}. The best results, experimentally², using withdrawal weighting was a peak-to-peak ripple level of about 2 dB; down from about 8 dB for uniform reflectors. To further reduce the off resonance ripple we have developed a reflector which is withdrawal weighted in lightly weighted sections (high reflectivity per unit length) and weighted with segmented lines^{8,9} where weighting is heaviest (low reflectivity). This combined type of reflector, shown schematically in Fig. 6, allows an experimental reduction of off-resonance ripple to 1 dB or less, while permitting reduced photolithographic mask costs compared to the costs of a mask with purely segmented-line reflectors. The combined type reflector may also be used to reduce mask costs in devices such as reflective array filters¹⁰ and compressors, which require right angle reflections.

The surface wave transducers used for UHF devices are of the recessed-aluminum configuration¹¹ of Fig. 5(b) with overlap weighting¹² to eliminate higher order transverse mode distortions. The recessed-transducer configuration has very low surface wave reflectivity (the reflectivity of other configurations will either cause distortions¹³ or result in reduced electro-acoustic-coupling¹⁴) allowing an undistorted response with maximum coupling, and the configuration is compatible with straight-forward fabrication procedures. The transducer electrode period is the same as that of the reflectors, and the electrodes are positioned so as to have their centers on the peak of the voltage standing-wave pattern in the cavity. For grooved reflectors on quartz, the electrode centers must be an integer number of half-wavelengths ($M\lambda_0/2$) from the inside edge of a reflector.

A knowledge of the three surface wave velocities involved in the device (free surface: $v_s = 3157.8$; the velocity in the transducers; and that in the reflectors) is required to properly design a SAW resonator. We have experimentally determined⁷ how these latter two velocities vary with etch depth or metal thickness and the velocity reduction from the free surface value is in the range of 0.1 to 0.3%. Typical parameters for two-port UHF devices are: reflector length $750\lambda_0$ (for a cosine weighting), transducer length $\approx 30\lambda_0$, cavity length (edge to edge) $\approx 75\lambda_0$, etch depth $\approx .01\lambda_0$ ($.015\lambda_0$ at 1.4 GHz), and acoustic aperture $\approx 50\lambda_0$. In general shallower grooves, percentage-wise, allow longer cavities with no additional longitudinal modes. As a guide, the edge-to-edge

length should be less than twice the distance from the reflector edge to the effective center of reflection.

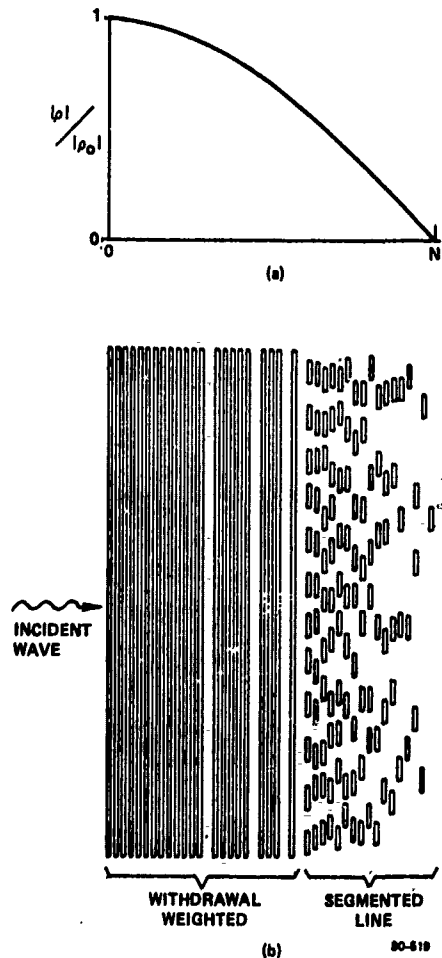


Fig. 6 Schematic diagram of combined type (withdrawal-weighted-plus segmented lines) reflector (b), for a given relative reflectivity distribution (a). This type of reflector permits devices to be fabricated with off-resonance peak-to-peak ripple levels of 1 dB or less.

The resonator design data is utilized by computer routines that develop and place on magnetic tape the digitizing instructions required for an optical pattern generator, such as the Electromask 2000¹⁵. A 10X reticle is produced that is used to make the low reflectivity chrome master containing an array of patterns at 1X. Utilizing masks such as shown in Fig. 7, we have produced as many as 12 UHF devices on a substrate, which was subsequently diced.



Fig. 7 Photograph of a portion of a chrome photolithographic mask with an array of two resonators plus reflector exposure blocks. Masks with 4 to 6 such patterns are used depending on device frequency.

Resonator Fabrication

We fabricate resonators using optical contact printing to replicate the mask pattern on a photoresist coated substrate, and ion beam etching to form the reflector grooves and transducer recesses. We are able to obtain good quality masks with linewidths down to 0.55 microns from our corporate mask-making facility. These masks are replicated by ensuring intimate mask-substrate contact. Our procedures are effective in good measure because the total pattern area is small; not more than 15 x 15 mm for an array of 6 patterns at 800 MHz. Further, it has been recognized¹⁶ that contact printing will allow replication of patterns with linewidths below 0.4 μ m, the lower limit depending on the wavelength of light used. Replication is performed in a conventional mask aligner with a standard ultraviolet light source having a peak intensity at about 3500 Å.

The quartz substrates are synthetic and have a standard "surface wave" finish but are specified to contain no crystallographic growth zone boundaries. The photoresist used is Shipley¹⁷ AZ-1350 spun onto a thickness of about 8000 Å. The remainder of the fabrication process is given in detail in Ref. 13 and only the salient features are reported here. The entire array of resonator patterns is exposed into the photoresist which is then developed. The entire pattern is then ion-beam etched to the desired depth. This form of etching is used because of the high degree of control and repeatability possible. We have found, however, that small variations in etch depth, on

the order of 5 to 8%, have little effect on the resonance frequency since it is the cavity length which is the primary factor in setting the frequency. The entire pattern is then metalized, with about 100 Å of chromium for adhesion plus enough aluminum to fill the etched grooves. Note that the reflectors, as well as transducer grooves, are metalized. The lift-off technique is then employed to leave a clear substrate with metal filled grooves. The substrate is then coated with resist a second time and only the reflector sections are exposed using the exposure blocks seen in Fig. 7. Following resist development, the metal in the reflector grooves is chemically etched away, the remaining resist is washed off, and the substrate is diced.

To insure maximum Q and minimal aging rates, SAW resonators must be packaged in a vacuum and in an ultra-clean manner similar to the schemes currently employed for bulk acoustic mode resonators. The objectives in packaging are to minimize contamination of the surface, particularly by carbonaceous materials, and to mount the substrate so as to minimize strains and effects of shock and vibration. Surface contamination is a potentially more serious problem with SAW resonators, than with bulk devices, since the entire active surface is exposed, and most of the surface wave energy is confined to within about two wavelengths of the surface. Strains developed in mounting will relax with time leading to increased aging and these must be made as small as possible initially. However, since only a portion of one surface of the substrate contains surface wave energy, the possibility exists for mounting schemes which are different than bulk mode resonators. One mounting scheme is shown in Ref. 5, in which the substrate is held above the header surface by several mounting clips, and the lid is welded on in an ultra-high vacuum. A second possibility, which is under evaluation and is described in detail in Ref. 18, is that of using an all quartz system consisting of a base (on which the SAW device is placed), a spacer ring, and a lid all bonded using a glass frit. A third possibility, suitable in certain applications, is that of bonding the substrate, on one end only, to the flatpack, or T0-8 type header, base.

Applications

An 840 MHz two-port SAW resonator filter is being manufactured for use as the oscillator stabilizing element in a Sperry radar system test set. The device specifications required a center frequency of $840 \pm .126$ MHz, a linear-monotonic phase shift between the -3 dB points, a maximum 3.5 dB loss and a minimum Q of 1000 when electrically matched. In excess of 100 such devices are required. The devices being produced meet or exceed the required specifications, and the salient device performance characteristics, when sealed in dry nitrogen at atmospheric pressure, are listed in Table 2.

Table 2

840 MHz SAW Resonator Performance

	Best	Typical
Matched loss	2.4 dB	2.8 dB
Matched Q	2000	1500
Rejection level	18 dB down	16 dB down
Unloaded Q (vacuum)	13,900	12,000
Input power (continuous)	>+14 dBm	

The frequency response of a typical 840 MHz resonator is given in Fig. 8 where both narrow and wide-band views are shown. The matched insertion loss is 2.5 dB and the loaded Q is 1500. The large amplitude ripple off-resonance exists because weighted reflectors were not used in this design.

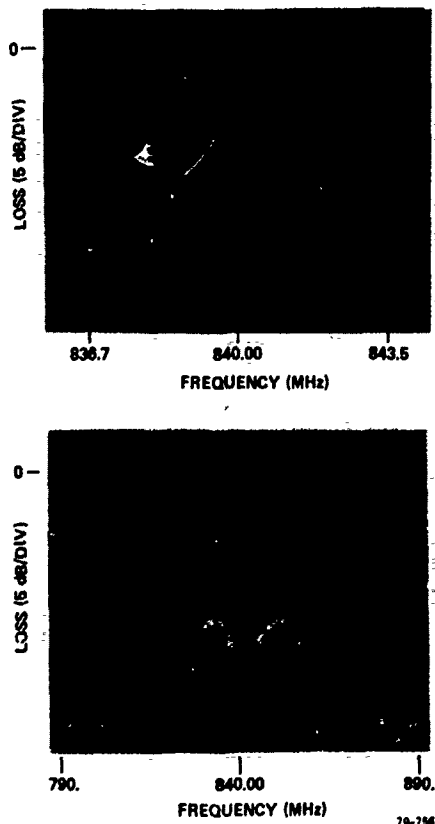


Fig. 8 Frequency response of an electrically matched 840 MHz two-port SAW resonator being used to stabilize a radar system test set oscillator. The minimum loss is 2.5 dB with a loaded Q of 1500.

The oscillator schematic diagram is given in Fig. 9, in which only the transistor biasing network is omitted. A photograph of the oscillator assembly¹⁹ is shown in Fig. 10, where the resonator is in the 3/8" (square) flatpack. The SAW oscillator has effected an order of magnitude reduction in volume (19 in³ for the unit being replaced vs 1.7 in³ for the SAW oscillator), a deletion of one power supply, and a reduction in power consumption by a factor of 6. Also, this SAW oscillator delivers +26 dBm output power, while utilizing a single RF transistor, and so may be considered a source of 840 MHz power and not simply a signal source. The resonator operates with an input power of +14 dBm, and the single side-band noise-to-carrier ratio at 10 KHz offset from the carrier is less than -130 dBc. Further details of the oscillator performance are presented in Ref. 20.

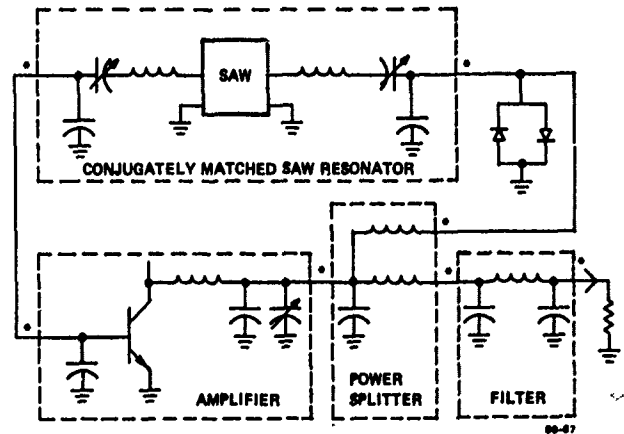


Fig. 9 840 MHz SAW oscillator schematic diagram including matching networks.

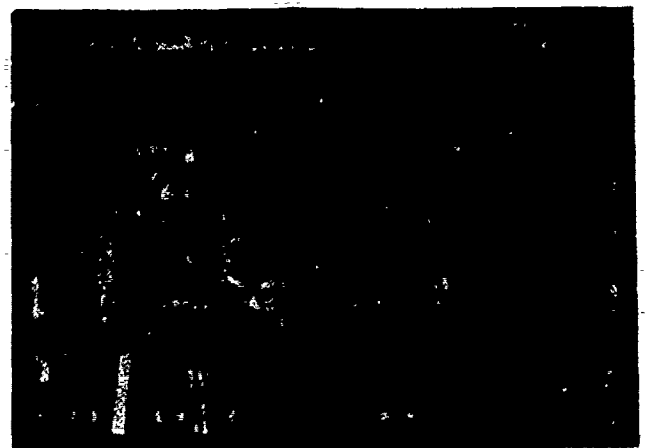


Fig. 10 Photograph of an 840 MHz SAW resonator stabilized oscillator assembly. The resonator is in the 3/8" square flatpack.

A 500 MHz resonator has been designed for use as the noise suppression filter in a low-noise frequency source²¹. The salient device specifications require a maximum matched insertion loss of 2.5 dB, continuous power handling capacity of +15 dBm and an out-of-band rejection of 22 dB, minimum. The frequency response characteristic is shown in Fig. 4 and important device performance features are listed in Table 3.

Table 3

500 MHz SAW Resonator Performance

Matched Loss	1.7 dB
Matched Q	2800
Unloaded Q	≈22000 (1.06 x published Q max)
Rejection	22 dB

These devices must meet stringent environmental specifications and they will be thoroughly evaluated for suitability prior to actual use. Packaging will be in a T0-8 header and the devices will be sealed in a high vacuum.

A UHF SAW resonator stabilized oscillator has limitations relating to temperature stability and aging which may be overcome, for very low noise, highly-stable oscillators, by phase locking a SAW oscillator to a multiplied bulk mode crystal oscillator. The functional diagram for such a phase-locked source is shown in Fig. 11. A SAW oscillator will, generally speaking, exhibit higher noise levels than a multiplied crystal source for low Fourier frequencies ($F < 5\text{KHz}$). However, for Fourier frequencies above this approximate value, the SAW oscillator operates with lower FM noise levels. Phase-locking allows one to obtain the low close in noise associated with a bulk crystal oscillator; the low mid-Fourier-frequency-range noise of the SAW oscillator; the long term aging rates and temperature stability characteristics of the bulk oscillator; and relatively high RF output power levels.

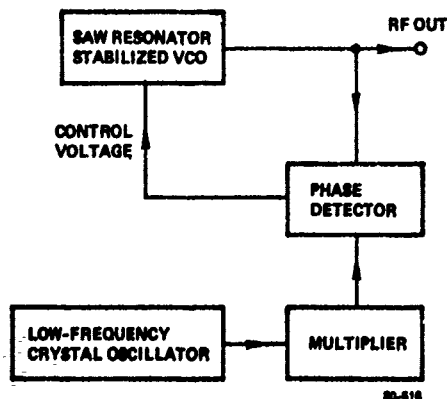


Fig. 11 Schematic diagram of a UHF source which consists of a SAW oscillator phase-locked to a low frequency crystal source.

Summary

We have shown that single-pole SAW resonator filters, with characteristics suitable for systems applications, may be produced at frequencies in excess of 1.4 GHz. The performance characteristics of devices at 1.43 GHz, 840 MHz and 500 MHz have been presented, design considerations and fabrication procedures have been discussed, and several actual or potential systems applications are outlined. The resonator characteristics of high frequency, low insertion loss, distortion-free/linear-phase response, high power-transfer capacity, and small size are seen to allow significant reductions in sub-system size, weight, complexity, and power consumption.

Acknowledgements

The author would like to thank Mr. Raymond St. Cyr for his effort in developing fabrication procedures and producing the devices discussed herein, Dr. Martin Block for his enthusiastic cooperation in developing the 500 MHz noise suppression filter, and Dr. Herman van de Vaart for his continuing support and encouragement in the pursuit of this work.

References

1. T. L. Szabo and A. T. Slobodnik, Jr., "Acoustic Surface Wave Diffraction and Beam Steering", Air Force Cambridge Research Lab Report - TR-73-0302, p. 171, May 1973.
2. W. J. Tanski, "SAW resonators utilizing withdrawal weighted reflectors," *IEEE Trans. Sonics and Ultrasonics*, Vol. SU-26, pp. 404-410, Nov. 1979.
3. C. O. Newton, "A study of the propagation characteristics of the complete set of SAW paths on quartz with zero temperature coefficient of delay", *Proc. 1979 Ultrasonics Symposium*, pp. 632-636 (IEEE Cat. No. 79 CH 1482-9).
4. B. K. Sinha and H. F. Tiersten, "Zero temperature coefficient of delay for surface waves in quartz", *Appl. Phys. Letters* **34**, No. 12, pp. 817-819, June 1979.
5. W. R. Shreve, J. A. Kusters, and C. A. Adams, "Fabrication of SAW resonators for improved long term aging", *Proc. 1978 Ultrasonics Symposium*, pp. 573-579 (IEEE Cat. No. 78 CH 1344-1).
6. R. L. Rosenberg and L. A. Coldren, "Scattering analysis and design of SAW resonator filters", *IEEE Trans. Sonics and Ultrasonics*, Vol SU-26, pp. 205-230, May 1979.
7. W. J. Tanski, "GHz SAW resonators," *Proc. 1979 Ultrasonics Symposium* pp. 815-823 (IEEE Cat. No. 79CH1482-9 SU).
8. P. S. Cross, "Surface acoustic wave resonator filters using tapered gratings," *IEEE Trans. Sonics and Ultrasonics*, Vol. SU-25, pp. 313-319, Sept 1978.

9. G. L. Matthaei and F. Barmann, "SAW resonators using low-loss 'waffle-iron' reflectors," Proc. 1976 Ultrasonics Symposium, pp. 415-418 (IEEE Cat. No. 76 Ch 1120-5 SU).
10. L. P. Solie, "A SAW filter using a reflective dot array (RDA)," Proc. 1976 Ultrasonics Symposium, pp. 309-312 (IEEE Cat. No. 76 CH 1120-5SU).
11. W. J. Tanski, "A configuration and circuit analysis for one-port SAW resonator," J. Appl. Phys, pp. 2559-2560, April 1978.
12. H. A. Haus, "Modes in SAW grating resonators," J. Appl. Phys. vol. 48, pp. 4955-4961, Dec. 1977.
13. W. J. Tanski, "Surface acoustic wave resonators on quartz," IEEE Trans. on Sonics and Ultrasonics, Vol. SU-26, pp. 93-104 (March 1979).
14. P. S. Cross, W. R. Shreve, and T. S. Tan, "Synchronous IDT SAW resonators with Q above 10,000," Proc. 1979 Ultrasonics Symposium pp. 824-829, (IEEE Cat. No. 79 CH 1482-9 SU).
15. Electromask Inc., Woodland Hills, CA 91364.
16. H. I. Smith, "Fabrication techniques for surface-acoustic-wave and thin-film optical devices," Proc. IEEE, vol. 62, pp. 1361-1387, 1974.
17. Shipley Company, Inc., 2300 Washington St., Newton, MA 02163, USA.
18. G. R. Montress, R. A. Wagner and M. Gilden, "Stable microwave SAW oscillators for aging studies," Proc. 1979 Ultrasonics Symposium, pp. 886-890 (IEEE Cat. No. 79 CH 1482-9 SU).
19. This oscillator was designed by Philip Dragonetti and Edward Kosco at the Sperry Microwave Electronics Division in Clearwater, Florida.
20. P. Dragonetti, E. Kosco, W. Tanski and R. St. Cyr, "An 840 MHz SAW resonator stabilized radar system oscillator," Proc. 1980 Int. Systems and Circuits Symposium, (Houston, Texas, April 1980).
21. Frequency Electronics Inc. of New Hyde Park, NY is evaluating this resonator, particularly with regard to environmental conditions, for use in an ultra-low noise frequency source.

SH-TYPE SURFACE ACOUSTIC WAVES ON ROTATED Y-CUT QUARTZ

T. NISHIKAWA, A. TANI, K. SHIRAI and C. TAKEUCHI

FUJITSU LIMITED

1015 Kamikodanaka, Nakahara-Ku, Kawasaki, 211, JAPAN

Summary

This paper describes theoretical and experimental studies of SH-type surface acoustic waves on rotated Y-cut quartz.

Surface skimming bulk waves or shallow bulk acoustic waves propagating near the surface of a substrate have recently been reported (1-7). These waves have been analyzed assuming a free surface. We analyzed these waves taking into account electrical and mechanical loading effects. The calculated and experimental results indicate that the acoustic properties, such as effective electro-mechanical coupling coefficients and displacement distributions, are largely dependant on the thickness of the layer and that these waves should be treated as SH-Type surface acoustic waves, or Love waves (8-11), if the propagation path is very short or layered with film. In addition, these results indicate that lower insertion loss devices can be obtained if the thickness of interdigital electrodes is increased.

Introduction

Rayleigh waves on ST-cut quartz are commonly used for SAW (surface acoustic wave) devices because of their good temperature characteristics. But their comparatively low phase velocity makes it difficult for high frequency SAW devices to be realized. Also bulk waves, such as shear wave mode (1.6fo) and longitudinal wave mode (1.8fo), cause spurious responses.

Recently, bulk waves propagating near the surface of a substrate, called surface skimming bulk waves (SSBW) or shallow bulk acoustic waves (SBAW) have been reported (1-7). These bulk waves have many advantages over conventional Rayleigh waves, such as good temperature characteristics, higher phase velocity and fewer spurious responses, and are considered to be suitable for higher frequency devices. Some analytical methods for SSBW have been reported, but in these methods, electrical and mechanical loading effects of interdigital electrodes were ignored and the surface was assumed to be free.

In high frequency operation, however, these factors cannot be ignored. Therefore, we analyzed these waves taking into account electrical and mechanical loading effects. An approximated IDT (interdigital transducer) model assuming a layered surface, was used for the calculations. This paper describes calculated and experimental results for these waves; such as the phase velocity, frequency temperature coefficients, electro-mechanical coupling coefficients and distributions of displacement for depth. In addition, some experimental results for these waves on 36° rotated Y-cut quartz, having high phase velocity and zero temperature coefficient, are presented.

Analysis

Fig. 1 shows the rotated Y-cut quartz. θ is the angle of rotation and the Z' (or X_3) axis is the wave propagation direction. Since it is extremely difficult to obtain exact solutions regarding mechanical loading effects of IDT, we assumed, for our analysis, that the entire surface was covered with a layer, of thickness as shown in Fig. 2 (12). The coordinate system (X_1, X_2, X_3) for SH-type SAW propagation on the layered surface is shown in Fig. 3.

Assuming uniformity of displacements ($U_i, i=1,2,3$) and electric potential (ψ) in the X_1 direction, we consider the wave propagation in the X_3 direction. Let the displacements and electric potential be

$$\begin{pmatrix} U_1 \\ U_2 \\ U_3 \\ \psi \end{pmatrix} = \begin{pmatrix} A_1 \\ A_2 \\ A_3 \\ A_4 \end{pmatrix} \cdot e^{jnX_2} \cdot e^{j(\omega t - \xi X_3)} \quad (1)$$

The stress equation of motion and charge equation of electrostatics are shown below:

$$T_{ij,i} = \rho \ddot{u}_j \quad (2)$$

$$D_{i,i} = 0 \quad (3)$$

Substituting (1) into (2) and (3), we obtain the following frequency equation.

$$\begin{pmatrix} a_{11} & a_{12} & 0 & 0 \\ a_{21} & -a_{22} & 0 & 0 \\ 0 & 0 & a_{33} & a_{34} \\ 0 & 0 & a_{43} & a_{44} \end{pmatrix} \begin{pmatrix} A_1 \\ A_4 \\ A_2 \\ A_3 \end{pmatrix} = 0 \quad (4)$$

where

$$a_{11} = C_{66}K^2 - 2C_{56}K + C_{55} - \bar{C}_{66}X^2$$

$$a_{12} = e_{26}K^2 - (e_{25} + e_{36})K + e_{35}$$

$$a_{22} = (\epsilon_{22}K^2 - 2\epsilon_{23}K + \epsilon_{33})$$

$$a_{33} = C_{22}K^2 - 2C_{24}K + C_{44} - \bar{C}_{66}X^2$$

$$a_{34} = C_{24}K^2 - (C_{44} + C_{23})K + C_{34}$$

$$a_{44} = C_{44}K^2 - 2C_{34}K + C_{33} - \bar{C}_{66}X^2$$

$$a_{ij} = a_{ji}, \quad K = \eta/\xi, \quad \bar{C}_{66} = C_{66} + e^2_{26}/\epsilon_{22}$$

$$X = V_s/V_b, \quad V_b = \sqrt{\bar{C}_{66}/\rho}, \quad V_s: \text{Phase velocity}$$

As shown in (4), the frequency equation is very simple compared with that for Rayleigh waves. Only the displacement U_1 is coupled with electric potential (U_2, U_3 are not). This indicates that U_1 and ψ should be analyzed as SH-type SAW. Moreover, the fact that U_2 and U_3 cannot be generated by piezoelectricity implies that no spurious response occurs.

General solutions for U_1 and ψ can be obtained by solving the following fourth degree equation in terms of K for a given X ,

$$\begin{vmatrix} C_{66}K^2 - 2C_{56}K + C_{55} - \bar{C}_{66}X^2 & e_{26}K^2 - (e_{25} + e_{36})K + e_{35} \\ e_{26}K^2 - (e_{25} + e_{36})K + e_{35} & (\epsilon_{22}K^2 - 2\epsilon_{23}K + \epsilon_{33}) \end{vmatrix} = 0 \quad (5)$$

and selecting two roots satisfying the boundary conditions where X_2 approaches infinity. The solutions are given by:

$$U_1 = \sum_{n=1}^2 C(n) A_1(n) \cdot e^{j\xi K(n) X_2} \cdot e^{j(\omega t - \xi X_3)} \quad (6)$$

$$\psi = \sum_{n=1}^2 C(n) A_4(n) \cdot e^{j\xi K(n) X_2} \cdot e^{j(\omega t - \xi X_3)} \quad (7)$$

The general solution for displacement (U'_1) in the layer is obtained from the stress equation of motion and is given by the following expression.

$$U'_1 = \sum_{n=3}^4 C(n) \cdot e^{j\xi K(n) X_2} \cdot e^{j(\omega t - \xi X_3)} \quad (8)$$

$$\text{where } K(3) = -K(4) = \sqrt{(V_s/V_c)^2 - 1}$$

$$V_c = \sqrt{\mu/\rho'}$$

μ, ρ' : Lamé constant and density of metal film

The boundary conditions between the substrate and the layer are shown as follows:

$$X_2 = 0; \quad U_1 = U'_1 \quad (9)$$

$$T_{12} = T'_{12} \quad (10)$$

$$\psi = 0 \quad (11)$$

$$X_2 = h; \quad T'_{12} = 0 \quad (12)$$

Substituting general equations, (6), (7) and (8) into the above boundary conditions, we obtain the following homogeneous equation.

$$\begin{pmatrix} S(1) & S(2) & -\mu K(3) & -\mu K(4) \\ A_1(1) & A_1(2) & -1 & -1 \\ 0 & 0 & S(3) & S(4) \\ A_4(1) & A_4(2) & 0 & 0 \end{pmatrix} \cdot \begin{pmatrix} C(1) \\ C(2) \\ C(3) \\ C(4) \end{pmatrix} = 0 \quad (13)$$

where

$$S(1) = (C_{66}K(1) + C_{56})A_1(1) + (e_{26}K(1) + e_{36})A_4(1)$$

$$S(2) = (C_{66}K(2) + C_{56})A_1(2) + (e_{26}K(2) + e_{36})A_4(2)$$

$$S(3) = \mu K(3) \cdot e^{j\xi K(3)h}$$

$$S(4) = \mu K(4) \cdot e^{j\xi K(4)h}$$

The phase velocity of SH-type SAW is obtained when the determinant of the matrix (13) is zero.

Calculated Results

The calculated phase velocity of SH-type SAW on rotated Y-cut quartz is shown in Fig. 4. The curve was calculated with an $A\lambda$ layer thickness of 0.01λ (λ : wavelength). The phase velocity of Rayleigh waves is also shown in the figure. The phase velocity on 36° rotated Y-cut quartz can be seen to be 1.6 times that of Rayleigh waves on ST cut quartz.

Fig. 5 shows the first and second order frequency temperature coefficients when the thickness of the $A\lambda$ layer is 0.01λ . Seven frequency points were calculated at 10°C intervals from -50°C to $+55^\circ\text{C}$ and temperature coefficients were obtained from the method of least squares. It can be found that the angles of rotation where the first order temperature coefficient is zero are 36.2° and 129.5° . The temperature characteristics of these rotation angles are shown in Fig. 6, compared with those of Rayleigh waves on ST-cut. The second order temperature coefficients of these rotation angles are as follows:

$$\theta = 36.2^\circ \quad T_F^{(2)} = -56 \times 10^{-9}/^\circ\text{C}^2$$

$$\theta = 129.5^\circ \quad = -20 \times 10^{-9}/^\circ\text{C}^2$$

$$\text{ST-Cut} \quad = -39 \times 10^{-9}/^\circ\text{C}^2$$

Fig. 7 shows the distributions of displacement for depth on Al layered 36° and 130° rotated Y-cut quartz. As the thickness of the layer increases the displacements concentrate more to the surface. Also, the effects of the Al layer thickness at 36° is larger than that at 130° . This is because the phase velocity at 36° (5,080m/sec) is very large compared with that of the Al shear wave (3,100m/sec), while in the case of 130° rotation, its phase velocity (3,330m/sec) approximates to that of Al shear wave, resulting in minimal effect on the displacement. In high frequency operation, SH-type SAW devices can be easily obtained on 36° rotated Y-cut quartz using a thin Al layer. (For example, a frequency 800MHz and an Al thickness (h) of 1,000Å are equivalent to $h/\lambda = 1.5 \times 10^{-2}$) Fig. 8 shows the distributions of displacement when gold is used instead of aluminum; mechanical loading effects of a gold layer are very large compared with those of Al, because gold's shear wave velocity (1,250m/sec) is very low and its density is very large. The displacements concentrate more to the surface even though the layer is very thin.

Since the displacement distribution depends largely on the thickness of the layer, effective electro-mechanical coupling coefficients should also change. Therefore the coupling coefficients, $2\Delta V/V$, were calculated from the difference of the phase velocities obtained from electrical boundary conditions (11) and (14).

$$X_2=0; \quad D_2=0 \quad (14)$$

The coupling coefficients with Al layer thicknesses of 0.01λ and 0.02λ are shown in Fig. 9. The coupling coefficients depend strongly on the thickness of the layer.

Experimental Results

Table 1 shows an outline of the samples used in the experiments. 36° rotated Y-cut quartz was used for the substrate because of its high phase velocity and good temperature characteristics. The configuration was of the three transducer type, Type-1 being a double electrode transducer and Type-2 a conventional one. The pathlength between input and output transducers was designed to be very short ($\lambda/4$) to avoid increasing propagation loss on the free surface. A photograph of the sample is shown in Fig. 10. The enclosure is of the T0-8 type.

Attenuation characteristics of Type-1 transducer with interdigital electrodes thicknesses of 1,000Å and 2,000Å are shown in Fig. 11. The center frequency and insertion loss are significantly changed. These results indicate that mechanical loading effects of IDTs cannot simply be ignored. Attenuation characteristics of Type-2 transducer are shown in Fig. 12. Due to internal wave reflections, the characteristics are similar to those of resonator type transducer and low insertion loss is obtained (13). Fig. 13 shows wide band attenuation characteristics. As shown before,

there is no spurious response caused by bulk waves.

The phase velocity and coupling coefficients were obtained from the characteristics shown in Fig. 11. The phase velocity was calculated from the center frequency and coupling coefficients were obtained from the minimum insertion loss at the center frequency using an IDT cross field model (14, 15). Experimental and calculated results are shown in Fig. 14 and can be seen to closely agree. These results indicate that the approximated IDT model, assumed before, is viable and that waves can be treated as SH-type SAW if the propagation path is very short or layered with a metal film.

Fig. 15 shows the frequency temperature characteristics. The experimental results were obtained from the phase change at each temperature. The turnover temperature difference between calculated and experimental values was within 5°C and the second order temperature coefficient was found to be $-60 \times 10^{-9}/^\circ\text{C}^2$ and calculated of $-56 \times 10^{-9}/^\circ\text{C}^2$.

Aging characteristics are shown in Fig. 16. SAW oscillators were assembled and operated continuously for the observation period. Over 100 days the frequency change was seen to be limited to within 2ppm.

Conclusion

We analyzed SH-type SAW assuming that SSBW would change to SH-type SAW if the surface was layered with film. The calculated and experimental results were in close agreement.

The results indicate that the assumption is true even in IDT regions, if the propagation path is very short or if it is layered with film. This type of wave, especially on 36° rotated Y-cut quartz, is considered to be very practical for higher frequency devices because of its high phase velocity, good temperature characteristics, lack of spurious response and lower insertion loss.

Acknowledgment

The authors would like to thank Messrs. M. Otsuki and T. Kojima of FUJITSU LIMITED for their consistent guidance and encouragement.

References

1. M. F. Lewis, Proc. 1977 IEEE Ultrasonics Symposium, P. 744
2. T. I. Browning, et al., Proc. 31st Annual Frequency Control Symposium, P. 258, (1977)
3. K. H. Yen, et al., Proc. 31st Annual Frequency Control Symposium, P. 266, (1977)
4. T. I. Browning, et al., Proc. 1978 IEEE Ultrasonics Symposium, P. 586
5. D. L. Lee, Proc. 1978 IEEE Ultrasonics Symposium, P. 675
6. K. H. Yen, et al., Proc. 1978 IEEE Ultrasonics Symposium, P. 680
7. G. W. Farnell, IEEE Trans. SU-26, NO3, P. 202, (1979)

8. Y. Ota, et al., Paper of Technical Group on Ultrasonics, IECE of JAPAN, US69-3 (1969)
9. M. Onoe, Trans. IECE of JAPAN, 52-A, NO.10, P. 403 (1969)
10. M. Onoe, et al., The committee of Electro-Mechanical Functional Devices, IEE of JAPAN, Sept. 92-258 (1979)
11. T. Nishikawa, et al., The committee of Electro-Mechanical Functional Devices, IEE of JAPAN, Feb. 86-242 (1979)
12. J. Minowa, et al., Paper of Technical Group on Ultrasonics, IECE of JAPAN, US76-23 (1976)
13. Y. Koyamada, et al., Paper of Technical Group on Ultrasonics, IECE of JAPAN, US77-35 (1977)
14. K. Kuroda, et al., Paper of Technical Group on Ultrasonics, IECE of JAPAN, US75-14 (1975)
15. W. R. Smith, et al., IEEE Trans. MTT-23, NO.11, P. 853 (1975)
16. R. Bechmann, Proc. IRE, Aug., P. 1812 (1962)

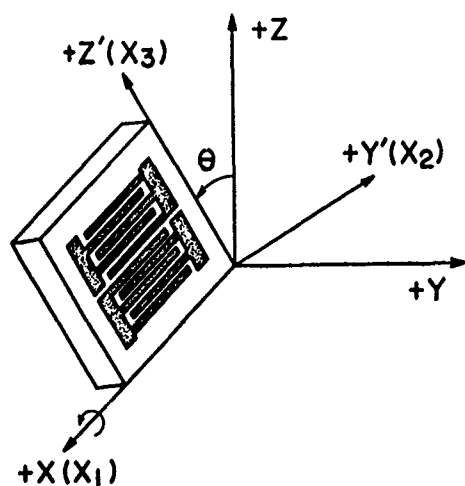


Fig. 1 Rotated Y-cut quartz

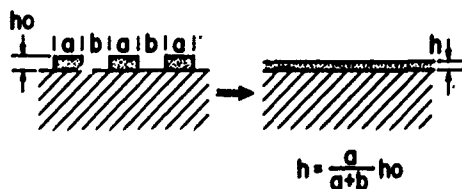


Fig. 2 Approximated IDT model

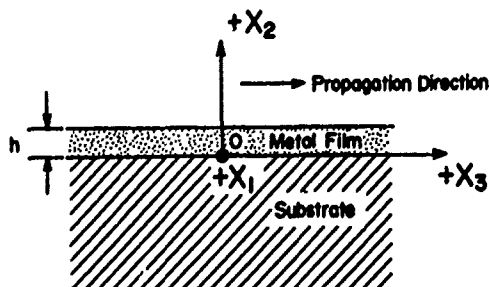


Fig. 3 Coordinate system for SH-type SAW propagation

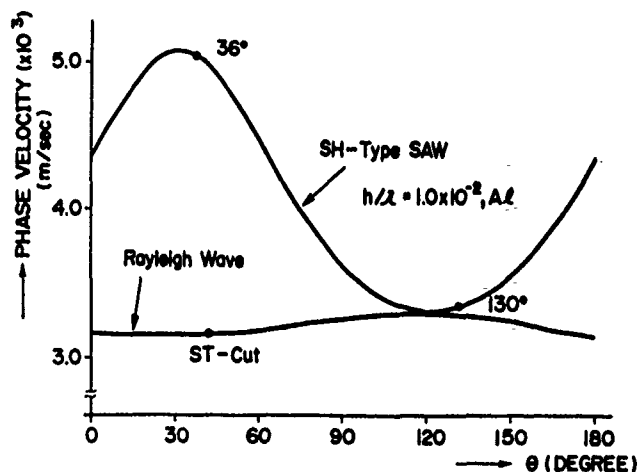


Fig. 4 Phase velocities of SH-type and Rayleigh waves on rotated Y-cut

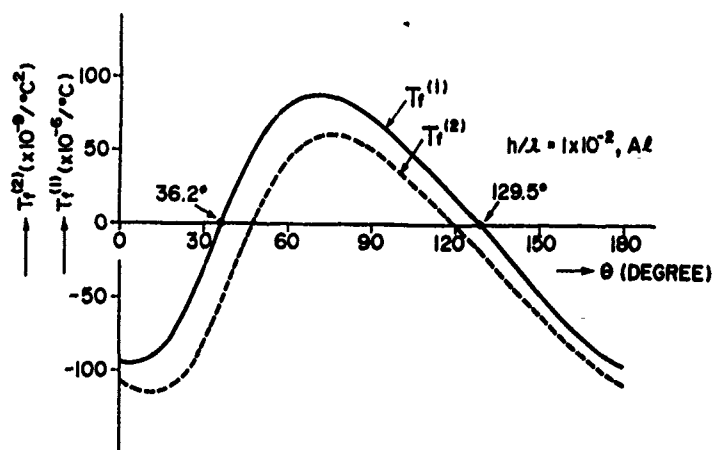


Fig. 5 Frequency temperature coefficients

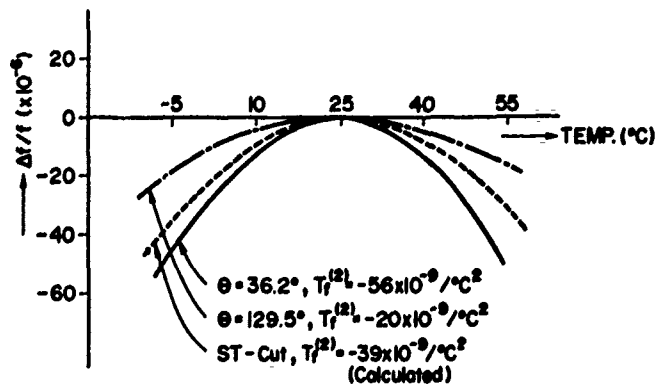


Fig. 6 Frequency temperature characteristics

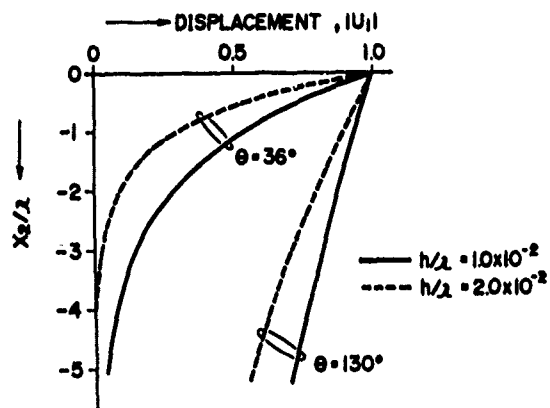


Fig. 7 Distributions of displacement when the surface is layered with aluminum

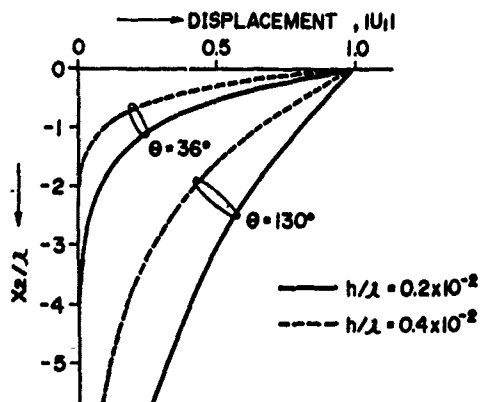


Fig. 8 Distributions of displacement when the surface is layered with gold

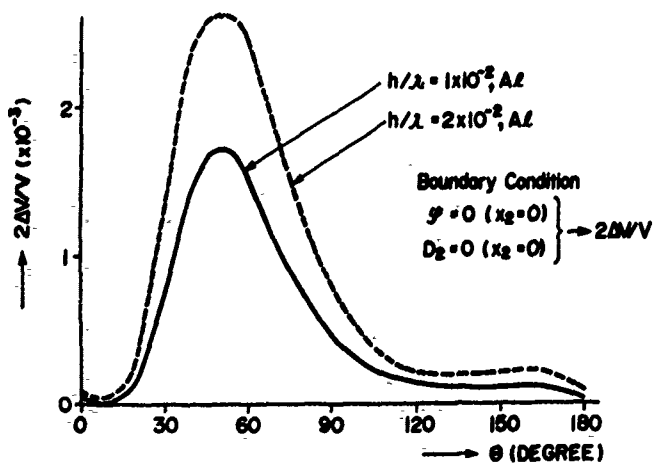


Fig. 9 Electro-mechanical coupling coefficients.

	TYPE-1	TYPE-2
SUBSTRATE		
Rotation Angle (θ)	36°00'	36°00'
TRANSDUCER		
Configuration		
Finger Pairs	80-160-80	100-200-100
Wavelength (λ)	11.9 μ m	7.92 μ m
Fingerwidth	$\lambda/8$	$\lambda/4$
Pathlength (d)	$\lambda/4$	$\lambda/4$

Table 1 Experimental samples

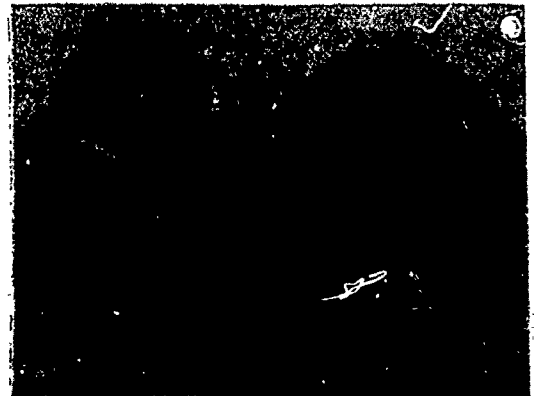


Fig. 10 Photograph of sample.

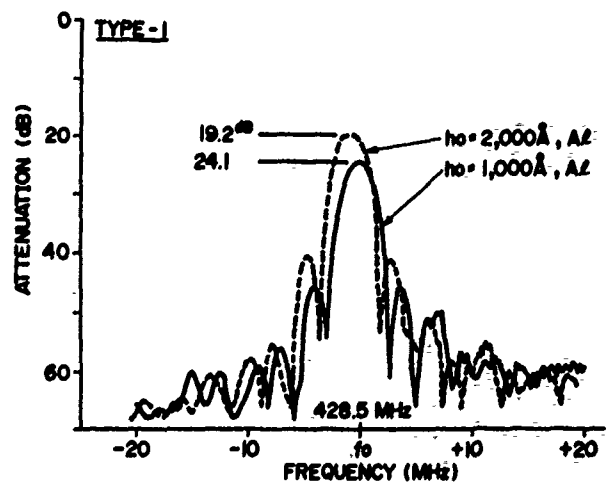


Fig. 11 Attenuation characteristics of Type-1

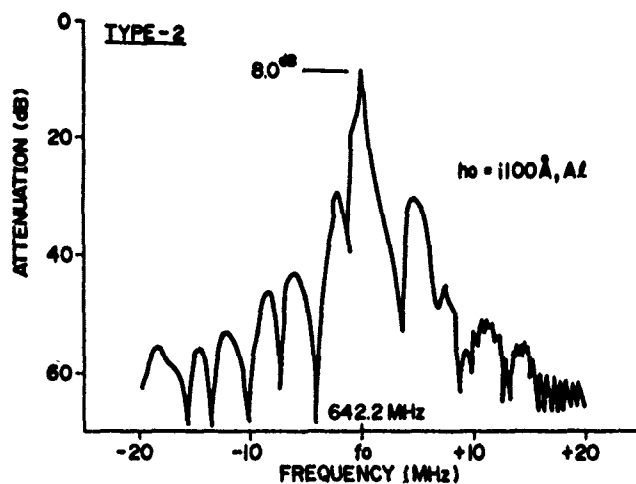


Fig. 12 Attenuation characteristics of Type-2

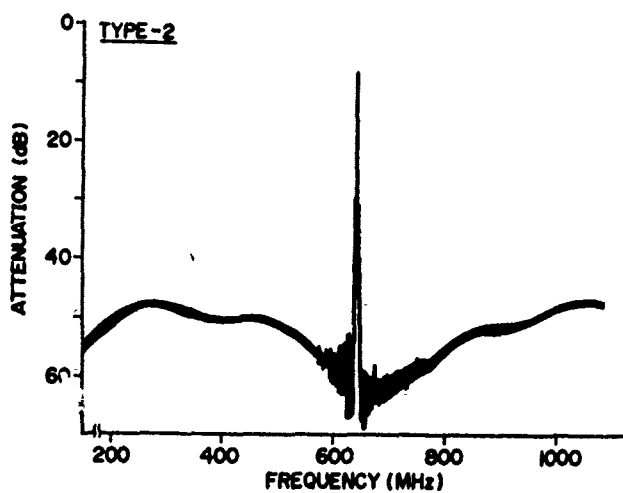


Fig. 13 Wide band attenuation characteristics of Type-2

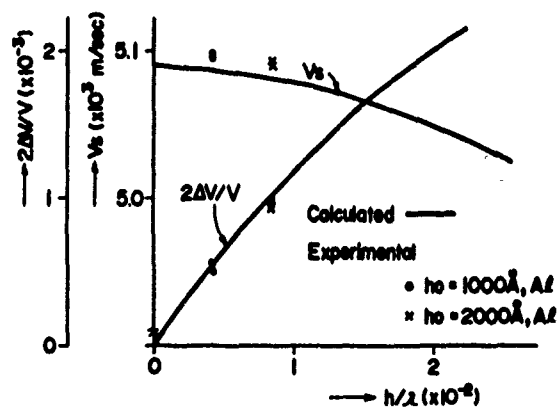


Fig. 14 Phase velocity and coupling coefficients on 36° rotated Y-cut

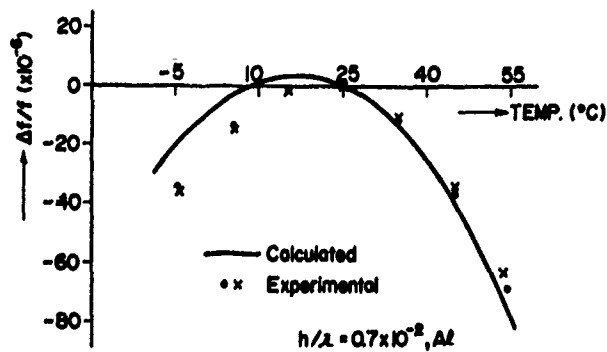


Fig. 15 Frequency temperature characteristics

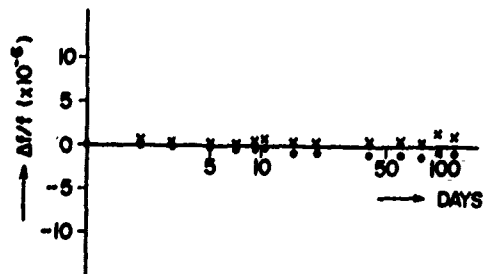


Fig. 16 Aging characteristics

ANALYSIS OF AGING DATA ON SAW OSCILLATORS*

T. E. Parker

Raytheon Research Division
Waltham, Massachusetts 02154

Summary

The long-term frequency stability (aging) of oscillators is an important parameter for many applications, and with the recent interest in surface acoustic wave (SAW) controlled oscillators, this has been an area of investigation. As a result, improved long-term stability of SAW oscillators has been reported when high-quality packaging techniques have been used. This paper presents an analysis of new aging data accumulated over the last three years on several types of packages. All packages were high-quality hermetic enclosures, and the mounting was strictly mechanical, with no organics or silicone rubbers used.

The test oscillators included both delay lines and resonators in the 300 to 400 MHz range. All were fabricated on rotated Y-cut quartz plates (40°), and either gold or aluminum metallization was used. The packages include brazed and welded flatpacks, cold-welded HC 38/U and TO-8 enclosures, and a novel all-quartz approach. Other variables included back-filling, post-seal bake, and surface treatment with silicones to reduce 1/f noise. The tests were all conducted at a temperature of ~30°C

Introduction

For SAW controlled oscillators to be competitive with multiplied, low-frequency, crystal-controlled oscillators, they must demonstrate a frequency stability similar to or better than that of quartz crystal oscillators. In the area of short-term stability, the SAW oscillator has clearly demonstrated superior performance in certain areas of the noise spectrum. However, one area where the SAW oscillator lags behind that of crystal oscillators is long-term frequency stability (or aging). Because SAW oscillators are naturally used at higher frequencies, it is questionable whether the long-term stability of SAW devices will ever match that of the best low-frequency quartz crystals. However, SAW oscillators begin to become competitive for many applications when a stability on the order of 1 ppm per year is

reached. Previously published results^{1,2} have shown that low aging requires a clean hermetic package which contains no materials that will outgas (such as elastomers or epoxies). SAW resonators packaged by techniques established for bulk wave devices, which clearly meet these criteria have shown a drift of from under 1 ppm to almost 7 ppm in the first year.³ In order to reduce this drift so that it is consistently under 1 ppm, it is important to have some idea of what the aging mechanism is for a device sealed in a high-quality package. To help obtain this information, an investigation of aging in SAW oscillators has been going on at Raytheon for more than four years. The philosophy behind this investigation has been to use a variety of packaging and fabrication techniques in order to identify the factors which may influence long-term stability. Though circumstances have introduced more variables than were intended, the data is sufficient to indicate that certain factors are more important to long-term stability than others. Specifically, the data suggests that given a high-quality hermetic package and a mechanical means of holding the substrate (no organics or elastomers), the physical and/or chemical state of the transducer metallization has more effect on the long-term stability than the ultimate cleanliness of the enclosure.

Experimental Conditions

A total of forty SAW-controlled oscillators either have been or are currently under aging test at Raytheon. In this paper we will report on the observed long-term frequency drift of thirty-one of these oscillators. Frequencies of operation range from 200 to 400 MHz, and most of the devices are delay lines. However, the aging data also includes results from two SAW resonators and one surface-skimming bulk-wave (SSBW) delay line. The devices were all fabricated on rotated Y-cut quartz substrates and most devices had transducers made with 1000 Å of aluminum. However, five devices with 500 Å gold transducers were also evaluated. All of the devices were operated as oscillators and the long-term drift was obtained by monitoring the frequency of operation. All of the oscillators were maintained at an ambient temperature of 20°C (the temperature of the SAW device was around 30°C), and corrections to the frequency for any temperature variations were made using measured temperature coefficients. The accuracy of the frequency

*Supported in part by NASA Contract NAS5-25117.

counter used in these measurements was maintained at one part in 10^9 by monitoring the 3.58 MHz color subcarrier on network TV broadcasts.

High-quality, wideband, commercial rf amplifiers were used in the oscillators to keep the phase shift through the electronics to a minimum and to provide maximum stability. For delay lines a gain of 20 dB was required, and the amplifiers were chosen to provide a power level of about 20 milliwatts incident on the SAW device. For the resonators only 10 dB of gain was required, and an incident power of 5 milliwatts was used. Throughout these measurements the power levels remained constant to a few tenths of a dB.

Most of the devices being reported on in this paper were packaged in conventional enclosures. These include flatpacks (Tekform #50272), which were either brazed or welded shut, and HC 36/U crystal packages, which were sealed by cold welding. Of these three approaches, the cold-welded HC 36/U enclosure was clearly the cleanest package. The sealing was done by U.S. Army ERADCOM at Fort Monmouth, New Jersey, in cooperation with NASA contract NAS5-25117. The high-vacuum sealing equipment that was used has an established record of producing bulk-wave devices with very low aging rates. The brazed flatpacks were sealed at Raytheon (also in a high-vacuum system), but with this technique the highest temperature occurs at the time of sealing. Thus the degree of substrate contamination can be expected to be higher than that from cold-welding. The flatpacks that were sealed by welding were clearly done in the least clean environment, since the sealing was done in a plastic drybox which was flushed with dry nitrogen. The sealing was accomplished by overlapping spot welds. In all cases the packages and substrates were UV-cleaned prior to sealing.

The substrate mounting was done by either 10-mil gold wire straps,¹ or by the spring arrangement shown in Fig. 1. All of the devices packaged in flatpacks used gold wire straps, while most of the devices in the HC 36/U enclosures used the spring arrangement. Neither of these techniques is necessarily being recommended as a practical method for holding substrates, but they were used because they eliminated the need for adhesives or rubbers.

In addition to the conventional packages, three devices were also sealed in an all-quartz package. In this arrangement the SAW substrate also serves as part of the enclosure. A matching cap of quartz is used to protect the active area from contamination. The details of this package will be presented later in the text along with the aging data. Finally, some very preliminary results will be presented for SAW devices mounted in cold-welded TO-8 enclosures. The sealing of the TO-8's was done at Raytheon, but in a manner very similar to that used for the HC 36/U enclosures.

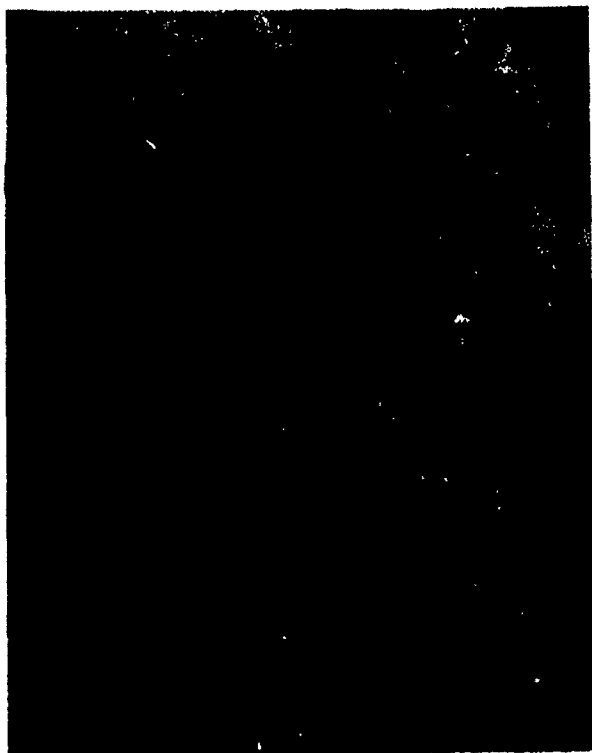


Figure 1. SAW delay line mounted in HC36/U using spring holder.

Analysis of Aging Data

The aging data for thirty-one oscillators will be presented and discussed in this section. Table 1 lists these oscillators along with the pertinent packaging and performance parameters of each one. The parameters in Table 1 are self-explanatory except for T_f , which is the elapsed time (in weeks) from when the transducers were fabricated until the start of the aging test. Also, an "R" after the frequency indicates that the device is a resonator; all other devices are delay lines.

Figure 2 shows the observed fractional frequency change as a function of time (in weeks) for seven devices that were fabricated with aluminum transducers. Four devices sealed in brazed flatpacks are shown with various dashed lines; two devices in HC 36/U enclosures are shown with dotted lines; and a single device in a welded flatpack is shown with a solid line. All of the devices show an upward drift in frequency (at least initially), and this is consistent with the results of Ref. 3. However, the magnitude of the drift does not correlate well with package cleanliness. The devices in the brazed packages consistently show the largest drift, but the drift of the device in the welded flatpack (No. 5) is nearly identical to the two in HC 36/U enclosures. Number 5 is a resonator and the one feature that dis-

TABLE 1. PACKAGING PARAMETERS OF THE TEST OSCILLATORS

Osc. No.	Substrate Number	(MHz) Frequency	Transducer Metal	Package (Type Seal)	Atmosphere	Preaged	T _f (weeks)
1	Q514D	311	Cr-Al	Flatpack (brazed)	Vacuum	No	2.4
2	Q601A	401	Al	Flatpack (brazed)	Vacuum	No	0.9
3	Q617A	401	Al	Flatpack (brazed)	Vacuum	No	0.9
4	Q638A	401	Al	Flatpack (brazed)	Argon	No	1.9
5	Q1120A	310(R)	Al	Flatpack (welded)	Nitrogen	No	12
6	Q514A	311	CR-Al	HC36/U	Vacuum	No	~26
7	Q1089A	401	Al	HC36/U	Vacuum	No	6.3
8	Q638B	401	Al	Flatpack (brazed)	Vacuum	Yes (11 days at 90°C)	3.0
9	Q969A	401	Al	Flatpack (welded)	Nitrogen	Yes (07 days at 90°C)	4.4
10	Q970A	401	Al	Flatpack (welded)	Nitrogen	Yes (11 days at 90°C)	3.9
11	Q1009A	345	Al	Flatpack (welded)	Nitrogen	Yes (11 days at 90°C)	3.5
12	Q1085C	401	Al	HC36/U	Vacuum	Yes (10 days at 100°C)	9.3
13	Q1089C	401	Al	HC36/U	Vacuum	Yes (10 days at 100°C)	7.3
14	Q1093A	401	Al	HC36/U	Vacuum	Yes (07 days at 200°C)	6.3
15	Q604	401	Au	Flatpack (brazed)	Vacuum	No	1.0
16	Q619B	401	Au	Flatpack (brazed)	Vacuum	No	2.7
17	QEC2	401	Au	HC36/U	Vacuum	No	~39
18	Q1088A	401	Au	HC36/U	Vacuum	No	6.3
19	Q1091B	401	Au	HC36/U	Vacuum	Yes (10 days at 100°C)	6.3
20	Q1088B	401	Au	HC36/U	Leak	No	---
21	Q977	310	Al	All Quartz	Air	No	---
22	Q1148	310(R)	Al	All Quartz	Air	No	---
23	Q1150	310	Al	All Quartz	Air	No	---
24	Q1157A	401	Al	Flatpack (brazed)	Vacuum	No (silicone treated)	10
25	Q1057A	218(SSBW)	Al	Flatpack (brazed)	Vacuum	No	---
26	Q1239A	401	Al	TO-8	Vacuum	No	11.5
27	Q1239C	401	Al	TO-8	Vacuum	No	11.0
28	Q1239D	401	Al	TO-8	Vacuum	No	12.0
29	Q1246A	401	Al	TO-8	Vacuum	No	0.6
30	Q1246C	401	Al	TO-8	Vacuum	No	1.3
31	Q1246B	401	Al	TO-8	Vacuum	No (pad)	1.3

tinguishes it from the rest is the very small amount of scatter on this curve.

Figure 3 shows the aging data for six devices with aluminum transducers that were subjected to a 100°C bake (for up to eleven days) after sealing but before the start of the aging test. Under these conditions the aging characteristics have changed drastically. Here, half of the devices have aged downward and show a relatively complex pattern with up to two sign changes in the slope. The ones drifting upward, however, are not drastically different from the unbaked devices in Fig. 2. Whether a device drifts up or down does not seem to depend on the package type and further reinforces the possibility that the mechanism causing the observed aging is not strongly dependent on cleanliness. However, the mechanism does appear to be influenced by the temperature of the environment. This is further reinforced by the data in Fig. 4, which shows the aging of a device subjected to a 200°C bake after sealing. This device has been extremely stable and after seventy-one weeks of operation is still within 0.5 ppm of the starting frequency.

The scatter in the data of Figs. 2, 3, and 4 is partially due to incomplete correction for temperature variation; in addition, fluctuations are sometimes caused by power outages or by disturbances in the aging chamber when oscillators are being replaced. However, some of the fluctuations appear to occur spontaneously and therefore may be inherent in the oscillator. It is significant in this regard that the two resonators which have been tested are among those with the least scatter.

Though the aging data in Figs. 2 and 3 does not correlate well with package type, there is a parameter which does appear to be significant. This is illustrated in Fig. 5, where the total frequency drift after ten weeks is plotted, for ten oscillators, as a function of the time from transducer fabrication to start of the aging test, T_f . The ten data points in Fig. 5 are from the oscillators in Figs. 2 and 3 that aged upward during the first ten weeks of operation. Though particular package types tend to cluster around certain ranges of T_f , it is clear from Fig. 5 that large values of T_f result in less frequency drift, even within a package type. The significance of this is even more important when it is noted that most of the period from transducer fabrication to the start of the aging test occurred before the device was sealed. Thus the relaxation process that causes the aging appears to be going on even before the device is sealed or operating. Consequently, there is a lower rate of drift once the aging test is started. Thus the evidence from the data presented so far is that package type is not particularly significant to aging but that transducer fabrication is. Therefore, likely candidates for aging mechanisms are chemical or physical changes in the transducer metal.

A useful technique for helping to identify possible aging mechanisms is to evaluate the fit of the data to specific mathematical models. Three models that have been successfully used on bulk-wave devices are

$$\frac{\Delta F}{F} = A \log(Bt + 1) \quad (1)$$

$$\frac{\Delta F}{F} = A(1 - e^{-Bt}) \quad (2)$$

$$\frac{\Delta F}{F} = A(t)^B \quad (3)$$

where t is time and A and B are fit parameters. The first model is applicable to chemisorption, oxidation, and stress relief processes;⁶ while the second applies to first-order chemical reactions, or adsorption and desorption of a physisorbed monolayer.⁶ The last model has been identified with diffusion processes when B is near $1/2$.⁷

The aging data from Figs. 2 and 3 was fitted to these three models, but some restrictions were required. Specifically, the fitting routine could handle only two fit parameters and therefore was limited to the presence of only one mechanism at a time. This meant that aging curves which showed one or more distinct changes in direction could not be fitted. Also curves which were dominated by scatter (Fig. 4) were not used. Thus only seven curves were fitted (Nos. 1, 2, 5, 6, 7, 10, and 13), and it was found that overall the logarithmic model (Eq. 1) gave the best results. (This is also consistent with Ref. 3.)

It is interesting to note that the logarithmic model (Eq. 1) has exactly the same mathematical form even if the observation does not start at the same time as the actual relaxation process. If, for example, the observation starts at a time t_0 after the relaxation starts, the expression for the observed change in frequency $\Delta F'/F$ becomes

$$\frac{\Delta F'}{F} = A \log(B't' + 1) \quad (4)$$

where t' is the time elapsed after t_0 and $B' = B/(Bt_0 + 1)$. Of course, $t = t_0 + t'$. Note that the parameter A is unchanged and that B' is smaller than B for $t_0 > 0$. Figure 6 illustrates how this influences the shape of the aging curves. The data and the fitted curves are plotted for two oscillators with different values of T_f . As can be seen, the values of A differ by only 50 percent, while the values of B' differ by almost a factor of 36. The latter is not equal to the relative values of T_f , but it is certainly clear that large values of T_f result in small values of B' . Thus we see that not only is the magnitude of the drift dependent on T_f (Fig. 5), but that the shape of the curve (as manifested in B') is also consistent with the hypothesis that the relaxation process starts at or near the time of the transducer fabrication, which, in many cases occurred well before the start of the aging tests. The fact that the logarithmic model gives the best fit suggests that likely causes for the changes in the transducer metal are internal stress relaxation or oxidation.

In addition to devices with aluminum transducers, five devices with gold transducers were tested. Gold is not a very practical transducer material because of the significant slowing of the wave under the gold, but it is a very stable

material and it was felt that it would provide a good contrast to the aluminum. Figure 7 shows the observed frequency drift of the devices with gold transducers. As indicated, three were in cold-weld enclosures, and two were in brazed flatpacks. Only No. 19 was subjected to a post-seal bake (100°C for ten days). As expected the aging was different from aluminum devices but surprisingly, it was not significantly better. Distinctly different results were obtained for the two package types and, in general, all the curves have a flatter shape than those observed for aluminum devices. Numbers 17 and 18 are clearly the best of the group and, significantly, No. 17 has a large value for T_f . The latter is a particularly impressive device since after nearly two years of operation it is still within a few tenths of a part per million of the starting frequency. Curves 15, 18, and 19 were fitted to the three models discussed earlier, but none clearly stood out as giving a better fit. This may be due in part to the relatively shallow curvature present for all the devices.

Though few conclusions can be drawn about the aging mechanisms for gold devices, the distinctly different characteristics from the aluminum devices lends further support to the hypothesis that the transducer metallization is the source of the aging on the aluminum devices.

One final piece of information can be presented about aging of devices in conventional packages, and this is the effect of package leaks on aging. Figure 8 illustrates what happens when a leak develops. Oscillators 1, 2, and 3 all were found to be leak-free at the beginning of the aging measurements, and all were found to have leaks when their operation was terminated. It was felt that the observed shift to downward drift was caused by the occurrence of a leak and this was confirmed by No. 20, which was known to have a leak at the beginning of the test. Since on all of the devices the leak rate was large enough for the package to fill to atmospheric pressure in a matter of one or two weeks, it is felt that the continued downward drift in Fig. 8 was most likely due to a continued diffusion of moisture into the package which was subsequently adsorbed into the surface of the quartz.

In addition to conventional packages, aging measurements were also carried out on devices using a novel all-quartz package.⁵ The construction of this package is illustrated in Fig. 9. The SAW substrate constitutes the bottom of the package, and a matching rotated Y-cut quartz plate is used for the cover. The transducers are recessed to provide a flat surface, and a cavity is etched into the top plate to prevent coupling to the top inside surface. The joining faces of the top and bottom plates are polished optically flat and are joined by a modified optical bond. The modification to this bonding technique is that the quartz surfaces were first coated with a few monolayers of a high-temperature silicone compound. This served to prevent the migration of moisture into the cavity and also reduced the $1/f$ phase noise of the SAW device.⁸ Electrical connections were made by plating over the exposed ends of each busbar.

Figure 10 shows the observed frequency drift of three devices packaged in this manner. The sudden drop in frequency near week 20 for oscillators 22 and 23 coincided with two power interruptions which shut down the oscillators and environmental chamber for two multi-hour time intervals within a period of three weeks. The same power interruptions seemed to have very little effect on oscillator 21. Nevertheless, all three oscillators are doing exceptionally well. After more than a year of operation, all are still within 1 ppm of their starting frequency and No. 21 has been doing particularly well during the period from fifty-five weeks to the present. During this time the frequency has generally been constant to within a few parts in 10^8 . Note that No. 22 is a resonator and does not age significantly differently from the two delay lines, except that the aging curve of the resonator may be somewhat smoother.

The author feels that the good aging of these devices does not necessarily reflect on the quality of the all-quartz package but that it is more likely due either to the silicone treatment or to some other step in the sealing process which is substantially different from that used with the conventional packages. Some support for the former is given in Fig. 11, which shows the aging of a silicone-treated device in a brazed flatpack. As can be seen, except for a dip around week 24, the frequency stability has been quite good for nearly one year.

Figure 12 shows the aging characteristic of another special case. Here the acoustic device does not utilize surface waves but rather the so-called surface skimming bulk wave⁹ (or shallow bulk acoustic wave).¹⁰ The observed aging is not large but is very erratic. The erratic nature may be due to the large number of electrodes (660 double electrode fingers in each transducer) required to obtain a low insertion loss with a long delay time.

Finally, some very recent aging data has been obtained on SAW devices with aluminum transducers which were sealed in TO-8 packages (26 through 31 in Table 1). Though only ten weeks of data is available on these six devices, it clearly shows that the three devices with values of T_f near eleven weeks are drifting less than the three with smaller values of T_f around one week. The fact that all the devices came from the same batch of quartz clearly eliminates the quartz itself as the source of the aging mechanism. In addition, one device had an aluminum pad added between the transducer to increase the amount of metallization. As expected, this device is showing the largest frequency drift. However, the aging data shows that apparently a new variable has been introduced, since after ten weeks of operation none of the six devices has drifted more than 1 ppm. This is considerably less drift than would have been expected from any of the devices, even those with large values of T_f . At this time, differences between the sealing procedures for the various packages are being investigated to determine what caused the reduced aging.

Conclusions

This aging investigation has demonstrated that drift of less than 2 ppm in the first year can be obtained on a significant fraction of the devices when reasonably clean packages are used. It can also be expected that further drift will occur at a decreasing rate in the following years. Furthermore, the data strongly suggest that the transducer metallization (at least for aluminum) is very likely the source of the relaxation mechanism which causes the frequency drift. Apparently this mechanism is sensitive to temperature and other process variables and thus increases the possibility that aging rates well under 1 ppm in the first year are possible under practical production conditions.

Acknowledgements

The author would like to acknowledge the valuable assistance of Clarence Dunnrowicz and John Lang in fabricating and sealing the devices, and the measurements made by Merton Bennett. The valuable assistance of Tom Lukaszek and John Vig in handling the sealing of the devices at ERADCOM is also gratefully acknowledged.

References

1. T. E. Parker, "Aging characteristics of SAW controlled oscillators," 1977 IEE Ultrasonics Symposium, 862, 1977.
2. D. T. Bell, "Aging processes in SAW resonators," 1977 IEEE Ultrasonics Symposium, 851, 1977.
3. W. R. Shreve, J. A. Kusters, and C. A. Adams, "Fabrication of SAW resonators for improved long term aging," 1978 IEEE Ultrasonics Symposium, 573, 1978.
4. J. R. Vig and J. W. LeBus, "UV/ozone cleaning of surfaces," IEEE Trans. Parts, Hybrids, Packaging PHP-12, 365, 1976.
5. A similar package has been reported by G. K. Montress, R. A. Wagner, and M. Gilden, "Stable microwave SAW oscillators for aging studies," 1979 IEEE Ultrasonics Symposium, 886, 1979.
6. A. W. Warner, D. B. Fraser, and C. D. Stockbridge, "Fundamental studies of aging in quartz resonators," IEEE Trans. Sonics Ultrason. SU-12, 52, 1965.
7. G. L. Dybwad, "Aging analysis of quartz crystal units with TiPdAu electrodes," Proc. 31st Symposium on Frequency Control, 144, 1977.
8. T. E. Parker, "1/f phase noise in quartz SAW devices," Electron. Lett. 15, 296, 1979; "1/f phase noise in quartz delay lines and resonators," 1979 IEEE Ultrasonics Symposium, 878, 1979.
9. T. I. Browning and M. F. Lewis, "New family of bulk acoustic wave devices employing interdigital transducers," Electron. Lett. 13, 128, 1977.
10. K. H. Yen, K. L. Wang, and R. S. Kagiwada, "Efficient bulk wave excitation on ST quartz," Electron Lett. 13, 37, 1977.

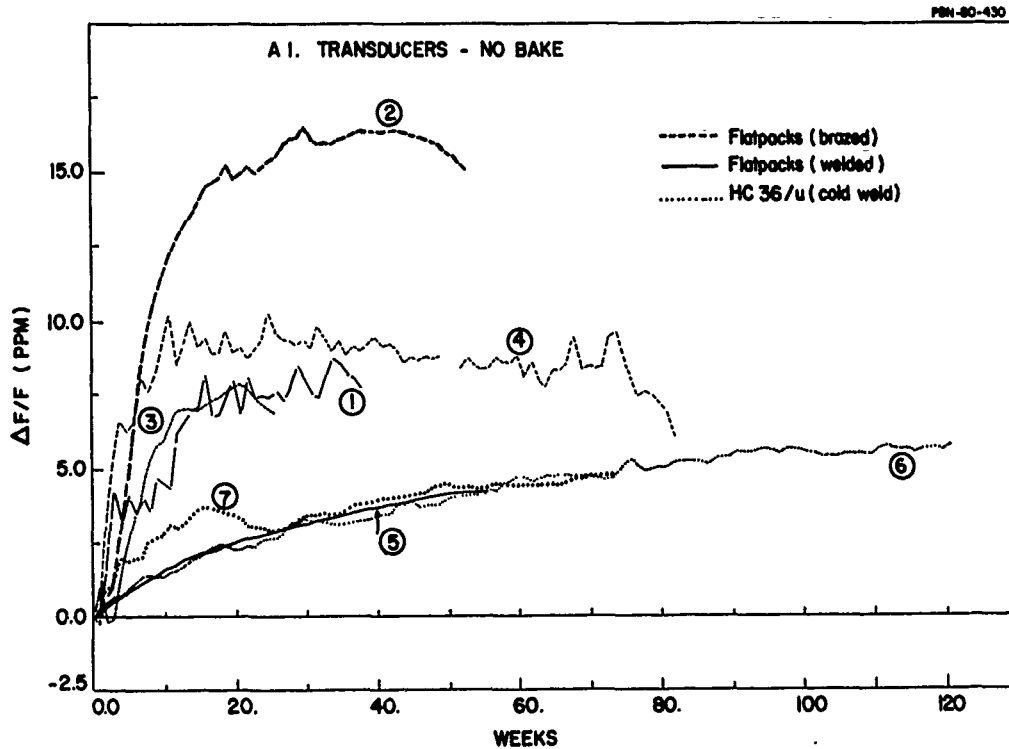


Figure 2. Aging of devices with aluminum transducers which were not subjected to a post-seal bake.

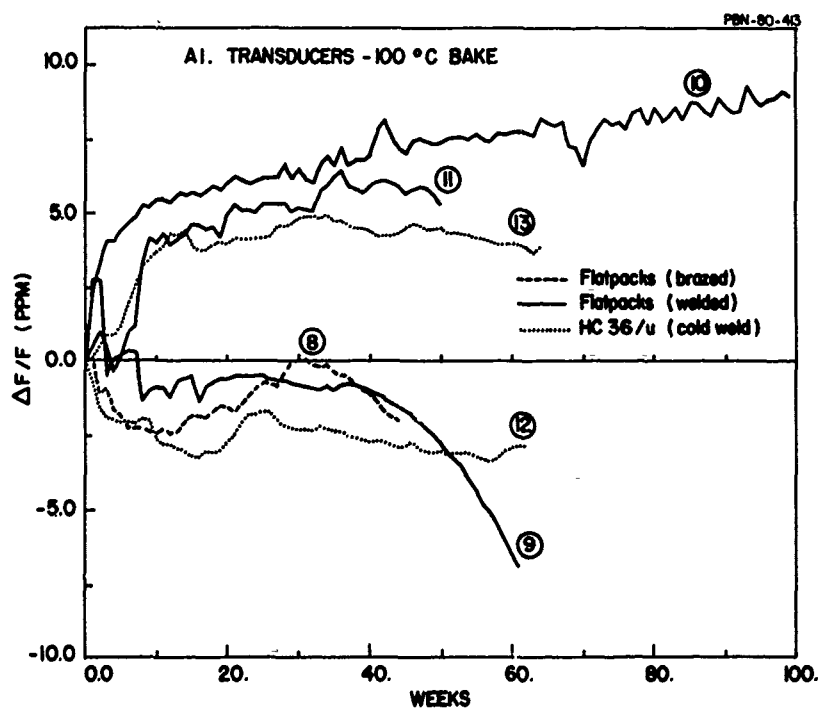


Figure 3. Aging of devices with aluminum transducers which were subjected to a 100°C bake after sealing.

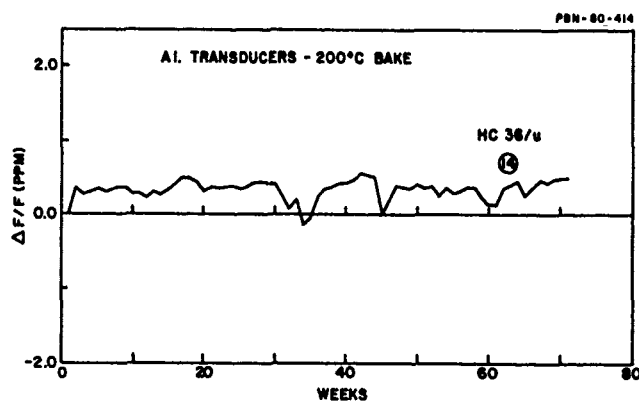


Figure 4. Aging of a device with aluminum transducers which was subjected to a 200°C post-seal bake.

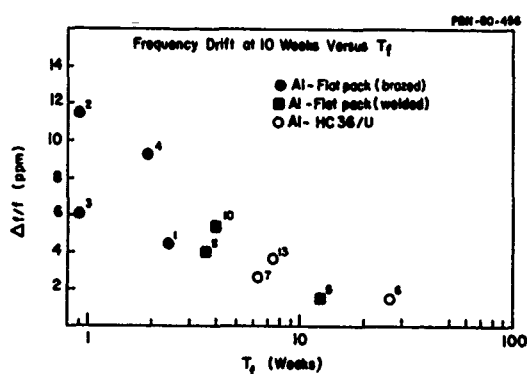


Figure 5. Frequency drift in first ten weeks as a function of the time from transducer fabrication to start of the aging test, T_f . The numbers refer to the oscillator from which each data point was derived.

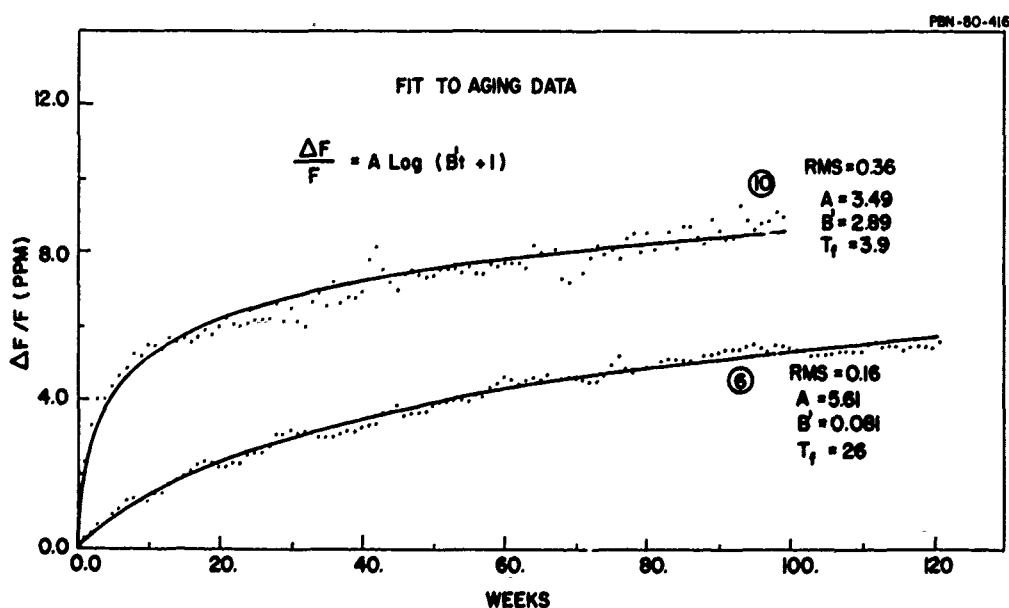


Figure 6. Fit of log curve to aging data for two oscillators with different values of T_f .

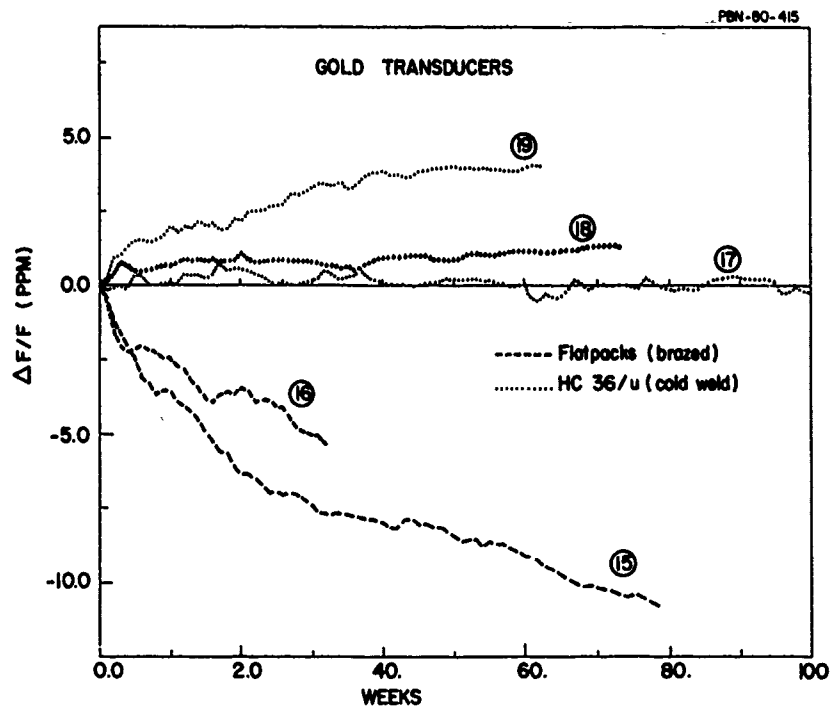


Figure 7. Aging of devices with gold transducers.

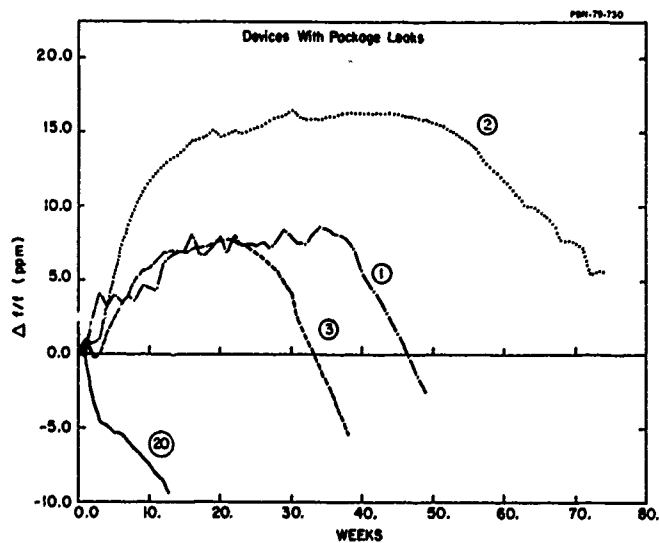


Figure 8. Aging of devices with package leaks.

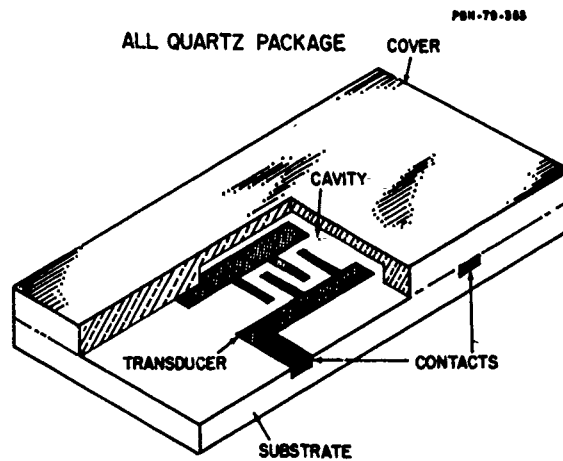


Figure 9. Illustration of the construction of an all-quartz package.

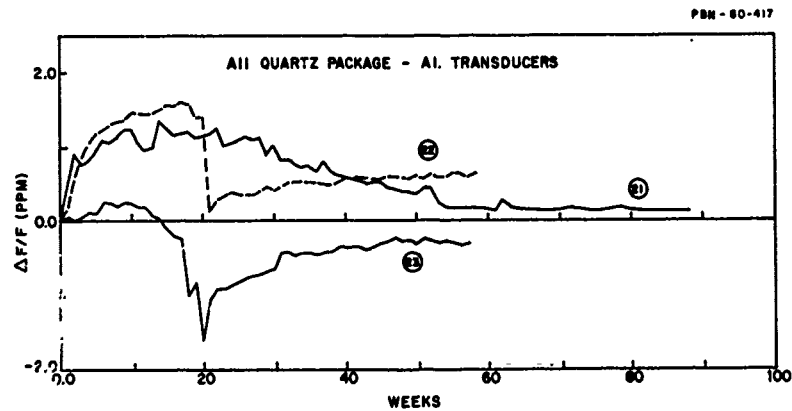


Figure 10. Aging of devices with aluminum transducers using the all-quartz package.

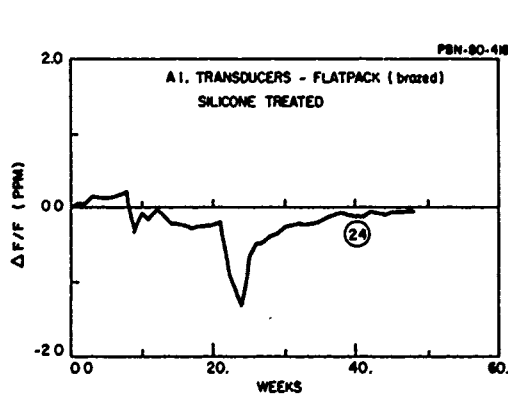


Figure 11. Aging of a silicone-treated device in a braze flatpack.

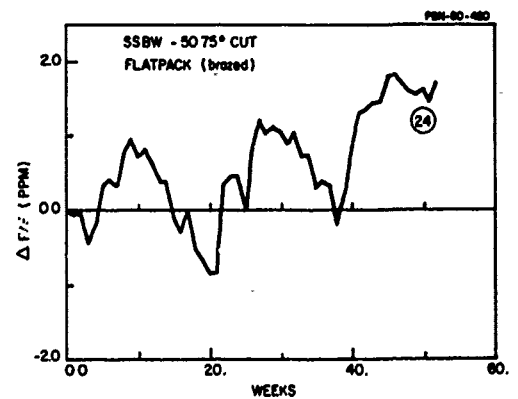


Figure 12. Aging of a surface-skimming bulk-wave device in a braze flatpack.

NUMERICAL ANALYSIS OF DOUBLY ROTATED* CUT SAW DEVICES

D.F. Williams and F.Y. Cho
Motorola Government Electronics Division

ABSTRACT

Results of a numerical study of the properties of surface acoustic waves (SAW) on doubly rotated cuts of alpha quartz are presented. First and second order TCF's have been calculated on a $10^\circ \times 10^\circ \times 10^\circ$ grid spanning the range of angles (XY wlt) 0 to $30^\circ/-90^\circ$ to $90^\circ/0$ to 180° . The Finite Difference method was employed. SAW velocities were calculated at -50°C , 25°C , and 100°C . The corresponding frequencies were determined and curve fitted. Angular maps created from the data base by these calculations were used to identify zero first and second order TCF surfaces. Families of cuts with zero first order TCF and small second order TCF's have been identified and further explored on smaller angular grids (as small as $1.0^\circ \times 1.0^\circ \times 1.0^\circ$).

The results of Sinha and Tiersten's approach are correlated with the finite difference method and used to find cuts with zero first order TCF.

Families of cuts on alpha quartz with SAW temperature stability superior to that found on ST cut Quartz are identified. Coupling coefficients, power flow angles, phase-temperature plots and other parameters are given for selected cuts.

INTRODUCTION

Quartz is one of the most commonly used substrates for fabricating surface acoustic wave (SAW) devices. In SAW narrowband filter, oscillator and resonator applications, the temperature stability of the device is an important design parameter. Currently, almost all temperature stable SAW devices fabricated on quartz use the ST cut¹. This cut exhibits a parabolic frequency dependence in temperature. For many applications, the temperature dependence of devices fabricated on ST quartz is too large. Thus it is desirable to find crystal cuts with superior temperature performance. Of course, many other design parameters must be considered when choosing a crystal cut. Some of the more important parameters are the piezoelectric coupling coefficient, acoustic losses, dependence of device performance on cut misorientation, excitation of bulk modes, and beam steering angle. These parameters are all determined for a given cut.

The objective of this paper is to locate crystal cuts which exhibit lower SAW temperature coefficients of delay than the ST cut. The method used to characterize and calculate the temperature dependence of a crystal orientation is discussed. Use is made of computer models to investigate the temperature dependence of different cuts of crystal for SAW devices. Calculated and measured results are presented and compared. Finally, plans for future experimental work are outlined.

CALCULATION OF TEMPERATURE COEFFICIENTS

Defining τ as the delay time for an acoustic wave to propagate between two points on the surface of the crystal, we wish to find orientations for which τ is constant in temperature. It has been shown that determining the temperature dependence of τ (time delay) is equivalent to determining the temperature dependence of F frequency via the relation $F \propto 1/\tau$.²

The most straightforward method for calculating the frequency-temperature characteristics of a SAW device is the Finite Difference method^{3,4}. The Rayleigh wave velocities are calculated for different temperatures, yielding the values $V_R(T_i)$, $i=1,2,\dots,n$. This is done by first calculating the fundamental constants at the temperature T_i of interest. These constants⁴ are then rotated into the coordinate system of interest. An iterative procedure³ is used to calculate a velocity V_s for which Christoffel's equation and the boundary conditions are satisfied simultaneously. Linear regression is used to calculate the temperature dependence of a Rayleigh wave and requires a complete solution of the problem to be performed at several temperatures.

Sinha and Tiersten⁵ have provided a computer program to calculate the first order TCD using a perturbation approach. The constants used in this program were derived from the original experimental data of Bechmann, Ballato, and Lukaszek⁶, and properly includes coordinate axis skewing. A comparison of results using the Finite Difference method and the first order temperature derivatives calculated by Sinha and Tiersten's program shows the later method to be more accurate⁵, and angular orientations of the zero TCF⁽¹⁾ surfaces calculated by the two programs differ by as much as 3 degrees on off axis cuts. Although the program does not calculate the second and third order TCD's, it verifies and refines results for the first order TCD. Both computer programs were used extensively in this study.

ANALYTICAL APPROACH

IRE standard angle definitions (YX wlt) PHI/THETA/PSI for quartz were used throughout the investigation.⁷ Using the Finite Difference approach with the available crystal constants, the calculated results show that the zero TCF⁽¹⁾ surfaces do not intersect with the zero TCF⁽²⁾ surfaces, based on the interpolated results of the $10^\circ \times 10^\circ \times 10^\circ$ resolution. It is not likely that a finer resolution will provide contrary information because TCF⁽¹⁾ and TCF⁽²⁾ are relatively slow varying functions. A list of the crystal elastic constants and their temperature derivatives on which these calculations are based are given in reference 6. Calculations were performed on a $10^\circ \times 10^\circ \times 10^\circ$ grid over the angular ranges $0 \leq \text{PHI} \leq 30^\circ$, $0 \leq \text{PSI} \leq 180^\circ$, and $-90^\circ \leq \text{THETA} \leq 90^\circ$. These initial calculations defined the "angular volumes" of low TCF orientations. Calculations were then performed on a $2.5^\circ \times 2.5^\circ \times 2.5^\circ$ grid near promising orientations. In this way, the entire angular range was explored and a large computer-based data file built. Maps of first and second order TCF's were generated.⁸ Despite the number and density of points at which the first and second order TCF's were calculated, wherever TCF⁽¹⁾ was found to be less than or equal to zero, we found TCF⁽²⁾ to be less than 0.

The investigative approach used has been to first locate the surfaces of zero TCF⁽¹⁾ (the most significant term) with the Finite Difference program. Near these surfaces of zero TCF⁽¹⁾, low values of TCF⁽²⁾ are sought, using already calculated results of the Finite Difference programs. Where low values of TCF⁽²⁾ have been found, the perturbation approach was used to more accurately locate the zero TCF⁽¹⁾ surface, this being the most significant term in the total temperature dependence. TCF⁽³⁾'s are then calculated to assure that their effect on the total temperature dependence is small. To date, this has always been found to be the case.

*Work supported by U.S. Army Electronics Command, Fort Monmouth, N.J., under contract DAAK 20-79-C-0275

RESULTS OF THE INVESTIGATIVE APPROACH

Table 1 consists of a summary of the results of using the investigative approach described above. Out of the many areas with low TCF cuts, some of which have been identified in this program and some previously identified.^{1,2,4,8,9,10} There are three where especially low TCF cuts have been located. These areas are centered near (YX wlt) 0/27/138, (YX wlt) 7/27/135.5, and (YX wlt) 15/40/40. These orientations have zero TCF⁽¹⁾, calculated by Sinha and Tiersten approach, with TCF⁽²⁾ and TCF⁽³⁾ calculated using the Finite Difference approach. These areas are chosen because of zero TCF⁽¹⁾ and low TCF⁽²⁾. TCF⁽³⁾ can be mostly cancelled out by TCF⁽¹⁾ if the propagation direction is slightly rotated away from the zero TCF⁽¹⁾ direction, so that the TCF⁽²⁾ term will dominate the performance characteristics. The angular resolution in these areas is 1° x 1° x 1°. The cuts potentially have one half to one third the temperature coefficients of ST-Cut quartz.

Table 1. Propagation Characteristics of Selected Orientations

ANGLES OF ZTCF ⁽¹⁾ DEGREES (S AND T'S PROGRAM)			TCF ⁽²⁾ /°C ² (X10 ⁻⁸) FINITE DIFFERENCE PROGRAM	TCF ⁽³⁾ /°C ³ (X10 ⁻¹⁰) FINITE DIFFERENCE PROGRAM
PHI	THETA	PSI		
6	26	136.31	-1.4	
6	27	135.93	-1.3	0.67
6	28	135.59	-1.3	0.57
7	26	135.99	-1.5	
7	27	135.64	-1.4	
7	28	135.27	-1.3	0.65
8	26	135.74	-1.4	0.65
8	27	135.36	-1.4	
8	28	134.97	-1.3	
1	26	137.78	-1.2	0.68
1	27	137.48	-1.2	0.65
1	28	137.17	-1.1	0.67
0	26	138.07	-1.2	0.67
0	27	137.78	-1.1	0.68
0	28	137.49	-1.1	0.62
-1	26	138.37	-1.2	0.60
-1	27	138.09	-1.2	0.62
-1	28	137.80	-1.1	0.73
14	39	40.195	-1.0	0.64
14	40	40.415	-1.0	0.66
14	41	40.64	-1.0	0.75
15	39	39.79	-1.0	0.63
15	40	40	-1.0	0.74
15	41	40.23	-1.0	0.73
16	39	39.4	-1.0	0.68
16	40	39.605	-1.0	0.66
16	41	39.825	-1.1	0.60

To insure the suitability of the cuts described above for SAW applications, the coupling coefficients, SAW velocity, and powerflow angles have been calculated for these cuts and are summarized in Table 2. Inverse velocity plots have been made for orientations with promising SAW temperature characteristics to check for the possibility of leaky surface waves and minimum values of f_b were calculated and compared with f_{SAW} . The polar plots of the inverse velocities for a (YX wlt) 0/27/137.8 and 7/27/135.59 are shown in Figure 1 and Figure 2, respectively. The inverse surface wave velocity for 0/27/137.8 is 3.06×10^{-4} , that for 7/27/137.8 is 3.03×10^{-4} . These values are larger than the maximum $(1/v_{bulk}) \cos \theta$ ($< 2.9 \times 10^{-4}$), therefore, the analysis indicates that a leaky mode does not exist (see Table 2 for the SAW velocities).

Table 2. Propagation Characteristics of Selected Orientations

ANGLES OF ZTCF ⁽¹⁾ , DEGREE. (S AND T'S PROGRAM)			VELOCITY (MSEC)	K ² (X10 ⁻³)	POWER FLOW ANGLE (DEGREES)
PHI	THETA	PSI			
6	26	136.31	3296.84	1.12	-0.3
6	27	135.93	3293.60	1.12	-0.2
6	28	135.59	3290.63	1.12	-0.1
7	26	135.99	3303.33	1.12	-0.5
7	27	135.64	3299.70	1.12	-0.4
7	28	135.27	3296.33	1.12	-0.3
8	26	135.74	3310.15	1.12	-0.7
8	27	135.36	3306.11	1.12	-0.6
8	28	134.97	3302.32	1.10	-0.5
1	26	137.78	3268.80	1.10	+0.7
1	27	137.48	3267.44	1.10	+0.9
1	28	137.17	3266.36	1.10	+1.0
0	26	138.07	3264.09	1.12	+0.9
0	27	137.78	3263.09	1.10	+1.1
0	28	137.49	3262.35	1.10	+1.2
-1	26	138.37	3259.65	1.10	+1.1
-1	27	138.09	3259.01	1.10	+1.3
-1	28	137.80	3258.64	1.08	+1.5
14	39	40.195	3298.50	0.96	-7.7
14	40	40.415	3306.67	0.96	-8.1
14	41	40.64	3315.19	0.94	-8.6
15	39	39.79	3301.82	0.96	-7.8
15	40	40.00	3310.14	0.94	-8.3
15	41	40.23	3319.09	0.98	-8.6
16	39	39.4	3305.38	0.96	-8.0
16	40	39.605	3314.03	0.98	-8.4

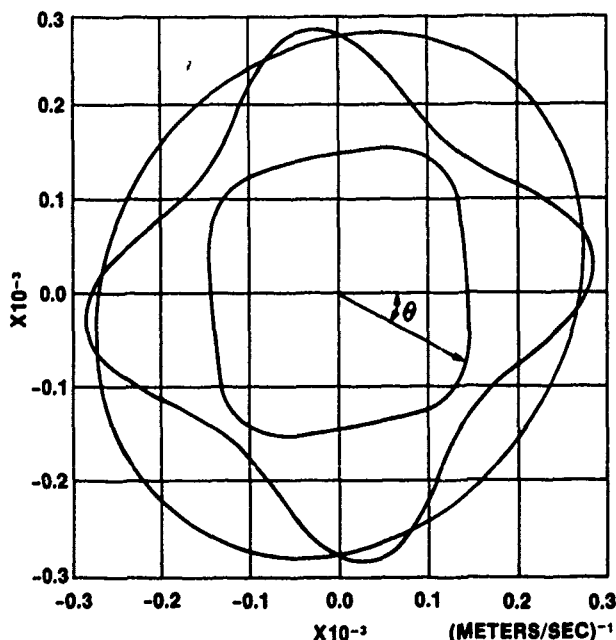


Figure 1. Polar Plots of Inverse Velocities for a (YX wlt) 0/27/137.8

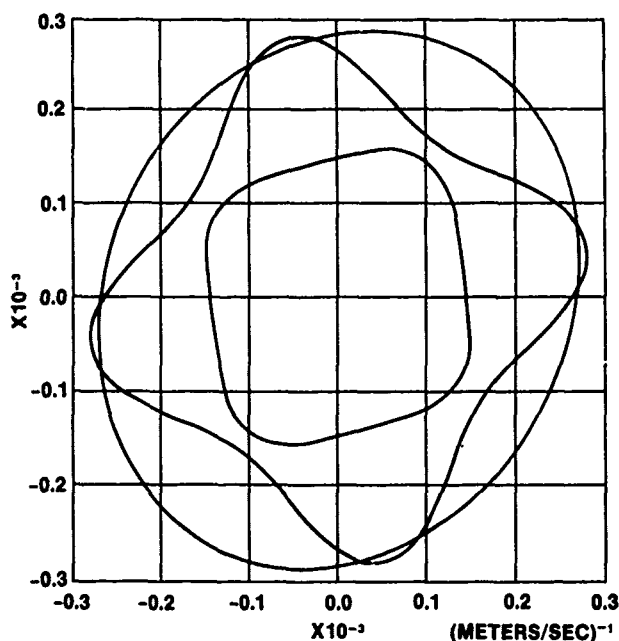


Figure 2. Polar Plots of Inverse Velocities for a (YXwlt) 7/27/135.59

In cutting quartz and aligning masks on it, there is always some maximum achievable accuracy. Thus it is useful to know how all of the acoustic quantities considered vary with angle. Quantities such as TCD, phase velocity, power flow angle, $\Delta V/V$, and bulk wave velocity surfaces, are of interest to this program. These quantities can be accurately determined by directly calculating the quantities at $\phi = (\phi_0 + \Delta\phi)$, $\theta = (\theta_0 + \Delta\theta)$, and $\psi = (\psi_0 + \Delta\psi)$ with the same computer program discussed earlier.

Calculation of the angular dependence on the first, second, and third order TCD's is, of course, our primary task. Of these three quantities, the first order TCF is most sensitive to angular variation. Quantities such as velocity (Table 2), power flow angles (Table 2), BAW velocities (Figures 1 and 2), coupling coefficients (Table 3), and second and third order TCF's (Table 1) do not vary quickly with angle. This is not the case for TCF⁽¹⁾. Table 3 contains a summary of $\partial \text{TCF}^{(1)}/\partial\psi$. The large values of $\partial \text{TCF}^{(1)}/\partial\psi$ impose strict fabrication tolerances on the SAW cuts and mask alignment. Fabrication accuracy to within 6 minutes is required to keep the total temperature variation due to TCF⁽¹⁾ within 45 ppm for $\partial \text{TCF}^{(1)}/\partial\psi \approx 3(\text{PPM}/^\circ\text{C})/\text{degree}$ over the temperature range -50°C to 100°C . Table 4 contains summaries of $\partial \text{TCF}^{(1)}/\partial\phi$ and $\partial \text{TCF}^{(1)}/\partial\theta$. These values impose fabrication tolerances on the rotated quartz plate angles ϕ and θ of 12 minutes to keep the total temperature variation due to $\partial \text{TCF}^{(1)}/\partial\phi$ within 45 ppm over the temperature range -50°C to 100°C . This linear temperature variation may be compensated for by varying ψ on any particular cut if all other cut parameters vary slowly with angle.

Table 3. $\partial \text{TCF}^{(1)}/\partial\psi$ for Selected Cuts

ANGLES OF ZTCF ⁽¹⁾ , DEGREES (S AND T'S PROGRAM)			$\partial \text{TCF}^{(1)}/\partial\psi$
PHI	THETA	PSI	
6	26	136.31	+2.7 (PPM/C°)/DEGREE
6	27	135.93	+2.7
6	28	135.59	+2.7
7	26	135.99	+2.7
7	27	135.64	+2.7
7	28	135.27	+2.7
8	26	135.74	+2.7
8	27	135.36	+2.7
8	28	134.97	+2.7
1	26	137.78	+2.8
1	27	137.48	+2.8
1	28	137.17	+2.8
0	26	138.07	+3.0
0	27	137.78	+3.0
0	28	137.49	+3.0
-1	26	138.37	+3.0
-1	27	138.09	+3.0
-1	28	137.80	+3.0
14	39	40.195	-3.5
14	40	40.415	-3.5
14	41	40.64	-3.5
15	39	39.79	-3.5
15	40	40	-3.5
15	41	40.23	-3.5
16	39	39.4	-3.7
16	40	39.605	-3.7
16	41	39.825	-3.7

Table 4. $\partial \text{TCF}^{(1)}/\partial\phi$ and $\partial \text{TCF}^{(1)}/\partial\theta$ for Selected Cuts

ANGLES OF ZTCF ⁽¹⁾ (S AND T'S PROGRAM), DEGREE			$\partial \text{TCF}^{(1)}/\partial\phi$	$\partial \text{TCF}^{(1)}/\partial\theta$
PHI	THETA	PSI		
7	27	135.64	-0.7(PPM/C°)/DEGREE	-0.5(PPM/C°)/DEGREE
0	27	137.78	-0.8	-0.8
15	40	40.00	+1.5	-0.7

EXPERIMENTAL VERIFICATION

Wafers with the orientation listed in Table 1 are being fabricated. Considerable care has been taken to reduce fabrication tolerances of the devices fabricated for this study. For these cuts, ϕ and θ are known to be within ± 4 minutes. ψ is known to be within ± 15 minutes. Two wafers with orientation (YX wlt) $8.05^\circ/25.9^\circ/135.7^\circ$ and (YX wlt) $6.57^\circ/26.88^\circ/134.9^\circ$ as well as a commercially supplied ST-cut wafer have been tested. A delay line oscillator was used to measure the temperature dependence of the SAW delay time. The experimental apparatus is shown in Figure 3. No coils were used to match the devices in order to eliminate inductance changes in the matching circuit over the temperature range tested. The complete experimental error is estimated to be within ± 10 ppm.

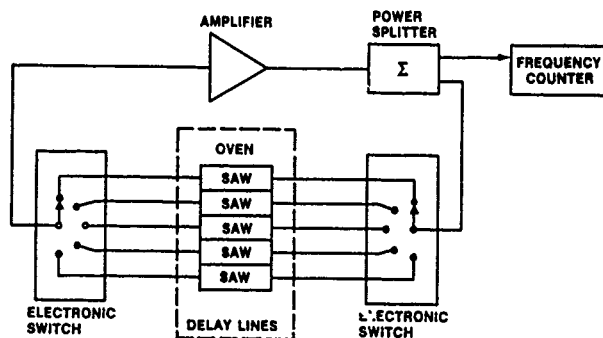


Figure 3. Measurement System

The frequency-temperature behavior of the device fabricated on the commercially supplied ST-cut wafer (YX wlt) 0/42.75/0 (angular tolerance is not known) is shown in Figure 4. Both the calculated and experimental results are plotted. Plots of the measured frequency-temperature behavior of the two devices fabricated at Motorola are shown in figure 5 and 6.

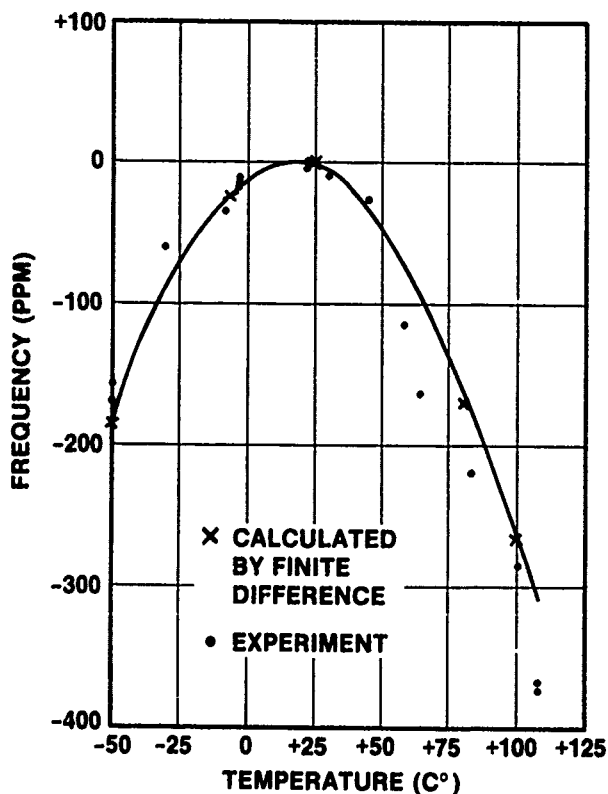


Figure 4. (YXwlt) 0/42.75/0 ST-CUT

The linear term in temperature is virtually absent in the device fabricated at (YX wlt) 6.57/26.88/134.9 (figure 5). The linear frequency term in the device fabricated at (YX wlt) 8.05/25.9/135.7 (figure 6) could be compensated for by a rotation of the mask by about 0.5 degrees. This small rotation would not, according to our calculations, appreciably affect TCF⁽²⁾. Both devices have a calculated second order TCF⁽²⁾ of about -0.15×10^{-7} , about half as large as that of ST-Cut Quartz. This result is borne out by the experimental measurements, a linear regression analysis which shows a TCF⁽²⁾ of -0.16×10^{-7} . These results are summarized in Table 5.

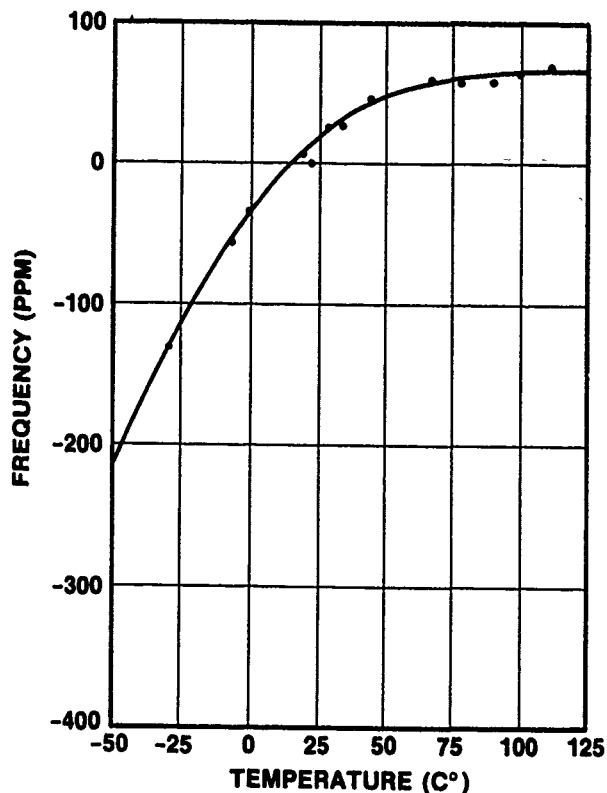


Figure 5. (YXwlt) 8.05/25.9/135.7

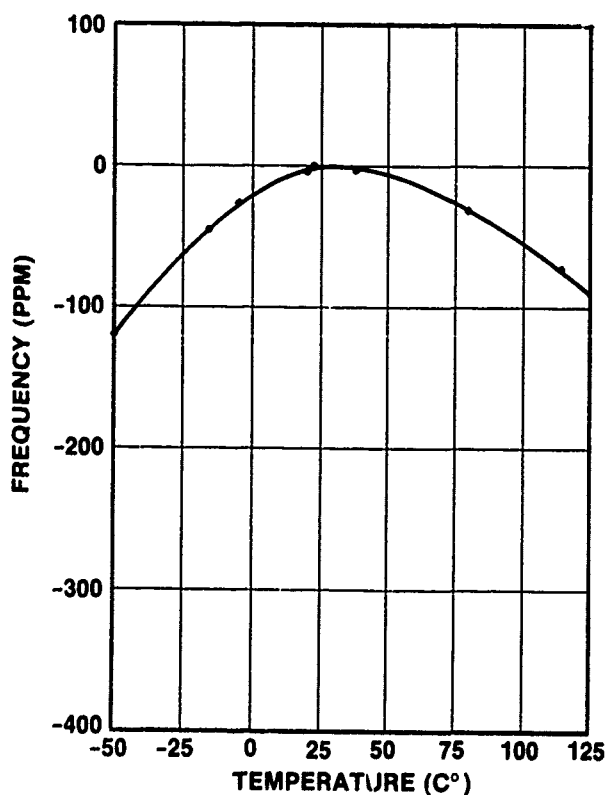


Figure 6. (YZwlt) 6.57/26.88/134.9

Table 5. Comparison of Experimental and Calculated Results

Angles			Calculated				Measured		
Phi	Thet	Psi	TCF ^{††}	TCF ^{†††}	TCF ^{2†††}	TCF ^{3†††}	TCF ¹	TCF ²	TCF ³
0	42.75	0†	-0.07 X 10 ⁻⁴	0.06 X 10 ⁻⁴	-0.40 X 10 ⁻⁷	0.11 X 10 ⁻¹⁰	-0.1 X 10 ⁻³	-0.37 X 10 ⁻⁷	-0.17 X 10 ⁻¹⁰
8.05	25.9	135.7	-0.01	0.74	-0.15	0.42	0.16	-0.16	0.58
6.57	26.88	134.9	-0.24	0.55	-0.15	0.48	0.025	-0.16	0.47

†Wafer obtained commercially. Angular tolerance is unknown.

††Calculated using Sinha and Tiersten's program.

†††Calculated using Finite Difference Approach.

The agreement between the experimental and calculated results has been excellent to date. Calculations using the Finite Difference method indicate that the doubly rotated wafers in fabrication should possess a slightly improved frequency response with $TCF^{(2)} = -0.1 \times 10^{-7}$ (see Table 1) but does not include the effects of coordinate axis skewing⁵ taken into account by the Sinha and Tiersten computer program, which may become significant for these cuts which are farther off of the crystalline axes.

SUMMARY

The results of a study of the temperature coefficients of frequency on doubly rotated cuts of quartz were presented. Both a Finite Difference technique³ and a Perturbation technique developed by Sinha and Tiersten⁵ were used to select orientations with temperature stability superior to ST-Cut quartz. Experimental results are found to be in agreement with the calculations and show a two fold improvement in frequency stability over the ST-Cut.

ACKNOWLEDGEMENTS

The authors wish to thank Dr. A. Ballato for stimulating technical discussions; we wish to thank Mr. D. Green, Mr. R. Welles, Mr. J. Balacio, Mr. R. Caputo, Ms. C. Peterson and Ms. L. Fredericks in the material and fabrication areas.

REFERENCES

- 1"Surface Acoustic Wave Delay Lines with Small Temperature Coefficient", Schulz, Manfred B., Proc. IEEE, Sept. 1970, pp. 1361-1632.
- 2"Higher Order Temperature Coefficients of Quartz SAW Oscillators", D. Handen, M. Michael, J.J. Gagnepain, Frequency Control Symposium, 1978, pp. 77-86.

3"Numerical Computation of Acoustic Surface Waves in Layered Piezoelectric Media-Computer Program Descriptions", William Jones, William Smith, Donald Perry, Final Report F19628-70-C-0027, prepared for Air Force Cambridge Research Laboratories by Hughes Aircraft Company.

4"The Temperature Coefficients of Acoustic Surface Wave Velocity and Delay on Lithium Niobate, Lithium Tantalate, Quartz, and Tellurium Dioxide", Andrew Slobodnik, Report #AFCRL-72-0082, Air Force Cambridge Research Laboratories.

5"The Temperature Dependence of the Velocity of Surface Waves in Quartz", B.K. Sinha and H.F. Tiersten, IEEE, 1978, Ultrasonics Symposium, pp. 662-665.

6"Higher Order Temperature Coefficients of the Elastic Stiffnesses and Compliances of Alpha-Quartz", R. Bechmann, A. Ballato, T. Lukaszek, IRE, Aug. 1962, pp. 1812-1822.

7"Standards on Piezoelectric Crystals 1949", Pro. IRE 14, Dec. 1949, pp. 1378-1395.

8"Numerical Analysis of Doubly Rotated Cut SAW Devices", Williams and Cho, 1979 USP, IEEE Cat. No. 79CH 1482-9SU.

9"Surface and Shallow Bulk Acoustic Waves Propagating on Doubly Rotated Quartz Substrates," A. Ballato, T. Lukasek, K. Yen, R. Kagiwada, Technical Report DELET-TR-79-23, U.S. Army Electronics Technology and Devices Laboratory, Fort Monmouth, N.J.

10"A New Cut of Quartz Giving Improved Temperature Stability to SAW Oscillators", Ian Browning and Meirion Lewis, Proc. 32nd Annual Symposium on Frequency Control, 1978, pp. 87-92.

OBSERVATIONS OF EFFECTS INDUCED BY DIELECTRIC COATINGS ON SSBW AND SAW DEVICES

Carl N. Helmick Jr. and David J. White

Physics Division, Research Department (Code 3814)
Naval Weapons Center, China Lake, CA 93555

Abstract

We have reported previously on the effects of thin dielectric overlays on narrow-band SAW devices, showing that Al_2O_3 and ZnS are potentially useful materials for fine-tuning the center frequency up or down. Our study has now been expanded to include SSBW devices as well. Currently we are investigating an extensive sampling of closely related SAW and SSBW delay lines, all fabricated on rotated Y cuts of quartz and employing the same transducer design, but differing in (1) substrate rotation angle (+35 to 43°), (2) coating (ZnS, Al_2O_3 , or nothing), and (3) propagation direction (0 or 90° with respect to the X axis). Preliminary results, comprising room-temperature data on ten coated samples, are reported here. The coated SAW lines show no surprises, but the coated SSBW lines display interesting behavior. ZnS overlays produce even stronger center-frequency shifts than on SAW devices. In addition, both ZnS and Al_2O_3 reduce insertion loss substantially, provided the coating thickness does not exceed about 0.02λ . These effects are attributed to trapping or guiding by the dielectric surface layer, i.e., the transformation of shallow bulk waves into Love waves. Some implications of this behavior are discussed. Additional measurements (including temperature dependence and aging) are planned and will be reported later.

Introduction

In previous studies we have demonstrated that the deposition of a thin overlay of a suitable nonconducting material on a narrow-band SAW (surface acoustic wave) device can be employed to adjust its center frequency up or down by as much as 1% without appreciably degrading performance.^{1,2} The technique is thus potentially useful as a practical means of fine-tuning the center frequency of narrow-band SAW devices to meet the stringent tolerances often encountered in specific applications, either as a post-fabrication operation or as a final trimming step in production.

In particular for quartz SAW delay lines, we found ZnS (whose acoustic velocity is slower than that of quartz) to be an excellent coating material for decreasing the center frequency. Similarly, Al_2O_3 (a faster material than quartz) was found to be useful for increasing the center frequency. In either case, a relative frequency shift of 0.5% re-

quired an overlay thickness of about 0.007λ (i.e., about 300 nm for a 70-MHz SAW device). Insertion loss increased typically 1 or 2 dB for such coatings. In addition, for devices fabricated on quartz substrates having a parabolic temperature dependence (e.g., AT and ST cuts), we observed that both overlay materials decreased the turnover temperature (temperature where the slope of the frequency-temperature characteristic passes through zero) some 25 to 50°C.

Subsequent work has been directed toward making a number of improvements in experimental technique and instrumentation (related to device fabrication, coating, packaging, and characterization), and the scope of the study has been broadened to include SSBW (surface-skimming bulk wave) as well as SAW devices. Presently we are engaged in the investigation of the effects produced by dielectric overlays on a series of closely related quartz SAW and SSBW delay lines, all fabricated on rotated Y cuts of quartz and employing the same transducer design. The devices differ only in (1) substrate rotation angle (three cuts in the range 35 to 43°), (2) coating material (ZnS, Al_2O_3 , or nothing), and (3) transducer orientation (propagation parallel or perpendicular to the crystalline X axis).

We now wish to report the preliminary results of room-temperature observations made on ten of these coated devices, comparing center frequency and insertion loss before and after coating, for both classes of device. First, however, we shall review the general properties of SSBW and SAW devices as they relate to the present study.

SSBW and SAW Properties Compared

Surface-skimming bulk waves, also known as shallow bulk acoustic waves (SBAW's), are shear-horizontal (SH) bulk waves that travel just below the surface, gradually spreading into the bulk material as they propagate.³⁻⁶ SSBW's can be generated and received by interdigital transducers (IDT's) on piezoelectric crystals in the same manner as SAW's (Rayleigh waves). They and other bulk modes can often be excited in addition to Rayleigh waves on SAW devices. (Still other surface and pseudo-surface modes exist for certain material symmetries and orientations, but these will not be discussed here.) When these bulk modes accompany the desired Rayleigh surface wave, they are usually regarded as spurious and can sometimes cause interference or distortion.

It has been recognized since 1976, however, that the shallow SH mode can be specifically isolated and employed to good advantage in acoustic devices, possessing most of the desirable features of SAW devices (planar geometry, compact size, design versatility, etc.). SSBW/SBAW devices can utilize the design and fabrication techniques already developed for SAW devices.

The two modes — SSBW (shallow SH) and SAW (Rayleigh) — differ in the details of velocity, coupling efficiency, and temperature coefficient of delay, as these are all strong functions of material, orientation, and propagation mode. Fortunately, there exist several materials and orientations having favorable combinations of propagation properties for SSBW's.

For example, the rotated Y cuts of quartz are of particular interest because of the existence of temperature-compensated orientations. Conventional SAW devices typically use the ST cut (42.75° rotated Y cut) with propagation parallel to the X axis. This orientation possesses a parabolic temperature dependence, with turnover temperature at room temperature, and the IDT couples maximally to the Rayleigh mode (SAW).

There is, however, some weaker coupling to bulk modes at higher frequencies in these devices, with the fast quasi-shear (quasi-SH) and quasi-longitudinal modes typically being observable in narrow-band delay lines.^{4,5} These appear at frequencies well above the SAW frequency, where they become phase matched to the IDT's for propagation (nearly) parallel to the surface. In addition, wide-band SAW devices can suffer from interference or distortion due to the slow quasi-shear (quasi-shear-vertical [SV]) mode within or very near the pass-band, as its velocity is not much above the Rayleigh velocity.

When the same transducers are oriented 90° off the X axis, however, coupling occurs only to a pure SH mode (i.e., the SSBW/SBAW), whose velocity is about 1.6 times that of the Rayleigh SAW generated in the 0° orientation (5.1 v/c 3.16 km/s). Furthermore, the temperature coefficient is related to that of the corresponding conventional bulk-wave configuration, so that the proper choice of cut can yield a temperature dependence equal or superior to that of the SAW on ST-cut quartz.³ SSBW's on AT-cut quartz, for example, are approximately equivalent to conventional (perpendicular) bulk waves in BT-cut quartz, as the two cuts are about 90° apart.

Thus, an AT-90° SSBW device differs in the following important respects from an ST-0° (or ST-X) SAW device:

1. Only one mode (viz., the SSBW = SBAW = SH) mode couples to the transducers, yielding a cleaner spectrum.
2. The center frequency (which scales as propagation velocity for a given transducer size) is about 60% higher, enabling higher frequency devices to be fabricated for a given IDT size (important for operating frequencies above 500 MHz, where transducer resolution tolerances become critical for SAW's).
3. Insertion loss tends to be somewhat higher, especially for long propagation paths, due to beam-

spreading loss. (Surface power falls as λ/R , where R is the path length = center-to-center transducer separation.) However, it is possible to minimize this extra loss through care in transducer design and fabrication and (as will be discussed later) the use of surface modifications that reduce spreading of the beam.

One more comment may be made. Since SSBW's travel somewhat below the surface, they are generally expected to be less affected by surface contaminants than SAW's, therefore yielding narrow-band devices (such as oscillators) with improved aging stability. Extensive aging tests of SSBW devices do not appear to have been reported yet, so this expectation remains to be verified.

Experimental Devices and Measurements

All devices currently under investigation are delay lines employing the same narrow-band design, based on a mask supplied to us by Andersen Laboratories. The two transducers (not identical) utilize split fingers with overlap weighting. One transducer consists of 170 periods, with three fingers per period; it operates at the second harmonic. The other transducer consists of 144 periods, with four fingers per period; it operates at the third harmonic. The finger spacings are such that the resonant wavelengths λ_0 are the same, here 22.8 μm . The ground bus for each transducer completely encloses the finger region, following a trapezoidal path. Both apertures are 65 wavelengths, the center-to-center separation is 464 wavelengths, and the gap between finger regions is 73 wavelengths.

The transducers, aluminum 100 to 110 nm thick, are formed on bare quartz substrates using standard photolithographic techniques. The bottom surface and the end edges of the substrate are roughened prior to transducer fabrication to suppress (scatter) any reflected waves.

This design is being used to make some three dozen devices, comprising three substrate cuts, two propagation directions, and three coating conditions, as follows:

1. The substrates are rotated Y cuts of quartz having rotation angles +35.25° (AT cut), +39.0°, and +42.75° (ST cut).
2. Transducer orientations are either (a) perpendicular to the quartz X axis (denoted here as the 90° direction), yielding only the SSBW; or (b) parallel to the X axis (denoted here as the 0° direction), yielding primarily the Rayleigh SAW, but also two smaller peaks at higher frequencies, due to the onset of the quasi-SH and quasi-longitudinal modes.
3. Coatings are ZnS (slow layer), Al_2O_3 (fast layer), or nothing. The thickness of the dielectric layer ranges from 50 to 600 nm (h/λ from 0.2% to 2.6%) for different samples. Uniform coatings are deposited over the entire device, employing E-beam evaporation for ZnS and formerly for Al_2O_3 . Because of consistency problems encountered with the latter in our evaporation setup, we have changed to reactive sputtering as a means for depositing high-purity Al_2O_3 coatings. Unfortunately, the sputtering system was out of operation until quite recently, so that we have obtained only one device to date.

with a sputtered Al_2O_3 coating. All of our overlays are assumed to be polycrystalline and unaligned, i.e., effectively isotropic.

The delay lines are currently at various stages of fabrication, packaging, and room-temperature characterization. Such characterization consists so far of transmission measurements performed on the unmatched devices, including the recording of wide- and narrow-band frequency sweeps plus careful measurements of center frequency, insertion loss, and phase vs. frequency in the passband. These measurements are performed before and after coating, with some double checks made at other times to ascertain consistency and stability.

Following completion of the room-temperature characterizations and final package sealing, representative samples will be measured as a function of temperature and then monitored in oscillator circuits for aging behavior.

Presently we have satisfactory room-temperature data on ten coated devices (four SAW and six SSBW). In Table 1 we have listed center frequencies and insertion loss for each device, along with the changes produced by the overlay. Although our investigation is far from complete, we believe these preliminary results are of sufficient interest to report now.

Additional measurements are planned and will be reported later.

Room-Temperature Results

As can be seen from Table 1, for the particular transducer design used, the uncoated SAW center frequencies were about 139.5 MHz and the uncoated SSBW center frequencies were about 60% higher, ranging from 221 to 226 MHz, depending on cut. Uncoated insertion loss at center frequency (unmatched) was around 20 dB for the SAW lines and 27 dB for the SSBW lines, there being a moderate amount of sample-to-sample variation, especially for the SSBW lines. Group delay times were about 3.1 μs for the uncoated SAW lines and 1.9 μs for the SSBW lines.

The coating-induced changes for the SAW lines were about as expected on the basis of our earlier work,^{1,2} with ZnS decreasing center frequency approximately linearly with thickness over the range observed. The rate of frequency change was about -4.5 kHz/nm, verified up to a thickness of 305 nm (0.013 λ), at which thickness the frequency had decreased by 1.5%. Insertion loss was degraded by no more than 2 dB for these coatings.

The results for the coated SSBW devices were at

TABLE 1. Room-Temperature Effects Observed on Coated SAW and SSBW Devices.

Samples listed in order of increasing coating thickness h for each mode and coating material.

λ_0 = surface wavelength defined by transducers = 22.8 μm ,

f_0 = center frequency, IL = insertion loss.

PROP. MODE	OVERLAY		QUARTZ SUBSTRATE		UNCOATED DEVICE		COATING-INDUCED CHANGES		
	Material	h (μm) [h/λ_0]	Cut-Orient.	ID #	f_0 (MHz)	IL (dB)	Δf_0 (MHz) [$\Delta f_0/f_0$]	$\Delta f_0/h$ (MHz/ μm)	ΔIL (dB)
SAW	ZnS	0.160 [0.70%]	AT-0°	C8	139.51	18.5	-0.79 [-0.57%]	-4.9	+2
		0.255 [1.12%]	ST-0°	C7	139.62	22	-1.03 [-0.74%]	-4.0	+2
		0.275 [1.21%]	AT-0°	C3	139.41	19	-1.40 [-1.00%]	-5.1	+1
		0.305 [1.34%]	AT-0°	C4	139.38	22	-1.50 [-1.08%]	-4.9	±0
SSBW	ZnS	0.201 [0.88%]	AT-90°	D9	225.93	36	-2.90 [-1.28%]	-14.4	-13
		0.250 [1.10%]	39°-90°	D5	224.34	28	-1.18 [-0.53%]	-4.7	-7
		0.300 [1.32%]	ST-90°	D11	221.59	28	-2.93 [-1.32%]	-9.8	-12
		0.370 [1.62%]	39°-90°	D13	224.39	27	-5.33 [-2.38%]	-14.4	-7
		0.530 [2.33%]	39°-90°	D7	224.31	24.5	-11.87 [-5.29%]	-22.4	+5
	Al_2O_3	0.147 [0.65%]	39°-90°	D6	224.29	24	-0.30 [-0.13%]	-2.0	-6

first surprising to us, because of the widespread expectation that SSBW's are less influenced by (non-conducting, nonperiodic) surface contaminants than true surface (e.g., Rayleigh) waves.³⁻⁶ Our data reveal that the frequency shift induced by a thin ZnS coating is about double that for the SAW case, roughly -10 kHz/nm for h/λ up to about 2%, though there is appreciable scatter in the limited sampling to date.

For $h/\lambda > 2\%$ the frequency shift was even more pronounced, with a rather large (5.3%) frequency decrease observed for the 530-nm ZnS coating. The one Al_2O_3 -coated sample also displayed a negative frequency shift, though much smaller than for a ZnS coating of comparable thickness. This is contrary to the effect observed for SAW devices,^{1,2} as Al_2O_3 is a fast layer and tends to increase the velocity of Rayleigh waves.

Note that Al_2O_3 is a fast layer even in the SSBW case, as its isotropically averaged velocity is 6.4 km/s, which is 25% higher than the uncoated SSBW velocity. (This assumes the film density is close to that of the bulk.)

Another notable feature of the dielectric-coated SSBW lines is the substantial improvement (6 to 13 dB) in insertion loss resulting from all the coatings except the thickest. The SSBW lines show somewhat less individual variation in loss values after coating than before, tending to be about the same as for the uncoated SAW lines — although one coated SSBW line (#D11) ended up with lower loss than any of the uncoated SAW lines. In contrast to the others, the SSBW line with the thickest coating (530 nm) displayed increased loss, suggesting that signal enhancement ceases for $h/\lambda > 2\%$.

Some observations were also made of frequency and insertion loss for the higher-order modes also present on the SAW devices. These are not shown in the table, as documentation was not as complete on these "spurious" modes for the devices made early in the study. Their general characteristics, however, can be readily summarized.

Two transmission peaks were seen above the Rayleigh frequency, similar to those reported by Browning and Lewis.^{4,5} A fast-shear response (quasi-SH mode) appeared in the 225-226 MHz range, and a quasi-longitudinal response occurred at about 254.5 MHz (the latter usually, but not always, weaker than the former). No evidence of waves reflected from the ends or the bottom surface was seen.

When the SAW devices (0° propagation direction) were coated with ZnS or Al_2O_3 , very little change was seen in the quasi-longitudinal mode, but a substantial negative frequency shift (typically -10 kHz/nm), often accompanied by signal enhancement, was seen for the quasi-SH mode on ZnS-coated devices. It was, in fact, the observation of coating-induced effects on the quasi-SH mode of 0° devices that prompted us to investigate more carefully the effects of dielectric coatings on the SH mode (SSBW/SBAW) on 90° devices.

Discussion

The substantial negative frequency shift pro-

duced by a thin ZnS coating on an SSBW delay line is larger than expected on the basis of simply a velocity perturbation. Even a fast layer, Al_2O_3 , was found to decrease the center frequency, albeit to a lesser extent. One way to account for this is to assume that the dielectric bends the SSBW, initially propagating at a shallow angle with respect to the surface, so that it propagates (more nearly) parallel to the surface.

For example, consider a tilted plane bulk wave, propagating at an inclination angle θ into the bulk material. If λ is the bulk wavelength, then its projection on the surface, λ_a , is given by:

$$\lambda_a = \lambda / \cos \theta = v / f \cos \theta. \quad (1)$$

At the center frequency (phase-matched condition), we have $\lambda_a \equiv \lambda_0$, where λ_0 is the operating wavelength of the IDT's — a fixed geometrical property of the finger spacing. Therefore the right-hand side of eq. (1) is invariant with respect to any coatings.

Now let the subscripts 1 and 2 denote two conditions: uncoated and coated, respectively. Equating $v/f \cos \theta$ for these two conditions yields:

$$\frac{f_{02}}{f_{01}} = \frac{v_2}{v_1} \cdot \frac{\cos \theta_1}{\cos \theta_2} \quad (2)$$

= (velocity factor) \times (bending factor),

where f_{0i} = center frequency, v_i = velocity in the transducer region (composite medium), and θ_i = launch angle ($\theta_2 < \theta_1$). For a slow layer like ZnS ($v_2 < v_1$), both factors are less than 1, leading to a strong decrease in f_0 . For Al_2O_3 , a fast layer, the velocity factor is greater than 1 and the bending factor less than 1, with the former evidently dominant, leading to a mild frequency decrease.

This simple model is at best incomplete, but it nonetheless illustrates the influence of both velocity and angle modifications. One must consider in more detail the propagation of acoustic waves in layered media, which has been extensively reviewed by Farnell and Adler.⁷ Relevant qualitative features will be outlined here.

In a medium consisting of a semi-infinite substrate covered by a thin layer, two surface-guided modes can be identified if anisotropy is not excessive: A Rayleigh-like wave, having primarily sagittal-plane displacements, and a Love wave, having primarily horizontal displacements (i.e., a [quasi-]SH surface-guided wave). For either of these surface-guided modes, more of the mode energy is drawn into the layer as the relative thickness (h/λ) increases.

Thus if we add a dielectric overlay to a SAW device, we do not change the fundamental nature of the Rayleigh wave. It remains a Rayleigh(-like) wave after coating, but with modified velocity (generally shifted in the direction of the layer's shear velocity), along with the addition of dispersion (through the parameter h/λ). The effect of a thin coating on Rayleigh-wave velocity can be viewed as a perturbation, and velocity can be calculated approximately, at least for high-symmetry cases, as a

first-order correction (expanding in terms of h/λ or hK) to the uncoated velocity.⁸

The situation is quite different when applying a dielectric overlay to an SSBW device, even for very small h , as the coating transforms the initially diffracting bulk SH wave into a surface-guided SH Love wave. This accounts for the "bending" assumed in eq. (2), and is what has been variously referred to by others as "energy trapping," "ducting," "surface guiding," "confining," or the "addition of a slowing mechanism."^{3,5,6,9,10,11} Periodic surface grooves or other topological variations,^{9,10} or a metallic grating,⁶ between the transducers have already been used or considered as methods for trapping SSBW's, and we now have demonstrated that a similar effect results from the deposition of a dielectric coating. The layer (dielectric in this case) traps or guides the SSBW along the surface, so that (less) energy is radiated or diffracted into the bulk, leading to a reduction in insertion loss.

For a sufficiently thick coating the signal enhancement will saturate, the limiting value presumably being that for a Rayleigh surface wave. If the coating thickness is increased beyond an optimum range, sufficient wave energy will be drawn into the nonpiezoelectric layer that electromechanical coupling to the IDT's is diminished, leading to an increase (degradation) of insertion loss (see Ref. 7, pp. 122-123). This evidently is what happened in our sample #D7 ($h/\lambda = 2.33\%$). (Note, however, that the coating's effect on frequency was showing no signs of saturating at that thickness — actually becoming more pronounced.)

The case of Al_2O_3 (fast layer) on quartz SSBW devices raises some interesting questions, as in theory there is no real Love-wave solution for a fast layer on a planar substrate.⁷ Yet we appear to have an actual example of such a wave with our Al_2O_3 -coated SSBW line. Its signal strength was enhanced, as with ZnS, implying energy trapping by the Al_2O_3 layer, although the frequency was not shifted upward. Gulyaev and Polzikova¹¹ have shown that surface shear-wave velocity can be increased by a fast layer on a convex curved surface, but not on a planar surface. Although additional experimental and theoretical clarification is obviously needed in the present situation, it appears at this point that for Al_2O_3 on planar quartz devices (a) a (pseudo-) Love wave exists for at least some range of layer thickness and velocity values; (b) guiding or energy trapping occurs for SSBW's, though possibly not quite as complete as with a slow layer; and (c) SH propagation velocity is not increased above that of the uncoated substrate, although the decrease may be small. Consequently, upward frequency tuning of SSBW devices seems unlikely.

Conclusions

We have demonstrated that the deposition of a thin dielectric coating on an SSBW/SBAW device produces two effects: energy trapping and negative frequency shift. Either or both of these effects could prove useful in some applications of these devices.

It appears that a thin layer of any different

material, electrically conducting or nonconducting, deposited on the surface of an SSBW device — or presumably adsorbed by it — will have a pronounced effect on the frequency and amplitude characteristics. The surface perturbation effectively transforms the shallow-bulk, inward-spreading SH wave into a surface-guided Love wave. Consequently, the oft-presumed immunity of SSBW/SBAW devices to minor surface contaminants (of importance in the aging behavior of precision oscillators) is called into question. Clearly there is a need for closer examination of this point.

On the other hand, it may prove advantageous deliberately to exploit the evidently strong sensitivity of SSBW devices to (adsorbed) foreign materials as a *detection mechanism*. SAW and conventional bulk-wave devices have been employed or considered as sensors for chemical analysis, gas chromatography, air-pollution monitoring, and the detection of hazardous vapors.^{12,13} SSBW devices may offer increased sensitivity in some of these applications, and perhaps allow greater flexibility in the use of selective chemical absorbants without quenching the wave.

References

1. C.N. Helmick Jr., D.J. White & R.L. King, "Fine Tuning of Narrow-Band SAW Devices Using Dielectric Overlays," 1977 *Ultrasonics Symp. Proc.*, p. 659.
2. C.N. Helmick & D.J. White, "Observations of Aging and Temperature Effects on Dielectric-Coated SAW Devices," 1978 *Ultrasonics Symp. Proc.*, p. 580.
3. A. Ballato & T.J. Lukaszek, "Shallow Bulk Acoustic Wave Progress and Prospects," *IEEE Trans. MTT-27*, 1004 (1979); has extensive bibliography.
4. T.I. Browning & M.F. Lewis, "New Family of Bulk-Acoustic-Wave Devices Employing Interdigital Transducers," *Electronics Ltrs.* 13, 128 (1977).
5. M. Lewis, "Surface Skimming Bulk Waves, SSBW," 1977 *Ultrasonics Symp. Proc.*, p. 744.
6. K.H. Yen, K.F. Lau & R.S. Kagiwada, "Shallow Bulk Acoustic Wave Filters," 1978 *Ultrasonics Symp. Proc.*, p. 680.
7. G.W. Farnell & E.L. Adler, "Elastic Wave Propagation in Thin Layers," in *Phys. Acoustics*, Vol. 9, ed. W.P. Mason & R.N. Thurston (Academic Press, New York, 1972), pp. 35-127.
8. L. Bjerkan & K. Fossheim, "An Approximate Method for the Rayleigh Wave Dispersion in Materials Covered with a Thin Film," *J. Phys. D* 10, 925 (1977).
9. B.A. Auld & B-H Yeh, "Theory of Surface Skimming Wave Guidance by a Corrugated Surface," 1979 *Ultrasonics Symp. Proc.*, p. 786.
10. Yu.V. Gulyaev & V.P. Plessky, "Shear Surface Acoustic Waves in Periodic Structures," *Wave Electronics* 4, 7 (1979).
11. Yu.V. Gulyaev & N.I. Polzikova, "Shear Acoustic Surface Waves on a Cylindrical Surface of a Solid Coated with a Layer of a Different Material," *Sov. Phys. Acoust.* 24, 287 (1978).
12. H. Wohltjen & R. Dessy, "Surface Acoustic Wave Probe for Chemical Analysis" (in three successive parts), *Anal. Chem.* 51, 1458, 1465, 1470 (1979).
13. Y. Tomita et al., "Detection of Explosives with a Coated Piezoelectric Quartz Crystal," *Anal. Chem.* 51, 1475 (1979).

SENSITIVITIES OF SAW OSCILLATORS TO TEMPERATURE, FORCES AND PRESSURE : APPLICATION TO SENSORS

D. Hauden, S. Rousseau, J.J. Gagnepain

Laboratoire de Physique et Métrologie des Oscillateurs du C.N.R.S.
associé à l'Université de Franche-Comté-Besançon
32, av. de l'Observatoire - 25000 Besançon - France

Abstract

The paper describes the sensitivity of SAW oscillators to external thermal and mechanical perturbations. It is known that the sensitivity results from the non linear elastic behavior of the crystal which couples the surface wave to the static bias. The method which is used consists in calculating the static bias in the thin plate approximation by means of Mindlin's polynomial method and then in calculating the non linear coupling coefficients. The frequency shift is obtained by using a perturbation method which takes into account the surface wave penetration depth. Three types of sensors are studied : temperature, force and pressure.

- The temperature probe is made of a doubly-rotated quartz plate which has at the same time high sensitivity and good linearity.

- The influences of bending and uniaxial forces on rectangular quartz-plates, and of diametrically applied forces on circular plates as a function of the azimuthal angle are studied.

- The sensitivity to hydrostatic pressure is studied in the cases of bulky plates and of a thin diaphragm. If bulky plate sensitivity is small, the diaphragm exhibits very large frequency shifts.

Introduction

The characteristics of surface acoustic waves are modified by external effects as temperature and mechanical perturbations, i.e., forces, pressures, acceleration fields. Such sensitivity is almost entirely due to the non linear elastic properties of the crystal. Usually those phenomena are unwanted in stable SAW oscillators, because they are at the origin of the main causes of frequency instabilities. However they can advantageously be used for sensor applications, if the SAW is made selectively sensitive to a given physical quantity, the measurement of which thus is transposed into frequency measurement. High resolution can be obtained, because frequency measurements are the most accurate ones.

In the present paper thermal and mechanical effects are considered as quasistatic effects, in account of their large time constants with respect to that one of the high frequency wave. The

temperature distribution is supposed to be homogeneous in the all volume, and therefore the thermal behavior is represented by a static frequency-temperature characteristic which is related to the temperature coefficients of the material¹. The dynamic thermal behavior of the crystal is neglected. Under mechanical perturbations stress and strains fields are induced, which are function of the applied surface and volume forces. The static bias and the wave are coupled by the non linear properties of the crystal² which in the problems here considered are the third order elastic terms. The static deformation is calculated by using Mindlin's polynomial expansion³ and the corresponding velocity and/or frequency shifts^{4,5} are obtained by means of a perturbation method.

Temperature sensor

The anisotropy of quartz crystal enables to modify the frequency-temperature characteristic (F-T) by choosing appropriate crystal orientation (cut angles ϕ and θ defined following the IEEE notation YX $\omega\phi/\theta$) and the propagation direction (angle ψ with respect to the modified OX axis). This characteristic is represented by the well-known relation

$$f(T) = f(T_0) [1 + \alpha_f^{(1)}(T-T_0) + \alpha_f^{(2)}(T-T_0)^2 + \alpha_f^{(3)}(T-T_0)^3] \quad (1)$$

where $\alpha_f^{(1)}$, $\alpha_f^{(2)}$, and $\alpha_f^{(3)}$ are the first, second and third order temperature coefficients (T.C.'s) measured at the reference temperature T_0 . The ideal characteristic of a temperature sensor will correspond to zero second and third order T.C.'s and simultaneously to a first order one as large as possible. In this case the device will have at the same time good linearity and sensitivity.

The frequency shifts versus temperature of SAW oscillators were calculated for a large number of quartz cuts with different propagation directions⁶. Among different configurations with properties corresponding to the above specifications a cut was selected (considerations of coupling factor, power flow angle are also to be taken into account) as shown on fig. 1 (this cut was called LST cut), and corresponds to $\phi = 11^\circ 24'$, $\theta = 59^\circ 24'$ and $\psi = 35^\circ$. The calculated velocity is 3360 m/s. The T.C.'s are

$\alpha_f^{(1)} = 40 \text{ ppm/}^\circ\text{C}$, $\alpha_f^{(2)} = -4.10^{-5} \text{ ppm/}^\circ\text{C}^2$ and $\alpha_f^{(3)} = -3.10^{-7} \text{ ppm/}^\circ\text{C}^3$. In fact it appears that the value of the third order T.C. is certainly without any meaning because of the lack of precision at this order in the knowledge of the fundamental coefficients.

The electromechanical coupling factor is equal to 0.09 % and power flow direction angle is -3.3° .

Experimentally the selected cut was tested over a temperature range from -25°C to 100°C . The characteristic is shown on fig. 2. At a reference temperature of 25°C the measured frequency is equal to 93.15 MHz and corresponds to a phase velocity of 3356 m/s. The corresponding T.C.'s obtained from the experimental F-T characteristic are :

$$\alpha_f^{(1)} = 31 \text{ ppm/}^\circ\text{C} \text{ and } \alpha_f^{(2)} = -2.10^{-3} \text{ ppm/}^\circ\text{C}^2$$

The sensitivity of the probe is $3.2 \cdot 10^{-4} \text{ }^\circ\text{C/Hz}$ and the measured linearity defect is about 0.1°C for the range -25°C , $+75^\circ\text{C}$.

If one considers that the SAW oscillator using such a delay line has an intrinsic stability between $3 \cdot 10^{-10}$ and 10^{-9} over a few seconds, resolutions in temperature measurement of the order of $10 \mu^\circ\text{C}$ to $30 \mu^\circ\text{C}$ can be obtained.

On the other hand, the planar structure of the probe, as shown on fig. 3, enables to achieve faster response time by using the lower crystal surface as sensitive surface.

Velocity shifts under mechanical perturbation

The elastic equations of a finite amplitude wave propagating in a medium of specific mass ρ_0 , submitted to a mechanical bias can be written with respect to the natural state a_i :

$$\rho_0 \ddot{u}_i = (\overline{A}_{ikjm} u_{j,m})_{,k} \quad (2)$$

The boundary conditions corresponding to a stress free surface are :

$$\overline{A}_{ikjm} u_{j,m} = 0 \text{ for } a_2 = 0 \quad (3)$$

The coefficients \overline{A}_{ikjm} represent the non linear coupling between the static deformation and the high frequency wave. They are related to the static components

$$\overline{A}_{ikjm} = C_{ikjm} + \delta_{ij} \overline{T}_{km} + C_{ikjmu\nu} \overline{S}_{uv} + C_{pkjm} \overline{U}_{i,p} + C_{ikpm} \overline{U}_{j,p} \quad (4)$$

where C_{ikjm} and $C_{ikjmu\nu}$ are the second and third order elastic constants, \overline{T}_{km} , \overline{S}_{uv} and $\overline{U}_{i,p}$ the static stresses, strains and displacements gradients.

They can be presented as modified elastic constants following

$$\overline{A}_{ikjm} = C_{ikjm} + \overline{H}_{ikjm} \quad (5)$$

Generally, the non linear coupling terms \overline{H}_{ikjm} are function of the space variable a_i . The unperturbed wave components u_i^0 for the Rayleigh wave can be written :

$$u_i^0 = \sum_{p=1}^3 A_p u_i^0(p) e^{-\chi_p a_2} e^{i\omega_0(t - \frac{a_1 + \beta_p a_2}{V_0})} \quad (6)$$

with $\chi_p = \omega_0 \alpha_p / V_0$, β_p and α_p are the real and imaginary parts of the p complex depth coefficients q_p .

Although the wave penetration depth is small, it is not possible to consider the non linear coupling term \overline{H}_{ikjm} only at the free surface. The calculations has to take into account the functional dependence of \overline{H}_{ikjm} along the plate thickness by using a polynomial expansion :

$$\overline{H}_{ikjm} = \sum_n \overline{\alpha}_{ikjm}^{(n)} a_2^n \quad (7)$$

These coefficients are considered as small terms with respect to the second order elastic constants C_{ikjm} . Thus a perturbation method can be directly applied and leads to the relative velocity shifts for a Rayleigh wave :

$$\frac{\Delta V}{V_0} = \frac{\sum_n \left[\sum_{p,q} \frac{A_p u_i^0(p) A_q u_i^0(q) \overline{\alpha}_{ikjm}^{(n)} \overline{\alpha}_{ikjm}^{(n)}}{(q_p - q_q) (i \frac{\omega_0}{V_0} (q_p - q_q))^n} \right]}{2 \rho_0 V_0^2 \sum_{p,q} \frac{A_p u_i^0(p) A_q u_i^0(q)}{q_p - q_q}} \quad (8)$$

This equation is general and can be used whatever the perturbation is. For each particular problem the static stress and strain distribution will be calculated.

Following Mindlin³ if thin plates of thickness $2h$ are considered, the mechanical displacements \overline{U}_i are written :

$$\overline{U}_i = \sum_n \overline{U}_i^{(n)} a_2^n \quad (9)$$

The corresponding strains and stresses are developed the same way :

$$\overline{S}_{ij}^{(n)} = (1/2) [\overline{U}_{i,j}^{(n)} + \overline{U}_{j,i}^{(n)} + (n+1) (\delta_{2j} \overline{U}_i^{(n+1)} + \delta_{2i} \overline{U}_j^{(n+1)})] \quad (10)$$

where δ_{ij} is the Kronecker symbol.

Then strain-stress relations become :

$$\overline{T}_{ij}^{(n)} = C_{ijk\ell} \sum_m H_{mn} \overline{S}_{k\ell}^{(m)} \quad (11)$$

where H_{mn} is a constant, equal to zero if $m+n$ is odd and equal to $2h^{(m+n+1)}$ if $m+n$ is even.

Sensitivity to external forces

Bending forces

A rectangular plate of length L , clamped on one end and submitted to a bending force F distributed on the other end is represented by a bi-dimensional model in the (a_1, a_2) plane. The edge conditions are :

$$\begin{aligned} \bar{U}_1 = \bar{U}_2 = \bar{U}_{1,2} \text{ at } a_1 = a_2 = 0 \\ T_{11} = 0 \quad T_{12} = F \text{ at } a_1 = L \end{aligned} \quad (12)$$

(L is the plate length)

The static displacements field is :

$$\begin{aligned} \bar{U}_1 &= -K [C_{22} C_{66} a_2 a_1^2 + (\bar{C}_{12}^2 + C_{11} C_{66}) a_2^3/3] \\ \bar{U}_2 &= K [C_{22} C_{66} a_1^3/3 + h^2 \bar{C}_{12}^2 + C_{12} C_{66} a_2^2] a_1 \\ \bar{U}_3 &= 0 \end{aligned} \quad (13)$$

with $K = 3F/4h^3 C_{66} \bar{C}_{12}^2$ and $\bar{C}_{12}^2 = C_{12}^2 - C_{11} C_{22}$

Fig. 4 shows the calculated sensitivities of singly rotated quartz cuts as a function of θ . Y and ST cuts were measured and their force-frequency coefficients are compared to the theoretical evaluations in table I. The SAW is propagating along OX at 88 MHz ($L = 17$ mm, $2h = 2$ mm and width = 15 mm).

	sensitivity Hz/N	
	measured	calculated
ST,X	1140	1200
Y,X	740	930

Table I

Axial forces

The rectangular plate is submitted to an axial force. Conditions at the clamped end are the same. On the other end they become :

$$T_{11} = F \quad T_{12} = 0 \quad \text{at } a_1 = L$$

The displacement field is easily obtained and corresponds to an homogeneous distribution :

$$\begin{aligned} \bar{U}_1 &= K C_{22} a_1 \\ \bar{U}_2 &= -K C_{12} a_2 \\ \bar{U}_3 &= 0 \end{aligned} \quad (14)$$

with $K = F/2h \bar{C}_{12}^2$

Theoretical sensitivities for singly rotated cuts are presented on fig. 5. They are also compared to the experimental values measured on ST and Y cut quartz plates, in table II.

	sensitivity (Hz/N)	
	measured	calculated
ST,X	58	54
Y,X	90	45

Table II

The discrepancy between theory and experiment in the case of Y cut is large and is attributed to lack of precision in the mechanical set used for applying the force.

Diametrically applied forces on circular plates

A circular plate of thickness $2h$ and diameter D is submitted to diametrically applied forces. The stress distribution is purely radial and exact solutions can be calculated even in the case of anisotropic bodies as a function of the force azimuthal angle α .

Figure 6 shows the force sensitivities of a SAW propagating along the Oa_1 axis of the circular plate versus α . Calculations are performed for ST and Y cuts and compared with measured values of Y cut. The SAW propagation direction is along the X-axis (noted a_1 on the figure). Plate diameter is 40 mm and thickness $2h$ is 2 mm.

The values $\alpha = 0^\circ, 90^\circ$ correspond to a maximum of sensitivity, for both cuts, and are appropriate for sensor applications. But it can be also observed that for $\alpha = 45^\circ, 135^\circ$ (Y cut) and $\alpha = 50^\circ, 130^\circ$ (ST cut), the sensitivity becomes zero and therefore such angles can be used for desensitizing the SAW to spurious mounting influence in the case of stable oscillators.

Sensitivity to hydrostatic pressure

The sensitivity of SAW delay line to hydrostatic pressure is generally small. Indeed, strains and stresses field are homogeneous in the all volume of the crystal plate. For a plate (of thickness $2h$) fixed at its lower surface, the static displacements due to the application of a uniform pressure P are :

$$\begin{aligned} \bar{U}_1 &= -P [\sigma_1 a_1 + 2\sigma_6 (a_2 + 2h) + \sigma_5 a_3] \\ \bar{U}_2 &= -\sigma_2 P (a_2 + 2h) \\ \bar{U}_3 &= -P [\sigma_5 a_1 + 2\sigma_4 (a_2 + 2h) + \sigma_3 a_3] \end{aligned} \quad (15)$$

with $\sigma_i = \sum_{j=1}^3 s_{ij} \epsilon_j$ $i = 1$ to 6 ;
 s_{ij} are the stiffness constants.

The corresponding strains can be written :
 $\epsilon_i = -\sigma_i P$.

Figure 7 shows theoretical and experimental frequency shifts of a ST-cut quartz SAW oscillator at 105 MHz submitted to hydrostatic pressure from 0 to 35 PSI. The sensitivity is about 25 Hz/PSI and is rather low for sensor applications.

As already presented^{10,11}, a thin anisotropic plate clamped at its edges and submitted to a pressure, is deformed by an important bending. The sensitivity can still be increased by using a thin circular diaphragm.

For describing such an anisotropic diaphragm stiffly clamped all around, a three-dimensional model is necessary. In account of the difficulty to solve it directly, the problem was splitted into two parts :

- a cross section in the $a_1 a_2$ plane, normal to the main surfaces of the diaphragm, is first considered, with the boundary conditions $T_{22} = 0$ at $a_2 = 0$, $T_{22} = P$ at $a_2 = -2h$ and the edge conditions $U_1 = U_2 = U_{1,2} = 0$ at $a_2 = 0$ and $a_1 = R$. The stress and strain distribution are easily calculated in this bi-dimensional problem by using the polynomial method.

- then the solutions are transposed to any cross-section normal to the main surfaces (fig. 8). The stress and strain distributions are calculated at a point M whatever its position is in the cross section. By superposing at the point M the solutions corresponding to the all possible cross sections (this is equivalent to performing an integration over 360°) the total stresses and strains are obtained at the point M.

The perturbation method gives the corresponding pressure-sensitivity at a point of the surface. The mean (and true) sensitivity is obtained by averaging over the path length (δ) and over the beam width (w) given by the transducer location and geometry (fig. 9).

Fig. 10 gives the pressure-sensitivity for a Y-cut of quartz as a function of the mean position of the transducers on the a_3 axis. The diaphragm thickness is 246 μm and its diameter is 10 mm. The nominal oscillator frequency is 105 MHz.

For $w = 1,5$ mm, three experimental points have been obtained and the calculation is in good agreement with them. At the center of the diaphragm ($a_3 = 0$), the sensitivity is 1.4 KHz/PSI and is almost the opposite of that one at $a_3 = 4$ mm. Using this property, dual channel sensor with a sensitivity twice as large has been built¹².

The differential device also enables to decrease largely the temperature influence by com-

pensating effect. The temperature coefficient of a clamped diaphragm is larger than the corresponding TC of a free-to-expand plate (2.5 KHz/ $^\circ C$ for a Y-cut diaphragm) as calculated by considering a circular plate submitted to axial forces distributed along its periphery. It is possible to choose a particular cut for avoiding this effect, but the easiest solution is to use two channels which reduce the frequency-temperature shifts within 1 KHz over a temperature range from $-40^\circ C$ to $+80^\circ C$.

The influence of the quartz anisotropy was also studied. On fig. 11 are presented the sensitivities of two doubly rotated cuts with zero first order temperature coefficients. They can be compared with Y and ST cut sensitivities given on the same figure. All these four sensitivities correspond to a thickness over diameter ratio normalized to unity.

Conclusion

SAW delay lines and resonators can advantageously be used as sensors in account of their large sensitivities and also of their high frequencies, which allow small sizes. The linearities which could be achieved are still to be precized. The second advantage of SAW sensors is related to their planar structure, which can be held and mounted easily, and designed for the best thermal and mechanical characteristics.

Acknowledgements

The authors wish to thank Dr. P. Hartemann of Thomson-C.S.F. for the experimental values of the pressure sensor sensitivities and Dr. C. Peugeot for providing the doubly rotated quartz crystal samples.

References

1. R. Bechman, A.D. Ballato, T.J. Lukaszek, "Higher order temperature coefficients of the elastic stiffness and compliances of alpha-quartz", U.S.A.E.L.R.D.L. Technical Report 2261, Fort Monmouth, N.J. 1963.
2. J.C. Baumhauer, H.F. Tiersten, "Non linear electroelastic equations for small fields superposed on a bias", J. Acoust. Soc. Am., 54, n° 4, 1018, (1973).
3. R.D. Mindlin, "An introduction to the mathematical theory of vibrations of elastic plates", Monograph USASCEL, Fort Monmouth, N.J., 1955.
4. H.F. Tiersten, B.K. Sinha, "A perturbation analysis of the attenuation and dispersion of surface waves", J. Appl. Phys., 49, jan. 1978.
5. D. Hauden, "Etude des propriétés non linéaires des ondes élastiques de surface : application aux oscillateurs et capteurs à quartz", Thèse Besançon, juin 1979.

6. D. Hauden, M. Michel, J.J. Gagnepain, "Higher order temperature coefficients of quartz SAW oscillators", Proceedings of 32nd annual frequency control Symposium, May 1978.
7. R.N. Thurston, "Wave propagation in fluids and normal solids", Physical Acoustics, vol. 1A, Academic Press, New-York, 1964.
8. D. Janiaud, L. Nissim, J.J. Gagnepain, "Analytical calculation of initial stress effects on anisotropic crystals : application to quartz resonators", Proceedings of 33rd annual frequency control Symposium, May 1979.
9. S. Rousseau, "Sensibilité à la pression de lignes à ondes de surface : étude d'un capteur à quartz", Thèse Besançon, LPMO, Mars 1980.
10. J.F. Dias, H.E. Karrer, "Stress effects in acoustic surface wave circuits and applications to pressure and force transducers", IEEE International Solid State Circuits Conference, 1974.
11. T.M. Reeder, D.E. Cullen, M. Gilden, "SAW oscillator pressure sensors", 1975, IEEE Ultrasonics Symposium Proceedings IEEE, cat. 75CH0994-4SU.
12. P. Hartemann, D. Hauden, "Capteurs de pression à ondes élastiques de surface. Journées Industrielles de la Société Française de Physique, Toulouse, 18 mars 1980.

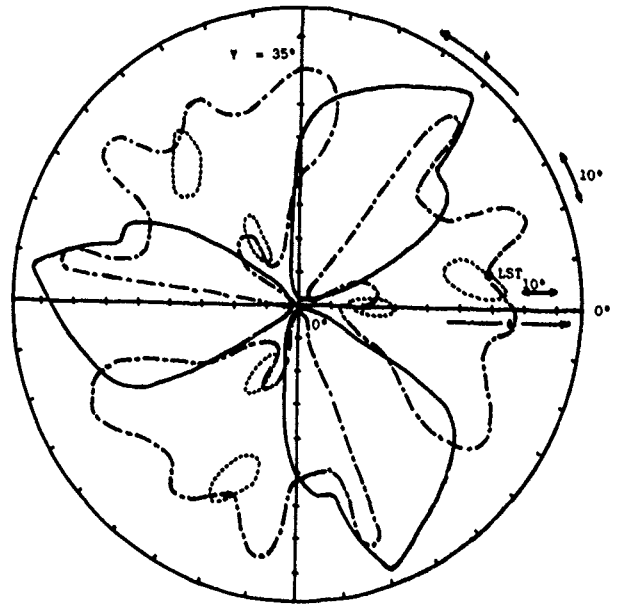


Fig. 1 : Loci with zero
First (—), second (---) and third (-.-) order temperature coefficients obtained by calculation.

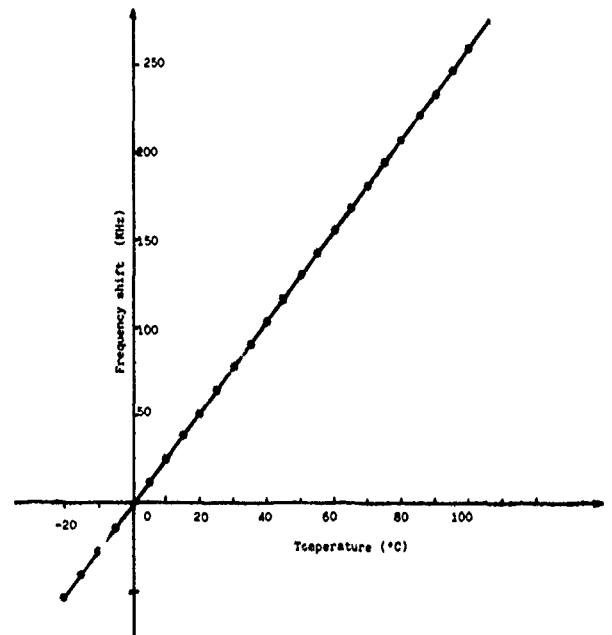


Fig. 2 : Frequency-temperature characteristic measured on the LST quartz crystal. Sensitivity 3100 Hz/°C, Linearity 0.1°C from -25 to + 75°C.

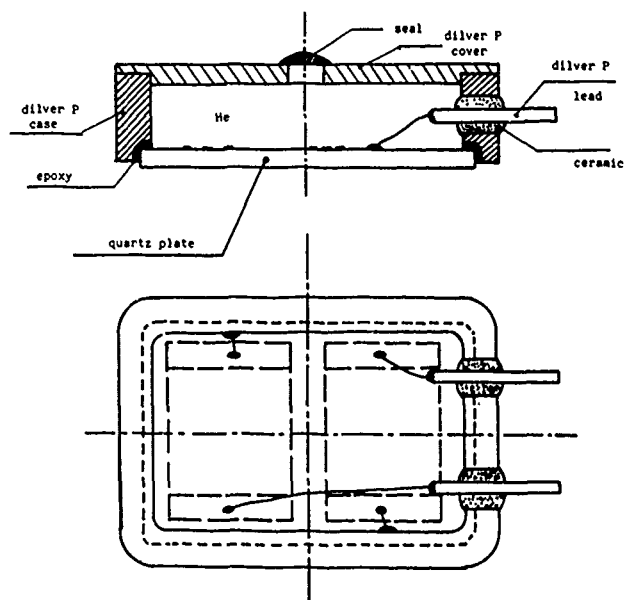


Fig. 3 : Configuration of the SAW LST temperature sensor.

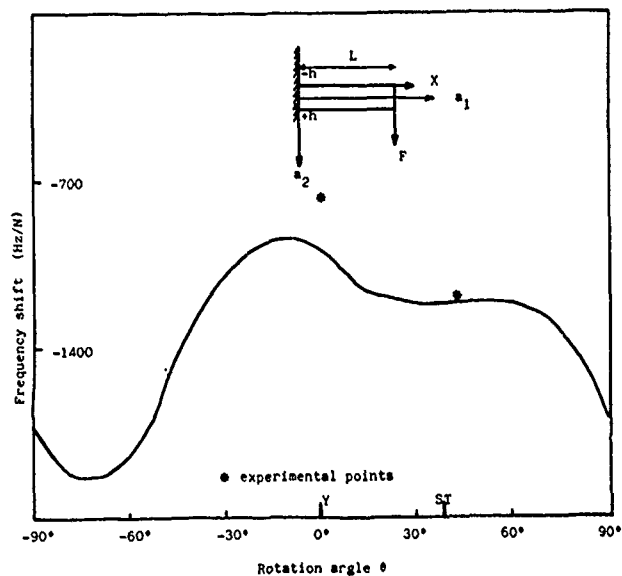


Fig. 4 : Sensitivity versus θ of a SAW propagating on a $Y+\theta^\circ$ rectangular quartz plate clamped on one end and submitted to a bending force on the other end.

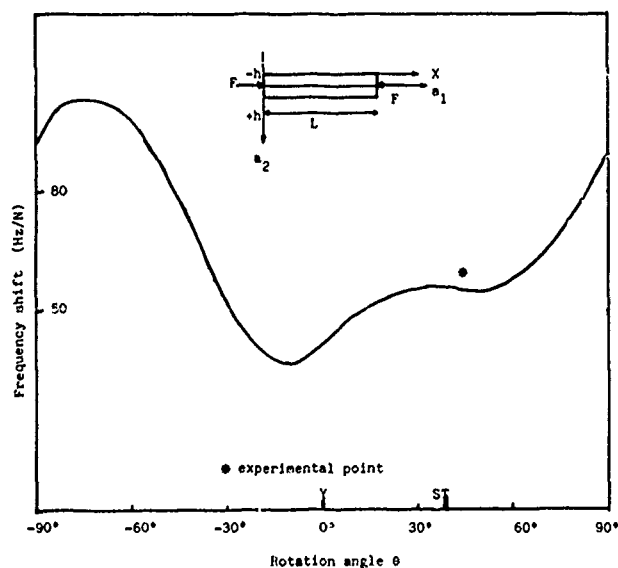


Fig. 5 : Sensitivity versus θ of a SAW propagating on a $Y+\theta^\circ$ rectangular quartz plate clamped on one end and submitted to an axial force on the other end.

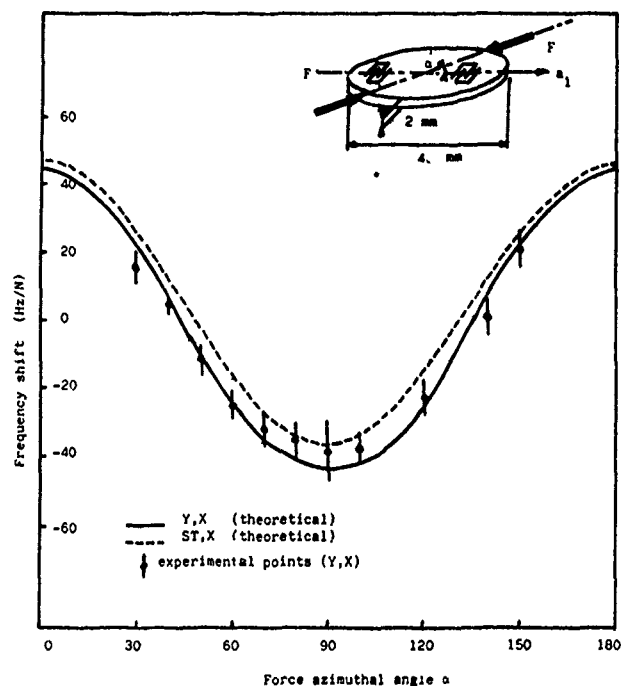


Fig. 6 : Sensitivity of a SAW propagating on circular Y, X and ST,X quartz plates submitted to diametrically applied forces of azimuthal angle α .

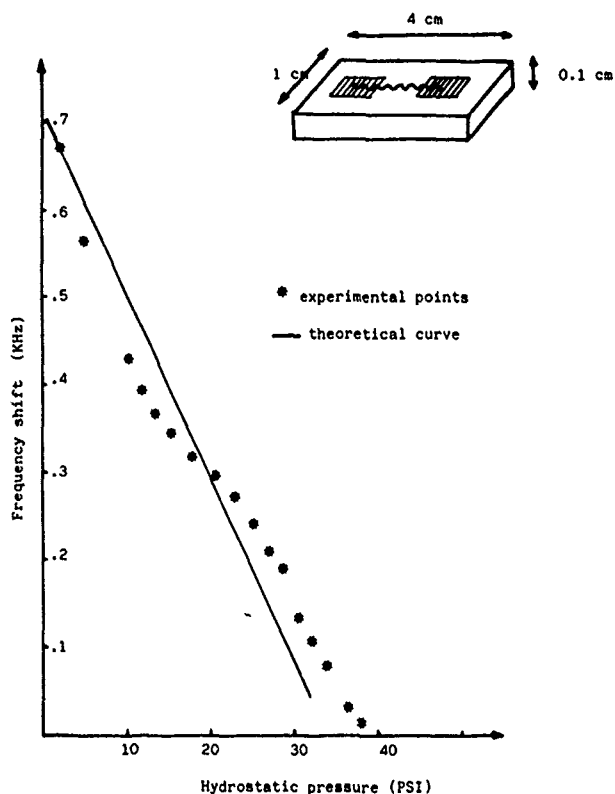


Fig. 7 : Experimental sensitivity to hydrostatic pressure of a bulky ST,X quartz plate.

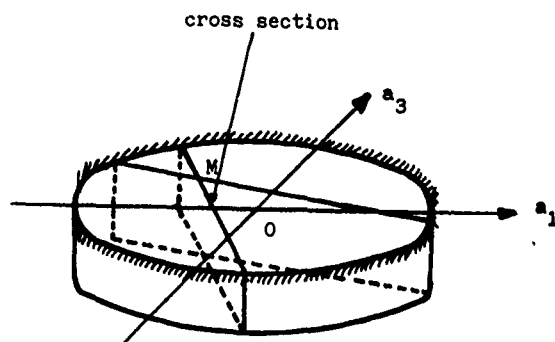


Fig. 8 : Configuration of a circular diaphragm showing the cross sections used in the calculation of the stress and strain distributions at a point M.

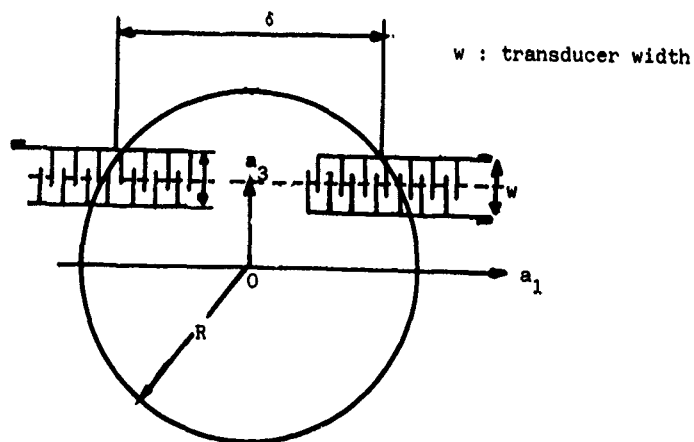


Fig. 9 : Position of the transducers.

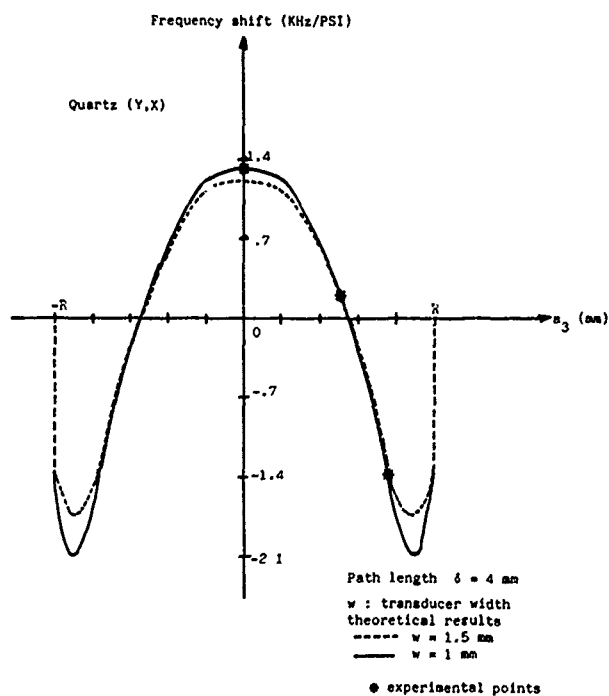


Fig. 10 : Sensitivity of the pressure sensor as a function of the position of the transducers.

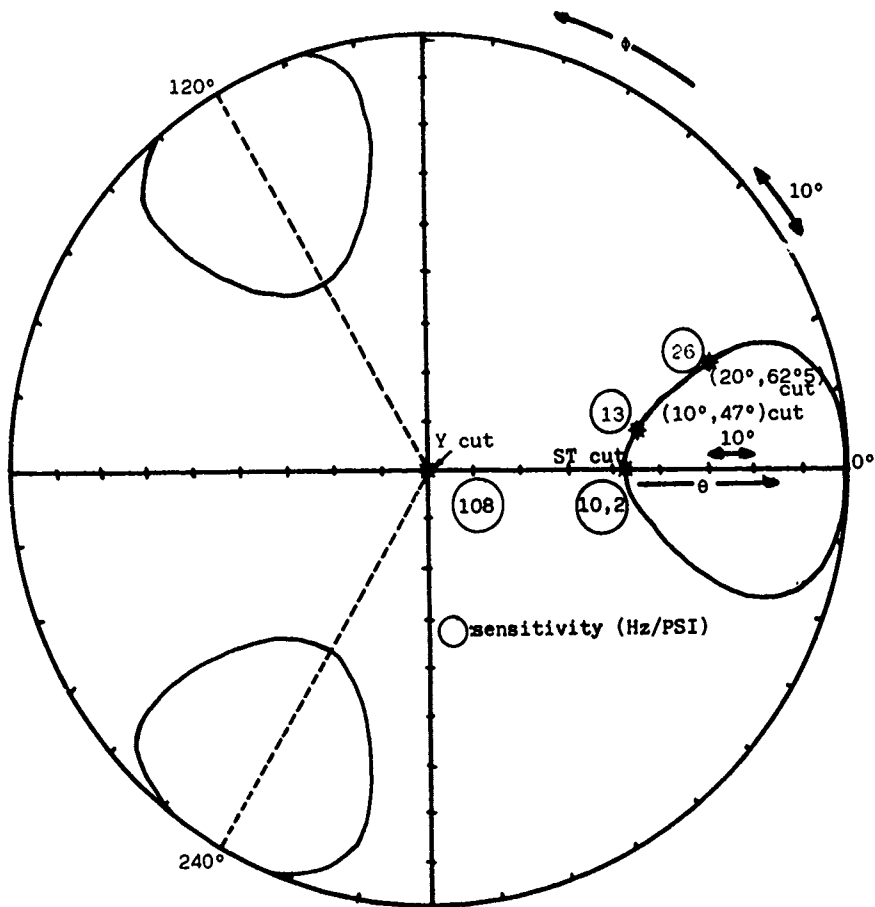


Fig. 11 : Sensitivities of singly rotated Y, ST, and doubly rotated (20°, 62.5°) and (10°, 47°) cuts.

LONGEVITY PERFORMANCE OF CESIUM BEAM FREQUENCY STANDARDS

Andrew C. Johnson
U.S. Naval Observatory, Washington, DC.

Melinda M. Force and Terry N. Osterdock
Hewlett-Packard Company, Santa Clara, CA

Field Survey

Abstract

The results are reported of a survey conducted to assess the useful lifetime performance of Cesium Beam Frequency Standards. The source sample includes organizations which operate Cesium Beam Frequency Standards in support of timekeeping, space tracking, communications, navigation and calibration.

Also, presented is an analysis of the lifetimes of various Cesium Beam Tubes, the major component within the Cesium Beam Frequency Standard. The data for this analysis are taken from the records of the Hewlett-Packard Company.

Introduction

The review of Cesium Beam Frequency Standard performance in field operation was undertaken to provide a statistical base for sound planning and programming of future operational requirements and to provide visibility of maintenance/repair requirements.

The information presented in this paper is the result of the joint, yet separate efforts, of the U.S. Naval Observatory and Hewlett-Packard Company.

a. The U.S. Naval Observatory portion is based on the results of the response to a questionnaire, which was sent to addresses selected at random from the U.S. Naval Observatory mail list.

b. The Hewlett-Packard portion is based on the result of an in-house review of the maintenance service records with regards to cesium beam tube replacement. The data base includes the entire population of Cesium Beam Tubes, produced since 1968 and used in HP Model 5061A and HP Model 5062C Cesium Beam Frequency Standard.

Questionnaire:

The questionnaire (Figure 1) used by the U.S. Navy Observatory included provisions for the following information:

1. Reporting Activity:
2. Control No: - Admin Control
3. Model No.
4. Serial No.
5. Service Date - Initial date placed in service (new or after repair)
6. Failure Date - Date of fault reported
7. Repair Date - Date of repair of reported fault
8. Application
9. Fault Location

Responses to questionnaire were received from a cross section of the international time/frequency community to include elements of communications, navigation, satellite tracking, calibration and national standards laboratories.

Of the ninety-one questionnaires mailed, thirty-eight responses were received as of 7 May 1980. Of these, twenty-six provided useful information on a total of seventy-four cesium-beam oscillators (HP 5061). No other model is covered in the current field survey report.

Results.

Though relatively small, this sample reveals some interesting data. First a look at the number of failures against time (Figure 2). Note the age of the oldest reported oscillator is a bit over twelve years. The other notable items on this graph is the high initial failure rate which is again matched in the third year. Then it tends to taper and level off at around five failures per year.

The plot of failures by type module (Figure 3) reveals that the high non-performers are the A2 battery charger, A9 Operational Amplifier and the A12 cesium beam tube. However, with a larger sample these rankings may change.

The cesium beam tube total may be out of proportion yet realistic because better records both maintenance and procurement are available on high dollar items. While the less expensive items may be routinely processed through maintenance and procurement channels.

Another highlight is the other category which included A16 Clock Assembly, A17 Terminal Board, A18 +3500 VDC power supply, A19 -2500 VDC power supply and other stoppages.

The Phase Detector module A8 appears to be the most reliable, note that no failures were reported for this module.

The cost of the modules and module identification are shown for information (Figure 4). There is no apparent relation between cost and failures or reliability. In one case the high cost item was the item on which the failure reports were also high. The A2, A9 and A12 failures are presented on the next three plots. For the A12, Cesium Beam Tube (Figure 5), it appears that after the initial failures, there is a year or two of low failure.

I suspect that the third-year lump is due to the new high performance tubes and the second lump at five years is the regular tube.

The A2, battery charger (Figure 6), appears to suffer the high initial failure and like the A12 cesium beam tube, it then enjoys a year of low failures and increases in second and third years. After the middle of the fourth year there were few significant failures.

The A9 Operational Amplifier (Figure 7), seems to have a rather flat failure rate still loaded toward the early years.

The plot of Other Failures (Figure 8), against time is interesting only in that it does not show the high initial rate and more closely reflects the curve one would like to see. This may be due to the fact that it is a catchall for random failures. Note that its peak in the first six months of the fourth year lags.

The data presented has not been averaged. It is simply a tabulation of information collected. An attempt was made to remove all non-operational time from the service time. When a module was repaired or replaced it started as a new item with zero service time.

Cesium Beam Tube Longevity

This portion of the paper will discuss the Beam Tube, the single most expensive item within the Frequency Standard. The reliability and, even more importantly, the lifetime of the beam tube is of prime importance to the user because it is a perishable item. The beam tube does, in fact, have a finite intrinsic lifetime due to the nature of the physics of the device.

This analysis of the beam tube lifetime data includes all of the beam tubes produced by HP since 1968, when the 5061A was first introduced. We will not be discussing the older 5060A data since a number of users have opted to replace older units with the 5061A. Because of this, HP has not been getting back all of the dead beam tubes to determine their respective lifetimes. The source of the lifetime data is the shipment and return-for-credit exchange dates less an appropriate length of time to account for shipment time and non-use time due to delays in getting the old beam tube back to HP.

We will discuss:

1. the meaning of the curves we will be using
2. the definition of a 5-7 year life
3. identify the 3 beam tubes
4. discuss the lifetime and reliability of each
5. the validity of the data.

Understanding the Curves

The format we shall use for presenting the data is as shown in Figure 9. We compare the percentage of beam tubes returned vs the age of the tube. The curve is cumulative and, therefore, we would expect it to eventually get to 100%. The question is how long before it gets there. The curves do represent the entire population of tubes and, therefore, include all failures whether catastrophic or normal end of life. The curves on the high performance tube also includes a number of tubes whose oven temperatures were purposely turned up to achieve even greater performance but at an acknowledged decrease in lifetime.

Lifetime Defined

The design life for most beam tubes is 5-7 years. This is a compromise between longevity and superior performance. We could turn up the temperature of the beam tube and improve its performance but likewise shorten the lifetime. For most applications, 5-7 years with an acceptable safety margin is the standard. We might expect - for an ideal design (dashed line Figure 9) to have no failures in the 1st 5 years. At the end of 7 years perhaps 50% would have died and the remaining 50% would die in greater than 7 years. However, due to the randomness of any manufacturing process - we expect a low percentage of beam tubes dying before 5 years. An estimate of 4%/year might be appropriate resulting in a curve which moves upward by 20% as shown in Figure 9 (solid line).

Cesium Beam Tube Characteristics

The cesium beam tube is a precision manufactured device requiring very tight tolerances and stringent requirements for cleanliness. The 3 beam tubes we shall discuss are shown in Figure 10: the mini tube, high performance and standard tubes.

Figure 11 shows the components of the 5062 mini tube as an example of the physical make-up of cesium beam tubes. The key components are the oven, state selector magnets, interactive cavity, ionizer, electron multiplier and the mass spectrometer. Other important components not shown are the Vac Ion Pump and Gettering Material.

5062C Mini Tube

The 5062C Mini Cesium Beam tube uses 12 beams of cesium and a very short interactive cavity with sufficient cesium and getting to last significantly longer than the 5 to 7 year design life. Figure 12 shows the actual life characteristics for those tubes shipped between 1974 and June 1977. In early 1977 we experienced a higher level of returns due to low beam current tube. From the failure analysis we determined the cause to be the electron multiplier. Due to the high level of beam flux the gain of the electron multiplier degraded rapidly causing death of the tube.

Owners of the instruments were informed that the Electron Multiplier Voltage and Cesium Oven Temperature needed to be turned down. As a result of that turn-down and a later retrofit of some electronics, the beam tube life was extended such that 44% of those early tubes are still in an operational status. After June of 1977 the instruments shipped from the factory included the turndown as well as the new electronics. Approximately a factor of 2 improvement in lifetime was achieved as shown by the second curves. February 1978 marked the first shipment of beam tubes from the newly renovated clean room facility. The resultant change in lifetime performance is dramatic as shown by the bottom curve.

High Performance Beam Tube

The next beam tube we will look at is the high performance 5061A Option 004. This tube was specifically designed with a longer interactive cavity, higher beam flux (using dual beams) and greater gettering capacity than the standard tube. Its purpose is to be more accurate and have greater short term time domain stability than previously available frequency standards. Its design life was also 5 to 7 years with a large design safety margin. I might point out that it is also possible to turn up the oven temperature in a standard beam tube to get improved performance but with significantly shorter lifetime. The Hewlett-Packard High Performance Cesium Beam Tube was specifically designed for improved performance without significantly lower life.

Figure 13 shows the early tube data. During the 1972-74 timeframe we experienced a number of early failures due to the cesium oven. This discovery resulted in an oven redesign. The beam tubes that did make it past the early problems have led useful and productive lives and after 6 1/2 years there are still more than 45% operating.

The oven redesign resulted in a better lifetime characteristic in the middle curve. The bottom curve shows the data for the beam tubes produced after the clean room facilities were renovated. Again the same type of improvement that we had for the 5062C tube.

Standard 5061A Cesium Beam Tube

Let us now turn to the standard 5061A cesium beam tube data to see how it has performed over the years. This beam tube is also in a 16" long envelope like the HP Option 004 high performance tube or rather just the reverse since the standard tube was first introduced in the HP 5060A in 1964.

The standard HP 5061A beam tube life characteristic is interesting because it has a reputation in the industry which sets it apart from all other beam tubes regardless of manufacturer. The data on this graph explains why it has that reputation. This graph shows the beam tubes produced between April 1968 and November 1971. After 10 years there are still over 50% operational.

As we examine Figure 14 we might question the validity of the data. The owner of the 5061A, whose beam tube has failed, will normally return the old tube for credit to keep his cost to a minimum. However, a certain number of owners may not return the dead beam tube. Perhaps they want to put it on display, take the instrument out of service, or even take the beam tube apart. We estimate that fewer than 5 to 10% of the beam tubes would fall into this category. Adding to the validity of this data we find a number of tubes from this batch whose lifetime has actually been 10, 11 and, in several cases, 12 years. The data obtained directly from the users and presented earlier in this paper supports this data.

The middle curve shows those tubes produced between November 1971 and June 1974. This particular batch has a little higher rate in the early years but crosses over in the 5 3/4 year point.

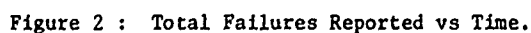
The last curve shows more recent tube history. It appears that the curves for the standard tubes are fairly consistent with minor variations.

As you can see from the data for this tube, which was designed for a 5 to 7 year lifetime, it has not only exceeded our wildest expectations but has demonstrated a lifetime in excess of 10 years for a large percentage of users.

Conclusion

The data on the cesium beam tube has shown us some very interesting results. The standard beam tube life is exceptional. The high performance and the mini tube are performing as expected for a 5-7 year design life - now that early problems are solved.

Figure 1 : Cesium Beam Frequency Standard Performance Questionnaire.



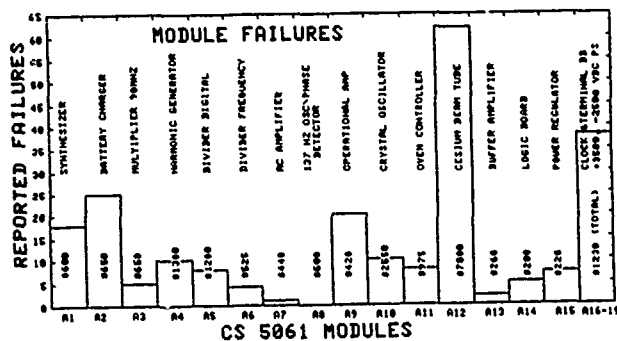


Figure 4 : Module Failures with associated costs.

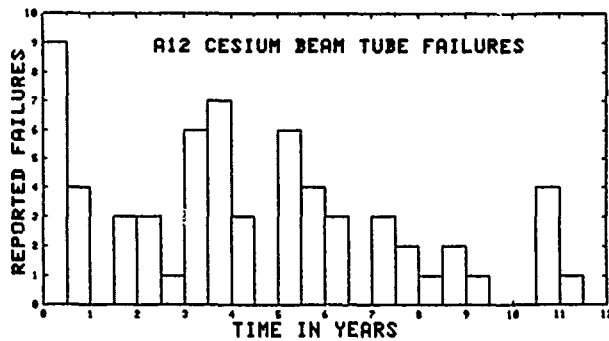


Figure 5 : A12 Cesium Beam Tube Failures.

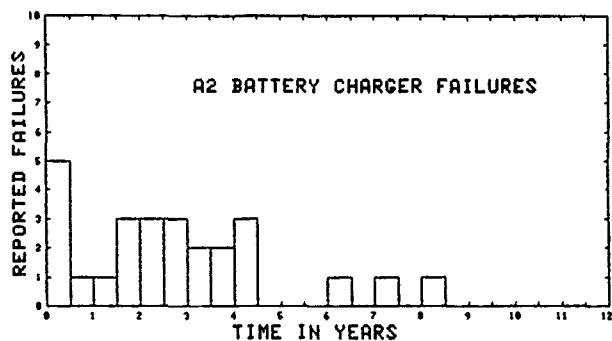


Figure 6 : A2 Battery Charger Failures.

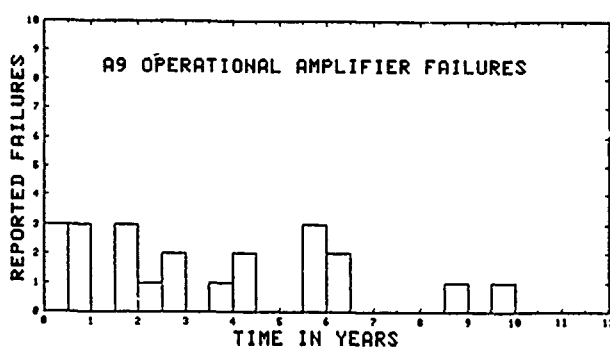


Figure 7 : A9 Operational Amplifier Failures.

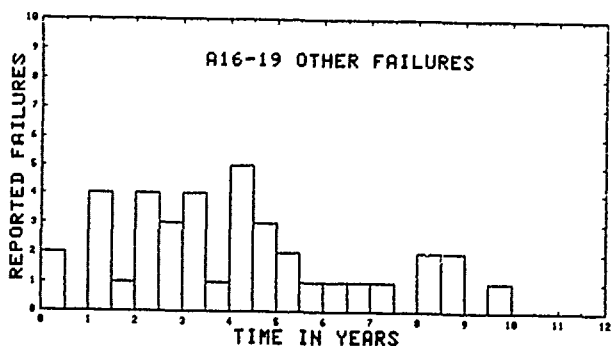


Figure 8 : A16-19 Other Failures.

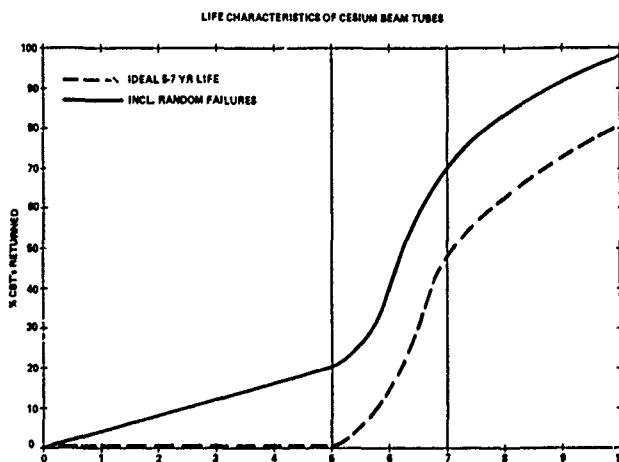


Figure 9 : Ideal 5-7 year life Characteristics of Cesium Beam Tubes.

Cesium Beam Tubes		
Instrument	Beam Tube	Characteristics
HP 5062C	Mini Tube	8" long cylindrical envelope Line width: 1.500 Design life: 5 to 7 years Nr. of Beams: 12
HP 5061A	High Performance Option 004	16" cylindrical envelope Line width: 4.50 Design life: 5 to 7 years Nr. of Beams: 2
	Standard	16" cylindrical envelope Line width: 6.00 Design life: 5 to 7 years Nr. of Beams: 1

Figure 10: Cesium Beam Tube Characteristics.

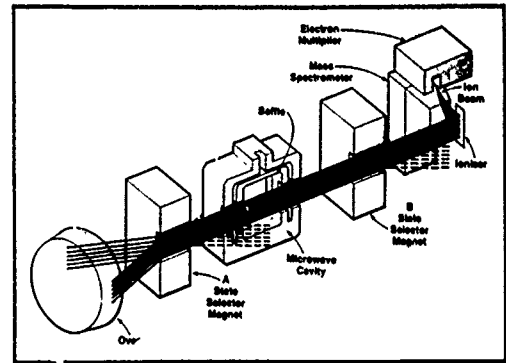


Figure 11: Cesium Beam Tube interval components.

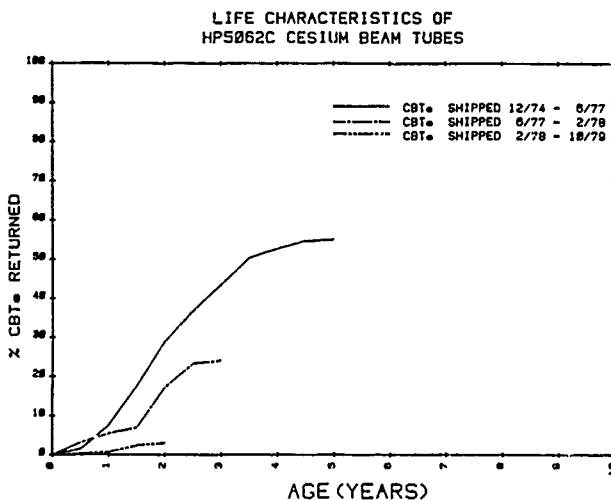


Figure 12: Life Characteristics of HP 5062C Cesium Beam Tubes.

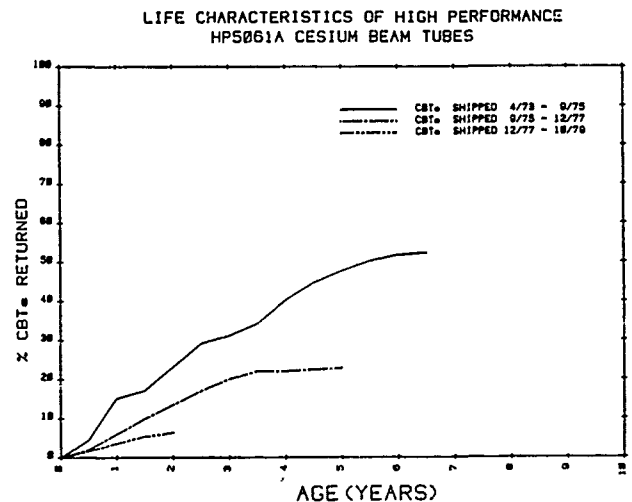


Figure 13: Life Characteristics of High Performance HP 5061A Cesium Beam Tubes.

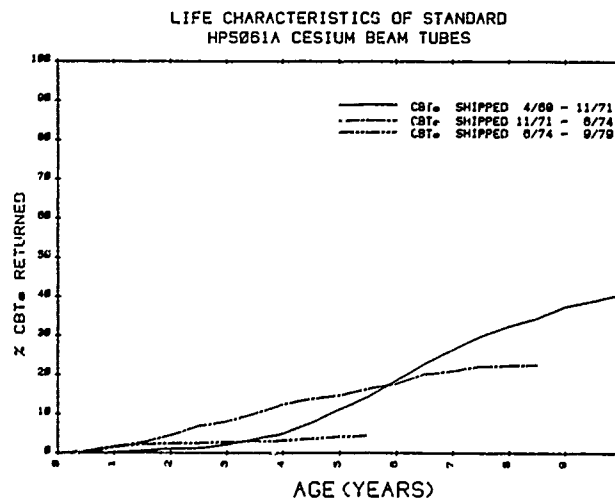


Figure 14: Life Characteristics of Standard HP 5061A Cesium Beam Tubes.

INITIAL TEST RESULTS OF USNO GPS TIME TRANSFER UNIT

Kenneth Putkovich

U. S. Naval Observatory
Washington, D. C.

Summary

The U. S. Naval Observatory (USNO), as part of its mission in the field of Precise Time and Time Interval (PTTI), is vitally interested in the development of new concepts, techniques, and equipments for the generation and dissemination of PTTI. The advent of the Global Positioning System (GPS), with its predicted capability for time transfers on a worldwide basis to the ten-nanosecond level, promises to be a vehicle for unprecedented improvements in worldwide timekeeping.

The USNO secured funding and coordinated an effort to build a GPS receiver for time transfer. The GPS Time Transfer Unit (GPS/TTU) that was the result of these efforts was initially tested in late 1979 and was found to perform well within the ± 100 nanosecond range required in the procurement specification. Additional testing at the USNO was conducted to verify the relationship between Coordinated Universal Time (UTC) and GPS time and to evaluate the performance of the satellites as vehicles for time transfer. The data being gathered are being made available via an automated data link to anyone interested. Analysis of the data gathered to date has revealed several areas of uncertainty that must be resolved if the system is to be used to its fullest potential. Improvements to the GPS/TTU to enhance its operation are also being planned.

Introduction

This paper will deal specifically with the description, testing and evaluation of the performance of the GPS/TTU and an evaluation of GPS as a means of time transfer at the present time. A brief description of the GPS system is provided as background to aid in achieving some understanding of the overall system. More detailed information is available in the literature.¹

Background

The GPS, as originally planned, was to consist of a space segment of twenty-four satellites and a ground segment of a Master Control Site (MCS) and five or more Monitor Sites (MS), one of which was to be located at the USNO. The function of the monitor sites is to receive transmissions from each of the satellites, referred to a local clock, and to retransmit this information to the

MCS over secure data communications links. The function of the MCS is to correlate this information with other information, perform the necessary calculations to determine current satellite performance parameters and upload this information to the satellite on a daily, or as needed, basis. This upload provides current information on clock performance, adjusts the clocks as necessary and provides updated navigation data. The satellites were to be equally distributed in three planes inclined to the equatorial plane of the earth by 63° and intersecting the equatorial plane at 120° intervals.

Due to funding cutbacks, present plans call for a space segment of eighteen satellites. The elimination of six satellites from the system will have little adverse affect on PTTI, since at least one satellite will always be in view and only one is necessary for time recovery. Studies are presently underway to determine the best orbital configuration for navigation.

GPS Satellite Signal²

Data are transmitted from the satellites on two carrier frequencies, the primary (L_1) is at 1575.42 MHz and the secondary (L_2) is at 1227.6 MHz. The L_1 or primary transmission is modulated by both a precision (P) code and a coarse/acquisition (C/A) code simultaneously. The L_2 or secondary transmission is modulated by either a P or C/A code. The data stream is transmitted at 50 bits per second and is common to both the P and C/A codes on both the L_1 and L_2 bands. All signals are derived from the same onboard clock. A complete data message is a frame of 1500 bits repeated every six seconds. Each frame is divided into five 300-bit subframes which are further subdivided into ten 30-bit words. The first two words of each subframe contain telemetry and code handover information. The last eight words of Subframe 1 contain clock corrections, an age of data word and ionospheric delay model coefficients. The last eight words of Subframes 2 and 3 contain the space vehicle's ephemeris and associated age of data words. The last eight words of Subframe 4 contain an alphanumeric message of interest to users. The last eight words of Subframe 5 contain an Almanac (an abbreviated version of information in Subframes 2 and 3) for each of the satellites in the constellation. Each Subframe 5 contains information on a single satellite. Thus the com-

plete Almanac for the entire satellite constellation requires reception of a sequence of frames. The length of the sequence is dependent on the number of satellites in orbit with twenty-four being the maximum.

In order to recover time relative to GPS, a user must be able to reliably receive the satellite signal and demodulate and decode the data stream. Utilizing this information, he can calculate a corrected pseudorange, compare it to a pseudorange measured against his clock, and from the difference, determine his clock difference. The GPS/TTU described in the following paragraphs was designed to perform that function for application at a fixed, known location.

Time Transfer System

The Time Transfer System (Figures 1 and 2) consists of four major components - the receiver, the processor, the pseudorange counter and the software operating system. Only a brief description of each of these subsystems will be provided as a detailed description would be beyond the scope and intent of this paper. Stanford Telecommunications, Inc. (STI) designed and built the receiver, developed the software and integrated the computer/receiver/software system.

GPS Receiver

The receiver (Figure 3) is a single channel, spread spectrum Doppler tracking receiver capable of tracking and decoding the C/A code on the L_1 frequency. It receives the signal (from antenna with nearly hemispherical coverage) through a low noise preamplifier. Preselective filtering in the preamplifier and further filtering at the receiver limit the effect of out-of-band noise. The signal is then down converted to an IF frequency and fed to code loop and correlator which track the C/A code and despread the spread spectrum signal. A carrier tracking loop then demodulates the signal and provides both C/A code epochs and navigation data to detection and synchronization circuits which provide the satellite outputs to both the measurement and computer systems.

Manual intervention by an operator is required to initialize acquisition and tracking of any satellite by the receiver. After the operator has ascertained which satellites are visible, the space vehicle identification number and an estimate of Doppler frequency are provided to the receiver via either front panel switches or the system console. From that point on acquisition and tracking is automatic.

Processor

The processor is a Hewlett-Packard 1000 Series computer, Model 20, with 64k words of semiconductor memory and a memory based (RTE-M) operating system. It provides the means of controlling, collecting and storing the navigation and time data from the satellite receiver and the pseudorange counter, of making the necessary calculations to determine satellite range and rela-

tive clock offsets and of displaying and storing the received and reduced data. The processor interfaces with the receiver through an RS-232C data communications link and an IEEE-488-1975 general purpose instrumentation bus. The decoded navigation data from the receiver is passed to the processor over the RS-232C data link. The IEEE-488-1975 bus provides a two-way communications and control link between the processor and the receiver and counter. Over this bus pass the receiver status information, satellite identification and Doppler estimates, counter control and measured pseudorange, and the other interactive digital signals required for system operation.

The system console provides the major interface between the system and the operator. The interactive keyboard and display are used to input time and location for system initialization, to select various modes of operation from a menu provided by the operating system and display a variety of raw and processed data. Additional software features for recording and processing data can be invoked by operating the switch registers on the processor front panel. A variety of information, including the space vehicle message, ephemeris data, results of data reductions, and various statistical factors can be selected for display in several formats.

The console minicartridge magnetic tape systems provide the means of entering the operating system and receiver data base (geodetic coordinates, receiver bias and UTC-GPS time offset) and for recording the parameters recovered from the satellite message and those measured on the pseudorange counter.

System Software

The software system consists of a Hewlett-Packard RTE-M operating system, and an application program designed to operate the receiver and data collection systems, apply the algorithms required to correct and reduce the received data and to output the reduced data in a usable form.

The RTE-M is a real-time executive operating system for the management of the operations and resources of HP 1000 Model 20 computer systems. It supports multiprogramming and program development in Fortran IV, has a file manager for file maintenance on mini cartridges and includes drivers for a number of peripheral subsystems, including the IEEE-488-1975 instrumentation bus.

The application program consists of a main program which handles program initialization, time transfer initialization, control of the continuous time transfer solutions and an out-of-view satellite control and 23 subroutines which perform diagnostics, calculate dates, recover satellite data, etc.

Pseudorange Counter

The pseudorange counter is a Hewlett-Packard Model 5328A with a programmable, high resolution time interval module and IEEE-488-1975 bus compat-

ibility. It is used exclusively to measure pseudorange every six seconds by measuring the time interval between a one pulse per six seconds generated from a station reference clock and that recovered from the received C/A code. While tracking a satellite the counter is under the exclusive control of the processor and provides pseudorange (to a ten-nanosecond, single measurement, resolution) to the processor every six seconds via the data bus.

Testing

Initial Tests

Initial tests of the time transfer capability of the TTU were carried out as part of the unit acceptance tests. A pair of portable atomic clocks was carried to the MCS at Vandenberg AFB in California. The ensemble of atomic clocks which constitute the GPS master clock were measured against the portable clocks with particular attention to the clock serving as reference for the Vandenberg Monitor Site. Pertinent system delays in the monitor receiver were also measured and verified with site personnel. The portable clocks were then transported to the STI facility in Sunnyvale, where a series of time transfers were made using the portable clocks as reference for the TTU. The clocks were then returned to Vandenberg (to establish a baseline for GPS time) and then taken back to Sunnyvale for a final series of measurements. The results of this initial series of measurements are presented in Figure 4. As can be seen from the plot, time transfers with a precision of better than ± 50 nanoseconds were achieved. Having established that the TTU performed to well within the contractual specifications, it was shipped to the USNO for more extensive testing.

USNO Testing

The TTU was put in operation at USNO in early January of this year. Operational difficulties were encountered from the outset. Although the data that were collected appeared to be reasonably good, acquiring and tracking satellites was a continuous problem. Intermittent signal loss, indications of malfunctions in the receiver acquisition and tracking loops and periodic loss of program control made the system difficult to use and quite ineffective. The receiver was shipped to STI for repair in February. After being lost in transit for five weeks, STI made a few relatively simple repairs and returned the unit to the USNO in early April. Poor performance when the receiver was placed back in service was traced to the antenna preamplifier. Replacement of the preamplifier corrected the problem and brought the TTU to a performance level that leaves little to be desired. At present any satellite that rises above the horizon can be acquired and tracked.

To date, the USNO program has consisted of acquiring, tracking, and recording data on all satellite passes visible from the USNO on weekdays from about 1000 to 2000 UT. As the TTU requires an operator, manpower and funding diffi-

culties limit testing to normal working hours. Unfortunately the satellite constellation has precessed to the point where the visibility from the USNO is optimum in the early morning hours (See Figure 14), making data collection even more difficult.

The first group of data presented, Figures 5 through 8, are intended to give an overview as to the general characteristics of the data rather than the qualitative value of the information it contains. The final plots of data, Figures 9 through 13, contain all the information collected with the TTU during the test period. All plots of data show the difference between the USNO Master Clock and GPS (MC - GPS) on the y-axis and date (in either Modified Julian Date or GPS Epoch) on the x-axis. (GPS Epoch which is presently offset from UTC by 2 seconds is counted in seconds beginning with 00:00:00 on Sunday and is reset to zero at that time.)

Figure 5 is a plot of data recovered from every six-second transmission from SV #6 over a period of about one hour on 6 February 1980. (SV is one of several designators for the satellites.) The pass is centered around the time of greatest satellite elevation. Figure 6 is the same data smoothed by taking 20 sample (2 minute) averages.

Figure 7 is a plot of SV #5 centered approximately at highest elevation and smoothed by taking 50 sample (5 minute) averages over the nearly two hours of data taken on 28 April. Two things become apparent if one compares this figure with the previous one. The slopes are different and the data from SV #5 is more nonlinear. The difference in slopes can be attributed to the space vehicle clocks, the GPS clock or a combination of the two. The linearity difference that is apparent can be attributed to the differences in the groundtrack of the two satellites (see Figure 15) and the inability of the mathematical models used in correcting the data to compensate for the different azimuth/elevation profiles. SV #6 "flies by" the USNO on a westerly track, rising in the northwest, gaining highest elevation in the west and setting in the southwest. SV #5, on the other hand, rises in the southwest, gains highest elevation to the north and sets in the southeast.

Figure 8 shows a pass for SV #8 taken on 8 February which includes a satellite upload from the MCS. The upload should be indicative of the combined GPS master clock and satellite performance. Thirty nanoseconds over a one day period equates to a $\pm 3 \times 10^{-13}$ difference between the two.

Figure 9 through 13 are the data collected during a twenty-day period in April and May. With the exception of SV #7, performance among the other satellites was fairly consistent over the period, showing among other things an offset for the GPS master clock of approximately -2.7×10^{-13} and an approximate time offset of 12 to 13 microseconds. Close examination of these plots also reveals some significant steps in time which show

good consistency within the GPS system but raise some questions as to uniform performance against an external time scale. The two portable clock trips that were recently completed revealed the same problem in that correlation between portable clock data and TTU measurements made at a one week interval could not be achieved to better than several hundred nanoseconds. I suspect that time jumps due to changes in operating clocks, system delays, etc., are accounted for in the control system software in order to maintain internal synchronization. To an external observer they appear as steps in time. This is well illustrated by examining the y-axis differences of all the plots presented in this paper.

Conclusion

It has been demonstrated that time transfers utilizing GPS and a GPS/TTU can be made to a precision of approximately fifty nanoseconds with little difficulty. By employing techniques similar to those used in TV Line-10 transfers, where simultaneous, common view measurements against a stable transmitter yield measurements with ten-nanosecond uncertainty, intercontinental time transfer at a ten-nanosecond level should be possible. However, before day-to-day stability against an external reference such as UTC can be achieved, in the same sense as LORAN-C, a more comprehensive approach to the control and synchronization of the ground clocks must be developed.

The USNO is pursuing improvement of GPS timing and attempting to make it available to users as soon as possible. The data collected by the GPS/TTU are made available via our recently inaugurated PTTI digital data service. In the future this data will also be published in our Time Service publications. Modifications to the TTU software to allow programmed, automatic tracking of every satellite every day and automatic transfer of the data to our on-line data acquisition system computer will considerably enhance the timeliness and quantity of data available. Finally, a program to improve linkage of the GPS MCS clock ensemble to the USNO Master Clock is being pursued with the aim of eliminating the presently observed discontinuities and reducing the ground clock offsets.

Reference

1. Global Positioning System, The Institute of Navigation, Washington, DC, 1980.
2. System Specification for the NAVSTAR Global Positioning System, USAF Space and Missile Systems Organization, 31 January 1979.

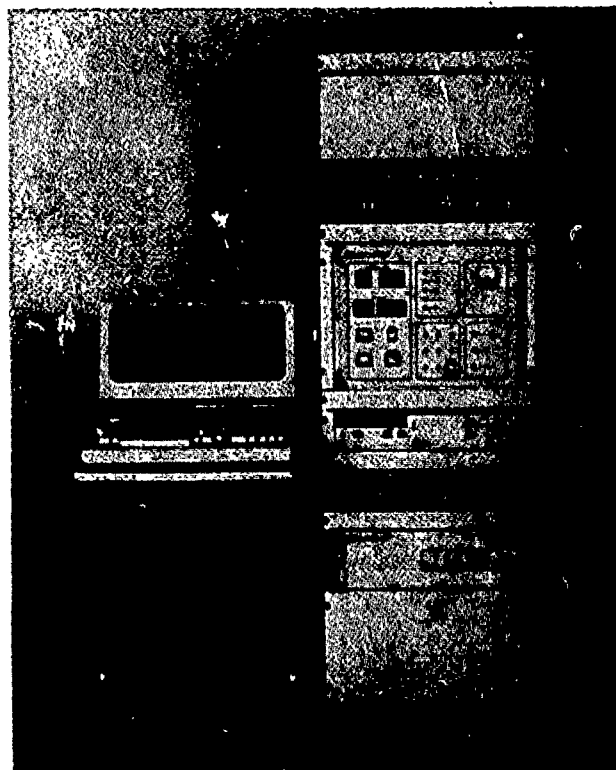
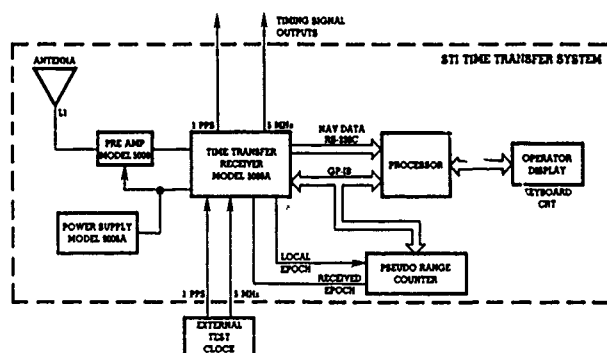
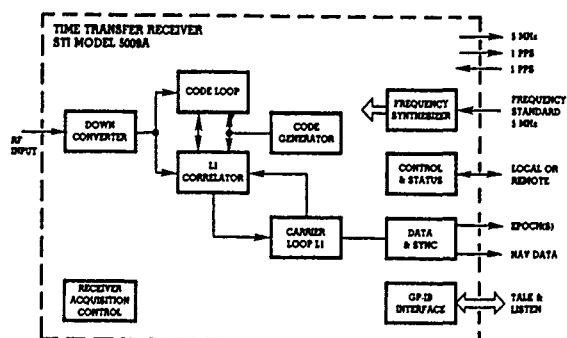


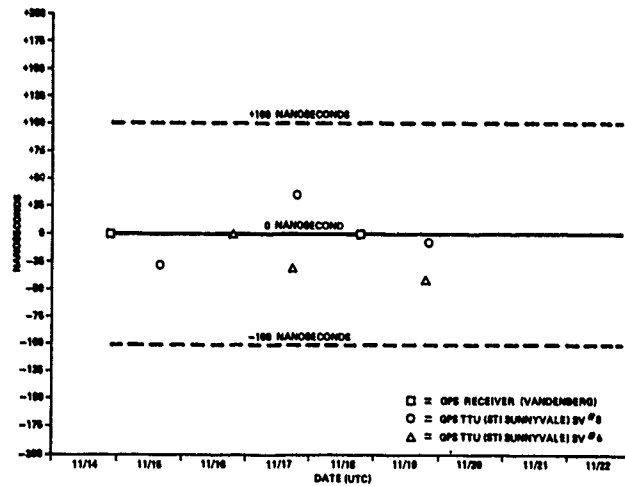
Figure 1. GPS/TTU System (less antenna)



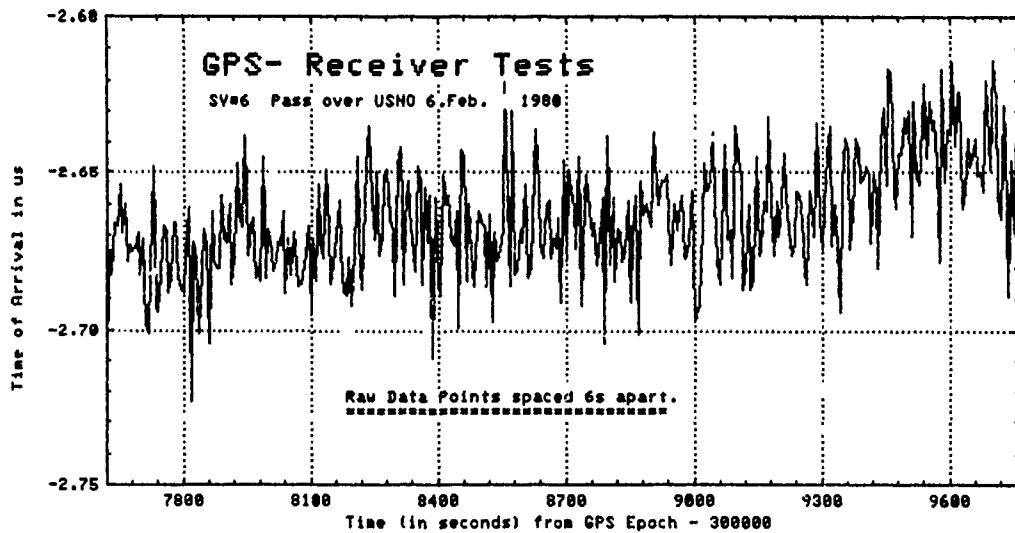
" 2. GPS/TTU Block Diagram



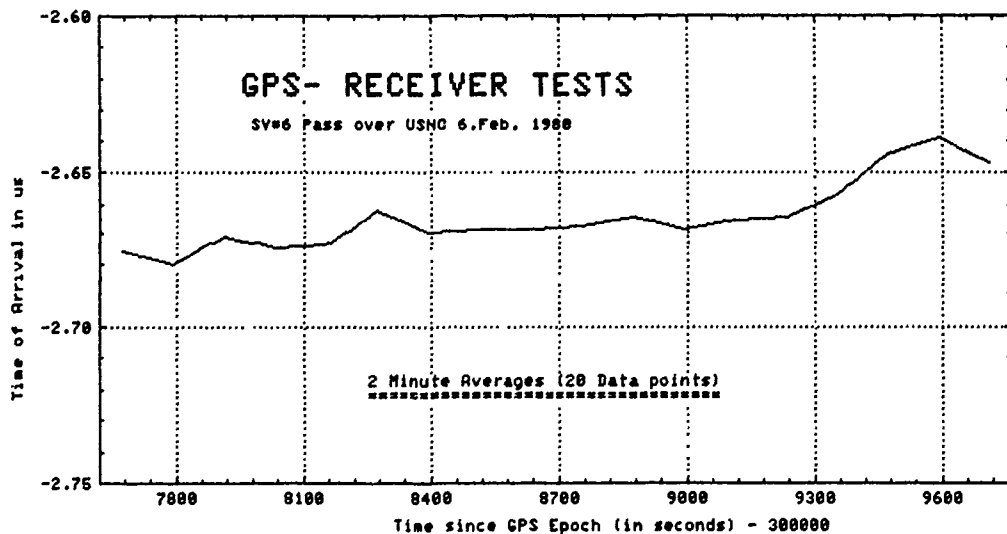
" 3. GPS Receiver Block Diagram



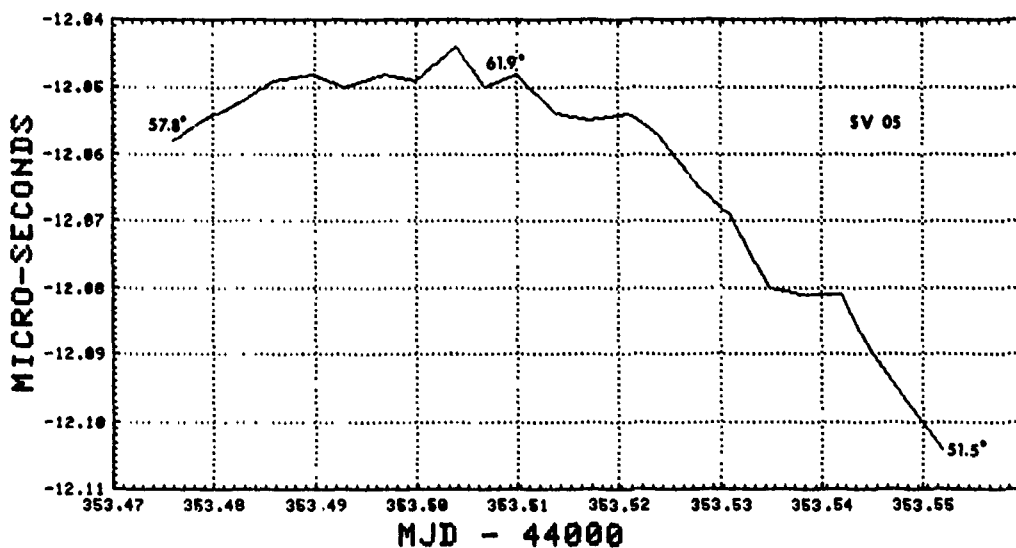
" 4. GPS/TTU Preliminary Test Results



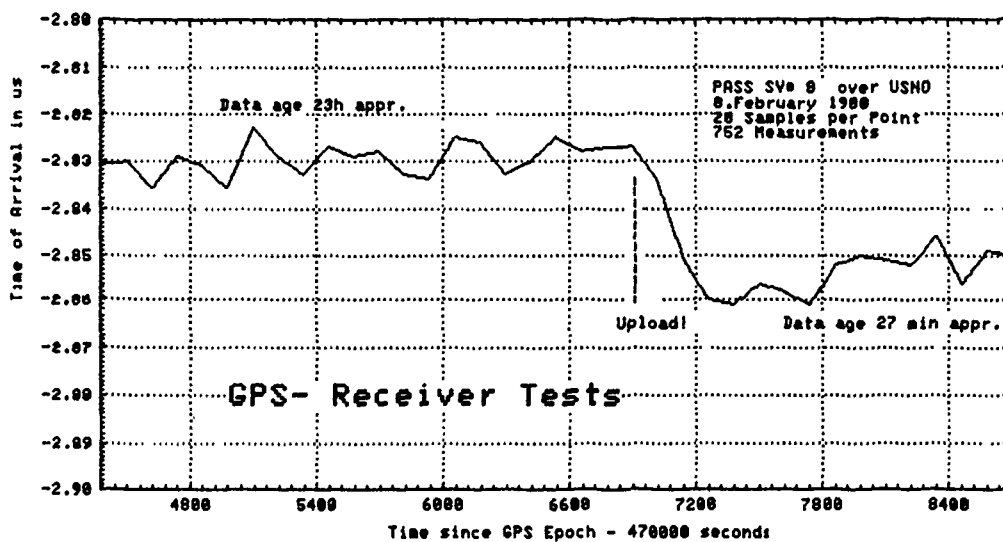
" 5. Raw Data SV #6



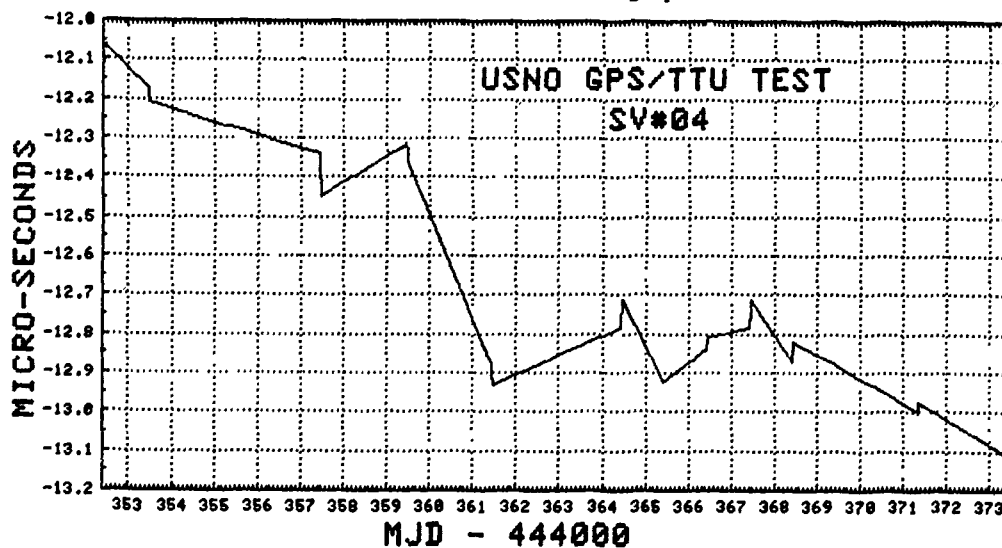
" 6. Smoothed Data SV #6



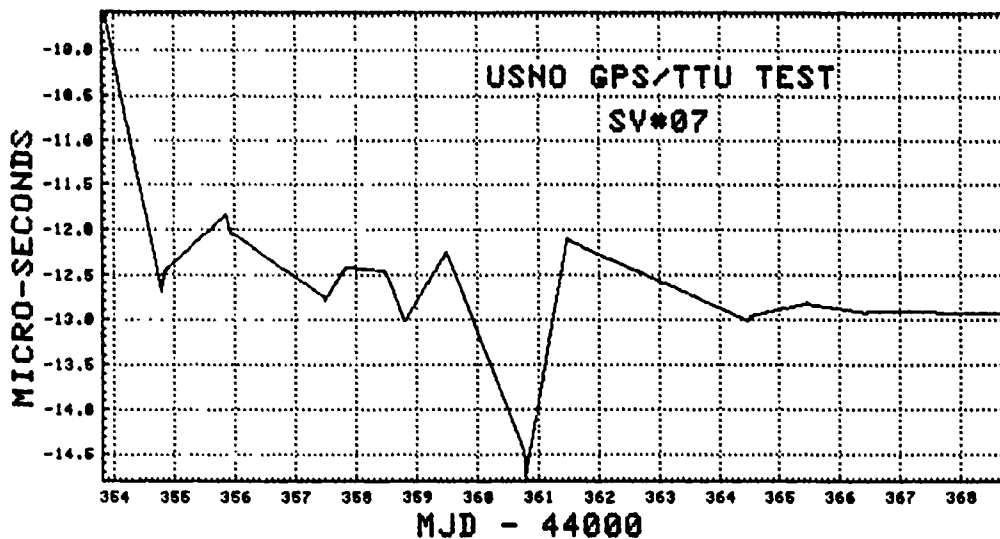
" 7. SV #5 Data Showing Elevation



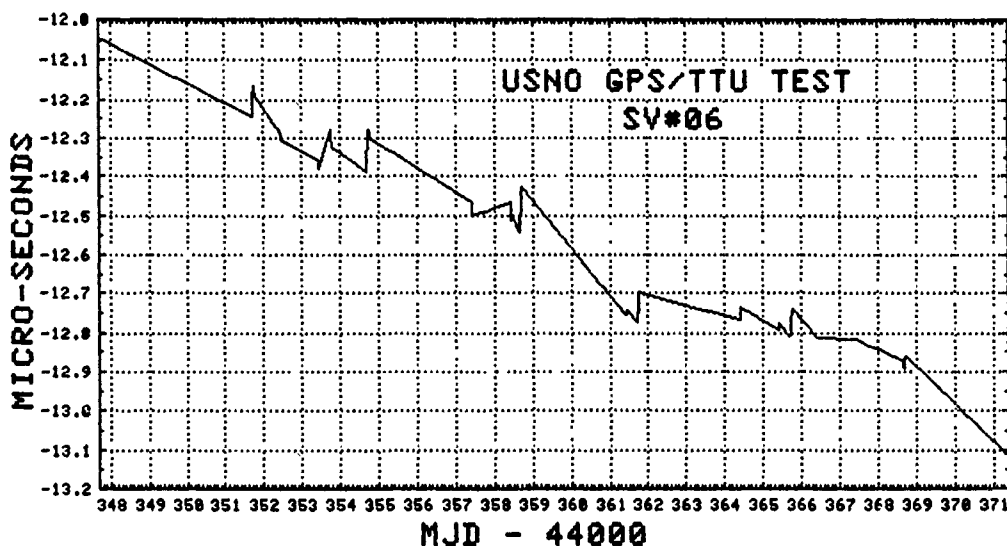
" 8. SV #8 Data Showing Upload



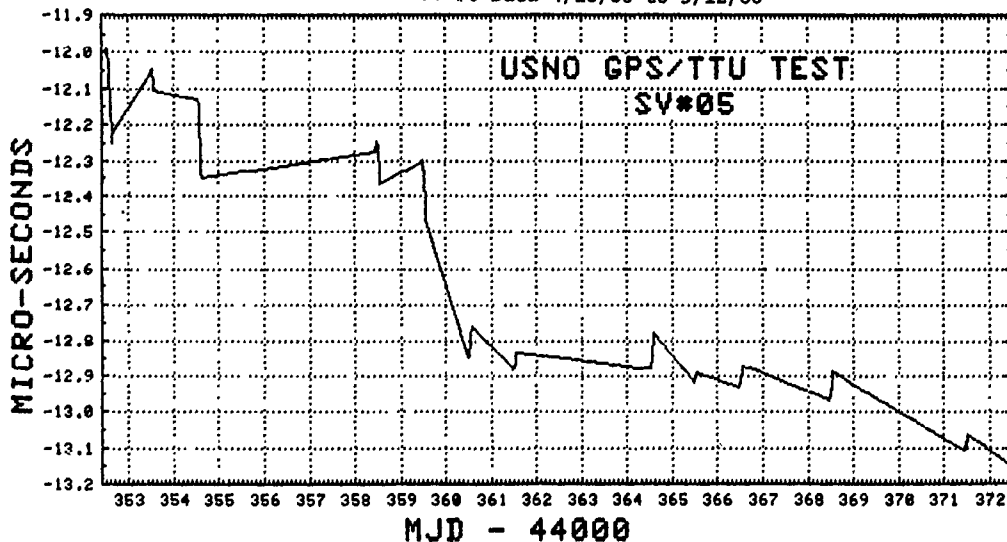
" 9. SV #4 Data 4/23/80 to 5/14/80



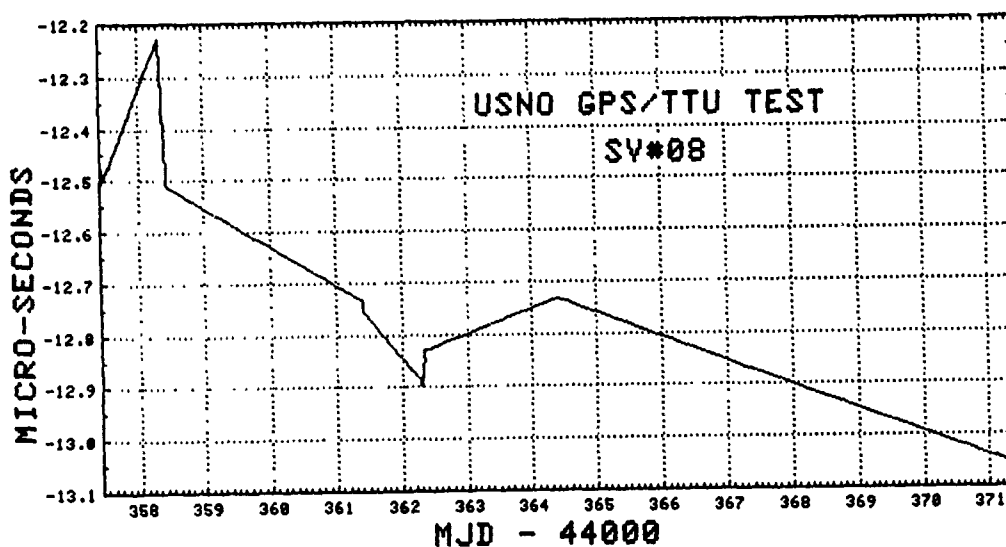
" 10. SV #5 Data 4/23/80 to 5/13/80



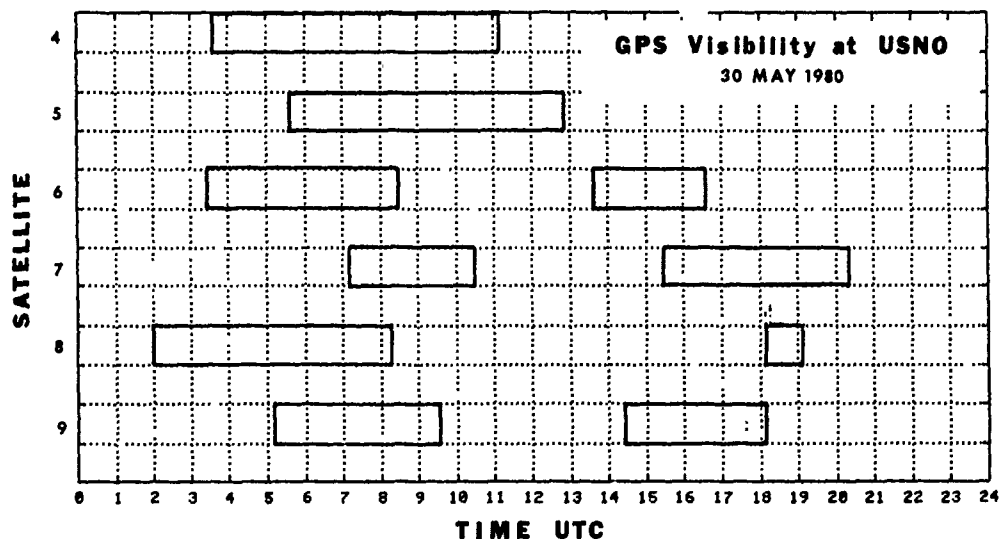
" 11. SV #6 Data 4/18/80 to 5/12/80



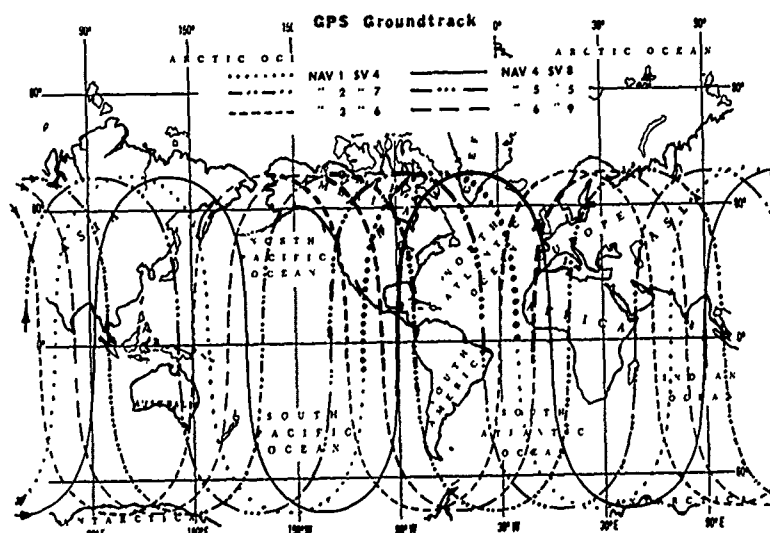
" 12. SV #7 Data 4/25/80 to 5/09/80



" 13. SV #8 Data 4/28/80 to 5/12/80



" 14. Approximate GPS Visibility at USNO Diagram



" 15. Approximate GPS Groundtrack (heavy lines indicate USNO visibility)

ACCURATE TIME AND FREQUENCY TRANSFER DURING COMMON-VIEW OF A GPS SATELLITE

David W. Allan and Marc A. Weiss

National Bureau of Standards
Boulder, Colorado

Summary

Even though the GPS is primarily a navigation system, if two clocks at known coordinates A and B are in common-view of a single GPS satellite, receivers at these two clock sites may coincidentally receive transmitted GPS clock times. By subtracting the received times of arrivals as measured by clocks A and B at the two sites while compensating for the propagation delays, one has an accurate measure of the time difference between clock A and clock B.

When all of the error contributions are assessed, it appears that 1 ns time stability and 10 ns of time accuracy should be achievable in measuring remote clocks--at distances of the order of a few thousand km. The primary error sources are as follows: uncertainties in the satellite ephemeris, differential ionospheric delays, uncertainties in tropospheric delay estimation, and uncertainties in receiver delays.

We have chosen this common-view approach because it provides an opportunity for a high accuracy (10 ns) relatively low cost receiver due to the common-mode error cancellation achievable.

Introduction

The fact that GPS time is based on atomic clocks, plus the fact that the GPS satellite ephemerides are accurately known, leads to some significant national and international time comparison opportunities. Even though GPS is fundamentally a navigation system, accurate time is also available.¹ It is assumed in this document that users wishing to measure or compare time on the earth will know their location to within similar uncertainties attributable to the time errors in GPS. The civilian or C/A (clear access)-code will always be available and can be used for general access system design.

There are four interesting methods to employ GPS for accurate time transfer or for accurate time and frequency comparisons (see Fig. 1):

First, Clock A and a GPS receiver are used to deduce from a GPS satellite's ephemeris, from clock A's location, and from received GPS time decoded from the same satellite, the time difference (Clock A - GPS time). This method is the simplest and least accurate (estimated to be better than about 100 ns with respect to GPS time),² but has global coverage, is in the receive-only mode, requires no other data, yields receiver prices that could be competitive on a mass production basis, and could service an unlimited audience. Also, GPS time will be referred to UTC(USNO) and will be known with respect to UTC(BIH), UTC(NBS), and other major timing centers.

Second, Clock A and Clock B at different locations anywhere on earth can be compared by making successive observations of the same GPS satellite clock, at least one of which will appear above their horizons with delayed view times of less than 12 hours. This is analogous to the clock flyover mode reported by J. Besson³ and others. The time prediction error for the satellite cesium clocks to be used in the GPS satellites will be about 5 ns over 12 hours. Since the same GPS satellite clock will be viewed by both A and B, biases in the satellite ephemeris may tend to cancel depending upon geometry, etc. Accuracies of from 10 ns to 50 ns are anticipated. This method requires communication of the data between A and B, and hence the logistics may limit the customers.

Third (see Figures 1 & 2), two users with Clock A and Clock B at different locations, but in simultaneous common-view of a single GPS satellite clock, can take advantage of common mode cancellation of ephemeris errors in determining the time

difference ($t_A - t_B$). The satellite clock error contributes nothing. Since the GPS satellites are at about 4.2 earth radii (12 hour orbits), for continental distances between A and B (≤ 3000 km) the angle \angle (A-Satellite-B) will be $\leq 10^\circ$, and the effects of satellite ephemeris errors will be reduced by a factor of more than 10 over the first method. Using a fairly straightforward receiver system, an accuracy of about 10 ns in measuring the time difference ($t_A - t_B$) appears probable. This again requires data communication between A and B. With improved ephemerides and propagation delay characterization, the accuracy limit for this method appears to be about 1 ns. The receiver should be relatively inexpensive, and given the reasonable costs of data modems and the potential accuracies achievable via this method, it makes it very attractive and cost effective for national, and in some instances, for international time comparisons.

Fourth, a method being developed for Geodesy by JPL (Jet Propulsion Laboratory)⁴ has baseline accuracy goals of about 2 cm over baselines of the order of 100 km. This method can be inverted to do time comparisons with subnanosecond accuracies. The two clocks A and B separated by about 100 km have two broadband receivers with tunable tracking antennae such that sequentially, 4 satellites can be tracked concurrently at A and B. The data are cross-correlated after the fact, the same as in long baseline interferometry, to determine location and time difference ($t_A - t_B$). The data density is high and the baselines are relatively short, but the accuracy is excellent.

It appears that as GPS becomes fully developed, GPS time may become operational world time. Methods 1, 2, or 3 above would yield significant improvements in national and international time comparisons. If commercial vendors take advantage of some of these methods, receiver costs could be made reasonable. The same basic receiver could be used in methods 1, 2, or 3; the main difference would be in the software support, modems, and local clocks. Method 3 (common-view) coupled with LASSO would provide an ideal future method for the generation of International Atomic Time, TAI, and

of UTC at the nanosecond accuracy level. This method has the most attractive accuracy/cost ratio and is being pursued by NBS. The theoretical advantages and disadvantages are reported herein.

System Error Analysis

Errors Resulting from Satellite Ephemeris Location Uncertainty

The time transfer error is dependent upon the ephemeris or position error of a satellite. Common-view time transfer yields a great reduction in the effect of these errors between two stations, A and B, as compared to transfer of time from the satellite to the ground. Common-view time transfer is accomplished as follows:

- 1) Stations A and B receive a common signal from a satellite and each records the local time of arrival, t_A and t_B respectively.
- 2) From a knowledge of station and satellite position in a common coordinate system, the range between the satellite and each of the stations is computed, r_A and r_B respectively.
- 3) The time of transmission of the common signal according to each station, A and B, is computed by subtracting from the times of arrival, the times of propagation from the satellite to each of the respective stations, i.e., the time to travel the distances, r_A and r_B , are τ_A and τ_B (the range delays) and are given by $\tau_A = r_A/c$ and $\tau_B = r_B/c$ where c is the speed of light. This speed is subject to other corrections as are treated later.
- 4) Finally, the time difference, τ_{AB} , of station A's clock minus station B's clock at the times the signals arrived is:

$$\tau_{AB} = (t_A - \tau_A) - (t_B - \tau_B) = (t_A - t_B) - (\tau_A - \tau_B).$$

If the ephemeris of the satellite is off, the computed ranges from the stations to the satellite will be off an amount dependent on the way the ephemeris is wrong and the geometrical configuration of the satellite-station systems. The advantage of common-view time transfer is that the computed bias is affected not by range errors to individual stations, but by the difference of the two range errors. Thus, much of the ephemeris error cancels out. To see how this works in detail, suppose the ephemeris data implies range delays of τ_A^i and τ_B^i , but the actual position of the satellite, if known correctly, would give range delays of $\tau_A = \tau_A^i - \Delta\tau_A$ and $\tau_B = \tau_B^i - \Delta\tau_B$. Then the error in time transfer would be $\Delta\tau_{AB} = \Delta\tau_B - \Delta\tau_A$, where $\tau_{AB} = \tau_{AB}^i - \Delta\tau_{AB}$ is the true time difference (clock A - clock B) and where τ_{AB}^i is the computed time difference from the actual time of arrival measurements and ephemeris data. Thus, $\Delta\tau_{AB}$, the time transfer error due to ephemeris error, depends not on the magnitude of the range errors, but on how much they differ.

The error in time transfer, $\Delta\tau_{AB}$, as mentioned above, depends on the locations of the two stations and of the satellite, as well as the orientation of the actual position error of the satellite. Figures 3 through 18 at the end of the paper give $\Delta\tau_{AB}$ for some ground stations of interest with different discrete levels of error shown as contour graphs dependent on where the satellite is. There are four sets of contour graphs for each pair of ground stations; for current and future typical ephemeris errors,⁴ and for whether the satellite is going north or south in its orbital plane. Within a particular graph, the contour level at a point corresponds to the root-mean-square value of $\Delta\tau_{AB}$ when the common view satellite is directly above that location. The current values of ephemeris error for the GPS satellites are estimated at about 10 meters in-track, i.e., in the satellite's direction of motion; 7 meters cross-track, and 2 meters radial.⁵ This corresponds to 41.23 ns rms error (square root of the sum of squares/c). The projected values for 1985 are 7 m in-track, 3 m cross-track, and 0.6 m radial, corresponding to 25.46 ns rms

error.⁵ Notice that the rms errors make an elongated ellipsoid and are dependent on satellite direction. Thus, to compute the range errors to a given pair of stations for a given satellite location, one needs to know the satellite direction at that location. The satellite moves in a fixed plane in space with the earth rotating under it.

The program which computed the figures used an orbital plane making an angle of 63° with the ecliptic with the satellite moving west to east in the plane. As an approximation, the orbit was assumed circular at 4.2 earth radii (12 hour period). At a given latitude, the satellite direction in degrees east of north is determined by the orbital plane and whether the direction is northerly or southerly. Corrections for the earth's rotation need to be included. Thus, each figure was created by: 1) choosing a given pair of ground stations, a set of values for ephemeris error, and whether the satellite was moving north or south in its orbital plane; 2) for a given location on a map containing the ground stations, finding the satellite direction (a function of latitude only) and three independent position error vectors from the three different types of ephemeris error; and 3) approximating $\Delta\tau_{AB}$ for each of the independent position error vectors, then finding the square root of the sum of their squares for the total $\Delta\tau_{AB}$ at that location. In this way a chart of values of $\Delta\tau_{AB}$ was computed, which were then plotted in contour plots superimposed on a world map in cylindrical projection. Clearly, there are regions shown where the satellite will be below the horizon for one or both stations, so the maps are over-inclusive in this regard.

The $\Delta\tau_{AB}$ were approximated in the following way. Let us fix a coordinate system at the earth's center to define basis vectors. Then let \underline{A} and \underline{B} be the position vectors of stations A and B, respectively, and \underline{S} the position vector of the satellite. Then the range vectors, pointing to the satellite from the ground stations, are:

$$\underline{R}_A = \underline{S} - \underline{A} \text{ and } \underline{R}_B = \underline{S} - \underline{B}.$$

Let e_A and e_B be the unit vectors in the directions of R_A and R_B respectively. Then the ranges are:

$$r_A = e_A \cdot (\underline{S} - \underline{A}) \text{ and } r_B = e_B \cdot (\underline{S} - \underline{B}).$$

If \underline{S} is the satellite position according to its ephemeris, but the true position is $\underline{S} + \Delta \underline{S}$ then the new unit vectors, e'_A and e'_B , are the same as the old to first order:

$$e_A \cdot e'_A = 1 - \frac{\alpha^2}{2} + \dots = \cos(\alpha), \text{ where } \alpha \text{ is the angle between } e_A \text{ and } e'_A.$$

So, to first order, the new ranges are:

$$r'_A = e'_A \cdot (\underline{S} + \Delta \underline{S} - \underline{A}).$$

Thus, the range errors are approximately:

$$\Delta r_A = r'_A - r_A = e'_A \cdot \Delta \underline{S} \text{ and } \Delta r_B = r'_B - r_B = e'_B \cdot \Delta \underline{S}$$

so:

$$\Delta \tau_{AB} = (\Delta r_B - \Delta r_A)/c = \frac{1}{c}(e'_B - e'_A) \cdot \Delta \underline{S}.$$

We see that the time transfer error increases as the vectors pointing to the satellite from the ground stations become less parallel up to the maximum of $\sqrt{2}$ times the ephemeris error when they are perpendicular, down to zero when they are parallel. Because of the dot product, some interesting and very helpful situations may arise. For example, if the path of the satellite were at right angles to the line between stations A and B and were half-way in between the two stations, the effect of the ephemeris errors due to radial and on-track go to zero! Since the GPS satellites are so far out, 4.2 earth radii approximately, the direction vectors pointing to the satellite tend to be close to parallel, thus cancelling most of the ephemeris error in all cases where common-view is available.

Errors Resulting from Ionosphere

The ionospheric time delay is given by $\Delta t = 40.3/cf^2 \cdot \text{TEC}$ (seconds) where TEC is the total number of electrons, called the Total Electron Content, along the path from the transmitter to the receiver, c is the velocity of light in meters per second, and f is the carrier frequency in Hz. TEC is usually expressed as the number of electrons in a unit cross-section column of 1 square meter area along the path and ranges from 10^{16} electrons per meter squared to 10^{19} electrons per meter squared. At the 1.575 GHz C/A carrier frequency for the GPS satellite system and for a TEC of 10^{18} electrons per meter squared, one computes the delay of 54 ns which is possible for low latitude parts of the world. For these low latitudes and solar exposed regions of the world, time delays exceeding 100 ns are possible especially during periods of solar maximum. Clearly, the TEC parameter is of great importance in the GPS system. Shown in Fig. 19 is a reproduction of a figure taken from a paper by J. A. Klobuchar,⁶ this figure clearly shows during a solar maximum year, 1968, that the range of delays vary from about 5 to 40 ns, being maximum near the equator and near the noon path. Fig. 20 is also from Klobuchar's paper and shows the actual vertical electron content at Hamilton, MA looking towards the ATS-3 satellite for every day of the year, and here again one sees the variations from the order of 5 ns to 40 ns.

In studying these graphs, one observes two very important things: 1) the total delay at nighttime and/or high latitude is much smaller than at daytime, and 2) one notices that the correlation in absolute delay time covers much larger distances when one moves away from the equator and the vicinity of noon; the conclusion being that a significant amount of common-mode cancellation will occur through the ionosphere at large distances if all observations are made at either high latitudes and/or at nighttime. These cancellation effects, as can be seen from Fig. 20 over several thousand km, will cause errors of less than 5 ns. For short baselines less than

1000 km, this common-mode cancellation will cause errors of the order of or less than about 2 ns.

Clearly, this gives a definite direction as to how one should proceed using the common-view GPS time and frequency transfer technique proposed in this paper. Even though the total ionospheric delay may be very large at certain times and places, there are ways to pick and choose, which would allow one to get large amounts of common-mode cancellation and which would allow one to achieve with some care, time and frequency transfer accuracies approaching a nanosecond.

Beyond the common-mode cancellation, if one had access to the measurements of the total electron content, then clearly one could use the model to actually calculate the delay over the two paths of interest, or if the monitor stations for the TEC were nearby, given reasonable correlations from one monitor station to another, one could interpolate the TEC so that on an ongoing basis, the differential delay variations could be calculated again to the order of a nanosecond. Also, if one used both the L_1 and L_2 frequencies from the GPS satellite, the TEC could be calculated.

Errors Resulting From Troposphere

In transferring time between ground stations via common-view satellite, one records the time of arrival of the signal and computes the time of transmission by subtracting the propagation time. The propagation time is found by dividing the range to the satellite by the velocity of light. However, moisture and oxygen in the troposphere have an effect on the velocity of propagation of the signal, thus affecting the computed time of transmission and therefore, the time transfer. This effect is dependent on the geometry, the latitude, the pressure, and the temperature, and may vary in magnitude from 3 ns to 300 ns.⁷ However, by employing reasonable models and using high elevation angles, the uncertainties in the differential delay between two sites should be well below 10 ns. Later on, if needed, the magnitude of the troposphere delay can be calculated with uncertainties which will approach a nanosecond.

Error Considerations in Receiver Design

Since the primary goal of the NBS receiver design is accuracy in time and frequency transfer, the approach taken tends to be somewhat different than perhaps may be considered in a navigation receiver. The fundamental concern is that whatever time delay exists within the receiver that it be extremely stable (of the order of a nanosecond). This, of course, can be most easily accomplished if the total additional delay (beyond cables) is minimized through the receiver. We also are working toward minimum parts cost, while still providing full automation in capability. In addition, we are designing into the current units being built by NBS, self contained microprocessor control and a (1 ns) time interval counter.

The total receiver will have high accuracy, is designed to be very stable, and will be totally automated and self-contained. This allows one to take maximum advantage of appropriate seeing time of the satellites, minimize ionospheric delay and delay variations; to maximize the common-mode cancellations between two sites. We estimate a total receiver delay, excluding cables, to be less than 30 ns and the receiver stability to be less than 2 ns. Receivers can be straightforwardly calibrated in a side-by-side mode as to the differential delay, and since one uses the concept of common-mode between two sites, only the differential delay is important for accurate time and frequency transfer between sites A and B.

Current and Future System Accuracy Potential and System Cost

When one combines all of the possible errors from any of the potential error sources, one obtains an absolute accuracy of time transfer of better than 10 ns, and a time stability of the order of a nanosecond. This means that on a 24 hour basis, one could measure absolute frequency differences between remote sites to a few parts in 10^{14} . We anticipate a front end parts and assembly cost (not including development costs) of well under \$10,000. This includes the computer and

automatic control system as well as a 1 ns time interval counter; but, of course, does not include the necessary testing documentation and costs incurred by a vendor if they were to develop and put into production such a system. The concept being developed has the significant advantage that the main costs will be front end costs as the system should be unintensive after being set in operation. It also has the significant advantage over two-way satellite systems, in that it is in the receive only mode, which should allow a much larger user audience for this kind of receiver as well as avoiding all of the problems of FCC clearance, etc. for having a transmitter, which is necessary for a two-way satellite system. There have been some discussions that because of the excellent signal-to-noise on the C/A code that the signal strength would be degraded, so that adversary users would be denied the full accuracy of the system. From a time and frequency point of view, this would not be a serious problem if there was a degradation in signal-to-noise, because one could simply do averaging and since there is plenty of time to average over a pass, this should still give comparable accuracy results.

The future accuracy potential is quite exciting because there is significant anticipated improvement in the accuracy of the ephemerides for the satellites, and that error contribution should be reduced considerably. The ionospheric delay can, in fact, be calibrated at or below the nanosecond level, and the tropospheric delay can also be modeled to a few nanoseconds. As we gain more experience with receiver design and total delay and delay stability, it is believed that its accuracy can also be improved to the nanosecond level or below. Ultimately, over the next several years this common-view approach could be developed with accuracies of the order of a nanosecond.

Conclusions

In conclusion, we have shown that one-way satellite transmission from a GPS satellite in common-view at two sites allows one to do accurate time transfer to 10 ns or better. This accuracy

is achieved because of common-mode cancellations of several contributing errors in the system. The system furthermore has the potential to achieve accurate time transfer of the order of a nanosecond. The estimated stability of the receiver delays and all contributing error delays should yield stabilities of the order of 1 ns, which means that on a 24 hour basis, frequency transfer can occur with an accuracy of about 1 part in 10^{14} . Two prototypes are being built at the National Bureau of Standards to test these ideas.

Acknowledgements

We are indebted to our sponsor SAMSO and the several competent contributors to the development of Global Positioning System, in particular, to Dr. John A. Klobuchar and to Albert Bierman; to Dick Davis and Al Clements and their great initiative in the receiver design concepts, which will be published after prototypes have been built and tested. We also wish to express our indebtedness to Dr. G. M. R. Winkler, Mr. James L. Jespersen, and Dr. S. Jarvis for very helpful suggestions in the text.

References

1. Spilker, James J., "Global Positioning System: Signal Structure and Performance Characteristics," Stanford Telecommunications, Inc. Report, 1 June 1978, STI-TM-8802.
2. Putkovick, K., "Initial Test Results of USNO GPS Time Transfer Unit," Proceedings of Frequency Control Symposium, Philadelphia, PA, 28-30 May 1980.
3. Besson, J. (1970), "Comparison of National Time Standards by Simple Overflight," IEEE Trans. on Instrumentation and Measurement IM-19(4), 227-232.
4. MacDoran, Peter F., (1979), "Satellite Emission Radio Interferometric Earth Surveying, SERIES - GPS Geodetic System," Bulletin Geodesique.
5. Private Communication, Albert Bierman, Aerospace Corp.
6. Klobuchar, J. A. (1978), "Ionospheric effects on Satellite Navigation and Air Traffic Control Systems," NATO AGARD proceedings, Lecture Series No. 93, Recent Advances in Radio and Optical Propagation for Modern Communication, Navigation, and Detection Systems.
7. Jespersion, James L.; Private Communication.

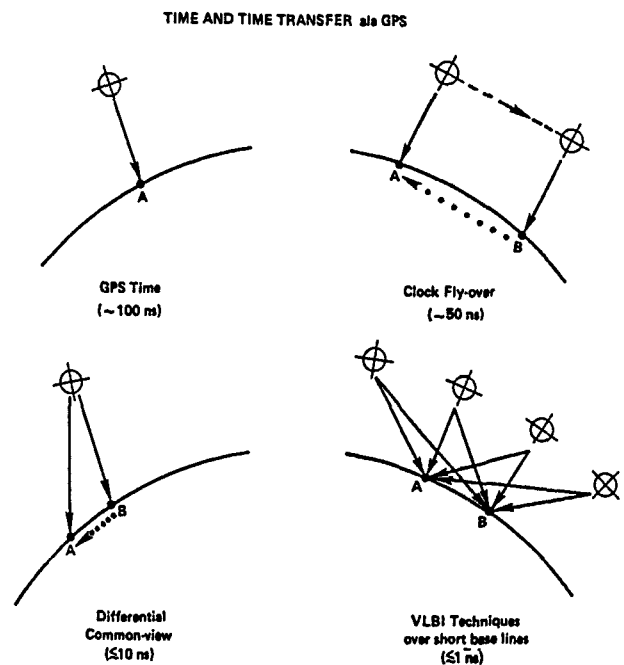


Figure 1. Four methods of time transfer and their approximate accuracies using GPS:

Upper left, using data from the satellite to find GPS time and comparing a local clock with the GPS time scale.

Upper right, using one satellite to decode GPS time at two different locations and times to compare both clocks with the GPS time scale and hence with each other.

Lower left, measuring the time of arrival of a common signal from a satellite at two locations to compare the computed time of transmission according to the two clocks and thus compare the clocks.

Lower right, recording signals from four satellites at two stations to determine locations and time differences.

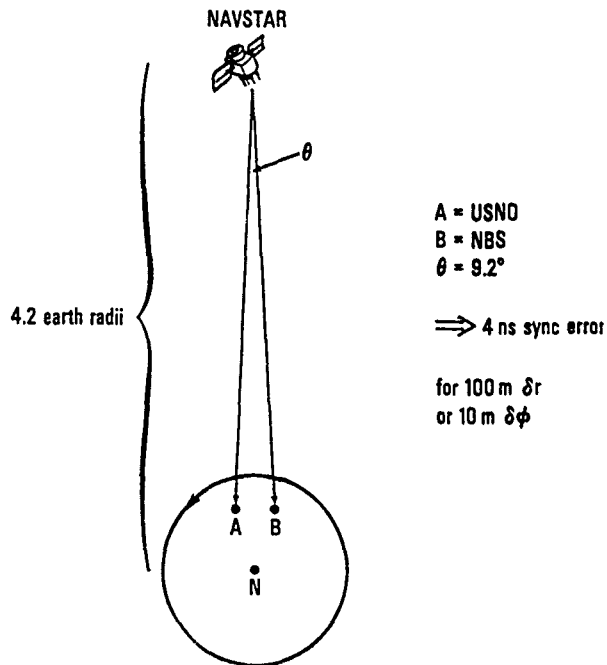
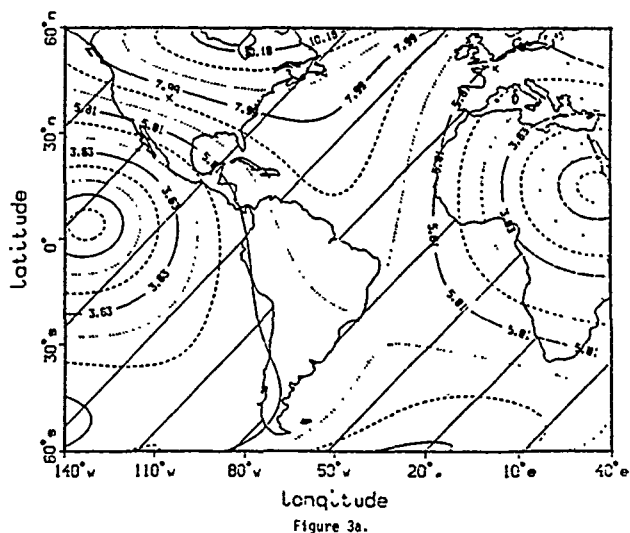


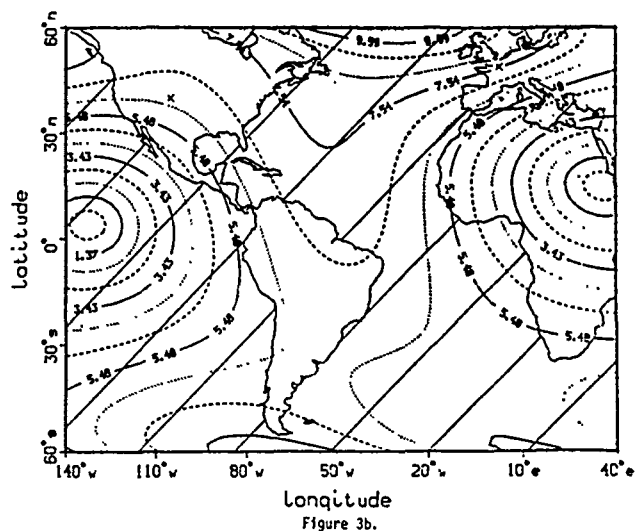
Figure 2. Time transfer via a satellite in common view of two ground stations indicating that fairly large errors (100 m = 333 ns radial error or 10 m = 33 ns in-track or cross-track error) in satellite ephemeris can cancel to a few ns time transfer error.

Figures 3-18. Contour graphs of the error in common-view time transfer for various choices of ground stations, satellite direction, and ephemeris error. The odd-numbered figures use current ephemeris error estimates: 10 m in-track, 7 m cross-track, and 2 m radial corresponding to 41.23 ns rms (square root of the sum of the squares divided by the speed of light). The even-numbered figures use error values projected for 1985: 7 m in-track, 3 m cross-track, and 0.6 m radial corresponding to 25.46 ns rms. The satellite direction is always northerly in the "a" figures and southerly in the "b" figures. The ground station locations are marked with an "x". The contours in a given figure are spaced for equal error values with error increasing as one goes from dotted to dashed to solid to dotted lines. Figures 3a, 3b, 4a, and 4b are examples of all four combinations; the odd numbered "a" figures and the even numbered "b" are deleted thereafter because their contour may be inferred from studying Figures 3a, 3b, 4a, and 4b along with the station combination of interest.

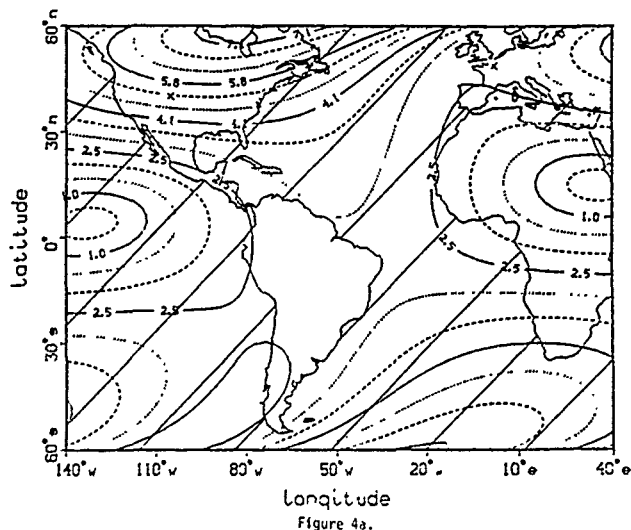
from rms ephemeris error = 41.23 ns
units=nanoseconds,direction=north
.727 ns between contours



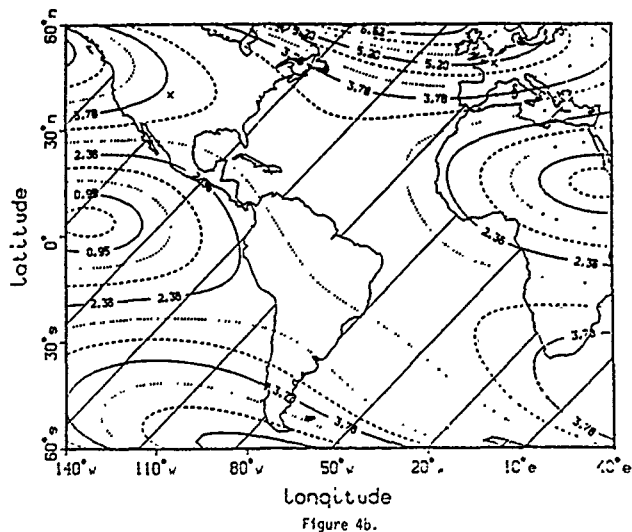
from rms ephemeris error = 41.23 ns
units=nanoseconds,direction=south
.685 ns between contours



from rms ephemeris error = 25.46 ns
units=nanoseconds,direction=north
.509 ns between contours



from rms ephemeris error = 25.46 ns
units=nanoseconds, direction=south
.473 ns between contours



NBS-NRC Time Transfer Error

from rms ephemeris error = 41.23 ns
units=nanoseconds,direction=south
.200 ns between contours

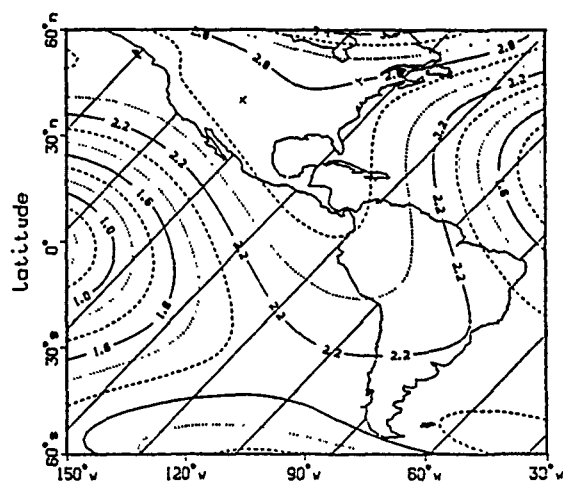


Figure 5b.

NBS-NRC Time Transfer Error

from rms ephemeris error = 25.46 ns
units=nanoseconds,direction=north
.167 ns between contours

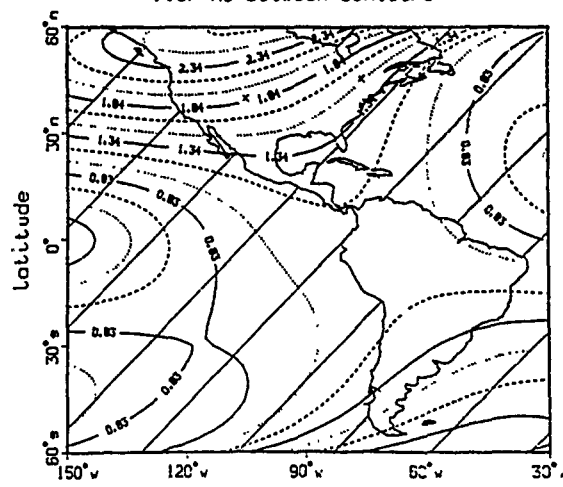


Figure 6a.

NBS-PTB Time Transfer Error

from rms ephemeris error = 41.23 ns
units=nanoseconds,direction=south
.609 ns between contours

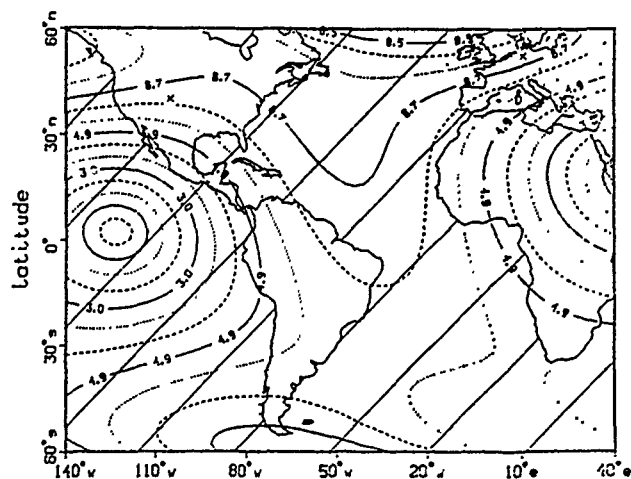


Figure 7b.

NBS-PTB Time Transfer Error

from rms ephemeris error = 25.46 ns
units=nanoseconds,direction=north
.477 ns between contours

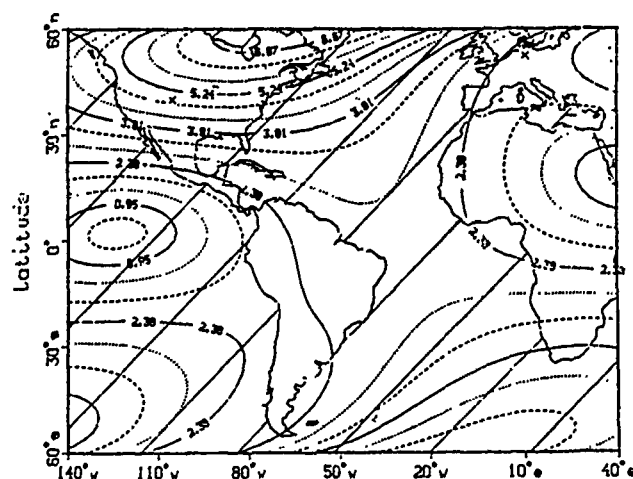


Figure 8a.

NBS-RRL Time Transfer Error

from rms ephemeris error = 41.23 ns

units=nanoseconds, direction=south

.784 ns between contours

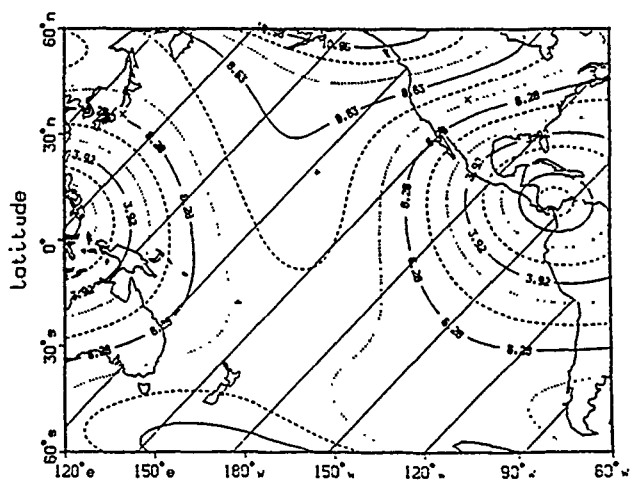


Figure 9b.

NBS-RRL Time Transfer Error

from rms ephemeris error = 25.46 ns

units=nanoseconds, direction=north

.561 ns between contours

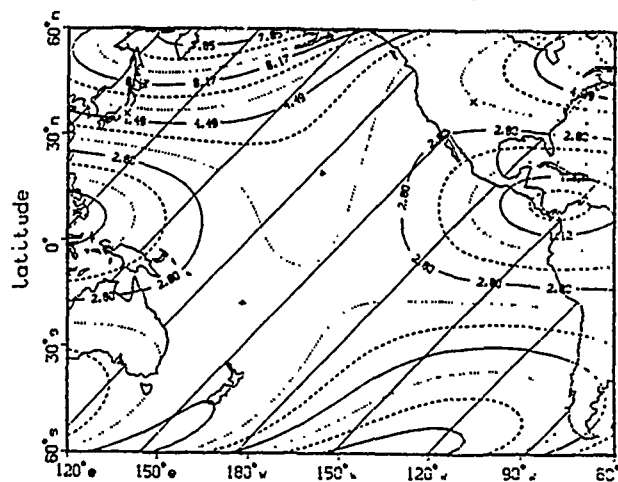


Figure 10a.

NBS-USNO Time Transfer Error

from rms ephemeris error = 41.23 ns

units=nanoseconds, direction=south

.202 ns between contours

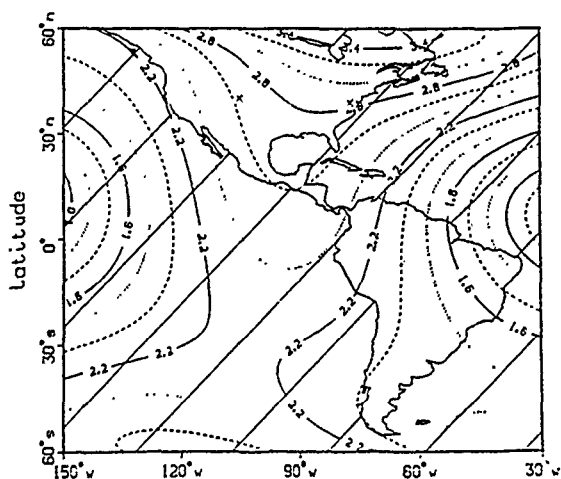


Figure 11b.

NBS-USNO Time Transfer Error

from rms ephemeris error = 25.46 ns

units=nanoseconds, direction=north

.147 ns between contours

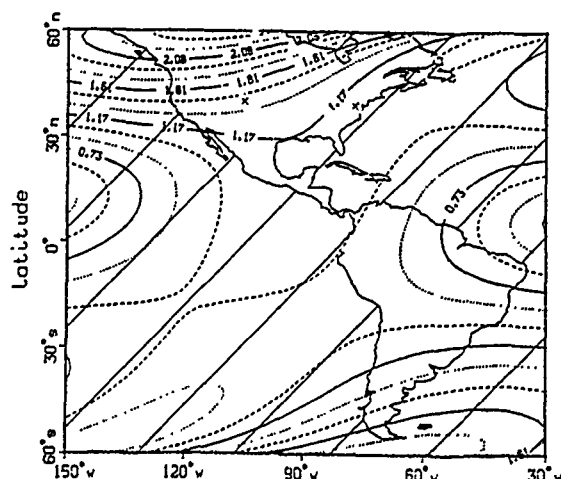


Figure 12a.

NBS-Vandenberg Time Transfer Error

from rms ephemeris error = 41.23 ns
units=nanoseconds,direction=south
.102 ns between contours

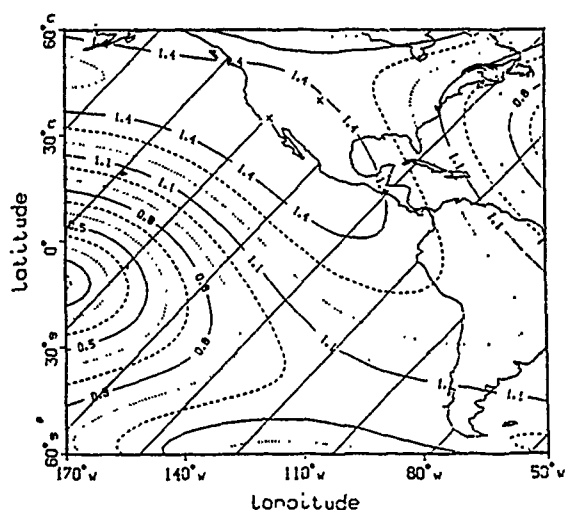


Figure 13b.

NBS-Vandenberg Time Transfer Error

from rms ephemeris error = 25.46 ns
units=nanoseconds,direction=north
.091 ns between contours

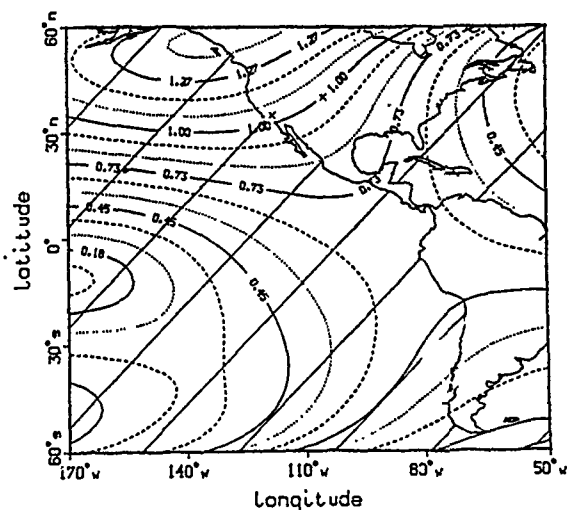
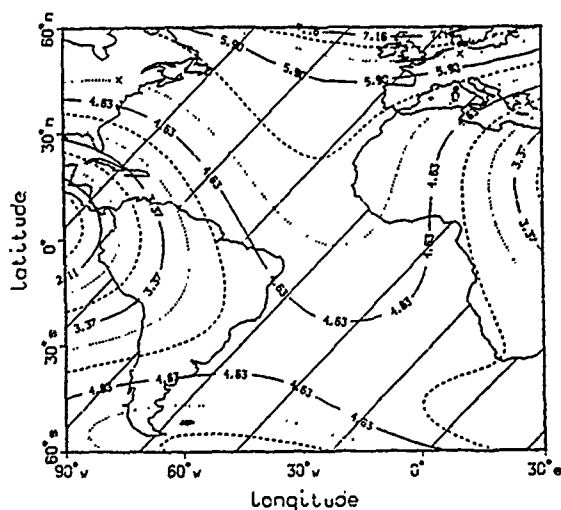


Figure 14a.

NRC-PTB Time Transfer Error

from rms ephemeris error = 41.23 ns
units=nanoseconds,direction=south
.421 ns between contours



USNO-BIH Time Transfer Error

from rms ephemeris error = 41.23 ns
units=nanoseconds,direction=south
.468 ns between contours

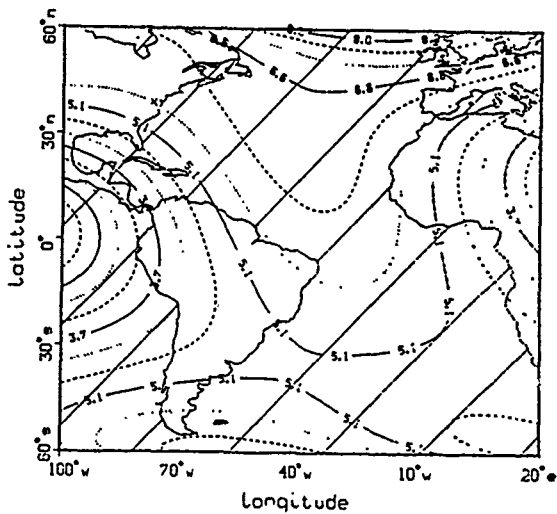


Figure 17b.

USNO-BIH Time Transfer Error

from rms ephemeris error = 25.46 ns
units=nanoseconds, direction=north

.385 ns between contours

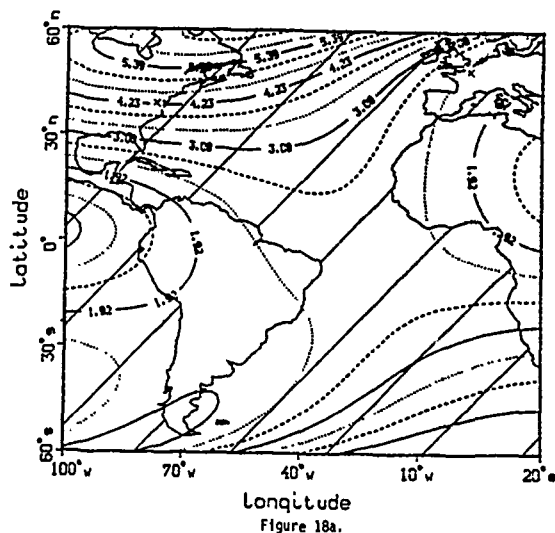
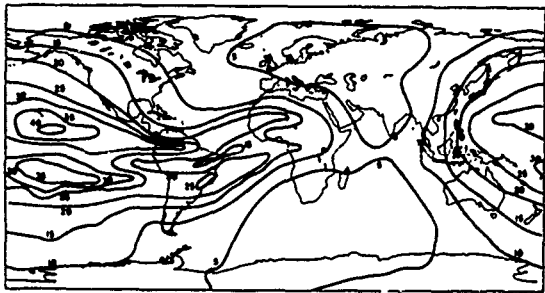


Figure 18c

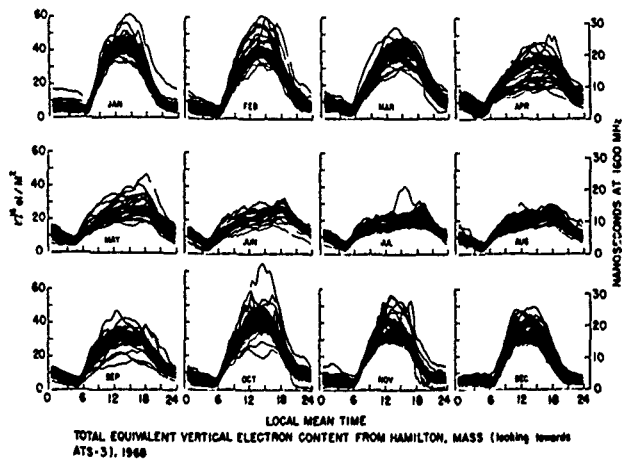
IONOSPHERIC TIME DELAY (BENT MODEL)
(NANOSECONDS AT 16 GHz)

00 h UT, MARCH 1968



Worldwide average vertical ionospheric time delay at 1.4 GHz for 00 hours universal time March, 1968, an average solar maximum year.

Figure 19.



Monthly overplots of equivalent vertical TSC from Hamilton, Massachusetts for the year 1960, a solar maximum year.

Figure 20.

TIME RELATED ASPECTS OF THE POSITION LOCATION REPORTING SYSTEM

John E. Lioy

Office of the Project Manager, PLRS/TIDS

ABSTRACT

The Position Location Reporting System (PLRS) is being developed for use by the U.S. Army and U.S. Marine Corps for position location, navigation and limited data communications.

PLRS is a synchronous time-ordered network utilizing a common spread spectrum waveform, with many units in the network time-sharing a single frequency band. To support hundreds of users in near real time, PLRS employs frequency-hopping and a direct sequence pseudo-noise spectrum-spreading technique, combined with data encryption and interleaving, which provides meaningful Electronic Warfare (EW) protection.

The technique employed to locate the position of system users is multilateration. It is based on determining range to a User Unit by measuring the time-of-arrival (TOA) of signal bursts from units at known locations. Every User Unit incorporates a time base generator which is effectively synchronized with and periodically corrected by the system timing source (Rubidium Standard) at the Master Unit (MU). Each User Unit in the network is assigned one or more unique time slots during which it transmits and all other programmed units receive.

INTRODUCTION

The PLRS Master Unit data base provides information such as position location, which is communicated to the user. The information on these users is also displayed for the field commander's use. Position locations are typically accurate to within ten meters. Users can also send and receive information through the master unit to other units. When programmed by the Master Unit to do so, each User Unit in the network reports the TOA of any signal bursts it has received from other specified units. The MU compares the reported time of message receipt with the known time of transmission, and converts the difference into range between sender and receiver. When the ranges between a given unit and three or more previously located units are known, the position of the unit in three dimensions can be calculated. The use of more than three measurements for a unit can increase the accuracy of the location to within a few meters.

The system consists of two major components as shown in Fig. 1. The Master Unit, or MU automatically manages a network of up to 370 active users and also displays their positions on a CRT. The User Unit (UU) configuration except for mounting antenna and power adapter is the same for man-pack, surface vehicle or aircraft applications. Each unit contains all of the electronics necessary to be programmed and located by the MU, and to transmit and receive digital data.

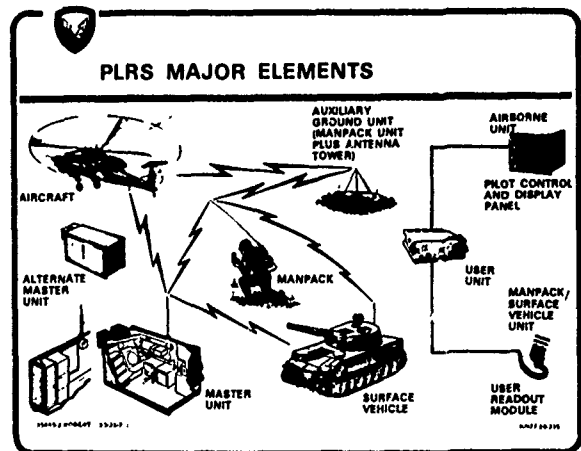


Figure 1

The Master Unit is configured in a S-280 shelter. It includes a time of arrival processor (TOAP) network control processing (NCP), a display control processor (DCP), a Command Response Unit (CRU) for network control, a graphics display and a rubidium standard for system timing.

The user unit measure time of arrival (TOA) on messages transmitted from other units in its assigned communications path.

Each user unit contains a transducer which measures its altitude. This information is also transmitted to the MU for an altitude refinement which can be used to reduce positioning inaccuracies due to unfavorable user geometries.

A real-time position tracking system has finite computer and communication capacity. It is essential these resources be used efficiently, maximizing the frequency of new position updates to enhance user capacity and positioning accuracy. Time ordered systems, maintaining precise time synchronization among user unit time bases, potentially satisfies this need. Early time ordered systems employed frequent user time base correction at the expense of system resources. Many communication transmissions are eliminated by the scheme employed in PLRS. In PLRS, each user's oscillator offset and drift is modeled at and determined with respect to the Master Unit's time reference. This perceived time error is accounted for in position update calculations. This scheme allows the one-way TOA approach and achieves accurate positioning using small inexpensive oscillators at the user unit. This paper explains this and other time-related aspects of the PLRS.

TYPICAL ARMY AREA OF OPERATIONS

The PLRS Employment Concept envisions a total of five active Master Units per corps, all inter-operating and sharing the common time-frequency resource as a single, coordinated non-interfering network. The Master Units would be deployed to the rear of four-on-line divisions and the reserve division in the corps area. The majority of User Units would be deployed near the FEBA, with still other User Units used as relays to support communications between Master Units. In this manner, the entire corps area is covered, and User Units can travel freely within this area without loss or interruption of services. (See Figure 2)

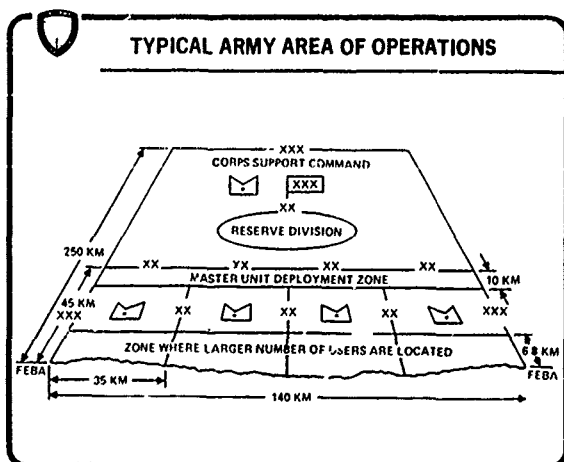


Figure 2

PLRS COVERAGE VIA RELAYING

In order to acquire units that are beyond Line-of-Sight (LOS) of the Master Unit, the PLRS employs an automatic Integral Relay Concept. This technique allows for any user to be programmed and serve as a relay. Up to three levels of relaying can be accommodated. Units that are within LOS of the MU are called "A" Level Users. Units that are within LOS of the "A" Level are called "B" Level Users. This concept is extended to the D Level. This automatic relaying feature allows for the adaptive rerouting of information in cases where communication paths are broken by rough terrain, battle damage or interference. (See Figure 3)

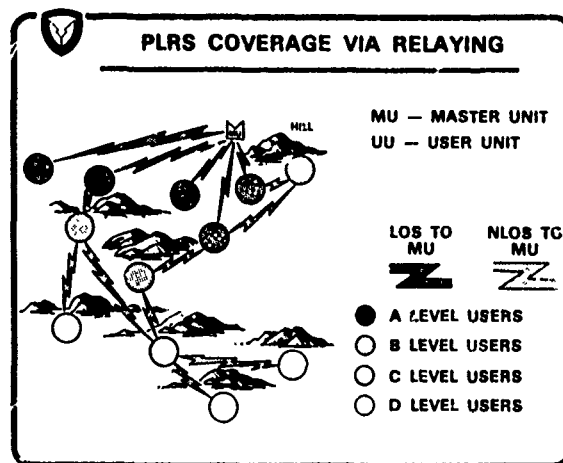


Figure 3

MULTILATERATION TECHNIQUE

Position accuracies of 7-15 meters for ground users is achieved by multilateration. (See Figure 4) Accurate position location requires each user to be within Line-of-Sight of at least three other users with known positions. The distances between the unit to be updated and the three known users is calculated by measuring the length of time it took for this (UU No. 3) user's signal to arrive at each of the three known user locations. By knowing what precise time User Unit No. 3 will transmit and the time of arrival of this message at three known locations, the Master Unit can calculate the intersection of the three distances from the three known users to update the position of Unit No. 3.

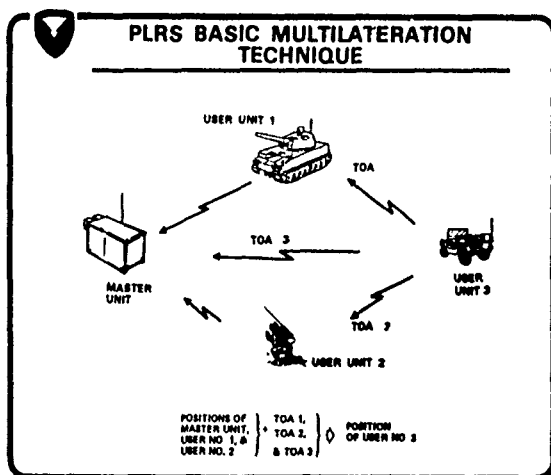


Figure 4

MU/UU DATA FLOW

Figure 5 illustrates the Data flow between the Master Unit and the User Units.

The Master Unit sends outbound command messages to the User Units who report back Time-of-Arrival measurements. The User can request information from the MU by Data Input messages. The MU answers these requests via the Data Output messages, which are displayed on the URO. The MU also interfaces with Command and Control elements.

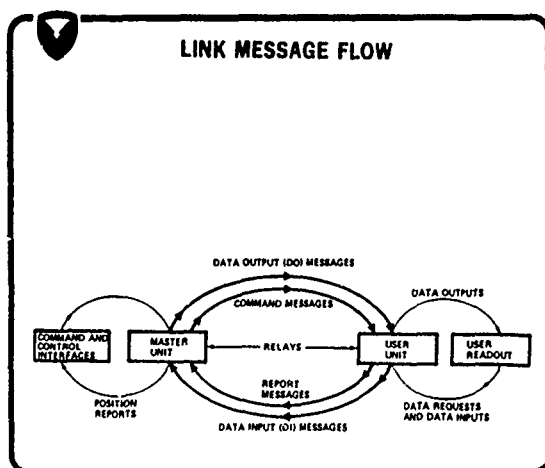


Figure 5

SYNCHRONOUS TIME DIVISION MULTIPLE ACCESS

The PLRS is a Time Division Multiple Access System (TDMA) employing direct sequence spectrum spreading and frequency hopping over a frequency range of 420-450 MHz. The PLRS network members have effectively synchronized time bases thereby allowing for one way Time of Arrival (TOA) measurements to be made between network members. These TOA measurements are converted to ranges at the Master Station. Position location is performed by providing the TOA measurements from the network members to the MU processor where new position location updates are calculated. Every User Unit has its own time that it should transmit or perform other programmed operations. Once this time base is synchronized with the Master Unit's time base, then messages can be sent or received and range measurements made. The Master Unit's time base acts as the prime timing source for the entire network correcting each of the User Unit clocks whenever they require it. In this way, the timing oscillators included in the User Units need to have only moderate stability, and can be inexpensive production type

The fundamental time division of the PLRS is the time slot. Each of the PLRS units in a network takes turns transmitting a burst of radio frequency energy in a time slot while the selected PLRS units listen. The time slot is approximately 2 milliseconds long.

The frame is 128 slots and is precisely 250 milliseconds in length. The significance of the frame is that it represents the maximum rate at which a User Unit can generate a report message that can be processed by the Master Unit.

The epoch has 256 frames consisting of 32,768 time slots with a length that is precisely 64 seconds long. It represents the minimum rate at which a User Unit can generate a report message that can be processed by the Master Unit. The PLRS network can be said to be periodic with respect to the epoch. This is why there is a carousel type arrangement displayed in Figure 6.

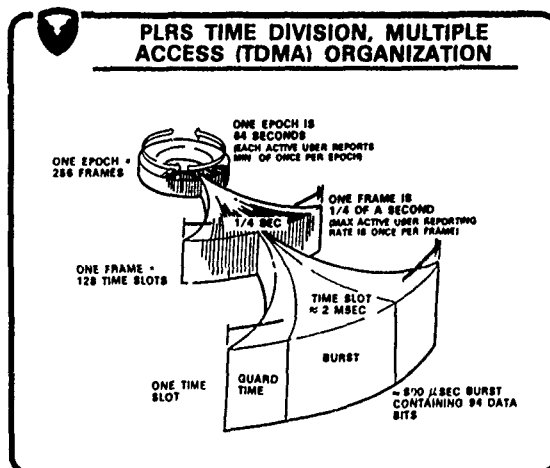


Figure 6

The main advantage of fully synchronous operation is that more time slots are made available for network users. Since the Master Unit does not have to contact a User Unit each time it wants to transmit for ranging, a great number of time slots are freed for other uses or users.

PLRS BURST WAVEFORM DESCRIPTION

The PLRS transmission waveform consists of a single burst of energy per time slot, as shown in Figure 7. The 824.6 microsec burst consists of 4123 PN (Pseudo Noise) Chips. The PN Chip is the basic signalling element of the PLRS CPSM Waveform. The PLRS PN Chip, of 200 nSec duration, phase modulates the transmitted PLRS carrier frequency.

The PLRS burst transmission consists of five segments: (1) Power Rise; (2) Preamble; (3) Buffer; (4) Data; and (5) Power Fall.

The Power Rise and Fall times are used to reduce the pulsed sidebands which rapid RF power switching would create.

The 320-chip-long Preamble of the PLRS waveform allows the User Unit to synchronize (by correlating the received message with a stored PN reference pattern) to incoming PLRS signals that arrive at an unknown time (due to unknown range between users) within a timeslot.

In the Buffer and Data portions of the PLRS waveform, 19 PN chips are grouped (actually MOD 2 summed) with each data symbol. The buffer portion of the PLRS message contains 12 symbols, while the data portion contains 182 symbols. The buffer portion of the PLRS message allows the User Unit to refine the carrier phase and time tracking processes prior to actual data demodulation.

The 182 symbol Data portion of the message is an interleaved, error correction encoded version of the 104-bit baseband data message. Ten bits of message validation (parity) are appended to 94 bits of actual data to form the 104-bit message. The first 19 bits of this message include 14 bits of unit ID or barometric pressure plus a 5-bit message header. The last 75 bits of the 94 bit message are the 75 bits of information used either for User Unit control and reporting with PLRS link messages or 75 bits of data from the user data I/O device.

The information transmitted, (in the UHF band - 420 - 450 MHz), is spread to a bandwidth of approximately 3 MHz (3 dB) by modulation with a 5 Mpps pseudonoise code sequence. Each time a User Unit or Master Unit transmits a burst, that signal burst is spread by the 5 Mpps code. The spread spectrum signaling format provides a low density signal spectrum that reduces detection by would-be interceptors and that offers minimum interference to other co-channel users.

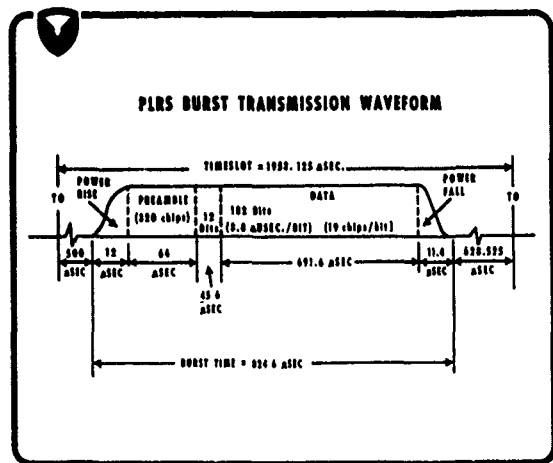


Figure 7

DATA TRANSMISSION PROCESS

Figure 8 illustrates the functional processing done to transmit a PLRS burst transmission. Raw digital data in groups of 94 bits per message are fed to the Validation Encoding Logic. The message validation encoding process uses a cyclic redundancy checking algorithm to generate 10 parity bits which are appended to the 94 bits of data.

The resulting 104 bits are then encrypted by the SDU and sent to the error correction encoding function. Error correction encoding is a 7/4 Hamming coding process that adds 3 check bits to each 4 unencoded bits. Thus, the 104 input bits result in 182 (7/4 x 104) encoded symbols. These 182 symbols are then interleaved to minimize burst error interference. After interleaving, the PN code is modulo 2 added to the data stream, the signal then is passed through the CPSM modulator, and finally the signal is amplified and frequency converted for transmission at UHF. The receiving process is the exact inverse of the transmit process.

The data process of message validation, error correction, and interleaving provide a great deal of data protection. Interleaving of error correction encoded symbols protects data against burst signal interference up to 100 microseconds in duration. Error correction encoding and decoding allows a lower data detection threshold Signal-to-Noise Ratio over an unencoded system and tolerates one symbol per word in error, with perfect correction. Message validation detects whether the received message contains any residual, uncorrected errors. The combination of these data protection techniques provides nearly error-free digital data communication in the PLRS system. One other technique, that of unique addressing and message acknowledgement, is used for critical PLRS messages. The message requiring acknowledgement must be correctly responded to by the commanded User Unit or the MU will repeat the message.

This process ensures that critical commands are received totally error-free before they are acted upon by a User Unit.

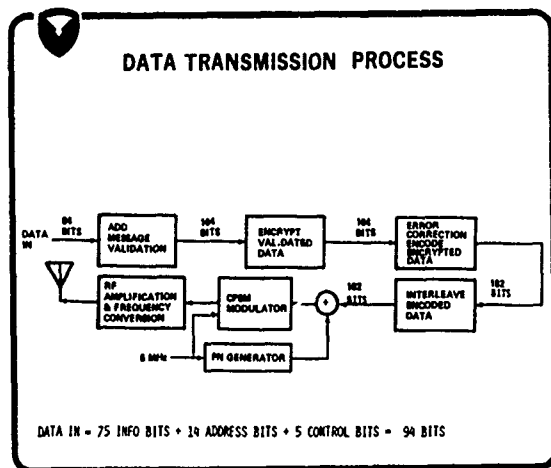


Figure 8

TRANSACTION GROUP

The 128 time slots in each frame are organized as eight groups of sixteen non-contiguous time slots. Figure 9 shows one group. Each group of sixteen time slots may be used for a complete set of two-way information. Transfers (or transactions) between the MU and a set of up to four User Units. Thus, each of these groups is termed a Transaction Group (TG). Each of the four UU's involved in a TG is operating at a different relay level, relative to the MU. These levels are defined as levels A, B, C and D as they progress outward from the MU, as designated on the vertical axis. The sixteen time slots in each TG are defined sequentially by time slot indices (TSI) 0 to 15, as designated on the horizontal axis. Although not shown on the slide, within each TSI time interval, eight time slots occur (numbered time slots 0 to 7). Each of these eight time slots is utilized for a transaction involving a member of a different set of up to four User Units. Thus, eight TG's are time interleaved across each frame.

TIME SYNCHRONIZATION

To maintain time synchronization, the system performs time difference measurements (See Figure 10). When the MU transmits, a UU measures the resultant TOA and reports that TOA back to the MU in the unit's assigned transmission time slot. The MU then compares the TOA report with its own TOA measurement of the UU's signal to determine the UU's Clock Offset. When required, the MU commands the UU to correct its timing. For units not in

direct communication with the MU, a lower level unit transmits instead of the MU. The timing offset is then relative to this lower level unit, thus forming a timing chain back to the MU. A simplified version of the discrete Kalman filter called the CLOC (Central Logic Oscillator Control) filter is used to obtain estimates of each UU's clock offset and drift rate with respect to the MU's clock (or oscillator). With this knowledge, precise one-way TOA ranging is possible without using prohibitively large and expensive highly stable oscillators at each UU. CLOC provides, as required, commanded corrections to each UU's clock offset and/or frequency to keep all UU's nominally synchronized with one another.

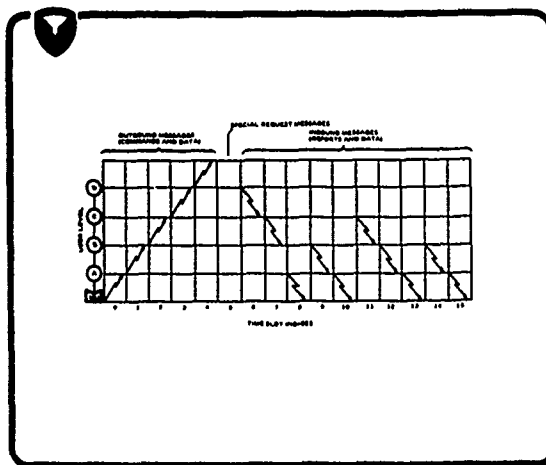


Figure 9

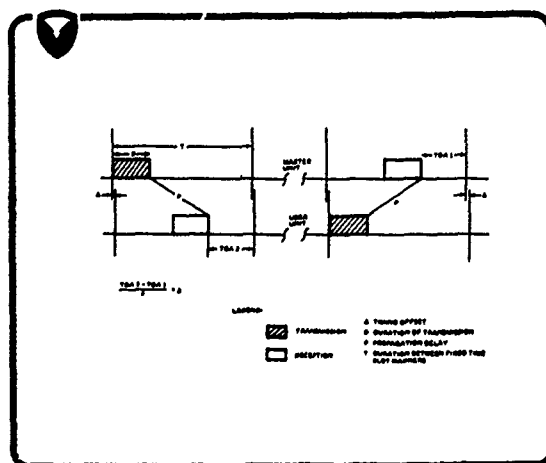


Figure 10

OPERATION OF THE CLOC FILTER

To perform one-way TOA ranging, it is necessary that the difference between the time reference of the Master Unit (MU) and the time reference of the User Unit (UU) be known. This difference is expressed as the clock offset of the UU with respect to the MU. The function of the CLOC filter is to estimate this clock offset, as well as the UU's clock drift rate (i.e., the rate at which the offset changes with time).

The filter processes pairs of TOA inputs from two cooperating units (See Figure 11). In the case of an A level UU (one that communicates directly with the MU), the pair of units is the MU and the A level, UU. The relative offset information is given by the difference of the paired TOAs. In this case, the relative offset is the absolute offset since the MU is assumed to have perfect timing. In the case of a B level UU, one that communicates with the MU via an A level relay, the pair of cooperating units is the A level UU and the B level UU. In this case, the clock offset and drift of the B level UU with respect to the MU is determined by knowing the absolute offset of the lower level (A-level in this case) unit and the relative offset afforded by the paired TOAs. The process is analogous for C level and D level UUs. The operation of the CLOC filter is the same for all units forming the inputting pairs.

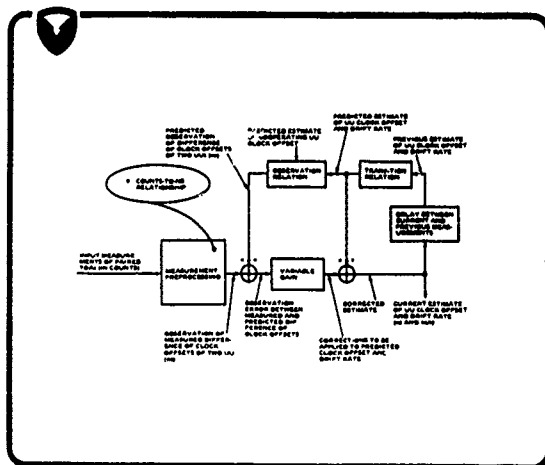


Figure 11

Clock Offset Estimation The input measurements received by the CLOC filter are in 12.5-ns counts representing TOA measurements from each of a pair of cooperating units. A 12.5-ns increment is selected as a result of a tradeoff between hardware circuitry considerations and TOA accuracy requirements. The measurement preprocessing stage subtracts one input TOA count from the other and converts the result to nanoseconds. The output of the preprocessing stage is thus the currently measured clock offset of one unit with respect to the other. This measurement is compared with the

previously predicted relative offset to obtain the current measurement residual. An adaptive gain is applied to the measurement residual to provide a correction factor for the predicted estimate of the clock offset of the unit with respect to the MU which is a necessary input for one-way TOA ranging. An adaptive gain is applied to the measurement residual to account for: (1) the fact that each UU, because of dual relay assignments, cooperates with two other lower level units (thus, two sources of timing), (2) the length of time since the cooperating unit's clock offset was estimated.

The current estimate of clock offset is fed back to the CLOC filter to provide the previous offset and predicted estimate of offset for comparison with the next pair of input TOA measurements involving the same two cooperating units. The offset is predicted by linearly extrapolating the current estimate to account for the delay between measurements. The delay between measurements is counted by keeping track of when this UU was updated last. The current estimate of relative offset thus becomes the previous estimate for the next pair of input measurements involving the UU.

Application of the measurement relation consists of taking the current predicted estimate of the UU clock offset and the predicted estimate of the cooperating UU's clock offset and subtracting these two to form the relative offset. The predicted estimate of offset for the cooperating UU is simply obtained by extrapolating its previous clock offset to the time of occurrence of the current paired TOA measurements. This yields the predicted measurement of relative offset, to which the measured relative offset is applied to form the measurement residual.

Clock Drift Rate Estimation - The correction to the clock offset is partially applied to the drift rate after taking into account the passage of time since the last estimate of drift rate.

Clock Correction Commands to UU - Whenever the resultant MU estimates of UU offset or drift rate falls outside prescribed limits, a command is sent to the UU to correct its clock offset or frequency or both. Thus, each UU's clock is permitted to drift while still maintaining nominal network synchronism, hence, the name "drift synchronization".

MERCURY ION FREQUENCY STANDARD : PRELIMINARY RESULTS

Michèle Jardino, Michel Desaintfuscien, Roland Barillet,
Jacques Viennet, Pierre Petit and Claude Audoin

Laboratoire de l'Horloge Atomique
Equipe de Recherche du CNRS
associée à l'Université Paris-Sud
Bâtiment 221
91405 Orsay - France

Summary

A laboratory experiment which is aimed to evaluate the properties of a frequency standard using the hyperfine transition of stored mercury ions is described.

About 10^6 ions of ^{199}Hg isotope are confined in a cylindrical radiofrequency trap. The hyperfine transition at a frequency of about 40.5 GHz is observed via optical pumping produced by the ultraviolet light at 194 nm which is emitted by an electrodeless $^{202}\text{Hg}^+$ lamp.

Presently achieved linewidth and signal to noise ratio are reported. Storage time, optical pumping and relaxation rates are given.

A frequency control loop which locks the frequency of a 5 MHz quartz crystal oscillator to the hyperfine frequency of stored mercury ion is described. In this system, pulses delivered by the photomultiplier are processed digitally. Optimal conditions for the interrogation of the hyperfine transition are specified.

Preliminary results on the experimentally achieved frequency stability are reported. We obtained $\sigma(\tau) = 3.6 \times 10^{-11} \tau^{-1/2}$ for $35 \text{ s} < \tau < 3500 \text{ s}$. This frequency stability is comparable to that of commercially available cesium beam frequency standards. Prospects for improvement by a factor of 10 at least are discussed.

Introduction

Storage of ions in a radiofrequency trap is a very promising, and now well known technique^{1,2} for interrogating, during long times, a microwave transition, free from wall perturbation and first order Doppler effect³.

Stored $^{199}\text{Hg}^+$ looks attractive⁴⁻¹¹ for application to frequency standards, mainly on account of the high value of the frequency of its hyperfine transition, at 40.5 GHz.

We have developed experimental techniques for the measurement of the various relaxation times involved in the microwave transition of stored $^{199}\text{Hg}^+$ ions¹², and we report, here, for the first time, the experimentally measured frequency sta-

bility of a quartz crystal oscillator which is frequency controlled by the $\Delta m_F = 0$ transition of $^{199}\text{Hg}^+$ stored in a radiofrequency trap.

Experimental set-up for the observation of the hyperfine transition of $^{199}\text{Hg}^+$

As shown in figure 1, a fortuitous matching⁴ of $^{199}\text{Hg}^+$ and $^{202}\text{Hg}^+$ energy levels is used to selectively pump $^{199}\text{Hg}^+$ from the $F = 1$ to the $F = 0$, hyperfine ground state, via an upper excited state¹³. A microwave excitation mixes the two $F = 1$ and $F = 0$ states and, consequently, increases the number of ions in the $F = 1$ level when its frequency is close enough to the frequency of the hyperfine transition in the ground state. The fluorescence light emitted by the ions in the excited state is proportional to the ion number in the $F = 1$ level. This light is then used to probe the hyperfine transition¹³.

In our experimental set-up, depicted in figure 2, ions are confined in a copper cylindrical trap¹⁴. The ring diameter is $2r_0 = 38 \text{ mm}$. The height of the trap is $2z_0 = r_0\sqrt{2} = 27 \text{ mm}$. Two holes provided in the cylinder⁸ allow the pumping light to pass through the trap. A third aperture is used to apply the microwave excitation. The upper cap of the trap is made of a mesh whose transparency is 90 %, in order to observe the fluorescence light. An electron beam is introduced into the trap through a hole drilled at the center of the lower cap. It ionizes neutrals of a low pressure mercury vapor.

The values of the d.c. and a.c. components of the confining voltages are fixed to store a maximum number of ions in the trap^{15,16}. They are, respectively : $V_{dc} = 18 \text{ V}$ and $V_{ac} = 250 \text{ V}$. The frequency of the a.c. voltage is 250 kHz. In such conditions, the depth of the effective potential well is 20 eV about.

The trap is set in a quartz envelope, with a flat window transparent to the U.V. pumping radiation, at 194 nm. At the opposite of the window, a light trap reduces back scattering of the incoming light. An ion-sputtering pump provides a background pressure smaller than 10^{-7} Pa . Two mu-metal magnetic shields reduce the earth magnetic field intensity and its fluctuations, and two Helmholtz coils create an adjustable homogeneous magnetic field parallel to the trap axis.

This work has been sponsored by CNRS and DRET.

The pumping light at 194 nm is produced by an electrodeless spherical lamp, 25 mm in diameter. It contains about 10 mg of mass 202 isotope of mercury. The pumping beam is carefully collimated by two sharp edged diaphragms, in order to reduce the intensity of the light scattered from the pumping beam. A flux of about $5 \cdot 10^{12}$ photons at 194 nm enters the trap. The fluorescence light is observed at right angle from the direction of the pumping beam, in a large solid angle of 1.84 steradians. A solar blind photomultiplier and an interference filter are used in the detection path in order to block the spurious light at wavelength different from 194.2 nm, coming from the pumping beam, the thermocathode and from the atoms excited by electron impact.

As shown in figure 3, the microwave excitation at 40.5 GHz is produced, by frequency synthesis, from the 5 MHz quartz crystal oscillator which is to be locked on the hyperfine transition. In a first stage, the frequency of the oscillator is multiplied up to 8 GHz. It is then mixed with a signal at 101.469... MHz delivered by a frequency synthesizer driven by the same 5 MHz oscillator. The upper side band at about 8.1 GHz is frequency multiplied by a factor of 5. A horn couples the microwave excitation at 40.5... GHz to the ions. The 5 MHz oscillator can be controlled by a servo loop in such a way that the frequency of the microwave excitation equals the frequency of the hyperfine transition. This control loop will be described latter.

Resonance line

It can be shown¹² that the number $n_1(\omega)$ of ions in the $F = 1$ state is given by :

$$n_1(\omega) = \frac{3I_0}{4Y_s} \left(1 - \frac{Y_p}{\Gamma_1}\right) + \frac{I_0 Y_p}{2Y_s \Gamma_1} \frac{S}{1+S} \frac{1}{1 + \frac{(\omega - \omega_0)^2}{2\sqrt{1+S}}} \quad (1)$$

where I_0 is the number of ions produced every second in the trap by electron impact ; Y_s is the inverse of the ion storage time ; Y_p is the optical pumping rate ; Γ_1 and Γ_2 are the total longitudinal and transverse relaxation rates, respectively ; S is the saturation factor of the resonance line ; ω_0 is the resonant angular frequency and ω is the angular frequency of the interrogating microwave signal. 17,18 :

We have

$$\Gamma_1 = \gamma_1 + \gamma_s + \gamma_p \quad (2)$$

and

$$\Gamma_2 = \gamma_2 + \gamma_s + \gamma_p/2 \quad (3)$$

where γ_1 and γ_2 are the longitudinal and the transverse relaxation rates between hyperfine levels. They are related to charge exchange collisions¹⁹ spin exchange collisions, motion in an inhomogeneous d.c. magnetic field and residual Doppler broadening.

The first term of the right hand side of equation (1) gives an indication of the efficiency of the optical pumping in comparison with relaxation processes. The second one is the term of interest. It increases with the intensity of the pumping light. The full width half maximum of the line is :

$$\delta\omega = 2\Gamma_2\sqrt{1+S} \quad (4)$$

The ion cloud is very dilute : its density at the center of the trap is typically 10^6 ions/cm³. It is nevertheless possible to observe the resonance line with a good signal to noise ratio, as it is shown in figure 4. Each point of this record has been obtained by accumulating during 1 s, the pulses delivered by the photomultiplier.

The width of the Lorentzian curve is 8.8 Hz only, for a saturation factor of 3. The resonant frequency being 40.5 GHz, the quality factor of the line is close to 5×10^9 .

The height of the line is about 11 % of the background. The background light is composed of the stray light due to imperfections in the optical system and of that part of the fluorescence light which remains when the microwave excitation is not applied (see equation 1). Typical values of these components, presently achieved in our experimental set-up, are shown in figure 5.

Measurement of the relaxation time constants of the ions

Measurement of the time constants of the various relaxation processes acting on the stored ions is of interest to analyze the physical mechanisms involved and to be able to optimize the operating conditions.

The longitudinal and transverse relaxation rates γ_1 and γ_2 , the storage rate γ_s and the pumping rate γ_p of the ions confined in the trap and excited by P the pumping light can be measured by studying the fluorescence light in various steady state and transient state experiments¹².

Figure 6 shows a sketch of the experimental procedure

- the width of the line gives the value of the total transverse relaxation rate Γ_2 when extrapolated to zero microwave power as shown by equation (4). The value of the saturation factor, for a given microwave power is there known,
- the ratio of the fluorescence background and of the height of the resonance line gives the value of Γ_1/γ_p . See equation (1),
- the transient behavior of the fluorescence signal after the microwave excitation is switched off¹² gives Γ_1 , and, consequently γ_p ,
- the transient behavior of the fluorescence signal when ions, excited by a ¹⁹⁹Hg⁺ lamp, are allowed to be stored in the trap gives the value of γ_s ¹², and consequently of γ_1 and γ_2 .

This last experiment is made possible because the d.c. component of the voltage applied to the trap can be switched rapidly between two values. One of them is such that ions cannot be confined, and the other one corresponds to optimum storage capability. Such an experiment cannot be done with a Rb cell for instance.

The following set of relaxation rates has been measured :

$$\begin{aligned} \gamma_1 &= 1.0 \pm 0.6 \text{ s}^{-1} \\ \gamma_2 &= 8.4 \pm 1.1 \text{ s}^{-1} \\ \gamma_s &= 2.3 \pm 0.3 \text{ s}^{-1} \\ \gamma_p &= 2.6 \pm 0.3 \text{ s}^{-1} \end{aligned} \quad (5)$$

Frequency control of a 5 MHz quartz crystal oscillator by the frequency of the hyperfine transition of the ions

The synthesizer used in the frequency synthesis chain is modulated such that the angular frequency of the microwave interrogating signal is square-wave frequency modulated with a period of 3 s, between two values ω_1 and ω_2 on both sides of the resonance line. The frequency of the VCXO is controlled in order that the fluorescence intensity is the same for both frequencies (figure 7).

The two values of the response of the atomic medium are not compared analogically, as usual, but digitally, as shown in figure 8. Photoelectron pulses delivered by the photomultiplier are up-counted when the angular frequency is ω_1 and down-counted when the angular frequency is ω_2 . The result of an up then down cycle is added to the previous ones and stored in a buffer register. It can easily be shown that this process acts as an integrator followed by a sampling and hold circuit, which operates on a quantity proportional to $\omega_0 - (\omega_1 + \omega_2)/2$.

The digital information delivered by the buffer register is converted into an analog voltage. It is applied to the varactor of the oscillator via an integrator with transfer function

$$H(p) = \frac{1 + T_1 p}{T_2 p} \quad (6)$$

The effect of a slow drift of the background light intensity, if any, is removed. This is done with the following algorithm, depicted on figure 9: one counts up during the first quarter of the cycle, down during the second and third quarters and up again during the last quarter. A dead-time of about 0.1 s between countings eliminates the spurious effect of transient regimes in the frequency of the microwave signal and in the response of the ions.

Optimal conditions for the interrogation of the transition

It can be shown that the one-sided power spectral density S_y of fractional frequency fluctuations of the controlled quartz crystal oscillator is approximately given by x^* :

$$S_y = \frac{1}{2} \frac{S_l}{\omega_0^2 \left| \frac{\partial l}{\partial \omega} (\omega_0 \pm \omega_m) \right|^2} \quad (7)$$

S_l is the one-sided power spectral density of the flux of photo-electrons. l is the mean value of this flux when the microwave angular frequency is $\omega_0 \pm \omega_m$. $\omega_m = (\omega_1 - \omega_2)/2$ is the depth of the angular frequency modulation.

The optimum value of ω_m is such that $\left| \frac{\partial l}{\partial \omega} \right|$ is a maximum. It can be seen, from equation (1), that this is obtained for $\omega_m = (\omega_m)_{opt}$ given by:

$$(\omega_m)_{opt} = \sqrt{3} \delta \omega / 6 \approx 0.29 \delta \omega \quad (8)$$

x^* This expression is valid for Fourier frequencies smaller than the cut-off frequency of the closed loop system.

Equation (7) then becomes:

$$S_y = \frac{8}{27} \frac{\delta \omega^2}{\omega_0^2 l_l^2} S_l \approx 0.30 \frac{\delta \omega^2}{\omega_0^2 l_l^2} S_l \quad (9)$$

where l_l is the flux of photoelectrons which represents the height of the atomic line x^* . It can be seen, from equations (1) and (4) that the quantity $\delta \omega / l_l$ is a minimum when the saturation factor S equals its optimum value S_{opt} given by:

$$S_{opt} = 2 \quad (10)$$

We then have:

$$\left(\frac{l_l}{\delta \omega} \right)_{max} = K n \frac{\gamma_p^2}{\Gamma_1 \Gamma_2} \quad (11)$$

where n is the total number of stored ions and K is a constant which depends on the efficiency of the optical system.

Obviously, the quantities K , n and $\gamma_p^2 / \Gamma_1 \Gamma_2$ must be made as large as possible. This means that: i) the solid angle for observation of the fluorescence light, and the quantum efficiency of the photomultiplier must be large; ii) the storage conditions are optimized, the ion creation rate and the storage time are large enough and iii) the pumping rate γ_p is the main contribution to total relaxation rates Γ_1 and Γ_2 .

Equation (9) also shows that S_l should be as small as possible. This practically means that the light scattered from the optical pumping beam must be made as small as possible.

If one assumes that the fluctuations on the flux of photoelectrons are only due to shot noise, it can easily be seen from equation (9) that the square root of the two sample variance 2σ of the fractional frequency fluctuations of the controlled quartz crystal oscillator is the following:

$$\sigma_y(\tau) = 0.54 \frac{\delta \omega}{\omega_0} \frac{(l_l)^{1/2}}{l_l} \frac{1}{\tau^{1/2}} \quad (12)$$

where l_l is the flux of photoelectrons for $\omega = \omega_0 \pm \omega_m$. It has been experimentally checked that the power spectral density S_l is close to the shot noise limit.

Measured frequency stability of a 5 MHz quartz crystal oscillator controlled by the hyperfine transition of $^{199}\text{Hg}^+$

The fractional frequency stability of a 5 MHz quartz crystal oscillator which is controlled by the hyperfine transition of $^{199}\text{Hg}^+$ has been measured. The reference oscillator was a 5 MHz VCXO phase controlled by a hydrogen maser 21 . The frequency of the two oscillators was multiplied up to 400 MHz, as shown in figure 10. The fluctuations of the period of the beat note are processed in order to measure the square root $\sigma_y(\tau)$ of the two-sample variance of the fractional frequency fluctuations of the oscillator. The $\sigma_y(\tau)$ graph, in

x^* l_l is the difference between the flux of photoelectrons when $\omega = \omega_0$ and $|\omega - \omega_0| \gg \delta \omega$.

the range $10 \text{ s} < \tau < 3500 \text{ s}$ is shown in figure 11. We have, in that range :

$$\sigma_Y(\tau) = \frac{3.6 \times 10^{-11}}{\sqrt{\tau}} \quad (13)$$

In this measurement, the parameters ω_m and S were adjusted to their optimum values, given by equations (8) and (10), and relaxation rates were similar to those given by equations (5).

For the purpose of comparison, the specified frequency stability of three models of commercially available Cs beam frequency standards is depicted in the same figure. The achieved frequency stability is thus quite comparable to that of manufactured Cs beam frequency standards.

Prospects for further improvements

The performances of a frequency standard based on the hyperfine transition of stored $^{199}\text{Hg}^+$ are promising. Improvement of the frequency stability looks possible when the present conditions of operation of our experimental set-up are compared to those discussed previously in this paper.

Stray light detected by the photomultiplier

The background light contributions shown in figure 5 should be made as small as possible. In our measurements, the stray light is responsible for 83 % of the background. Reducing it to zero would improve the frequency stability, characterized by $\sigma_Y(\tau)$, by a factor 2.1.

Hyperfine line shape

Equations (2) and (3) show that the asymptotic value of the ratio $\gamma_p^2/\Gamma_1\Gamma_2$ - which defines the effect of the line shape on the frequency stability - is 2. The typical value obtained in our experiments is .1. This shows that the frequency stability could be improved by another factor of 20 by reducing the relaxation rates γ_1 , γ_2 and γ_s . It is possible to decrease the value of γ_s at least by introducing a light buffer gas such as helium, under low pressure (10^{-3} Pa) in the vacuum tank. Another benefit of the buffer gas would be to improve the number of stored ions.

The other way to obtain a larger value of the ratio $\gamma_p^2/\Gamma_1\Gamma_2$ is to enhance the intensity of the pumping light. If the other relaxation rates are kept constant, the effect on the stability is less pronounced than in the previous method, if rejection of the light scattered from the pumping beam is not simultaneously improved. In that case, the frequency stability should be increased by a factor of about 3.

We then conclude that it seems possible to improve the short term frequency stability of the controlled quartz crystal oscillator by a factor of 10 at least.

Obviously, the long term frequency stability and reproducibility of this new atomic frequency standard must be investigated. This requires measurement of pressure shifts (effect of collisions with neutral mercury and with buffer gas, when added), of light shift, of second order and residual first order (if any) Doppler shifts with and without light buffer gas.

Acknowledgments.

We would like to thank the "Centre de Spectrométrie Nucléaire et Spectrométrie de Masse" ²² which kindly supplied mercury isotopes.

References

1. W. Paul, O. Osberghaus and E. Fischer, Forschungsb.-Wirtsch.-Verkehrsministerium Nordrhein-Westfalen, n° 415 (1958) 1
2. H.G. Dehmelt, Advances in Atomic Physics. New York, Academic Press 3 (1967) 53
3. R.H. Dicke, Phys. Rev. 89 (1953) 472
4. F.G. Major, NASA Report X-521.69.167, Goddard Space Flight Center (1969)
5. F.G. Major and G. Werth, Phys. Rev. Lett. 30 (1973) 1155
6. F.G. Major and G. Werth, Applied Physics 15 (1978) 201
7. M.D. Mc Guire, R. Petsch and G. Werth, Phys. Rev. 17 (1978) 1999
8. M.D. Mc Guire, Proc. of the 31st Annual Symposium on Frequency Control - Atlantic City (1977) p. 612
9. M. Jardino, F. Plumelle, M. Desaintfuscién and C. Audoin, 11th EGAS Conference - Orsay - France July 1979
10. G. Werth, 10th International Congress of Chronometry - Geneva - Switzerland, Sept. 1979 Proc. : Vol. 2, p. 13
11. M. Jardino, F. Plumelle, M. Desaintfuscién and C. Audoin, 10th International Congress of Chronometry - Geneva - Switzerland, Sept. 1979 Proc. : Vol. 2, p. 17
12. M. Jardino and M. Desaintfuscién, to be published in I.E.E.E. Trans. on Instr. and Meas. Sept. 1980
13. A. Kastler, J. Phys. Radium 11 (1950) 255
14. M.N. Benilan and C. Audoin, Int. J. of Mass. Spectrometry and Ion Physics 11 (1973) 421
15. R. Iffländer and G. Werth, Metrologia 13 (1977) 167
16. F. Plumelle, M. Desaintfuscién, J.L. Duchêne and C. Audoin, to appear in Optics Communications
17. J.P. Barrat and C. Cohen-Tannoudji, J. Phys. Radium 22 (1961) 329
18. J. Vanier, Phys. Rev. 168 (1968) 129
19. D. Rapp and W.E. Francis, J. of Chem. Physics 37 (1962) 2631
20. J.A. Barnes, A.R. Chi, L.S. Cutler, D.J. Healey, D.B. Leeson, T.E. Mc Guinag, J.A. Mullen, W.L. Smith, R.L. Sydnor, R.F.C. Vessot and G.M.R. Winkler, I.E.E.E. Trans. on Instr. and Meas. IM-20 (1971) 105
21. P. Petit, J. Viennet, R. Barillet, M. Desaintfuscién and C. Audoin, Metrologia 10 (1974) 61
22. K. Alexandre, J. Camplan, M. Ligonnière, R. Meunier, J.L. Sarrouy, H.J. Smith and B. Vassent, Nucl. Instr. and Meth. 84 (1970) p. 45

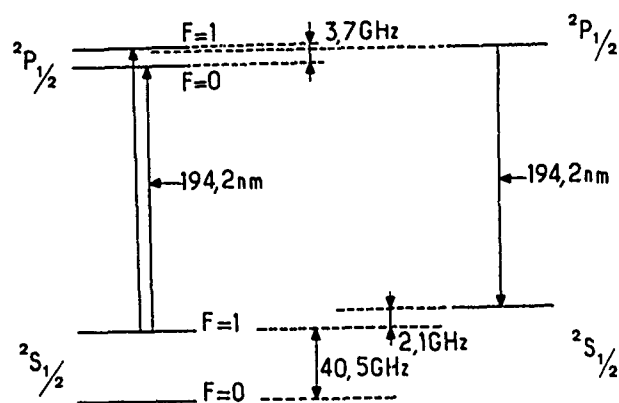


Fig. 1 : Simplified energy diagram of the $^{199}\text{Hg}^+$ and $^{202}\text{Hg}^+$ levels involved in the experiment.

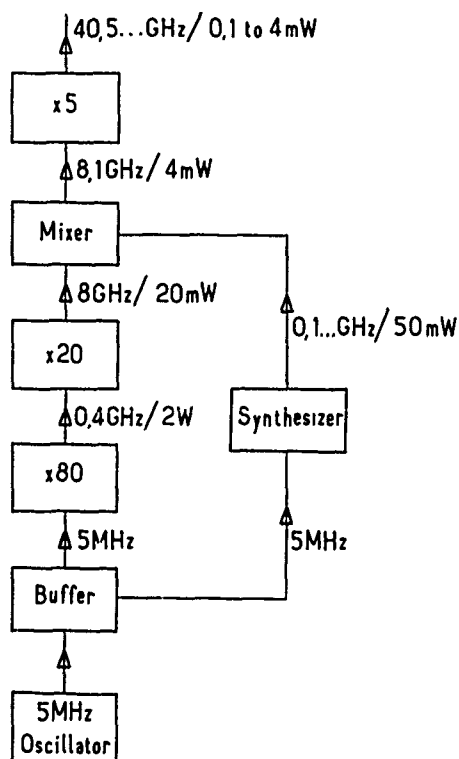


Fig. 3 : Frequency synthesis of the 40.5 GHz excitation.

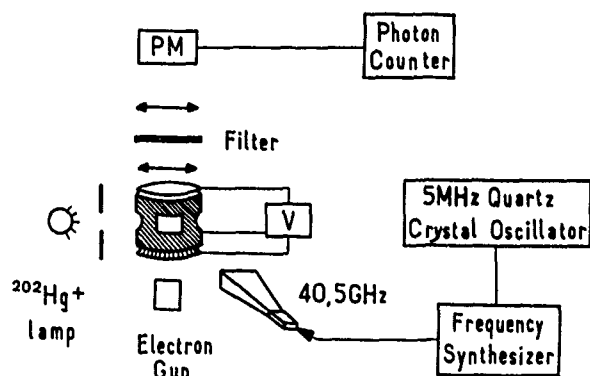


Fig. 2 : Schematic of the experimental set-up.

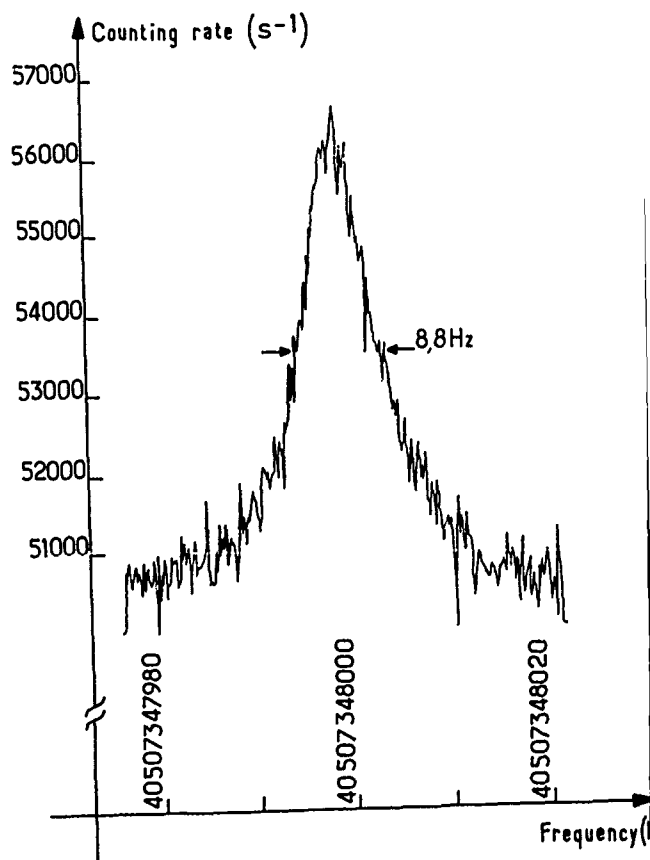


Fig. 4 : Experimental record of a $^{199}\text{Hg}^+$ microwave resonance line.

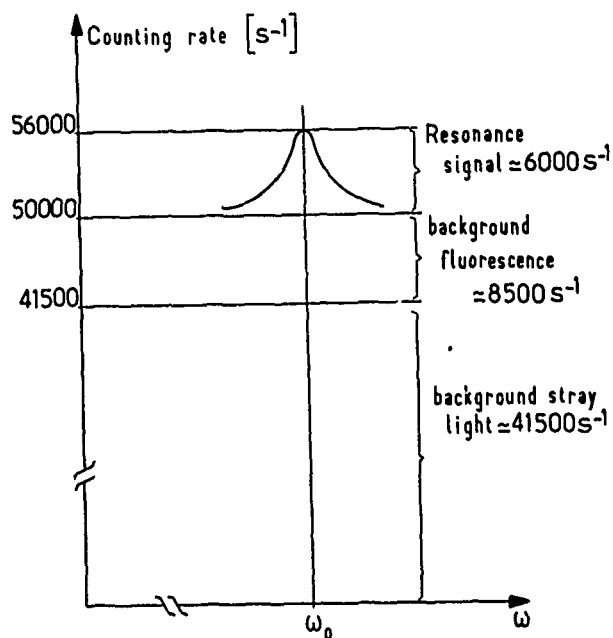


Fig. 5 : Typical values of the background stray light, the background fluorescence and the resonance curve height.

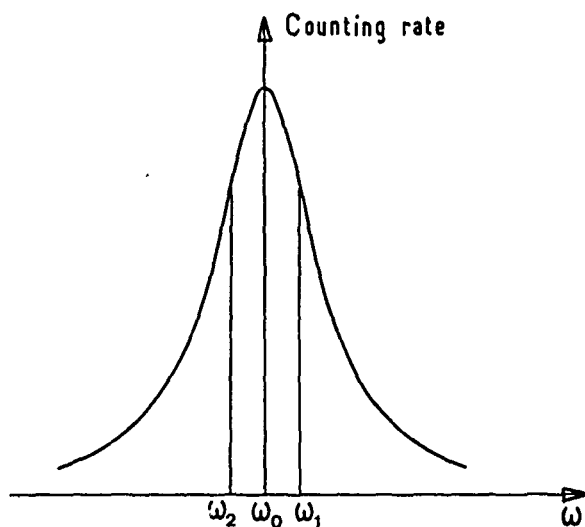


Fig. 7 : Frequencies used for the interrogation of the resonance line.

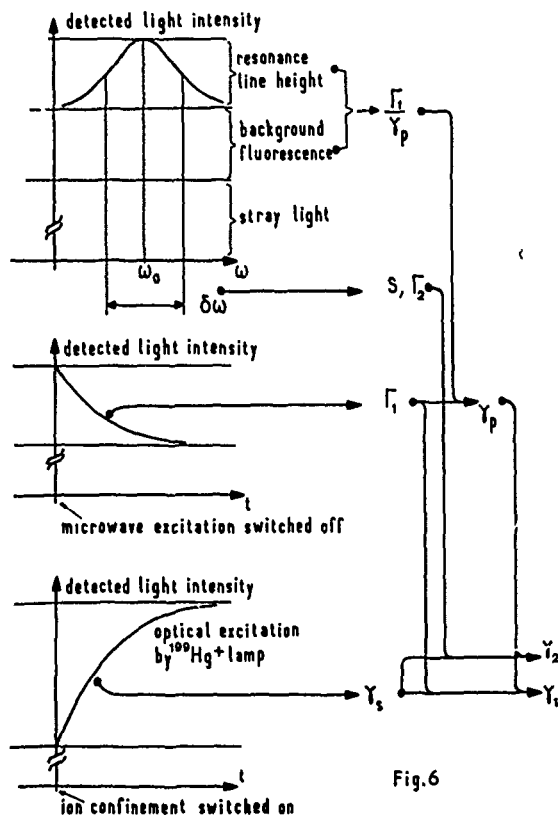


Fig.6

Fig. 6 : Scheme of the different experimental steps for measuring the relaxation time constants of the ions.

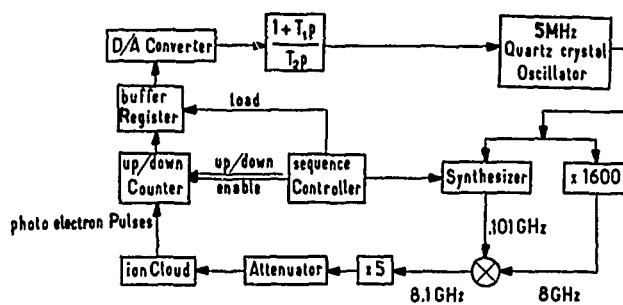


Fig. 8 : Scheme of the digitally based control loop of the 5 MHz oscillator.

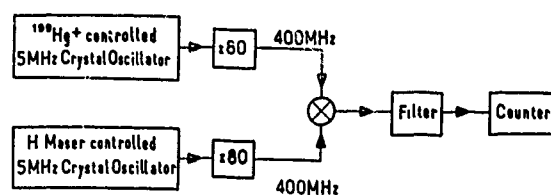
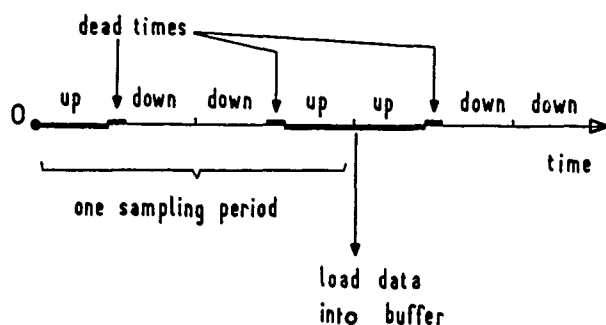


Fig. 10 : Measurement of the $^{199}\text{Hg}^+$ controlled 5 MHz oscillator frequency stability.

Fig. 9 : Counting sequence which eliminates slow drift of the background light intensity.

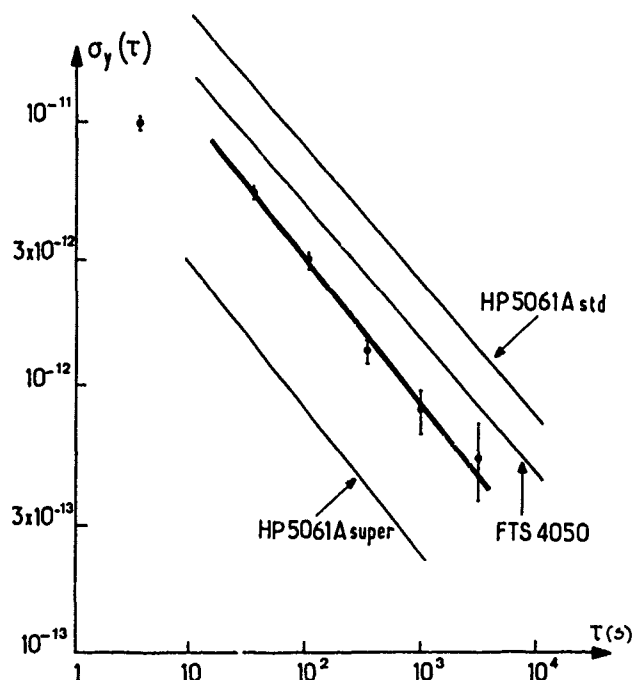


Fig. 11 : Measured fractional frequency stability of the $^{199}\text{Hg}^+$ controlled 5MHz quartz crystal oscillator. Open circles represent experimental points. Error bars are specified. The bold line represents the least-square fit of experimental data. Thin lines show the specified frequency stability of three commercially available Cs beam frequency standards.

NEW HYDROGEN MASER DESIGNS

H. E. Peters

Sigma Tau Standards Corporation
P.O. Box 1877, 1014 Hackberry Lane
Tuscaloosa, Alabama 35403

Summary

Two new atomic hydrogen maser frequency standards have been designed at Sigma Tau Standards Corporation which incorporate significant improvements over older designs, and which should enhance the future utility and practical applicability of these standards.

The first of these standards, the "Small Hydrogen Maser," is based upon a new approach to cavity resonator and storage bulb assembly design which provides a factor of two or more reduction in linear dimensions, and a factor of eight or more reduction in weight and volume over older designs.¹ This new approach to a reasonably price hydrogen maser is being supported by the United States Air Force² and the first breadboard test maser using the new principle is presently under construction. Features of this new design, as well as laboratory results will be presented in this paper.

The second hydrogen maser design has been undertaken with the support of the United States National Bureau of Standards.³ This maser is conventional in principle, but incorporates several improvements in subsystems such as the vacuum system, state selector, temperature control, receiver electronics, and instrumentation. The most significant new feature is in the construction of the cavity resonator. The new maser incorporates a dielectric (fused silica) cavity cylinder within an aluminum outer cavity which is itself well isolated and under exceptionally good temperature control. Thus transient effects, thermal gradients, and pulling due to RF leakage are minimized.

Key words (for information retrieval)
Frequency Standard, Hydrogen Maser, Maser Standard.

Introduction

Atomic hydrogen masers of all designs, sizes, shapes have certain basic features in common, and advances in design technique usually apply generally. The present paper will be concerned only with active oscillator hydrogen masers, and emphasize in particular those features which are novel.

The only fundamental differences in the two designs to be presented is in the storage bulb and cavity configuration. But to enhance the basic size advantage of the first design, the "Small Hydrogen Maser" (SHM), a significant effort has been made to miniaturize and optimize subsystems such as hydrogen supply, source, and state selection, in addition to the primary goal which was to demonstrate a new approach to realization of a small storage bulb and resonator structure. Thus most of the new design features described herein were associated with the small hydrogen maser development.

The Small Hydrogen Maser

The basic principles upon which the small hydrogen maser is based were presented two years ago at the 32nd Annual Frequency Control Symposium.¹ The most important design criteria considered for this new maser, in order of precedence were: 1. Long term stability - no degradation of performance in relation to the best conventional hydrogen masers; 2. Short and medium term stability of 1×10^{-14} (100 seconds) and less than 1×10^{-14} (1,000 seconds) over the normal variations of environment and power supply; 3. Size 10 inches diameter by 20 inches long, exclusive of pump and controls; 4. Weight 50 pounds maximum; 6. Power required 50 watts maximum.

Figure 1 is a generalized drawing of the small hydrogen maser which identifies the main parts. Figure 2 is a photograph of the lower assembly showing the hydrogen supply system, source dissociator, and excitation circuit. Figure 3 is a picture of the vacuum enclosure just after welding and leak checking, and shows the disposition of the external vacuum pump. An 8 liter per second pump is illustrated, however a 20 liter per second pump is being used on the first maser breadboard test assembly to facilitate various operational tests and evaluations. Figure 4 shows most of the mechanical parts just prior to assembly.

Storage Bulb Resonator

The most important part of the small hydrogen maser concept is the atom storage bulb and resonator structure, seen in Figures 1 and 4. The bulb is fused quartz, two inches diameter by seven inches long, with four copper electrodes attached

to the outer surface; it is coated internally with FEP 120 teflon, and is supported by a pyrex glass tube attached to the outer cavity cylinder bottom. The outer cavity cylinder is made of OFHC copper. The loaded Q of the first unit is 10,000 and it has a filling factor of .70. The temperature sensitivity of frequency of this assembly is $5 \times 10^{-6}/^{\circ}\text{C}$, which is a very significant improvement (a factor of 7) over designs of large masers using aluminum cavities.

Several other bulb and cavity configurations were tested prior to deciding upon the above. Cavity Q's of over 16,000 were obtained with a 3 inch diameter by 7 inch long bulb having 8 electrodes on its surface and mounted in a 6.6 inch diameter by 11 inch long outer cavity. Adequate Q's were also obtained with 2, 3, and 4 electrodes on 2 inch diameter by 7 inch long bulbs in a range of sizes of the outer cylinder. The present design was chosen for first tests as it combines a high filling factor with adequate Q, has a relatively low temperature variation of frequency, and minimizes the magnetic field volume which must be kept homogeneous over the bulb region.

State Selection

A novel state selection system has been designed for tests in this maser. It uses two miniature quadrupole magnet focusers in series, with a low field shielded region between where the magnetic field reverses direction. Both the two upper hyperfine states are focused upon passage from the source through the first state selector, but the reversal of field between focusers changes the (1, 1) state to a (1, -1) state, i.e. the magnetic moment changes sign in relation to the field; thus only (1, 0) state atoms are focused upon passage through the second state selector, and pass into the storage bulb.

With the above system the maser will oscillate with up to a factor of 2 lower cavity Q and/or one may use much longer storage times. Thus cavity pulling will be reduced, and the design safety factor for operation under adverse conditions is improved. One of the new state selectors can be seen next to the storage bulb assembly in Figure 4.

Hydrogen Supply and Source

to minimize the size and weight of the hydrogen supply, a new hydrogen supply system has been designed and constructed. It consists of a small storage bottle using a metal hydride absorber followed by a palladium silver purifier and control valve and thermistor pirani gauge. An electronic servo stabilizes the pressure in the source dissociator bulb. The storage bottle is seen in Figures 2 and 4. The sealed off bottle contains 2.62 grams of hydrogen absorbed in 200 grams of LaNiAl metal, which is sufficient for over 50 years of maser operation. The hydrogen may be easily replenished when required. Also in Figure 2 the palladium purifier (in black silicone

rubber thermal insulation) and pirani gauge assembly may be seen, as well as the pyrex glass source dissociator and excitation circuit.

Magnetic Shields

Four concentric cylindrical magnetic shields are used, these may be seen in Figure 4. Two of these are within the vacuum enclosure, and two are outside. The shielding factor of this configuration is calculated as 1×10^6 , and so the small hydrogen maser should be relatively insensitive to external field variations.

The Full Size Hydrogen Maser

The technology of atomic hydrogen masers in the full size format is relatively mature, with a developmental history of approximately 20 years. However most units in use in the field are of older designs which do not represent the latest state of knowledge; and due to the disadvantages of cost, size, and weight there have been no recent units developed which are commercially available. Yet for many purposes in time and frequency standards work the hydrogen maser would be invaluable. As a first step in a program with the ultimate goal of acquiring state of the art hydrogen maser standards, the United States National Bureau of Standards³ contracted with Sigma Tau Standards Corporation to provide design drawings and circuitry for a hydrogen maser frequency and time standard representative of the latest technical knowledge. This work is now complete.

The full size Hydrogen Maser has the following anticipated characteristics and design goals:

Stability maximums, short term 1×10^{-13}
1 second varying as T^{-1} , long term
 2×10^{-15} at 1 day.

Settability, by direct digital synthesis with
a range of $\pm 5 \times 10^{-7}$, resolution $\pm 3 \times 10^{-15}$.

Reproducibility, $\pm 2 \times 10^{-13}$.

Accuracy $\pm 2 \times 10^{-12} \pm$ IAT error.

Automatic cavity tuning capability.

Magnetic Field sensitivity, $\pm 1 \times 10^{-14}$ for
 ± 1 Gauss Ambient.

Other environmental factors no worse than
 $\pm 1 \times 10^{-14}$ for normal laboratory variations.

Power input 115/220 VAC 100W, 22-30VDC
70W, with facility for uninterrupted power
and automatic charging of internal or
external batteries.

Controls, full instrumentation with multiplexed
external monitoring capability and multifunc-
tion alarms.

Some other design characteristics of interest are, bulb size 5.4 liter volume, design line Q 3×10^9 or higher, cavity Q 4×10^6 , filling factor .50, oscillator power output 2×10^{-13} watts minimum, 3 level cavity thermal control system, cavity fused silica with copper metalization within an aluminum external cavity. The maser has a dual vacuum system so that the storage bulb is pumped separately for maximum elimination of background gasses. Both pumps are replaceable without breaking the main vacuum seals. The overall dimensions are 45 inches high by 19 inches square.

Aluminum vs Dielectric Cavity Construction

One of the most important features, which departs from the design practice of other masers constructed by the writer, is the composite dielectric - metal cavity design. This deserves a short discussion.

In the operational history of hydrogen masers using aluminum cavities over many years,⁴ the thermal drift data for the temperature control system has become well known because these masers used cavity auto-tuners and data on cavity frequency corrections were most usually recorded. Typically the daily linear drift corrections were about 1×10^{-14} or less as referred to the maser output frequency. From this the equivalent thermal control system drift is calculated to be of the order of 3×10^{-5} °C per day or less. Since aluminum has a thermal expansion coefficient of about 2.5×10^{-5} per °C at the cavity temperature, one might expect that masers using a lower expansion coefficient material, such as fused silica, for the cavity would have a much lower drift. For example, a cavity related daily drift of only 2×10^{-16} might be expected.

In practice, masers using low expansion dielectric materials for the cavity have not performed significantly better than those using aluminum. Consideration of inherent material stability properties would lead one to suppose that proper design of a maser using a low expansion dielectric material for the cavity, in conjunction with the good thermal regulation systems used with the metal cavity masers, would lead to an order of magnitude or better long term drift performance. Such a design has been incorporated in the new large hydrogen maser.

Large Maser Cavity Assembly Design

Figure 5 is a drawing showing the essentials of the cavity assembly used in the new large hydrogen maser. There is a large quartz storage bulb supported within a fused silica cylinder which has copper metallization internally. This cylinder is supported within an outer aluminum cavity structure thermodynamically similar to that used on good aluminum cavity masers in the past. Temperature control is used to fine tune the frequency of this composite cavity, but due to the silica "liner" the sensitivity is approximately 3 KHz per °C, instead of 35 KHz per °C for aluminum. Other factors, such as lower coupling,

better thermal shielding, and improved sensors have also been incorporated into this design; therefore improved long term stability performance is anticipated.

Relative Merits - Large vs Small Maser

The most significant advantage of the large hydrogen maser over the small one relates to the storage bulb size. The maser wall shift, as well as the maximum line Q achievable, depends explicitly upon the surface area to volume ratio of the bulb. This reduces, for similarly shaped bulbs, to a variation with the inverse diameter. Thus the large maser, with a 5.4 inch diameter bulb, will have a wall shift about 2.7 times smaller than that of a small maser with a 2 inch diameter bulb, and the large maser will have a similarly better line Q. Thus for very long term stability on an auto-tuned maser, for reproducibility and accuracy as required by basic frequency and time standards laboratories, the large maser has a significant advantage.

In most other respects the small hydrogen maser has the advantage. Oscillation level and power output are not significantly different. Thus the SHM should exhibit the excellent stability characteristics inherent in hydrogen masers. Magnetic shielding is easier in the small hydrogen maser, less power is required for thermal control, it is smaller and weighs less. Last but not least, the SHM physical structure is an order of magnitude less expensive than that of the large maser. Since the electronics required for the hydrogen maser are not any more extensive, or as complicated, as those required for other types of atomic frequency standard such as cesium or rubidium, the SHM may easily become very competitive in cost in the future, while providing much better stability performance than other standards.

References

1. Harry E. Peters, "Small, Very Small, and Extremely Small Hydrogen Masers," Proceedings, 32nd Annual Symposium on Frequency Control, US Army Electronics Command, Fort Monmouth, N. J. (1978).
2. USAF, Deputy For Electronic Technology, Air Force Systems Command, Hanscom AFB, Massachusetts.
3. U. S. Department of Commerce, National Bureau of Standards, Boulder, Colorado.
4. V. S. Reinhardt et al., "NASA Atomic Hydrogen Standards Program - An Update," Proceedings, 30th Annual Symposium on Frequency Control, US Army Electronics Command, Ft Monmouth, N. J. (1976).

References 1. and 4. are available from The Electronic Industries Association, 2001 Eye Street, N. W., Washington, D. C. 20006.

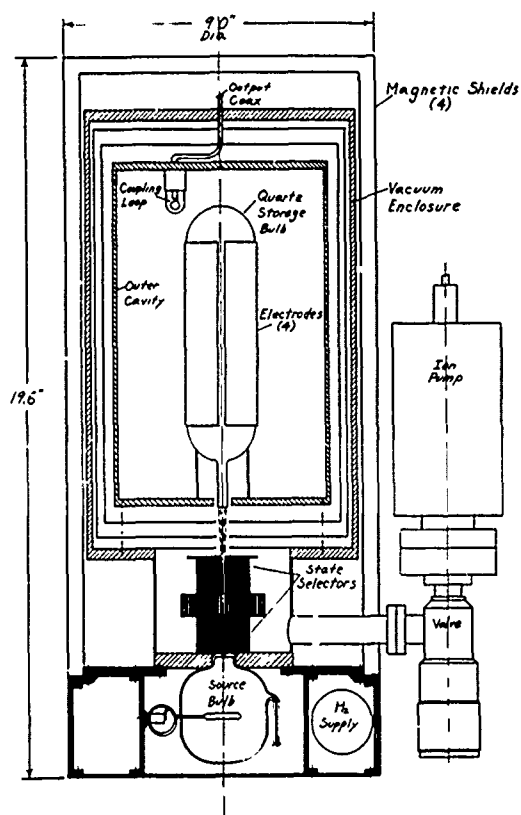


Figure 1.
Small Hydrogen Maser Basic Structure

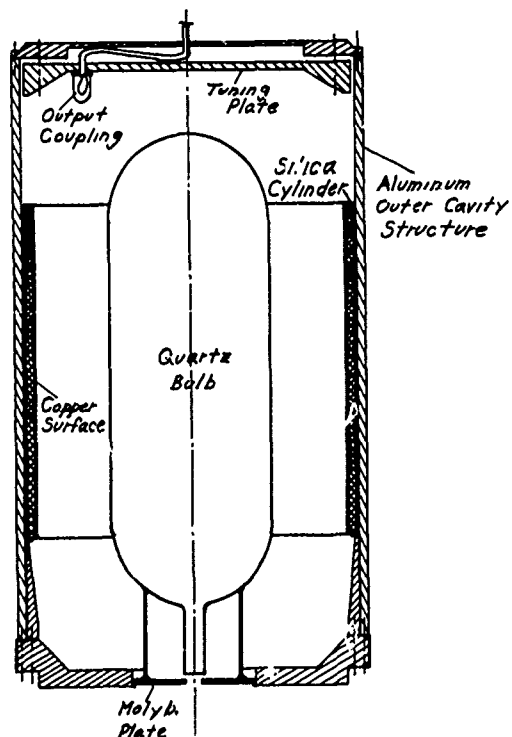


Figure 5.
Full Size Hydrogen Maser Cavity Structure

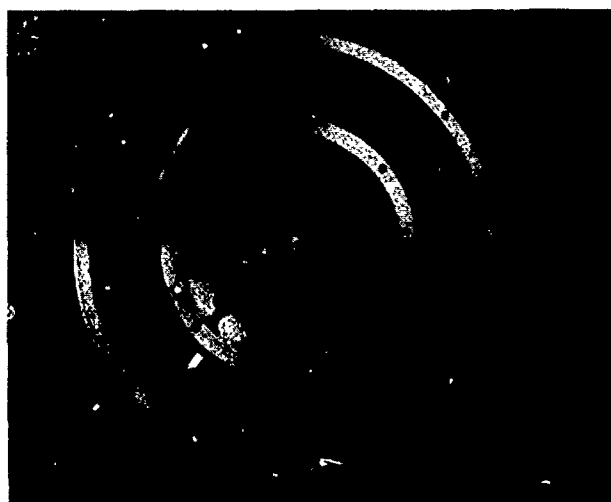


Figure 2.
Small Hydrogen Maser Lower Assembly

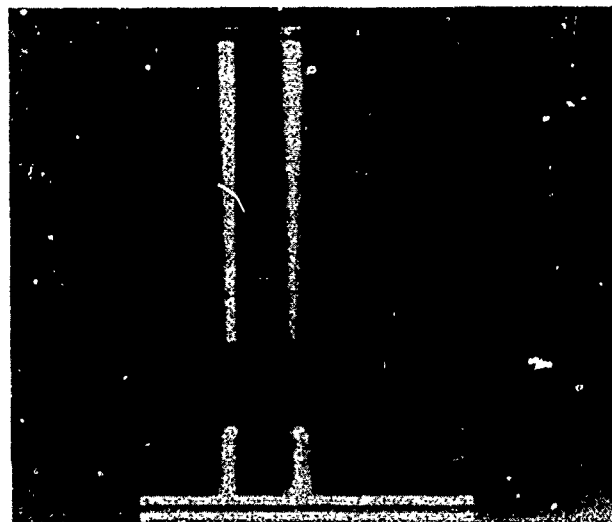


Figure 3.
Small Hydrogen Maser Vacuum Enclosure and Ion Pump



Figure 4.
Small Hydrogen Maser Parts

AN OSCILLATING COMPACT HYDROGEN MASER^{*}

Harry T.M. Wang

Hughes Research Laboratories
Malibu, CA 90265

Summary

An oscillating compact hydrogen maser is described. The maser employs a versatile, compact microwave cavity design, resulting in significant size and weight reductions compared to a conventional hydrogen maser. The Q of the compact cavity is electronically enhanced to enable sustained maser oscillation, thus improving the signal-to-noise ratio and allowing relatively simple signal processing electronics to be used. The long-term stability of the maser is improved by a cavity frequency stabilization servo system; this system employs a reference derived from the atom transition frequency. Preliminary test results indicate a root Allan variance of better than 8 parts in 10^{15} for an averaging time of 10^4 sec. The data also indicate that stability will continue to improve with averaging time.

Introduction

The development of compact hydrogen masers has been stimulated by a desire to utilize the excellent stability and accuracy of the conventional hydrogen maser in applications where there are severe size and weight constraints. Walls and Hellwig¹ have shown that the long-term stability of a maser frequency standard could be improved using a low- Q cavity and operating the maser as a frequency-sensitive amplifier (passive mode). This approach removes the necessity of a bulky high- Q cavity since the oscillation condition does not have to be met. Consequently, several compact cavity designs² and atom interrogation techniques^{3,4,5} have been proposed and tested. However, due to the relatively low Q of the compact cavities, there is a sacrifice in the signal-to-noise ratio and a more complex signal-processing system must be used.

An alternate approach is to electronically enhance the Q of the compact cavity to produce sustained maser oscillation. This improves the signal-to-noise ratio and the atoms detect the center of the resonant line since maser oscillation is sustained at a frequency where the gain of the system is a maximum. Thus, simpler signal-processing circuitry similar to that of a conventional maser could be used. Furthermore, the unique self-diagnostic feature of an active maser — the spin-exchange tuning process — is retained. On the

other hand, due to the higher effective cavity Q , the output frequency of an oscillating maser is more susceptible to cavity drift pulling. However, since all compact cavity designs are sensitive to thermal variations, a cavity frequency stabilization servo system is mandatory to assure long-term stability performance regardless of whether an active or passive approach is adopted. For that matter, the long-term performance of a conventional maser could be improved by the cavity stabilization servo system described below.

In this paper, we describe a compact hydrogen maser where sustained maser oscillation is obtained using a cavity Q -enhancement technique. The fabrication of and preliminary test results from the maser operating with a cavity-stabilization servo system that employs a reference derived from the atomic transition frequency are discussed.

Q-Enhanced Maser Oscillator

The principle of operation of a Q -enhanced maser oscillator is shown schematically in Figure 1. As in a conventional maser, a state-selected beam of hydrogen atoms is focused into a storage bulb placed inside a compact microwave cavity tuned to the hyperfine transition frequency of ground-state hydrogen atoms. The interaction of the atoms with the cavity electromagnetic field causes the atoms to radiate. The losses in the compact cavity are such that the maser oscillation condition is difficult to satisfy. This limitation is overcome by positive feedback, as shown in Figure 1. A portion of the externally amplified maser output is fed back into the cavity. The attenuator in the feedback loop determines the amount of feedback, while the phase shifter adjusts propagation delays to ensure that the feedback signal is in phase with the electromagnetic field in the cavity. Thus, the cavity losses are effectively reduced or cavity Q -enhanced and sustained maser oscillation can be obtained.

The interaction of the atoms with the cavity electromagnetic field $H(r)$ in the presence of relaxation processes is described by the density matrix rate equations.³ To account for the effect of feedback, the electromagnetic field inside the cavity of quality factor Q and resonating at frequency ω_c can be represented by a solution of the differential equation

$$\ddot{H}(t) + \frac{\omega_c}{Q} \dot{H}(t) + \omega_c^2 H(t) = \alpha \ddot{\rho}_{24} - \frac{\omega_c^2}{Q} H_f(t) \quad (1)$$

where the first and second terms on the right side of the equation are due, respectively, to the radiating atoms and the feedback contribution to the field intensity, $H_f(t)$. Notice that the feedback is written in this way to avoid introducing cavity-coupling coefficients. The constant α relates the induced field to the oscillating moment, which is proportional to the off-diagonal density matrix element ρ_{24} as defined in Ref. 3.

The coupled differential equations describing the time evolution of the density matrix elements and the cavity electromagnetic field are nonlinear and exact solutions cannot be found. However, a good approximate description of the operation of the Q-enhanced maser oscillator is given by a linearized solution. To this first-order approximation, it can be shown that the phase shift θ between the cavity rf field and the oscillating atomic moment (in addition to the normal quadrature relationship) is given by

$$\tan \theta = \frac{\frac{2Q}{\omega_c} (\omega_c - \omega) - \epsilon \sin \phi}{1 - \epsilon \cos \phi}, \quad (2)$$

where $\epsilon = |H_f|/|H|$ is the fractional contribution of feedback to the cavity rf field intensity, and ϕ is the feedback delay. The maser oscillation frequency is given by

$$\omega - \omega_c \approx \left[\frac{2Q^1}{\omega_c} (\omega_c - \omega) - \frac{m^1 \lambda}{4\sigma} - \frac{\epsilon \sin \phi}{1 - \epsilon \cos \phi} \right] \frac{1}{T_2}, \quad (3)$$

where Q^1 is the effective cavity Q, defined by

$$Q^1 = \frac{Q}{1 - \epsilon \cos \phi}. \quad (4)$$

The spin exchange shift contribution to the maser oscillation frequency is given by the second term inside the brackets of Eq. 3; $m^1 = mQ/Q^1$ is a geometrical constant (m is defined in Ref. 3), λ is the spin exchange shift parameter, σ is the spin exchange cross-section, and $1/\pi T_2$ is the atomic transition linewidth. When the feedback is in phase (i.e., $\phi = 0$), Eqs. 2 and 3 are identical to the expressions for a conventional maser. As shown in Eq. 4, the effective cavity Q is a maximum when $\phi = 0$, and this condition is automatically satisfied in a Q-enhanced maser oscillator. Thus, the self-diagnostic feature of spin-exchange tuning is retained in a Q-enhanced maser oscillator.

Cavity Stabilization Technique

The cavity in a Q-enhanced oscillator is not an isolated component as in a conventional maser. The cavity resonance frequency is sensitive to phase shift in the feedback loop. In fact, the

cavity and the feedback loop form a resonant system that is susceptible to environmental perturbations. It is therefore essential to have a cavity frequency stabilization servo system.

The cavity servo employs a voltage-biased varactor reactance tuner for cavity frequency adjustment and takes advantage of the fact that the atomic line Q is about 5 orders of magnitude higher than the cavity Q. As shown in Figure 2, if the desired cavity frequency is f_0 , then two test signals of equal amplitude at frequencies f_1 and f_2 symmetrically situated with respect to f_0 and at half-power points of the cavity response will be alternately injected into the cavity by square wave modulating the test signal source. If the cavity response is represented by the solid curve in Figure 2, then the rectified test signals have the same amplitude and there would be no error signal at the modulating frequency. On the other hand, if the cavity has drifted so that the response is represented by the dotted curve, cavity transmissions at frequencies f_1 and f_2 are quite different. The rectified test signals produce a square wave at the modulating frequency. This error signal is synchronously detected and additional gain is provided by a smoothing integrator, the output of which is used to bias the varactor reactance tuner so that the cavity response is slewed back to the desired solid curve.

Notice that the use of discrete test signals f_1 and f_2 situated thousands of transition linewidths away from the atom transition frequency minimizes interference with the atom radiation process. Furthermore, to assure long-term cavity stability, the test signals are phase locked to the output of the frequency standard, and hence to the atom resonance frequency. Thus, the servo system is inherently superior to any cavity stabilization scheme based on thermal and/or mechanical designs.

A functional block diagram of the oscillating compact hydrogen maser signal-processing system is shown in Figure 3. The cavity Q enhancement and frequency stabilization servo are located, respectively, in the central portion and in the left side of the diagram. The front end microwave electronics is common to both systems. After the first conversion, the signal is divided into two channels by a power divider. In one channel, a narrow crystal band pass filter (BW = 4 kHz) passes maser oscillation signal to the clock signal processing circuits; in the other channel, the signals are rectified and synchronously detected for the cavity stabilization servo system. To minimize interference with the radiating atoms due to switching sidebands that might be generated, the test signal synthesizer is switched to generate alternately the two test frequencies at a relatively low rate of 10 Hz. The spacing of the frequencies f_1 and f_2 is selected to be 30 kHz since strong maser oscillation could be obtained with an enhanced cavity width of that magnitude.

Compact Maser Fabrication

A schematic of the physics unit of the oscillating compact hydrogen maser is shown in Figure 4.

The source of the state-selected atomic hydrogen beam (consisting of an rf dissociator and a hexapole magnet) is fabricated using a conventional design. For flux modulation in spin exchange tuning of the maser, a bistable, magnetically latched beam shuttle is used to create about a 30% flux differential. The beam shuttle is compact and light and consumes power only during switching from one state to the other (40 mA at 5 V for about 1 msec). More importantly, it allows the source to operate at fixed parameters of pressure and rf drive level. This mode of operation is desirable for long-term source reliability. Vacuum maintenance is provided by a combination of getter and ion pumps. The former has the advantage that, after activation, it would pump hydrogen at room temperature without any power consumption. However, its pumping speed for other contaminants is fairly low. On the other hand, in the clean environment inside a maser, the contaminant outgassing is insignificant unless allowed to accumulate. Thus, the gas load to the ion pump can be throttled down and a correspondingly small ion pump can be employed, resulting in appreciable system size and weight reductions. The vacuum chamber is made of aluminum and is connected to the source manifold by a titanium tube which provides mechanical support with low thermal leakage to the microwave interaction region. The solenoid, which generates a uniform quantization field, is wound on a light-weight fiber-glass form and is equipped with a second-order field gradient correction coil driven from the same current source as the main coil. Magnetic shielding is provided by four layers of concentric cylindrical shields with conical end caps based on a design by Wolf.⁶

The compact cavity and storage bulb design and fabrication has been described elsewhere.² Briefly, the cavity consists of a section of 6 in. O.D. x 1/8 in. wall x 6 in. long clear fused quartz tubing with aluminum end plates. The inner surface of the quartz tubing is plated with high-conductivity silver coating. Input and output coupling loops as well as a varactor reactance tuner are mounted on the bottom aluminum end plate. With symmetrical input-output coupling coefficients of 0.2 each, the loaded cavity Q is about 9400 and the reactance tuning range is adjustable to one full cavity width without significant Q degradation. In practice, the tuning range is limited to about 1/3 of the cavity width to relax the bias voltage stability requirement. The storage bulb, 4 in. O.D. x 4-1/2 in. long, provides mechanical support for the cylindrical loading capacitor. The capacitor consists of four equally spaced electrodes fabricated from 0.02 in. copper shims and attached to the bulb by low-loss epoxy cement. The bulb is coated on the inside with FEP 120 Teflon by standard techniques. The cavity-storage bulb subassembly is mounted inside the aluminum vacuum chamber by pre-loaded polyimide (Vespel) springs that provide longitudinal compression as well as lateral retention. This mechanical design gives both mechanical stability and thermal isolation.

Separate temperature controls are provided at the top, middle, and bottom sections of the vacuum

chamber as well as at the next-to-outer-most layer of the magnetic shields. To minimize dc stray fields, double bifilar heater windings and ac heater currents are used.

Except for the front-end components, the signal-processing electronics is housed in a rack separate from the physics unit. Another thermal control unit is used to regulate the temperature of an aluminum plate on which the front-end microwave electronic components are mounted. These components include the critical feedback loops and the integrator that drives the reactance tuner. The plate is located just below the lower end cap of the outer most magnetic shield. The location is chosen to minimize the length of the transmission line used in maser input-outgoing coupling. An outer aluminum vessel covering the top of the maser physics unit provides additional isolation from ambient thermal variations as well as electromagnetic interference. Although the combination provides only relatively coarse temperature regulation for the electronic components, it significantly reduces thermally induced fluctuations in the system and contributes to improved performance of the cavity Q-enhancement and stabilization servo systems.

Experimental Results

Strong maser oscillation was obtained with an enhanced cavity Q of 35,500 in spite of the fact that a poor bulb coating gives an atomic line Q of only 6×10^8 . (An atomic line Q of 1×10^9 had been measured in a bulb of similar geometry in a separate test bed maser.) Stability performance using a VLG-11 maser (a full size conventional maser) as reference is shown in Figure 5. The data were taken with a measurement bandwidth of 1 Hz without any corrections to the effect of the reference maser. The measured pair stability (root Allan Variance) of 3.5×10^{-15} for an averaging time of 10^4 seconds gives an indication of the excellent performance of the Q-enhanced compact maser oscillator with cavity stabilization. The performance can be expected to improve from better storage bulb coating and the resulting higher line Q as well as from improved receiver noise performance.

Under contractual requirements, the maser was delivered to the Naval Research Laboratory (NRL) in Washington, D.C. for further tests and evaluation. Preliminary test results at NRL are shown in Figure 6.⁷ It should be noted that the data were taken after an initial warm up but without optimizing the operating parameters. The ruggedness of the device is shown by the fact that it withstood well the rigor of transcontinental shipment. The apparent degradation in performance could be attributed to several factors. First, the measurement bandwidth for the data in Figure 6 is 1 kHz versus 1 Hz for those of Figure 5. The noise contribution would be more severe for the larger bandwidth. Second, when the data for Figure 6 were taken, the environment was not very conducive to stability testing due to construction work in the vicinity. Third, maser operating parameters could be

optimized. Nevertheless, data from both pre- and post-delivery testing (Figures 5 and 6, respectively) indicate excellent long-term stability and can be expected to improve with averaging time. In fact, the data give no indication of the flicker floor of the device. This raises an interesting problem in long-term stability testing since the stability of conventional masers starts to degrade significantly beyond about 10^4 sec. Although we believe that the long-term stability of conventional masers can benefit from a cavity-stabilization servo such as discussed here, the existing conventional masers have relied on thermal and/or mechanical designs.

Conclusions

We have shown the viability of the concept of Q-enhancement in atomic frequency standards. Excellent long-term stability of a Q-enhanced maser oscillator equipped with a properly designed cavity stabilization servo has been demonstrated. In conjunction with the versatility of the compact cavity design, the technology of a portable hydrogen frequency standard with excellent performance is ready to be exploited.

Acknowledgment

The design, fabrication, and testing of the oscillating compact hydrogen maser was the cooperative effort of several people. The contributions of Ted Calderone, Roy Hasselquist, Jack Lewis, Adrian Popa, and Joe Schmidt are gratefully acknowledged. I also wish to thank Stu Wolf and Joe White of NRL for providing the magnetic shield design and post-delivery test data, respectively. In addition, useful discussions were held with Dick Abrams, Bill Bridges, and Stu Crampton.

References

- * This work has been supported by the Office of Naval Research under Contract N00014-78-C-0139 administered by the Naval Research Laboratory.
- 1. F.L. Walls and H. Hellwig, "A New Kind of Passively Operating Hydrogen Frequency Standard," Proc. 30th Annual Symposium on Frequency Control, 473, 1976.
- 2. H.T.M. Wang, J.B. Lewis and S.B. Crampton, "Compact Cavity for Hydrogen Frequency Standard," Proc. 33rd Annual Symposium on Frequency Control, 543, 1979.
- 3. H.T.M. Wang, "Hydrogen Frequency Standard Using Free-Induction Technique," Proc. 33rd Annual Symposium on Frequency Control, 536, 1979.
- 4. D.A. Howe, F.L. Walls, H.E. Bell, and H. Hellwig, "A Small Passively Operated Hydrogen Maser," Proc. 33rd Annual Symposium on Frequency Control, 554, 1979.
- 5. G. Busca and H. Brandenberger, "Passive H. Maser," Proc. 33rd Annual Symposium on Frequency Control, 563, 1979.
- 6. S.A. Wolf, Naval Research Laboratory (Private Communication).
- 7. Joe White, Naval Research Laboratory (Private Communication).

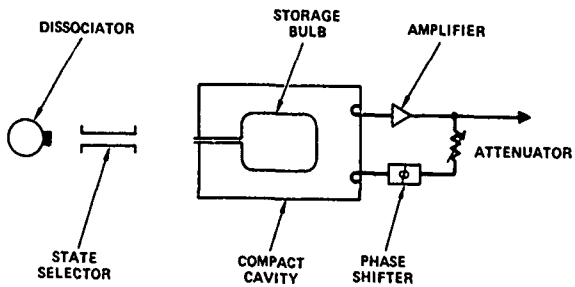


Figure 1. Schematic of a Q-enhanced maser oscillator.

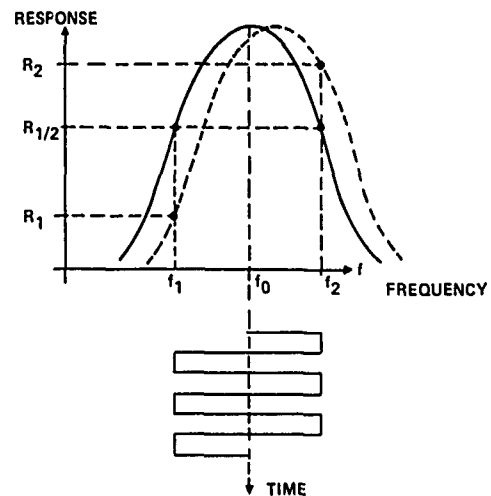


Figure 2. Concept for cavity frequency stabilization servo system.

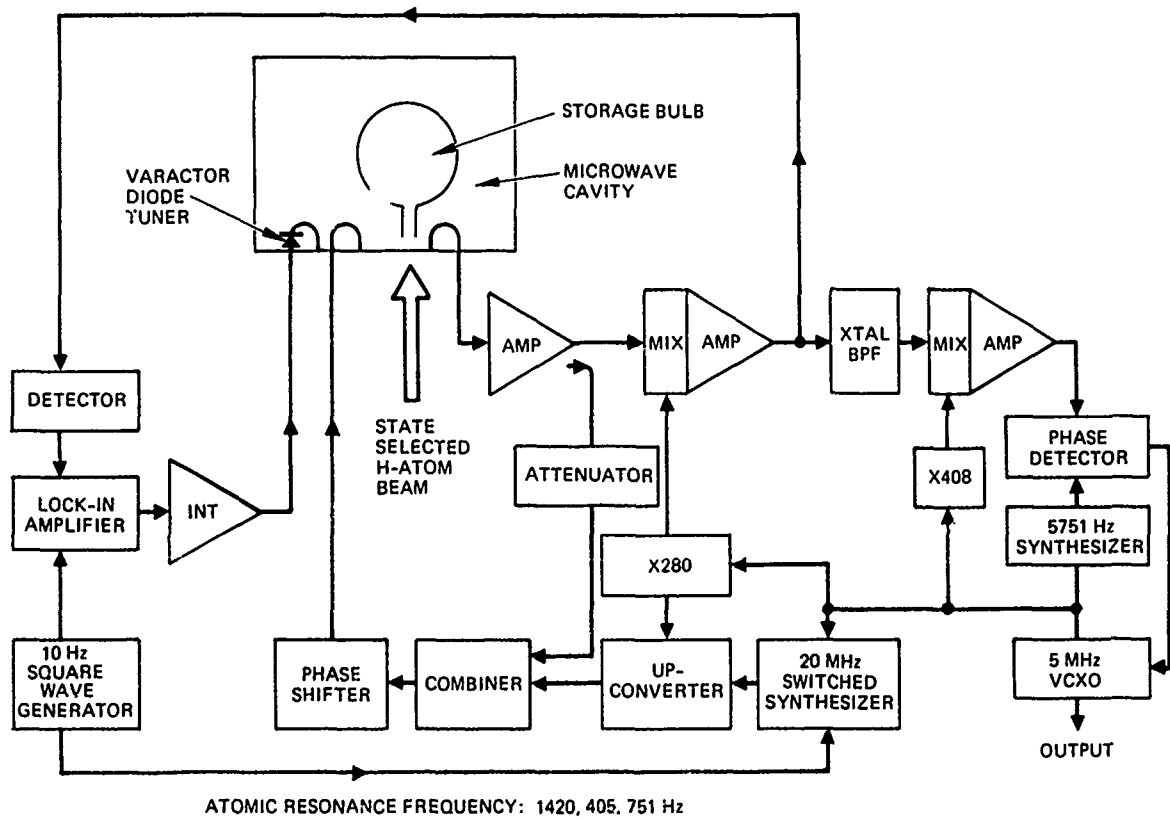


Figure 3. Functional block diagram of Q-enhanced maser oscillator with cavity stabilization servo system.

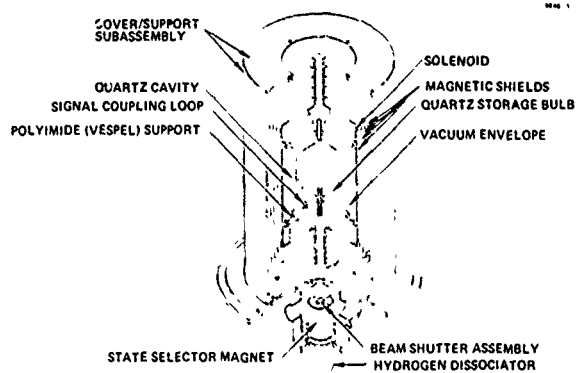


Figure 4. Schematic of the physics unit of the oscillating compact hydrogen maser.

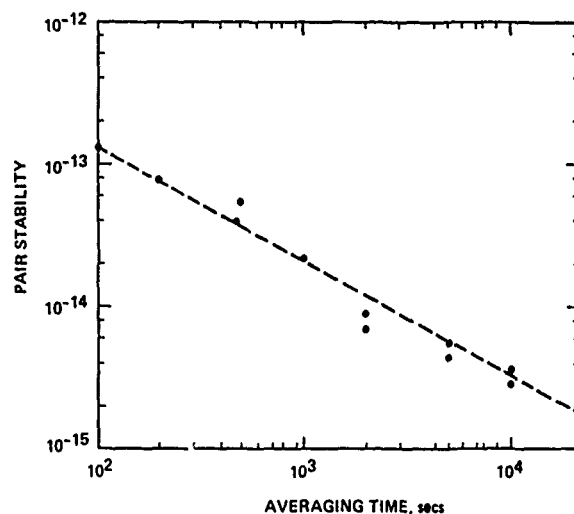


Figure 5. Stability data of oscillating compact hydrogen maser (measurement bandwidth = 1 Hz)

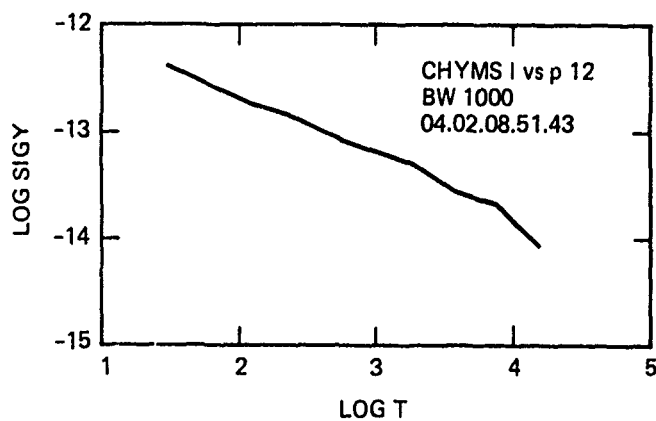


Figure 6. Stability data of oscillating compact hydrogen maser (measurement bandwidth = 1 kHz).

RESULTS OF THE DEVELOPMENT OF THE LIGHT WEIGHT CESIUM STANDARD

Marvin Meirs, Iancu Pascaru and Martin Bloch

Frequency Electronics, Inc.
New Hyde Park, New York 11040

Summary

The paper discusses the test results on the light weight portable military Cesium Beam Frequency Standard. The description and operation of this clock was reported in the 33rd Frequency Control Symposium. The Portable Real Time Clock (PRTC) presently being manufactured by Frequency Electronics, Inc., is used as a precision clock for the communication system on the 616A program and for other applications where a portable cesium standard is needed.

The Cesium Beam Frequency Standard will weigh approximately 35 lbs. and utilizes a cesium tube weighing just 11.5 lbs. The projected life expectancy of this tube is greater than 5 years. The test results on this tube show significant improvements in signal to noise ratio, linewidth, and background noise. Typical figures are 58 db/Hz signal to noise ratio, a factor of six for the signal to background ratio and less than 800 linewidth. The details of design and fabrication of the Cesium Standard are presented as well as test results.

Introduction

The Portable Real Time clock has been designed and fabricated by Frequency Electronics, Inc. for use as a portable aircraft Cesium Standard.

The small size, light weight, good performance and simplicity of maintenance due to its module construction are the main characteristics of this new clock.

The Cesium Standard as presently constructed provides 5 MHz, 3 MHz and 1 MHz frequency outputs as well as 1PPS, 1PPM and time-of-day time code signals. The front panel consists of a real time of day display and monitor circuitry to indicate system performance characteristics. Figure 1 is a photograph of this unit. Shown in Figure 2 is the Portable Real Time Clock alongside the Master Regulating Clock which is the larger 19 inch rack mounted system.

Design

The PRTC was designed to replace the presently manufactured MRC meeting all environmental

and electrical performance characteristics with a significant reduction in size and weight. The PRTC is 5.2 inches high by 13.25 inches wide by 19.5 inches deep. A block diagram of the PRTC is shown in Figure 3.

The 5 MHz OCVCXO is multiplied to 9200 MHz by the multiplier module (X1840). The synthesizer produces a frequency of 7.36822840 which it generates from the 5 MHz oscillator. The difference between these two frequencies is used to feed the cesium beam resonator. The error signal from the cesium resonator is amplified and integrated and used as the control signal for the 5 MHz oscillator, which closes the loop. The 5 MHz signal is then used to generate 1 MHz and 3 MHz outputs as well as to drive the real time-of-day clock and generate the timing outputs.

A top view of the Cesium Standard without its cover is shown in Figure 4 and shows the configuration of many of the modules.

Figure 5 is a bottom view which shows the chassis wiring.

The power supply for the PRTC was designed to minimize power supply ripple and spikes. A block diagram of the power supply is shown in Figure 6. This switching regulator uses pulse width modulation and permits us to generate all of the system required voltages with less than 20 millivolts of spikes and ripple. The efficiency of this power supply is approximately 63 percent.

One of the major design efforts on this program was the redesign of the Cesium Beam tube to reduce both size and weight. The weight was reduced from 21.5 lbs. to 11.5 lbs. and the size was reduced to about 60 percent of the previous volume. Along with this significant reduction in weight and size, performance of the new tube is better than that of the previous one. Figure 7 shows a comparison of the two tubes.

Figure 8 is a photograph of the first light weight tube manufactured.

To date, three tubes have been fabricated and a compilation of the data is shown in Table I.

Performance

The PRTC performance results have, in general, been far better than that required by the specification. Table II shows some of the

TABLE I

TUBE CHARACTERISTICS FOR LIGHT WEIGHT CESIUM RESONATOR

Line Width	< 800 Hz
Signal to Noise	> 58 db/Hz
Signal to Background	> 6
Short Term Stability	1 to 3×10^{-11} $\sqrt{5}$
Weight	11.5 lbs.
Volume	115 cubic inches
Life Expectancy	5 to 7 years

TABLE II

PERFORMANCE RESULTS - PRTC

PARAMETER	SPECIFICATION	ACTUAL
Accuracy	$\pm 3 \times 10^{-11}$	$\pm 1 \times 10^{-11}$
	- 28° C to + 65° C	
Reproducibility	$\pm 1 \times 10^{-11}$	$\pm 0.5 \times 10^{-11}$
Settability	$\pm 2 \times 10^{-12}$	$\pm 1 \times 10^{-12}$
Stability		
Averaging Time (sec.)		
1	7×10^{-11}	3×10^{-11}
10	2.2×10^{-11}	0.95×10^{-11}
100	7×10^{-12}	3×10^{-12}
1,000	2.2×10^{-12}	0.95×10^{-12}
10,000	7×10^{-13}	3×10^{-13}

The frequency stability data for averaging times up to 66,000 seconds has been taken and plotted on Figure 9. Although there has not been sufficient time to take complete stability data, indications are that the stability floor will be below 1×10^{-13} for averaging times in excess of 10^5 seconds.

Figure 10 is a plot of the single sideband phase noise of the 5 MHz output signal with the worst case AT cut crystal. Although this is considerably better than the specification requirement, plans are being made to use an SC cut crystal in the 5 MHz oscillator to even further improve the sideband noise.

The one specification characteristic which will be improved further is the weight. The original design objective was a weight of less than 30 lbs. The actual weight of these prototype units was 38.65 lbs. The breakdown of weight by

TABLE III

WEIGHT ANALYSIS, PRTC

MODULE	WEIGHT (LBS.)		
	DESIGN OBJECTIVE	ACTUAL PROTOTYPE UNITS	ANTICIPATED PRODUCTION UNITS
A0 Chassis	8.0	9.3	8.3
A1 Cesium Beam Tube	11.0	11.5	11.5
A3 Error Signal Controller	1.0	1.0	1.0
A5 Multiplier	0.9	1.25	1.25
A7 Synthesizer	0.7	0.9	0.9
A8 5 MHz OCVCXO	0.8	1.0	1.0
A9 Clock	2.0	0.75	0.75
A10 1 MHz/3MHz Divider	0.3	0.45	0.45
A11 Power Supply	2.0	3.5	2.5
A17 Battery Pack	3.0	4.5	4.5
Front Panel, Covers and Miscellaneous	—	4.5	3.0
Total	29.7	38.65	35.15

module is shown in Table III. As indicated by this table, most of the additional weight is in the power supply, battery and front panel of the unit. Future production units will be manufactured to bring the weight down to approximately 35 lbs.

Table IV is a power analysis of the PRTC by module. The specification requirement of 48 watts was met. However, the actual clock dissipated more power than the original anticipated design objectives. This was primarily due to the additional power dissipation in the power supply. The power supply efficiency was sacrificed in order to obtain low noise and ripple.

Conclusions

A light weight portable cesium clock has been designed which exceeds most of its performance requirements. Performance of this clock with regard to noise and stability is better than that of larger units and no performance or functions have been sacrificed to obtain the smaller size. Further tests are scheduled to obtain more data and qualify the unit to full military airborne environmental conditions.

Acknowledgment

We would like to acknowledge the support of Dr. N. Yannoni of RADC on this program.

TABLE IV
POWER ANALYSIS, PRTC

MODULE	POWER (WATTS)	
	DESIGN OBJECTIVE	ACTUAL PROTOTYPE UNITS
A1 Cesium Beam Tube	10.0	10.0
A3 Error Signal Controller	1.5	1.5
A5 Multiplier	2.5	3.5
A7 Synthesizer	1.0	0.9
A8 5 MHz OCVCXO	1.6	2.5
A9 Clock	4.5	7.0
A11 Power Supply	7.8	16.3
A17 Battery Pack	0.9	2.0
Total	31.3	43.7

Specification = 48 Watts maximum.

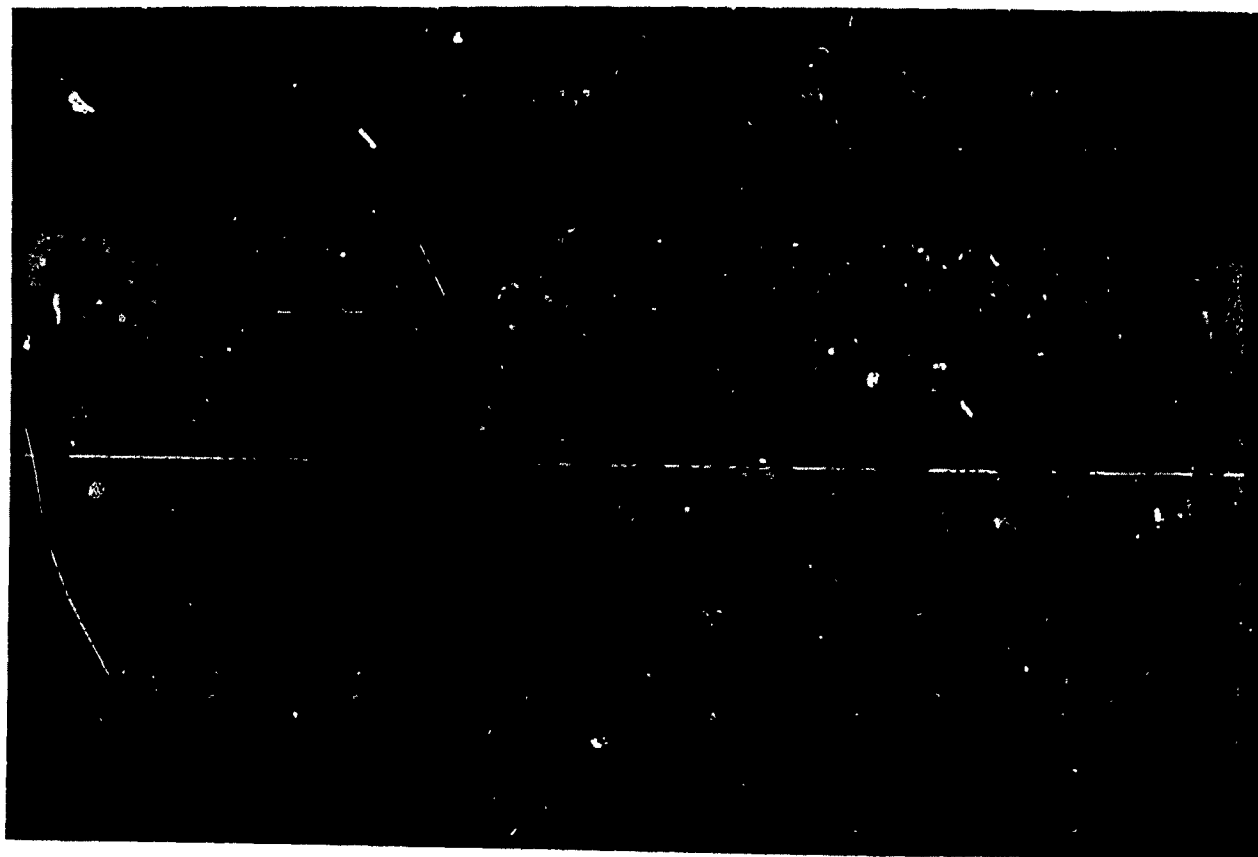


Figure 1. Cesium Beam Primary Frequency Standard,
Model FE-5450A

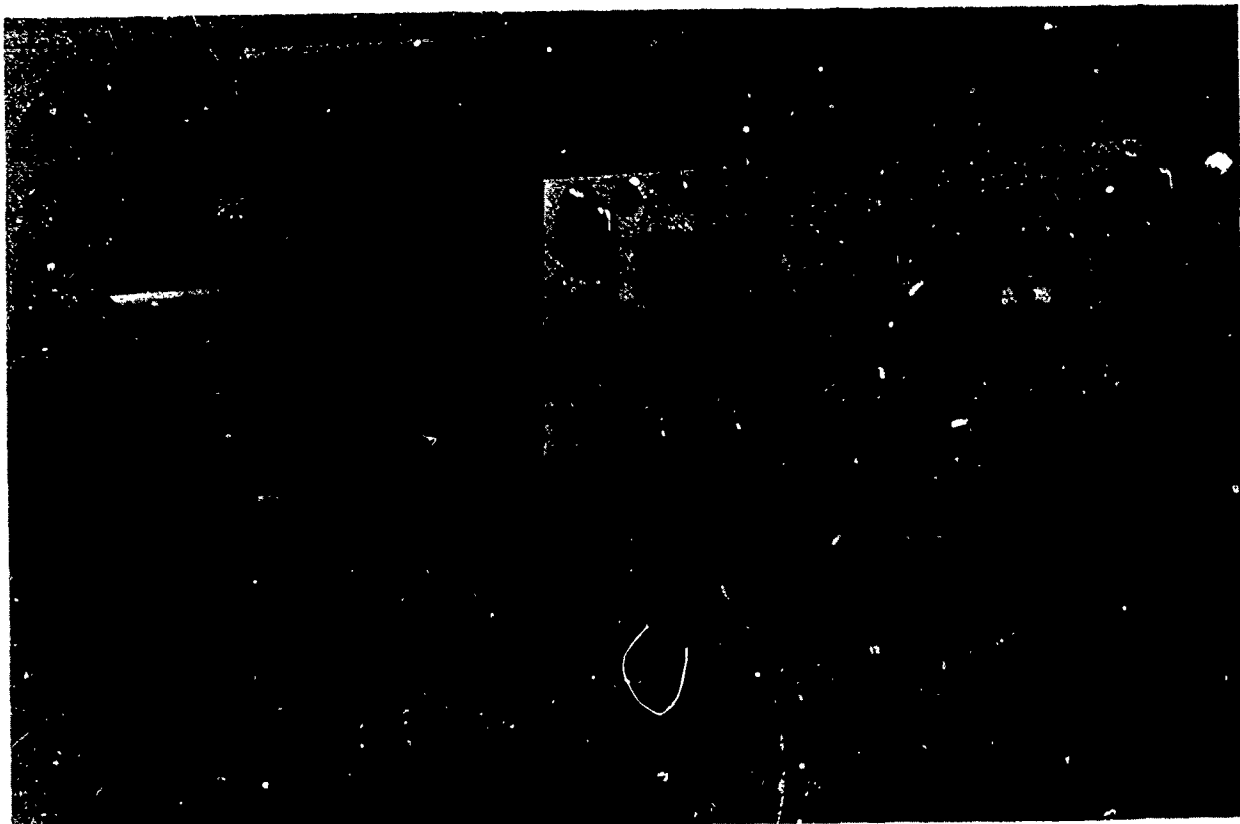


Figure 2. Portable and Rack Mount Cesium Standards

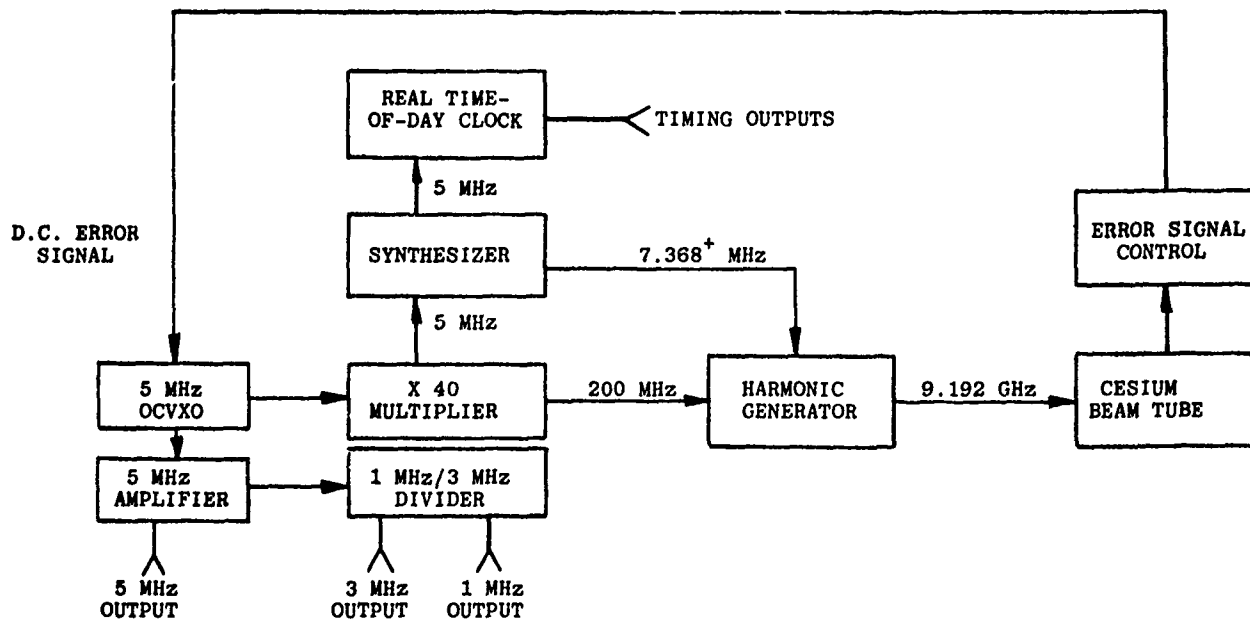


Figure 3. PRTC Block Diagram, Model FE-5450A

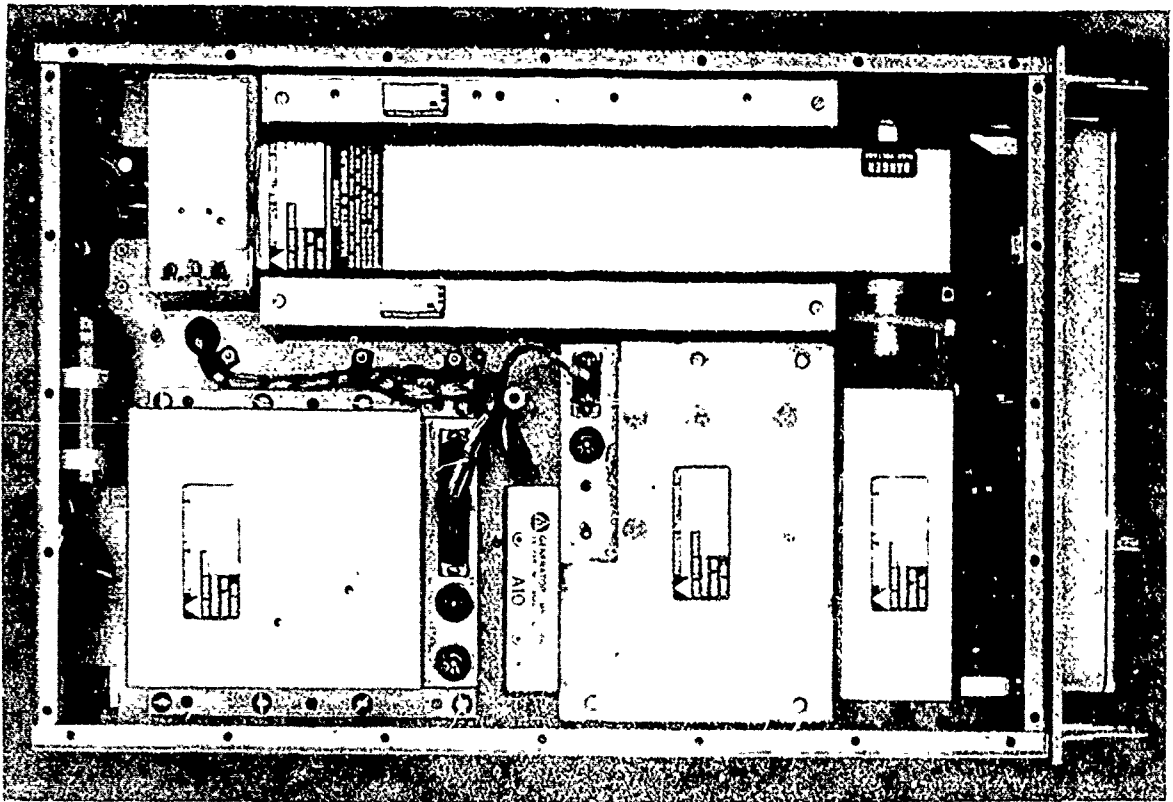


Figure 4. Top View, PRTC

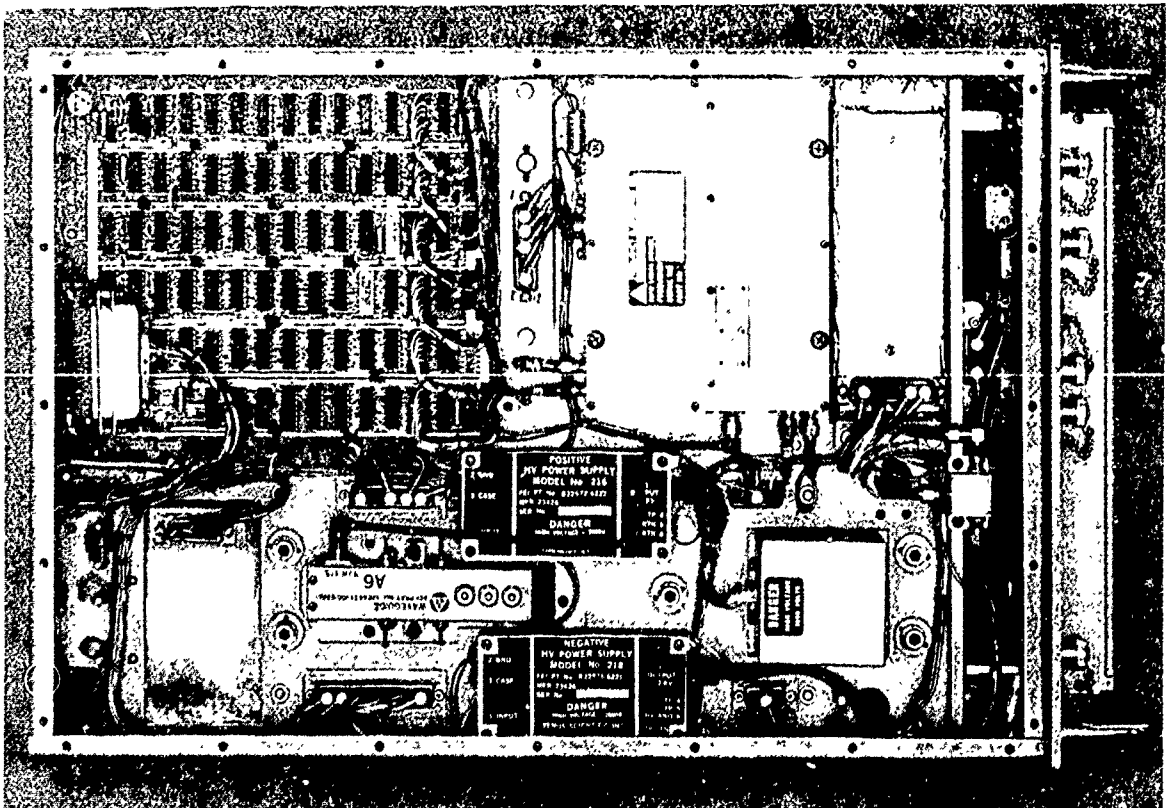


Figure 5. Bottom View, PRTC

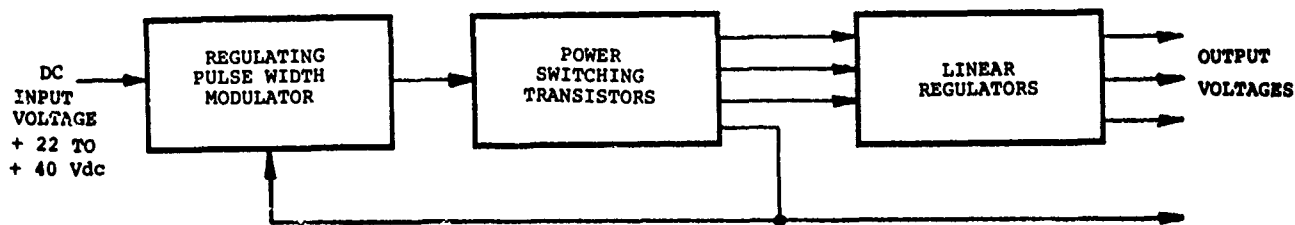


Figure 6. Block Diagram, PRTC Power Supply

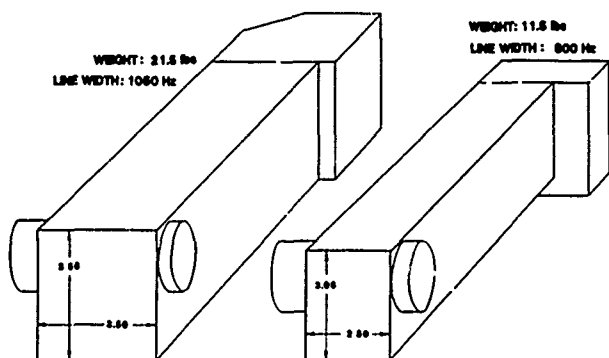


Figure 7. Comparison of Standard Cesium Resonator Vs. Light-Weight Cesium Resonator

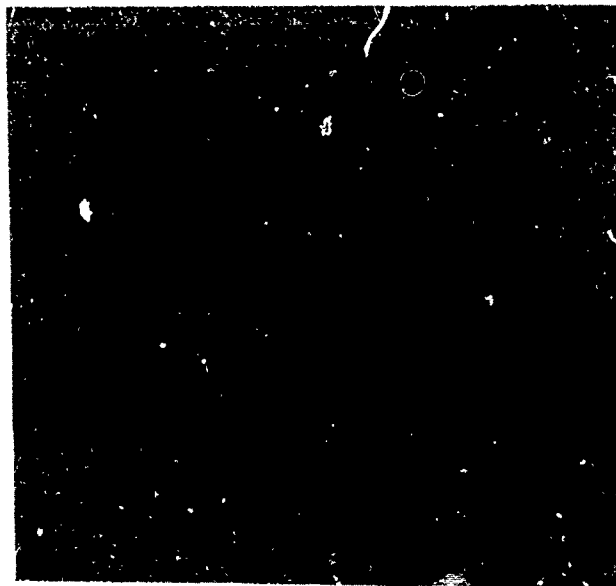


Figure 8. Light Weight Cesium Beam Tube

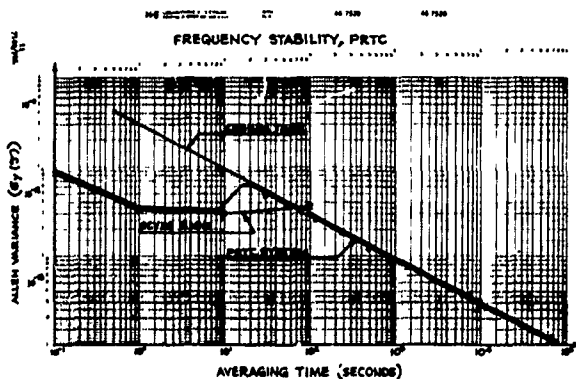


Figure 9. Frequency Stability, PRTC

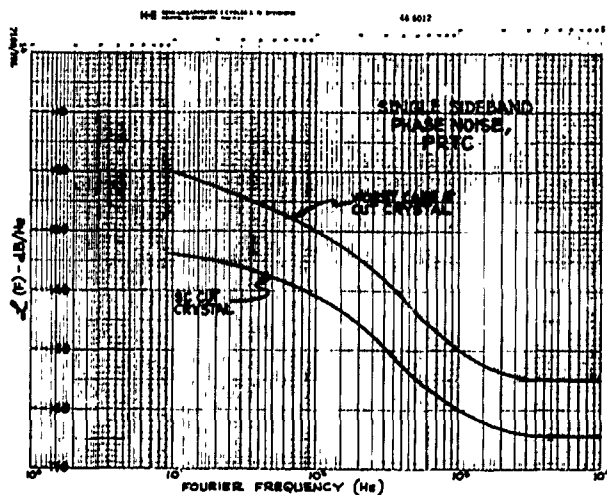


Figure 10. Single Sideband Phase Noise, PRTC

POSSIBLE AVENUES OF IMPROVEMENT OF THE SHORT AND LONG TERM STABILITY
OF OPTICALLY PUMPED PASSIVE RUBIDIUM FREQUENCY STANDARDS

L.G. Bernier, A. Brisson, M. Têtu, J.Y. Savard, J. Vanier

Laboratoire d'Electronique Quantique
Département de Génie Electrique
Université Laval, Québec, CanadaAbstract

The paper describes work done on the Passive Rubidium Frequency Standard in order to identify and possibly improve its frequency stability in the short and long term region. In relation to the short term region, experiments are described which permit the identification of the major sources of noise and measurements are reported. A theoretical model is developed and conclusions are drawn relative to the optimization of the various parameters. In relation to the long term region, earlier work has shown that the power shift created by inhomogeneous broadening in the presence of a buffer gas and light shift could be a cause of instabilities. To avoid that effect we have started experiments on a wall coated cell without buffer gas and we report results on the wall shift and its temperature dependence. Although that type of cell avoids the power shift, it is observed that the temperature dependence of the wall shift is relatively large. These results are discussed in terms of earlier data obtained on rubidium masers.

Introduction

The optically pumped passive rubidium frequency standard [1] is probably one of the atomic standards that has found the most spreaded use in the field. To a small size it associates a good short term frequency stability and a relatively good long term frequency stability [2], [3]. Although, in many cases, the specifications of presently available units are quite satisfactory, the standard could also be used in situations where better stability is required if its actual characteristics could be improved [4]. In particular one may wonder if the actual short term stability presently achieved is at the theoretical limit and if the long term stability could be improved by a change in the actual design of the absorption cell. In practice it is found that the sources of instabilities either in the short term or in the long term region can be separated and studied quite independently. Along these lines of thought, we have started fundamental work on both aspects of the problem and this paper is a report on the theoretical and experimental results we have obtained.

Short term stability

A block diagram of the passive rubidium frequency standard is shown in Figure 1. Figure 2 shows a typical result of short term stability as

obtained with commercial units. The main questions are: "What is the theoretical limit of the short term stability? Is it possible to improve the short term stability by optimizing parameters in the optical package? Is it possible to do so without affecting the long term stability?"

In practice it is found that the short term stability is limited by the presence of a white frequency noise [5]. This gives rise to a short term stability in the time domain given by

$$\sigma^2(\tau) = \frac{1}{2} \frac{h_0}{\tau} \quad (1)$$

where $\sigma^2(\tau)$ is the Allan variance, h_0 is a constant which gives the noise amplitude and τ is the averaging time [6]. The origin of the noise giving rise to this behaviour is shot noise at the photodetector and it gives the fundamental limit to the frequency stability as shown below.

Theoretical calculation of the contribution of shot noise to $\sigma(\tau)$

The model used to make the calculations is illustrated in Figure 3. The important points are as follows.

- The optical package coupled to the lock-in detector produces a signal proportional to the derivative of the resonance line creating a discriminator pattern. The line is assumed Lorentzian.

- The model is linear and the shot noise at the photodetector appears as white noise of spectral density $S_1 = 2 e I_0$, where e is the electronic charge and I_0 is the photocurrent.

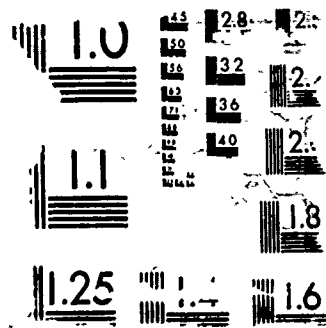
- Finally it is assumed that the frequency of modulation and the depth of modulation are much less than the absorption line width.

The complete calculation is given in Appendix A and the main results are as follows.

The slope of the discriminator pattern near the center of the resonance line is given by

$$\frac{1(v)}{dv} = \frac{8e}{\Delta v^2} \alpha I_0 \quad (2)$$

where $1(v)$ is the modulation current peak amplitude at the photodetector, I_0 is the photocurrent, α is the fractional absorption depth, Δv is the full line width at half the height, $2e$ is the peak to peak amplitude of modulation of the interrogating r.f. signal. These parameters are illustrated in Figure 4.



The signal at the maximum of the discriminator pattern is given by

$$i_0 = \frac{9\epsilon\alpha I_0}{4\sqrt{3}\Delta\nu} \quad (3)$$

It is shown in the Appendix that the spectral density of the fractional frequency fluctuations are given by

$$S_y(f) = \frac{3^3}{2^{10}Q_L^2(S/N)^2} \quad (4)$$

In the time domain this corresponds to a stability expressed by

$$\sigma(\tau) = \frac{0.11}{Q_L(S/N)} \frac{1}{\tau^{\frac{1}{2}}} \quad (5)$$

Here, Q_L is the line Q, defined as

$$Q_L = \frac{\nu_0}{\Delta\nu} \quad (6)$$

and (S/N) is the signal to noise ratio. Within the limit of shot noise as mentioned above, the signal to noise ratio is given by

$$\left(\frac{S}{N}\right)^2 = \frac{3^3\epsilon^2\alpha^2 I_0}{2^6\Delta\nu^2 e} \quad (7)$$

From this expression and equation [5] it is seen that for good short term stability, the detector must detect as much as possible of the transmitted light flux creating optical pumping and the photocurrent I_0 . The absorption factor α is constant up to a certain value of I_0 where it saturates; it also depends on the width $\Delta\nu$. Consequently, the expression above can be optimized only through calculations on the atomic system itself.

With a line Q of 2×10^7 , and a signal to noise ratio of 75 dB, a stability of 1×10^{-12} is predicted for an averaging time of 1 second.

In practice however the line is broadened by the interrogating power; furthermore the modulation amplitude may not be weak relative to the line width. In that case the frequency stability is still given by a formula of the form:

$$S_y(f) = \frac{k^2}{Q_L^2(S/N)^2} \quad (8)$$

where k is given by

$$k = \frac{Q_L i'_0}{D' \nu_0} \quad (9)$$

with $i'_0 = \frac{i_0}{I_0}$ and $D' = \left(\frac{1}{d\nu}\right) \frac{\nu_0}{I_0}$.

These parameters are found experimentally.

Servo loop equations

In the frequency standard itself the above frequency stability is transferred to a crystal oscillator. The system is shown in Figure 5 and is described by a linear model. The equations describing the servo loop, for frequency fluctuations, are [7], [8]:

$$S_{y_q}^k(f) = |H_1(f)|^2 S_{y_q}^f(f) + |H_2(f)|^2 S_{y_r}(f), \quad (10)$$

$$|H_1(f)|^2 = \frac{(f/f_n)^2}{1+(f/f_n)^2}, \quad |H_2(f)|^2 = \frac{1}{1+(f/f_n)^2} \quad (11)$$

where it is assumed that an integrator with transfer function:

$$F(p) = \frac{1}{pt_1}, \quad (12)$$

is used.

Here $t_1 = RC$ is the time constant of the integrator and $p = j2\pi f$. f_n is defined as

$$f_n = \frac{nK_v K_r}{2\pi t_1} \quad (13)$$

The various terms are as follows: K_v is the equivalent frequency discriminator sensitivity of the atomic ensemble coupled to the phase sensitive detector in volts per radian per second; it is equal to $2\pi D$; K_r is the voltage controlled crystal oscillator coefficient in radian per second per volt; $S_{y_q}^f(f)$ is the free running quartz-crystal oscillator spectral density; $S_{y_r}(f)$ is the equivalent spectral density of the atomic reference; finally $S_{y_q}^k(f)$ is the spectral density of the locked quartz crystal oscillator.

It is observed that $H_2(f)$ is essentially a low pass filter for the atomic reference spectral density, while $H_1(f)$ is a high pass filter for the quartz crystal oscillator fluctuations. Consequently f_n must be adjusted for best overall performances depending on the values of $S_{y_q}^f$ and S_{y_r} .

Experimental results on short term frequency stability

We have made measurements on the various parameters studied above. These measurements were done on a test bench in which the optical package consisted of a natural rubidium lamp, an absorption cell containing natural rubidium and a mixture of N_2 and K_r as buffer gas in a TE₁₁₁ cavity. The photodetector was a PIN diode and the signal was detected with a commercial lock-in amplifier.

Noise measurements: A typical discriminator pattern observed with the set up is shown in Figure 6. The noise at the PIN diode was measured as a function of frequency with maximum light intensity available. The results are shown in Figure 7. The noise was also measured as a function of light intensity or photocurrent. The results are shown in Figure 8. It should be mentioned here that the actual level of light and photocurrent in the present set up is much lower than is normally used in practice. This is due to three causes. First, the PIN diode used has a very small surface of detection, limiting the signal to noise ratio as shown by equation [7], since I_0 is proportional to the surface of the detector. Secondly, the lamp was placed at a distance somewhat larger than normal from the absorption cell; this was made necessary in order to have an arrangement in which the light intensity could be varied easily. Finally, we did not use an isotopic filter in the system and that limited the signal to noise ratio.

In the results shown, it is observed first,

that the noise output is proportional to I_0 and the relation $S_1 = 2eI_0$ is obeyed. The dotted line in Figure 8 is the actual theoretical limit of the noise. Secondly, the noise is white at frequencies above 10 Hz. Below 10 Hz, there is a flicker component in the noise output. Thus, modulation at a frequency of 100 Hz followed by synchronous detection avoids completely that last noise contribution. This is the frequency that we have use for modulation.

In our case, at the operating light intensity, the noise is thus 2.1×10^{-26} [A²/Hz]. The signal as measured experimentally is 9.2×10^{-11} [A] (peak). This gives a signal to noise ratio of 53 dB. In some other systems a signal to noise ratio as high as 75 dB has been observed in a one Hertz bandwidth.

Frequency stability measurements

The frequency stability was measured in the frequency domain directly at 6.834 GHz. The measurement was done by beating directly the signal at 6.834 GHz with the output signal of a rubidium maser which has a very good spectral purity. The set up is shown in Figure 9. A phase-lock loop was used to lock the synthesizer to the beat signal in order to be able to make phase stability measurements [9]. The signal resulting from this phase comparison was then analysed with a spectrum analyser.

The results of this measurement with the crystal oscillator not locked to the rubidium resonance signal are shown in Figure 10. Figure 11 gives the results for the case where the crystal oscillator is locked to the atomic resonance line. The level of $S_y(f)$ for $f < 25$ Hz is 4.5×10^{-20} . This is in very good agreement with the value calculated from the level of shot noise reported above. In fact this is only 0.2 dB higher than the shot noise contribution. Above 25 Hz the servo loop act as a high pass filter for the quartz oscillator fluctuations and the spectral density observed is that of the quartz crystal oscillator.

It should be mentioned that the $S_y(f)$ reported here gives a resulting stability worst than what is usually encountered in practice. This is due to the reason given above. In the present set up we have a signal to noise ratio of 53 dB. The measured line Q at the temperature of operation was $Q_1' = 3.4 \times 10^6$ and $Q_2 = 1.9 \times 10^6$ for $2e = \Delta\nu$. From equation 8, this would give a time domain frequency stability of 1.5×10^{-10} for an averaging time of 1 second. This is entirely consistent with the spectral density reported in Figure 11. That relatively poor stability consequently, has allowed the verification of the theoretical predictions with a very simple crystal oscillator and without elaborate techniques.

Discussion

From the results reported above we can conclude that the limit of short term stability in the passive rubidium frequency standard is well understood. The theory which describes that limit is based on well known phenomena and servo-system concepts. Furthermore experimental and theoretical

results are in good agreement. Thus attempts to optimize the system can be done on a reliable mathematical basis. In this line of thought, it is clear that the main parameters are line Q and S/N.

The line Q is entirely controlled by the line width. For a fixed frequency, it can be increased only by reducing the relaxation rate. This rate is controlled by wall and buffer gas relaxation. The buffer gases which appear to give the lowest relaxation rates are nitrogen and the noble gases such as helium, neon and argon. The relaxation rate of Rb⁸⁷ in these gases is not known exactly. However it is known for Rb⁸⁵ at 3 GHz [10]. In Rb⁸⁷, we would expect the rate for Rb⁸⁵ multiplied by the square of the ratio of the frequencies $(6.8/3)^2$. This would give a line Q of the order of 1.3×10^8 in nitrogen for example. In practice however the line is broadened by spin exchange interaction, interrogating r.f. power and pumping light intensity. In that case we do not expect at normal operating temperatures a line Q better than $\sim 2.5 \times 10^7$. With parafilm, in a 1 inch bulb, a line Q of nearly 3×10^7 is obtained at 60 °C.

On the other hand the (S/N) is given by equation [7]. It is proportional to the fractional absorption depth α , the total optical pumping photocurrent I_0 and within certain limits to the modulation amplitude ϵ . The (S/N) is also proportional to the inverse line width as is the line Q. Consequently any reduction in line width results in an increased line Q, an increased S/N and a sharp improvement in short term stability. In the context of the parafilm coated cell this result appears to be rather important. On the other hand, for a given fractional absorption depth α , the signal is proportional to I_0 the optical pumping photocurrent. Consequently, it is advantageous to detect the total light intensity that creates the resonance signal α . However, although the S/N increases with I_0 , there is a point where α saturates and decreases with I_0 . Above that point, there is not much gain in increasing I_0 . Furthermore, in a system using hyperfine filtering, the line width is given by

$$\Delta\nu = \Delta\nu_0 + \frac{1}{2} \frac{\Gamma}{\pi} \quad (14)$$

where Γ is the pumping rate in photons per atoms per second and $\Delta\nu_0$ includes all other interactions [11]. There is thus an optimum light intensity at which the system can be set at in order to obtain optimum signal to noise ratio and line Q. In practice and up to now this has been done experimentally.

Long term stability

Some of the physical processes causing long term instabilities in the passive rubidium frequency standard are believed to take place in the absorption cell itself. Such are the power shift and wall interactions varying with time. The power shift acts through the inhomogeneous broadening caused by the light shift [12]. Wall interactions including adsorption of rubidium may cause time dependent fluctuations of rubidium density and changes in gas density in the absorption cell. One

method of avoiding these effects is to use a cell without buffer gas, coated with a substance that prevent relaxation. Parafint, a long chain wax, has been found to be very efficient in that respect. However, one has to know several parameters such as relaxation rates, wall shift and temperature coefficient of the wall shift, before concluding on the actual practicality of the technique.

We have made measurements on a parafint coated cell attached directly to a vacuum system. The cell made of quartz was placed in a TE₀₁₁ cavity as shown in Figure 12. The rest of the system was identical to that shown in Figure 1 except that an isotopic filter could be placed in the path of the light. The signal to noise ratio obtained with the arrangement in best conditions was 75 dB in a one Hertz bandwidth. The line Q was of the order of 2.7×10^7 .

The results on the wall shift are shown in Figure 13. At 60 °C, the shift is of the order of - 210 Hz and the temperature coefficient is + 1.4 Hz/°C. These results are slightly different from those obtained by Brewer [13].

It would be possible to operate a standard with such a cell. The S/N ratio and the line Q are such that a stability of $\sim 1 \times 10^{-12}$ for a 1 sec. averaging time can be expected. The wall coating temperature dependence may be a problem, however. Nevertheless it is expected that at higher temperatures that dependence will be smaller as found in Rb⁸⁵. On the other hand its long term stability remains to be investigated. However, a rubidium maser incorporating a bulb filled with 10 Torr of N₂ and coated with parafint has now been in operation for nearly 5 years without any signal amplitude degradation. The surface is thus expected to be rather stable and non reactive with rubidium. The remaining question is its frequency stability with time and this has not been measured yet.

Conclusion

In the present paper we have examined carefully the limits of stability of the passive rubidium frequency standard. In the short term region, calculations show that the limit is due to the presence of white frequency noise. Experiments confirm these calculations. It is shown that improvement in short term stability could be obtained by increasing the line Q and the signal to noise ratio. In cells using buffer gases, the limits are set by the buffer gas relaxation rate, spin exchange interactions, light broadening and interrogation power broadening. The contribution of the buffer gas to the line width is a function of pressure. In practice it appears that a line Q of the order of 2.5×10^7 is feasible in normal operating conditions. In the parafint coated cell described in this article a line Q of the order of 2.7×10^7 was realized in optimum conditions and a signal to noise ratio of 75 dB was obtained in a 1 Hz bandwidth.

The same parafint coated cell had been used previously in a power shift experiment [14]. It was shown that the removal of the buffer gas permitted a large reduction in power shift and, thus, it is hoped that the technique could be used to

improve long term stability. However the measurements reported show that the wall shift and the temperature coefficient are quite large. Nevertheless, from results obtained on rubidium 85 it is believed that at a temperature of about 80 °C the temperature sensitivity would be much reduced [10]. In that case the cell could be used without excessive demand on the temperature control. These studies are underway.

Acknowledgement

The authors would like to thank MM. R. Blier and Y. Chalifour for their constant technical support. This work was supported jointly by the Department of National Defense, the Natural Sciences and Engineering Research Council, Canada and the Ministère de l'Éducation, Province of Quebec.

Appendix

Calculation of $\sigma(\tau)$ and $S_y(f)$ in the case where the stability is limited by shot noise.

The profile of the light intensity transmitted through the absorption cell and detected at the photocell is assumed to be of the form shown in Figure 4. It can be expressed as:

$$I(v) = I_0(1 - \alpha \frac{g(v)}{2T_2}) \quad , \quad A-1$$

where I_0 is the photocurrent, T_2 is the transverse relaxation time and $g(v)$ is the line shape assumed to be Lorentzian.

$$g(v) = \frac{2T_2}{1 + T_2^2(v-v_0)^2} \quad . \quad A-2$$

The full line width at half the height is given by

$$\Delta v = \frac{1}{\pi T_2} \quad . \quad A-3$$

The discriminator pattern is essentially the derivative of A-1

$$\frac{dI(v)}{dv} = 2\pi\alpha I_0 |g(v)|^2 (v-v_0) \quad . \quad A-4$$

The width between the discriminator maxima is

$$\delta v = \frac{1}{\sqrt{3}\pi T_2} \quad . \quad A-5$$

The peak signal amplitude at the peak of the discriminator pattern is

$$i_0 = \frac{9\alpha\epsilon I_0}{4\sqrt{3}\Delta v} \quad A-6$$

and the slope at the center of the discriminator is

$$\frac{i(v)}{dv} = \frac{8\epsilon}{\Delta v^2} \alpha I_0 \quad . \quad A-7$$

The addition of shot noise at the photodetector appears as a frequency instability with a spectral density given by

$$S_y(f) = \frac{4\epsilon I_0}{(v_0)^2 (1/dv)^2} \quad A-8$$

In this expression we take into account the discriminator action of the atomic reference combined with the lock-in detector. The signal to noise ratio is defined as

$$\left(\frac{S}{N}\right)^2 = \frac{(\text{signal power at maximum of discriminator})}{(\text{shot noise power})}$$

$$\left(\frac{S}{N}\right)^2 = \frac{(i_0^2/2)}{2eI_0} \quad \text{A-9}$$

From these expression, simple algebra gives

$$\left(\frac{S}{N}\right)^2 = \frac{3^3 a^2 \epsilon^2 I_0}{2^6 e \Delta \nu^2}$$

$$S_y(f) = \frac{3^3}{2^{10} Q_L^2 (S/N)^2}$$

The time domain frequency stability is then given by

$$\sigma(\tau) = \frac{0.11}{Q_L (S/N)} \tau^{-\frac{1}{2}}$$

where we have used the relations [6]

$$S_y(f) = h_0$$

$$\sigma^2(\tau) = \frac{1}{2} \frac{h_0}{\tau}$$

valid for white frequency noise. These expressions are similar to those obtained by Lacey *et al.* [15] although they have been derived in a different way. There is, however, a factor of 2 difference in the frequency stability $S_y(f)$, our value being smaller than the value they obtain.

Bibliography

- [1] R.J. Carpenter, E.C. Beaty, P.L. Bender, S. Saito, R.O. Stone, IRE. Trans. Instr. 1-9, 132, 1960.
- [2] E. Jechart, Elecktronik 12, 457, 1974.
- [3] I. Matsuda, T. Sato, N. Kuromochi, H. Fukuyo, Bul. Tokyo Inst. of Tech. 125, 9, 1974.
- [4] Example: A proposal for a Canadian very long-baseline array, 1980.
- [5] See for example: C. Audoin and J. Vanier, Journal of Physics E. Scient. Inst., 9, 697, 1976.
- [6] J.A. Barnes *et al.*, IEEE Trans. on Instr. and Meas., 20, 105, 1971.
- [7] J. Vanier, M. Têtu, L.G. Bernier, IEEE Trans. on Instr. and Meas., 28, 188, 1979.
- [8] L.S. Cutler and C.L. Searle, Proc. IEEE 54, 136, 1966.
- [9] M. Têtu, R. Brousseau and J. Vanier, IEEE Trans. on Instr. and Meas., June 1980.
- [10] J. Vanier, J.F. Simard and J.S. Boulanger, Phys. Rev. 9, 1031, 1974.
- [11] G. Missout, J. Vanier, Can. J. Phys., 53, 1030, 1975.
- [12] A. Risley, G. Busca, Proc. of the 32nd Annual Symposium on Frequency Control, p. 506, 1978.
- [13] R.G. Brewer, J. Chem. Phys., 38, 3015, 1963.
- [14] A. Risley, S. Jarvis, J. Vanier, Proc. of the 33rd Annual Symposium on Frequency Control, 477, 1979.

[15] R.F. Lacey, A.L. Helgesson and J.H. Holloway, Proc. of the IEEE, 54, 170, 1966.

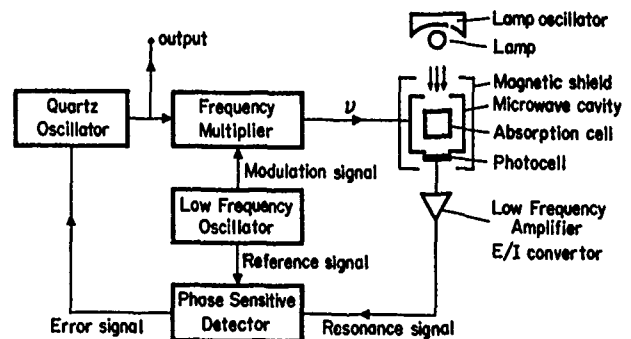


Figure 1

Block diagram of the passive rubidium frequency standard.

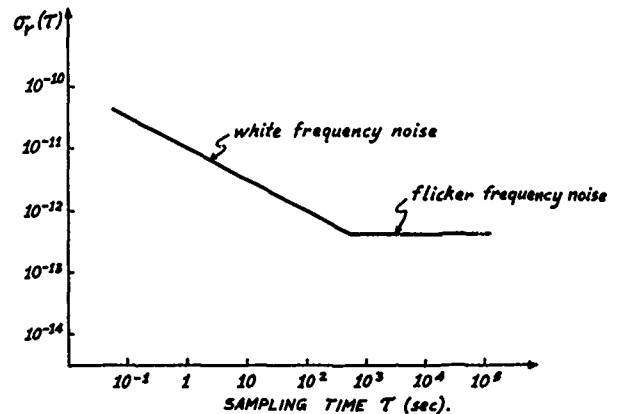


Figure 2

Plot of frequency stability $\sigma(\tau)$ for a typical commercial rubidium frequency standard.

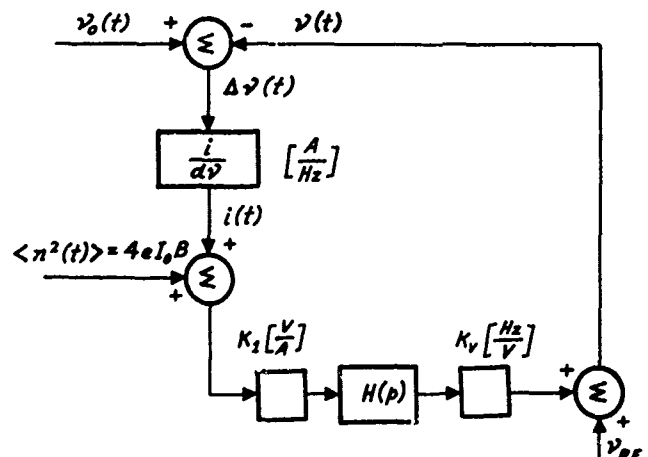
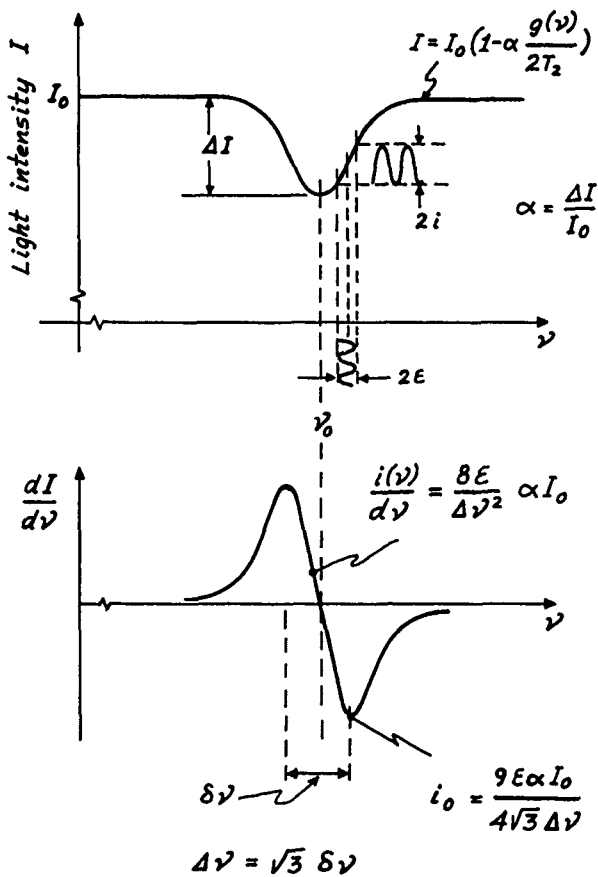


Figure 3

Linear model used in the calculations of the short term frequency stability.



Line shape and error signal

Figure 4

Line shape and discriminator pattern.

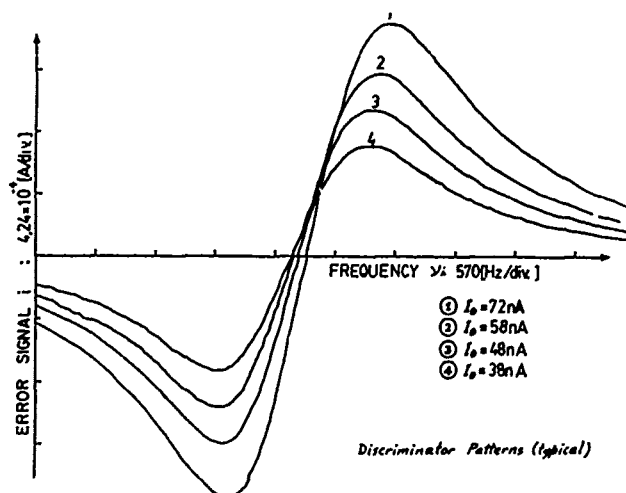


Figure 6

Discriminator pattern obtained experimentally with a PIN diode used as detector. The various curves are for different light intensities.

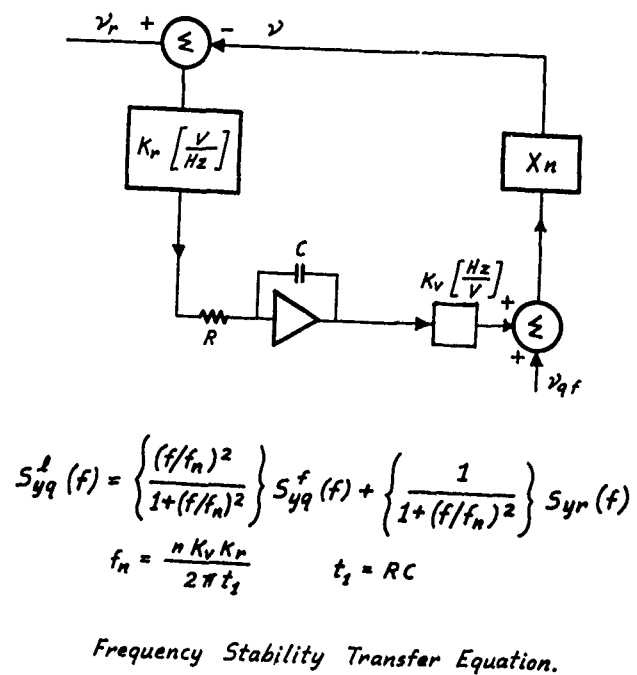


Figure 5

Block diagram used for the servo loop equations.

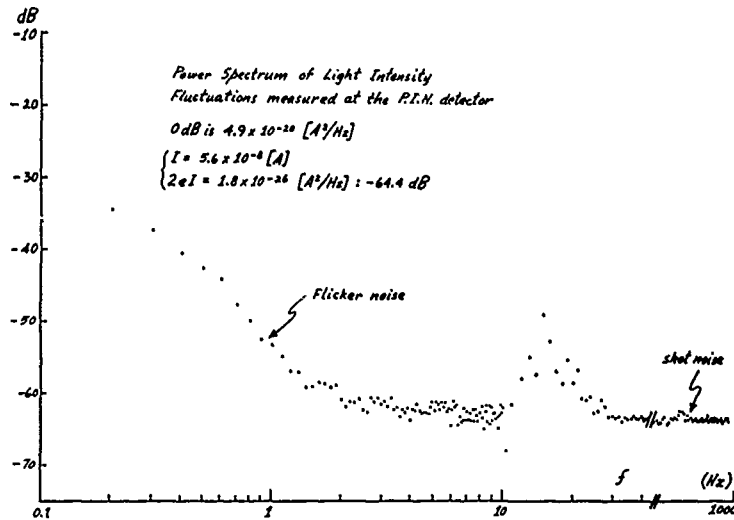


Figure 7 Current shot noise against frequency.

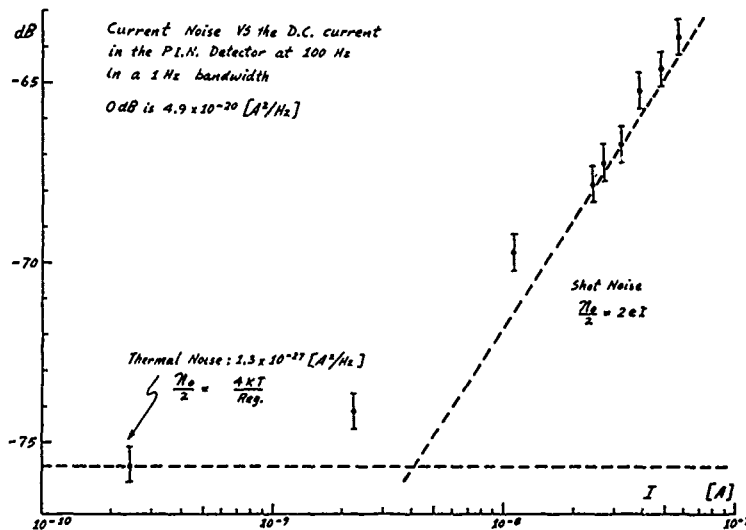


Figure 8 Current shot noise against photocurrent.

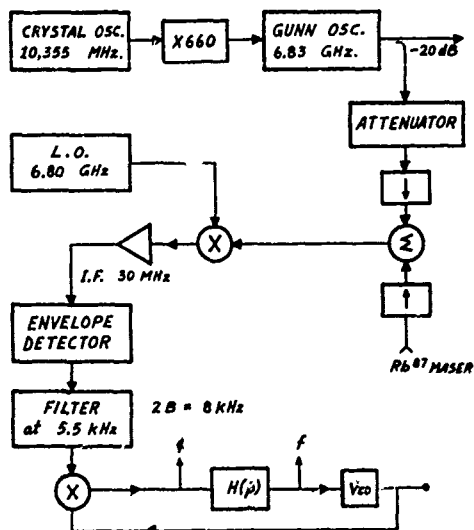


Figure 9

Block diagram of the experimental set up used to measure $S_y(f)$.

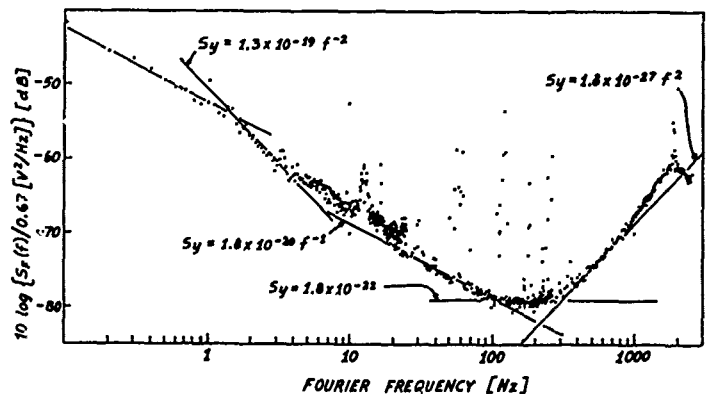


Figure 10

Fractional frequency stability spectral density $S_y(f)$ for the free running crystal oscillator.

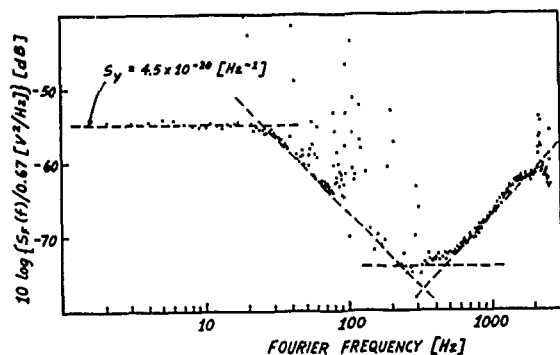


Figure 11

Same as Figure 10 for the crystal oscillator locked to the atomic resonance line.

OSC. 100 MHz Oscillator
 Rb⁸⁷ Lamp
 Filter Rb⁸⁵ + 70 Torr Ar

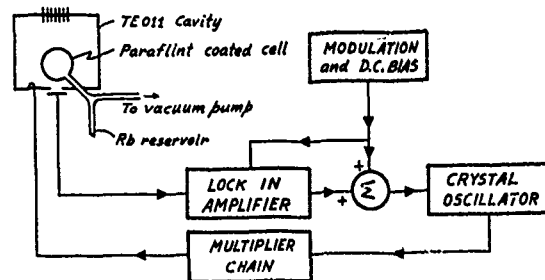


Figure 12

Block diagram of the system used in measurements with the paraflint coated cell.

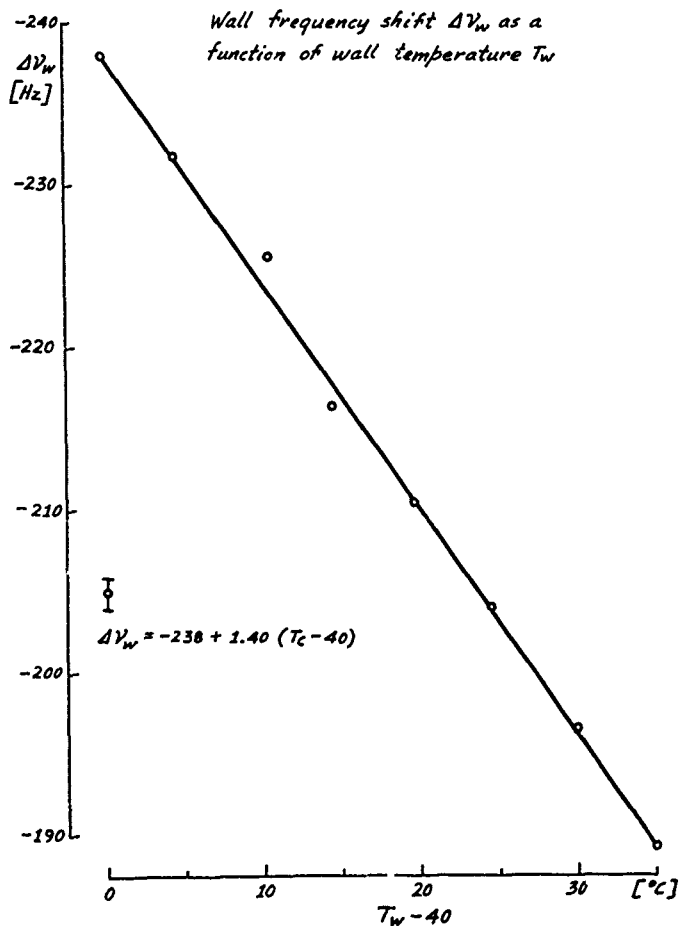


Figure 13

Experimental results showing the temperature dependence of the hyperfine frequency of rubidium 87 in a paraflint coated cell.

TEMPERATURE INDUCED FREQUENCY CHANGES IN ELECTRODED AT-CUT QUARTZ TRAPPED ENERGY RESONATORS

D.S. Stevens and H.F. Tiersten
Department of Mechanical Engineering,
Aeronautical Engineering & Mechanics
Rensselaer Polytechnic Institute
Troy, New York 12181

Abstract

A system of approximate plate equations for the determination of thermal stresses in electroded piezoelectric plates is applied to AT-cut quartz trapped energy resonators. The change in resonant frequency resulting from the thermally induced biasing stresses and strains is determined from an equation for the perturbation of the eigenfrequency of the piezoelectric solution due to a bias. The changes in resonant frequency with temperature are calculated for a number of harmonic and anharmonic overtone trapped energy modes for rectangular electrodes oriented in various directions with respect to the diagonal axis on AT-cut quartz plates. In this way the dependence of the change in frequency per °K on both the orientation of the rectangular electrodes and the electrode geometry is determined.

1. Introduction

A perturbation analysis of the linear electroelastic equations for small fields superposed on a bias has been performed¹. The change in resonant frequency due to any bias such as, e.g., a residual stress may readily be obtained from the resulting equation for the perturbation of the eigenfrequency if the bias is known. In addition, a system of approximate plate equations for the determination of thermal stresses in thin piezoelectric plates coated with large much thinner films was derived² from Mindlin's plate equations³⁻⁵. The resulting approximate equations simplify the treatment of many thermal stress problems considerably, and the three-dimensional detail not included in the approximate description is not deemed to be important for our purposes. Furthermore, an analysis of AT-cut quartz trapped energy resonators with rectangular electrodes vibrating in the usual coupled thickness-shear and thickness-twist modes has been performed⁶.

In this paper the aforementioned system of approximate static thermoelastic plate equations for the anisotropic plated crystal plate is applied to AT-cut quartz plates with large rectangular electrodes oriented in various directions with respect to the diagonal axis of the AT-cut quartz plate. The approximate three-dimensional displacement field resulting from the solution of the plate equations is readily determined from the description. Since the rectangular electrodes have an arbitrary orientation with respect to the diagonal axis of the AT-cut quartz plate, the existing

approximate solution for the eigenmodes of the trapped energy resonator⁶ must be modified essentially to account for the coupling of the symmetric and antisymmetric trapped energy modes. Since the direct inclusion of the coupling coefficient, which is not too large, would drastically alter the existing approximate solution⁶, the influence of the coupling of the antisymmetric mode on the eigenfrequency of the symmetric mode is treated by means of a perturbation procedure. The substitution of the thermoelastic three-dimensional displacement field into the above-mentioned equation for the perturbation of the eigenfrequency along with the approximate solution for the vibrating modes in trapped energy resonators and the first temperature derivatives of the fundamental elastic constants of quartz⁷ enables the calculation of the temperature dependence of the resonant frequencies of electroded AT-cut quartz trapped energy resonators due to the thermally induced biasing deformation as a function of the orientation of the rectangular electrodes with respect to the diagonal axis. The influence of the temperature dependence⁸⁻¹⁰ of the motional capacitive effect of the electrodes on the resonant frequency of thickness vibrations of the electroded portion of the plate resulting from the temperature dependence of the pertinent (for thickness vibrations of AT-cut quartz plates) piezoelectric and dielectric constants is included in the treatment. Results are presented for rectangular gold electrodes with different aspect ratios oriented in various directions on AT-cut quartz plates for a number of harmonic and anharmonic trapped energy modes. In particular, it is shown that a square electrode minimizes the orientational dependence of the change in frequency with temperature. In addition, the change in frequency with temperature of the fundamental trapped energy mode for rectangular electrodes oriented along the diagonal axis of the AT-cut quartz plate is obtained as a function of the ratio of the electrode geometry to the plate thickness. These latter results are related to the dependence of the apparent shift in angle of the zero temperature cut on the electrode geometry.

2. Perturbation Equations

For purely elastic nonlinearities the equation for the first perturbation of the eigenvalue obtained from the perturbation analysis¹ mentioned in the Introduction may be written in the form

$$\Delta_{\mu} = H_{\mu}/2\omega_{\mu}, \quad \omega = \omega_{\mu} - \Delta_{\mu}, \quad (2.1)$$

where ω_μ and ω are the unperturbed and perturbed eigenfrequencies, respectively, and

$$H_\mu = - \int_V \tilde{K}_{LY}^n g_{Y,L}^\mu dV, \quad (2.2)$$

where V is the undeformed volume of the piezoelectric plate at the reference temperature T_0 . In (2.2) g_Y^μ denotes the normalized mechanical displacement vector, and \tilde{K}_{LY}^n denotes the portion of the Piola-Kirchhoff stress tensor resulting from the biasing state and a change in the elastic constants $\Delta g_{LYM\alpha}$ in the presence of the g_Y^μ , and is given by

$$\tilde{K}_{LY}^n = (\hat{C}_{LYM\alpha} + \Delta C_{2LYM\alpha}) g_{\alpha,M}^\mu, \quad (2.3)$$

where

$$\hat{C}_{LYM\alpha} = T_{LM}^1 \delta_{Y\alpha} + C_{LYM\alpha B} E_{AB}^1 + C_{LYKM}^w w_{\alpha,K} + C_{2LYKM}^w w_{Y,K}, \quad (2.4)$$

and

$$T_{LM}^1 = C_{LMKN} E_{KN}^1 - v_{LM} (T - T_0), \\ E_{KN}^1 = \frac{1}{2} (w_{K,N} + w_{N,K}). \quad (2.5)$$

The quantities T_{LM}^1 , E_{AB}^1 and w_K denote the static biasing stress, strain and displacement field, respectively. Thus, in this description the present position x is related to the reference position X by

$$x(X_L, t) = X_L + w(X_L) + u(X_L, t). \quad (2.6)$$

The coefficients C_{LMKN} and $C_{LYM\alpha B}$ denote the second and third order elastic constants, respectively, v_{LM} denotes the thermoelastic coupling coefficients and T denotes the present temperature.

The normalized eigensolution g_Y^μ and \tilde{F}^μ is defined by

$$g_Y^\mu = \frac{u_Y^\mu}{N_\mu}, \quad \tilde{F}^\mu = \frac{\tilde{\phi}^\mu}{N_\mu}, \quad N_\mu^2 = \int_V \rho u_Y^\mu u_Y^\mu dV, \quad (2.7)$$

where u_Y^μ and $\tilde{\phi}^\mu$ are the mechanical displacement and electric potential, respectively, which satisfy the equations of linear piezoelectricity

$$\tilde{K}_{LY}^L = C_{LYM\alpha} u_{\alpha,M} + e_{MLY} \tilde{\phi}_{,M}, \\ \tilde{p}_L^L = e_{LMY} u_{Y,M} - \epsilon_{LM} \tilde{\phi}_{,M}, \quad (2.8)$$

$$\tilde{K}_{LY,L}^L = \rho \tilde{u}_Y^\mu, \quad \tilde{p}_{L,L}^L = 0, \quad (2.9)$$

subject to the appropriate boundary conditions, and ρ is the mass density. Equations (2.8) are the linear piezoelectric constitutive relations and (2.9) are the stress equations of motion and charge equation of electrostatics, respectively. The upper cycle notation for many dynamic variables and the capital Latin and lower case Greek index notation is being employed for consistency with Ref.1, as is the remainder of the notation in this section.

At this point we note that if the relative change in the piezoelectric constants with temperature were of the same order of magnitude as the relative change in the elastic constants, the temperature dependence of the piezoelectric constants would indeed be negligible in the description because of the small piezoelectric coupling in quartz. However, this is not actually the case and the relative temperature dependence of the piezoelectric coefficients is nearly two orders of magnitude larger than that of the elastic coefficients¹¹. As a consequence at least certain aspects of the temperature dependence of the piezoelectric constants must be included if the description presented here is to be physically meaningful. Although the perturbation theory in Ref.1 includes the full electroelastic interaction, it was not retained here because the temperature derivatives of the complete piezoelectric and dielectric tensors is not presently known. Moreover, the existing temperature derivatives of the fundamental elastic constants of quartz⁷ effectively contain a portion of the influence of the temperature dependence of the piezoelectric and dielectric constants, primarily that resulting from the piezoelectric stiffening of the waves. Nevertheless, the influence of the temperature dependence of the piezoelectric and dielectric constants on that of the motional capacitive (shorting) effect of the electrodes on that of the resonant frequency of thickness vibrations of the electroded portion of the plate is not contained in the purely elastic perturbation integral in (2.2). In view of the foregoing, the general electroelastic perturbation integral in Ref.1 has been appropriately modified¹² to include the influence of only the linear term in the thickness eigensolution in the electroded region and the temperature dependence of the one pertinent piezoelectric constant, with the result

$$H_\mu = - \int_V \left[\tilde{K}_{LY}^n g_{Y,L}^\mu - 2C_{266}^2 k_{26}^2 \frac{\Delta e_{26}}{e_{26}} g_{1,2} \frac{g_1(h)}{h} \right] dV, \quad (2.10)$$

where the usual compressed matrix notation for the tensor indices has been introduced, a cross-section of the electroded AT-cut quartz plate is shown in Fig.1 along with associated coordinate system and

$$k_{26}^2 = e_{26}^2 / \epsilon_{66} e_{22}, \quad (2.11)$$

where e_{26} and e_{22} are the significant piezoelectric and dielectric constants here.

3. Temperature Induced Biasing State

It has been shown² that referred to the coordinate system shown in Fig.1 the static purely extensional thermoelastic plate equations for the plated crystal plate may be written in the form

$$\chi_{AB,A}^{(0)} = 0, \quad \chi_{AB,A}^{(2)} = 0, \quad (3.1)$$

where A, B, C, D take the values 1 and 3 and skip 2 and $\chi_{AB}^{(0)}$ and $\chi_{AB}^{(2)}$ are the zero and second order plate stress resultants, respectively, for the electroded crystal plate. For homogeneous temperature

states and identical electrodes on the upper and lower surfaces the extensional constitutive equations may be written in the form

$$\begin{aligned}\chi_{AB}^{(0)} &= 2h(\gamma_{ABCD} + \frac{2h'}{h} \gamma'_{ABCD}) E_{CD}^{(0)} + 2h \left(\frac{1}{3} \gamma_{ABCD} + \right. \\ &\quad \left. \frac{2h'}{h} \gamma'_{ABCD} \right) E_{CD}^{(2)} - 2h \left(\beta_{AB} + \frac{2h'}{h} v_{AB}^{*'} \right) (T - T_0), \\ \chi_{AB}^{(2)} &= \frac{2}{3} h^3 \left(\gamma_{ABCD} + \frac{6h'}{h} \gamma'_{ABCD} \right) E_{CD}^{(0)} + \frac{2}{5} h^5 \left(\gamma_{ABCD} + \right. \\ &\quad \left. \frac{10h'}{h} \gamma'_{ABCD} \right) E_{CD}^{(2)} - \frac{2}{3} h^3 \left(\beta_{AB} + \frac{6h'}{h} v_{AB}^{*'} \right) (T - T_0),\end{aligned}\quad (3.2)$$

where

$$v_R^{*'} = v'_R - v'_{2C2R}/c'_{22}, \quad (3.3)$$

in the compressed notation and we have introduced the usual compressed matrix notation for tensor indices according to the scheme

$$R, S = 1, 3, 5; \quad W, V = 2, 4, 6, \quad (3.4)$$

and

$$\gamma_{RS} = c_{RS} - c_{RW} c_{WV}^{-1} c_{VS}, \quad \beta_R = v_R - c_{RW} c_{WV}^{-1} v_V. \quad (3.5)$$

The γ_{RS} are Voigts' anisotropic plate elastic constants and the β_R are the associated anisotropic plate thermoelastic constants. For the case of anisotropic extension considered here the three-dimensional strains E_{KL} , which are needed in the perturbation equation, are related to the plate strains by

$$E_{KL} = \frac{1}{2} (w_{K,L} + w_{L,K}) = E_{KL}^{(0)} + \chi_{KL}^{(2)} E_{KL}^{(2)}. \quad (3.6)$$

The plate strains $E_{AB}^{(n)}$ ($n=0, 2$), which occur in (3.2), are given by

$$E_{AB}^{(n)} = \frac{1}{2} (w_{A,B}^{(n)} + w_{B,A}^{(n)}), \quad (3.7)$$

and the remaining plate strains, which are needed in (3.6) as well, may be obtained from

$$\begin{aligned}E_W^{(0)} &= -c_{WV}^{-1} c_{VS} E_S^{(0)} + c_{WV}^{-1} v_V (T - T_0), \\ E_W^{(2)} &= -c_{WV}^{-1} c_{VS} E_S^{(2)}.\end{aligned}\quad (3.8)$$

The foregoing has been for the electroded portion of the plate. In the unelectroded portion the situation is somewhat simpler and we have the ordinary stress equations of equilibrium

$$T_{ML,M}^1 = 0, \quad (3.9)$$

along with the constitutive equations (2.5)₁. Since the outside edges of the plate are traction free along with the unelectroded major surfaces, we have

$$\hat{N}_M T_{ML}^1 = 0, \quad (3.10)$$

on all unelectroded surfaces, where \hat{N}_M denotes the unit normal to all unelectroded surfaces of the

plate at $T=T_0$. From (3.9) and (3.10) we have

$$T_{ML}^1 = 0, \quad (3.11)$$

for the unelectroded portion of the plate. Since the thermoelastic coupling constants v_{ML} are related to the coefficients α_{JK} by the usual relation

$$v_{ML} = c_{MLJK} \alpha_{JK}, \quad (3.12)$$

from (2.5)₁, (3.11) and (3.12), we have

$$E_{JK}^1 = \alpha_{JK} (T - T_0), \quad (3.13)$$

in the unelectroded region.

By virtue of (3.11), along the edges of the electroded region of the plate, we have

$$N_A \chi_{AB}^{(0)} = 0, \quad N_A \chi_{AB}^{(2)} = 0, \quad (3.14)$$

where N_A denotes the outwardly directed unit normal to the edge of the electrode at $T=T_0$. The solution satisfying (3.14) and (3.1) takes the form

$$\chi_{AB}^{(0)} = 0, \quad \chi_{AB}^{(2)} = 0. \quad (3.15)$$

This solution is unique to within static homogeneous plate rotations of zero and second order. Substituting from (3.2) into (3.15), we obtain

$$\begin{aligned}(\gamma_{RS} + \frac{2h'}{h} \gamma'_{RS}) E_S^{(0)} + h^2 \left(\frac{\gamma_{RS}}{3} + \frac{2h'}{h} \gamma'_{RS} \right) E_S^{(2)} \\ = \left(\beta_R + \frac{2h'}{h} v_R^{*'} \right) (T - T_0), \\ (\gamma_{RS} + \frac{6h'}{h} \gamma'_{RS}) E_S^{(0)} + h^2 \left(\frac{3}{5} \gamma_{RS} + \frac{6h'}{h} \gamma'_{RS} \right) E_S^{(2)} \\ = \left(\beta_R + \frac{6h'}{h} v_R^{*'} \right) (T - T_0).\end{aligned}\quad (3.16)$$

Equations (3.16) constitute six inhomogeneous linear equations which may readily be solved for the six plate strains $E_S^{(0)}$ and $E_S^{(2)}$. When $E_S^{(0)}$ and $E_S^{(2)}$ have been determined from (3.16), $E_{KL}^{(0)}$ and $E_{KL}^{(2)}$ are readily determined from (3.8). Then the three-dimensional biasing strain can be obtained from (3.6), which is for anisotropic extension. There is no flexure because the resonator has identical electrodes and is subject to a homogeneous temperature change $(T - T_0)$.

It is well known that in static linear elasticity the solution to a boundary value problem is unique only to within a static homogeneous (global) infinitesimal rigid rotation¹³. Similarly, the solution to a static linearly elastic boundary value problem using the approximate plate equations is unique¹² only to within homogeneous infinitesimal n th order plate rotations $\Omega_{KL}^{(n)}$, where¹⁴

$$\Omega_{KL}^{(n)} = \frac{1}{2} (w_{L,K}^{(n)} - w_{K,L}^{(n)} + (n+1) (\delta_{2K} w_L^{(n+1)} - \delta_{2L} w_K^{(n+1)}))_1, \quad (3.17)$$

and the three-dimensional small rotation field Ω_{KL} is given by

$$\Omega_{KL} = \frac{1}{2} (w_{L,K} - w_{K,L}) = \sum_{n=0}^2 x_2^{(n)} \Omega_{KL}^{(n)}. \quad (3.18)$$

We now note that when the equations of equilibrium for the plate stress resultants, (3.1), are satisfied trivially, as is the case here, the relaxation of the stress resultants, (3.15), results in homogeneous plate strains $\bar{\epsilon}_{KL}^{(n)}$ and homogeneous plate rotations $\bar{\Omega}_{KL}^{(n)}$, which are consistent with three-dimensional strain gradient-rotation gradient relations^{1,2}. Accordingly, with (3.6) and (3.18) we have

$$\bar{w}_{L,K} = \bar{E}_{KL}^{(0)} + x_2^2 \bar{E}_{KL}^{(2)} + \bar{\Omega}_{KL}^{(1)}, \quad (3.19)$$

in which we have introduced bars to denote the electroded region and where the biasing displacement gradients $\bar{w}_{L,K}$ are known linear functions of $(T - T_0)$, as is the consistent^{1,2} rotation field $\bar{\Omega}_{KL}^{(1)}$. Thus, we may now obtain $\bar{\epsilon}_{L\gamma M\alpha}$ in (2.4) as a known linear function of $(T - T_0)$ in the electroded region. In the unelectroded region the homogeneous strain state is given by (3.13) and the static homogeneous (global) infinitesimal rigid rotation is indeed arbitrary. In fact, the change in frequency due to a homogeneous infinitesimal rigid rotation has been shown to vanish². Consequently, we may select the homogeneous infinitesimal rigid rotation to take any value that is convenient and in particular to vanish, and we have

$$\bar{\Omega}_{KL}^{(1)} = \frac{1}{2} (w_{L,K} - w_{K,L}) = 0, \quad (3.20)$$

which with (2.5)₂ and (3.13) yields

$$w_{J,K} = \alpha_{JK} (T - T_0). \quad (3.21)$$

The substitution of (3.13), (3.21) and (3.11) in (2.4) yields $\bar{\epsilon}_{L\gamma M\alpha}$ as a known linear function of $(T - T_0)$ in the unelectroded region.

4. Eigenmodes in Trapped Energy Resonators

A plan view of a rectangular electrode with the electrode axis X , rotated by an angle γ with respect to the diagonal axis X_1 of the AT-cut quartz plate is shown in Fig.2. Referred to the $X_1 - X_3$ axes, it has been shown⁶ that the differential equations of coupled thickness-shear and thickness-twist vibrations for the unelectroded and electroded portions of the plate can be written in the respective forms

$$M_n u_{,11} + c_{55} u_{,33} - \frac{n^2 \pi^2}{4h^2} \bar{c}_{66} u - \rho \ddot{u} = 0, \quad (4.1)$$

$$M_n \bar{u}_{,11} + c_{55} \bar{u}_{,33} - \frac{n^2 \pi^2}{4h^2} \hat{c}_{66} \bar{u} - \rho \ddot{\bar{u}} = 0, \quad (4.2)$$

where the bar refers to the electroded region of the plate, we have suppressed the index 1 on u and \bar{u} and

$$M_n = c_{11} + (c_{12} + c_{66})r + \frac{4(x\bar{c}_{66} - c_{66})(c_{22}r + c_{12})\cot n\pi/2}{c_{22}n\pi}, \quad (4.3)$$

$$\bar{c}_{66} = c_{66} + \frac{e_{26}^2}{\epsilon_{22}}, \quad \hat{c}_{66} = \bar{c}_{66} \left(1 - \frac{8k_{26}^2}{n^2 \pi^2} - 2R\right),$$

$$r = \frac{c_{12} + c_{66}}{\bar{c}_{66} - c_{22}}, \quad k_{26}^2 = \frac{e_{26}^2}{\bar{c}_{66} \epsilon_{22}},$$

$$R = \frac{2\rho' h'}{\rho h}, \quad \kappa = \sqrt{\frac{\bar{c}_{66}}{c_{22}}}, \quad (4.4)$$

and ρ' is the mass density. When Eqs.(4.1) and (4.2) are transformed to the electrode axes X_1 and X_3 they take the respective forms

$$A_{11} u_{,11} + A_{13} u_{,13} + A_{33} u_{,33} + \left(\rho \omega^2 - \frac{n^2 \pi^2}{4h^2} \bar{c}_{66}\right) u = 0, \quad (4.5)$$

$$A_{11} \bar{u}_{,11} + A_{13} \bar{u}_{,13} + A_{33} \bar{u}_{,33} + \left(\rho \omega^2 - \frac{n^2 \pi^2}{4h^2} \hat{c}_{66}\right) \bar{u} = 0, \quad (4.6)$$

in which we have introduced the time dependence $\exp(i\omega t)$ and u and \bar{u} are space dependent only and

$$A_{11} = M_n \cos^2 \gamma + c_{55} \sin^2 \gamma, \quad A_{13} = (c_{55} - M_n) \sin 2\gamma$$

$$A_{33} = M_n \sin^2 \gamma + c_{55} \cos^2 \gamma. \quad (4.7)$$

The existence of the material coefficient A_{13} in Eqs.(4.5) and (4.6) results in the occurrence of mixed derivative terms, which essentially couple the antisymmetric to the symmetric trapped energy modes and prevent the existing⁶ simple approximate solution for the trapped energy modes from being extended to the present asymmetric case in a straightforward way^{1,2}. Moreover, in the worst possible case encountered here

$$A_{13} = .326 \sqrt{A_{11}^2 + A_{33}^2}. \quad (4.8)$$

Consequently, we simply ignore A_{13} in (4.5) and (4.6) in obtaining the trapped energy eigensolutions and find its influence on the eigenfrequencies by means of a perturbation procedure to be discussed later.

A plan view showing one quadrant of the trapped energy resonator with the rectangular electrode is shown in Fig.3 along with the electrode coordinate system and the labeling of the four distinct regions considered in the solution. In accordance with the earlier work⁶ the edge conditions are

$$\begin{aligned}
\bar{u} &= u^S, \quad \bar{u}_1 = u^S_1 \text{ at } x_1 = \pm l, \quad |x_3| < b, \\
\bar{u} &= u^T, \quad \bar{u}_3 = u^T_3 \text{ at } x_3 = \pm b, \quad |x_1| < l, \\
u^T &= u^C, \quad u^T_1 = u^C_1 \text{ at } x_1 = \pm l, \quad |x_3| > b, \\
u^S &= u^C, \quad u^S_3 = u^C_3 \text{ at } x_3 = \pm b, \quad |x_1| > l. \quad (4.9)
\end{aligned}$$

As shown earlier⁵, in the absence of A_{13} the symmetric eigensolutions satisfying (4.6) in the electroded region and (4.5) in the unelectroded regions marked T and S and the edge conditions in (4.9) are given by

$$\begin{aligned}
\bar{u} &= \bar{B} \sin \frac{n\pi x_2}{2h} \cos \bar{\xi} x_1 \cos \bar{v} x_3, \\
u^S &= B^S \sin \frac{n\pi x_2}{2h} e^{-\bar{\xi}^S (x_1 - l)} \cos \bar{v} x_3, \\
u^T &= B^T \sin \frac{n\pi x_2}{2h} \cos \bar{\xi} x_1 e^{-\bar{v}^T (x_3 - b)}, \\
u^C &= B^C \sin \frac{n\pi x_2}{2h} e^{-\bar{\xi}^S (x_1 - l)} e^{-\bar{v}^T (x_3 - b)}, \quad (4.10)
\end{aligned}$$

provided the transcendental equations

$$\bar{\xi} \tan \bar{\xi} l = \left[\frac{\gamma_n}{A_{11}} - \bar{\xi}^2 \right]^{1/2}, \quad \bar{v} \tan \bar{v} b = \left[\frac{\gamma_n}{A_{33}} - \bar{v}^2 \right]^{1/2}, \quad (4.11)$$

are satisfied where

$$\gamma_n = \bar{\epsilon}_{66} \frac{n^2 \pi^2}{2h^2} \left[\frac{4k_{26}^2}{n^2 \pi^2} + R \right]. \quad (4.12)$$

For a given h , l and b values of $\bar{\xi}$ and \bar{v} for the respective symmetric trapped energy modes are the roots of the respective equations in (4.11). The symmetric eigenfrequency ω_1 is then found^{1,2} by substituting (4.10)₁ in (4.6) and $\bar{\xi}^S$ and \bar{v}^T are obtained^{1,2} by substituting (4.10)₂₋₃, respectively, in (4.5). The relations between the amplitudes in the different regions are⁸

$$\begin{aligned}
B^S &= \bar{B} \cos \bar{\xi} l, \quad B^T = \bar{B} \cos \bar{v} b, \\
B^C &= \bar{B} \cos \bar{\xi} l \cos \bar{v} b. \quad (4.13)
\end{aligned}$$

In addition to the $u_1^S(\bar{u}_1)$ displacement field satisfying (4.5) [(4.6)] there is an accompanying $u_2(\bar{u}_2)$ displacement field which for convenience^{1,5} we take in the form^{1,2}

$$\begin{aligned}
\bar{u}_2 &= \left(\bar{B}_2^{(1)} \cos \frac{n\pi x_2}{2h} + \right. \\
&\quad \left. \bar{B}_2^{(2)} \cos \frac{n\pi x_2}{2h} \right) \sin \bar{\xi} x_1 \cos \bar{v} x_3, \quad (4.14)
\end{aligned}$$

where

$$\begin{aligned}
\bar{B}_2^{(1)} &= \frac{r \bar{\xi}^S \bar{B} 2h}{n\pi}, \\
\bar{B}_2^{(2)} &= (-1)^{(n+1)/2} \frac{(c_{22}^r + c_{12}^r) \bar{\xi}^S \bar{B} 2h}{c_{22} n\pi \sin n\pi/2}, \quad (4.15)
\end{aligned}$$

and

$$\begin{aligned}
u_2^S &= \left(B_2^{(1)S} \cos \frac{n\pi x_2}{2h} + \right. \\
&\quad \left. B_2^{(2)S} \cos \frac{n\pi x_2}{2h} \right) e^{-\bar{\xi}^S (x_1 - l)} \cos \bar{v} x_3, \\
u_2^T &= \left(B_2^{(1)T} \cos \frac{n\pi x_2}{2h} + \right. \\
&\quad \left. B_2^{(2)T} \cos \frac{n\pi x_2}{2h} \right) \sin \bar{\xi} x_1 e^{-\bar{v}^T (x_3 - b)}, \quad (4.16)
\end{aligned}$$

where

$$\begin{aligned}
B_2^{(1)S} &= \frac{r \bar{\xi}^S \bar{B} 2h}{n\pi}, \\
B_2^{(2)S} &= \frac{(-1)^{(n+1)/2} (c_{12} + r c_{22}) \bar{\xi}^S \bar{B} 2h}{c_{22} n\pi \sin n\pi/2}, \\
B_2^{(1)T} &= \frac{r \bar{\xi}^T \bar{B} 2h}{n\pi}, \\
B_2^{(2)T} &= \frac{(-1)^{n+1/2} (c_{12} + r c_{22}) \bar{\xi}^T \bar{B} 2h}{c_{22} n\pi \sin n\pi/2}, \quad (4.17)
\end{aligned}$$

and with

$$\begin{aligned}
\bar{\xi}^S &= (\bar{\xi}^2 \cos^2 \gamma + \bar{v}^2 \sin^2 \gamma)^{1/2}, \quad \bar{\xi}^T = (\bar{\xi}^2 \cos^2 \gamma + \bar{v}^2 \sin^2 \gamma)^{1/2}, \\
\bar{v}^S &= (\bar{\xi}^2 \sin^2 \gamma + \bar{v}^2 \cos^2 \gamma)^{1/2}, \quad \bar{v}^T = (\bar{\xi}^2 \sin^2 \gamma + \bar{v}^2 \cos^2 \gamma)^{1/2} \quad (4.18)
\end{aligned}$$

Since the coefficient A_{13} essentially couples the antisymmetric with the symmetric solutions, the nearby normalized antisymmetric solution must be included in the perturbation term in the integral for the perturbation of the eigenfrequency. In fact, since the perturbation term from the symmetric solution integrates to zero, the perturbation takes the form^{1,2}

$$\delta \mu = - \frac{1}{2 s \omega_\mu} \int_V A_{13} A_{g,13}^{\mu} S_{g,1}^{\mu} dV, \quad (4.19)$$

where

$$S_{g,1}^{\mu} = \frac{S_{u,1}^{\mu}}{S_N^{\mu}}, \quad A_{g,1}^{\mu} = \frac{A_{u,1}^{\mu}}{A_N^{\mu}}, \quad (4.20)$$

and $S_{u,1}^{\mu}$ is the symmetric trapped energy eigensolution presented in (4.10) and $A_{u,1}^{\mu}$ is the nearby antisymmetric trapped energy eigensolution, which is obtained by replacing $\cos \bar{\xi} x_1$ and $\cos \bar{v} x_3$ in (4.10) by $\sin \bar{\xi} x_1$ and $\sin \bar{v} x_3$, respectively, and, of course, the tangent functions in (4.11) are replaced^{1,2} by cotangent functions. The perturbed frequency ω_1 resulting from the existence of A_{13} is given by

$$\omega_\mu = s \omega_\mu + \delta \mu. \quad (4.21)$$

5. Temperature Dependence of Resonant Frequency

Before the temperature dependence of the resonant frequency of an AT-cut quartz trapped energy resonator can be calculated, the temperature dependence of e_{26} must be estimated from experimental data. This estimate can be most accurately made using data on the temperature dependence of the thickness vibrations of both unelectroded and electroded AT-cut quartz plates. Since this data does not appear to be presently available, we have used the best data we could find¹⁶ in obtaining the estimate of de_{26}/dT , which is on the difference in the temperature dependence of the resonant frequencies of both the fundamental and fifth overtone trapped energy modes. We used the difference in the two temperature dependences, rather than either one separately, because the measurements¹⁶ were made with circular electrodes and the analysis was for circumscribed square electrodes. From the data and the analysis we obtain the estimate¹²

$$(1/e_{26})de_{26}/dT = 1.3 \times 10^{-4}/^{\circ}\text{K}. \quad (5.1)$$

We are now in a position to calculate the change in frequency with temperature from (2.1) for any one trapped energy mode, where from (2.10) for the trapped energy modes we have¹²

$$H_{\mu} = -4 \int_{-h}^h dx_2 \left[\int_0^b dx_1 \left(\int_0^b (\bar{\theta} + \bar{C}) dx_3 + \int_b^{\infty} \bar{\theta}^T dx_3 \right) + \int_0^b dx_1 \left(\int_0^b \bar{\theta}^S dx_3 + \int_b^{\infty} \bar{\theta}^C dx_3 \right) \right], \quad (5.2)$$

where θ for each of the four regions is given by

$$\begin{aligned} \theta = & (\hat{c}_{1111} + \Delta c_{1111}) (g_{1,1} \cos^2 \gamma + g_{3,3} \sin^2 \gamma) \\ & + (\hat{c}_{2121} + \Delta c_{2121}) g_{2,2} + (\hat{c}_{2222} + \Delta c_{2222}) g_{2,2}^2 \\ & + (\hat{c}_{3131} + \Delta c_{3131}) (g_{1,1} \sin^2 \gamma + g_{3,3} \cos^2 \gamma) \\ & + 2(\hat{c}_{1122} + \Delta c_{1122}) g_{2,2} g_{1,1} + 2(\hat{c}_{2112} + \Delta c_{2112}) g_{2,2} g_{1,1}, \end{aligned} \quad (5.3)$$

with the appropriate superscript understood and

$$\bar{C} = -2c_{2122}^2 \frac{1}{e_{26}} \frac{de_{26}}{dT} (T - T_0) \bar{g}_{2,2} \frac{\bar{g}(h)}{h}. \quad (5.4)$$

The $\hat{c}_{LYM\alpha}$ in (5.3) are known as linear expressions in $(T - T_0)$ from the analysis in Sec.3 and the change in the elastic constants with temperature $\Delta g_{LYM\alpha}$ are given by

$$\Delta c_{2LYM\alpha} = (dc_{2LYM\alpha}/dT) (T - T_0), \quad (5.5)$$

where the $dc_{2LYM\alpha}/dT$ are obtained from the first temperature derivatives of the fundamental elastic constants of quartz⁷ $dc_{LYM\alpha}/dT$ referred to the principal axes by the tensor transformation relation

$$\frac{d}{dT} \tilde{c}_{LYM\alpha} = a_{LY}^a a_{YE}^a a_{MF}^a a_{\alpha G}^a \frac{d}{dT} \tilde{c}_{DEFG}, \quad (5.6)$$

where the $a_{Y\alpha}$ are the matrix of direction cosines for the transformation from the principal axes to the coordinate system containing the axes referred to the electroded plate. When the conventional IEEE notation¹⁷ for doubly-rotated plates is written in the form $(Y, X, w, l) \psi, \theta$, where $\psi = 0$, the rotation angles ψ and θ are the first two Euler angles, and for the AT-cut, $\psi = 0^{\circ}$ and $\theta = 35.25^{\circ}$, from which the $a_{\alpha G}$ can be determined. Clearly, the transformation relations for the second and third order elastic, piezoelectric and dielectric constants, and coefficients of linear expansion may be written in the respective forms

$$\begin{aligned} \tilde{c}_{KLMN} &= a_{KD}^a a_{LE}^a a_{MF}^a a_{NG}^a \tilde{c}_{DEFG} \\ \tilde{c}_{KLMNAB} &= a_{KD}^a a_{LE}^a a_{MF}^a a_{NG}^a a_{AH}^a a_{BI}^a \tilde{c}_{DEFGHI}, \\ \tilde{e}_{KLM} &= a_{KD}^a a_{LE}^a a_{MF}^a \tilde{e}_{DEF} \\ \tilde{\alpha}_{KL} &= a_{KM}^a a_{LN}^a \tilde{\alpha}_{MN}, \quad \alpha_{KL} = a_{KM}^a a_{LN}^a \tilde{\alpha}_{MN}, \end{aligned} \quad (5.7)$$

where the tensor quantities with the upper cycle are referred to the principal axes of the crystal.

Calculations have been performed using the known values of the second order elastic, piezoelectric and dielectric constants of quartz¹⁸, the third order elastic¹⁹ and thermoelastic²⁰ constants of quartz and the recently obtained⁷ temperature derivatives of the fundamental elastic constants of quartz. The results of the calculations are presented in Figs.4-8. Figure 4 shows the calculated change in frequency with temperature for an AT-cut quartz plate 1.7 mm thick with 4000 Å thick rectangular gold electrodes as a function of the electrode orientation for the fundamental trapped mode for three b/l ratios for $l/h = 20$. The orientational dependence for the square electrodes is much smaller than for the rectangular electrodes because the squareness tends to reduce the influence of the anisotropy. Figure 5 shows the change in frequency with temperature for the fundamental trapped mode as a function of the l/h ratio for three b/l ratios with $\gamma = 0$. The thickness of both the AT-cut quartz plate and the electrodes is the same as for Fig.4 and, indeed, is maintained for all the figures. Figure 5 clearly shows that the change in frequency with temperature is a rather significant function of the electrode configuration, vanishes when there is no electrode and is asymptotic to the pure thickness vibration value at an l/h ratio of about 70 for the square electrode. This means that the apparent shift in angle for the zero temperature cut depends somewhat significantly on the electrode configuration. Figure 6 shows the change in frequency with temperature due to the presence of the electrodes¹² for the cases treated in Fig.5. Since a portion of the aging rate is a result of the relaxation of residual stress in the electrodes, the change in frequency shown in Fig.6 is the portion of the actual change in the frequency that contributes to the aging rate. Note that the change in frequency with temperature due to the electrodes shown in Fig.6 is about two orders of

magnitude smaller than the actual change shown in Fig. 5. Figure 7 shows the change in frequency with temperature of the fundamental and third and fifth harmonic overtones, as a function of γ for square gold electrodes with $l/h=20$. It can be seen from the figure that both the actual change in frequency and the orientational dependence is much smaller in the harmonics than in the fundamental. Figure 8 shows the change in frequency with temperature of some of the anharmonic overtones of the fifth harmonic as compared with the fifth harmonic as a function of γ for square gold electrodes with $l/h=20$. The figure indicates that the change in frequency with temperature of the anharmonics is considerably larger than that of the fifth harmonic and that the orientational dependence of that of the anharmonics with a different number of nodes in the two directions in the plane of the plate is much greater than for those with the same number of nodes in the two directions.

The results presented here can readily be checked experimentally by successive deposition of differently oriented rectangular electrodes on one quartz plate.

Acknowledgements

We wish to thank R.C. Smythe of Piezo Technology, Inc. for a valuable comment, A. Ballato of the U.S. Army Electronics Technology and Devices Laboratory for several informative discussions and T.J. Lukaszek of the above laboratory for kindly providing the data used in the estimation of $(1/e_{26})de_{26}/dT$.

This work was supported in part by the Army Research Office under Contract No. DAAG 29-79-C-0088, the Office of Naval Research under Contract No. N00014-76-C-0368 and the National Science Foundation under Grant No. ENG 7827637.

References

- H.F. Tiersten, "Perturbation Theory for Linear Electroelastic Equations for Small Fields Superposed on a Bias," *J. Acoust. Soc. Am.*, **64**, 832 (1978).
- H.F. Tiersten and B.K. Sinha, "Temperature Dependence of the Resonant Frequency of Electroded Doubly-Rotated Quartz Thickness-Mode Resonators," *J. Appl. Phys.*, **50**, 8038 (1979).
- R.D. Mindlin, "An Introduction to the Mathematical Theory of the Vibration of Elastic Plates," U.S. Army Signal Corps Eng. Lab., Fort Monmouth, New Jersey (1955). Signal Corps Contract DA-36-03956-56772.
- R.D. Mindlin, "High Frequency Vibrations of Crystal Plates," *Quart. Appl. Math.*, **19**, 51 (1961).
- H.F. Tiersten, *Linear Piezoelectric Plate Vibrations* (Plenum, New York, 1969), Chap. 13.
- H.F. Tiersten, "Analysis of Trapped Energy Resonators Operating in Overtones of Coupled Thickness-Shear and Thickness-Twist," *J. Acoust. Soc. Am.*, **59**, 879 (1976).
- B.K. Sinha and H.F. Tiersten, "First Temperature Derivatives of the Fundamental Elastic Constants of Quartz," *J. Appl. Phys.*, **50**, 2732 (1979).
- M. Onoe, "Relationship Between Temperature Behavior of Resonant and Antiresonant Frequencies and Electromechanical Coupling Factors of Piezoelectric Resonators," *Proc. IEEE*, **57**, 702 (1969).
- A. Ballato, "Apparent Orientation Shifts of Mass-Loaded Plate Vibrators," *Proc. IEEE*, **64**, 1449 (1976).
- A. Ballato and G.J. Iafrate, "The Angular Dependence of Piezoelectric Plate Frequencies and Their Temperature Coefficients," *Proceedings of the 30th Annual Symposium on Frequency Control*, U.S. Army Electronics Command, Fort Monmouth, New Jersey, 141 (1976).
- R. Bechmann, "Influence of the Order of Overtone on the Temperature Coefficient of AT-Type Quartz Resonators," *Proc. IRE*, **43**, 1667 (1955).
- For more detail see D.S. Stevens and H.F. Tiersten, "Temperature Dependence of the Resonant Frequency of Electroded AT-Cut Quartz Trapped Energy Resonators," to be issued as a technical report, Rensselaer Polytechnic Institute, Troy, New York.
- A.E.H. Love, *A Treatise on the Mathematical Theory of Elasticity*, 4th ed. (Cambridge University Press, Cambridge, 1927) also (Dover, New York, 1944) Secs. 18 and 118.
- The expressions for the n th order plate rotations are obtained by substituting from the thickness expansion for the mechanical displacement field into the expression for the three-dimensional small local rotation and proceeding exactly as in the determination of the n th order plate strains obtained in Ref. 3.
- The proper approximate expression for u_2 has been obtained only when $\gamma=0$. When $\gamma \neq 0$ the direct extension of the expression for u_2 is very cumbersome, especially for integrating over the rectangular electrode. Consequently, we use the simpler expression in Eq. (4.14), which reduces to the proper one when $\gamma=0$ and $\gamma=\pi/2$. We do not believe that this simplification results in appreciable error for the purpose for which it is used in this work^{1,2}.
- T.J. Lukaszek, private communication.
- "Standards on Piezoelectric Crystals, 1949," *Proc. IRE*, **37**, 1378 (1949). Since the transformation programs were written before the new IEEE Standard on Piezoelectricity - IEEE Std 176 - 1978 was issued, it was more convenient to use the crystallographic conventions based on the old 1949 Standards.
- R. Bechmann, "Elastic and Piezoelectric Constants of Alpha-Quartz," *Phys. Rev.*, **110**, 1060 (1958).
- R.N. Thurston, H.J. McSkimin and P. Andreatch, Jr., "Third Order Elastic Constants of Quartz," *J. Appl. Phys.*, **37**, 267 (1966).
- F. Kohlrausch, *Lehrbuch der prakt. Physik*, 16. Aufl. 5, 158 (1930). Constants employed in Ref. 21.
- R. Bechmann, A.D. Ballato and T.J. Lukaszek, "Higher Order Temperature Coefficients of the Elastic Stiffnesses and Compliances of Alpha-Quartz," *Proc. IRE*, **50**, 1812 (1962).

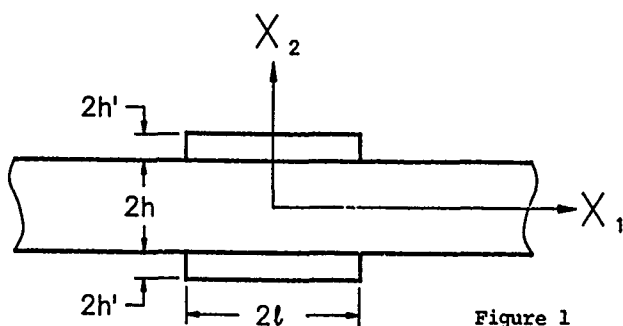


Figure 1
Cross-section of the Trapped Energy Resonator

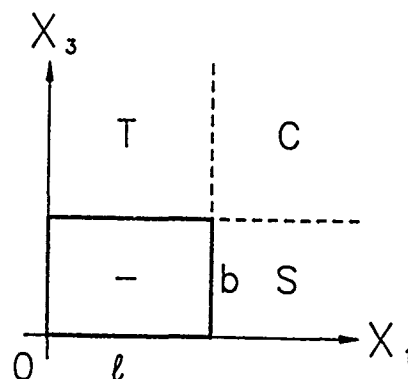


Figure 3
Plan View Showing One Quadrant of the Electroded Plate

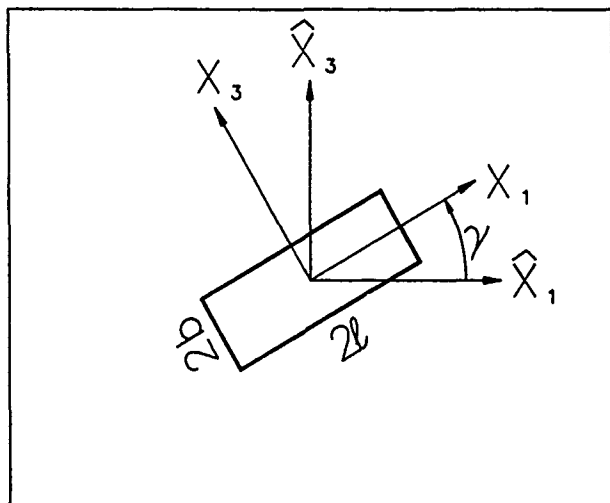


Figure 2
Plan View Showing Orientation of the Rectangular Electrodes with Respect to the Diagonal Axis of the AT-cut Quartz Plate

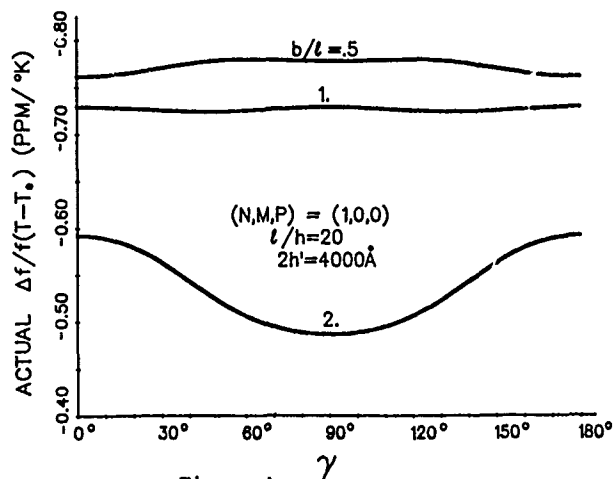


Figure 4

Change in the Resonant Frequency per °K for the Fundamental Trapped Mode as a Function of the Orientation of the Electrodes with Respect to the Diagonal Axis of the 1.7 mm Thick AT-Cut Quartz Plate. The curves are for three different aspect (b/l) ratios of the 4000 Å thick gold electrodes with $l/h = 20$.

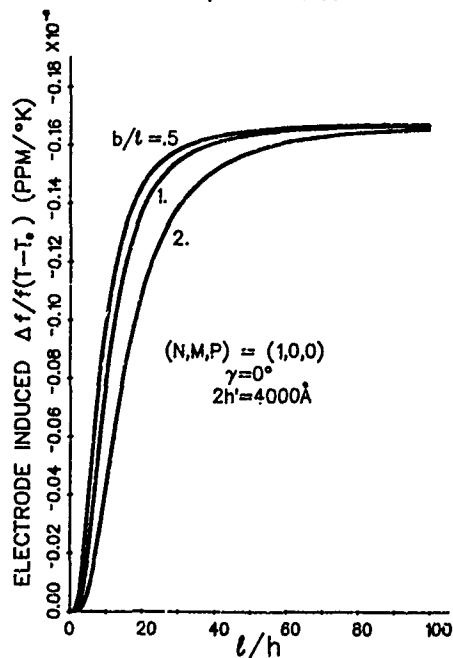


Figure 6

Change in the Resonant Frequency per °K due to the Electrodes for the Cases Treated in Fig. 5

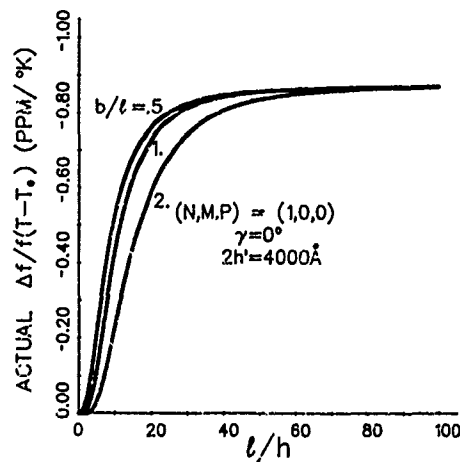


Figure 5

Change in the Resonant Frequency per °K for the Fundamental Trapped Mode as a Function of the l/h Ratio for Three b/l Ratios of 4000 Å Thick Rectangular Gold Electrodes Oriented Along the Diagonal Axis ($\gamma = 0$) of the 1.7 mm Thick AT-Cut Quartz Plate

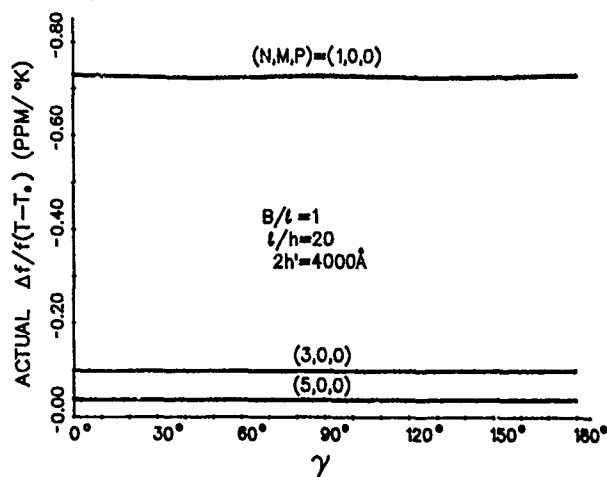


Figure 7 Change in the Resonant Frequency per $^{\circ}\text{K}$ for the Fundamental and Third and Fifth Harmonic Overtone Trapped Modes as a Function of the Orientation of the Electrodes with Respect to the Digonal Axis of the 1.7 mm Thick AT-Cut Quartz Plate. The square gold electrodes are 4000 Å thick and $t/h=20$. The notation N,M,P denotes the number of nodes in the X_2, X_1, X_3 -directions.

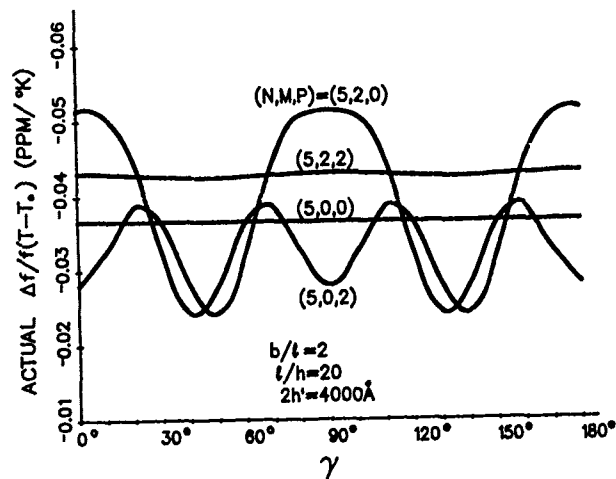


Figure 8 Change in the Resonant Frequency per $^{\circ}\text{K}$ for the Fifth Harmonic and Some of the Anharmonic Overtones of the Fifth Harmonic Trapped Modes as a Function of the Orientation of the Electrodes for the Geometry Considered in Fig.7

TRANSIENT THERMALLY INDUCED FREQUENCY EXCURSIONS IN
DOUBLY-ROTATED QUARTZ THICKNESS-MODE RESONATORS

B.K. Sinha

Schlumberger-Doll Research

P.O. Box 307, Old Quarry Road, Ridgefield, Connecticut 06877

H.F. Tiersten

Department of Mechanical Engineering, Aeronautical Engineering & Mechanics
Rensselaer Polytechnic Institute, Troy, New York 12181

Abstract

The temperature distribution in the quartz plate is obtained from the uncoupled heat conduction equation subject to appropriate initial and boundary conditions. The time-dependent thermally induced biasing state is determined from the exact equations of static linear thermoelasticity for the unelectroded plate and from a system of approximate thermoelastic extensional plate equations for the electroded plate. The time-dependent change in resonant frequency resulting from the thermally induced biasing state is determined from an equation for the perturbation of the eigenfrequency due to a bias. Results are presented for a number of thermally compensated as well as uncompensated cuts of quartz for some physically meaningful temperature inputs.

1. Introduction

A perturbation analysis of the linear electroelastic equations for small fields superposed on a bias has been performed¹. The change in resonant frequency due to any bias such as, e.g., a residual stress may readily be obtained from the resulting equation for the perturbation of the eigenfrequency if the bias is known. In addition, a system of approximate plate equations for the determination of thermal stresses in thin piezoelectric plates coated with large much thinner films was derived² from Mindlin's plate equations³⁻⁵. The resulting approximate equations simplify the treatment of many thermal stress problems considerably, and the three-dimensional detail not included in the approximate description is not deemed to be important for our purposes.

When a quartz resonator is subject to a change in the ambient temperature, it undergoes a time-dependent, inhomogeneous temperature distribution which causes the resonant frequency to drift in time^{6,7} until the new thermal equilibrium state is reached. In this paper the time-dependent, inhomogeneous temperature distribution in the quartz plate is obtained from the uncoupled heat conduction equation for thickness dependence only, subject to the appropriate initial and boundary conditions. Since the heat conduction is sufficiently slow compared to the speed of elastic waves, the mechanical inertia terms can be neglected in the stress equations of motion, thereby reducing them to the quasi-static stress equations of equilibrium. Accordingly, the time-dependent thermally

induced biasing deformation state is determined from the exact equation of static linear thermoelasticity for the unelectroded plate and from the aforementioned system of approximate static thermoelastic plate equations² for the electroded plate. Here, however, the approximate equations are extended to the case of inhomogeneous temperature distributions. In earlier work^{8,9} on thermal transients in unelectroded plates, static equations other than the stress equations of equilibrium and boundary conditions other than the traction free conditions used in the purely static case were employed and we do not understand the reason for this. Since the mechanical inertia is negligible in the slowly varying transient case, the static equations and boundary conditions hold just as in the homogeneous time-independent case.

In the case of both the unelectroded and electroded plates the substitution of the quasi-static thermoelastic three-dimensional displacement field into the above mentioned equation for the perturbation of the eigenfrequency along with the solution¹⁰ for thickness-modes in doubly-rotated quartz plates and the first temperature derivatives of the fundamental elastic constants of quartz¹¹ enables the calculation of the temperature dependence of the resonant frequencies of doubly-rotated quartz thickness-mode resonators due to the time-dependent thermally induced biasing deformation.

The calculated time-dependent change in resonant frequency resulting from the thermally induced biasing state shows that in a thermally uncompensated cut the influence of the electrodes on the change in frequency is small and the frequency shift increases essentially monotonically from one equilibrium state to another. On the other hand, since in a thermally compensated cut the change in frequency in the absence of the electrodes is essentially negligible, the thermally induced biasing deformation state resulting from the presence of the electrodes is the dominant factor causing the frequency change. As a consequence, the calculated frequency shift increases in time considerably beyond the new equilibrium resonant frequency before relaxing to that final equilibrium frequency, in conformity with existing experimental data^{6,7}. The existence of and magnitude of this increase beyond the final equilibrium value depends strongly on the rate of change of the surface temperature and the thermal time constant of the quartz plate. Results are presented for both step and exponential temperature changes. The calculations also show

that when electrodes are not present the time-dependent resonant frequency changes monotonically from one equilibrium state to the other, even for thermally compensated cuts.

2. Perturbation Equations

For purely elastic nonlinearities the equation for the first perturbation of the eigenvalue obtained from the perturbation analysis mentioned in the Introduction may be written in the form

$$\Delta_\mu = H_\mu / 2\omega_\mu, \quad \omega = \omega_\mu - \Delta_\mu, \quad (2.1)$$

where ω_μ and ω are the unperturbed and perturbed eigenfrequencies, respectively, and

$$H_\mu = - \int_V \tilde{K}_{LY}^n g_{Y,L}^\mu dV, \quad (2.2)$$

where V is the undeformed volume of the piezoelectric plate at the reference temperature T_0 . In (2.2) g_Y^μ denotes the normalized mechanical displacement vector, and \tilde{K}_{LY}^n denotes the portion of the Piola-Kirchhoff stress tensor resulting from the biasing state and a change in the elastic constants $\Delta g_{LYM\alpha}$ in the presence of the g_Y^μ , and is given by

$$\tilde{K}_{LY}^n = (\hat{C}_{LYM\alpha} + \Delta C_{2LYM\alpha}) g_{\alpha,M}^\mu \quad (2.3)$$

where

$$\begin{aligned} \hat{C}_{LYM\alpha} = & T_{LM}^1 \delta_{Y\alpha} + C_{LYM\alpha B}^1 E_{AB}^1 + C_{LYKM}^1 w_{\alpha,K} \\ & + C_{2LYKM}^1 w_{Y,K}, \end{aligned} \quad (2.4)$$

and

$$\begin{aligned} T_{LM}^1 = & C_{2LMKN}^1 E_{KN}^1 - v_{LM}(T - T_0), \\ E_{KN}^1 = & \frac{1}{2} (w_{K,N} + w_{N,K}). \end{aligned} \quad (2.5)$$

The quantities T_{LM}^1 , E_{AB}^1 and w_K denote the static biasing stress, strain and displacement field, respectively. Thus, in this description the present position y is related to the reference position \tilde{x} by

$$y(X_L, t) = \tilde{x} + w(X_L) + u(X_L, t). \quad (2.6)$$

The coefficients g_{LMKN} and $g_{LYM\alpha B}$ denote the second and third order elastic constants, respectively, v_{LM} denotes the thermoelastic coupling coefficients and T denotes the present temperature.

The normalized eigensolution g_Y^μ and $\tilde{\varphi}^\mu$ is defined by

$$g_Y^\mu = \frac{u_Y^\mu}{N_\mu}, \quad \tilde{\varphi}^\mu = \frac{\varphi^\mu}{N_\mu}, \quad N_\mu^2 = \int_V \rho u_Y^\mu u_Y^\mu dV, \quad (2.7)$$

where u_Y^μ and φ^μ are the mechanical displacement and electric potential, respectively, which satisfy the equations of linear piezoelectricity

$$\tilde{K}_{LY}^L = \tilde{C}_{LYM\alpha} u_{\alpha,M} + e_{MLY} \tilde{\varphi}_{,M},$$

$$\tilde{D}_L^L = e_{LMY} u_{Y,M} - \epsilon_{LM} \tilde{\varphi}_{,M}, \quad (2.8)$$

$$\tilde{K}_{LY,L}^L = \rho \ddot{u}_Y, \quad \tilde{D}_{L,L}^L = 0, \quad (2.9)$$

subject to the appropriate boundary conditions, and ρ is the mass density. Equations (2.8) are the linear piezoelectric constitutive relations and (2.9) are the stress equations of motion and charge equation of electrostatics, respectively. The upper case notation for many dynamic variables and the capital Latin and lower case Greek index notation is being employed for consistency with Ref.1, as is the remainder of the notation in this section. The change in the pertinent piezoelectric thickness constants with temperature that was discussed in the work^{1,2} on the temperature dependence of trapped energy resonators was not included here because they are not known for doubly-rotated orientations and for the pure thickness vibrations considered here those terms only introduce a constant difference in the temperature behavior of the fully electroded and unelectroded plate which depends on the orientation of the crystal.

3. Temperature Induced Biasing State

A schematic diagram of the electroded crystal plate is shown in Fig.1 along with the associated coordinate system. It has been shown³ that referred to this coordinate system the static (here quasi-static) purely extensional thermoelastic plate equations for the plated crystal plate may be written in the form

$$\chi_{AB,A}^{(0)} = 0, \quad \chi_{AB,A}^{(2)} = 0, \quad (3.1)$$

where A, B, C, D take the values 1 and 3 and skip 2 and $\chi_{AB}^{(0)}$ and $\chi_{AB}^{(2)}$ are the zero and second order plate stress resultants, respectively, for the electroded crystal plate. For inhomogeneous temperature states and identical electrodes on the upper and lower surfaces the extensional constitutive equations may be written in the form⁴

$$\begin{aligned} \chi_{AB}^{(0)} = & 2h \left(\gamma_{ABCD} + \frac{2h'}{h} \gamma'_{ABCD} \right) E_{CD}^{(0)} + 2h^3 \left(\frac{1}{3} \gamma_{ABCD} + \frac{2h'}{h} \gamma'_{ABCD} \right) E_{CD}^{(2)} - 2h \left(\beta_{AB}^{(0)} + \frac{2h'}{h} \beta_{AB}^{(2)} \right) (\bar{T} - T_0), \\ \chi_{AB}^{(2)} = & \frac{2}{3} h^3 \left(\gamma_{ABCD} + \frac{6h'}{h} \gamma'_{ABCD} \right) E_{CD}^{(0)} + \frac{2}{5} h^5 \left(\gamma_{ABCD} + \frac{10h'}{h} \gamma'_{ABCD} \right) E_{CD}^{(2)} - \frac{2}{3} h^3 \left(\beta_{AB}^{(2)} + \frac{6h'}{h} \beta_{AB}^{(2)} \right) (\bar{T} - T_0), \end{aligned} \quad (3.2)$$

where \bar{T} is the electrode temperature, $\beta_A^{(0)}$ and $\beta_A^{(2)}$ are defined in terms of integrals over the inhomogeneous temperature distribution through the thickness^{1,4}

$$\beta_R^{*'} = v_R' - v_{2R}' c_{22}' / c_{22}', \quad (3.3)$$

and we have introduced the compressed notation for tensor indices according to

$$R, S = 1, 3, 5; \quad W, V = 2, 4, 6, \quad (3.4)$$

$$\gamma_{RS} = c_{RS} - c_{RW} c_{WV}^{-1} c_{VS}. \quad (3.5)$$

The γ_{RS} are Voigt's anisotropic plate elastic constants and the $\beta_R^{(*)}$ are the effective anisotropic plate thermoelastic constants. For the case of anisotropic extension considered here the three-dimensional strains E_{KL} , which are needed in the perturbation equation, are related to the plate strains by

$$E_{KL} = \frac{1}{2} (w_{K,L} + w_{L,K}) = E_{KL}^{(0)} + X_2^2 E_{KL}^{(2)}. \quad (3.6)$$

The plate strains $E_{AB}^{(n)}$ ($n=0,2$), which occur in (3.2), are given by

$$E_{AB}^{(n)} = \frac{1}{2} (w_{A,B}^{(n)} + w_{B,A}^{(n)}), \quad (3.7)$$

and the remaining plate strains, which are needed in (3.6) as well, may be obtained from¹⁴

$$E_W^{(0)} = -c_{WV}^{-1} c_{VS} E_S^{(0)} + c_{WV}^{-1} \left(\frac{9}{4} v_V^{(0)} - \frac{5}{4} v_V^{(2)} \right) (\bar{T} - T_0),$$

$$E_W^{(2)} = -c_{WV}^{-1} c_{VS} E_S^{(2)} + \frac{15}{4h} c_{WV}^{-1} (v_V^{(2)} - v_V^{(0)}) (\bar{T} - T_0), \quad (3.8)$$

In Fig.1, the X_2 -coordinate axis is normal to the major surfaces of the plate at $T=T_0$. Since the outside edges of the plate are traction free, we have

$$N_A \chi_{AB}^{(0)} = 0, \quad N_A \chi_{AB}^{(2)} = 0 \quad \text{on outside edges}, \quad (3.9)$$

where N_A denotes the outwardly directed unit normal to the edge of the plate at $T=T_0$. The solution satisfying (3.1) and (3.9) takes the form

$$\chi_{AB}^{(0)} = 0, \quad \chi_{AB}^{(2)} = 0. \quad (3.10)$$

This solution is unique to within static homogeneous plate rotations of zero and second order. Substituting from (3.2) into (3.10), we obtain

$$\left(\gamma_{RS} + \frac{2h'}{h} \gamma_{RS}' \right) E_S^{(0)} + h^2 \left(\frac{\gamma_{RS}}{3} + \frac{2h'}{h} \gamma_{RS}' \right) E_S^{(2)}$$

$$= \left(\beta_R^{(0)} + \frac{2h'}{h} \beta_R^{(2)} \right) (\bar{T} - T_0),$$

$$\left(\gamma_{RS} + \frac{6h'}{h} \gamma_{RS}' \right) E_S^{(0)} + h^2 \left(\frac{3}{5} \gamma_{RS} + \frac{6h'}{h} \gamma_{RS}' \right) E_S^{(2)}$$

$$= \left(\beta_R^{(2)} + \frac{6h'}{h} \beta_R^{(0)} \right) (\bar{T} - T_0). \quad (3.11)$$

Equations (3.11) constitute six inhomogeneous linear equations which may readily be solved for the six plate strains $E_S^{(0)}$ and $E_S^{(2)}$. When $E_S^{(0)}$ and $E_S^{(2)}$ have been determined from (3.11), $E_W^{(0)}$ and $E_W^{(2)}$ are readily determined from (3.8). Then the three-dimensional biasing strain can be obtained from (3.6), which is for anisotropic extension. There is no flexure because the resonator has identical electrodes which are subject to the same temperature change $(\bar{T} - T_0)$.

It is well known that in static linear elasticity the solution to a boundary value problem is unique only to within a static homogeneous (global) infinitesimal rigid rotation¹³. Similarly, as

noted in Sec.3 of Ref.12, the solution to the static approximate plate equations is unique only to within homogeneous infinitesimal n th order plate rotations $\Omega_{KL}^{(n)}$, and when the equations of equilibrium for the plate stress resultants, (3.1), are satisfied trivially, as is the case here, the relaxation of the stress resultants, (3.10), results in homogeneous plate strains $E_{KL}^{(n)}$ and plate rotations $\Omega_{KL}^{(n)}$, which are consistent with three-dimensional strain gradient - rotation gradient relations¹⁴. Accordingly, as in Ref.12, we may write

$$w_{L,K} = E_{KL}^{(0)} + X_2^2 E_{KL}^{(2)} + \Omega_{KL}^1, \quad (3.12)$$

which provides the biasing displacement gradients $w_{K,N}$ as a known time-dependent linear function of $(T - T_0)$ and where Ω_{KL}^1 is the consistent¹⁴ rotation field. Thus, we may now obtain \hat{c}_{LYM} in (2.4) as a known linear function of $(T - T_0)$ for the electroded plate.

The foregoing has been for the fully electroded plate. In the case of the unelectroded plate the situation is somewhat simpler and since as noted in the Introduction, the mechanical inertia can be neglected in the stress equations of motion, we have the quasi-static stress equations of equilibrium

$$T_{ML,M}^1 = 0, \quad (3.13)$$

along with the constitutive equations (2.5)₁. Since the outside edges of the plate are traction free along with the major surfaces, we have

$$N_M T_{ML}^1 = 0, \quad (3.14)$$

where N_M denotes the unit normal to all surfaces of the plate at $T=T_0$. From (3.13) and (3.14) we have

$$T_{ML}^1 = 0, \quad (3.15)$$

for the unelectroded plate. Since the thermoelastic coupling constants v_{ML} are related to the coefficients α_{JK} by the usual relation

$$v_{ML} = c_{MLJK} \alpha_{JK}, \quad (3.16)$$

from (2.5)₁, (3.15) and (3.16), we have

$$E_{JK}^1 = \alpha_{JK} (\bar{T} - T_0). \quad (3.17)$$

In the case of the unelectroded plate the time-dependent inhomogeneous strain state is given by (3.17) and we note that when the quasi-static stress equations of equilibrium, (3.13), are satisfied trivially, as is the case here, the vanishing of the stresses, (3.15) results in time-dependent inhomogeneous strains E_{KL}^1 and consistent¹⁴ rotations Ω_{KL}^1 , where

$$\Omega_{KL}^1 = \frac{1}{2} (w_{L,K} - w_{K,L}), \quad (3.18)$$

which with (2.5)₂ and (3.17) yields¹⁴

$$w_{J,K} = \alpha_{JK}(T - T_0) + \Omega_{JK}^1, \quad (3.19)$$

where Ω_{JK}^1 is linear in $(T - T_0)$. The substitution of (3.17), (3.19) and (3.15) in (2.4) yields \tilde{c}_{LYM} as a known linear function of $(T - T_0)$ in the unelectroded region.

4. Temperature Dependence

The temperature behavior of the plate shown in Fig. 1 is obtained by satisfying the uncoupled one-dimensional heat conduction equation

$$k_{22} \frac{\partial^2 T}{\partial x_2^2} = C_s \frac{\partial T}{\partial t}, \quad (4.1)$$

subject to appropriate initial and boundary conditions at $x_2 = \pm h$. In (4.1) k_{22} is the thermal conductivity in the x_2 -direction and C_s is the specific heat. If the surfaces are subject to a step rise in temperature $(T - T_0)$, the initial and boundary conditions are

$$T(x_2, t) = T_0, \quad t = 0, \quad (4.2)$$

$$T = \bar{T}, \quad \text{at } x_2 = \pm h. \quad (4.3)$$

The solution to Eq. (4.1) subject to conditions (4.2) and (4.3) can be written in the form¹⁵

$$T(x_2, t) = \bar{T} - \frac{4(\bar{T} - T_0)}{\pi} \sum_{n=0}^{\infty} \frac{(-1)^n}{(2n+1)} e^{-\kappa_{22}^2 \zeta_n^2 t} \cos \zeta_n x_2, \quad (4.4)$$

where

$$\kappa_{22} = k_{22}/C_s, \quad \zeta_n = (2n+1)\pi/2h. \quad (4.5)$$

If the surfaces of the plate are subject to a time varying exponential rise in surface temperature from T_0 to \bar{T} , the initial and boundary conditions are

$$T(x_2, t) = T_0, \quad t = 0, \quad (4.6)$$

$$T = \bar{T}(1 - e^{-\beta t}), \quad \text{at } x_2 = \pm h, \quad (4.7)$$

and we note that the magnitude of β determines the sharpness of the temperature rise. The solution to (4.1) subject to conditions (4.6) and (4.7) can be written in the form¹⁵

$$T(x_2, t) = \bar{T} - (\bar{T} - T_0) e^{-\beta t} \frac{\cos(\beta/\kappa_{22})^{1/2} x_2}{\cos(\beta/\kappa_{22})^{1/2} h} - \frac{4\beta}{\pi} (\bar{T} - T_0) \sum_{n=0}^{\infty} \frac{(-1)^n}{(2n+1)} \frac{e^{-\kappa_{22}^2 \zeta_n^2 t} \cos \zeta_n x_2}{(\beta - \kappa_{22}^2 \zeta_n^2)}, \quad (4.8)$$

provided $\beta \neq \kappa_{22}^2 \zeta_n^2$. Equations (4.4) or (4.8) can readily be used in the appropriate equations in Sec. 3 to obtain the displacement gradients $w_{K,L}$ as

a known function of x_2 and t and the given temperature data.

5. Time Dependent Change in Resonant Frequency with Temperature

The solution for thickness-modes in arbitrarily anisotropic piezoelectric plates with shorted electrodes on the major surfaces, which are normal to the x_2 -direction, may be written in the form¹⁰

$$u_Y = \sum_{n=1}^3 B^{(n)} \beta_Y^{(n)} \sin \eta_n x_2 e^{i\omega t},$$

$$\varphi = \left[\frac{e_{22Y}}{\epsilon_{22}} u_Y + iX_2 \right] e^{i\omega t}, \quad (5.1)$$

where

$$L = -\frac{1}{h} \sum_{n=1}^3 B^{(n)} \frac{e_{22Y}}{\epsilon_{22}} \beta_Y^{(n)} \sin \eta_n h, \quad (5.2)$$

and the $\beta_Y^{(n)}$ are the normalized eigenvectors of the linear homogeneous algebraic system for the eigenvalues of $\tilde{c}^{(n)}$ of the piezoelectrically stiffened elastic constants, which is given by

$$(\bar{c}_{2Y\alpha 2} - \bar{c}^{(n)} \delta_{Y\alpha}) \beta_\alpha^{(n)} = 0, \quad \bar{c}_{2Y\alpha 2} = c_{2Y\alpha 2} + \frac{e_{22Y} e_{22\alpha}}{\epsilon_{22}}, \quad (5.3)$$

and the $B^{(n)}$ are given by

$$B^{(n)} = -\beta_\alpha^{(n)} e_{22\alpha} L / \bar{c}^{(n)} \eta_n [\cos \eta_n h - R \eta_n h \sin \eta_n h]. \quad (5.4)$$

Substituting from (5.4) into (5.2), we obtain

$$L \left[1 - \sum_{n=1}^3 (k^{(n)})^2 / \eta_n h (\cot \eta_n h - R \eta_n h) \right] = 0, \quad (5.5)$$

where

$$(k^{(n)})^2 = \frac{\beta_Y^{(n)} e_{22Y} \beta_\alpha^{(n)} e_{22\alpha}}{\bar{c}^{(n)} \epsilon_{22}}, \quad R = \frac{2\rho' h'}{\rho h}. \quad (5.6)$$

The condition for a nontrivial solution of the scalar equation (5.5) is

$$\sum_{n=1}^3 (k^{(n)})^2 / \eta_n h (\cot \eta_n h - R \eta_n h) = 1, \quad (5.7)$$

the roots of which determine the resonant frequencies of thickness vibration of piezoelectric plates driven by the application of a voltage across the surface electrodes. From this unperturbed thickness eigensolution, we can determine the normalized eigensolution we need for the perturbation formulation in Sec. 2 simply by writing

$$g_Y = u_Y/N, \quad \hat{f} = \tilde{\varphi}/N, \quad (5.8)$$

where, from (2.7)₃ and (5.1), we find

$$N^2 = \rho \sum_{m=1}^3 \sum_{n=1}^3 B^{(m)} \beta_Y^{(m)} B^{(n)} \beta_Y^{(n)} \left[\frac{\sin(\eta_m - \eta_n)h}{\eta_m - \eta_n} - \frac{\sin(\eta_m + \eta_n)h}{\eta_m + \eta_n} \right]. \quad (5.9)$$

The change in the frequency of thickness vibrations with time-dependent temperature changes of any electroded quartz plate may now be determined from (2.1), which we rewrite here for any one mode in the form

$$\Delta_M = H_M / 2\omega_M, \quad \omega = \omega_M - \Delta, \quad (5.10)$$

where for the case of thickness vibrations, we have

$$H_M = - \int_{-h}^h \tilde{K}_{2Y}^n g_{Y,2}^M dx_2. \quad (5.11)$$

From (2.3) for the thickness-mode being perturbed here, we have

$$\tilde{K}_{2Y}^n = (\hat{c}_{2Y2\alpha} + \Delta c_{2Y2\alpha}) g_{\alpha,2}^M, \quad (5.12)$$

where $\hat{c}_{2Y2\alpha}$ is known as a space and time-dependent linear expression in $(T - T_0)$ from the analyses in Secs. 3 and 4 and

$$\Delta c_{2Y2\alpha} = (dc_{2Y2\alpha}/dT) (T - T_0). \quad (5.13)$$

The $dc_{2Y2\alpha}/dT$ are obtained from the temperature derivatives of the fundamental elastic constants of quartz $dc_{0\alpha\beta\gamma}/dT$ referred to the principal axes, which have now been determined¹¹, by the tensor transformation relation

$$\frac{d}{dT} c_{2Y2\alpha} = a_{2D}^a a_{YE}^a a_{2F}^a a_{\alpha G}^a \frac{d}{dT} c_{DEFG}, \quad (5.14)$$

where the a_{YE} are the matrix of direction cosines for the transformation from the principal axes to the coordinate system containing the axis normal to the plane of the plate. When the conventional IEEE notation⁶ for doubly-rotated plates is written in the form $(Y, X, W, \ell)\eta, \theta$ where $\psi = 0$, the rotation angles ϕ and θ are the first two Euler angles, from which the a_{YE} for any doubly-rotated plate can be determined in the usual manner¹⁴. Clearly, the transformation relations for the second and third order elastic, piezoelectric and dielectric constants, and coefficients of linear expansion may be written in the respective forms

$$\begin{aligned} c_{2KLMN} &= a_{KD}^a a_{LE}^a a_{MF}^a a_{NG}^a \tilde{c}_{DEFG}, \\ c_{3KLMNAB} &= a_{KD}^a a_{LE}^a a_{MF}^a a_{NG}^a a_{AH}^a a_{BI}^a \tilde{c}_{DEFGHI}, \\ e_{KLM} &= a_{KD}^a a_{LE}^a a_{MF}^a \tilde{e}_{DEF}, \\ \epsilon_{KL} &= a_{KM}^a a_{LN}^a \tilde{\epsilon}_{MN}, \quad \alpha_{KL} = a_{KM}^a a_{LN}^a \tilde{\alpha}_{MN}, \end{aligned} \quad (5.15)$$

where the tensor quantities with the upper cycle are referred to the principal axes of the crystal.

Calculations of the resonant frequency, called ω_M here, for the particular unperturbed thickness-mode of interest may now be performed¹⁴ by finding the appropriate root ω_M of (5.7), with (5.3)₁ and the relations

$$\tilde{c}^{(n)} = \rho \omega_M^2 / \eta_n^2. \quad (5.16)$$

Then the perturbation integral H_1 can be evaluated by employing (5.12) and (5.8)₁ in (5.11) and performing the integrations¹⁴. Such calculations have been performed using the known values of the second order elastic, piezoelectric and dielectric constants of quartz¹⁷, the third order elastic¹⁸ and thermoelastic¹⁹ constants of quartz and the recently obtained¹¹ temperature derivatives of the fundamental elastic constants of quartz. Specific calculations have been made for a number of singly and doubly-rotated quartz plates 1.7 mm thick. Typical results of some of the calculations are presented in Figs. 2-10, each of which shows the relative change in frequency with time for the fundamental and third and fifth harmonics of the C-mode for different orientations of the quartz plate and surface and temperature conditions. Figures 2-4 are for the thermally compensated AT-cut quartz plate. Figure 2 is for the unelectroded resonator subject to a step rise in surface temperature. It can be seen from the figure that the frequency changes monotonically in time and reaches the new equilibrium value in about one-half second. Figure 3 is for a resonator with 2000 Å thick gold electrodes on the surfaces, which are subject to a step rise in temperature. The figure shows that the change in frequency overshoots the final equilibrium value considerably before relaxing to that value in a very short time. Figure 4 is for the same electrodes as Fig. 3, but the surfaces are subject to the exponential change in temperature discussed in Sec. 4 for a rise time $(1/\beta)$ of 1/10 of a second. Again the figure shows, even more clearly this time, that the change in frequency overshoots the final equilibrium value considerably before relaxing to that value in a very short time. Figures 5-7 are for the thermally compensated BT-cut quartz plate. Figures 5-7 for the BT-cut are respectively similar to Figs. 2-4 for the AT-cut and reveal the same type of behavior in each instance. Figures 8-10 are for the thermally uncompensated LC-cut quartz plate which in fact is used as a thermometer because its resonant frequency is linearly sensitive to temperature. Figure 8 is for the unelectroded resonator subject to a step rise in temperature and, as before, the frequency changes monotonically to the final equilibrium value. Figure 9 is for an electroded resonator subject to a step rise in surface temperature and shows that the frequency changes monotonically in time to the final equilibrium value in essentially the same way as in the unelectroded case shown in Fig. 8. Clearly, this behavior of the thermally uncompensated cut is in contradistinction to the behavior of the electroded compensated cuts shown in Figs. 3 and 6, in which the frequency shifts considerably beyond the final equilibrium value before relaxing to that value. Figure 10 is for an electroded resonator subject to an exponential change in surface temperature with a rise time of 300 sec and shows, of course, that the frequency changes monotonically to the

final equilibrium value in a considerably longer time than in the case of the step rise. It should be noted that in the case of the thermally uncompensated cuts, in which the change in frequency overshoots the final equilibrium value for the case of the step rise and exponential rise in surface temperature for short rise times, the overshoot is nonexistent for long rise times. Finally, Figs. 11-13 are for the thermally compensated SC-cut quartz plate. Figures 11 and 12 for the SC-cut are respectively similar to Figs. 2 and 3 for the AT-cut and 5 and 6 for the BT-cut and clearly reveal the same type of behavior in each instance. On the other hand Fig. 13, which is for an electroded resonator subject to an exponential change in surface temperature with a large rise time of 300 sec, does not exhibit the overshoot and instead exhibits monotonic behavior to the final equilibrium frequency similar to that of Fig. 11 for the unelectroded plate subject to a step rise in temperature, but in a considerably longer time because of the large rise time. This is in accordance with the above-mentioned behavior of electroded thermally compensated cuts for long exponential rise times.

Acknowledgements

One of the authors (BKS) wishes to thank Dr. R.P. Potter for his support and encouragement. The work of the other author (HFT) was supported in part by ARO Contract No. DAAG 29-79-C-0088 and NSF Grant No. ENG 7827637.

References

1. H.F. Tiersten, "Perturbation Theory for Linear Electroelastic Equations for Small Fields Superposed on a Bias," *J. Acoust. Soc. Am.*, **64**, 832 (1978).
2. H.F. Tiersten and B.K. Sinha, "Temperature Dependence of the Resonant Frequency of Electroded Doubly-Rotated Quartz Thickness-Mode Resonators," *J. Appl. Phys.*, **50**, 8038 (1979).
3. R.D. Mindlin, "An Introduction to the Mathematical Theory of the Vibration of Elastic Plates," *U.S. Army Signal Corps Eng. Lab.*, Fort Monmouth, New Jersey (1955). Signal Corps Contract DA-36-03956-56772.
4. R.D. Mindlin, "High Frequency Vibrations of Crystal Plates," *Quart. Appl. Math.*, **19**, 51 (1961).
5. H.F. Tiersten, *Linear Piezoelectric Plate Vibrations* (Plenum, New York, 1969), Chap. 13.
6. A.W. Warner, "Use of Parallel-Field Excitation in the Design of Quartz Crystal Units," *Proceedings of the 17th Annual Frequency Control Symposium*, U.S. Army Electronics Research and Development Laboratory, Fort Monmouth, New Jersey, 248 (1963).
7. A. Ballato and J. Vig, "Static and Dynamic Frequency-Temperature Behavior of Singly and Doubly-Rotated, Oven-Controlled Quartz Resonators," *Proceedings of the 32nd Annual Symposium on Frequency Control*, U.S. Army Electronics Research and Development Command, Fort Monmouth, New Jersey, 180 (1978).
8. R. Holland, "Nonuniformly Heated Anisotropic Plates: I. Mechanical Distortion and Relaxation," *IEEE Trans. Sonics Ultrason.*, **SU-21**, 171 (1974).
9. G. Théobald, G. Marianneau, R. Prétot and J.J. Gagnepain, "Dynamic Thermal Behavior of Quartz Resonators," *Proceedings of the 33rd Annual Symposium on Frequency Control*, U.S. Army Electronics Research and Development Command, Fort Monmouth, New Jersey, 239 (1979).
10. H.F. Tiersten, "Thickness Vibrations of Piezoelectric Plates," *J. Acoust. Soc. Am.*, **35**, 53 (1963).
11. B.K. Sinha and H.F. Tiersten, "First Temperature Derivatives of the Fundamental Elastic Constants of Quartz," *J. Appl. Phys.*, **50**, 2732 (1979).
12. D.S. Stevens and H.F. Tiersten, "Temperature Induced Frequency Changes in Electroded AT-Cut Quartz Trapped Energy Resonators," *Proceedings of the 34th Annual Symposium on Frequency Control*, U.S. Army Electronics Research and Development Command, Fort Monmouth, New Jersey, these proceedings (1980).
13. A.E.H. Love, *A Treatise on the Mathematical Theory of Elasticity*, 4th ed. (Cambridge University Press, Cambridge, 1927) also (Dover, New York, 1944) Secs. 18 and 118.
14. For more detail see B.K. Sinha and H.F. Tiersten, "Transient Temperature Dependence of the Resonant Frequency of Doubly-Rotated Quartz Resonators," to be issued as a technical report, Rensselaer Polytechnic Institute, Troy, New York.
15. H. Carslaw and J. Jaeger, *Conduction of Heat in Solids* (Oxford University Press, 1959).
16. "Standards on Piezoelectric Crystals, 1949," *Proc. IRE*, **37**, 1378 (1949). Since the transformation programs were written before the new IEEE Standard on Piezoelectricity - IEEE Std 176 - 1978 was issued, it was more convenient to use the crystallographic conventions based on the old 1949 Standards.
17. R. Bechmann, "Elastic and Piezoelectric Constants of Alpha-Quartz," *Phys. Rev.*, **110**, 1060 (1958).
18. R.N. Thurston, H.J. McSkimin and P. Andreatch, Jr., "Third Order Elastic Constants of Quartz," *J. Appl. Phys.*, **37**, 267 (1966).
19. F. Kohlrausch, *Lehrbuch der prakt. Physik*, 16. Aufl. 5. 158 (1930). Constants employed in Ref. 20.
20. R. Bechmann, A.D. Ballato and T.N. Lukaszek, "Higher Order Temperature Coefficients of the Elastic Stiffnesses and Compliances of Alpha-Quartz," *Proc. IRE*, **50**, 1812 (1962).

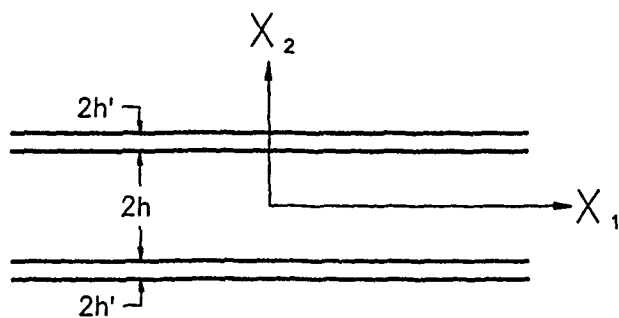


Figure 1

Figure 1. Schematic diagram of the electroded crystal plate along with the associated coordinate system.

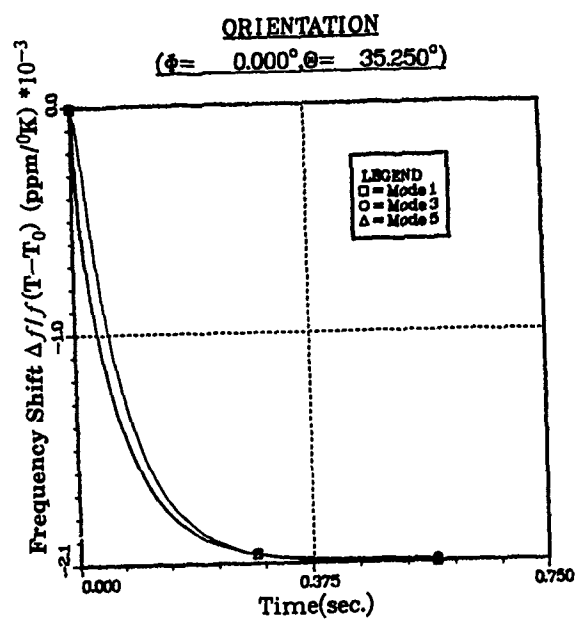


Figure 2

Time-dependent Frequency Shift per $^\circ\text{K}$ for Unelectroded Quartz Resonator Subject to a Step Rise in Surface Temperature. Quartz plates are 1.7 mm thick for all figures.

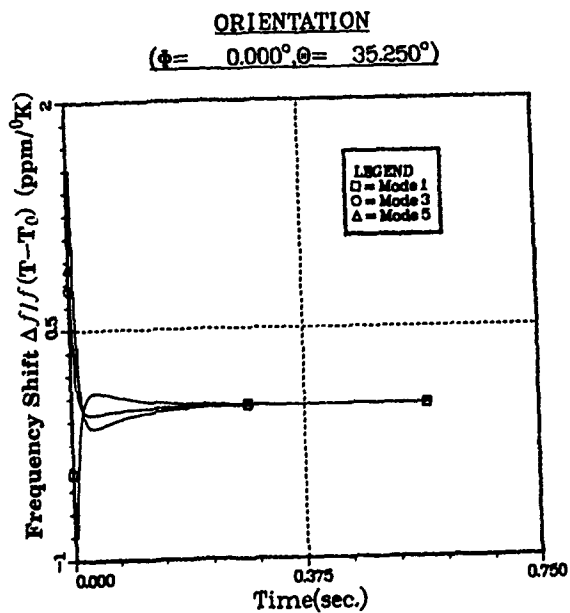


Figure 3

Time-dependent Frequency Shift per $^\circ\text{K}$ for Quartz Resonator with 2000 Å Thick Gold Electrodes Subject to a Step Rise in Surface Temperature

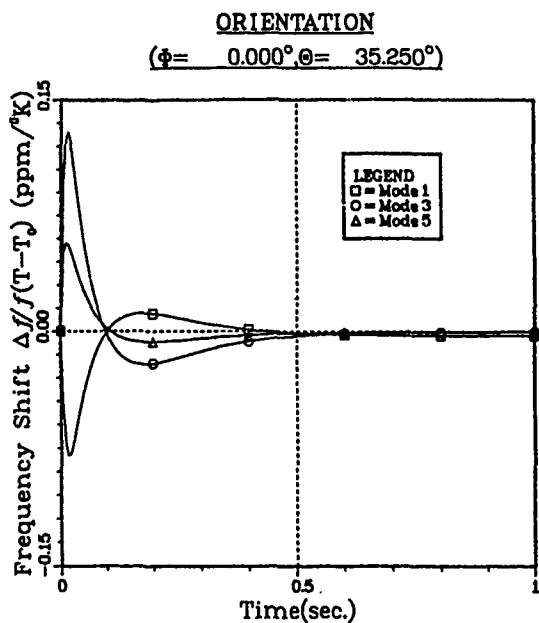


Figure 4

Time-dependent Frequency Shift per $^\circ\text{K}$ for Quartz Resonator with 2000 Å Thick Gold Electrodes Subject to a Surface Temperature $\bar{T}(1 - e^{-\beta t})$ for $\beta = 10.0 \text{ sec}^{-1}$

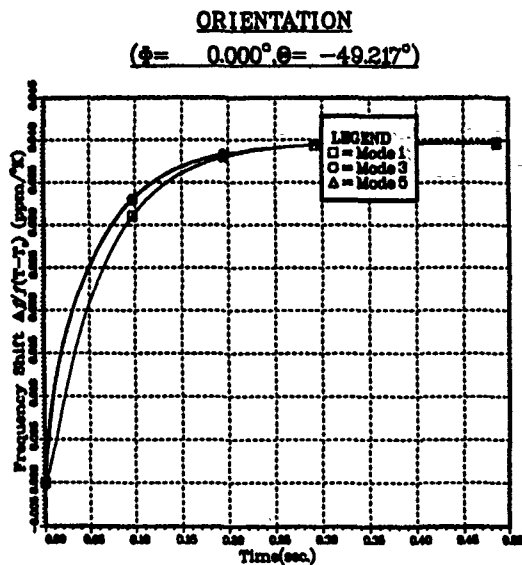


Figure 5

Time-dependent Frequency Shift per $^\circ\text{K}$ for Unelectroded Quartz Resonator Subject to a Step Rise in Surface Temperature

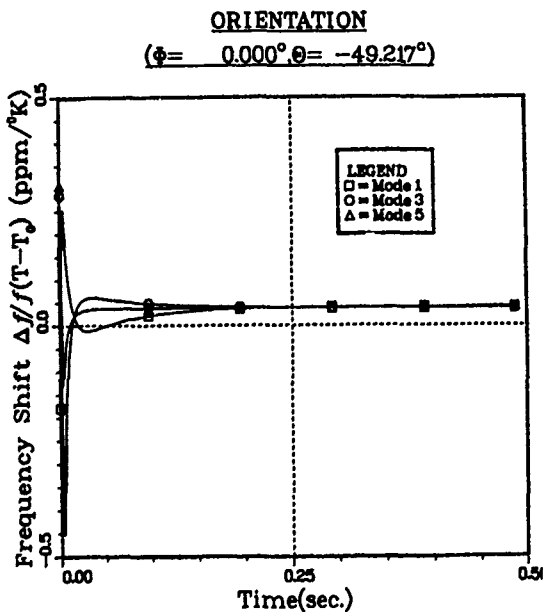


Figure 6

Time-dependent Frequency Shift per $^\circ\text{K}$ for Quartz Resonator with 2000 Å Thick Gold Electrodes Subject to a Step Rise in Surface Temperature

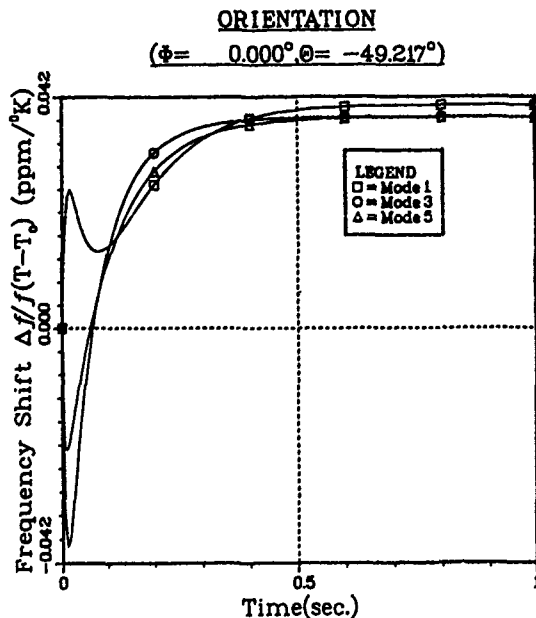


Figure 7

Time-dependent Frequency Shift per $^\circ\text{K}$ for Quartz Resonator with 2000 Å Thick Gold Electrodes Subject to a Surface Temperature $\bar{T}(1 - e^{-\beta t})$ for $\beta = 10.0 \text{ sec}^{-1}$

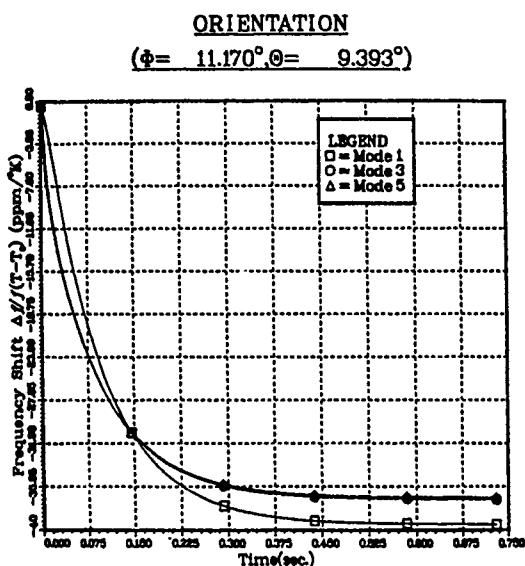


Figure 8

Time-dependent Frequency Shift per $^\circ\text{K}$ for Unelectroded Quartz Resonator Subject to a Step Rise in Surface Temperature

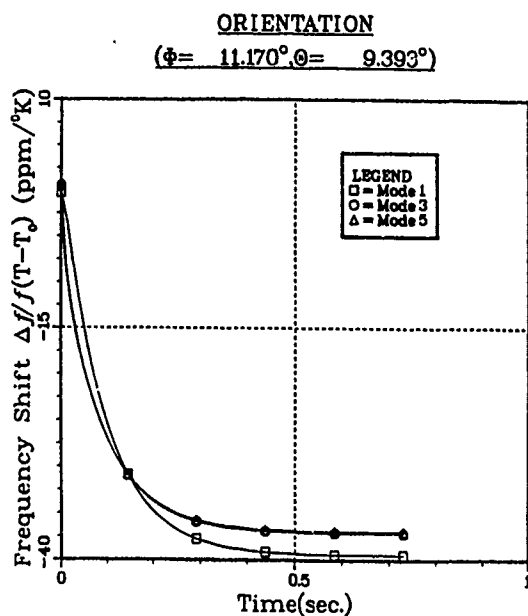


Figure 9

Time-dependent Frequency Shift per $^\circ\text{K}$ for Quartz Resonator with 2000 Å Thick Gold Electrodes Subject to a Step Rise in Surface Temperature

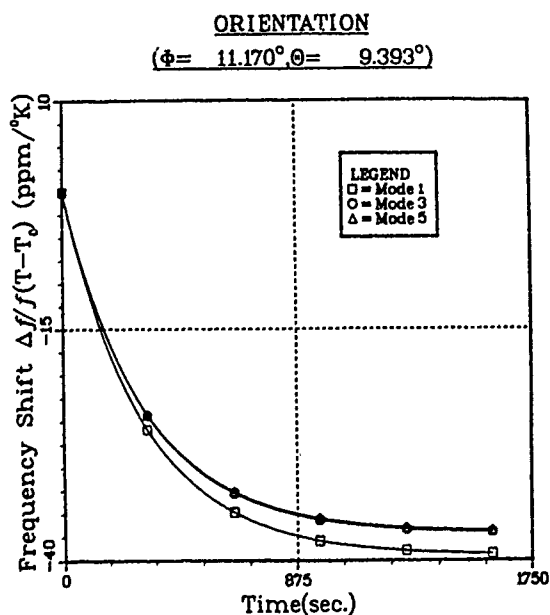


Figure 10

Time-dependent Frequency Shift per $^\circ\text{K}$ for Quartz Resonator with 2000 Å Thick Gold Electrodes Subject to a Surface Temperature $\bar{T}(1 - e^{-\beta t})$ for $\beta = 1/300 \text{ sec}^{-1}$

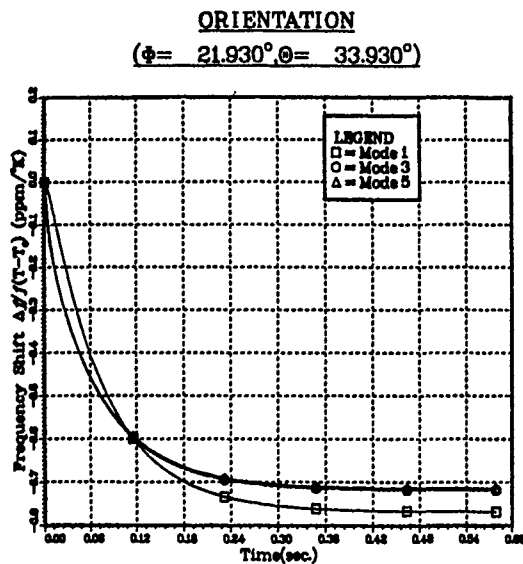


Figure 11

Time-dependent Frequency Shift per $^\circ\text{K}$ for Unelectroded Quartz Resonator Subject to a Step Rise in Surface Temperature

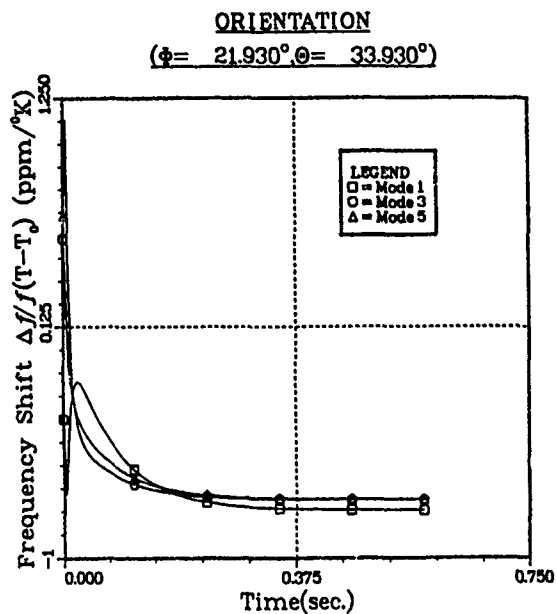


Figure 12

Time-dependent Frequency Shift per $^\circ\text{K}$ for Quartz Resonator with 2000 Å Thick Gold Electrodes Subject to a Step Rise in Surface Temperature

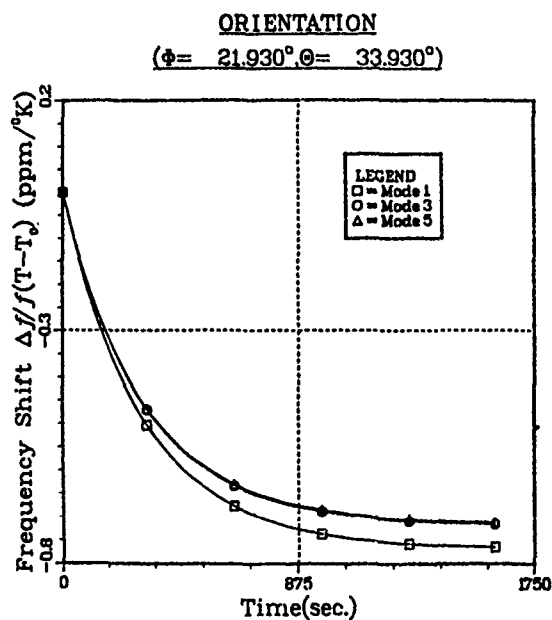


Figure 13

Time-dependent Frequency Shift per $^\circ\text{K}$ for Quartz Resonator with 2000 Å Thick Gold Electrodes Subject to a Surface Temperature $\bar{T}(1 - e^{-\beta t})$ for $\beta = 1/300 \text{ sec}^{-1}$

NONLINEAR EFFECT OF INITIAL STRESSES IN DOUBLY-ROTATED CRYSTAL RESONATOR PLATES

P. C. Y. Lee and Kuang-Ming Wu*

Department of Civil Engineering
Princeton University
Princeton, NJ 08544

Summary

The changes in the resonance frequencies of circular, quartz plates of doubly-rotated cuts are investigated when the plates are subject to in-plane initial stresses. Two types of initial stresses are considered: (a) The plate is subject to a pair of static diametral forces, and (b) The plate is supported by a number of ribbon supports attached to the edge of the plate and subject to steady acceleration.

The governing equations of motion for plates under initial stresses derived previously¹ are solved by the perturbation method. In these equations, the spatial variation of initial stress and strain fields and the nonlinear effect due to the presence of the third-order elastic stiffnesses in the stress-strain relations are taken into account. The present result is an extension of our previous investigations^{1,2} in two aspects: (1) The stress-strain relations for crystals when referred to the plate axes are of triclinic symmetry, hence the result can be applied to plates of any cut-orientation, and (2) The coupled equations of motion for plate vibrations have been extended to include the extensional mode in addition to the thickness-shear and flexural modes.

In the case of plates subject to diametral forces, the changes of resonance frequencies (represented by the force sensitivity coefficient K_f) are predicted as a function of the force orientation for various cut orientations such as AT, (yxwℓ)10°/33.9°, FC, IT, SC, and rotated X-cut. The predicted results are compared to the experimental values of Ballato,³ Ballato and Lukaszek,⁴ and the calculated values of EerNise⁴ by the variational method.

In the case of plates subject to acceleration, a special three-point mount configuration of which two supports are 180° apart and the third is 90° from the first two in forming a "T" shape is chosen for the study. The changes of resonance frequencies (represented by the acceleration sensitivity coefficient K_a) are predicted as a function of the direction of acceleration for an SC-cut plate and for a given orientation of the "T" shaped three-point mount. By examining the predicted values of $|K_a|_{\max}$ (proportional to the "2g" tip over results) as function of α the orientation of the

of the "T" shaped mount, it is found that the minimum acceleration-sensitivity occurs at orientation angles $\alpha = -15^\circ$ and $\alpha = +75^\circ$, while the maximum acceleration-sensitivity occurs at $\alpha = +15^\circ$ and $\alpha = -75^\circ$. The predicted value $\alpha = -15^\circ$ for SC-cut has been observed experimentally by A. Warner.

Equations of Motion for Crystal Plates Under Initial Stresses

The stress equations of motion for plates under in-plane initial stresses are reduced to:

$$\begin{aligned} & \frac{\partial}{\partial x_1} \left[(1+U_{1,1}^{(0)}) t_1^{(1)} + U_{1,3}^{(0)} t_5^{(1)} \right] + \frac{\partial}{\partial x_3} \left[(1+U_{1,1}^{(0)}) t_5^{(1)} + \right. \\ & \quad \left. U_{1,3}^{(0)} t_3^{(1)} \right] - \left[(1+U_{1,1}^{(0)}) t_6^{(0)} + U_{1,3}^{(0)} t_4^{(0)} \right] \\ & \quad = \frac{2}{3} b^3 \rho \ddot{u}_1^{(1)} \\ & \frac{\partial}{\partial x_1} \left[U_{2,1}^{(0)} t_1^{(0)} + U_{2,3}^{(0)} t_5^{(0)} + (1+U_2^{(1)}) t_6^{(0)} + U_{2,1}^{(1)} t_1^{(1)} + \right. \\ & \quad \left. U_{2,3}^{(1)} t_5^{(1)} + T_1^{(0)} u_{2,1}^{(0)} + T_5^{(0)} u_{2,3}^{(0)} + \frac{\partial}{\partial x_3} \left[U_{2,1}^{(0)} t_5^{(0)} + \right. \right. \\ & \quad \left. \left. U_{2,3}^{(0)} t_1^{(0)} + (1+U_2^{(1)}) t_4^{(0)} + U_{2,1}^{(1)} t_5^{(1)} + U_{2,3}^{(1)} t_1^{(1)} + \right. \right. \\ & \quad \left. \left. T_5^{(0)} u_{2,1}^{(0)} + T_3^{(0)} u_{2,3}^{(0)} \right] = 2b\rho \ddot{u}_2^{(0)} \right. \\ & \frac{\partial}{\partial x_1} \left[(1+U_{1,1}^{(0)}) t_1^{(0)} + U_{1,3}^{(0)} t_5^{(0)} + T_1^{(0)} u_{1,1}^{(0)} + T_5^{(0)} u_{1,3}^{(0)} \right] + \\ & \quad \frac{\partial}{\partial x_3} \left[(1+U_{1,1}^{(0)}) t_5^{(0)} + U_{1,3}^{(0)} t_3^{(0)} + T_5^{(0)} u_{1,1}^{(0)} + \right. \\ & \quad \left. T_3^{(0)} u_{1,3}^{(0)} \right] = 2b\rho \ddot{u}_1^{(0)} \end{aligned} \quad (1)$$

In the above equations, thickness-shear, flexural, and extensional modes are included. The thickness-twist, thickness-stretch, and face-shear modes are neglected, since their amplitudes of vibration are very small in the vicinity of the thickness-shear cut-off frequencies as compared to those of the former three modes.⁵

*Present address: GM Research Lab., GM Technical Center, Warren, MI 48909.

Also, from Ref. 1 we have the incremental stress-strain relations

$$\begin{aligned} t_p^{(0)} &= 2b(c_{pq} + c_{pqr}E_r^{(0)})\kappa_{(p)}\kappa_{(q)}\eta_q^{(0)} \\ t_p^{(1)} &= \frac{2}{3}b^3(c_{pq} + c_{pqr}E_r^{(0)})\eta_q^{(1)} \end{aligned} \quad (2)$$

and the incremental strain-displacement relations

$$\begin{aligned} \eta_1^{(0)} &= (1+u_{1,1}^{(0)})u_{1,1}^{(0)} + u_{2,1}^{(0)}u_{2,1}^{(0)} \\ \eta_4^{(0)} &= u_{1,3}^{(0)}u_{1,1}^{(0)} \\ \eta_5^{(0)} &= u_{1,3}^{(0)}u_{1,1}^{(0)} + u_{2,3}^{(0)}u_{2,1}^{(0)} \\ \eta_6^{(0)} &= (1+u_{2,1}^{(1)})u_{2,1}^{(0)} + (1+u_{1,1}^{(0)})u_{1,1}^{(1)} \end{aligned} \quad (3)$$

$$\begin{aligned} \eta_1^{(1)} &= u_{2,1}^{(1)}u_{2,1}^{(0)} + (1+u_{1,1}^{(0)})u_{1,1}^{(1)} \\ \eta_5^{(1)} &= u_{2,3}^{(1)}u_{2,1}^{(0)} + u_{1,3}^{(0)}u_{1,1}^{(1)} \\ \eta_2^{(0)} &= \eta_3^{(0)} = \eta_2^{(1)} = \eta_3^{(1)} = \eta_4^{(1)} = \eta_6^{(1)} = 0 \end{aligned}$$

For free harmonic vibrations, we may let:

$$\begin{aligned} u_1^{(1)} &= \Gamma e^{i\omega t} \\ u_2^{(0)} &= vbe^{i\omega t} \\ u_1^{(0)} &= ube^{i\omega t} \end{aligned} \quad (4)$$

By substituting (4) into (3) and (2), and then the resulting relations into (1), we obtain the displacement equations of motion for the increment vibrations

$$\begin{aligned} \bar{T}_1\Gamma_{,11} + \bar{T}_2\Gamma_{,1} + \bar{T}_3\Gamma + \bar{T}_4v_{,11} + \bar{T}_5v_{,1} + \\ \bar{T}_6u_{,11} + \bar{T}_7u_{,1} = -\Omega^2\Gamma \\ \bar{F}_1\Gamma_{,11} + \bar{F}_2\Gamma_{,1} + \bar{F}_3\Gamma + \bar{F}_4v_{,11} + \bar{F}_5v_{,1} + \\ \bar{F}_6u_{,11} + \bar{F}_7u_{,1} = -\Omega^2v \\ \bar{E}_1\Gamma_{,11} + \bar{E}_2\Gamma_{,1} + \bar{E}_3\Gamma + \bar{E}_4v_{,11} + \bar{E}_5v_{,1} + \\ \bar{E}_6u_{,11} + \bar{E}_7u_{,1} = -\Omega^2u \end{aligned} \quad (5)$$

where \bar{T}_i , \bar{F}_i , and \bar{E}_i ($i = 1, 2, \dots, 7$) are coefficients which depend on material properties as well as on the initial stress field. For instance, we have

$$\bar{T}_1 = \frac{b^2}{3\kappa^2 c_{66}} \left\{ (1+u_{1,1}^{(0)}) [c_{11}^{(0)} (1+u_{1,1}^{(0)}) + c_{15}^{(0)} u_{1,3}^{(0)}] + u_{1,3}^{(0)} [c_{51}^{(0)} (1+u_{1,1}^{(0)}) + c_{55}^{(0)} u_{1,3}^{(0)}] \right\}$$

$$\begin{aligned} \bar{T}_2 = \frac{b^2}{3\kappa^2 c_{66}} \left\{ [c_{11}^{(0)} (1+u_{1,1}^{(0)}) + c_{15}^{(0)} u_{1,3}^{(0)}] (1+u_{1,1}^{(0)}) \right\}_{,1} + \\ \left\{ [c_{51}^{(0)} (1+u_{1,1}^{(0)}) + c_{55}^{(0)} u_{1,3}^{(0)}] (1+u_{1,1}^{(0)}) \right\}_{,3} + \\ \left\{ [c_{51}^{(0)} (1+u_{1,1}^{(0)}) + c_{55}^{(0)} u_{1,3}^{(0)}] u_{1,3}^{(0)} \right\}_{,1} + \\ \left\{ [c_{31}^{(0)} (1+u_{1,1}^{(0)}) + c_{35}^{(0)} u_{1,3}^{(0)}] u_{1,3}^{(0)} \right\}_{,3} \end{aligned} \quad (6)$$

where

$$c_{pq}^{(0)} = c_{pq} + c_{pqr}E_r^{(0)} \quad (7)$$

Each of these coefficients can be separated into two parts:²

$$\begin{aligned} \bar{T}_i &= T_i + t_i \\ \bar{F}_i &= F_i + f_i \\ \bar{E}_i &= E_i + e_i \end{aligned} \quad (8)$$

where T_i , F_i , and E_i are associated with vibrational motion without initial stresses and are dependent on material properties only, while t_i , f_i , and e_i are contributed by initial fields and are space-dependent.

By setting the initial fields equal to zero in (6), we obtain

$$\begin{aligned} T_1 = \frac{b^2}{3\kappa^2 c_{66}} c_{11} \quad T_3 = T_5 = -\kappa_6^2 \\ T_7 = \frac{\kappa_1 \kappa_6 c_{61}}{\kappa c_{66}} \quad F_2 = F_4 = \frac{b}{3} \end{aligned} \quad (9)$$

$$\begin{aligned} F_6 = E_2 = E_4 = \frac{bc_{61}}{3\kappa c_{66}} \quad E_6 = \frac{bc_{11}}{3\kappa^2 c_{66}} \\ T_2 = T_4 = T_6 = F_1 = F_3 = F_5 = F_7 = E_1 = E_3 = E_5 = \\ E_7 = 0 \end{aligned}$$

Solution By Perturbation Method

Equation (5) can be expressed in the matrix form

$$LV = \lambda V \quad (10)$$

where $\lambda = -\Omega^2$ is the eigenvalue, $V = \{\Gamma v u\}^T$ is the displacement vector, and L is the linear differential operator which can be separated into two parts as follows:

$$L = L_0 + Q$$

where

$$L_0 = \begin{bmatrix} T_{1\partial_{11}} + T_3 & T_5\partial_1 & T_7\partial_1 \\ F_2\partial_1 & F_4\partial_{11} & F_6\partial_{11} \\ E_2\partial_1 & E_4\partial_{11} & E_6\partial_{11} \end{bmatrix} \quad (11)$$

$$Q = \begin{bmatrix} t_{1\partial_{11}} + t_2\partial_1 + t_3 & t_4\partial_{11} + t_5\partial_1 & t_7\partial_1 \\ f_{1\partial_{11}} + f_2\partial_1 + f_3 & f_4\partial_{11} + f_5\partial_1 & f_6\partial_{11} + f_7\partial_1 \\ e_{2\partial_1} + e_3 & e_4\partial_{11} + e_5\partial_1 & e_6\partial_{11} + e_7\partial_1 \end{bmatrix} \quad (12)$$

Note that L_0 is the part of the operator associated with motions without the influence of initial stresses, while Q is the part of the operator that includes all the effects of initial fields. From the initial stress and strain fields obtained previously,^{1,2} calculations show that the values of t_i , f_i , and e_i are of several orders of magnitude smaller than those of T_i , F_i , and E_i . Hence it is appropriate to employ the perturbation method to obtain the changes in frequencies due to initial fields.

Let V_n and λ_n be the eigenvector and eigenvalue satisfying Eq. (10), therefore

$$LV_n = \lambda_n V_n \quad (13)$$

where

$$L = L_0 + Q$$

$$\lambda_n = \lambda_n^0 + \lambda_n^{(1)} \quad (14)$$

$$V_n = V_n^0 + \sum_m a_{nm}^{(1)} V_m^0$$

Note that $\lambda_n^{(1)}$, $a_{nm}^{(1)}$ are the first-order perturbations and are of the same order of Q . If we substitute Eq. (14) into Eq. (13) and collect the terms of the same order, we have

$$L_0 V_n^0 = \lambda_n^0 V_n^0 \quad (15)$$

$$\sum_m a_{nm}^{(1)} L_0 V_m^0 + Q V_n^0 = \lambda_n^{(1)} V_n^0 + \lambda_n^0 \sum_m a_{nm}^{(1)} V_m^0 \quad (16)$$

Multiplying (16) by V_n^0 and employing the property that the V_n^0 form a complete and orthogonal set, we obtain,

$$\lambda_n^{(1)} = \frac{V_n^0 \cdot Q \cdot V_n^0}{V_n^0 \cdot V_n^0} \quad (17)$$

After the normalization $V_n^0 \cdot V_n^0 = 1$, we have

$$\lambda_n^{(1)} = V_n^0 \cdot Q \cdot V_n^0 \quad (18)$$

It can be shown that the changes of resonance frequencies can be obtained by²

$$\frac{\Delta f}{f_0} = \frac{1}{2\lambda_n^0} \int_A V_n^0 \cdot Q \cdot V_n^0 dA \quad (19)$$

In (19) we see that Q defined in (12) contains all the effect from the initial stresses and V_n^0 and λ_n^0 are governed by (15) which are the equations of free vibrations of the crystal plates without the influence of initial stresses.

Thickness-shear, Flexural and Extensional Vibrations of Doubly Rotated Quartz Plates

In the present section, we shall solve Equations (15) with traction-free boundary conditions. Equations (15) in matrix form can be obtained from (5) by replacing \bar{T}_i , \bar{F}_i , and \bar{E}_i by T_i , F_i , and E_i , respectively, and by making use of (9)

$$\begin{aligned} T_1 \Gamma_{,11} + T_3 \Gamma + T_5 v_{,1} + T_7 u_{,1} &= -\Omega^2 \Gamma \\ F_2 \Gamma_{,1} + F_4 v_{,11} + F_6 u_{,11} &= -\Omega^2 v \\ E_2 \Gamma_{,1} + E_4 v_{,11} + E_6 u_{,11} &= -\Omega^2 u \end{aligned} \quad (20)$$

By assuming the vibrational form of solutions

$$\begin{aligned} \Gamma &= \sum_{q=1}^3 A_{1q} \cos \xi_q x_1 \\ v &= \sum_{q=1}^3 A_{2q} \sin \xi_q x_1 \\ u &= \sum_{q=1}^3 A_{3q} \sin \xi_q x_1 \end{aligned} \quad (21)$$

and substituting (21) into (20), we obtain the dispersion relation

$$\begin{vmatrix} 3\Omega^2 - \bar{\xi}_q^2 \bar{c}_{11} & -\bar{\xi}_q^2 \bar{c}_{16} & -\bar{\xi}_q \bar{c}_{16} \\ -\bar{\xi}_q^2 \bar{c}_{16} & 3\Omega^2 - \bar{\xi}_q^2 \bar{c}_{66} & -\bar{\xi}_q \bar{c}_{66} \\ -\bar{\xi}_q \bar{c}_{16} & -\bar{\xi}_q \bar{c}_{66} & \Omega^2 - \bar{c}_{66} - \frac{\bar{\xi}_q^2 \bar{c}_{11}}{3\kappa_1^2} \end{vmatrix} = 0 \quad (22)$$

where $\bar{c}_{pq} = \kappa(p)\kappa(q)c_{pq}/\kappa^2 c_{66}$

$$\bar{\xi} = \xi_q b$$

and the amplitude ratios

$$A_{1q} : A_{2q} : A_{3q} = 1 : \alpha_{2q} : \alpha_{3q}$$

where

$$\alpha_{2q} = \frac{\begin{vmatrix} \bar{\xi}_q \bar{c}_{16} & -\bar{\xi}_q^2 \bar{c}_{16} \\ \bar{\xi}_q \bar{c}_{66} & 3\Omega^2 - \bar{\xi}_q^2 \bar{c}_{66} \end{vmatrix}}{D}$$

$$\alpha_{3q} = \begin{vmatrix} 3\Omega^2 - \bar{\xi}_q^2 \bar{c}_{11} & \bar{\xi}_q \bar{c}_{16} \\ -\bar{\xi}_q^2 \bar{c}_{16} & \bar{\xi}_q \bar{c}_{66} \end{vmatrix} / D \quad (23)$$

$$D = \begin{vmatrix} 3\Omega^2 - \bar{\xi}_q^2 \bar{c}_{11} & -\bar{\xi}_q^2 \bar{c}_{16} \\ -\bar{\xi}_q^2 \bar{c}_{16} & 3\Omega^2 - \bar{\xi}_q^2 \bar{c}_{66} \end{vmatrix}$$

In (22), the correction factors $\kappa(p)$ are introduced as follows

$$\kappa(p) = \begin{cases} 1 & \text{if } p = 3, 5 \\ \kappa = \pi/\sqrt{12} & \text{if } p = 2, 4 \\ \kappa_1 & \text{if } p = 1 \\ \kappa_6 & \text{if } p = 6 \end{cases} \quad (24)$$

κ_1 is introduced for the adjustment of the slope of the extensional branch (E_1) and κ_6 for the correction of the thickness-shear cut-off frequency as compared to the dispersion relations of the six coupled modes of vibrations.⁵ The values of κ_1 and κ_6 for various cuts of quartz plates are listed below.

Doubly rotated quartz plates ($\gamma \times \omega \times l$) ϕ/θ , $\theta = 33.9^\circ$	κ_1	κ_6
AT-cut, $\phi = 0^\circ$	1.0	1.0
$\phi = 10^\circ$	1.0116	0.9818
FC-cut, $\phi = 15^\circ$	1.0214	0.963
IT-cut, $\phi = 19.1^\circ$	1.0252	0.9492
SC-cut, $\phi = 21.9^\circ$	1.0252	0.9397
Rotated-X-cut, $\phi = 30^\circ$	1.0146	0.918

Dispersion curves computed from (22) for an SC-cut plate are shown in Fig. 1 by the solid lines as compared with those in dashed lines of the six coupled equations of motion.⁵

For the resonance frequencies and the incremental displacement field, we should look for a two-dimensional solution satisfying both the governing equations of motion and the traction-free conditions of a circular crystal plate. An analytical solution for such a problem is extremely complicated and difficult to obtain, if not impossible. However, we note that at the thickness-shear resonance frequencies the vibrational motion is trapped mostly in the middle portion of a plate which is either contoured or plated with electrodes in the middle portion of the plate.^{6,7} Also, the thickness-shear resonance frequencies are insensitive to the width of a rectangular plate as shown by Sykes⁸ and one-dimensional solutions^{9,10} give very accurate predictions when they are compared with experimental data. Therefore, in this section of the paper, the circular plate is approximated by a square plate of equivalent area and the one-dimensional solution will be obtained to predict the resonance frequencies and displacement field.

For a square plate with the length of the sides $2a (= \sqrt{\pi}R)$, the traction-free conditions at the edges $X_1 = \pm a$ are

$$t_1^{(0)} = t_6^{(0)} = t_1^{(1)} = 0 \quad \text{at } X_1 = \pm a \quad (25)$$

where R is the radius of the circular plate.

From (2), the one-dimensional stress-displacement relations become

$$t_1^{(0)} = 2bk_1 [\kappa_1 c_{11} u_{1,1}^{(0)} + \kappa_6 c_{16} (u_{2,1}^{(0)} + u_1^{(1)})]$$

$$t_6^{(0)} = 2bk_1 \kappa_6 [\kappa_1 c_{61} u_{1,1}^{(0)} + \kappa_6 c_{66} (u_{2,1}^{(0)} + u_1^{(1)})]$$

$$t_1^{(1)} = \frac{2}{3} b^3 c_{11} u_{1,1}^{(1)} \quad (26)$$

Substitution of (21) into (26) and (25) leads to the homogeneous equations

$$iM_{pq} \{A_{1q}\} = 0 \quad p, q = 1, 2, 3 \quad (27)$$

where

$$M_{1q} = \kappa_1 [\kappa_1 c_{11} \alpha_{3q} \xi_q + \kappa_6 c_{16} (\alpha_{2q} \xi_q + 1)] \cos \xi_q a$$

$$M_{2q} = \kappa_6 [\kappa_1 c_{61} \alpha_{3q} \xi_q + \kappa_6 c_{66} (\alpha_{2q} \xi_q + 1)] \cos \xi_q a$$

$$M_{3q} = c_{11} \xi_q \sin \xi_q a \quad (28)$$

For nontrivial solutions of (27), we have

$$\det M_{pq} = 0 \quad (29)$$

which is the frequency equation for thickness-shear, flexural, and extensional vibrations.

The calculation of the resonance frequencies of an SC-cut plate are performed and illustrated in Fig. 2. By comparing Fig. 2 with Figs. 3 and 4, which are the corresponding frequency spectra calculated from the six-mode theory,⁵ we see that the three-mode theory gives very good predictions of the frequencies of thickness-shear, flexure, and extension.

From (27), we can also calculate the amplitude ratios

$$A_{11} : A_{12} : A_{13} = 1 : \beta_2 : \beta_3 \quad (30)$$

if we choose A_{11} as the reference. The displacement field can be written in terms of α_{pq} and β_q

$$v_n^0 = \begin{Bmatrix} \Gamma \\ v \\ u \end{Bmatrix} = A_{11} \begin{Bmatrix} \sum_{q=1}^3 \beta_q \cos \xi_q x_1 \\ \sum_{q=1}^3 \beta_q \alpha_{2q} \sin \xi_q x_1 \\ \sum_{q=1}^3 \beta_q \alpha_{3q} \sin \xi_q x_1 \end{Bmatrix} \quad (31)$$

The remaining constant A_{11} may be determined by normalizations

$$V_n^0 \cdot V_n^0 = \int_A \left\{ \Gamma \cdot v \cdot u \right\} \left\{ \begin{matrix} \Gamma \\ v \\ u \end{matrix} \right\} dA = 1$$

Changes in the Resonance Frequencies

Once the resonance frequencies (or λ_n^0) and displacement field V_n^0 are obtained from (29) and (31), then the frequency changes $\Delta f/f_0$ can be obtained by carrying out numerical integration over the electroded area A of the plate for various in-plane initial stress fields.^{1,2}

Plates Subject to a Pair of Diametral Forces

Following Ratajski's¹¹ definition of force sensitivity coefficient, we have

$$K_f = \frac{\Delta f}{f_0} \cdot \frac{1}{N} \cdot \frac{d}{f_0/m} = \frac{\Delta f}{f_0} \frac{bd}{N} \sqrt{\frac{\rho}{c_{66}}} \quad (32)$$

where N is the magnitude of applied diametral forces and m is the order of harmonic overtones of the thickness-shear frequency.

Computations of K_f as a function of ψ , the orientation of the diametral forces, are made for circular quartz plates of AT-cut ($yx\lambda$) 33.9°, ($yxw\lambda$) 10°/33.9°, FC-cut ($yxw\lambda$) 15°/33.9°, IT-cut ($yxw\lambda$) 19°/33.9°, SC-cut ($yxw\lambda$) 22°/33.9°, and Rotated-X-cut ($yxw\lambda$) 30°/33.9°. The results are shown in Figs. 5 to 10, respectively, and are compared with the experimental results of Ballato,³ Ballato and Lukaszek,⁴ and the calculated result of Eernise.⁴ Analytical calculations of the same problem had been made also by Janiand, Nissim, and Gagnepain.¹² The results of Refs. 4 and 12 both show the improvement of predicted frequencies by employing the initial stress field of anisotropic plate subject to a pair of diametral forces.

Plates Subject to Steady Accelerations

We define the acceleration sensitivity coefficient

$$K_a = \frac{\Delta f}{f_0} \cdot \frac{1}{F} \cdot \frac{d}{f_0/m} = \frac{\Delta f}{f_0} \frac{8/\pi}{ngd\sqrt{\rho c_{66}}} \quad (33)$$

where $F = ng\rho(\pi bd^2/2)$ is the magnitude of body force on the plate and ng the acceleration on the plate, in terms of the acceleration from gravity.

A circular, SC-cut ($yxw\lambda$) 23.75°, 33.9° quartz plate with a three-point mount was chosen for the acceleration sensitivity study. The support configuration is shown in the upper part of Fig. 11. The angle α denotes the orientation of the "T"-shaped support configuration, while the angle ψ indicates the orientation of the body force due to the acceleration.

In Fig. 11, K_f is computed and plotted as a function of ψ , for $\alpha = 0^\circ, -15^\circ, -30^\circ$, and -45° .

We see that both the magnitude and location of $|K_a|_{\max}$ change as the support orientation α changes. By repeating the above process of calculation, we obtain $|K_a|_{\max}$ as a function of α as shown by the solid lines in Fig. 12. We see that the minimum acceleration-sensitivity occurs at $\alpha = -15^\circ$ and $+75^\circ$, while the maximum acceleration-sensitivity occurs at $\alpha = +15^\circ$ and -75° .

The minimum acceleration-sensitivity angle $\alpha = -15^\circ$ for the "T"-shaped mount has been observed by A. Warner.¹³ The result shown in Fig. 12 is also consistent qualitatively with the experimental data by Kusters, Adams and Yoshida,¹⁴ for their result (Fig. 2 of Ref. 14) is for a two-point mount configuration. It should be noted that the convention for the mounting angles in Ref. 14 is the opposite of that employed in the present paper.

The 1949 IRE¹⁵ Standards are employed in the present paper. If one wants to carry out computations using the 1978 IEEE¹⁶ Standards, one must change the signs of the piezoelectric constants e_{11} and e_{14} accordingly.^{16,17} One also needs to change the signs of the second- and third-order elastic constants, which are suggested in the following table.

SIGN CHANGES OF THE MATERIAL CONSTANTS FOR QUARTZ

	1949 IRE STD	1978 IEEE STD
e_{11}	= (L/R) (+/-)	(L/R) (-/+) ^{16,17}
e_{14}	= (L/R) (-/+)	(L/R) (-/+) ^{16,17}
c_{14}	= (-)	(+)
c_{114}	= (-)	(+)
c_{124}	= (-)	(+)
c_{134}	= (+)	(-)
c_{144}	= (-)	(+)

Let X , Y , and Z be the axes of quartz crystals according to the 1949 IRE Standards and X' , Y' , and Z' be the axes of quartz crystals according to the 1978 IEEE Standards. All the sign changes given in the above table can be obtained by a rotation of 180° about the Z axis, i.e., by a coordinate transformation as follows:

$$\begin{aligned} X &\rightarrow -X' \\ Y &\rightarrow -Y' \\ Z &\rightarrow Z' \end{aligned} \quad (33)$$

The $|K_f|_{\max}$ vs. α relation according to the 1978 IEEE Standards is computed and shown in Fig. 12 in dashed lines for comparison.

References

1. Lee, P. C. Y., Wang, Y. S. and Markenscoff, X., Proc. 27th Ann. Freq. Cont. Symp. 1-6 (1973), also J. Acoust. Soc. Am., Vol. 57, 95 (1975).
2. Lee, P. C. Y. and Wu, K-M, Proc. 30th Ann. Freq. Cont. Symp. 1-7, (1976), also J. Acoust. Soc. Am., Vol. 63, 1039-1047 (1977).

3. Ballato, A. D., Proc. 14th Ann. Freq. Cont. Symp., 89-114 (1960).
4. Ballato, A., EerNisse, E. P. and Lukaszek, T., Proc. 31st Ann. Freq. Cont. Symp., 8-10, (1977).
5. Lee, P. C. Y. and Wu, Kuang-Ming, presented at the 33rd Freq. Control Symposium (1979).
6. Lee, P. C. Y. and Chen, S., J. Acoust. Soc. Amer., 46, 1193-1202 (1969).
7. Lee, P.C.Y., and Spencer, W. J., J. Acoust. Soc. Amer., Vol. 45, 637-645, (1969).
8. Sykes, R. A., "Quartz Crystals for Electric Circuits," R. A. Heising, Editor, D. Van Nostrand, New York (1946).
9. Mindlin, R. D. and Gazis, D. C., Proc. 4th U.S. Natl. Congr. App. Mech., 305-310 (1962).
10. Mindlin, R. D. and Lee, P. C. Y., Int. J. Solids Structures, Vol. 2, 125-139 (1966).
11. Ratajski, J. M., IBM No. 60-825-1940A, IBM Federal System Div., Electronics Center (1966)
12. Janiand, D., Nissim, L. and Gagnepain, J. J., Proc. 32nd Ann. Freq. Cont. Symp. 169-179, (1978).
13. Warner, A., private communication and Goldfrank, B and Warner, A., Proc. 34th Ann. Freq. Cont. Symp. (1980).
14. Kusters, J. A., Adams, C. A. and Yoshida, H., Proc. 31st Ann. Freq. Cont. Symp. 3-7, (1977).
15. "Standards on Piezoelectric Crystals, 1949," Proc. IRE, Vol. 37, No. 12, December 1949, 1348-1395.
16. IEEE Standard 176-1978, (1978).
17. Meeker, T. R., Proc. 33rd Ann. Freq. Cont. Symp., 176-180, (1979).

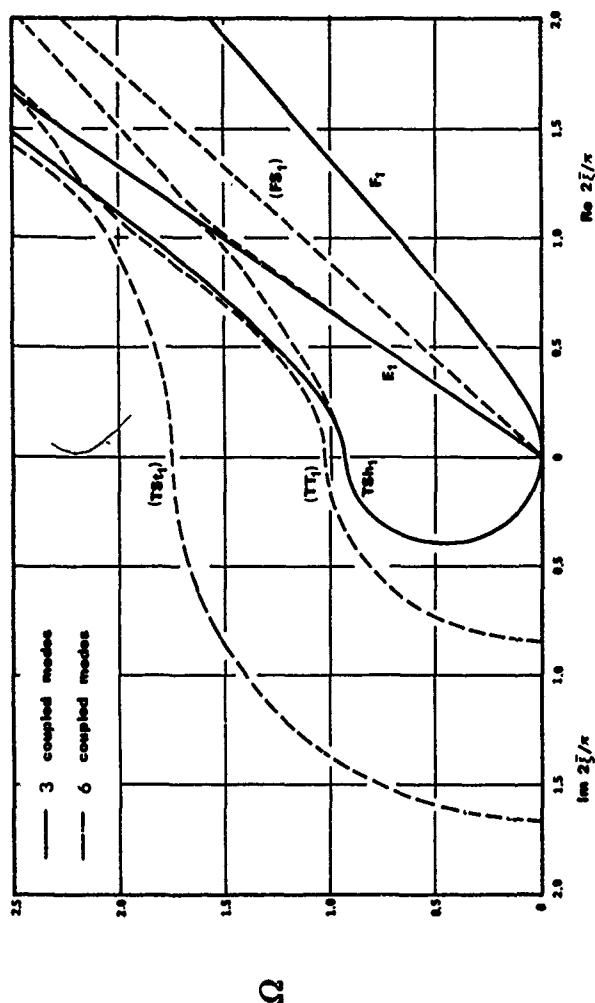


Fig. 1 Dispersion curves of SC-cut quartz plate for waves propagating in the x_1 -direction.

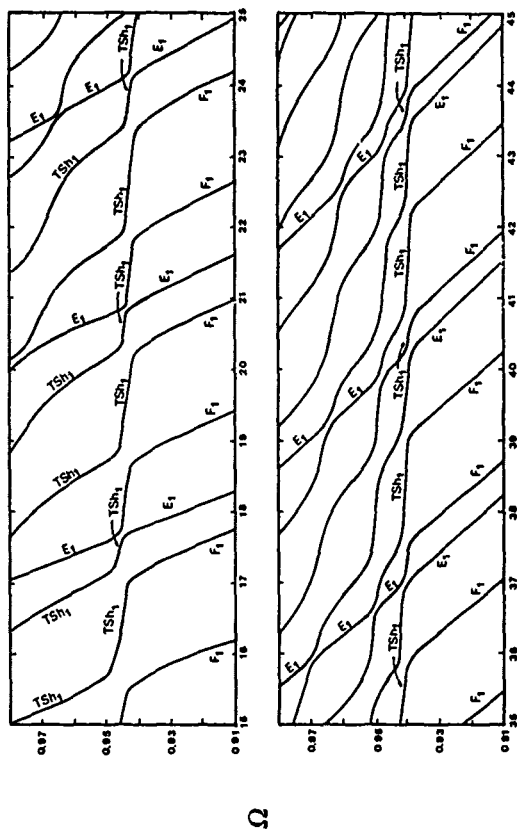


Fig. 2 Frequency spectra of SC-cut quartz plate for waves propagating in the x_1 -direction. (3 modes)

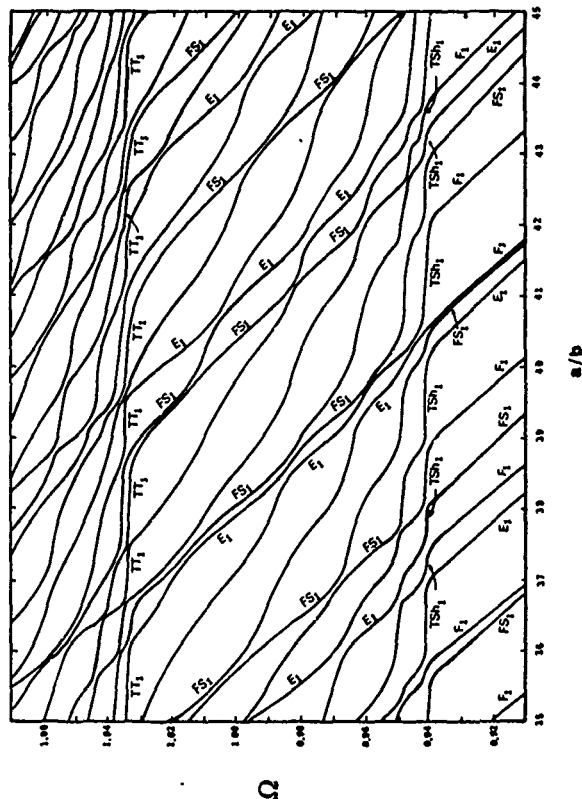


Fig. 3 Frequency spectrum of SC-cut quartz plate for waves propagating in the x_1 -direction ($15 \leq a/b \leq 25$). (6 modes)

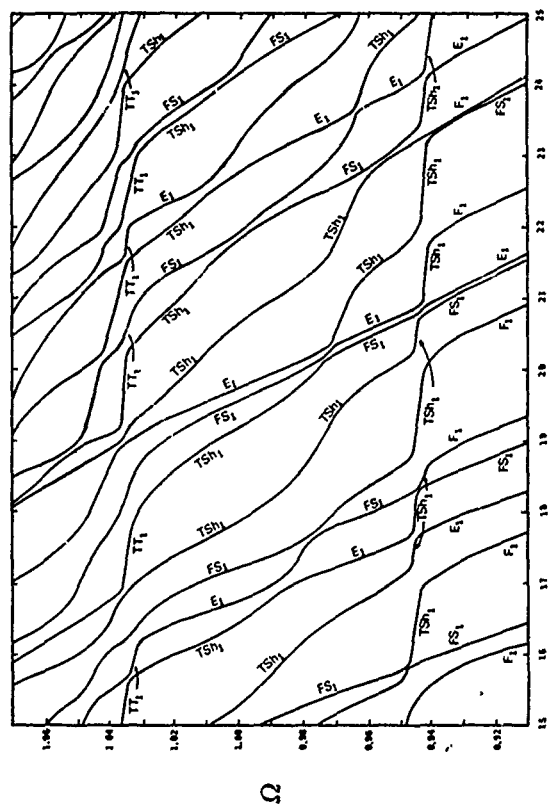


Fig. 4 Frequency spectrum of SC-cut quartz plate for waves propagating in the x_1 -direction ($35 \leq a/b \leq 45$). (6 modes)

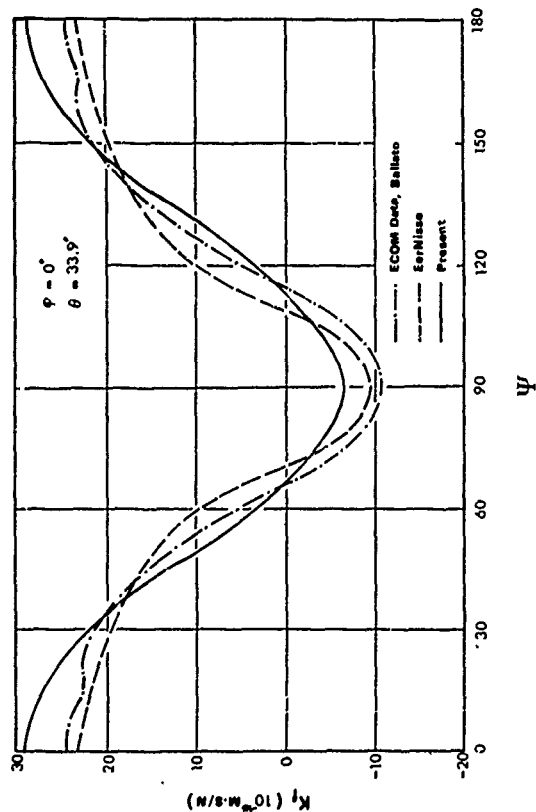


Fig. 5 Force sensitivity coefficient K_f as a function of the azimuth angle ψ of the pair of diametral forces, for AT-cut plate ($\psi = 33.9^\circ$).

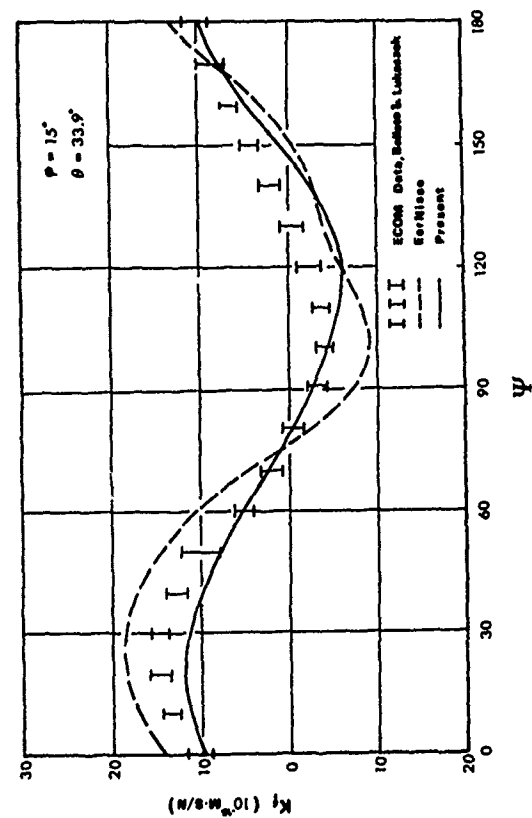


Fig. 7 K_f vs. ψ for FC-cut plate (yxwε) $15^\circ/33.9^\circ$.

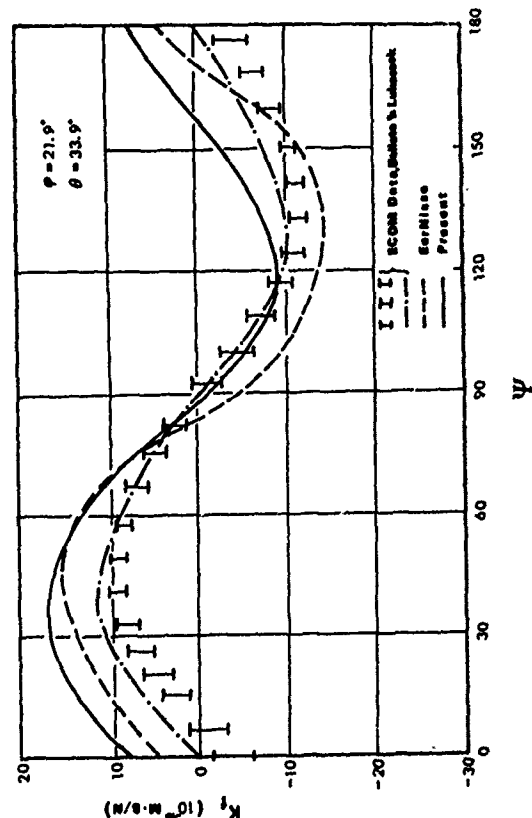


Fig. 9 K_f vs. ψ for SC-cut plate (yxwε) $21.9^\circ/33.9^\circ$.

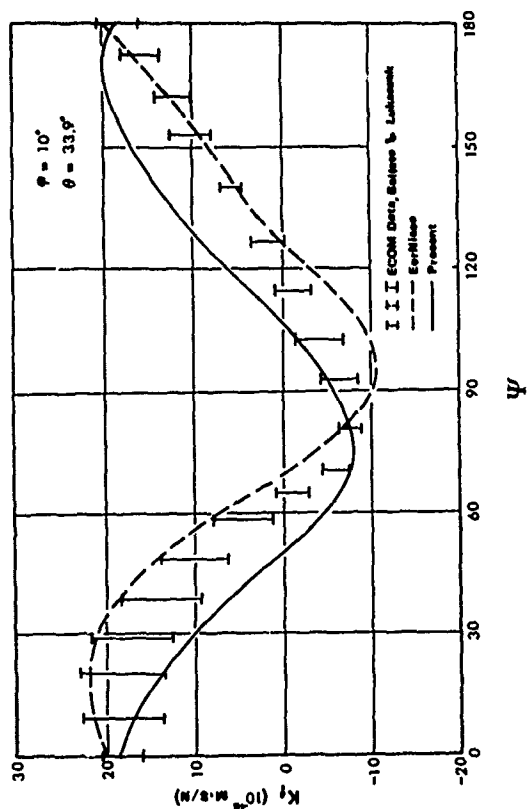


Fig. 6 K_f vs. ψ for quartz plate (yxwλ) $10^\circ/33.9^\circ$.

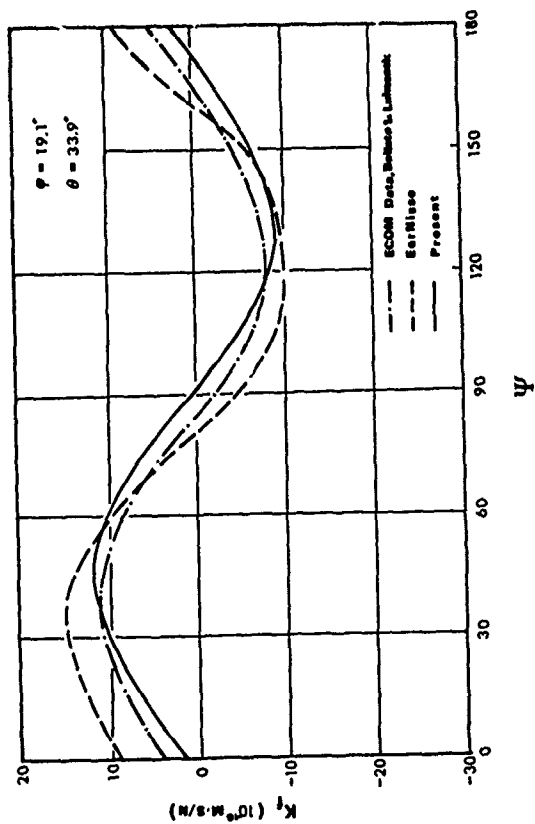


Fig. 8 K_f vs. ψ for IT-cut plate (yxwλ) $19.1^\circ/33.9^\circ$.

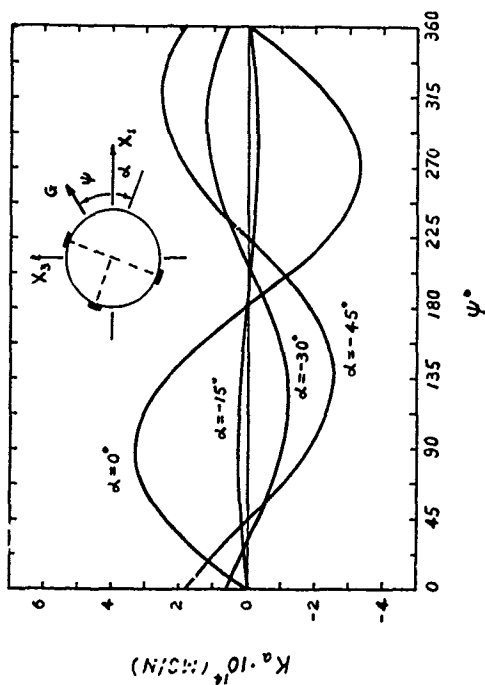


Fig. 11 Acceleration sensitivity coefficient K_a as a function of the orientation of body force, for SC-cut plate.

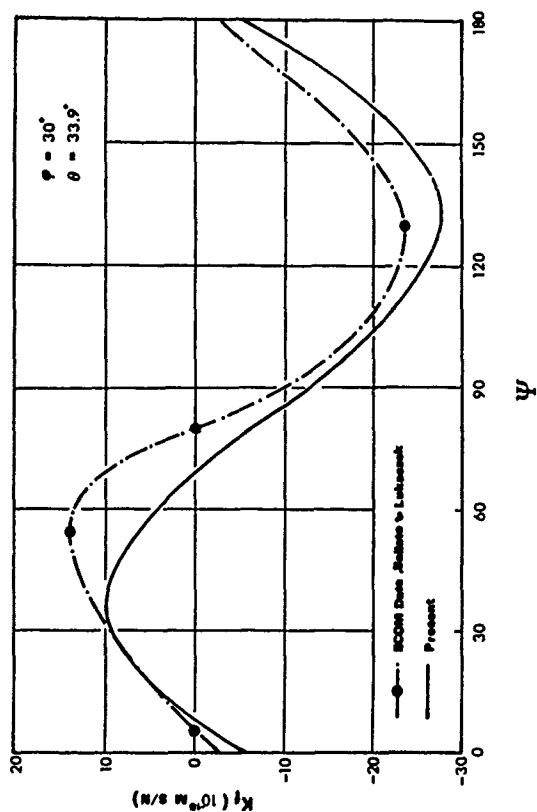


Fig. 10 K_f vs. ψ for Rotated-X-cut plate (yxw2) $30^\circ/33.9^\circ$.

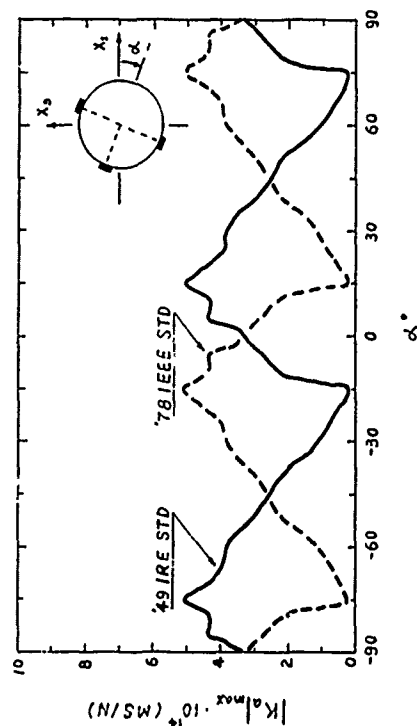


Fig. 12 $|K_a|_{\max}$ vs. α , for SC-cut plate.

THE FREQUENCY AND MOTIONAL CAPACITANCE OF PARTIAL CONTOURED
CRYSTAL RESONATORS

Daniel C.L. Vangheluwe

N.V. Philips' Gloeilampenfabrieken,
Eindhoven Nederland

Abstract

A solution of the equation of Tiersten for a rotated Y cut crystal with a partial cylindrical contour, operating in the thickness shear mode is found. The solution gives good agreement with the results of finite element calculations. An effective width b_{eff} is introduced, which is used to scale the problem. b_{eff} is the width of the active area of the crystal for the convex contour. With a different scaling factor, adapted to the problem of a partial spherical contour, a solution for the frequency for this case is found, which agrees with experiments. The maximum motional capacitance for large electrodes is calculated with the finite element method and it is found, to have a simple relationship to the width of the uncontroled part divided by b_{eff} . A method is given, to calculate the motional capacitance for intermediate values of the electrode area.

Introduction

The development of quartz crystals has a long history. However, the effect of concentration of the motion to the centre by contouring, which has been the practice for thickness shear resonators, has been poorly understood. Shockley explained for the first time the concentrating effect of the electrode in 1963. Until now, a comparable theory for a contoured crystal has not been given. This paper attempts a theoretical understanding of partial and full contouring and its consequences, such as a limitation of the motional capacitance and a change of the frequency.

Recently H. Tiersten¹⁾ has proposed a simplified equation of the motion of a rotated Y cut quartz crystal, with a contoured shape, operating in the thickness shear mode. In his analysis, the change in the thickness, which results from the contouring, is small, compared to the thickness of the crystal. Since the mode is highly trapped to the center of the crystal, the edge can be ignored, which simplifies the analysis. The equation of Tiersten is the result of a first order expansion of the decay number in the x and the z direction, which is assumed to be small, compared to the wavenumber in the

thickness direction. For a contoured crystal the decay number increases, which makes the expansion less accurate. In view of this we have examined the accuracy of the equation of Tiersten in predicting the frequency of both full and partial contoured crystals. For this purpose we have applied the finite element method to this problem, neglecting the z dependence. For those, interested in the method, we refer to an earlier article ²⁾.

The equation of Tiersten is solved for the partial contour after the parameters have been scaled in a proper way. This results in a frequency equation with a reduced number of parameters. The results of the finite element calculation are scaled also and compared with the solution of the frequency equation. The above method of scaling will also be used for the calculation of the motional capacitance and gives a simple quantitative description of the problem.

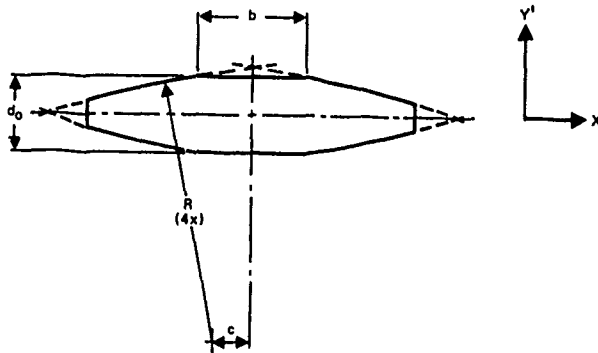
The Contour

The contouring of the crystal results in a slowly decreasing thickness in x and z direction as shown in figure 1. We will make a distinction between two types of contouring: 1) the cylindrical contour gives a decreasing thickness in only one direction and the thickness remains constant in the other direction, 2) the spherical contour has a thickness, decreasing uniformly in all directions between the x and z direction. As can be seen in figure 1, for $b=c=0$, we have a convex contour, which can be applied, either on one face of the crystal or on both faces. If the contouring is partial, b is the width of the central uncontroled part of the crystal, which we will call the facet. Further parameters of the contouring are, the radius R of the contour, the eccentricity c of the circle describing the contour (see figure 1). The distance c can be either positive or negative. For positive values c can be no greater than the width of the facet. For a slow decrease of the thickness and large R, we have to a first order approximation:

$$(1) \quad d(x)/d_0 = 1 + ((b/2 \cdot c)^2 - (x-c)^2)/(2Rd_0)$$

with $d(x)$ the thickness of the crystal as a

function of the distance x from the centre of the crystal.



PARTLY CONTOURED CRYSTAL SHOWN IN CROSS SECTION

The frequency

The cylindrical contour

The equation of Tiersten ¹⁾ results from a first order approximation of the dispersion relation of the thickness shear mode, assuming that the wave numbers in x and z direction are small, compared to the wavenumber in thickness direction. In the following analysis we will use this equation with the derivative of the motion with respect to z put to zero. We will thus consider only the problem of the cylindrical contour to start with. Introducing the equation of the thickness dependence (1) into the equation of Tiersten gives:

$$M_n \frac{d^2 u}{dx^2} + \gamma \omega^2 u \quad (2a)$$

$$- \frac{n^2 \pi^2 c_{66}}{d_0^2} u \left(1 - \frac{(b/2-c)^2 - (x-c)^2}{R d_0} \right) = 0$$

with the displacement in the x direction and M_n a constant, which depends on the elasticity coefficients of quartz ¹⁾ with c_{11} the most important contributor and n the harmonic number. For the facet the thickness is constant and we have:

$$M_n \frac{d^2 u}{dx^2} - \frac{n^2 \pi^2 c_{66}}{d_0^2} u + \gamma \omega^2 u = 0 \quad (2b)$$

In order to scale the distances, we introduce an effective width, b_{eff} , which we define as:

$$b_{eff} = 2 (R d_0^3 M_n / (n^2 c_{66}))^{1/4}$$

and with the scaled distances $y = \sqrt{\gamma} \pi (x-c) / b_{eff}$

and $y_0 = \sqrt{\gamma} \pi (b/2-c) / b_{eff}$ equations (2a) (2b) are rewritten as:

$$\frac{d^2 u}{dy^2} + (k^2 + (y_0^2 - y^2)/4) u = 0 \quad \dots y > y_0 \quad (3a)$$

$$\frac{d^2 u}{dy^2} + k^2 u = 0 \quad \dots y < y_0 \quad (3b)$$

In the above equations, k is the factor containing the frequency and from the preceding equations, it follows that:

$$k^2 = \left(\frac{n^2 \pi^2}{8} \right) \left(\frac{c_{66}}{M_n} \right) \left(\frac{b_{eff}^2}{d_0^2} \right) \left(\frac{f^2}{f_{0n}^2} - 1 \right) \quad (4)$$

with f_{0n} the frequency of the thickness shear mode for an infinite plate with a thickness d_0 and with $f_{0n} = n(c_{66}/\rho)^{1/2}/2d_0$. The frequency or k in this case follows from the boundary conditions which are: (i) zero derivative with respect to y at the centre or a solution symmetrical in y for the facet, (ii) a solution which decays to zero for large y , if we neglect the edge of the crystal. Besides this the solutions in the two regions must be matched at $y=y_0$, which means, that the displacement and its derivative with respect to y must be continuous at that point. With the choice of $\cos(ky)$ as a solution of (3b) the first condition is met. For the contoured region (y larger than y_0) the solution must be a parabolic cylindrical function $3)$, which decays to zero for large y and which is symmetric in y . The Whittaker function $3)$ $U(a, y)$ fulfils these requirements. In its asymptotic form it behaves as $\exp(-y^2/4)$. $y^{-a-1/2}$, similar to the solution given by Tiersten ¹⁾ for the plano convex contour. The conditions of continuity at $y=y_0$ then give the following frequency equation:

$$\tan\left(\frac{\pi k}{2k_0}\right) = - \frac{\frac{d}{dy} (U(a, y_0))}{k U(a, y_0)} \quad (5)$$

$$\text{with } k_0 = \sqrt{\gamma} \pi / 8 (b_{eff}/b) \quad \text{and } a = -(k^2 + y_0^2/4).$$

For the limiting case $b/2=c$, equation (5) simplifies to:

$$\tan\left(\frac{\pi k}{2k_0}\right) = \frac{\sqrt{2} \cdot T(3/4 - k^2/2)}{k \cdot T(1/4 - k^2/2)} \quad (6)$$

with T the Gamma function ³⁾. For the complete convex case, with $b=c=0$, k_0 becomes infinitely large and a solution of (7) is only possible

when $T(1/4-k^2/2)=0$ or $k^2=0.5$. The latter condition is equal to the solution of Tiersten ¹⁾, as may be found using equation (4).

It will be clear at this point, that the solution from (5) depends on two parameters only. The first one, k_0 represents the width of the facet and the second, y_0 the eccentricity of the circle, describing the contour. The other parameters R and d_0 have been eliminated by scaling. Figure 2 gives the solutions for two special cases, $c=0$ and $c=b$ as a function of the width of the facet, normalised to b_{eff} . The case $c=0$ is mostly used, but the case $2c=b$ may turn up in a tube tumbling process where the mutual grinding between crystals or dummies becomes significant. As can be seen in figure 2 the latter case is more sensitive to variations in the width of the facet. As can be seen in figure 2, k increases with further contouring (smaller b) and the question arises, whether the first order approximation of the wave number is accurate enough.

In order to investigate this we made some calculations with a finite element program called ASKA ²⁾ of a cross section of the crystal, which is the xy plane. The xy plane was divided into 120 elements of a more complicated structure ²⁾. In the x direction we had 60 elements, and in the y direction 2 with a total of 1210 degrees of freedom. The problem is not solved for all these degrees of freedom, but an iterative method finds only the lowest eigen frequencies, which is sufficient to find the frequency of the thickness shear mode.

The results can only be compared if b_{eff} is known. Our first definition of b_{eff} is not adequate for this purpose because it depends on the equation of Tiersten. We have looked therefore at another method to determine b_{eff} . For the complete convex contour (plano convex), the solution for the motion has the form given by Tiersten: $\exp(-2x^2/b_{eff}^2)$. We have found, that the amplitude, calculated with ASKA for this type of contour has the same x dependence, from which a value of b_{eff} can be derived. As can be seen from the above solution b_{eff} defines the region of activity for the complete convex case. From the equation of Tiersten it follows, that b_{eff} is proportional to $(Rd_0)^{1/4}$. We found the same linear relationship with ASKA up to values of $b_{eff}/d_0=8$, with a slightly smaller constant of proportionality K , as indicated in the table below.

From the above it follows, that we can also calculate b_{eff} from measurements of the amplitude versus x . We used the measurements with light modulation of Sauerbrey ⁴⁾ for different values of R to compare with the above results. As can be seen in the table below the value of K derived from the measurements of Sauerbrey agrees with the results from ASKA. The value of K derived from the equation of Tiersten

is slightly larger but this can be corrected for by making M_n smaller.

Table 1. Comparison of the constant of proportionality K of b_{eff} and $(Rd_0)^{1/4}$ for the fundamental frequency, $n=1$.

	constant K
H.Tiersten from def. with M_n	2.79
Sauerbrey from measurement	2.65
calculated with the finite element method	2.67
Stoddard from C_1	2.78

b_{eff} for a contour on both faces is found with ASKA calculations to be $2^{1/4}$ smaller than for a contour on one face. This is equivalent to an increase in the spacial rate of change of the thickness by a factor two and in the first order approximation in equation (1) to halving the radius of curvature R .

Having calculated b_{eff} from the ASKA calculations, we compared this result with the solution of equation (5) for the fundamental ($n=1$) and $c=0$. The absolute accuracy of the frequency calculated with ASKA is 0.5%, but the relative accuracy of the frequency for different contours is expected to be much better than that. Figure 3 gives the results after scaling. As can be seen in figure 3, the scaling of the ASKA results works well. The results of ASKA and equation (5) are quite close, with the ASKA results giving slightly smaller values. The results of equation (5) for $c=0$ can be corrected to agree with the results from ASKA in figure 3 when a value of $M_n=10.24$ instead of 11.01 is used. The latter value was calculated from equations given by Tiersten ¹⁾, omitting the mass loading effect of the electrodes. (The mass loading effect was also excluded in the ASKA calculations). The difference in M_n when the piezoelectric effect is accounted for, is too small to be of any influence here. As a conclusion, it appears, that a small reduction in the value of M_n is sufficient to correct for the approximations made by Tiersten for the cylindrical contour. With the above correction, the solution of equation (5) gives accurate values of the frequency for a partial contoured crystal.

The spherical contour

Until now we have neglected the z dependence of the displacement and we have considered a change of the thickness in the x direction only. Apart from bar type crystals, most crystals are spherical with a spherical contour. In the solution given by Tiersten for the complete convex contour, the z dependence is included ¹⁾. With the scaling factor of figure 3, the solution for the spherical case is larger by a factor $(1 + \sqrt{c_{55}/M_n})^{1/2}$, which gives 2.94 for

the AT cut. Experimental values given by Tiersten give for the fundamental an average value of 2.65. This value is also found in our own experiments, from which the results are given in figure 4. By comparing figures 3 and 4, it can be seen, that a simple multiplication of the solution in figure 3 using the above factor 2.94 does not give the values found from experiments for the spherical contour.

The solution of the spherical problem from equation (2) with the z dependence included, is not straightforward, because the boundary between the facet and the contour is circular. Therefore it is not possible to find an analytic solution as in case of the cylindrical contour. Any solution of the spherical problem must approach the frequency of a circular flat crystal for large b . In this limiting case, k is proportional to $1/b$ for both the spherical and the cylindrical case. Thus the solution for the cylindrical case is also valid for the spherical case for large b . This suggests the use of the solution for the cylindrical case with an adjusted scaling factor. If we multiply k and k_0 from equation (6) with a factor 1.25, a solution is obtained which agrees with the experiments in figure 4, except for large values of b/b_{eff} , where the edge in the experiments is too close to the facet.

We concluded from this, that the frequency for the spherical contour, can be estimated from the adapted solution of the cylindrical contour. A correction of the scaling factor of 1.25 must then be used to account for the different geometry.

The motional capacitance

The motional capacitance C_1 results from the equivalent circuit of a crystal at resonance. The energy content of C_1 is equal to the kinetic energy of motion at resonance, from which the following expression is derived in the appendix:

$$C_1 = \frac{8 k_{16}^2}{\pi^2} \left(\frac{\epsilon^S A_{av}}{d_0} \right) \quad (7)$$

with k_{16} the coupling factor for the thickness shear, ϵ^S the dielectric constant for constant strain and A_{av} the active area of the crystal. A_{av} is calculated from the motion by an averaging procedure which has been derived in the appendix. As is known, the contour imposes a definite maximum C_1 on the crystal. This is due to the restriction of the area in motion, A_{av} , notwithstanding the area covered by the electrode. For the convex cylindrical contour the motion from the equation of Tiersten gives for C_1 with very large electrodes:

$$A_{av} = b_z b_{eff} \quad (8)$$

with b_z the width in the z direction and b_{eff} the effective width in the x direction as defined on page 3. If we assume for the spherical contour a displacement in the x direction, which has circular symmetry around the y axis, we arrive at:

$$A_{av} = b_{eff}^2 \quad (9)$$

with the method given in the appendix, for very large electrodes. Stoddard ⁵⁾ gives a design equation for the minimum L_1 of planoconvex crystals, which can be calculated back to C_1 . His equation is similar to equation (7) with A_{av} from equation (9). Full agreement between the equations is obtained for a value of the coupling factor of 8%, which is slightly less than the theoretical value of 8.8% for the AT cut. The difference with the theoretical value is probably a correction for the electrode trapping, which results in a smaller value for C_1 .

Stoddard ⁵⁾ also defines an equivalent diameter D , which after insertion in his design equation for L_1 , would yield the minimum motional inductance of the convex crystal. Stoddard gives the following empirical relation for D :

$$D = 3.14 (Rd_0)^{1/4}$$

From this definition it follows, that

$\pi D^2/4 = A_{av}$ and with (9), we derive that $b_{eff} = 2.78(Rd_0)^{1/4}$, which is in reasonable agreement with values found earlier and given in table 1.

Using the integration method given in the appendix, we calculated the maximum C_1 from the motion obtained with ASKA for a number of cases with a partial contour. The integration was first performed for the cylindrical case with the z dependence neglected. The result can be seen in figure 5 as a function of b/b_{eff} . For the spherical contour, we assumed a circular symmetric displacement, which resulted in figure 6. For low values of b/b_{eff} the amplitude is concentrated towards the centre and C_1 for large electrodes is nearly constant. For large values of b/b_{eff} the facet overrules the contour and the case of a flat crystal with C_1 proportional to b for the cylindrical case and to b^2 for the spherical case, is approached. For an electrode diameter, which is small compared to b_{eff} , A_{av} is equal to the area of the electrode, because the crystal is fully active between the electrodes. For intermediate values of the electrode diameter, C_1 can be obtained by partial integration over the electrode.

Conclusions

A solution of the equation of Tiersten for the partial cylindrical contour has been found, which agrees with finite element calculations when a small correction to M_n is applied. The solution not only gives accurate values of the frequency for the cylindrical contour, but also for the spherical contour, if the scaling of the parameters of the frequency equation is adapted. The scaling depends on b_{eff} , which can be calculated directly from the radius of curvature and the thickness of the crystal.

A method is given, to calculate C_1 from the displacement as a function of distance. The maximum motional capacitance for the complete convex contour follows directly from b_{eff}^2 , which can be interpreted as the average active area of the crystal. After the width of the facet is scaled with b_{eff} , a simple relationship with the maximum C_1 is found from finite element calculations. As a conclusion, the solution of the equation of Tiersten and the scaling with b_{eff} couples simplicity to a good quantitative description of the problem. The results can be improved by taking into account the anisotropy of the crystal and the trapping due to mass-loading of the electrodes.

Acknowledgements

I wish to thank D.L.A.Tjaden of the Nat. Lab. of Philips N.V. for providing the analytical solution in this article and to R.F.Milsom for the helpfull discussion and the presentation of the paper.

References

- 1) H.F.Tiersten, Proc. of the 31st A.S.F.C., 44 (1977).
- 2) D.Vangheluwe, Proc. of the 32nd A.S.F.C., 134 (1978).
- 3) M.Abramowitz, I.A.Stegun, Handbook of Mathematical Functions, Dover Publ., 686 (1965).
- 4) G.Sauerbrey, Proc. of the 21st A.S.F.C., 68 (1967).
- 5) W.G.Stoddard, Proc. of the 17th A.S.F.C., 272 (1963).

note: A.S.F.C.= Annual Symposium on Frequency Control (U.S.Army, fort Monmouth)

Appendix

Calculation of the motional capacitance

The motional capacitance C_1 can be derived from the following energy balance. At resonance, the crystal can be represented electrically by the capacitance C_1 in series with the motional inductance L_1 , through which a current I flows. Because these electrical components represent the motion of the crystal, their energy content,

which is $I^2 L_1$ or $I^2 / \omega^2 C_1$ is equal to the potential energy or the kinetic energy of motion at resonance, giving the following equation:

$$I^2 / (\omega^2 C_1) = \int c^D S^2 dV \quad (1)$$

with c^D the stiffness for constant dielectric displacement D and S the strain for the mode in question. The integral must be taken over the volume of the crystal. The current I can be eliminated from the above equation, using the well known piezoelectric relation:

$$T = c^D S + hD \quad (2)$$

$$E = D/\epsilon^S + hS$$

T is the shear stress in the xy plane and E is the electric fieldstrength in the y direction h is a constant of piezoelectricity and the usual subscripts have been omitted for simplicity. At resonance the voltage across the electrodes vanishes, making the left part of the second equation of (2) zero when it is integrated over y . This gives a direct relation between D and S . The current in equation (1) is replaced by the surface integral over the electrode of dD/dt and D can be replaced by $-\epsilon^S hS$. As a result, S can be eliminated from the energy balance and the following expression for C_1 results, after introducing the coupling factor $k_{16} = h(\sqrt{\epsilon^S/c^D})$

$$C_1 = \left(\frac{8k_{16}^2}{\pi^2} \right) \left(\frac{\epsilon^S}{d_0} \right) \frac{\left(\int S dx dz \right)^2}{\int S^2 dx dz} = \left(\frac{8k_{16}^2}{\pi^2} \right) \left(\frac{\epsilon_{av}^S}{d_0} \right) \quad (3)$$

A_{av} is an area obtained by averaging S . The integral in the numerator must be taken over the area of the electrode and the integral in the denominator over the area of the crystal.

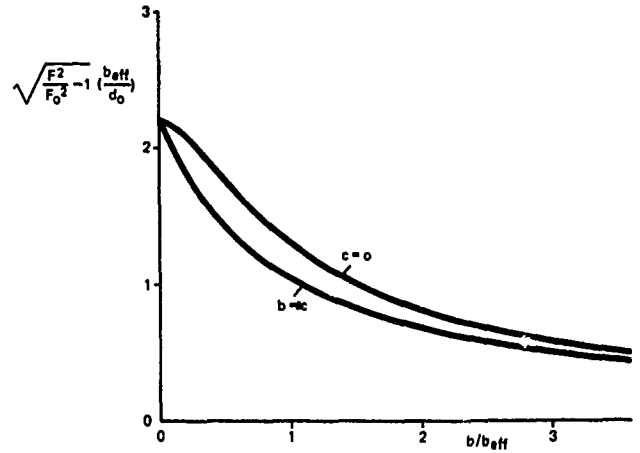


Fig. 2

The normalized frequency as a function of the normalized width of the facet, for a cylindrical facet, according to the equation of Tiersten.

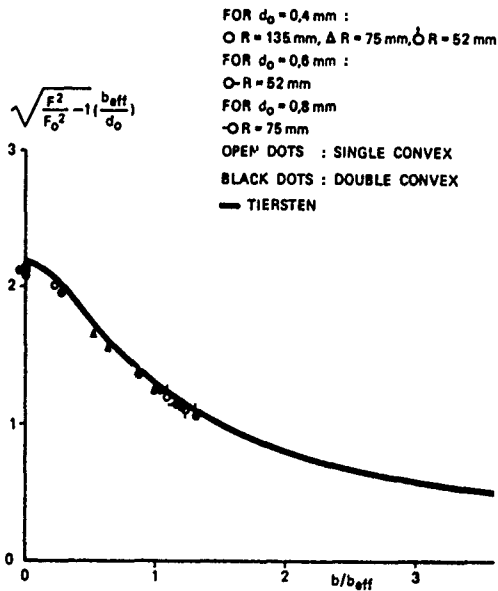


Fig. 3

The solution of the equation of Tiersten, compared with the results obtained with the finite element method (dots), for the cylindrical contour.

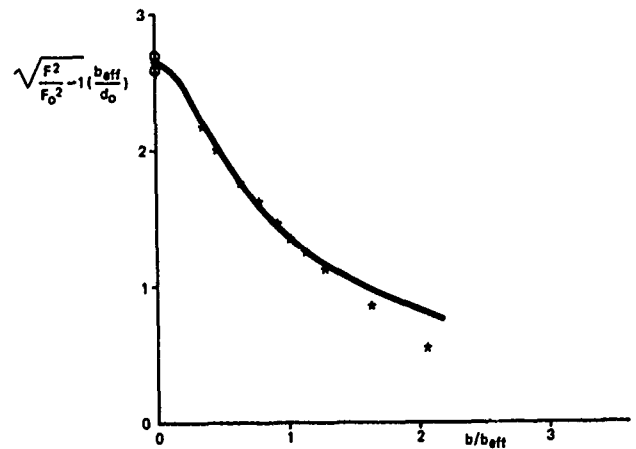


Fig. 4

Measurements (points) for a spherical contour on a circular crystal (6.5 MHz). The full line is the solution of the equation of Tiersten with the scaling factor adapted to give agreement with the measurement.

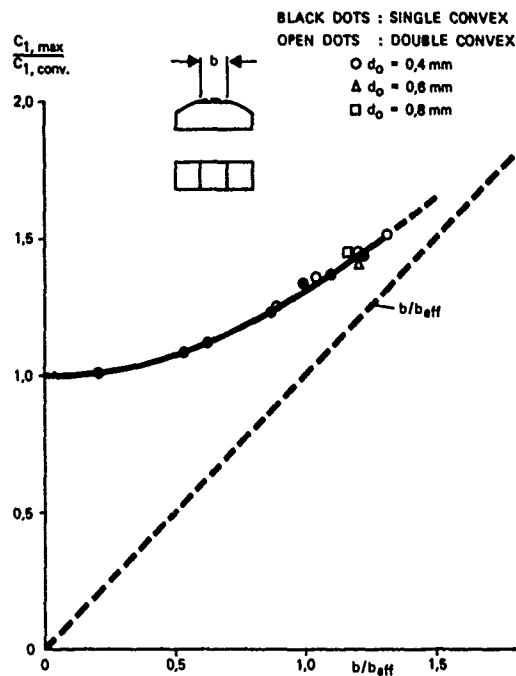


Fig. 5

The motional capacitance for a large electrode as a function of the normalized width of the facet, for the cylindrical contour.

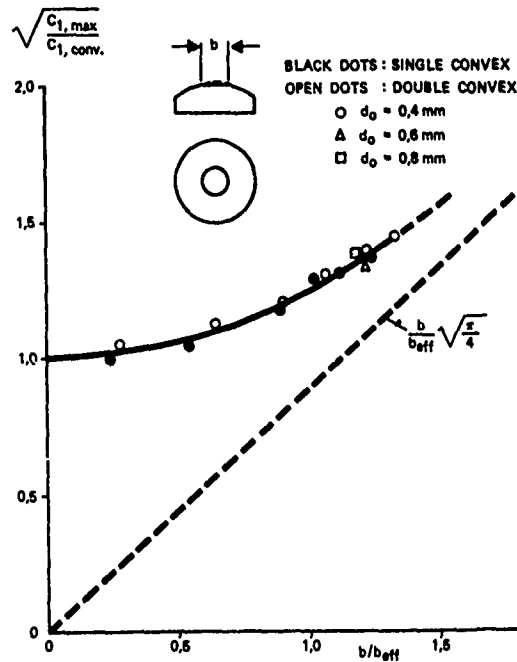


Fig. 6

The motional capacitance for a large electrode as a function of the normalized width of the facet, for the spherical contour.

DECOUPLED FAMILIES OF CONTOUR MODES OF PLANAR THIN PLATES

C. Bourgeois

Centre Electronique Horloger S.A.
Neuchâtel, Switzerland

Summary

The different possible parities of the displacement, compatible with the variational formulation of linear elasticity, determine the decoupled families of modes of planar thin plates. Eleven groups of modes have been found, depending on the symmetries of the plates and on the symmetries of the elastic constants of the material. Four of these groups are similar to the families of rectangular plates described by Lloyd and Redwood¹. The seven others correspond to the combinations of two or four of the previous groups.

A computer procedure, based on variational techniques, has been developed to study the properties of contour modes of thin plates of any shape and any crystallographic orientation. Typical vibration patterns of each family are discussed. Resonant frequency, displacement pattern and frequency-temperature behavior of some modes are compared with various published data.

Introduction

The majority of resonant elastic structures are described by linear differential equations and boundary conditions. The contour modes of thin mechanically free plates fall into this category.

Lloyd and Redwood¹ showed that the differential equations of orthotropic rectangular plates are satisfied by four distinct families of contour modes: the diagonal-shear modes, the dilatation-type modes and the flexure modes along each axis of symmetry of the plate.

There are actually no known analytical solutions to the vibration problems of finite elastic bodies, even in the isotropic case, if one excepts the special case of Lamé modes. Consequently, it is necessary to rely on approximation techniques. Among these, the most powerful methods are based either on finite-difference, or on variational techniques. Thus Holland and EerNisse² used the Rayleigh-Ritz technique to approximate the modes of rectangular isotropic plates.

Variational formalism

In an orthogonal coordinate system, and in tensor notation, Holland and EerNisse showed that the Lagrangian appropriate to linear elasticity is expressed as

$$L = \frac{1}{2} \iiint_V (u_{i,j} c_{ijkl} u_{k,l} - \rho \omega^2 u_i u_i) dV$$

where V is the volume of the solid, c_{ijkl} is the stiffness tensor, ρ is the density, $u_{i,j}$ is the local displacement; the comma denotes differentiation and all subscripts range from 1 to 3. The different modes of vibration correspond to the stationary Lagrangian.

In the plane stress approximation, the Lagrangian can be expressed as

$$L = \frac{1}{2} \iint_S (u_{i,j} \gamma_{ijkl} u_{k,l} - \rho \omega^2 u_i u_i) dS$$

where S is the surface of the plate, γ_{ijkl} is the usual planar stiffness tensor. The indices range from 1 to 2 for a Z-cut plate.

One can demonstrate that the variation of the Lagrangian leads to the differential equation:

$$\rho \omega^2 u_i + \gamma_{ijkl} u_{k,lj} = 0$$

and to the boundary condition:

$$\gamma_{ijkl} u_{k,l} n_j = 0$$

where n_j is the outward-pointing normal vector.

Holland and EerNisse chose Fourier expansions of the displacement as trial functions. One can show however that power expansions yield more exact frequencies. The calculation of the temperature dependence has been carried out very carefully to minimize numerical errors. This precludes the use of iterative methods for the various matrix operations. The same scheme has to be imposed at different temperatures⁴.

Symmetries of plates and

symmetries of modes

Let us consider the five symmetries of a plate, in a set XY of rectangular axes, as shown in Fig. 1. The axes will be chosen as close as possible to the symmetries of the plate. These five symmetries are

- 1) plate with X and Y as axes of symmetry
- 2) plate with a center of symmetry
- 3) plate with X as axis of symmetry
- 4) plate with Y as axis of symmetry
- 5) plate without symmetry.

The special case of a plate with a center of rotation will be considered later.

Each displacement can be described by the sum of four trial functions, corresponding to the different possible combinations of parities with respect to the X and Y axis:

$$u_1 = u_1^{EO} + u_1^{OE} + u_1^{EE} + u_1^{OO}$$

$$u_2 = u_2^{OE} + u_2^{EO} + u_2^{OO} + u_2^{EE}$$

The superscripts refer to even or odd parity.

Let us now introduce these expressions into the Lagrangian and the differential equations, expressed in engineering notation as

$$L = \frac{1}{2} \iint_S [\gamma_{11} u_{1,1}^2 + \gamma_{22} u_{2,2}^2 + \gamma_{66} (u_{1,2} + u_{2,1})^2 + 2\gamma_{12} u_{1,1} u_{2,2} + 2(\gamma_{16} u_{1,1} + \gamma_{26} u_{2,2})(u_{1,2} + u_{2,1}) - \rho \omega^2 (u_1^2 + u_2^2)] dS$$

$$\rho \omega^2 u_1 + \gamma_{11} u_{1,11} + \gamma_{66} u_{1,22} + (\gamma_{66} + \gamma_{12}) u_{2,12}$$

$$+ \gamma_{16} (2u_{1,12} + u_{2,11}) + \gamma_{26} u_{2,22} = 0$$

$$\rho \omega^2 u_2 + \gamma_{22} u_{2,22} + \gamma_{66} u_{2,11} + (\gamma_{66} + \gamma_{12}) u_{1,12}$$

$$+ \gamma_{26} (2u_{2,12} + u_{1,22}) + \gamma_{16} u_{1,11} = 0$$

The elastic coupling effects between the trial functions appears in the differential equations, while the kinetic coupling effects, due to a lack of symmetry of the plate, appears in the Lagrangian through the integral over the surface.

Modes of high symmetry

Four groups of modes exist in orthotropic plates ($\gamma_{16} = \gamma_{26} = 0$) with X and Y as axes of symmetry. These four families are decoupled in the differential equations and in the Lagrangian. They were described by Lloyd and Redwood, and are characterized by

- 1) u_1^{EO} and u_2^{OE} : diagonal-shear modes
- 2) u_1^{OE} and u_2^{EO} : dilatation-type modes
- 3) u_1^{OO} and u_2^{EE} : modes of flexure along the X axis
- 4) u_1^{EE} and u_2^{OO} : modes of flexure along the Y axis

Fig. 2a through 2d illustrate the symmetries of these modes, where the arrows correspond to displacements of the same amplitude. They are characterized as follows:

- 1) diagonal-shear modes:
-symmetric about the center of the plate
-antisymmetric about the X and Y axes
- 2) dilatation-type modes:
-symmetric about the center of the plate
-symmetric about the X and Y axes
- 3) modes of flexure along the X axis:
-symmetric about the Y axis
-antisymmetric about the X axis
- 4) modes of flexure along the Y axis:
-symmetric about the X axis
-antisymmetric about the Y axis

where antisymmetry corresponds to symmetry followed by phase inversion.

Fig. 3 illustrates the first modes of each family of the SL cut³. The SL mode is the second diagonal-shear mode.*

Fig. 4 and 5 illustrate the DT mode of a square plate and of a circular plate respectively.

Modes with a center of symmetry and

modes with a center of antisymmetry

Two families of modes have either a center of symmetry or a center of antisymmetry. The first family corresponds to the coupling of the diagonal-shear modes with the dilatation-type modes. The second family corresponds to the coupling of the flexure modes along the X axis with the flexure modes along the Y axis. These two families

* The frequencies as well as the frequency-temperature behavior are the computed values.

The frequency constant relates to the width of a rectangular plate, or to the diameter of a circle.

correspond either to elastic coupling in anisotropic plates with the axes of symmetry X and Y, or to kinetic coupling in plates with a center of symmetry. They are characterized by

$$1) u_1 = u_1^{EO} + u_1^{OE} \text{ and } u_2 = u_2^{OE} + u_2^{EO} ;$$

modes with a center of symmetry.

$$2) u_1 = u_1^{OO} + u_1^{EE} \text{ and } u_2 = u_2^{EE} + u_2^{OO}$$

modes with a center of antisymmetry.

Fig. 2e and 2f illustrate the symmetries of these two modes.

Fig. 6 illustrates the first modes of these two families for the ZT cut⁴. In this case, the anisotropy of the plate produces a weak elastic coupling between the two basic families. The ZT mode is the fourth mode with a center of symmetry. No coupling effect appears on the displacement pattern. This is due to the fact that γ_{12} as well as γ_{26} vanish at 25°C.

Fig. 7 illustrates the first modes with a center of symmetry for the GT cut. The GT mode corresponds to the fourth mode.

Fig. 8 illustrates the kinetic coupling in the case of an isotropic Z-cut plate with a center of symmetry.

Modes with an axis of symmetry and modes with an axis of antisymmetry

Two families of modes are either symmetric or antisymmetric about X. The first family corresponds to the coupling of the dilatation-type modes with the flexure modes along the Y axis. The second family corresponds to the coupling of the diagonal-shear modes with the flexure modes along the X axis. These two families correspond to kinetic coupling in plates symmetric about X. They are characterized by

$$1) u_1 = u_1^{EE} + u_1^{OE} \text{ and } u_2 = u_2^{OO} + u_2^{EO} ;$$

modes symmetric about X

$$2) u_1 = u_1^{OO} + u_1^{EO} \text{ and } u_2 = u_2^{EE} + u_2^{OE} ;$$

modes antisymmetric about X.

Fig. 2g and 2h show the symmetries of these two modes.

Fig. 9 illustrates the first mode of these two families for an isotropic Z-cut plate.

Two other families of modes, similar to the previous ones are either symmetric or antisymmetric about Y, as shown in Fig. 2i and 2j.

Modes without symmetry

The last family of modes has no symmetry and is characterized by the coupling of all the four basic families. This type of modes occurs either in anisotropic plates symmetric about an axis, or in plates without symmetry, as shown in Fig. 10.

Plates with a center of rotation

Let us consider the two cases of plates with a center of rotation as shown in Fig. 11. One of these possesses additional axes of symmetry.

The displacement patterns will be related to the symmetry of the plate as long as the elastic constants have the same order of rotation. With the rotation equations given by Love⁵, one can demonstrate that this is only possible for isotropic plates. In appropriate polar coordinates, the Lagrangian and the differential equations are expressed as

$$L = \frac{1}{2} \iint \left[-\rho \omega^2 (u_r^2 + u_\theta^2) + \gamma_{11} (u_{r,r} + \frac{1}{r} (u_r + u_{\theta,\theta}))^2 + \gamma_{66} ((u_{\theta,r} - \frac{1}{r} (u_\theta - u_{r,\theta}))^2 - \frac{4}{r} u_{r,r} (u_r + u_{\theta,\theta})) \right] ds$$

$$\rho \omega^2 u_r + \gamma_{11} (u_{r,rr} + \frac{1}{r} (u_{r,r} + u_{\theta,r\theta}) - \frac{1}{r^2} (u_r + u_{\theta,\theta})) - \gamma_{66} (\frac{1}{r} u_{\theta,r\theta} + \frac{1}{r^2} (u_{\theta,\theta} - u_{r,\theta\theta})) = 0$$

$$\rho \omega^2 u_\theta + \gamma_{66} (u_{\theta,rr} + \frac{1}{r} (u_{\theta,r} - u_{r,\theta\theta}) - \frac{1}{r^2} (u_\theta - u_{r,\theta})) + \gamma_{11} (\frac{1}{r} u_{r,\theta\theta} + \frac{1}{r^2} (u_{r,\theta} + u_{\theta,\theta\theta})) = 0$$

One can show that four decoupled families of modes, similar to the previous basic families, exist in plates with a center of rotation and axes of symmetry. They can be described by trial functions expressed as a power series in the radius r, and as sine or cosine series of the polar angle θ as follows:

$$1) \text{ shear modes: } u_r = \sum r^i \cos(j\theta) \text{ and}$$

$$u_\theta = \sum r^i \sin(j\theta)$$

$$2) \text{ dilatation-type modes:}$$

$$u_r = \sum r^i \sin(j\theta) \text{ and}$$

$$u_\theta = \sum r^i \cos(j\theta)$$

3) modes symmetric about an axis:

$$u_r = \sum r^i \cos(j\theta) \text{ and}$$

$$u_\theta = \sum r^i \sin(j\theta)$$

4) modes antisymmetric about an axis:

$$u_r = \sum r^i \sin(j\theta) \text{ and}$$

$$u_\theta = \sum r^i \cos(j\theta)$$

where p is the order of the center of rotation.

These different types of modes are characterized as follows:

- the shear modes are antisymmetric about each axis of symmetry of the plate
- the dilatation-type modes are symmetric about each axis of symmetry of the plate
- the modes with an axis of symmetry are symmetric about one of the axis of symmetry of the plate
- the modes with an axis of antisymmetry are antisymmetric about one of the axis of symmetry of the plate.

Fig. 12 illustrates the first modes of each of these families for a Z-cut equilateral triangle. One can observe that the frequency of the mode with an axis of symmetry and the frequency of the mode with an axis of antisymmetry are identical. More generally, in the case of plates with a center of rotation of odd order, the frequencies as well as the frequency-temperature behaviors of modes with an axis of symmetry are identical to those of modes with an axis of antisymmetry. This is due to the fact that the difference of the displacement patterns of equal modes, belonging to the same family, corresponds to a pattern showing the symmetry of the other family.

In a plate with a center of rotation of even order, there is always an axis of symmetry perpendicular to another axis of symmetry. Thus a mode with an axis of symmetry can also be considered as a mode with an axis of antisymmetry. Furthermore there are two types of axes of symmetries in such plates. Consequently, there are also two types of modes with an axis of symmetry having the same frequencies. Fig. 13 illustrates the first modes of each type for a Z-cut square plate.

In the case of plates with a center of rotation, but without an axis of symmetry, there are two families of modes corresponding respectively to the kinetic coupling of the shear-modes with the dilatation-type modes, and to the coupling of the modes with an axis of symmetry and the modes with an axis of antisymmetry, as illustrated in Fig. 14. The first family has a center of rotation of the same order as the plate, or a submultiple in the case of even order.

Three-dimensional modes

A similar analysis shows that for three-dimensional modes, 51 decoupled families are possible. They depend on 8 basic families. The 43 other families can be characterized as follows:

- 12 groups result from the elastic coupling of 2 basic families;
- 2 groups result from the elastic coupling of 4 basic families;
- 16 groups result from the kinetic coupling of 2 basic families;
- 12 groups result from the kinetic coupling of 4 basic families;
- 1 group result from the kinetic coupling of all 8 basic families.

References

1. P. Lloyd and M. Redwood, "Finite-difference method for the investigation of vibrations of solids and the equivalent-circuit characteristics of piezoelectric resonators, Parts I and II", J. Acoust. Soc. Am., Vol. 39, pp.346-361, February 1966.
2. R. Holland and E.P. EerNisse, "Design of Resonant Piezoelectric Devices", (M.I.T. Press 1969), Chap. 3.
3. L.T. Sogn, "Quartz Piezoelectric Element", U.S. Patent 3 072 806.
4. J. Hermann and C. Bourgeois, "A New Quartz Crystal Cut for Contour Mode Resonators", Proc. 33th Annual Symposium on Frequency Control, pp. 255-262, May 1979.
5. A.E.H. Love, "A Treatise on the Mathematical Theory of Elasticity", New York: Dover 1944, p. 153.

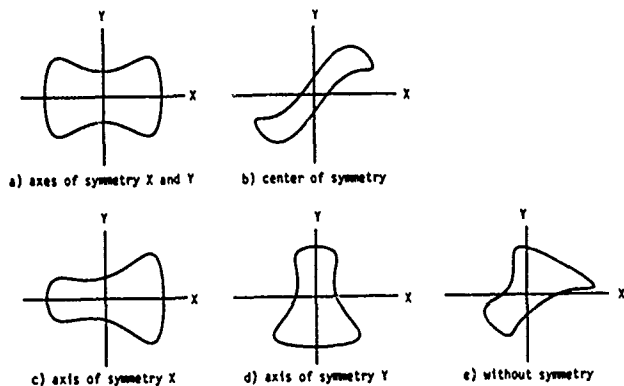


Fig. 1

SYMMETRIES OF PLATES

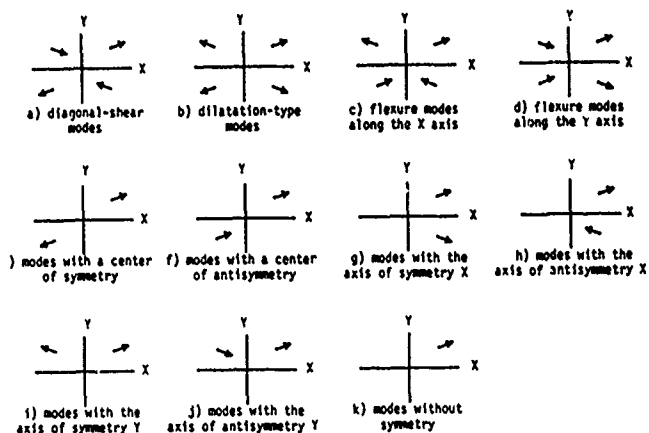


Fig. 2

SYMMETRIES OF MODES

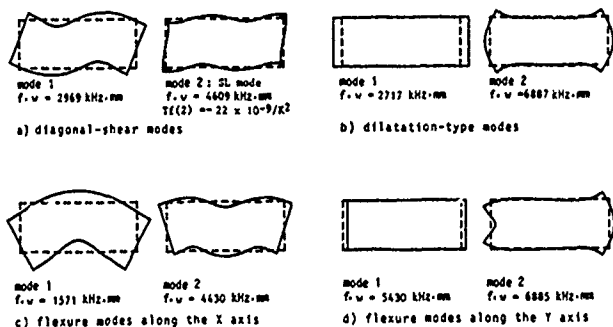


Fig. 3

SL CUT (YX1) -51°17'



Fig. 4

DT MODE OF A SQUARE PLATE (YX1) -52°30'



Fig. 5

DT MODE OF A CIRCULAR PLATE (YX1) -52°

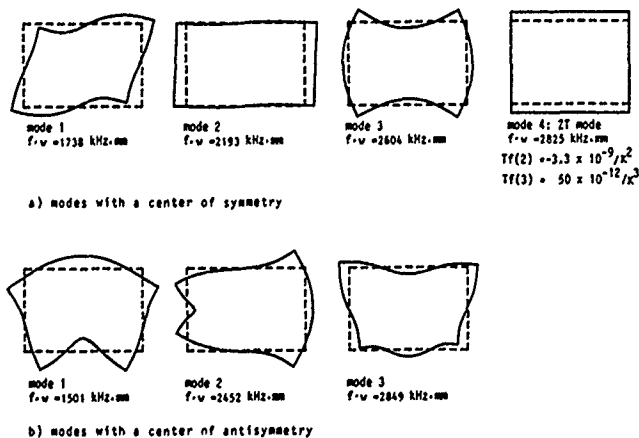


Fig. 6

ZT CUT (ZX wt) 26°20'10°

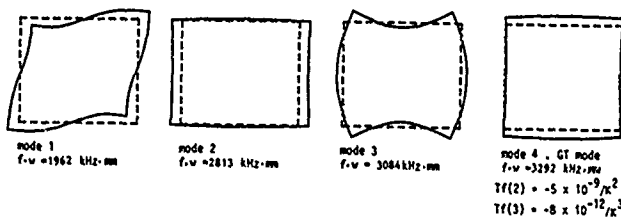


Fig. 7 GT CUT (YZ wt) $51^{\circ}7.5'/45^{\circ}$

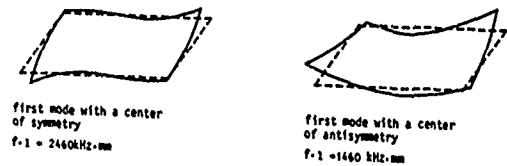


Fig. 8

Z-CUT PLATE WITH A CENTER OF SYMMETRY

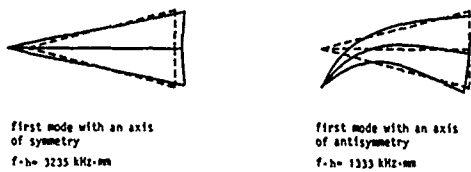


Fig. 9 Z-CUT PLATE WITH AN AXIS OF SYMMETRY

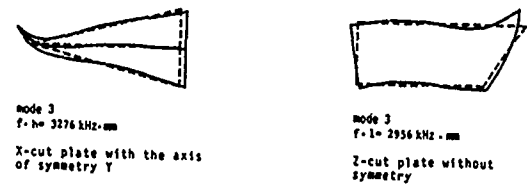


Fig. 10 MODES WITHOUT SYMMETRY

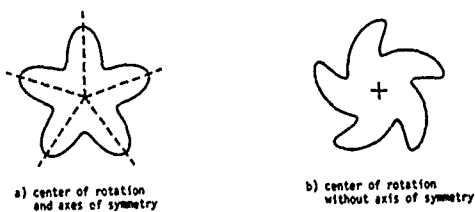


Fig. 11

SYMMETRIES OF PLATES WITH A CENTER OF ROTATION

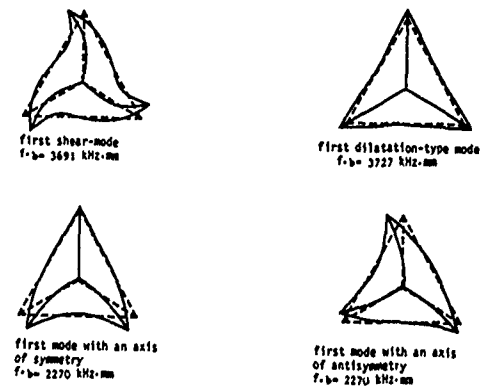
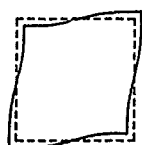
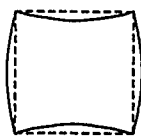


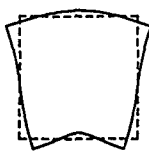
Fig. 12 Z-CUT EQUILATERAL TRIANGLE



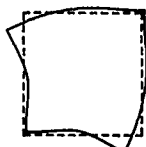
first shear-mode
f.l= 2234 kHz.mm



first dilatation-type mode
f.l= 2345 kHz.mm



first mode with an axis
of symmetry of the first type
f.l= 2267 kHz.mm



first mode with an axis
of symmetry of the second type
f.l= 2267 kHz.mm

Fig. 13

Z-CUT SQUARE PLATE



first mode with a twofold
center of symmetry
f.l= 1695 kHz.mm



first mode with a fourfold
center of symmetry
f.l= 3139 kHz .mm



first mode with a center
of antisymmetry
f.l= 1738 kHz .mm

Fig. 14

Z-CUT PLATE WITH A FOURFOLD
CENTER OF ROTATION AND
WITHOUT AXIS OF SYMMETRY

TEMPERATURE DEPENDENCE OF THE FORCE FREQUENCY EFFECT FOR THE AT-, FC-, SC-, AND ROTATED X-CUTS

Errol P. Bernisse*
Quartex, Inc.
1020 Atherton Drive
Salt Lake City, UT 84107

Summary

Measurements have been made of the temperature dependence of the force frequency effect for the FC- and SC-cuts of quartz resonators from 25°C to over 100°C. Results for the AT-cut are included for comparison purposes. Also, corrected earlier Rotated X-cut results are included. All cuts are summarized together to represent the commonly-used doubly rotated Y-cut family.

It is found that the azimuthal angles where K_f is zero, which are of interest for mounting locations, shift with temperature for all four cuts. The shifts can be large and should be taken into account when developing the optimum mounting points of a crystal for oven-controlled applications.

Introduction

The force-frequency effect is the shift in resonant frequency of circular, thickness shear-mode resonators caused by diametrically opposed point forces applied on the perimeter in the plane of the resonator blank. The effect arises from the nonlinear elastic effects which couple the initial stress of the applied forces to the resonant vibrations. The effect causes undesirable frequency shifts with the influences of mounting stresses and acceleration. It has been studied extensively around room temperature for frequency control applications.¹⁻⁶ The primary motivation of these early studies was to identify locations where mountings could be applied with a minimum of influence by the mounting structures on frequency stability.

The temperature dependence of K_f has been investigated previously for the AT-cut^{7,8} and Rotated X-cut.⁹ The present work presents new data for the AT-, FC-, and SC-cuts and corrected data for the Rotated X-cut. Thus, four orientations are now known in the doubly rotated family (YXwz)φ,θ.¹⁰ For all four orientations, a shift is seen with temperature in the azimuthal angles where K_f is zero. Historically, two-point mounting structures for the resonators are placed in the vicinity of these azimuthal angles to reduce sensitivity to mounting stresses and acceleration. The temperature sensitivity of these mounting

points varies with choice of cut, but the general conclusion holds for all four cuts summarized here that experimental determination of the optimum mounting points should be done at the anticipated operating temperature of the oven. If this is not done, the mounting locations determined at room temperature can be as much as 5° or more away from optimum at an oven temperature of 80°C.

Experimental Technique

The experimental technique used here has been described earlier.⁹ Briefly, a circular resonator is held in a circle of 20 individual fingers. Any opposing pair of fingers can be periodically squeezed with a motor/cam arrangement. The crystal is used in an oscillator circuit whose output is beat against a reference signal. The difference frequency is frequency discriminated and measured with a phase-lock amplifier locked to the motor/cam. Repeatability is better than 5%. The entire finger assembly fits into a tube furnace for temperature measurements.

The force frequency coefficient K_f (in m s/N) is defined as

$$\frac{\Delta f}{f} = K_f \frac{F N_0}{d\tau}$$

where F is applied force in N, N_0 is frequency constant in m/s, d is resonator diameter in m, τ is resonator thickness in m, and $\Delta f/f$ is fractional frequency shift. The azimuthal angle ψ defines the location on the perimeter where F is applied. It is measured for the (YXwz)φ, θ cuts counterclockwise around the y" axis from the x" axis.⁶

One inch diameter, flat circular resonator samples with thickness for fundamental thickness shear-mode operation around 6MHz were obtained for each of the cuts investigated, plated with Cr/Au key hole pattern electrodes, and measured in the multi-finger apparatus. The finger assembly was inserted into a tube furnace to vary temperature. The K_f response at each of the ten pairs of fingers was measured and then temperature was changed. Typical data are shown in Figure 1 where K_f is plotted vs. temperature for selected azimuthal angles on the SC-cut. Note that K_f varies linearly with temperature within the scatter in the data. The lines are least-squared fits of a straight line. The slope of the

*The raw experimental data reported here were taken while the author was at Sandia Laboratories.

straight lines are used here as dK_f/dT .

Azimuthal angle ψ was determined to within $\pm 2^\circ$ by noting finger pair location relative to a flat on the resonator edge placed by the crystal supplier. An error of 90° occurred in identifying ψ for the earlier⁹ Rotated X-cut data. The earlier published K_f vs. temperature results for this cut are repeated here in Figure 2 with the correct ψ values. The scatter in data seen in Figures 1 and 2 is typical for all four cuts measured.

The general data will be presented as K_f vs. azimuthal angle and as dK_f/dT vs. azimuthal angle since behavior of K_f with T is linear within the experimental error. The K_f data will be plotted for both 25°C and the highest temperature measured for each cut. In terms of the $(YX\omega l)\phi, \theta$ family, the AT-, FC-, SC-, and Rotated X-cuts correspond to ϕ values of $0^\circ, 15^\circ, 22^\circ$, and 30° , respectively, with θ adjusted near -35° to give a zero temperature coefficient of frequency. Figures 3 through 6 show the measured results for these four cuts.

Figure 3 contains the AT-cut results. The lines for K_f in the upper half have been added for viewing purposes only. The ψ values for zero K_f at 25°C are 65° and 115° . At 78°C these angles change to 60° and 120° . For transducer applications one is interested in the ψ angles where dK_f/dT is zero; these are 40° and 140° as seen in the lower half of Figure 3. The line in the lower half of Figure 3 is the experimental result of reference 7. The results in Figure 3 for both K_f and dK_f/dT are in good agreement with the earlier AT-cut results.^{3,7}

Figure 4 contains the results for the FC-cut. Lines have been added through the data points for viewing ease. For zero K_f at 25°C , ψ is 79° and 137° . At 160°C , these change to 65° and 142° . The zeros of dK_f/dT occur around $\psi = 44^\circ$ and 143° .

Figure 5 contains the SC-cut results with lines through the data for viewing purposes. The zeros of K_f occur at $\psi = 1^\circ$ and 89° . At 120°C , the zeros occur at 83° and 170° . The dK_f/dT is zero at $\psi = 63^\circ$ and 149° .

Figure 6 contains the Rotated X-cut results with lines added for viewing. The zeros of K_f occur at $\psi = 13^\circ$ and 87° . At 275°C , these zeros occur at $\psi = 79^\circ$ and 178° . The dK_f/dT characteristic has zero at $\psi = 52^\circ$ and 137° .

Figure 7 summarizes K_f vs. ψ at 25°C and dK_f/dT vs. ψ by plotting the smooth curves drawn through the data in Figures 3 through 6. In all cases, the locations of zero K_f have appreciable temperature dependencies. Taken as a family, one location of the zeros of K_f at 25°C ranges from $\psi = 65^\circ$ to 89° and back to 87° as ϕ goes from 0° to 30° . Nowhere in this ψ range does dK_f/dT become zero when K_f is zero. The other location for the zero of K_f at 25°C varies from $\psi = 115^\circ$ to 193° (13°) as ϕ goes from 0° to 30° . Somewhere between the FC- and SC-cuts ($\phi = 15^\circ$ to 22°) there

is a cut of quartz where K_f and dK_f/dT are both zero at the same azimuthal angle.

Note in the lower half of Figure 3 that the area beneath the dK_f/dT wave is larger for negative values than for positive values, thus the integral of dK_f/dT is negative and the integral of K_f over ψ changes downward with increasing temperature for the AT-cut. Similar conclusions are reached for the FC- and Rotated X-cuts from Figures 4 and 6. For the SC-cut in Figure 5, the integral of dK_f/dT is nearly zero, so the integral of K_f over ψ , which is zero for this cut, stays near zero at all temperatures. This happy circumstance means that the stress compensation feature of the SC-cut is relatively temperature insensitive.

Conclusions

Four members of the $(YX\omega l)\phi, \theta$ family of doubly rotated cuts of quartz have been investigated for the temperature dependence of the force frequency effect, the AT-, FC-, SC-, and Rotated X-cuts. For all four cuts, the results show that the azimuthal angles where K_f is zero shift with temperature. If these ψ values where K_f is zero are chosen as mounting points to minimize mounting and acceleration effects on frequency stability, the ultimate operating temperature must be taken into account. Otherwise, the ψ angles will be in error. For instance, if the SC-cut is mounted at $\psi = 1^\circ$ where K_f is zero for 25°C , but the crystal is then used in an 80°C oven, the ψ for a zero of K_f should really be at -4° (176°), so there is a 5° error and K_f at the $\psi = 1^\circ$ mounts at 80°C will be appreciable.

Acknowledgements

The discrepancy in the Rotated X-cut data was noted as a result of discussions with D. Koehler.

References

1. A. D. Ballato, "Effects of Initial Stress on Quartz Plates Vibrating in Thickness Modes," in *Proc. 14th Annu. Frequency Control Symposium*, May-June 1960, p. 89.
2. R. W. Keyes and F. W. Blair, "Stress Dependence of the Frequency of Quartz Plates," *Proc. IEEE*, Vol. 55, No. 4, Apr. 1967, p. 565.
3. J. M. Ratajski, "Force-Frequency Coefficient of Singly-Rotated Vibrating Quartz Crystals," *IBM J. Res. Dev.*, Vol. 12, No. 1, Jan. 1968, p. 92.
4. P. C. Y. Lee, Y. S. Wang, and X. Markenscoff, "Elastic Waves and Vibrations in Deformed Crystal Plates," in *Proc. 27th Annu. Frequency Control Symposium*, June 1973, p. 1.
5. A. Ballato, E. P. EerNisse, and T. Lukaszek, "Force-Frequency Effect in Doubly Rotated Quartz Resonators," in *Proc. 31st Annu. Frequency*

Control Symposium, June 1977, p. 8.

⁶ E. P. EerNisse, T. J. Lukaszek, and A. Ballato, "Variational Calculation of Force-Frequency Constants of Doubly Rotated Quartz Resonators," IEEE Trans. on Sonics and Ultrasonics, Vol. SU-25, No. 3, May 1978, p. 132.

⁷ C. R. Dauwalter, "The Temperature Dependence of the Force Sensitivity of AT-cut Quartz Crystals," in Proc. 26th Annu. Frequency Control Symposium, 1972, p. 108.

⁸ M. Onoe, et. al., "Quartz Crystal Accelerometer Insensitive to Temperature Variations," in Proc. 31st Annu. Frequency Control Symposium, June 1-3, 1977, p. 62.

⁹ E. P. EerNisse, "Temperature Dependence of the Force Frequency Effect for the Rotated X-cut," in Proc. 33rd Annu. Frequency Control Symposium, 1979, p. 300.

¹⁰ IEEE Standard on Piezoelectricity, IEEE Std. 176-1978.

Figure 1. Representative data for the SC-cut shown as K_f vs. temperature for selected values of azimuthal angle ψ . Lines are least squared error fit.

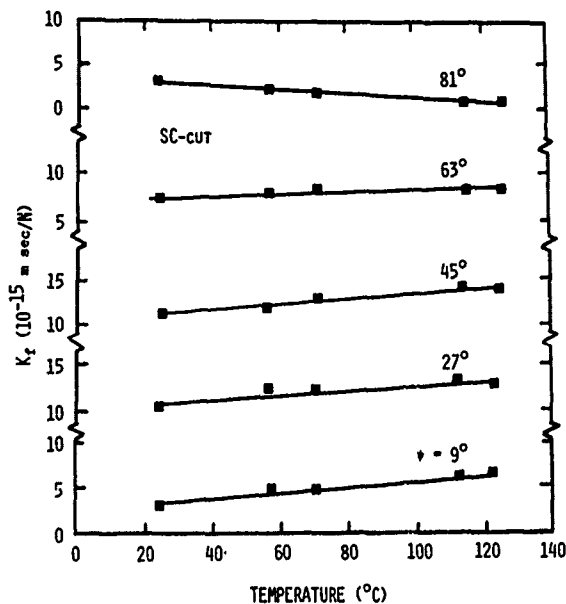
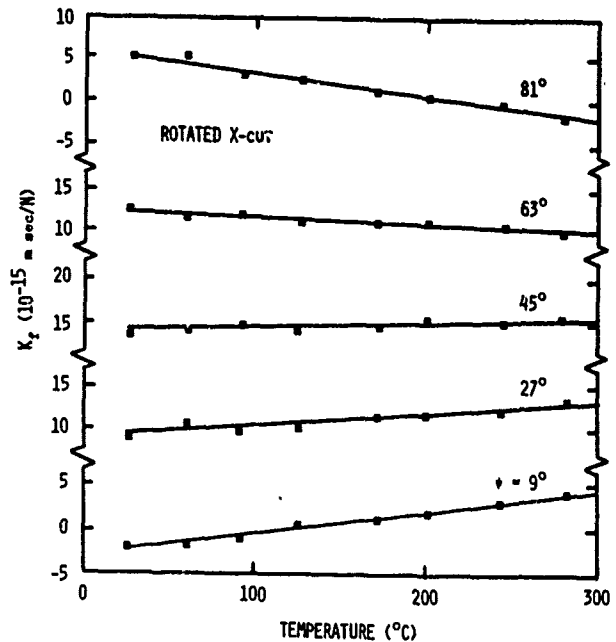


Figure 2.

Representative data for the Rotated X-cut shown as K_f vs. temperature for selected values of azimuthal angle ψ . Lines are least squared error fit.

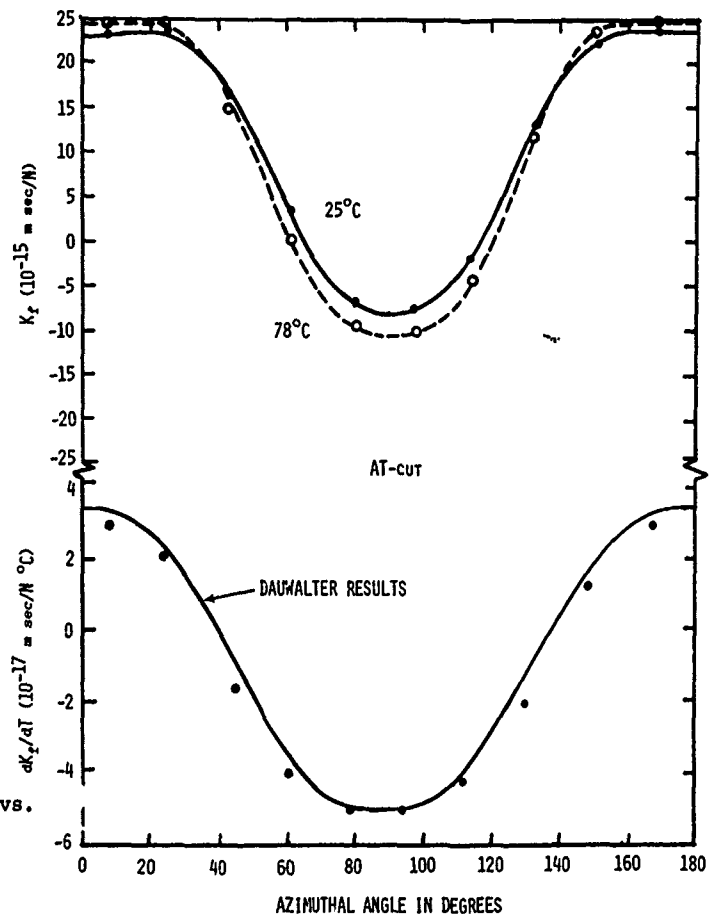


Figure 3. K_f at 25°C and 78°C vs. ψ for the AT-cut, lines are added for viewing purposes. dK_f/dT vs. ψ for the AT-cut, line is result published in reference 7.

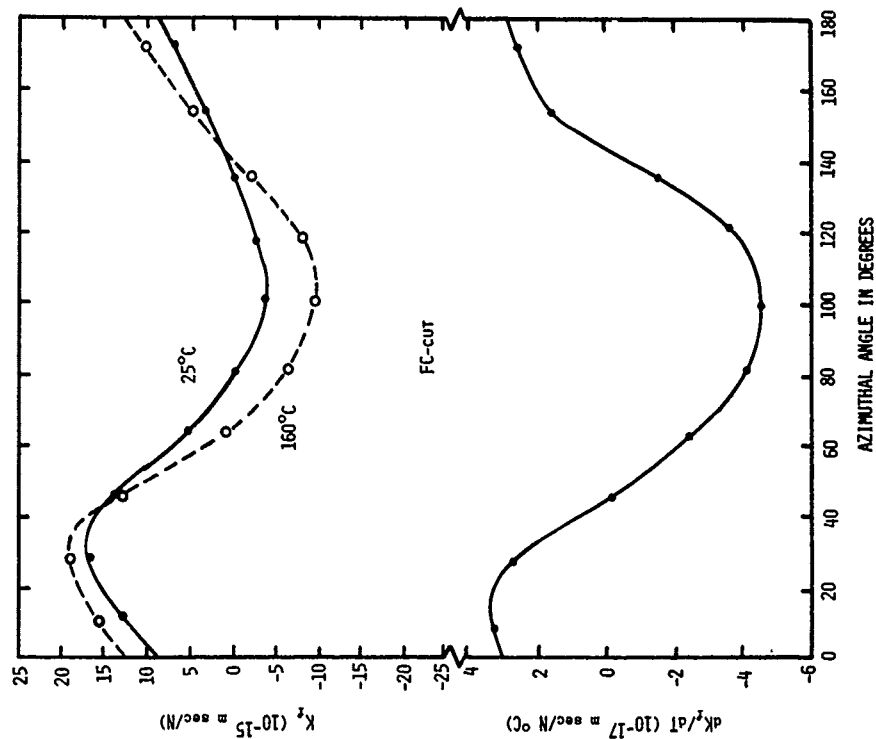


Figure 4.

K_F at 25°C and 160°C vs. ψ and dK_F/dT vs. ψ for the FC-cut, lines added for viewing purposes.

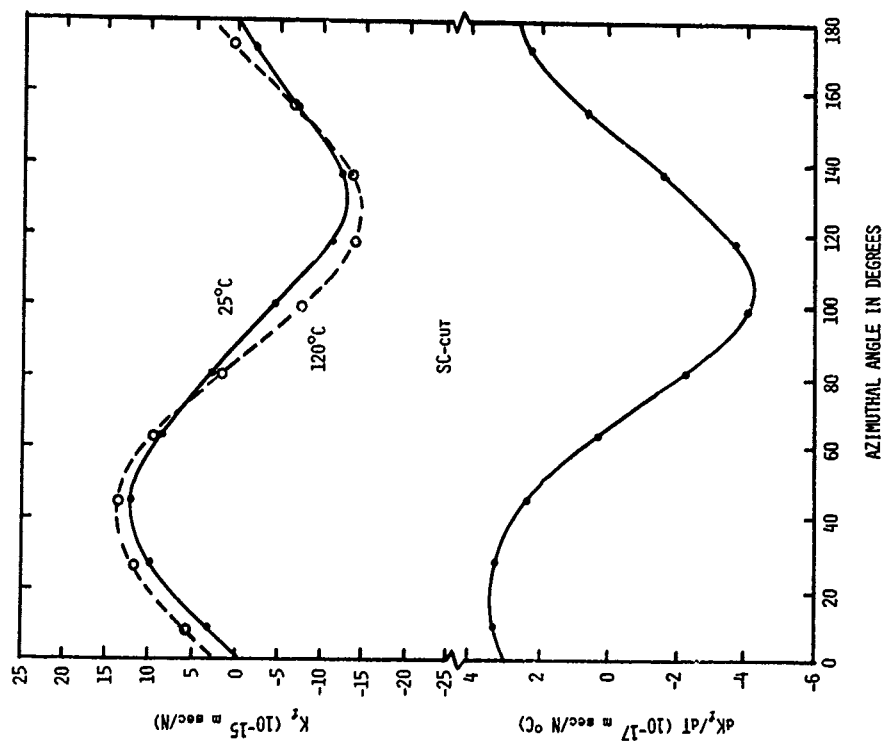


Figure 5.

K_F at 25°C and 120°C vs. ψ and dK_F/dT vs. ψ for the SC-cut, lines added for viewing purposes.

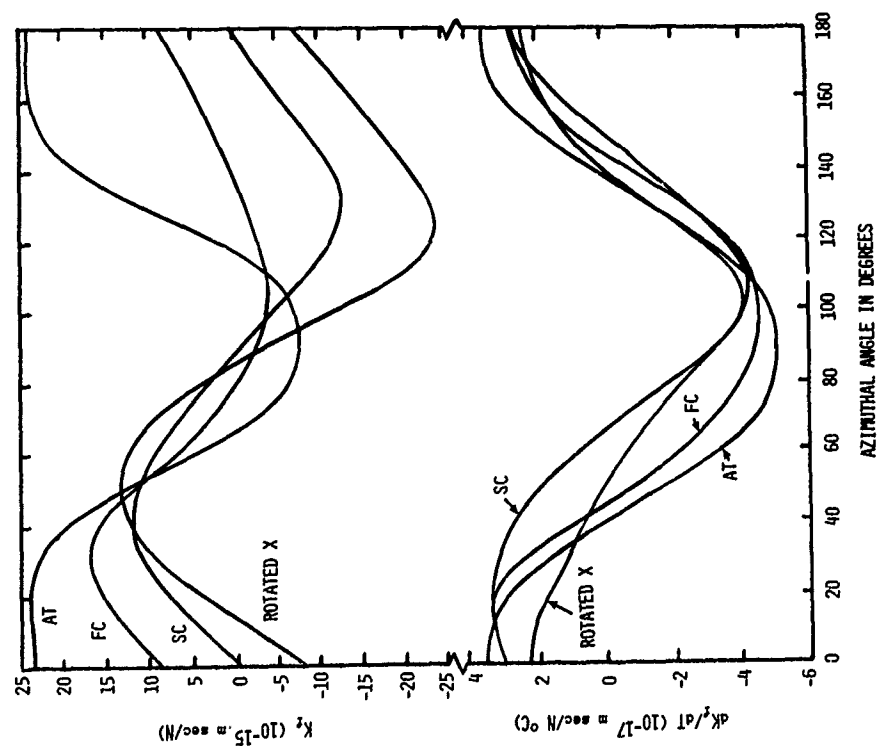


Figure 7.

Summary of experimental results for K_f at 25°C vs. ψ and dK_f/dT vs. ψ for the AT-, FC-, SC-, and Rotated X-cuts.

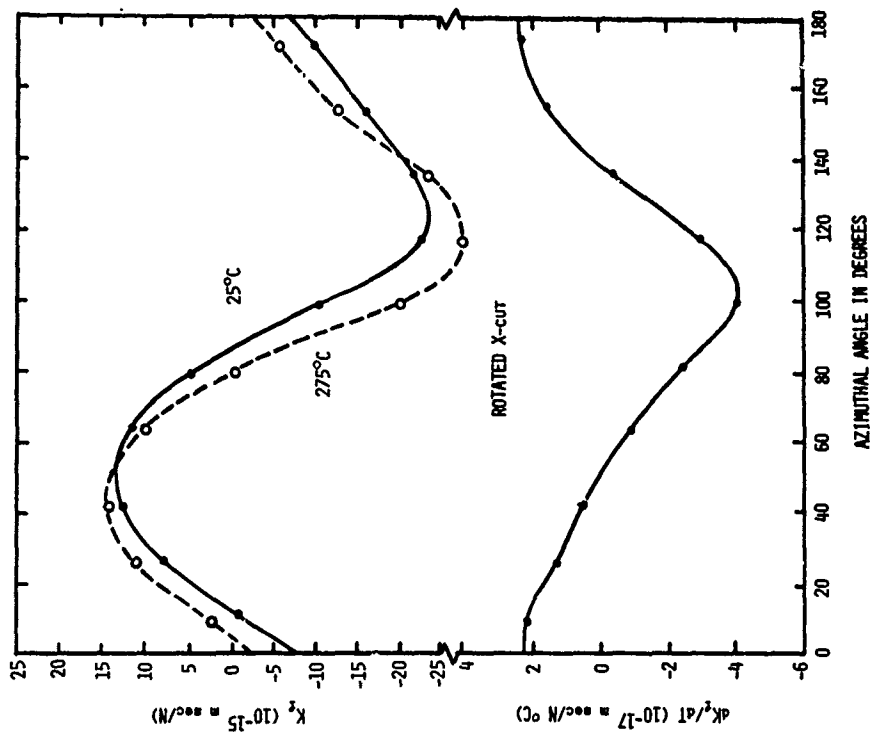


Figure 6.

K_f at 25°C and 275°C vs. ψ and dK_f/dT vs. ψ for the Rotated X-cut. Lines added for viewing purposes.

SUBTLE EFFECTS IN HIGH STABILITY VIBRATORS

A. Ballato, T. J. Lukaszek, & G. J. Iafrate

US Army Electronics Technology & Devices Laboratory
USAERADCOM, Fort Monmouth, NJ 07703

Abstract

The quest for high stability crystal vibrators for advanced frequency control applications has led in the very recent past to a number of far-reaching developments. As the level of frequency stability has improved over the years, various factors that were once imperceptible have become nonnegligible, and their influences have had to be dealt with - eliminated, reduced, or compensated. The task of adding to the list continues. At present the most obvious contributors to resonator performance have been enumerated. It is important to continue to catalog less obvious effects, and to evaluate critically at what level their influences make an appearance in the error budget of the resonator.

We consider a number of influences that are more-or-less "subtle". Each is examined to see what contribution it makes to resonator performance. It is apparent that some have to be taken into account in present-day applications; others may become important as future stability specifications become even more stringent.

Key Words

Resonators, Frequency Control, Acoustic Waves, Quartz Crystals, Bulk Acoustic Waves, Piezoelectric Crystals, Equivalent Networks, Acceleration Effects, Vibration Effects, Quartz Resonators, Twinning, Electrode Stresses.

Introduction

The year 1980 marks the centenary of the discovery of piezoelectricity by the brothers Curie, and the fifty-eighth year of the quartz oscillator! The past thirty years or so have seen the development of cultured quartz from coin-sized pieces, shown in Fig. 1, to large crystals that constitute the bulk of the usage today (Fig. 2). Since the introduction of the quartz crystal-controlled oscillator by Cady, each decade of time has seen approximately one order of magnitude frequency stability improvement. Progress in timekeeping is seen on a broad time scale in Fig. 3, adapted from Reference 2; a similar chart is given in Reference 3. Further improvements will depend upon less-obvious factors than have been considered to date. This paper briefly treats a number of such topics.

Magnetic Fields

Quartz, and other high purity dielectric crystals, can be considered to be nonmagnetic for our purposes here. A vibrating crystal with metallic, nonmagnetic electrodes is, however, affected by external magnetic fields. Eddy currents are produced in the electrodes by their motions in the fields; these change the critical frequencies of the vibrator, and lower its Q. The situation is depicted in Fig. 4, where the vibrator leads are considered attached to the remainder of the oscillator and the combination adjusted to the resonance condition of the vibrator (zero reactance at all times). The case with magnetic field parallel to crystal thickness is treated.

For a pure shear mode, the retarding force density at the plate surfaces is

$$-j\omega\sigma B^2 u, \quad (1)$$

with σ the electrical conductivity of the electrode, and u the mechanical displacement at the surfaces. Electrodes of thickness h' will thus produce resistances of

$$R = \sigma A B^2 h' \quad (2)$$

for areas of value A . Using conventional notation⁴, this leads to an expression for the input admittance of the single mode vibrator, including the effects of electrode inertia⁵:

$$Y_{in} = j\omega C_0 + j\omega C_0 \cdot \{ (X/(k^2 \tan X) - 1 - X^2 \mu/k^2) + (jXRY_0/k^2) \}^{-1}. \quad (3)$$

Resonance and antiresonance frequencies are determined from the zeros of the susceptance function as the roots of

$$(X - (k^2 + \mu X^2) \tan X) \cdot (1 - \mu X \tan X) + X \cdot (RY_0)^2 \cdot \tan^2 X = 0. \quad (4)$$

When $R=0$, the first expression in brackets yields the condition for resonance, and the second that for antiresonance. From the expression for Y_{in} the network in Fig. 5 is obtained for $\mu=0$ (massless electrodes). Inclusion of mass merely replaces the resistances at C-D and E-F by series R-L combinations. Figure 6 is the bisected version of Fig. 5.

Departures from the resonance frequency as function of R are found by perturbation, with RY_0 the small parameter. The expression for frequency shift is

$$\Delta f/f \approx - (2/\pi)^2 (RY_0)^2 \quad (5)$$

$$\text{with } RY_0 = \sigma h^2 B^2 / (\rho v), \quad (6)$$

ρ the quartz mass density, and v the acoustic velocity of the mode in question. It is seen from (5) and (6) that the frequency shift is quartic in the magnetic field strength. Table 1 gives frequency shift values for an AT cut having 10,000 Å copper electrodes; only for fields about ten thousand times larger than that of the earth (the first entry in the table) is the effect perceptible.

This analysis has been extended to the multi-mode case, and the situation of a lateral magnetic field, with corresponding network representations.⁵

Ambient Vibrations

Insensitivity to acceleration is one of the most prominent criteria by which to judge high stability resonators. At present, the rule-of-thumb number relating frequency shift to applied acceleration is 2×10^{-9} per g, although efforts are underway to reduce this value. (See the references given in Reference 6). It appears that a sensitivity of 1×10^{-11} /g is a reasonable goal for the next few years. These two sensitivity figures have been used in conjunction with published values for acceleration levels in various environments⁷⁻¹² to produce the frequency shift entries shown in Table 2.

From Table 2 it is seen that the decrease in acceleration sensitivity to parts in 10^4 per g and beyond is highly desirable. The smallest entry in the table is due to microseisms⁸⁻¹². Figure 7, taken from Reference 10, shows the very interesting spectrum of microseisms observed at the earth's surface. It appears that the spectrum of displacement versus period plotted on log-log scales consists of portions of +2 and -2 slope peaking rather sharply around a period of about 7 seconds. The maximum amplitude of acceleration is approximately 4 micro-g's, and is constant along the +2 slope line. For oscillators with high acceleration sensitivity this source of disturbance would have to be eliminated by mounting supports even for isolated, underground installations. Building vibrations are far greater than microseisms, and their noise spectra must be considered in the installation of precision oscillators. In certain locations, the accelerations due to earthquakes must be allowed for, although the vibrations found in urban environments produce accelerations associated with earthquakes of magnitude 3-4 on the Richter scale⁹. This scale is defined, for shallow shocks, as the \log_{10} of the maximum trace amplitude in micrometers with which the standard short-period torsion seismometer would register that earthquake at an epicentral distance of 100 km.

One crystal resonator structure having decreased

acceleration sensitivity for accelerations in the thickness direction is the ring-supported configuration⁶. Several varieties of these are displayed in Fig. 8 and Fig. 9; they bear a resemblance to grooved resonators¹³⁻¹⁵ except that the membrane of quartz connecting the support ring to the active portion is wider to allow for energy trapping.

Mass Imbalance

In treatments of resonator electroding, it is usually tacitly assumed that both electrodes are of equal size and thickness. The practical reality is usually just the opposite. It is very difficult to guarantee that the thicknesses are equal in the first place; to make matters worse, final frequency adjustment is usually made with a burst of material applied to a single side. Add to this situation the facts that registration of both electrodes is never perfect, that the electrode tabs are asymmetrically disposed, and that sometimes a larger electrode is used on one side to improve statistical uniformity of C_1 by compensating for mis-registration, then it is seen that symmetry of the plate resonator about the mid-plane is seldom, if ever, achieved.

The single-mode case is treated, by way of example, for a simple electrode mass imbalance in the one-dimensional approximation. The equivalent network is that of Fig. 5 with the mechanical ports C-D and E-F having the equal resistances R replaced by unequal transmission lines representing the thick electrodes. When the electrodes are thin enough for propagation of the acoustic waves to be neglected within the electrodes, the transmission lines are replaced with lumped inductances; the mass imbalance results in unequal inductance values and prevents the network from being bisected, as in Fig. 6. When bisection can take place, the transmission line representing the crystal plate of thickness $2h$ is replaced by one of half this value and the construction for the critical frequencies is that given in Fig. 10; the formulas are those of the bracketed terms in (4) separately set to zero. An AT-cut resonator with symmetrical electrodes of equal thickness produced the mode spectrograph of Fig. 11. Strong responses are found at the odd harmonics, and nothing is visible at the even harmonics.

It is appropriate now to quote from Cady, p 308:

"There are circumstances under which a plate may conceivably vibrate in a thickness mode at or close to an even harmonic frequency. The shape, size, and location of the electrodes may be such as to produce a driving field in the plate that varies in the direction of the thickness. Or the plate may be twinned or have other defects such that the excitation is not uniform. Finally, the plate may be in contact with an electrode of considerable mass, so that in effect one has a composite resonator."

When the electrodes are of unequal mass, and circuit bisection is not possible, the construction becomes that of Fig. 12, where the critical frequencies are determined by intersection with a tangent function of argument $2X$ instead of X . The expression for input impedance is

$$Z_{in} = (1/j\omega C_0) \cdot \left\{ 1 - \frac{k^2 (\tan X/X)}{((1-\bar{\mu}X \tan X) + \frac{\Delta^2 X^2}{(1+\bar{\mu}X \cot X)})} \right\}, (7)$$

where $\bar{\mu} = (\mu_1 + \mu_2)/2$ and $\Delta = (\mu_1 - \mu_2)/2$. Equation (7) has been written in terms of argument X for the tangent and cotangent functions. The anti-resonant frequencies (denoted $f_A^{(M)}$ for M odd, and $f_R^{(M)}$ for M even) are found from the vanishing of the bracketed term in (7) as roots of

$$\tan 2X = \frac{-(\mu_1 + \mu_2) X}{(1 - \mu_1 \mu_2 X^2)}. (8)$$

These are shown in Fig. 12 along with the high and low frequency asymptotes of the right hand side of (8). The roots for the resonant frequencies are found from the zeros of (7).

The even-harmonic resonances produced by the unequal mass-loadings on the crystal plate surfaces ($\mu_1 \neq \mu_2$) are very sharp compared to the odd harmonics as may be seen from Fig. 13. It is thus possible to use such resonances for stabilizing the frequency of an oscillator - at least in principle. Figure 14 shows a blow-up of the second harmonic of the case of Fig. 13; Fig. 15 shows the fourth harmonic, and Fig. 16 the fourteenth harmonic. Compare the width of the resonance of Fig. 16 with that of Fig. 17 showing the fifteenth harmonic. In general, for large M , the frequency of response approaches $(M-1)$.

When the resonator of Fig. 11 was overcoated with electrode material on one side only, the mode spectrum of Fig. 18 was produced. The second harmonic becomes present due to the imbalance, and it is sharp; however, it is also very weak. Figure 19 is a vertically expanded version; it has a strength of only about 8 dB and is more than 50 dB below the fundamental.

Another unsymmetrical structure that leads to even harmonics is the composite resonator; see Reference 16 for additional references. This structure is shown in Fig. 20, with the equivalent network given in Fig. 21. Here the quartz substrate must be represented by a transmission line because of its thickness; as it shrinks in size the situation of Fig. 5 with inductors is approached.

Apart from producing even harmonics, the presence of asymmetry in resonators (due to unequal electrodes, bevelling, contouring, etc.) is very probably a major cause of "activity dips", or "bandbreaks".^{17,18} These are illustrated in Fig. 22, which is taken from Reference 19. Both the frequency versus temperature and the conductance

versus temperature curves suffer anomalous dips as the interfering mode's influence is manifest at a particular temperature. The second harmonic mode "divided by two" via the nonlinear elastic constants can produce dips at the fundamental.

Electrode Influence

Some time ago the effect of equal electrode coatings was demonstrated in regard to frequency shift and change of the frequency-temperature, $(f-T)$ curve of a resonator.²⁰⁻²⁵ The calculations dealt only with the influence of inertial mass; no elastic properties were assumed for the electrodes, nor were they presumed to apply any stresses to the crystal. This was done so that the inertial influence of the electrode could be compared with elastic and stress effects. Results from the one dimensional theory for the change in apparent orientation angle are given in Fig. 23 and Fig. 24.²⁵

Table 3 gives apparent orientation angle shifts as function of mass loading and harmonic number for an AT plate having the following parameters:

$$\begin{aligned} f^{(1)} &= 5.0 \text{ MHz} \\ \phi_a &= 14. \text{ mm} \\ \phi_e &= 6. \text{ mm} \end{aligned}$$

The electrodes are of evaporated aluminum, of equal thickness on both sides. These data are to be compared with the data appearing in Table 10 of References 23 and 24 for chromium and indium. The comparison is given in graphical form for all three metals plus the inertial mass theory in Fig. 25. It is seen that Al and In have slopes that agree with theory, but are displaced; the curves for Cr are consistent among themselves, but differ in sign from the theory. The results in Fig. 25 indicate the importance of electrode material, deposition method, and conditions of deposition on the behavior of the finished resonator. Figure 26 shows the decrease in inflection temperature with increasing mass of evaporated aluminum, for resonators with the parameters described above.

It should also be borne in mind that stresses in the electrodes can produce activity dips, even when the electrodes are of equal mass. Consequently, the practice of furnishing the quartz plate with a thin layer of Ni or Cr to insure adhesion of gold, e.g., ought to be re-examined in view of the stress levels produced by these metals, both intrinsically, and as a function of temperature.

X-Ray Angle Changes²⁶

The angles locating the X-ray planes in a crystal are functions of temperature and external stress. For example, the plane at $38^\circ 13'$ used for orienting AT cuts is only found at this angle at a certain temperature. For high precision applications the angle shift with temperature is not negligible. We give an approximate calculation to establish the order of magnitude of the angle change.

Consider a rotated-Y-cut plate of crystal in the rhombic, tetragonal, trigonal, hexagonal, or cubic systems. (These have no off-diagonal thermoelastic coefficients.) At temperature T the plate angle will be determined from

$$\tan \theta = (X_2/X_3). \quad (9)$$

With a change in temperature to $T+\Delta T$, the axes become, in the linear approximation

$$\left. \begin{aligned} X_2' &= X_2 (1 + \alpha_{22} \Delta T) \\ X_3' &= X_3 (1 + \alpha_{33} \Delta T) \end{aligned} \right\} \quad (10)$$

We are thus led to a relation between $\Delta\theta$ and ΔT :

$$\tan \Delta\theta = \{(A-1) \tan \theta / (1 + A \tan^2 \theta)\} \quad (11)$$

where

$$A = (1 + \alpha_{22} \Delta T) / (1 + \alpha_{33} \Delta T). \quad (12)$$

Equations (11) and (12) are used to calculate the angle changes in Table 4; beyond about 10 kelvins the linear approximation is not accurate except as to order of magnitude. For the tetragonal, trigonal and hexagonal systems, since $\alpha_{22} = \alpha_{11}$, the result is independent of angle ϕ . In particular, for the upper zero temperature locus for thickness mode plates θ is approximately constant and the result holds therefore for the AT, FC, IT, and SC cuts. The relation appearing in Table 4, viz.,

$$\Delta\theta \sim \frac{1}{2} (\alpha_{11} - \alpha_{33}) \cdot \Delta T \cdot \sin 2\theta \quad (13)$$

is obtained from equations (11) and (12) and shows that $\Delta\theta$ depends on the difference between α_{11} and α_{33} for rotated-Y-cuts (or for doubly rotated cuts when $\alpha_{22} = \alpha_{11}$). For the cubic system this difference is zero, so $\Delta\theta$ is always zero in this system. For quartz, the effective value of α in the thickness direction of rotated-Y-cut plates is shown in Fig. 27. For the Y cut, $\alpha = \alpha_{22} = \alpha_{11}$, while for $\theta = \pm 90^\circ$ (Z cut), $\alpha = \alpha_{33}$.

Twinning

The types of twinning that may occur in quartz are shown in Fig. 28 along with the changes in axes and handedness.²⁷ We briefly explore the effects of twinning on the piezoelectric constants of crystals in Class 18.

(a) Dauphiné: $X_1 \leftrightarrow X_1$; $X_2 \leftrightarrow X_2$; $X_3 \leftrightarrow X_3$.

$$e_{11} \leftrightarrow -e_{11}; e_{14} \leftrightarrow e_{14}.$$

(b) Brazil: $X_1 \leftrightarrow X_1$; $X_2 \leftrightarrow X_2$; $X_3 \leftrightarrow X_3$.

$$e_{11} \leftrightarrow -e_{11}; e_{14} \leftrightarrow -e_{14}.$$

(c) Combined: $X_1 \leftrightarrow X_1$; $X_2 \leftrightarrow X_2$; $X_3 \leftrightarrow X_3$.

$$e_{11} \leftrightarrow -e_{11}; e_{14} \leftrightarrow -e_{14}.$$

Consider e_{26} , the piezoelectric constant driving the pure shear mode in rotated-Y-cuts of quartz:

$$\text{Untwinned: } e_{26}' = (e_{11} \cos \theta + e_{14} \sin \theta) \cdot (-\cos \theta).$$

$$(a) \text{ Dauphiné: } e_{26}' = (-e_{11} \cos \theta + e_{14} \sin \theta) \cdot (-\cos \theta).$$

$$(b) \text{ Brazil: } e_{26}' = (e_{11} \cos \theta + e_{14} \sin \theta) \cdot (+\cos \theta).$$

$$(c) \text{ Combined: } e_{26}' = (e_{11} \cos \theta - e_{14} \sin \theta) \cdot (-\cos \theta).$$

Consider further a plate of unity area, with a fraction 'a' of this area twinned. For simplicity, assume the twinning is complete throughout the thickness, and that the distribution of motion is uniform even though twinned. Then the composite e_{26}' should be:

(a) Dauphiné:

$$e_{26}' = [(1-2a) e_{11} \cos \theta + e_{14} \sin \theta] \cdot (-\cos \theta).$$

(b) Brazil:

$$e_{26}' = [(1-2a) e_{11} \cos \theta + (1-2a) \sin \theta] \cdot (-\cos \theta).$$

(c) Combined:

$$e_{26}' = (e_{11} \cos \theta + (1-2a) e_{14} \sin \theta) \cdot (-\cos \theta).$$

In the case of Brazil twinning:

$$e_{26}' (\text{twinned}) = (1-2a) \cdot e_{26}' (\text{untwinned}). \quad (14)$$

Equation (14), when written in terms of the resonator capacitance ratio becomes:

$$r (\text{twinned}) = r (\text{untwinned}) / (1-2a)^2. \quad (15)$$

Cosmic Rays²⁸⁻⁴⁰

Cosmic rays, and other unshieldable radiation sources, produce cumulative contributions to long term aging. Knowing the radiation sensitivity of natural and cultured quartz under a variety of treatments permits an evaluation of resonator performance due to this source.

The raw data are contained in Fig. 29 to Fig. 31.²⁸ Using the values for the photon flux given and a number of simplifying assumptions, the frequency shift due to this source is given in Table 5 for two values of quartz sensitivity. The unit "rad" is defined as

"The standard unit of absorbed dose, equal to energy absorption of 100 ergs per gram (0.01 joule per kilogram)."³⁶

Similarly for neutrons, the assumptions listed at the bottom of Table 6 lead to the order-of-magnitude figures given in the table for three values of altitude. As may be seen, for neutrons the estimate leads one to conclude that resonators in satellites may indeed experience non-negligible shifts even prescinding from the conservative assumption of total energy absorption.

Acknowledgment

The authors wish to thank Profs. R. D. Mindlin and Jack Oliver, Drs. H. A. Leupold, E. Hafner, J. Vig, B. K. Sinha, R. Kinloch, and J. Ziegler, and Messrs. J. Kwiecien, G. Waldeck and J. Sherman for their contributions. We wish to thank R. Kinloch of Sawyer Research Products, Inc. for permission to use Fig. 2, J. Ziegler of IBM for permission to use Figs. 29 - 31, and J. Oliver of Cornell University for permission to use Fig. 7.

REFERENCES*

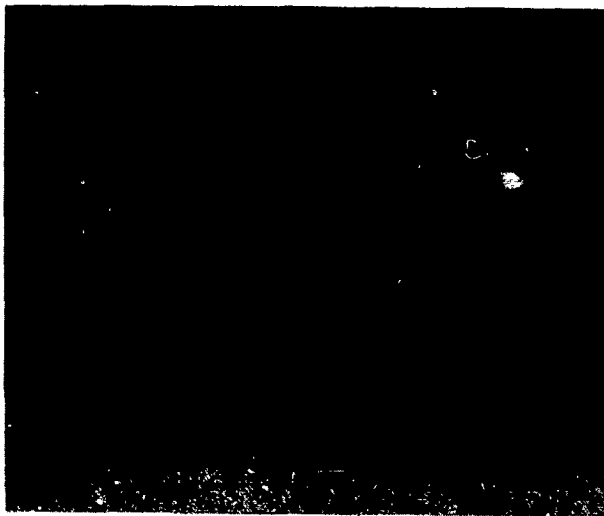
1. W.G. Cady, Piezoelectricity, McGraw-Hill, New York, 1946; Dover, New York, 1964, p.308.
2. J.A. Barnes, "Basic concepts of precise time and frequency," in Time and Frequency: Theory and Fundamentals, (B.E. Blair, ed.), National Bureau of Standards Monograph 140, Washington DC 20402, May 1974, Chapter 1, pp. 1-40.
3. W.A. Marrison, "The evolution of the quartz crystal clock," *Bell Syst. Tech. J.*, vol. 27, July 1948, pp. 510-588.
4. A. Ballato and T.J. Lukaszek, "Mass-loading of thickness-excited crystal resonators having arbitrary piezo-coupling," *IEEE Trans. Sonics Ultrason.*, vol. SU-21, October 1974, pp. 269-274.
5. A. Ballato, "Quartz resonators in magnetic fields," to be published.
6. A. Ballato, "Crystal resonators with increased immunity to acceleration fields," *IEEE Trans. Sonics Ultrason.*, vol. SU-27, July 1980.
7. AMC Pamphlet 706-117, Engineering Design Handbook, "Environmental Series, Part Three, Induced Environmental Factors," HQ, US Army Materiel Command, Alexandria, VA 22333, January 1976, Chapters 4, 5, & 6.
8. C.M. Harris and C.E. Crede, Eds., Shock and Vibration Handbook, McGraw-Hill, New York 1961. Volume 1, Basic Theory and Measurements; Volume 2, Data Analysis, Testing, and Methods of Control; Volume 3, Engineering Design and Environmental Conditions.
9. C.F. Richter, "Instrumental earthquake magnitude scale," *Bull. Seismol. Soc. Amer.*, vol. 25, January 1935, pp. 1-32.
10. J.N. Brune and J. Oliver, "The seismic noise of the earth's surface," *Bull. Seismol. Soc. Amer.*, vol. 49, October 1959, pp. 349-353.
11. J.W. Guyton, "Review of seismological information on ground vibrations," Technical Report No. 63-50, The Geotechnical Corporation, Garland, TX, May 1963, 13 pp.
12. United Kingdom Atomic Energy Authority, The Detection and Recognition of Underground Explosions, Whitefriars Press, London, 1965, 118 pp.
13. M. Nakazawa, "Analysis of vibrational mode in concaved quartz crystal plate with probe method," paper of Tech. Group on EA 76-43. *Inst. Electr. Comm. Eng. Jpn.*, pp. 23-28, 1976.
14. M. Nakazawa and S. Wakui, "On the grooved AT-cut quartz crystal," submitted to *J. Inst. Electr. Comm. Eng. Jpn.*
15. M. Nakazawa, "Improving frequency-temperature characteristics of grooved AT-cut plates," these proceedings.
16. A. Ballato and T. Lukaszek, "Distributed network modeling of bulk waves in crystal plates and stacks," Technical Report ECOM-4311, US Army Electronics Command, Fort Monmouth, NJ 07703, May 1975, 19 pp.
17. B.J. Isherwood and C.A. Wallace, "The analysis of unwanted-mode vibration patterns in AT-cut quartz oscillator crystals, revealed by x-ray diffraction topography: I. Interpretation of the x-ray diffraction topographs," *J. Phys. D: Appl. Phys.*, vol. 8, 1975, pp. 1827-1842.
18. F.N. Goodall and C.A. Wallace, "The analysis of unwanted-mode vibration patterns in AT-cut quartz oscillator crystals, revealed by x-ray diffraction topography: II. A partial theoretical description of the unwanted mode," *J. Phys. D: Appl. Phys.*, vol. 8, 1975, pp. 1843-1850.
19. A. Ballato and R. Tilton, "Electronic activity dip measurement," *IEEE Trans. Instrum. Meas.*, vol. IM-27, March 1978, pp. 59-65.
20. A. Ballato and T. Lukaszek, "Mass effects on crystal resonators with arbitrary piezo-coupling," *Proc. 27th AFCS*, June 1973, pp. 20-29.
21. A. Ballato and T. Lukaszek, "Mass-loading effects on crystal resonators excited by thickness electric fields," Technical Report ECOM-4270, US Army Electronics Command, Fort Monmouth, NJ 07703, October 1974, 80 pp.
22. A. Ballato, "Normalized frequencies and deviations as function of coupling, mass-loading, and harmonic: numerical results for thickness excitation," Technical Report ECOM-4354, US Army Electronics Command, Fort Monmouth, NJ 07703, September 1975, 164 pp.
23. A. Ballato and T. Lukaszek, "Frequency-temperature coefficients of mass-loaded plate vibrators," Technical Report ECOM-4356, US Army Electronics Command, Fort Monmouth, NJ 07703, September 1975, 49 pp.

24. A. Ballato and T. Lukaszek, "Higher-order temperature coefficients of frequency of mass-loaded piezoelectric crystal plates," Proc. 29th AFCS, May 1975, pp. 10-25.
25. A. Ballato, "Apparent orientation shifts of mass-loaded plate vibrators," Proc. IEEE, vol. 64, September 1976, pp. 1449-1450.
26. E. Knolmayer, "Exact netplane data for quartz, LiTaO_3 , LiNbO_3 , and berlinite," these proceedings.
27. C. Frondel, *The System of Mineralogy*. Wiley, New York, 1962, Seventh Edition, vol. 3.
28. J.F. Ziegler and W.A. Lanford, "Effect of cosmic rays on computer memories," Science, vol. 206, 16 November 1979, pp. 776-788.
29. T.C. May, "Soft errors in VLSI: present and future," IEEE Trans. Components, Hybrids, and Mfg. Technol., vol. CHMT-2, No. 4, December 1979, pp. 377-387.
30. J.A. Woolley, L.E. Lamar, N.H. Stradley, and D.M. Harshbarger, "Low alpha-particle-emitting ceramics: what's the lower limit?," IEEE Trans. Components, Hybrids, and Mfg. Technol., vol. CHMT-2, No. 4, December 1979, pp. 388-390.
31. S.W. Levine, "Alpha emission measurements of lids and solder preforms on semiconductor packages," IEEE Trans. Components, Hybrids, and Mfg. Technol., vol. CHMT-2, No. 4, December 1979, pp. 391-395.
32. D.H. Phillips, "Cosmic radiation effects in spacecraft microelectronics: Part I," Military Electronics/Countermeasures, vol. 5, August 1979, pp. 88-92.
33. D.H. Phillips, "Cosmic radiation effects in spacecraft microelectronics: Part II," Military Electronics/Countermeasures, vol. 5, September 1979, pp. 87-93.
34. D.J. Redman, R.M. Sega, and R. Joseph, "Alpha particle-induced soft errors in microelectronic devices, Part I," Military Electronics/Countermeasures, vol. 6, March 1980, pp. 42-47.
35. D.J. Redman, R.M. Sega, and R. Joseph, "Alpha particle-induced soft errors in microelectronic devices, Part II," Military Electronics/Countermeasures, vol. 6, April 1980, pp. 40-48.
36. D.N. Lapedes, Ed., *Dictionary of Scientific and Technical Terms*, McGraw-Hill, New York, 1974.
37. R. Bechmann, "Radiation effects in quartz - a bibliography," Nucleonics, vol. 16, March 1958, pp. 122, 138.
38. Index to the proceedings of the frequency control symposium 1956 (10th) to 1976 (30th). Proc. 30th AFCS June 1976, Category 3: Radiation effects on resonators, p. 502.
39. E.A. Gerber, "Precision frequency control and selection, a bibliography," Proc. 33rd AFCS, May-June 1979, Section 1.3, pp. 604-606.
40. E.A. Gerber, "Precision frequency control and selection, a bibliography," these proceedings, Section 1.3.

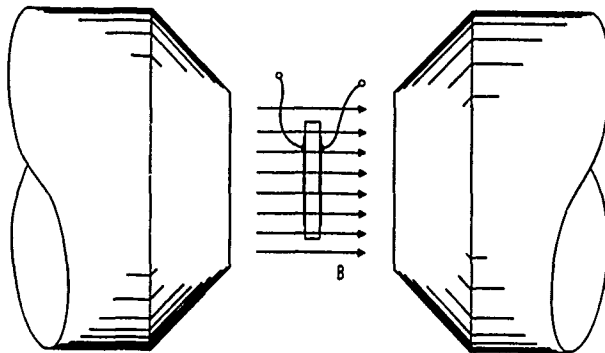
* AFCS: Annual Frequency Control Symposium, US Army Electronics R&D Command, Fort Monmouth, NJ 07703.



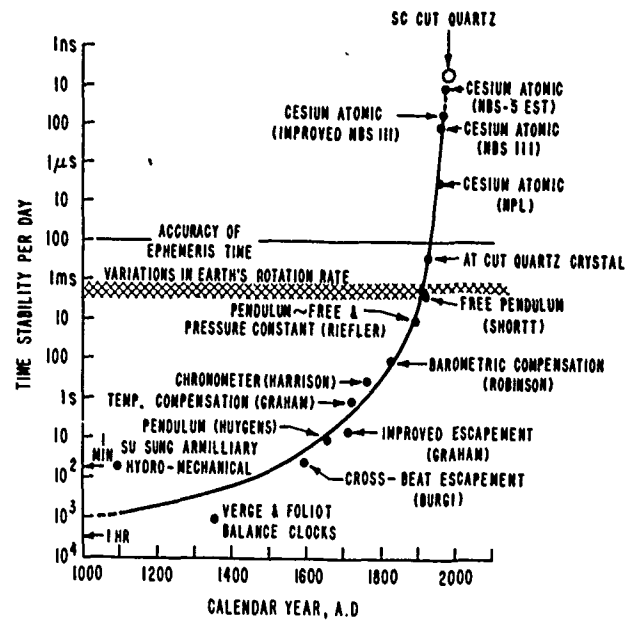
1. Early cultured quartz.



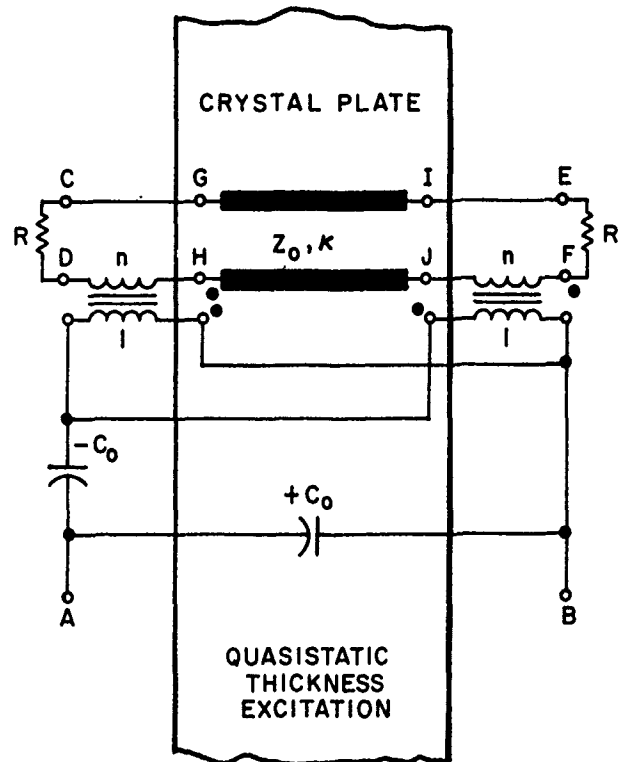
2. Modern cultured quartz.



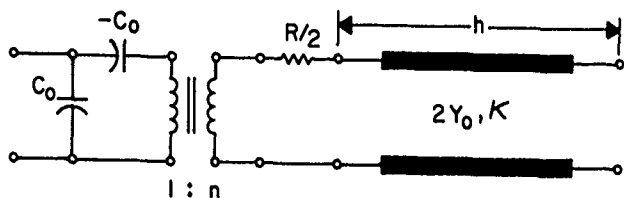
4. Crystal resonator in magnetic field.



3. Progress in timekeeping.



5. Network for resonator in magnetic field.



6. Bisected version of Fig. 5.

QUARTZ RESONATORS IN MAGNETIC FIELDS

$$\Delta F/F \approx -(\frac{1}{2})^2 \cdot R^2 Y_0^2$$

$$RY_0 = \sigma h^2 B^2 / (\rho v)$$

TESLA	KILO-GAUSS	$\Delta F/F$		KILO-OERSTED
		AT CUT	AMPERE/METER	
5.8 (-5)	0.58 (-3)	-2.2 (-28)	46.2	0.58 (-3)
0.1	1	-1.9 (-15)	7.9 (+4)	1
0.3	3	-1.5 (-13)	2.4 (+5)	3
1	10	-1.9 (-11)	7.9 (+5)	10
3	30	-1.5 (-9)	2.4 (+6)	30

Table 1. Quartz resonators in magnetic fields.

AMBIENT ACCELERATION EFFECTS				
ENVIRONMENT	ACCELERATION G UNITS	OSCILLATOR SENSITIVITY		NOTE
		2x10 ⁻⁹ /g	1x10 ⁻¹¹ /g	
		FREQUENCY SHIFT		
<u>ROAD VEHICLES</u>				
TRACTOR-TRAILER (3-80 Hz)	0.2 PEAK	4(-10)	2(-12)	1/
PANEL TRUCK	0.02 RMS	4(-11)	2(-13)	2/
ARMORED PERSONNEL CARRIER	0.5 TO 3 RMS	6(-9)	3(-11)	
<u>RAILROADS</u>				
STANDARD	1 PEAK	2(-9)	1(-11)	
SOFT-RIDE	0.1 PEAK	2(-10)	1(-12)	
CROSSING TRACKS/SWITCHES	6 PEAK	1.2(-8)	6(-11)	
NORMAL COUPLING & SWITCHING	30 PEAK	6(-8)	3(-10)	3/
<u>SHIPS</u>				
NORMAL CALM	0.02 TO 0.8	1.6(-9)	8(-12)	
ROUGH SEAS	0.8	1.6(-9)	8(-12)	
SLAM & EMERGENCY MANEUVERS	TO 3	6(-9)	3(-11)	

Table 2a. Ambient acceleration effects.

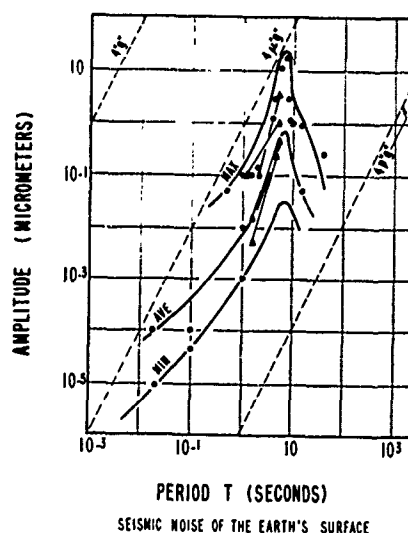
AMBIENT ACCELERATION EFFECTS				
ENVIRONMENT	ACCELERATION G UNITS	OSCILLATOR SENSITIVITY		NOTE
		2x10 ⁻⁹ /g	1x10 ⁻¹¹ /g	
		FREQUENCY SHIFT		
<u>AIRCRAFT</u>				
PROPELLER	0.3 TO 5 RMS	1(-8)	5(-11)	
HELICOPTER	0.1 TO 7 RMS	1.4(-8)	7(-11)	
JET	0.02 TO 2 RMS	4(-9)	2(-11)	4/
<u>ROCKETS</u>				
MISSILES (BOOST PHASE)	15	3(-8)	1.5(-10)	
ABLE-1 (MULTI-STAGE)	30	6(-8)	3(-10)	
VENUS ENTRY	310 MAX.	6.2(-7)	3.1(-9)	
<u>SEISMIC</u>				
EARTHQUAKE (EL CENTRO, CA, 1940)	0.33 MAX.	6.6(-10)	3.3(-12)	
MICROSEISMS	4x10 ⁻⁶ MAX.	8(-15)	4(-17)	
BUILDINGS (QUIESCENT)	0.02 RMS	4(-11)	2(-13)	5/

Table 2b. Ambient acceleration effects (cont.)

NOTES:

- 1/ PEAK AMPLITUDE LEVELS ARE APPROXIMATELY TEN TIMES RMS LEVELS FOR ROAD VEHICLES.
- 2/ FLATBED TRACTOR-TRAILER WITH AND WITHOUT 15 TON LOAD; 16 DIFFERENT ROAD CONDITIONS; VARIOUS SPEEDS; CROSSCOUNTRY (USA) TRIP. PEAK IS 1g AT 1 Hz, DECREASING TO 0.2 AT 3 Hz; RELATIVELY CONSTANT TO 80 Hz; INCREASING TO 1g AT 300 Hz. AIR-RIDE SUSPENSION (3-300 Hz): 0.01g RMS.
- 3/ HUMP (11 MPH): 450g PEAK; COUPLING SHOCK (3.4 MPH): 100g PEAK; COUPLING SHOCK (6 MPH): 700g PEAK.
- 4/ TRANSPORT PLANE IN TURBULENCE: 2 TO 3g RMS.
- 5/ SECOND FLOOR, HEXAGON BUILDING, FORT MONMOUTH, NJ: QUIESCENT LEVEL, WORKING HOURS: 20 MILLI-G, CONSTANT (0.1 TO 10 Hz); SPIKES TO 50 MILLI-G (1-10 Hz); SPIKES TO 100 MILLI-G (0.1 TO 1 Hz) - MACHINERY; BUILDING RESONANCES: 7-10 Hz.

Table 2c. Notes to Table 2.

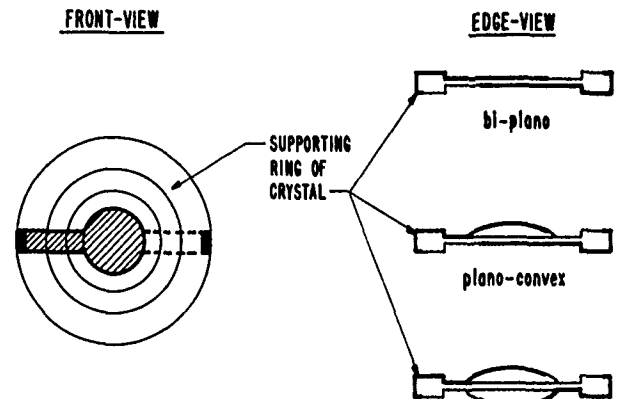


7. Seismic noise at the earth's surface.

(a) EDGE FORCES; ZERO DISPLACEMENTS
(b) EDGE TORQUES, ZERO SLOPES

The graph shows the dependence of the frequency shift Δf on the normalized frequency X . The x-axis is labeled X and has two main regions: FUNDAMENTAL and THIRD HARMONIC. The y-axis is labeled $\frac{1}{\mu X}$. Several curves are plotted: X/k^2 , $\text{TAN } X$, and $X/(k^2 + \mu X^2)$. Key points are marked: $f_{A\mu}^{(1)}$, $f_{R\mu}^{(1)}$, $f_{RO}^{(1)}$, $f_{AO}^{(1)}$, $f_{A\mu}^{(3)}$, $f_{R\mu}^{(3)}$, $f_{RO}^{(3)}$, and $f_{AO}^{(3)}$. A vertical dashed line is labeled $k/\sqrt{\mu}$.

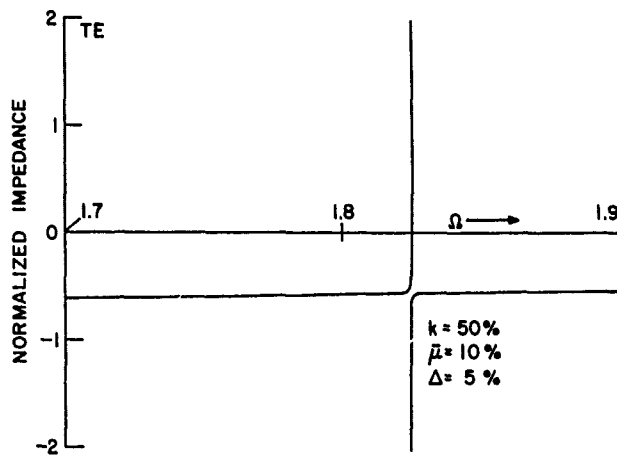
RING-SUPPORTED CRYSTAL RESONATORS



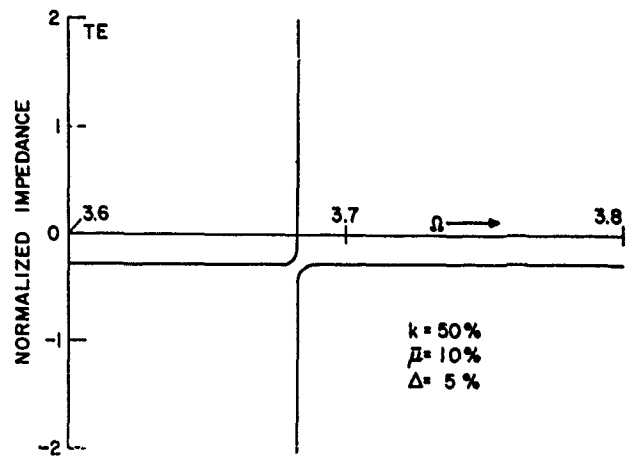
A high-contrast, black and white photograph showing a close-up of a textured surface, possibly a wall or ceiling. The surface is covered in a dense pattern of small, light-colored specks or fibers against a dark background. In the foreground, there is a dark, irregular shape that appears to be a shadow or a piece of material. The overall image has a grainy, high-contrast quality.

Figure 1 is a plot of Normalized Impedance TE versus Ω . The y-axis ranges from -2 to 2, and the x-axis ranges from 0 to 5. Four curves are shown, corresponding to different values of k (50%, 10%, 5%, and 2.5%), with $\mu = 10\%$ and $\Delta = 5\%$. The curves show that as k decreases, the impedance response shifts to higher frequencies and becomes flatter.

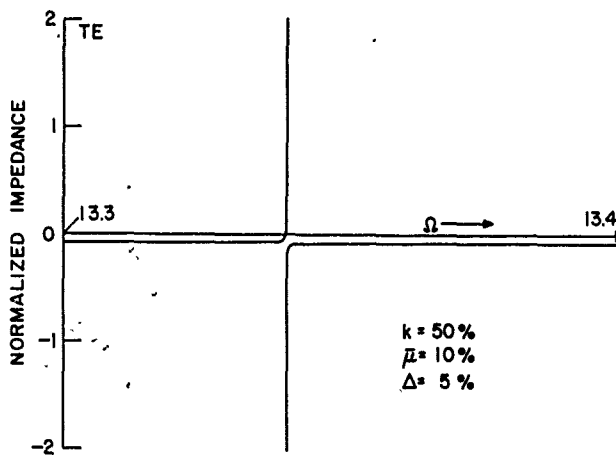
439



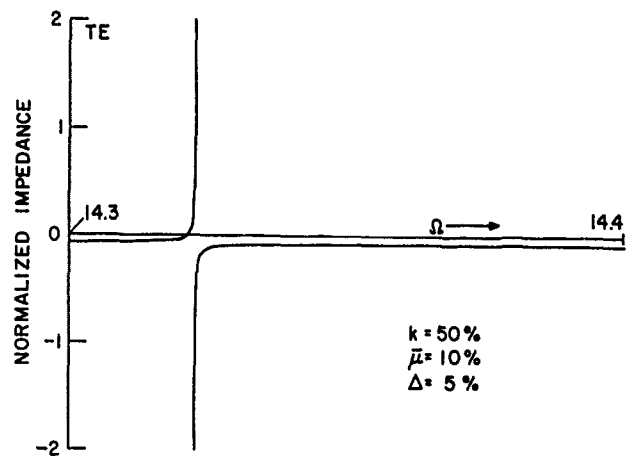
14. Spectrum near second harmonic.



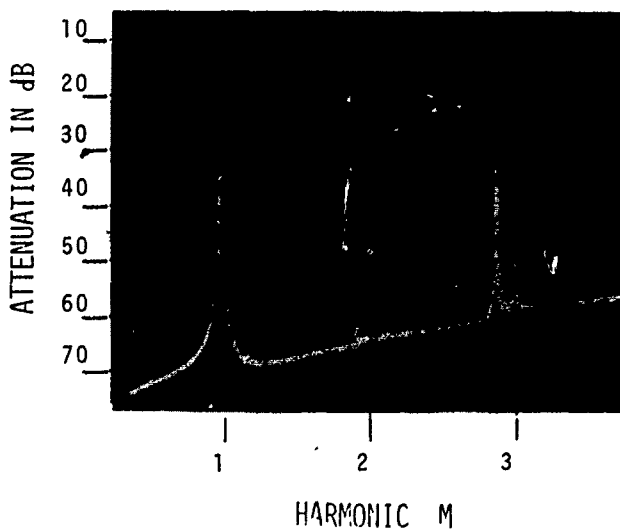
15. Spectrum near fourth harmonic.



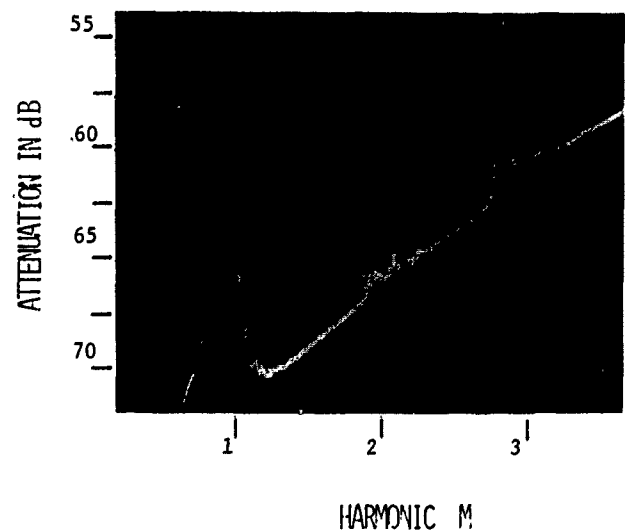
16. Spectrum near fourteenth harmonic.



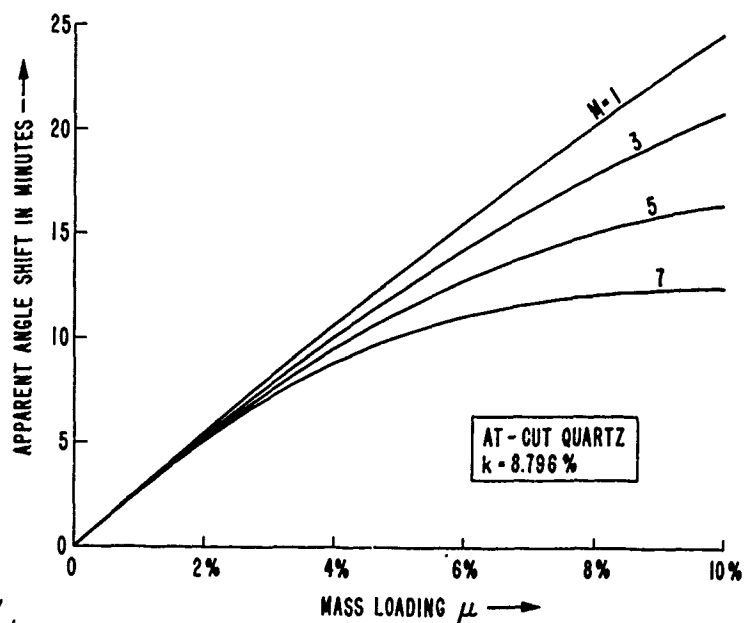
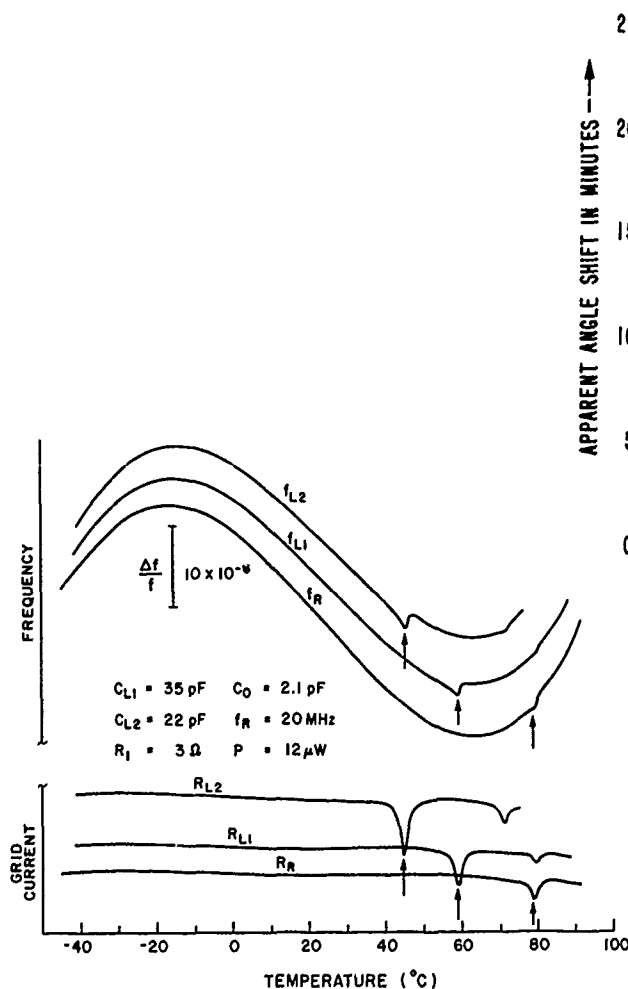
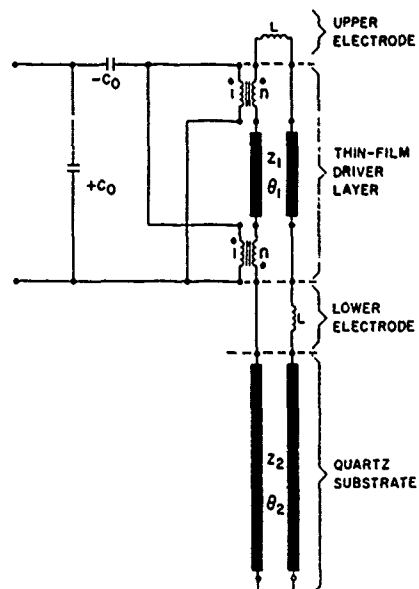
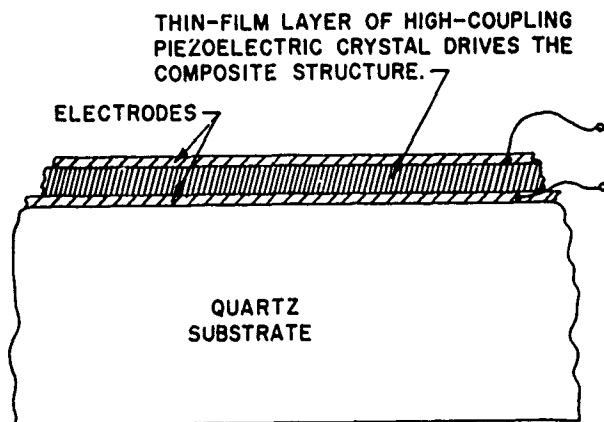
17. Spectrum near fifteenth harmonic.

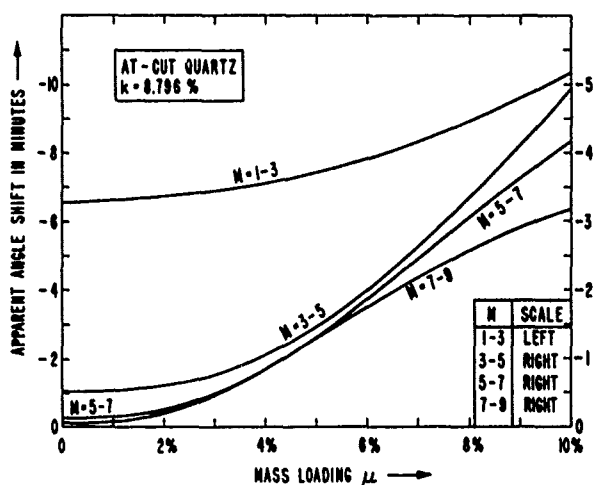


18. Experimental mode spectrum-electrode imbalance.

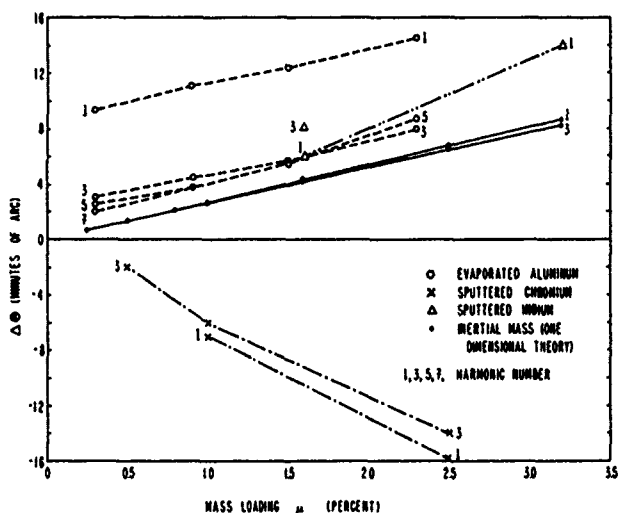


19. Attenuation scale expansion of Fig. 18.





24. Angle shift for change of harmonic.



25. Angle shift for various electrode materials.

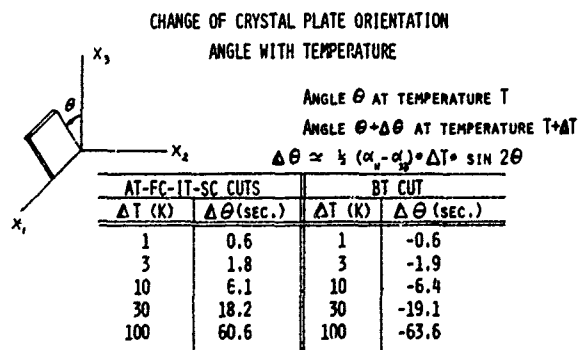
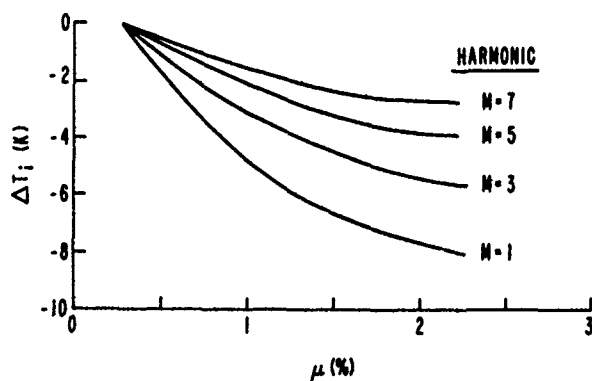


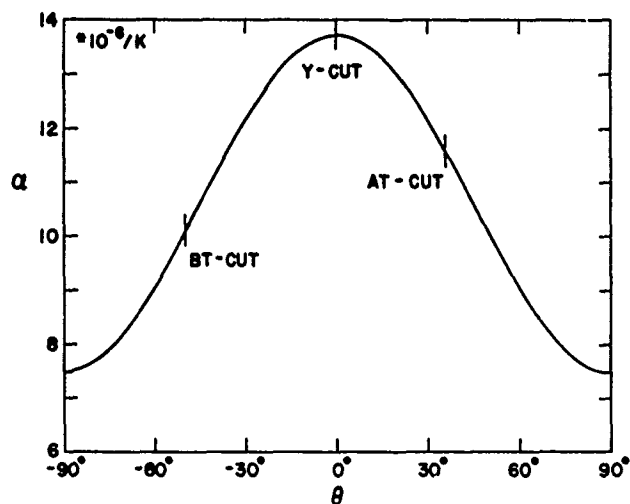
Table 4. Change of crystal plate orientation angle with temperature.

ALUMINUM ELECTRODES	HARMONIC NUMBER			
	1	3	5	7
0%				
0.3%	+9.4	+3.13	+2.6	+2.1
0.9%	+1.73	+1.37	+1.2	+1.68
1.5%	+1.29	+1.25	+1.76	
2.3%	+2.16	+2.25	+3.19	

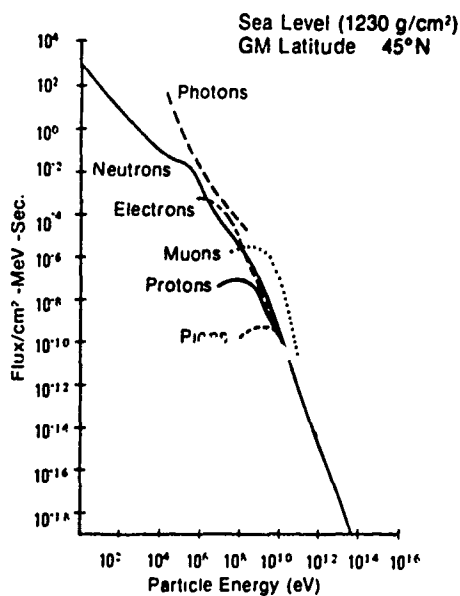
Table 3. Apparent angle shift in minutes of arc.



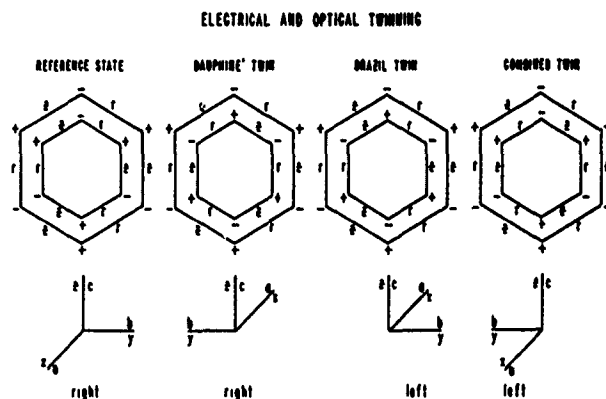
26. Inflection temperature change with increasing mass.



27. Thermoelastic coefficient for rotated-Y-cuts of quartz.



29. Cosmic ray flux.



28. Electrical and optical twinning.

SPECIFICATION: $\Delta F/F = 10^{-5}$

TIME FOR SPECIFIED SHIFT: $\tau(s) \approx 5 \cdot 10^{12} \cdot s$ YEARS

	NATURAL QUARTZ	SWEPT CULTURED
$\Delta F/F$	$\sim 10^{-11}/\text{RAD}$	$\sim 10^{-12}/\text{RAD}$
\mathcal{F}_P	~ 1	~ 1
$\tau(12)$	~ 5 YRS.	~ 50 YRS.
$\tau(14)$	~ 5 HOURS!	~ 0.5 YRS.

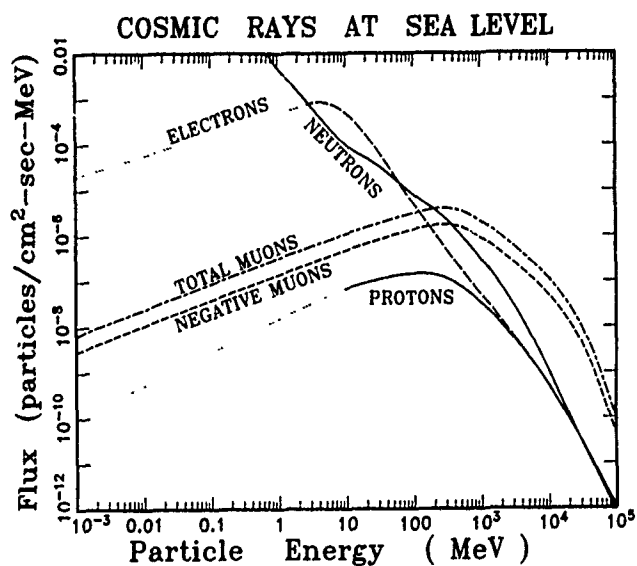
NOTES: 1/ UNPROTECTED CRYSTAL

2/ TOTAL ENERGY ABSORBED

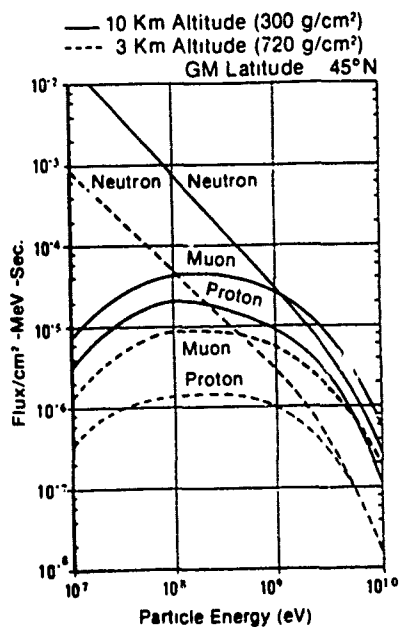
3/ SEA LEVEL

4/ \mathcal{F}_P IN PHOTONS/ $\text{CM}^2\text{-SEC}$

Table 5. Frequency shift for photons.



30. Cosmic rays at sea level.



SPECIFICATION: $\Delta F/F = 10^{-5}$

TIME FOR SPECIFIED SHIFT: $\tau(s) \approx 10^{14} \sim 5/4 \bar{J}_N$ YEARS

	SEA LEVEL	3 KM	10 KM
\bar{J}_N	$\sim 10^{-3}$	$\sim 10^{-2}$	~ 0.6
$\tau(12)$	$\sim 25,000$ YRS.	$\sim 2,500$ YRS.	~ 4 YRS.
$\tau(14)$	~ 250 YRS.	~ 25 YRS.	~ 16 DAYS!

NOTES: 1/ UNPROTECTED CRYSTAL

2/ TOTAL ENERGY ABSORBED

3/ $\Delta F/F \sim 10^{-21}$ CM²/NEUTRON

4/ \bar{J}_N IN NEUTRON-SEC/CM²

Table 6. Frequency shift for neutrons.

31. Cosmic ray flux at 3 and 10 km.

THE OVERLAPPING GROUND - A NEW MONOLITHIC CRYSTAL FILTER CONFIGURATION

James L. Dailing

MOTOROLA, INC.
Plantation, Florida

Abstract

The monolithic crystal filter has had widespread acceptance since its conception in the sixties even though it has one serious drawback - the limit of the ultimate attenuation. This limit, usually in the 40 dB range, is due to the stray capacitance between the input and output electrodes.

This paper presents a new configuration for the monolithic crystal filter electrodes which essentially eliminates the capacitance between the input and output. The result is that an ultimate attenuation of 60 to 80 dB can now be achieved with a single 2-pole monolithic crystal filter.

A secondary benefit of the new configuration over the standard monolithic crystal filter is that it can be used to obtain wider bandwidths if desired. In the past, limitation on the maximum bandwidth obtainable with standard monolithic crystal filters has caused difficulties for special purpose requirements.

I. Introduction

Filters have always played an important role in electrical engineering and, in particular, communications. We have seen that as system requirements and techniques become more sophisticated, filter requirements become more stringent. This is especially true in the mobile and portable communication field where, with the large and ever increasing number of radio and pager users, channels are narrow and closely spaced. Even though the discrete crystal filter with its unique narrow-band selective properties was able to fulfill the system requirements, the development of the monolithic crystal filter was a significant advance in the technology of selective networks. This is due to the fact that the monolithic crystal filter is at least 50% smaller than the discrete crystal filter and in addition is more economical. The result is that the monolithic crystal filter is now almost exclusively used instead of its discrete counterpart.

In spite of all its excellent attributes, the monolithic crystal filter has a significant limitation. This limitation is the degree of ultimate attenuation, typically about 40 dB. The monolithic crystal filter is, therefore, a selec-

tive device which has excellent close-in selectivity but mediocre far-out selectivity.

Analysis will show that the ultimate filter attenuation is being limited by capacitive feed-through from input to output. This has been considered a fundamental limitation for 2-pole crystal filters since very little could be done to improve it.

This paper describes a new configuration for the monolithic crystal filter electrodes which essentially eliminates the capacitive coupling from input to output. The result is that the ultimate attenuation has been increased to between 60 and 80 dB. Furthermore, the new configuration entails no additional cost. An additional benefit of the new configuration is that the bandwidth can be increased, if desired, for such requirements as data transmission.

II. Standard Type Structures

A standard structure for a 2-pole monolithic crystal filter is shown in Figure 1. The structure consists of two pairs of metallic electrodes (with their associated runners for connections) deposited on a thin piezoelectric wafer such as quartz. In this structure, the input and output electrodes are on one side of the wafer and their associated ground electrodes are on the opposite side. The signal, which is applied to the input electrode, is acoustically coupled through the piezoelectric material to the output electrode.

The equivalent electrical circuit for this standard configuration is shown in Figure 2. The values for the elements of this equivalent circuit, which represents a bandpass filter, are determined by the physical dimensions of the piezoelectric wafer, metallic electrodes, and intrinsic properties of the piezoelectric material. The parallel (coupling) inductor principally determines the bandwidth of the filter. A major factor in determining the value of this inductor is the distance (gap) between the input and output electrodes. This distance is usually very small (less than .5 mm). Due to the fact that this distance is so small, there is capacitive coupling between the input and output. This capacitance is shown as C_g in Figures 1 and 2.

The capacitance, C_g , causes transmission zeros to occur in the monolithic filter response as shown in Figure 3. These transmission zeros are seen experimentally and can be verified with a computer analysis program. As a consequence of the transmission zeros, there is the undesirable effect of flyback, also shown in Figure 3. At frequencies further removed from f_0 , the flyback returns to what is commonly referred to as the ultimate attenuation of the filter. At this point, the piezoelectric crystal has very little effect and the signal is merely coupling through the capacitance C_g . Ultimate attenuation is usually in the 40 dB range, with the capacitance, C_g , in the 10 fF range.

In the past, the 40 dB level of ultimate attenuation has been considered an inherent problem due to the fact that the crystal electrodes must be in close proximity for proper operation. The only solution to the problem was to use the "brute force" method of cascading two sections. Cascaded filters improve the ultimate attenuation, but the 4-pole response which results is often an overdesign. That is, often only a 2-pole response with good ultimate attenuation is needed. The result of the cascaded approach is that cost and size is doubled.

An alternate configuration has previously been reported¹ which reverses the output and ground electrodes as shown in Figure 4. This configuration has the effect of producing a 180° shift in the response as compared to the configuration shown in Figure 1. The equivalent circuit for the "reversed ground" structure has to be modified from that used for the structure in Figure 1, in order to accommodate the 180° phase shift. The modification is shown in Figure 5 where the coupling element has been changed from an inductor to a capacitor. This change eliminates the transmission zeros and associated flyback as can be shown by analysis.

The alternate "reversed ground" structure, however, still suffers from the problem of stray capacity between the input and output electrodes, as shown by the flux lines through the quartz in Figure 4. Even though the transmission zeros have been eliminated ultimate attenuation, as shown in Figure 6, remains in the 40 dB range. In other words, the capacitance between the input and output electrodes through the quartz is still in the 10 fF range. For every 6.0 dB improvement in the ultimate attenuation, the stray capacitance must be reduced by 50%. In order to increase the ultimate attenuation significantly, the stray capacitance must be substantially reduced.

III. Overlapping Ground Configuration

The capacitance from input to output can be reduced by using a Faraday shield. This can be accomplished by starting with the configuration shown in Figure 4 and extending the two ground electrodes into the gap area as shown in Figure 7a. This technique can be continued by extending the two ground electrodes further into the gap area

so that they overlap as shown in Figure 7b. By comparing the flux lines in Figure 7b with those in Figures 4 and 7a, it is possible to see qualitatively how the capacitance between the input and output is progressively reduced. The ground electrodes, in addition to being extended into the gap can be extended in the lateral direction as shown in Figure 8. This provides additional shielding, also improving the ultimate attenuation.

There is an additional benefit of extending the ground electrodes into the gap area. This added benefit is that by only extending the ground electrodes into the gap while keeping all other parameters constant increases the acoustic coupling and consequently filter bandwidth by as much as 50%. In a conventional monolithic crystal filter, the acoustic coupling decreases as the mass loading due to the electrodes increases. That is, the acoustic coupling decreases as the difference between the frequency in the unplated area (gap) and the frequency in the plated area (electrodes) increases. When the ground electrodes are extended into the gap, the difference between the frequency in the gap area and the frequency in the electrode area decreases so that the acoustic coupling increases. This increased acoustic coupling then provides the increased bandwidth.

A decrease in bandwidth could easily be accomplished by simply increasing the gap. This, in turn, further decreases the capacitance between the input and output electrodes, which helps improve the ultimate attenuation.

A significant point which must be emphasized is that the cost of a monolithic crystal filter with the overlapping ground should be the same as a standard monolithic crystal filter.

IV. Experimental Results

Numerous monolithic crystal filters with a center frequency of 45.0 MHz and bandwidths from 12.0 to 24.0 KHz have been made using the overlapping ground configuration or other variations described. The bandwidth of 24.0 KHz was not the maximum that could be obtained but only that observed using a configuration which would normally give a bandwidth of about 16.0 KHz without the overlapping grounds. An ultimate attenuation of 60 dB is relatively easy to obtain. When the monolithic crystal filter is measured in a well shielded fixture, the ultimate attenuation is close to 80 dB. The measured attenuation of such a filter in an HC-18 housing with a 3 dB bandwidth of 18.0 KHz is shown in Figure 9. The insertion loss is 1.0 dB. The 40 dB improvement in the ultimate attenuation to close to 80 dB means that the capacitance between the input and output electrodes has been reduced from the 10 fF range to the .1 fF range.

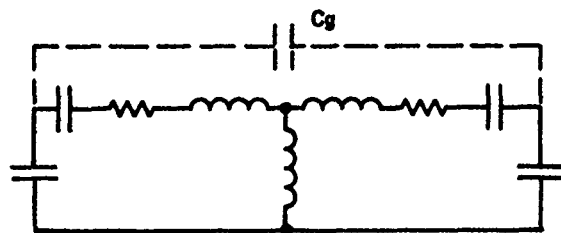
Other monolithic crystal filters at 17.9 MHz have been made using the overlapping ground configuration with results the same as for the units at 45.0 MHz including an ultimate attenuation of 75 to 80 dB.

V. Conclusion

A new configuration for the monolithic crystal filter has been described which in addition to reversing the output pair of electrodes, extends the two ground electrodes into the gap so that they overlap. The ground electrodes provide a Faraday shield between the input and output electrodes in order to reduce the stray capacitive coupling and thus increase the ultimate attenuation from the 40 dB range to the 70-80 dB range. A secondary benefit of the overlapping ground configuration is that wider bandwidth filters can now be obtained if desired. Monolithic crystal filters at 17.9 and 45.0 MHz have been constructed using the new configuration with equally good results. The measured attenuation of a 45.0 MHz filter was shown. One of the most significant points of this new configuration is that it can be accomplished with no additional fabrication costs.

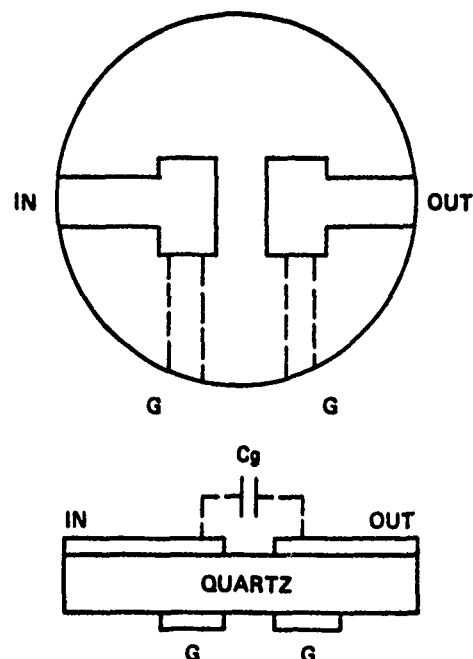
IV. References

1. Simpson, H. A., Finch, Jr. E. D., Weeman, R.K. "Composite Filter Structures Incorporating Monolithic Crystal Filters and LC Networks". Proc. of the 25th Annual Symposium on Frequency Control, 1971.
2. Dailing, James L., U. S. Patent 4,163,959 (August 7, 1979).



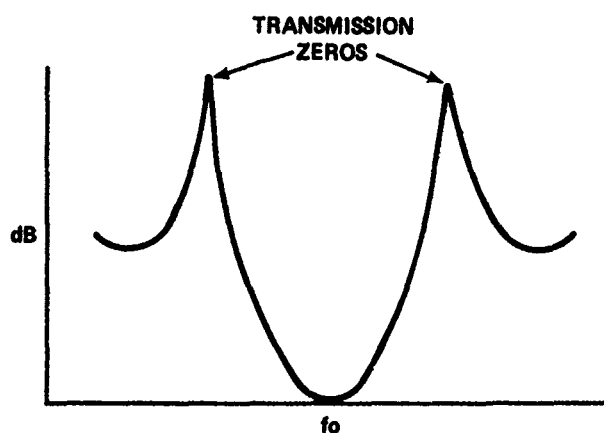
EQUIVALENT CIRCUIT FOR STANDARD MONOLITHIC CRYSTAL FILTER

Figure 2



STANDARD MONOLITHIC CRYSTAL FILTER

Figure 1



ATTENUATION-FREQUENCY RESPONSE OF STANDARD MONOLITHIC CRYSTAL FILTER

Figure 3

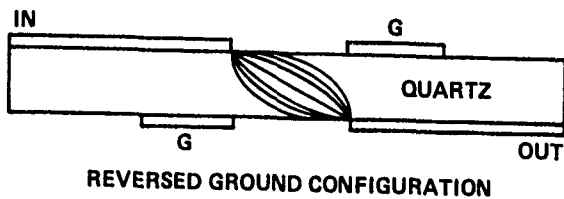


Figure 4

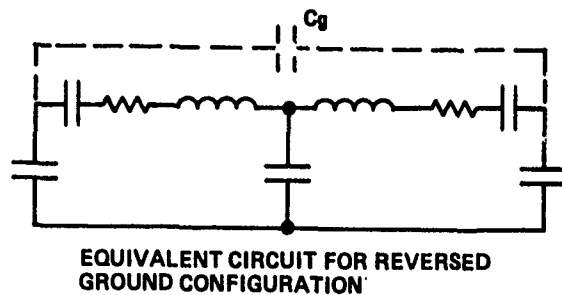
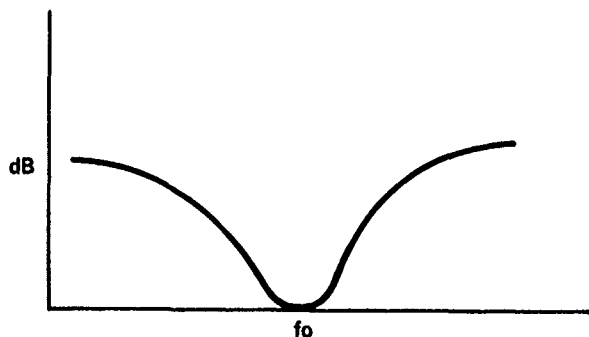
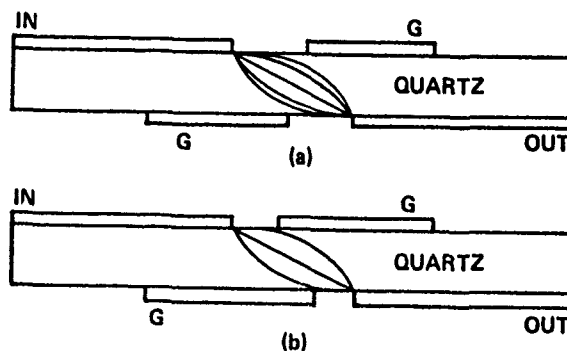


Figure 5



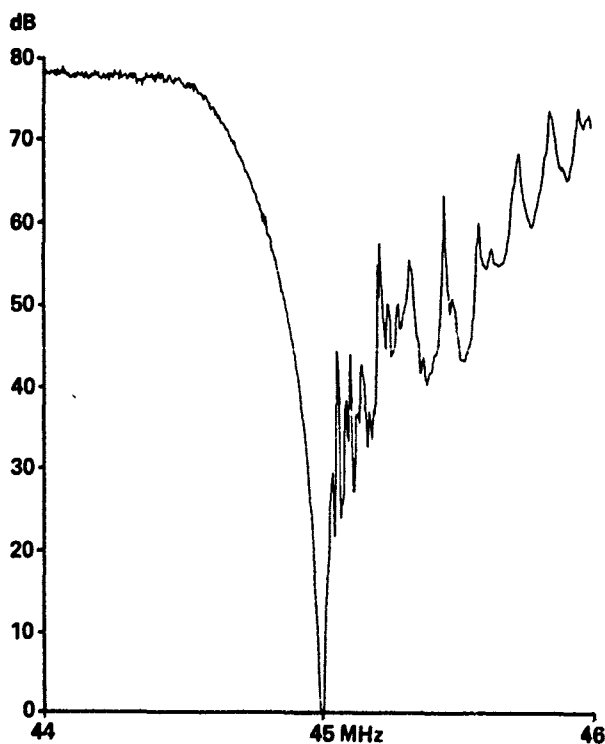
ATTENUATION-FREQUENCY RESPONSE OF REVERSED GROUND CONFIGURATION

Figure 6



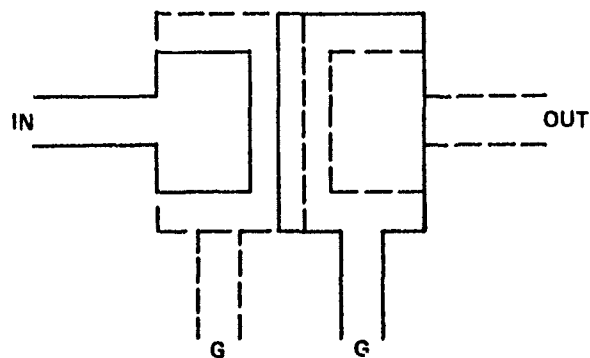
MONOLITHIC FILTER WITH FARADAY SHIELD

Figure 7



ATTENUATION - FREQUENCY RESPONSE OF 2-POLE MONOLITHIC CRYSTAL FILTER WITH FARADAY SHIELD

Figure 9



LATERAL EXTENSION AND OVERLAPPING OF GROUNDS

Figure 8

TACTICAL MINIATURE CRYSTAL OSCILLATOR

Harold W. Jackson

The Bendix Corporation
Communications Division
E. Joppa Road, Baltimore, Maryland 21204

Abstract

A small temperature controlled quartz oscillator having fast warmup and low power consumption has been developed using microelectronic packaging and vacuum insulating methods. In this paper the basic concepts, component characteristics, and circuit details are discussed. A simple model which describes the dynamic behavior of the quartz resonator and its thermal control system is also developed. The effects of component aging and circuit noise on the stability of the oscillator are evaluated, and a method of tuning the oscillator to final frequency is given.

Introduction

The Tactical Miniature Crystal Oscillator (TMXO) is a precision quartz oscillator designed for applications which require small size, fast warmup, and low power consumption. In order to achieve these characteristics, new methods have been developed for thermal insulation, thermal control, and electronics packaging. In some cases, the introduction of these new techniques has resulted in a departure from established design practice for precision quartz oscillators. To effectively utilize these techniques, it has been necessary to obtain a higher level of performance from components and circuits than was previously required. The objective of this paper is to briefly describe the major technical features of the design, and to discuss a few of the more interesting problems and results which are unique to this approach.

This work is supported by USAERADCOM,
Contract No. DAAB07-78-C-2990.

Basic Concepts

The most significant characteristic of the TMXO that differentiates it from more conventional oscillator designs is its mechanical construction. A key element in this construction is the use of hybrid microelectronic techniques. The electronics assembly is very small and tightly coupled mechanically and thermally. The small size and low mass makes it feasible to use a novel support and thermal isolation method which results in low power consumption in the thermal control elements.

A simplified sketch of the mechanical configuration of the TMXO is shown in figure 1. The electronics assembly consisting of two hybrid substrates and the

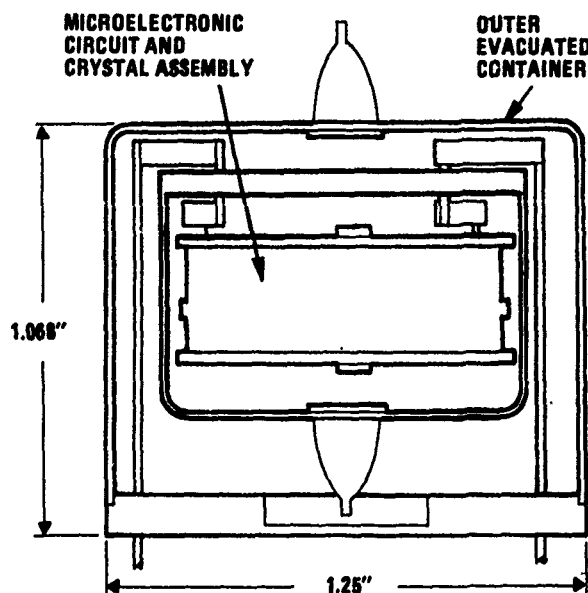


Figure 1. Simplified Mechanical Configuration of TMXO

crystal resonator is suspended by leads from the header of a hermetically sealed inner container. The inner container is in turn supported by a system of wires

(which also provide electrical connections) that feed through the header of the outer container. The outer container is also hermetically sealed and the space between the containers is evacuated. Removal of the gas between the inner and outer enclosures eliminates heat transfer due to gas conduction and convection and leaves only conduction through the wires and radiation as thermal coupling mechanisms between the inner container and the outside environment.

One of the hybrid substrates making up the electronics assembly contains the thermal control and voltage regulator circuits. The second substrate contains the oscillator, AGC, and buffer amplifier circuits. A photograph of the two circuits is shown in figure 2.



Figure 2. Electronic Assembly Substrates

The quartz resonator is contained in a ceramic flatpack enclosure similar to that proposed by Vig and Hafner¹ which is presently being developed by the Army. This packaging technique has demonstrated a significantly lower aging rate and less sensitivity to thermal cycling than standard crystal packages. The shape of this package is also very compatible with hybrid microelectronic techniques. The two flat sides of the flatpack are metalized so that the crystal can be bonded to the two substrates by soldering. This type of bonding is used to improve the thermal coupling between the crystal package and the heater elements attached to each substrate.

Quartz Resonator

The ceramic flatpack crystal resonator has been described previously.²⁻⁴ The discussion here will be limited to those characteristics of the resonator which impact on the design or performance of the TMXO. It should be pointed out that the flatpack resonators which have been evaluated for use in the TMXO were produced during the initial phases of the program and supplied essentially in an untested condition. Therefore, the results reported here should be taken as preliminary.

The ceramic flatpack crystal unit is not limited to any particular mode of vibration or cut of quartz plate, however, the TMXO development has been mostly concerned with fundamental AT cut resonators. Frequencies have been limited for the most part to the GPS frequency of 5.115 MHz although a few 10 MHz third overtone units have been evaluated. The fundamental mode resonator is attractive for TMXO application because of its smaller size, lower thermal capacity, and faster warmup.

Since the development of the ultra-precise 5th overtone resonator⁵ there has been little precedent for the use of fundamental mode resonators in precision oscillators. Because of this, little design guidance has been available relative to such questions as optimum crystal current, attainable levels of short term stability, aging rate limitations, etc. In order to optimize the design of the TMXO, an attempt has been made to answer some of these questions.

Short Term Stability

The design goal for short term stability (Allen variance) of the TMXO is 1×10^{-11} for a one second averaging time. The short term stability of the first TMXO crystal units evaluated ranged from parts in 10^{10} to parts in 10^{12} . This rather substantial variation in short term stability from unit to unit seemed to suggest

that fundamental mode units are not inherently noisy, but that the noisy performance must be due to other factors such as construction or processing.

In order to further confirm this, an arrangement was made with Bliley Electric Company to design and fabricate a 5 MHz fundamental mode resonator using basically the same construction and processing techniques used in their precision 5th overtone unit. The short term stability measurements (Allen variance) for the Bliley unit were as follows:

$\Delta f/f$	Averaging Time
2.9×10^{-11}	0.1 sec
1.0×10^{-11}	0.3 sec
3.6×10^{-12}	1.0 sec
1.2×10^{-12}	3.0 sec
1.0×10^{-12}	10.0 sec

The equivalent electrical parameters for the resonator were:

$$C_1 = 9 \times 10^{-15} \text{ Fd}$$

$$r = 2 \text{ ohms}$$

$$Q = 1.75 \times 10^6$$

For the Allen variance measurements the drive level was adjusted to 0.5mA.

The values shown for Allen variance are approaching the limits of the measurement equipment used and, therefore, the actual performance of the crystal unit may be somewhat better than indicated. In any case, the results tend to indicate that a fundamental resonator is capable of quite respectable short term stability.

The yield of ceramic flatpack resonators having acceptable short term stability is tending to improve as more units are fabricated and the design is refined.

Initial Aging

The ceramic flatpack enclosure seems to provide a substantial improvement in the initial aging characteristic of the resonator compared to other packaging techniques. A curve of frequency vs. time for a typical new resonator is shown in figure 3. After approximately one week, the aging rate has decreased to about $2 \times 10^{-10}/\text{day}$ and the better units will eventually reach $1 \times 10^{-10}/\text{day}$.

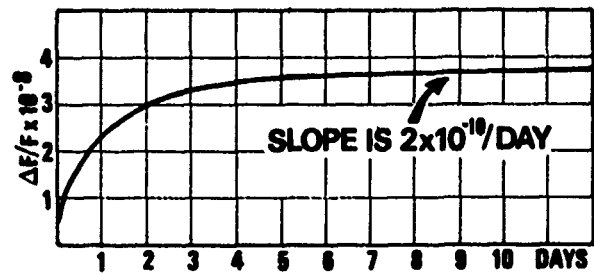


Figure 3. Initial Aging for TMXO Crystals

Frequency vs. Drive Level

The frequency vs. drive current for the 5.115 MHz TMXO crystals is shown in figure 4. Except for the slight minimum at 100uA, the curve is similar to that previously reported for 5th overtone units. At higher current levels the change in frequency is proportional to the square of the drive current as expected. Although the curve was corrected for the amplitude/phase characteristic of the oscillator circuit, it is possible that the minimum is due to experimental error.

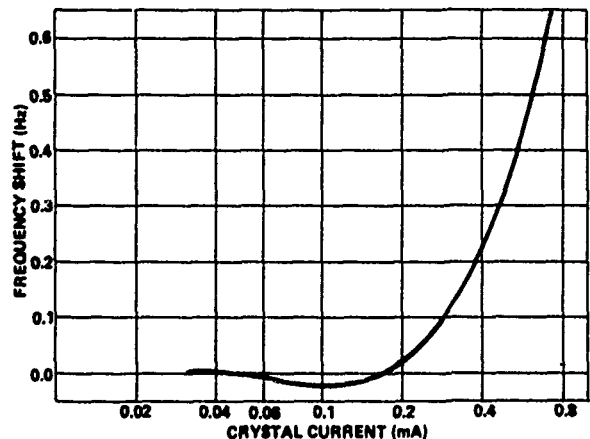


Figure 4. Crystal Frequency Vs. Drive Current

Warmup Time

A curve of frequency vs. time after starting from room temperature for the TMXO electronics assembly containing a 5.115 MHz fundamental resonator is shown in figure 5. When power is first applied, the thermal controller delivers full power and the temperature of the entire assembly increases at a rate of $1.5^\circ\text{K}/\text{sec}$. At approximately 42 seconds, the thermal sensor has reached its steady state value and the rate of change of temperature drops abruptly. Immediately following this, the frequency reaches its minimum value and

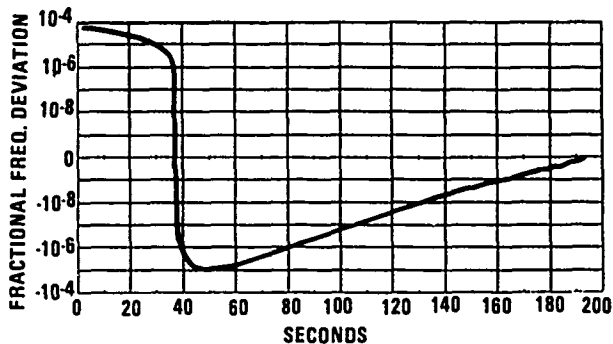


Figure 5. Warmup Curve for TMXO Electronics Assembly

starts to approach its final value at a rate of approximately one decade every twenty-five seconds. This exponential decay is characteristic of a single time constant system with the time constant equal to approximately eleven seconds. This time constant is determined primarily by the thermal capacity of the resonator and the thermal resistance between the resonator and package. For the flatpack package, the thermal path is primarily through the supports.

Temperature Retrace

An important crystal characteristic which has limited the performance of temperature controlled and temperature compensated crystal oscillators in the past is the shift in resonant frequency which results from temperature cycling. Initial testing of ceramic flatpack crystals with respect to the effects of temperature cycling have been quite encouraging. The frequency shift resulting from temperature cycling between -40°C and the UTP₉ for five cycles has ranged from 2×10^{-9} to 5×10^{-10} .

TMXO Crystal Characteristics

A summary of the equivalent electrical parameters of the TMXO crystal units is given in the following listing. The values given are representative of the latest 5.115 MHz fundamental mode resonators evaluated.

$$r = 3.2 \text{ ohms}$$

$$C_1 = 1.1 \times 10^{-14} \text{ Fd}$$

$$C_0 = 4 \times 10^{-12} \text{ Fd}$$

$$Q = 900K^*$$

$$\text{UTP} = 90 \text{ to } 100^{\circ}\text{C}$$

$$\Delta f/f < 1 \times 10^{-11} \text{ for 1 sec}$$

$$\text{Frequency Plating Tolerance} = \pm 5\text{ppm}$$

Thermal Control

Unlike other temperature controlled oscillators, the TMXO does not have an isothermal enclosure surrounding the crystal. Instead, the crystal package is heated directly by heat spreaders attached to each of the flat surfaces. This direct heating is necessary for fast warmup, and it is also convenient in minimizing the size of the electronics assembly. Direct heating, however, must be used with considerable care to avoid some very serious frequency stability problems.

One problem area is the potential for degradation of the short term stability of the oscillator by the effects of noise in the thermal control electronics. Since the quartz resonator is very sensitive to dynamic perturbations in the temperature, the stability of the oscillator is easily degraded by relatively small amounts of thermal noise. These effects are exaggerated in the TMXO because of its low thermal capacity and short thermal time constant which minimize the benefits of thermal integration found in more conventional oven controlled oscillators. Therefore, low frequency components of thermal noise are transmitted without attenuation to the resonator.

It was pointed out above that the warmup behavior of the crystal approximated that of a single time constant system. This suggests the possibility of modeling the dynamic frequency/temperature behavior of the crystal as a simple RC network. Such a model would allow the dynamic temperature response of the crystal to be analyzed using elementary circuit theory. The most obvious starting point would be a single section high pass filter which has the transfer function:

$$G_r(s) = \frac{Cs}{1 + RCs} \quad (1)$$

where $G_r(s)$ is the thermal transfer function of the resonator, and R and C are constants to be determined.*

We have seen from the warmup curve that the resonator recovers from a temperature step with a time constant of eleven seconds. We can therefore equate the product of R and C to eleven seconds.

Examining (1) we see that if the driving function were a linear ramp in

*No attempt is made to relate these constants to any physical characteristics of the resonator such as thermal capacity or thermal resistance. Use of the symbols R and C is merely to suggest an electronic analogy.

temperature, the response function would not contain a zero at the origin. Thus,

$$[\Delta f/f]_T(s) = \frac{a}{s} \cdot \frac{Cs}{1 + RCs} = \frac{aC}{1 + RCs} \quad (2)$$

where $[\Delta f/f]_T(s)$ is the response function of the resonator to a linear ramp, and a is the amplitude of the ramp in $^\circ\text{K/sec}$. If we now evaluate (2) at $s = 0$ (effectively neglecting the initial transient) we obtain:

$$[\Delta f/f]_T = aC \quad (3)$$

where $[\Delta f/f]_T$ is the steady state fractional frequency deviation or offset from the static frequency/temperature characteristic which results from a ramp in temperature. This quantity can be measured directly and for the TMXO crystals in the neighborhood of the UPT is equal to $2 \times 10^{-5}/^\circ\text{K/sec}$. Having thus determined a value for the constant C we may now write (1) as:

$$G_r(s) = \frac{2 \times 10^{-5}s}{1 + 11s} = \frac{1.8 \times 10^{-6}s}{s + .090} \quad (4)$$

A block diagram of the composite thermal controller and resonator model is shown in figure 6. The total system transfer function is seen to be the product of thermal controller transfer function and the crystal transfer function. The constant K in the thermal controller transfer function can either be calculated or measured and for the TMXO is equal to $.2 \text{ sec}^{-1}$. With all the system constants now determined, the system transfer function $G(s)$ may be written as:

$$G(s) = \frac{3.6 \times 10^{-7}s}{(s + .20)(s + .090)} \quad (5)$$

The actual measured response of the system with a 2mV sine wave excitation is shown in figure 7. There appears to be good agreement between the measured response and that predicted by (5).

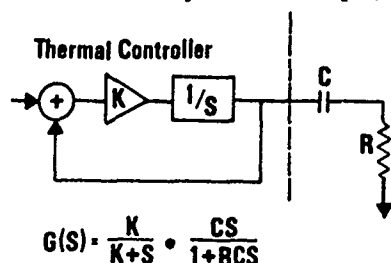


Figure 6. System Model Thermal Controller and Resonator

The preceding description of the dynamic frequency/temperature behavior of the quartz resonator has assumed that the amplitude of the temperature changes involved are small. If this were not the case, a complete description including the static temperature characteristic would be necessary. Although this could be done by superimposing the static and dynamic responses, such a description would not be necessary in most temperature controlled applications.

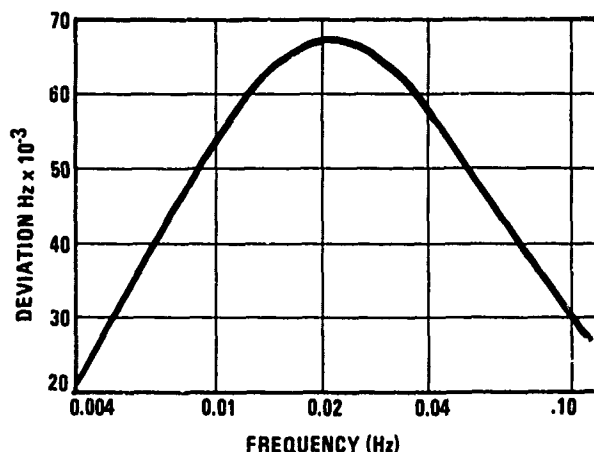


Figure 7. Frequency Response of Thermal Controller and Resonator

Having derived a satisfactory system model of the thermal controller and resonator, it is now possible to evaluate the effects of arbitrary perturbations such as that generated by noisy electronics. Fortunately, in the case of the TMXO, the system response is sufficiently narrow that the noise power density can be considered uniform in the neighborhood of the response peak. The fractional frequency deviation then is simply the product of the noise density, square root of the response bandwidth, the response amplitude at the peak, and the thermal sensor gain constant. Carrying out these calculations and assuming the noise density to be only due to thermal noise in the thermistor bridge (no excess noise), we obtain a value of $\Delta f/f = 1 \times 10^{-13}$.

If we require that there be no significant degradation in short term stability due to noise in the electronics, the effects of this noise should be kept below 2×10^{-12} . This implies that the noise figure of the system should be less than 26 dB at the frequency of maximum response (.14 rad/sec). Since $1/f$ noise is always a problem in this frequency region, careful attention must be paid to obtaining good noise performance in the thermistor bridge and amplifier circuits.

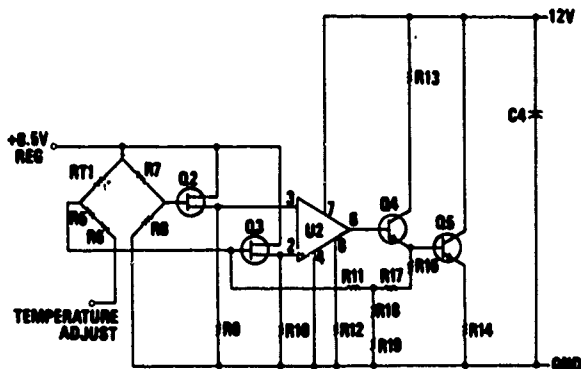


Figure 8. Thermal Control Unit

A schematic diagram of the thermal control circuit is shown in figure 8. The circuit consists of a thermistor bridge, voltage amplifier, and a power transistor used as a heater. The power transistor is actually two transistors, i.e., one for each substrate. In order to minimize the noise of the circuit, thin film resistors have been used in the thermistor bridge, and low noise FET transistors Q2 and Q3 have been included between the bridge circuit and operational amplifier U2 to minimize the effects of current noise in the input of U2.

Oscillator Circuit

A schematic diagram of the oscillator circuit is shown in figure 9. The resonator is used in the parallel mode in a circuit configuration sometimes referred to as a modified Colpitts. Bias current

for the oscillator transistor Q1 is supplied by transistor current source Q2 which is in turn controlled by the AGC detector. The nominal DC bias current in Q1 is 150 microamperes and the AGC gain is adjusted so that the nominal crystal current is 200 microamperes.

The output signal is taken from the emitter of Q1 and applied to buffer amplifier Q4. The output of Q4 is applied in parallel to the input of two identical amplifier stages; one of which drives the AGC detector and the other provides the final output.

The major considerations in the design of the oscillator circuit were minimization of the number of components, component size, and power consumption. The restriction on component size virtually eliminates the use of inductors for purposes such as the tuning of amplifier stages. The buffer amplifier stages are, therefore, designed to minimize parasitic capacity and Miller effects so that the useful frequency range of the circuit can be extended to 10 MHz while maintaining low bias currents in the transistor stages.

Tuning Procedures

Since there are no mechanically variable capacitors in the oscillator circuit, the circuit must be tuned before final assembly. To accomplish this, each crystal is placed in a special test oscillator where its required loading capacity is determined very accurately using a calibrated varactor. After determination of

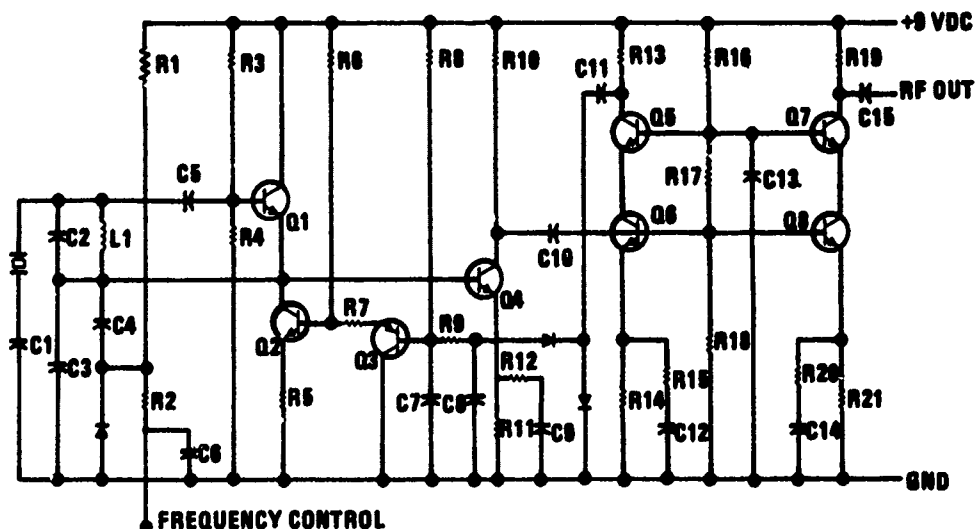


Figure 9. Oscillator and Buffer Amplifier Circuits

the loading capacity, a selection of two fixed capacitors is made so that the total capacity is within 3 pf of the required value. To complete the tuning procedure, the assembled oscillator substrate and crystal are placed in a test oven where the frequency error is determined. The final adjustment of loading capacity is then made by selecting a "tap" on a special porcelain trimmer capacitor designed for this purpose. The accuracy of the final selection is within 0.25 pf which corresponds to a frequency error of 1×10^{-7} . This residual error is within the range of the external voltage control input which is $\pm 2 \times 10^{-7}$.

Successfully determining the required loading capacity for the crystal requires that the test oscillator be as near as possible to the UTP temperature. Finding the turn point through a sequential series of adjustments on the test oven control can be quite time consuming because of the time necessary for the system to reach equilibrium after each adjustment. A method of sweeping the temperature has been developed which speeds up this process and gives good accuracy. The method is illustrated graphically in Figure 10. The temperature is first swept from low to high over a range of 20°K centered about the nominal value of the turn point temperature. As the temperature is swept, several readings of frequency and the oven monitoring thermistor resistance are recorded. The temperature slope for this sweep is $5 \text{ m}^{\circ}\text{K}/\text{sec}$. This procedure is then repeated with sweep going from high to low.

A quadratic curve is then fit to the data from the positive and negative sweeps individually using a least squares approx-

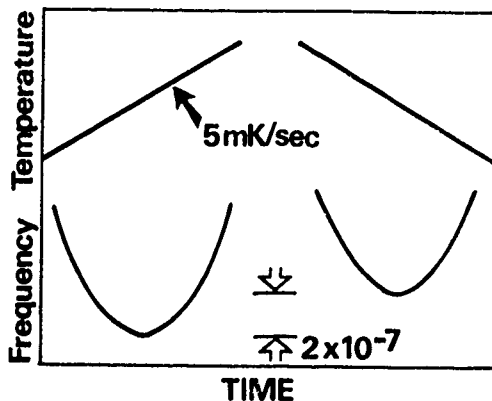


Figure 10. Crystal Turn Temperature Determination

imation. The minimum of each curve is then found by differentiation. The average value of the temperature at each minimum is then taken as the first estimate of the UTP temperature. After making this initial estimate, the entire process is repeated with the sweep range and rate reduced by a factor of ten. The error resulting from the application of this method is less than $20 \text{ m}^{\circ}\text{K}$.

Component Evaluation

The reactive elements in the resonator circuit used for tuning and phase inversion can seriously degrade the aging rate of the oscillator unless these components have excellent stability. The nominal value of loading capacity (100 pf) for the 5.115 MHz crystal will "pull" the frequency high by approximately 250 Hz. Therefore, if the aging rate of the loading capacitance were equal to $2 \times 10^{-6}/\text{day}$, the effect on oscillator aging due to loading capacitor drift would be $1 \times 10^{-10}/\text{day}$. This strongly suggests that the frequency plating tolerance should be improved to minimize the amount of pulling required, and that the components in the resonator circuit be as stable as possible. The following listing shows aging rates measured for capacitors with various dielectric materials, and the aging rate for a 2 microhenry toroid wound on a phenolic form with outside diameter equal to 0.12 inches. The data for the ceramic capacitor shown in the listing refers to an NPO type from one supplier. No other ceramic capacitors evaluated have demonstrated this stability.

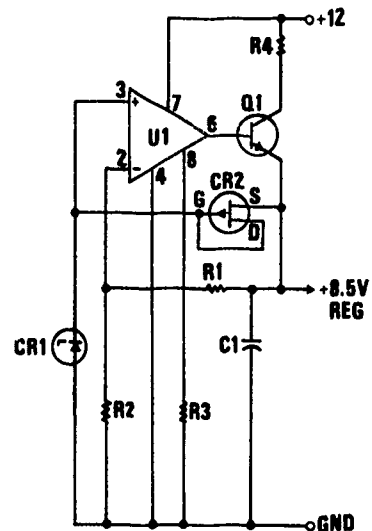


Figure 11. Voltage Regulator Circuit

ComponentRate

2 Microhenry Coil	-2 ppm/day
Porcelain Cap.	± 3 ppm/day
Ceramic Cap.	± 3 ppm/day
Silver Mica Cap.	-30 ppm/day
Glass Cap.	-70 ppm/day

Voltage Regulator

A schematic diagram of the voltage regulator circuit is shown in figure 11. The voltage reference for the circuit is a 1N821 temperature compensated reference diode which was selected because of its low 1/f noise. Feedback resistors R1 and R2 are low noise thin film resistors.

The amplitude of noise in the output of the regulator for the low pass bandwidth below 1 Hz is approximately 1 microvolt. The sensitivity of the oscillator circuit to supply variations is 4×10^{-8} /volt, which is not great enough to cause significant degradation in the short term stability of the oscillator.

Vacuum Maintenance

The maintenance of vacuum within the outer enclosure has been a serious problem in all previous work related to the TMXO. The current design concept which uses materials having low vapor pressure, seals the electronics assembly from the evacuated space, and uses an efficient getter, is believed to have effectively solved this problem.

Acknowledgments

The inspiration for the system model of the crystal resonator and thermal controller is due to Ballato⁶ wherein a "phenomenological" description of the dynamic frequency/temperature behavior of the crystal resonator is given in terms of rate of change of temperature. The author also wishes to acknowledge the contribution of Mr. Dwight Brown of the Bendix Communications Division who supplied much of the experimental data.

References

1. J. R. Vig and E. Hafner, "Packaging Precision Crystal Resonators," Technical Report ECOM 4134, U.S. Army Electronics Command, Fort Monmouth, N.J., July 1973.
2. E. Hafner and J. R. Vig; "Crystal Resonator Housing Configuration," U.S. Patent Nr. 3,931, 388, Jan. 6, 1976.
3. P. Wilcox, G. Snow, E. Hafner and J. R. Vig, "A New Ceramic Flatpack for Quartz Resonators," Proc. AFCS 28, June 1975, pp 202-210.
4. R. D. Peters, "Ceramics Flatpack Enclosures for Precision Quartz Crystal Units," Proc. AFCS 30, PP 224-231, June 1976.
5. A. W. Warner, "Design and Performance of Ultraprecise 2.5-mc Quartz Crystal Units," Bell Syst. Tech. J., vol. 39, pp 1193-1217, Sept. 1960.
6. Ballato, Arthur, "Static and Dynamic Behavior of Quartz Resonators," IEEE Transactions on Sonics and Ultrasonics, Vol. SU-26, No. 4, July 1979.

PERFORMANCE OF NEW OSCILLATORS DESIGNED FOR "ELECTRODELESS" CRYSTALS

R. J. Besson
Ecole Nationale Supérieure de Mécanique
et des Microtechniques-Besançon-France-

P. G. Girardet and E. P. Graf
Oscilloquartz S.A.
CH2002-Switzerland-

D. A. Emmons
Frequency and Time Systems, Inc.
Beverly, Massachusetts

Summary

Type BVA quartz crystal resonators are developed^{1,2,3,4} at the Ecole Nationale Supérieure de Mécanique et des Microtechniques in Besançon, France, and industrialized by Oscilloquartz S.A. in Neuchâtel, Switzerland⁹. Such resonators have led to quartz crystal oscillators with improved long term behaviour. As higher drive levels are allowed, better short term stability also ensues^{5,6}.

Experimental results have been obtained with three different oscillators and confirm the soundness of a frequency drift model, where aging is a non-monotonic function of resonator drive level. Results for 5MHz, 3rd and 5th overtone resonators are discussed.

To take full advantage of the BVA resonators, a new oscillator has been developed at OSA. The first results show good agreement between open loop measurements and the oscillator phase noise.

Introduction

First, some data concerning a very low cost test oscillator are presented. The goal is to rapidly obtain indications on the best possible use of BVA crystals in terms of performance versus drive level (up to 1.6 mW). An aging model can then be derived from these measurements. All results discussed refer to 5MHz resonators.

A commercial oscillator type FTS 1000 has been modified⁷ to be equipped with BVA AT cut and SC cut resonators. It has been verified that low aging rates are established quickly (in a few days or less) and that a "zero aging" drive level exists, in confirmation of results first obtained with the previous test oscillator. Measurements of short term stability, phase noise, aging and frequency retrace are reported.

The electronics of a new oscillator has been designed at OSA with the following objectives and data:

- the characteristics of the BVA resonators are utilized;
- the bandwidth of the loop amplifier is given by the quartz crystal resonator;
- we retain the possibility of measuring the amplifier's phase noise alone;

- we are able to measure the loaded Q of the resonator; and,
- correlation between passive measurements and final operating characteristics enables the detection of an incorrectly operating element early in the manufacturing process, thus eliminating costly disassembly and readjustment procedures.

Aging Model

To measure the long term behaviour of BVA resonators as a function of the drive level, the simple TTL oscillator shown in Figure 1 was used. Data gained with the same oscillator housed in a double thermostat are also indicated in the same figure.

From these measurements a model of the BVA resonator aging can be derived:

$$a_r = k P \left[1 + a \exp. \left(-\sqrt{\frac{P}{P_0} \cdot \frac{t}{\tau}} \right) \right] + a_1$$

AT 5th overtone natural quartz crystal

a_r :	aging rate
P:	dissipated power
a_1 :	intrinsic aging $-2 \cdot 10^{-11}/\text{day}$
k:	constant $0.022 \cdot 10^{-11}/\text{day} \cdot \mu\text{W}$
P_0 :	reference drive level 10μW
τ :	time constant 5 days
a:	constant 60

It is evident that optimum aging is achieved with a drive level of about 90μW.

Type FTS 1000 Oscillator Modified for BVA Resonators

BVA resonators have been installed in modified FTS 1000 oscillators⁷, for measurements of frequency stability on several types of AT and SC cut units. The occurrence of a low aging rate consistent with the model is confirmed. Test oscillators with drive level adjusted for the expected optimum drift rate have confirmed that low aging is achieved within several days after first turn-on.

Proc. 34th Ann. Freq. Control Symp., USAERADCOM, Ft. Monmouth, NJ 07703, May 1980

For SC cut quartz, the analytical model requires parameter constants which differ from the case of AT cut, and low aging at about 160 μ W is predicted. Figure 2 shows results for an SC cut 3rd overtone resonator which showed a change in the sign of the aging rate as drive power was increased beyond the optimal 160 μ W level. Here, the emphasis is not on quickly reaching the low aging point, but on documenting the time history under gradually increased drive level.

It is expected that one advantage of high drive level will be reduced white phase noise in the oscillator. In Figure 3 the performance of a 5th overtone AT cut resonator is shown for comparison at low and high drive level. It is seen that the change from 3 μ W to 72 μ W improves the white noise level to the measurement limit being imposed by the reference oscillator, a standard low drive level FTS 1000.

A further improvement in the white phase noise level is seen when two BVA resonators are compared directly. Figure 4 shows S_{ϕ} data for an SC cut 3rd overtone at 265 μ W drive level, versus an AT cut 5th overtone resonator at 84 μ W. The white noise is now limited by the noise floor of the measuring system as verified for the conditions of this measurement.

In the time domain, measured stability of BVA resonators has been excellent, and in particular no severe degradation in flicker-of-frequency performance is noted, even for the relatively high drive levels customary for these crystals. This represents a marked departure from the limitations of the usual plated resonators. In Figure 5 are presented Allan Variance results for BVA resonators measured with respect to standard low-drive-level, high stability oscillators. The Allan Variance is that for the oscillator pair in each case, and data at 1 second τ should be corrected downward by 20% for 1 second dead time. Thus, in the 1 to 100 second region it appears that $\sigma_y(\tau)$ is quite flat. For the SC cut 3rd overtone, the difference between 37 μ W and 285 μ W results may be partly due to the different reference oscillators, although they have in fact shown approximately 5×10^{-13} against each other. However, the BVA performance of $<4 \times 10^{-13}$ compared to about 7×10^{-13} is not a striking difference, considering the nearly 8-fold increase in resonator drive level.

Additional measurements for a BVA 3rd overtone SC cut resonator against a JPL hydrogen maser have shown a best result of σ (BVA) $\leq 1.4 \times 10^{-13}$ for averaging times equal to 40, 100 and 200 seconds, and 1.8×10^{-13} at 400 seconds. It is believed that long term wandering from spurious causes was limiting the performance for the longer time averages.

Model 8600 Oscillator

The electronics of a new oscillator has been designed at OSA and has already yielded results.

The block diagram of Figure 6 shows the following main features:

- the quartz crystal resonator with its pulling capacitor is located in the feed-back arm of the oscillator amplifier. Thus the combination resonator-loop amplifier is an amplifier the bandwidth of which is defined by the resonator's loaded Q.
- in the self-excitation path we see a broad-band filter for the attenuation of the harmonics; the bandwidth corresponds to a Q factor of approximately 5.
- for independent measurements of the loop amplifier the resonator can be replaced by an equivalent resistor. By cutting the self-excitation path and by feeding a corresponding frequency from an external quartz oscillator at point a, the phase noise of the amplifier alone can be measured. The transistor working points as well as operation of the AGC circuits are not modified in doing so.
- the resonator's loaded Q can be measured with a synthesizer connected at point a and with open self-excitation path.
- varying the AGC circuits' reference voltage leads to simple change of the quartz drive level.

Figure 7 shows the result of loop amplifier phase noise measurement with AGC. In this case, the quartz resonator has been replaced by a 82 ohm resistor and the self-excitation path was cut. This measurement in connection with a loaded Q value of 1.5×10^6 allows us to theoretically compute the spectral density S_{ϕ} of the operating oscillator⁸. Figure 8 displays the calculated and the measured S_{ϕ} data with a BVA resonator drive level of 80 μ W. This value approximately corresponds to an optimum aging characteristic of the BVA AT cut 5th overtone quartz crystal.

The run-in behaviour of a non-preaged oscillator with BVA resonator is shown in Figure 9.

All results have been gained at constant temperature in a thermostat analogous to the one used in our B-5400 oscillator. The thermostat has been adjusted at the BVA resonator's turn-over temperature of about 70°C.

Conclusion

Evaluation of BVA resonator performance using a variety of different oscillator circuits in separate laboratories has given comparable results for short term stability and long term drift.

Results of low aging with a simple test oscillator in the early phases of laboratory research, and more recently, as the resonators have approached industrial production, are confirmed by operation in a commercial oscillator. Aging is predictable and becomes a settable parameter.

Measurements of oscillator phase noise close to the carrier show good agreement with observed flicker noise in the time domain. The large drive level allowed by the BVA technique permits substantial reduction in the white phase noise level.

The advent of better resonators has now forced overall improvements in oscillator circuits.

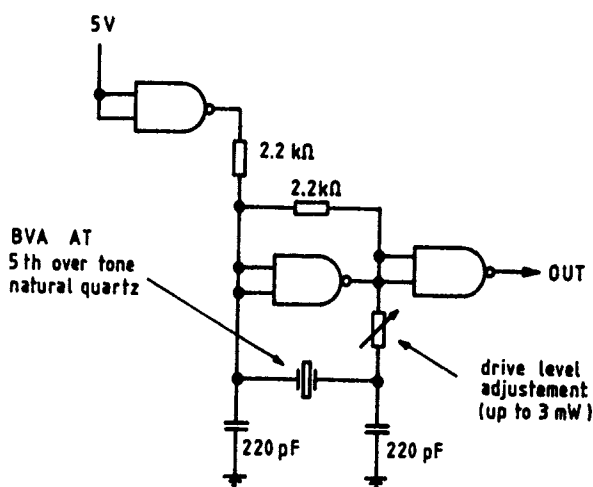
Acknowledgements

We wish to acknowledge the cooperation of Paul Kuhnle at Jet Propulsion Laboratory in making the hydrogen maser comparison; and the support of Dr. N. Yannoni at ESD-RADC, under contract No. F19628-80-C-0037 for portions of this work.

References

- (1) R.J. Besson, Proc. 30th Annual Frequency Control Symposium pp 78-83 (1976) and 31st AFCS pp 147-152 (1977).
- (2) French patents No. 7601035, 7616289, 7717309, 7802261, 7828728, 7835631, 7918553 and corresponding patent or patents pending in other countries.
- (3) R.J. Besson, Proc. 10th Annual PTII Applications and Planning Meeting pp 101-128 November 1978.
- (4) R.J. Besson, U.R. Peier, Conf. A 1.8 Proceedings Congress International de Chronometrie pp 57-61 September 1979.
- (5) S.R. Stein, C.M. Manney Jr., F.L. Walls, J.E. Grey, NBS and R.J. Besson, ENSCMB, Proc. 32nd AFCS pp 527-530 (1978).
- (6) A. Berthaut and R.J. Besson, CR Acad Sc Paris, November 1979.
- (7) R.J. Besson and D.A. Emmons, Proc. of the 11th Annual PTII Applications and Planning Meeting, pp 457-468 (1979).
- (8) D.J. Healey III, Proc. 26th Annual Frequency Control Symposium, pp 29-42 (1976).
- (9) R.J. Besson and U.R. Peier, "Further Advances on BVA Quartz Resonators", 34th Annual Frequency Control Symposium, Philadelphia, PA, May 28-30, 1980.

FIG. 1 TEST OSCILLATOR



Drive - level P	Aging α_f
1591 μ W	$33.3 \cdot 10^{-11}$ / day
90 μ W	≈ 0
50 μ W	$- 0.9 \cdot 10^{-11}$ / day
10 μ W	$- 1.8 \cdot 10^{-11}$ / day
1 μ W	$- 2 \cdot 10^{-11}$ / day

APPROXIMATE DRIVE LEVEL (MICROWATTS)	AGING RATE $\Delta f/f$ (per day)	TIME ELAPSED FROM 1st TURN-ON (DAYS)
10	$+4 \times 10^{-10}$	8
37	$+9 \times 10^{-11}$ (45 day average)	70
124	$+3 \times 10^{-11}$	120
284	-9×10^{-12}	135
160	approx. zero	165

BVA RESONATOR AGING VERSUS DRIVE LEVEL

FIGURE 2

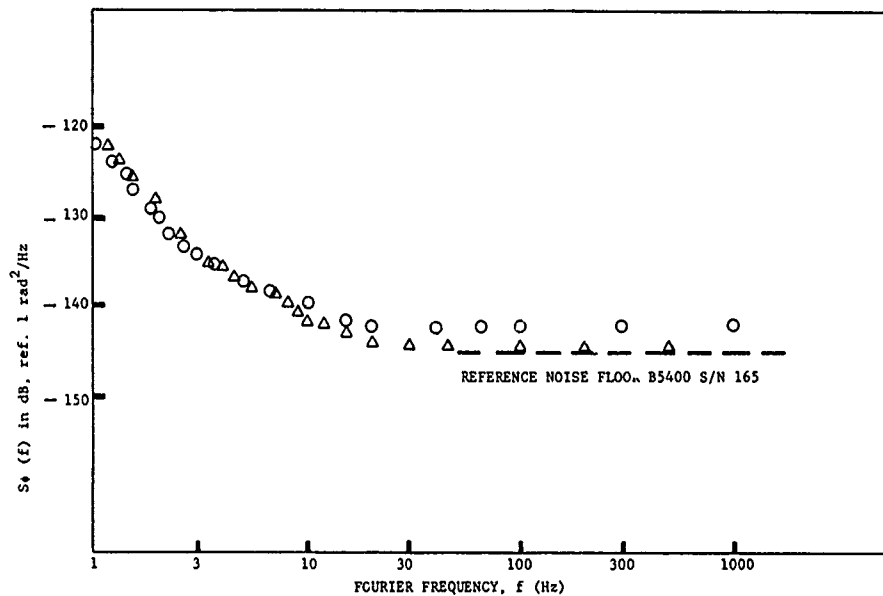


Figure 3. MEASURED PHASE NOISE; BVA RESONATOR (AT, 5th OT)
IN COMMERCIAL FTS 1000; DRIVE LEVEL 3 μW (O) and 72 μW (Δ)

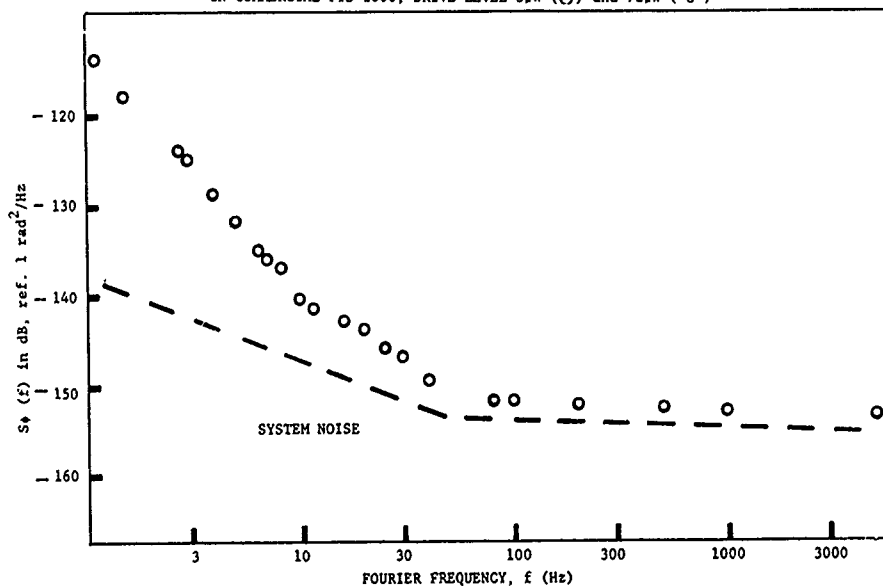


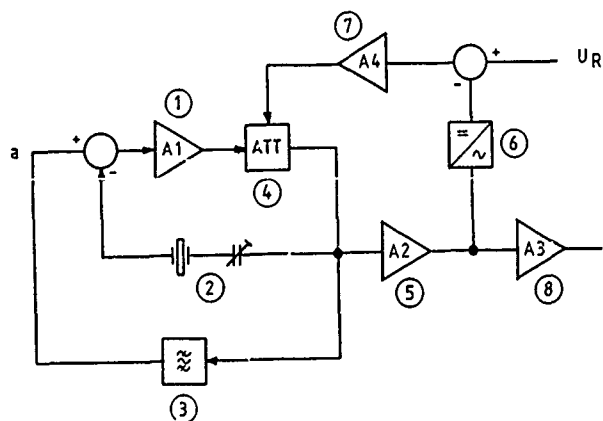
Figure 4. PHASE NOISE SPECTRAL DENSITY FOR BVA (SC, 3rd OT, 265 μW DRIVE LEVEL)
VERSUS BVA (AT, 5th OT, 84 μW)

RESONATOR BVA	DRIVE LEVEL	REFERENCE OSCILLATOR	$\sigma_y(\tau)$ in units 10^{-13}					
			τ (sec)	1	3	10	30	100
2-125 SC, 3rd	37 μ W	1000 S/N 12		*6.5	3.6	3.5	3.7	5.1
	285 μ W	85400 S/N 165		*8	6.5	5.2	7.4	
2-28 AT, 5th	72 μ W	1000 S/N 12		*8	6.0	6.4	6.8	
			*Dead Time Correction x 0.8 (1 sec)					

TIME DOMAIN STABILITY - ALLAN VARIANCE (TWO SOURCES)

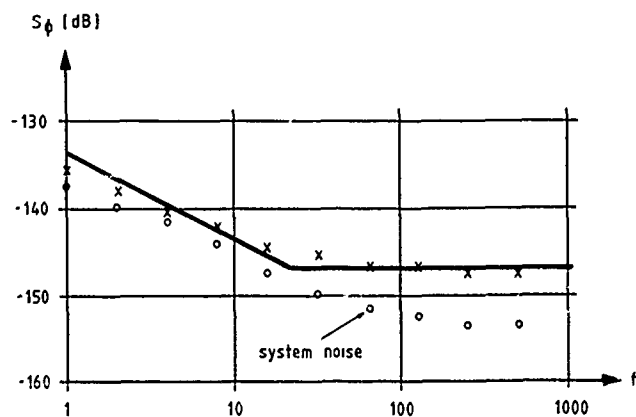
FIGURE 5

FIG 6 FUNCTIONAL DIAGRAM MODEL 8600



- ① Loop amplifier
- ② Resonator
- ③ LC filter
- ④ Passive attenuator
- ⑤ ⑧ Buffer amplifier
- ⑥ Rectifier
- ⑦ AGC amplifier

FIG 7 PHASE NOISE LOOP-AMPLIFIER



$$S_{\phi} = C(1 + A \cdot f^{-1})$$

$$C = 1.995 \cdot 10^{-15}$$

$$A = 14.85$$

FIG. 8 PHASE NOISE MODEL 8600, BVA AT 5th

BVA # 1 (2.48) - # 4 (2.110)

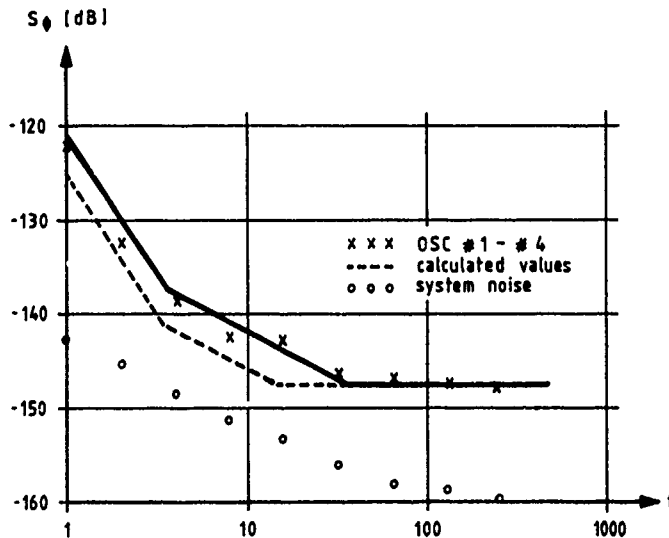
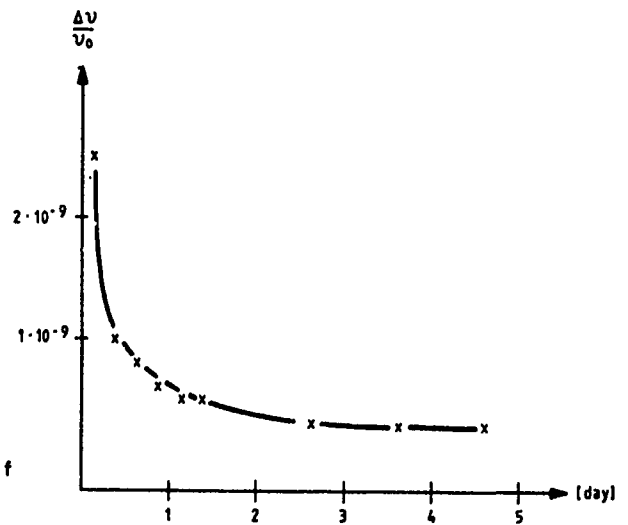


FIG. 9 RETRACE AFTER 12 DAYS OF OPERATION AND 6 HOURS OFF

8600 # 4 BVA AT 5th (2.110)



$$S_\phi = AC \left(\frac{V_0}{2Q_L} \right)^2 \cdot f^{-3} + C \left(\frac{V_0}{2Q_L} \right)^2 \cdot f^{-2} + AC f^{-1} + C$$

$$S_\phi = 8.23 \cdot 10^{-14} \cdot f^{-3} + 5.54 \cdot 10^{-15} \cdot f^{-2} + 2.96 \cdot 10^{-14} \cdot f^{-1} + 1.995 \cdot 10^{-15}$$

$$Q_L = 1.5 \cdot 10^6$$

A FAST WARMUP, SC CUT CRYSTAL OSCILLATOR

Marvin Meirs, Paul Sherman, Martin Bloch and John Ho

Frequency Electronics, Inc.
New Hyde Park, New York 11040

Summary

This paper discusses the design and development of a quartz oscillator for use in the Tail Warning Radar program. Excellent warmup characteristics have been achieved by using an SC cut crystal in an improved proportional controlled oven. Stability of $1\text{pp}10^{-8}$ are realized after only 5 minutes.

The oscillator operates at 10 MHz and utilizes a 3rd overtone SC cut crystal in a TO-8 enclosure. The proportional control oven has been reduced in size to obtain the smallest mass for fast warmup. This paper presents the mechanical and circuit design of this oscillator. Test results for warmup, temperature stability, and other characteristics are discussed.

Additional data is presented on SC cut crystals with regard to "g" sensitivity and radiation sensitivity. The radiation data shows sensitivities one to two orders of magnitude better than achieved with AT crystal.

Introduction

Table I is a summary of the electrical performance requirements for this oscillator. The main concern of this oscillator was the 1×10^{-7} stability after only five minutes of warmup. Actual results showed 5×10^{-8} at -55°C and better than 1×10^{-8} at room temperature. All performance requirements were met or exceeded.

Design

The mechanical package requirements of this oscillator is shown in Figure 1. The basic size is 3.34 x 3.34 x 1.22 inches deep. The 1.22 inches was the limiting factor with regard to oven designs and power dissipation. More room in this dimension could have reduced power consumption by 50 percent. However, this room was not available for this application. The detailed assembly for this unit is shown in Figure 2. The oscillator was designed using a double oven in order to get heat to the crystal in the fastest possible time. This drawing shows the outer oven with the outer oven controller and amplifier/regulator boards which were located outside of the ovens. Figure 3

TABLE I

TABLE OF PERFORMANCE CHARACTERISTICS

OCCO, MODEL FE-2163A

ITEM	PARAMETER	SPECIFICATION	ACTUAL
1	Output Frequency	10,0543478 MHz	10,0543478 MHz
2	Output Power	0 dBm, and ± 5.0 dBm	0 dBm, and ± 5.0 dBm
3	Frequency Stability per 24 Hours	$4 \text{ pp}10^{-10}$	$2 \text{ pp}10^{-10}$
4	Frequency Stability After 5 Minutes Warmup @ -55°C to $+75^{\circ}\text{C}$	$\pm 1 \text{ pp}10^{-7}$	$\pm 3 \text{ pp}10^{-8}$
5	DC Power + 25 Vdc + 15 Vdc	800 mA 100 mA	800 mA @ Turn-on, 175 mA @ 25°C 350 mA @ -55°C 14 mA
6	Weight	20 oz.	16 oz.

shows the construction of the inner oven assembly. Only the TO-8 quartz crystal was located inside of this inner oven. Actual photographs of this unit can be seen in Figures 4 and 5 where the unit has been disassembled to show the detailed construction. The schematic diagram for the entire unit is shown in Figure 6. A Colpitts oscillator configuration was chosen for its ease of use and minimization of components. The quartz crystal (Y1) is an SC cut 3rd overtone at approximately 10 MHz. A varactor, CR7, is incorporated to provide external frequency control. The circuitry was designed for use with two independent power supplies, a +25 vdc for the ovens and a +15 vdc for the oscillator and amplifier circuits.

It should be noted that after alignment and initial testing the entire assembly is foamed to provide both thermal insulation and mechanical rigidity to withstand the shock and vibration environments for this aircraft application.

Performance Results

Figure 7 shows the warmup data for an oscillator which was plotted both at 25°C and -55°C . Figure 8 is data on another oscillator

that was taken at -55°C but with expanded resolution. As can be seen, parts per 10^{-8} stability are achieved in a very short time.

The SC cut crystals have a turnover of $85^{\circ}\text{C} \pm 3^{\circ}\text{C}$ for operation over the temperature range of -55°C to $+75^{\circ}\text{C}$. A plot of frequency and impedance around the turnover point is shown in Figure 9. Typical Q's for these crystals is 1.5 million.

Although "g" sensitivity was not a specification requirement data was taken to evaluate this parameter for the SC crystal. Table II shows static "g" sensitivity for 13 of these oscillators. The average "g" sensitivity was $6 \times 10^{-10}/\text{g}$, a factor of 2 better than a typical AT crystal.

Radiation Performance Results

Radiation data was taken on SC cut crystals in conjunction with oscillators to be used on a space probe to Jupiter. This data was taken using a Cobalt 60 radiation source, and radiation rates from 10 to 150 Rads/sec. Cumulative radiation doses of 1 million Rads were applied. Figure 10 shows a radiation exposure of 10 Rad/sec. for 700 seconds after a 25,000 Rad preconditioning. The sensitivity during this exposure was $3.3 \times 10^{-12}/\text{rad}$. This same unit after 250,000 Rads preconditioning showed a slope of $7 \times 10^{-13}/\text{Rad}$ for the same exposure rate and time. This is shown in Figure 11.

Another of the oscillator's when subjected to the same rate after 750,000 Rads of preconditioning showed a slope of $5 \times 10^{-14}/\text{Rad}$. This is shown in Figure 12. This improvement in slope can be seen in Figure 13 when the unit was exposed to 150 Rad/sec. for 24 minutes. This curve shows an initial slope of $1 \times 10^{-13}/\text{Rad}$ which flattens to $1.7 \times 10^{-14}/\text{Rad}$ near the end of the exposure. Figure 14 is an accumulated 1,000,000 Rad exposure on this unit. The total frequency change was 2×10^{-8} for an average slope of $2 \times 10^{-14}/\text{Rad}$. A group of crystals to be used on this program was then subjected to radiation doses of 250,000 Rads and 1,000,000 Rads to determine their radiation sensitivity. These results are summarized in Table III. This table accumulates the results on the testing of 19 crystals. The first 11 of these crystals had previously been subjected to a 25,000 Rad preconditioning. Sensitivities on the units with previous preconditioning averaged $2.8 \times 10^{-13}/\text{Rad}$. Those with no preconditioning averaged $6.2 \times 10^{-12}/\text{Rad}$. All these units after the 250,000 Rads of preconditioning were better than $3 \times 10^{-13}/\text{Rad}$ and averaged $6.5 \text{ PP}10^{14}/\text{Rad}$.

Conclusions

The data presented here shows significant improvements in performance characteristics by the use of the SC cut crystal. This stress compensated crystal permits fast warmup with minimum overshoot and ringing due to abrupt

TABLE II
STATIC "g" SENSITIVITY (pp10¹⁰/2g)
OCZO, MODEL PR-2163A

UNIT	"X" AXIS	"Y" AXIS	"Z" AXIS
23	+ 7	+ 17	- 2
19	+ 1	0	+ 10
15	+ 4	+ 7	+ 1
20	- 1	+ 14	- 7
16	+ 7	+ 2	+ 6
14	- 5	+ 9	- 2
17	+ 3	- 18	0
18	+ 13	+ 3	+ 2
22	+ 3	+ 4	+ 6
21	+ 1	+ 10	+ 4
30	+ 6	+ 13	- 5
31	+ 7	- 10	+ 2
33	- 5	+ 16	0

TABLE III
SC CRYSTAL RADIATION SENSITIVITY
OCZO, MODEL PR-2163A

CRYSTAL	250 \times 10 ³ RADS		1 \times 10 ⁶ RADS	
	FREQUENCY CHANGE (pp10 ⁻⁸)	SENSITIVITY (pp10 ¹³ /RAD)	FREQUENCY CHANGE (pp10 ⁻⁸)	SENSITIVITY (pp10 ¹³ /RAD)
003	- 0.23	- 9.2	- 0.17	- 1.7
005	- 0.09	- 3.6	+ 0.004	+ 0.04
2900	- 0.10	- 4.0	---	---
001A	- 0.05	- 2.0	- 0.04	- 0.4
003A	- 0.07	- 2.8	- 0.05	- 0.5
007A	- 0.04	- 1.6	- 0.04	- 0.4
2888	- 0.04	- 1.6	+ 0.004	+ 0.04
2891	- 0.05	- 2.0	- 0.05	- 0.5
2889	- 0.06	- 2.4	- 0.05	- 0.5
2890	- 0.02	- 0.8	+ 0.01	+ 0.1
2909	- 0.01	- 0.4	- 0.07	- 0.7
3536	- 0.97	- 38.3	+ 0.02	+ 0.2
3530	- 2.21	- 88.4	+ 0.09	+ 0.9
3529	- 3.01	- 120.4	+ 0.26	+ 2.6
3537	- 1.17	- 46.8	+ 0.01	+ 0.1
3534	- 1.43	- 57.2	- 0.08	- 0.8
3532	- 1.17	- 46.8	- 0.04	- 0.4
3535	- 1.48	- 59.2	+ 0.05	+ 0.5
3531	- 1.13	- 45.2	- 0.16	- 1.6

temperature change. Data taken on "g" sensitivity indicated a factor of 2 improvements over AT crystals without significant effort to optimize this parameter.

Radiation sensitivities 1 to 2 orders of magnitude better than AT crystals have been achieved. Test data to levels of 1,000,000 Rads for crystals, and crystal/oscillator combinations show rates of $10^{-14}/\text{Rad}$. These performance results show great improvement over previously obtainable results and indicate that the SC cut crystal would be a good choice for many future oscillator requirements.

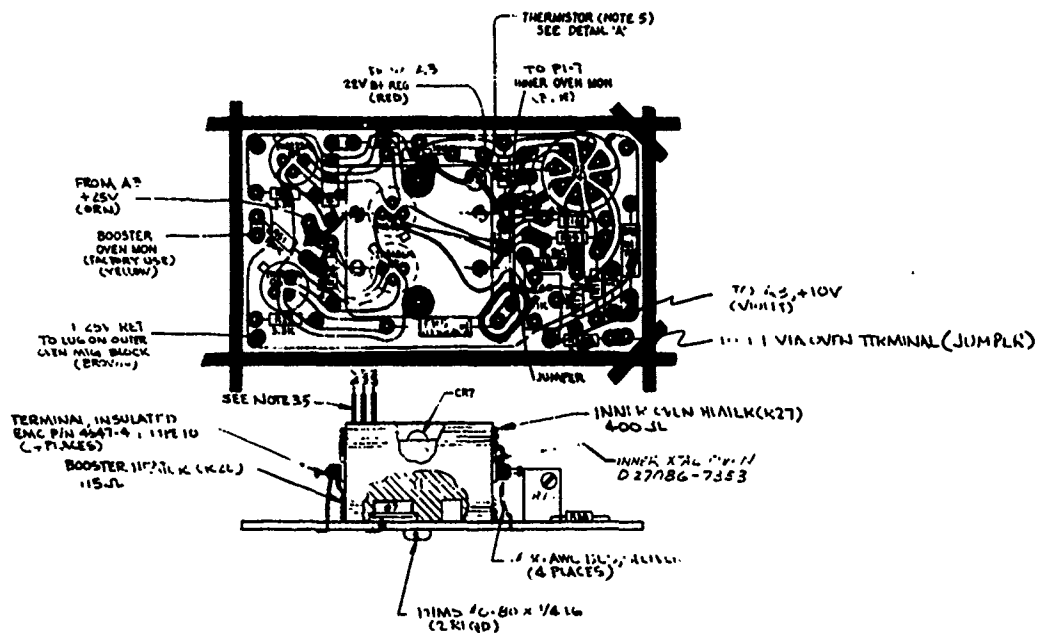


Figure 3. PC Assy, Inner/Booster, Oven Control, A1A2

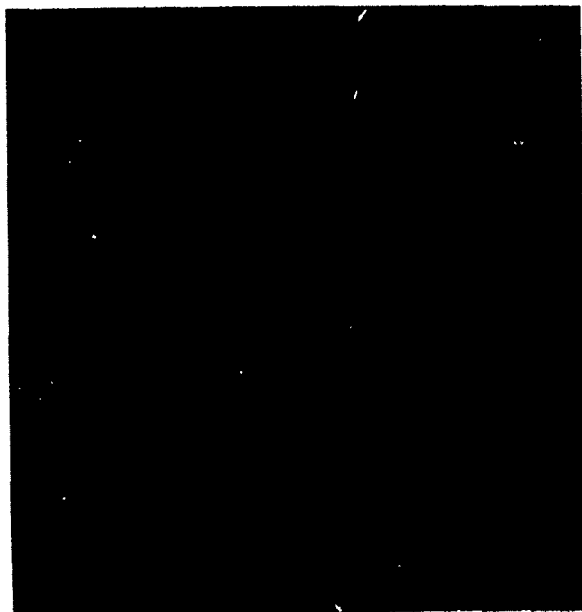


Figure 4. Top View of Fast Warm-up Oscillator, SC Cut Crystal, Model FE-2163A



Figure 5. Disassembled View of Fast Warm-up Oscillator, SC Cut Crystal, Model FE-2163A

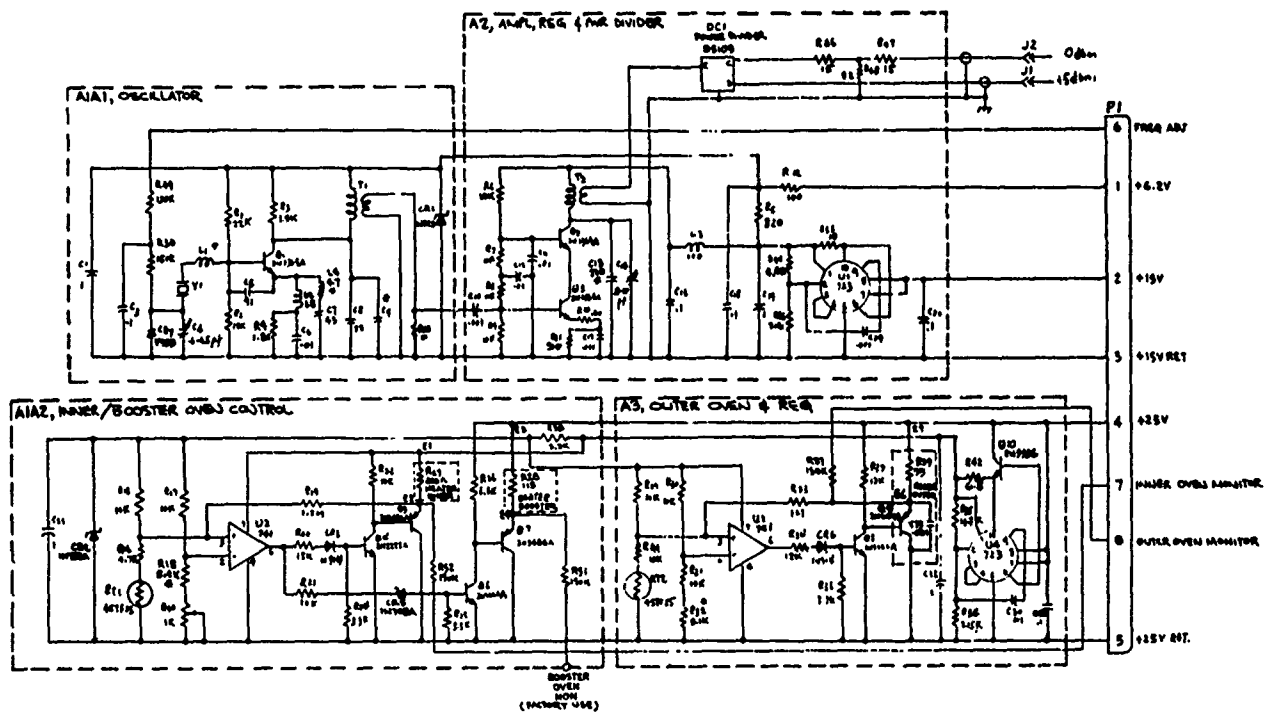


Figure 6. Crystal Oscillator (OCXO), Schematic Diagram, 10.054347.8 MHz

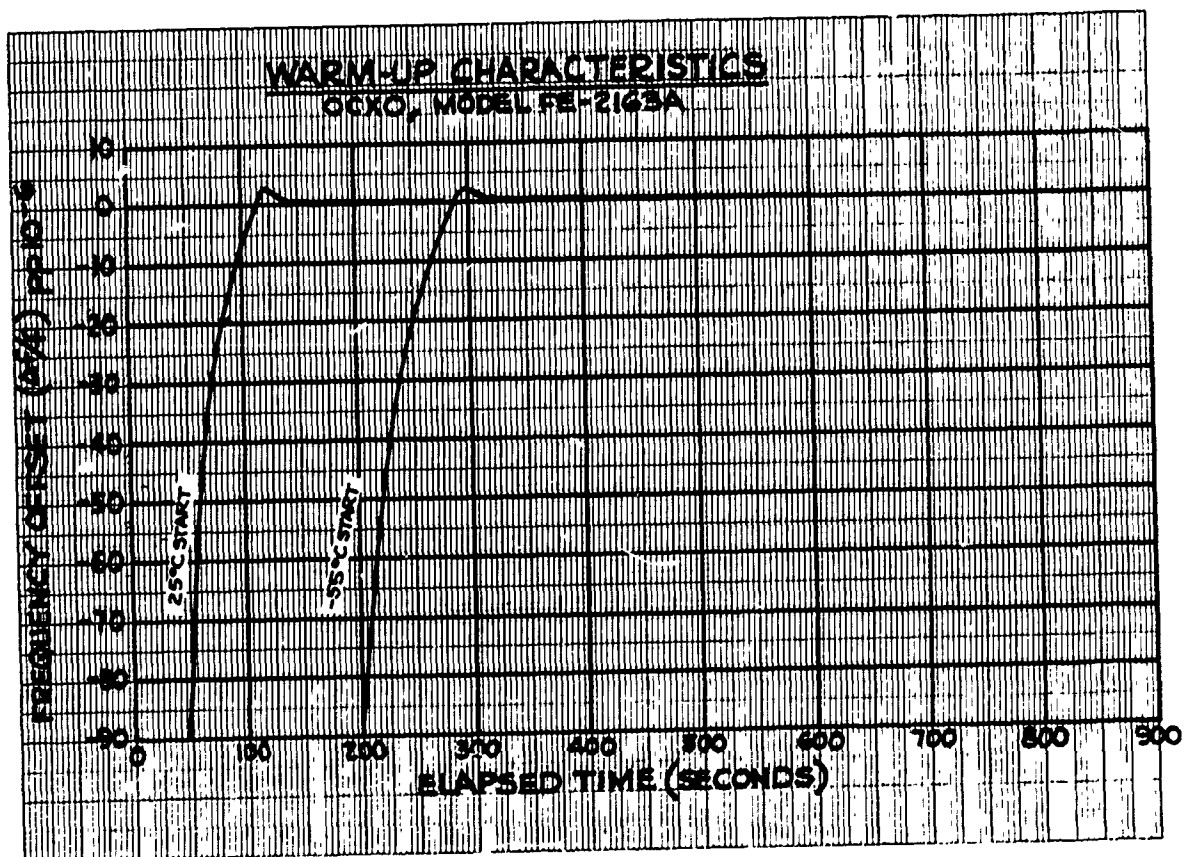


Figure 7. Warm-Up Characteristics, OCXO, Model FE-2163A

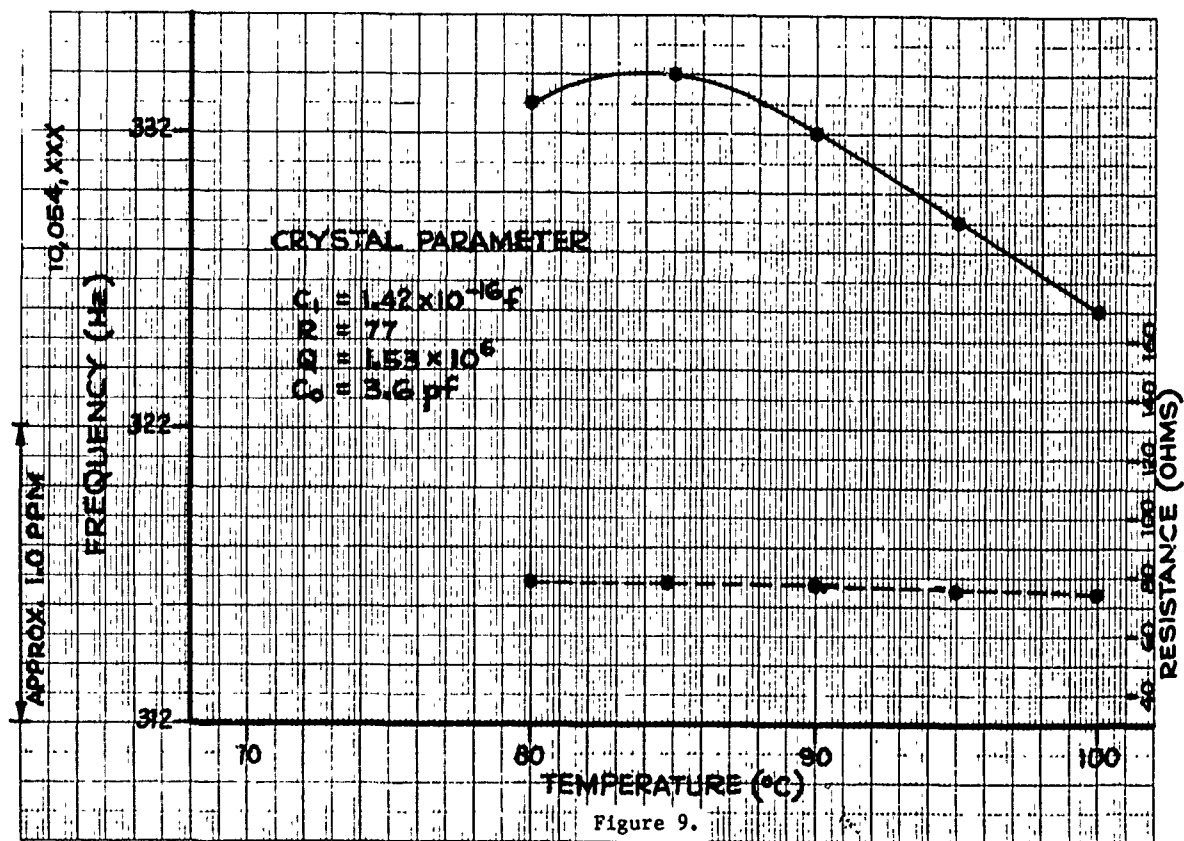
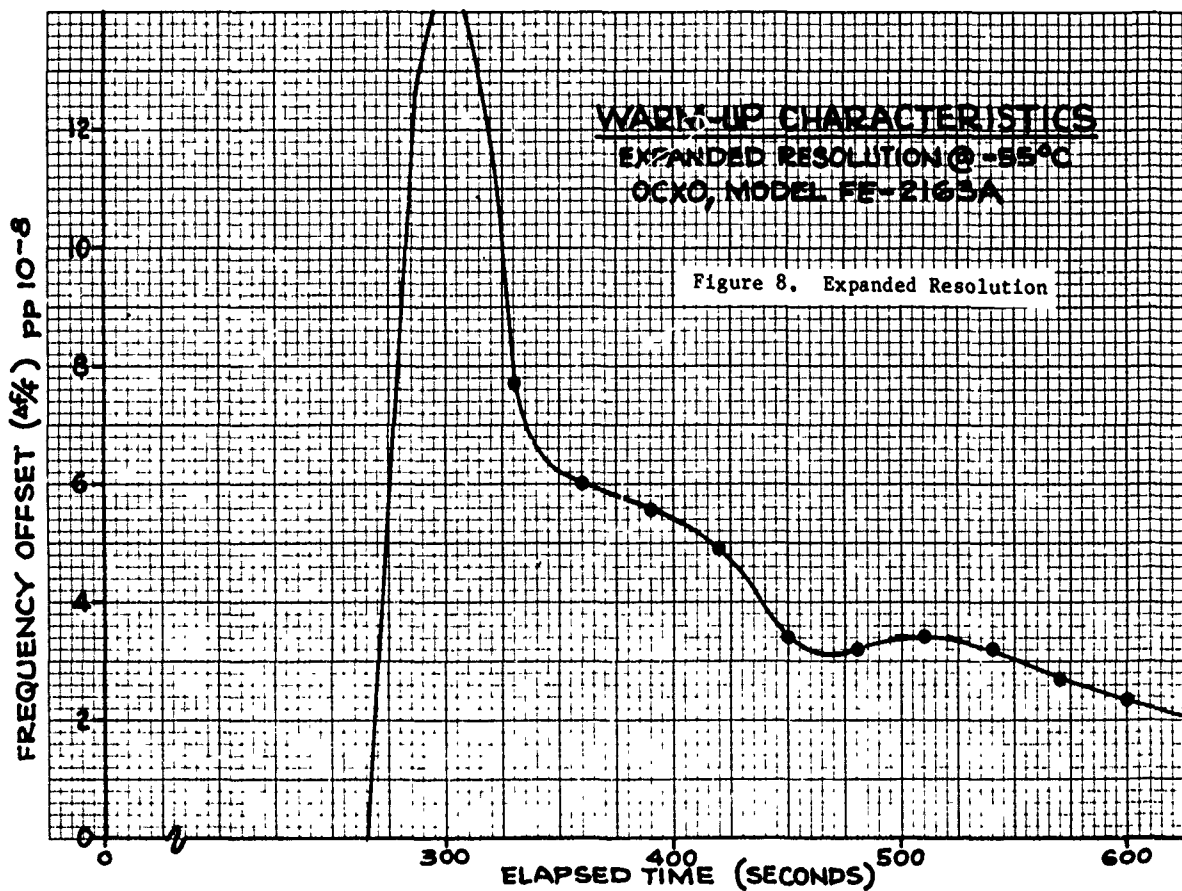


Figure 9.

SC CUT CRYSTAL TURNOVER GRAPH

DATE 09/14/79
TIME 09:56:00

DRIFT FOR Or10r/s7k1

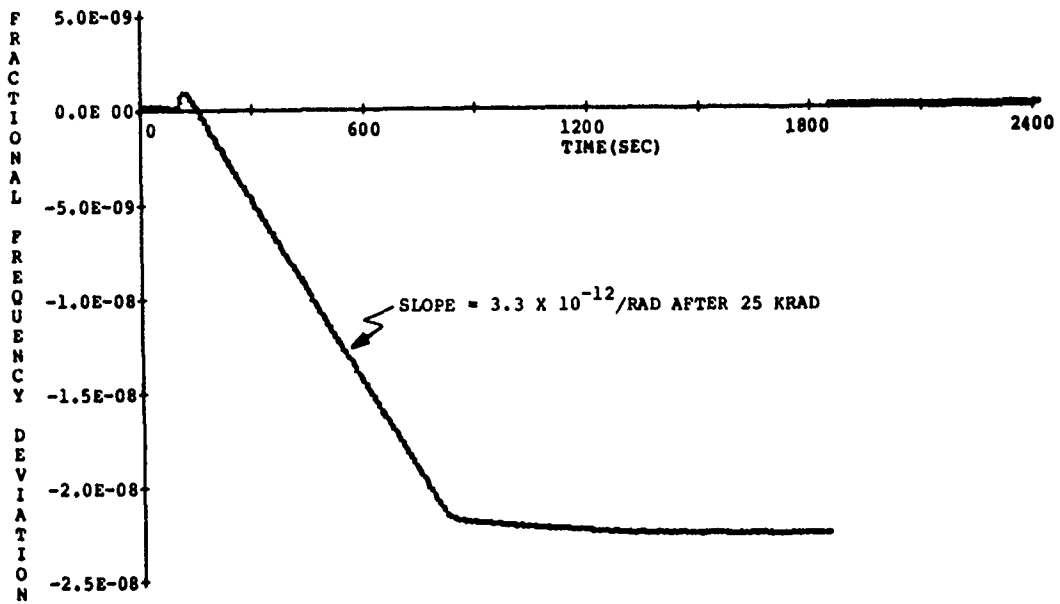


Figure 10. Orbiter Radiation, 10 Rad/Sec For
700 Seconds, 25 Krad Preconditioning

DATE 09/14/79
TIME 14:08:28

DRIFT FOR Or10r/s7k2

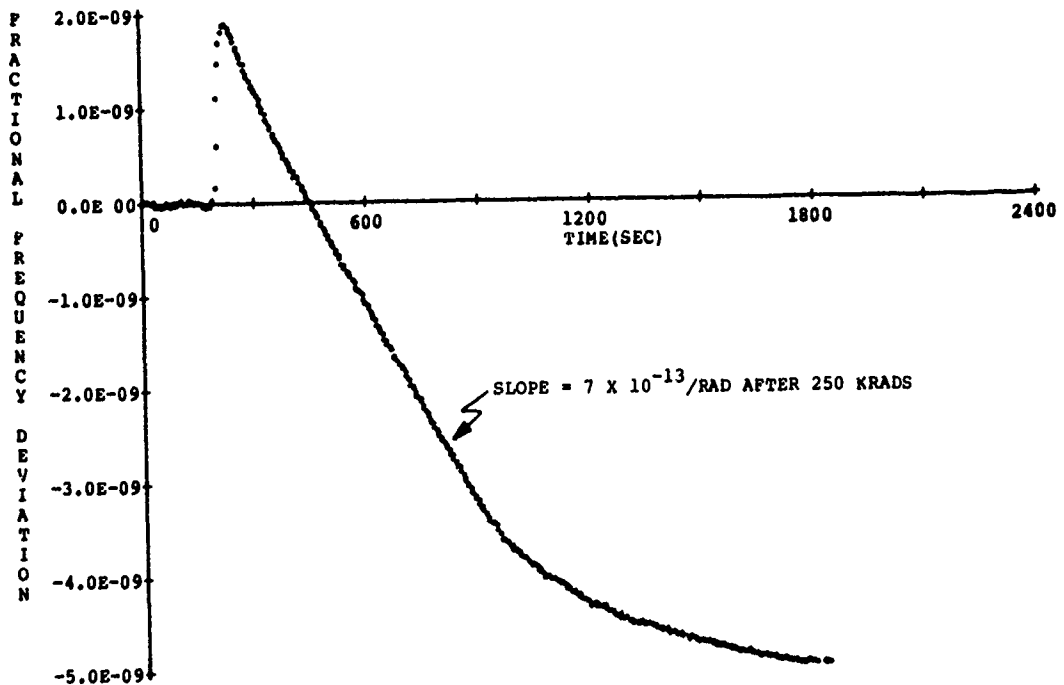


Figure 11. Orbiter Radiation, 10 Rad/Sec For 700
Seconds, 250 Krad Preconditioning

REQUIREMENTS AND EVALUATION OF THE CIRCUITRY, EXCLUDING THE CRYSTAL,
IN CRYSTAL OSCILLATORS

Benjamin Parzen*

Frequency Electronics, Inc.
New Hyde Park, New York 11040

Summary

In any crystal oscillator, the oscillator is made up of two distinct parts:

(1) The crystal.

(2) The remaining circuitry, hereinafter called the amplifier.

It would be very desirable to evaluate each one independently. However, it is very difficult to completely evaluate the crystal by itself, but it turns out that the amplifier is easily amenable to such evaluation and that quantitative limits can be set for the performance of the amplifier, relative to the oscillator performance, under certain amplifier operating conditions of the amplifier.

The basic principle consists of replacing the crystal with a different type of feedback element which renders the oscillator more unstable by many orders of magnitude compared to that when the crystal is used. The new oscillator performance is then measured and related to the performance that would be obtained when the crystal is used.

The procedure is illustrated by application to the Pierce, Colpitts and Clapp oscillator circuits.

Key words (for information retrieval)
Oscillators, Frequency Stability.

Introduction

In any crystal oscillator, the oscillator is made up of two distinct parts:

(1) The crystal resonator.

(2) The remaining circuitry, hereinafter called the amplifier.

It would be very desirable to evaluate each one independently. At the present state of the art, it is impossible to simply and completely evaluate the crystal by itself although extensive work has been carried out to independently determine the crystal short term performance^{1, 2}.

However, it turns out that the amplifier is readily amenable to such evaluation and that quantitative limits can be set for the performance of the amplifier, relative to the oscillator performance, under certain operating conditions of the amplifier and the crystal described later.

This paper derives the approximate relations between the oscillator and amplifier performance, for a given crystal, and describes the experimental technique for measuring the amplifier performance. The derivation is extremely simple. Yet it yields much information on the design of oscillators and the measurement of the amplifier performance.

It should be noted that the material presented herein is particularly applicable to the medium and long term frequency stability and yields very little information about the short term stability since the crystal resonator impedance far from the operating frequencies is not considered in the derivation and in the experimental measurement procedure. However, it is hoped that, in the future, the treatment will be extended to include the short term stability.

The amplifier evaluation would be extremely useful for the three following broad categories of applications:

(1) In new designs, it permits the budgeting of the performance of the amplifier for an overall oscillator performance and the experimental confirmation of whether the budget is being met.

(2) In old designs, or in manufacture of oscillators based on already available designs, the situation often arises that the oscillator performance is unsatisfactory and the crystal designer is convinced that the fault lies in the circuitry while the circuit designer is equally convinced that it is a crystal problem. At present, the solution for this dilemma has been to replace the crystal and/or the circuitry until satisfactory performance is finally achieved, usually at great cost of time and money. The amplifier evaluation procedure would markedly facilitate the resolution of this problem.

(3) It supplies information on the crystal medium and long term performance.

*Mr. Parzen is a Consultant to Frequency Electronics, Inc.

The Amplifier and Feedback Elements Concepts

Figure 1 shows the block diagram of a typical oscillator using the amplifier concept. It will be noted that it consists of only two elements:

- (1) The feedback element
- (2) The amplifier

In a crystal oscillator, the feedback element would be the crystal. In a non-crystal oscillator, the feedback element would be a resonator or part of a resonator. The amplifier is the rest of the oscillator including the oven and any other means for maintaining the electrical, mechanical and thermal environment.

A very important and necessary condition is that the feedback element is considered "perfect" meaning that the element characteristics are completely stable, i.e., independent of the environment and time, which condition can usually be practically satisfied during the time necessary for measuring the amplifier performance. Obviously, the total instability of the actual crystal oscillator is the sum of the amplifier instability, referred to the given perfect crystal and the instability of the actual crystal. Conversely, the instability of the actual crystal is the difference between the actual oscillator instability and the instability of the amplifier referred to the perfect crystal.

It will be noted in Figure 1 that the feedback element has associated with it a reactance, X_{FE} which is a function of only the operating frequency. Also the amplifier has associated with it a reactance X_A which is a function not only of the physical reactances in the amplifier, but also includes the contributions of the active circuitry and the environmental conditions.

General Relationships

In any oscillator, for a given feedback element = FE_n

We can write:

$$\frac{\Delta v_{FE_n}}{v} = \frac{\Delta v_{FE_n}}{\Delta X_{FE_n}} \cdot \frac{\Delta X_{FE_n}}{v} \quad (1)$$

Where, in general

$$X_{FE_n} = f(X_A) \quad (2)$$

depending upon v and the oscillator design

and for $\Delta v \ll v$ (3)

v can be assumed constant.

We shall now apply the above relations to the Pierce, Colpitts and Clapp oscillators.

Relationships in the Pierce, Colpitts and Clapp Oscillators

(2) now becomes:

$$X_{FE_n} \approx X_A \quad (4)$$

from which

$$\Delta X_{FE_n} \approx \Delta X_A \quad (5)$$

where all X symbols imply magnitude only.

If we make FE_n to be a crystal, it is well known that:

$$\Delta X_{Xtal} \approx \frac{2 Q_{Xtal} R_{Xtal} \Delta v_{Xtal}}{v} \quad (6)$$

so that (1), (5), and (6) yield:

$$\frac{\Delta v_{Xtal}}{v} \approx \frac{\Delta X_A}{2 Q_{Xtal} R_{Xtal}} \quad (7)$$

Now let us see what happens when we replace the crystal with the feedback element of Figure 2 and using the same amplifier.

From Figure 2, we have for FE_2 ,

$$X_{FE_2} = 2\pi L v \quad (8)$$

$$\Delta X_{FE_2} = 2\pi L \Delta v_{FE_2} \quad (9)$$

And from (4) and (5)

$$\frac{\Delta v_{FE_2}}{v} \approx \frac{\Delta X_A}{X_A} \quad (10)$$

Combining (7) and (10)

$$\frac{\Delta v_{FE_2}}{v} \approx \frac{\Delta v_{Xtal}}{v} \cdot \frac{2 Q_{Xtal} R_{Xtal}}{X_A} \quad (11)$$

or the converse,

$$\frac{\Delta v_{Xtal}}{v} \approx \frac{\Delta v_{FE_2}}{v} \cdot \frac{X_A}{2 Q_{Xtal} R_{Xtal}} \quad (11A)$$

Example 1:

$$Q_{Xtal} = 100,000, R_{Xtal} = 20\Omega, X_A = 100\Omega$$

$$\frac{\Delta v_{Xtal}}{v} \text{ desired} = 10^{-9}$$

$$\text{then } \frac{\Delta v_{FE_2}}{v} \approx 10^{-9} \cdot \frac{2 \times 100,000 \times 20}{100}$$

$$\approx 4(10)^{-5}$$

Example 2:

$$Q_{Xtal} = 2(10)^{-6} \quad R = 100\Omega \quad X_A = 400\Omega$$

$$\frac{\Delta U_{Xtal}}{U} \text{ desired} = 10^{-12}$$

$$\text{then } \frac{\Delta U_{FE_2}}{U} \approx 10^{-12} \cdot \frac{2 \times 2(10)^6 \cdot 100}{400}$$
$$\approx 1(10)^{-6}$$

It is interesting to note that for maximum permissible amplifier instability, Q_{Xtal} and R_{Xtal} should be maximized and X_A should be minimized. Also for equal Q_{Xtal} the crystal with greater R_{Xtal} (which is equivalent to smaller motional capacitance) will permit greater amplifier instability. Example 2 illustrates the severe requirement imposed on the amplifier. This is emphasized by noting that the Q of the oscillator with FE_2 is less than 4 for a stability of $1(10)^{-6}$, an achievement which offhand appears impossible but direct experiment has proven to be possible, a fact corroborated by the existence of crystal oscillators having stabilities of $(10)^{-12}$.

Experimental Procedure for the Pierce, Colpitts and Clapp Oscillators

We are presented with an oscillator having known crystal parameters and required stability. We have the task of determining whether the amplifier is adequate for this application.

We proceed as follows:

(1) Remove the crystal.

(2) Replace the crystal by the feedback element of Figure 2 making R the same as R_{Xtal} and L that value which will yield approximately the same operating frequency. This is facilitated by determining the approximate value of X_A with the H.P. 4815 vector impedance meter and calculating and trimming L until the right frequency is obtained. The oscillator is then energized and the current in FE_2 should be approximately the same as in the crystal. FE_2 is

realized by a stable inductor in series with a stable resistor and this normally is a relatively easy procedure. The output frequency is then monitored by a frequency counter and the stability $\frac{\Delta U_{FE_2}}{U}$ determined.

This is compared against that called for by (11). If it is less, then the amplifier is satisfactory. Otherwise an effort should be made to improve it as necessary.

Further Comments

The evaluations described in the previous sections apply specifically to the Pierce, Colpitts and Clapp Oscillator circuits. However, similar evaluations can be made for other types of oscillators in which case other forms of feedback elements will be required.

Sometimes when replacing the crystal by a different element, the oscillator may not perform properly (e.g., it may squegg). This is due to the fact that the crystal is narrow band around several discrete frequencies while the feedback element may be broad band. This is corrected by changing some of the time constants in the oscillator bias and filter circuits.

Conclusions

A method has been developed for evaluating the performance of a crystal oscillator, excluding the crystal. This method should prove to be a powerful tool for oscillator design and in the diagnosis of existing unsatisfactory oscillators.

References

1. F. L. Walls, A. E. Wainright "Measurement of the Short Term Stability of Quartz Crystal Resonators and the Implications for Crystal Oscillator Design and Applications" IEEE Trans. on Instrumentation and Measurement Vol IM-24 No. 1 March 1975.
2. J. T. Gagnepain "Fundamental Noise Studies of Quartz Crystal Resonators". Proc 29 SFC Fort Monmouth, N.J. 1976.

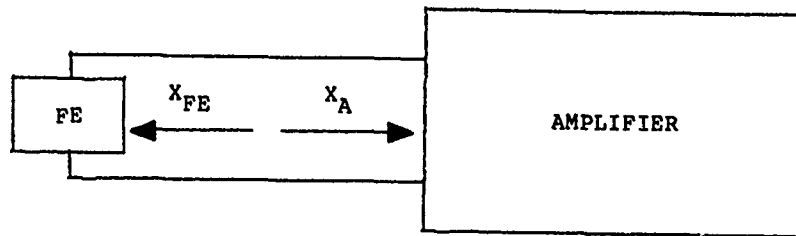
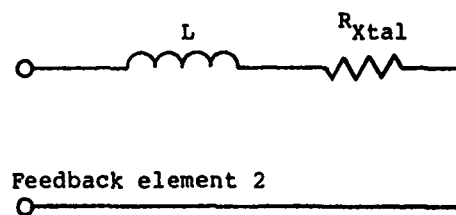


Figure 1
Block Diagram of Oscillator



L is chosen so that the oscillator frequency is approximately the same as the crystal oscillator frequency.

Figure 2
Feedback Element 2

MINIATURE PACKAGED CRYSTAL OSCILLATORS

D. M. Embree
Bell Telephone Laboratories, Incorporated
Reading, Pennsylvania

R. E. Paradysz
Bell Telephone Laboratories, Incorporated
Allentown, Pennsylvania 18103

V. R. Saari
Bell Telephone Laboratories, Incorporated
Holmdel, New Jersey

R. J. McClure
Western Electric Company
Reading, Pennsylvania 19604

Abstract

Miniature crystal controlled oscillators have been developed for general timing applications from 18 KHz to 22 MHz. This paper will address principally oscillators in the 0.5 MHz to 22 MHz region. The lower frequency devices are nearly identical except for tailoring of resonators and integrated circuits to lower frequencies. The oscillators are packaged in TO-5, TO-8 and DIP compatible metal cold welded hermetic packages. The oscillators were developed to provide high reliability and manufacturing simplicity. The heart of the various configurations is a silicon integrated circuit (SIC) oscillator. The SIC is composed of a linear oscillator amplifier with amplitude gain control followed by wave shaping circuitry to provide TTL output signals. The SIC is provided with beam lead connections and occupies an area of less than 70 mils square. Beam leads on the SIC are thermal compression bonded to a metallized ceramic substrate forming a hybrid integrated circuit (HIC). The HIC may have deposited components and functional SICs depending on the application. The crystal is added to the HIC and assembled and sealed within its appropriate enclosure. The oscillators are designed to function from -40°C to $+95^{\circ}\text{C}$ with stabilities of ± 100 ppm and ± 25 ppm from 0°C to $+70^{\circ}\text{C}$. Generally AT cut crystals in the 8 MHz to 22 MHz region are used in the oscillator. For low frequency applications the appropriate divider SIC is added to the HIC. A voltage controlled crystal oscillator is also available in a HIC configuration. These devices exhibit frequency tuning characteristics of 100 ppm per volt. This circuit uses thin film circuitry and applique devices in addition to the beam lead SICs. Oscillator frequency sensitivity to power supply voltage variations is typically 0.5 ppm per volt up to 22 MHz.

The output circuits in the oscillators are capable of driving five (5) medium power TTL loads with rise and fall times of less than 10 ns. The output symmetry of the oscillators is between 45-55 percent and 50-50 percent depending upon whether an output divider is used. Aging data at different temperatures up to 150°C has been used to estimate

the activation energy for the aging process and end of life frequency shifts. The nominal oscillator aging after twenty years at 90°C has been estimated to be about 10 ppm.

Introduction

Miniature crystal controlled oscillators have been developed for low-cost high volume applications. The main objectives in the development of these oscillators has been design simplicity and high reliability. The oscillators cover a frequency range from 18 KHz to 22 MHz and share similar technology over the entire frequency range. Metal hermetic cold welded enclosures and silicon integrated circuits utilizing beam lead technology are used throughout the oscillator design. The oscillators use +5VDC power supply voltage. Figure 1 illustrates some of the many miniature oscillators available in the dual-in-line compatible and TO-8 size enclosures. Wire mounted CT, DT and E element resonators are used as well as circular AT cut resonators. The heart of each device is the integrated circuit oscillator which may be followed by another integrated circuit performing additional functions.

The discussion in this paper will be limited to the high frequency oscillators using AT cut resonators. The technology for the lower frequency devices is identical except for resonators and integrated circuits which are optimized for lower frequencies.

The high frequency oscillators operate over a frequency range of 0.5 MHz to 22.0 MHz, with frequency stabilities of ± 100 ppm for all causes over a temperature range of -40°C to $+95^{\circ}\text{C}$. Stabilities of ± 25 ppm may be achieved for temperatures of 0°C to 70°C . Sensitivity to power supply voltage variations is less than 0.5 ppm per volt. The typical power consumption is 175 mw up to 8 MHz and 85 mw from 8 MHz to 22 MHz. Failure rates lower than 100 FITS at 95°C have been projected from tests conducted at 150°C . The oscillators are available in DIP compatible as well as TO-5 and TO-8 packages. The DIP compatible package offers the full frequency range from 0.5 MHz to 22.0 MHz while TO-5 and TO-8 packages are limited to the 8.0 MHz to

22.0 MHz frequency range. The oscillators provide TTL output signals capable of driving 5 medium power loads with rise and fall times of less than 10 ns. The output symmetry is typically 45% to 55% but at frequencies below 8 MHz the symmetry approaches 50%.

The oscillator enclosures are metal cold-welded packages that are in DIP compatible, TO-5 or TO-8 outlines as illustrated on Figure 2. The DIP compatible package, being 0.5 inches wide X 0.8 inches long X 0.3 inches high, has been designed to a proposed IEC package outline while the TO-5 and TO-8 packages are already industry standards. The DIP compatible enclosure is used over a frequency range from 0.5 MHz to 22.0 MHz. This enclosure has the largest internal volume and greatest flexibility for packaging. The TO-8 package is used in the 8 MHz to 22 MHz frequency range. The TO-5 package is generally used in the 10 MHz to 22 MHz region. This package is used in applications where space is at a premium and cost is less important.

The package assembly discussion will be limited to the DIP compatible configuration since the design is most flexible and does not have the space limitations of the smaller TO-5 and TO-8 packages. The assembly of the TO-5 and TO-8 packages is similar to the DIP configuration but scaled down in size.

Hybrid integrated circuits (HIC's) are used in conjunction with every packaged oscillator. The HIC is a conglomeration of several components mounted on a ceramic substrate. The ceramic substrate is metalized with interconnect paths and bonding pads to which silicon devices, crystal mounting ribbons and in some cases thin film resistors and capacitors are attached. Thermal compression bonding is used to attach these components to the ceramic substrate.

The crystal designs chosen for the packaged oscillator have been chosen for low-cost and high reliability. An AT cut plano-plano-plate with a maximum diameter of 0.320 inches conveniently fits into the DIP compatible package. The crystal is designed with less than 25 ohms resistance and all unwanted resonances are suppressed more than 10 dB. The frequency range of the crystal units is 8 MHz to 22 MHz.

A cutaway assembly of the dual-in-line oscillator package is illustrated in the photograph on Figure 3. The HIC used in this illustration includes an oscillator followed by a 4 bit ripple counter. The oscillator SIC is the smaller 20 beam device toward the rear of the HIC. The four bit ripple counter is the lower 30 beam device toward the front of the HIC. These devices are mounted on a ceramic substrate 0.370 inches wide by 0.495 inches long. The HIC allows the selection of one of four output frequencies available from the output of the ripple counter. Appearing on one of the four land areas to the right of the four bit divider are the oscillator output frequencies of $f/2$, $f/4$, $f/8$ and $f/16$. Selection of the desired output frequency is accomplished by connecting the appropriate divided output to the adjacent output

stripe with conductive epoxy. This particular HIC is used for output frequencies in the 0.5 MHz to 8.0 MHz range. Crystals in the 8 MHz to 16 MHz band are used for this application. The assembly of the package starts by first forming the crystal ribbon to accept the crystal plate. A drop of conductive epoxy is put on the center of the enclosure base. The HIC is then pressed into the base forcing the epoxy away from the center of the base. This provides mechanical attachment and low thermal resistance of the HIC to the enclosure base. The terminal wires are then formed over the land areas in each corner of the HIC. Silver-loaded conductive epoxy completes the electrical connection between the terminal wires and the land areas on the HIC. The crystal is then installed between the formed mounting ribbons and epoxied in place.

The epoxy is then cured at 150°C for one hour. After the epoxy has been cured the crystal is adjusted to frequency. In this operation, the oscillator is powered in a vacuum environment and gold is evaporated onto the crystal plate until the appropriate output frequency has been reached. The packaged crystal oscillator is then evacuated and sealed. There are many variations of circuit combinations available in packaged crystal oscillators. A unique design which has potential in phase lock loops and where remote tuning is desired is the voltage controlled crystal oscillator (VCXO). This oscillator is available in the DIP compatible package at frequencies in the 0.5 MHz to 22.0 MHz band. The functional block diagrams of the two circuits which are used to cover the frequency range from 0.5 MHz to 22 MHz are illustrated on Figures 4A and 4B. The HICs consist of the oscillator SIC and a divider (for frequencies from 0.5 MHz to 8.0 MHz) or buffer gate (for frequencies from 8.0 MHz to 22.0 MHz) plus the addition of a varactor diode in the crystal network. Biasing of the varactor diode is accomplished with two thin film resistors and a capacitor. The oscillator tuning characteristic is illustrated in Figure 5. The frequency vs. voltage sensitivity about the nominal +2.5 volts is about ± 100 ppm per volt.

Oscillator Integrated Circuit Design

The heart of each packaged crystal oscillator is a complimentary bipolar integrated circuit (CBIC) oscillator using beam lead technology. The oscillator is stabilized by an external quartz crystal that is designed to operate to 22 MHz providing TTL output signals with crystal resistance of up to 25 ohms. Rise and fall times are less than 10 nsec with on times of 45% to 50%. Typical power consumption is 40 mw. The oscillator incorporates several features which are listed below:

1. The oscillator circuit, designed of mixed differential stages, has high common mode rejection to interfering noise.
2. The symmetry between power supply and ground using complementary PNP and NPN transistors in CBIC technology makes the circuit tend naturally toward a symmetric output.

3. Push-pull loading provides low impedance connections at both terminals of the crystal to maintain a very high loaded circuit Q.
4. The average loop gain is reduced to unity over a cycle at a relatively low level of crystal current by a clipping circuit introduced at a point in the feedback loop where it does not appreciably affect the crystal termination impedances. The oscillator is not allowed to be limited by device saturation.
5. The push-pull, common-mode scheme of the oscillator tends to place NPN and PNP emitter junctions in series pairs. This reduces the manufacturing spread of offset voltages and produces high yield.
6. The bias voltages applied to the heart of the circuit float at levels established by means of a chain of diodes. This isolates the oscillating loop from external interferences.
7. Flip-flop action is designed into a novel TTL output circuit to reduce the cross-over current spikes which are injected into supply and ground. The interaction between the pull-down and push-up output devices is minimized.

Circuit Details

A schematic diagram of the oscillator circuit is presented in Figure 6. The following discussions break this diagram up into several parts for the sake of clarity.

The Oscillating Loop

A simplified picture of the oscillating circuit is given in Figure 7. The crystal is connected as the feedback network across a nearly zero-phase amplifier consisting of a push-pull common-base input stage and a push-pull emitter-follower output stage. The bias currents of all of the shown semiconductor devices except Q13 and Q14 are set, by circuitry to be discussed later, to be approximately equal. The clipper-transistor bias currents (Q13 and Q14) are so low as not to materially affect the small-signal gain. The network has two output points.

In Figure 8, the same network is shown again with different emphasis. The loop has been opened, permitting the ac emitter node voltage of Q9/Q10 to assume values much different from the values at the Q6/Q8 emitter node. The indicated incremental currents are defined as representing the instantaneous state of the fundamental oscillation when it is still small in amplitude. For the fundamental sine wave, the crystal appears as a small resistance R_x , which is typically about 5 ohms. The current I represents the common value of emitter bias current. All base currents and parasitics are neglected.

The imbalance parameters $k = \frac{1}{1 + \frac{1}{m}}$ and m arise

from the push-pull nature of the amplifier. (The latter quantity m is artificially defined to simplify the expressions.) The clipper transistor that is being cut off by the signal swing (in the half cycle implied by the current arrows), namely Q13, is neglected. The other clipper transistor is represented through its determinate relationship with the current kI and the voltage $-v$, which is considered as being applied to the base of Q10. The open-loop crystal terminal voltages (emitters of Q6/Q8 and Q9/Q10) are expressed in two ways, based on the voltages at the bases of the respective transistors and the corresponding emitter currents.

a. Start-Up Value of Loop Gain

To determine the small-signal loop gain for the fundamental mode of oscillation, we recognize that the crystal-driving terminal (Q9/Q10) is terminated in R_x plus the open-loop input impedance of the amplifier, which is a complicated function to express. But this is equivalent to equating the drive-terminal voltage to G times the voltage which the tank applies to the dissipative part of the circuit. This gives the equation shown at the bottom of Figure 8. For small signal, $k \approx 1$, $m \approx G$, $-v \approx$ the base voltage of Q9 and $\ln(1+x) \approx x$. Thus, we can write

$$\begin{aligned} -V_T \frac{I}{I} - 2R_x \frac{I}{I} G &= -I R - V_T \frac{I}{I} + V_T \frac{I}{I} G \\ \frac{I}{I} + 2R_x \frac{I}{I} G &= R + \frac{I}{I} \end{aligned}$$

where $V_T \approx 26$ mV, the thermal voltage of a junction and $\frac{I}{I} = r_e$. Thus

$$G = \frac{R + r_e}{2(r_e + R_x)} = \frac{200 + 21.6}{2(21.6 + 5)} = 4.16$$

Actually, this last expression for G could have been obtained from the closed-loop circuit diagram by inspection, for the same current flows in two parallel input meshes of resistance $2r_e + 2R_x$, and in two parallel resistances $R + r_e$ whose terminal voltage equals the EMF in the input mesh.

Thus the start-up value of loop gain for a nominal chip and a 5 ohm crystal has been calculated to be approximately 4.16, which will ensure growth of the oscillation. Computer analysis using the SPICE program has given a gain value consistent with this and has also shown that the small-signal phase angle will be about 14° at 10 MHz and 29° at 20 MHz. The crystal resistance can go as high as 31.6 ohms before reducing this gain to 2.08; AT-cut crystal units in the range 4-27 MHz will dependably have less series resistance than that.

b. Steady-State Amplitude of the Oscillation-Approximate Analysis

Let us now see if we can stop the growth of the oscillation both before any of the transistors saturates and at a controlled low value of

crystal-current amplitude. Let us assume, now, that the currents labeled in Figure 8 represent the peak values reached in the branches indicated. The oscillation will stop growing after both gain paths through the amplifier are interrupted simultaneously at the peaks of the current swings. The growth will stop when the fundamental-mode power flowing out of the tank circuit just equals the fundamental-mode power flowing into the tank circuit from Q9/10. The voltage waveform at the emitter node of Q9/10 will be nearly square, as shown in Figure 8. At the limit of the half cycle, the current in Q9 is essentially cut off by the relatively fast drop of the base voltage of Q9; the drop in the emitter node voltage is limited by the clipping action of Q14, represented by the forced independent voltage $-v$ at the base of Q10.

The fundamental sine-wave component of a 50 percent duty-cycle square wave has an amplitude equal to $\frac{1}{\pi} = 1.27$ times the amplitude of the square wave. This implies that the fundamental sine wave amplitude at the R_X terminal will be 1.27 times the peak voltage at the Q9/10 emitter when the loop is closed and no net additional power is flowing into the tank. Thus we can write

$$\begin{aligned} \frac{1}{\pi} V_B \ln(1 + \frac{1}{I}) - R_X(1+k)i &= 1R - V_T \ln(1 + \frac{1}{I}) \\ &- V_T \ln(1 - m \frac{1}{I}) \\ V_T \ln(1 - m \frac{1}{I}) &= \frac{1}{\pi} V_B - R + \frac{1}{\pi} R_X(1+k)i \\ &+ V_T(\frac{1}{\pi} - 1) \ln(1 + \frac{1}{I}) \end{aligned}$$

Let us consider setting v at such a value that $i = .81 \approx .96$ mA, which implies a crystal current amplitude of $(1+k)i = 1.49$ mA. Does this value of v result in a Q14 quiescent current satisfying the assumption that it is at least two orders of magnitude below the level I ? For $R = 200$ (Figure 1), $R_X = 5$ ohms and $k = 0.555$ the above equation gives

$$\begin{aligned} .026 \ln(1-.8m) &= \frac{1}{\pi} - 200 + \frac{20}{\pi} (1.555) (.00096) \\ &+ .026(\frac{1}{\pi} - 1) \ln 1.8 = -.178 \end{aligned}$$

$$1 - .8m = .00105$$

$$m = 1.249$$

(Note that $m \neq 1$.)

The value of v that our choice implies is obtained from the lower loop expressions for the Q9/10 emitter voltage in Figure 8, taking the factor G equal to unity because of the current continuity in the closed-loop situation. Thus we can write

$$\begin{aligned} \frac{1}{\pi} V_T \ln(1 + \frac{1}{I}) + R_X(1+k)i &= v - V_T \ln[1 + (1+k-m) \frac{1}{I}] \\ \frac{1}{\pi} [.026 \ln 1.8 + 5(1.555)(.00096)] &= v - .026 \ln[1 \\ &+ .307(.8)] \text{ which gives} \end{aligned}$$

$$v = .0347$$

The total current in Q10 at this point is

$$I + (1+k-m)i = (1+.246)I$$

Note that the current in the transistor (Q9) being cut off during this half cycle has swung much further (I) than the current in the transistor (Q10) that is maintaining a low terminating resistance for the crystal (0.246I).*

Figure 10 shows how a given value of v implies a value v_{CLP} of voltage (a dc value) applied to the base of the clipper transistor Q14. Since the V_{BE} 's of all of the transistors are stated in reference to a condition when a current $I = 1.2$ mA flows in an emitter junction of unit size, this value of v_{CLP} is in reference to V_0 , which is nearly the average of the voltages at the emitters of Q7 and Q12 (Figure 6 and 11). This point will become clearer in the next section, which discusses the biasing scheme of the oscillator.

Putting into Figure 10 the values of k , i and v obtained earlier, one can find, after two successive approximations that v_{CLP} would be about -65 mV. But this implies a quiescent (start-up) value of Q14 current of $I \exp[-(65/26)] = .082I$, which is not consistent with our assumption (and desire) that the value be two orders of magnitude below I . The derived value would result in a resistance of 260 ohm being present across R at start-up, which would pull the loop gain dangerously low. A doubling of this resistance value would preserve sufficient gain.

Setting i to 1.26I in the equations gives $-v = -56$ mV, $v_{CLP} = -84$ mV and $(1+k)i = 2.18$ mA. Since -84 mV is the value of v_{CLP} actually chosen (Figure 11), the predicted crystal current amplitude is 2.2 mA. This will still be sufficiently small as not to saturate any transistors, although it is higher than one might like from considerations of crystal lifetime. The computer has predicted approximately this amplitude for 6.7 MHz but a considerably lower value (about 1.3 mA) for 20 MHz, evidently due to capacitance and transit-time effects.

2. The Biasing Scheme

The bias voltages applied to the heart of the oscillator are established by means of the network shown in Figure 11. Current flowing through the diode-connected transistor Q30 induces a small initial current in Q28 and twice that amount of current in Q29, which has two units of emitter area. Neglecting base currents, all of the Q29 current is pulled through Q4 and Q3 and then Q27. This results in roughly four times the initial value of Q28 current being forced through Q2 into Q28 as positive feedback. Thus the currents build up until the 24 ohm resistors in series with the emitters of Q26 and Q28 stop the rise. By the time this happens, substantial current also flows in the path through Q7 and Q12, and this adds to the Q27 and Q28 currents. With the resistance values and emitter-area ratios indicated, the currents settle approximately to the values shown in the diagram, where $I \approx 1.2$ mA, a value almost independent of

* The number .246 will appear as $\frac{1}{2}$ in a later discussion.

supply voltage and temperature. (This has been verified by computer analysis.) Now the ratio of emitter-current densities in Q27 and Q26 (also Q28 and Q29) is 3:1, and the corresponding junction voltage difference is 28.6 mV, which appears across each 24 ohm resistor.

Only one of the emitter resistors of Q26/Q29 is necessary, but the other one has been added to achieve as high a degree of balance as can be obtained simply.

Two pairs of the output voltages differ by $B + b$, where b is the drop obtained with the current I flowing through a resistance value R . Note that B denotes the V_{BE} of either an NPN or a PNP transistor biased at $I_E = I$. When the output pairs are actually used to set up currents equal to I in the rest of the circuit, the junctions that appear across the voltage differences are always of the correct type to result in clean cancellation of the B 's.

The extra emitters of Q13 and Q14, connected as they are, reduce the Q2/3 currents relative to the resistor currents. This reduces the Q6/8 current just sufficiently to compensate for the average of the other Q13/14 emitter currents, which draw out of the base nodes of Q9/10. This technique keeps the Q9/10 bias current (and hence the output circuit biases) under control over a wide temperature range. This is important because the Q13/14 bias currents do not track the basic bias current I .

3. The TTL Output Circuit

It is important that the current impulses shot into the supply and ground as the TTL output switches be suppressed as much as is practical without unduly lengthening the TTL rise or fall times. Thus the positive-current and negative-current output devices (Q22 and Q23, respectively, in Figure 6) should not simultaneously receive drive currents sufficient to turn them on strongly. Therefore, the collector currents of Q17 and Q19 should never simultaneously be larger than about .8 mA; whereas, they individually need to swing to a value of at least 2 mA (better yet 3 mA) to provide the speed needed. The circuit arrangement in Figure 12 provides these features.

The voltage across the bottom $\frac{R}{2}$ resistor in Figure 12 is

$$n_1 I \frac{R}{2} = \frac{n_1 b}{2} = \frac{1}{2} [b - V_T \ln[(1+n_1) n_1] + (1-n_2)b - V_T \ln[(1+n_2) n_2]] \\ = \frac{b}{2} (1+n_1-n_2) - \frac{V_T}{2} \ln \left[\frac{n_1^2 (1+n_1)(1+n_2+2)}{n_2^2 (1+n_2)} \right]$$

At the center of the switching range, the collector currents of Q9 and Q10 are equal to I . Here we have

$$n_1 = n_2 = 0 \text{ and } n_1 = n_2 = n$$

This gives us

$$\frac{R}{2} n = b - nb - 2V_T \ln[n(1+n)]$$

which, for $b = .24$, gives

$$n = .655 \\ nI = .787 \text{ mA}$$

Hence the crossover current level of Q17/19 is low enough.

Now we shall calculate the maximum value of the Q19 (or Q17) current. From our earlier analysis of the steady state amplitude of oscillation we can see that the values of n_1 and n_2 corresponding to this state are 1 and .246, respectively. Noting that $n_2 \neq 0$ here, we now get

$$\frac{b}{2} n_1 = 2b - V_T \ln \left[\frac{n_1^3 (1.246)}{12n_1 + .078} \right] = 2b - 3V_T \ln n_1 - .006 \\ .12n_1 + .078 \ln n_1 - .47 = 0$$

for which the solution is

$$n_1 = 3.06 \\ n_1 I = 3.68 \text{ mA}$$

Hence the indicated value of the maximum current is high enough.

The nominal values of crossover and maximum Q17/19 current resulting from computer analysis are .67 mA and 3 mA (Figure 16), respectively, which are somewhat lower (and more desirable) than the approximate values calculated above. The reason is that the Q9/10 current is a bit larger than I .

It should be observed that the network of Figure 12 does not flip into the other state as soon as the equality level of Q9 and Q10 current is crossed. The differential input to Q15/16 must swing considerably past zero before the off pair of transistors (either Q16/17 or Q15/19) is brought back into conduction. The fact that Q9 and Q10 alternately cut off ensures that the flipping eventually does happen. The symmetry of the circuit preserves the desired 50 percent duty cycle.

An actual small deviation from the design thus far indicated helps (according to both computer and breadboard results) in preserving the approximate 50 percent duty cycle up to 20 MHz. The clipping action of Q13 has been inhibited somewhat by means of the imbalance of the resistor arrangement between the emitters of Q7 and Q12 (Figure 11). This appears to compensate for the imbalance in the parasitic capacitances associated with the NPN and PNP transistors. The effect seems to be that the cutting-off of Q10 in the appropriate half cycle is better assured at high frequencies. This promotes timely action of the flip-flop.

The flip-flop network drives the output network shown in Figure 13, where Q24 and Q25 are antisaturation devices. The diode Q20 shifts the level of the high-state output downward so that the rise and fall times do not raise the duty cycle above 50 percent when a 5-volt supply is used. The 10K resistor maintains a little bias current in the diodes in the zero output state.

Transient Analysis with the Computer

A transient analysis of the oscillator was obtained with a computer, using the SPICE program. The crystal was modeled with two series RLC networks placed in parallel, representing the fundamental and third-harmonic modes, and a shunt capacitance of 10 pf. The two series combinations chosen for a 6.67 MHz (20 MHz) computation were 5 ohms, 24 μ h (8 μ h), 24 pf (8 pf) for the fundamental resonator and 15 ohms, 24 μ h (8 μ h), 24/9 pf (8/9 pf) for the third-harmonic resonator. The resulting waveforms are shown in Figures 14-16 for 6.67 MHz and Figure 17 for 20 MHz.

In order to facilitate getting crystal-current build-up (energy storage) in the crystal within a reasonably short computation time, a voltage step function was applied in series with the equivalent circuit of the crystal at time zero. The magnitude was chosen (by trial and error) to start the crystal current amplitude slightly below or slightly above the steady state level. Thus the oscillation would either grow or decrease slightly from this level. The loaded Q of the crystal was chosen arbitrarily very low (about 30) so that the growth or decay would be noticeable.

Figure 14 shows a waveform for the emitter node of Q6/8 (crystal output terminal) that would be nearly a sinusoid were the small voltage represented by the top waveform (the reference voltage at the base of Q6) subtracted from it.

Figure 15 shows the clipper actions on the base voltages of Q9 and Q10 and also shows the collector voltages of Q9 and Q10 moving about 1R \approx 240 mV up or down from the quiescent (starting) level as Q9 and Q10 alternately cut off.

Figure 16 shows the TTL output voltage predicted assuming a 30 pf load. The rise and fall times are still very adequate, and the duty cycle is very nearly 50 percent. Other computer results (not shown) indicated that a 0.1 μ h placed in the supply lead or ground (still assuming the 30 pf load capacitance) would not seriously degrade the results.

Reliability

An extrapolated 20 year end of life lower 3 dB frequency has been obtained from isothermal studies. Data was obtained from 40 oscillators divided into three groups and aged at 25°C, 61°C and 150°C. The logarithms of the negative median extrapolated frequency shifts are plotted versus temperature in Figure 18. In Figure 18 the temperature scale is linear in the variable $[1/(T^\circ C + 273.16)]$. The solid line in Figure 18 is a least square fit to the medians of the frequency shifts extrapolated to 20 years. Actual aging times are 11,000, 14,000 and 40,000 hours for these samples. The equation of the solid lines is

* The crystal current in this particular case was started considerably below the steady-state amplitude, but no qualitative error in the waveforms has resulted from this.

$$DF = DF \frac{E_a}{RT}$$

with $DF = -.344 \times 10^5$ ppm (frequency) and $E_a = 0.26$ eV or 6074 calories. In this equation $T = T^\circ + 273.16$ and $R = 8.616975 \times 10^{-5}$ eV per K or 1.987 calories per K.

The failure rate of the oscillators has been predicted to be less than 100 FITS at 90°C. The prediction was made using the data collected from forty oscillators distributed over these stress temperatures. The most significant data is from the twelve units that were thermal stressed at 150°C. The only failure occurred at 32000 hours and the test was terminated at 40,000 hours. The 150 degree maximum stress temperature was chosen to be compatible with the conductive epoxy used in the device assembly.

Acknowledgments

The authors wish to express their appreciation to the many people in Bell Laboratories and Western Electric who have made significant contributions to the packaged crystal oscillator development. A special note of appreciation to the Western Electric Transmission Components and Development Department (27500) for quartz crystal resonators and oscillator models development and the Bell Laboratories Components Technology Department (4261) for the HIC development.

References

- (1) V. R. Saari, Private communication.
- (2) V. R. Saari, U.S. Patent No. 4,065,728, Crystal Oscillator Including a Pair of Push Pull Complementary Transistor Amplifiers.
- (3) S. H. Oster, I. R. Oak, G. T. Pearman, R. C. Rennick and T. R. Meeker, "A6 Monolithic Crystal Filter Design for Manufacture and Device Quality", Proceedings of the 29th Annual Symposium on Frequency Control, 1975.
- (4) D. S. Peck and C. H. Zierdt, Jr., "The Reliability of Semiconducting Devices in the Bell System", Proc. IEEE, February 1974, pp. 185-211.
- (5) J. D. Holmbeck, "Frequency Tolerance Limitations with Logic Gate Clock Oscillators", Proceedings of the 31st Annual Frequency Control Symposium, 1977.
- (6) R. B. Leighton, Principles of Modern Physics, McGraw Hill, New York (1955), pp. 722.
- (7) Handbook of Chemistry and Physics, 37th Edition, Chemical Rubber Publishing Co., Cleveland (1955), pp. 2895.

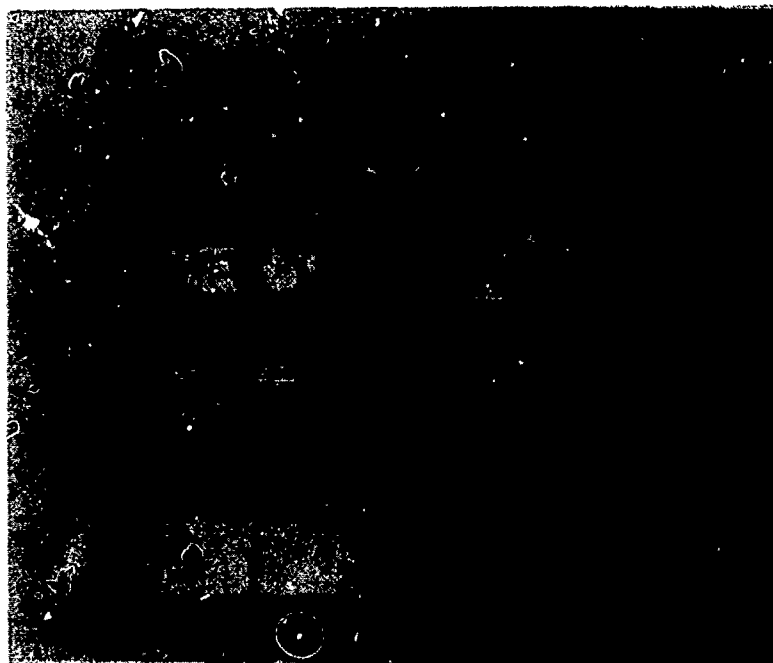


Figure 1 Miniature Oscillators from 18KHz to 22MHz

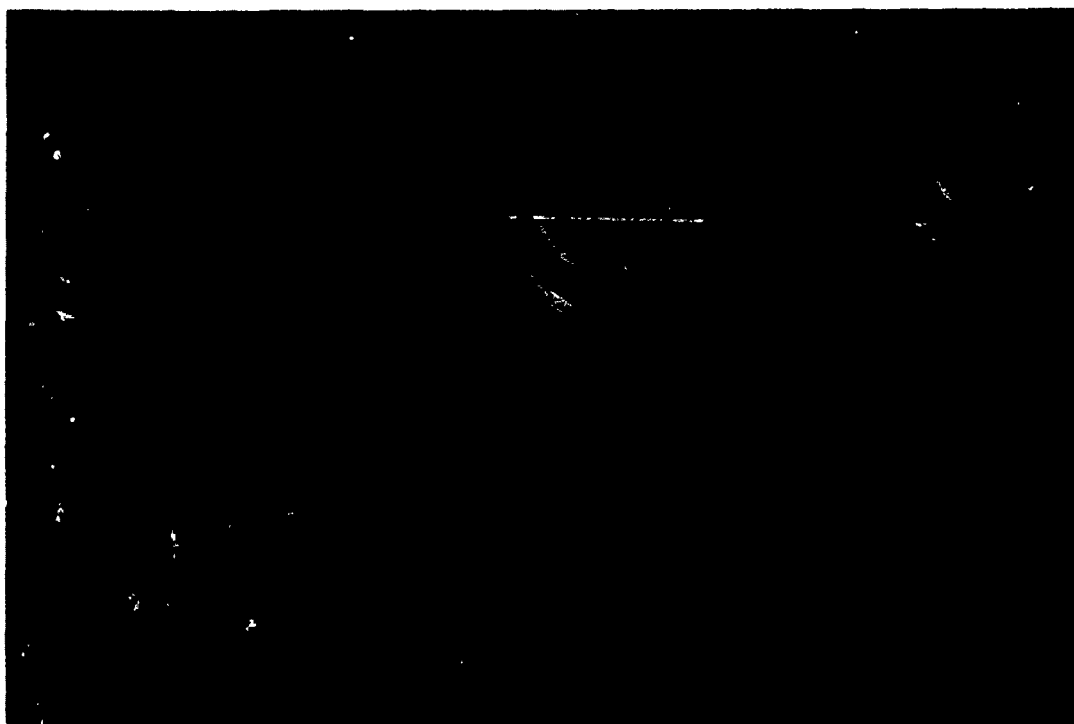


Figure 2 DIP Compatible, TO-8 and TO-5 Oscillator Enclosures



Figure 3 Cutaway Oscillator Assembly

HIC BLOCK DIAGRAM FOR 0.5 MHz TO 8.0 MHz

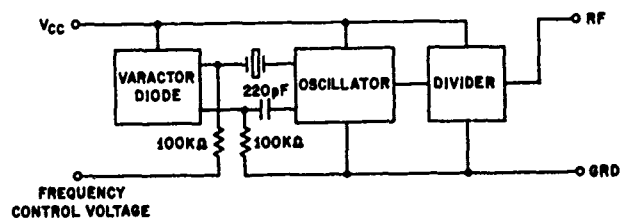


FIGURE 4A

HIC BLOCK DIAGRAM FOR 8.0 MHz TO 22.0 MHz

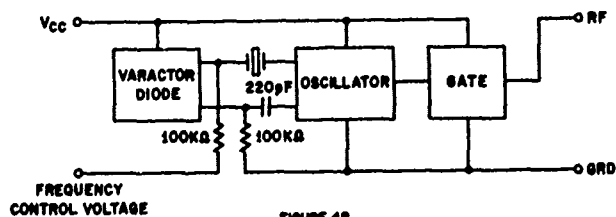


FIGURE 4B

VOLTAGE CONTROLLED OSCILLATOR TUNING CHARACTERISTIC

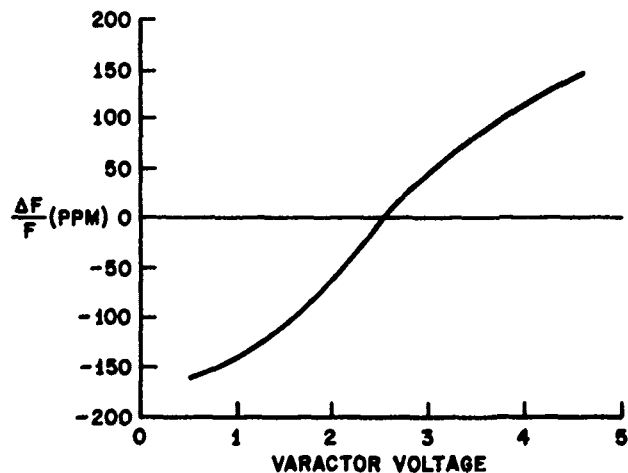


FIGURE 5

OSCILLATOR CIRCUIT (5020)

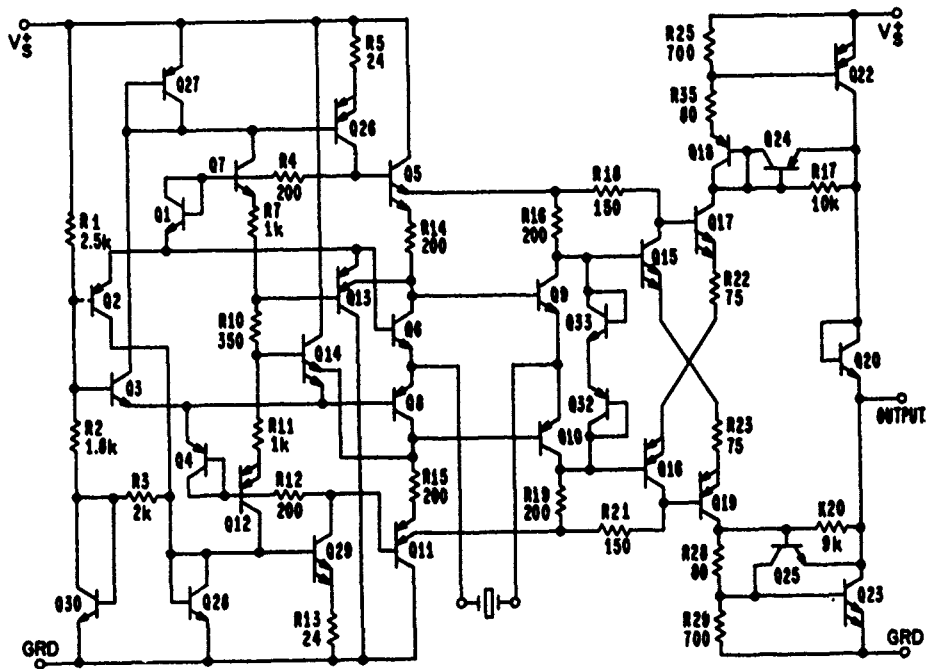


FIGURE 6

SIMPLIFIED OSCILLATOR CIRCUIT

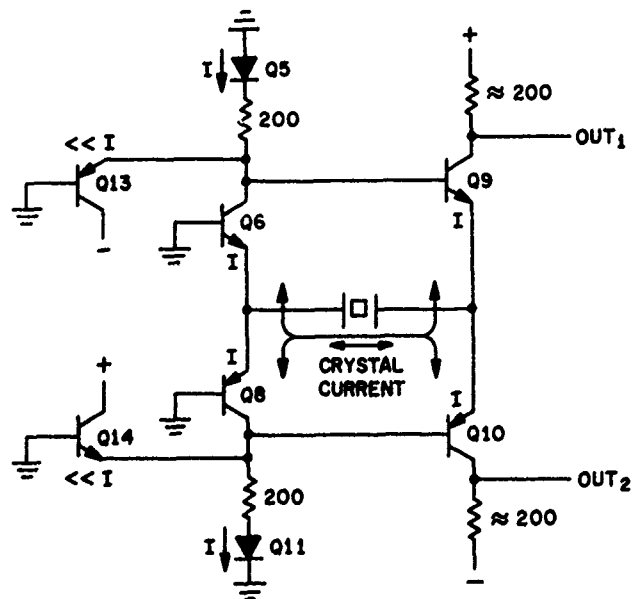
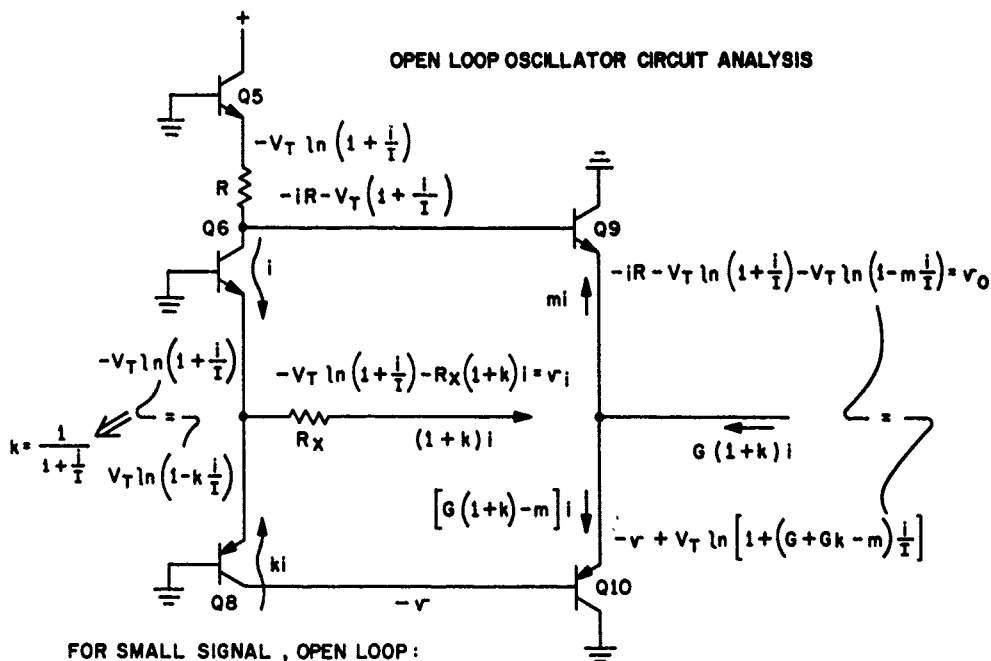


FIGURE 7



$$G v_i = v_o$$

$$G \left[-V_T \ln \left(1 + \frac{i}{I}\right) - R_X (1+k) i \right] = iR - V_T \ln \left[\left(1 + \frac{i}{I}\right) \left(1 - m \frac{i}{I}\right) \right]$$

FIGURE 8

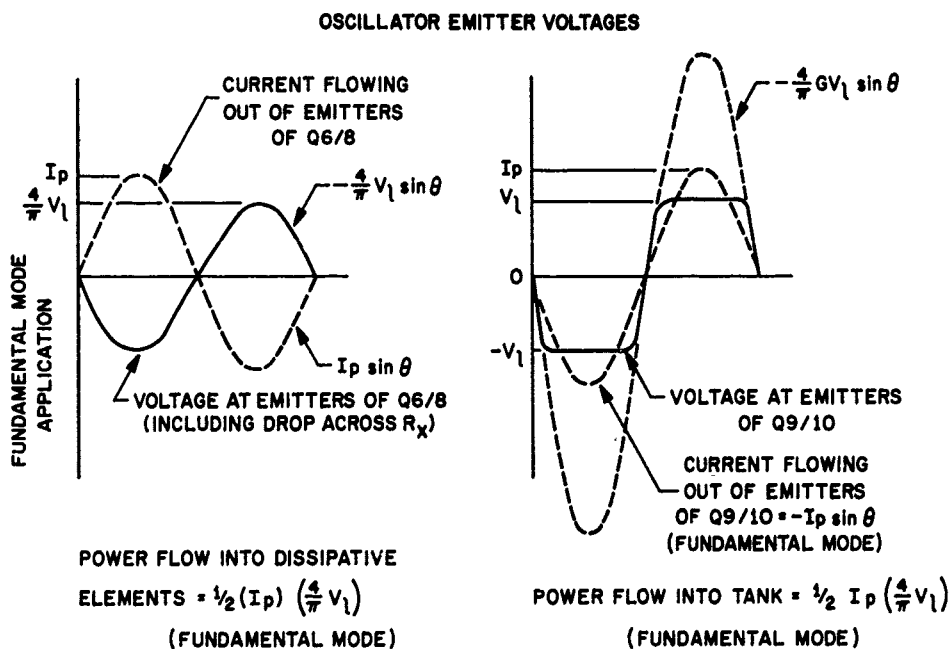
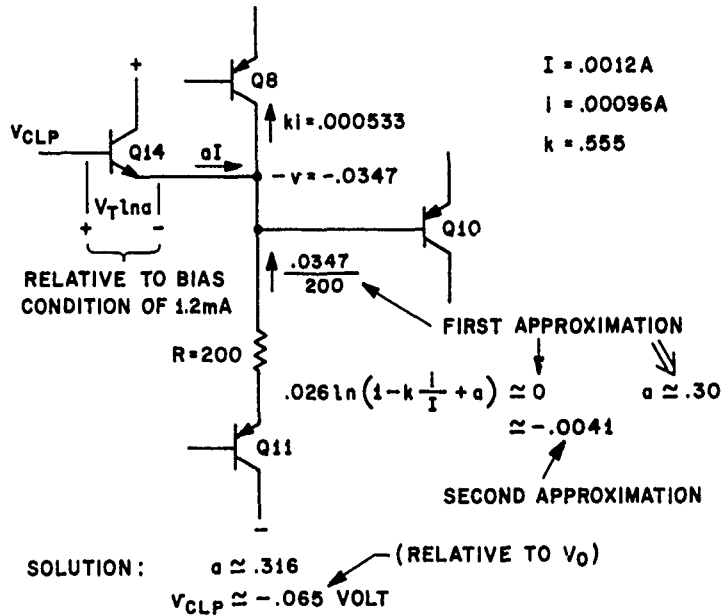
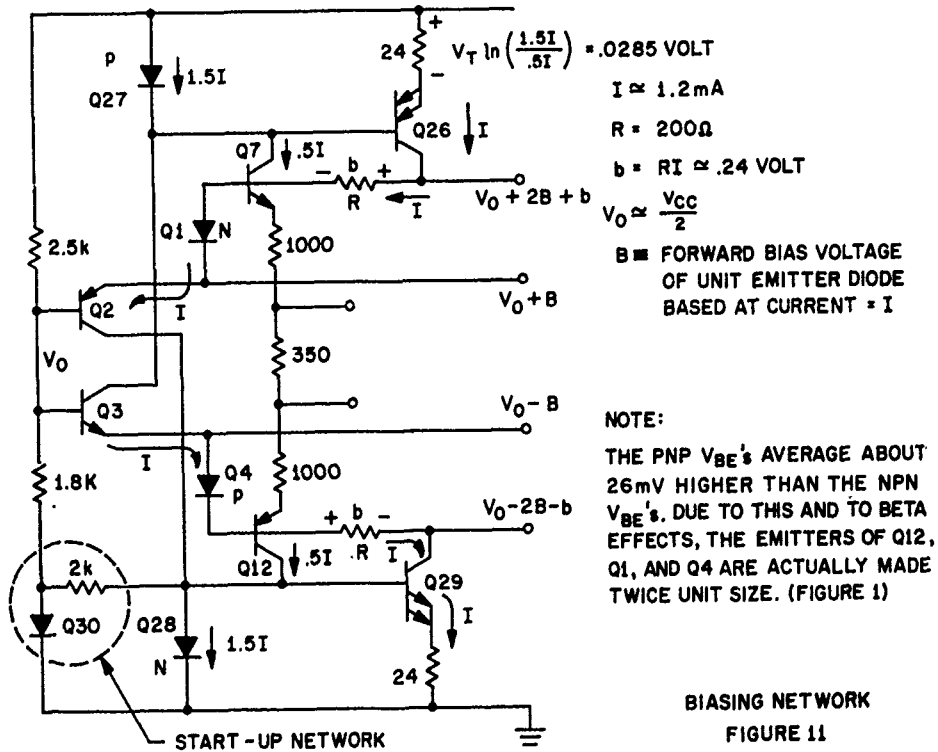


FIGURE 9

ANALYSIS OF VOLTAGE LIMITING OF Q14

**FIGURE 10**

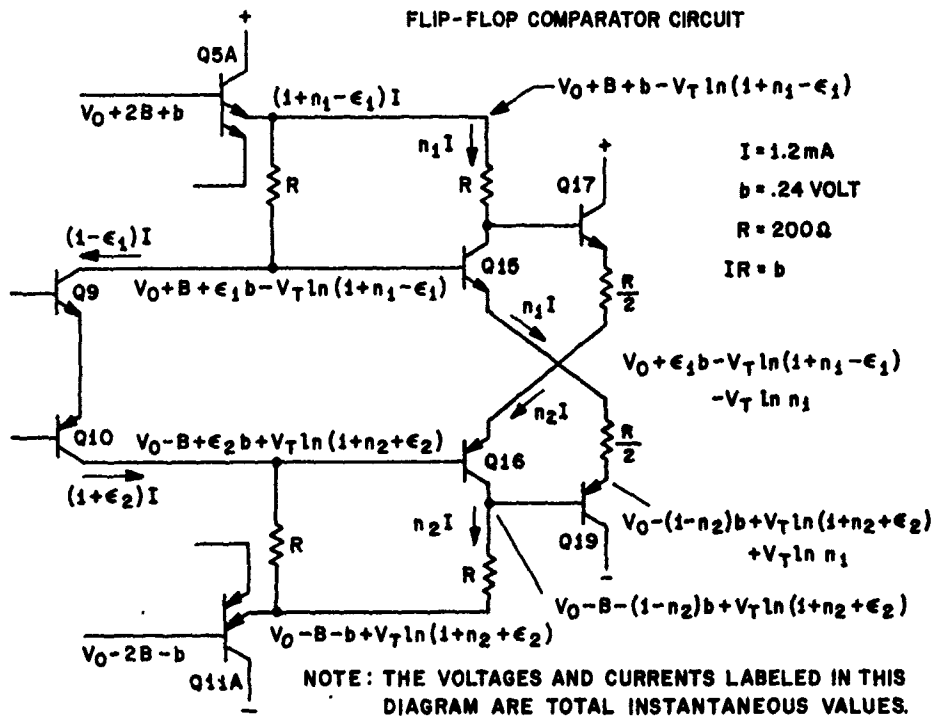


FIGURE 12

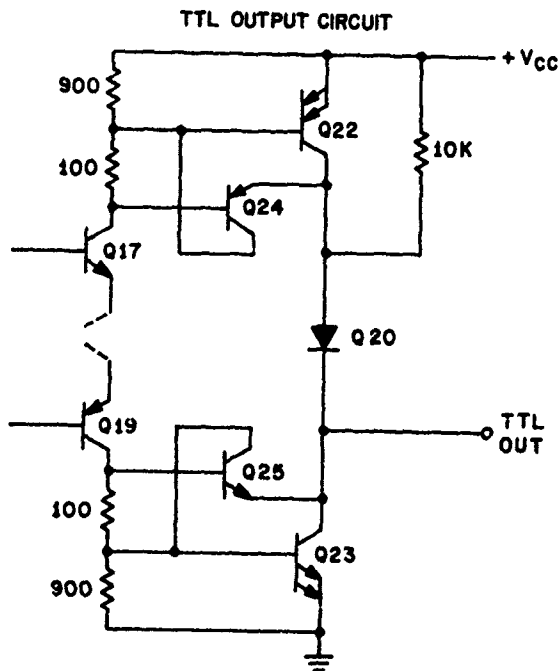


FIGURE 13

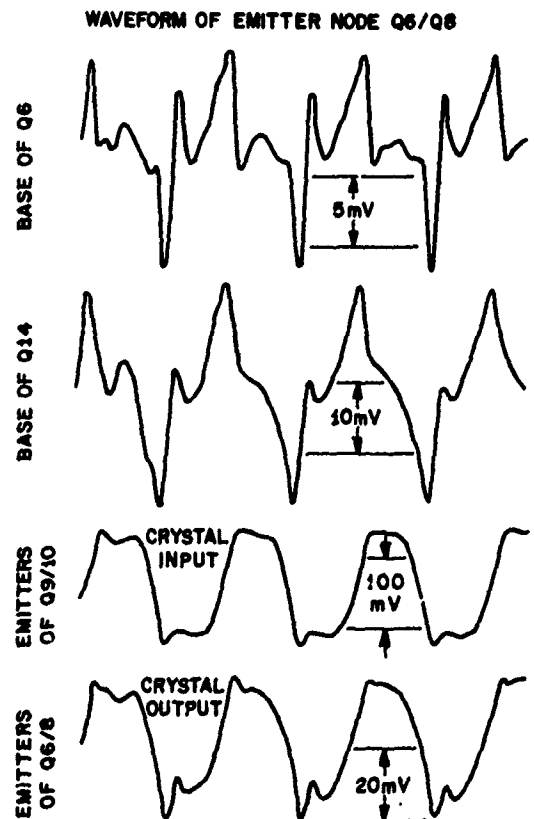


FIGURE 14

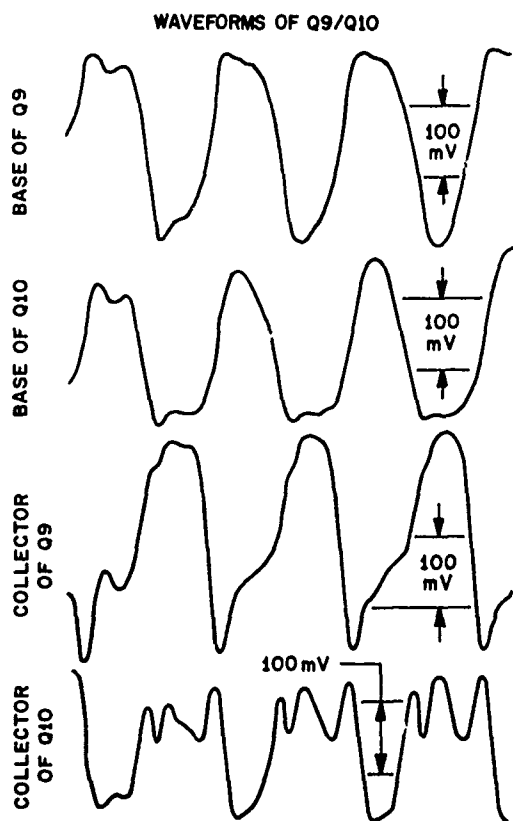


FIGURE 15

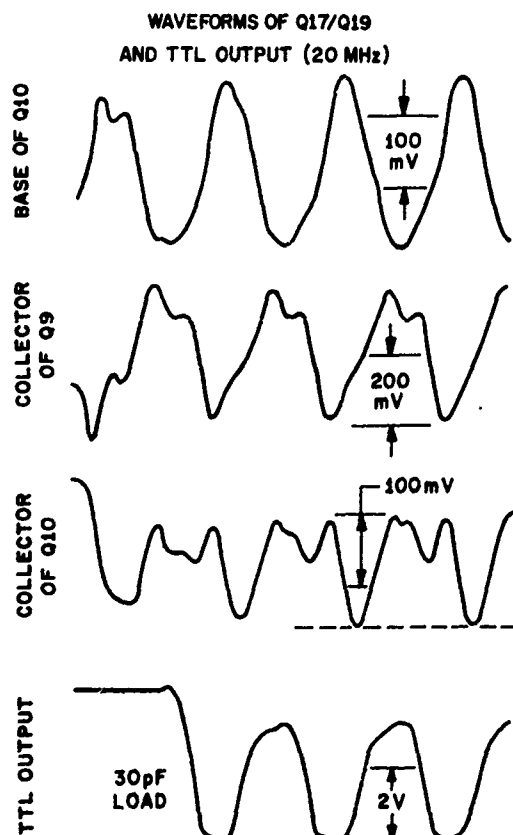


FIGURE 17

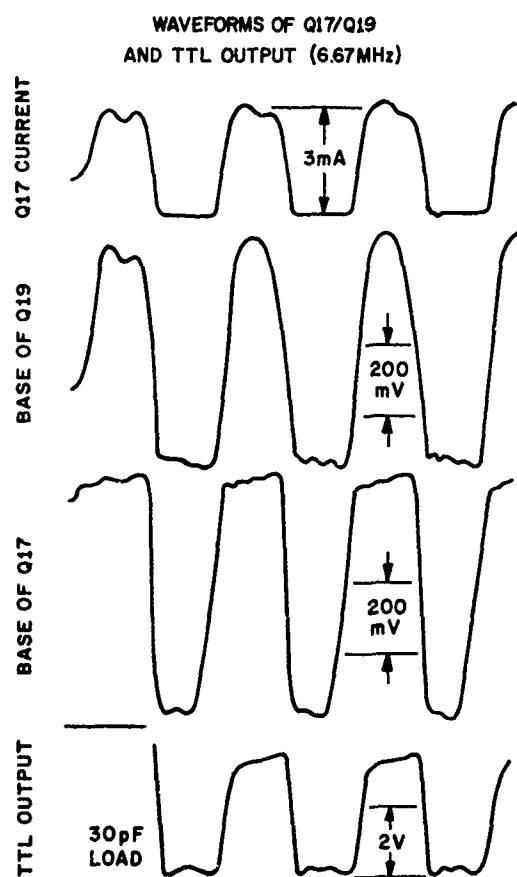


FIGURE 16

TEMPERATURE DEPENDENCE OF MEDIAN FREQUENCY SHIFTS
EXTRAPOLATED TO 20 YEARS

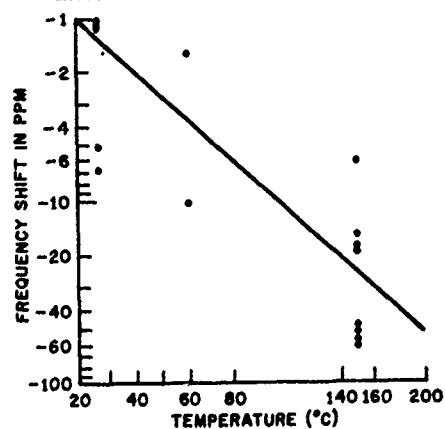


FIGURE 18

DIRECT-TEMPERATURE COMPENSATED CRYSTAL OSCILLATOR
FOR ADVANCED VHF/UHF RADIO COMMUNICATION SYSTEMS

S. Okano, T. Mitsuoka and T. Ohshima

Toyo Communication Equipment Co., Ltd.

Summary

A compact TCXO having a volume of 2.5 cc, maximum power consumption of 15 mW, and frequency stability of ± 2 ppm from -30°C to $+60^{\circ}\text{C}$ has been developed by connecting a temperature compensation circuit directly to a crystal resonator to meet the recent demand for VHF and UHF narrow band FM mobile radio equipment.

The essential point in this compensation method is independent temperature compensation at the low temperature and high temperature portions. Our approach in the analysis and design of this compensation method, studies on the main electronic components, and the performance of the unit as an actual compact TCXO and a TC-VCXO with voltage control function are described.

Key words (for information retrieval)
Oscillator, Crystal, Temperature Compensated, Direct Compensation, Thermistor, Sensitivity, Negative Resistance, Voltage Controlled.

Introduction

The utilization of higher frequency bands and narrower communication channels is being planned, or has already been implemented, to meet the demand for more effective utilization of frequencies and expanded communications volume in recent VHF and UHF band radio communication systems. The frequency stability of these advanced radio communications systems must be 50 % better than present frequency stability (± 5 ppm). This frequency stability is higher than the theoretical frequency temperature characteristic of a crystal, and the crystal oscillator must, therefore, have a function that compensates for the inherent frequency temperature characteristic of the crystal. The following temperature compensation methods have been studied and used for some time:

- 1) Compensation using the temperature characteristic of the reactance element of the oscillator circuit.
- 2) Compensation by adding a circuit consisting of a reactance element (L or C) and a temper-

ature sensing element to the oscillator circuit, and using the equivalent reactance temperature characteristics.^{1),2)}

- 3) Compensation by controlling a voltage controlled oscillator having a variable reactance element or circuit as the load capacitance by means of a temperature compensated voltage generator.³⁾

- 4) Compensation by digital processing for sophisticated temperature compensation.⁴⁾

These methods are classified as "direct type," in which the temperature compensation element or circuit is connected directly to the crystal oscillator loop such as methods 1) and 2), and "indirect type," in which the reactance of the oscillator circuit is controlled indirectly such as methods 3) and 4). High grade compensation is easily obtained with the indirect type, but it is complex. The direct type using method 2)

- a) does not provide a good grasp of the high frequency characteristic of the temperature sensing element.

- b) the equivalent resistance of the compensation circuit changes with temperature, resulting in a large change in the oscillation level.

Therefore, high compensation performance and good output characteristics are not obtained and it is not used industrially to any appreciable extent.

However, this method effectively meets the demands for compact size, low power consumption, and low cost and is well suited for use in advanced radio communication equipment. Such an idea has already been put forward by S. Boor, W. Horton, and R. Angove²⁾ as a compensation circuit consisting of a thermistor and capacitor connected in parallel. We developed this further, and applied it not only to temperature compensation in the low temperature portion, but also to temperature compensation in the high temperature portion. From the industrial standpoint, our design permits adjustment of the temperature compensation amount by adjusting the resistance value of the compensation circuit. Theoretical considerations were added to this temperature compensation circuit, independent temperature compensation of the low portion and high portion was refined, and newly developed miniature thermistors and electronic chip parts were used. A compact TCXO unit having a volume of 2.5 cc and a power consumption of 15 mW was built and

a ± 2 ppm frequency temperature characteristic over the -30°C to $+60^{\circ}\text{C}$ ambient temperature range was obtained. This TCXO may also be used as a high-frequency-stability crystal modulator by adding a voltage control function. Our approach to theoretical temperature compensation analysis and design in the development of this TCXO is described and the characteristics of the actual TCXO are introduced.

Compensation Principles

The simplest artificial temperature-sensitive reactance circuit network using a thermistor is the parallel circuit of thermistor and capacitor. The equivalent series capacitance and equivalent series resistance when this circuit is converted to a series circuit are represented by the following equation. The curves are plotted in Fig. 1.

$$\left. \begin{aligned} \frac{C_s}{C_p} &= 1 + \left(\frac{1}{Qx} \right)^2 \\ \frac{R_s}{R_{po}} &= \frac{x}{1 + (Qx)^2} \end{aligned} \right\} \quad (1)$$

Where, $X = R_p/R_{po}$ and $Q = X_{so}/R_{so} R_{po}$, R_{so} and X_{so} are the values of R_p , R_s , and X_s at the reference temperature. The horizontal axis of Fig. 1 is a logarithmic scale of the resistance value of the thermistor normalized by the value at the reference temperature, with the direction reversed. Therefore, the horizontal axis corresponds to the plus temperature direction. If the reference temperature is 25°C and B constant of the thermistor is 3000°K , $x=10$ corresponds to -30.4°C , $x=0.1$ corresponds to $+113^{\circ}\text{C}$. The Q of the circuit at the reference temperature is the parameter in this figure.

From the industrial standpoint, a compensation circuit should have function independently at the low temperature portion and high temperature portion. That is, the low temperature compensation circuit should not affect the normal temperature and high temperature portions, and the high temperature compensation circuit should not affect the normal temperature and low temperature portions. Introducing such a partial compensation concept,

- 1) prevents the temperature compensation amount from becoming too large and maintains stability against environmental changes,
- 2) permits "independent-temperature compensated design" at the required high temperature portion and low temperature portion and simplifies temperature characteristic adjustment.

When this circuit parameter $Q = 0.1$ (referring to Fig. 1), since the series capacitance at the normal temperature or high temperature portions can be made sufficiently large and the series capacitance can be abruptly lowered as the temperature drops, a compensation circuit that raises the frequency when the temperature drops at the low temperature portion can be built by connecting a

capacitor in series with this circuit. On the other hand, when $Q=10$, a compensation circuit that lowers the frequency when the temperature rises at the high temperature portion can be built. Temperature compensation of an AT-cut crystal having a zero or plus frequency temperature coefficient at room temperature is possible by connecting these two compensation circuits in series.

TEMPERATURE COMPENSATION CIRCUIT DESIGN

1. Two-point compensation

The simplest compensation circuit design is two-point compensation. The B constant of the thermistor in the compensation circuit shown in Fig. 2 is predetermined, because the B constant of actual thermistors is well matched and matching to within $\pm 1\%$ is not very difficult. Therefore, when the two temperature points are decided, x corresponding to these points is determined. These are made x_1 and x_2 . If the equivalent capacitances at which the frequency deviation at these two points becomes zero are made C_{s1} and C_{s2} ,

$$\left. \begin{aligned} C_{s1} &= C_p \left(1 + \frac{1}{Q^2 x_1^2} \right) \\ C_{s2} &= C_p \left(1 + \frac{1}{Q^2 x_2^2} \right) \end{aligned} \right\} \quad (2)$$

Solving these simultaneous equations,

$$\left. \begin{aligned} Q &= \sqrt{\frac{C_{s1}/x_2^2 - C_{s2}/x_1^2}{C_{s2} - C_{s1}}} \\ C_p &= \frac{x_1^2 C_{s1} - x_2^2 C_{s2}}{x_1^2 - x_2^2} \end{aligned} \right\} \quad (3)$$

Therefore, circuit constants R_{po} and C_p are found from Eq. (3)

The good compensation characteristics obtained even with simple two-point compensation is shown below by using the results of computer simulation. Koga and Aruga's elastic constants⁵⁾ were used as the frequency-temperature characteristics of a crystal in this simulation. Of course, a better compensation characteristics is obtained by making the primary coefficient large, by selecting an angle of cut to the minus side from this critical angle, but since the compression rate is large, it is undesirable. Fig. 2 is an example of low temperature portion compensation and two compensation points are 25°C and -30°C . The resonator is the fundamental frequency and the specified load capacitance is 20 pF and the B constant of the thermistor is 3000°K . In this figure, when $Q = 0.09$, C_s changes slightly near 20 pF and compensation characteristics is obtained from -40°C with about 1.4 ppm ripple. The affect of this compensation circuit on the high temperature portion is

an extremely small -0.4 ppm at $+70^\circ\text{C}$. Fig. 3 is an example of high temperature portion compensation and, shows the reduction of Q value by adding series capacitor C_s . The two compensation points are 25°C and 70°C . When $C_s = \infty$, the best compensation characteristics is obtained and the ripple is held to about 1.4 ppm up to $+73^\circ\text{C}$. The affect on the low temperature portion is an extremely low $+0.5$ PPM at -30°C . Therefore, a compensation circuit network that is effective over the entire temperature range can be built by substituting this circuit network for C_s of Fig. 2. However, since the Q is high at $C_s = \infty$, R_{po} rises and the reactance component of the thermistor cannot be ignored. Lowering Q permits use of a low resistance thermistor, but since the compensation effect deteriorates somewhat, the Q should be selected according to the frequency-temperature stability. Fig. 4 is an example of the overall compensation characteristic when two compensation circuit networks are combined. In this case, the Q of the high temperature compensation circuit was selected at about 10 and the Q of the low temperature compensation circuit was selected at about 0.09, considering the mutual affects of the two circuits. In this example, the ripple is about 2 PPM from -40°C to $+70^\circ\text{C}$ and an adequate temperature compensation characteristics is obtained. Of course, it goes without saying that better compensation can be obtained by making the temperature range narrower.

2. Actual compensation circuit

When the manufacture of this direct-temperature compensated crystal oscillator, if the frequency-temperature stability to be obtained is a comparatively simple compensation of ± 3 to 5 PPM, selecting one of several compensation circuit networks based on the frequency-temperature characteristics data of the crystal and combining it with the pertinent crystal is suitable. Of course, adjusting the frequency deviation by adjusting the resistance of the thermistor at the required temperature (for example, -30°C or 70°C) is also extremely effective in increasing compensation performance, but in this case, the reliability and stability of the thermistor is not adequately confirmed. On the other hand, adjusting the resistance by (1) trimming a fixed resistor, (2) adjusting a variable resistance, or (3) changing fixed resistors is simple and stability and reliability are very good.

We used a method that adjusts the compensation characteristic by adding a trimming resistor to basic compensation circuit for this reason. Fig. 5 gives the circuit diagram and the parameters needed for calculation. (a) is for low temperature use and (b) is for high temperature use. R_1 is the thermistor and R_2 is the trimming resistor. The resistance value of the thermistor normalized by the resistance value at the reference temperature is made a and the resistance value of the trimming resistor is made b. Fig. 6 and Fig. 7 show the adjusting effect obtained by varying b, using two-point compensation simulation. Inserting a fixed resistor of about $b = 10$ at the low temperature circuit and a fixed resistor of about $b = 0.1$ is at

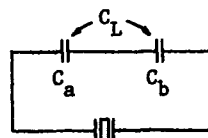
the high temperature circuit, the compensation characteristics is suppressed and increased the ripple, but these were within a range at which our target frequency temperature characteristic was easily obtained. If b is varied 8 - 12 at the low temperature side and 0.05 - 0.2 at the high temperature side, a change of ± 3 PPM or greater can be obtained at -30°C and $+70^\circ\text{C}$.

3. Sensitivity

The sensitivity of the component parts was grasped by computer simulation. The effect of thermistor resistance is very important and is described here by calculating the element sensitivity of the thermistor. As is well known, the sensitivity versus oscillation frequency f_L of load capacitance C_L is.

$$S_{C_L}^{f_L} = \frac{-CoC_L}{2\sqrt{(C_o+C_L)^2}} = -C_L \cdot S \quad (4)$$

Where, S is the trim sensitivity according to the Sherman definition.⁶⁾ Redrawing the equivalent reactance circuit,



Where C_a Equivalent series capacitance of compensation circuit network.

C_b Equivalent series capacitance of frequency adjustment or tuning circuit. The sensitivity of f_L with respect to C_a is obtained.

$$S_{C_a}^{f_L} = \frac{f_L}{S_{C_L}^{f_L}} \cdot S_{C_L}^{f_L} = \frac{-C_o C_a C_b^2}{2\sqrt{(C_o C_a + C_o C_b + C_a C_b)^2}} \quad (5)$$

The sensitivity of the compensation circuit is,

$$S_x^a = - \frac{2}{1+Q^2 x^2} \quad (6)$$

Moreover, the relationship between x and a is,

$$\left. \begin{aligned} S_a^x &= \frac{b}{a+b} \quad (\text{for low temperature}) \\ S_a^x &= \frac{a}{a+b} \quad (\text{for high temperature}) \end{aligned} \right\} (7)$$

These equations are used to find the element sensitivity of the thermistor.

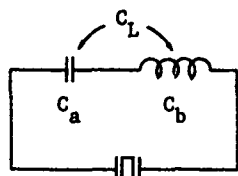
The sensitivity of the low temperature compensation circuit when b shown in Fig. 2 is maximum is calculated as an example.

$C_p = 98$ pF, $Q = 0.09$, C_a (25°C) = 12,141 pF, C_a (-30°C , $x = 9.76$) = 224 pF, $C_b = 20$ pF, $C_o = 3$ pF, and $\sqrt{f} = 225$. Substituting these in the fol-

lowing.

$$\begin{aligned} \frac{f_L}{S_x} &= \frac{f_L}{S_{C_a}} \cdot \frac{C_a}{S_x} = \frac{C_o C_a C_b^2}{\gamma (C_o C_a + C_o C_b + C_a C_b)^2 (1 + Q^2 x^2)} \\ &= 8.3 \times 10^{-7} \text{ (at } 25^\circ\text{C)} \\ &= 2.47 \times 10^{-5} \text{ (at } -30^\circ\text{C)} \end{aligned} \quad (8)$$

This shown that the element sensitivity of the thermistor is extremely low at 25°C and the frequency change for a 1% thermistor resistance change is less than 2.5×10^{-7} even at -30°C . However, the crystal is usually oscillated at the series resonant frequency by inserting a coil in series at the 3rd overtone mode. Therefore, the equivalent reactance circuit is represented as shown below.



$$\text{where, } C_b = -1/\omega^2 L$$

Thus, Eq. (5) can be applied unaltered. Since $C_a = C_b = 0$ at the series resonant frequency,

$$\frac{f_L(S)}{S_{C_a}} = \frac{-C_o}{2\gamma C_a} = \frac{-C_1}{2C_a} \quad (9)$$

The element sensitivity ratio when there is no coil is shown by,

$$\frac{f_L(s)}{S_{C_a}} / \frac{f_L(C_L=C_a)}{S_{C_a}} = 1 + \left(\frac{C_o}{C_a}\right)^2 \quad (10)$$

If C_a and C_o are reduced by the same amount, the element sensitivity increases by a factor of four.

Oscillation circuit design

The conditions required of a direct-temperature compensated oscillator circuit are a negative resistance large enough to cover the compensation circuit network loss and a stable output level against variation in this loss. The equivalent circuit of the Colpitts oscillator that we used is shown in Fig. 8. Here, R is the bias resistance and other equivalent input parallel resistances. The common-collector transistor circuit is represented by a follower. R_F represents the stabilizing resistor and transistor emitter resistor. The plotted imaginary part and real part are also shown in this figure. As can be seen from these curves, the circuit oscillates at a frequency $x = 1$ or greater, where the negative resistance appears. In actual oscillation circuit design, a prototype circuit designed on this consideration is built,

the negative resistance is measured, and the frequency range covered and the constants of the corresponding parts are decided.

To maintain a high negative resistance, the output should not be taken from the emitter. The affect on the negative resistance when a load resistance was connected to the emitter, was analyzed by using the model shown in Fig. 9. The load resistance was made R_L . Since a stabilized resistor is not generally used in this type of oscillator; R_F represents the transistor emitter resistance. In this case, the equation of the real part of the input impedance becomes complex and is shown by.

$$\begin{aligned} \frac{\text{Re}(Z_{in})}{R} &= \left\{ \frac{R_s}{R_L} \left(\frac{R_s}{R_L} - x^2 \right) + \frac{x^2}{Q^2} \frac{R}{R_L} \left(\frac{C_1}{C_P} + \frac{R_L}{R} \right) \right\} / \Delta \\ \text{where,} \quad \Delta &= \left(\frac{R_s}{R_L} - x^2 \right)^2 + x^2 \frac{1}{Q^2} \frac{R^2}{R_L^2} \left(\frac{C_1}{C_P} + \frac{R_L}{R} \right)^2 \\ R_s &= R_F + R_L, \quad C_P = C_1 + C_2 \end{aligned} \quad (11)$$

definition of Q and x are same to in Fig. 8.

The above equation when R_L/R is made a, $C_1 = C_2 = C$ and $Q = 5$ is plotted in Fig. 9. As can be seen from these curves, R_L contributes substantially to the negative resistance, and reducing parameter a has the same effect as if Q were reduced. $a = 1$ is equivalent to reducing Q to 4, and $a = 0.5$ is equivalent to reducing Q to 3. This problem can be solved by taking the output from the collector. The Colpitts oscillator collector current equation has already been given in another reference⁷⁾. according to this equation, as the oscillation level increases, the flow angle decreases and the peak value increases. But since the fundamental frequency component becomes constant when the O-P value of the sine wave voltage between the base-emitter becomes large enough, stable output level can be obtained by obtaining a sine wave through a tank circuit etc.

We stressed obtaining a constant peak value even with a resistance load by selecting the proper transistor. That is, a comparatively small signal transistor was selected and the h_{FE} saturation characteristic was used. Fig. 10 shows the output voltage change versus the loss when a switching transistor and a high frequency small signal transistor were used. This data was obtained by inserting a series resistance into the oscillation loop of a practical oscillator using a single transistor and measuring the output level change with a peak detection type level meter. The harmonic frequency component observed with a spectrum analyzer is also shown. As can be seen from this figure, the change in the output level of a small signal transistor for a change of 0 - 100 ohms was held to a peak value of about 2 dB. The change in the fundamental frequency component was also an excellent 1 dB or less. Fig. 11 shows the temperature dependence of the

output level (peak value) of a practical oscillator. The emitter level change is also shown for comparison purposes. The level change suppression effect is clearly shown in this figure.

Study of main components

Fig. 12 shows exterior views and interior views of actual direct-temperature compensated crystal oscillators. The resistors, capacitors, transistors, and other electronic parts are on chips. Since these chips are abundantly available and their reliability and mounting technology have been firmly established, small size and low price are possible. The use of these miniature parts and adoption of the direct-temperature compensation method makes possible a 1/3 - 1/4 reduction in volume compared to conventional discrete components. The crystal is a Type UM-1 miniature crystal used in the fundamental mode at 10 - 30 MHz and in the 3rd overtone mode above 30 MHz. The package is metal and is sealed by resistance welding to obtain an aging characteristics of ± 1 PPM or less/year. The AT-cut crystal frequency characteristic was designed the zero or plus temperature coefficient at room temperature, considering the shift of the oscillation circuit temperature characteristic and the frequency temperature characteristics caused by insertion of the load capacitance as shown at "a" in Fig. 13. When the frequency stability is comparatively loose, an angle of cut slightly to the bottom right from the zero temperature coefficient was designed and the high temperature side temperature compensation was omitted as shown by "b" of Fig. 13. Since variations in the inter-electrode capacitance and capacitance ratio affect the compensation characteristic, the crystal must be specified with care.

Since the thermistor determines the compensation performance, its electrical characteristics are extremely important. As is generally known, the characteristics of a thermistor are for DC and the characteristics at high frequencies are unclear. Accurate measurement of the high frequency characteristics, especially the temperature dependence, of a thermistor is difficult, but according to our studies, (1) a thermistor can be considered to be a resistor and capacitor parallel circuit at a certain frequency range, (2) the electrostatic capacitance is proportional to the electrode area and changes very little with temperature, and (3) as the resistance value and operating frequency increases the parallel resistance component tends to decrease. Fig. 14 shows the electrical characteristics of the 30 Ω chip thermistor that we used. The characteristics are stable with respect to both temperature and frequency. The results of 85°C accelerated aging of a low resistance thermistor are shown in Fig. 15. The resistance value change about +5 % in 100 days. The amount of change is proportional to the logarithm of time and post-shipment changes can be suppressed to a negligible value by baking. Fig. 16 shows the change in the frequency temperature characteristic before and after aging of an oscillator biased for approximately 1 year without baking. As can be seen from this figure, both

frequency-temperature characteristics show good agreement. From the result of element sensitivity calculation, the thermistor aging change in this case is assumed to be 1 % or less.

Actual data

Fig. 17 shows the typical temperature characteristics of an oscillator unit at which only the low temperature portion is compensated. A good temperature compensation effect is obtained at both the fundamental and 3rd overtone. The change in the output level is within ± 1 dB. Fig. 18 shows the distribution of the frequency temperature characteristics of a 3rd overtone oscillator unit at which only the low temperature portion is compensated. Fig. 19 shows the distribution of a fundamental mode oscillator unit at which the high temperature portion is also compensated. In both cases, compensation circuit networks corresponding to the temperature characteristic of the crystal were selected and used. A better characteristic was obtained by adjusting the resistance of the compensation circuit network. Fig. 20 shows the frequency aging at an ambient temperature of 25°C. The output frequency long-term stability depends on the long-term stability of the crystal and the aging change of the thermistor has virtually no affect.

Frequency modulation function

A frequency modulation function is often demanded of the oscillator used in an FM radio equipment transmitter. In this case, a VCXO (Voltage Controlled Crystal Oscillator) is employed. Since a VCXO can be given a good frequency modulation function from DC, it is applicable as a modulator for tone control signals and digital signals, as well as voice signals. Impressing the modulation input voltage on the varactor of an indirect-temperature compensation circuit is disadvantageous because the temperature compensation action changes the operating point of the varactor diode, resulting in a change in the modulation sensitivity and a worsening of the modulation distortion. Generally, the modulation distortion of a VCXO depends more on the operating point of the varactor diode than the operating point of the load capacitance of the crystal resonator. Separating the modulation function and temperature compensation function is convenient from both the standpoint of design and adjustment. When these two functions are separated, the use of a direct-temperature compensation circuit that uses few parts is advantageous. Fig. 21 shows the various characteristics of the VCXO as a frequency modulator. These characteristics adequately meet the demands of radio equipment. The C/N characteristic, in particular, is identical to that of a conventional crystal oscillator as shown in Fig. 22.

Conclusions

The compensation ability of a direct-temperature compensation system was shown by simulation. The two-point compensation design method and an effective trimming resistance were introduced. Element sensitivity was used to show the

affect of aging of the thermistor, the main element. It was also shown that there are no problems in actual measurement. The necessary equations to calculate the negative resistance margin for compensation circuit network loss were introduced. The technique to obtain an output level stable against changes in this loss was also shown. The direct-temperature compensation TCXO is a compact, low cost unit that fills the gap between PXO (Packaged Crystal Oscillator) and conventional indirect-temperature compensation TCXO. This type of oscillator is applicable to 150 or 400 MHz band modifiable radio communications 12.5 kHz spacing systems and 800 MHz band mobile radio communications 25 kHz spacing systems and further developments are expected.

References

- 1) Koerner, L.F., "Methods of Reducing Frequency Variations in Crystals Over a Wide Temperature Range," IRE Nat. Conv. Rec., Vol.4, Part 8, 1956, pp48-54.
- 2) S.B.Boor, W.H.Horton and R.B.Angove, "Passive Temperature Compensation of Quartz Crystal for Oscillator Applications," Proc. 19th AFCS, 1965, pp105-124
- 3) G.R.Hykes and D.E.Newell, "A Temperature - Compensated Frequency Standard," Proc. 15th AFCS, 1961, pp297-317
- 4) M.Onoe, I.Imagishi and H.Jariai, "Temperature Compensation of Crystal Oscillator by Microprocessor," Proc. 32nd AFCS, 1978, pp398-402
- 5) M.Aruga, "Adiabatic Elastic Constants of Quartz Crystal and their Temperature Dependence," Bulletin of the Tokyo Institute of Technology, Ser. A, Nov. 2, 1956
- 6) J.H.Sherman, "Trim Sensitivity, A Useful Characterization of a Resonator," Proc. 33rd AFCS, 1979, pp181-185
- 7) M.E.Frerking, "Crystal Oscillator Design and Temperature Compensation," Van Nostrand Reinhold, 1978, p202

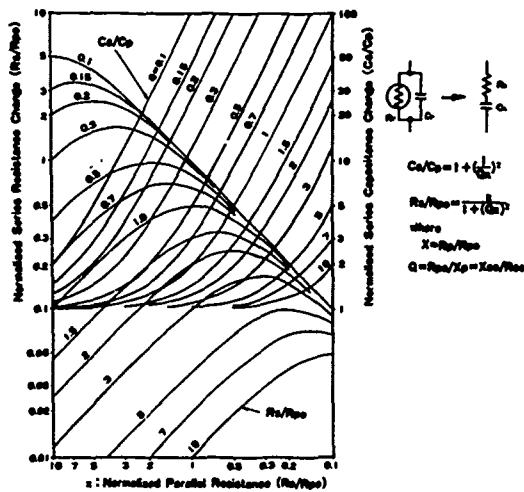


Fig.1 Parallel-Series Conversion

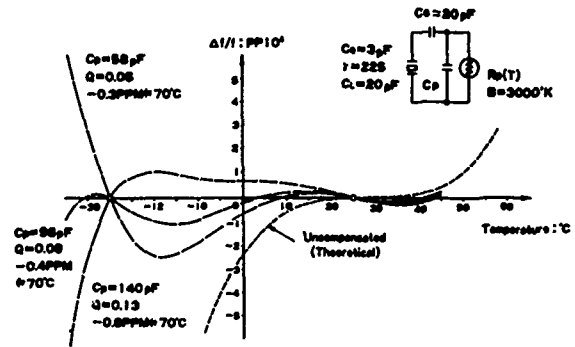


Fig.2 Basic Two-Point Compensation (Low Temperature Portion)

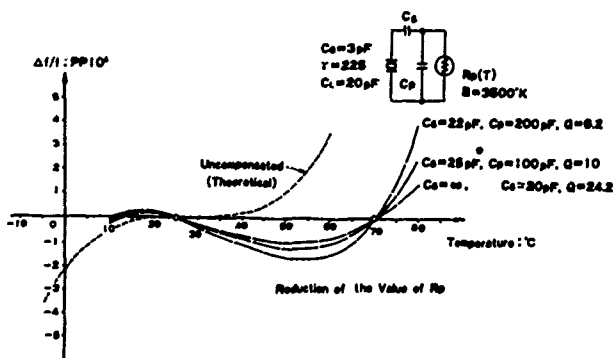


Fig.3 Basic Two-Point Compensation (High Temperature Portion)

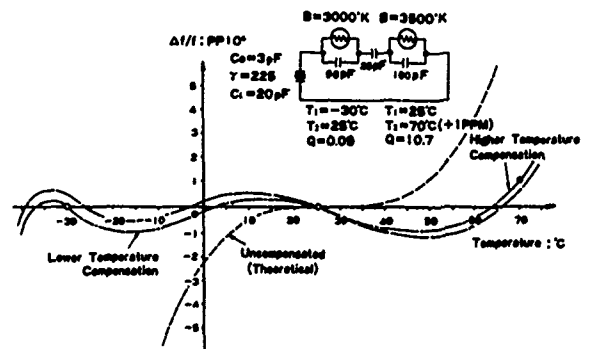


Fig.4 Combination of Low and High Temperature Compensation

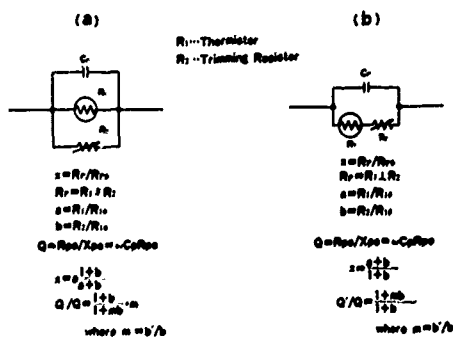


Fig.5

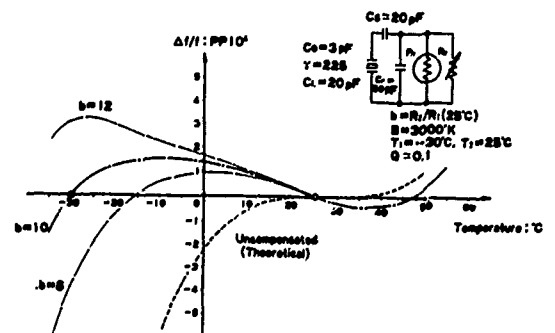


Fig.6 Simulation of Two-Point Compensation With Trimming Resistor (Low Temperature Portion)



Fig.12 Photograph of Actual Direct-TCXO s

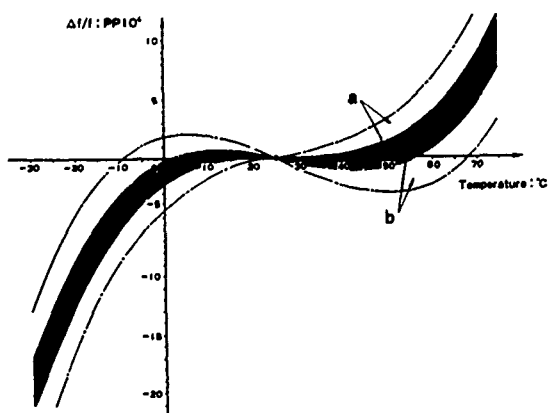


Fig.13 Required Frequency-Temperature Characteristics

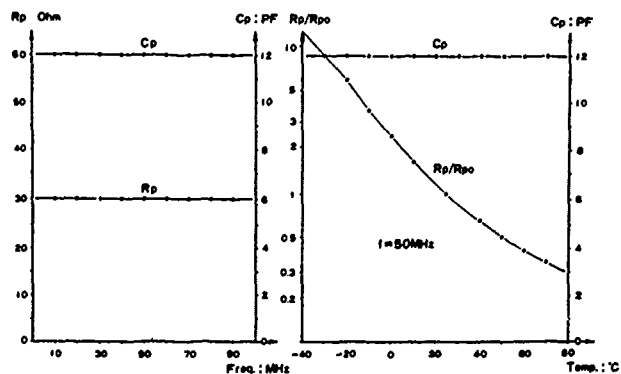


Fig.14 Electrical Characteristics of 30-Ohm Thermistor at High Frequency

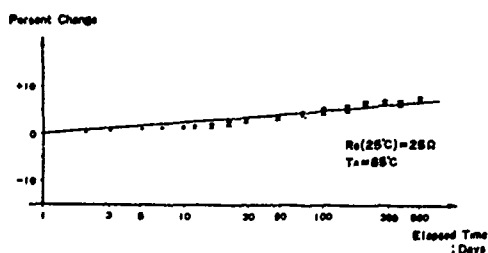


Fig.15 Accelerated Test of Thermistor Stability

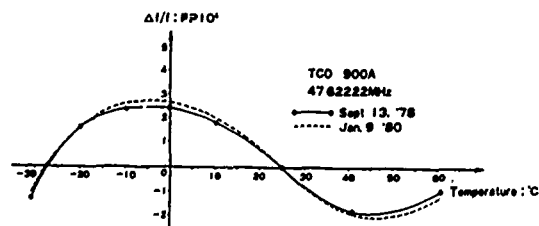
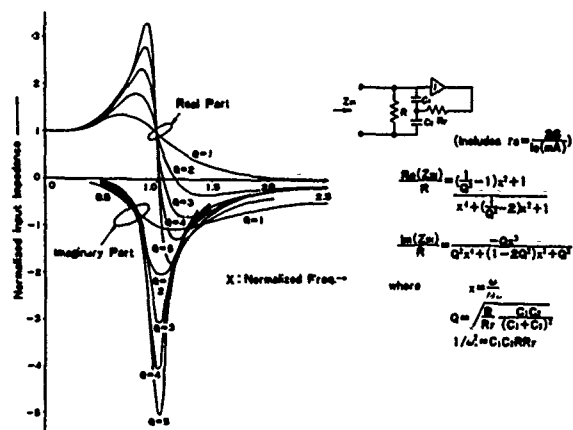
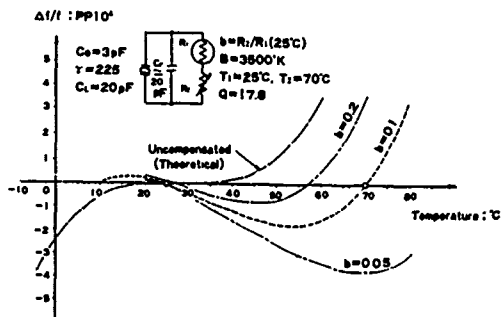


Fig.16 F-T Characteristics, Before and After Aging



**Fig.7 Simulation of Two-Point Compensation With Trimming Resistor
(High Temperature Portion)**

Fig.8 Input Impedance of Negative Resistance Generator

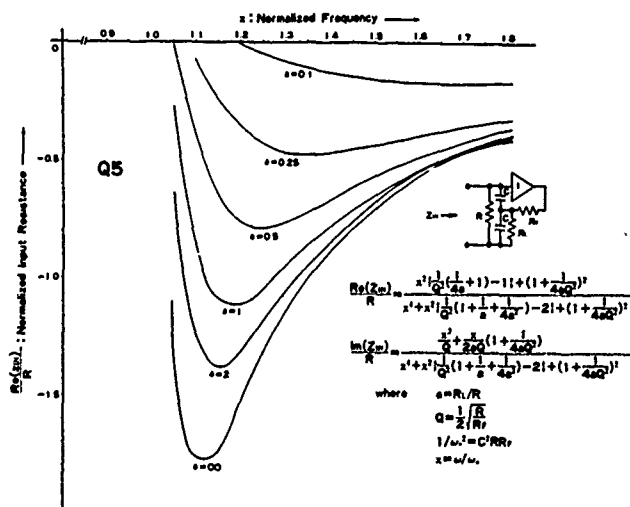


Fig.9 Negative Resistance Change vs. Emitter Load

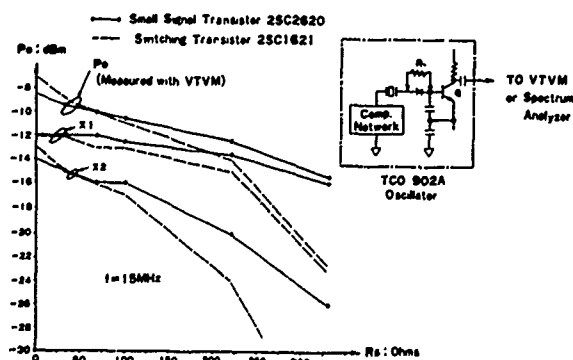


Fig.10 Output Voltage Change vs. Loss

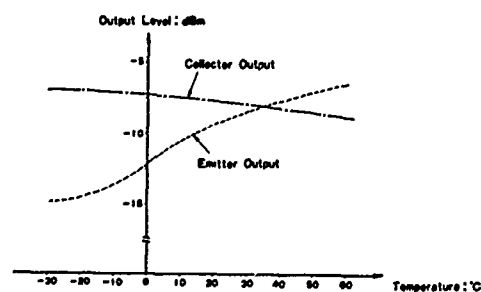


Fig.11 Temperature Dependence of Output Level in Practical Oscillator

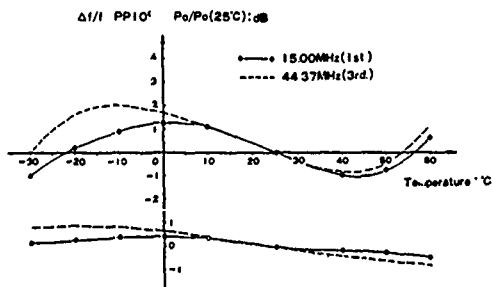


Fig.17 Typical Characteristics of Practical Oscillator

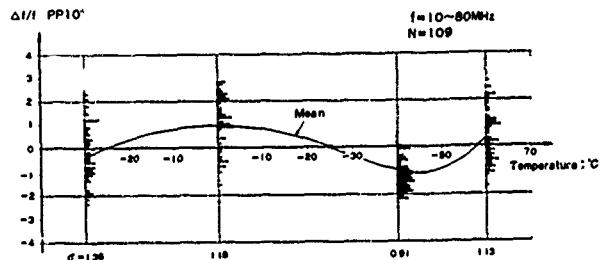


Fig.18 F/T Distributions, Low-Temperature Compensated

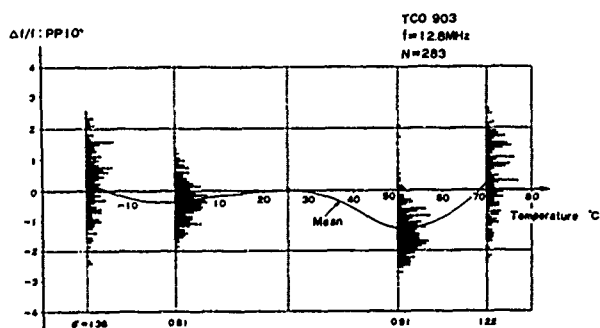


Fig.19 F/T Distributions, Both Low and High Temperature Compensated

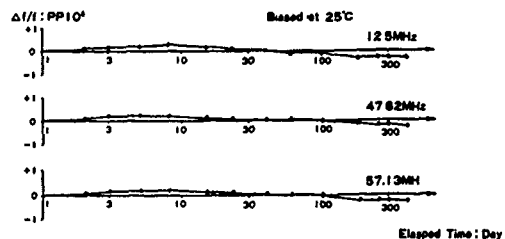


Fig.20 Typical Aging Data

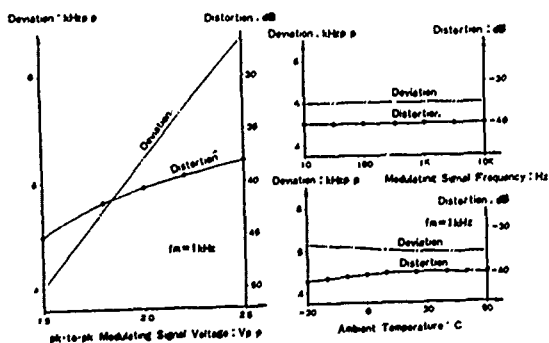


Fig.21 Frequency Modulation Characteristics
(Measured After X6 Frequency Multiplication.)

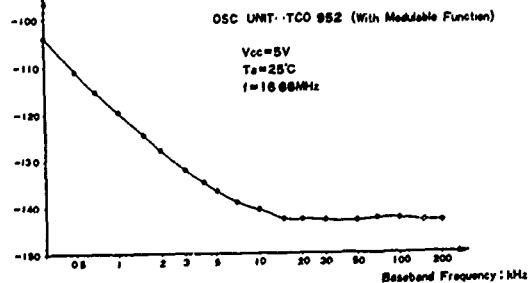


Fig.22 Typical Short Term Stability of TC-VCXO

INTEGRATED CIRCUIT COMPENSATION OF A.T. CUT
CRYSTAL OSCILLATORS

T. Keller, D. Marvin, and R. Steele

Motorola Communications Group
Franklin Park, Illinois

Summary

This paper discusses several important aspects of a new temperature compensation scheme that utilizes a custom designed linear integrated circuit to provide a piecewise nonlinear compensated AT cut TCXO for use in volume production. The IC is designed to provide temperature performance to ± 2 ppm from -40°C to $+95^{\circ}\text{C}$. The principle market for this TCXO is in mobile and portable two-way communication systems with available supply voltages as low as 4.5VDC and permissible compensation current drains of less than 1mA.

This heart of the compensation circuit is a bipolar IC consisting of an internal voltage regulator, a linear response voltage versus temperature detector, three individually controlled differential amplifiers for cold, linear and hot temperature ranges and current summing amplifiers. External to the IC are resistors that are adjusted to individually tailor the response of each circuit.

Included in this paper is a description of the compensation circuit, a discussion of temperature compensation techniques and typical performance characteristics.

Introduction

The design of portable two-way communications equipment, as shown in Figure 1, has created a unique set of oscillator requirements not collectively found in other products. These requirements include:

1. Temperature stability specifications meeting the need of the marketplace and FCC regulations. Minimally this is ± 5 ppm from -30°C to $+70^{\circ}\text{C}$. For 800MHz radios performance to ± 2 ppm is required. Certain mobile applications require performance to ± 2 ppm from -40°C to $+95^{\circ}\text{C}$.

2. The oscillators must be capable of direct frequency modulation (DFM) to handle a wide variety of digital as well as audio transmissions. Modulation must remain within 5% of the room reference modulation level while maintaining a

a distortion of less than 4% as the TCXO is tested over the temperature range.

3. The package size must be as small as possible, as the marketplace demands the lightest, smallest radio possible for user convenience.

4. Current drain for the oscillator in portable applications must be as low as possible in order to maximize battery lifetime. Typically the oscillator draws 15% to 35% of the entire standby current. Sideband noise performance of better than -155dB/Hz must be maintained at this low current level.

5. The oscillator should operate from a low voltage power supply to allow the battery to produce a maximum ampere-hour rating from a given volume.

6. The frequency output of the TCXO should be at as high a frequency as possible. This reduces the degradation of the signal to noise ratio caused by the multiplication that would otherwise be required. Other advantages of higher frequency operation are that the overall radio volume is reduced, the current drain is lowered by the reduction of the number of frequency multiplication stages and the reliability is improved. This is generally accomplished by selecting a harmonic of a third or fifth overtone oscillator.

These specifications, coupled with volume production, ease of manufacturing and low product cost requirements, were best met with the use of thick-film design techniques. Thick-film construction and stringent reliability requirements dictate that there be minimal parts change-out during the compensation procedure. Therefore, such existing techniques as thermistor-capacitor or thermistor-resistor-varactor compensation were not practical as parts change-out is required to meet temperature stability requirements. Theoretical approaches determining the proper selection of compensation components without iteration, such as Swanson and McVey¹, while being valuable for low volume precision TCXO's require highly characterized and consistent parts and repeatable third order performance. Such techniques are inconsistent with the cost goals of this product. Compensation schemes providing central compensation for several TCXO's in a radio meet many of the requirements, but fail to allow for unit to unit

nonlinearities. This can create a problem when compensating the oscillators to ± 2 ppm.

Digital compensation schemes, while providing superior performance for frequency versus temperature requirements of less than ± 1 ppm draw too much current and consume excessive space for an oscillator with the above requirements.

In order to meet the oscillator specifications, a series of compensation requirements was generated. These include:

1. Of all options studied, the combination of minimal size, low cost and high reliability would be best met by developing a custom integrated circuit compensation network with little interaction among the various temperature ranges. Changes could therefore be made in one range with minimal changes occurring in the other temperature ranges.

2. As the space available is quite limited the number of degrees of freedom available for oscillator compensation had to be minimized. Therefore, as much control as possible had to be built into the I.C.

3. In addition to compensating for the theoretical Bechmann equation, the circuit must allow for minor oscillator or crystal anomalies such as nonlinear temperature characteristics in the capacitors, coils and varactors or variations in crystal response induced by stress.

4. All adjustments must be made by laser trimming resistors and not by replacing parts. This will increase product reliability by having minimal rework performed on the oscillator.

5. All adjustments must leave the nominal varactor voltage unchanged. Distortion in modulated units will thus not be increased by operation at an undesired varactor bias point and no further parts adjustment would be necessary to return the oscillator to nominal frequency.

6. The crystal angle range to be compensated had to be maximized in order to reduce the cost of the crystals by reducing the crystal testing labor and reducing the amount of scrapped material. This requires that the compensation range be fairly large.

7. Current drain had to be kept as low as possible; less than 0.7mA nominal for a -30°C to 70°C temperature range and less than 1.2mA nominal for a -40°C to $+95^{\circ}\text{C}$ range.

8. Voltage requirements had to be as low as practical, allowing only enough voltage to swing the varactor to compensate a circuit of appropriate sensitivity.

Compensation Description

The technique selected to meet these criteria is illustrated in Figure 2. This IC contains

three separate current versus temperature generators, each operating in its own temperature range and generating a changing output current as a function of temperature. These currents are summed in the current summing amplifiers and converted to voltage to drive the varactor in the load resistors. One temperature sensor drives all three generators and all voltages are controlled by an integral voltage regulator.

For convenience, the three temperature ranges are referred to as cold, linear and hot. The linear range is the region between the two turnover temperatures, while the cold is the region below the lower turnover temperature and the hot is the region above the upper turnover temperature.

All three temperature range generators, as in Figure 3, work in a similar fashion. Each generator is a differential amplifier with emitter degeneration. One input is tied to a reference voltage established by a resistive voltage divider consisting of resistors with carefully controlled temperature coefficients of resistance connected to a voltage regulator. The other input is a voltage from the temperature sensing network. The first of these voltages remains essentially constant versus temperature, while the second changes at a constant rate of $-8\text{mV}/^{\circ}\text{C}$. The rate of change of the output current is adjusted by the value of the resistor in the current source.

Figure 4 illustrates the range of curves possible from the linear section with the ordinate showing the current injected by the differential amplifier into the current summing amplifier. The linear curve is essentially linear in the central portion while becoming third order at its extremes. The hot and cold sections operate in a similar fashion with typical outputs illustrated in Figures 5 and 6. When the output currents of the linear, cold and hot circuits are summed, a response such as that shown in Figure 7 is generated. As curves for higher angle crystals are generated, the turnover temperatures move out, just as they do in an AT cut crystal. This is achieved by the careful selection of the internal resistor values in the differential amplifiers.

While the circuit could have been constructed to provide an equivalent Bechmann² curve with one adjustment driving all three differential amplifiers, it was decided to use a three adjustment technique to allow added versatility. While a theoretical crystal follows Bechmann's curves, an entire oscillator can readily deviate from the theoretical. This technique permits the compensation to correct to some degree for both crystal and circuit anomalies. Thus, mounting strain induced crystal variations, variations in the IC build and linear and nonlinear variations in oscillator temperature performance can be corrected. The total adjustment range is large enough to accommodate the desired angle range. Figures 4, 5 and 6 show the change in circuit current possible for changes in the respective linear, cold and hot resistors.

In addition to the adjustments mentioned, two other adjustments are made. Variations from IC to IC, not to mention variations from crystal to crystal require an adjustment in the location of the inflection temperature in the compensation circuit. This is accomplished by adjusting R_1 in Figure 2. Secondly, different circuits such as fundamental, third overtone and fifth overtone, modulation requirements and stability requirements necessitate that the varactor be driven at different voltages and that different circuit sensitivities be established. Both of these functions are controlled by adjusting the load resistors R_{L1} and R_{L2} of Figure 2.

An internal voltage regulator is included to provide each oscillator with a predetermined voltage supply characteristic. As the unit is quite susceptible to voltage variations as a result of the varactor and the high sensitivity required by direct frequency modulation in the transmitter TCXO, it is mandatory to have a regulator within each oscillator. As the regulator is internal to the oscillator, the effect of its voltage versus temperature characteristic on frequency is removed during compensation. The regulator is designed so as to supply an output voltage with as little internal drop as necessary. This regulator will still work with as low as a 0.2VDC series drop. The temperature sensor is four diodes connected in series and run with a fixed current provided by the voltage regulator. Each diode has a linear temperature coefficient of $-2\text{mV}/^\circ\text{C}$ so that the total temperature slope is $-8\text{mV}/^\circ\text{C}$. Again the effects of nonlinearities are corrected during compensation.

Due to the circuit complexity of this design, an empirical approach utilizing basic differential amplifier techniques was used during the initial phases. This was then refined using an inhouse circuit analysis computer program. In addition to refining the design the program was also used for tolerance studies and worst case design analysis.

Compensation Techniques

The compensation circuit is laser trimmed in three distinct steps. In the first of these, the load resistors on the output of the current to voltage converter are trimmed to value with no circuitry other than the thick film resistors present. This trim is done along with all of the other resistors not requiring later adjustment. All of the parts including the I.C. are mounted next and the inflection point setting resistor is trimmed while room temperature is being monitored to provide proper setting. The oscillator is now in a state where all of the differential amplifier control resistors are undervalue so that they can later be adjusted upward to the value required. At this point the oscillator is ready to enter the automated data acquisition and laser resistor trimming system of Figure 8. The oscillator is cycled over the appropriate temperature range and frequency readings are made at predetermined temperatures to determine the slope of the oscillator compensation in the linear,

cold and hot ranges. The minicomputer controls the temperature chamber, the frequency counter and the network switching among the 48 oscillators being simultaneously tested. All of the frequency versus temperature data is stored on a disc for later retrieval. Upon completion of the temperature run the TCXO's are taken to the YAG laser resistor trimming system. At the laser station, the oscillator's sensitivity in ppm/volt and the initial value of the resistors in the differential amplifiers current sources are measured and this data is fed to the minicomputer. This data along with the recalled temperature data is processed in an algorithm and new resistor values are fed to the laser station. The laser then trims the resistor to the appropriate value and the oscillators are given a varification test.

Experimental Data

Such an integrated circuit has been designed and chips have been made. These chips have been mounted in commercial chip carriers for ease of handling and are attached to the substrate with normal solder reflow techniques. Several oscillator designs for various requirements have been built and tested. The oscillator in Figure 9 is designed to provide $\pm 2\text{ppm}$ performance from -40°C to $+95^\circ\text{C}$. Total current drain for the compensation circuit is less than 1.2mA and the circuit is able to utilize a crystal with an angle range of three minutes. Figure 10 shows initial crystal frequency versus temperature performance and total oscillator performance. This oscillator and several other models are now being produced using the system of Figure 8, in volume and are being used in several radio lines. Applications not requiring -40°C to $+95^\circ\text{C}$ performance are being built with a compensation current of less than 0.7mA.

Conclusions

A new temperature compensation scheme for AT cut bulk resonators has been reviewed. This scheme generates a piecewise non-linear approximation utilizing differential amplifier techniques and has been incorporated into an integrated circuit. By design the hot, cold and linear compensation regions can be made so that interactions are reduced to a minimal level, thus providing a simple compensation technique without having to replace any parts. It provides a low cost and reliable method of producing miniature TCXO's in volume. Oscillators are now being shipped that achieve $\pm 2\text{ppm}$ from -40°C to $+95^\circ\text{C}$ performance.

Acknowledgment

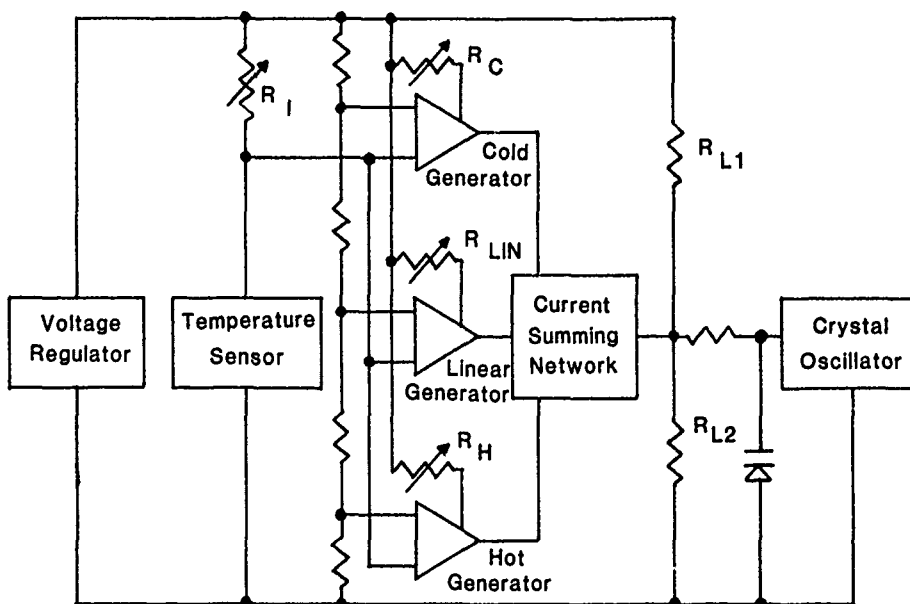
The authors wish to thank Al Kraybill of the Motorola technical staff whose help in the conception, design and analysis of the integrated circuit has been invaluable.

References

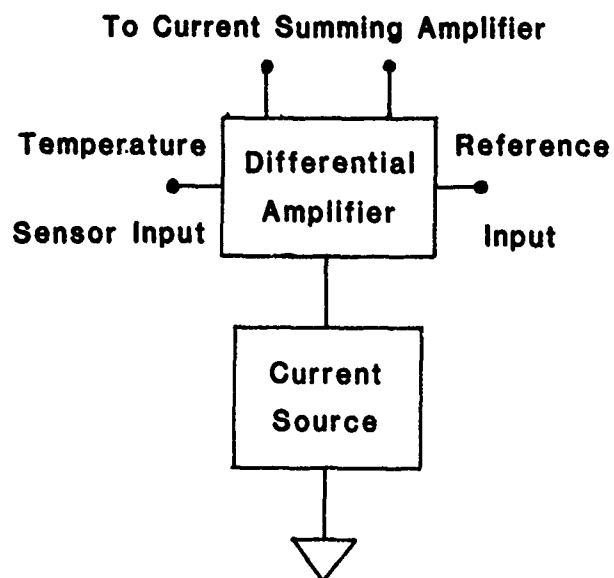
1. Swanson, C.T., and McVey, E.S., "A Non-iterative Solution for a Two-Thermistor TCXO", PROCEEDINGS OF THE 33RD ANNUAL SYMPOSIUM ON FREQUENCY CONTROL, pp. 425-430, 1979
2. Bechmann, R., "Frequency - Temperature - Angle Characteristics of AT-Type Resonators Made of Natural and Synthetic Quartz", INST. OF RADIO ENGINEERS. Vol. 44, pp. 1600-1607, November 1956
3. Mroch, A. and Hykes, G., "A Miniature High Stability TCXO Using Digital Compensation". PROCEEDINGS OF THE 30TH ANNUAL SYMPOSIUM ON FREQUENCY CONTROL, pp. 292-300, 1976
4. Scott, P., "Design Considerations for a Digitally Temperature Compensated Crystal Oscillator", PROCEEDINGS OF THE 31ST ANNUAL SYMPOSIUM ON FREQUENCY CONTROL, pp. 407-411, 1977



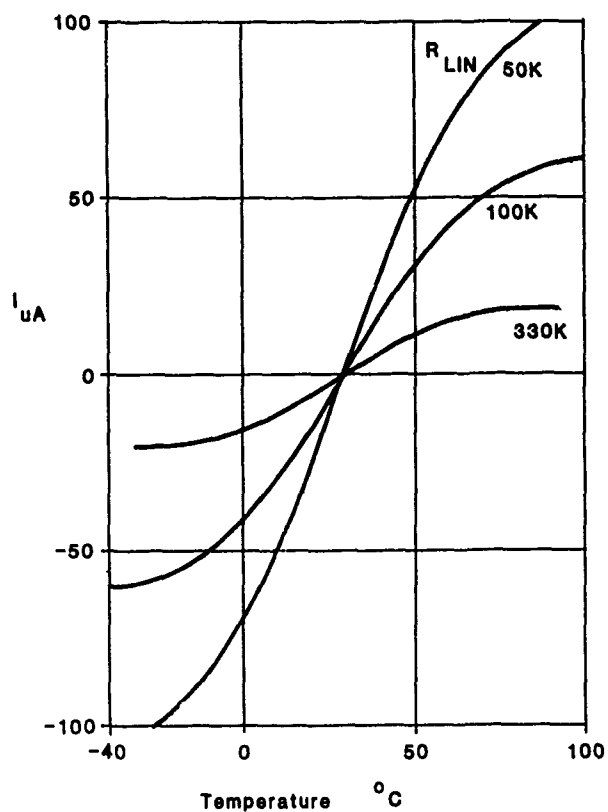
1. Portable Radio with TCXO's



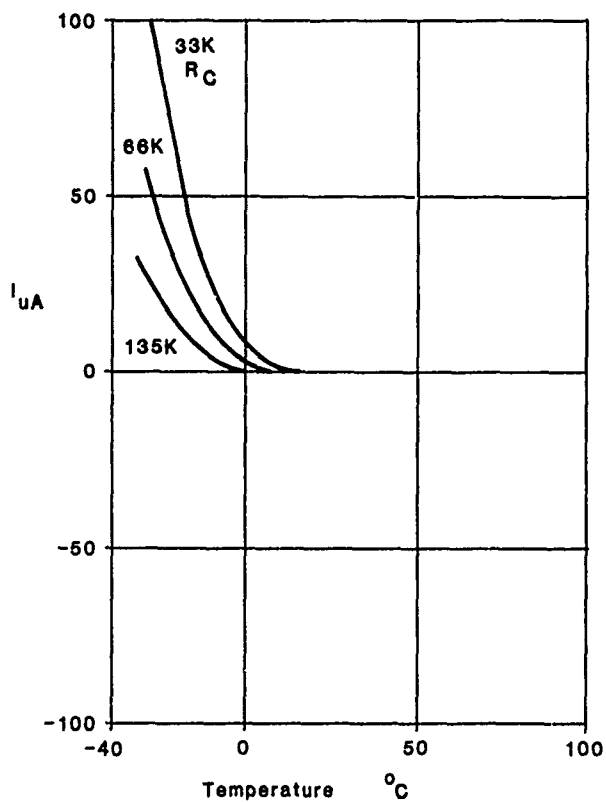
2. Block Diagram of Compensation



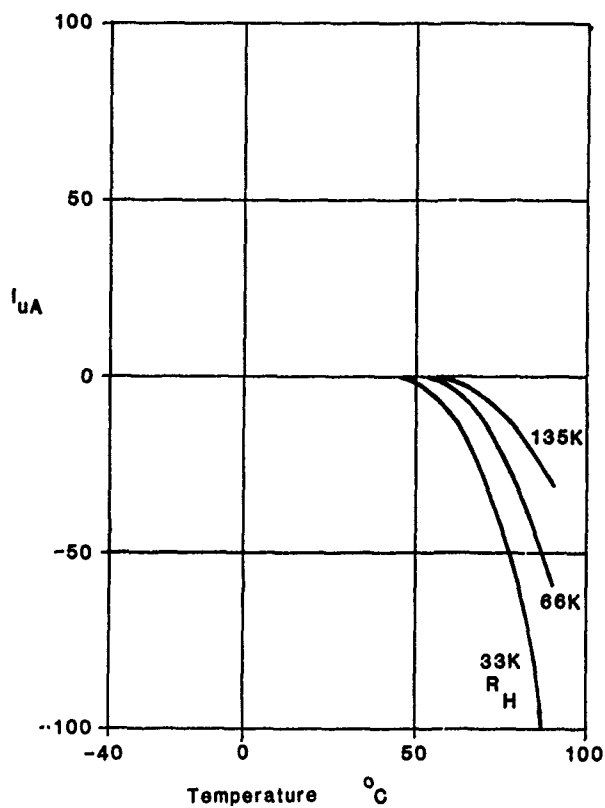
3. Block Diagram of Current Versus Temperature Generator



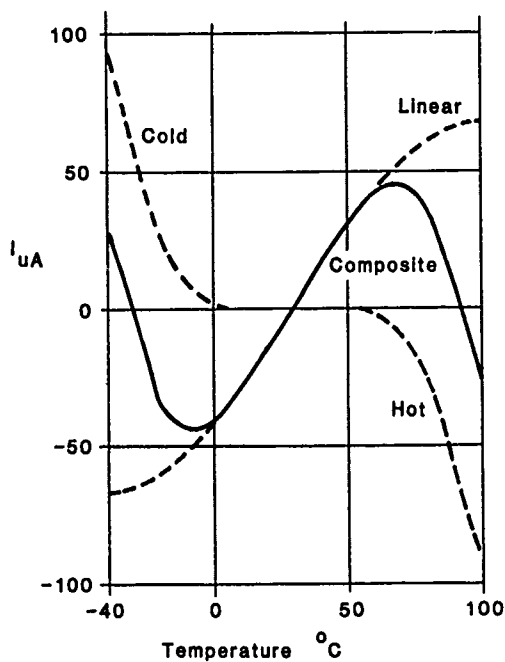
4. Linear Response



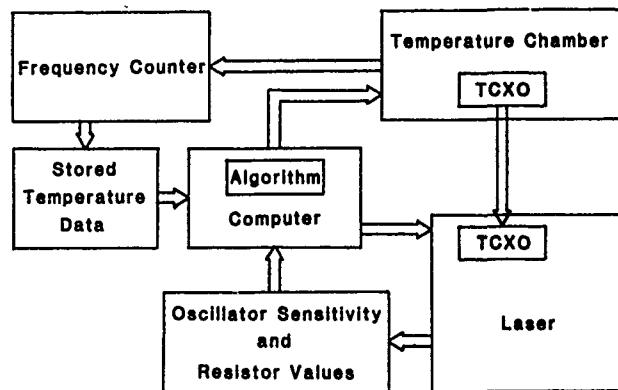
5. Cold Response



6. Hot Response



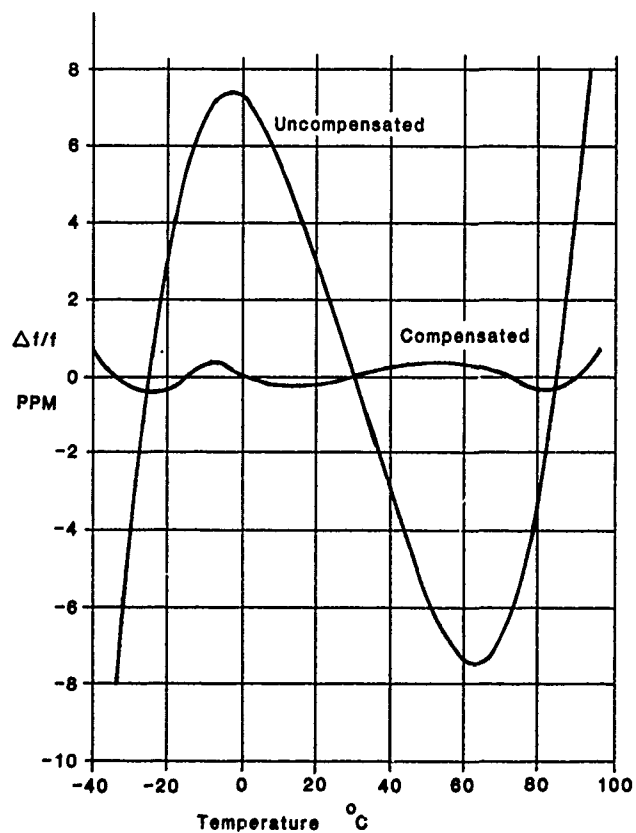
7. Composite Response



8. Automatic Data Acquisition and Laser Resistor Trimming System



9. Oscillator with IC Compensation



10. Frequency versus Temperature Characteristic with and without Compensation

TCXO ERROR DUE TO AGING ADJUSTMENT

Walter D. Galla
Isotemp Research, Inc.
Charlottesville, Virginia

and

Eugene S. McVey
University of Virginia
Charlottesville, Virginia

Abstract

The reactance associated with a crystal must be adjusted to maintain the desired frequency of an oscillation when aging occurs. In the case of TCXOs this reactance change modifies the circuit trim sensitivity which, in turn, results in temperature compensation frequency error that depends on crystal aging, turn-to-turn frequency deviation and circuit configuration. The analysis of TCXO error due to aging adjustment for three basic circuit configurations is presented and illustrated with sample calculations. The series mode circuit is the best of the three configurations.

Introduction

As is well known, TCXOs use temperature sensitive means to modify the reactance associated with crystals to produce an effect which ideally is equal and opposite to crystal and circuit temperature related frequency variations. The reactance associated with the crystal is also varied to compensate aging and, unfortunately, this variation in reactance changes the trim sensitivity.¹ Thus the temperature compensation is dependent on aging adjustments. There appear to be no easy ways to avoid the trim sensitivity problem, so it is important to define its extent for commonly used circuit configurations and suggest specification procedures to assure oscillator users that TCXO performance will be adequate when aging corrections are made.

The problem of TCXO error due to aging adjustment is not new, but apparently has received little attention in the literature. Gruen et al² introduce the problem in a report and suggest a circuit configuration to reduce the effect, but their treatment contains only the one configuration and no analytical guidelines for a designer or user of oscillators. The use of ganged components and field calibration procedures have been omitted in the search for solutions to the problem (Gruen, et al² also dismiss these possibilities).

Three generic circuits are analyzed and sensitivity equations are presented for designer use. Sample calculations demonstrate significant differences in the ability of the circuits to tolerate aging adjustments. Change in crystal characteristics and functions of load capacitance have not

been taken into account in the manner of Ballato³ but this can be done.

Parallel Trimmer Configuration

One of the basic configurations has the frequency trimming capacitor C_T in parallel with the crystal as shown in Fig. 1. The varicap C_V used for TCXO operation and other circuit capacitors may be combined into an equivalent capacitor C_{eq} as shown in Fig. 2 where

$$\frac{1}{C_{eq}} = \frac{1}{C_V} + \frac{1}{C_S} \quad (1)$$

and C_S is the combination of C_b and C_e . The crystal load capacitance is

$$C_L = C_T + C_{eq} \quad (2)$$

The term C_V may contain series and parallel elements as required to accommodate circuit operation. However, in all cases the capacitor networks may be reduced to the equivalents used. As usual, the motional capacitance is defined as C_1 .

The well known relationship

$$\frac{\Delta f}{f} = - \frac{C_1 \Delta C_L}{2(C_0 + C_L)^2} \times 10^6 \text{ PPM} \quad (3)$$

provides a good approximation of crystal frequency behavior for this configuration. The relationship between C_V and C_L to use in (3) to account for varicap frequency pulling is obtained by using the value of C_{eq} from (1) in (2) which is differentiated to obtain

$$\frac{\partial C_L}{\partial C_V} = \frac{1}{C_V^2 \left(\frac{1}{C_V} + \frac{1}{C_S} \right)^2} \quad (4)$$

For incremental variations (4) may be used in (3) to obtain

$$\frac{\Delta f}{f} = - \frac{C_1 \Delta C_V}{2 C_V^2 \left(\frac{1}{C_V} + \frac{1}{C_S} \right)^2 (C_0 + C_L)^2} \times 10^6 \text{ PPM} \quad (5)$$

We now seek the sensitivity of this relationship to changes in C_T (which is varied to compensate crystal aging). This sensitivity is

$$\frac{\partial(\frac{\Delta f}{f})}{\partial C_T} = \frac{C_1 \Delta C_V}{C_V^2 (\frac{1}{C_V} + \frac{1}{C_S})^2 (C_O + C_L)^3} \times 10^6 \quad (6)$$

For small changes (6) may be written as

$$\Delta(\frac{\Delta f}{f}) = \frac{C_1 \Delta C_V \Delta C_T}{C_V^2 (\frac{1}{C_V} + \frac{1}{C_S})^2 (C_O + C_L)^3} \times 10^6 \text{ PPM} \quad (7)$$

This can be used as the basic TCXO error equation for the parallel circuit configuration. Enter ΔC_V for the maximum $\Delta f/f$ required to TCXO the crystal. Enter ΔC_T required for maximum aging compensation. The result will be the worst case TCXO error.

Equation (7) may be written directly in terms of the maximum TCXO pull, p , and aging, a , where these values are in PPM. From (5), $\Delta f/f$ equals p and

$$\Delta C_V = - \frac{2pC_V^2 (\frac{1}{C_V} + \frac{1}{C_S})^2 (C_O + C_L)^2}{C_1} \times 10^{-6} \text{ pf} \quad (8)$$

Differentiate (2) to establish

$$\Delta C_T = \Delta C_L \quad (9)$$

Then, from (3) and (9)

$$\Delta C_T = - \frac{2a(C_O + C_L)^2}{C_1} \times 10^{-6} \text{ pf} \quad (10)$$

Using the values from (8) and (10) in (7) gives

$$\Delta(\frac{\Delta f}{f}) = \frac{4ap(C_O + C_L)}{C_1} \times 10^{-6} \text{ PPM} \quad (11)$$

This is the basic TCXO error equation for the parallel configuration in terms of the aging specification and the crystal pull specification.

Example

Determine the TCXO error resulting from aging compensation for a parallel circuit configuration with the specifications:

$$C_1 = 0.0125 \text{ pf}$$

$$C_O = 3 \text{ pf}$$

$$C_L = 27 \text{ pf}$$

$$a = 5 \text{ PPM (maximum aging)}$$

$$p = 15 \text{ PPM (maximum crystal pull for temperature compensation)}$$

From (11)

$$\begin{aligned} \Delta(\frac{\Delta f}{f}) &= \frac{4(5)(15)(3+27)}{0.0125} \times 10^{-6} \\ &= 0.72 \text{ PPM} \end{aligned}$$

This means that an oscillator which compensates 15 PPM of crystal change due to temperature variation when it is new will compensate only 14.28

PPM after being adjusted to accommodate +5 PPM of aging or 15.72 after accommodating -5 PPM aging. Thus, to meet the ambient temperature specification 0.72 PPM should be allocated to aging effects. Unfortunately, the example specifications used are not uncommon, so a serious design problem may exist. The problem may be minimized by using a better crystal to reduce aging, minimize the pull range, p , or use a better circuit configuration.

Series Trimmer Configuration

The series circuit configuration is shown in Fig. 3. The trimmer and its associated capacitance is C_T (C_O is not included) and contains the varicap C_V and other circuit capacitance C_S such that

$$\frac{1}{C_{eq}} = \frac{1}{C_V} + \frac{1}{C_S} \quad (12)$$

For this circuit

$$C_L = \frac{C_{eq} C_T}{C_{eq} + C_T} \quad (13)$$

The change in load capacitance due to varicap variation is

$$\frac{\partial C_L}{\partial C_V} = \frac{C_S^2 C_T^2}{(C_{eq} + C_T)^2 (C_S + C_V)^2} \quad (14)$$

so for small changes

$$\frac{\Delta f}{f} = - \frac{C_1 C_T^2 C_S^2 \Delta C_V}{2(C_{eq} + C_T)^2 (C_S + C_V)^2 (C_O + C_L)^2} \quad (15)$$

The change in this $\Delta f/f$ due to a change in C_T for a given ΔC_V is

$$\frac{\partial(\frac{\Delta f}{f})}{\partial C_T} = \frac{4ap(C_O + C_L)C_O}{C_1 C_L} \quad (16)$$

From (11) and for small ΔC_T

$$\Delta(\frac{\Delta f}{f}) = \frac{C_O}{C_L} [\Delta(\frac{\Delta f}{f}) \text{ parallel case}] \quad (17)$$

The series configuration is superior to the parallel case by the factor C_O/C_L , a rather dramatic result because approximately an order of magnitude is involved.

Example

Use the specifications of the parallel circuit configuration and compute TCXO error due to aging corrections.

From (17) and the previous example

$$\begin{aligned} \Delta(\frac{\Delta f}{f}) &= \frac{3(0.72)}{27} \\ &= 0.080 \text{ PPM} \end{aligned}$$

This is almost negligible for a 1 PPM oscillator, but would be significant in the case of a 0.2 PPM specification.

Series Mode Operation

In the first two cases the crystals are operated in the parallel mode. In this example the crystal is operated in the series mode, so an external inductor L_2 is required to allow frequency adjustment above and below the series mode frequency. This case also differs from the other cases in that it will be assumed that C_T is the variable component for both aging correction and temperature compensation.

We are denied the use of (3) in this configuration and must derive an appropriate $\Delta f/f$ equation. For the idealized circuit, the impedance of the crystal will be equal and opposite to the external circuit impedance when oscillation occurs, i.e.,

$$\frac{(j\omega L_1 - \frac{j}{\omega C_m}) (-\frac{j}{\omega C_o})}{j\omega L_1 - \frac{j}{\omega C_m} - \frac{j}{\omega C_o}} = -j\omega L_2 + \frac{j}{\omega \frac{C_T C_2}{C_T + C_2}} \quad (18)$$

This assumes idealized operation, i.e., no phase shift other than 90° or 180° increments as required in associated oscillator circuitry. Clear fractions of ω in (18) to obtain

$$\omega^4 - \left[\frac{1}{\frac{C_T C_2}{L_2 C_T + C_2}} + \frac{1}{\frac{L_1 C_o C_1}{L_1 C_o + C_1}} + \frac{1}{L_2 C_o} \right] \omega^2 + \frac{1}{(L_1 \frac{C_o C_1}{C_o + C_1}) (L_2 \frac{C_T C_2}{C_T + C_2})} + \frac{1}{(L_1 C_1) (L_2 C_o)} = 0 \quad (19)$$

Define

$$\omega_o = (L_1 C_1)^{-1/2} \quad (20)$$

$$\omega_1 = (L_2 C_o)^{-1/2} \quad (21)$$

$$\omega_2 = (L_2 \frac{C_T C_2}{C_T + C_2})^{-1/2} \quad (22)$$

$$\omega_3 = (L_1 \frac{C_o C_1}{C_o + C_1})^{-1/2} \quad (23)$$

Then (19) becomes

$$\omega^4 - (\omega_1^2 + \omega_2^2 + \omega_3^2) \omega^2 + \omega_o^2 \omega_1^2 + \omega_2^2 \omega_3^2 = 0 \quad (24)$$

Make a substitution

$$\lambda = \omega^2 \quad (25)$$

and (24) is reduced from a quartic to the quadratic

$$\lambda^2 - (\omega_1^2 + \omega_2^2 + \omega_3^2) \lambda + \omega_o^2 \omega_1^2 + \omega_2^2 \omega_3^2 = 0 \quad (26)$$

whose solution is

$$\lambda = \frac{\omega_1^2 + \omega_2^2 + \omega_3^2 \pm [(\omega_1^2 + \omega_2^2 + \omega_3^2)^2 - 4(\omega_o^2 \omega_1^2 + \omega_2^2 \omega_3^2)]^{1/2}}{2} \quad (27)$$

There are two values of λ in (27) and according to (25) each value of λ yields two pairs (values) of ω which are the negative of each other. We

would expect complex conjugates in this situation. Use (27) in (25) and write in terms of the frequency variable f where the 2π factor cancels; write as f_s which will be the series mode oscillation frequency for the total circuit. Use the minus sign in (27) because f_s must be lower than the sum of f_1 , f_2 and f_3 , i.e.,

$$f_s = \{f_1^2 + f_2^2 + f_3^2 - [(f_1^2 + f_2^2 + f_3^2)^2 - 4(f_o^2 f_1^2 + f_2^2 f_3^2)]^{1/2}\}^{1/2} \div 2 \quad (28)$$

Now determine the variation of f_2 with respect to C_T . All the frequency terms are independent of C_T except f_2 . Differentiation yields

$$\frac{df_s}{dC_T} = -(C_2 \{f_2 - [(f_1^2 + f_2^2 + f_3^2)^2 - 4(f_o^2 f_1^2 + f_2^2 f_3^2)]^{1/2}\}^{-1/2} \times [(f_1^2 + f_2^2 + f_3^2) f_2 - 2f_2 f_3^2]) \div 8\pi C_T f_s [L_2 C_T C_2 (C_T + C_2)]^{1/2} \quad (29)$$

Rewrite for incremental changes, divide both sides of the equation by f_o and substitute f_2 for its value to obtain

$$\frac{\Delta f_s}{f_o} = -\Delta C_1 C_1 f_2^2 \{1 - [(f_1^2 + f_2^2 + f_3^2)^2 - 4(f_o^2 f_1^2 + f_2^2 f_3^2)]^{1/2} [(f_1^2 + f_2^2 + f_3^2)]\}^{-1/2} + 4C_1 (C_T + C_2) f_o f_s \quad (30)$$

Negligible error is introduced if the $f_o f_s$ term is used to cancel the f_2^2 term to obtain

$$\frac{\Delta f}{f_o} = -\{[(f_1^2 + f_2^2 + f_3^2)^2 - 4(f_o^2 f_1^2 + f_2^2 f_3^2)]^{1/2} - f_1^2 - f_2^2 + f_3^2\} \times \frac{C_2 \Delta C_T 10^6}{4C_T (C_T + C_2)} \div [(f_1^2 + f_2^2 + f_3^2)^2 - 4(f_o^2 f_1^2 + f_2^2 f_3^2)]^{1/2} \text{ PPM} \quad (31)$$

where a factor has been added to convert to PPM.

No obvious simplifications present themselves as is the case when (3) is derived, so (31) will be the principle result for making calculations. Although one could now take the derivative of (31) with respect to C_T , the result appears to be more difficult to work with than just applying (31) with the initial value of C_T and then again with C_T after maximum aging and then taking the difference of the two answers to determine temperature compensation error. The use of (31) will be illustrated with an example.

Example

Determine TCXO error resulting from aging compensation for series mode operation with the specifications:

- $a = 5 \text{ PPM}$
- $p = 15 \text{ PPM}$
- $f_o = 10 \text{ MHz}$
- $C_o = 3 \text{ pf}$

$$C_1 = 0.0125$$

$$C_T = 10 \text{ pf}$$

$$C_2 = 120 \text{ pf}$$

From (20)

$$L_1 = 0.0202642 \text{ h}$$

Design so that $f_0 = f_2$ (in which case (28) reduces to f_0 or f_2 as expected) and from (22)

$$L_2 = 27.4411539 \text{ } \mu\text{h}$$

From (21) and (23)

$$f_1 = 17\,541\,160.4 \text{ Hz}$$

$$f_3 = 10\,020\,820.76 \text{ Hz}$$

Now calculate C_T from (31) for $p = 15$:

$$15 = 62.44270 \Delta C_T \text{ PPM}$$

$$\Delta C_T = 0.2402202 \text{ pf}$$

The change in C_T for the specified a using the previous calculation is

$$\Delta C_T = \frac{0.2402202(5)}{.15}$$

$$= 0.080073400 \text{ pf}$$

The new C_T for positive aging will be

$$C_T = 10 + 0.080073400$$

$$= 10.080073 \text{ pf}$$

With this value of C_T

$$f_2 = 9\,963\,269.17$$

and from (31)

$$\frac{\Delta f}{f} = 62.203873 \text{ } C_T \text{ PPM}$$

For the C_T built into the oscillator for temperature compensation (0.2402202) this gives a

$$\frac{\Delta f}{f} = 14.943 \text{ PPM}$$

instead of the required 15 for an error of

$$\Delta\left(\frac{\Delta f}{f}\right) = 15 - 14.943$$

$$= 0.0574 \text{ PPM}$$

This is the best of the three examples considered, but would still be significant for an oscillator with an 0.2 PPM temperature ambient specification.

Conclusions

It is apparent that a better configuration than those considered will be required to realize the potential of digital compensation unless very good crystals (expensive crystals) are used and the temperature range is constrained to keep the turn-to-turn frequency variation relatively small. It is concluded that TCXOs should be tested with output frequency adjusted to the maximum aging compensation value.

Bibliography

1. Sherman, J.A., "Trim Sensitivity, A Useful Characterization of a Resonator," p. 181-185, Proc. 33rd Annual Symposium on Frequency Control, 1979.
2. Gruen, H.E., Dominguey, C.D., Hardt, I.E., Kidman, R.D., "Frequency Temperature Compensation Techniques for Quartz Crystal Oscillators," Quarterly Report No. 9, Contract DA 36-039 AMC-02282(E), Oct., 1964.
3. Ballato, A., "Frequency-Temperature-Load Capacitance Behavior of Resonators for TCXO Application," IEEE Transactions on Sonics and Ultrasonics, Vol. SU-25, No. 4, July 1978.

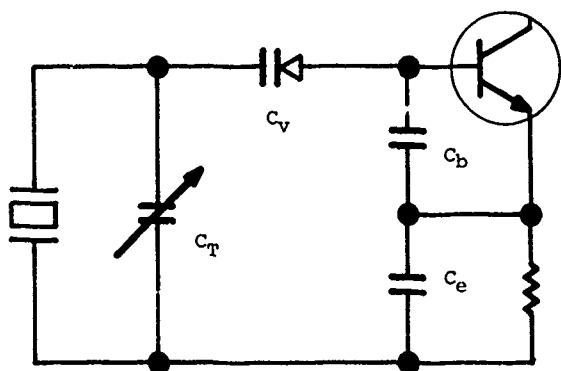


Figure 1. Oscillator with parallel trimmer

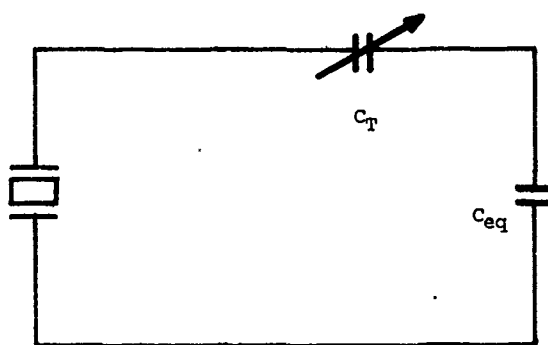


Figure 3. Series trimmer circuit configurations

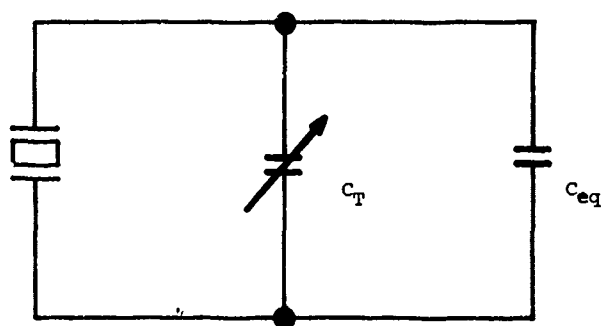


Figure 2. Crystal and associated circuitry for parallel trimmer configuration

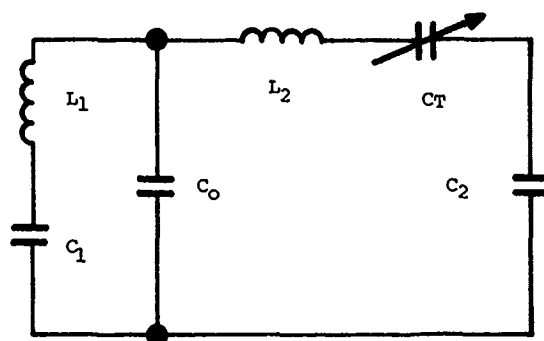


Figure 4. Series mode operation circuit

PRECISION FREQUENCY CONTROL AND SELECTION

A Bibliography, continued

E. A. GERBER
US Army Electronic Technology and Devices Laboratory (ERADCOM)
Fort Monmouth, New Jersey 07703

The bibliography published in the Proceedings of the 33rd Annual Symposium on Frequency Control (1979) covers the years 1968 to 1978. The continuation covers articles published or listed in abstract services in 1979 through April 1980. The same selection criteria as last year's have been used. The categories are:

1. Acoustic Resonators and Devices

- 1.1 Properties of Natural and Synthetic Piezoelectric Crystals and Materials
 - 1.1.1 Quartz
- 1.2 Theory and Properties of Piezoelectric Resonators and Waves
 - 1.2.1 Bulk Acoustic Waves (BAW) and Resonators
 - 1.2.2 Surface Acoustic Waves (SAW) and Resonators
- 1.3 Radiation Effects on Resonators
- 1.4 Resonator and Devices Technology
- 1.5 Piezoelectric and Electromechanical Filters
 - 1.5.1 Bulk Acoustic Wave Filters
 - 1.5.2 Surface Acoustic Wave Filters
 - 1.5.2.1 SAW Bandpass and Bandstop Filters
- 1.6 Stability, Reliability and Aging of Resonators
- 1.7 Resonator and Device Measurement and Specifications
- 1.8 Precision Oscillators
 - 1.8.1 Bulk Acoustic Wave Oscillators
 - 1.8.2 Surface Acoustic Wave Oscillators
 - 1.8.3 Frequency Standards and Clocks (other than Quantum Devices)
- 1.9 Temperature Control and Compensation

2. Quantum Electronic Devices and Standards

- 2.1 Microwave Frequency and Time Standards
 - 2.1.1 (Passive) Beam Standards
 - 2.1.2 Gas Cell Standards
 - 2.1.3 Hydrogen Maser
 - 2.1.4 Other Gas Masers

- 2.2 Laser Frequency Standards
 - 2.2.1 He-Ne Lasers
 - 2.2.2 Other Laser Standards

3. Other Topics

- 3.1 Frequency and Time, Their Measurement and Stability
 - 3.1.1 Digital Measurements
- 3.2 Frequency and Time Coordination, Comparison and Distribution
- 3.3 Other Means for Precision Frequency Control
- 3.4 Applications
- 3.5 Miscellaneous

4. Anonymous/Unknown Authors

1.1

Adachi, M.; Kawabata, A.

"Elastic and piezoelectric properties of potassium lithium niobate (KLN) crystals." (Dept. of Electronics, Faculty of Engng., Kyoto Univ., Kyoto, Japan) Jpn. J. Appl. Phys. (Japan), vol 17, no. 11, p. 1969 - 74 (Nov. 1978).

Chai, B. H.-T.; Ozimek, E.J.

"Experimental Data on the Piezoelectric Properties of Berlinite" Corporate Research Center, Allied Chemical Corporation, Morristown, NJ 07960; Ultrasonics Symposium Proceedings, New Orleans, LA, USA, 26-28 Sept 1979 (New York, USA: IEEE 1979), pp 577-583.

Detaint, J.; Feldmann, M.; Henaff, J.; Poignant, H.; & Toudic, Y.; CNET

"Bulk and Surface Acoustic Wave Propagation in Berlinite" 31st Annual Symposium on Frequency Control, US Army Electronics Command, Fort Monmouth, NJ, pp 70-79 (1977). Copies available from the Electronic Industries Association, 2001 Eye Street, N.W., Washington, DC 20006

DeVries, Adrian J.; Everett, P.; Gilchrist, D.F.; Hansen, K.; Wojcik, T.J.

"Acoustic Effects of Filamentary Defects in Y-Z LiNbO₃" Zenith Radio Corporation, 1000 Milwaukee Ave., Glenview, Illinois 60025; Ultrasonics Symposium Proceedings, New Orleans, LA, USA, 26-28 Sept 1979, (New York, USA: IEEE 1979), pp 584-588

Cullen, G.W.; Duffy, M.T.; Wang, C.C.

"The Preparation and Properties of heteroepitaxial III-V and II-VI compounds for surface acoustic wave and electrooptic devices." In book: Heteroepitaxial semiconductors for electronic devices, Berlin, Germany: Springer-Verlag (1978), Cullen, G.W.; Wang, C.C., Eds., pp. 150-81.

Fukuda, T.; Matsumura, S.; Hirano, H.; Ito, T.

"Growth of LiTaO₃ single crystal for SAW device applications." (Toshiba Res. & Dev. Center, Tokyo Shibaura Electric Co. Ltd., Kawasaki, Japan.) J. Cryst. Growth (Netherlands), vol. 46, no 2, p 179-84 (Feb. 1979)

Halliburton, L.E., Oklahoma State University; Kappers, L.A., University of Connecticut; Armington, A.F. & Larkin, J., Rome Air Development Center.

"Radiation Effects in Berlinite" 31st Annual Symposium on Frequency Control, US Army Electronics Command, Fort Monmouth, NJ, pp 62-69, (1977). Copies available from the Electronic Industries Association, 2001 Eye Street, N.W. Washington D.C. 20006

Kolb, E.K.; Barns, R.L.; Laudise, R.A.; Rosenberg, R.L.

"Solubility, Crystal Growth & Perfection of Aluminum Orthophosphate" Bell Laboratories. 31st Annual Symposium on Frequency Control, US Army Electronics Command, Fort Monmouth, NJ, pp 88-79, (1977). Copies available from the Electronic Industries Association, 2001 Eye Street, N.W., Washington D.C. 20006

Lec, R.; Soluch, W.

"The elastic, piezoelectric, dielectric and acoustic properties of LiIO₃ crystals" Tlee & Radio Rest. Inst., Warsaw, Poland. 1977 Ultrasonics Symposium Proceedings, Phoenix, AZ, USA, 26-28 Oct 1978 (New York, USA: IEEE 1977), pp 389-92

Miller, R.L.; Arai, G.; Cocco, A.; Knowles, T.; Wallner, J.

"Filamentary Domain-Reversal Defects in Y-Z LiNbO₃: Structure, Composition, and Visualization Techniques" Zenith Radio Corp., 1000 Milwaukee Ave., Glenview, Illinois 60025. Ultrasonics Symposium Proceedings, New Orleans, LA, USA, 26-28 Sept 1979 (New York, USA: IEEE 1979) pp. 589-594

O'Connell, R.M.; Carr, P.H.

"New materials for surface acoustic wave devices" Rome Air Dev. Center, Deputy for Electronic Technol., Hanscom AFB, MA, USA. 1978 Ultrasonics Symposium Proceedings, Cherry Hill, NJ, USA, 25-27 Sept. 1978 (New York, USA: IEEE 1978) pp 590-3

Ozimek, E.J. & Chai, B. H.-T.

"Piezoelectric Properties of Single Crystal Berlinite", Allied Chemical Corporation. 31st Annual Symposium on Frequency Control, US Army Electronics Command, Fort Monmouth, NJ, pp 80-87, (1977). Copies available from the Electronic Industries Association, 2001 Eye Street, N.W., Washington D.C. 20006

Rauber, A.

"Chemistry and Physics of Lithium Niobate" Inst. fur Angewandte Festkorperphys., Fraunhofer-Gesellschaft, Freiburg, Germany; In book: Current topics in materials science, vol. 1, E. Kaldis, Ed. pp. 481-601, Amsterdam, Netherlands: North-Holland (1978)

Whatmore, R.W.; O'Hara, C. (Allen Clark Res. Centre, Plessey Res. (Caswell) Ltd., Towcester, England), Cockayne, B.; Jones, G.R.; Lent, B. "Ca_{1/2}Al_{1/2}O₃₃: a new piezoelectric material." Mater. Res. Bull (USA), vol 14, no. 8, pp 967-72 (Aug 1979).

1.1.1

Asahara, J.

"Superior large autoclaves produce synthetic quartz crystals." Toyo Communication Equipment Co. Ltd., Koza-gun, (Kanagawa, Japan). JEE (Japan), no 144, pp 36-9 (Dec. 1978)

- Brice, J.C.; Cole, A.M.
 "The characterization of synthetic quartz by using infra-red absorption" Philips Res. Labs., Redhill, England. Proceedings of the 32nd Annual Symposium on Frequency Control 1978, Atlantic City, NJ., USA, 31 May - 2 June 1978, (Washington D.C., USA: Electronic Industries Assoc. 1978)pp 1-10
- Chakraborty, D.
 "Suitability of coloured quartz crystals for resonator plates". Univ Munster, Munster, Germany. J. Mater. Sci, (GB), vol. 13, no. 11, pp 2529-30 (Nov. 1978)
- Cline, T.W.; Laughner, J.W.; Newnham, R.E.; Cross, L.E.
 "Electrical and acoustic emission during ferro-bielastic twinning in quartz". (Materials Res. Lab., Pennsylvania State Univ., University Park, PA, USA) Proceedings of the 32nd Annual Symposium on Frequency Control 1978, Atlantic City, NJ., USA, 31 May - 2 June 1978, (Washington D.C., USA: Electronic Industries Assoc. 1978)pp 43-9
- Griscom, D.L.
 "Point Defects in α -Quartz". Naval Research Laboratory. 31st Annual Symposium on Frequency Control, US Army Electronics Command, Fort Monmouth, NJ, pp 98-109, (1977). Copies available from the Electronic Industries Association, 2001 Eye Street, N.W. Washington D.C. 20006
- Krishna, M.M.
 "Rotated elastic constants, coupling factors and conversion efficiencies of AC and BC quartz". Dept. of Electronics & Communications Engng., Univ. of Roorkee, Roorkee, India. Indian J. Pure & Appl. Phys., vol. 16, no. 8. pp 735-8 (Aug 1978)
- Lipson, H.G.; Euler, F.; Armington, A.F.
 "Low temperature infrared absorption of impurities in high grade quartz". Rome Air Dev. Center, Deputy for Electronic Technol., Hanscom AFB, MA, USA. Proceedings of the 32nd Annual Symposium on Frequency Control 1978, Atlantic City, NJ, USA, 31 May - 2 June 1978 (Washington, D.C., USA, Electronic Industries Assoc. 1978)pp 11-23
- Mindlin, R.D.
 "The Sesquicentennial of the First Crystal Plate Equations" Columbia University. 31st Annual Symposium on Frequency Control, US Army Electronics Command, Fort Monmouth, NJ, pp 1-3, (1977) Copies available from the Electronic Industries Association, 2001 Eye Street, N.W. Washington D.C. 20006
- Yoda, H.
 "Japan achieves new synthetic quartz crystal technology" Nihon Dempa Kogyo Co. Ltd., Shibuya-ku, Tokyo, Japan. JEE (Japan), no. 144, pp 31-5, (Dec. 1978)
- Boy, J.-J.; Gillet, D.
 "Electro-acoustic effects on the phase velocities of the acoustic and electromagnetic waves in a piezoelectric crystal" Lab. de Chronometrie et Piezoelectrique, Ecole Nat. Supérieure de Chronometrie et Micromécanique, Besançon, France. C.R. Hebd. Seances Acad. Sci. Ser. B (France), vol. 287, no. 8, pp 203-6 (9 Oct 1978) In French
- Gulyaev, Y.V.; Plessky, V.P.
 "Shear surface acoustic waves at the periodically nonuniform boundary between two solids" Inst. of Radio & Electronics, Acad. of Sci., Moscow, USSR; Electron. Lett. (GB), vol 15, no. 2, pp 63-4, (18 Jan 1979)
- Harmon, D.L.; Josse, F.; Vetelino, J.F.
 "Surface Skimming Bulk Waves in Y-rotated quartz-experimental characterization and filter device implementation" Dept. of Electrical Engineering, University of Maine, Orono, ME 04469; Ultrasonics Symposium Proceedings, New Orleans, LA, USA, 26-28 Sept 1979 (New York, USA: IEEE 1979) pp 791-796
- Klimenko, B.I.; Perelomova N.V.; Blistanov, A.A.; Bondarenko, V.S.
 "Anisotropy and phase velocities of propagation of elastic waves in lithium niobate". Moscow Inst. of Steel & Alloys, Moscow, USSR. Sov. Phys-Crystallogr (USA), vol 23, no. 1, pp 114-14 (Jan.-Feb. 1978). Translation of: Kristallografiya (USSR), vol. 23, no. 1, pp 210-16 (Jan.-Feb. 1978)
- Lau, K.F.; Yen, K.H.; Wilcox, J.Z.; Kagiwada, R.S.
 "Analysis of Shallow Bulk Acoustic Wave Excitation by Interdigital Transducers" TRW Defense and Space Systems Group. 31st Annual Symposium on Frequency Control, US Army Electronics Command, Fort Monmouth, NJ pp 388-395, (1977). Copies available from the Electronic Industries Association, 2001 Eye Street, N.W. Washington D.C. 20006
- Matthaei, G.L.
 "Variational solutions for acoustic resonator problems from the 'reaction' point of view." Dept. of Electrical Engng. & Computer Sci., Univ. of California, Santa Barbara, CA, USA. 1978 Ultrasonics Symposium Proceedings, Cherry Hill, NJ, USA, 25-27 Sept. 1978 (New York, USA: IEEE 1978) pp 157-62
- Nakagawa, Y.; Dobashi, T.; Saigusa, Y.
 "Bulk-wave generation due to the nonlinear interaction of surface acoustic waves." Yamanashi Univ., Kofu-city, Japan. J. Appl. Phys. (USA), vol 49, no. 12, pp 5924-7 (Dec. 1978)
- Nelson, D.F.
 "Nonlinear electroacoustics of crystals" Bell Lab, Murray Hill, NJ, USA. 1978 Ultrasonics Symposium Proceedings, Cherry Hill, NJ, USA, 25-27 Sept. 1978 (New York, USA: IEEE 1978) pp 357-62

Paige, E.G.S.; Whittle, P.
"Multistrip coupler performance for surface-skimming bulk waves on lithium tantalate." Dept. of Engng. Sci., Univ. of Oxford, Oxford, England. Electron. Lett. (GB), vol. 15, no. 13, pp 347-6 (21 June 1979)

Paige, E.G.S.; Whittle, P.
"Coupling of surface skimming bulk waves with a multistrip coupler" Dept. of Engineering Science, University of Oxford, Parks Road, Oxford, OXI 3PJ, England. Ultrasonics Symposium Proceedings, New Orleans, LA, USA, 26-28 Sept. 1979, (New York, USA: IEEE 1979) pp 802-805

Togami, Y.; Chiba, T.
"Observation of surface waves and bulk waves in a surface acoustic wave device by frequency-shift holography." NKK Broadcasting Sci. Res. Labs., Tokyo, Japan), NKK Tech J. (Japan), vol. 31, no. 1, pp 22-38 (1979). In Japanese

Yen, K.H.; Lau, K.F.; Kagiwada, R.S.
"Temperature stable shallow bulk acoustic wave devices." TRW Defense & Space Systems Group, Redondo Beach, CA, USA. Proceedings of the 32nd Annual Symposium on Frequency Control 1978, Atlantic City, NJ, USA, 31 May - 2 June 1978 (Washington, D.C., USA; Electronic Industries Assoc. 1978) pp 95-101

Yen, K.H.; Lau, K.F.; Kagiwada, R.S.
"Recent Advances in Shallow Bulk Acoustic Wave Devices." TRW Defense and Space Systems Group, Redondo Beach, California 90278; Ultrasonics Symposium Proceedings, New Orleans, LA, USA, 26-28 Sept 1979 (New York, USA: IEEE 1979) pp 776-785

"Surface-Skimming bulk wave devices." Radio & Electron. Eng. (GB) vol. 49, no. 6, pp 288 (June 1979)

1.2.1

Ballato, A.; Lukaszek, T.
"Shallow bulk acoustic wave devices." US Army Electronics Technol. & Devices Lab., Fort Monmouth, NJ, USA; 1979 IEEE MTT-S International Microwave Symposium Digest, Orlando, FL, USA, 30 April - 2 May 1979 (New York, USA: IEEE 1979) pp 162-4

Barcus, L.C.
"Holographic displacement amplitude measurements of four anharmonic AT modes." Univ. of Lowell, Lowell, MA, USA; Proceedings of the 32nd Annual Symposium on Frequency Control 1978, Atlantic City, NJ, USA, 31 May - 2 June 1978 (Washington D.C., USA: Electronic Industries Assoc. 1978) pp 202-6

Baryshnikova, L.F.; Lyamov, V.E.
"Excitation of an acoustic harmonic and its energy flux in piezoelectric crystals." Sov. Phys-Solid State (USA) vol. 20, no. 4, pp 640-3 (April 1978) Translation of Fiz. Tverdogo Tela (USSR) vol. 20, no. 4, pp 1109-14 (April 1978)

Baryshnikova, L.F.; Lyamov, V.E.
"Harmonic generation in piezoelectric crystals under the action of homogeneous external fields." Phys. Faculty, M.V. Lomonosov Moscow State Univ., Moscow, USSR. Sov. Phys-Acoust. (USA), vol. 24, no. 4, pp 167-70 (July-Aug 1978). Translation of Akust. Zh. (USSR), vol. 24, no. 4, pp 465-72 (July-Aug 1978)

Burly, P.V.; Il'in, P.P.; Kucherov, I.Ya.
"Control of elastic wave velocity in piezoelectric plates." Ukr. Fiz. Zh (USSR) vol 24, no. 4, pp 561-2 (April 1979) In Russian

Chowdhury, B.R.
"A note on disturbances in a piezoelectric resonator." Bethune Collegiate School, Calcutta, India) Indian J. Theor. Phys., vol. 26, no. 2, pp 89-95, (June 1978).

Dulmet, B.; Gillet, D.; Maitre, P.
"Definition of a Q-factor for electroless resonators operating at high frequencies." Ecole Nat. Supérieure de Chronometrie et de Micromécanique, Besançon, France. C.R. Hebd. Seances Acad. Sci. Ser. B (France), vol. 287, no. 13, pp 293-6, (13 Nov. 1979) In French

Gilinskiy, I.A.; Popov, V.V.
"Theory of wave excitation in piezoelectric crystals by narrow metallic electrodes." Radio Eng. & Electron. Phys. (USA), vol. 23, no. 2, pp 102-10 (Feb 1978). Translation of Radiotekh & Electron (USSR), vol 23, no. 2, pp 392-400 (Feb 1978)

Goodell, J.; Sundelin, R.
"Frequency Characteristics of Bulk Microwave Acoustic Resonators" Westinghouse Advanced Technology Lab, Box 1521, Baltimore, MD 21203, Ultrasonics Symposium Proceedings, New Orleans, LA, USA, 26-28 Sept 1979 (New York, USA: IEEE 1979) pp 123-127

Gridnev, S.A.; Postnikov, V.S.; Prasolov, B.N.; Turkov, S.K.
"Damping of low-frequency elastic vibrations in LiNbO_3 ." Polytech. Inst., Voronezh, USSR. Sov. Phys. Solid State (USA), vol 20, no. 5, pp 747-50, (May 1978). Translation of: Fiz. Tverdogo Tela (USSR), vol. 20, no. 5, pp 1299-303 (May 1978)

Kokorin, Yu.I.; Zaitseva, B.I.; Sysoev, A.M.; Malyshevskii, N.G.; Kidyarov, B.I.
"Polarization effect in piezoelectric resonators executing longitudinal vibrations." Inst. of Phys. Acad. of Sci., USSR. Sov. Phys.-Crystallogr. (USA), vol. 23, no. 1, pp 118-19 (Jan-Feb 1978). Translation of: Kristallografiya (USSR), vol. 23, no. 1 pp 217-18 (Jan-Feb 1978)

Lakes, R.S.
"Prediction of anelastic loss in piezoelectric solids: Effect of geometry." Biomedical Engng. Program, Univ. of Iowa, Iowa City, IA, USA) Appl. Phys. Lett. (USA), vol. 34, no. 11, pp 729-30 (1 June 1979)

Milsom, R.F.

"Three-Dimensional Variational Analysis of Small Crystal Resonators." Philips Research Laboratories, UK; 31st Annual Symposium of Frequency Control, US Army Electronics Command, Fort Monmouth, NJ pp 263-270, (1977). Copies available from the Electronic Industries Association, 2001 Eye Street, N.W. Washington D.C. 20006

Mitra, G.B.; Kar, Leela

"A preliminary study of the changes in X-rays reflected by a piezoelectric crystal when subjected to an oscillatory electric field." Dept of Phys. Indian Inst. of Technol., Kharagpur, India. Indian J. Phys. Part A, vol. 53A, no. 1-2, pp 158-67 (Jan-Mar 1979)

Mochizuki, Y.

"A new method to analyse vibrations of resonators by the combination of plate equations and finite element method." Shizuoka Univ., Shizuoka, Japan. Proceedings of the 32nd Annual Symposium on Frequency Control 1978, Atlantic City, NJ, USA, 31 May - 2 June 1978 (Washington, D.C., USA: Electronic Industries Assoc. 1978) pp 120-33

Momosaki, E.; Kogure, S.; Inoue, M. Sonoda, T.

"New Quartz Tuning Fork with Very Low Temperature Coefficient." Suwa Seikosha Co., Ltd. 31st Annual Symposium of Frequency Control, US Army Electronics Command, Fort Monmouth, NJ, pp 247-254, (1977). Copies available from the Electronic Industries Association, 2001 Eye Street, N.W. Washington D.C. 20006

Moore, R.A.; Hopwood, F.W.; Haynes, T.; McAvoy, B.R.

"Bulk Acoustic Resonator for Microwave Frequencies" Westinghouse Electric Corporation. 31st Annual Symposium of Frequency Control, US Army Electronics Command, Fort Monmouth, NJ, pp 444-448 (1977) Copies available from the Electronic Industries Association, 2001 Eye Street, N.W. Washington D.C. 20006

Murphy, J.; Gad, M.M.

"A versatile program for computing and displaying the bulk acoustic wave properties of anisotropic crystals." Thin Film Technol. Dept., Westinghouse R&D Center, Pittsburgh, PA, USA; 1978 Ultrasonics Symposium Proceedings, Cherry Hill, NJ USA, 25-27 Sept. 1978 (New York, USA: IEEE 1978) pp 172-81

Nakazawa, M.

"Specific directions of plane elastic waves in thin LiTaO_3 and LiNbO_3 crystal plates." Faculty of Engng., Shinshu Univ., Wakasato, Nagano, Japan. Int. J. Electron. (GB) vol. 46, no. 3, pp 289-98, (March 1979)

Nelson, D.F.

"Three-field electroacoustic parametric interactions in piezoelectric crystals." Bell Labs., Murray Hill, NJ, USA; J. Acoust. Soc. Am (USA), vol. 64, no. 3, pp 891-5 (Sept. 1978)

Ostrovskii, I.V.; Polovina, A.I.

"Acoustic correlation in a piezoelectric plate resonator." T.G. Shevchenko State Univ., Kiev, Ukrainian SSR; Sov. Phys.-Solid State (USA) vol. 20, no. 11, pp 1979-80 (Nov. 1978) Translation of: Fiz. Tverdogo Tela (USSR), vol 20, no. 11, pp 3430-2, (Nov. 1978).

Paul, H.S.; Sarma, K.V.

"Forced torsional vibrations of a semi-infinite piezoelectric medium of (622) class." Dept of Math., Indian Inst. of Technol., Madras, India; Proc. Indian Natl. Sci. Acad. Part A., vol 44, no. 6, pp 362-8 (Nov. 1978)

Sekimoto, H.; Ariga, M.

"Dispersion characteristics near cutoff frequencies for thickness waves in high coupling piezoelectric plates." Faculty of Technol., Tokyo Metropolitan Univ., Tokyo, Japan; Trans. Inst. Electron. & Commun. Eng. Jpn. Sect. E. (Japan), vol E61, no. 10, pp 830-1 (Oct. 1978)

Shimizu, H.; Yamada, K.

"Energy-trapping for backward-wave mode thickness-vibrations by controlling piezoelectric reaction." Faculty of Engng., Tohoku Univ., Sendai, Japan; Trans. Inst. Electron. & Commun. Eng. Jpn. Sect. E (Japan) vol E62, no. 1, pp 21-2 (Jan 1979)

Srinivase Rao, B.

"Wave propagation in piezoelectric medium of hexagonal symmetry." Dept. of Math., Government Coll., Rajahmundry, India; Proc. Indian Acad. Sci. Sect. A. vol. 87A, no. 5, pp 125-36 (May 1978)

Strashilov, V.L.; Borisov, M.I.; Branzalov, K.P.; Mirtcheva, D.S.

"An application of thickness-shear approximation to the analysis of multielectroded monolithic (piezoelectric) structures." Inst. of Solid State Phys., Acad. of Sci., Sofia, Bulgaria; Wave Electron. (Netherlands) vol. 4, no. 1, pp 67-70 (Sept. 1979)

Tiersten, H.F.; Smythe, R.C.

"An analysis of contoured crystal resonators operating in overtones of coupled thickness shear & thickness twist." Dept. of Mech. Engng., Aeronautic Engng. & Mech., Rensselaer Polytech. Inst., Troy, NY, USA; J. Acoust. Soc. Am. (USA) vol. 65, no. 6, pp 1455-60 (June 1979)

Uno, T.

"Mode dependency of temperature characteristics of trapped energy mode LiTaO_3 resonators excited by parallel electric field." Yokosuka Electrical Communication Lab., NTT, Yokosuka, Japan; Trans. Inst. Electron. & Commun. Eng. Jpn. Sect E (Japan), vol. E62, no. 4, pp 258 (April 1979)

Watanabe, H.; Nakamura, K.; Shimizu, H.

"Energy trapping of width-extensional vibrations caused by a contribution of complex branches of dispersion curves." Faculty of Engng., Tohoku Univ Sendai, Japan; Trans Inst. Electron & Commun. Eng. Jpn. Sect. E (Japan, Vol. E61, no. 12, pp 980-1, (Dec 1978)

1.2.1.1

Balbi, J.H.; Duffaud, J.A.; Besson, R.J.
"A new nonlinear analysis method and its application to quartz crystal resonator problems." Faculte des Sci., Besancon, France; Proceedings of the 32nd Annual Symposium on Frequency Control 1978 Atlantic City, NJ., USA, 31 May - 2 June 1978, (Washington, D.C., USA, Electronic Industries Assoc. 1978) pp 162-8.

Bahadur, H.; Parshad, R.; Hepworth, A.; Lall, V.K.
"Some observations using scanning electron microscope for studying the ultrasonic vibrations of quartz crystals." Nat. Phys. Lab., New Delhi, India; Proceedings of the 32nd Annual Symposium on Frequency Control 1978, Atlantic City, NJ, USA, 31 May - 2 June 1978 (Washington D.C. USA: Electronic Industries Assoc. 1978) pp 207-19

Ballato, A.; Vig, J.R.
"Static and dynamic frequency-temperature behavior of singly and doubly rotated, oven-controlled quartz resonators." US Army Electronics Technol & Devices Lab., USAERADCOM, Fort Monmouth, NJ, USA; Proceedings of the 32nd Annual Symposium on Frequency Control 1978, Atlantic City, NJ, USA, 31 May - 2 June 1978 (Washington, D.C., USA: Electronic Industries Assoc. 1978) pp 180-8

Ballato, A.
"Resonators Compensated for Acceleration Fields." USAERADCOM; 31st Annual Symposium of Frequency Control, US Army Electronics Command, Fort Monmouth, NJ, pp 322-336 (1977) Copies available from the Electronic Industries Association, 2001 Eye Street, N.W. Washington D.C. 20006

Ballato, A.
"Static and dynamic behavior of quartz resonators." US Army Electron. Technol. & Devices Lab., Fort Monmouth, NJ, USA; IEEE Trans. Sonics & Ultrason. (USA), vol. SU-26, no. 4, pp 299-306 (July 1979)

Besson, R.
"A new type of quartz resonator design." ENS de Mecanique et des Microtech., Besancon, France; C.R. Hebd, Seances Acad, Sci, Ser. B (France), vol. 288, no. 16, pp 245-8 (2 May 1979) In French

Besson R.; Gagnepain, J.-J.; Janiaud, D.
"Design of a Bulk Wave Quartz Resonator Insensitive to Acceleration." ENSCMB; LPMO; & ONERA 31st Annual Symposium of Frequency Control, US Army Electronics Command, Fort Monmouth, NJ, pp 337-345 (1977) Copies available from the Electronic Industries Association, 2001 Eye Street, N.W. Washington, D.C. 20006

Bye, K.L.; Cosier, R.S.
"An X-ray double crystal topographic assessment of defects in quartz resonators." Philips Res. Labs., Redhill, England; J. Mater. Sci, (GB), vol. 14, no. 4, pp 800-10 (April 1979)

EerNisse, E.P.
"Rotated X-cut quartz resonators for high temperature applications." Sandia Labs., Albuquerque, NM, USA; Proceedings of the 32nd Annual Symposium on Frequency Control 1978, Atlantic City, NJ, USA, 31 May - 2 June 1978 (Washington, D.C., USA: Electronic Industries Assoc. 1978) pp 255-9

EerNisse, E.P.
"Temperature Dependence of the Force Frequency Effect for the Rotated X-Cut" Sandia Laboratories. 31st Annual Symposium of Frequency Control, US Army Electronics Command, Fort Monmouth, NJ, pp 300-305, (1977). Copies available from the Electronic Industries Association, 2001 Eye Street, N.W. Washington D.C. 20006

Fletcher, E.D.; Douglas, A.J.
"A Comparison of the Effects of Bending Moments on the Vibrations of AT and SC (or TCC) cuts of Quartz" Philips Research Laboratories, UK; 31st Annual Symposium of Frequency Control, US Army Electronics Command, Fort Monmouth, NJ, pp 346-350, (1977). Copies available from the Electronic Industries Association, 2001 Eye St., N.W. Washington D.C. 20006

Hermann, J.; Bourgeois, C.
"A New Quartz Crystal Cut for Contour Mode Resonators." Centre Electronique Horloger S.A.; 31st Annual Symposium of Frequency Control, US Army Electronics Command, Fort Monmouth, NJ, pp 255-262 (1977). Copies available from the Electronic Industries Association, 2001 Eye Street, N.W. Washington D.C. 20006

Janlaud, D.; Nissim, L.; Gagnepain, J.-J.
"Analytical calculation of initial stress effects on anisotropic crystals: application to quartz resonators." ONERA, Chatillon, France; Proceedings of the 32nd Annual Symposium on Frequency Control 1978, Atlantic City, NJ, USA, 31 May - 2 June 1978 (Washington, D.C., USA: Electronic Industries Assoc. 1978), pp 169-79.

Kato, T.; Ueda, H.
"Frequency Temperature Characteristics of Rectangular AT-Cut Quartz Plates" Citizen Watch Co., Ltd.; 31st Annual Symposium of Frequency Control, US Army Electronics Command, Fort Monmouth, NJ, pp 271-276 (1977). Copies available from the Electronic Industries Association, 2001 Eye Street, N.W. Washington D.C. 20006

Kazelle, I.; Zelenka, I.
"Temperature dependence of the oscillation frequency of AT-cut quartz resonators between resonance and antiresonance frequencies." Industrial Textile Inst. Liberec, Czechoslovakia. Sov. Phys.-Crystallogr. (USA), vol. 23, no. 3, pp 363-4 (May-June 1978). Translation of Kristallografiya (USSR), vol. 23, no. 3, pp 650-2 (May-June 1978)

Krishna, M.M.

"Rotated elastic constants, coupling factors and conversion efficiencies of AC and BC quartz." Dept. of Electronics & Communications Engng., Univ. of Roorkee, Roorkee, India; Indian J. Pure & Appl. Phys., vol. 16, no. 8, pp 735-8 (Aug 1978).

Lee, P.C.Y.; Zee, C.; Brebbia, C.A.

"Thickness-shear, thickness-twist, and flexural vibrations of rectangular AT-cut quartz plates with patch electrodes." Dept. of Civil Engng., Princeton Univ., Princeton, NJ, USA; Proceedings of the 32nd Annual Symposium on Frequency Control 1978, Atlantic City, NJ, USA, 31 May - 2 June 1978 (Washington, D.C., USA: Electronic Industries Assoc. 1978) pp 108-19

Lukaszek, T.J.; Ballato, A.

"Resonators for Severe Environments" USAERADCOM; 31st Annual Symposium on Frequency Control, US Army Electronics Command, Fort Monmouth, NJ, pp 311-321 (1977). Copies available from the Electronic Industries Association, 2001 Eye Street, N.W. Washington D.C. 20006

Meeker, T.R.

"Extension, Flexure, and Shear Modes in Rotated X-Cut Quartz Rectangular Bars"; Bell Telephone Laboratories; 31st Annual Symposium on Frequency Control, US Army Electronics Command, Fort Monmouth, NJ, pp 286-292 (1977). Copies available from the Electronic Industries Association, 2001 Eye Street, N.W. Washington D.C. 20006

Peschl, I.H.

"The quartz crystal. Structure, mode of operation and characteristics." Funkschau (Germany), vol. 51, no. 7, pp 369-72 (30 March 1979). In German.

Sinha, B.K.; Tiersten, H.F.

"Temperature derivatives of the fundamental elastic constants of quartz." Dept. of Mech. Engng., Rensselaer Polytech. Inst., Troy, NY, USA; Proceedings of the 32nd Annual Symposium on Frequency Control 1978, Atlantic City, NJ, USA, 31 May - 2 June 1978 (Washington, D.C., USA: Electronic Industries Assoc. 1978) pp 150-4

Sinha, B.K.; Tiersten, H.F.

"Temperature Induced Frequency Changes in Electroded Contoured Quartz Crystal Resonators." Rensselaer Polytechnic Institute; 31st Annual Symposium on Frequency Control, US Army Electronics Command, Fort Monmouth, NJ, pp 228-234 (1977). Copies available from the Electronic Industries Association, 2001 Eye Street, N.W. Washington D.C. 20006

Tiersten, H.F.; Sinha, B.K.

"Temperature induced frequency changes in electroded doubly-rotated quartz thickness-mode resonators." Dept. of Mech. Engng., Rensselaer Polytech. Inst., Troy, NY, USA; Proceedings of the 32nd Annual Symposium on Frequency Control 1978, Atlantic City, NJ, USA, 31 May - 2 June 1978 (Washington, D.C., USA: Electronic Industries Assoc. 1978) pp 155-61

Tiersten, H.F.; Ballato, A.

"Nonlinear Vibrations of Quartz Rods." Rensselaer Polytechnic Institute and USAERADCOM; 31st Annual Symposium on Frequency Control, US Army Electronics Command, Fort Monmouth, NJ, pp 293-299 (1977). Copies available from the Electronic Industries Association, 2001 Eye St., N.W. Washington D.C. 20006

Toki, M.; Tsuzuki, Y.

"Motional inductance of plano-convex AT-cut quartz crystal resonators." Faculty of Engng., Yokohama Nat. Univ., Yokohama, Japan; Trans. Inst. Elect. & Commun. Eng. Jpn. Sect. E (Japan), vol. E52, no. 3, pp 154-5 (March 1979)

Vangheluwe, D.C.L.

"Finite element analysis of AT-cut crystals" N.V. Philips' Gloeilampenfabr., Eindhoven, Netherlands; Proceedings of the 32nd Annual Symposium on Frequency Control 1978, Atlantic City, NJ, USA, 31 May - 2 June 1978 (Washington, D.C. USA: Electronic Industries Assoc. 1978) pp 134-4

Yaroslavskii, M.I.; Fedorkov, A.P.

"Low-frequency heat-sensitive quartz resonators." Meas. Tech (USA) vol. 21, no. 1, pp 110-11 (Jan. 1978). Translation of: Izmer. Tekh. (USSR), vol. 21, no. 1, pp 71 (Jan 1978)

Yamashita, S.; Motte, S.; Takahashi, K.; Echigo, N.; Watanabe, A.; Kubota, K.

"New Frequency-Temperature Characteristics of 4.19 MHz Beveled Rectangular AT-Cut Quartz Resonator." Daini Seikosha Co., Ltd.; 31st Annual Symposium on Frequency Control, US Army Electronics Command, Fort Monmouth, NJ, pp 277-285 (1977). Copies available from the Electronic Industries Association, 2001 Eye St., N.W. Washington D.C. 20006

Zumsteg, A.E.; Suda, P.; Zingg, W.

"Energy trapping of coupled modes in rectangular AT-cut resonators." SSIH Electronic SA, Bienne, Switzerland; Proceedings of the 32nd Annual Symposium on Frequency Control 1978, Atlantic City, NJ, USA, 31 May - 2 June 1978 (Washington, D.C., USA: Electronic Industries Assoc. 1978) pp 260-6

1.2.2

Ballato, A.; Lukaszek, T.J.; Yen, K.H.; Kagiwada, R.S.

"SAW and SBAW on Double Rotated Cut Quartz" USAERADCOM, Fort Monmouth, NJ 07703 & TRW Defense and Space Systems Group, Redondo Beach, CA 90278; Ultrasonics Symposium Proceedings, New Orleans, LA, USA, 26-28 Sept 1979 (New York, USA: IEEE 1979), pp 797-80

Browning, T.I.; Lewis, M.F.; Milson, R.F.

"Surface acoustic waves on rotated Y-cut TiTaO_3 " Royal Signals & Radar Establ., Malvern, England; 1978 Ultrasonics Symposium Proceedings, Cherry Hill, NJ, USA, 25-27 Sept. 1978 (New York, USA: IEEE 1978) pp 586-9

- Burlii, P.V.; Il'in, P.P.; Kuchеров, I. Ya.
"Investigation of the effects of electrical screening of a surface on the propagation of elastic waves in piezoelectric plates." Kiev T.G. Shevchenko Gov. Univ., USSR; Ukr. Fiz. Zh. (USSR), vol. 23, no. 10, pp 1730-2 (Oct. 1978) In Russian
- Cross, P.S.; Shreve, W.R.; Tan, T.S.
"800 MHz SAW Resonators with Q above 10,000." Hewlett-Packard Laboratories, 1501 Page Mill Rd., Palo Alto, CA 94304 & Hewlett-Packard Co., 1400 Fountain Grove Parkway, Santa Rosa, CA 95404; Ultrasonics Symposium Proceedings, New Orleans, LA, USA, 26-28 Sept 1979 (New York, USA: IEEE 1979) pp 824-829
- Deka, M.; Claus, R.O.
"Measurements of surface waves on an optical flat by reflective interferometry." Virginia Polytech. Inst. & State Univ., Blacksburg, VA, USA; Proceedings of Southeastcon 1979, Roanoke, VA, USA, 1-4 April 1979 (New York, USA: IEEE 1979) pp 193-6.
- Gulyaev, Y.V.; Plessky, V.P.
"Shear surface acoustic waves in periodic structures on solids." Inst. of Radio Engng. & Electron., Acad. of Sci., Moscow, USSR; Wave Electron. (Netherlands), vol. 4, no. 1, pp 7-29 (Sept 1979)
- Harmon, D.; Morency, D.; Soluch, W.; Vetelino, J.F.; Mittleman, S.D.
"Experimental determination of the SAW properties of X-axis boule cuts in berlinite." Dept. of Electrical Engng., Univ. of Maine, Orono, ME, USA; 1978 Ultrasonics Symposium Proceedings, Cherry Hill, NJ, USA, 25-27 Sept. 1978 (New York, USA: IEEE 1978) pp 594-7
- Hartemann, P.
"Influence of annealing on the surface-acoustic-wave velocity increase induced by ion implantation in quartz." Lab. Central de Recherches, Thomson-CSF, Orsay, France; J. Appl. Phys. (USA), vol. 49, no. 10, pp 5334-5 (Oct. 1978)
- Hauden, D.; Michel, M.; Gagnepain, J.J.
"Higher order temperature coefficients of quartz SAW oscillators." Lab. de Phys. et Metrologie des Oscillateurs, CNRS, Besancon, France; Proceedings of the 32nd Annual Symposium on Frequency Control 1978, Atlantic City, NJ, USA, 31 May - 2 June 1978 (Washington, D.C., USA: Electronic Industries Asso. 1978) pp 77-86
- Haydl, W.H.; Hiesinger, P.; Kohlbacher, G.; Schmitt, P.
"Design and performance of SAW-resonators and resonator-filters." Inst. fur Angewandte Festkorperphys. der Fraunhofer Gesellschaft, Freiburg, Germany; Agard Conference Proceedings No. 230. Impact of Charge Coupled Devices and Surface Acoustic Wave Devices on Signal Processing and Imagery in Advanced Systems, Ottawa, Canada, 11-15 Oct. 1977 (Neuilly-sur-Seine, France: AGARD 1978) pp 3.3/1-7
- Henaff, J.; Feldmann, M.
"Computed coupling and temperature coefficients of ASW in TI, VS₂, and TI₁laSe₄." Dept. TCR/DEF, CNET, Issy-lesMoulineaux, France; 1977 Ultrasonics Symposium Proceedings, Phoenix, AZ, USA, 26-28 Oct. 1978 (New York, USA: IEEE 1977) pp 696-700
- Jhunjhunwala, A.; Vetelino, J.F.
"Spectrum of Acoustic Waves Emanating from a Line Source on a Piezoelectric Crystal" Dept. of Electrical Engineering, University of Maine, Orono, ME 04469; Ultrasonics Symposium Proceedings, New Orleans, LA, USA, 26-28 Sept. 1979 (New York, USA: IEEE 1979) pp 945-950
- Koyamada, Y.; Yoshikawa, S.
"Long IDT coupled mode analysis" Nippon Telegraph & Telephone Public Corp., Tokyo, Japan; Electr. Commun. Lab. Tech. J. (Japan), vol. 27, no. 7, pp 1557-72 (1978). In Japanese
- Koyamada, Y.; Yoshikawa, S.; Ishihara, F.
"One-port SAW resonators using long IDTs and their application to narrow band filters." Electr. Commun. Lab. Tech. J. (Japan), vol. 27, no. 8, pp 1663-77 (1978). In Japanese
- Koyamada, Y.; Yoshikawa, S.
"Coupled mode analysis for a long IDT." Nippon Telegraph & Telephone Lab., Musashino-shi, Tokyo, Japan; Rev. Electr. Commun. Lab (Japan), vol. 27, no. 5-6, pp 432-44 (May-June 1979)
- Koyamada, Y.; Yoshikawa, S.; Ishihara, F.
"One-port SAW resonators using long IDTs and their application to narrow band filters." Nippon Telegraph & Telephone Lab., Musashino-shi, Tokyo, Japan Rev. Electr. Commun. Lab. (Japan), vol. 27, no. 5-6, pp 445-58 (May-June 1979).
- Krashennnikov, M.V.; Chaplik, A.V.
"Plasma-acoustic waves on the surface of a piezo-crystal." Zh. Eksp. & Teor. Fiz. (USSR), vol. 75, no. 5, pp 1907-18 (Nov. 1978) In Russian. English translation in: Sov. Phys. JETP (USA)
- Lewis, M.F.
"Temperature Compensation Techniques for SAW Devices" Royal Signals & Radar Establishment, St. Andrews Road, Malvern, Worcs. WR14 3PS, UK; Ultrasonics Symposium Proceedings, New Orleans, LA, USA, 26-28 Sept 1979 (New York, USA: IEEE 1979) pp 612-622.
- McAvoy, B.R.; Murphy, J.; de Klerk, J.
"Temperature compensation in bulk mode microwave resonators." Westinghouse Res. & Dev. Center, Pittsburgh, PA, USA; 1977 Ultrasonics Symposium Proceedings, Phoenix, AZ, USA, 26-28 Oct. 1978 (New York, USA: IEEE 1977) pp 403-7
- Moore, R.A.; Newman, B.A.; McAvoy, B.R.; Murphy, J.
"Temperature characteristics of microwave acoustic resonators." Advanced Technol. Lab., Westinghouse Defense & Electronics System Center, Baltimore, MD, USA; 1979 IEEE MTT-S International Microwave Symposium Digest, Orlando, FL, USA, 30 April - 2 May 1979 (New York, USA: IEEE 1979) pp 171-3

Morency, D.G.; Soluch, W.; Vetelino, J.F.; Mittleman, S.D.; Harmon, D.; Surek, S.; Field, J.C. "Experimental measurement of the SAW properties of berlinite." Dept. of Electrical Engng., Univ. of Maine, Orono, ME, USA; Proceedings of the 32nd Annual Symposium on Frequency Control 1978, Atlantic City, NJ, USA, 31 May - 2 June 1978 (Washington, D.C., USA: Electronic Industries Assoc. 1978) pp 196-201

Nakamura, K; Kazumi, M. "SH-type and Rayleigh-type surface waves on rotated Y-cut LiTaO₃." Faculty of Engng., Tohoku Univ., Sendai, Japan; 1977 Ultrasonics Symposium Proceedings, Phoenix, AZ, USA, 26-28 Oct. 1978, (New York, USA: IEEE 1977) pp 819-22

O'Connell, R.M.; Slobodnik, A.J., Jr.; Carr, P.H. "Material choice for optimum SAW device performance" Deputy for Electronic Technol., Hanscom AFB, MA, USA; Agard Conference Proceedings No. 230. Impact of Charge Coupled Devices and Surface Acoustic Wave Devices on Signal Processing and Imagery in Advanced Systems, Ottawa, Canada, 11-15 Oct. 1977 (Neuilly-sur-Seine, France: AGARD 1978) pp 2.1/1-19.

O'Connell, R.M.; Carr, P.H. "Progress in closing the lithium niobate-ST cut quartz piezoelectric coupling gap." Rome Air Dev. Center, Deputy for Electronic Technol., Hanscom AFB MA, USA, 31 May - 2 June 1978 (Washington, D.C., USA Electronic Industries Assoc. 1978) pp 189-95

O'Connell, R.M. "A New Cut of Quartz with Orthogonal Temperature-Compensated Propagation Directions for Surface Acoustic Wave Applications." Rome Air Development Center; 31st Annual Symposium on Frequency Control, US Army Electronics Command, Fort Monmouth, NJ, pp 402-405 (1977). Copies available from the Electronic Industries Association, 2001 Eye Street, N.W. Washington D.C. 20006

Oliner, A.A. (Ed.) "Acoustic surface waves." Berlin, Germany: Springer-Verlag (1978), 350 pp

Parker, T.E.; Wichansky, H. "Temperature-compensated surface-acoustic-wave devices with SiO₂ film overlays." Raytheon Res. Div., Waltham, MA, USA; J. Appl. Phys. (USA), vol. 50, no. 3, pt. 1, pp 1360-9 (March 1979)

Parker, T.E.; Lee, D.L. "Stability of Phase Shift on Quartz SAW Devices." 31st Annual Symposium on Frequency Control, US Army Electronics Command, Fort Monmouth, NJ, pp 379-387 (1977). Copies available from the Electronic Industries Association, 2001 Eye Street, N.W. Washington D.C. 20006

Schwelb, C.; Adler, E.L.; Farnell, G.W. "Effect of anisotropy on waveguide modes in SAW resonators." Dept. of Electrical Engng., Concordia Univ., Montreal, Canada; 1977 Ultrasonics Symposium Proceedings, Phoenix, AZ, USA, 26-28 Oct. 1978, (New York USA: IEEE 1977) pp 867-72

Sinha, B.K.; Tiersten, H.F. "On the temperature dependence of the velocity of surface waves in quartz." Dept. of Mech. Engng., Aeronautical Engng. & Mech., Rensselaer Polytech. Inst., Troy, NY, USA; 1978 Ultrasonics Symposium Proceedings, Cherry Hill, NJ, USA, 25-27 Sept. 1978 (New York, USA: IEEE 1978) pp 662-6

Tanski, W.J. "Developments in resonators on quartz." Sperry Res. Center, Sudbury, MA, USA; 1977 Ultrasonics Symposium Proceedings, Phoenix, AZ, USA, 26-28 Oct. 1978 (New York, USA: IEEE 1977) pp 900-4

Tanski, W.J. "Surface acoustic wave resonators on quartz." Sperry Res. Center, Sudbury, MA, USA; IEEE Trans. Sonics & Ultrason. (USA), vol. SU.26, no. 2, pp 93-104 (March 1979)

Tanski, W.J.; Wittels, N.D. "SEM observations of SAW resonator transverse modes" Sperry Res. Center, Sudbury, MA, USA; Appl. Phys. Lett. (USA), vol. 34, no. 9, pp 537-9 (1 May 1979)

Tanski, W.J. "GHz SAW Resonators" Sperry Res. Center, Sudbury, MA, USA; Ultrasonics Symposium Proceedings, New Orleans, LA, USA, 26-28 Sept. 1979 (New York, USA: IEEE 1979) pp 815-823

Vandeweghe, J.; Lagasse, P.E.; Tromp, H.; Hoffman, G.; Naten, T.; Slecckx, F. "Acoustic surface wave resonators for broadband applications." Lab for Electromagnetism & Acoustics, Univ. of Gent, Gent, Belgium; Proceedings of the 8th European Microwave Conference, Paris, France, 4-8 Sept. 1978 (Sevenoaks, England: Microwave Exhibitions & Publishers Ltd. 1978) pp 663-7

Vandeweghe, J.; Lagasse, P.E.; Naten, T. "Distributed feedback acoustic surface wave resonators." Lab. Electromagnetism & Acoustics, Univ. of Gent, Gent, Belgium; 1978 Ultrasonics Symposium Proceedings, Cherry Hill, NJ, USA, 25-27 Sept. 1978 (New York, USA: IEEE 1978) pp 438-41

Vetelino, J.F.; Jhunjhunwala, A.; Field, J.C. "The surface acoustic wave properties of bismuth silicon oxide." Dept. of Electrical Engng., Univ. of Maine, Orono, ME, USA; 1977 Ultrasonics Symposium Proceedings, Phoenix, AZ, USA, 26-28 Oct. 1978 (New York, USA: IEEE 1977) pp 675-8

Williams, D.F.; Cho, F.Y. "Numerical Analysis of Double Rotated Cut SAW Devices." Motorola Government Electronics Division, Scottsdale, AZ 85252; Ultrasonics Symposium Proceedings, New Orleans, LA, USA, 26-28 Sept. 1979 (New York, USA: IEEE 1979) pp 627-631

Yamanouchi, K.; Iwahashi, K.; Shibayama, K. "Temperature dependence of Rayleigh waves and piezoelectric leaky surface waves in rotated Y-cut LiTaO₃ and SiO₂/LiTaO₃ structures." Res. Inst. of Electrical Communication, Tohoku Univ. Sendai, Jpn. Wave Electron (Netherlands), vol. 3, no. 4, pp 319-33 (April 1979)

Yashiro, J.; Goto, N.
 "Analysis of bulk waves in surface-acoustic wave devices." Dept. of Electrical & Electronic Engng. Tokyo Inst. of Technol., Tokyo, Japan; IEE J. Microwave Opt. & Acoust. (GB), vol. 2, no. 6, pp 187-93 (Nov. 1978)

1.3

Bahadur, H.; Parshad, R.
 "Some new findings on the effect of nuclear and X-irradiation on the oscillating characteristics of quartz crystals." Nat. Phys. Lab., New Delhi, India; Indian J. Phys. Part A vol. 53A, no. 1-2, pp 239-59 (Jan-March 1979)

Euler, F.; Ligor, P.; Kahan, A.; Pellegrini, P.; Flanagan, T.M.; Wrobel, T.F.
 "Steady state radiation effects in precision quartz resonators." Deputy for Electronic Technol. Hanscom AFB, MA, USA; Proceedings of the 32nd Annual Symposium on Frequency Control 1978, Atlantic City, NJ, USA, 31 May - 2 June 1978 (Washington, D.C., USA: Electronic Industries Assoc. 1978) pp 24-33

Koehler, D.R.; Young, T.J.; Adams, R.A.
 "Radiation induced transient thermal effects in 5 MHz AT-cut quartz resonators." Sandia Labs., Albuquerque, NM, USA; 1977 Ultrasonics Symposium Proceedings, Phoenix, AZ, USA, 26-28 Oct. 1978 (New York, USA: IEEE 1977) pp 877-81

Koehler, D.R.
 "Radiation Induced Frequency Transients in AT, BT and SC Cut Quartz Resonators." Sandia Laboratories; 31st Annual Symposium on Frequency Control, US Army Electronics Command, Fort Monmouth, NJ, pp 118-121 (1977). Copies available from the Electronic Industries Association, 2001 Eye Street, N.W. Washington D.C. 20006

Lipson, H.G.; Euler, F. Ligor, P.A.
 "Radiation Effects in Swept Premium-Q Quartz Material, Resonators and Oscillators." Rome Air Development Center; 31st Annual Symposium on Frequency Control, US Army Electronics Command, Fort Monmouth, NJ, pp 122-133 (1977). Copies available from the Electronic Industries Association, 2001 Eye Street, N.W. Washington D.C. 20006

Martin, J.J.; Halliburton, L.E.; Markes, M. Koumvakalis, N.; Sibley, W.A. & Brown, R.N.; Armington, A.
 "Radiation-Induced Mobility of Interstitial Ions in Synthetic Quartz." Oklahoma State University, and Rome Air Development Center; 31st Annual Symposium on Frequency Control, US Army Electronics Command, Fort Monmouth, NJ pp 134-147 (1977). Copies available from the Electronic Industries Association, 2001 Eye Street, N.W. Washington D.C. 20006

Pellegrini, P.; Euler, F.; Kahan, A.; Flanagan, T.M.; Wrobel, T.F.
 "Steady-state and transient radiation effects in precision quartz oscillators." Rome Air Dev. Center, Hanscom AFB, MA, USA; IEEE Trans. Nucl. Sci., (USA), vol. ns. 25, no. 6, pp 1267-73 (Dec. 1978) (IEEE Annual Conference on Nuclear and Space Radiation Effects, Albuquerque, NM, USA, 18-21 July 1978)

Young, T.J.; Koehler, D.R.; Adams, R.A.
 "Radiation induced frequency and resistance changes in electrolyzed high purity quartz resonators." Sandia Labs., Albuquerque, NM, USA; Proceedings of the 32nd Annual Symposium on Frequency Control 1978, Atlantic City, NJ, USA, 31 May - 2 June 1978 (Washington D.C., USA: Electronic Industries Assoc 1978) pp 34-42

1.4

Ang, D.
 "A Microprocessor Assisted Anodizing Apparatus for Frequency Adjustment." Tyco Crystal Products; 31st Annual Symposium on Frequency Control, US Army Electronics Command, Fort Monmouth, NJ, pp 364-367 (1977). Copies available from the Electronic Industries Association, 2001 Eye Street, N.W. Washington D.C. 20006

Bloch, M.B.; Meirs, M.P.; Strauss, A.
 "Results of temperature slewing quartz crystals for anomalous responses." Frequency Electronics Inc., New Hyde Park, NY, USA; Proceedings of the 32nd Annual Symposium on Frequency Control 1978, Atlantic City, NJ, USA, 31 May - 2 June 1978 (Washington, D.C., USA: Electronic Industries Assoc. 1978) pp 344-53

Brandmayr, R.; Filler, R. Vig, J.
 "Etching Studies on Quartz" USAERADCOM; 31st Annual Symposium on Frequency Control, US Army Electronics Command, Fort Monmouth, NJ, pp 351-358 (1977). Copies available from the Electronic Industries Association, 2001 Eye Street, N.W. Washington D.C. 20006

Clastre, J.; Pegeot, C.; Leroy, P.Y.
 "Goniometric measurements of the angles of cut of doubly rotated quartz plates." Univ. de Bordeaux, Talence, France; Proceedings of the 32nd Annual Symposium on Frequency Control 1978, Atlantic City NJ, USA, 31 May - 2 June 1978 (Washington, D.C., USA: Electronic Industries Assoc. 1978) pp 310-16

Darces, J.F.; Merigoux, H.
 "Final X-ray control of the orientation of round or rectangular quartz slides for industrial purposes." Lab. de Cristallographic, Univ. de Franche-Comte, Besancon, France; Proceedings of the 32nd Annual Symposium on Frequency Control 1978, Atlantic City, NJ, USA, 31 May - 2 June 1978 (Washington, D.C., USA: Electronic Industries Assoc. 1978) pp 304-9

Dolochycki, S.J.; Staples, E.J.; Wise, J.; Schoenwald, J.S.; Lim, T.C.
"Hybrid SAW Oscillator Fabrication and Packaging" Science Center, Rockwell International; 31st Annual Symposium on Frequency Control, US Army Electronics Command, Fort Monmouth, NJ pp 274-78 (1977). Copies available from the Electronic Industries Association, 2001 Eye Street, N.W. Washington D.C. 20006

Dworsky, L.N.
"Discrete element modelling of AT-quartz devices." Motorola Inc., Plantation, FL, USA; Proceedings of the 32nd Annual Symposium on Frequency Control 1978, Atlantic City, NJ, USA, 31 May - 2 June 1978 (Washington, D.C., USA: Electronic Industries Assoc. 1978) pp 142-9

Dybwad, G.L.
"Simplified fixtures with improved thin film deposition uniformity on quartz crystals." Bell Telephone Labs. Inc., Allentown, PA, USA; Proceedings of the 32nd Annual Symposium on Frequency Control 1978, Atlantic City, NJ, USA, 31 May - 2 June 1978 (Washington D.C., USA: Electronic Industries Assoc. 1978) pp 286-9

Filler, R.L.; Vig, J.R.; Frank, J.M.; Peters, R.D.
"Polyimide bonded resonators." US Army Electronics Technol. & Devices Lab., Fort Monmouth, NJ, USA; Proceedings of the 32nd Annual Symposium on Frequency Control 1978, Atlantic City, NJ, USA: Electronic Industries Assoc. 1978) pp 290-8

Fuchs, D.
"Basic considerations on metal canned enclosures for the encapsulation of quartz crystal units." Jenaer Glaswerk Schott & Gen., Landshut, Germany; Proceedings of the 32nd Annual Symposium on Frequency Control 1978, Atlantic City, NJ, USA: 31 May - 2 June 1978 (Washington D.C., USA: Electronic Industries Assoc. 1978) pp 321-5

Fuchs, D.
"New Metal Enclosures for Resistance Welding Developed to Meet MIL-Specifications." Jenaer Glaswerk Schott & Gen.; 31st Annual Symposium on Frequency Control, US Army Electronics Command, Fort Monmouth NJ, pp 186-188 (1977). Copies available from the Electronic Industries Association, 2001 Eye Street, N.W. Washington D.C. 20006

Hartemann, P.
"Microwave surface-acoustic-wave components." Thomson-CSF Res. Center, Orsay, France; Agard Conference Proceedings No. 230. Impact of Charge Coupled Devices and Surface Acoustic Wave Devices on Signal Processing and Imagery in Advanced Systems, Ottawa, Canada, 11-15 Oct. 1977 (Neuilly-sur-Sein, France: AGARD 1978) pp 212/1-9

Hickernell, F.S.; Bush, H.J.
"The monolithic integration of surface acoustic wave and semiconductor circuit elements on silicon for matched filter device development." Motorola Government Electronics Div., Scottsdale, AZ, USA; Agard Conference Proceedings No. 230. Impact of Charge Coupled Devices and Surface Acoustic Wave Devices on Signal Processing and Imagery in Advanced Systems, Ottawa, Canada, 11-15 Oct. 1977 (Neuilly-sur-Seine, France: AGARD 1978) pp 3.5/1-13

Kagiwada, R.S.; Yen, K.H.; Lau, K.F.
"High frequency SAW devices on $\text{AlN}/\text{Al}_2\text{O}_3$." TRW Defense & Space Systems Group, Redondo Beach, CA, USA; 1978 Ultrasonics Symposium Proceedings, Cherry Hill, NJ, USA, 25-27 Sept. 1978 (New York, USA: IEEE 1978) pp 598-601

Kasai, T.; Noda, J.; Suzuki, J.
"Lapping characteristics of LiTaO_3 single crystals: study on precision machining of opto-electronic crystals. I." J. Jpn. Soc. Precis. Eng. (Japan), vol. 44, no. 11, pp 1360-6 (Nov. 1978) In Japanese.

Kobayashi, Y.
"Fully automated piezgoniometer (automatic quartz plate classifier)." Rigaku Corp., Tokyo, Japan; Proceedings of the 32nd Annual Symposium on Frequency Control 1978, Atlantic City, NJ, USA, 31 May - 2 June 1978 (Washington, D.C., USA: Electronic Industries Assoc. 1978) pp 317-20

MacDonald, D.B.; Shaffer, C.F.; Blocker, T.G., III; Vail, R.C.
"Development of a two-step E-beam lithography process for submicron surface acoustic wave (SAW) device fabrication." Texas Instruments, Dallas, TX, USA; Opt. Eng. (USA), vol. 18, no. 1, pp 53-8 (Jan-Feb 1979)

Ney, R.J.; Hafner, E.
"Continuous Vacuum Processing System for Precision Quartz Crystal Units." General Electric Neutron Devices Department & USAERADCOM; 31st Annual Symposium on Frequency Control, US Army Electronics Command, Fort Monmouth, NJ, pp 368-373 (1977). Copies available from the Electronic Industries Association, 2001 Eye Street, N.W. Washington D.C. 20006

Nickols, S.E.; Fay, R.M.
"Bonding of piezoelectric materials." IBM Corp., Armonk, NY, USA; IBM Tech. Disclosure Bull. (USA) vol. 21, no. 7, pp 2986 (Dec. 1978)

Oguchi, K.; Momosaki, E.
" $+50^\circ$ X micro quartz resonator by lithographic process." Res. & Dev. Dept., Suwa Seikosha Co. Ltd., Suwa, Japan; Proceedings of the 32nd Annual Symposium on Frequency Control 1978, Atlantic City, NJ, USA, 31 May - 2 June 1978 (Washington, D.C., USA: Electronic Industries Assoc. 1978) pp 277-81

Peschl, H.
"The quartz (crystal): Assembly, operation and properties. II." Funkschau (Germany), vol. 51, no. 8, pp 451-4 (12 April 1979) In German. For pt. I see ibid., vol. 51, no. 7, pp 369 (1979)

xeche, J.J.H.

"Frequency tuning of quartz resonators by plasma anodization." Proceedings of the 32nd Annual Symposium on Frequency Control 1978, Atlantic City, NJ, USA, 31 May - 2 June 1978 (Washington D.C., USA:Electronic Industries Assoc. 1978) pp 299-303

Suda, P.; Zumsteg, A.E.; Zingg, W.
Anisotropy of Etching Rate for Quartz in Ammonium Bifluoride." SSIH QUARTZ Division; 31st Annual Symposium on Frequency Control, US Army Electronics Command, Fort Monmouth, NJ, pp 359-363 (1977). Copies available from the Electronic Industries Association, 2001 Eye Street, N.W. Washington D.C. 20006

Tanski, W.J.

"SAW resonators at 1.29 GHz with Q values approaching the material limit." Sperry Res. Center, Sudbury, MA, USA; Electron. Lett. (GB), vol. 15, no. 12, pp 339-40 (7 June 1979)

Warner, A.; Goldfrank, B.; Meirs, M.; Rosenfeld, M.
"Low 'g' Sensitivity Crystal Units and Their Testing." Frequency Electronics, Inc.; 31st Annual Symposium on Frequency Control, US Army Electronics Command, Fort Monmouth, NJ, pp 306-310 (1977). Copies available from the Electronic Industries Association, 2001 Eye Street, N.W. Washington D.C. 20006

Wilhelmy, H.J.

"A man and his work: Jurgen Staudte and the crystal tuning fork." Elektronik (Germany), vol. 28, no. 1, pp 38-42 (11 Jan 1979) In German

Yamashita, S.; Echigo, N.; Kawamura, Y.; Watanabe, A.; Kubota, K.
"A 4.19 MHz beveled miniature rectangular AT-cut quartz resonator." Daini Seikosha Co. Ltd., Tokyo, Japan; Proceedings of the 32nd Annual Symposium on Frequency Control 1978, Atlantic City, NJ, USA, 31 May - 2 June 1978 (Washington, D.C., USA: Electronic Industries Assoc. 1978) pp 267-76

1.5

Albsmeier, M.H.

"Mechanical filters in communications systems." Siemens AG, Munich, Germany; Rev. HF (Belgium), vol. 11, no. 1-2, pp 44-9 (1979)

Deschamps, R.G.

"Evidence for the existence of poles on the attenuation frequency curve of a magnetostrictive bar filter and calculation of the corresponding characteristics." Soc. Anonyme de Telecommunications, Paris, France; C.R. Hebd. Seances Acad. Sci, Ser. B (France), vol. 287, no. 9, pp 231-4 (16 Oct. 1978) In French

Gunther, A.E.; Albsmeier, H.; Traub, K.
"Mechanical channel filters meeting CCITT specification." Geschäftsbereich Weitverkehrstechn., Siemens AG, München, Germany; Proc. IEEE (USA), vol. 67, no. 1, pp 102-8 (Jan. 1979)

Hribsek, M.F.

"The Design and Application of Electromechanical Single Silicon Beam Filters." University of Belgrade; 31st Annual Symposium on Frequency Control, US Army Electronics Command, Fort Monmouth, NJ, pp 173-175 (1977). Copies available from the Electronic Industries Association, 2001 Eye Street, N.W. Washington D.C. 20006

Kawana, T.; Kawahata, H.

"Preshift Mechanical Filter for Voice Frequency Telegraph Transmission System." Transmission Division, Nippon Electric Co., Ltd., Kawasaki, Japan; Ultrasonics Symposium Proceedings, New Orleans, LA, USA, 26-28 Sept 1979 (New York, USA: IEEE 1979), pp 119-122

Onoe, M.

"Crystal, ceramic, and mechanical filters in Japan" Inst. of Industrial Sci., Univ. of Tokyo, Tokyo, Japan; Proc. IEEE (USA), vol. 67, no. 1, pp 75-102 (Jan 1979)

Sato, N.; Yakuwa, K.; Kazama, K.; Fujisaki, M.
"A pole-type mechanical filter channel bank." Nippon Telegraph & Telephone Public Corp., Tokyo, Japan; NTC 78. Conference Record of the IEEE 1978 National Telecommunications Conference, Pt. II, Birmingham, AL, USA, 3-6 Dec. 1978 (New York, USA: IEEE 1978), pp 30.4/1-5

Schultz, J.J.

"Economical diode-switched crystal filters." CQ Radio Amat. J. (USA) vol. 34, no. 7, pp 33-5, 91 (July 1978)

Zmudzki, B.

"Piezoelectric tuning fork filters." Elektronika (Poland), vol. 19, no. 12, pp 525-6 (1978). In Polish

1.5.1

Allemandou, P.; Beaudet, D.

"Design of mechanical filters having attenuation poles." Ecole Polytech., Paris, France; Onde Electr. (France), vol. 59, no. 1, pp 59-61 (Jan. 1979) In French

Fleischmann, U.

"Calibration of quartz filters with adjustable bandwidth." Funkschau (Germany) vol. 51, no. 1, pp 41-2 (5 Jan 1979) In German

Hardcastle, J.A.

"Ladder crystal filter design." Radio Commun, (GB), vol. 55, no. 2, pp 116-20 (Feb. 1979). For previous pt. see ibid, vol. 53, no. 9, pp 687 (1977)

Swanson, T.W.; Herzig, P.A.

"A polyolithic crystal filter employing a Rhodes transfer function." ECI Div., E-Systems, St. Petersburg, FL, USA; Proceedings of the 32nd Annual Symposium on Frequency Control 1978, Atlantic City, NJ, USA, 31 May - 2 June 1978 (Washington, DC, USA: Electronic Industries Assoc. 1978) pp 233-42

Lafevre, M.R.

"State of the art and new developments in piezo-electric monolithic filters." CNET, Paris, France; Rev. HF (Belgium), vol. 11, no. 1-2, p. French (1979).

Lefevre, R.

"Monolithic Crystal Filters With Very High Q Factor and Low Spurious Level." CNET; 31st Annual Symposium on Frequency Control, US Army Electronics Command, Fort Monmouth, NJ, pp 148-158 (1977). Copies available from the Electronic Industries Association, 2001 Eye Street, N.W. Washington D.C. 20006

Makino, T.; Hashima, A.

"A highly stabilized MIC Gunn oscillator using a dielectric resonator." Wireless Res. Lab., Matsushita Electric Industrial Co. Ltd., Osaka, Japan; IEEE Trans. Microwave Theory & Tech. (USA), vol. MTT-27, no. 7, pp 633-8 (July 1979)

McLean, D.I.; Graziani, A.F.; Royer, J.J.

"New Discrete Crystal Filters for Bell System Analog Channel Banks." Bell Telephone Laboratories; 31st Annual Symposium on Frequency Control, US Army Electronics Command, Fort Monmouth, NJ, pp 166-172 (1977). Copies available from the Electronic Industries Association, 2001 Eye Street, N.W. Washington D.C. 20006

Neubig, B.

"Monolithic quartz filters" Tech. Univ., Berlin, Germany; Funkschau (Germany), vol. 50, no. 10, pp 438-41 (5 May 1978). In German

Watanabe, N.; Tsukamoto, K.

"A torsional mode 10-element pole-type mechanical channel filter." Musashino Electrical Communication Lab., NTT, Musashino, Japan; Trans. Inst. Electron. & Commun. Eng. Jpn. Sect. E (Japan), vol. E61, no. 8, pp 642-3 (Aug. 1978)

Sawamoto, K.; Watanabe, N.; Tsukamoto, K.

"A torsional mode even elements pole-type mechanical channel filter." Electr. Commun. Lab. Tech. J. (Japan), vol. 27, no. 8, pp 1689-702 (1978). In Japanese,

Schreckenbach, W.;

"Design and materials requirements for monolithic, multiple-electrode crystal filters, using ceramics, with special reference to filters for 10.7 MHz." VEB Keramische Werke, Hermsdorf, Germany; Hermsdorfer Tech. Mitt. (Germany), vol. 19, no. 53, pp 1701-4 (May 1979). In German.

Sekine, T., Konno, M.; Sugawara, S.

"A mechanical filter with two attenuation poles consisting of three resonators." Faculty of Engng. Gifu Univ., Kakumuhara, Japan; Trans. Inst. Electron. & Commun. Eng. Jpn. Sect. E (Japan), vol. E61, no. 7, pp 549 (July 1978)

Siffert, P.; Kerboul, J.

"A selective linear phase crystal filter." Service Filtrés de la Compagnie d'Electronique et de Piezo-Electricite, Sartrouville, France; Proceedings of the 32nd Annual Symposium on Frequency Control 1978 Atlantic City, NJ, USA, 31 May - 2 June 1978 (Washington, D.C., USA: Electronic Industries Assoc. 1978) pp 244-9

Simmonds, T.H., Jr.

"The evolution of the discrete crystal single-sideband selection filter in the Bell System." Bell Labs., North Andover, MA, USA; Proc. IEEE (USA), vol. 67, no. 1, pp 109-15 (Jan 1979)

Siwa, M.

"Crystalline piezoelectric filters." Elektronika (Poland), vol. 19, no. 11, pp 456-62 (1978) In Polish.

Smythe, R.D.

"Some recent advances in integrated crystal filters" Piezo Technol, Inc., Orlando, FL, USA; Proceedings of the 32nd Annual Symposium on Frequency Control 1978, Atlantic City, NJ, USA, 31 May - 2 June 1978 (Washington, D.C., USA: Electronic Industries Assoc. 1978) pp 220-32

Sugawara, S.; Konno, M.

"Spurious responses and their suppression in torsional mode mechanical filter." Faculty of Engng., Yamagata Univ., Yonezawa, Japan; Trans. Inst. Electron. & Commun. Eng. Jpn. Sect. E (Japan), vol. E61, no. 9, pp 737-8 (Sept. 1978)

Sugawara, S.; Konno, M.

"Spurious responses and their suppression in the mechanical filter with flexure mode resonators." Faculty of Engng., Yamagata Univ., Yonezawa, Japan; Trans. Inst. Electron. & Commun. Eng. Jpn. Sect. E (Japan), vol. E61, no. 11, pp 911-12 (Nov. 1978)

Uno, T.

"A LiTaO₃ monolithic crystal filter by parallel field excitation." Yokosuka Elect. Communication Lab., NTT, Yokosuka, Japan; Trans. Inst. Electron. & Commun. Eng. Jpn. Sect. E (Japan), vol. E61, no. 11, pp 915-16 (Nov. 1978)

Yakuwa, K.; Kojima, T.; Okuda, S.; Shirai, K.; Kasai, Y.

"A 128-kHz mechanical channel filter with finite-frequency attenuation poles." Fujitsu Ltd., Kawasaki, Japan; Proc. IEEE (USA), vol. 67, no. 1, pp 115-19 (Jan 1979)

Zelenka, J.

"A monolithic filter employing thickness dilational modes of vibration." Electrical Engng. Dept., Mech. & Textile Engng. Coll., Liberec, Czechoslovakia; TESLA Electron. (Czechoslovakia), vol. 11, no. 4, pp 105-110 (Dec. 1978)

"Cheap crystal filter" Elektor (GB), vol. 4, no. 7-8, pp 58-9 (July-Aug. 1978)

Berzelius

"Filters for surface waves." *Radioind. Electron.-Telev. (Italy)*, vol. 3, no. 4, pp 197-201 (April 1979) In Italian.

Bidenko, V.A.; Grankin, I.M.; Nelin, E.A.; Progrebnyak, V.P.

"Synthesis of surface acoustic wave filters with asymmetric amplitude-frequency response." *Izv. VUZ Radioelektron (USSR)*, vol. 22, no. 5, pp 87-8 (May 1979) In Russian

Biran, A.; Chalzel, A.; Gafni, H.

"Low-Sidelobe SAW Cascade Filter." *RAFAEL - Armament Development Authority, Ministry of Defense, Haifa, Israel; Ultrasonics Symposium Proceedings, New Orleans, LA, USA, 26-28 Sept 1979 (New York, USA: IEEE 1979) pp 570-573*

Carr, P.H.

"Systems applications of SAW filters and delay lines." Deputy for Electronic Technol. Hanscom AFB, MA, USA; Agard Conference Proceedings No. 230. Impact of Charge Coupled Devices and Surface Acoustic Wave Devices on Signal Processing and Imagery in Advanced Systems, Ottawa, Canada, 11-15 Oct. 1977 (Neuilly-sur-Seine, France: AGARD 1978) pp 3.4/1-12

Chiba, T.

"SAW filter as applied to the group-delay equalizer in the TV relay station transmitter." *NHK (Japan Broadcasting Corporation) Technical Research Laboratories, Kinuta, Setagaya, Tokyo, Japan 157. Ultrasonics Symposium Proceedings, New Orleans, LA, USA, 26-28 Sept 1979 (New York, USA: IEEE 1979) pp 545-549*

Coldren, L.A.; Rosenberg, R.L.; Rentschler, J.A.

"Monolithic transversely coupled SAW resonator filters." *Bell Labs., Holmdel, NJ, USA; 1977 Ultrasonics Symposium Proceedings, Phoenix, AZ, USA, 26-28 Oct. 1978 (New York, USA: IEEE 1977) pp 888-93*

Coldren, L.A.; Rosenberg, R.L.

"Surface-acoustic-wave resonator filters." *Bell Labs., Holmdel, NJ, USA; Proc. IEEE (USA) vol. 67, no. 1, pp 147-58 (Jan 1979)*

Coldren, L.A.

"The temperature dependence of SAW resonator filters using folded acoustic coupling." *Bell Labs., Holmdel, NJ, USA; Ultrasonics Symposium Proceedings, New Orleans, LA, USA, 26-28 Sept 1979 (New York, USA: IEEE 1979) pp 830-835*

Cross, P.S.

"Surface acoustic wave resonator-filters using tapered gratings." *Bell Telephone Labs., Holmdel, NJ, USA; 1977 Ultrasonics Symposium Proceedings, Phoenix, AZ, USA, 26-28 Oct. 1978 (New York, USA: IEEE 1977) pp 894-9*

Cuozzo, F.C.

"Numerical simulation of SAW interdigital filters using an equivalent electrical model." *IBM CER, La Gaude, France; 1977 Ultrasonics Symposium Proceedings, Phoenix, AZ, USA, 26-28 Oct. 1978 (New York, USA: IEEE 1977) pp 642-7*

Desbois, J.

"The Problem of the Accuracy in the Fabrication of Multipole SAW Resonator Filters." *Thomson-CSF, ASM Division, 06802 Cagnes-sur-Mer France; Ultrasonics Symposium Proceedings, New Orleans, LA, USA, 26-28 Sept. 1979 (New York, USA: IEEE 1979) pp 841-844*

Drummond, B.

"A 24 MHz Nyquist SAW filter for the 1450 demodulator." *Tekscope (USA)*, vol. 10, no. 3, pp 10-12 (1978)

Drummond, B.

"Surface-acoustic wave filters for broadcast demodulators." *Tektronix UK Ltd., London, England; Electron. Ind. (GB)*, vol. 5, no. 6, pp 59, 61 (June 1979)

Gerard, H.M.; Yao, P.S.; Otto, O.W.

"Performance of a programmable radar pulse compression filter based on a chirp transformation with RAC filters." *Hughes Aircraft Co., Fullerton, CA, USA; 1977 Ultrasonics Symposium Proceedings, Phoenix, AZ, USA, 26-28 Oct. 1978 (New York, USA: IEEE 1977) pp 947-57*

Gerard, H.M.

"Principles of surface wave filter design." *Hughes Aircraft Co., Fullerton, CA, USA; In book: Acoustic surface waves, A.A. Oliner (Ed.), pp 61-96. Berlin, Germany: Springer-Verlag (1978), 350 pp*

Halgas, F.A.; Godfrey, J.T.; Sundelin, R.; Moore, R.A.; Weinert, R.W.; Isaacs, T.J.

"Comparative performance of SAW filters on sulfosalt versus quartz substrates." *Systems Dev. Div. Westinghouse Electric Corp., Baltimore, MD, USA; 1977 Ultrasonics Symposium Proceedings, Phoenix, AZ, USA, 26-28 Oct. 1978 (New York, USA: IEEE 1977) pp 798-802*

Haspel, M.

"Surface-acoustic-wave dispersive filter implementation of quasi-linear FM matched filter pairs." *Elta Electronics Industries Ltd., Ashdod, Israel; 1977 Electrical and Electronics Engineers in Israel Tenth Convention, TelAviv, Israel, 10-13 Oct. 1977 (New York, USA, IEEE 1978) pp 231-6*

Hickernell, F.S.; Olson, D.E.; Adamo, M.D.; Bush, H.J.

"Monolithic surface wave transversal filter." *Motorola Government Electronics Div., Scottsdale, AZ, USA; 1977 Ultrasonics Symposium Proceedings, Phoenix, AZ, USA, 26-28 Oct. 1978 (New York, USA: IEEE 1977) pp 615-18*

- Hohkawa, K.; Yoshikawa, S.; Ishihara, F.
"Surface acoustic wave filters without apodization loss." Musashino Electrical Communication Lab., NTT, Musashino, Japan; Trans. Inst. Electron. & Commun. Eng. Jpn. Sect. E. (Japan), vol. E62, no. 2, pp 91-2 (Feb. 1979)
- Huber, C.; Lane, J.; Newman, B.A.; Godfrey, J.T.; Grauling, C.H.; Moore, R.A.
"A low sidelobe SAW contiguous (sic) filterbank using MDC LiTaO₃." Systems Dev. Div., Westinghouse Electric Corp., Baltimore, MD, USA; 1977 Ultrasonics Symposium Proceedings, Phoenix, AZ, USA, 26-28 Oct. 1978 (New York, USA: IEEE 1977) pp 568-72
- Jack, M.A.; Paige, E.G.S.
"Fourier transformation processors based on surface acoustic wave chirp filters." Dept. of Electrical Engng., Univ. of Edinburgh, Edinburgh, Scotland; Wave Electron. (Netherlands), vol. 3, no. 3, pp 229-47 (Nov. 1978)
- Kodama, T.
"Optimization Techniques for SAW Filter Design." Toshiba Research and Development Center, Toshiba Corporation, Kawasaki, 210 Japan; Ultrasonics Symposium Proceedings, New Orleans, LA, USA, 26-28 Sept 1979 (New York, USA: IEEE 1979) pp 522-526
- Kosck, M.
"Influence of manufacturing inaccuracies on transmission properties of acoustic surface wave filters" Coll. of Mech. & Textile Engng., Liberec, Czechoslovakia; TESLA Electron. (Czechoslovakia), vol. 11, no. 1, pp 27-8 (March 1978)
- MacDonald, D.B.
"Fabrication of L-band pulse compression filters." Texas Instruments, Dallas, TX, USA; 1977 Ultrasonics Symposium Proceedings, Phoenix, AZ, USA, 26-28 Oct. 1978 (New York, USA: IEEE 1977) pp 792-7
- Malocha, D.C.; Wilkus, S.
"Low loss capacitively weighted TV IF filter." Advanced Technol. Lab., Texas Instruments Ind., Dallas, TX, USA; 1978 Ultrasonics Symposium Proceedings, Cherry Hill, NJ, USA, 25-27 Sept. 1978 (New York, USA: IEEE 1978) pp 500-3
- Milsom, R.F.
"A diffraction theory for SAW filters on non-parabolic high-coupling orientations." Allen Clark Res. Centre, Plessey Co. Ltd., Caswell, Towchester, England; 1977 Ultrasonics Symposium Proceedings, Phoenix, AZ, USA, 26-28 Oct., 1978 (New York, USA: IEEE 1977) pp 827-33
- Minowa, J.; Nakagawa, K.; Okuno, K.; Kobayashi, Y.; Morimoto, M.
"400 MHz SAW timing filter for optical fiber transmission systems." Yokosuka Electrical Communication Lab., Nippon Telegraph & Telephone Public Corp., Yokosuka, Japan; 1978 Ultrasonics Symposium Proceedings, Cherry Hill, NJ, USA, 25-27 Sept. 1978 (New York, USA: IEEE 1978) pp 490-3
- Hiyashiro, F.
"TV SAW filters utilize X-112⁰Y.LiTaO₃ crystals." Toshiba R&D Center, Kawasaki, Japan; JEE (Japan), no. 137, pp 46-7, 56-7, 70 (May 1978)
- Moule, G.I.; Newton, C.O.; Paige, E.G.S.
"Performance of a surface acoustic wave variable slope chirp filter." Royal Signals & Radar Establ., Malvern, England; 1977 Ultrasonics Symposium Proceedings, Phoenix, AZ, USA, 26-28 Oct. 1978 (New York, USA: IEEE 1977) pp 611-14
- Nishiyama, S.; Otomo, J.
"400 MHz SAW filters achieved with LiNbO₃." Nihon Dempa Kogyo Co. Ltd., Saitama, Japan; JEE (Japan), no. 137, pp 48-51 (May 1978)
- Nonaka, H.; Arai, S.; Ieki, H.
"ZnO thin films provides economical SAW filters." Murata Mfg. Co. Ltd., Koyoto, Japan; JEE (Japan), no. 137, pp 36-8 (May 1978)
- Noro, Y.; Hazama, K.
"Surface acoustic wave filters." Solid State Phys. (Japan), vol. 13, no. 6, pp 359-65 (June 1978). In Japanese
- Potter, B.R.
"L-Band Low Loss Filters" Texas Instruments; 31st Annual Symposium on Frequency Control, US Army Electronics Command, Fort Monmouth, NJ, pp 396-401 (1977). Copies available from the Electronic Industries Association, 2001 Eye Street, N.W. Washington D.C. 20006
- Potter, B.R.
"L-Band Low-Loss SAW Filters." Texas Instruments Incorporated, MS 88, P.O. Box 226015, Dallas, TX 75266; Ultrasonics Symposium Proceedings, New Orleans, LA, USA, 26-28 Sept 1979 (New York, USA: IEEE 1979) pp 533-536
- Rosenberg, R.L.; Coldren, L.A.
"Fast synthesis of finite-loss SAW resonator filters." Bell Labs., Holmdel, NJ, USA; 1977 Ultrasonics Symposium Proceedings, Phoenix, AZ, USA, 26-28 Oct. 1978 (New York, USA: IEEE 1977) pp 822-7
- Rosenberg, R.L.; Coldren, L.A.
"Scattering analysis and design of SAW resonator filters." Bell Labs., Holmdel, NJ, USA; IEEE Trans. Sonics & Ultrason. (USA), vol. SU-26, no. 3, pp 205-30 (May 1979)
- Savage, E.B.
Fast computation of s.a.w. filter responses including diffraction." Dept. of Electrical & Computer Engng., Univ. of California, Santa Barbara, CA, USA; Electron. Lett. (GB), vol. 15, no. 17, pp 538-9 (16 Aug. 1979)
- Sato, H.; Meguro, T.; Yamanouchi, K.; Shibayama, K.
"Small ripple acoustic surface wave filter using piezoelectric thin film unidirectional transducer." Res. Inst. of Electrical Commun., Tohoku Univ., Sendai, Japan; 1977 Ultrasonics Symposium Proceedings, Phoenix, AZ, USA, 26-28 Oct 1978 (New York, USA: IEEE 1977) pp 740-3

- Schmidt, R.V.; Cross, P.S.
"Externally coupled resonator-filter (ECRF)." Bell Labs., Holmdel, NJ, USA; IEEE Trans. Sonics & Ultrason. (USA), vol. SU.26, no. 2, pp 88-93 (March 1979)
- Schoenwald, J.S.
"Ultra low shape factor SAW filters using asymmetrically truncated transducers." Sci. Center, Rockwell Internat., Thousand Oaks, CA, USA; 1978 Ultrasonics Symposium Proceedings, Cherry Hill, NJ, USA, 25-27 Sept. 1978 (New York, USA: IEEE 1978) pp 478-81
- Shibayama, K.; Yamanouchi, K.; Sato, H.
"UHF range surface acoustic wave filters using unidirectional interdigital transducers." Res. Inst. of Electrical Communication, Tohoku Univ., Sendai, Japan; Proc. Jpn. Acad. Ser. B (Japan, vol. 54, no. 6, pp 294-9 (June 1978)
- Slobodnik, A.J., Jr.; Laker, K.R.; Szabo, T.L.; Kearns, W.J.; Roberts, G.A.
"Low sidelobe SAW filters using overlap and withdrawal weighted transducers." RADC/EEA, Hanscom AFB, MA, USA; 1977 Ultrasonics Symposium Proceedings Phoenix, AZ, USA, 26-28 Oct. 1978 (New York, USA: IEEE 1977) pp 757-62
- Slobodnik, A.J., Jr.; Szabo, T.I.; Laker, K.R.
"Miniature surface-acoustic-wave filters." RADC, Hanscom AFB, MA, USA; Proc. IEEE (USA), vol. 67, no. 1, pp 129-46 (Jan 1979)
- Slobodnik, A.J., Jr.; Roberts, G.A.; Silva, J.H.; Kearns, W.J.; Sethares, J.C.; Szabo, T.L.
"Switchable SAW filter banks at UHF." Electromagnetic Sci. Div., Rome Air Dev. Center, Hanscom AFB, MA, USA; IEEE Trans. Sonics & Ultrason. (USA), vol. SU.26, no. 2, pp 120-6 (March 1979)
- Smith, W.R.
"SAW filters for CPSM spread spectrum communication" Hughes Aircraft Co., Fullerton, CA, USA; 1977 Ultrasonics Symposium Proceedings, Phoenix, AZ, USA, 26-28 Oct. 1978 (New York, USA: IEEE 1977) pp 524-8
- Stocker, H.; Kowatsch, M. Seifert, F.
"Technique, construction and application of SAW filters." Inst. fur Phys. Elektronik, Tech. Univ. Wien, Wien, Austria; Elektronikschau (Austria), vol. 54, no. 12, pp 26-30 (1978). In German.
- Tani, K.
"ZnO thin film SAW filters improve TV images." Matsushita Electronic Components Co. Ltd., Osaka, Japan; JEE (Japan), no. 137, pp 39-45 (May 1978)
- Temmyo, J.; Yoshikawa, S.
"On the fabrication and performance of SAW delay line filters for GHz SAW oscillators." Musashino Communications Lab., Nippon Telegraph & Telephone Public Corp., Musashino-shi, Tokyo, Japan; IEEE Trans. Sonics & Ultrason. (USA), vol. SU-25, no. 6, pp 367-71 (Nov. 1978)
- Tsukamoto, M.
"TTE suppressed surface acoustic wave filter." Wireless Res. Lab., Matsushita Electric Industrial Co. Ltd., Kadoma, Osaka, Japan; Appl. Phys. Lett. (USA), vol. 33, no. 7, pp 559-60 (1 Oct. 1978)
- Tsukamoto, M.
"Characteristics of a SAW filter with three inclined and tapered transducers." Wireless Res. Lab. Matsushita Elec. Ind. Co. Ltd., Kadoma, Osaka, Japan; J. Appl. Phys. (USA), vol. 50, no. 5, pp 3146-52 (May 1979)
- Ugrinovic, K.; Lazarevic, Z.
"Surface acoustic wave in the radar signal processing." Centar za Organizaciju i Veze Skupstine Opcine, Split, Yugoslavia; Elektrotehnika, Zagreb (Yugoslavia, no. 3-6, pp 199-201 (1978) In Croatian
- White, P.D.; Stevens, R.
"Surface acoustic wave resonator filters." Philips Res. Labs., Redhill, England; Conference on Radio Receivers and Associated Systems, Southampton, England, 11-14 July 1978 (London, England: IERE 1978) pp 93-100
- Yamaguchi, M.; Hashimoto, K.; Kogo, H.
"Withdrawal of interdigital electrodes for sidelobe reduction of SAW filters by implicit enumeration algorithm for 0-1 type integer optimization." Faculty of Engng., Chiba Univ., Chiba, Japan; Trans. Inst. Electron. & Commun. Eng. Jpn. Sect. E (Japan), vol. E61, no. 8, pp 631-2 (Aug. 1978)
- Yamaguchi, M.; Temma, T.; Kogo, H.
"Waveguide-type s.a.w. filter using energy focusing interdigital transducers." Dept. of Electrical Engng Chiba Univ., Yayoi-cho, Chiba-shi, Japan; IEE J. Microwave Opt & Acoust. (GB), vol. 3, no. 4, pp 161-8 (July 1979)
- Yamanouchi, K.; Shibayama, K.
"Low insertion loss acoustic surface wave filters" Oyo Buturi (Japan), vol. 47, no. 12, pp 1170-5 (Dec 1978) In Japanese. (11 refs.)
- Znamenskiy, A.E.
"Filters using acoustic surface waves." Telecommun. & Radio Eng. Part I (USA), vol. 31, no. 12, pp 10-15 (Dec 1977) Translation of: Elektrosvyaz (USSR), vol. 31, no. 12, pp 33-9 (Dec. 1977)

1.5.2.1

- Allen, D.E.; Shepard, J.W.
"Surface acoustic wave filters for deep space applications" Motorola Government Electronics Div., Scottsdale, AZ, USA; 1977 Ultrasonics Symposium Proceedings, Phoenix, AZ, USA, 26-28 Oct. 1978 (New York, USA: IEEE 1977) pp 529-31

Broux, G.; Claes, R.; Deleers, J.J.

"Surface acoustic wave filters for IF-stages in TV receivers. II. Measurement techniques." GTE Sylvania, Tienen, Belgium; Radio Mentor Electron. (Germany), vol. 44, no. 6, pp 223-4 (June 1978) In German.

Broux, G.; Claes, R.; Deleers, J.J.

"The use of filters for surface acoustic waves for the design of circuits for IF stages of television sets." Antenna (Italy), vol. 50, no. 10, pp 369-76, (Oct. 1978). In Italian.

Broux, G.; Claes, R.; Deleers, J.J.

"The use of surface acoustic wave filters for the design of IF stages of television sets." Antenna (Italy), vol. 50, no. 11, pp 413-17 (Nov. 1978) In Italian

Browning, T.I.; Gunton, D.J.; Lewis, M.F.; Newton, C.O.

"Bandpass filters employing surface skimming bulk waves." Royal Signals & Radar Establ., Malvern, England; 1977 Ultrasonics Symposium Proceedings, Phoenix, AZ, USA, 26-28 Oct. 1978 (New York, USA: IEEE 1977) pp 753-6

Gerard, H.M.; Judd, G.W.

"500 MHz bandwidth RAC filter with constant groove depth." Hughes Aircraft Co., Fullerton, CA, USA; 1978 Ultrasonics Symposium Proceedings, Cherry Hill NJ, USA, 25-27 Sept. 1978 (New York, USA: IEEE 1978), pp 734-7

Hazama, K.; Yamada, J.; Ishigaki, M.; Toyama, T.
"Design of mass productive fabrication techniques of high performance SAW TV IF filters." Consumer Products Res. Center, Hitachi Ltd., Yokohama, Japan; 1978 Ultrasonics Symposium Proceedings, Cherry Hill, NJ, USA, 25-27 Sept. 1978 (New York, USA: IEEE 1978) pp 504-8

Hazama, K.; Kishimoto, K.; Yuhara, A.; Ishigaki, M.; Matsuura, S.
"SAW Comb Filter for TV Channel Indicating System" Ultrasonics Symposium Proceedings, New Orleans, LA, USA, 26-28 Sept 1979 (New York, USA: IEEE 1979) pp 550-554

Hohkawa, K.; Yoshikawa, S.

"SAW filter design using linear programming technique." Nippon Telegraph & Telephone Public Corp., Tokyo, Japan; Rev. Electr. Commun. Lab. (Japan), vol. 26, no. 5-6, pp 755-66 (May-June 1978)

Hunsinger, B.

"SAW Filter Applications in Consumer Electronics." Coordinated Science Laboratory, Univ. of Illinois, Urbana, Illinois 61801; Ultrasonics Symposium Proceedings, New Orleans, LA, USA, 26-28 Sept 1979 (New York, USA: IEEE 1979), pp 541-544

Kinoshita, Y.; Hikita, M.; Tabuchi, T.; Kojima, H.
"Broadband resonant filter using surface-shear-wave mode and twinturn reflector." Central Res. Labs., Hitachi Ltd. Tokyo, Japan; Electron. Lett. (GB), vol. 15, no. 4, pp 130-1 (15 Feb. 1979)

Malocha, D.C.; Goll, J.H.; Heard, M.A.

"Design of a Compensated SAW Filter Used in a Wide Spread MKS Waveform Generator." Texas Instruments Inc. & Contitronix, Inc.; Ultrasonics Symposium Proceedings, New Orleans, LA, USA, 26-28 Sept 1979 (New York, USA: IEEE 1979), pp 518-521

Minowa, J.

"A method for accurately adjusting the center frequency of surface acoustic wave filters." Nippon Telegraph & Telephone Public Corp., Tokyo, Japan; Rev. Electr. Commun. Lab. (Japan), vol. 26, no. 5-6, pp 797-807 (May-June 1978)

Minowa, J.; Takai, K.

"Narrow pass band surface acoustic wave filters for transmission system applications." Electrical Communication Labs., Nippon Telegraph & Telephone Public Corp., Tokyo, Japan; Rev. Electr. Commun. Lab. (Japan), vol. 26, no. 11-12, pp 1675-85 (Nov. Dec. 1978)

Morgan, D.P.

"Microwave acoustic devices." Allen Clark Res. Centre, Plessey Res. (Caswell) Ltd., Towcester, England; Proceedings of the 8th European Microwave Conference, Paris, France, 4-8 Sept. 1978 (Sevenoaks, England: Microwave Exhibitions & Publishers Ltd. 1978) pp 378-88

Moulic, J.R.

"A broadband surface-wave filter with -50-dB stopbands and 1-dB passband ripple." IBM Federal Systems Div., Owego, NY, USA; 1977 Ultrasonics Symposium Proceedings, Phoenix, AZ, USA, 26-28 Oct. 1978 (New York, USA: IEEE 1977) pp 673-4

Penimuri, D.; Havens, D.P.;

"Surface-acoustic-wave filters prove versatile in VHF applications." Collins Div., Rockwell Internat. Corp., Newport Beach, CA, USA; Electronics (USA), vol. 52, no. 14, pp 115-20 (5 July 1979)

Potter, B.R.; Shoquist, T.L.

"Multipassband low loss SAW filters." Texas Instruments Inc., Dallas, TX, USA; 1977 Ultrasonics Symposium Proceedings, Phoenix, AZ, USA, 26-28 Oct. 1978 (New York, USA: IEEE 1977) pp 736-9

Rosenberg, R.L.; Coldren, L.A.

"A new wider-band SAW Resonator filter on quartz." Bell Laboratories, Holmdel, NJ 07733; Ultrasonics Symposium Proceedings, New Orleans, LA, USA, 26-28 Sept 1979 (New York, USA: IEEE 1979) pp 836-840

Savage, E.B.; Matthaei, G.L.

"Compensation for diffraction in SAW filters" Dept. of Electrical and Computer Engineering, Univ. of California, Santa Barbara, CA 93106; Ultrasonics Symposium Proceedings, New Orleans, LA, USA, 26-28 Sept 1979 (New York, USA: IEEE 1979) pp 527-532.

Schoenwald, J.

"Diffraction loss compensation in very low shape factor wideband SAW filters." Teledyne MEC, Palo Alto, CA, USA; 1977 Ultrasonics Symposium Proceedings, Phoenix, AZ, USA, 26-28 Oct. 1978 (New York, USA: IEEE 1977) pp 706-9

Kearns, W.J.; Roberts, G.A.; Silva, J.H.; Noonan, J.P.; Slobodnik, A.J., Jr.; Fenstermacher, T.E. "SAW Butterworth contiguous filters at UHF." Rome Air Dev. Center, Hanscom AFB, MA, USA; IEEE Trans. Sonics & Ultrason. (USA), vol. SU-26, no. 3, pp 246-53 (May 1979)

Stevens, R.; White, P.D.; Mitchell, R.F.; Moore, P.; Redwood, M.

"Stopband level of 2-port SAW resonator filters." Philips Res. Labs., Redhill, England; 1977 Ultrasonics Symposium Proceedings, Phoenix, AZ, USA, 26-28 Oct. 1978 (New York, USA: IEEE 1977) pp 905-8

Stigall, R.E.; Hartmann, C.S.

"Phase and magnitude distortion compensation in a low-loss T₁ SAW filter." Texas Instruments, Inc., Dallas, TX, USA; 1977 Ultrasonics Symposium Proceedings, Phoenix, AZ, USA, 26-28 Oct. 1978 (New York, USA: IEEE 1977) pp 729-32

Suthers, M.S.; Campbell, C.K.

"Use of a charge distribution model in SAW band-pass filter design." Bell Northern Research, Ottawa, Ontario, Canada & McMaster University, Hamilton, Ontario, Canada; Ultrasonics Symposium Proceedings, New Orleans, LA, USA, 26-28 Sept. 1979 (New York, USA: IEEE 1979) pp 565-569

Tani, K.; Senda, K.; Niikawa, T.; Tazuke, K.

"ZnO surface acoustic wave filter for TV set." Ceramics Dept., Matsushita Electronic Components Co. Ltd., Osaka, Japan; Natl. Tech. Rep. (Japan), vol. 24, no. 1, pp 134-43 (Feb. 1978). In Japanese.

Valov, V.I.

"Surface acoustic-wave filters connected in series" Izv. VUZ Radioelektron. (USSR), vol. 22, no. 1, pp 105-7 (Jan 1979) In Russian.

Webb, D.C.

"SAW filters simplify signal sorting." Naval Res. Lab., Washington, D.C., USA; Microwave Syst. News (USA), vol. 8, no. 9, pp 75, 77-8, 81, 83-4 (1 Sept 1978)

Williamson, R.C.

"Case studies of successful surface-acoustic-wave devices." Lincoln Lab., MIT, Lexington, MA, USA; 1977 Ultrasonics Symposium Proceedings, Phoenix, AZ, USA, 26-28 Oct. 1978 (New York, USA: IEEE 1977) pp 460-8

Yamaguchi, M.; Hashimoto, K.; Hogo, H.

"Suboptimization of electrode-withdrawal weighted SAW filters." Faculty of Engng., Chiba Univ., Chiba-shi, Japan; IEEE Trans. Sonics & Ultrason. (USA), vol. SU-26, no. 1, pp 53-9 (Jan 1979)

1.6

Adams, C.A.; Kusters, J.A.

"Improved long-term aging in deeply etched SAW resonators." Hewlett-Packard Co., Santa Clara, CA, USA; Proceedings of the 32nd Annual Symposium on Frequency Control 1978, Atlantic City, NJ, USA, 31 May - 2 June 1978 (Washington, D.C., USA: Electronic Industries Assoc 1978) pp 74-6

Beil, D.T., Jr.

"Aging processes in SAW resonators." Texas Instruments, Dallas, TX, USA; 1977 Ultrasonics Symposium Proceedings, Phoenix, AZ, USA, 26-28 Oct. 1978 (New York, USA: IEEE 1977) pp 851-6

Quesada, V.

"Study of the instability of quartz resonators." Astron. Internat. Latitude Station, Carloforte-Cagliari, Italy; Mem. Soc. Astron. Ital. (Italy), vol. 48, no. 4, pp 659-63 (Dec. 1977) In Italian

Shreve, W.R.

"Aging in quartz SAW resonators." Texas Instruments Inc., Dallas, TX, USA; 1977 Ultrasonics Symposium Proceedings, Phoenix, AZ, USA, 26-28 Oct. 1978 (New York, USA: IEEE 1977) pp 857-61

Yaroslavskii, M.I.; Sorokin, K.V.; Lavrova, T.P.; Karaul'nik, A.E.; Petrozhitskaya, I.N.; Motin, P.E.; Shin, V.; Efremov, O.N.; Lyubimov, L.A.

"High-stability quartz resonators." Meas. Tech. (USA), vol. 20, no. 8, pp 1175-7 (Aug. 1977). Translation of: Izmer. Tekh. (USSR), vol. 20, no.8, pp 54-5 (Aug. 1977)

1.7

Beaver, W.D.; Van Loben Sels, W.E.; Wang, M.

"Quartz Crystal Measurements by a 'Phase-Amplitude' Method." Comtec Economation Inc.; 31st Annual Symposium on Frequency Control, US Army Electronics Command, Fort Monmouth, NJ, pp 189-200 (1977). Copies available from the Electronic Industries Association, 2001 Eye Street, N.W. Washington, D.C. 20006

Besson, R.; Decailliot, M.

"Application of sideband modulation oscillators for measurement of quartz resonators stability." Ecole Nat. Supérieure de Chronometrie et Micromécanique, Besançon, France; C.R. Hebd. Seances Acad. Sci. Ser. B (France), vol. 288, no. 3, pp 57-60 (22 Jan 1979) In French

Darymov, V.I.; Koshelev, F.P.; Kurin, M.N.
Krivobokov, V.P.

"Method of determining the thickness of the broken layer on the surface of quartz." Kirov Polytech. Inst., Tomsk, USSR; Ind. Lab. (USA), vol. 44, no. 3, pp 355-6 (March 1978). Translation of: Zavod. Lab. (USSR), vol. 44, no. 3, pp 302-3 (March 1978)

Grzeszykowski, M.

"Quartz resonator parameters wide band active meter" Pr. Inst. Tele- & Radiotech. (Poland), no. 77, pp 69-73 (1978) In Polish

Hughes, S.J.; Parfitt, R.W.; Hardy, J.S.

"The measurement of load resonance characteristics of quartz crystals using the zero phase II-network" Royal Aircraft Establ., Farnborough, England; Proceedings of the 32nd Annual Symposium on Frequency Control 1978, Atlantic City, NJ, USA, 31 May - 2 June 1978 (Washington, D.C., USA: Electronic Industries Assoc. 1978) pp 337-43

Malinowski, G.; Hafner, E.

"Automatic microcircuit bridge measurements on quartz crystal units." US Army Electronics Technol. & Devices Lab., Fort Monmouth, NJ, USA; Proceedings of the 32nd Annual Symposium on Frequency Control 1978, Atlantic City, NJ, USA, 31 May - 2 June 1978 (Washington, D.C., USA: Electronic Industries Assoc. 1978) pp 354-64

Meeker, T.R.

"A Review of the New IEEE Standard on Piezoelectricity." Bell Telephone Laboratories; 31st Annual Symposium on Frequency Control, US Army Electronics Command, Fort Monmouth, NJ, pp 176-180 (1977). Copies available from the Electronic Industries Association, 2001 Eye St. NW Washington DC 20006

Roberts, G.E.

"A Four-Frequency Process For Accurately Measuring Coupled-Dual Resonator Crystals." General Electric; 31st Annual Symposium on Frequency Control, US Army Electronics Command, Fort Monmouth, NJ, pp 159-165 (1977). Copies available from the Electronic Industries Association, 2001 Eye Street, N.W. Washington D.C. 20006

Sherman, J.H., Jr.

"Trim Sensitivity - A Useful Characterization of a Resonator." General Electric; 31st Annual Symposium on Frequency Control, US Army Electronics Command, Fort Monmouth, NJ, pp 181-185 (1977). Copies available from the Electronic Industries Association, 2001 Eye Street, N.W. Washington, D.C. 20006

Smolarski, A.; Wojcicki, M.

"Quartz resonators series resonance frequency direct measuring method." Pr. Inst. Tele- & Radiotech. (Poland), no. 77, pp 55-9 (1978). In Polish.

Swanson, T.W.

"Crystal filter AM-PM conversion measurements." ECI Div., E-Systems, St. Petersburg, FL, USA; Proceedings of the 32nd Annual Symposium on Frequency Control 1978, Atlantic City, NJ, USA, 31 May - 2 June 1978 (Washington, D.C., USA: Electronic Industries Assoc. 1978) pp 250-4

Tsuzuki, Y.; Tiki, M.; Adachi, T.; Yanagi, H.

"Automatic Measurement of Parameters of VHF Quartz Crystal Resonators." Yokohama National University; 31st Annual Symposium on Frequency Control, US Army Electronics Command, Fort Monmouth, NJ, pp 201-205 (1977). Copies available from the Electronic Industries Association, 2001 Eye Street, N.W. Washington D.C. 20006

Uchino, K.; Cross, L.E.

"A High-Sensitivity AC Dilatometer for the Direct Measurement of Piezoelectricity and Electrostriction." The Pennsylvania State University; 31st Annual Symposium on Frequency Control, US Army Electronics Command, Fort Monmouth, NJ, pp 110-117 (1977). Copies available from the Electronic Industries Association, 2001 Eye Street, N.W. Washington D.C. 20006

Watson, N. J.

"110MHz spectrum analyser, TF 2370. Crystal testing and measurements." Marconi Instrum. (GB), vol. 16, no. 2, pp 35-6 (Summer 1978)

Yamaguchi, T.; Hamano, K.

"Interferometric method of measuring complex piezoelectric constants of crystals in a frequency range up to about 50 kHz." Dept. of Phys., Tokyo Inst. of Technol., Oh-okayama, Meguro, Tokyo, Japan; Jpn. J. Appl. Phys. (Japan), vol. 18, no. 5, pp 927-32 (May 1979)

Yamamoto, S.; Sugawara, S.; Tomikawa, Y.; Konno, M.

"A method for measuring equivalent circuit elements of a piezoresonator." J. Acoust. Soc. Jpn. (Japan), vol. 34, no. 8, pp 455-61 (Aug 1978) In Japanese.

1.8.1

Apal'kov, V.K.; Mitrofanov, V.P.; Shiyon, V.S.

"Frequency stability of oscillator with sapphire resonator." M.V. Lomonosov Moscow State Univ., Moscow, USSR; Sov. Phys.-Dokl. (USA), vol. 23, no. 9, pp 671-2 (Sept 1978). Translation of: Dokl. Akad. Nauk SSSR, vol. 242, no. 1-3, pp 578-80, (Sept 1978)

Arnoldt, M.

"Improved frequency stability circuit for 10 MHz quartz crystal." Funk-Tech. (Germany), vol. 33, no. 23, pp WS 380-1 (Dec. 1978) In German

Bexlyud'ko, V.Ya.; Zelenskii, A.A.; Solodovnik, V.F.

"Differential quartz oscillator with a wide relative tuning range." Khar'kov Aviation Inst., Khar'kov, Ukrainian SSR; Instrum. & Exp. Tech. (USA) vol. 21, no. 4, pt. 2, pp 1004-6 (July-Aug 1978). Translation of: Prib. Tekh. Eksp. (USSR), vol 21, no 4, pt 2, pp 147-9 (July-Aug 1978)

- Burgoon, R.; Wilson, R.L.
"Performance Results of an Oscillator Using the SC Cut Crystal." Hewlett-Packard; 31st Annual Symposium on Frequency Control, US Army Electronics Command, Fort Monmouth, NJ, pp 406-410 (1977). Copies available from the Electronic Industries Association, 2001 Eye St., NW Washington, DC 20006
- Burgoon, R.; Wilson, R.L.
"Design Aspects of an Oscillator Using the SC Cut Crystal." Hewlett-Packard; 31st Annual Symposium on Frequency Control, US Army Electronics Command, Ft. Monmouth, NJ, pp 411-416 (1977). Copies available from the Electronic Industries Association, 2001 Eye Street, N.W. Washington, D.C. 20006
- Chiba, S.
"High stability reactance oscillator by zero input impedance amplifier." Nagano Tech. Coll., Nagano, Japan; Trans. Inst. Electron. & Commun. Eng. Jpn. Sect. E. (Japan), vol. E61, no. 7, pp 575 (July 1978)
- Garner, P.J.
"Voltage controlled crystal oscillators." Philips Res. Labs., Redhill, England; Conference on Radio Receivers and Associated Systems, Southampton, England, 11-14 July 1978 (London, England: IERE 1978) pp 227-35
- Gauthier, N.
"Integrated quartz oscillator for TTL clock circuits." *Toute Electron.* (France), no. 434, pp 53-5 (July 1978) In French
- Gersbach, J.E.
"Crystal oscillator" IBM Corp., Armonk, NY, USA; IBM Tech. Disclosure Bull. (USA), vol. 21, no. 9, pp 3584-5 (Feb. 1979)
- Gniewinska, P.
"Development trends of quartz crystal units and oscillators." Inst. Tele-i Radiotech., Warszawa, Poland; *Elektronika* (Poland), vol. 19, no. 7-8, pp 309-14 (1978) In Polish
- Horiba, Y.; Nakao, Y.; Komatsu, T.; Tomisawa, O.; Ohkubo, T.
"Design for low power dissipation in CMOS quartz oscillator of watch use." LSI Dev. Lab. Mitsubishi Electric Corp., Itami, Japan; Trans. Inst. Electron & Commun. Eng. Jpn. Sect. E. (Japan), vol. E61, no. 10, pp 859-60 (Oct. 1978)
- Ivanek, F.
"Frequency stabilisation." Farinon Electric, San Carlos, CA, USA; *Onde Electr.* (France), vol. 59, no. 1, pp 55-8 (Jan 1979) In French
- Kavun, E.P.
"High-power crystal oscillator." *Instrum. & Exp. Tech.* (USA), vol. 21, no. 3, pt. 1, pp 685-6 (May-June 1978). Translation of: *Prib. Tekh. Eksp.* (USSR), vol. 21, no. 3, pt. 1, pp 128-9 (May-June 1978)
- Kodama, S.; Sato, Y.
"An Analysis of Unwanted Frequency Oscillation in a Crystal Controlled Oscillator." Nippon Electric Co., Ltd.; 31st Annual Symposium on Frequency Control, US Army Electronics Command, Fort Monmouth, NJ, pp 417-424 (1977). Copies available from the Electronic Industries Association, 2001 Eye Street, N.W. Washington, D.C. 20006
- Kulagin, E.V.; Pikhtele, A.I.; Sokolov, V.P.; Fateev, B.P.
"Natural fluctuations in a quartz crystal oscillator with automatic gain control." *Radiophys. & Quantum Electron.* (USA), pp 1125-30. Translation of *Izv. VUZ Radiofiz.* (USSR), vol. 21, no. 11, pp 1618-26 (Nov. 1978)
- Okano, S.; Ikeda, Y.
"Crystal oscillators facilitate future frequency control." Toyo Communication Equipment Co., Ltd., Koza-gun, Kanagawa, Japan; *JEE* (Japan), no. 144, pp 40-3 (Dec. 1978)
- Popov, G.Y.; Dishkov, P.S.; Donchev, S.D.
"Hybrid integrated circuit of quartz generator." *Elektro Prom.-st. & Priborostr.* (Bulgaria), vol. 14, no. 2, pp 65-6 (1979). In Bulgarian (2 refs.)
- Przyjemski, J.M.
"Improvement in system performance using a crystal oscillator compensated for acceleration sensitivity" Charles Stark Draper Lab., Inc. Cambridge, MA, USA; Proceedings of the 32nd Annual Symposium on Frequency Control 1978, Atlantic City, NJ, USA, 31 May - 2 June 1978 (Washington, D.C., USA: Electronic Industries Assoc. 1978), pp 426-31
- Rohde, U.L.
"Mathematical analysis and design of an ultra stable low noise 100 MHz crystal oscillator with differential limiter and its possibilities in frequency standards." Dept. of Electrical Engng., Univ. of Florida, Gainesville, FL, USA; Proceedings of the 32nd Annual Symposium on Frequency Control 1978, Atlantic City, NJ, USA, 31 May - 2 June 1978 (Washington, D.C., USA: Electronic Industries Assoc. 1978) pp 409-25
- Savage, E.
"How to build crystal oscillators." *Radio Electronics*, New York, NJ, USA; *Radio-Electron.* (USA), vol. 49, no. 7, pp 66-7 (July 1978)
- Swanson, C.T.; McVey, E.S.
"A Non-Iterative Solution for a Two-Thermistor TCXO." University of Virginia; 32nd Annual Symposium on Frequency Control, US Army Electronics Command, Fort Monmouth, NJ, pp 425-430 (1977). Copies available from the Electronic Industries Association, 2001 Eye St., NW Washington DC 20006
- Van Der Windt, J.; Grassi, R.
"To specify a time-base oscillator, you'd better know your crystals." Philips Test & Measuring Instruments, Jarfalla, Sweden; *Electron. Des.* (USA) vol. 26, no. 24, pp 126-9 (22 Nov. 1978)

Watanabe, A.

"Quartz oscillator in Japan - mainly used for the wrist watch." Watch Res. & Dev. Dept., Daini Seikousha, Tokyo, Japan; Bull. Jpn. Soc. Precis. Eng. (Japan), vol. 12, no. 2, pp 61-6 (June 1978)

"A voltage controlled quartz oscillator using a reactance diode." Elektron. Entwickl. (Germany), vol. 13, no. 10, pp 62 (Oct. 1978) In German.

"Practical oscillator calculations. VII. Quartz crystal oscillators." Funk-Tech. (Germany), vol. 33, no. 23, pp 270-4 (Dec. 1978) In German.

1.8.2

Allison, R.; Goldman, S.J.

"Vibration effects on close in phase noise of a 300 MHz surface wave resonator oscillator." Texas Instruments Ind., Dallas, TX, USA; Proceedings of the 32nd Annual Symposium on Frequency Control 1978, Atlantic City, NJ, USA, 31 May - 2 June 1978 (Washington, D.C., USA: Electronic Industries Assoc. 1978) pp 66-73

Chen, C.L.; Field, M.E.

"Injection locking phenomena in SAW oscillators." School of Electrical Engng., Purdue Univ., West Lafayette, IN, USA; 1977 Ultrasonics Symposium Proceedings, Phoenix, AZ, USA, 26-28 Oct. 1978 (New York, USA: IEEE 1977) pp 923-6

Eschler, H.; Sanchez-Hermosilla, L.; Bulst, W.E.; Schucht, P.

"Design and construction of SAW oscillators for secondary radar systems." Siemens AG, Munchen, Germany; Proceedings of the 32nd Annual Symposium on Frequency Control 1978, Atlantic City, NJ, USA, 31 May - 2 June 1978 (Washington, D.C., USA: Electronic Industries Assoc. 1978) pp 58-65

Gilden, M.; Montress, G.K.; Cullen, D.E.; Wagner, R.A.; Reeder, T.M.

"Design of stable SAW oscillators operating above 1 GHz." United Technol. Res. Center, East Hartford, CT, USA; 1978 Ultrasonics Symposium Proceedings, Cherry Hill, NJ, USA, 25-27 Sept. 1978 (New York, USA: IEEE 1978) pp 452-7

Henaff, J.

"Use of surface acoustic wave oscillators in telecommunications systems." Onde Elect. (France), vol. 59, no. 8-9, pp 95-101 (Aug-Sept 1979) In French

Henaff, J.

"Application of SAW-oscillators to digital communications." C.N.E.T.; Dpt. TCR/DEF, 92131 Issy-les-Moulineaux, France; Ultrasonics Symposium Proceedings, New Orleans, LA, USA, 26-28 Sept 1979 (New York, USA: IEEE 1979) pp 855-860

Hohkawa, K.; Yoshikawa, S.

"Surface acoustic wave oscillator with maximally flat temperature coefficient." Masashino Electrical Communication Lab., NTT, Tokyo, Japan; J. Acoust. Soc. Jpn. (Japan), vol. 35, no. 1, pp 11-20 (Jan 1979). In Japanese.

Hohkawa, K.; Yoshikawa, S.

"Temperature Stable Oscillators Employing Parallel Connected SAW resonators." Musashino Electrical Communication Laboratory, Nippon Telegraph and Telephone Public Corporation, 3-9-11 Midoricho, Musashino, Tokyo, Japan 180; Ultrasonics Symposium Proceedings, New Orleans, LA, USA, 26-28 Sept 1979 (New York, USA: IEEE 1979) pp 623-626

Lee, D.L.

"Design Considerations for Electronically Compensated SAW Delay Line Oscillators." Raytheon Research Division, 28 Seyon St., Waltham, Massachusetts 02154; Ultrasonics Symposium Proceedings, New Orleans, LA, USA, 26-28 Sept 1979 (New York, USA: IEEE 1979) pp 849-854

Leja, I.; Parker, T.E.

"High Efficiency SAW Oscillator using a Dual Gate GaAs FET." Raytheon Missile Systems Division, Hartwell Rd., Bedford, Mass. 01730 & Raytheon Research Division, 28 Seyon St., Waltham, Mass 02154; Ultrasonics Symposium Proceedings, New Orleans, LA, USA, 26-28 Sept 1979 (New York, USA: IEEE 1979) pp 865-869

Levesque, P.; Valdois, M.; Hauden, D.; Gagnepain, J.J.; Hartemann, P.; Uebersfeld, J.

"Theoretical and Experimental Analysis of SAW quartz oscillator Acceleration Sensitivity." Onera - CNRS - Thomson-L.C.R. - Universite Paris VI; Ultrasonics Symposium Proceedings, New Orleans, LA, USA, 26-28 Sept 1979 (New York, USA: IEEE 1979) pp 896-899

Montress, G.K.; Wagner, R.A.; Gilden, M.

"Stable Microwave SAW Oscillators for Aging Studies" United Technologies Research Center, East Hartford, Connecticut 06108; Ultrasonics Symposium Proceedings, New Orleans, LA, USA, 26-28 Sept 1979 (New York, USA: IEEE 1979) pp 886-890

Moriizumi, T.; Kyuma, K.; Hyakutake, J.; Yasuda, T.

"A monolithic surface-wave oscillator using a SAW amplifier and periodic gratings." Tokyo Inst. of Technol., Tokyo, Japan; 1977 Ultrasonics Symposium Proceedings, Phoenix, AZ, USA, 26-28 Oct. 1978 (New York, USA: IEEE 1977) pp 932-5

Parker, T.E.

"Aging characteristics of SAW controlled oscillators" Raytheon Res. Div. Waltham, MA, USA; 1977 Ultrasonics Symposium Proceedings, Phoenix, AZ, USA, 26-28 Oct. 1978 (New York, USA: IEEE 1977) pp 862-6

Parker, T.E.

"1/f phase noise in quartz SAW devices." Raytheon Res. Div., Waltham, MA, USA; Electron. Lett. (GB) vol. 15, no. 10, pp 296-8 (10 May 1979)

Salmon, S.K.

"Surface acoustic wave oscillators at UHF." Philips Res. Labs., Redhill, England; Conference on Radio Receivers and Associated Systems, Southampton, England, 11-14 July 1978 (London, England IERE 1978) pp 101-6

Temmyo, J.; Yoshikawa, S.
"Design and characteristics of a 2 GHz SAW delay line oscillator." Musashino Elec. Communication Lab., NTT, Musashino, Japan; Trans. Inst. Electron. & Commun. Eng. Jpn. Sect. E. (Japan), vol. E61, no. 11, pp 885-90 (Nov. 1978)

Thorpe, J.C.; Yen, K.H.
"2.2 GHz Surface Acoustic Wave Oscillator." TWR Defense & Space Systems Group, Redondo Beach, CA 90278; Ultrasonics Symposium Proceedings, New Orleans, LA, USA, 26-28 Sept 1979 (New York, USA: IEEE 1979) pp 882-885

Valdois, M.; Levesque, P.; Hartemann, P.
"Influence of acceleration on surface acoustic wave oscillators." ONERA, Chatillon, France; Agard Conference Proceedings No. 230. Impact of Charge Coupled Devices and Surface Acoustic Wave Devices on Signal Processing and Imagery in Advanced Systems, Ottawa, Canada, 11-15 Oct. 1977 (Neuilly-sur-Seine, France: AGARD 1978) pp 2.5/1-6 In French.

Valdois, M.; Levesque, P.; Hartemann, P.
"Acceleration dependence of the surface acoustic wave oscillator frequency." ONERA, Chatillon, France; 1977 Ultrasonics Symposium Proceedings, Phoenix, AZ, USA, 26-28 Oct. 1978 (New York, USA: IEEE 1977), pp 936-8

Vasi'jevic, D.
"SAW oscillators." Elektrotehnicki Fakultet, Belgrade, Yugoslavia; Tehnika (Yugoslavia), vol. 33, no. 12, pp 1797-9 (1978) In Croatian

Volluet, G.
"Tunable magnetoelastic surface wave oscillators." Thomson-CSF Res. Center, Orsay, France; Agard Conference Proceedings No. 230. Impact of Charge Coupled Devices on Signal Processing and Imagery in Advanced Systems, Ottawa, Canada, 11-15 Oct. 1977 (Neuilly-sur-Seine, France: AGARD 1978) pp 2.6/1-10

Weglein, R.D.; Otto, O.W.
"Microwave SAW oscillators." Hughes Res. Labs., Malibu, CA, USA; 1977 Ultrasonics Symposium Proceedings, Phoenix, AZ, USA, 26-28 Oct. 1978 (New York, USA: IEEE 1977) pp 913-22

Wise, J.; Dolochycki, S.J.; Staples, E.J.
"The design of SAW oscillators for low noise communications systems." Electronics Research Center, Rockwell International, Thousand Oaks, CA 91360; Ultrasonics Symposium Proceedings, New Orleans, LA, USA, 26-28 Sept 1979 (New York, USA: IEEE 1979) pp 870-873

1.8.3

Akahane, Y.
"Highly precise standard signal circuit for time-piece." Suwa Seikosha Co. Ltd., Suwa, Japan; Proceedings of the 32nd Annual Symposium on Frequency Control 1978, Atlantic City, NJ, USA, 31 May - 2 June 1978 (Washington, DC, USA: Electronic Industries Assoc. 1978) pp 403-8

Allan, D.W.; Hellwig, H.
"Time deviation and time prediction error for clock specification, characterization, and application." Time & Frequency Div., Nat. Bur. of Stand., Boulder, CO, USA; IEEE 1978 Position Location and Navigation Symposium, San Diego, CA, USA, 6-9 Nov. 1978 (New York, USA: IEEE 1978) pp 29-36.

Arnoldt, M.
"Universally applicable quartz time base." Funk-Tech. (Germany), vol. 33, no. 18, pp 289-90 (Sept. 1978) In German

Bergmann, G.
"A quartz crystal controlled clock generator using ICL technique." Elektroniker (Switzerland), vol. 17, no. 7, pp 1-5 (1978). In German

Hajek, J.
"Non-autonomous clocks." Jemna Mech. & Opt. (Czechoslovakia), vol. 24, no. 1, pp 17-21 (Jan. 1979). In Czech

Korzen, W.
"The precision low-frequency signal generator type T66." Grundig Inf. (Germany), vol 26, no. 1, pp 25-31 (1979) In German

Kraengel, W.D., Jr.
"Standby crystal time base backs up line-powered clock." Electronics (USA), vol. 52, no. 7, pp 104-5 (29 March 1979)

Lender, R.; Szepan, R.
"Digital clock CADM extends R&S standard-frequency line." Rohde & Schwarz, Munich Germany; News Rohde & Schwarz (Germany), vol. 18, no. 82, pp 4-7 (1978)

Pogson, I.
"Quartz crystal driver for Yaesu Musen clock." Electron. Aust. (Australia), vol. 40, no. 11, pp 44-6 (Feb. 1979)

Prokysek, J.
"On the problems of setting the accuracy of crystal-controlled electronic clocks and watches." Jemna Mech. & Opt. (Czechoslovakia), vol. 24, no. 1, pp 23-6 (Jan 1979) In Czech

Rutman, J.
"Characterization of phase and frequency instabilities in precision frequency sources: fifteen years of progress." Obs. de Paris, Paris, France; Proc. IEEE (USA), vol. 66, no. 9, pp 1048-75 (Sept 1978)

Stein, S.R.; Manney, C.M., Jr.; Walls, F.L.; Gray, J.E.; Besson, R.J.
"A systems approach to high performance oscillators" Nat. Bur. of Stand., Boulder, CO, USA; Proceedings of the 32nd Annual Symposium on Frequency Control 1978, Atlantic City, NJ, USA, 31 May - 2 June 1978 (Washington, D.C., USA: Electronic Industries Assoc. 1978), pp 527-30

1.9

Browning, I.; Lewis, M.
"A new cut of quartz giving improved temperature stability to SAW oscillators." RSRE, Malvern, England; Proceedings of the 32nd Annual Symposium on Frequency Control 1978, Atlantic City, NJ, USA, 31 May - 2 June 1978 (Washington, D.C., USA: Electronic Industries Assoc. 1978) pp 87-94

Frerking, M.E.
"The Application of Microprocessors to Communications Equipment Design." Rockwell International; 31st Annual Symposium on Frequency Control, US Army Electronics Command, Fort Monmouth, NJ, pp 431-435 (1977). Copies available from the Electronic Industries Association, 2001 Eye Street, N.W. Washington D.C. 20006

Gniewinska, B.; Kwiatkowska, D.; Rozwadowski, M.
"Temperature gradient free change of state (crystal oven); Elektronika (Poland), vol. 19, no. 12, pp 511-12 (1978). In Polish

Kinsman, R.G.
"Temperature compensation of crystals with parabolic temperature coefficients." Motorola Communications Systems Div.; Schaumburg, IL, USA; Proceedings of the 32nd Annual Symposium on Frequency Control 1978, Atlantic City, NJ, USA, 31 May - 2 June 1978 (Washington D.C., USA: Electronic Industries Assoc. 1978) pp 102-7

Kusters, J.A.; Fischer, M.C.; Leach, J.G.
"Dual model operation of temperature and stress compensated crystals." Hewlett-Packard Co., Santa Clara, CA, USA; Proceedings of the 32nd Annual Symposium on Frequency Control 1978, Atlantic City, NJ, USA, 31 May - 2 June 1978 (Washington, D.C., USA: Electronic Industries Assoc. 1978) pp 389-97

Onoe, M.; Yamagishi, I.; Nariai, H.
"Temperature compensation of crystal oscillator by microprocessor." Inst. of Industrial Sci., Univ. of Tokyo, Tokyo, Japan; Proceedings of the 32nd Annual Symposium on Frequency Control 1978, Atlantic City, NJ, USA, 31 May - 2 June 1978 (Washington, D.C., USA: Electronic Industries Assoc. 1978) pp 398-402

Teramachi, Y.; Horie, M.; Kataoka, H. Musha, T.
"Frequency Response of Quartz Oscillator to Temperature Fluctuation." Institute of Technology; 31st Annual Symposium on Frequency Control, US Army Electronics Command, Fort Monmouth, NJ, pp 235-238 (1977). Copies Available from the Electronic Industries Association, 2001 Eye Street, N.W. Washington D.C. 20006

Theobald, G.; Marianneau, G.; Pretot, R.; Gagnepain, J.J.
"Dynamic Thermal Behavior of Quartz Resonators." CNRS; 31st Annual Symposium on Frequency Control, US Army Electronics Command, Fort Monmouth, NJ, pp 239-246 (1977). Copies Available from the Electronic Industries Association, 2001 Eye Street, N.W. Washington D.C. 20006

Warwick, G.A.; Gosling, W.; Prescott, A.J.
"A digital technique for temperature compensation of crystal oscillators." School of Electrical Engng., Univ. of Bath, Bath, England; Conference on Radio Receivers and Associated Systems, Southampton, England, 11-14 July 1978 (London, England: IERE 1978) pp 207-16

2.1

Fruhauf, T.; Szepan, R.
"Crystal, rubidium, caesium: complete standard-frequency line." News Rohde & Schwarz (Germany), vol. 18, no. 80, pp 4-9 (1978).

Garvey, R.M.; Hellwig, H.W.; Jarvis, S., Jr.; Wineland, D.J.
"Two-frequency separated oscillating fields technique for atomic and molecular beam spectroscopy." Time & Frequency Div., Nat. Bur. of Stand., Boulder, CO, USA; IEEE Trans. Instrum. & Meas. (USA), vol. IM-27, no. 4, pp 349-54 (Dec. 1978) (CPEM '78 Conference of Precision Electromagnetic Measurement, Ottawa, Canada, 26-29 June 1978)

Hall, J.L.
"Stabilized lasers and precision measurements." Univ. of Colorado, Boulder, CO, USA; Science (USA) vol. 202, no. 4364, pp 147-56 (13 Oct. 1978)

Percival, D.B.
"Estimation of the spectrum of fractional frequency deviates." US Naval Obs., Washington, DC, USA; Proceedings of the 32nd Annual Symposium on Frequency Control 1978, Atlantic City, NJ, USA, 31 May - 2 June 1978 (Washington, D.C. USA: Electronic Industries Assoc. 1978) pp 542-8

Shimoda, K.
"Invention of masers and lasers." Faculty of Sci. Univ. of Tokyo, Tokyo, Japan; J. Inst. Electron. & Commun. Eng. Jpn. (Japan), vol. 62, no. 2, pp 113-17 (Feb. 1979) In Japanese (36 refs.)

Strumia, F.
"Analysis of new microwave and optical frequency standards based on ions storage." Phys. Dept., Pisa Univ., Pisa, Italy; Proceedings of the 32nd Annual Symposium on Frequency Control 1978, Atlantic City, NJ, USA, 31 May - 2 June 1978 (Washington, D.C., USA: Electronic Industries Assoc. 1978) pp 444-52

Townes, G.H.
"Townes recalls the early days." Laser Focus (USA) vol. 14, no. 8, pp 52-8 (Aug. 1978)

Vanier, J.; Tetu, M.; Bernier, L.-G.
"Transfer of frequency stability from an atomic frequency reference to a quartz crystal oscillator" Dept. de Genie Electrique, Univ. Laval, Quebec, Canada; Proceedings of the 32nd Annual Symposium on Frequency Control 1978, Atlantic City, NJ, USA, 31 May - 2 June 1978 (Washington DC, USA: Electronic Industries Assoc. 1978) pp 520-6

Walls, F.L.; Wineland, D.J.; Drullinger, R.E.
 "New possibilities for frequency standards using laser cooling and detection of stored ions." Time & Frequency Div., Nat. Bur. of Stand., Boulder, CO, USA; Proceedings of the 32nd Annual Symposium on Frequency Control 1978, Atlantic City, NJ, USA, 31 May - 2 June 1978 (Washington, DC, USA: Electronic Industries Assoc. 1978) pp 453-9

2.1.1

Audoin, C.; Jardino, M.; Cutler, L.S.; Lacey, R.F.
 "Frequency offset due to spectral impurities in cesium-beam frequency standards." Univ. Paris-Sud, Orsay, France; IEEE Trans. Instrum. & Meas. (USA), vol. 1M-27, no. 4, pp 325-9 (Dec. 1978) (CPEM '78 Conference on Precision Electromagnetic Measurement, Ottawa, Canada, 26-29 June 1978).

Becker, G.
 "Research on Cs beam frequency standards at the PTB: beam optics, Majorana transitions." Phys.-Tech. Bundesanstalt, Braunschweig, Germany; IEEE Trans. Instrum. & Meas. (USA), vol. 1M-27, no. 4, pp 319-25 (Dec. 1978). (CPEM '78 Conference on Precision Electromagnetic Measurement, Ottawa, Canada, 26-29 June 1978)

Emmons, D.A.; Rogers, P.J.
 "New Cesium Beam Tube Utilizing Hexapole State Selection." Frequency & Time Systems, Inc.; 31st Annual Symposium on Frequency Control, US Army Electronics Command, Fort Monmouth, NJ, pp 490-493 (1977). Copies available from the Electronic Industries Association, 2001 Eye Street, N.W. Washington D.C. 20006

Hahn, S.L.; Radecki, K.W.
 "Features of a silver beam magnetic resonance apparatus as a frequency standard." Inst. of Radioelectronics, Warsaw Tech. Univ., Warsaw, Poland; IEEE Trans. Instrum. & Meas. (USA), vol. 1M-27, no. 4, pp 335-8 (Dec. 1978) (CPEM '78 Conference on Precision Electromagnetic Measurement, Ottawa, Canada, 26-29 June 1978)

Iijima, S.; Fujiwara, K.; Kobayashi, H.; Kato, T.
 "Effect of environmental conditions on the rate of a cesium clock." Tokyo Astron. Obs., Univ. of Tokyo, Tokyo, Japan; Ann. Tokyo Astron. Obs. (Japan), vol. 17, no. 1, pp 50-67 (1978).

Jumonji, H.; Tanaka, K.; Toyama, J.; Takaoka, H.; Kariya, K.; Kawada, J.
 "A new low voltage, maintenance-free, cesium beam tube for a frequency standard." Yokosuka Electrical Communication Lab., NTT, Tokyo, Japan; Proceedings of the 32nd Annual Symposium on Frequency Control 1978, Atlantic City, NJ, USA, 31 May - 2 June 1978 (Washington, DC, USA: Electronic Industries Assoc. 1978) pp 460-5

Kobayashi, M.; Nakagiri, K.; Urabe, S.; Shibuki, M.; Saburi, Y.

"Design of and preliminary results on a cesium-beam standard at the Radio Research Laboratories." Radio Res. Labs., Koganei, Tokyo, Japan; IEEE Trans. Instrum. & Meas. (USA), vol. 1M-27, no. 4, pp 343-8 (Dec. 1978) (CPEM '78 Conference on Precision Electromagnetic Measurement, Ottawa, Canada, 26-29 June 1978).

DeMarchi, A.; Bava, G.P.
 "Stability limits for frequency standards using divergent beams." Istituto Elettrotecnico Nazionale, Torino, Italy; Metrologia (Germany), vol. 14, no. 4, pp 179-83 (1978)

McCaskill, T.; White, J.; Stebbins, S.; Buisson, J.
 "NTS-2 cesium frequency stability results." Naval Res. Lab., Washington, DC, USA; Proceedings of the 32nd Annual Symposium on Frequency Control 1978, Atlantic City, NJ, USA, 31 May - 2 June 1978 (Washington, D.C., USA: Electronic Industries Assoc. 1978) pp 560-6

Mungall, A.G.
 "A new concept in atomic time keeping: the continuously operating long-beam primary cesium clock." Div. of Phys. Nat. Res. Council, Ottawa, Ontario, Canada; IEEE Trans. Instrum. & Meas. (USA), vol. 1M-27, no. 4, pp 330-4 (Dec. 1978) (CPEM '78 Conference on Precision Electromagnetic Measurement, Ottawa, Canada, 26-29 June 1978)

Pascaru, I.; Meirs, M.
 "Development of a Light Weight, Military, Cesium Standard." Frequency Electronics, Inc.; 31st Annual Symposium on Frequency Control, US Army Electronics Command, Fort Monmouth, NJ, pp 484-489 (1977). Copies available from the Electronic Industries Association, 2001 Eye Street, N.W. Washington D.C. 20006

Rovera, G.; Leschiutta, S.; Busca, G.; Strumia, F.
 "Parameters affecting the stability of an optically pumped cesium frequency standard." Istituto Elettrotecnico Nazionale, Torino, Italy; Proceedings of the 32nd Annual Symposium on Frequency Control 1978, Atlantic City, NJ, USA, 31 May - 2 June 1978 (Washington, D.C., USA: Electronic Industries Assoc. 1978) pp 466-8

2.1.2

Brunet, M.
 "Rubidium standards." Mes. Regul. Autom. (France), vol. 43, no 6-7, pp 67-75 (June-July 1978). in French

Risley, A.; Busca, G.
 "Effect of line inhomogeneity on the frequency of passive Rb frequency standards." Nat. Bur. of Stand., Boulder, CO, USA; Proceedings of the 32nd Annual Symposium on Frequency Control 1978, Atlantic City, NJ, USA, 31 May - 2 June 1978 (Washington D.C., USA: Electronic Industries Assoc. 1978) pp 506-13

Risley, A.; Jarvis, S., Jr.; Vanier, J.
 "Study of the Dependence of Frequency upon Microwave Power of Wall-Coated and Buffer-Gas-Filled Passive Rb⁸⁷ Frequency Standards." National Bureau of Standards & Université Laval; 31st Annual Symposium on Frequency Control, US Army Electronics Command, Fort Monmouth, NJ, pp 477-483 (1977). Copies available from the Electronic Industries Association, 2001 Eye Street, N.W. Washington DC 20006

2.1.3

Audoin, C.; Lesage, P.; Viennet, J.; Barillet, R.
 "Analysis of H-maser autotuning systems." Lab. de l'Horloge Atomique, Univ. Paris-Sud, Orsay, France; Proceedings of the 32nd Annual Symposium on Frequency Control 1978, Atlantic City, NJ, USA, 31 May - 2 June 1978 (Washington, DC, USA: Electronic Industries Assoc. 1978) pp 531-41

Beverini, N.; Vanier, J.
 "Tuning of hydrogen maser cavity by means of a variable capacitance diode." Dept. de Génie Électrique, Univ. Laval, Quebec, Canada; IEEE Trans. Instrum. & Meas. (USA), vol. IM-28, no. 2, pp 100-4 (June 1979)

Busca, G.; Brandenberger, H.; Ebauches, S.A.
 "Passive H Maser." 31st Annual Symposium on Frequency Control, US Army Electronics Command, Fort Monmouth, NJ, pp 563-568 (1977). Copies available from the Electronic Industries Association, 2001 Eye Street, N.W. Washington DC 20006

Elkin, G.A.; Zhestkova, N.D.; Paramzin, V.A.
 "Measuring wall-induced frequency shift in a hydrogen oscillator." Meas. Tech. (USA), vol. 20, no. 10, pp 1453-5 (Oct. 1977). Translation of: Izmer. Tekh. (USSR), vol. 20, no. 10, pp 39-40 (Oct. 1977)

Gneorghi, O.C.; Mandache, C.M.
 "On a hydrogen dissociator for maser." Inst. for Phys. & Technol. of Radiation Devices, Bucharest, Rumania; Rev. Roum. Phys. (Rumania), vol 24, no. 3-4, pp 317-23 (1979)

Howe, D.A.; Walls, F.L.; Bell, H.E.; Hellwig, H.
 "A Small, Passively Operated Hydrogen Maser." National Bureau of Standards; 31st Annual Symposium on Frequency Control, US Army Electronics Command, Fort Monmouth, NJ, pp 554-562 (1977). Copies available from the Electronic Industries Association, 2001 Eye Street, N.W. Washington D.C. 20006

Lesage, P.; Audoin, C.
 "Amplitude Noise in Actively and Passively Operated Hydrogen Masers." CNRS; 31st Annual Symposium on Frequency Control, US Army Electronics Command, Fort Monmouth, NJ, pp 515-535 (1977). Copies available from the Electronic Industries Association, 2001 Eye Street, N.W. Washington D.C. 20006

Levine, M.W.; Vessot, R.F.; Mattison, E.M.
 "Performance evaluation of the SAO VLG-11 atomic hydrogen masers." Center for Astrophys., Harvard Coll. Obs., Cambridge, MA, USA; Proceedings of the 32nd Annual Symposium on Frequency Control 1978, Atlantic City, NJ, USA, 31 May - 2 June 1978 (Washington, D.C., USA: Electronic Industries Assoc. 1978) pp 477-85

Mattison, E.M.; Blomberg, E.L.; Nystrom, G.N.; Vessot, R.F.C.
 "Design and Testing of a Small Passive Hydrogen Maser." Smithsonian Astrophysical Observatory; 31st Annual Symposium on Frequency Control, US Army Electronics Command, Fort Monmouth, NJ, pp 549-553 (1977). Copies available from the Electronic Industries Association, 2001 Eye Street, N.W. Washington D.C. 20006

Morris, D.
 "Time-dependent frequency shifts in the hydrogen maser." Div. of Phys., Nat. Res. Council of Canada, Ottawa, Ontario, Canada; IEEE Trans. Instrum. & Meas. (USA), vol. IM-27, no. 4, pp 339-43 (Dec. 1978) (CPEM '78 Conference on Precision Electromagnetic Measurement, Ottawa, Canada, 26-29 June 1978).

Peters, H.E.
 "Small, very small, and extremely small hydrogen masers." Sigma Tau Standards Corp., Tuscaloosa, AL, USA; Proceedings of the 32nd Annual Symposium on Frequency Control 1978, Atlantic City, NJ, USA, 31 May - 2 June 1978 (Washington, D.C., USA: Electronic Industries Assoc. 1978) pp 469-76

Rueger, L.J.; Bates, A.; Stillman, L.; Norton, J.; Blackburn, C.M.; Reinhardt, V.A.
 "NASA NR hydrogen maser." Appl. Phys. Lab., Johns Hopkins Univ., Laurel, MD, USA; Proceedings of the 32nd Annual Symposium on Frequency Control 1978, Atlantic City, NJ, USA, 31 May - 2 June 1978 (Washington, D.C., USA: Electronic Industries Assoc. 1978) pp 486-91

Sabisky, E.S.; Weakliem, H.A.
 "An operating development model spacecraft hydrogen maser." RCA David Sarnoff Res. Center, Princeton, NJ, USA; Proceedings of the 32nd Annual Symposium on Frequency Control 1978, Atlantic City, NJ, USA, 31 May - 2 June 1978 (Washington, DC, USA: Electronic Industries Assoc. 1978) pp 499-500

Savard, J.-Y.; Busca, G.; Rovea, S.; Petit, P.; Desaintfussien, M.
 "Effects of coherently excited Zeeman transitions on a hydrogen maser hyperfine transition." Dept. de Génie Électrique, Univ. Laval, Quebec, Ontario, Canada; Can. J. Phys. (Canada), vol. 57, no. 6, pp 904-16 (June 1979)

Vessot, R.F.C.; Mattison, E.M.; Blomberg, E.L.
 "Experiments with a Cryogenic Hydrogen Maser." Smithsonian Astrophysical Observatory; 31st Annual Symposium on Frequency Control, US Army Electronics Command, Fort Monmouth, NJ, pp 511-514 (1977). Copies available from the Electronic Industries Assoc., 2001 Eye St., N.W. Washington DC 20006

Walls, F.L.; Howe, D.A.

"A passive hydrogen maser frequency standard." Nat. Bur. of Stand., Boulder, CO, USA; Proceedings of the 32nd Annual Symposium on Frequency Control 1978 Atlantic City, NJ, USA, 31 May - 2 June 1978 (Washington, DC, USA: Electronic Industries Assoc. 1978) pp 492-8

Wang, H.T.M.

"Hydrogen Frequency Standard Using Free Induction Technique." Hughes Research Laboratories; 31st Annual Symposium on Frequency Control, US Army Electronics Command, Fort Monmouth, NJ, pp 536-542. (1977). Copies available from the Electronic Industries Association, 2001 Eye Street, N.W. Washington D.C. 20006

Wang, H.T.M.; Lewis, J.B.; Crampton, S.B.

"Compact Cavity for Hydrogen Frequency Standard." Hughes Research Laboratories & Williams College; 31st Annual Symposium on Frequency Control, US Army Electronics Command, Fort Monmouth, NJ, pp 543-548 (1977). Copies available from the Electronic Industries Association, 2001 Eye Street, N.W. Washington D.C. 20006

2.1.4

Laine, D.C.; Al-Jumaily, A.M.

"Injection priming of a pulsed molecular-beam maser oscillator." Dept. of Phys. of Keele, Keele, England; Electron. Lett. (GB), vol. 15, no. 1, pp 21-3 (4 Jan 1979)

Vanier, J.; Nguyen, D.H.; Busca, G.; Tetu, M.

"Study of the effect of light shifts and buffer gas shifts on the hyperfine transition of ⁸⁵Rb: influence of the long term frequency stability of the rubidium maser." Dept. de Genie Electrique, Univ. Laval, Quebec, Canada; Can. J. Phys. (Canada), vol. 57, no. 9, pp 1380-7 (Sept. 1979)

Wineland, D.J.; Howe, D.A.; Mohler, M.B.; Hellwig, H.W.

"Special purpose ammonia frequency standard - a feasibility study." Nat. Bur. of Stand., Boulder, CO, USA; IEEE Trans. Instrum. & Meas. (USA), vol. IM-28, no. 2, pp 122-32 (June 1979)

2.2

Bava, E.; DeMarchi, A.; Godone, A.

"Direct synthesis of the frequency of a long distance infrared source." Istituto Elettrotecnico Nazionale, Torino, Italy; Alta Freq. (Italy), vol. 47, no. 12, pp 851-8 (Dec. 1978) In Italian

Bergquist, J.C.; Wineland, D.J.

"Laser to Microwave Frequency Division Using Synchrotron Radiation." National Bureau of Standards; 31st Annual Symposium on Frequency Control, US Army Electronics Command, Fort Monmouth, NJ, pp 494-497 (1977). Copies available from the Electronic Industries Association, 2001 Eye Street, N.W. Washington D.C. 20006

Chebotaev, V.P.

"Use of ultranarrow resonance in spectroscopy and for stabilizing gas laser frequencies." Inst. for Semiconductor Phys., Acad. of Sci., Novosibirsk, USSR; Sov. J. Quantum Electron. (USA), vol. 8, no. 9, pp 1130-5 (Sept. 1978). Translation of: Kvantovaya Elektron., Moskva (USSR), vol. 5, no. 9, pp 2004-14 (Sept 1978)

Yuan-Wu, Chi

"A survey of optical frequency standards." Kexue Tongbao (China), vol. 23, no. 8, pp 452-8 (Aug. 1978). In Chinese. English translation in: Kexue Tongbao (Scientia) (USA)

DeMarchi, A.; Godone, A.; Bava, E.

"Comparison of Different Tuning and Modulation Techniques for F.I.R. Lasers." Istituto Elettrotecnico Nazionale; 31st Annual Symposium on Frequency Control, US Army Electronics Command, Fort Monmouth, NJ, pp 504-510 (1977). Copies available from the Electronic Industries Association, 2001 Eye Street, N.W. Washington D.C. 20006

Efimov, G.V.; Semenovskaya, N.A.; Tkachenko, V.S.; Fertik, N.S.; Chuprakov, A.V.

"Investigation of the frequency response of piezoelectric transducers used in frequency stabilization of lasers." Avtometriya (USSR), no. 2, pp 136-9 (March-April 1978). In Russian. English translation in: Autom. Monit. & Meas. (GB)

Hall, J.L.

"Stabilized lasers and precision measurements." Univ. of Colorado, Boulder, CO, USA; Science (USA), vol. 202, no. 4364, pp 147-56 (13 Oct 1978)

Rutman, J.

"Standard frequency generators in the submillimeter infrared and visible light regions of the electromagnetic spectrum." LPTE, Paris, France, Onde Electr. (France), vol. 59, no. 3, pp 91-6 (March 1979) In French

Vergunov, V.B.; Vol'nov, M.I.; Tyurikow, D.A.

"Electronic system for stabilizing the difference frequency of two lasers." Phys. Inst., Acad. of Sci., Moscow, USSR; Instrum. & Exp. Tech. (USA), vol. 21, no. 3, pt. 2, pp 765-6 (May-June 1978). Translation of: Prib. Tekh. Eksp. (USSR), vol. 21, no. 3, pt. 2, pp 197-8 (May-June 1978)

Vlasov, A.N.

"Long-term instability and irreproducibility of a gas laser frequency and requirements to be satisfied by automatic frequency control systems." Sov. J. Quantum Electron. (USA), vol. 8, no. 7, pp 866-869, (July 1978). Translation of: Kvantovaya Elektron., Moskva (USSR), vol. 5, no. 7, pp 1518-1548 (July 1978).

2.2.1

- Bondarenko, A.N.; Krinitsyn, Yu. M.
"Frequency stabilisation in a He-Ne laser at $\lambda=0.63 \mu$ operating in competitive oscillation mode." *Avtometriya* (USSR), no. 3, pp 115-19 (May-June 1978). In Russian. English translation in: *Autom. Monit. & Meas.* (GB)
- Bondarenko, A.N.; Vologdin, V.K.; Krinitsyn, Yu.M.
"Stabilized two-frequency He+Ne Laser for 0.63-wavelength." *Instrum. & Exp. Tech.* (USA), vol. 21, no. 4, pt. 2, pp 1090-2 (July-Aug 1978). Translation of: *Prib. Tekh. Eksp.* (USSR), vol. 21, no. 4, pt. 2, pp 225-8 (July-Aug 1978)
- Cerez, P.; Bennett, S.J.
"New developments in iodine-stabilized He-Ne lasers." *Univ. de Paris-Sud, Orsay, France; IEEE Trans. Instrum. & Meas.* (USA), vol. IM-27, no. 4, pp 396-8 (Dec. 1978). (CPEM '78 Conference on Precision Electromagnetic Measurement, Ottawa, Canada, 26-29 June 1978).
- Cerez, P.; Brillet, A.; Man, C.
"Frequency stabilised He-Ne lasers." *Lab. de l'Horloge Atomique, Univ. Paris-Sud, Orsay, France; Rev. Phys. Appl. (France)*, vol. 14, no. 2, pp 347-51 (Feb. 1979). In French.
- Cerez, P.; Bennett, S.J.
"Helium-neon laser stabilized by saturated absorption in iodine at 612 nm." *Lab. de l'Horloge Atomique, Univ. de Paris-Sud, Orsay, France; Appl. Opt.* (USA), vol. 18, no. 7, pp 1079-83 (1 April 1979)
- Kekung, C.; Hsueh-ping, C.; Chia-chi, C.; Cheng-hsian, L.
"Methane saturated absorption stabilized He-Ne laser." *Kexue Tongbao (China)*, vol. 23, no. 12, pp 734-6 (Dec. 1978). In Chinese. English translation in: *Kexue Tongbao (Scientia)* (USA) (no refs.)
- Dandwate, V.D.; Puntambekar, P.N.; Sen, D.
"Iodine stabilised He-Ne laser." *Nat. Phys. Lab., New Delhi, India; Pramana (India)*, vol. 12, no. 5, pp 465-74 (May 1979)
- Deki, K.; Yamamoto, H.; Ohta, T.
"Frequency stabilization of a gas laser utilizing the magnetic field tuning dip." *Faculty of Engng.; Doshisha Univ., Kyoto, Japan; Trans. Inst. Electron. & Commun. Eng. Jpn. Sect. E (Japan)*, vol. E62, no. 1, pp 56-7 (Jan 1979)
- Ferguson, J.B.; Morris, R.H.
"Single-mode collapse in 6328-A He-Ne lasers." *Phys. Dept., San Diego State Univ., San Diego, CA, USA; Appl. Opt.* (USA), vol. 17, no. 18, pp 2924-9 (15 Sept. 1978)
- Gelikonov, V.M.; Zaitsev, Yu. T.; Malykin, G.B.
"Laser frequency self-stabilization effect in the presence of rapid perturbations." *Inst. of Appl. Phys., Acad. of Sci., Gorki, USSR; Sov. J. Quantum Electron. (USA)*, vol. 9, no. 2, pp 227-9 (Feb. 1979). Translation of: *Kvantovaya Elektron.*, Moskva (USSR) vol. 6, no. 2, pp 381-3 (Feb. 1979).

Gubin, M.A.; Nikitin, V.V.; Petrovskii, V.N.; Protsenko, E.D.; Tyurikow, D.A.; Yatsenko, L.P.
"Investigation of the stability and frequency shifts of a two-mode He-Ne-CH₄ laser." *P.N. Lebedev Phys. Inst., Acad. of Sci., Moscow, USSR; Sov. J. Quantum Electron. (USA)*, vol. 9, no. 1, pp 34-9 (Jan 1979). Translation of *Kvantovaya Elektron.*, Moskva (USSR), vol 6, no. 1, pp 63-71 (Jan 1979).

Nakazawa, M.; Musha, T.; Tako, T.
"Frequency stabilization of a 3.39 μ m HeNe laser with no frequency modulation." *Graduate School of Nagatsuda, Tokyo Inst. of Technol., Yokohama, Japan; Trans. Inst. Electron. & Commun. Eng. Jpn. Sect. E (Japan)*, vol. E62, no. 1, pp 51-2 (Jan 1979)

Nakazawa, M.; Musha, T.; Tako, T.
"Frequency-stabilized 3.39- μ m He-Ne laser with no frequency modulation." *Dept. of Appl Electronics, Tokyo Inst. of Technol., Yokohama, Japan; J. Appl. Phys. (USA)*, vol. 50, no. 4, pp 2544-7 (April 1979)

Nai-cheng, S.; Chia-Lua, A.; Yao-hsiang, W.; I-min, S.; Han-chien, S.
"Performance investigation of iodine saturated absorption stabilized He-Ne lasers." *Kexue Tongbao (China)*, vol. 23, no. 12, pp 730-3 (Dec. 1978). In Chinese. English translation in: *Kexue Tongbao (Scientia)* (USA) (6 refs.)

Tanaka, K.; Morinaga, A.
"Preliminary experiment for stabilizing unmodulated He-Ne laser to an iodine hyperfine component." *Nat. Res. Lab. of Metrology, Tokyo, Japan; J. Appl. Phys. (USA)*, vol. 50, no. 1, pp 38-40 (Jan 1979)

2.2.2

Andreev, P.S.; Gusev, A.A.; Kruzhlov, S.V.; Pakhomov, L.N.; Petrun'kin, V.Yu.
"Stabilized single-frequency travelling-wave YAG:Nd³⁺ laser." *M.I. Kalinin Polytech. Inst. Leningrad, USSR; Sov. Tech. Phys. Lett. (USA)*, vol. 4, no. 3, pp 137-8 (March 1978). Translation of: *Pis'ma V Zh. Tekh. Fiz.* (USSR), vol. 4, no. 5-6, pp 339-43 (March 1978)

Avtonomov, V.P.; Alexandrescu, R.; Dumitras, D.; Duta, D.
"Possible stabilization of the frequency of a CO₂ laser using an external Stark cell containing 1-1 difluoroethane." *P.N. Lebedev Phys. Inst., Acad. of Sci., Moscow, USSR; Sov. J. Quantum Electron. (USA)*, vol. 9, no. 2, pp 204-6 (Feb. 1979). Translation of: *Kvantovaya Elektron.*, Moskva (USSR), vol. 6, no. 2, pp 351-4 (Feb. 1979)

Champagne, L.F.
"Electron beam controlled, neon stabilized XeF laser." *Optical Sci. Div., Naval Res. Lab., Washington, DC, USA; Proceedings of the Fourth Colloquium on Electronic Transition Lasers, Munich, Germany, 20-22 June 1977 (Berlin, Germany: Springer-Verlag 1978)*, pp 32-6

Pei-lin, C.; Lien-fang, C.; Soo-soo, Y.; Shing-fang, H.

"Investigation of the frequency stabilization of a dual frequency laser." Dept. of Fundamental Courses, Tsinghua Univ., Peking, China; J. Tsing Hua Univ. (China), no. 3, pp 21-31 (1978). In Chinese.

Jitschin, W.; Meisel, G.

"Fast frequency control of a CW dye jet laser." Inst. für Angewandte Phys., Univ. Bonn, Bonn, Germany; Appl. Phys. (Germany), vol. 19, no. 2, pp 181-4 (June 1979)

Kubodera, K.; Otsuka, K.; Miyazawa, S.

"Stable LiNdP_{10} miniature laser." Nippon Telegraph & Telephone Public Corp., Musashino Elec. Communication Lab., Tokyo, Japan; Appl. Opt. (USA) vol. 18, no. 6, pp 884-90 (15 March 1979)

Lund, M.W.; Cogan, J.N.; Davis, J.A.

"Low-cost method for stabilization of a CO_2 laser for use in far infrared laser pumping." Dept. of Phys., San Diego State Univ., San Diego, CA, USA; Rev. Sci. Instrum. (USA), vol. 50, no. 6, pp 791-2 (June 1979)

Ohtsu, M.; Tako, T.

"Frequency stability of an H_2CO -stabilized He-Xe laser in an axial magnetic field." Res. Lab. of Precision Machinery & Electronics, Tokyo Inst. of Technol., Yokohama, Japan; Jpn. J. Appl. Phys. (Japan), vol. 17, no. 12, pp 2169-70 (Dec. 1978)

Ohtsu, M.; Koyama, R.; Tako, T.

"Improvements in the long-term frequency stability of the He-Xe laser at $3.51 \mu\text{m}$." Res. Lab. of Precision Machinery & Electronics, Tokyo Inst. of Technol., Yokohama, Kanagawa, Japan; Jpn. J. Appl. Phys. (Japan), vol. 18, no. 8, pp 1621-2 (Aug 1979)

Oraevskii, A.N.

"Development of a highly stable optical frequency standard utilizing an atomic beam." P.N. Lebedev Phys. Inst., Acad. of Sci., Moscow, USSR; Sov. J. Quantum Electron. (USA), vol. 8, no. 8, pp 1053-5, (Aug 1978). Translation of: Kvantovaya Elektron., Moskva (USSR), vol. 5, no. 8, pp 1850-3 (Aug 1978)

Spieweck, F.

"Frequency stabilization of Ar^+ lasers by saturated absorption in external I_2 cells (at 582 THz)." Phys.-Tech. Bundesanstalt, Braunschweig, Germany; IEEE Trans. Instrum. & Meas. (USA), vol. IM-27, no. 4, pp 398-400 (Dec. 1978). (CPEM '78 Conference on Precision Electromagnetic Measurement, Ottawa, Canada, 26-29 June 1978).

Tsao, J.Y.; Sharp, R.C.; Yablonovitch, E.

"Digital feedback stabilization of a single-axial-mode CO_2 TEA laser." Div. of Appl. Sci., Harvard Univ., Cambridge, MA, USA; Rev. Sci. Instrum. (USA) vol. 50, no. 8, pp 1023-4 (Aug 1979)

van Oorschot, B.P.J.; van der Hoeven, C.J.

"A recently developed iodine-stabilised laser." Nat. Phys. Res. Lab., CSIR, Pretoria, S. Africa; J. Phys. E. (GB), vol. 12, no. 1, pp 51-5 (Jan 1979)

Vladimirkii, K.V.; Norvaishas, A.A.

"Stability of lasing on an asymmetrical inhomogeneously broadened line. II." Sov. Phys.-Lebedev Inst. Rep. (USA), no. 10, pp 32-6 (1977). Translation of: Sb. Kratk. Soobshch. Fiz. AN SSR Fiz. Inst. P.N. Lebedev, no. 10, pp 37-41 (1977)

Wang, C.P.; Varwig, R.L.

"Frequency stabilization of HF lasers by means of beat signals and anomalous dispersion." Ivan A. Getting Labs., Aerospace Corp., El Segundo, CA, USA; J. Appl. Phys. (USA), vol. 50, no. 6, pp 3838-40 (June 1979).

3.1

Baird, K.M.; Hanes, G.R.; Evenson, K.M.; Jennings, D.A.; Petersen, F.R.

"Extension of absolute-frequency measurements to the visible: frequencies of ten hyperfine components of iodine." Nat. Res. Council, Ottawa, Canada; Opt. Lett. (USA), vol. 4, no. 9, pp 263-4 (Sept. 1979)

Bezrukov, S.M.; Preobrazhenskii, N.I.

"Increased accuracy in audio-frequency measurements with the S4-12 and S4-53 spectrum analyzers." Leningrad Inst. of Nuclear Phys., Acad. of Sci., USSR; Instrum. & Exp. Tech. (USA), vol. 21, no. 3, pt. 2, pp 714-16 (May-June 1978). Translation of: Prib. Tekh. Eksp. (USSR), vol. 21, no. 3, pt. 2, pp 152-3 (May-June 1978)

Bologlu, A.; Barber, V.A.

"Microprocessor-controlled harmonic heterodyne microwave counter also measures amplitudes." Hewlett-Packard J. (USA), vol. 29, no. 9, pp 2-4, 6-7, 9-12, 14-16 (May 1978)

Burgoon, R.; Fischer, M.C.

"Conversion between time and frequency domain of intersection points of slopes of various noise processes." Hewlett-Packard Co., Santa Clara, CA, USA; Proceedings of the 32nd Annual Symposium on Frequency Control 1978, Atlantic City, NJ, USA, 31 May - 2 June 1978 (Washington, DC, USA: Electronic Industries Assoc. 1978) pp 514-19

Bushuev, F.I.; Ivakin, V.M.

"Electronic converter of the unit time dimension." Meas. Tech. (USA), vol. 21, no. 6, pp 788-9 (June 1978). Translation of: Izmer. Tekh. (USSR), vol. 21, no. 6, pp 38-9 (June 1978)

Drake, J.M.; Rodriguez-Izquierdo, G.

"Analogue setup for fast-response frequency measurement." Electron. Eng. (GB), vol. 50, no. 614, pp 41, 43, (Oct. 1978)

- Englert, R.
"Circuit for measuring very low frequencies." Elektronik (Germany), vol. 27, no. 15, pp 67-8 (21 Dec. 1978) in German.
- Godone, A.; DeMarchi, A.; Bava, E.
"A New Compact Multiplier Chain for Precise Frequency Measurements up to 20 THz." Istituto Elettrotecnico Nazionale; 31st Annual Symposium on Frequency Control, US Army Electronics Command, Fort Monmouth, NJ, pp 498-503 (1977). Copies available from the Electronic Industries Association, 2001 Eye Street, N.W. Washington D.C. 20006
- Hellwig, H.; Wineland, D.J.; Evenson, K.M.
"Time, frequency and physical measurement." Nat. Bur. of Stand., Boulder, CO, USA; Phys. Today (USA) vol. 31, no. 12, pp 23-30 (Dec. 1978)
- Jennings, D.A.; Petersen, F.R.; Evenson, K.M.
"Frequency measurement of the 260-THz (1.15- μ m) He-Ne laser." Time & Frequency Div., Nat. Bur. of Stand., Boulder, CO, USA; Opt. Lett. (USA), vol. 4, no. 5, pp 129-30 (May 1979)
- Jones, C.H.
"A test equipment for the measurement of phase and frequency instability in VHF and SHF sources." Royal Signals & Radar Establ., Ministry of Defence, Christchurch, England; Radio & Electron. Eng. (GB), vol. 49, no. 4, pp 187-96 (April 1979)
- Kimel'blat, V.I.
"Evaluation of measuring accuracy of middle frequency and band-width for radio-receiving apparatus" Meas. Tech. (USA), vol. 21, no. 4, pp 541-3 (April 1978). Translation of: Izmer. Tekh. (USSR), vol. 21, no. 4, pp 60-1 (April 1978)
- Kolbasin, A.I.; Pavlenko, Yu. F.
"Transfer of the dimension of a unit deviation of frequency from the special state standard to prototype means of measurement." Meas. Tech. (USA), vol. 21, no. 6, pp 806-9 (June 1978). Translation of Izmer. Tekh. (USSR), vol. 21, no. 6, pp 49-50 (June 1978)
- Koppe, H.
"Frequency measurement using a microcomputer - a program and an instruction program." Elektron. Präz. (Germany), vol. 14, no. 5, pp 30, 35-6, 39 (May 1979). In German.
- Loose, P.
"Modern electronic-based timing systems." Electron. Eng. (GB), vol. 15, no. 622, pp 81, 83-4 (May 1979)
- Ohman, B.
"New task for the telecommunication authority - national measurement standards for time and frequency." Tele (Swed. Ed.) (Sweden), vol. 84, no. 4, pp 14-24 (1978). In Swedish
- Pacheu, Y.
"Analogue frequency meter." Electron. & Appl. Ind. (France), no. 262S, pp 15-16 (15 Jan 1979). In French.
- Percival, D.B.
"The U.S. Naval Observatory clock time scales." US Naval Obs., Washington, DC, USA; IEEE Trans. Instrum. & Meas. (USA), vol. IM-27, no. 4, pp 376-85 (Dec. 1978). (CPEM '78 Conference on Precision Electromagnetic Measurement, Ottawa, Canada, 26 - 29 June 1978).
- Petrov, A.F.; Zhukov, E.T.; Kosharnovskii, G.V.; Breslavets, V.P.; Fedulov, V.M.
"Frequency comparator based on a delay line." Meas. Tech. (USA), vol. 20, no. 10, pp 1456-8 (Oct 1977). Translation of: Izmer. Tekh. (USSR), vol. 20, no. 10, pp 40-2 (Oct. 1977)
- Rama Murthy, T.V.; Kumar, M.K.
"A measurement technique for low frequencies." Systems Engng. Div., Nat. Aeronautical Lab., Bangalore, India; J. Phys. E (GB), vol. 12, no. 3, pp 187-8 (March 1979)
- Speake, B.
"The accurate setting of microwave frequencies." Caledonian Microwave Ltd., Elgin, Moray, Scotland; Commun. Int., (GB), vol. 6, no. 2, pp 19, 21 (Feb. 1979)
- Szepean, R.
"Determining accuracy of receiver-controlled frequency standards." Rohde & Schwarz, Munich, Germany; News Rohde & Schwarz (Germany), vol. 18, no. 82, pp 23-6 (1978).
- Tooley, M.
"In-line crystal calibrator." Pract. Wireless (GB), vol. 55, no. 5, pp 49-50, 55 (May 1979)
- van den Steen, L.
"A low frequency meter with instantaneous response" TNO Medical Biological Lab., Rijswijk, Netherlands; IEEE Trans. Biomed. Eng. (USA), vol. BME-26, no. 3, pp 137-40 (March 1979)
- van Straaten, J.
"A one-chip LSI frequency meter in the I^2L technology for FM and AM receivers." N.V. Philips Gloeilampenfabrieken, Nijmegen, Netherlands; IEEE Trans. Commun. Electron. (USA), vol. CE-25, no. 1, pp 134-43 (Feb. 1979)
- Voss, R.F.
"1/f Noise." IBM; 31st Annual Symposium on Frequency Control, US Army Electronics Command, Fort Monmouth NJ, pp 40-46 (1977). Copies available from the Electronic Industries Association, 2001 Eye Street, N.W. Washington D.C. 20006
- Woschni, E.G.
"Application of microprocessors to the calculation of error correction for the synchronisation effect in highly accurate frequency measurements." Wiss. Z. Tech. Hochsch. Karl-Marx-Stadt (Germany), vol. 20, no. 5, pp 665-8 (1978). In German.

"A system of measurement and display of frequency for a AM/FM receiver." *Electron. & Appl. Ind.* (France), no. 271, pp 55-6 (15 June 1979) In French

3.1.1

Arai, M.

"Frequency counter trends: μ -processors facilitate improvements." *Iwatsu Electric Co. Ltd.*, Tokyo, Japan; *JEE* (Japan), no. 136, pp 30-1 (April 1978)

Arai, M.

"Universal counters are becoming intelligent." *Iwatsu Electric Co., Ltd.*, Tokyo, Japan, *JEE* (Japan), no. 136, pp 32-4 (April 1978)

Bodea, M.; Danila, T.

"Autoranging, digital time-interval meter." *Bul. Inst. Politeh. 'Gheorghe Gheorghiu-Dej' Bucuresti Ser. Electroteh.* (Rumania), vol. 40, no. 2, pp 57-63 (April-June 1978) In Rumanian

De Costanzo, L.

"Radio receiver frequency counter/clock." *Electron. Ind.* (GB), vol 5, no. 8, pp 16-17 (Aug. 1979)

Cardwell, W.T., Jr.

"Frequency counter in a probe." *Radio-Electron.* (USA), vol. 49, no. 10, pp 67, 72-3, 100-1, 103 (Oct. 1978)

Colburn, J.; Owen, B.

"600 MHz portable frequency counter." *Optoelectronics Inc.*, Ft. Lauderdale, FL, USA; *Radio-Electron.* (USA), vol. 50, no. 1, pp 39-43, 90 (Jan 1979)

Conway, A.; Urdaneta, N.

"Selecting a frequency counter." *Teleph. Eng. & Manage.* (USA), vol. 82, no. 15, pp 77-8 (1 Aug 1978).

Conway, A.; Urdaneta, N.

"Considerations in selecting a frequency counter." *Communications* (USA), vol. 15, no. 12, pp 22-3 (Dec. 1978)

Hamanaka, A.

"New frequency counter series features high reliability." *Anritsu Electric Co. Ltd.*, Tokyo, Japan; *JEE* (Japan), no. 142, pp 50-4 (Oct 1978)

Koch, E.

"An all-waveband receiver with a digital frequency display and a quartz clock." *Funkschau* (Germany), vol. 51, no. 5, pp 236-9 (2 March 1979) In German.

McCarthy, E.P.

"A digital instantaneous frequency meters." *Electrical Engng. Dept., Univ. of Salford*, Salford, England; *IEEE Trans. Instrum. & Meas.* (USA), vol. IM-28, no. 3, pp 224-6 (Sept. 1979)

McClellan, G.

"Prescaler and LSI chip form 135-MHz counter." *Electronics* (USA), vol. 51, no. 26, pp 97, 99 (21 Dec. 1978)

Pritchard, N.B.

"A frequency counter for a 144 MHz transmitter." *Radio Commun.* (GB), vol. 55, no. 5, pp 410-15 (May 1979)

Schommartz, G.

"On the measurement dynamics of digital frequency meters." *Wilhelm-Pieck-Univ., Rostock, Germany; MSR* (Mess. Steuern Regeln) (Germany), vol. 22, no. 5, pp 261-7 (May 1979). In German.

Schreiber, H.

"Active test head for a frequency counter." *Funk-Tech.* (Germany), vol. 33, no. 14, pp 241-2 (July 1978). In German.

Simpson, L.

"Upgraded 200 MHz digital frequency meter. II. Construction details." *Electron. Aust.* (Australia), vol. 40, no. 6, pp 60-3 (Sept. 1978)

"A frequency counter for radio receivers."

Elektronischau (Austria), vol. 55, no. 7, pp 56-7, (1979). In German

"A universal counter on one chip." *Elektronischau* (Austria), vol. 54, no. 11, pp 48 (1978). In German

"Yaesu Musen YC-500S frequency counter." *Electron. Aust.* (Australia), vol. 40, no. 1, pp 103 (April 1978)

"A special IC revolutionizes the design of universal counters." *Elektron. Prax.* (Germany), vol. 14, no. 4, pp 14-18 (April 1979) In German

"Microprocessor and LSI: two features of a universal 100 MHz counter." *Electron. & Appl. Ind.* (France), no. 270, pp 23-6 (1 June 1979) In French.

3.2

Berger, U.

"DCF-77 clock with microprocessor. II." *Funkschau* (Germany), vol. 50, no. 12, pp 579-82 (2 June 1978) In German.

Belotserkovskii, D. Yu.; Il'in, V.G.; Nazarov, K.I.; Fedorov, Yu.A.; Cherenkov, G.T.

"The USSR time and frequency state service." *Meas. Tech.* (USA), vol. 21, no. 8, pp 1037-40 (Aug 1978). Translation of: *Izmer. Tekh.* (USSR), vol. 21, no. 8, pp 10-11 (Aug 1978).

Bhat, C.L.; Razdan, H.

"A clock synchronization circuit using transmitted time-codes." *Bhabha Atomic Res. Centre, Nuclear Res. Lab., Srinagar, Kashmir, India; Def. Sci. J.* (India) vol. 28, no. 3, pp 153-6 (July 1978)

Binelli, P.; Detoma, E.; D'Ottavio, A.; Leschiutta, S.; Marconicchio, F.
"Methods of transmission and applications of time and frequency signals, transmitted by SIRIO satellite." Telespazio S.p.A., Roma, Italy; XXV Congresso Internazionale per L'Elettronica (25th International Scientific Congress on Electronics), Rome, Italy, 13-15 March 1978 (Rome, Italy: Ressegna Internazionale Elettronica Nucleare ed Aerospaziale 1978), pp 397-406. In Italian.

Bocaniciu, T.
"Utilisation of standard television signal for distant testing of measuring apparatus for time and frequency." Inst. Nat. de Metrologie, Bucuresti, Rumania; Metrol. Apl. (Rumania), vol. 25, no. 4, pp 180-3 (1978). In Rumanian.

Cermak, J.; Buzek, O.
"Time sharing in the OMA 50 kHz Czechoslovak station." Ustavy Radiotechniky a Elektroniky, CSAV, Praha, Czechoslovakia; Slaboprouty Obz. (Czechoslovakia), vol. 40, no. 2, pp 53-6 (1977) In Czech.

Clark, T.A.; Ryan, J.W.; Counselmann, C.C., III; Ford, P.G.; Hanson, L.B.; Hinteregger, H.F.; Kelpczynski, W.J.; Knight, C.A.; Robertson, D.S.; Rogers, A.E.E.; Shapiro, I.I.; Whitney, A.R.
"Synchronization of clocks by very-long-baseline interferometry." Goddard Space Flight Center, NASA, Greenbelt, MD, USA; IEEE Trans. Instrum. & Meas. (USA), vol. IM-28, no. 3, pp 184-7 (Sept. 1979)

Costain, C.C.; Boulanger, J.-S.; Daams, H.; Miller, L.G.; Guinot, B.; Fréon, G.; Parcelier, P.; Brunet, M.; Azoubib, J.
"Two-Way Time Transfers between National Research Council (Ottawa) and Paris Observatory via the 'Symphonie' Satellite." National Research Council; Observatoire de Paris; CNES; & Bureau International de l'Heure; 31st Annual Symposium on Frequency Control, US Army Electronics Command, Fort Monmouth NJ, pp 473-476 (1977). Copies available from the Electronics Industries Association, 2001 Eye Street, N.W. Washington D.C. 20006

Dittmann, H.; Kalau, M.
"The national time and frequency standard of the German Democratic Republic." Radio Fernsehen Elektron. (Germany), vol. 27, no. 6, pp 381-2 (1978) In German

Fedorov, Yu, A.; Bol'shakov, V. Ya.
"Comparing frequencies of highly stable oscillators by means of television signals." Meas. Tech. (USA) vol. 21, no. 6, pp 786-8 (June 1978). Translation of: Izmer. Tekh. (USSR), vol. 21, no. 6, pp 37-8, (June 1978)

Giles, P.G.; Hart, P.J.; Thomas, I.
"Radio clock for reception and display of MSF time-code transmission." Mullard Application Lab., London, England; Mullard Tech. Commun. (GB), vol. 14, no. 140, pp 402-23 (Oct. 1978)

Hoult, N.S.
"A Rugby, MSF, time-code clock." Jesus Coll., Cambridge, England; Radio Commun. (GB), vol. 55, no. 2, pp 122-7 (Feb. 1979)

Iordachescu, T.; Matei, M.
"Comparison of time and frequency calibration standards by means of LORAN-C type standard frequency signals." Metrol. Apl. (Rumania), vol. 25, no. 4, pp 184-6 (1978). In Rumanian

Iordachescu, T.; Matei, M.
"Comparison of the time and frequency standard with standard frequency signals type LORAN-C." Metrol. Apl. (Rumanian), vol. 25, no. 4, pp 184-90 (1978). In Rumanian.

Klose, M.
"Frequency measurement in radio monitoring." Rohde & Schwarz, Munich, Germany; Commun. Int. (GB), vol. 5, no. 12, pp 38, 40, 44 (Dec. 1978)

Percival, D.B.
"The U.S. Naval Observatory clock time scales." US Naval Obs., Washington, DC, USA; IEEE Trans. Instrum. & Meas. (USA), vol. IM-27, no. 4, pp 376-85 (Dec. 1978) (CPEM '78 Conference on Precision Electromagnetic Measurement, Ottawa, Canada, 26-29 June 1978).

Ptacek, V.
"The long-term stability of time comparisons using the TV method." Astron. Inst., Czechoslovak Acad. of Sci., Praha, Czechoslovakia; Bull. Astron. Inst. Czech. (Czechoslovakia), vol. 29, no. 6, pp 372-5 (1978).

Sen, A.K.; Saha, B.; Saha, S.K.; Trehan, S.K.; Sehra, J.S.; Ghosh, R.N.
"Standardisation and calibration of various equipment by the use of standard frequency transmissions" Centre of Advanced Study in Radio Phys. & Electronics, Univ. of Calcutta, Calcutta, India; J. Inst. Electron. & Telecommun. Eng. (India), vol. 24, no. 8, pp 320-3 (Aug. 1978)

Smith, C.
"Time: who needs it? (Time signals from satellites)" Nat. Bur. of Stands., Boulder, CO, USA; Dimensions NBS (USA), vol. 62, no. 7-8, pp 16-19 (July-Aug 1978)

Strohbehn, K.; Brown, R.G.
"Filtering precision time signals." Electrical Engng. Dept., Iowa State Univ., Ames, IA, USA; 21st Midwest Symposium on Circuits and Systems, Ames, IA, USA, 14-15 Aug 1978 (North Hollywood, CA, USA: Western Periodicals Co. 1978), pp 476-80.

Szezan, R.
"Determining accuracy of receiver-controlled frequency standards." Rohde & Schwarz, Munich, Germany; News Rohde & Schwarz (Germany), vol. 18, no. 82, pp 23-6 (1978).

3.3

Bobryshev, V.D.; Verkin, B.I.; Dmitriev, V.M.; Prentslau, N.N.
"Cryogenic high-frequency stable systems with mode-conversion cavities." Physico-Tech. Inst. of Low Temperatures, Acad. of Sci., Kharkov, Ukrainian SSR; Cryogenics (GB), vol. 18, no. 11, pp 601-6 (Nov. 1978)

Bushnell, T.R.; Buswell, R.N.
"Cavity controlled oscillators." Watkins-Johnson Co., Palo Alto, CA, USA; Commun. Int. (GB), vol. 5, no. 6, pp 20, 23-4, 26 (June 1978)

Minakova, I.I.; Nazarov, V.I.; Panov, V.I.; Popel'nyuk, V.D.
"Frequency stabilization of a solid-state oscillator with a superconducting sapphire resonator." M.V. Lomonosov Moscow State Univ., Moscow, USSR; Sov. Tech. Phys. Lett. (USA), vol. 4, no. 2, pp 71-2 (Feb. 1978). Translation of: Pis'ma V Zh. Tekh. Fiz. (USSR), vol. 4, no. 3-4, pp 172-6 (Feb. 1978).

Saito, T.; Arai, Y.; Komizo, H.; Itoh, Y.; Nishikawa, T.
"A 6 GHz highly stabilized GaAs FET oscillator using a dielectric resonator." Fujitsu Labs. Ltd. Kawasaki Japan; 1979 IEEE MTT-S International Microwave Symposium Digest, Orlando, FL, USA, 30 April - 2 May 1979 (New York, USA: IEEE 1979) pp 197-9

Stein, S.R.; Turneure, J.P.
"Superconducting resonators: High stability oscillators and applications to fundamental physics and metrology." Frequency & Time Stand. Section, Nat. Bur. of Stand., Boulder, CO, USA; AIP Conf. Proc. (USA), no. 44, pp 192-213 (1978)

3.4

Assmus, F.
"Development of the clock and watch industry in the electronic age." Polytech. Tijdschr. Elektrotech. Elektron. (Netherlands), vol. 33, no. 12, pp 733-47 (Dec. 1978) In Dutch.

Groux, G.; Claes, R.; Deleers, J.J.
"Surface-wave filters for TV IF stages. III." Radio Mentor Electron. (Germany), vol. 44, no. 7, pp 267-70 (July 1978) In German

Delgado Penin, J.A.
"SAW devices as IF filters in TV receivers." Mundo Electron. (Spain), no. 84, pp 97-102 (April 1979) In Spanish.

Dorogov, V.N.; Shavaiko, S.N.
"Inductive gauge with quartz resonator." Moscow Inst. of Electronic Machines, Moscow, USSR; Sov. J. Nondestr. Test. (USA), vol. 14, no. 7, pp 672-2 (July 1978). Translation of: Defektoskopiya (USSR), vol. 14, no. 7, pp 109-10 (July 1978).

Drummond, W.S.; Roth, S.A.
"Applications of high performance SAW transversal filters in a precision measurement instrument." Appl. Res. Group, Tektronix Inc., Beaverton, OR, USA; 1978 Ultrasonics Symposium Proceedings, Cherry Hill, NJ, USA, 25-27 Sept. 1978 (New York, USA: IEEE 1978) pp 494-9

Farrell, J.J.
"Crystals and NMOS: frequency controlled MPU's." Motorola Semiconductor Products Inc., Austin, TX, USA; Proceedings of the 32nd Annual Symposium on Frequency Control 1978, Atlantic City, NJ, USA, 31 May - 2 June 1978 (Washington, DC, USA: Electronic Industries Assoc. 1978) pp 334-6

Nabeyama, H.; Shimano, M.; Hazama, K.; Yamada, J.; Koro, Y.
"New color television receiver with SAW IF filter and one-chip PIF IC." Consumer Products Res. Center Hitachi Ltd., Yokohama, Japan; IEEE Trans. Consum. Electron. (USA), vol. CE-25, no. 1, pp 50-9 (Feb. 1979)

Nichols, S.A.; Woodring, D.G.
"Applications of atomic frequency standards to SATCOM spread spectrum systems." Naval Res. Lab., Washington, DC, USA; Proceedings of the 32nd Annual Symposium on Frequency Control 1978, Atlantic City, NJ, USA, 31 May - 2 June 1978 (Washington, DC, USA: Electronic Industries Assoc. 1978) pp 555-9

Nield, P.N.
"Frequency stabilization of communication receivers" Dept. of Electrical Engng., Univ. of Aston, Birmingham, England; Conference on Radio Receivers and Associated Systems, Southampton, England, 11-14 July 1978 (London, England: IERE 1978) pp 217-26

Nishiguchi, Y.; Nosaka, S.
"Quartz crystal units allow smaller, thinner watches" Kyoto Ceramic Co., Ltd., Yamashina-ku, Kyoto, Japan; JEE (Japan), no. 144, pp 48-51 (Dec. 1978)

Pogson, I.
"Quartz crystal driver for Yaesu Musen clock." Electron. Aust. (Australia), vol. 40, no. 11, pp 44-6 (Feb. 1979)

Prokysek, J.
"On the problems of setting the accuracy of crystal-controlled electronic clocks and watches." Jemna Mech. & Opt. (Czechoslovakia), vol. 24, no. 1, pp 23-6 (Jan 1979). In Czech.

Ramadan, B.; Piyakis, K.; Kos, J.F.
"High accuracy quartz crystal thin film monitor." Dept. of Phys & Astron., Univ. of Regina, Regina, Saskatchewan, Canada; Rev. Sci. Instrum. (USA), vol. 50, no. 7, pp 867-71 (July 1979)

Roth, S.A.; Zook, J.K.; Nicholas, D.; Ericson, K.; Drummond, W.S.

"Systems considerations in the design of a SAW-filter based television demodulator." Tektronix Ind., Beaverton, OR, USA; Conference Record of the Twelfth Asilomar Conference on Circuits, Systems and Computers, Pacific Grove, CA, USA, 6-8 Nov. 1978 (New York, USA: IEEE 1978) pp 568-72

Rozwadowski, M.; Czarnecki, A.; Szule, W.; Zynca, A. "A quartz thermometer with temperature resolution of 10-40C." Elektronika (Poland), vol. 19, no. 10, pp 431 (1978). In Polish

Salmon, S.K.

"Practical aspects of surface acoustic wave oscillators." Philips Res. Labs., Redhill, England; 1979 IEEE MTT-S International Microwave Symposium Digest, Orlando, FL, USA, 30 April - 2 May 1979 (New York, USA: IEEE 1979) pp 165-7

Sander, W.; Haydl, W.H.

"SAW filter application for phased array radar." Forschungsinst. für Funk und Mathematik, Wachtberg-Werthhoven, Germany; AGARD Conference Proceedings No. 230. Impact of Charge Coupled Devices and Surface Acoustic Wave Devices on Signal Processing and Imagery in Advanced Systems, Ottawa, Canada, 11-15 Oct. 1977 (Neuilly-sur-Seine, France: AGARD 1978) pp 3.10/1-11

Sare, A.

"Application of LORAN-C system in comparison of time and frequency." Elektrotehnicki Fakultet, Zagreb, Yugoslavia; Elektrotehnika, Zagreb (Yugoslavia), no. 3-6, pp 164-6 (1978). In Croatian.

Schlenzig, K.

"Extended application of quartz clocks." Radio Fernsehen Elektron. (Germany), vol. 28, no. 1, pp 55-7 (1979). In German.

Seguin, M.; Knapp-ziller, M.; Foure, J.-L.

"Surface acoustic wave filters in telephony carrier systems." Onde Electr. (France), vol. 59, no. 8-9, pp 82-8 (Aug. Sept. 1979) In French.

Stapies, E.J.; Schoenwald, J.S.; Dolochycki, S.J.; Wise, J.; Lim, T.C.

"Application of SAW oscillators to low-noise communications systems." Sci. Center, Rockwell Internat Thousand Oaks, CA, USA; 1979 IEEE MTT-S International Microwave Symposium Digest, Orlando, FL, USA, 30 April - 2 May 1979 (New York, USA: IEEE 1979) pp 168-70

Stein, S.R.; Walls, F.L.

"Composite oscillator systems for meeting user needs for time and frequency." Time & Frequency Div., Nat. Bur. of Stand., Boulder, CO, USA; IEEE 1978 Position Location and Navigation Symposium, San Diego, CA, USA, 6-9 Nov. 1978 (New York, USA: IEEE 1978) pp 22-8

Stigall, R.E.; Shreve, W.R.

"SAW devices for use in a high performance television tuner." Texas Instruments Inc., Dallas, TX, USA; Proceedings of the 32nd Annual Symposium on Frequency Control 1978, Atlantic City, NJ, USA, 31 May - 2 June 1978 (Washington, DC, USA: Electronic Industries Assoc. 1978) pp 50-7

Tebo, A.R.

"Applications of helium-neon lasers in the infrared" Electro-Opt. Syst. Des. (USA), vol. 11, no. 4, pp 54-6 (April 1979)

Veith, R.; Kriedt, H.; Rehak, M.

"A video IF unit employing a surface wave filter. I" Funkschau (Germany), vol. 51, no. 5, pp 226-32 (2 March 1979) In German

von Willisen, F.K.

"The quartz watch: its life and times." IEEE Spectrum (USA), vol. 16, no. 6, pp 18-23 (June 1979)

V'yukhin, V.N.; Vanyushev, B.V.; Chernyshov, A.I.

"High-speed two-channel generator of a grid of quartz-controlled frequencies (for control of acoustooptical deflector)." Inst. of Automation & Electrometry, Acad. of Sci., Novosibirsk, USSR; Instrum. & Exp. Tech. (USA), vol. 21, no. 4, pt. 2, pp 1001-3 (July-Aug. 1978). Translation of: Prib. Tekh. Eksp. (USSR), vol. 21, no. 4, pt. 2, pp 145-7 (July-Aug 1978)

Warashina, N.

"Crystal oscillators and units improve frequencies for measuring instruments." Kinsekisha Lab. Co. Ltd., Komae-city, Tokyo, Japan; JEE (Japan), no 144, pp 44-7 (Dec. 1978)

Webb, D.C.; Davis, K.L.

"Surface wave devices for surveillance receivers." Naval Res. Lab., Washington, DC, USA; Conference Record of the Twelfth Asilomar Conference on Circuits, Systems and Computers, Pacific Grove, CA, USA, 6-8 Nov. 1978 (New York, USA: IEEE 1978) pp 573-7

Williams, N.

"Crystals, synthesizers and the phase-locked loop. I." Electron. Aust. (Australia), vol. 40, no. 9, pp 111-13 (Dec. 1978)

"Some problems with the change over to electric clocks." Sdelovaci Tech. (Czechoslovakia), vol. 27, no. 2, pp 62 (Feb. 1979) In Czech.

"Trends in quartz wristwatches." Funkschau (Germany) vol. 50, no. 25, pp 1278-9 (1 Dec. 1978) In German.

Alley, C.

"Relativity and Clocks" University of Maryland; 31st Annual Symposium on Frequency Control, US Army Electronics Command, Fort Monmouth, NJ, pp 4-39 (1977). Copies available from the Electronic Industries Association, 2001 Eye Street, N.W. Washington, D.C. 20006

Kartaschoff, P.

"Frequency and time." London, England: Academic Press (1978), xv + 260 pp.

Kurokawa, S.

"Japan's quartz crystal industry sees international cooperation as its panacea." Nomura Res. Inst., Kajiwara, Kamakura-city, Kanagawa, Japan; JEE (Japan), no. 144, pp 28-30 (Dec. 1978)

Langer, E.

"The piezoelectric effect and its applications. A simple tutorial on the physics and techniques for piezoelectric devices. IV." Nachr. Elektron. (Germany), vol. 33, no. 7, pp 237-8 (July 1979). In German. For pt. III see *ibid.*, vol. 33, no. 6, pp 205 (1979)

Warashina, N.

"Crystal oscillators and units improve frequencies for measuring instruments." Kinsekisha Lab. Co. Ltd., Komae-city, Tokyo, Japan; JEE (Japan), no. 144, pp 44-7 (Dec. 1978)

AUTHOR INDEX

AUTHOR	PAGE	AUTHOR	PAGE	AUTHOR	PAGE
C. A. Adams	167	H. Kawashima	131	J. S. Schoenwald	273
D. W. Allan	334	T. Keller	498	P. Sherman	463
C. Andricos	202	E. Knolmayer	102	K. Shirai	286
D. Ang	41	S. Kogure	160	T. Shrout	25
J. Asahara	120	K. Kohra	14	B. K. Sinha	393
N. Asanuma	120	A. M. Kong	237	T. Sonoda	160
C. Audoin	353	J. A. Kusters	167	E. J. Staples	273
J. F. Balascio	65	J. Lamboley	112	R. Steele	498
A. Ballato	431	K. F. Lau	221,237	D. S. Stevens	384
R. Barillet	353	P.C.Y. Lee	403	R. A. Sundelin	243
L. G. Bernier	376	N. C. Lias	65	C. K. Suzuki	14
R. J. Besson	175,457	P. A. Ligor	72	C. Takeuchi	286
R. Betsch	25	T. C. Lim	273	A. Tani	286
M. Bloch	370,463	J. E. Lioy	347	W. J. Tanski	278
C. Bourgeois	419	H. G. Lipson	72	M. Tetu	376
A. Brisson	376	T. J. Lukaszek	221,431	H. F. Tiersten	384,393
F. Y. Cho	302	G. Marianneau	52	M. Toki	58
L. E. Cross	25	M. E. Markes	1	Y. Toudic	93
J. L. Dailing	445	J. J. Martin	1, 81	R. A. Tracy	217
J. F. Darces	112	D. Marvin	498	Y. Tsuzuki	58
R. Davidheiser	252	E. M. Mattison	228	J. P. Valentin	194
P. E. Debely	34	T. R. Meeker	85	D. C. L. Vangheluwe	412
M. Desaintfuscién	353	M. Meirs	370,463	J. Vanier	376
P. Desrousseaux	269	H. Merigoux	112	R. F. C. Vessot	228
J. Detaint	93	A. J. Miller	85	J. Viennet	353
R. J. Dinger	34	T. Mitsuoka	488	J. R. Vig	187
D. J. Dodson	221	E. Momosaki	160	H. T. M. Wang	364
S. P. Doherty	81	R. A. Moore	243	A. Warner	183
G. L. Dybwad	46	J. Murphy	243	M. A. Weiss	334
E. P. EerNisse	426	B. R. McAvoy	243	D. J. White	307
D. M. Embree	475	R. J. McClure	475	D. F. Williams	302
D. A. Emmons	457	H. McKinstry	25	J. Wise	273
F. Euler	72	E. S. McVey	504	P. V. Wright	262
B. F. Farrell	228	M. Nakazuma	152	K. M. Wu	403
R. L. Filler	187	R. Neurgaonkar	25	K. H. Yen	237
M. M. Force	320	T. Nishikawa	286	A. Zahorchak	243
J. J. Gagnepain	52,255,312	A. S. Nowick	9		
W. D. Galla	504	O. Ochiai	131		
E. A. Gerber	509	T. Ohshima	488		
P. G. Girardet	457	S. Okano	488		
B. Guldgrank	183	Y. Oomura	140		
J. Goodell	243	T. N. Osterdock	320		
E. P. Graf	457	R. E. Paradysz	475		
J. Gros Lambert	255	T. E. Parker	292		
L. E. Halliburton	1	B. Parzen	471		
D. Hauden	255,312	I. Pascaru	370		
H. A. Haus	262	C. Pegeot	233		
T. Haynes	243	U. R. Peier	175		
C. N. Helmick, Jr.	307	E. M. Perdue	213		
J. Ho	463	H. E. Peters	360		
F. W. Hopwood	217,243	P. Petit	353		
M. Y. Huang	221	F. Pirio	269		
G. J. Iafrate	431	M. Planat	255		
F. Iwasaki	14	H. Poignant	93		
H. W. Jackson	449	K. Putkovich	326		
H. Jain	9	S. Rousseau	312		
M. Jardino	353	V. R. Saari	475		
A. C. Johnson	320	H. Sato	131		
R. S. Kagiwada	237	G. Sauvage	233		
O. Kawano	58	J. Y. Savard	376		

CLASSIFICATIONS AND STANDARDS GERMANE TO FREQUENCY CONTROL

Institute of Electrical and Electronic Engineers

Order through: IEEE Service Center
445 Hoes Lane
Piscataway, NJ 08854
(201/981-0060)

- 176-1978 Piezoelectricity \$ 9.00
- 177-1966 Piezoelectric Vibrators, Definitions and Methods of Measurements for (ANSI C83.17-1970) \$ 4.00
- 180-1962 Ferroelectric Crystal Terms, Definitions of \$ 3.00
- 319-1971 Piezomagnetic Nomenclature \$ 4.00

Electronic Industries Association

Order through: Electronic Industries Assn.
2001 Eye Street, N.W.
Washington, D.C. 20006

- (a) Holders and Sockets
 - RS-192-A, Holder Outlines and Pin Connections for Quartz Crystal Units. (Standard Dimensions for older types.) \$ 6.80
 - RS-367, Dimensional and Electrical Characteristics Defining Receiver Type Sockets. (Including crystal sockets.) \$20.20
 - RS-417, Crystal Outlines (Standard dimensions and pin connections for current quartz crystal units - 1974) \$ 7.80
- (b) Production Tests
 - RS-186-E, (All Sections), Standard Test Methods for Electronic Component Parts \$42.00
- (c) Application Information
 - Components Bulletin No.6, Guide for the Use of Quartz Crystals for Frequency Control \$ 4.90

International Electrotechnical Commission

Order through: American National Standards Institute
1430 Broadway
New York, New York 10018

*ANSI can quote prices on specific IEC publications on a day to day basis only. All IEC and ISO standards have been removed from its Standards Catalog. Call ANSI, NYC (212/354-3300) for prices.

- IEC Publication 122-1 (1976)
Quartz crystal units for frequency control and selection. Part 1: Standard values and test conditions. (Second edition)
- IEC Publication 122-2 (1962) Section 3:
Guide to the Use of Quartz Oscillator Cry-

stals, including Amendment 1 (1969)

IEC Publication 122-3 (1977) Part 3: Standard Outlines and pin connections. (Second edition)

IEC Publication 283 (1968) Methods for the Measurement of Frequency and Equivalent Resistance of Unwanted Resonances Filter Crystal Units

IEC Publication 302 (1969) Standard Definitions and Methods of Measurement for Piezoelectric Vibrators Operating Over the Frequency Range up to 30 MHz

IEC Publication 314 (1970) Temperature Control Devices for Quartz Crystal Units, including Supplement 314A
Contents: General Characteristics & Standards; Test Conditions; Pin Connections

IEC Publication 314A (1971) First Supplement to Publication 314 (1970) Contents: Guide to the Use of Temperature Control Devices for Quartz Crystal Units.

IEC Publication 368 (1971) Piezoelectric Filters, including Amendment 1, Amendment 2, and Supplement 368A and 368B Contents: General Information & Standard Values; Test Conditions

IEC Publication 368A (1973) First Supplement to Publication 368 (1971) Contents: Guide to the Use of Piezoelectric Filters

IEC Publication 368B (1975) Second Supplement to Publication 368 (1971) Contents: Piezoelectric Ceramic Filters

IEC Publication 444 (1973) Basic Method for the Measurement of Resonance Frequency and Equivalent Series Resistance of Quartz Crystal Units by Zero Phase Technique in a π - Network

IEC Publication 483 (1976) Guide to Dynamic Measurements of Piezoelectric Ceramics with High Electromechanical Coupling

Department of Defense

Order through: Naval Publication & Form Center
5801 Tabor Avenue
Philadelphia, PA 19120

MIL-C-3098 Crystal Unit, Quartz, General Specification For

MIL-H-10056 Holders (Enclosures), Crystal, General Specification For

MIL-STD-683 Crystal Units, Quartz; And Holders, Crystal

MIL-F-28734 Frequency Standards, Cesium Beam, General Specifications For

MIL-O-55310 Oscillators, Crystal, General Specification For

MIL-F-18327 Filters, High Pass, Low Pass, Band Pass Suppression and Dual Functioning, General Specification For

MIL-O-39021 Oven, Crystal, General Specification For

MIL-O-55240 Oscillators, Audio Frequency

MIL-F-28811 Frequency Standard, Cesium Beam Tube

PROCEEDINGS

ANNUAL FREQUENCY CONTROL SYMPOSIA

A complete index to the Proceedings of the Frequency Control Symposia for 1956 (10th) through 1976 (30th) is available as part of the 1976 (30th) Proceedings.

The Proceedings of the 33rd (1979) and 34th (1980) Symposia contain a bibliography of the world-wide literature on precision frequency control and selection compiled by Dr. E. A. Gerber for the years 1968-1978 and 1979 with part of 1980, respectively.

<u>NO.</u>	<u>YEAR</u>	<u>DOCUMENT NO.</u>	<u>OBTAIN FROM*</u>	<u>COST</u>
10	1956	AD 298322	NTIS	\$28.00
11	1957	AD 298323	"	30.00
12	1958	AD 298324	"	31.00
13	1959	AD 298325	"	33.00
14	1960	AD 246500	"	22.00
15	1961	AD 265455	"	19.00
16	1962	PB 162343	"	24.00
17	1963	AD 423381	"	29.00
18	1964	AD 450341	"	29.00
19	1965	AD 471229	"	32.00
20	1966	AD 800523	"	32.00
21	1967	AD 659792	"	28.00
22	1968	AD 844911	"	30.00
23	1969	AD 746209	"	17.00
24	1970	AD 746210	"	19.00
25	1971	AD 746211	"	19.00
26	1972	AD 771043	"	18.00
27	1973	AD 771042	"	23.00
28	1974	AD A011113	"	21.00
29	1975	AD A017466	"	23.00
30	1976	AD A046089	"	27.00
31	1977	AD A088221	"	30.00
32	1978		EIA	20.00
33	1979		"	20.00
34	1980		"	20.00

*NTIS - National Technical Information Service
Sills Building
5285 Port Royal Road
Springfield, Virginia 22161

NTIS prices are as of September 1980 and are subject to change.

*EIA - Annual Frequency Control Symposium
C/O Electronic Industries Association
2001 Eye Street
Washington, DC 20006

Remittance must be enclosed with all orders. For orders placed with NTIS from outside the United States, double the domestic price list per copy for handling and mailing.

When referencing these Proceedings, please use the format shown in the following examples:

- (1) D. E. Newell and R. H. Bangert, "Temperature Compensation of Quartz Crystal Oscillators", Proceedings, 17th Annual Symposium on Frequency Control, US Army Electronics Command, Fort Monmouth, NJ, pp 491-508, (1963). National Technical Information Service Accession Nr. AD 423381.
 - (2) I. Pascary and M. Meirs, "Development of a Light Weight, Military, Cesium Standard", 33rd Proceedings Annual Symposium on Frequency Control, US Army Electronics Command, Ft. Monmouth, N.J. pp 484-489. Copies available from Electronic Industries Association, 2001 Eye Street, NW, Washington, D.C. 20006.
-